Indian Institute of Metals Series

Raghumani S. Ningthoujam
A. K. Tyagi *Editors*

Handbook of Materials Science, Volume 2

Magnetic Materials

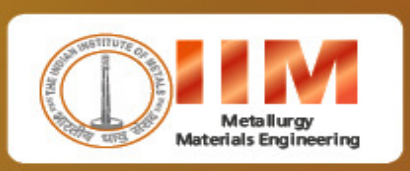

Springer

Indian Institute of Metals Series

Series Editor
U. Kamachi Mudali
Vice Chancellor, HBNI, DAE, Mumbai, India

Editorial Board
Divakar Ramachandran
IGCAR, Kalpakkam, India

Bikramjit Basu
Materials Research Center, IISc, Bangalore, India

Suman K. Mishra
CGCRI, Kolkata, India

N. Eswara Prasad
Ex-DMSRDE, Kanpur, India

S. V. S. Narayana Murty
Material Development and Production Group, VSSC, Valiamala, India

R. N. Singh
Mechanical Metallurgy Division, BARC, Mumbai, India

R. Balamuralikrishnan
DRDO, DMRL, Hyderabad, India

About the Book Series:

The study of metallurgy and materials science is vital for developing advanced materials for diverse applications. In the last decade, the progress in this field has been rapid and extensive, giving us a new array of materials, with a wide range of applications, and a variety of possibilities for design of new materials, processing and characterizing the materials. In order to make this growing volume of knowledge available, an initiative to publish a series of books in Metallurgy and Materials Science was taken during the Diamond Jubilee year of the Indian Institute of Metals (IIM) in the year 2006, and has been published in partnership with Springer since 2016.

This book series publishes different categories of publications: textbooks to satisfy the requirements of students and beginners in the field, monographs on select topics by experts in the field, professional books to cater to the needs of practising engineers, and proceedings of select international conferences organized by IIM after mandatory peer review. The series publishes across all areas of materials sciences and metallurgy. An panel of eminent international and national experts serves as the advisory body in overseeing the selection of topics, important areas to be covered, and the selection of contributing authors.

Editors
Raghumani S. Ningthoujam and A. K. Tyagi

Handbook of Materials Science, Volume 2
Magnetic Materials

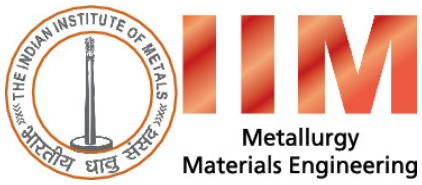

Editors
Raghumani S. Ningthoujam
Chemistry Division, Bhabha Atomic Research Centre, Mumbai, Maharashtra, India

A. K. Tyagi
Homi Bhabha National Institute, Mumbai, Maharashtra, India

ISSN 2509-6400 e-ISSN 2509-6419
Indian Institute of Metals Series
ISBN 978-981-97-4645-3 e-ISBN 978-981-97-4646-0
https://doi.org/10.1007/978-981-97-4646-0

© The Editor(s) (if applicable) and The Author(s), under exclusive license to Springer Nature Singapore Pte Ltd. 2024

This work is subject to copyright. All rights are solely and exclusively licensed by the Publisher, whether the whole or part of the material is concerned, specifically the rights of translation, reprinting, reuse of illustrations, recitation, broadcasting, reproduction on microfilms or in any other physical way, and transmission or information storage and retrieval, electronic adaptation, computer software, or by similar or dissimilar methodology now known or hereafter developed.

The use of general descriptive names, registered names, trademarks, service marks, etc. in this publication does not imply, even in the absence of a specific statement, that

such names are exempt from the relevant protective laws and regulations and therefore free for general use.

The publisher, the authors and the editors are safe to assume that the advice and information in this book are believed to be true and accurate at the date of publication. Neither the publisher nor the authors or the editors give a warranty, expressed or implied, with respect to the material contained herein or for any errors or omissions that may have been made. The publisher remains neutral with regard to jurisdictional claims in published maps and institutional affiliations.

This Springer imprint is published by the registered company Springer Nature Singapore Pte Ltd.
The registered company address is: 152 Beach Road, #21-01/04 Gateway East, Singapore 189721, Singapore

Preface

The growth of human civilization has always depended on materials. Thus, evolution of materials has been an integral part of human beings right from the primitive times. The importance of materials can be gauged by the fact that various historic ages have been named based on the materials used by the people belonging to a particular era, such as Stone Age, Bronze Age, Iron Age, Concrete Age, Steel Age, Silicon Age, etc. Some of the earlier processes like forging and smelting have played a key role in the growth of materials and their large-scale deployment for the benefit of humankind. However, during the initial phase, the materials were used without much understanding of the factors responsible for their functioning. For example, Romans who were great innovators of glasses and invented the glass window could not predict how important this material would be in future. It is believed that the first metal tool appeared perhaps only six thousand years ago as a result of knowledge of melting and casting processes. Materials that have immensely changed our lives are wood, clay, bronze, iron, steel, cement, polymers, aluminum, glasses, and semiconductors. It shall not be wrong to claim that the twenty-first century is going to witness a tremendous progress in the field of materials science as the need for advanced materials in various areas like engineering, electronics, communications, healthcare, societal sectors, natural resources management, and generation of wealth from waste is going to exhibit rapid growth. Even the demand for materials for high-tech sectors shall witness exponential growth. Net-zero target will also be intricately linked with the advancement in the field of materials science. The quest for developing better, efficient, and cost-effective materials has been a constant endeavor and shall

continue forever. It is generally believed that materials are going to play the most important role to achieve the sustainable development goals, in particular for clean energy, clean water, climate change, health care, industries, innovation & infrastructure, etc. In this context, there is an urgent need to develop efficient materials consisting of earth-abundant elements. The solution for some of the challenges such as production of green hydrogen and green synthesis of ammonia will also come from advanced materials. The rational design of newer and efficient materials by interplay of synthesis methodologies, crystallographic structures, morphologies, and dimensionality is going to be of paramount importance. In the coming years, a diverse range of materials will have to be developed to meet these goals. In view of this, it was felt appropriate to publish a Handbook of Materials Science comprising of ten volumes on optical materials, magnetic materials, catalytic materials, photocatalytic materials, nuclear materials, sensor materials, materials for healthcare, energy materials, materials for environmental applications and soft materials.

Volume 2 (Magnetic Materials): In general, materials responding to the applied magnetic fields are referred to as magnetic materials. Magnetic materials are classified on the basis of their response to applied magnetic fields: ferromagnetic, ferrimagnetic, antiferromagnetic, paramagnetic, and diamagnetic materials. Such types of materials are used in various applications. Nowadays, new concepts and new materials in terms of metallic, superconducting, semiconducting, and insulating properties are coming up. If applied magnetic fields are either polarized or circular and random, electron spin–magnetic interactions are dramatically different. There are recent reports on topological insulators, large drop in resistivity, angular GMR, angular CMR, triangular types of

magnetic interactions, and variation of magnetic properties upon changing dimensions from 0D, 1D, 2D to 3D. In this volume, the basic concept of magnetism, units and dimensions, conversion factors, classification, ferrites, nitrides, carbides, generation of magnetism in graphene because of association of defects or addition of impurities, spin-crossover in iron and cobalt complexes, magnetism in bulk and thin film metallic glass systems, ferromagnetism in 2D materials, defect engineering, phase transition, externally driven interface in 3D Ising model, proving magnetism in thin films and super-lattices using polarized neutron reflectivity, magnetism in organic molecules, molecular magnets, quantum magnets, uses of superparamagnetic nanoparticles in hyperthermia, diagnosis and therapy, and various applications of magnetic materials in sensors, healthcare, catalysis, data storage, environmental, water treatment, industrial area, etc., are provided.

We are immensely thankful to all the authors for their rich contributions toward this handbook series. Although due efforts have been taken to make the book as error-free as possible some may have crept in unnoticed. We shall be thankful to the readers for bringing such unintentional errors to our notice. Finally, we sincerely hope that our efforts will be of use to a wide range of researchers working in the field of materials science.

Raghumani S. Ningthoujam
A. K. Tyagi
Mumbai, India

Contents

1 Basic Concept of Magnetic Materials and Summary of All the Chapters
Raghumani S. Ningthoujam and A. K. Tyagi

2 Magnetic Materials: Fundamentals and Applications
Seema Verma

3 Units, Dimensions, and Conversion Factors in Magnetism: Basic Understanding
Manas Srivastava, Ruchi Agrawal and Raghumani S. Ningthoujam

4 Classification of Ferrites, Synthesis and Properties of Spinel Ferrite Nanoparticles and Their Applications
Vibha H. Ojha, Abha H. Oza, Ruchi Agrawal and Raghumani S. Ningthoujam

5 Applications of Magnetic Materials
Ruchi Agrawal, Manas Srivastava and Raghumani S. Ningthoujam

6 Defects-Induced Multifunctional Properties in $BiFeO_3$
Subhajit Nandy, Pavana S. V. Mocherla and C. Sudakar

7 Basic Concepts of Nitride Magnetic Materials and Their Applications
Pragnya P. Mishra and Rabi N. Panda

8 Fundamental Aspects of Nanomagnetism and Its Versatile Applications
Asnit Gangwar, P. A. Hassan and K. C. Barick

9 Ferromagnetic Functional Materials
A. P. Srivastava

10 Origin of Magnetism, Synthesis, Characterization and Perspective Application of Magnetic Graphene

Mohit Kumar Singh, Sunil Kumar and Ranjan K. Sahu

11 Externally Driven Interface in 3D Ising Model: A Monte Carlo Study
Manish K. Sahai and A. K. Bakshi

12 Selected Examples of Iron and Cobalt Complexes Exhibiting Spin-Crossover Behavior
Monika Rana, Venkata Nikhil Raj Mothikari and Anuj Kumar Sharma

13 Magnetism in Bulk and Thin Film Metallic Glass Systems
Debarati Bhattacharya

14 Recent Developments in Magnetic Nanocrystalline Metal Oxides and Their Biomedical Applications
Kashmiri Deka and Vikas L. Mathe

15 Ferromagnetism in Two-Dimensional TMD Materials via Doping, Phase Transition and Defect Engineering
Rohini Sanikop, Bidisha Priyadarsini Jena, Vikasmita Samanta and C. Sudakar

16 Magnetic Nanoparticles-Based Coated Materials
Shankar B. Dalavi, Anagha B. Patil and Rabi N. Panda

17 Probing Magnetism in Thin Films and Superlattices Using Polarized Neutron Reflectivity
Surendra Singh and Harsh Bhatt

18 Introduction and Classification of Organic Molecule Based Magnetic Materials
Pramod Bhatt and S. M. Yusuf

19 HSP90: An Emerging Molecular Target for Improvement of Nanoparticle Based Magnetic Hyperthermia Therapy

Neena G. Shetake, Amit Kumar,
Raghumani S. Ningthoujam and Badri Narain Pandey

20 Magnetic–Luminescent Nanocomposites for Cancer Hyperthermia Therapy
Goutam Singh Ningombam and
Nongmaithem Rajmuhon Singh

About the Editors

Dr. Raghumani S. Ningthoujam obtained M.Sc. in Chemistry from Manipur University, India, in 1994. He was awarded Ph.D. in Chemistry from Indian Institute of Technology (IIT) Kanpur in area of superconducting, electron transport and magnetic properties of nanostructured transition metal nitrides in 2004. He joined Bhabha Atomic Research Centre (BARC), Mumbai, as Scientific Officer in 2006 after completion of Dr. K. S. Krishnan Fellowship. Currently, he is working in area of luminescent and magnetic nanomaterials and their applications in sensors, imaging, diagnosis and therapy. He did Post-Doctoral Fellowship at University of Victoria, Canada, in the area of quantum dots. Presently, he is Scientific Officer (G) at Chemistry Division, BARC, Mumbai. He has published about 160 papers in the refereed journals, 7 review articles and 4 books. In recognition of his significant contributions to the chemical science, he has been awarded DAE-Scientific and Technical Excellence Award in 2012 and Young Achiever Award, SSPS 2010. He has been elected as Fellow, The National Academy of Sciences, India (FNASc), in 2016 and Fellow, Maharashtra Academy of Sciences (FMASc), in 2013.

Dr. A. K. Tyagi is presently Dean, Homi Bhabha National Institute (HBNI), Mumbai and honorary Professor at JNCASR, Bengaluru. He occupied various positions at Bhabha Atomic Research Centre (BARC) such as Director, Chemistry Group, BARC and Director, Bio-Science Group. He was a Distinguished Scientist, DAE. His research interests are in the field chemistry of materials which includes functional materials, nanomaterials, nuclear

materials, energy materials, metastable materials, hybrid materials and structure-property correlation. He has published about 650 papers in journals and several books and has supervised 32 Ph.D. students. In recognition of his significant contributions to the field of chemistry of materials, he has been conferred with many prestigious awards, such as DAE Homi Bhabha Science and Technology Award, JNCASR's National Prize in Solid State and Materials Chemistry (2018), Acharya PC Ray Memorial Award from Indian Science Congress Association (2020), JC Bose National Fellowship. He is Elected Fellow of the Indian Academy of Sciences (FASc), National Academy of Sciences, India (FNASc), Royal Society of Chemistry, UK (FRSC), Indian National Academy of Engineering (FNAE), Indian National Science Academy (FNA), Asia Pacific Academy of Materials, Word Academy of Ceramics and The World Academy of Sciences (FTWAS).

© The Author(s), under exclusive license to Springer Nature Singapore Pte Ltd. 2024
R. S. Ningthoujam, A. K. Tyagi (eds.), *Handbook of Materials Science, Volume 2*, Indian Institute of Metals Series
https://doi.org/10.1007/978-981-97-4646-0_1

1. Basic Concept of Magnetic Materials and Summary of All the Chapters

Raghumani S. Ningthoujam[1, 2] ✉ and A. K. Tyagi[1, 2] ✉
(1) Chemistry Division, Bhabha Atomic Research Centre, Mumbai, 400085, India
(2) Homi Bhabha National Institute, Mumbai, 400094, India

✉ **Raghumani S. Ningthoujam (Corresponding author)**
Email: rsn@barc.gov.in

✉ **A. K. Tyagi**
Email: aktyagi@barc.gov.in
Email: aktyagi@hbni.ac.in

Keywords Magnetic materials – Spin glass – Superparamagnetic – Dimensionality – Molecular magnets

1.1 Introduction

Materials can be divided into two types: Non-magnetic and magnetic materials. Non-magnetic materials are materials that do not show the force of attraction or repulsion to others. These are considered as diamagnetic materials. Examples are dry wood, plastic, gold, silver, copper, etc.

Magnetic materials are the materials which can produce the force of attraction or repulsion to others. Examples are iron, nickel, and cobalt. Details can be obtained from following book references (Cullity and Graham 2011; Kittel 2005; Dutta 1986; Malik et al. 1989).

In the presence of magnetic field (H), all materials are classified as.

1. Diamagnetic materials

2. Paramagnetic materials

3. Ferromagnetic materials

4. Ferrimagnetic materials

5. Antiferromagnetic materials

Magnetization (M) in the presence of applied magnetic field (H) is known as magnetic susceptibility ($\chi = M/H$). These are expressed as volume susceptibility (χ_v) and mass or specific susceptibility (χ_g). Diamagnetic materials show negative susceptibility. It means that in the presence of H, induced magnetic field from material is opposite to the direction of applied magnetic field. Paramagnetic materials, ferromagnetic materials, Ferrimagnetic materials, and antiferromagnetic materials show positive susceptibility. Paramagnetic materials have a very low value of χ ($\sim a \times 10^{-6}$ emu/g/Oe and 'a' is a number). Ferromagnetic and ferrimagnetic materials have a high value of χ ($\sim a \times 10–10^{3}$ emu/g/Oe and 'a' is a number)). Antiferromagnetic materials have a medium value of χ ($\sim 10^{-1}$–10 emu/g/Oe and 'a' is a number). Ferromagnetic and ferrimagnetic materials have Curie temperature (T_C),

whereas antiferromagnetic materials have Neel temperature (T_N). Below T_C, materials become ferromagnetic or ferrimagnetic, and above these, all become paramagnetic. When we apply magnetic field (H) to a material, a relation between magnetic flux density (B) and magnetization (M) is given by

$$B = H + 4\pi M. \tag{1.1}$$

In the CGS unit, B, H, and M are expressed in Gauss, Oersted, and emu/g, respectively. Equation (1.1) can be expressed as

$$\frac{B}{H} = 1 + 4\pi\frac{M}{H}, \tag{1.2}$$

$$\mu = 1 + 4\pi\chi. \tag{1.3}$$

Here, μ (= B/H) and χ (M/H) are known as magnetic permeability and susceptibility, respectively. These are important parameters in understanding property of any material.

(1) For empty space, $\chi = 0$, $\mu = 1$.

(2) For diamagnetic material, χ is small and negative, and μ is slightly less than 1.

(3) For paramagnetic and antiferromagnetic materials, χ is small and positive, and μ is greater than 1.

(4) For ferromagnetic and ferrimagnetic materials, both χ and μ are large and positive.

(5) For superconducting material, χ is $-1/(4\pi) = -0.079$ emu/cm^3/Oe and μ is zero as $B = 0$.

Thus, perfect diamagnetic materials will be superconducting materials below their superconducting

transition. Examples of diamagnetic materials are paper, polythene, He, Au, Ag, Cu, ZnO, etc. Examples of paramagnetic materials are Na, O_2, FeO, etc. Examples of ferromagnetic materials are Fe, Co, Ni, FeNi, FePt, FeCo, Fe_4N, Ni_3N, Fe–Co–N, etc. (Cullity and Graham 2011; Kittel 2005; Dutta 1986; Malik et al. 1989; Ningthoujam and Gajbhiye 2015; Sharma et al. 2010a; Gajbhiye et al. 2002, 2004a, b, 2008). Examples of ferrimagnetic materials are Fe_3O_4, $NiFe_2O_4$, $MnFe_2O_4$, $ZnFe_2O_4$, etc. (Cullity and Graham 2011; Umare et al. 2008; Shukla et al. 2008; Ningthoujam et al. 2008; Joshi et al. 2020; Akhlaghi and Najafpour-Darzi 2021). Examples of antiferromagnetic materials are MnO, NiO, α-Fe_2O_3, etc. (Cullity and Graham 2011; Joshi et al. 2021). Examples of superconducting materials are VN, MoN, Hg, MgB_2, etc. (Ningthoujam and Gajbhiye 2010, 2015; Ningthoujam et al. 2002; Gajbhiye and Ningthoujam 2004; Nagamatsu et al. 2001). Magnetic and electric components are observed in electric current in a wire (i.e., a charged particle is passing through a wire). They are perpendicular to each other. When an alternating current (i) with frequency (f) is passing through a coil with a number of turns (n) with length the of coil (L) with diameter (D), magnetic field (H) can be generated: This gives rise to electromagnetism.

In magnetization versus applied magnetic field curve (M-H plot) and magnetization versus temperature curve (M-T plot), ferromagnetic and ferrimagnetic particles have the intrinsic parameters such as saturation magnetization (M_s), coercivity (H_c), remanence magnetization (M_r), and Curie temperature (T_c). Above T_c, it becomes paramagnetic. Thus, the ferromagnetic or ferrimagnetic materials have spontaneous magnetization in the absence of magnetic field. The ferromagnetic and ferrimagnetic particles are broadly divided into three: soft, hard, and

superparamagnetic particles. In general, soft magnetic materials have low coercivity ($H_c < 500$ Oe), whereas hard magnetic materials have high coercivity ($H_c > 1000$ Oe). The hard magnetic materials are known as the permanent magnetic materials. Examples of soft magnetic materials are Fe, Co, Ni, CoNi, $NiFe_2O_4$, Fe_3O_4, Fe_4N, Ni_3N, Fe–Co–N, etc. (Cullity and Graham 2011; Ningthoujam and Gajbhiye 2015; Sharma et al. 2010b; Ningthoujam et al. 2009). Examples of hard magnetic materials are $CoFe_2O_4$, $SrFe_{12}O_{19}$, FePt, CoPt, FePd, NdFeB, SmCo, alnico (composition of alnico alloy = 8–12% Al, 15–26% Ni, 5–24% Co, up to 6% Cu, 1% Ti, and the rest is Fe) (Cullity and Graham 2011; http://magworld.physics.auth.gr/world/basics/9; https://www.electrical4u.com/hard-magnetic-materials/; Mohapatra et al. 2023; Robert 2012). Superparamagnetic particles have zero coercivity and zero remanence and their magnetization increases with applied magnetic field and behaves as paramagnetic. It is particle size-dependent magnetic material. Below, a particular temperature known as a blocking temperature, it behaves as ferromagnetic material.

In the M-H curve, diamagnetic materials have a negative value in susceptibility; and paramagnetic materials have a positive value in susceptibility and there is an increase of susceptibility with applied magnetic field. There are two types of paramagnetic materials: Curie and Pauli paramagnetic materials (Kittel 2005). In the case of Pauli paramagnetic materials, magnetic susceptibility of materials is almost independent of temperature (χ-T plot), whereas in case of Curie paramagnetic materials, magnetic susceptibility decreases with temperature. In case of antiferromagnetic materials, there are two coercivity values in negative and positive applied magnetic fields in M-H plot. They have Neel temperature (T_N) and above T_N, it behaves as paramagnetic in χ-T plot.

1.2 Origin of Magnetic Moment of a System

An atom has nucleus core surrounded by electrons. Magnetic contribution from nucleus is almost negligible as compared to that of electrons (Cullity and Graham 2011; Kittel 2005; Dutta 1986; Malik et al. 1989). Magnetic moment of an atom is mainly contributed by spin and orbital magnetic moment. It is the vector sum.

When an electron of charge (e) and mass (m) moves in an orbit with an angular velocity (ω), its magnetic moment (μ_l) is given by

$$\mu_l = \sqrt{l\,(l+1)}\frac{eh}{4\pi m}, \tag{1.4}$$

$$\mu_l = \sqrt{l\,(l+1)}\beta \tag{1.5}$$

where "*l*" is the orbital (azimuthal) angular momentum quantum number. "*h*" is Planck's constant.

$\beta = \frac{eh}{4\pi m}$ is the Bohr magnetron and its value is 0.927×10^{-20} ergs/Oe.

Also, electron is also spinning its own axis and its magnetic moment (μ_s) is given by

$$\mu_s = 2\sqrt{s\,(s+1)}\frac{eh}{4\pi m}, \tag{1.6}$$

$$\mu_s = 2\sqrt{s\,(s+1)}\beta \tag{1.7}$$

where s is the spin quantum number. $s = ½\ n$ (n is the number of unpaired electrons present in *s*, *p*, *d*, or *f* orbitals). If $n = 0$, there are no unpaired electrons, system becomes non-magnetic or diamagnetic in general.

The spin and orbital magnetic moments can also be written as

$$\mu_s = g\sqrt{s\,(s+1)}\beta \tag{1.8}$$

$$\mu_l = g\sqrt{l\,(l+1)}\beta \tag{1.9}$$

where "*g*" is called the gyromagnetic ratio, which is a ratio of magnetic moment to angular momentum. For spin magnetic moment, *g* is equal to 2, whereas *g* is equal to 1 for orbital magnetic moment.

For atom having many electrons, there is a resultant spin angular vector S, which is given by

$$S = \sqrt{s\,(s+1)}\frac{h}{2\pi}. \tag{1.10}$$

Similarly, there is a resultant orbital angular vector *L*, which is given by

$$L = \sqrt{l\,(l+1)}\frac{h}{2\pi}. \tag{1.11}$$

The coupling of *S* and *L* can give a resultant vector *J* or *L*-*S* coupling known as Russel Saunders coupling.

The effective magnetic moment (μ_{eff}) is given by

$$\mu_{eff} = \mu_J = g\sqrt{J\,(J+1)\,\beta}, \tag{1.12}$$

And

$$g = 1 + \frac{J\,(J+1) + S\,(S+1) - L\,(L+1)}{2J\,(J+1)}, \tag{1.13}$$

where *S* is the resultant spin quantum number, *L* is the resultant orbital quantum number, and *J* is the resultant *L*-*S* coupling quantum number.

There is another coupling scheme that involves the coupling of the spin and orbital vectors of individual electrons (j vectors). Then coupling of all individual j vectors gives rise to j–j coupling.

In a multielectron system, there is Coulombic attraction and repulsion among electrons. It can have multiplicity with width among levels. This is represented by a term symbol, which decides the ground state and excited states. It is represented by

$$^{2S+1}L_J, \tag{1.14}$$

where $2S + 1$ represents the spin multiplicity, L represents the orbital quantum number, and $J = S + J$ to $S - J$ with positive values. The symbols S, P, D, F, G, H, I, ... have been used for $L = 0$, 1, 2, 3, 4, 5, 6,..., respectively. According to Hund's rules, the lowest energy ground state of the multielectron system:

1. The ground state (lowest energy) will be the highest value of the spin multiplicity. 2. The term symbol with the largest L value will be the ground state when there are several terms with same spin multiplicity. 3. The term with the lowest J value will be the ground state for a half-filled or less than half-filled shell. 4. The term with the highest J value will be the ground state for a more than half-filled shell.

Term symbols for a few examples are provided in Table 1.1. Magnetic moments of 3d- and 4f-block ions are provided in Tables 1.2 and 1.3, respectively. In the case of 3d ions, spin magnetic moment (μ_{spin}) is close to the experiment value, whereas, in the case of 4f ions, spin–orbit coupling magnetic moment (μ_J) is close to the experiment value. It is indicated that spin magnetic contribution is more dominating over orbital magnetic contribution in 3d-block ions. In 4f-block ions, orbital magnetic contribution is significant in its magnetic moment. The ground state term symbol with $J = 0$ suggests diamagnetic property. Therefore, He and Ne atoms are diamagnetic. In the case of

Eu^{3+} ($4f^6$), the ground state term symbol is $^7F_0$ suggesting that Eu^{3+} ion will be diamagnetic, but is paramagnetic experimentally (Table 1.3). This can be explained that width of $^7F_0$ and $^7F_1$ levels (nearest levels) is about 350 cm^{-1}, which is close to room temperature energy of 210 cm^{-1}. Because of this, electron populations at $J = 0$ are also occupying $J = 1$ partially at room temperature and thus, there is a mixing of $J = 0$ and $J = 1$. Now, it is no longer diamagnetic. Instead, it exhibits paramagnetic behavior.

Table 1.1 Term symbols for a few examples of atoms

Atom	S	L	J	The ground state term symbol
H ($1s^1$)	½	0	½	$^2S_{1/2}$
He ($1s^2$)	0	0	0	$^1S_0$ (for $J = 0$, material is diamagnetic)
Li ($1s^2 2s^1$)	½	0	½	$^2S_{1/2}$
Ne ($1s^2 2s^2$)	0	0	0	$^1S_0$ (for $J = 0$, material is diamagnetic)
B ($1s^2 2s^2 2p^1$)	½	1	½, 3/2	$^2P_{1/2}$
Ti^{3+} ($3d^1$)	½	2	3/2, 5/2	$^2D_{3/2}$
Ce^{3+} ($4f^1$)	½	3	5/2, 7/2	$^2F_{5/2}$
Eu^{3+}($4f^6$)	3	3	0, 1, 2, 3, 4, 5, 6	$^7F_0$ (expected to be diamagnetic as J = 0, but it is paramagnetic)
Tb^{3+}($4f^8$)	3	3	0, 1, 2, 3, 4, 5, 6	$^7F_6$

Table 1.2 Calculated and experimental values of magnetic moments of $3d^{3+}$ ions (Dutta 1986; Malik et al. 1989)

$3d^{n+}$ ions with configurations	*n*	Ground term = $^{2S+1}L_J$	S = n/2	L	*J*	μJ (B. M.)	μS+L (B. M.)	μspin only (B. M.)	μexp (B.M.)
$Ti^{3+}(3d^1)$	1	$^2D_{3/2}$	½	2	3/2	1.55	3.01	1.73	1.7–1.8
$V^{3+}(3d^2)$	2	$^3F_2$	1	3	2	1.63	4.49	2.83	2.8–3.1
V^{2+}, $Cr^{3+}(3d^3)$	3	$^4F_{3/2}$	3/2	3	3/2	0.70	5.21	3.87	3.7–3.9
Cr^{2+}, $Mn^{3+}(3d^4)$	4	$^5D_0$	2	2	0	0.00	5.50	4.90	4.8–4.9
Mn^{2+}, $Fe^{3+}(3d^5)$	5	$^6S_{5/2}$	5/2	0	5/2	5.92	5.92	5.92	5.7–6.0
Fe^{2+}, $Co^{3+}(3d^6)$	4	$^5D_4$	2	2	4	6.71	5.50	4.90	5.0–5.6
$Co^{2+}(3d^7)$	3	$^4F_{9/2}$	3/2	3	9/2	6.63	5.21	3.87	4.3–5.2
$Ni^{2+}(3d^8)$	2	$^3F_4$	1	3	4	5.59	4.49	2.83	2.9–3.9
$Cu^{2+}(3d^9)$	1	$^2D_{5/2}$	1/2	2	5/2	3.55	3.01	1.73	1.9–2.1

The symbol "*n*" is the number of unpaired electrons in 3d-orbitals

$\mu_J = \mathrm{g}\sqrt{J\,(J+1)}B.M.$ (Bohr magnetron).

$\mu_{S+L} = \sqrt{\mathrm{L}\,(\mathrm{L}+1)+4\mathrm{S}\,(\mathrm{S}+1)}B.M.$

$\mu_{spinonly} = \sqrt{4\mathrm{S}\,(\mathrm{S}+1)}B.M.$

$\mu_{spinonly} = \sqrt{\mathrm{n}\,(\mathrm{n}+2)}B.M.$

$g = 1 + \frac{J(J+1)+S(S+1)-L(L+1)}{2J(J+1)}$

Table 1.3 Calculated and experimental values of magnetic moments of $4f^{3+}$ ions (Dutta 1986; Malik et al. 1989)

Ln^{3+} ions with configurations	*n*	Ground term = $^{2S+1}L_J$	S = n/2	L	*J*	*G*	μJ (B. M.)	μspin only (B. M.)	$\mu_{exp.}$ (B.M.)
$La^{3+}(4f^0)$	0	$^1S_0$	0	0	0	–	0.00	0.0	0.00 (Diamagnetic)

Ln^{3+} ions with configurations	*n*	Ground term = $^{2S+1}L_J$	S = n/2	L	*J*	*G*	μJ (B. M.)	μspin only (B. M.)	$\mu_{exp.}$ (B.M.)
$Ce^{3+}(4f^1)$	1	$^2F_{5/2}$	½	3	5/2	6/7	2.54	1.7	2.3–2.5
$Pr^{3+}(4f^2)$	2	$^3H_4$	1	5	4	4/5	3.58	2.8	3.4–3.6
$Nd^{3+}(4f^3)$	3	$^4I_{9/2}$	3/2	6	9/2	8/11	3.62	3.9	3.5–3.6
$Pm^{3+}(4f^4)$	4	$^5I_4$	2	6	4	3/5	2.70	4.9	–
$Sm^{3+}(4f^5)$	5	$^6H_{5/2}$	5/2	5	5/2	2/7	0.84	5.9	1.5–1.6
$Eu^{3+}(4f^6)$	6	$^7F_0$	3	3	0	-	0.00	6.9	3.4–3.6
$Gd^{3+}(4f^7)$	7	$^8S_{7/6}$	7/2	0	7/2	2	7.94	7.94	7.8–8.0
$Tb^{3+}(4f^8)$	6	$^7F_6$	3	3	6	3/2	9.70	6.9	9.4–9.6
$Dy^{3+}(4f^9)$	5	$^5H_{15/2}$	5/2	5	15/2	4/3	10.60	5.9	10.4–10.5
$Ho^{3+}(4f^{10})$	4	$^5I_8$	2	6	8	5/4	10.60	4.9	10.3–10.5
$Er^{3+}(4f^{11})$	3	$^4I_{15/2}$	3/2	6	15/2	6/5	9.60	3.9	9.4–9.6
$Tm^{3+}(4f^{12})$	2	$^3H_6$	1	5	6	7/6	7.60	2.9	7.1–7.4
$Yb^{3+}(4f^{13})$	1	$^2F_{7/2}$	½	3	7/2	8/7	4.50	1.7	4.4–4.9
$Lu^{3+}(4f^{14})$	0	$^1S_0$	0	0	0	–	0.00	0.0	0.00 (diamagnetic)

The symbol "*n*" is the number of unpaired electrons in 4f-orbitals

$\mu_J = \mathrm{g}\sqrt{J\left(J+1\right)}B.M.$ (Bohr magnetron)

$\mu_{spinonly} = \sqrt{4\mathrm{S}\left(\mathrm{S}+1\right)}B.M$

$\mu_{spinonly} = \sqrt{\mathrm{n}\left(\mathrm{n}+2\right)}B.M$

$g = 1 + \frac{J(J+1)+S(S+1)-L(L+1)}{2J(J+1)}$

When one atom interacts with another one (same or different) to form chemical bonds, its magnetic property

will be different from constituents. H atom is paramagnetic in terms of spin magnetic moment, but when it has a chemical bonding with another H atom to form H_2, it becomes diamagnetic. Fe atom is paramagnetic, when it forms bcc (body-centered cubic) lattice with many Fe atoms through metallic bonding, system becomes ferromagnetic. When Fe atoms form chemical bonding (ionic bonding) with oxygen atoms such as compounds α-Fe_2O_3, ɣ-$Fe_2O_{3,}$ and Fe_3O_4, the first compound becomes antiferromagnetic, whereas the second and third compounds become ferrimagnetic. O_2 molecule is paramagnetic. Saturation magnetization (M_s) of bcc Fe decreases when compounds with oxygen are formed. M_s values for bcc Fe and Fe_3O_4 are 217 and 92 emu/g, respectively (Cullity and Graham 2011). Even, when Co lattice changes from hcp (hexagonal close packed) to fcc (face-centred cubic) structure, magnetic moment decreases significantly. Thus, from these, we can see the different behavior of magnetism in different materials.

Magnetism of materials comes from the main sources:

1. Exchange interaction
2. Spin–orbit coupling
3. Dipolar interaction
4. Superexchange interaction
5. Double exchange interaction.

The first and second sources are observed in all materials (Cullity and Graham 2011; Kittel 2005; Dutta 1986; Malik et al. 1989). The third source is observed in the case of

concentrated particles. In non-interacting particles, it is almost negligible. The fourth and fifth ones are observed when interaction between spins of metal ions through a negative ion (O^{2-} or S^{2-}) (Cullity and Graham 2011; Phuc et al. 2003; Anderson 1950). Link can be represented by M–O–M, M–O–M$^{/}$, where M or M$^{/}$ can have same oxidation states or different oxidation states. M and M$^{/}$ are different elements. In general, superexchange interaction will introduce antiferromagnetic property, whereas double exchange will introduce ferromagnetic property. Examples are Fe_3O_4, $CoFe_2O_4$, $LaMnO_3$, and $La_{0.7}Sr_{0.7}MnO_3$. In the case of Fe_3O_4 (inverse spinel cubic structure), Fe^{2+} ($3d^{6+}$) in octahedral site is coupling with Fe^{3+}($3d^{5+}$) in tetrahedral site through antiferromagnetic interaction. This is of superexchange type (Fe^{2+}–O–Fe^{3+}). Similarly, Co^{2+} ($3d^{7+}$) in octahedral site is coupling with Fe^{3+}($3d^{5+}$) in tetrahedral site through antiferromagnetic interaction. This is of superexchange type (Co^{2+}–O–Fe^{3+}). In the case of $LaMnO_3$ (perovskite structure), there is Mn^{3+}–O–Mn^{3+}, which gives rise to antiferromagnetic through coupling of magnetic spins of Mn^{3+} ($3d^{4+}$). In the case of $La_{0.7}Sr_{0.7}MnO_3$, there is a mixture of Mn^{3+} ($3d^{4+}$) and Mn^{4+} ($3d^{3+}$) ions. Mn^{3+}–O–Mn^{3+}orMn^{4+}–O–Mn^{4+} gives rise to antiferromagnetic interaction. This is of superexchange type. There is another interaction through double exchange interaction mechanism in Mn^{3+}–O–Mn^{4+}. One electron from Mn^{3+} ($3d^{4+}$) can be transferred to Mn^{4+} ($3d^{3+}$) ion through $O(\uparrow\downarrow)$ from left to right. The left Mn^{3+} becomes Mn^{4+}, whereas the right Mn^{4+} becomes Mn^{3+}. In this, $O(\uparrow\downarrow)$ helps in electron transfer process. In the same process, an electron can be transferred from the right Mn^{3+} to the left Mn^{4+} one through $O(\uparrow\downarrow)$. This is known as double exchange mechanism, which makes the system electrons spin in the

same direction, and thereby, the system becomes ferromagnetic.

1.3 Spin Glass and Ferromagnetic Systems

Spin glass system is a class of magnetism in which spins present in system attain frustration (Cable et al. 1986; Toro et al. 1999). It gives rise to antiferromagnetic interaction. This is like a disordered spin in a system. A few examples are Fe in Cu, Mn in Mn, Co in Au, and FeCo in Cu. Here, a few fractions of magnetic spins (Fe, Co, Mn, or FeCo) are distributed at a large distance, i.e., without dipolar interaction. Individual atomic spins see each other with different directions. Here, matrices Cu and Au are diamagnetic, but metallic in electrical conductivity. In zero field cooled study, it follows antiferromagnetic behavior. It shows transition: its magnetic susceptibility (χ) increases from low temperature and then decreases with further increase of temperature. The point with maximum susceptibility is known as a spin glass transition.

Ferromagnetic system has spontaneous magnetization in the absence of applied magnetic field. It consists of domain and domain walls (Cullity and Graham 2011). A domain is a region in which atomic spins are aligned in the same direction. Domain walls are the interface region between neighboring domains. In the absence of magnetic field, all domains are oriented in different directions. At high magnetic field, domain walls get collapsed and all domains align along applied magnetic field (H). The system becomes a single domain.

When the size of ferromagnetic particles decreases, their magnetization decreases due to the rotation of domain spins from easy direction. With further decrease in particle size, every particle can act as single domain and it

can have the highest coercivity (H_c). With further decrease in particle size, each domain gets rotated from easy direction to opposite direction. At that time, system does not have magnetization in the absence of magnetic field. It behaves as paramagnetic ($H_c = 0$ Oe). This system is known as superparamagnetic particles. It shows the superparamagnetic blocking temperature (T_B), below which it behaves ferromagnetic and above which, it behaves as paramagnetic. However, with a decrease in particle size, it gets associated with surface dangling bonds (Mørup et al. 2013). Area of surface dangling bonds increases with a decrease in particle size. It gives antiferromagnetic at surface and ferromagnetic at core at low temperature. If such individual particles are closer to each other, there is an antiferromagnetic interaction among small particles. This also introduces the concept of spin glass in system (Aslibeiki et al. 2010; Topkaya et al. 2012). Below T_B, there is a peak (T_g), which is considered as spin glass. To distinguish T_B and T_g, low-temperature AC magnetic susceptibility (χ_{AC}) study is required. T_g is frequency-dependent, whereas T_B is almost frequency-independent ($f < 1000$ Hz). In general, superparamagnetic system is exhibited only when there is no interaction among single domains, whereas spin glass system is introduced only when there is dipolar interaction among domains. The relaxation time (τ) for the superparamagnetic particles is given by Cullity and Graham (2011)

$$\tau = \tau_0 exp\left(\frac{E_a}{k_B T}\right), \tag{1.15}$$

where τ is the relaxation time, E_B is the anisotropy energy barrier, and k_B is the Boltzmann constant.

1.4 When Particle Size Decreases

When particle size decreases, their intrinsic properties change due to the decrease of exchange interaction in a system. The diamagnetic particle in bulk system becomes weak ferromagnetic when particle size decreases to nanosize. ZnO is diamagnetic, but it becomes weak ferromagnetic in nanosized particles (Straumal et al. 2016). Ferromagnetic particles decrease their saturation magnetization with decrease in particle size (Cullity and Graham 2011). Antiferromagnetic particles become ferromagnetic with decrease in particle size. Antiferromagnetic NiO shows the spin glass with decrease in particle size (Tiwari and Rajeev 2005). Non-stoichiometry is observed in small-sized particles (5 nm) of Fe_3O_4 confirmed by the Mossbauer study (Hah et al. 2021).

1.5 When Dimensionality Reduces

When the dimensionality of system changes from 3 to 2D or 1D or 0D, there are many changes in its chemical and physical properties including magnetic property (Glavin and Nam 2023; Gutiérrez 2020). Bulk 3D MoS_2 is a semiconductor, but its band gap increases when dimensionality changes to 2D. Bond breaking or vacancy in lattice may occur when dimensionality changes. Even chemical and physical stabilities change with their dimensionality. Transition metal chalcogenides (TMCs) such as MX_2 (M = Mo, W; X = S, Te, Se,), h-BN, graphene, and layered oxides are examples of 2D-layered structures. MX_2 can have various structures of 2D form: 1 T (tetragonal), 2H (hexagonal), and 3R (rhombohedral). Ferromagnetic properties of materials can be generated by introduction of defects in lattice or dangling bonds or doping of transition metals or adding free radicals.

Graphite belongs to 3D structure, but 2D, 1D, and 0D nanostructures can be generated, namely graphene, nanowire, and fullerene nanostructures.

Zero-dimensional molecular magnets have shown an interesting phenomenon in terms of exciting and unusual properties such as quantum magnetism and quantum information science (for quantum computer) (Coronado 2020). One example of 0D molecular magnet is $[Mn_{12}O_{12}(ac)_{16}(H_2O)_4]$. Here, 12 Mn^{n+} ions interact with each other. One-dimensional, 2D, and 3D molecular magnets are now synthesized in laboratory.

1.6 Applications

Many magnetic materials have been used in various areas including data storage, read access memory, industry, removal of toxic ions, drug carrier, magnetic-based separation, catalysis, photo-catalysis, hyperthermia, sensors, ferrofluids, etc. (Schwerdt et al. 2012; Chung 2020; Wang et al. 2019; Yu et al. 2019; Meissner and Ochsenfeld 1933; Geim et al. 1998; Yaghoubi 2013; Rajan et al. 2022; Joshi et al. 2019; Srivastava et al. 2023).

1.7 Summary of All the Chapters

Chapter 2 deals with the basic understanding of magnetism: Diamagnetic, paramagnetic, ferromagnetic, ferromagnetic, and antiferromagnetic materials. Intrinsic magnetic parameters such as saturation magnetization, Curie temperature, coercivity, and remanence magnetization are the characteristics of ferromagnetic compounds. Minimization of magnetostatic energy through the subdivision of magnetic domains in ferromagnetic particles is mentioned. The association of domain rotation and domain wall displacement during measurement of

magnetization with the applied magnetic field (M-H curve) is explained in an easy way. Various types of magnetic anisotropy including intrinsic forms such as magnetocrystalline anisotropy, shape anisotropy, and stress anisotropy are mentioned. The magnetism of spinel ferrite and hexaferrite crystal structures is explained. When particle size decreases from micron to nanosize (multidomain to single domain), the effect on magnetization and coercivity is mentioned. The importance of superparamagnetic particles is provided.

Chapter 3 deals with the units and dimensions of magnetic physical quantities. The mathematical equations related to magnetic materials are provided in a simpler form. This makes an easy way of presentation. The conversion factor from the CGS unit to the MKS or SI unit or vice versa is given in a table. This is very useful for researchers and readers. The origins of diamagnetic, paramagnetic, ferromagnetic, or ferromagnetic and antiferromagnetic properties are explained. When particle size decreases, what happens in magnetic properties? This was addressed in this chapter. Many examples of single-domain and multidomain systems are given by taking metallic and insulating particles. Use of ferrofluids in hyperthermia applications and their heat generation is elaborately explained. Using Mossbauer spectroscopy, superparamagnetic doublets, and ferromagnetic sextets are explained by varying particle sizes. Fe_3O_4 bulk particles show the sextets indicating ferromagnetic nature and nanoparticles with size 5–10 nm show superparamagnetic doublets at room temperature, but they become ferromagnetic at lower temperature, which is less than that of the blocking temperature and even become ferromagnetic at high magnetic field at room temperature. In the case of particle size 5–10 nm, non-stoichiometry has been developed and this is demonstrated by isomershift

ratio of Fe^{n+} ions at the B site to Fe^{n+} ions at the A site. In bulk, this ratio is 2:1, but it becomes 3:1. Agglomerated Fe_3O_4 nanoparticles can be reduced by dispersion in a suitable medium, which is confirmed by the Mossbauer study.

Chapter 4 deals with the definition of ferrites that are compounds of ferric oxide (Fe_2O_3) and MO (MgO, NiO, MnO, ZnO, CuO, FeO) or Ln_2O_3 (Y_2O_3, La_2O_3, Gd_2O_3, Dy_2O_3). Each ferrite crystal structure consists of 2 or 3 substructures in which Fe^{3+} ions can occupy. Oxygen ions occupy the fcc lattice, where metal ions including Fe^{3+} are occupying interstitial sites (tetrahedral, octahedral, and trigonal bipyramid). In cubic crystal structure, Fe^{3+} ions are occupying both tetrahedral and octahedral sites partially, whereas, in hexagonal structure, Fe^{3+} ions are occupying three sites: tetrahedral, octahedral, and trigonal bipyramid sites partially. Classification of ferrites is provided on the basis of crystal structures: spinel, hexagonal, garnet, and orthoferrites. Spinel structure is further divided into three types: normal, inverse, and mixed types. The different synthesis methods and characterization techniques are provided in an easy way. Ferromagnetic particles have spontaneous magnetization and are explained by the association of domains and domain walls. With decrease in particle size, surface area increases. In nanosize systems, intrinsic properties of ferromagnetic particles change. Initially, each particle can attain single domain, which can have the highest coercivity. With further decrease in particle size, coercivity decreases and, finally, it attains zero at which stage, particles are known as superparamagnetic particles. There is a transition known as the blocking temperature (T_B) at which transition from ferromagnetic to superparamagnetic state takes place. This can be measured using ZFC and FC curves. In nanosize

range, magnetic nanoparticles experience the following: canting spin structure and lattice defects. In spinel ferrite, Fe^{3+} ions in the B site (octahedral site) have a deficiency in occupancy that induces strain in system.

Chapter 5 deals with the applications of magnetic materials in different fields. Every material can be of diamagnetic or paramagnetic or ferromagnetic or ferrimagnetic or antiferromagnetic material. Depending on their properties, they are used in different applications. The materials can be in the form of metals, alloys, oxides, sulfides, phosphate, vanadates, silicates, composites, or core–shell. Diamagnetic materials are materials which have no unpaired electrons in atom/ion (as the atomic orbitals are completely filled) and their magnetic moment is opposite to the applied magnetic field and independent of temperature. They are used for electromagnetic shielding to protect the sensitive electronic devices and scientific and medical equipment from the strong magnetic field interference as they absorb the high-frequency radiations. A perfect diamagnetic material is known as a "Superconductor", which has zero resistance. Various applications of superconductors and magnetic materials in different technologies include cables, induction heaters, motors, generators, maglev, electric aircraft, MRI, NMR, and accelerator. Paramagnetic materials are materials which contain an unpaired electron due to which they have a small magnetic moment. Their magnetic moment is aligned in the direction of the applied magnetic field. They have been used in many applications such as MRI, magnetic refrigeration, and magnetocaloric devices. Ferromagnetic or ferrimagnetic materials are materials with spontaneous magnetization in the absence of a magnetic field. Each particle consists of magnetic domains and domain walls. A domain is a region in which unpaired electrons are aligned in one direction. They have been used

in many applications including GMR, Spintronic devices, transformers, data storage, etc. Antiferromagnetic materials are the materials where the magnetic spins are antiparallel to each other, resulting in a small net magnetic moment. They possess small and positive magnetic susceptibility. They have been used as memory and logic elements for conventional and neuromorphic computing applications. Small-sized magnetic nanoparticles exhibit interesting properties, which make them useful in many applications including catalysis, sensors, magnetic-based separation of toxic ions from water, biological areas (hyperthermia and carrier for drug), etc.

Chapter 6 deals with the $BiFeO_3$ compound having multiferroic property. This shows the rhombohedrally distorted perovskite structure and shows weak coupling between the ferroelectric ($T_C \sim 1120$ K) and magnetic ($T_N \sim 643$ K) order parameters above room temperature. If defects are induced in the lattice of the $BiFeO_3$ compound, what does it happen in properties? Three types of defects, namely point defects (interstitials and vacancies), line defects (edge and screw dislocations), and planar defects (stacking faults, twin boundaries) are observed in many systems. Due to the presence of defects in system, strain is induced. It changes its magnetic, ferroelectric, magnetodielectric, optical/electronic, photovoltaic, photocatalytic, and photoferroelectric properties of $BiFeO_3$. It is to be noted that the term “Ferroic” is used in a material, which can have capable of retaining a spontaneous and switchable parameter, whereas “Multiferroics” is a material having properties like ferromagnetism (magnetic moment), ferroelectricity (electric dipole moment), and ferroelasticity (strain). Uses of $BiFeO_3$ in magnetic, ferroelectric, magnetodielectric, optical/electronic, photovoltaic, photocatalytic, and photoferroelectric applications are provided. Upon

decrease of particles, their properties vary as compared to bulk.

Chapter 7 deals with the basic concepts of nitride magnetic materials and their applications. Different classes of nitrides such as ionic, covalent, metallic, and interstitial nitrides with many examples are provided. Nitrides can be prepared by various routes: solid gas (metal and NH_3, metal and N_2), urea, and metal precursors. Compounds such as Fe_3N, Fe_4N, ε-$Co_xFe_{3-x}N$ ($0 \leq x \leq 0.4$), γ′-$Ni_xFe_{4-x}N$ ($0 \leq x \leq 0.8$), γ-Mo_2N, γ-$Co_{0.25}Mo_{1.75}N$, $FeMoN_2$, β-W_2N, and $CoWN_2$ are prepared. Their characterization techniques are mentioned. Introduction to Fine Particle Magnetism: Size Effect in Nanomaterials: Superparamagnetism and Surface Effects in Nanomaterials: Spin Canting are elaborately provided. Also, crystal structure, chemical bonding, and magnetism are discussed. Very interesting properties of metal nitrides are important parts of discussion in this chapter. A comparison of magnetic parameters of various nitride materials and selected potential applications of metal nitrides are provided.

Chapter 8 deals with the fundamental aspects of nanomagnetism and its versatile applications. Here, origin of nanomagnetism, and classification of magnetism such as diamagnetism, paramagnetism, ferromagnetism, ferrimagnetism and antiferromagnetism are discussed. Further, the classification of ferro/ferromagnetic materials such as soft, hard, and superparamagnetic materials is provided. Various synthesis routes of magnetic nanoparticles such as co-precipitation, sol–gel, thermal decomposition, microemulsion and emulsion, mechanical ball milling, and hydrothermal techniques are mentioned and these will help researchers working in magnetic materials. Finally, various applications of magnetic nanoparticles in areas of data storage, biomedical, sensors,

environmental, and energy storage and conversion are provided and these will be important for users.

Chapter 9 aims to give a brief summary about functional ferromagnetic materials. A concise historical development of magnetism and the understanding of the phenomenon of magnetism and its underlying science from the atomic scale to the bulk scale are provided. The soft and hard magnetic materials are discussed with many examples. The soft magnetic materials have high permeability ($\mu = B/H$) and low hysteresis loss (small M-H or B-H loop). On the other hand, the hard magnetic materials are opposite of the soft magnetic materials. Examples of many soft magnetic materials include iron (Fe), nickel (Ni), cobalt (Co), Fe_3C, Fe–Si, Fe–Ni, Fe–Co, 49Fe–49Co–2V, $MO.Fe_2O_3$ ($M = Fe$, Cu, Zn, Mn, or Ni) as well as non-crystalline materials (magnetic amorphous metallic glass of Fe–P–C alloy, amorphous metallic glass of composition $Co_{64.5}Fe_{3.5}Si_{16}B_{14}Ni_2$, $Fe_{78}Si_{13}B_9$ alloy) are mentioned. The hard magnetic materials are known as permanent magnets, which are defined by the dimensionless hardness parameter ($k = \sqrt{(K_1/(\mu_0 M_s^2)}$, where K_1, $\mu_{0,}$ and M_s are magnetocrystalline anisotropy constant, the vacuum permeability and the saturation magnetization, respectively. Examples of various hard magnetic materials including FePt, CoPt, hexaferrites ($Ba_{O.6}Fe_2O_3$, $Sr_{O.6}Fe_2O_3$), rare-earth magnets ($SmCo_5$, Sm_2Co_{17}), $RE_2Fe_{14}B$ ($RE = Nd$, Tb, Dy), $Sm_2Co_{17}N_3$, $Sm_2Fe_{17}N_{3,}$ and $NdFe_{11}TiN_x$ are provided. Nanoscale engineering can provide interesting magnetic properties, which are different from bulk. Also, low-dimensional magnetic materials can generate many magnetic interactions, which are different from bulk. Molecular magnetism is another fascinating and rapidly evolving field of research that explores the design, the synthesis, and the magnetic

properties of molecules and molecular complexes for future potential applications in quantum computers. Many applications of magnetic materials are mentioned in this.

Chapter 10 deals with the synthesis of magnetic graphene, its sources for magnetism, and its applications in various areas. Graphene is a carbon allotrope having high electrical conductivity, high mechanical strength, and high corrosion resistance from environment. Many have attempted to incorporate magnetism into graphene in order to advance its applications. In atom, its magnetic moment is contributed by its spin and orbital moments. In any material, magnetism comes from exchange interactions, super-exchange, and double-exchange mechanisms. However, pure graphene is diamagnetic as it does not have unpaired electrons. Magnetism in graphene can be generated in various ways: defects, dangling bonds, adsorption of free radicals, addition of functional groups, proximity effects, etc. Various synthesis routes such as ion-irradiation method, chemical methods such as non-covalent approach (hydrogen bonding, electrostatic interaction, π–π stacking interaction), and covalent approach (diazonium salts, nitrene, diazirines, in situ reduction method) are provided. Many techniques to characterize such magnetic graphene are mentioned. Applications of magnetic graphene in various areas such as biomedical, water treatment, chemical sensor, gas sensor, spin-dependent electronics, microwave absorption, catalyst, adsorption of heavy metal, photocatalysis, and energy storage are provided.

Chapter 11 deals with the externally driven interface in three-dimensional Ising model. A Monte Carlo simulation is used. It is very useful in thin film devices. Mapping of magnetization of surface/interface growth with dynamics is done. In bulk magnetic material, there are three major components of energy: (a) exchange interaction, (b) spin–orbit coupling, and (c) magnetic dipolar interaction. The

inter-atomic exchange interaction between two spin states of nearby atoms (labeled further as i and j) is related to $-J_{ij}S_iS_j$, where J_{ij} is the exchange integral or the exchange constant. For ferromagnetic ordering, J_{ij} is positive, whereas, for antiferromagnetic ordering, J_{ij} is negative. A spin–orbit coupling gives rise to magnetization direction to crystal lattice that is known as magnetocrystalline anisotropy. In such systems, spins are restricted to an axis and thus the model is known as the Ising model. Lattice with 1D, 2D, or 3D is modeled with 1D, 2D, or 3D Ising model, respectively. The evolution of microstructure of magnetization interface with field interface velocity (V_f) is demonstrated. This study will be useful in data storage media, spin manipulative devices, spin Seeback effect (spin caloritronics), write heads, and sensors.

Chapter 12 deals with the selected examples of iron and cobalt complexes exhibiting spin-crossover behavior. Molecules having d-block metal ions (d^4 to d^7) are important and their properties such as magnetism, color, conductivity, and physiochemical properties vary with temperature, pressure, or exposure to light as their spin can change from low spin to high spin which is known as spin-crossover (SCO). Such molecules belong to stimuli-responsive materials. A brief survey of the known chemistry of mononuclear Fe(II) and Co(II) octahedral systems with suitable N-donor ligands exhibiting SCO behavior is provided. Its characterization techniques such as magnetic susceptibility measurement, Mossbauer spectroscopy, UV–visible spectroscopy, vibrational spectroscopy, XRD method, and Light-Induced Excited Spin State Trapping (LIESST) measurement are mentioned. Its emerging applications in the area of sensing of gases such as ethanol and methanol, light emitting devices, bistability domain with an “ON” and an “OFF” position,

microelectromechanical systems (MEMS), muscle-mimicking actuator technologies, and optical storage devices are provided with many examples.

Chapter 13 deals with the magnetism in bulk and thin film metallic glass systems. The metallic glasses can have characteristic properties of bulk amorphous alloys such as high thermal stability, elevated mechanical strength, significant corrosion and wear resistance, and good electrical properties. In thin film, the amount of materials required for devices decreases significantly. In thin-film metallic glasses (TFMGs), ferromagnetic elements such as Fe, Co, and Ni can be incorporated. This provides the system with excellent soft magnetic properties of large saturation magnetization, low coercivity, and reduced hysteresis loss, making them invaluable in magnetic recording media, magneto-optical, and high-power device applications. Here, synthesis methods to prepare magnetic metallic glass materials are provided. During annealing, nanocrystalline magnetic particles are observed, which is different from bulk or amorphous phase. Many alloys (Fe–Si–B–Nb–Cu, Ni–Zr, have been prepared in glass matrix. Many characterization techniques are provided.

Chapter 14 deals with the developments in magnetic nanocrystalline metal oxides and their biomedical applications. Various magnetic nanocrystalline metal oxides such as spinels AB_2O_4, garnets, and hexaferrites are mentioned. Crystal structures of halite, corundum, rutile, and perovskite are given. Different synthesis methods such as coprecipitation, hydrothermal, thermal decomposition, microemulsion, sonochemical, and thermal plasma techniques are provided to prepare magnetic nanoparticles. After preparation, surface functionalization with appropriate ligands is required for use in biomedical applications. Many characterization techniques such as XRD, FTIR, electron microscopy, Raman spectroscopy, XPS,

UV–visible spectroscopy, VSM, etc. are mentioned. Types of magnetic materials are also described. Use of magnetic nanoparticles in biomedical areas such as MRI, PET, magnetic-based hyperthermia, drug delivery, etc., are mentioned.

Chapter 15 deals with various approaches to obtain long-range ferromagnetic ordering with Curie temperature near or above 300 K in 2D-TMDs (transition metal chalcogenides) through extrinsic mechanisms such as controlling the defects, dopants, and phase stability mechanisms. Diluted magnetic semiconductors (DMS) are the potential candidates for spintronics applications. Many examples of spintronics applications such as III−V [(In, Mn)Se] and II−VI [(Zn, Cr)Te] were mentioned. Approximately 60 TMDs known as MX_2 TMDs, with "M" being a transition metal element from group IV to VII and X a chalcogen (S, Se, or Te) are known. Some of them form a layered structure in which metals form strong covalent bonds with chalcogens in the intralayer, while weakly bonded van der Waals (vdW) interactions are formed between the adjacent MX_2 layers. In terms of crystal structure, MX_2 can have three different forms: 1T (tetragonal), 2H (hexagonal), and 3R (rhombohedral). Various methods to prepare TMDs are (i) mechanical cleavage, (ii) liquid-phase exfoliation, (iii) intercalation and exfoliation, (iv) thinning, (v) vapor deposition, and (vi) solution-based methods. Origin of magnetism in the MX_2 system is elaborately mentioned. Intrinsic and extrinsic ferromagnetisms are mentioned. Ferromagnetic interactions via bound magnetic polarons are also mentioned. Inducing ferromagnetism by incorporating unpaired spins in these TMDs, namely (a) by defect engineering, (b) by transition metal cation doping, and (c) by structural phase transition is provided. Many examples

of MoS_2, $MoSe_2$, WS_2, and $MoTe_2$ with or without doping are provided.

Chapter 16 deals with the surface-functionalized cobalt-based nanomaterials; such as Co, Co–Fe alloys, Co–Ni alloys, Co–Pt alloys, and cobalt ferrite ($CoFe_2O_4$) for various potential users. There are bottlenecks for applications in various fields at nanoscale, nontoxic synthesis methods, control on size, dispersion in aqueous medium and biocompatible surfaces, etc. It requires coating of such nanoparticles with various capping agents, i.e., PEG, PVP, oleic acid, oleyl amine, mesoporous silica, etc. Various synthesis routes for nanoparticles such as aqueous/organic mediated chemical reduction routes using $NaBH_4$, $Li(Et)_3BH$ (superhydride), and polyol as reducing agents are provided. and stabilized via coating the surface. Many characterization techniques such as XRD, electron microscopy, and VSM are mentioned. Various kinds of magnetic materials are discussed. Applications of coated magnetic nanoparticles in catalysis, electrocatalysis, MRI, hyperthermia, data storage, ferrofluid, magnetic recording head, and biosensing are provided.

Chapter 17 deals with the study of magnetism in thin films and superlattices using polarized neutron reflectivity. Various thin film techniques such as magnetron sputtering, electron beam epitaxy, pulsed laser deposition (PLD), molecular beam epitaxial (MBE), etc., have provided the creation of atomically precise ultra-thin films and epitaxial interfaces of dissimilar materials. This gives exotic physical phenomena, particularly at the interfaces, thereby providing a rigorous test for established theories of magnetism. The technological applications using thin-film heterostructures and superlattices in various areas are provided. Different techniques for probing magnetism in thin films and superlattices such as SEMPA, reflection high-energy electron diffraction (RHEED), scanning

tunneling microscopy (STM), and Auger spectroscopy, MFM, Magneto-optic Kerr effect (MOKE), Resonant X-ray scattering, and polarized neutron reflectivity are mentioned. Also, extensive studies on $CaMnO_3$ (CMO)/$CaRuO_3$ (CRO) superlattices, where CMO is an AFM insulator and CRO is a metallic paramagnet is done and after analysis, it is observed ferromagnetic character at interface. Other interfaces such as Gd/Co multilayer, Fe/Cu/Pt heterostructure, $La_{0.67}Sr_{0.33}MnO_3$ (LSMO)/$LaNiO_3$ (LNO) heterostructure, proximity and tunneling at interfaces in superconductor and ferromagnet oxide heterostructures, induced interface magnetism at ferromagnetic/multiferroic interface are studied. Application of magnetic thin films and superlattices are provided.

Chapter 18 deals with the study of molecule-based magnetic materials. Molecule-based magnetic materials are classified into two: (a) purely organic magnets and (b) organic–inorganic hybrid magnets. The spin will reside solely on the organic ligands in the case of purely organic magnets, whereas the spin carriers will either be active or passive in the case of hybrid magnets. Active means spin will reside on both the inorganic and organic ligands, whereas passive means the spin will reside only on the inorganic part. This is considered in the group of low-dimensional molecular structures. The exciting and unusual phenomena of quantum magnetism, condensed matter physics, and quantum information science (for quantum computer) can be generated. Lattice structure of various dimensionalities like 0D (single), 1D (chain), 2D (layer), and 3D (open framework) can be synthesized using an appropriate choice of molecular ligand or building blocks. These are possible using organic–inorganic hybrid magnets. One example of 0D (single) is $[Mn_{12}O_{12}(ac)_{16}(H_2O)_4]$ (where ac is acetate $= O_2CCH_3$)

discovered by Sessoli and co-workers. Nowadays, there are many compounds on 0D and this compound is known as single-molecule magnet. One example of 1D (layer) molecule is $[Co^{II}(hfac)_2(NITphOMe)]$, (Hhfac = hexafluoroacetylacetone, NITPhOMe = 4′-methoxy-phenyl-4,4,5,5-tetramethylimidazoline-1-oxyl-3-oxide), first reported by Gatteschi in 2001. This is known as single-chain magnet (SCM). An example of 2D (layer) is manganese hexafluoroacetylacetonate and this is considered as layered molecular compounds. 3D (open framework) includes the metal–organic frameworks (MOFs) and covalent organic frameworks (COF) that have porous crystalline material. Here, metal ions are linked by organic ligands. The compounds are important for gas storage such as for hydrogen, carbon dioxide, and methane and catalysts. One example is $(rad)_2Mn_2[Cu(opba)]_3(DMSO)_2{\cdot}2H_2O$, where DMSO is dimethyl sulfoxide, and rad^+ is 2-(4-*N*-methylpyridinium).

Chapter 19 deals with the study of HSP90: An emerging molecular target for improvement of nanoparticle-based magnetic hyperthermia therapy. Cancer is a major global health problem. Among treatments, surgery, chemo- and radiotherapy are the most common approaches. However, however, hyperthermia-based treatment was started long back. There are two types of hyperthermia treatments (HT): (1) generation of heat generation from ultrasound, radiowaves, or microwaves and (2) magnetic nanoparticle-based heat treatment under an AC magnetic field. Here, heat is generated at 40–43 °C which induces denaturation of cellular proteins and lipids, affecting important biological processes such as membrane transport, DNA replication/repair machinery, and cell proliferation/survival. The previous one has many side effects: (i) in-homogenous heating of the tumor, (ii) to reach hyperthermia temperature at the core of the tumor,

the surface needs to be heated at a much higher temperature and then it results in blisters, burn and pain to the patient. The second approach can avoid the above disadvantages. In a recent study, it was observed that there is a critical role of Heat Shock Proteins (HSPs), especially HSP90 expression in deciding the success or failure of HT. Magnetic nanoparticle-based heat treatment has provided newer opportunities to tackle the problem of HSR induced by HT or HSP90 inhibitors for enhancing their therapeutic capabilities. Also, HSP90-targeted NPs could be one of the ways for the treatment of cancer in future.

Chapter 20 deals with the study of magnetic-luminescent nanocomposites for cancer hyperthermia therapy. history of magnetic-based hyperthermia using micronsized particles and nanoparticles has been mentioned. The sources of heat generation from magnetic nanoparticles under the AC magnetic field are Neel relaxation, Brownian relaxation, hysteresis loss, and eddy currents. Many examples of magnetic nanoparticles such as Fe_3O_4, $MnFe_2O_4$, and Zn ferrite are provided. To make water dispersible, many capping agents and core@shell model using SiO_2 are provided. Also, utility of nanocomposite having magnetic property as well as luminescence property has been mentioned. Luminescent materials will be QDs, inorganic nanoparticles, and organic molecules. This gives advantages in terms of imaging, diagnosis, and therapy of cancer.

References

Akhlaghi, N., Najafpour-Darzi, G.: Manganese ferrite ($MnFe_2O_4$) Nanoparticles: from synthesis to application—a review. J. Ind. Eng. Chem. **103**, 292–304 (2021)
[Crossref]

Anderson, P.W.: Antiferromagnetism: theory of super exchange interaction. Phys. Rev. **79**, 350 (1950)
[Crossref]

Aslibeiki, B., Kameli, P., Salamati, H., Eshraghi, M., Tahmasebi, T.: Superspin glass state in $MnFe_2O_4$ nanoparticles. J. Magn. Magn. Mater. **322**, 2929–2934 (2010)
[Crossref]

Cable, J.W., Nicklow, R.M., Tsunoda, Y.: Spin dynamics of a Cu-Mn spin glass alloy. Physica B+C **136**, 318–321 (1986)

Chung, D.D.L.: Materials for electromagnetic interference shielding. Mater. Chem. Phys. **255**, 123587 (2020)
[Crossref]

Coronado, E.: Molecular magnetism: from chemical design to spin control in molecules, materials and devices. Nat. Rev. Mater. **5**, 87–104 (2020)
[Crossref]

Cullity, B.D., Graham, C.D.: Introduction to Magnetic Materials. John Wiley & Sons (2011)

Dutta, R.L.: Inorganic Chemistry. The New Book Stall, Calcutta (1986)

Gajbhiye, N.S., Sharma, S., Ningthoujam, R.S.: Synthesis of self-assembled monodisperse 3 nm FePd nanoparticles: phase transition, magnetic study and surface effect. J. Appl. Phys. **104**, 123906 (2008)
[Crossref]

Gajbhiye, N.S., Ningthoujam, R.S.: Structural, electrical and magnetic studies of nanocrystalline δ-MoN and γ-Mo_2N. Phys. Stat. Sol. **1**, 3449 (2004)

Gajbhiye, N.S., Ningthoujam, R.S., Weissmuller, J.: Synthesis and magnetic studies of nanocrystalline nickel nitride material. Phys. Stat. Sol. **189**, 691 (2002)

Gajbhiye, N.S., Panda, R.N., Ningthoujam, R.S., Bhattacharyya, S.: Magnetism of nanostructured iron nitride (Fe-N) systems. Phys. Stat. Sol. **1**, 3252 (2004b)

Gajbhiye, N.S., Ningthoujam, R.S., Weissmuller, J.: Mössbauer study of nanocrystalline ε-$Fe_{3-x}Co_xN$ system. Hyperfine Interact. **156**, 51 (2004)

Geim, A.K., Dubonos, S.V., Lok, J.G.S., Henini, M., Maan, J.C.: Paramagnetic Meissner effect in small superconductors. Nature **396**, 144–146 (1998)
[Crossref]

Glavin, N.R., Nam, S.W.: 2D layered materials and heterostructures: past, present, and a bright future. Matter **6**, 4–6 (2023)

Gutiérrez, H.R.: Two-dimensional layered materials offering expanded applications in Flatland. ACS Appl. Nano Mater. **3**, 6134–6139 (2020)

Hah, H.Y., Gray, S., Johnson, C.E., Johnson, J.A., Kolesnichenko, V., Kucheryavy, P., Goloverd, G.: Mössbauer spectroscopy of superparamagnetic Fe_3O_4 nanoparticles. J. Magn. Magn. Mater. **539**, 168382 (2021)
[Crossref]

http://magworld.physics.auth.gr/world/basics/9

https://www.electrical4u.com/hard-magnetic-materials/

Joshi, R., Perala, R.S., Srivastava, M., Singh, B.P., Ningthoujam, R.S.: Heat generation from magnetic fluids under alternating current magnetic field or induction coil for hyperthermia-based cancer therapy: basic principle. J. Radiat. Cancer Res. **10**, 156–164 (2019)
[Crossref]

Joshi, R., Singh, B.P., Ningthoujam, R.S.: Confirmation of highly stable 10 nm sized Fe_3O_4 nanoparticles formation at room temperature and understanding of heat-generation under AC magnetic fields for potential application in hyperthermia. AIP Adv. **10**, 105033 (2020)
[Crossref]

Joshi, R., Singh, B.P., Prajapat, C.L., Kashyap, Y., Nayak, C., Bhattacharyya, D., Ningthoujam, R.S.: Insights into the structural and microscopic origin of magnetic properties of the γ-Fe_2O_3@Mn_xO_y nanostructure. J. Phys. Chem. C **125**, 17971 (2021)
[Crossref]

Kittel, C.: Introduction to Solid State Physics. John Wiley & sons, Inc (2005)

Malik, W.U., Tuli, G.D., Madan, R.D.: Selected Topics in Inorganic Chemistry. S. Chand & Company Ltd. (1989)

Meissner, W., Ochsenfeld, R.: Ein neuer EffektbeiEintritt der Supraleitfähigkeit Naturwissenschaften **21**, 787–788 (1933)

Mohapatra, J., Joshi, P., Liu, J.P.: Low-dimensional hard magnetic materials. Progress Mater. Sci. **138**, 101143 (2023)

Mørup, S., Brok, E., Frandsen, C.: Spin structures in magnetic nanoparticles. J. Nanomater. 720629 (2013). https://doi.org/10.1155/2013/720629

Nagamatsu, J., Nakagawa, N., Muranaka, T., Zenitani, Y., Akimitsu, J.: Superconductivity at 39 K in magnesium diboride. Nature **410**, 63–64 (2001) [Crossref][PubMed]

Ningthoujam, R.S., Gajbhiye, N.S.: Electron-electron interaction effect and resistivity maximum in nanocrystalline and ordered superconducting γ-Mo_2N. Int. J. Nanotechnol. **7**, 932 (2010) [Crossref]

Ningthoujam, R.S., Gajbhiye, N.S.: Synthesis, electron transport properties of transition metal nitrides and applications. Prog. Mater. Sci. Mater. Sci. **50**, 50–154 (2015) [Crossref]

Ningthoujam, R.S., Sudhakar, N., Rajeev, K.P., Gajbhiye, N.S.: Electrical resistivity study of La, B doped nanocrystalline superconducting vanadium Nitride. J. Appl. Phys. **91**, 6051 (2002) [Crossref]

Ningthoujam, R.S., Gajbhiye, N.S., Sachil, S.: Reduction mechanism of Ni^{2+} into Ni nanoparticles prepared from different precursors: magnetic studies. Pramana J. Phys. J. Phys. **72**, 577 (2009) [Crossref]

Ningthoujam, R.S., S.S. Umare, Sharma, S.J., Shukla, R., Kurian, S., Vatsa, R.K., Tyagi, A.K., Tewari, R., Dey, G.K., Gajbhiye, N.S.: Magnetic and Mössbauer studies on nanocrystalline $Co_{1-x}Li_xFe_2O_4$ (x = 0, 0.2). Hyperfine Interact. **184**, 227 (2008)

Phuc, N.X., Bau, L.V., Khiem, N.V., Son, L.H., Nam, D.N.H.: Magnetic and transport properties of $La_{0.7}Sr_{0.3}Co1-yMnyO_3$—no double exchange between Mn and Co. Physica B: Condensed Matter. **327**, 177–182 (2003)

Rajan, A., Chandunika, R.K., Raju, F., Joshi, R., Sahu, N.K., Ningthoujam, R.S.: Synthesis and processing of magnetic based nanomaterials for biomedical applications. In: Tyagi, A.K., Ningthoujam, R.S. (eds.) Handbook on Synthesis Strategies for Advanced Material: Volume-II: Processing and Functionalization of Materials, Chapter 16, pp. 659–714. Springer Nature, Singapore (2022)

Robert, C.P.: Hexagonal ferrites: a review of the synthesis, properties and applications of hexaferrite ceramics. Prog. Mater. Sci. **57**, 1191–1334 (2012) [Crossref]

Schwerdt, J.I., Goya, G.F., Calatayud, M.P., Hereñú, C.B., Reggiani, P.C., Goya1, R.G.: Magnetic field-assisted gene delivery: achievements and therapeutic potential. Curr. Gene Therapy **12**, 116–126 (2012)

Sharma, S., Gajbhiye, N.S., Ningthoujam, R.S.: Synthesis and self-assembly of monodisperse Co_xNi_{100-x} (x = 50, 80) colloidal nanoparticles by homogenous nucleation. J. Colloids Interface Sci. **351**, 323 (2010b)
[Crossref]

Sharma, S., Gajbhiye, N.S., Ningthoujam, R.S.: Effect of annealing on magnetic properties of FePd and FePdPt nanoparticles. In: AIP Conference Proceeding, vol. 1313, pp. 125 (2010a)

Shukla, R., Ningthoujam, R.S., Umare, S.S., Sharma, S.J., Kurian, S., Vatsa, R.K., Tyagi, A.K., Gajbhiye, N.S.: Decrease of superparamagnetic fraction at room temperature in ultrafine $CoFe_2O_4$ particles by Ag doping. Hyperfine Interact. **184**, 217 (2008)
[Crossref]

Srivastava, M., Joshi, R., Singh, B.P., Ningthoujam, R.S.: Advances on magnetic nanoparticles based cancer therapy through hyperthermia: Basic understanding and history. In: Hassan, P.A., Balakrishnan, B., Tyagiin, A.K. (eds.) Engineered Biomaterials: Progress and Prospects. World Scientific Publishing Co Pvt. Ltd., Singapore (2023)

Straumal, B.B., Protasova, S.G., Mazilkin, A.A., Goering, E., Schütz, G., Straumal, P.B., Baretzky, B.: Ferromagnetic behaviour of ZnO: the role of grain boundaries. Beilstein J. Nanotechnol. **7**, 1936–1947 (2016)

Tiwari, S.D., Rajeev, K.P.: Signatures of spin-glass freezing in NiO nanoparticles. Phys. Rev. B **72**, 104433 (2005)
[Crossref]

Topkaya, R., Akman, Ö., Aktaş, B., Durmus, Z., Baykal, A.: Surface spin disorder and spin-glass-like behaviour in manganese-substituted cobalt ferrite nanoparticles. J. Nanopart. Res. **14**, 1156 (2012). https://doi.org/10.1007/s11051-012-1156-2

De Toro, J.A., López de la Torre, M.A., Riveiro, J.M., Sáez Puche, R., Gómez-Herrero, A., Otero-Díaz, L.C.: Spin-glass-like behavior in mechanically alloyed nanocrystalline Fe-Al-Cu. Phys. Rev. B **60**, 12918 (1999)

Umare, S.S., Ningthoujam, R.S., Sharma, S.J., Shrivastava, S., Kurian, S., Gajbhiye, N.S.: Mössbauer and magnetic studies on nanocrystalline $NiFe_2O_4$ particles prepared by ethylene glycol route. Hyperfine Interact. **184**, 235 (2008)
[Crossref]

Wang, L., Qiu, H., Liang, C., Song, P., Han, Y., Han, Y., Gu, J., Kong, J., Pan, D., Go, Z.: Electromagnetic interference shielding MWCNT-Fe_3O_4@Ag/epoxy

nanocomposites with satisfactory thermal conductivity and high thermal stability. Carbon **141**, 506–514 (2019)
[Crossref]

Yaghoubi, H.: The Most Important Maglev Applications, p. 537986 (2013)

Yu, K., Zeng, Y., Wang, G., Luo, X., Li, T., Zhao, J., Qian, K., Park, C.B.: rGO/Fe_3O_4 hybrid induced ultra-efficient EMI shielding performance of phenolic-based carbon foam. RSC Adv. **9**, 20643–20651 (2019)

© The Author(s), under exclusive license to Springer Nature Singapore Pte Ltd. 2024
R. S. Ningthoujam, A. K. Tyagi (eds.), *Handbook of Materials Science, Volume 2*, Indian Institute of Metals Series
https://doi.org/10.1007/978-981-97-4646-0_2

2. Magnetic Materials: Fundamentals and Applications

Seema Verma[1] ✉
(1) Indian Institute of Science Education and Research (IISER) Pune, Pune, Maharashtra, India

✉ **Seema Verma**
Email: sa.verma@iiserpune.ac.in

Keywords Magnetism – Magnetic materials – Ferrites – Superparamagnetism

2.1 Introduction

Magnetism was first noticed by the ancient Greek philosopher Thales in the sixth century BC. However, a comprehensive understanding of magnetism began to emerge after 1600, with the publication of “De Magnete” by the Englishman William Gilbert. The first naturally occurring magnetic material, known as lodestone or magnetite (Fe_3O_4), was abundant in the Magnesia district (modern Turkey), giving rise to the term “magnetism.” Since then, magnetism and magnetic materials have captured the interest of scientists and technologists due to their intriguing physical phenomena and their vital role in various applications. Many of our modern devices,

including electrical power generators, transformers, electric motors, computers, telephones, information storage media, actuators, electronic circuits, security alarm systems, diagnostic and therapeutic tools, heavily rely on magnetism and magnetic materials. In our daily lives, we are surrounded by magnetic materials, and for numerous applications, a well-established group of magnetic materials known as ferrimagnetic oxides or ferrites are commonly used.

It's noteworthy that ferrite materials, known for their weak permanent magnetism, were initially used in the lodestones by early navigators over two millennia ago. Although attempts to obtain various forms of ferrite materials and their commercialization began in the early twentieth century, their use faced challenges due to inferior magnetization properties compared to ferromagnetic alloys. The widespread commercial application of ferrite magnetic materials gained momentum after the 1950s, driven by advancements in technologies like radio, television, carrier telephony, microwave devices, computer circuits etc.

The intent of this chapter is to provide a brief introduction to different types of magnetic materials, magnetic phenomena and their role in exploring various applications focusing particularly on ferrite materials. It offers a concise classical and phenomenological description based on the concept of ferrimagnetism which is followed by a concise introduction to fine particle magnetism. Several excellent textbooks, including B.D. Cullity and C.D. Graham, *Introduction to Magnetic Materials*, (Cullity and Graham 2009) 2nd edn. John Wiley and Sons, 2009; Nicola A. Spaldin, *Magnetic Materials: Fundamental and Applications*, (Spaldin 2011) 2nd edn. Cambridge University Press, 2011; D. Jiles, *Introduction to Magnetism and Magnetic Materials*, (Jiles 1996) Chapman & Hall, 1996;

Paul Valenzuela, *Magnetic Ceramics*, (Valenzuela 1994) Cambridge University Press, 1994; J. Smit and H. P. J. Wijn, *Ferrites*, (Smit and Wijn 1959) Phillips technical library, 1959; C. Kittel. *Introduction to Solid State Physics*, (Kittel 1996) John Wiley and Sons, 1996 are recommended for readers seeking a more detailed exploration of the topics discussed in this chapter.

2.2 Fundamentals

Magnetic effects in condensed matter are caused by the quantized spin and orbital angular momenta of electrons. We can draw a connection between the spin and orbital motion of electrons and a current-carrying loop of wire with no resistance. The magnetic moments resulting from the spin and orbital motion are the same for the first Bohr orbital (n = 1), and this magnetic moment is known as the Bohr Magneton: $\mu_B = eh/4\pi mc$ (in cgs unit) $= 0.927 \times 10^{-20}$ erg/Oe (emu) where e is the charge on electron in esu, c is the velocity of light, m is the mass of the electron and h is the Planck's constant (Cullity and Graham 2009; Spaldin 2011; Jiles 1996).

Atoms consist of multiple electrons, each spinning on its axis and revolving around the nucleus. The overall magnetic moment of an atom is the sum of all the individual electron moments, taking into account their respective directions. This situation gives rise to two potential outcomes:

1. If the magnetic moment vectors of all electrons cancel each other out, the atom has a zero net magnetic moment. These atoms are non-magnetic and exhibit diamagnetism.

2. If the magnetic moment vectors of each electron partially cancel out, the atom retains a finite magnetic

moment. These atoms are magnetic, and depending on the interactions among the magnetic moment vectors, the substance made up of such atoms can be paramagnetic, ferromagnetic, ferrimagnetic, or antiferromagnetic.

In the presence of externally applied field of strength H the material gets magnetized and depending upon the types of magnetic materials the magnetic flux (Φ) i.e. amount of magnetic lines of forces passing through unit area (A) is different. In cgs units, magnetic flux ($\Phi = HA$) is measured in maxwells, equivalent to Oersted cm^2, while in SI units, it is defined as $\Phi = \mu_o$ HA. Here, μ_o represents the permeability of free space, with a value of $4\pi \times 10^{-7}$ Wb/Am, and the SI unit of flux is weber (Cullity and Graham 2009; Spaldin 2011; Jiles 1996).

A uniform magnetic field (H) can be generated by external electric currents outside the materials, be it from a solenoid, an electromagnet, or a permanent magnet. Electromagnets are constructed with an iron core surrounded by a coil of wire carrying a direct current. As the iron is exposed to the magnetic field (H), it becomes magnetized, and the degree of magnetization relies on the applied field's strength. The overall magnetic field observed is the combination of the external field (H) and the field produced due to the magnetization of the iron rod. Represented as M, the magnetization intensity leads to an additional $4\pi M$ lines of force passing through each square centimeter of the iron rod's surface. This results in the magnetic flux density or induction (B), measured by the total lines per square centimeter. Magnetic induction has dual contributions: one from the magnetic field (H) and the other from the magnetization (M) of the medium (here iron). Magnetization (M) is measured in magnetic moment per unit volume with cgs unit emu/cm^3. It is important to note that the value of magnetization can also be measured

to the unit of mass than that of volume as mass of the samples can be accurately measured and it is independent of the temperature. The specific mgnetization (σ) in emu/g is represented as,

$$\sigma = \frac{\mathrm{m}}{\mathrm{w}} = \frac{\mathrm{m}}{\mathrm{v}\rho} = \frac{M}{\rho} \tag{2.1}$$

where m, w, v and ρ are magnetic moment, mass, volume and density respectively.

As represented below, the ratio of M to H is called Susceptibility (χ),

$$\chi = \frac{M}{H} \tag{2.2}$$

If M is measured in magnetic moment per unit volume, susceptibility χ is referred as volume susceptibility, χ_{v} (see Eq. 2.3). If the magnetization is measured to the unit of mass then the susceptibility χ is referred as mass susceptibility, χ_{m} (see Eq. 2.4).

$$\chi_{\mathrm{v}} = \frac{M}{H} \tag{2.3}$$

$$\chi_{\mathrm{m}} = \frac{\chi_{\mathrm{v}}}{\rho} \tag{2.4}$$

The cgs units of volume and mass susceptibilities are emu/cm^3 Oe and emu/g Oe respectively. Another important quantity permeability, μ can be obtained by taking a ratio of magnetic induction B to the magnetic field H as shown below:

$$\mu = \frac{B}{H} \tag{2.5}$$

This indicates how permeable a material is to the magnetic field. The relationship between B, H, and M is a

unique property of the magnetic material. In cgs units, B, H, and M are related by,

$$B = H + 4\pi M \tag{2.6}$$

Therefore, total magnetic flux, Φ passing through unit area (A) observed i.e. $\Phi_{observed}$ (BA) due to magnetization will be different from $\Phi_{current}$ (HA). That means for different magnetic materials, the amount of magnetic lines of forces (Φ) passing through unit area (A) is different and this enables us to classify different magnetic materials:

(a) If $\Phi_{current} > \Phi_{observed}$; magnetic lines of forces are expelled out. For such materials susceptibility χ has a negative and small value. That means permeability μ is slightly less than 1. These kinds of materials are diamagnetic.

(b) If $\Phi_{current} \leq \Phi_{observed;}$ The observed flux in these materials are only about 0.02% greater than the flux due to the current applied. They are weakly magnetic therefore for such materials susceptibility χ is small and positive, and Permeability μ is slightly greater than 1. These kinds of materials are paramagnetic.

(c) If $\Phi_{current} <<< \Phi_{observed;}$ The observed flux is atleast 1000 times more than that due to the current. Both susceptibility, χ and permeability, μ are large and positive. These materials are known as ferromagnetic or ferrimagnetic (Cullity and Graham 2009; Spaldin 2011; Jiles 1996).

As $B = H + 4\pi M$ in cgs units

$$\mu = 1 + 4\pi\chi \tag{2.7}$$

In SI units, B, H and M are related by the vector sum of $\mu_o H$ and $\mu_o M$ which represents contribution to magnetic

induction from free space and magnetic induction from the magnetization of materials respectively:

$$B = \mu_o (H + M) \tag{2.8}$$

where μ_o is the permeability of free space or vacuum and is equal to $4\pi \times 10^{-7}$ Wb/A m or henry/m. The magnetic induction B is in weber/m^2 or tesla (T). Both magnetic field H and magnetization M are measured in A/m, therefore in SI unit susceptibility χ is a dimensionless quantity.

Also as $\mu = \mu_o (1 + \chi)$; $\mu/\mu_o = \mu_r = 1 + \chi$ where μ_r is the relative permeabilty. For free space i.e. in the absence of any magnetic materials, $M = 0$, hence $\chi = 0$. Therefore, $\mu = \mu_o$ and $\mu_r = 1$. This implies in SI unit the total magnetic flux density in a free space is, $B = \mu_o H$.

2.2.1 Diamagnetism

As discussed earlier, diamagnetism is a phenomena which occurs in all the atoms where the net magnetic moments associated with each atom are zero due to their filled electron shells. However, in the presence of an externally applied field there is a change in the orbital motion of the electrons. This effect where the orbital motion of the electrons changes on the application of applied field is known as the diamagnetic effect. As seen in Fig. 2.1, an electron revolving in an orbit constitutes an electric current and the magnetic moment μ is in the direction perpendicular to this current loop. In the absence of any externally applied field, magnetic moments of each current loops are alligned in such a way that they all get cancelled out completely giving zero net magnetic moments. However, as observed by Faraday, the moment external magnetic field is applied, the change in flux Φ through the current loop induces an electromotive force. This induced current will have its own magnetic field in the opposite direction so as to oppose the change in the flux. In other

words magnetic moment associated with the induced current always points in the direction opposite to that of the applied magnetic field. As electron orbits are resistance less, the induced current will remain constant and so magnetic moment will decrease as long as the field is kept on. The magnetic moment of the current loop containing one electron is the product of the current and the area of the loop. Current depends upon the charge and the frequency of orbital motion of electrons. If r is the orbital radii and Z is the total number of electrons, the magnetic moment in SI unit is expressed by the following Eq. 2.9 (Cullity and Graham 2009; Spaldin 2011).

$$\mu = -\frac{\mu_o Z e^2 H}{6m} < r^2 > \tag{2.9}$$

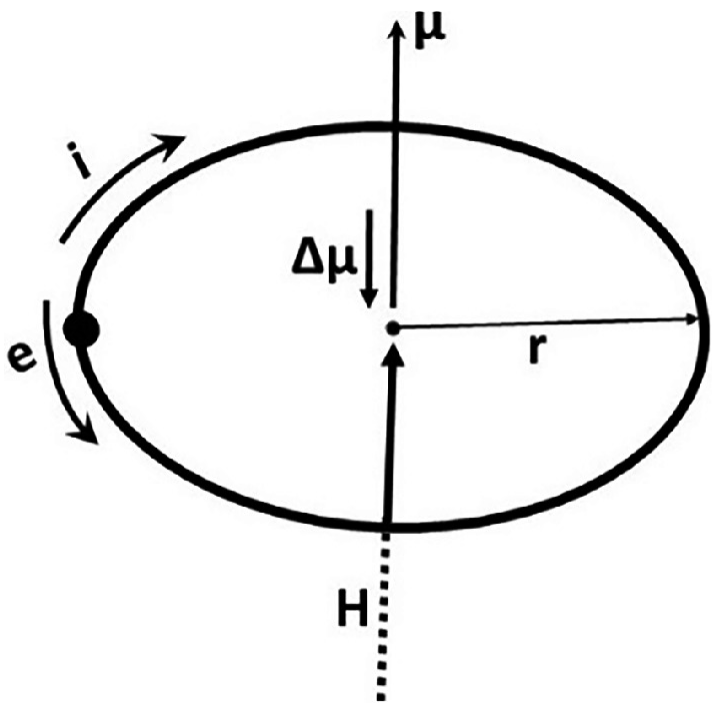

Fig. 2.1 Effect of field, H on the orbital magnetic moment. (Adapted and redrawn (Cullity and Graham 2009))

If the number of electrons per unit volume is N, m is the mass of the electron and c is the speed of light, then the

diamagnetic susceptibility, χ in SI unit is given by,

$$\chi = \frac{M}{H} = -\frac{\mathrm{N}\mu_o \mathrm{Z}e^2}{6m} < r^2 > \tag{2.10}$$

Susceptibility in SI unit is dimensionless. If we work in the CGS unit the expression for susceptibility is given by,

$$\chi = \frac{M}{H} = -\frac{\mathrm{N}\mathrm{Z}e^2}{6mc^2} < r^2 > \tag{2.11}$$

which has the units of emu/(cm^3 Oe).

This is the classical Langevin's theory of Diamagnetism (Spaldin 2011; Tyler 1931) which indicates susceptibility is temperature independent and its value is high for large atoms having higher Z and r values.

2.2.1.1 Diamagnetic Substances and Applications

Diamagnetism exists in all materials, however, it is only those that have no other magnetic properties are purely termed as Diamagnetic materials. It is important to note that diamagnetism in all materials are usually suppressed due to the presence of a much stronger effect as observed in paramagnetic or ferromagnetic materials. All noble gases are diamagnetic because they have closed shell electronic configuration. Superconductors under certain conditions are perfect diamagnetic materials.

2.2.2 Paramagnetism

Paramagnetism arises due to the incomplete cancellation of the magnetic moment vectors, therefore atoms, ions or molecules on the whole are left with a finite permanent magnetic moment. The source of permanent magnetic moment is a result of uncompensated spin or orbital angular momentum of electrons. In the absence of an externally applied field, these magnetic moment vectors are

randomly oriented due to thermal energy. This results in zero net magnetization value. However, as soon as an external magnetic moment is applied the magnetic moments get aligned towards the direction of the field resulting in net magnetization. That means, in the absence of any opposing force or thermal agitation, there is a possibility of complete alignment of the magnetic moments even in the presence of a very weak magnetic field. However, it has been observed that for most of the paramagnets, the thermal agitation is very large due to which even at a very high magnetic field of strength as high as 10 T; the magnetization acquired is only 2% of the saturation value. Therefore, the Paramagnets possess small, positive susceptibility. In these materials, the diamagnetic response is always present, however, the atomic or ionic magnetic moment values are much greater than that of the induced diamagnetic moments. Paramagnetism is governed by the competitive effect between the magnetic field applied which aligns the magnetic moment vectors and the thermal energy which causes their randomization. Langevin proposed a simple model to explain this competitive effect both in qualitative and quantitative manner. To grasp the classical theory of paramagnetism, Langevin examined a unit volume of paramagnetic gas with n atoms, each having a magnetic moment μ. He assumed that interactions between these magnetic moments were negligible (Cullity and Graham 2009). Imagine each of these vectors extending from the center of a sphere with a unit radius (refer to Fig. 2.2) (Spaldin 2011.

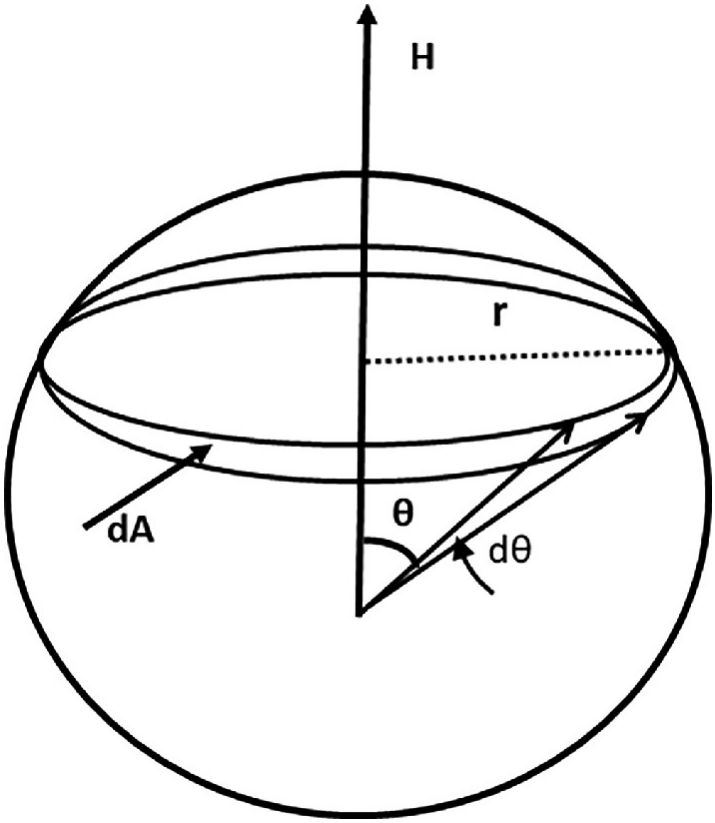

Fig. 2.2 Fraction of paramagnetic moment vectors drawn through the center of a sphere, that are inclined at an angle θ and θ + dθ to the field axis. (Adapted and redrawn Spaldin 2011)

When no field is applied, number of magnetic moment vectors passing through the unit area of the sphere surface is the same at any point. Therefore, a small number dn of magnetic moment vectors inclined at an angle θ and θ + dθ to the field axis should be proportional to fractional surface area dA. That is,

$$\mathrm{dn} \propto \mathrm{dA} \tag{2.12}$$

$$\mathrm{dA} = 2\pi \sin\theta \, d\theta \text{ for a sphere of unit radius} \tag{2.13}$$

The moment external field is applied; all the magnetic moment vectors would get aligned towards the direction of the field. At thermal equilibrium the magnetic moment vectors will get aligned at an angle θ with the direction of the field. The energy of interaction is given by,

$$\mathrm{E_p} = -\mu \cdot \mathrm{H} = -\mu \mathrm{H} \cos\theta \tag{2.14}$$

Using Maxwell—Boltzmann distribution law, the number of such orientation is proportional to the Boltzmann factor given by,

$$e^{-E_p/kT} \text{or } e^{\mu \mathrm{H} \cos\theta/kT} \tag{2.15}$$

where k is the Boltzmann constant

According to Statistical mechanics, the probability of finding the magnetic moments between θ and θ + dθ to the field axis is proportional to the fractional surface area $(2\pi \mathrm{r}^2 \sin\theta d\theta)$ and the Boltzmann factor i.e.

$$\mathrm{dn} \propto \mathrm{dA}.e^{-\mathrm{Ep/kT}} \tag{2.16}$$

$$\mathrm{dn} = \mathrm{K}2\pi \mathrm{r}^2 \sin\theta d\theta.e^{-\mathrm{Ep/kT}} \tag{2.17}$$

when K is the proportionality constant. For unit radii of the sphere,

$$\mathrm{dn} = \mathrm{K}2\pi \sin\theta d\theta.e^{\mu H \cos\theta/kT} \tag{2.18}$$

$$\mathrm{n} = \int_0^n dn = 2\pi \mathrm{K} \int_o^\pi e^{\mu \mathrm{H} \cos\theta/kT} \sin\theta d\theta \tag{2.19}$$

Each magnetic moment vector contributes an amount of $\mu \cos\theta$ to the magnetization aligned with the applied magnetic field. Therefore, the total magnetization of the entire system can be determined by multiplying dn by the contribution $\mu \cos\theta$ and then integrating it across the total number i.e.

$$\mathrm{M} = \int_o^n \mu \cos\theta.dn \tag{2.20}$$

Substituting the value of dn and after carrying out the integration, we obtain,

$$\mathrm{M} = \mathrm{n}\mu \left[\cot \mathrm{h} \left(\frac{\mu \mathrm{H}}{kT}\right) - \left(\frac{\mathrm{kT}}{\mu \mathrm{H}}\right)\right] \tag{2.21}$$

$$\mathrm{M} = \mathrm{MoL}\,(\mathrm{x}) \tag{2.22}$$

When Mo = nμ which is the saturation magnetization, maximum magnetization value a material can possess i.e. it is a state of complete alignment of magnetic moment vectors and attainment of the complete saturation. Value of $\mathrm{x} = \frac{\mu \mathrm{H}}{kT}$ and

$$\mathrm{L}(\mathrm{x}) = \cot h(\mathrm{x}) - \left(\frac{1}{\mathrm{x}}\right). \tag{2.23}$$

L(x) is known as Langevin function (Cullity and Graham 2009; Spaldin 2011; Jiles 1996; Langevin 1905). The form of L(x) is shown below in Fig. 2.3. Here L(x) is expressed as a function of x.

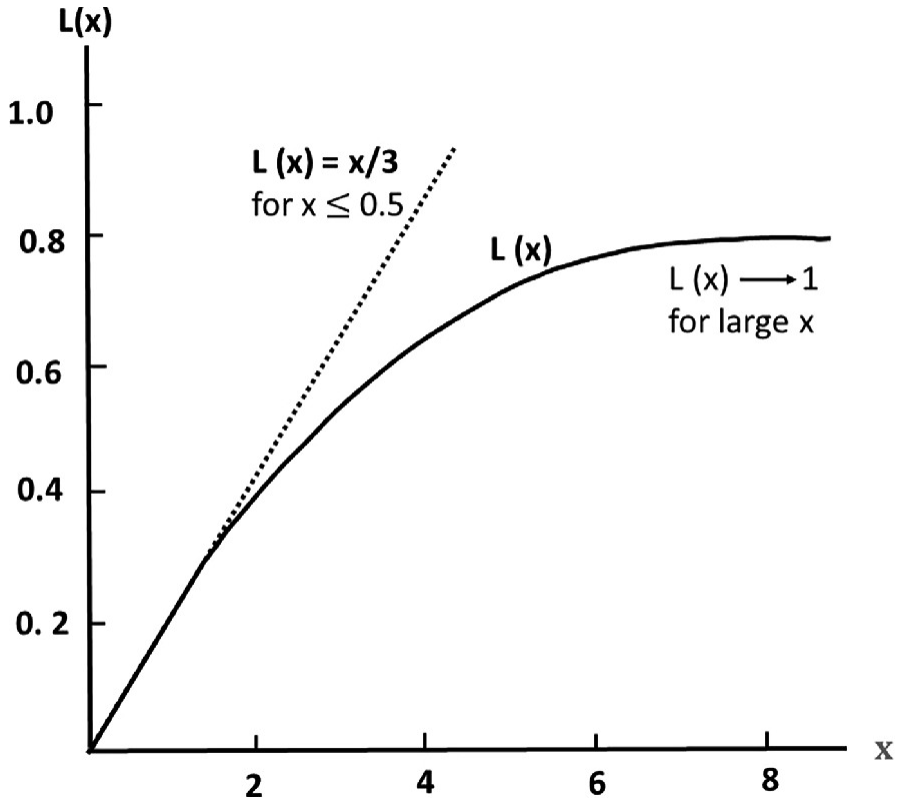

Fig. 2.3 Langevin Function, L(x). (Adapted and redrawn Cullity and Graham 2009)

At large x $\left(= \frac{\mu H}{kT}\right)$, $\mathrm{L}(\mathrm{x}) \to 1 \text{and for } \mathrm{x} \leq 0.5$, it forms a straight line having a slope of 1/3. Langevin theory of

Paramagnetism leads to two important conclusions:

(i) Saturation occurs when ‘x’ is very large. i.e. either by applying a very high field or lower temperature, or both, M would approach Mo (nμ). In other words, complete alignment of magnetic moment vectors towards the direction of the field lead to saturation.

(ii) For very small value of ‘x’, at ordinary temperature and normal field strength the curve shows linear behaviour, coinciding with the tangent to the curve at the origin. If we expand the Langevin function using Taylor series we obtain,

$$\mathrm{L}(\mathrm{x}) = \frac{\mathrm{x}}{3} - \frac{\mathrm{x}^3}{45} + \ldots\ldots\ldots \tag{2.24}$$

For a very small value of x it reduces to,
$\mathrm{L}(\mathrm{x}) \cong \frac{\mathrm{x}}{3}$ after substituting the values, we get,

$$\frac{\mathrm{M}}{\mathrm{Mo}} = \frac{\mu \mathrm{H}}{3kT} \tag{2.25}$$

$$\mathrm{M} = \frac{\mathrm{n}\mu^2\ \mathrm{H}}{3kT} \text{i.e.} \tag{2.26}$$

$$\frac{M}{\mathrm{H}} = \chi_{\mathrm{v}} = \frac{\mathrm{n}\mu^2}{3kT} \tag{2.27}$$

where χ_{v} is volume susceptibility. As $\mathrm{n} = \mathrm{N}_A\rho/\mathrm{A}$ when N_A is the Avogadro’s number, ρ is the density and A is the atomic mass. After substituting its value, we get,

$$\frac{M}{\rho H} = \frac{N_A\mu^2}{3\mathrm{A}kT} \tag{2.28}$$

$$\chi_{\mathrm{m}} = \frac{C}{T} \tag{2.29}$$

where $\mathrm{C} = \frac{N_A \mu^2}{3\mathrm{A}k}$ is a constant called Curie constant. The expression, $\chi_\mathrm{m} = \mathrm{C}/\mathrm{T}$ is called Curie law which indicates that susceptibility is inversely proportional to temperature. Thus Curie law holds good only for $\mu H \ll kT$. As discussed earlier, Langevin theory is based upon the assumption that the magnetic moment vectors associated with the atoms, molecules or the ions do not interact with each other. They are acted upon by the applied field and thermal randomization and so the net magnetization is the competitive effect of the two. Interestingly, it was observed experimentally that many paramagnetic materials do not obey Curie's law, rather they obey a more generic law called Curie–Weiss law. According to this law, susceptibility χ_m is related to temperature by a general expression,

$$\chi_\mathrm{m} = \frac{\mathrm{C}}{\mathrm{T} - \theta} \tag{2.30}$$

when θ has the dimension of temperature and it can be either positive or negative. Paramagnetic materials which obey Curie–Weiss law show spontaneous magnetization and behave as a ferromagnetic material below certain critical temperature called Curie temperature, Tc. In order to explain this phenomena, Weiss suggested that the elementary magnetic moment vectors do interact with each other unlike the assumption made by Langevin which was related to the presence of fictitious internal molecular field, $\mathrm{H_m}$. Weiss also assumed that the intensity of the internal molecular field, $\mathrm{H_m}$ is proportional to the magnetization M of the material

$$\text{i.e. } \mathrm{H_m} \propto \mathrm{M} \tag{2.31}$$

$$\text{or } \mathrm{H_m} = \gamma \mathrm{M} \tag{2.32}$$

where γ is the molecular field constant. Total field ($\mathrm{H_{total}}$) experienced by the material is,

$$H_{total} = H_{ext} + H_m \tag{2.33}$$

Therefore, the Curie law is given by,

$$\chi_m = \frac{M}{\rho H_{total}} = \frac{C}{T} \tag{2.34}$$

After substituting the value of H_{total} the value of susceptibility is obtained as,

$$\frac{M}{\rho H_{ext}} = \frac{C}{T - C\rho\gamma} \tag{2.35}$$

$$\chi_m = \frac{C}{T - \theta} \tag{2.36}$$

where $\theta = C\rho\gamma$ which is the measure of the interaction (Spaldin 2011). In substances following Curie law, where $\theta = C\rho\gamma$, there's no internal molecular field as $\theta = C\rho\gamma = 0$. However, for substances following Curie–Weiss law, when $T = C\rho\gamma$, susceptibility diverges, indicating the transition to a spontaneously ordered phase, leading to Ferromagnetism. Near the transition temperature (Tc), the value of θ is approximately equal to Curie temperature. Below Tc, paramagnetic materials exhibit ferromagnetism, while above Tc, thermal energy overpowers the internal molecular field (H_m), destroying magnetic ordering. Positive θ values show the molecular field reinforcing the applied field, increasing magnetization. Negative θ values indicate the internal molecular field opposing the applied field, decreasing magnetization. Antiferromagnetism, with negative θ, has a transition temperature (Néel temperature, T_N) occurring at a positive temperature. Variation of the mass susceptibility with temperature is shown in Fig. 2.4. Further discussion will be given in the later section of the chapter

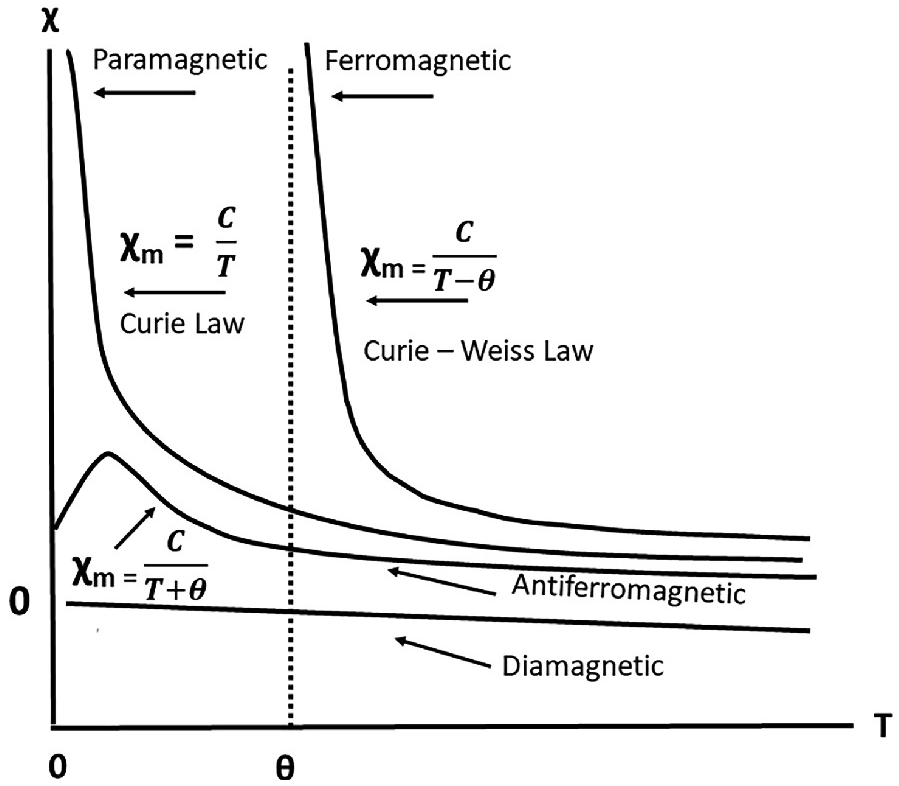

Fig. 2.4 Variation of Mass Susceptibility with temperature

In the quantum mechanical theory of paramagnetism, magnetic moment vectors (μ) are limited to specific directions in response to an applied field (H). This limitation is known as spatial quantization, primarily represented by the total angular momentum (J). In an atom with multiple electrons, the total angular momentum (J) is defined by combining the total orbital angular momentum (L) and total spin momentum (S). This combination, J = L + S is typically called Russel-Saunders coupling. The effective net magnetic moment (μ_{eff}) of an atom is connected to the total angular momentum (J) and the spectroscopic splitting factor (g factor). This relationship is expressed as $\mu_{\text{eff}} = \mathrm{g}\sqrt{\mathrm{J}(\ \mathrm{J}+1)}\mu_B$ Additionally, the magnetic moment component (μ_H) in the direction of the magnetic field is denoted by $\mu_{\mathrm{H}} = \mathrm{g}\mathrm{M}_{\mathrm{J}}\mu_{\mathrm{B}}$, where M_J is the quantum number associated with the total magnetic moment (J). Allowed

values for M_J include $J,\ J-1,\ J-2\cdots-J$, resulting in a total of $(2J+1)$ numbers representing μ_H.

So if we incorporate the space quantization rules and follow the procedure similar to the classical theory of Paramagnetism, we obtain (Cullity and Graham 2009),

$$M = ngJ\mu_B\left[\frac{2J+1}{2J}\coth\left(\frac{2J+1}{2J}\right)x' - \frac{1}{2J}\coth\frac{x'}{2J}\right] \tag{2.37}$$

where $x' = \frac{gJ\mu_B H}{kT} = \frac{\mu_H H}{kT}$

$$\text{i.e. } ngJ\mu_B = n\mu_H = Mo \tag{2.38}$$

i.e. product of total number of atoms per unit volume and the maximum moment of atoms aligned at the direction of the magnetic field applied is the saturation magnetization value. This gives,

$$\frac{M}{Mo} = \frac{2J+1}{2J}\coth\left(\frac{2J+1}{2J}\right)x' - \frac{1}{2J}\coth\frac{x'}{2J} \tag{2.39}$$

Expression on the right hand side is called Brillouin function and is abbreviated as $B(J,x')$. We can have two cases:

$$\text{If } x' \ll 1, \text{we have, } \coth x' \cong \frac{1}{x'} + \frac{x'}{3} \tag{2.40}$$

This gives,

$$B(J,x') \cong \frac{x'(J+1)}{3J} \tag{2.41}$$

After substituting its value, we obtain a result for the susceptibility which is,

$$\chi_v = \frac{M}{H} = \frac{nJ(J+1)g^2\mu_B}{3kT} = \frac{n\mu_{eff}^2}{3kT} = \frac{C}{T} \tag{2.42}$$

Mass susceptibility χ_m is given by,

$$\chi_{\mathrm{m}} = \frac{\chi_{\mathrm{v}}}{\rho} = \frac{M}{\rho H} = \frac{\mathrm{n}\mu_{\mathrm{eff}}^2}{3\rho \mathrm{kT}} = \frac{\mathrm{N}\mu_{\mathrm{eff}}^2}{3A\mathrm{kT}} = \frac{\mathrm{C}}{\mathrm{T}} \tag{2.43}$$

when N is the Avogadro's number and A is the atomic weight. If μ_{eff}^2 refers to a molecule rather than an atom then atomic weight A needs to be replaced by molecular weight M´. Overall expression for susceptibility remains same as that of classical case of paramagnetism except that the value of Curie constant $\mathrm{C} = \frac{\mathrm{Nn}\mu_{\mathrm{eff}}^2}{3A\mathrm{k}}$.

Therefore, the expression for Curie law $\chi_{\mathrm{m}} = \frac{\mathrm{C}}{\mathrm{T}}$ is regained. The expression is represented in cgs unit and to obtain susceptibility in SI units this expression needs to be multiplied by μ_{o}

If $\mathrm{x}' \gg 1$ i.e. at low temperature and strong field the Brillouin function reduces to,

$$\mathrm{B}(\mathrm{J}, \mathrm{x}') \cong 1 \text{ i.e.} \tag{2.44}$$

$$\mathrm{M} \cong \mathrm{Mo} \cong \mathrm{ngJ}\mu_{\mathrm{B}} \tag{2.45}$$

This expression shows the state of magnetic saturation $(\mathrm{M} \cong \mathrm{Mo})$ and is analogous to the Langevin's classical expression of paramagnetism. That means Brillouin function has two important limits with respect to the value of J. When J = 1/2 there are only two allowed states and it reduces to

$$\frac{M}{Mo} = \tanh x' \tag{2.46}$$

However, when $\mathrm{J} \to \infty$, this reduces to Langevin function L(x). i.e. for large number of allowed magnetic moment vectors, the quantum mechanical results approach the classical one.

Knowing the value of J and that of the g-factor of the ion, we can calculate the effective magnetic moment value from the equation, $\mu_{\mathrm{eff}} = \mathrm{g}\sqrt{\mathrm{J}\ (\mathrm{J}+1)}\,\mu_{\mathrm{B}}$ The value of J can be

determined by applying Hund's rule. Generally, this formula works well for the paramagnetic salt with rare earth ions. However, for the first row transition metals, calculated value doesn't match with that of the experimental value, rather the magnetic moment values are closer if we completely ignore the orbital angular momentum value (L). This is known as quenching of the orbital angular momentum and this is due to the presence of the electric field gradient generated by the surrounding ions/ligands in the solids. This electric field causes the orbitals to be strongly coupled to the crystal lattice. So whenever an external magnetic field is applied to orient the magnetic moment vectors towards the direction of field, the lattice-orbit coupling resist the orientation. Therefore, the orbital magnetic moments (L) do not contribute to the total magnetization value and the observed value is equal to that of the spin only value. $\mu_{\text{eff}} = \text{g}\sqrt{\text{S}\ (\text{S}+1)}\,\mu_{\text{B}}$

A very good example to justify this is by taking a case of Mn^{3+} ($3d^4$) ions. The value of susceptibility as obtained from the above expression and $S = 2$ corroborate well with that of experimental value whereas after incorporating the orbital magnetic moments, the calculated susceptibility value is zero (Spaldin 2011; Kittel 1996).

2.2.3 Ferromagnetism

As discussed in the section of paramagnetism, ferromagnetism too is due to the presence of uncompensated magnetic moment vectors, however, unlike paramagnetism, this involves magnetic phenomena which is at least a million times stronger. This is due to the presence of a very strong internal molecular field, H_m which results in magnetic ordering leading to spontaneous magnetization below θ (γρC) value, even in the absence of an externally applied field. Above θ which is actually the Curie temperature Tc, the magnetically ordered

ferromagnet undergo phase transition to magnetically disordered paramagnet and its susceptibility follows Curie–Weiss law: $\chi_m = \frac{C}{T-\theta}$. Therefore, at Tc the interaction energy due to the internal molecular field i.e. $\mu_B H_m$ becomes approximately equal to the thermal energy ($k_B Tc$). For example, iron having $T_C \cong 1000$ K, approximate value of internal molecular field, $H_m \approx (10^{-16})\ (10^3)/10^{-20} \approx 10^7$ Oe. This is an extraordinarily large value! Therefore, for the ferromagnetic material at temperature well below the Curie temperature T_C, there exists spontaneous magnetic ordering even in the absence of an externally applied magnetic field owing to such strong internal magnetic field. However, there must be more to this as if there would have been only internal molecular field then every piece of iron, cobalt or nickel would have significant amount of magnetic moments. But in reality this is not the case rather they are present in their demagnetized state. In order to address this, Weiss made few very innovative assumptions which are as follows:

(i) Within each ferromagnetic material, there exist many small regions called domains. Each domain is separated from each other by a wall called domain wall.

(ii) Each domain is spontaneously magnetized to its saturation value, M_o. This is due to the presence of an internal molecular field H_m and is assumed to be proportional to the total magnetization of each domain i.e. $H_m = \gamma M$. Though, each of the domains are magnetized to its saturation value, in the absence of any externally applied field total magnetization of the material is zero. This is owing to the fact that the magnetic moment vectors of each domain are so oriented that they get cancelled out completely.

Therefore, we can consider a ferromagnetic material as being paramagnet having a huge internal molecular field. In other words, we can use theory of paramagnetism to understand ferromagnetism. As discussed earlier, Langevin theory of paramagnetism is given by, $\frac{\mathrm{M}}{\mathrm{Mo}} = \mathrm{L}(\mathrm{x}) = \coth(\mathrm{x}) - \left(\frac{1}{\mathrm{x}}\right)$ where L(x) is Langevin function and $\mathrm{x} = \frac{\mu \mathrm{H}}{k\mathrm{T}}$. At a fixed temperature say T, the variation of magnetization as a function of "x" $\left(= \frac{\mu H}{k\mathrm{T}}\right)$ is represented by a curve, say 1 (see Fig. 2.5). If the field acting on the material is only Weiss internal molecular field $\mathrm{H_m}$, i.e. in absence of any externally applied field the expression for "x" is given by, $\mathrm{x} = \frac{\mu \mathrm{H_m}}{k\mathrm{T}} = \frac{\mu\gamma \mathrm{M}}{k\mathrm{T}} = \frac{\mu\gamma \mathrm{M}}{k\mathrm{T}} \frac{\mathrm{Mo}}{\mathrm{Mo}}$.

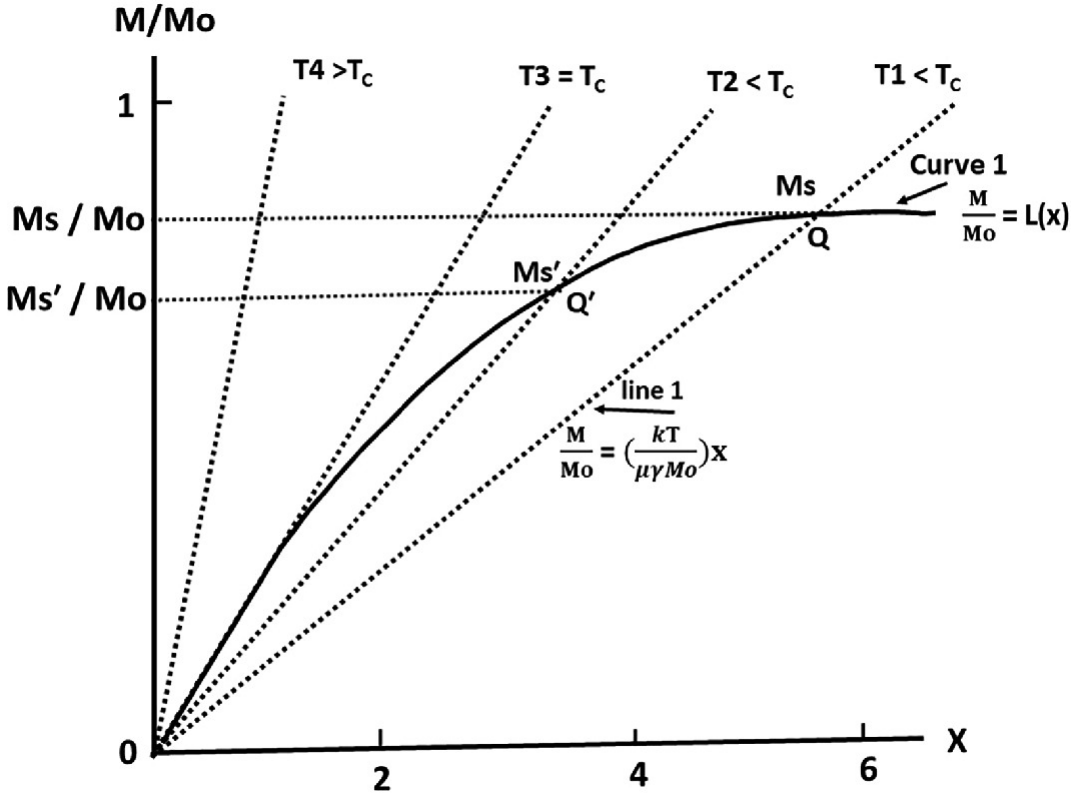

Fig. 2.5 Variation of spontaneous magnetization with temperature. Curve 1 represents Langevin function and dotted line 1 shows linear variation of magnetization with "x" when only Weiss internal molecular field $\mathrm{H_m}$ is present

Or,

$$\frac{\mathrm{M}}{\mathrm{Mo}} = (\frac{k\mathrm{T}}{\mu\gamma\mathrm{Mo}})\mathrm{x} \tag{2.47}$$

This clearly shows that $\frac{\mathrm{M}}{\mathrm{Mo}}$ varies linearly with “x”. The straight line passes through the origin and the slope is proportional to the absolute temperature. At some temperature T1, say it is lower to Curie Temperature Tc, the variation of magnetization is a straight line and is represented by the dotted line 1 of the Fig. 2.5. The straight line intersects the Langevin plot at Q which corresponds to the spontaneous magnetization, Ms owing to the presence of an internal molecular field. As we increase the temperature from T1 to T2, the line intersects the Langevin curve at Q′, which corresponds to lower spontaneous magnetization value of Ms′. At a temperature T3 equal to the Curie temperarture ($\mathrm{T_C}$) the line is tangent to the Langevin function at the origin. Intersection of the two curves at point 0 indicates magnetization corresponding to this point is unstable and hence spontaneous magnetization is zero. It is therefore important to note that the effect of increasing the temperature is to move the spontaneous magnetization Ms to lower and lower values on Langevin curve 1 and at a temperature equal to Tc, spontaneous magnetization vanishes. At any temperature above its Curie temperature, say T4, the material is paramagnetic because it is not spontaneously magnetized (Cullity and Graham 2009). Variation of spontaneous magnetization with temperature can be clearly understood from Fig. 2.5.

The value of Curie temperature can be evaluated from the slope of Langevin curve passing through origin, which is 1/3. i.e.

$$\frac{k\mathrm{T_C}}{\mu\gamma\mathrm{M_o}} = \frac{1}{3} \tag{2.48}$$

Or,

$$\mathrm{Tc} = \frac{\mu\gamma \mathrm{M_o}}{3k} \tag{2.49}$$

Therefore, for the materials, subjected to molecular field only, the slope of the straight line at any temperature is given by, $\frac{k\mathrm{T}}{\mu\gamma \mathrm{M_o}} = \frac{\mathrm{T}}{3\mathrm{T_c}}$. This represents the slope of the line with a particular value of Ms/Mo. In other words, the fraction of spontaneous magnetization Ms/Mo can be solely determined by the ratio T/Tc. Therefore, for different ferromagnetic materials, having different values of Mo and Tc, it will have the same value of Ms/Mo for any particular value of T/Tc. This is known as law of corresponding state (Cullity and Graham 2009). As we increase the temperature, thermal randomization increases leading to the overall decrease in the total magnetization. It is important to note that as we increase the temperature, number of atoms per unit volume may change due to thermal expansion. Therefore, while dealing with the change in magnetization with temperature, we must measure specific magnetization (σ) as this allow us to measure magnetic moment per unit mass. The relationship between σ and M is given by,

$$\frac{\sigma_\mathrm{s}}{\sigma_\mathrm{o}} = \frac{\mathrm{M_s}\rho_\mathrm{o}}{\mathrm{M_o}\rho_\mathrm{s}} \tag{2.50}$$

where σ_s and σ_o are the specific magnetization at TK and OK respectively. ρ_s and ρ_o are densities at these temperatures. Therefore, correct definition of the law of corresponding state is that materials having same value of σ_s/σ_o will also have the same value of T/Tc. The variation of specific magnetization with temperature for ferromagnetic materials Ni, Co and Fe is shown in Fig. 2.6.

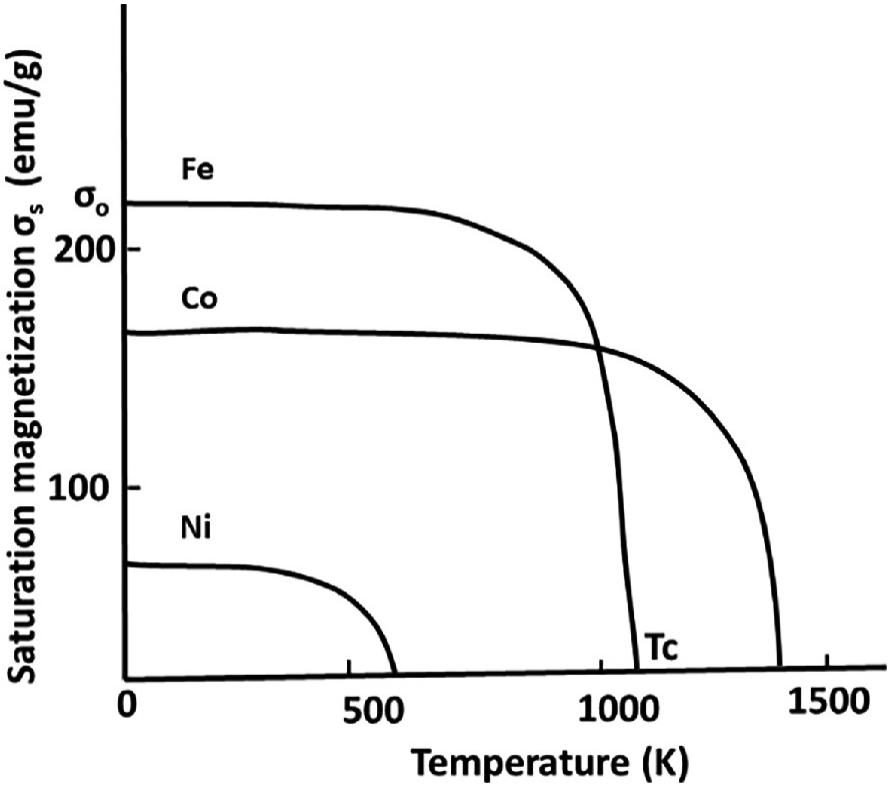

Fig. 2.6 Representation of variation of saturation magnetization of Fe, Co, and Ni as a function of temperature. (Adapted and redrawn Cullity and Graham 2009)

The magnetization is maximum at OK as the magnetic moment vectors are aligned in a particular direction under the influence of an internal molecular field. As we increase the temperature, the magnetization decreases due to thermal randomization and further at the Curie temperature T_C it undergoes ferromagnetic to paramagnetic transition.

To test the law of corresponding states, the experimental points, expressed as σs/σo vs T/Tc, were graphed. The results revealed a close conformity of the points to a single curve. However, it was observed that the curve's shape, as predicted by the classical Langevin function, didn't align well with the experimental values. A more accurate plot can be achieved by substituting the classical Langevin function with the quantum mechanical Brillouin function, utilizing an appropriately chosen J. The

more general expression for magnetization is then derived from this function:

$$\frac{\sigma}{\sigma o} = \frac{2J+1}{2J}\coth\left(\frac{2J+1}{2J}\right)x' - \frac{1}{2J}\coth\frac{x'}{2J} \tag{2.51}$$

$$\frac{\sigma}{\sigma o} = B(J, x') \tag{2.52}$$

when $x' = \frac{gJ\mu_B H}{kT}$. A change from magnetization, M to specific magnetization, σ also involves a change in the internal molecular field constant γ. As $H_m = \gamma M = \gamma\rho(M/\rho) = \gamma\rho\sigma$. Here γρ becomes the internal molecular field constant. Therefore, a linear variation of $\sigma/\sigma o$ with x' representing internal molecular field is given by the following equation,

$$\frac{\sigma}{\sigma o} = \left(\frac{kT}{gJ\mu_B\gamma\rho\sigma o}\right)x' \tag{2.53}$$

Figure 2.7 displays how the spontaneous magnetization values of Fe, Co, and Ni change with temperature. The predictions were made using the classical Langevin theory and the Brillouin function with J values of 1 and 1/2. The results show that Langevin theory with $J = \infty$ doesn't match the experimental data well (Tyler 1931). On the other hand, the theoretical curves based on the Brillouin function align quite well with the experiment, especially the curve for J = ½.

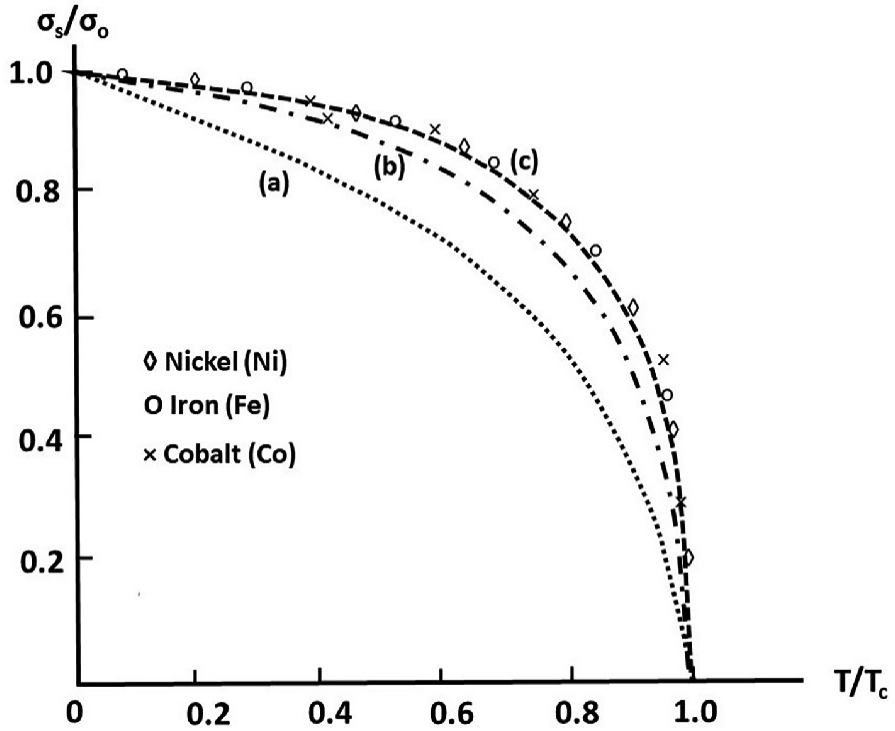

Fig. 2.7 Saturation magnetization versus temperature plots of iron (Fe), cobalt (Co), and nickel (Ni). The curves are calculated using the Langevin function with $J = \infty$ (**a**) and the Brillouin function with $J = 1$ (**b**) and $J = 1/2$ (**c**). (Adapted and redrawn Tyler 1931)

2.2.3.1 Origin of Weiss Internal Molecular Field: Exchange Interaction

The Weiss internal molecular field theory explains how ferromagnetic materials exhibit spontaneous magnetization below the Curie temperature, T_c and transition to behaving like paramagnetic materials above this temperature, following the Curie–Weiss law. However, it doesn't clarify the origin and nature of this internal molecular field. The field due to magnetic dipole–dipole interaction is only around 10^3 G, much lower than the actual molecular field strengths observed, like the Weiss molecular field in iron, which is as high as 10^7 G.

In 1928, Heisenberg proposed that the internal molecular field's physical origin results from the quantum mechanical exchange interaction between neighbouring

atoms. This exchange interaction arises from the Pauli Exclusion Principle, where any change in the relative orientation of two spins disturbs the spatial distribution of charges, allowing interaction between atoms. The strength of this exchange interaction depends on the overlap of wave functions and the relative orientation of spins (Cullity and Graham 2009; Spaldin 2011; Jiles 1996; Valenzuela 1994).

The Pauli exclusion principle enhances the probability of electron wave function overlap for antiparallel spins and tends to keep spins apart for parallel spins. This is a form of electrostatic interaction. Combining this with Columbic interaction results in different energies for spin configurations, parallel and antiparallel. Following Heitler-London theory, Heisenberg showed that the exchange energy between two atoms with spin angular momentum $S_i h/2\pi$ and $S_j h/2\pi$ is given by,

$$E_{ex} = -2J_{ex}S_i \cdot S_j = -2J_{ex}S_iS_j \cos\varphi \tag{2.54}$$

When Jex is the exchange integral and φ is the angle between the two spins.

If J_{ex} is positive, E_{ex} is minimum and hence more stable for the parallel alignment of the spins $(\cos\varphi = 1)$ whereas E_{ex} will take its maximum value when the spins are antiparallel $(\cos\varphi = -1)$. On the other hand, if J_{ex} is negative, then the lowest energy and hence most stable state is achieved for the antiparallel spins. Therefore, a positive value of exchange integral J_{ex} is a necessary condition for ferromagnetism to occur whereas a negative value of J_{ex}, lead to the occurrence of antiferromagnetism. In other words, quantum mechanically exchange interaction is a strong driving force for the cooperative parallel alignment of the magnetic moment vectors.

2.2.4 Antiferromagnetism

Antiferromagnetism occurs when the interaction between magnetic moments leads to the alignment of adjacent magnetic moment vectors in an antiparallel direction (refer to Fig. 2.8).

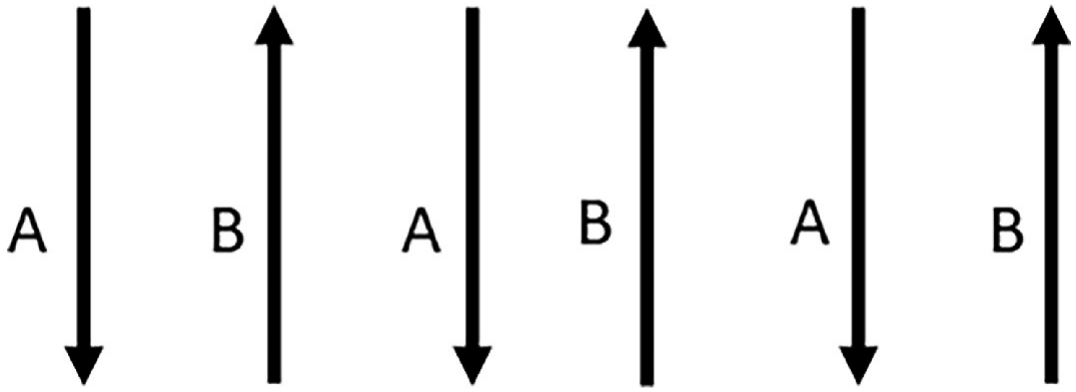

Fig. 2.8 Antiparallel alignment of spin magnetic moments in A and B sublattices showing antiferromagnetism

When there's no external magnetic field, neighbouring magnetic moment vectors cancel each other out, resulting in the material showing no overall magnetization. However, when an external magnetic field is applied, a small magnetization emerges in the direction of the field. This magnetization increases as the temperature rises, reaching its maximum at a critical temperature known as the Neel temperature, T_N. Beyond this temperature, the magnetization steadily decreases, indicating the material's transition to a paramagnetic state. In essence, the Neel temperature, T_N, serves a similar role to the Curie temperature, T_c, in ferromagnetic materials, marking the boundary between magnetically ordered (below) and magnetically disordered (above) regions on the temperature scale (See Fig. 2.4).

The theory of antiferromagnetism was first developed by Néel (1932) in 1932 where he utilized Weiss internal molecular field theory to explain the problem. In a crystal displaying antiferromagnetism, there are two identical

sublattices of magnetic ions, labelled A and B, with spontaneous saturation magnetization in the absence of an applied magnetic field. However, their magnetic moment vectors are aligned in opposite directions. For antiferromagnetic materials, the interactions between adjacent atoms A and B (A-B) are considered crucial, while A-A and B-B interactions can be ignored. Each sublattice, A and B, has its internal molecular field denoted as $\mathrm{H_m^A}$ and $\mathrm{H_m^B}$, respectively. Since the internal molecular field is proportional to magnetization, the field acting on sublattice A with magnetization value of $\mathrm{M_A}$ is proportional but opposite in direction to the magnetization $\mathrm{M_B}$ of sublattice B i.e. $\mathrm{H_m^A} = -\gamma \mathrm{M_B}$.

Similarily, for the internal molecular field which acts on the sublattice B,

$$\mathrm{H_m^B} = -\gamma \mathrm{M_A} \tag{2.55}$$

where $\mathrm{M_A}$ is the magnetization of the sublattice A. The minus sign shows that in antiferromagnetic alignment, the internal molecular field of one sublattice opposes the magnetization of the other sublattice. $\mathrm{T_o}$ find the total magnetization $(\mathrm{M_A} + \mathrm{M_B})$ of the material, we analyze their behavior above and below the Neel temperature, $\mathrm{T_N}$. Above this temperature, the material acts as paramagnetic, and the magnetization of the two sublattices, following Curie's law, can be expressed as,

$$\mathrm{M_A} = \frac{\mathrm{n}\mu^2 H_A}{3\mathrm{kT}} \tag{2.56}$$

$$\mathrm{M_B} = \frac{\mathrm{n}\mu^2 H_B}{3\mathrm{kT}} \tag{2.57}$$

Total magnetization M is given by,

$$\mathrm{M} = \mathrm{M_A} + \mathrm{M_B} \tag{2.58}$$

$$= \frac{n\mu^2}{3kT}(H_A + H_B) \tag{2.59}$$

If H is the externally applied field and H_m^A is the internal molecular field at sublattice A, then the effective field experienced by sublattice A is given by,

$$H_A = H + H_m^A = H + (-\gamma M_B) \tag{2.60}$$

Similarly,

$$H_B = H + H_m^B = H + (-\gamma M_A) \tag{2.61}$$

Therefore,

$$M = \frac{n\mu^2}{3kT}(H - \gamma M_B + H - \gamma M_A) \tag{2.62}$$

$$M = \frac{n\mu^2}{3kT}(2H - \gamma M) \tag{2.63}$$

This yields the expression for susceptibility as,

$$\chi = \frac{M}{H} = \frac{\frac{2n\mu^2}{3k}}{T + \frac{n\gamma\mu^2}{3k}} = \frac{C}{T + \theta} = \frac{C}{T - (-\theta)} \tag{2.64}$$

where,

$$C = \frac{2n\mu^2}{3k} \text{and } \theta = \frac{n\gamma\mu^2}{3k}$$

This expression is similar to the Curie–Weiss law applied to ferromagnetic materials above the critical temperature, T_c. The difference lies in the denominator, which contains the term $T + \theta$ instead of T-θ. Essentially, these materials have a negative value for θ. Since θ is directly linked to the internal molecular field coefficient, γ, the effect of the Weiss internal molecular field H_m in the paramagnetic region is to counteract the influence of the applied field H. While H attempts to align magnetic moment vectors in its

direction, H_m works to disalign them. In simpler terms, the exchange integral, J_{ex}, in antiferromagnetic materials is negative, resulting in a smaller susceptibility (χ) compared to ideal paramagnetic materials with zero internal molecular field. On the other hand, ferromagnetic materials with a large positive internal molecular field H_m exhibit much higher susceptibility.

Figure 2.9(A) illustrates the dependence of inverse susceptibility on the molecular field, H_m, for a constant Curie constant C. It demonstrates how χ changes with temperature T in two scenarios: one with a large positive molecular field, characteristic of ferromagnetic materials above their Curie temperature, and the other with a negative molecular field, typical of antiferromagnetic substances (Néel 1948). The alignment of magnetic moment vectors for these materials is depicted in Fig. 2.9(B)

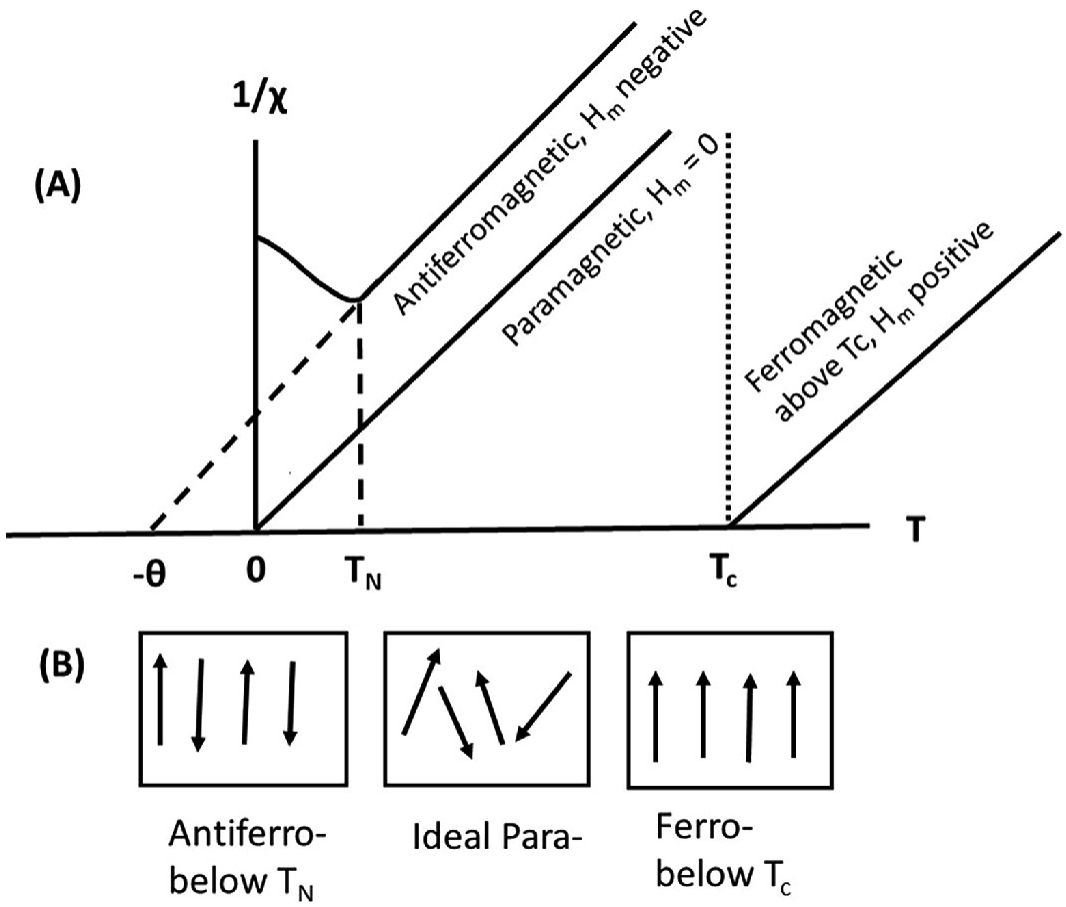

Fig. 2.9 Variation of inverse susceptibility as a function of temperature for a fixed Curie temperature (**A**) and alignment of magnetic moment vectors (**B**)

Weiss internal molecular theory of Antiferromagnetism predicts that at the Neel temperature T_N is equal to θ. Below Neel temperature, each of the sublattices are spontaneously magnetized along their preferred crystallographic axis, when field applied is zero. The spontaneous magnetization to its saturation value is due to the presence of strong internal molecular field created by other sublattice. Below T_N, system orders and therefore the susceptibility decrease with the decrease in the temperature as the extent of antiparallel alignment of the neighbouring spins increases. As $M_A = -M_B$, at 0 K, the net spontaneous magnetization is zero. However, an applied field can produce a small magnetization and the resulting susceptibility is governed by the angle which the applied

field makes with the preferred crystallographic axis. We can have two possibilities (Cullity and Graham 2009; Spaldin 2011): The field can be applied either (a) parallel, or (b) perpendicular to the preferred crystallographic axis. The susceptibility in these two directions can be determined separately whereas in powdered or the polycrystalline samples, which have no preferred orientation of the crystals, the average overall possible orientations is taken to calculate the net susceptibility, χ_p. It can be shown that below Neel temperature, susceptibility, $\chi_\perp$ is independent of temperature when the field is applied in the perpendicular direction. On the other hand, if the field is in the parallel direction the susceptibility, $\chi_\parallel$ decreases continuously and approaches zero at $T \rightarrow 0$ K as at 0 K the sublattices are perfectly aligned, antiparallel to each other. Therefore, at 0 K, the internal molecular field is so strong that it does not allow the magnetic moment vectors of sublattices to change their orientation even in the presence of an external magnetic field.

2.2.4.1 Antiferromagnetic Materials

Many antiferromagnetic materials are ionic compounds, including metallic oxides, sulfides, chlorides, and more. Chromium (Cr) and Manganese (Mn) have complicated antiferromagnetic structure, although their susceptibility does not obey Curie–Weiss law. The antiferromagntic ordering in the case of most of these ionic compounds occurs through indirect exchange interaction mechanism called superexchange interaction. Let's take the example of the ionic compound MnO. Manganese ion (Mn^{2+}) has five valence electrons in its 3d orbitals, filling all five and aligning them parallel to each other. On the other hand, the oxygen ion (O^{2-}) has an electronic configuration resembling neon, with filled shells and two superimposed

orbits—one with a net spin up and the other with a net spin down. When a Mn^{2+} ion with all up-spin gets close to an O^{2-} ion, covalent bonding can take place. In this process, the neighboring oxygen ion donates its down-spin electron, leaving an up-spin electron in the oxygen p orbital. This electron is then capable of being donated to the adjacent Mn^{2+} ion, completing the interaction. This way oxygen-mediated interaction leads to an overall antiferromagnetic alignment between the Mn^{2+} ions. The strength of the coupling between two antiparallel spins of metal ions is governed by the M–O–M angle and it is generally greatest if M–O–M is collinear or if the angle is 180° (Cullity and Graham 2009; Spaldin 2011). This type of anion mediated interaction between the metal ions is called superexchange interaction and the details are shown in the Fig. 2.10.

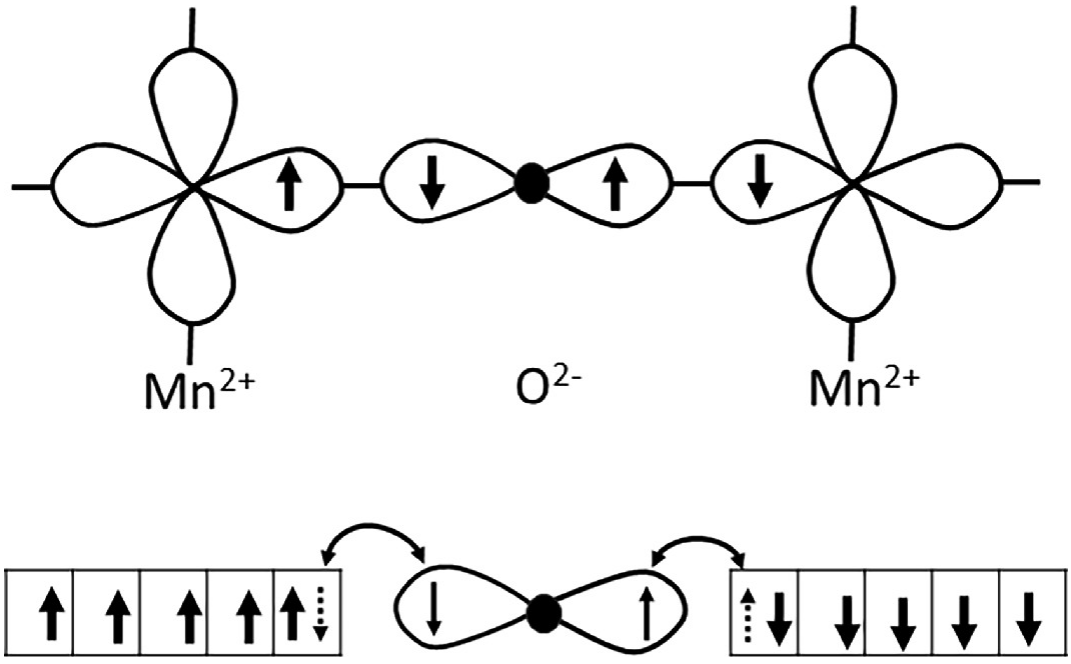

Fig. 2.10 Schematic representation of superexchange interactions in MnO. (Adapted and redrawn Spaldin 2011)

2.2.5 Ferrimagnetism

Ferrimagnetic materials are similar to antiferromagnets in which the magnetic moment vectors of two adjacent

sublattices couple through superexchange interaction leading to antiparallel alignment of the localized moments. However, unlike an antiferromagnet, the magnetization of the two neighbouring sublattices have different magnitudes which result in a non-zero value of overall magnetization. In fact, ferrimagnets are also related to ferromagnets as both exhibit hysteresis and below Curie temperature, T_c show spontaneous magnetization even in the absence of an externally applied field. Above T_C, the spontaneous magnetization is destroyed due to thermal randomization and the system behaves paramagnetically. The nature of temperature dependent magnetization curves in ferrimagnetic materials is distinctly different from that of the ferromagnetic materials as it can be seen in Fig. 2.11. Near the T_C value χ^{-1} versus T is curved for the ferrimagnetic materials. The orientation of the magnetic moment vectors for ferromagnetic and ferrimagnetic lattice below and above T_c are also represented in Fig. 2.11.

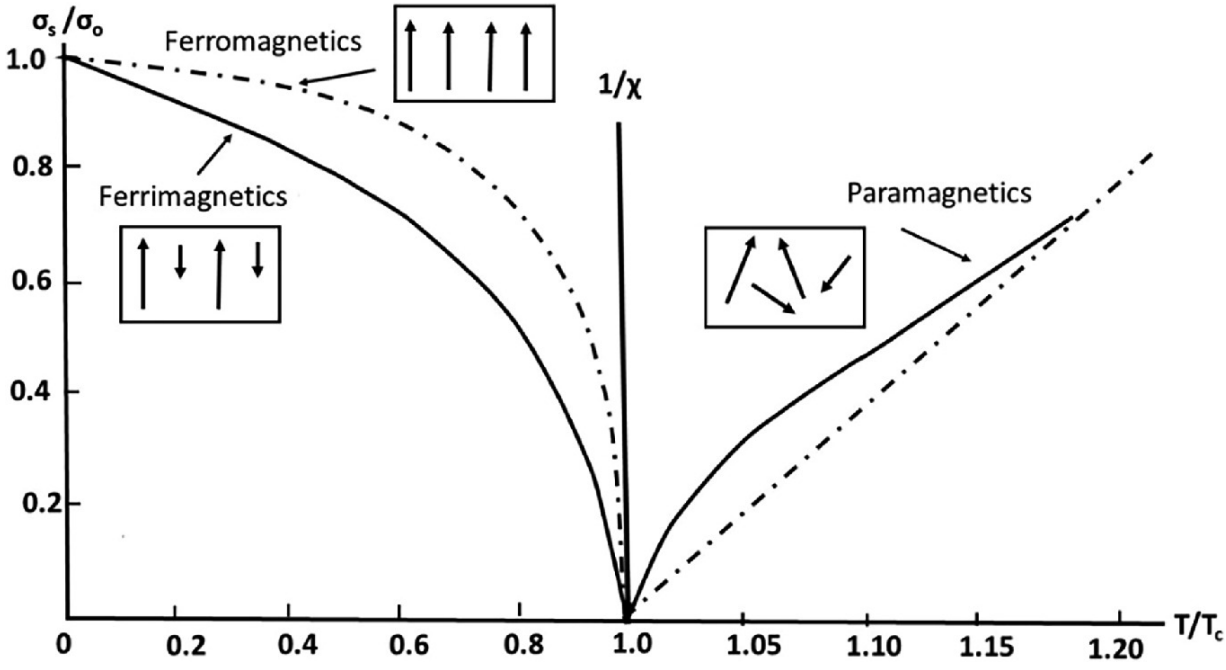

Fig. 2.11 Schematic representation of temperature dependent magnetization behaviour (specific magnetization and inverse susceptibility) in standard

Corresponding orientation of the magnetic moment vectors below and above T_c are represented inside the rectangular boxes.

Neel pioneered the theory of Ferrimagnetism using Weiss internal molecular field theory. However, unlike antiferromagnets, the A and B sublattices in ferrimagnets are not structurally identical. They may consist of different atomic species or have the same ions at sites with different symmetry. This means considering all three interactions: A-B, A-A, and B-B interactions. A-B interactions drive antiparallel alignment of magnetic moment vectors, while A-A and B-B interactions lead to parallel alignment. A detailed explanation of magnetization in ferrimagnets using internal molecular field theory is beyond the scope of this chapter. Important ferrimagnetic materials include certain double oxides of iron and another metal, known as ferrites. Depending on the crystal structure of ferrites, they are classified as (i) Cubic and (ii) Hexagonal ferrite materials.

2.2.5.1 Cubic Ferrites

Cubic ferrites possess a spinel crystal structure, named after the mineral spinel ($MgO.Al_2O_3$). This structure consists of eight formula units, 8 [$MO.\ Fe_2O_3$], or a total of $8 \times 7 = 56$ ions per unit cell. The face-centered cubic framework forms due to the closely packed large oxygen ions with a radius of about 0.14 nm. This arrangement leads to the creation of two distinct interstitial sites namely tetrahedral (A site) and octahedral (B site). The tetrahedral site, located at the centre of a tetrahedron with corners occupied by oxygen ions, contrasts with the octahedral site, surrounded by oxygen ions forming an octahedron. It’s noteworthy that while a unit cell contains 64 A sites and 32 B sites, out of these only 1/8th of the tetrahedral sites and 1/2 of the octahedral sites are occupied. Smaller cations

with ionic radii ranging from 0.04 nm to 0.09 nm fill these sites. Although various cation combinations may form a spinel structure, the specific site occupancy of cations is governed by factors such as covalent bonding effects and crystal field stabilization energies of transition metal cations (Cullity and Graham 2009; Spaldin 2011; Jiles 1996; Valenzuela 1994).

Cubic ferrites, as described by the general formula $MO.Fe_2O_3$, involve divalent metal ions M such as Mn^{2+}, Ni^{2+}, Fe^{2+}, Co^{2+}, Zn^{2+}, Mg^{2+} and so on. Among all, notably, cobalt ferrite ($CoO.Fe_2O_3$) stands out as a magnetically hard ferrite material, distinguishing itself from other ferrites that are generally magnetically soft. Magnetite, recognized as the oldest magnetic material known to humanity, also falls into the category of cubic ferrite materials with the formula $FeO.Fe_2O_3$ or Fe_3O_4. The crystal structure of the cubic ferrite is shown in the Fig. 2.12.

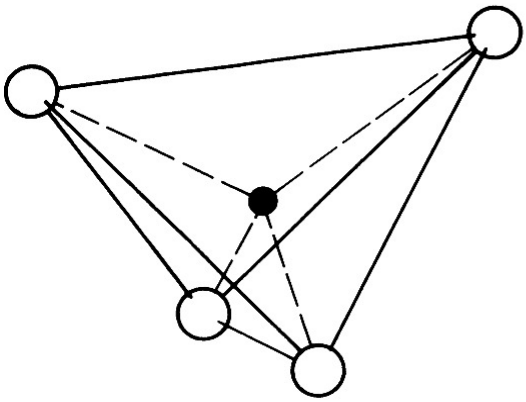

(a) Tetrahedral *A* site

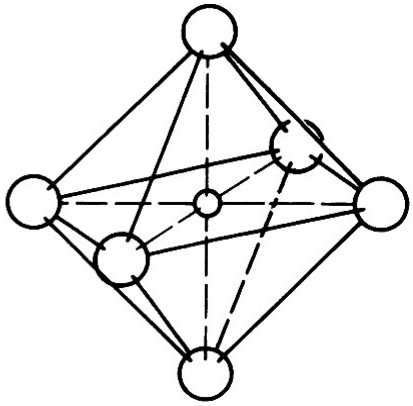

(b) Octahedral *B* site

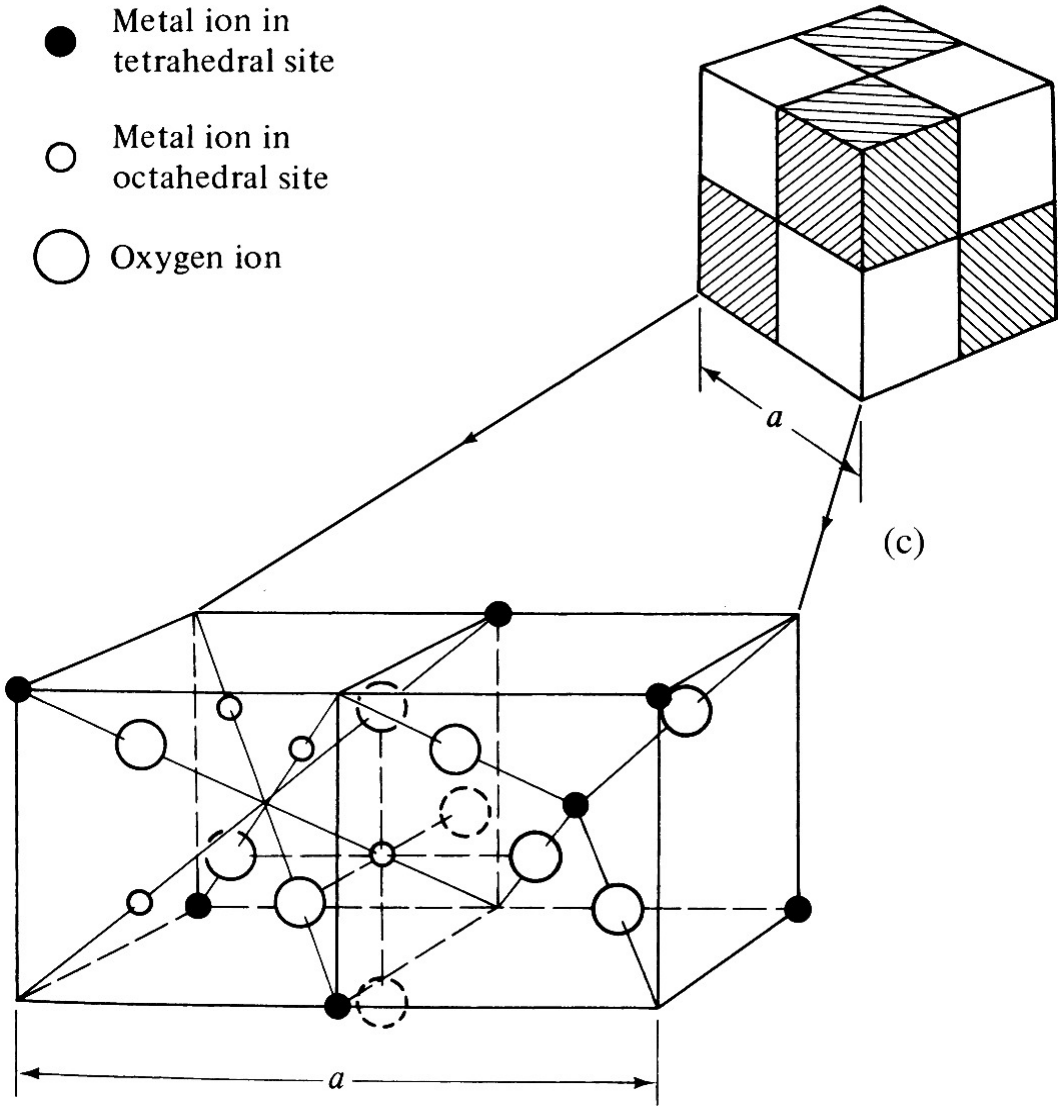

(c)

(d)

Fig. 2.12 Crystal structure of Cubic Ferrites. Source: (Cullity and Graham 2009). Reprinted by permission of John Wiley & Sons

Spinels come in two main types: normal and inverse, depending on how the cations are arranged. They are also named based on combinations of cation valency, like 2, 3 (seen in $NiFe_2O_4$), 1, 3 (found in $Li_{0.5}Fe_{2.5}O_4$), 2, 4 (as in Co_2GeO_4), 1, 3, 4 (as in $LiFeTiO_4$), and 1, 2, 5 (as in $LiNiVO_4$). When used in magnetic materials, $MgO.Al_2O_3$ spinels often see Al^{3+} replaced by Fe^{3+}. In normal spinel structures, M^{2+} ions are in tetrahedral A sites, and Fe^{3+} ions take up octahedral B sites, as seen in examples like zinc ferrite ($ZnO.Fe_2O_3$) and cadmium ferrite ($CdO.Fe_2O_3$). In inverse spinels, Fe^{3+} ions are evenly split between A and B sites, pushing divalent ions to the remaining B sites. Examples include ferrites of iron (Fe), cobalt (Co), and nickel (Ni), all displaying ferrimagnetism. There's also a possibility of intermediate cation distribution, where both A and B sites have divalent and Fe^{3+} cations. The degree of inversion is influenced by preparation techniques, especially the cooling rate, and this structure is termed mixed inverse spinel.

Most ferrites have an ionic bond, where cations are surrounded by anions, and vice versa. Because cations are quite far apart, strong ferromagnetic interactions are not common. This results in a prevalent antiferromagnetic arrangement in the magnetic ordering of ferrites, where cation interactions happen through anions, known as superexchange interaction. The strongest superexchange interaction occurs between octahedral and tetrahedral cations, forming A-O-B interactions at an angle of about 135°. In normal spinels like $ZnO.Fe_2O_3$ and $CdO.Fe_2O_3$, where divalent cations Zn^{2+} and Cd^{2+} lack magnetic moments for A-O-B magnetic ordering, the net Fe^{3+}– Fe^{3+} interaction is weak, leading to paramagnetism. On the

other hand, in inverse spinels, the saturation magnetization at 0 K relies on the magnetic moment of divalent cations. The dominant antiferromagnetic A-O-B interaction aligns the spin moments of Fe^{3+} ions on octahedral sites oppositely to those on tetrahedral positions, cancelling their magnetic moments. However, the moments of all divalent ions align in the same direction, contributing to the net magnetization. The saturation magnetization of a ferrimagnetic solid is calculated by multiplying the net spin magnetic moment of each divalent cation by the concentration of divalent cations (Cullity and Graham 2009).

Table 2.1 provides the saturation magnetization values per formula unit for certain significant ferrites, where 'n' represents the number of magnetic moments per formula unit.

Table 2.1 Magnetization data for various ferrite materials. (Adapted and compiled from Cullity and Graham 2009 and Smit and Wijn 1959)

			0 K		**300 K**	
Ferrites	T_C (K)	n (μ_B)	σ_o	M_0	σ_o	M_S
		(calc)	emu/g	emu/cm^3	emu/g	emu/cm^3
$FeO.Fe_2O_3$	858	4	98	510	92	480
$MnO.Fe_2O_3$	573	5	112	560	80	400
$CoO.Fe_2O_3$	793	3	90	475	80	425
$NiO.Fe_2O_3$	858	2	56	300	50	270
$CuO.Fe_2O_3$	728	1	30	160	25	135

In the ferrimagnetic region below the Curie temperature (Tc), each sublattice undergoes spontaneous magnetization due to the presence of an internal molecular field. However, the magnetizations of the two sublattices oppose each other. As each sublattice has its unique temperature

dependence, the overall temperature-dependent magnetization is determined by the difference in sublattice magnetization. This leads to a diverse range of magnetization curves anticipated for ferrite materials. Figure 2.13 illustrates magnetization curves for some spinels.

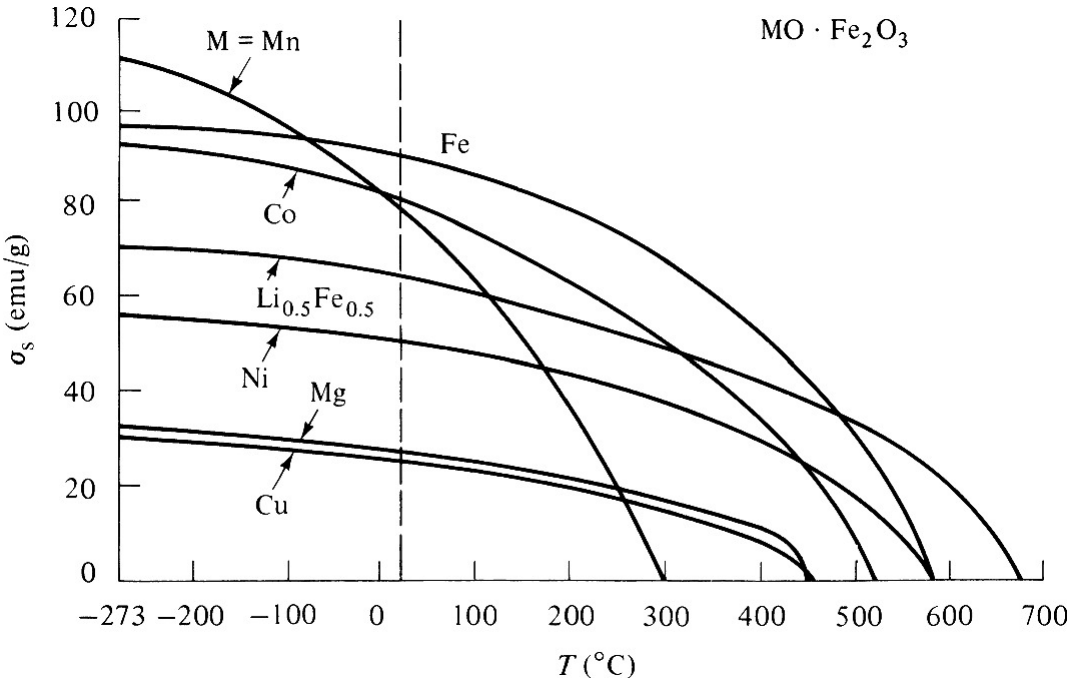

Fig. 2.13 Temperature-dependent saturation magnetization for various cubic ferrimagnets. Source: (Cullity and Graham 2009). Reprinted by permission of John Wiley & Sons

Additionally, depending upon the cations and their distribution in A and B sites of spinel structure, magnetic properties can be widely modified and precisely tuned for specific applications.

As the cubic ferrites are magnetically soft i.e. they can be easily magnetized and demagnetized giving thin hysteresis loop. Additionally, due to the high permeability, saturation magnetization value combined with low electrical conductivity, are particularly appropriate for high frequency applications as their high electrical resistivity reduces the formation of undesirable eddy currents and high permeability value helps in concentrating the flux

density inside the induction coil thereby enhancing the inductance value.

2.2.5.2 Hexagonal Ferrite Materials

Hexaferrites are a type of ferrites that share a hexagonal magnetoplumbite crystal structure. All hexaferrites exhibit ferrimagnetic properties, and their magnetization is closely connected to their specific crystal arrangement. The magnetic mineral magnetoplumbite was initially identified in 1925 with the composition $PbFe_{7.5}Mn_{3.5}Al_{0.5}Ti_{0.5}O_{19}$. The revelation that hexaferrites possess the magnetoplumbite crystal structure emerged post-World War II during research conducted at Philips Laboratories.

Based on this structure, first synthetic hexaferrite materials was found to be $PbFe_{12}O_{19}$. Further during 1950s number of isomorphous compounds were developed which included $BaFe_{12}O_{19}$ and $SrFe_{12}O_{19}$. It was in 1952 when the $BaFe_{12}O_{19}$ hexaferrite material was commercialized. It is important to note that the Fe ions in the Barium ferrites occupy the same positions as the mixture of Fe, Mn, Al and Ti in magnetoplumbite. Since their discovery, there has been a profound increase in the research work owing to their massive technological and commercial applications.

The family of hexaferrites is based on magnetoplumbite crystal structure which belong to the hexagonal space group $P6_3/mmc$. To describe the planes of hexagonal crystal structure, four miller indices h, k, l, i are needed. The last one indicating the c-axis and the first three (h, k, l) indicating the in-plane orientation of the unit vectors placed at 120^o from each other as it is seen in the Fig. 2.14.

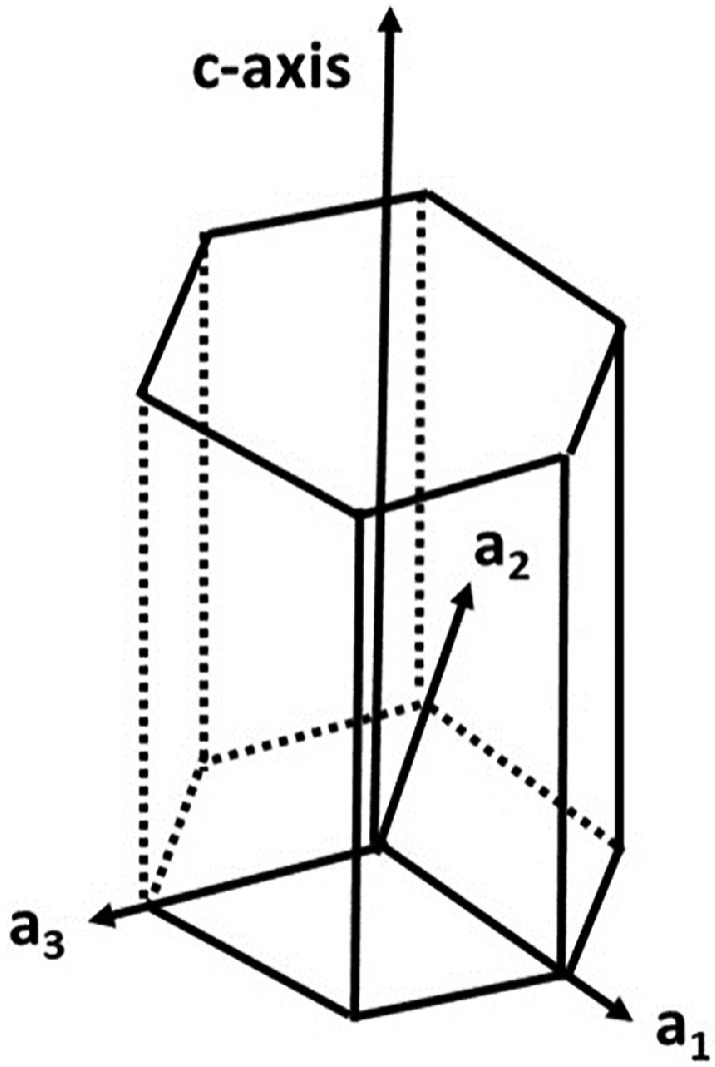

Fig. 2.14 Hexagonal crystal structure showing c—axis as easy axis of magnetization

The magnetoplumbite crystal structure is composed of closely packed oxygen anions and larger divalent cations like Ba^{2+}, Sr^{2+}, Pb^{2+}. The smaller Fe^{3+} cations fill the spaces in between. A hexagonal ferrite unit cell consists of two formula units, i.e. $2 \times 32 = 64$ atoms. To envision the crystal structure, picture it as having 10 oxygen layers in its basic unit, constructed from four building blocks labeled S, S*, R, and R*, all arranged along the c-axis. The S and S* blocks are spinels with two oxygen layers, featuring Fe^{3+} ions in the interstices. The Fe_6O_8 composition are obtained from the stacking sequence of oxygen ions in the ABCABC

(face-centered cubic, fcc) pattern, with four Fe^{3+} ions in octahedral sites, all with parallel spins, and two in tetrahedral sites, with spins opposite to the octahedral ones. The S and S* blocks are similar but are rotated 180° with respect to each other. The R block comprises three oxygen layers in an ABABAB (hexagonal closed-packed, hcp) sequence, with one oxygen anion replaced by a divalent ion. Each R block has six Fe^{3+} ions, five in octahedral sites with varying spin configurations, and one coordinated by five O^{2-} anions with a spin-up configuration. Thus, the R block has a composition of $BaFe_6O_{11}$. Similar to S and S* blocks, R and R* are equivalent but rotated 180° relative to each other (Spaldin 2011).

The magnetic structure of M-type hexaferrite, such as $BaFe_{12}O_{19}$, follows the Neel model of antiferromagnetism. In $BaFe_{12}O_{19}$, the only magnetic ions are Fe^{3+} ions, each having a moment of $5\mu_B$. These ions occupy three different interstitial sites: tetrahedral, octahedral, and hexahedral. Among the 24 Fe^{3+} ions per formula unit, four are in tetrahedral sites, 18 in octahedral, and two in hexahedral. Considering superexchange interactions, 16 Fe^{3+} ions point in one direction, while 8 spins point in the opposite direction. Therefore, the magnetic moment per unit cell is (16–8) (5) = 40 μ_B, or per formula ($BaO.6Fe_2O_3$), it is 20 μ_B.

The hexaferrites, benefiting from the hexagonal magnetoplumbite crystal structure, possess a distinct internal effective magnetic field, H_m. This field is associated with the magnetocrystalline anisotropy parallel to the c-axis, extending out of the hexagonal crystal's basal plane. This characteristic makes hexaferrites useful as permanent magnets, in magnetic recording media and data storage materials, as well as high-frequency electronic components and electromagnetic absorbers.

2.2.6 Magnetic Phenomena

2.2.6.1 Magnetic Domain and Hysteresis

Let's explore the idea of magnetic domains and hysteresis. According to the Weiss theory, a strong internal molecular field, H_m, can magnetize a material to its full saturation even without an external field. However, ferromagnetic materials like iron did not show net magnetization unless placed in an external field. In 1906, Weiss explained this by suggesting that in their demagnetized state, ferromagnetic materials are divided into small regions called domains. Each domain is spontaneously magnetized due to the internal molecular field, originating from quantum mechanical exchange interactions between neighbouring atoms, as explained by Heisenberg in 1928. The boundaries between two adjacent domains are called domain walls. Although the magnetic moment vectors of different domains are randomly oriented, they cancel each other out, resulting in zero net magnetization. In the presence of an external field, domains favourably oriented toward the field direction grow at the expense of unfavourably oriented domains. With a higher magnetic field, the magnetic moment vectors rotate toward the field direction, leading to material saturation. Therefore, magnetization involves two processes: (a) Domain wall motion and (b) Domain rotation.

Before we go any further, let's understand why these magnetic domains form. According to Neel, ferromagnetic materials form domain structures to minimize the total energy of the material. The exchange energy prefers a single domain structure where all magnetic moment vectors align in the same direction. Although a single domain minimizes exchange energy, there are other contributors to total energy, like magnetostatic energy, magnetocrystalline energy, magnetostrictive energy and domain wall energy. Among these, the driving force to form

domain structure is the minimization of magnetostatic energy.

For example, in a magnetized block of single domain ferromagnetic material, free poles at the ends create an external magnetic field that tries to magnetize the block in the opposite direction. This demagnetizing field causes magnetostatic energy. To minimize this energy, one way is to reduce the impact of the external demagnetizing field by subdividing domains into smaller ones. However, this subdivision can’t go on forever because forming domain walls requires additional energy. Thus, ferromagnetic materials have a domain structure made up of smaller domains, representing a state of minimum energy. To virtually eliminate magnetostatic energy, keeping all magnetic flux within the system, closure domains are formed. Figure 2.15 illustrates this entire process (Kittel 1996).

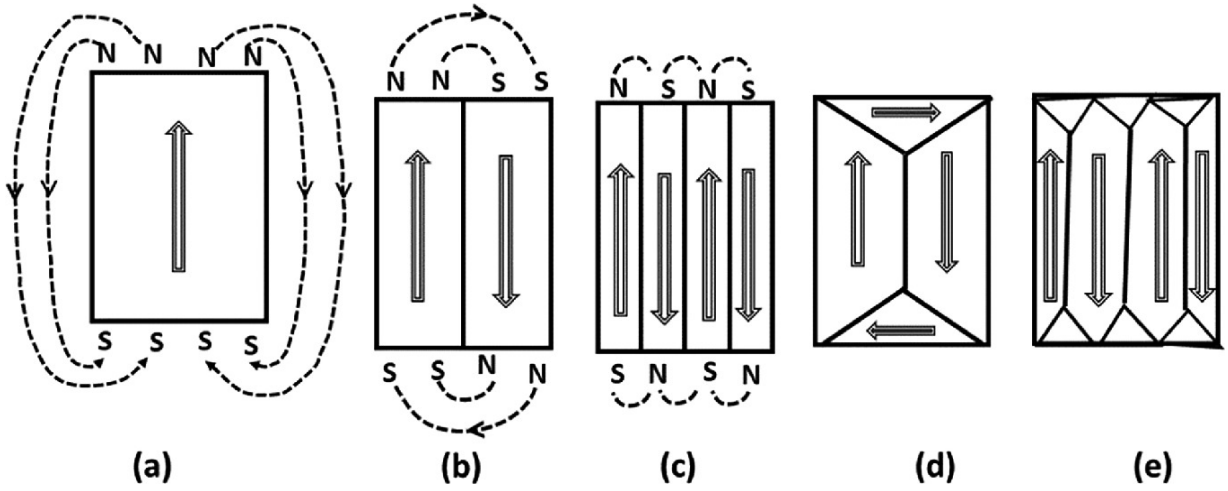

Fig. 2.15 Minimization of magnetostatic energy through the subdivision of magnetic domains. (Adapted and redrawn Kittel 1996)

The formation of a domain wall happens when the competitive effects of exchange energy and magnetocrystalline energy balance out. Exchange energy likes magnetic moment vectors to align parallel, so it prefers a wide domain wall, where the change in angle

between neighbouring domains is as small as possible. This means the 180° difference in spin alignments between adjacent domains can be spread among many spins, favouring a thick domain wall (Cullity and Graham 2009; Spaldin 2011; Kittel 1996).

Conversely, magnetocrystalline anisotropy is most effective when magnetic moment vectors align parallel to their easy axis of magnetization. However, since the magnetic moment vectors inside the wall aren't along the easy axis, magnetocrystalline anisotropy tends to narrow down the wall thickness. In the end, a balance between exchange energy (which tries to make the wall as wide as possible) and magnetocrystalline energy (which tries to make the wall as thin as possible) results in minimization of the total energy within the material's boundary, leading to an optimal wall thickness.

The domains and domain walls that are most energetically favourable are those that avoid forming magnetic poles, as this prevents contributions to magnetostatic energy. An illustrative example of such a wall is the twist 180° boundary (Kittel 1996). Fig. 2.16 provides a visual representation of the changes in the orientation of magnetic dipole moments within a 180° twist boundary, showcasing the intricacies of this process.

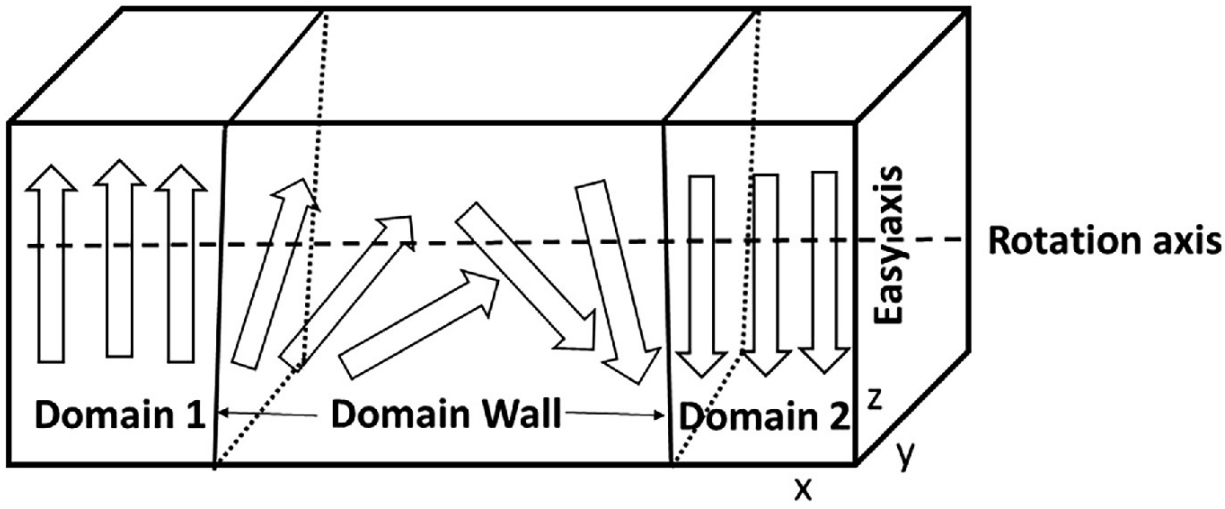

Fig. 2.16 Orientation of magnetic moment vectors within a 180° twist boundary. (Adapted and redrawn Kittel 1996)

As mentioned before, when a ferromagnetic material is exposed to an external magnetic field, it becomes magnetized. This magnetization process includes two key steps:

(a) Domain Wall Motion: This step involves the growth of domains that are already aligned favourably with the applied magnetic field. Further, these domains expand at the cost of less favourably aligned domains.

(b) Rotation of Magnetic Moments: In this step, the magnetic moment vectors of various domains rotate in the direction of the external magnetic field.
Figure 2.17 provides a visual representation of these two magnetization processes.

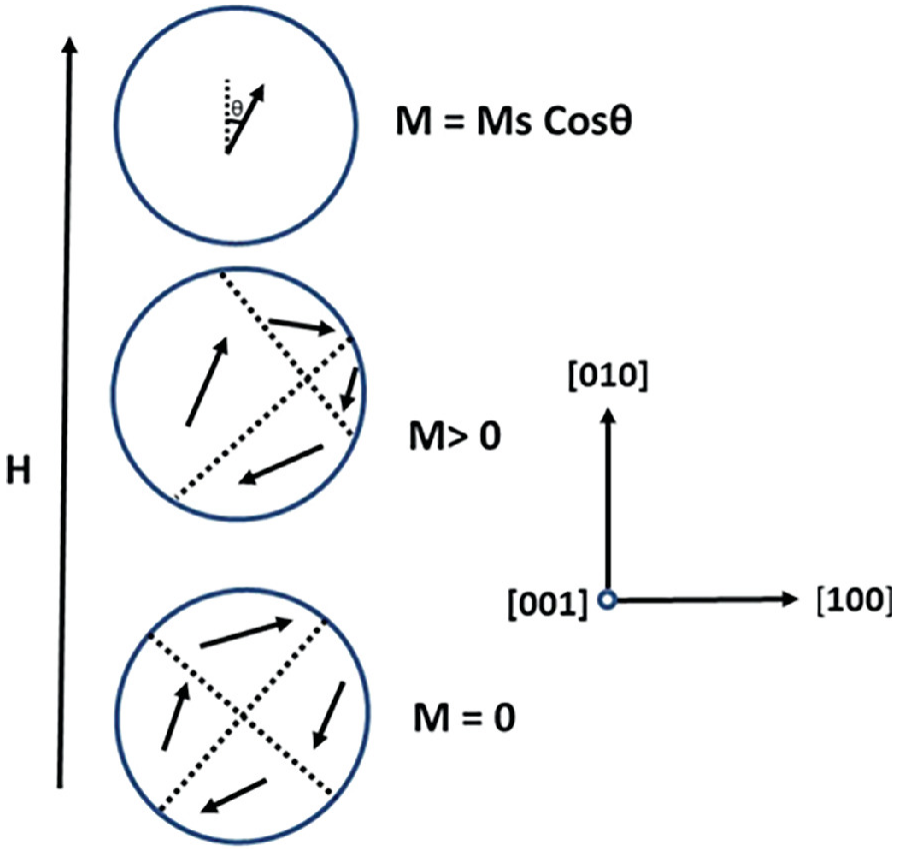

Fig. 2.17 Alteration in the arrangement of domains throughout the magnetization process

Figure 2.18 illustrates the process of magnetization and the resulting hysteresis. When a ferromagnetic material encounters a small magnetic field, especially along the [010] crystallographic axis, the domains aligned with the field direction grow, displacing less favourably oriented domains. This leads to a small magnetization, represented by the initial part (OA) of the hysteresis curve. This displacement of domain boundaries is called domain wall motion, and it's mostly reversible.

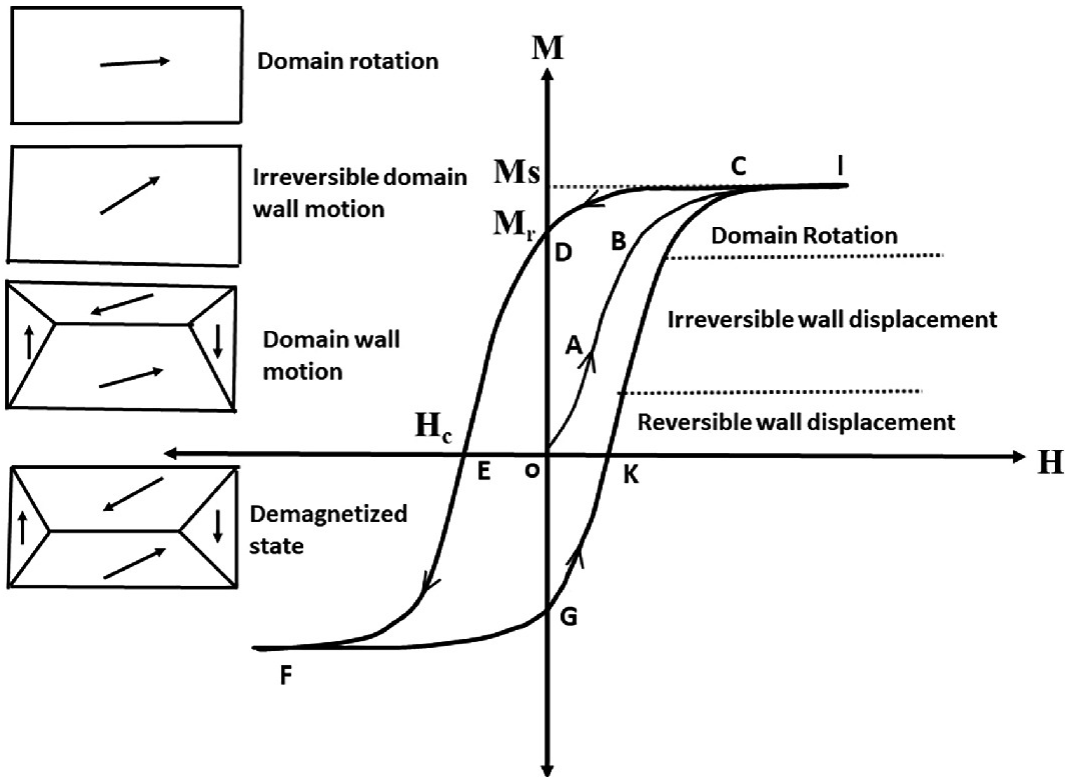

Fig. 2.18 Hysteresis loop and corresponding domain structure

As the applied field strengthens, more domains contribute to a substantial increase in magnetization (portion AB). The domain wall motion in this phase becomes irreversible. With further increase in the strength of the field, the favourably oriented domains keep growing until they reach their maximum limit. The magnetic

moment vectors are still aligned along the easy axis of magnetization. Continued field strengthening causes the magnetic moment vectors to rotate from the easy axis to the field direction. The magnetization value increases, reaching its maximum, known as saturation magnetization, Ms (portion BCI), where all magnetic moment vectors align with the field direction. While going back when the magnetic field decreases to zero, the magnetization doesn't follow the initial curve but lags behind. Some non-zero magnetization persists even when the field is zero, termed remanent magnetization or remanence, M_r. To reduce this magnetization to zero, a reverse magnetic field must be applied, known as coercive field (H_c) or coercivity.

A similar pattern occurs in the reverse magnetization when the strength of the reverse magnetic field is increased and then decreased to zero. This non-reversible behaviour in the magnetization curve, forming the closed loop CEFGKC, is termed the Hysteresis loop. The crucial points along this loop are M_s, M_r, and H_c, and their values are significant in determining the suitability of a magnetic material for a specific purpose. Materials with high M_r and large H_c are labeled as hard magnetic materials and are crucial for making permanent magnets. On the flip side, materials that can be easily magnetized and demagnetized, having small M_r and H_c values, are referred to as soft magnetic materials. These materials find applications in transformer cores and electronic circuits.

2.2.6.2 Magnetic Anisotropy

Magnetic anisotropy refers to the dependence of magnetic properties on the direction in which they are measured. Essentially, the characteristics of a magnetic material are significantly influenced by the direction of measurement. The nature of magnetic anisotropy plays a crucial role in determining the suitability of a magnetic material for a

specific application. Various types of magnetic anisotropy exist, including intrinsic forms such as magnetocrystalline anisotropy, shape anisotropy, and stress anisotropy. Additionally, anisotropy can be induced through processes like annealing or irradiation. Another noteworthy form of anisotropy, acting at interfaces, is known as exchange anisotropy (Cullity and Graham 2009; Spaldin 2011; Jiles 1996; Valenzuela 1994).

Among these, magnetocrystalline anisotropy, or crystal anisotropy, is particularly vital as it strongly influences magnetization. In the following discussion, we will briefly explore magnetocrystalline anisotropy shedding light on their significance in understanding and utilizing magnetic materials.

2.2.6.3 Magnetocrystalline Anisotropy

Magnetocrystalline anisotropy originates from the fact that there is a tendency of magnetic moment vectors to remain aligned along the preferred crystallographic axis. That means the ease of obtaining saturation magnetization is different for different crystallographic axis. The preferred axis along which the saturation is achieved at quite low field is called easy axis of magnetization. Different materials with different crystal structures have different easy axes of magnetization. For example, single crystal sample of iron (Fe) having body centered cubic crystal structure M_s is most easily obtained when measured along <100> , less easily when measured along <110> and it is most difficult when measured along <111> crystallographic axis. The crystallographic axis along which huge amounts of magnetic field is applied to achieve saturation magnetization is called hard axis of magnetization. Therefore, for iron sample, <100> is the easy axis of magnetization whereas <111> is the hard axis of magnetization. For face cantered cubic Ni sample, the easy

axis of magnetization is <111> and hard axis of magnetization is <100> . For Fe and Ni which are cubic and they have three axes. On the other hand, cobalt being hexagonal, its single c-axis acts as its easy axis of magnetization.

The magnetocrystalline anisotropy energy can be studied by creating a {110} disk from a single crystal of material, as illustrated in Fig. 2.19. Then, measure the magnetization curve with varying magnetic fields along [001], [110], and [111] crystallographic axes within the disk. Figure 2.20 shows schematic magnetization curves for single crystals of ferromagnetic Fe and Ni, with the magnetic field applied along both their easy and hard axes.

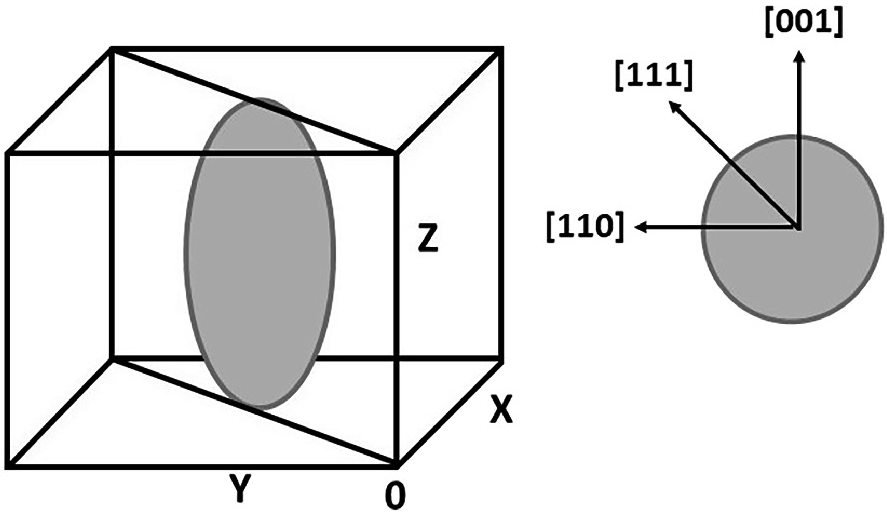

Fig. 2.19 Single crystal with cubic crystal structure is cut in the form of a disk parallel to {110} plane. (Adapted and redrawn Spaldin 2011)

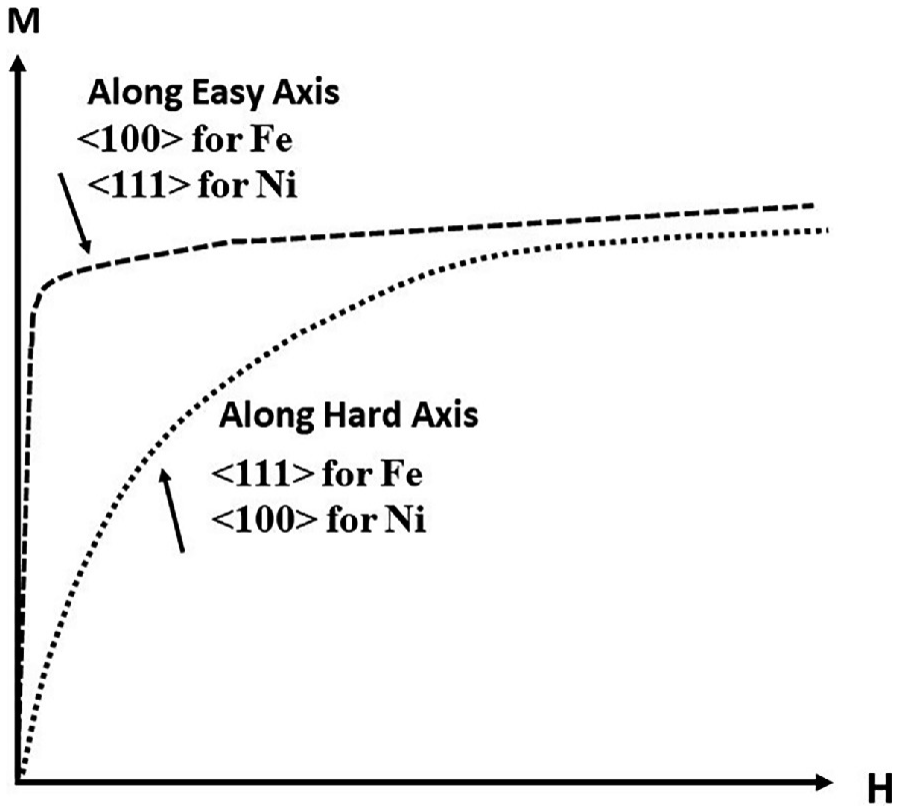

Fig. 2.20 Illustration of magnetization curve when the field is applied along the easy and hard axes of a single crystal

It's crucial to understand that saturation magnetization is reached along both the easy and hard axes. However, a significantly larger applied magnetic field is needed to achieve saturation along the hard axis compared to the easy axis.

This concept provides insights into demagnetized states of materials. In this state, materials spontaneously align their magnetic moments with the easy axis of magnetization. When an external magnetic field is applied in a different direction, it must work against the anisotropy force to rotate the magnetic moment vectors away from the easy axis toward the direction of the applied field. The energy needed for this rotation is called anisotropy energy. Magnetocrystalline anisotropy, originating from spin–orbit coupling, is a result of the resistance encountered when trying to reorient the electronic orbits as the external field attempts to align the spin magnetic moment of a domain

system. This resistance, measured as the energy required to overcome spin–orbit coupling, defines the magnetocrystalline anisotropy energy (Cullity and Graham 2009; Spaldin 2011; Jiles 1996; Valenzuela 1994). Therefore, the systems with strong orbit-lattice coupling exhibit quenched orbital magnetic moments, with the total magnetic moment arising solely from the spin magnetic moments of the system.

2.2.7 Fine Particles Magnetism

Magnetism in fine particles has traditionally been explained through the size effect, which is rooted in the magnetic domain structure of these materials. As discussed in the domain formation section, the balance between magnetocrystalline energy and exchange energy leads to a optimum domain wall width of around 100 nm. Therefore, particles smaller than this threshold lack sufficient space for domain walls, resulting in the formation of single domain particles. The idea is that when we talk about the state with the lowest free energy in ferromagnetic particles, smaller particles tend to have a uniform magnetization (single domain particles), while larger ones show non-uniform magnetization (multi-domain particles). To simplify, as particle size decreases towards a critical diameter say d_{sd}, it becomes energetically unfavourable for domain walls to form, classifying particles as single domain. This implies that changes in magnetization no longer happens through domain wall motion; instead, they need the coherent rotation of spins, resulting in higher coercivities. As the particle size further decreases below d_{sd}, coercivity decreases due to thermal effects until it drops to zero at another critical size say d_{sp}. Experimental investigations into how coercivity relates to particle size show a behaviour similar to what's illustrated in Fig. 2.21.

This entire concept provides insights into how magnetism behaves in particles of different sizes.

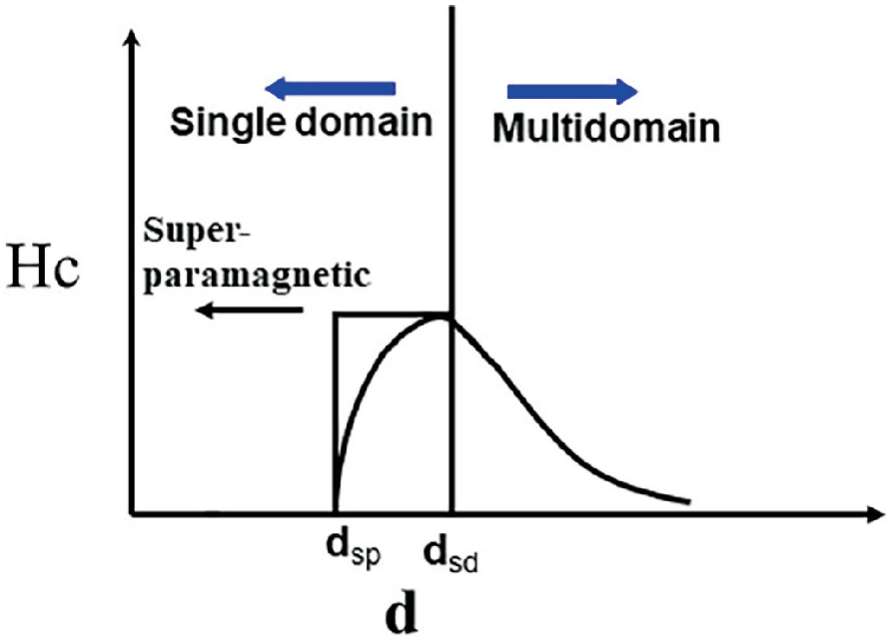

Fig. 2.21 Variation of coercivity with particle size (diameter). Critical size d_{sd} and d_{sp} represent single domain and superparamagnetic particle size

An essential aspect of magnetic nanoparticles is that their magnetic anisotropy energy, expressed as $E_A = KV$, where K represents the anisotropy constant, and V is the particle's volume. In simpler terms, magnetic anisotropy ensures that the magnetic moment vectors stay aligned with the particle's easy axis of magnetization. As the particle size gets smaller, the magnetic anisotropy energy barrier (KV) also decreases. When the size drops below a critical value (d_{sp}), thermal agitation energy (k_BT, where k_B is the Boltzmann constant) begins to overcome the magnetic anisotropy energy. Consequently, there's a spontaneous reversal of the particle's magnetization from one easy axis to another, leading to fluctuations in the magnetization direction, causing the average magnetic moments to become zero. In this state, the material behaves similarly to paramagnetism. However, instead of individual atoms, the entire particle's magnetic moment

tends to align with the magnetic field, while thermal agitation attempts to disalign them. This phenomenon is called superparamagnetism and occurs in materials with very small crystallites. A key difference between paramagnetic and superparamagnetic particles is that the magnetic moment per atom in a typical paramagnetic particle is a few Bohr magnetons, whereas a 5 nm iron superparamagnetic particle typically has a magnetic moment around 10,000 μ_B. Two conditions must be met for superparamagnetic behaviour: (a) zero coercivity, meaning no hysteresis, and (b) magnetization, when plotted against the field at different temperatures, superimposes when expressed as a function of H/T (Cullity and Graham 2009).

In the superparamagnetic state, when the magnetic anisotropy energy (E_A) becomes comparable to the thermal activation energy (k_BT), the direction of magnetization begins to flip randomly, leading to rapid superparamagnetic relaxation. The temperature at which thermal activation energy surpasses the magnetic anisotropy energy barrier, causing nanoparticles to undergo superparamagnetic relaxation, is termed the superparamagnetic blocking temperature (T_B).

Superparamagnetic particles are typically identified by certain characteristics observed in temperature-dependent measurements. For instance, there is a maximum or a peak in the temperature variation of ac susceptibility and zero-field-cooled (ZFC) magnetization when measured in a small dc magnetic field. The temperature corresponding to this peak is the superparamagnetic blocking temperature, T_B where nanoparticles undergo superparamagnetic relaxation. When the sample is cooled under a magnetic field (FC), the magnetization remains nearly constant or dips below the blocking temperature. As the temperature increases above T_B, it aligns with the ZFC magnetization. The bifurcation between ZFC and FC magnetization curves

is due to the existence and distribution of energy barriers of the magnetic anisotropy and the slow relaxation of the nanoparticles below T_B. This unique temperature dependence, along with the divergence of ZFC and FC magnetization below T_B, defines the distinctive features of superparamagnetism (Hansen and Morup 1999; Verma et al. 2014). Below the blocking temperature, an opening up of the magnetic hysteresis loop is also anticipated. Figure 2.22 illustrates a typical magnetic behaviour of an assembly of non-interacting superparamagnetic particles with random distribution of anisotropy axis.

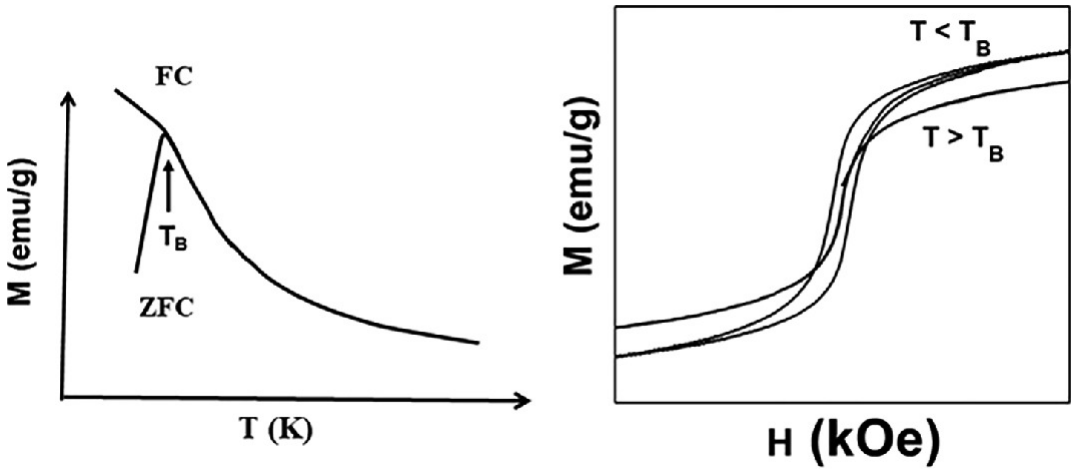

Fig. 2.22 Standard field-cooled (FC) and zero-field-cooled (ZFC) magnetization curves for an assembly of magnetic nanoparticles, with emphasis on the blocking temperature (T_B) displayed on the left. Illustration of magnetization behaviour below and above the blocking temperature (T_B) in relation to the magnetic field depicted on the right

Acknowledgements

The author gratefully acknowledges Woman Scientist research grant from Department of Science & Technology, Government of India (SR/WOS-A/CS-12/2019), IISER Pune and DST nanoscience unit of IISER, SRNM/NS-42/2009 for research support.

References

Cullity, B.D., Graham, C.D.: Introduction to Magnetic Materials, 2nd edn. Wiley (2009)

Hansen, M.F., Morup, S.: Estimation of blocking temperatures from ZFC/FC curves. J. Magn. Magn. Mater. **203**, 214–216 (1999)
[Crossref]

Jiles, D.: Introduction to Magnetism and Magnetic Materials. Chapman & Hall (1996)

Kittel, C.: Introduction to Solid State Physics. Wiley (1996)

Langevin, P.: Magn´etisme et th´eorie des ´electrons. Ann. Chim. Phys. **5**, 70 (1905)

Néel, L.: Ann. de Physique **18**, 5–105 (1932)

Néel, L.: Propri´et´es magn´etique des ferrites: Ferrimagn´etisme et antiferromagn´etisme. Ann. Phys. **3**, 137 (1948)

Smit, J., Wijn, H.P.J.: Ferrites, Phillips technical library (1959)

Spaldin, N.A.: Magnetic Materials: Fundamental and Applications, 2nd edn. Cambridge University Press (2011)

Tyler, F.: The magnetization-temperature curves of iron, cobalt an nickel. Philos. Mag. **11**, 596 (1931)
[Crossref]

Valenzuela, P.: Magnetic Ceramics. University Press, Cambridge (1994)

Verma, S., Kumar, A., Pravarthana, D., Deshpande, A., Ogale, S.B., Yusuf, S.M.: Off-stoichiometric nickel cobaltite nanoparticles:thermal stability, magnetization, and neutron diffraction studies. J. Phys.Chem. C **118**, 16246–16254 (2014)

© The Author(s), under exclusive license to Springer Nature Singapore Pte Ltd. 2024
R. S. Ningthoujam, A. K. Tyagi (eds.), *Handbook of Materials Science, Volume 2*, Indian Institute of Metals Series
https://doi.org/10.1007/978-981-97-4646-0_3

3. Units, Dimensions, and Conversion Factors in Magnetism: Basic Understanding

Manas Srivastava[1], Ruchi Agrawal[1, 2] and Raghumani S. Ningthoujam[1, 2] ✉
(1) Chemistry Division, Bhabha Atomic Research Centre, Mumbai, 400085, India
(2) Homi Bhabha National Institute, Anushaktinagar, Mumbai, 400094, India

✉ **Raghumani S. Ningthoujam**
Email: rsn@barc.gov.in

Keywords Units and dimensions – Conversion factors – Magnetic materials – AC magnetic fields – Mossbauer – Magnetic nanoparticles

3.1 Introduction

The nature around us is colourful and diverse. Our surroundings play a lot of roles around us such as air, oxygen, gases, wind, sun, moon, planets, and water. The curiosity to understand the natural phenomena to generate some basic laws and find these events from surrounding is physics. For example, the rubbing of comb in hair, the moon revolving around the earth, and the rubbing of iron needle with magnetite can all be explained if we know the basic law of

Charles Coulomb (1736–1806) and John Michell (1724–1793). The understanding of these laws leads to generating the story of magnetism. As per the researchers, the story of magnetite begins with Lodestone. The first magnetic materials are known to Human kind around 2500 years back. The powerful thoughts of great scientists, namely Professor Richard Phillips Feynman, Sir Isaac Newton, Johannes Kepler, and Aristotle have provided a great idea of “understanding the nature”. In various scientific areas such as biology, chemistry, physics, and interdisciplinary branches, the study of nature is performed. This chapter covers units, dimensions, conversion factors, and magnetism and magnetic nanoparticles with applications. A detailed explanation about units, dimensions, conversion factors, and magnetism can be obtained from the suggested books mentioned after conclusions (Kumar and Obj 2021; Verma 1993; Cullity and Graham 2011; Kittel 2005).

3.2 Units

The beauty of nature is governed by physics. The unit is the most important parameter to compare physical quantities. It requires various standard techniques to determine physical quantities. An Elephant is heavier than Man, simpler to tell how much times heavier than Man? Justice to this answer lies in this chapter. However, the standard mass is known to us. Then, we can compare the weight of a Man with an Elephant with the help of unit mass. Suppose the mass of man is less than that of an elephant by 200 times.

On defining a unit, this can be done on the basis of two concepts:

(1) How many times the standard unit.

(2) The unit’s name.

For example, he has been studying for 4 h. Then, split the 4 h into two parts. First, the numeric term “4” means how

much time greater than the standard and the rest “hr” means that hour.

Who chooses this unit?

The first question that arrives in our mind is “How the standard unit is chosen?” The answer to this question automatically strikes in this way that the unit is accepted Internationally. Or else, each person personally chooses her/his own unit. Then, this causes conflict with the whole world. To freely communicate with the whole world, the International body was set up “Conférence Générale des Poids et Mesures” (CGPM) or General Conference on Weight and Measures in English that has decided on units.

3.3 Dimensions

There are the base quantities, which can derive all the physical quantities of interest. A quantity is expressed as a product of different powers of the base quantities. The dimension of a quantity in a base is expressed as the exponent of a base quantity. To make the concept clear in Units and Dimensions, we will consider physical quantity like a Magnetic field. We will learn later about this physical quantity.

On defining this physical quantity, let us consider an equation. When a magnetic field (H) is applied to a moving charge particle (q) with velocity (v), a force (F) is developed (Fig. 3.1). This is a vector quantity. This is known as the magnetic Lorentz force. This force is perpendicular to both H and v.

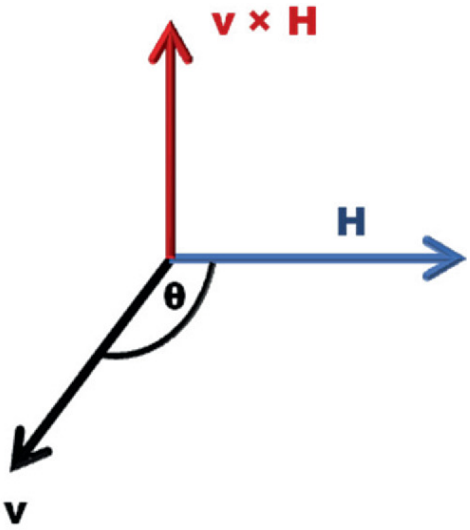

Fig. 3.1 The schematic diagram representing Lorentz force

$$F = qvH \tag{3.1}$$

It is strictly noted that the magnitude is not required in this type of calculation. Consider the SI units in this equation:

On simplifying the above equations:

$$F = \text{charge} \times \text{velocity} \times \text{magneticfield}$$

$$\text{F} = \text{current} \times \text{time} \times \left(\frac{\text{length}}{\text{time}}\right) \times \left(\frac{\text{force}}{\text{current} \times \text{length}}\right)$$

$$F = \text{current} \times \text{time} \times \left(\frac{\text{length}}{\text{time}}\right) \times \left(\frac{\text{mass} \times \text{acceleration}}{\text{current} \times \text{length}}\right)$$

$$\text{F} = \text{current} \times \text{time} \times \left(\frac{\text{length}}{\text{time}}\right) \times \left(\frac{\text{mass} \times \left(\frac{\text{velocity}}{\text{time}}\right)}{\text{current} \times \text{length}}\right)$$

$$\text{F} = \text{current} \times \text{time} \times \text{length} \times \text{time}^{-1} \times \left(\frac{\text{mass} \times \left(\left(\frac{\left(\frac{\text{length}}{\text{time}}\right)}{\text{time}}\right)\right)}{\text{current} \times \text{length}}\right.$$

$$F = \text{current} \times \text{time} \times \text{length} \times \text{time}^{-1} \times \text{mass} \times \text{length} \times \text{time}^{-2} \times \text{current}^{-1} \times \text{length}^{-1}$$

On simplifying this above term, we get

$$F = \text{mass} \times \text{length} \times \text{time}^{-2} \tag{3.2}$$

Therefore, dimensions of force are expressed as 1 in mass, 1 in length, and −2 in time. For convenience to the reader, Table 3.1 provides the base quantity, its symbol, symbol for dimension, base unit, and unit symbols.

Table 3.1 Base quantity, its symbol, symbol for dimension, base unit, and unit symbols. (Cullity and Graham 2011)

S. no	Base quantity	Symbol for quantity	Symbol for dimension	SI base Unit	SI unit symbol
1	Mass	M	M	Killogram	Kg
2	Length	L	L	Metre	M
3	Time	T	T	Second	S
4	Current	I	I	Ampere	A
5	Temperature	T	Θ	Kelvin	K
6	Amount of substance	N	N	Mole	Mol
7	Luminous intensity	I_v	J	Candela	Cd

Note Any symbol for dimension is represented by one letter only

Moreover, square brackets are used to express the physical quantities which are expressed in terms of the base quantities. It is strictly noted that the equation is dimensions but not magnitudes. Therefore, the Eq. (3.2) is written as

$$[\text{force}] = MLT^{-2} \tag{3.3}$$

It is strictly noted that this is an expression of physical quantity with respect to base quantities. This is known as the *dimensional formula*. We have derived the dimensional formula of force. The expression is MLT^{-2}. The outputs to the dimensional formula of force give us the following:

(1) The dimensional formula of force is represented by MLT^{-2}.

(2) The dimensions of force are expressed as 1 in mass, 1 in length, and −2 in time.

3.3.1 Use of Dimension

The mathematical equation contains many physical quantities. Each physical quantity is identical in terms of dimensions, i.e., one can subtract or add the same physical quantity. The result is homogeneity of dimensions in equations. Thus, magnetic fields cannot be added to force or force cannot be subtracted to charge. This method is known as the *Principle of Homogeneity of Dimensions* in an equation. This is the most important principle to verify whether an equation may be correct or not. For example, suppose we want to check the dimensions of an equation.

Let us check the equation which provides the relationship of magnetic field/flux density (B) produced at the centre of a circular coil having a radius of r with steady current (I) (Fig. 3.2).

$$B = \frac{\mu_0 I}{2\pi r} \tag{3.4}$$

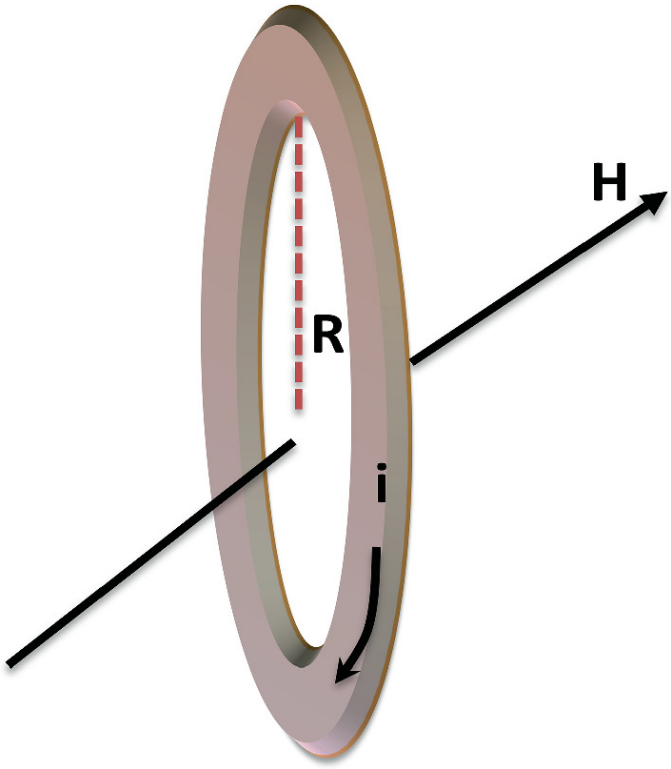

Fig. 3.2. Magnetic field /flux density (B) produced at the centre of a circular coil having a radius of (r) when a steady current (I) is flowing in a coil

μ_0 is permeability of free space ($4\pi \times 10^{-7}\ H/m$) and H = Henry. It is a constant value. When a magnetic field of one ampre/m is given in a material, a magnetic flux density is generated with a value of one tesla (T) or one weber/m^2. The magnetic permeability of a material is equal to one henry (H) per metre.

$$[B] = \left[\frac{\text{force}}{\text{current} \times \text{length}}\right]$$
$$= \left[MT^{-2}I^{-1}\right]$$
$$[\mu_0] = \left[MLT^{-2}I^{-2}\right]$$
$$[I] = [\boldsymbol{I}]$$
$$[\mathrm{r}] = [\mathbf{L}]$$

On substituting the values in the above Eq. (3.4), we get

$$[B] = \left[MT^{-2}I^{-1}\right] \tag{3.5}$$

$$\& \left[\frac{\mu_{0I}}{2\pi r}\right] = \left[\frac{\mu_{0I}}{r}\right] = \left[MT^{-2}I^{-1}\right] \tag{3.6}$$

Thus, the dimensions are the same for this equation.

3.3.2 Limitation

On performing the above exercise for Eq. (3.4), we come across many drawbacks. Suppose the equation for current carrying a wire is the same in dimensions but different in magnitude. The reason behind this is that the pure numbers are dimensionless. The pure number in this equation is "$\frac{1}{2\pi}$". So, we have come across the conclusion in Eq. (3.4) that the dimensionally correct equations must be correct but a dimensionally wrong equation is always wrong.

3.4 Conversions of Units with Fundamental Definitions

Using base quantities, the different sets of units can be derived. During conversion from one system to another, a conversion factor for the unit of derived quantity is required (Table 3.2). To make it clear, consider the physical quantity "force". Herein, we will now cover some fundamentals of magnetism related to the Definition of Dimensions. All of us know that the forces of attraction and repulsion between magnets are observed at an early age. How to measure this force? According to Charles Coulomb (1785), "the force F between two poles is proportional to the product of their pole strengths p_1 and p_2 and inversely proportional to the square of the distance d between them":

$$F = k\frac{P_1 P_2}{d^2} \tag{3.7}$$

Table 3.2 The fundamentals of units, dimensions, and conversion units (cgs/SI) of some basic magnetic parameters

S no	Quantity	Nature	Dimensions	Units	Symbol	Conversion unit (cgs/SI)	Remarks
1	Magnetic field strength, magnetic intensity	Vector	$\left[L^{-1}I\right]$	Am^{-1}	H	$\frac{Oe}{A{\cdot}m^{-1}} = \frac{10^3}{4\pi} = 79.6$	$B = \mu_0 (H + M)$
2	Magnetic flux	Scalar	$\left[ML^2T^{-2}I^{-1}\right]$	W (weber)	Φ	$\frac{Mx}{Wb} = \frac{Mx}{V{\cdot}S} = 10^{-8}$	$W = Tm^2$
3	Magnetic flux density, magnetic field	Vector	$\left[MT^{-2}I^{-1}\right]$	T (tesla)	B	$\frac{G}{T} = \frac{G}{Wb{\cdot}m^{-2}} = 10^{-4}$	$10^4 G\,(\text{gauss}) = 1T$
4	Magnetic moment	Vector	$\left[L^{-2}I\right]$	Am^2	m	$\frac{emu}{A{\cdot}m^2} = \frac{erg{\cdot}Oe^{-1}}{A{\cdot}m^2} = \frac{10A{\cdot}cm^2}{A{\cdot}m^2} = \frac{emu}{J{\cdot}T^{-1}} = 10^{-3}$	
5	Magnetization	Vector	$\left[L^{-1}I\right]$	Am^{-1}	M	$\frac{emu{\cdot}cm^{-3}}{A{\cdot}m^{-1}} = \frac{erg{\cdot}Oe^{-1}cm^{-3}}{A{\cdot}m^2} = 10^3$	$\frac{\text{Magnetic moment}}{\text{Volumne}}$
6	Magnetization per unit volume	Scalar	$\left[L^{-4}I\right]$	Am^{-4}	M		
7	Magnetization per unit mass	Scalar	$[M^{-1}L^{-1}I]$	Am^{-1}/kg	σ	$\frac{emu{\cdot}g^{-1}}{A{\cdot}m^2{\cdot}kg^{-1}} = \frac{erg{\cdot}Oe^{-1}{\cdot}g^{-1}}{A{\cdot}m^2{\cdot}kg^{-1}} = 1$	

Note Oe = oersted, Mx = maxwell, Wb = weber, G = gauss, T = tesla, I = ampere, g = gram, kg = kilogram, J = joule, cm = centimeter

Here, k is proportionality constant and if it is taken as 1 and the unit of force is measured in dyne and d in cm. On defining, a unit of magnetic pole strength is equal to the strength of a magnetic pole that repels another identical unit pole at a distance of 1 cm with a force of one dyne. One dyne is also defined as that force that provides an acceleration of 1 cm/sec^2 to a mass of 1 g. In the CGS unit, the weight of 1 g of mass is 981 dynes. A magnetic pole will create a field around it, and this magnetic field creates force around the second pole. This force is proportional to the product of the pole strength (p) and magnetic field strength or field intensity H:

$$F = kpH \tag{3.8}$$

Here, k is proportionality constant. According to the above two equations, we get

$$H = \frac{p}{d^2} \tag{3.9}$$

On defining the above equations, Michael Faraday (1791–1867) invented a very good idea that a magnetic field is represented by “lines of force”.

So, the magnetic field strength (H) is defined as the number of lines of forces passing through a unit area perpendicular to the field.

Thus, as per Maxwell,

1Oe is equal to 1 line of force/cm^2, which is also equal to 1 maxwell/cm^2.

We want to define the Faraday law of Electromagnetic Induction (Fig. 3.3).

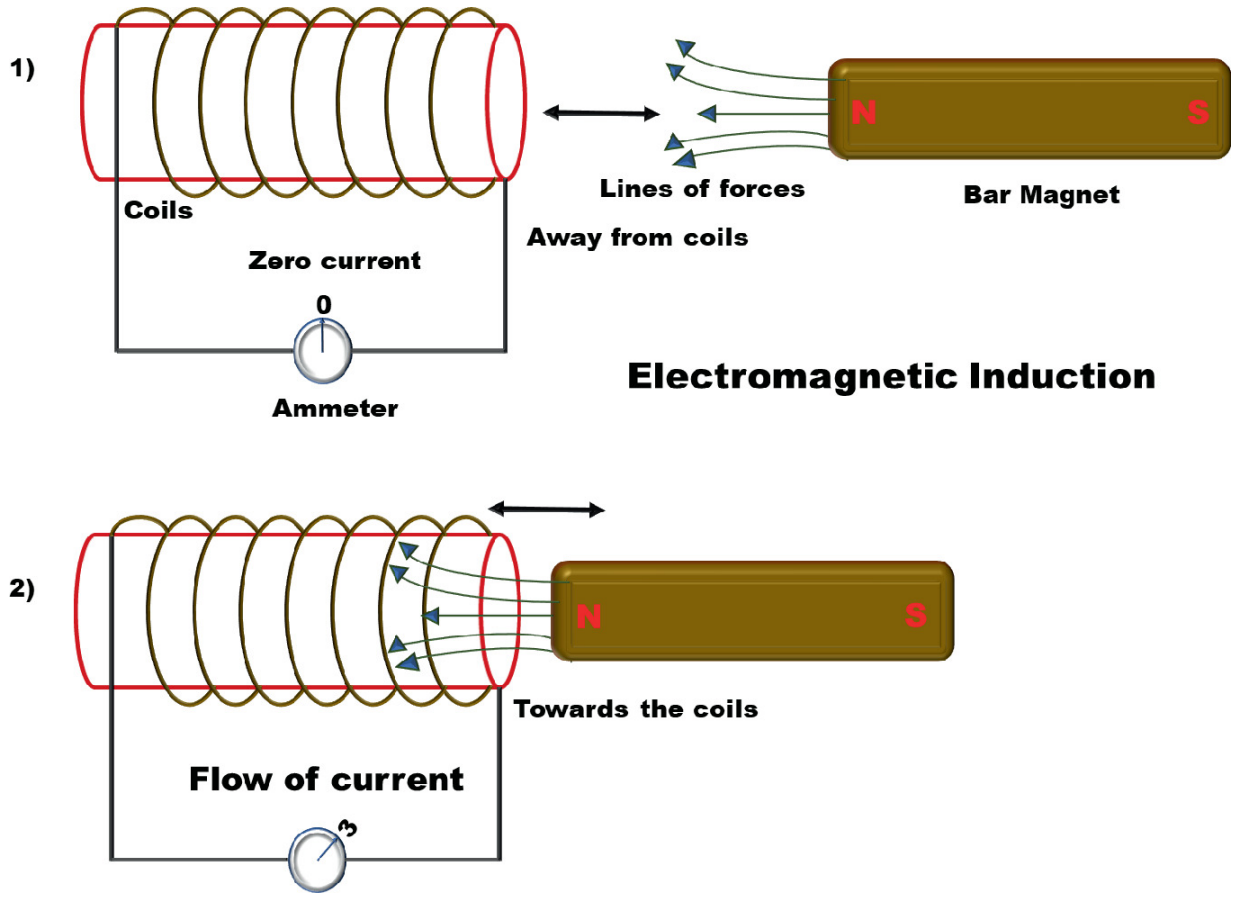

Fig. 3.3 The phenomenon of electromagnetic induction generation in the coils

It states that the EMF (electromagnetic force) induced in coils is directly proportional to the product of the number of turns and rate of change of flux.

$$\mathrm{EMF} = -\mathrm{N}\frac{\Delta\emptyset}{\Delta\mathrm{t}} \tag{3.10}$$

where $\mathrm{N} =$ number of turns; $\emptyset =$ magnetic flux.

3.5 Magnetic Moment

Consider a bar magnet with pole strength p situated near the end. The inter-pole distance of the bar magnet is l (Fig. 3.4).

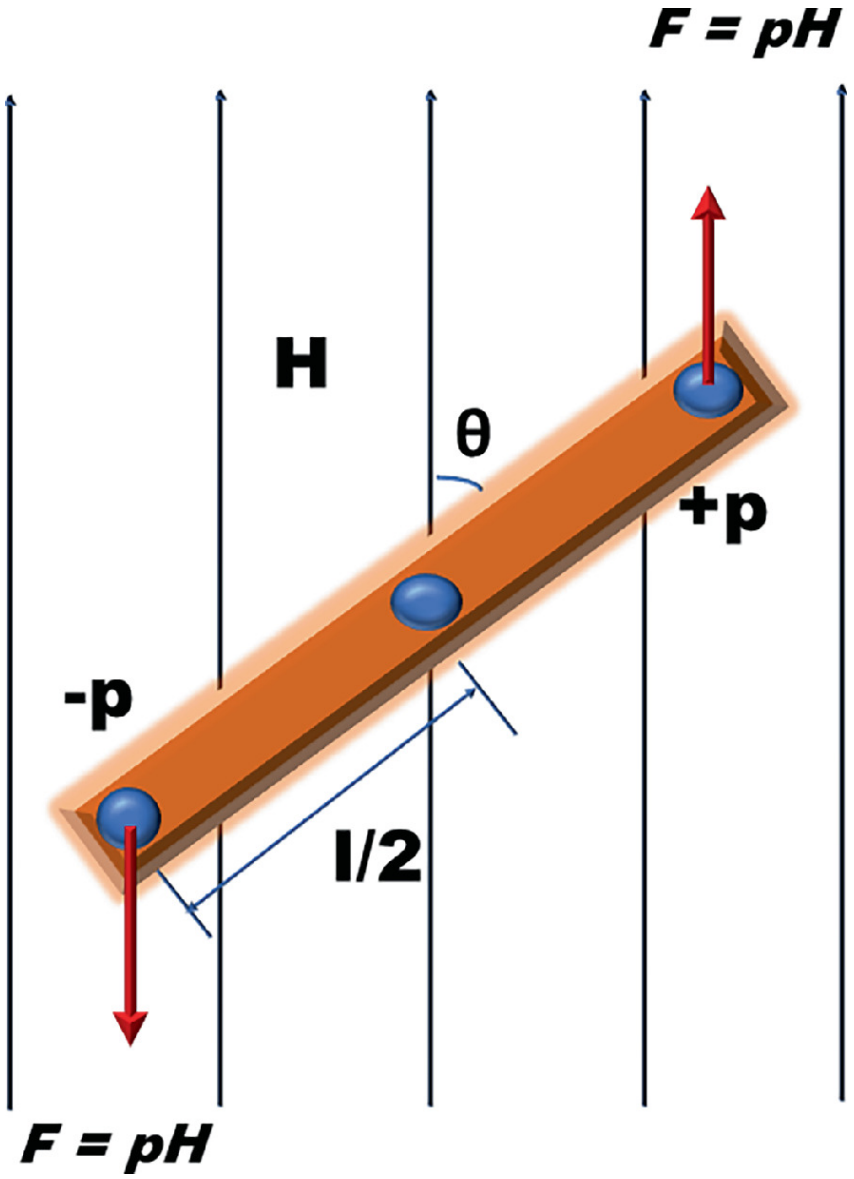

Fig. 3.4 Bar magnet in a uniform magnetic field

The couple acts on the bar magnet to align in the field direction. The resultant magnetic moment of the couple is given below:

$$\sum m_i = \mathrm{m} \tag{3.11}$$

whereas $\sum m_i$ is the sum of magnetic moments and m is the resultant magnetic moment.

The equation is summarized as follows:

$$(pH\sin\theta)(l/2) + (pHsin\theta)(l/2) = pHl\sin\theta \tag{3.12}$$

When $H = 1$ Oe and $\theta = 90^o$, the moment is given by.
On putting the above values in Eq. (3.12), we get

$$m = pl \tag{3.13}$$

On defining this equation, we have noted that the bar magnet is not parallel to the field. Why the bar magnet is not aligning to the field? The answer to this question is noted that a certain amount of potential energy has been stored in a bar magnet in the form of inertia. How to define this Potential energy? We have to go to the theory of classical mechanics for defining the potential energy. The work is required to be done against the field in turning through an angle $d\theta$. The equation is defined as

$$dE_P = 2\,(pHsin\theta)\,(l/2)d\theta = mHsin\theta d\theta$$

As per the definition of work done, we get

$$E_P = \int_{90^0}^{\theta} mHsin\theta d\theta$$

On solving the above equation, we get

$$E_P = -mHcos\theta \tag{3.14}$$

The vector notation,

$$E_P = -m \cdot H \ldots \tag{3.15}$$

So, the energy E_P is in ergs, and the unit of magnetic moment (m) is ergs/oersted or emu.

3.6 Intensity of Magnetization

When a few iron needles are sprinkled over a wire carrying a steady current (I) on a sheet of paper, the iron needles form a concentric circle due to a magnetic field. Then, it becomes magnetized. This depends on the strength of the field. How much quantity of the substance is required to magnetize? The answer to this question plays an important role to identify the degree of quantity. Already, we know that researches are

synthesizing many alloys and compounds. The researchers are trying hard to classify the magnetic properties of substances.

Consider 2 bar magnets with the same size and shape, and they have the same pole strength “p” and interpolar distances “d”. If two bar magnets are placed side by side, then poles add, its magnetic moment is (2p)d. If two bar magnets are placed end to end, then its interpolar distance becomes 2d, and thus its magnetic moment is p(2d).

In the above example, we can get double the magnetic moment through the increase of either the magnetic pole or length/interpolar distance by twice. However, the magnetic moment per unit volume remains the same. So, on defining the intensity of magnetization, we have come across some conclusions that it is independent of the morphology of magnetic materials.

The intensity of magnetization (M) is defined as the net magnetic moment per unit volume.

$$M = \frac{m_{net}}{v} \tag{3.16}$$

The unit of magnetization is erg/(oersted cm^3). This is also expressed as emu/cm^3. “emu” is defined as the electromagnetic unit of magnetic moment(1 emu = 1 erg/oersted or 1 erg/G and G is gauss).

The specific magnetization σ is defined as

$$\sigma = \frac{m}{w} \tag{3.17}$$

The unit of σ is written as emu/g.

In terms of *c.g.s* units:

$$B = H + 4\pi M \tag{3.18}$$

whereas B, H, and M are defined as Magnetic induction (Gauss), applied field (Oe), and Intensity of Magnetization (emu/g), respectively.

Next, how does a material respond to an applied magnetic field? So, the density of materials with their volume play an important role in defining the Intensity of Magnetization

(emu/cm^3). However, the conversion of units is an important factor in Magnetic materials. Also, how to convert “emu/g” to “emu/cm^3”?

The explanation to the above question is explained as follows:

$$\frac{\text{Susceptibility in } cgs \text{ unit}}{\text{Susceptibility in } SI \text{ unit}} = \frac{emug^{-1}Oe^{-1}}{Kg^{-1}\left(Am^2\right)\left(Am^{-1}\right)^{-1}} = 4\pi \times 10^{-3} \quad (3.19)$$

$$\frac{emu}{cm^3} = \frac{emu}{g} \times \frac{g}{cm^3} = \frac{emu}{g} \times \frac{10^{-3}Kg}{10^{-6}m^3} = \frac{emu}{g} \times 10^3 \times \frac{Kg}{m^3} = 10^3\rho\frac{emu}{g} \quad (3.20)$$

“ρ” = Density of materials (kg/m^3)

Now, susceptibility is an important term “How M varies with H?”. This is the ratio of two quantities:-

$$\chi = \frac{M}{H}\,\text{emu}/\left(\text{cm}^3\text{Oe}\right) \quad (3.21)$$

Susceptibilities are expressed in various ways such as mass, atomic, and molecular susceptibility.

The researcher is mainly interested in the variation of M with H. Variation of susceptibility versus temperature will provide the behaviour of magnetic materials: diamagnetic, paramagnetic, antiferromagnetic, or ferromagnetic or ferrimagnetic properties of materials. It gives susceptibility and what kind of substance? On the other hand, the engineer is only concerned about ferro- and ferrimagnetic materials. They want to know about the total flux density (B) produced through a given field.

The ratio of B with H is called as permeability (μ):

$$\mu = \frac{B}{H} \quad (3.22)$$

$$\text{So,} \quad \mu = 1 + 4\pi\chi \quad (3.23)$$

The various kinds of substances with their corresponding χ &μ : -

(1) Empty space. $\chi = 0,\ \mu = 1$.

(2) Diamagnetic materials. χ *is small and negative*, μ *slightly less than* 1.

(3) Para- and antiferromagnetic materials. χ *is small and positive*, μ *slightly greater than* 1.

(4) Ferro- and ferrimagnetic materials. χ *and* μ *is large and positive*, and both are functions of H.

(5) Superconducting materials. χ is $-1/(4\pi) = -0.079$ and μ is zero (B = H + 4πM)), here $\mathrm{B} = 0; \chi = \mathrm{M/H} = -1/(4\pi)$.

3.7 Classical Theory of Paramagnetism

In the year 1895, Pierre Curie derived Curie law. It states that "mass susceptibility is varied inversely with the absolute temperature for paramagnetics". The proportional constant "C" is called the Curie constant.

$$\chi = \frac{C}{T} \tag{3.24}$$

The basic limitation is that entities of magnetic moments do not interact via the application of fields and thermal agitations. The plot of$1/\chi$ *vs*. T gives a straight line for paramagnetic materials during Curie law and passes through the origin. In paramagnetic materials, it is assumed that atomic moments do not interact with each other or even in the presence of magnetic fields.

If there is an interaction among paramagnetic atoms/ions with or without a magnetic field, it does not follow Curie law. On this basis, Pierre Weiss (1865–1940) has proposed a modified equation:-

$$\chi = \frac{C}{T - \theta} \tag{3.25}$$

where θ is an interaction term. In the case of ferromagnetic materials, θ is called the Curie temperature (T_c). Most ferromagnetic materials become paramagnetic above the Curie temperature.

There is another paramagnetism, which does now follow the Curie behaviour (magnetic susceptibility decreases with the increase of temperature). Another one is known as the Pauli paramagnetism in which magnetic susceptibility does not change. This was introduced by Wolfgang Ernst Pauli in the 1940s, and this behaviour was observed in alkali metals and noble metals. At the Fermi energy, spin up and down states of conduction electrons are almost the same, and thus its density of states does not much change with temperature. The magnetic susceptibility of conduction electrons in metal will have two components: the Pauli paramagnetism (the spin magnetic moment under the magnetic field) and the Landau diamagnetism due to the orbital motion of conduction electrons.

3.8 Curie Point and Exchange Integral

The Heisenberg model is defined on the basis of Quantum–mechanical exchange interactions to explain magnetism. The exchange energy (U) is expressed as

$$U = -2JS_i.S_j \tag{3.26}$$

where “J” is the exchange integral.

Relation between exchange integral (J) and Curie point (T_c) has been expressed as

$$J = \frac{3k_BT_C}{2zS\,(S+1)} \tag{3.27}$$

On simplifying Eq. (3.26), Rush Brooke and Wood give the value of $k_BT_C/zJ = 0.28$, 0.325, and 0.346, respectively, for SC (simple cubic), BCC (body centred cubic), and FCC (face centred cubic) structures with S = ½. At Curie point, the

Heisenberg model gives exchange integral (J = 11.9 meV) for iron with S = 1.

3.9 Temperature-Dependent Magnetization in Cases of Ferromagnetic and Paramagnetic Materials

The magnetization in ferromagnetic materials decreases with the increase of temperature. This is due to the decrease in the alignment of magnetic domains. With further increase in temperature, random orientations of magnetic moments/domains increase. At a particular temperature, called the Curie Temperature (T_c), the number of spin up is equal to spin down, where spontaneous magnetization becomes zero. Above T_c, the property of material behaves as paramagnetic.

In the case of paramagnetic materials, the total magnetic moment in the direction of fields is acquired by the unit volume under consideration. Thus, the magnetization (M) is obtained by multiplying the number of atoms dn by $\mu cos\theta$ of each atom and integrating over the total number. Here θ is the angle of the magnetic moment of atom (μ) with respect to the magnetic field (H).

The total magnetization present in the material is given by

$$M = \int_0^n \mu cos\theta dn \tag{3.28}$$

On integration, we put variable 0 to π for θ.

$$\frac{M}{M_o} = \coth a - \frac{1}{a} \tag{3.29}$$

where $\mathrm{a} = \frac{\mu H}{kT}$

$n\mu$ is the maximum possible moment and it is indicated by M_o.

The Langevin function is expressed in series:

$$L(a) = \frac{M}{M_O} = \frac{a}{3} - \frac{a^3}{45} + \frac{2a^5}{945} - \ldots \tag{3.30}$$

The typical plot of L(a) with “a” is shown in Fig. 3.5.

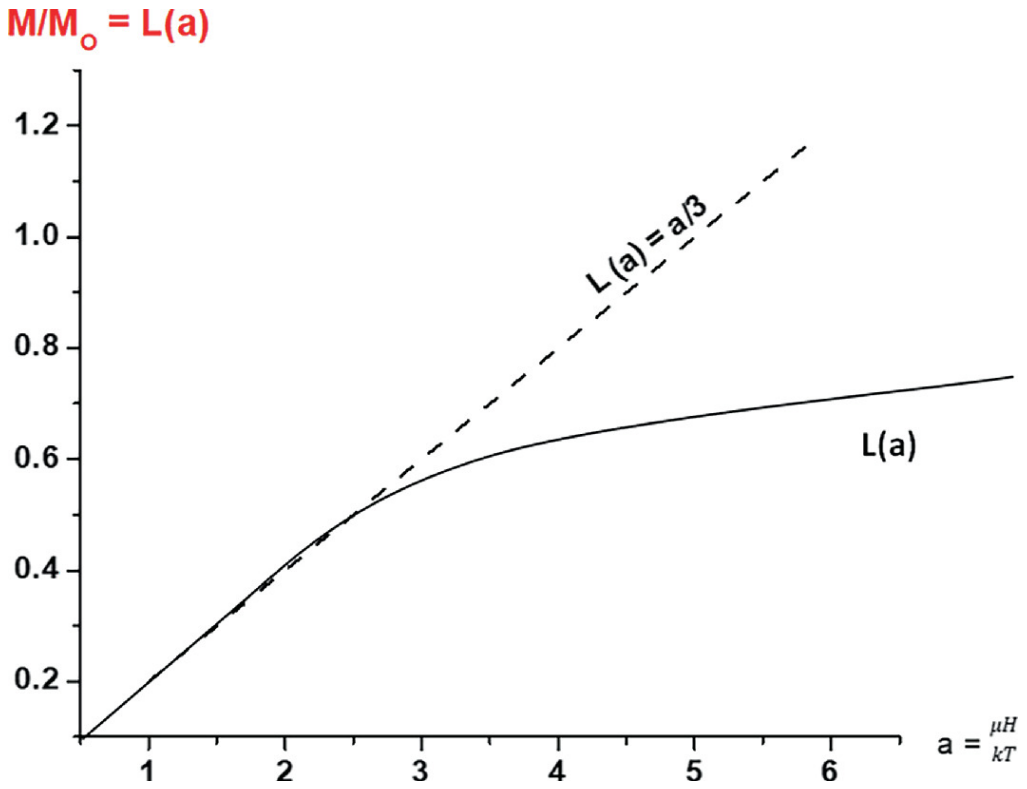

Fig. 3.5 Langevin function plot: M/M_O vs. $a = \mu H/kT$

On analysis of the Langevin function $L(a)$ with respect to “*a*”, there are two possibilities that occurred at large “*a*” and small “*a*”.

(1) When “*a*” tends to 1, it causes the disordering effect of thermal agitation.

(2) When “*a*” is less than 0.5, L(*a*) is practically straight line.

On the basis of the Langevin theory, it also leads to the Curie Law:

$$M = \frac{n\mu^2 H}{3kT} \tag{3.31}$$

$$\chi_V = \frac{M}{H} = \frac{n\mu^2}{3kT} \tag{3.32}$$

$$\chi_m = \frac{\chi_V}{\rho} = \frac{n\mu^2}{3\rho kT} \tag{3.33}$$

ρ is density and n is the number of atoms per unit volume, which is equal to Nρ/(A), where N = atoms/mole and A = atomic weight.

In terms of CGS and SI units, values in mass susceptibility are different.

$$\chi_V = \frac{C}{T} = \frac{N\mu^2}{3AkT}\left(emu/cm^3Oe\right)(CGS\text{units})\, or\, \left(Am^2/m^3Am^{-1}\right)(SI\text{units}) \tag{3.34}$$

$$\chi_m = \frac{C}{\rho T} = \frac{N\mu^2}{3\rho AkT}\left(emu/gOe\right)(CGS\text{units})\, or\, \left(Am^2/KgAm^{-1}\right)(SI\text{units}) \tag{3.35}$$

Let us consider oxygen having paramagnetic at 20 °C. In terms of CGS and SI units, the values of mass susceptibility are different. According to researchers what they want to express, we have to choose the correct units in magnetic materials.

$$\chi_m = 1.08 \times 10^{-4}\left(\frac{emu}{gOe}\right)(CGS\,\text{units}) \tag{3.36}$$

$$\begin{aligned}\chi_m =& 1.36 \times 10^{-6}\left(\frac{J/T}{KgAm^{-1}}\right) = 1.36 \times 10^{-6}\frac{Am^2}{KgAm^{-1}} \\ &= 1.36 \times 10^{-6}\frac{m^3}{Kg}\,(SI\,\text{units})\end{aligned} \tag{3.37}$$

How to convert the magnetic moment (μ) of the oxygen molecule in terms of Bohr magnetron at 25 °C (298 K)? So, the next step is to give a solution to the question with units and dimensions: -

$$\mu = \left(3M^*kT\chi/N\right)^{1/2} \tag{3.38}$$

where M = molecular mass, k = Boltzmann constant, T = temperature, χ = susceptibility, and N = Avogadro's number.

$$\mu = \left[\frac{3 \times 32 \times \left(\frac{g}{\text{mole}}\right) \times (1.38 \times 10^{-16}\left(\frac{erg}{K}\right) \times 298K \times \left(1.08 \times 10^{-4}\right)\left(\frac{emu}{gOe}\right)}{6.023 \times 10^{23}\left(\frac{\text{molecules}}{\text{moles}}\right)}\right]^{1/2} \quad \text{(CGS units)}$$

$$\mu = \left[\frac{3 \times 0.032 \times \left(\frac{Kg}{\text{mole}}\right) \times (1.38 \times 10^{-23}\left(\frac{J}{K}\right) \times 293K \times \left(1.36 \times 10^{-6}\right)\left(\frac{J/T}{KgAm^{-1}}\right)}{6.023 \times 10^{23}\left(\frac{\text{molecules}}{\text{moles}}\right)(4\pi \times 10^{-7})\left(\frac{T}{Am^{-1}}\right)}\right]^{1/2} \quad \text{(SI units)}$$

$$\mu = 2.64 \times 10^{-20}\frac{erg}{Oe}\,\text{per molecule}\,(cgs\,\text{units}) \tag{3.39}$$

$$\mu = 2.64 \times 10^{-23}\frac{Am^2}{\text{molecule}}\,(SI\,\text{units}) \tag{3.40}$$

Bohr Magnetron (μ_B) of oxygen molecule can be obtained by dividing the value of magnetic moment expressed in Eqs. (3.39) and (3.40) by the conversion factor.

$$\mu = \frac{2.64 \times 10^{-20}\frac{erg}{Oe}\text{per molecule}\,(cgs\text{units})}{0.927 \times 10^{-20}} \quad \text{or} \quad \frac{2.64 \times 10^{-23}\frac{Am^2}{\text{molecules}}\,(SI\text{units})}{0.927 \times 10^{-23}}$$

$$\mu = 2.85\mu_B \qquad \text{per molecule} \tag{3.41}$$

Let us calculate "a" after applying a high magnetic field of 1 Testa (10^4 Oe).

$$a = \frac{\mu H}{kT} = \left(\frac{2.64 \times 10^{-20}\frac{erg}{Oe}\text{per molecule}\,(cgs\text{units}) \times 10^4 Oe}{1.38 \times 10^{-16}erg/K \times 293K}\right)$$

$$a = 0.0065 \tag{3.42}$$

The value of the Langevin function is small enough than the slope a/3. Now, we want to consider the disordering effect of thermal agitation. For example, there are $N/32$ oxygen molecules per gram, and each with a moment of $2.64 \times 10^{-20} emu$.

If paramagnetic spins of oxygen molecules are fully parallel to each other, the specific magnetization (σ) of oxygen will be given by

$$\sigma = \frac{6.023 \times 10^{23} \times 2.64 \times 10^{-20}}{32} = 497 emu/g \tag{3.43}$$

On the other hand, the magnetization occurs in a field as strong as 10 T, which is equal to 10^5 Oe.

$$\sigma = \chi H = \left(1.08 \times 10^{-4}\right)\left(10^5\right) = 10.8 emu/g \tag{3.44}$$

Here, Eqs. (3.43) and (3.44) do not give the same value in specific magnetic magnetization. It is indicated that all spins in oxygen molecules are not parallel to each other. Also, to get the actual value of specific magnetization, the diamagnetic contribution of materials must be subtracted.

3.10 Temperature-Dependent Magnetization in Cases of Antiferromagnetic and Ferrimagnetic Materials

As the temperature of the surrounding environment of magnetic material increases, random orientations of magnetic moments occur. This changes the magnetic properties of materials. Let us discuss this on Antiferromagnetic and Ferrimagnetic properties.

3.10.1 Antiferromagnetism

In 1936, Néel introduced another property of materials called as Antiferromagnetism. Based on Néel, first, there should be the antiparallel alignment of neighbouring magnetic moments; second, the crystal structure of the materials should be divided into identical two substructures. The spins of a substructure are antiparallel to those of another substructure. Net of these gives rise to the moment of antiferromagnetic materials. In temperature-dependent magnetic study, there are ordering of moments below a particular temperature, and above this, it behaves with a paramagnetic nature. The transition point from the ordering of spins to paramagnetic is called the Néel

temperature. The equation of this Néel temperature (T_N) is given by the following relations:

$$\chi = \frac{C}{T + T_N} \tag{3.45}$$

Between substructures, magnetic interactions occur through superexchange (M-L-M). For example, MnO is antiferromagnetic with T_N at 122 K ($M = Mn^{2+}$, $L = O$). Mn^{2+}-O-Mn^{2+} interaction is of superexchange type.

In 1943, Guillaud suggested the different properties of compound Mn_2Sb. These properties of the compound are totally different than antiferromagnetic materials because they have opposite directions of magnetic moments with spontaneous magnetizations. This is lacking in antiferromagnetic materials.

3.10.2 Ferrimagnetism

The renowned scientist, in 1948, Louis Néel has invented the classical theory of Ferrimagnetism, the magnetic structure is subdivided into different substructures in crystallography. Substructures are generally represented by AO_4 (4 coordination around central metal ion “A” by oxygen to form tetragonal polyhedron) and BO_6 (6 coordination around central metal ion “B” by oxygen to form octahedron or trigonal bypyramid polyhedron). Such substructures can generate different types of ferrimagnetic materials such as spinel, hexaferrite, garnet, and orthoferrite. Néel has introduced the term ferrite as A and B ferric ions or ferrous/ferric ions mixture. There are negative exchange interactions between A and B sites meaning antiferromagnetic interactions. This is responsible for Ferrimagnetism in materials. The generalized formula for spinel ferrite materials will be MO. Fe_2O_3 ((AO) $[B_2O_3]$). The M represents divalent cations. The common example is FeO. Fe_2O_3, called Magnetite (Fig. 3.6).

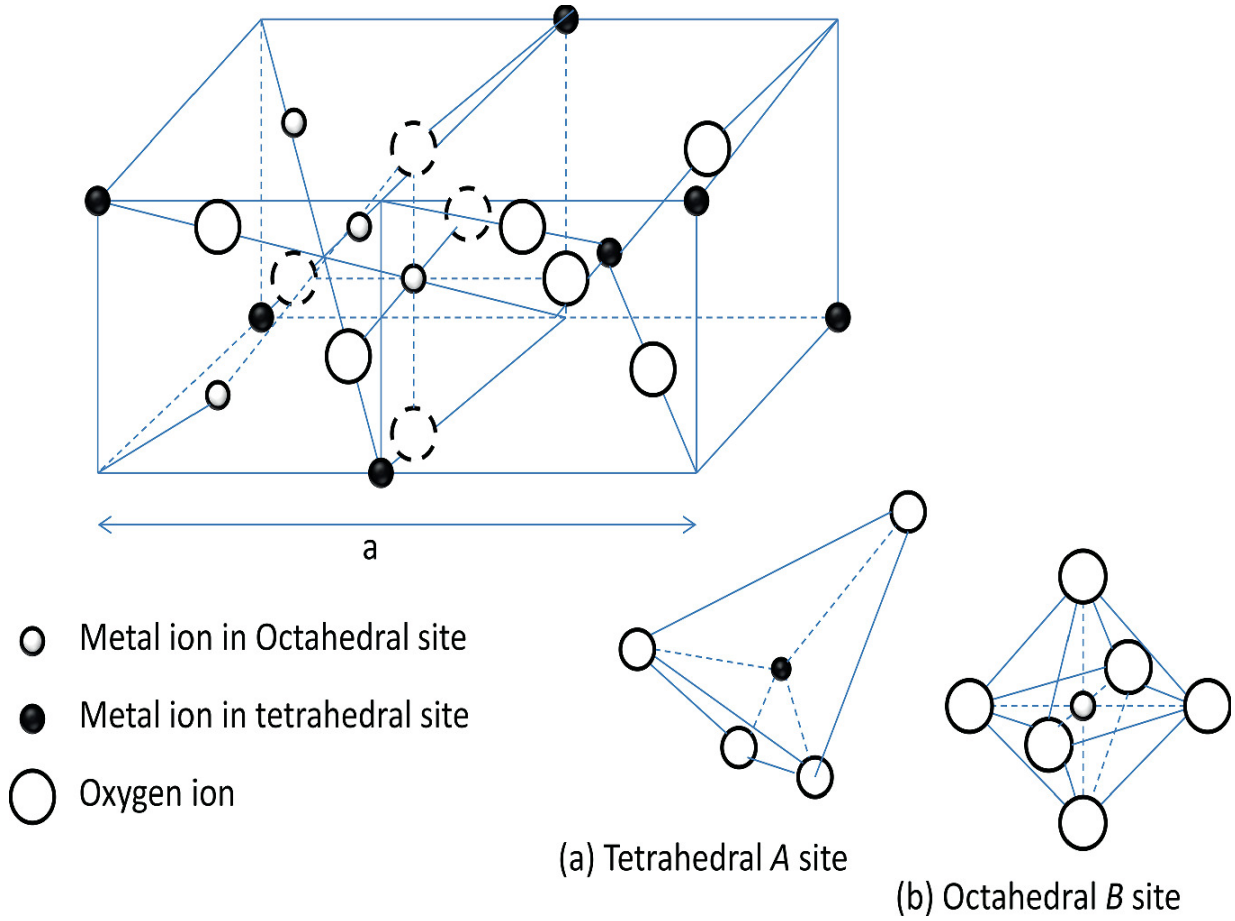

Fig. 3.6 Spinel structure: unit cell can be divided into octants; tetrahedral cations A, octahedral cations B, and O atoms (large circles) are shown in two octants. It is adapted and redrawn (Cullity and Graham 2011)

Bragg (1915) and Nishikawa (1915) defined spinel structures that formed due to cubic close-packed (FCC) of O atoms, and 1/8th tetrahedral sites are occupied by metal ions and 1/2th octahedral sites are occupied by other metal ions. The formula for the unit cell is AB_2O_4 and one unit cell has 8A,16B, 32O. It is formulated (Smit &Wijn, 1961) by taking A as a reference in the unit cell. Magnetite has an inverse cubic spinel structure where oxygen ions formed in fcc closed packing and cations distributions in tetrahedral and octahedral sites are indicated by the formula $(Fe^{3+})_A[Fe^{2+}Fe^{3+}]_B$. The saturation magnetization at room temperature of bulk magnetite is 90 emu/g, which is less than that of pure Fe (218 emu/g) indicating that there is a superexchange mechanism between iron ions through oxygen since iron ions

are occupying different substructures (A and B) with antiparallel spin interactions.

The space group of Fe_3O_4 is Fd3m. There are three types of spinel structures namely normal, inverse, and mixed. The magnetic property of materials is influenced by cation distribution in the tetrahedral and octahedral sites. The same ferrite magnetic material can have different properties due to cations distributions prepared by different preparation routes (such as temperature, pressure, and non-stochiometry).

3.11 Particle Size Effects

Magnetic properties of materials are discussed on the basis of micro-sized particles. When the size of a particle decreases from a micron to a nanometer, its magnetic properties change. Even, if particle size changes from 3D to 2D to 1D to 0D, the magnetic property of the material changes. Even diamagnetic particles can become a weak ferromagnetic because of non-stoichiometry (vacancy in lattice). Bulk ZnO is diamagnetic, but becomes weak ferromagnetic for nanoparticles (Straumal et al. 2016).

Here, we will discuss the particle size effect on the intrinsic properties of ferromagnetic materials: coercivity (H_c), remanent magnetization (M_r), saturation magnetization (M_s), and Curie temperature (T_c) (Cullity and Graham 2011; Gajbhiye et al. 2008). Let us see the M-H curve of ferromagnetic particles (Fig. 3.7).

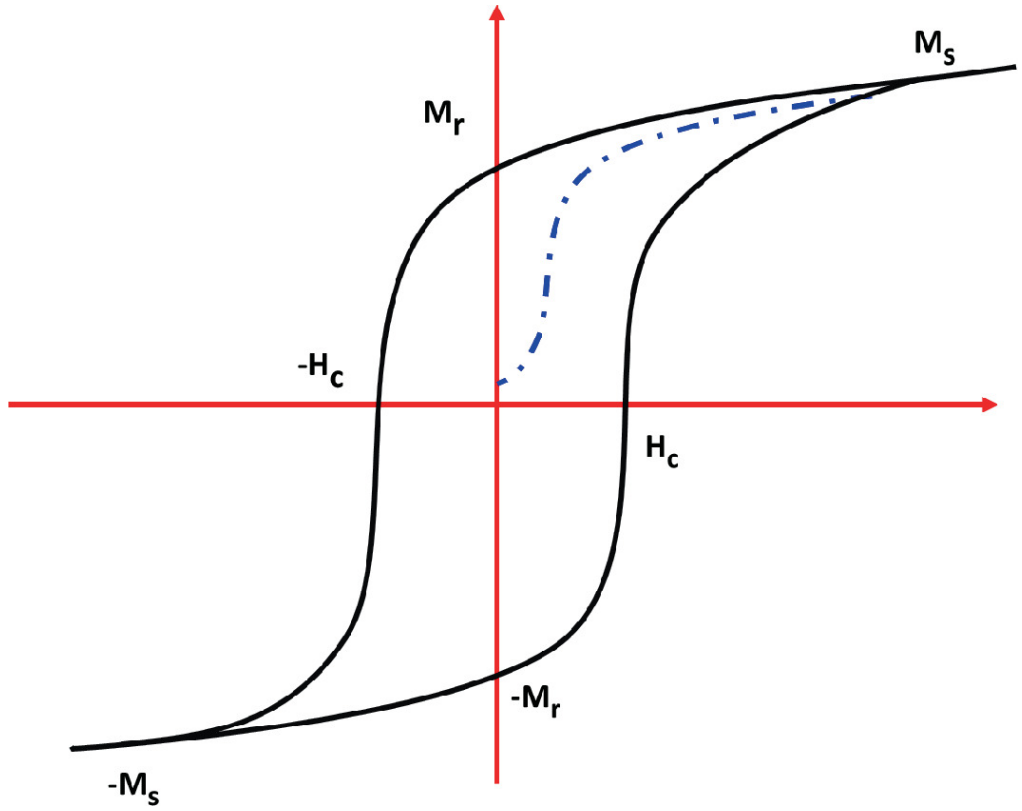

Fig. 3.7 Schematic representation of hysteresis loop (M–H curve)

The basic reason behind the variation of intrinsic properties of ferromagnetic material is a decrease in exchange interaction among domains. In the multi-domain system of micro-sized particles, each particle has many domains and domain walls. With the decrease of particles, the size of domain walls decreases significantly and finally each domain can exist without domain walls. Here, it becomes a stable domain and each particle acts as a domain and its H_c attains the maximum value as compared to that of bulk particles. Individual particles are considered as single domains. Again, further when the size of the particle decreases, H_c decreases and then goes to zero. These particles with $H_c \sim 0$ Oe are called as superparamagnetic particles (Fig. 3.8). The transition temperature from ferromagnetic to superparamagnetic character with the absence of hysteresis behaviour is termed as blocking temperature (T_b). In a superparamagnetic state, the relaxation of domain spins is about 10^{-9} s. This is considered as Neel's relaxation (τ_N).

Below T_b and above T_b, it behaves as ferromagnetic and paramagnetic, respectively. For the superparamagnetic state, the measurement time ($\tau_m \sim 0.1$ to 1 s) is much longer than τ_N. Thus, it cannot measure the magnetic moment of superparamagnetic particles and thus it shows zero coercivity ($H_c \sim 0$ Oe) and zero magnetization in the absence of an applied magnetic field. Temperature when the moments of particles are neither relaxed nor blocked ($\tau_m = \tau_N$) is called blocking temperature. The blocking temperature is much below than the Curie temperature. The magnetic moment of individual particle is about 10^3 to 10^5Bohr magneton in a superparamagnetic region (if it could be measured), but its net moment is zero like paramagnetic in the absence of an applied magnetic field (as all single domains have different orientations of moments). Even though the magnetic moment is high with a paramagnetic nature, the word “super” is used to add in the front of paramagnetic. Thus, the term “superparamagnetic” is used to identify them. In the absence of an applied magnetic field, superparamagnetic particles have zero magnetization.

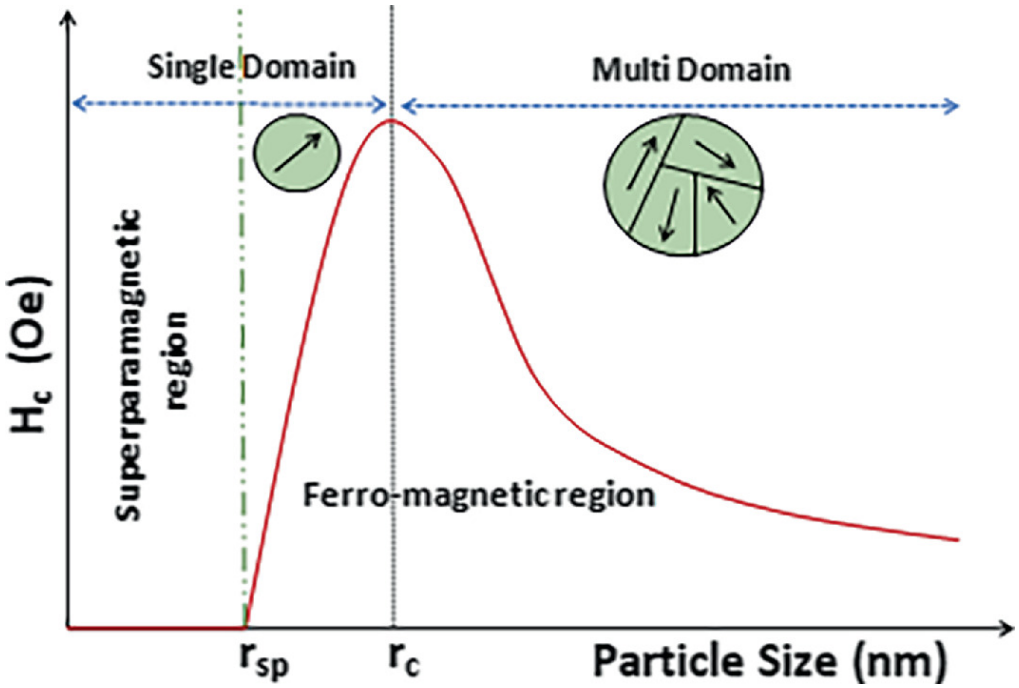

Fig. 3.8 The typical behaviour of H_C *versus* particle size (nm) in ferromagnetic materials

The critical size (d) of single domain MNPs is given by the following relation:

$$d = \frac{18\sqrt{AK}}{M_S^2 \mu_o} \tag{3.46}$$

where μ_o is the permeability of free space, A is the exchange stiffness, and K is the magneto-crystalline anisotropy.

Further, with the decrease in critical size, the anisotropy energy is even equal/lower than thermal energy. VSM or SQUID is not able to measure the superparamagnetic nature of materials because of a longer measurement time window (~1 s). In some cases of agglomerated nanoparticles or larger nanoparticles with T_b closed to room temperature, the Mossbeaur spectroscopy at room temperature can see superparamagnetic relaxation and ferromagnetic character since it has a time window (10^{-7} s), which is just more than the relaxation of superparamagnetic particles (10^{-9} s).

For bigger-sized particles (micrometer), magneto-crystalline energy (KV) is greater than thermal energy (kT). Magnetic spins cannot do flipping from 0 to 180° (Joshi et al. 2019). For the superparamagnetic particles, the thermal energy (kT) dominates over magneto-crystalline energy (KV), i.e., (KT >>> KV). Therefore, the relaxation of the magnetic moment along the easy axis is fast ($\tau < 10^{-9}$ s). These are demonstrated in Figs. 3.9 and 3.10. Here, thermal energy (kT = 0.026 eV at room temperature) is assumed constant. In this case, the measurement of magnetic moments of superparamagnetic is not possible by simple VSM or SQUID method. It means that the time of measurement (t_m) is longer than the relaxation time ($t_m >> \tau$). By averaging, the magnetic moment is almost zero in the demagnetized state; its H_c and M_r are almost zero while applying magnetic fields (from + ve to −ve fields).

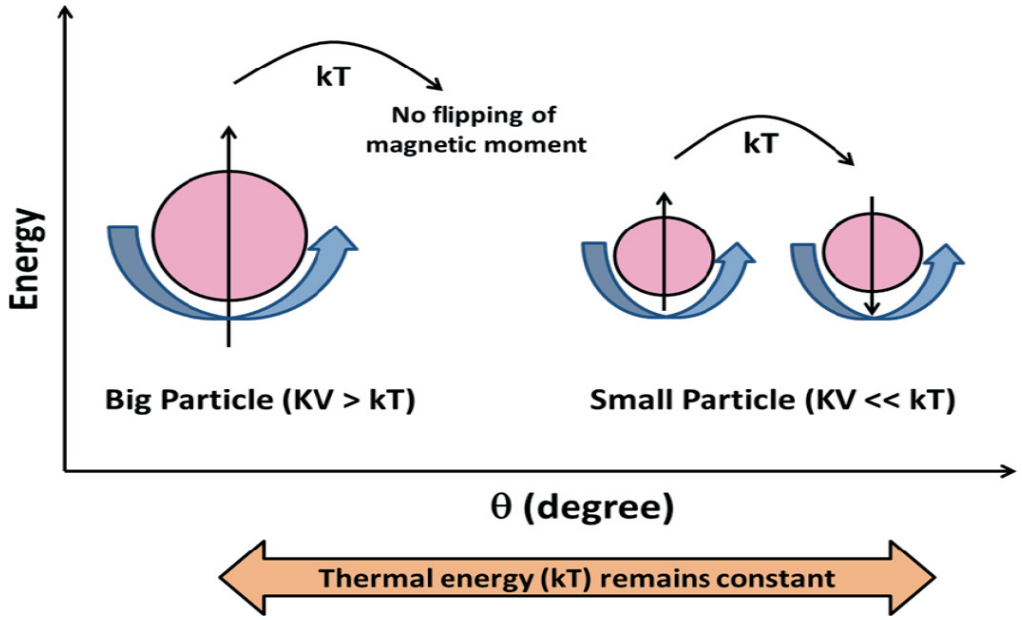

Fig. 3.9 No flipping of magnetic moment for big-sized particles, whereas flipping of magnetic moments for small-sized particles

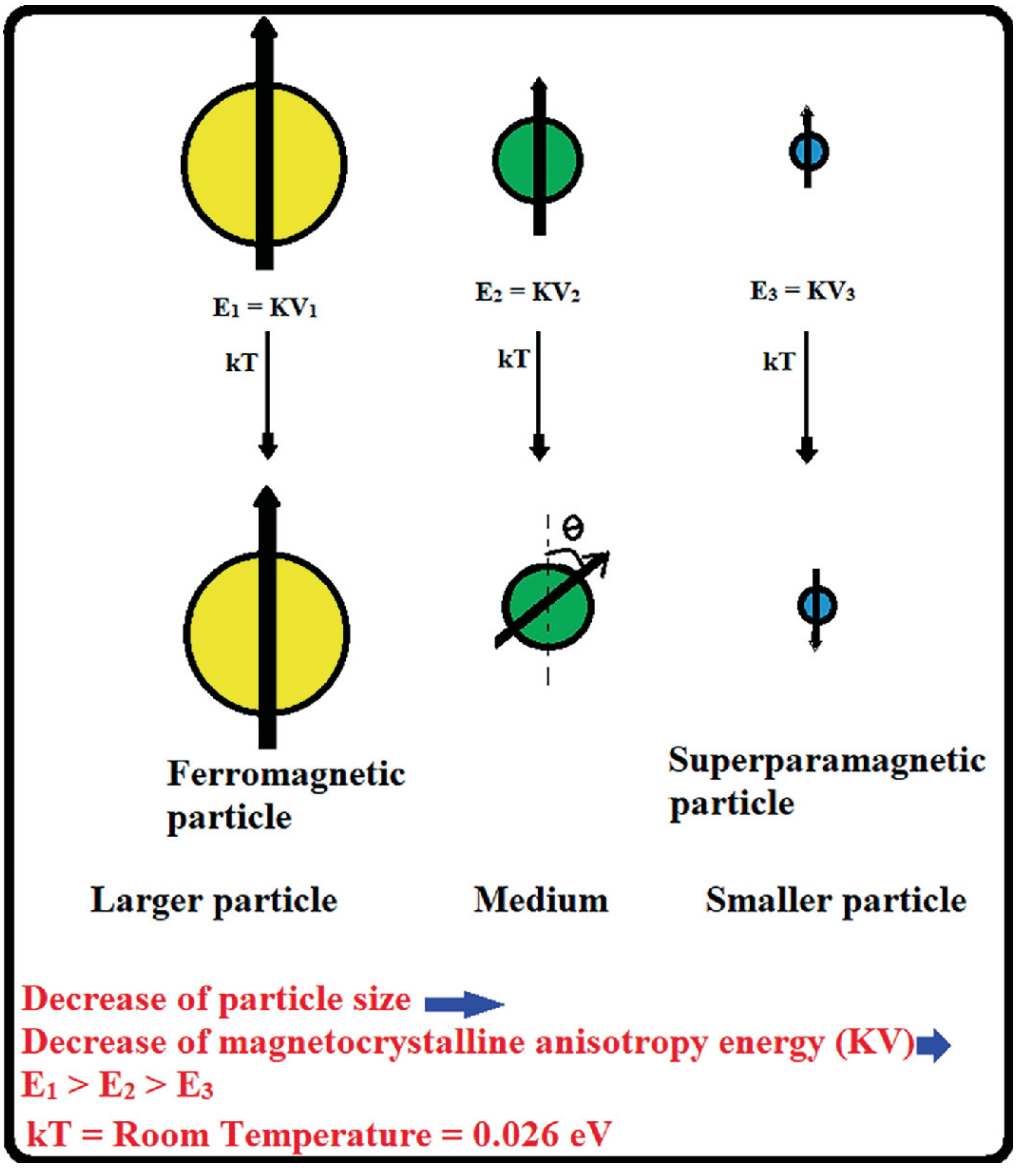

Fig. 3.10 Different orientations of magnetic moments with a decrease in particle size

The relaxation time (τ) is given by

$$\tau = \tau_0 exp\left(\frac{E_a}{k_B T}\right) \tag{3.47}$$

where τ = relaxation time

E_B = anisotropy energy barrier.

k_B = Boltzmann constant.

On the other hand, the physical rotation of particles in a liquid causes Brown relaxation (τ_B). This will be given by equation:

$$\tau_B = \frac{3V_h\eta}{k_BT} \tag{3.48}$$

where V_h = hydrodynamic volume

η = viscosity of the liquid.

If the Neel and Brownian relaxations are occurring simultaneously, then the effective relaxation (τ) is given by equation:

$$\frac{1}{\tau} = \frac{1}{\tau_N} + \frac{1}{\tau_B} \tag{3.49}$$

Using Eq. (3.46), we have the following relaxation formula:

$$\tau = \tau_0 exp\left(\frac{K_{eff}V}{k_BT}\right) \tag{3.50}$$

where $\tau_0 \sim 10^{-9}$–10^{-13} s. E_a is the energy barrier for a magnetic spin reversal from the easy direction to the opposite direction and this is equal to $K_{eff}V$, where K_{eff} is the anisotropic constant of particles and V is the volume of particles.

It is to be noted that a decrease in particle size can change the magnetic property of materials. Change in magnetic property comes from two main sources: spin relaxation and disorder in the system. Spin relaxation was already explained above. Disorder in the system arises from defects in lattice and/or surface dangling bonds. Surface dangling bonds give rise to spin canting, which reduces core ferromagnetic property. Overall, magnetization per gram reduces. Because of these two main sources, the magnetization of magnetic material gets reduced significantly. Accordingly, its coercivity and remanence magnetization are found to be different from the bulk. Figure 3.11 shows the behaviour of bulk and single domain particles: relaxation and surface dangling bonds or

surface spin canting. However, if the surrounding has chemical interactions with the surface of particles, its effects are highest in the case of small-sized particles due to the high surface area possessed by nanoparticles. Let us take a few examples. Ni nanoparticles with 100 nm size are stable in an ambient atmosphere for a few hours. In the case of Fe nanoparticles with the same size, it is unstable within a few minutes. At the initial stage, the surface reacts with oxygen present in the atmosphere. The surface becomes iron oxide, which is antiferromagnetic. After 1 day, the whole system becomes iron oxide. Thus, the magnetization study of nanoparticles must be done with an understanding of the material's stability. Fe_3O_4 nanoparticles become non-stoichiometry in a small size of 5 nm. This was confirmed by Mossbauer (discussed later). Reduction in magnetization of ferromagnetic nanoparticles with a decrease in particle size was confirmed by M-H and Mossbauer studies in many nanomaterials (Joshi et al. 2020; Gajbhiye et al. 2005; Ningthoujam and Gajbhiye 2008; Ningthoujam and Gajbhiye 2010; Sharma et al. 2018; Gajbhiye et al. 2004; Gajbhiye et al. 2004; Gajbhiye et al. 2005; Ningthoujam et al. 2008; Shukla et al. 2008; Umare et al. 2008; Ningthoujam et al. 2009; Sharma et al. 2010; Ningthoujam et al. 2012).

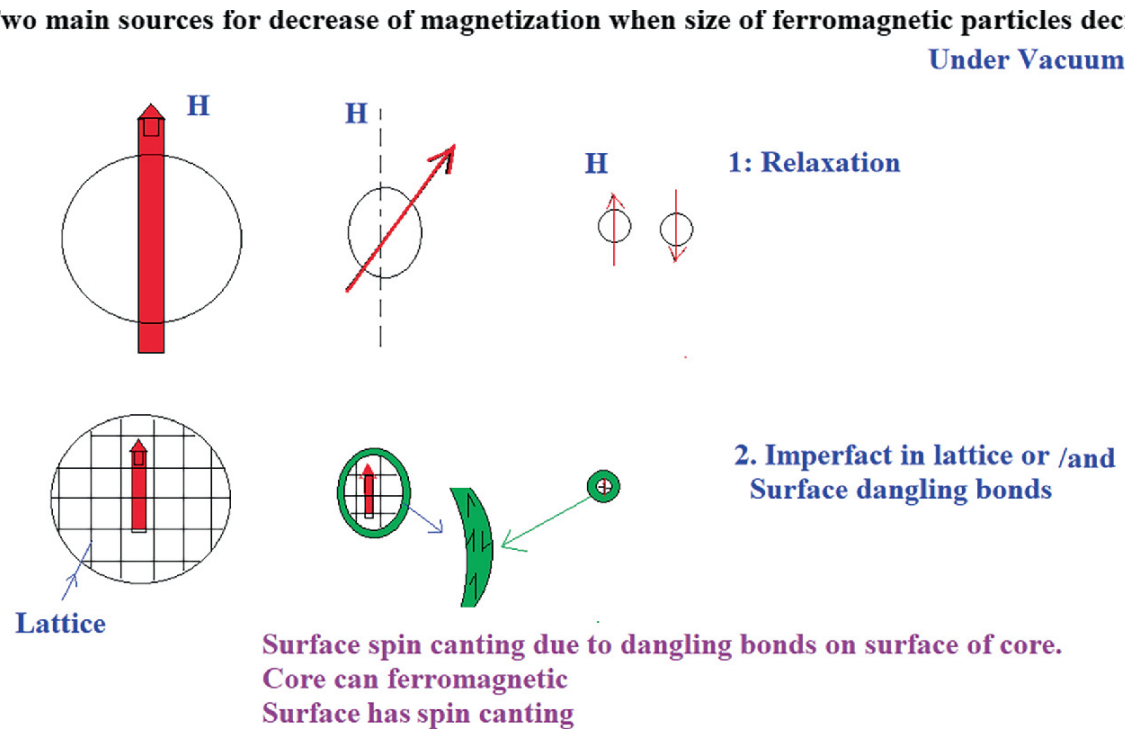

Fig. 3.11 Schematic diagram representing two main sources for the decrease of magnetization when the size of ferromagnetic or ferromagnetic particles decreases

3.11.1 Determination of Blocking temperature (T_b)

Superparamagnetic character depends on the size of the particles, effective anisotropy, applied magnetic field, and measuring time during the experiment. Blocking temperature can be determined by ZFC (zero field cool). In ZFC, the samples are cooled from high temperature (say 300 K) to low temperature (say 5 K) without applying a magnetic field, but in FC (field cool), samples are cooled from high temperature to low temperature with applying a magnetic field and then the magnetic moment is recorded with applying a small magnetic field (H = 10–100 Oe) (Gajbhiye et al. 2005; Ningthoujam and Gajbhiye 2008; Ningthoujam and Gajbhiye 2010). At the blocking temperature (T_B), both ZFC and FC curves meet (Fig. 3.12g) (Sharma et al. 2018). Below T_B, the divergence of curves occurs and above T_B, both curves go together in the same path. Below T_B, particles behave as ferromagnetic property, and above this, particles behave as

superparamagnetic behaviour. The particle size of Fe_3O_4 can be increased with the formation of the core–shell model (Fig. 3.12h, i) (Sharma et al. 2018). T_B increases with an increase in particle size. The curie temperature (T_c) is much far from T_B, i.e., $T_B << T_c$. In most cases, both ZFC and FC do not meet at T_B, instead meet at a T_{irr}(irreversible temperature), which is above T_B (Fig. 3.12h, i). This is due to the association of magnetic dipolar interaction in agglomerated superparamagnetic particles or broad particle size distribution. In pure superparamagnetic particles, it is assumed that there is no interaction among them like paramagnetic particles. In M-H curves, superparamagnetic particles of magnetite at room temperature have zero magnetization, but become ferromagnetic at 5 K (Fig. 3.12a–e) (Sharma et al. 2018). It is summarized that ferromagnetic single domains are blocked below T_b and above T_b, single domains behave superparamagnetic. The observation of the blocking temperature (T_b) was reported in many nanomaterials such as Fe_3N, Fe–Co–N, and Co (Gajbhiye et al. 2005; Ningthoujam and Gajbhiye 2008; Ningthoujam and Gajbhiye 2010). In some of magnetic nanoparticles, spin-glass nature was observed (Sharma et al. 2010; Sharma et al. 2013). This is due to coupling between surface spins of nanoparticles.

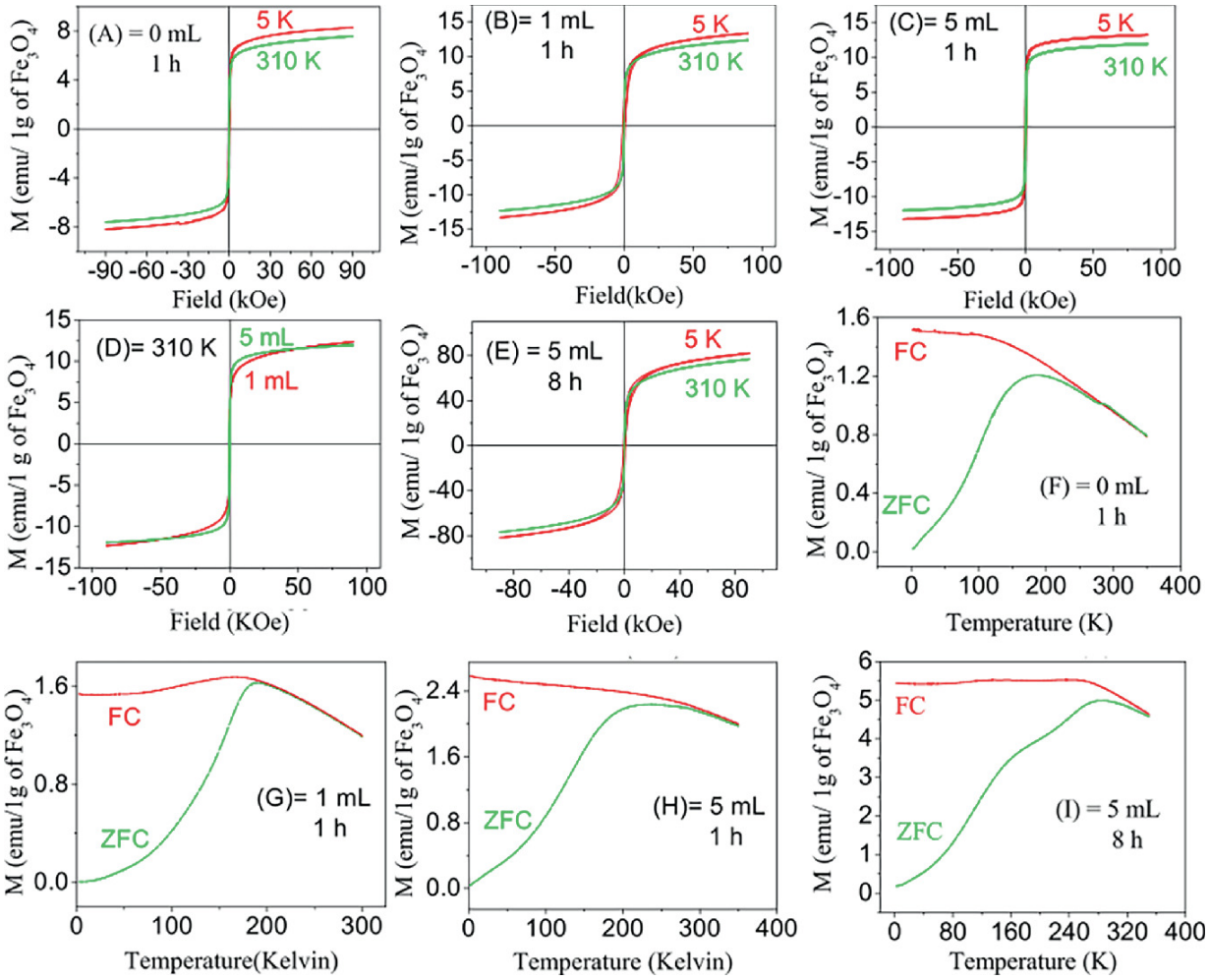

Fig. 3.12 Magnetization versus applied magnetic field (M–H) curves for superparamagnetic nanoparticles. **a** Core Magnetite (Fe_3O_4), Core–Shell Magnetite@ Magnetite (Fe_3O_4@Fe_3O_4) after addition of I mL of ferric oleate for 1 h duration of heating (**b**), addition of 5 mL of ferric oleate for 1 h (**c**), and addition of 5 mL of ferric oleate for 8 h (**e**). **d** Magnetization versus applied magnetic field (M-H) plots at 310 K for the addition of 1 mL and 5 mL of ferric oleate for 1 h. Their respective plots of magnetization versus temperature (M–T) under ZFC and FC measurements are provided in F–I. It is reproduced with permission from Springer Nature Publishers (Sharma et al. 2018)

3.11.2 Magnetic Properties of Particles Under Induction Coil

When ferromagnetic/superparamagnetic particles are kept under a radio-frequency AC field (induction coil), what does it happen? It generates heat due to hysteresis loss, eddy current, and relaxation process. The origin of magnetic heating via the inductive field depends on the size and magnetic properties of

particles. Hysteresis losses are observed in ferrimagnetic and ferromagnetic particles which have multiple domains (MD). MD contains subdomains where each domain has a definite magnetization direction. Between domains, there is an interface known as domain walls. When these are exposed to the magnetic field, the domain grows along an easy axis direction and others (domain walls) reduce in size. This phenomenon is called domain wall displacement. This phenomenon is irreversible under the decrease and increase of magnetic field amplitude which exhibits Hysteresis behaviour and produces heat under the AC magnetic field. However, we know that superparamagnetic particles consist of single domains. It is to be noted that there could be no heating due to hysteresis only under external DC magnetic fields. Under the AC magnetic field, the magnetic field is generated depending on the amount of current applied to the induction coil. This generated magnetic field can provide magnetic dipolar interaction among superparamagnetic particles. If there is magnetic dipolar interaction, it is no longer a single domain. Thus, it can generate a hysteresis loop under an AC magnetic field. This is one of the reasons producing heat. There are other factors which produce heat under AC magnetic fields such as eddy current and relaxation due to spin and Brownian motions. Magnetic spins undergo to rotate in overcoming the energy barrier $E \sim KV$, where K is the anisotropy constant and V is the volume of the particle. This energy dissipates when the particle moment relaxes to its equilibrium orientation (Neel relaxation). Due to Brownian motion, the rotation of the magnetic nanoparticles and collision among particles take place and relaxation takes place.

3.11.3 Concept of Heating from Magnetic Fluids Under AC Magnetic Field

Dispersed magnetic nanoparticles (MNPs) in a liquid can undergo two types of relaxation: Brownian and Neel’s spin relaxation (Srivastava et al. 2023; Ningthoujam et al. 2012). Brownian relaxation is applicable to all particles due to

particle rotation while Nèel's spin relaxation is applicable only to superparamagnetic nanoparticles in particular (magnetic moment rotation), respectively. Brownian relaxation is represented as (Fig. 3.13)

$$\tau_B = \frac{4\pi\eta r_h^3}{k_B T} \tag{3.51}$$

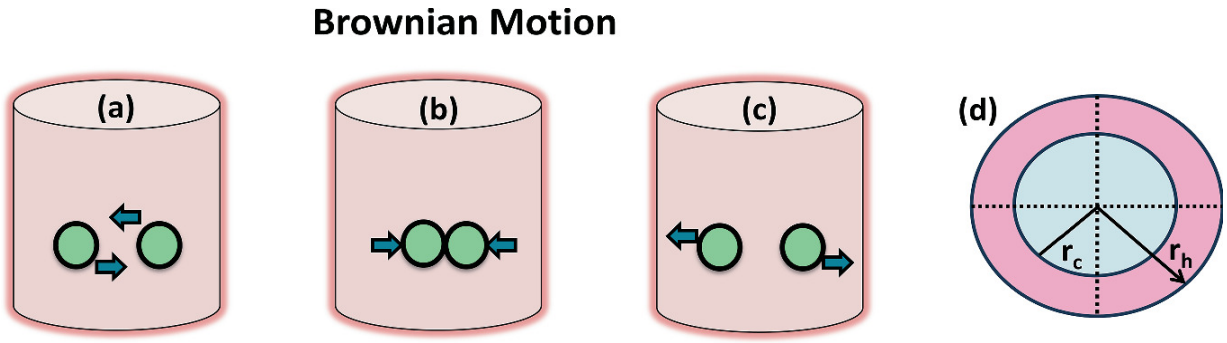

Fig. 3.13 Schematic representation of Brownian motion: small particles are suspended in a medium and can move in different directions. Here, small particles are **a** approaching, **b** collide each other, and **c** relax after collision. **d** Schematic representation of a spherical particle in a medium: a radius (r_c) and hydrodynamic radius (r_h)

where r_h is the hydrodynamic radius, η is the dynamic viscosity of carrier fluid, and T is the absolute temperature. On the other hand, Nèel's spin relaxation is given as

$$\tau_N = \tau_o e^{\Delta E/k_B T} \tag{3.52}$$

where τ_o is of the order of 10^{-9} s and ΔE is the anisotropic energy barrier which is equal to the product of anisotropic energy constant (K) and volume (V) of a single domain particle, k_B is Boltzmann's constant, and T is the absolute temperature. For the smaller nanoparticles, Nèel's spin relaxation is fast. It is to be noted that spin relaxation of the nanoparticles gets accelerated when magnetic nanoparticles (MNPs) with agglomeration are dispersed in a liquid. For agglomerated magnetic nanoparticles, magnetic dipolar interaction exists.

When we measured magnetization versus the applied magnetic field (M-H plot), we were able to see a hysteresis loop for ferromagnetic materials, which have saturation magnetization, coercivity, and remanance magnetization. In the case of superparamagnetic nanoparticles, we could not be able to observe hysteresis loss and also heat above 30 °C could not be observed. It is due to applying a constant direction of the magnetic field. In superparamagnetic nanoparticles, H_c is zero, and magnetization increases with applied magnetic field. Its spin relaxation takes place in 10^{-9} s. The measurement time using VSM or SQUID is about 0.5–1.0 s in a DC magnetic experiment which can't be able to see the superparamagnetic spin relaxation. On the other hand, the direction of current in AC magnetic field is changing over time. For the general study, 100–300 kHz frequency and the magnetic field generated from applied current up to 400 Oe are employed. At higher frequencies say MHz, the effect of polarization comes across. The permittivity of a medium depends on field frequency, whereas the permeability of a medium depends on the magnetic field. In the case of radio-frequency range (100–300 kHz frequency), measurement time will be ~10^{-6} s and this measurement time is closer to superparamagnetic relaxation. Therefore, some of the magnetic moments under the AC magnetic field can be observed.

The ferrofluids undergo power dissipation mainly due to (i) hysteresis loss, (ii) Brownian motion loss, (iii) Nèels spin relaxation, and (iv) Eddy current. Hysteresis loss in an AC magnetic field with a frequency (f) is given as

$$\text{Area under curve} = f \int MdH \tag{3.53}$$

where $\mathrm{f} = \omega/2\pi$ (ω is angular frequency). H is the applied magnetic field and M is magnetization. The behaviour of magnetic materials is defined by their magnetic susceptibility (χ), which is equal to the ratio of magnetization M to the applied magnetic field (H). In the AC magnetic field, χ is represented as

$$\chi = \chi' + \mathrm{i}\,\chi'' \tag{3.54}$$

i.e., Magnetic susceptibility has two components: $\chi^{/}$ (real part) and $\chi^{//}$ (imaginary part). The imaginary part is represented as

$$\chi'' = \frac{\omega\tau}{1 + (\omega\tau^2)}\chi \tag{3.55}$$

where τ is the total relaxation contributed by Brownian (τ_B) and Neel's relaxation (τ_N). Heat loss due to Eddy current which results from the interaction between oscillating magnetic field and conductive material. This Eddy current according to Faraday's and Lenz's laws is given by

$$\mathrm{ED} = \frac{(\mu\pi D f H)^2}{20\rho} \tag{3.56}$$

where D is the diameter of particle size, f is the frequency provided to particles, H is an applied magnetic field, and ρ is the electrical resistivity of material. Eddy current is observed in conducting material (metals) as its electrical resistivity is very low. However, in insulating systems such as ferrites (except Fe_3O_4), the eddy current is almost nil. Because of this, the ferrites are used in transformers.

3.12 Characterization of Magnetic Nanoparticles

3.12.1 VSM

A vibrating sample magnetometer (VSM) is a technique to measure the magnetic moment of a sample. Initially, the sample was kept in a constant magnetic field. When the sample is moved up and down using a transducer (piezoelectric), an alternating magnetic field is created by the sample and it induces an electric field in the pickup coils of the instrument. The induced current is proportional to the magnetization of the sample.

Figure 3.14 shows the MH curve of sample Ni_3N (crystallite size = 16 nm) measured from the VSM instrument (Gajbhiye et al. 2002). It is ferromagnetic with saturation magnetization of 1.67 emu/g and coercivity of 220 Oe. The saturation magnetization is less than that of Ni. The Curie temperature (T_c) is found to be 634 K. High-temperature Curie temperature is usually measured by VSM instrument.

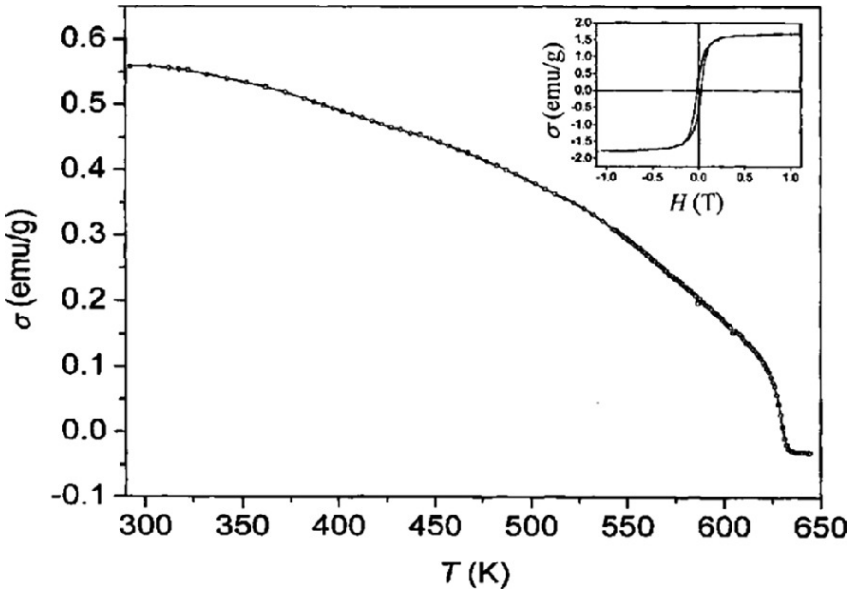

Fig. 3.14 Specific magnetization of Ni_3N with temperature (T) and magnetic field (H) as inset. Author's work (Gajbhiye et al. 2002)

3.12.2 SQUID

A SQUID (superconducting quantum interference device) is one of the sensitive magnetometers, which can measure extremely precise magnetic fields or magnetic moments. It consists of superconducting loops of Josephson junctions. Its sensitive is far better than that of VSM. Magnetization (M) versus magnetic field (H) of Fe_3O_4 nanoparticles and its core–shell nanoparticles were measured by using SQUID (Fig. 3.12) (Sharma et al. 2018). It shows the hysteresis loop at 5 K and no-hysteresis loop at 300 K indicating ferromagnetic character at 5 K and superparamagnetic at 300 K. Superconducting VN shows diamagnetic property below transition (9 K) and paramagnetic property above transition (Figs. 3.15 and 3.16)

(Sudhakar et al. 2004). Doping of B and La in VN decreases superconducting property. Similarly, MoN and Mo_2N show the paramagnetic nature above the superconducting transition (Gajbhiye and Ningthoujam 2004).

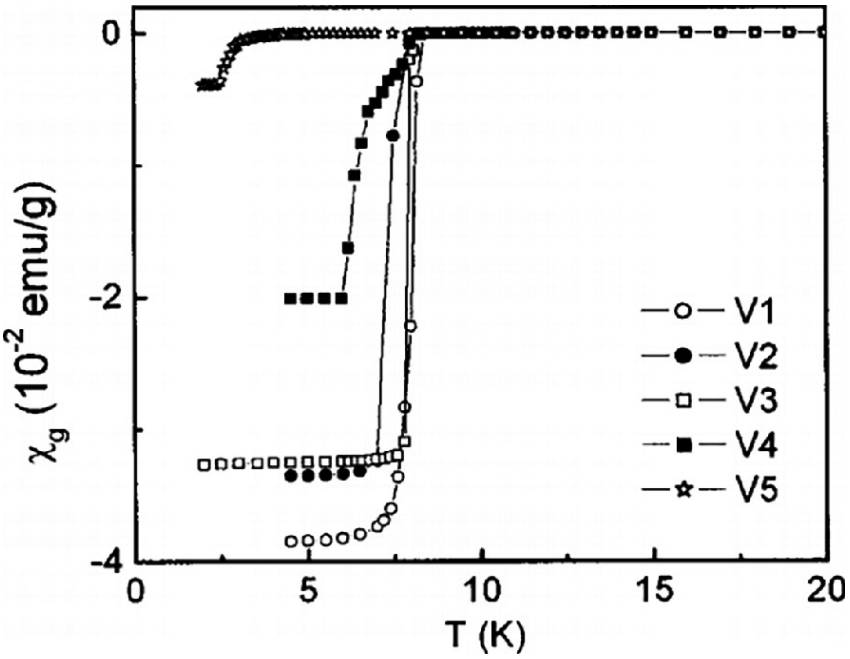

Fig. 3.15 The magnetic susceptibility at low temperatures for VN (V1) and VN doped with B, La samples (V2–V5). It shows the superconducting transitions (T_C) below 10 K. Superconducting property decreases with doping. It is reproduced with permission from AIP Publishers (Sudhakar et al. 2004)

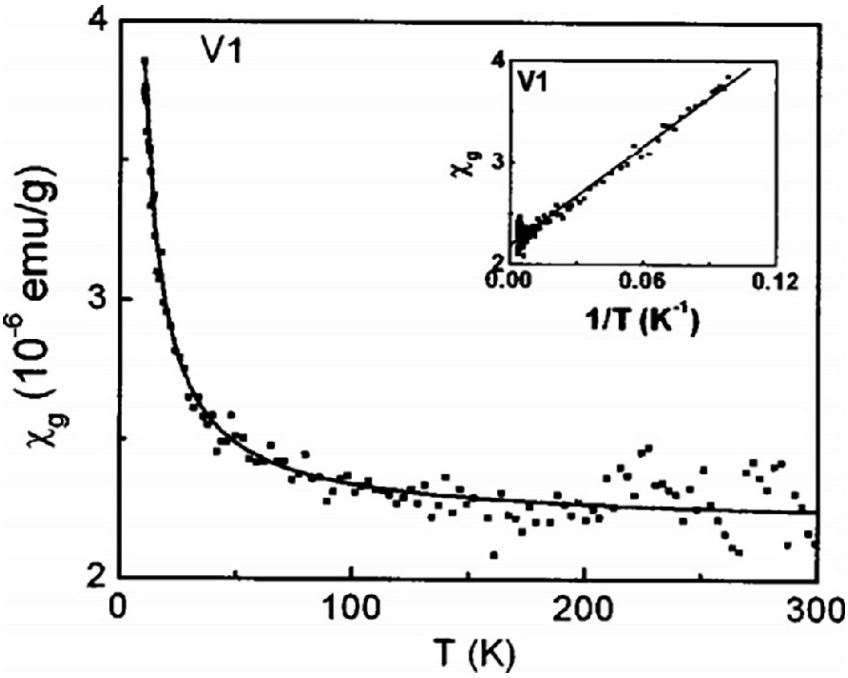

Fig. 3.16 The magnetic susceptibility of VN (V1) with temperature above T_C (10–300 K). The solid line is the best fit to the data $=_0 + \frac{C}{T}$. Inset: we plot the χ vs. 1/T indicating Curie law behaviour at low temperatures and the temperature-independent magnetic susceptibility (°) at higher temperatures. It is reproduced with permission from AIP Publishers (Sudhakar et al. 2004)

Cobalt nanoparticles in the range of 3 to 24 nm show the ferromagnetic character at 5 K (Fig. 3.17) (Gajbhiye et al. 2008). Saturation magnetization increases with the increase of particle size. Its coercivity (H_C) increases with an increase of particle size up to 10 nm and decreases with a further increase of particle size (Fig. 3.18) (Gajbhiye et al. 2008). Below 10 nm, particles behave in a single-domain nature, whereas above 10 nm, they behave in a multi-domain nature. Magnetization increases with the increase of particle size.

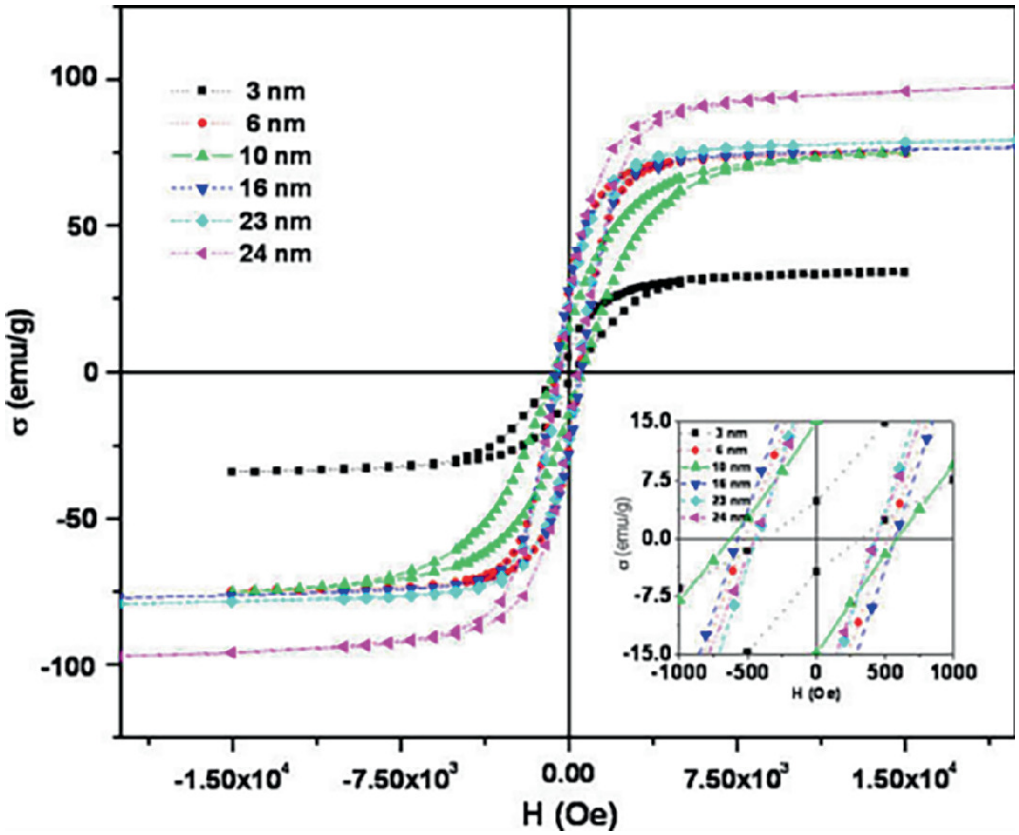

Fig. 3.17 Magnetization (σ -H) curves for Co nanoparticles of various sizes (3 to 24 nm) recorded at 5 K. Inset: The enlarged view of these curves nearly at 0 Oe field. It is reproduced with permission from Elsevier Publishers (Gajbhiye et al. 2008)

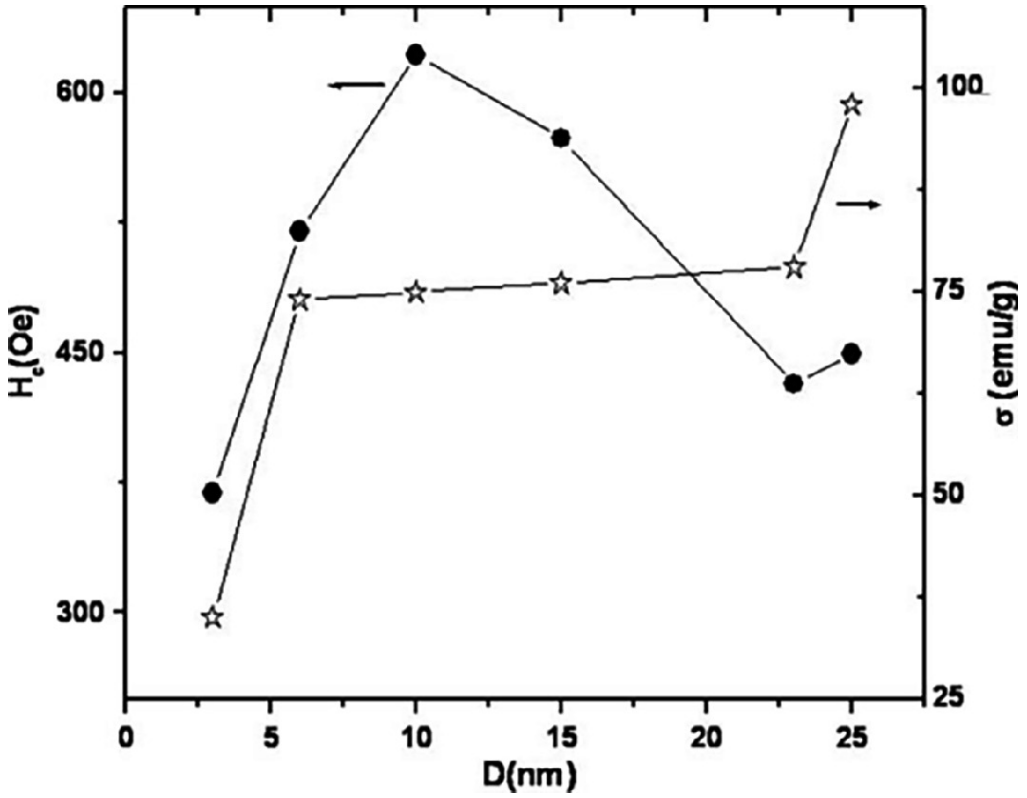

Fig. 3.18 Coercivity (H_C) vs. Particle sizes (D) for Co nanoparticles measured at 5 K (Left). The corresponding saturation magnetization (M_S) vs. Particle size (Right). It is reproduced with permission from Elsevier Publishers (Gajbhiye et al. 2008)

The high uniaxial anisotropy (K_u ~ (1–7) 10^7 ergs/cm^3) $L1_0$ phases of materials such as FePt, FePd, and CoPt are promising materials for the use of ultra-high-density magnetic recording. 3 nm FePdfcc phase nanoparticles show superparamagnetic at room temperature with blocking temperature at 58 K (ZFC and FC curves, Fig. 3.19); below this temperature (i.e., 5 K), it shows ferromagnetic property (Fig. 3.20) (Gajbhiye et al. 2008). When size increases to 10 nm with a face-centred tetragonal phase, particles show ferromagnetic properties at room temperature (Fig. 3.21) (Gajbhiye et al. 2008).

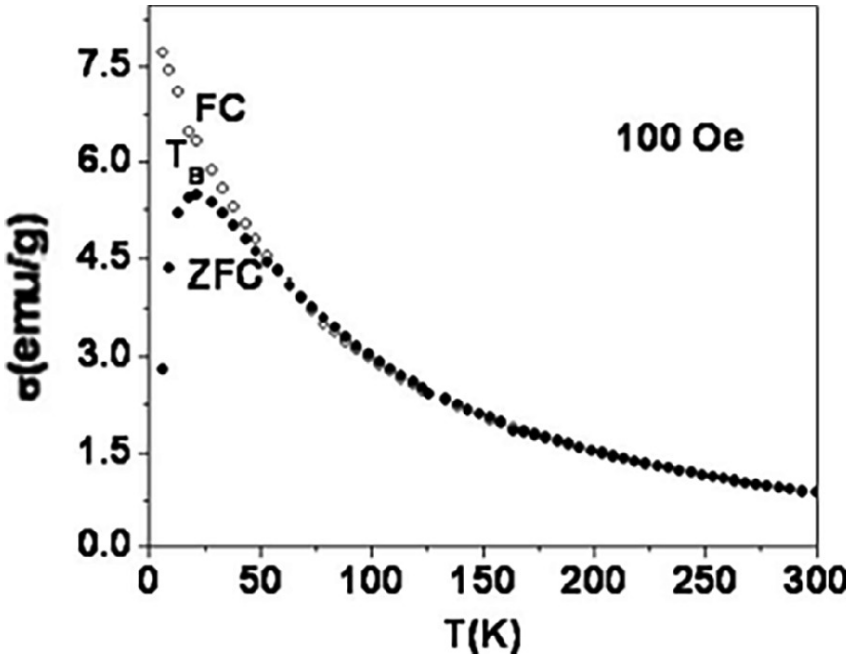

Fig. 3.19 The ZFC and FC curves for as-prepared fccFePd (3 nm size) particles. H is applied at 100 Oe. It is reproduced with permission from AIP Publishers (Gajbhiye et al. 2008)

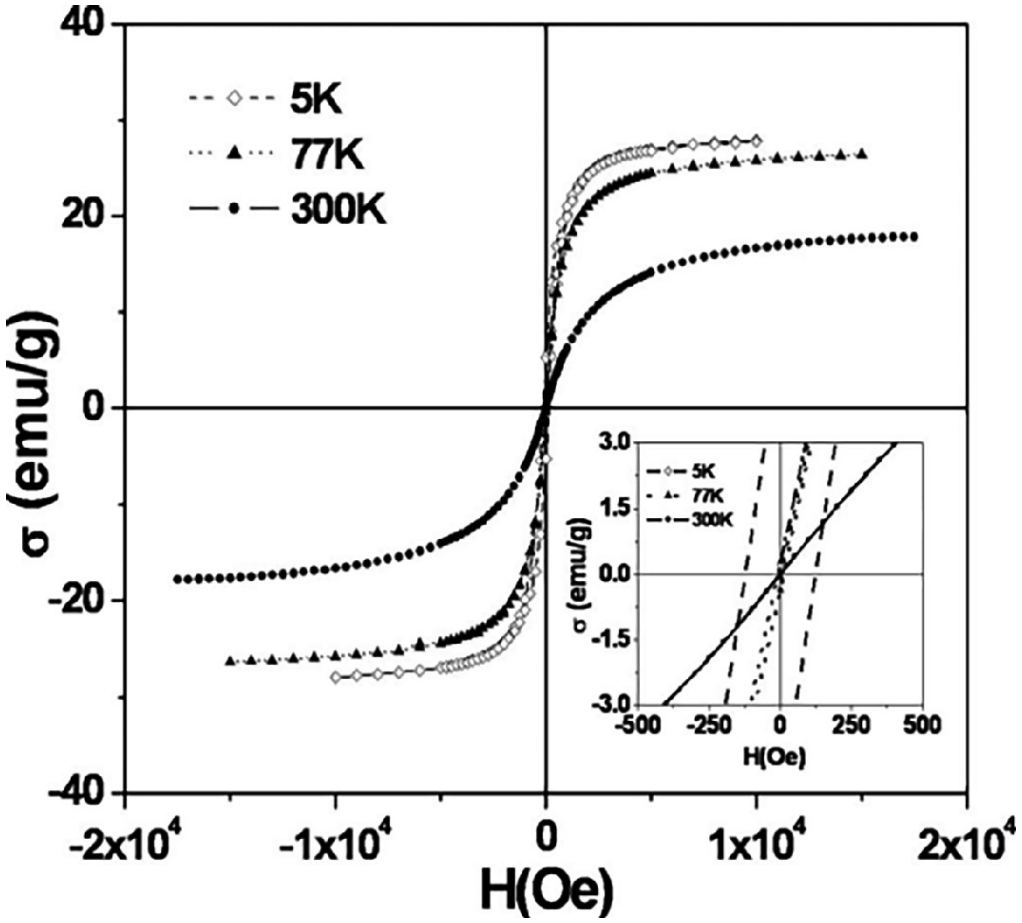

Fig. 3.20 Magnetization vs. applied magnetic field plots measured at 5, 77, and 300 K for as-synthesized fccFePd nanoparticles (3 nm). Inset: Enlarge view of these curves near 0 Oe. It is reproduced with permission from AIP Publishers (Gajbhiye et al. 2008)

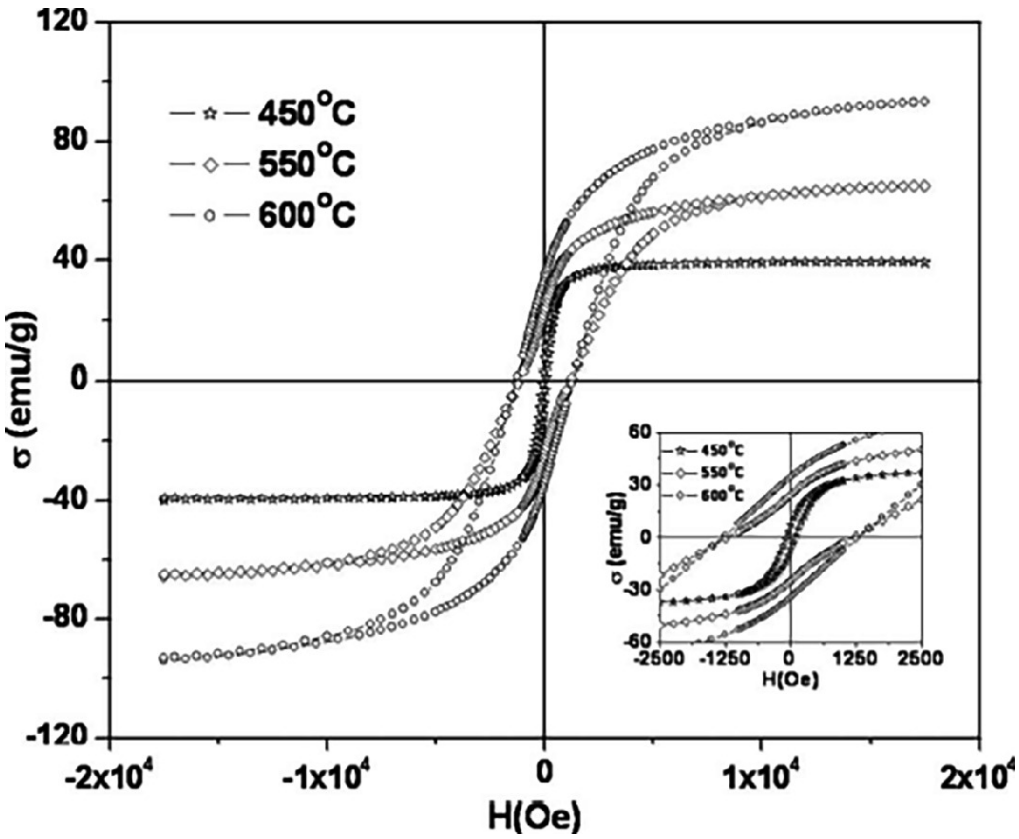

Fig. 3.21 Magnetization vs. applied field plots measured at 300 K for 450, 550, and 600 °C annealed FePd nanoparticles. Inset: Enlarge view of these curves near 0 Oe. It is reproduced with permission from AIP Publishers (Gajbhiye et al. 2008)

$Co_{50}Ni_{50}$ nanoparticles with a size of 25 nm show the superparamagnetic property at room temperature and ferromagnetic property at 5 K (Fig. 3.22) (Sharma et al. 2010). Even at 5 K, it does not attain saturation due to the contribution of superparamagnetic fraction arising from broad particle size distribution.

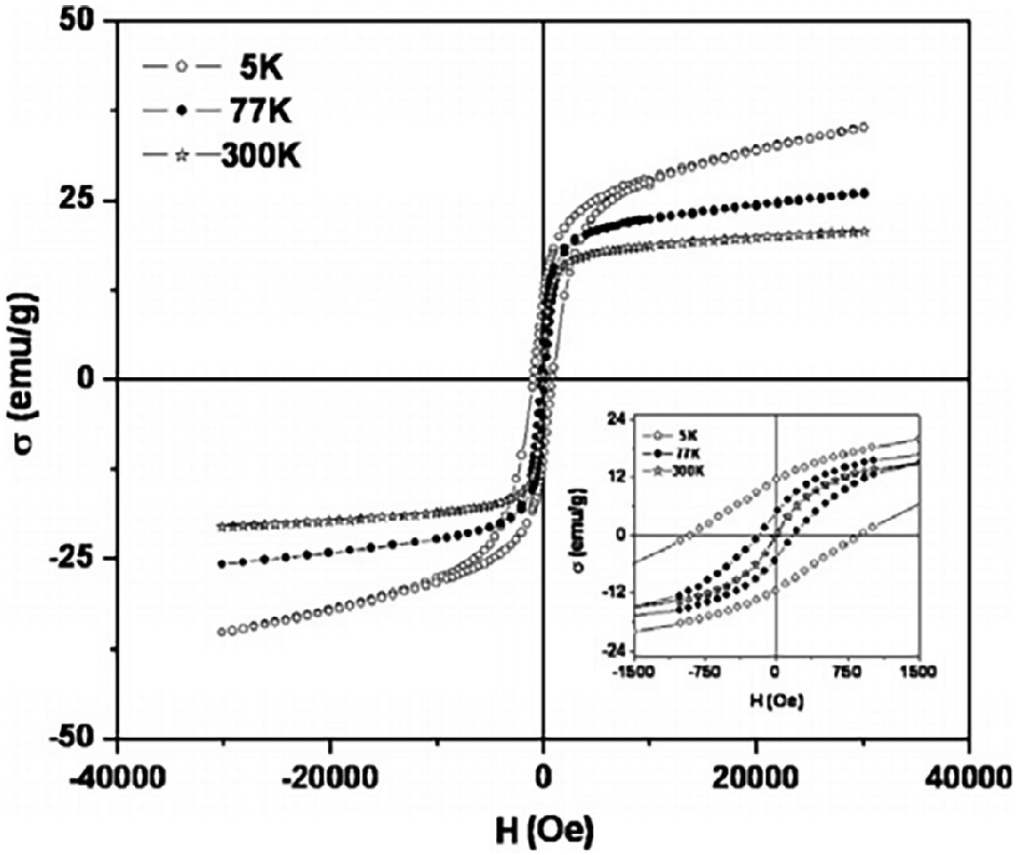

Fig. 3.22 Magnetization versus applied field plot measured at 5, 77, and 300 K for $Co_{50}Ni_{50}$. Inset: Enlarged view of these curves near 0 Oe. It is reproduced with permission from Elsevier Publishers (Sharma et al. 2010)

Core–shell nanoparticles (γ-Fe_2O_3@Mn_xO_y) show the superparamagnetic property at room temperature and exchange bias at 5 K. Here, γ-Fe_2O_3 is ferromagnetic, whereas Mn_xO_y is antiferromagnetic at 5 K. With an increase in the thickness of Mn_xO_y, exchange bias increases. The blocking temperature of the material decreases with the thickness of Mn_xO_y. This is shown in Fig. 3.23 (Joshi et al. 2021). Possible magnetic interactions between the core and shell of nanoparticles under different experimental conditions are shown in Fig. 3.24 (Joshi et al. 2021).

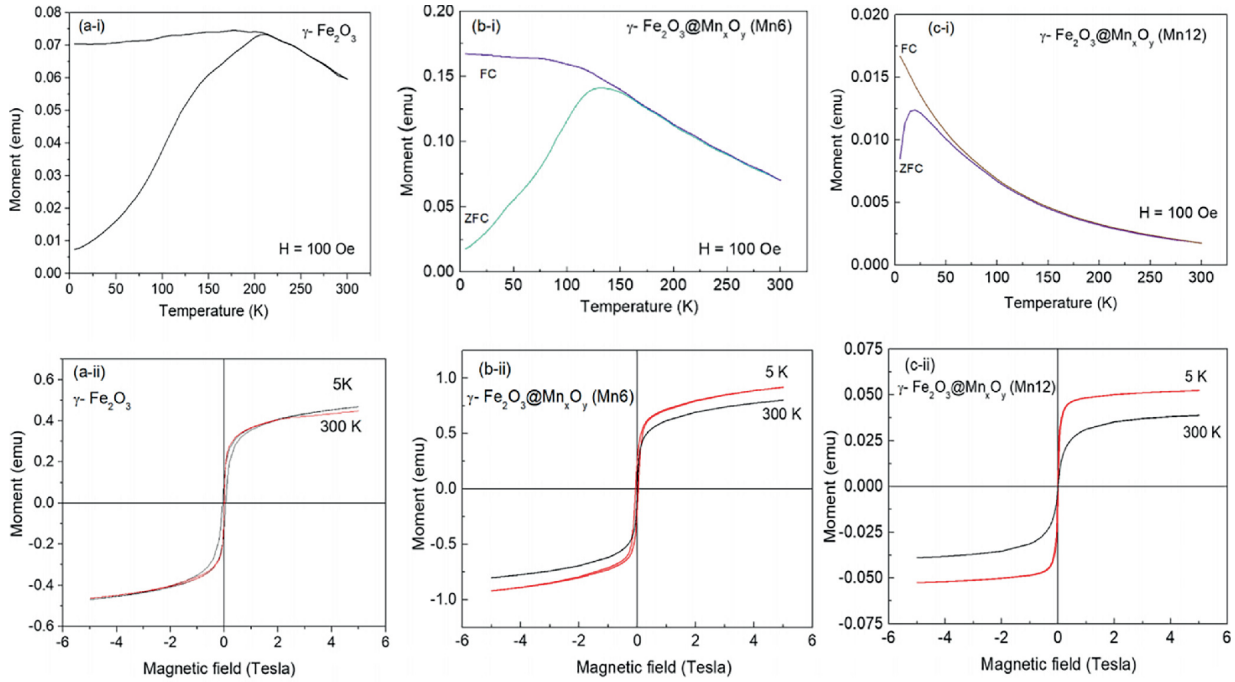

Fig. 3.23 Magnetization vs. temperature (ZFC and FC curves) and magnetization vs. magnetic field (M-H curves) for all the nanoparticles: (a-i,a-ii) γ-Fe_2O_3, (b-i,b-ii) γ-Fe_2O_3@Mn_xO_y (Mn6), and (c-I, c-ii) γ-Fe_2O_3@Mn_xO_y (Mn12). Mn6 and Mn12 correspond to the atomic percentage of Mn with respect to Fe. It is reproduced with permission from ACS Publishers (Joshi et al. 2021)

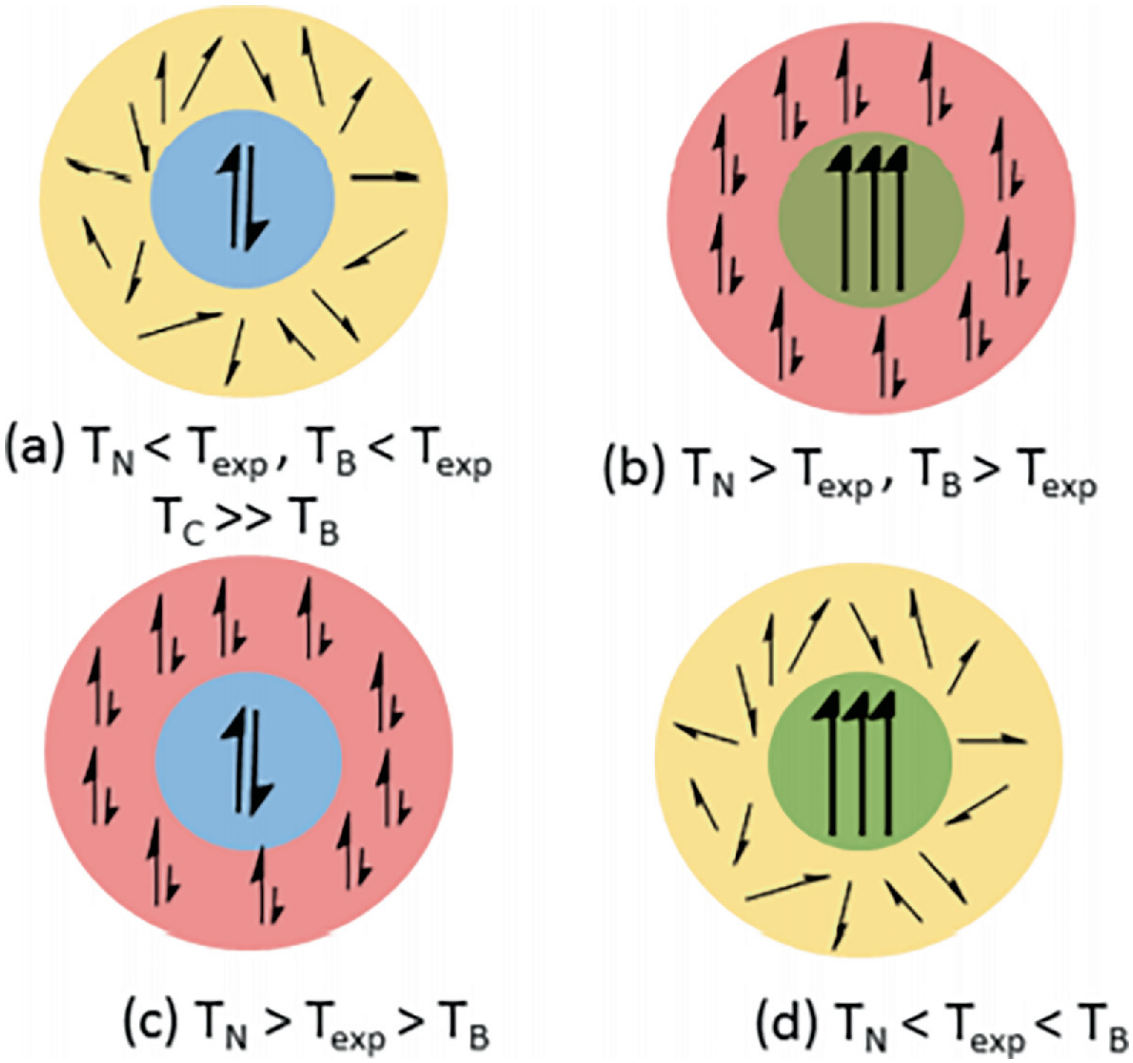

Fig. 3.24 Various possible magnetic interactions from core and shell of nanoparticles: superparamagnetic core and paramagnetic shell (**a**), ferromagnetic core and antiferromagnetic shell (**b**), superparamagnetic core and antiferromagnetic shell (**c**), and ferromagnetic core and paramagnetic shell (**d**). Here symbols are defined: T_N(Néel temperature), T_B(blocking temperature), T_C(Curie temperature), and T_{exp}(measurement temperature). It is reproduced with permission from ACS Publishers (Joshi et al. 2021)

3.13 Mössbauer Spectroscopy

The Mössbauer spectroscopy is a technique that can be used to study nuclear structure with the absorption and re-emission of gamma rays. To get the Mössbauer spectrum, the recoil-free emission and absorption in solids are required. The set up of this instrument requires a γ-ray source that is oscillated

towards and away from the sample at a constant velocity (drive), a sample, a detector, and a collimator to filter the γ-ray rays. The drive helps in getting resonance of absorption and re-emission of gamma rays by atoms/ions fixed in a solid. This was first observed by Rudolf Mössbauer in 1957 and he was awarded the Nobel Prize in Physics in 1961. Atoms with a nuclear spin quantum number (I = 1/2) at the ground state can undergo the Mossbauer transition to a higher excited state (I = 3/2). The ^{57}Co source is used for the Mossbauer spectroscopy of iron-containing compounds or samples. Through the capture of e^-, ^{57}Co undergoes decay to ^{57}Fe with a half-life of 272 days. The percentage of ^{57}Fe is 2.12% in nature and it has I = ½ in the ground state and I = 3/2 in the excited state. Three parameters such as isomer shift, quadrupole splitting, and hyperfine splitting can be derived. Depending on values, the behaviour of iron in particles such as paramagnetic, superparamagnetic, antiferromagnetic, and ferromagnetic or ferrimagnetic nature can be determined.

The three types of nuclear interaction are observed:

(1) Isomer shift: This is due to the difference in the electron densities at ground and excited states.

(2) Quadrupole splitting: This splitting arises due to atomic scale electric field gradients.

(3) Zeeman splitting: This is arrived due to non-nuclear magnetic fields.

This is a very sensitive technique which provides a higher energy resolution. This means that the Fe environment in a sample can be identified.

Mossbauer measurements of superparamagnetic iron oxide nanoparticles (SPIONPs) will be discussed here. The ferrimagnetic iron oxides (Fe_3O_4 and γ -Fe_2O_3) nanoparticles have shown their profound applications in medicine, MRI images, magnetic recording and bio separations, cell-labelling, etc.

3.13.1 Fe_3O_4

Fe_3O_4 has been known as the mineral magnetite which is a ferrimagnet containing Fe^{3+} and Fe^{2+} ions with the inverse spinel structure (Chakraborty et al. 2015; Majeed et al. 2014). This is a conductor at room temperature due to electron hoping from Fe^{2+} to Fe^{3+} site. 2 Fe^{3+} ions occupy the tetrahedral and octahedral sites of cubic structure, and 1 Fe^{2+} ion occupies the octahedral site. Oxygen ions occupy cubic close packing (ccp). Spins of Fe^{3+} at the tetrahedral site are antiparallel to those of Fe^{3+} at the octahedral site. Only the remaining Fe^{2+} at the octahedral site contributes to the magnetic moment of the Fe_3O_4 compound (i.e., $4\mu_B$). After conversion from $4\mu_B$ to magnetization, it becomes 92 emu/g. There is a transition (the Verwey transition) from the cubic structure at room temperature to a monoclinic structure at 119 K below which it is a non-conductor. This has a tendency to obtain non-stoichiometric with the formula $Fe_{3-\delta}O_4$ for magnetite nanoparticles, which can be identified by the Mossbauer spectroscopy (Lyubutin et al. 1926). However, the XRD (X-ray diffraction) pattern is not an effective tool to distinguish Magnetite (Fe_3O_4) and Maghmite (γ-Fe_2O_3), but the Mossbauer spectroscopy can distinguish both easily (Jiao et al. 2006; Lyubutin et al. 1926).

Bulk Fe_3O_4 shows the two sextets spectrum corresponding to Fe^{3+} at the tetrahedral site and $Fe^{2.5}$ (average of Fe^{3+} and Fe^{2+}) at the octahedral site indicating ferrimagnetic behaviour at room temperature. The hyperfine value of iron at the tetrahedral site (49.4 T) is more than that at the octahedral site (46.1 T). The intensity ratio of iron at octahedral and that at tetrahedral is 2:1 indicating that 2Fe in octahedral site and 1Fe in tetrahedral site. Quadrupole splitting values are almost zero. Isomer shifts at tetrahedral and octahedral sites are 0.28 and 0.67 mm/s, respectively (Fig. 3.25) (Hah et al. 2021).

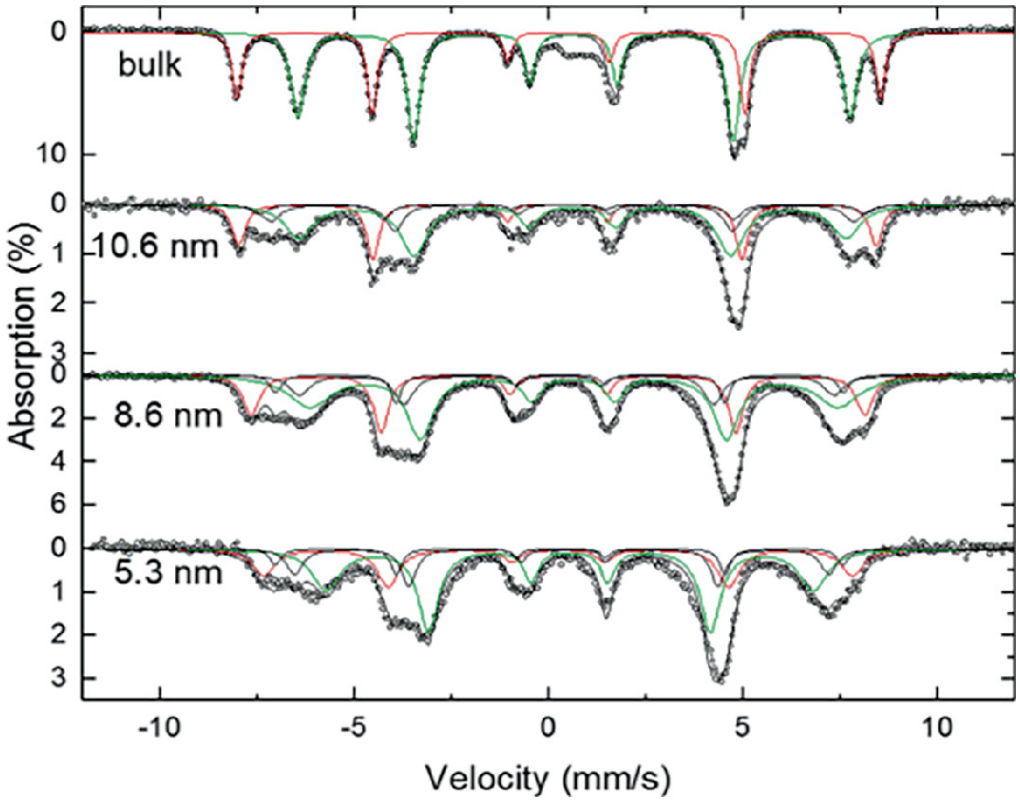

Fig. 3.25 Mössbauer spectra of Fe_3O_4 at room temperature with different particle sizes from 5 to 10 nm and bulk. A magnetic field with 20 kg is applied perpendicular to the γ-rays. The sextets spectrum is fitted with the Mossbauer program. Red lines (−) are the tetrahedral sites and green lines (−) are the octahedral sites. The lines shown in black (−) are from γ-Fe_2O_3 impurities. It is reproduced with permission from Elsevier Publishers (Hah et al. 2021)

When the particle size of Fe_3O_4 decreases to nanosize, hyperfine values at both tetrahedral and octahedral sites decrease. These can be studied by the Mossbauer spectroscopy (Fig. 3.26) (Hah et al. 2021). When size decreases to 10 nm, hyperfine at room temperature is almost nill. Doublet peaks appear with large line width. Isomer shift of 0.62 and quadrupole splitting of 0.34 are observed indicating superparamagnetic character. With further decrease of size down to 5 nm, line width decreases without much change in isomer shift and quadrupole splitting. For 10 nm particle size, hyperfine appears with a decrease of temperature for measurement say below 150 K (known as blocking temperature, T_b), which is demonstrated by the Mossbauer spectra recorded at different temperatures

(Fig. 3.27) (Hah et al. 2021). The T_b value decreases with a decrease in particle size. For 5 nm size, its T_b is ~60 K (Fig. 3.28) (Hah et al. 2021). In the presence of a magnetic field (say 20 kg), 5 nm size particles can become ferrimagnetic at room temperature (Fig. 3.25) (Hah et al. 2021). With a decrease in particle size, the isomer shift value at the octahedral site decreases, whereas that at the tetrahedral site is almost constant. It means that the amount of Fe^{2+} decreases with a decrease in particle size. On the basis of hyperfine values, the area ratio of octahedral and tetrahedral sites is 1.67:1 for 5 nm-sized particles as compared to bulk (2:1). This suggests that there are vacancies of Fe^{3+} at the octahedral site. Therefore, nanosize particles are non-stoichiometry.

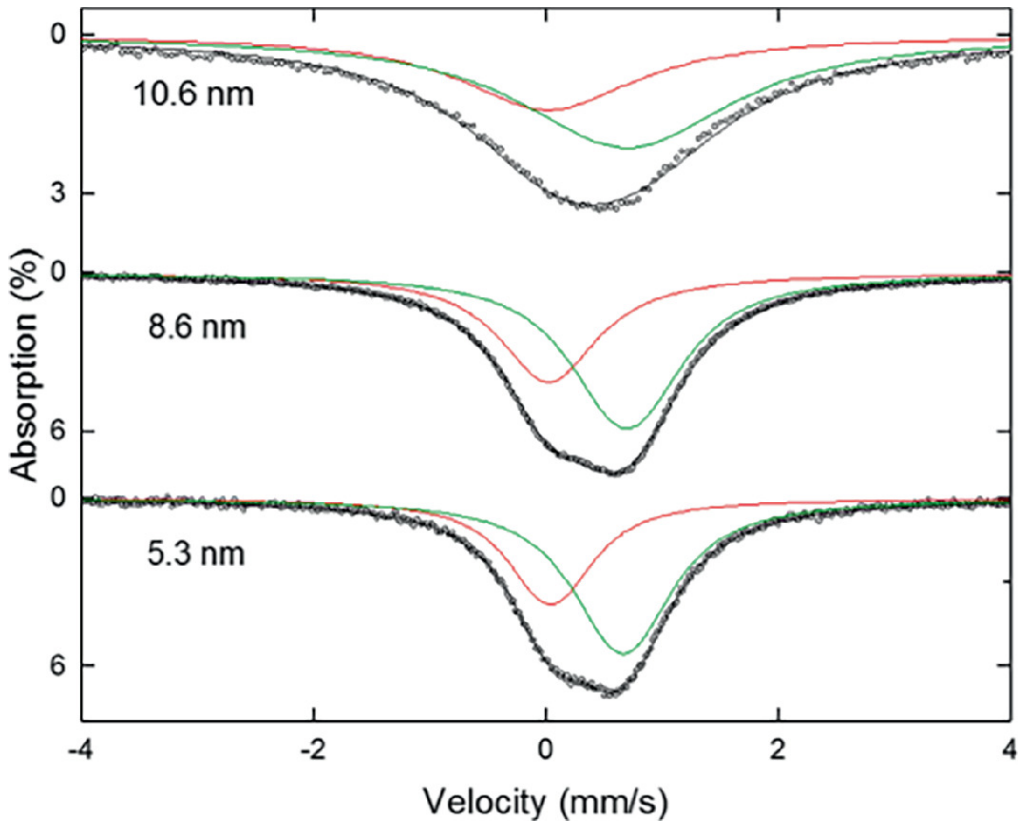

Fig. 3.26 Mössbauer spectra of Fe_3O_4 nanoparticles with sizes from 5 to 10 nm at room temperature. It is fitted with the Mossbauer program. Red lines (−) are the tetrahedral (A) sites and green lines (−) are the octahedral (B) sites. It is reproduced with permission from Elsevier Publishers (Hah et al. 2021)

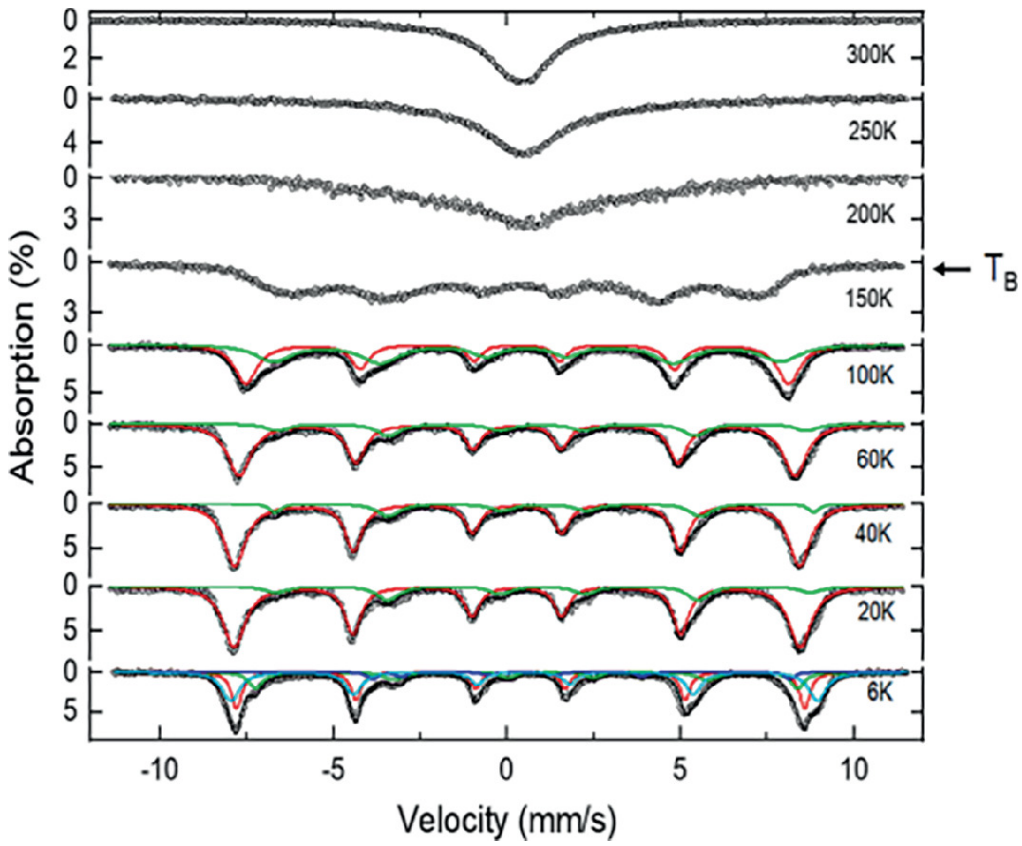

Fig. 3.27 Mössbauer spectra of Fe_3O_4 nanoparticles (10 nm) recorded at various temperatures. The blocking temperature T_B is found to be at 150 K. It is fitted with the Mossbauer program. Red lines (−) are the tetrahedral (**a**) sites and green lines (−) are the octahedral (**b**) sites. It is reproduced with permission from Elsevier Publishers (Hah et al. 2021)

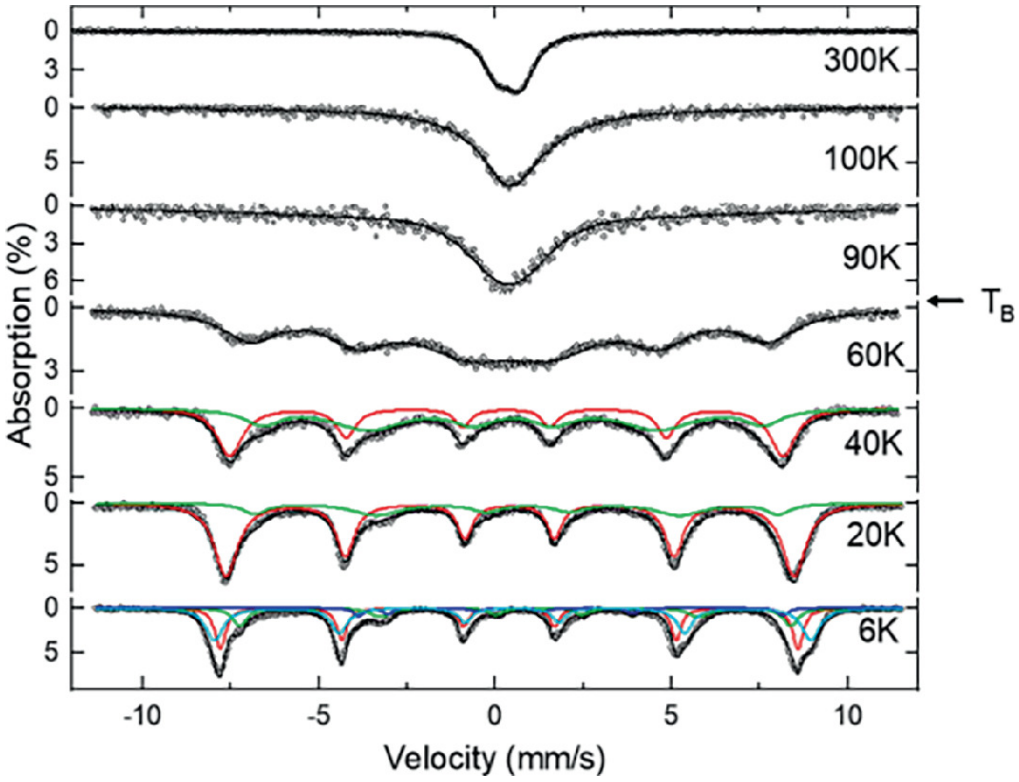

Fig. 3.28 Mössbauer spectra of Fe_3O_4 nanoparticles (5 nm) measured at various temperatures. The blocking temperature T_B is found to be at 60 K. Red lines (−) are the tetrahedral (**a**) sites and green lines (−) are the octahedral (**b**) sites. It is reproduced with permission from Elsevier Publishers (Hah et al. 2021)

3.13.2 $CoFe_2O_4$ and $NiFe_2O_4$

$CoFe_2O_4$ and $NiFe_2O_4$ nanoparticles with sizes of 9 and 30 nm show ferromagnetic properties, which can be predicted from Mossbauer spectra. Sextets spectrum could be observed. Interestingly, small sizer 9 nm particles have a superparamagnetic fraction (doublet peaks) (Fig. 3.29) (Gajbhiye et al. 2005).

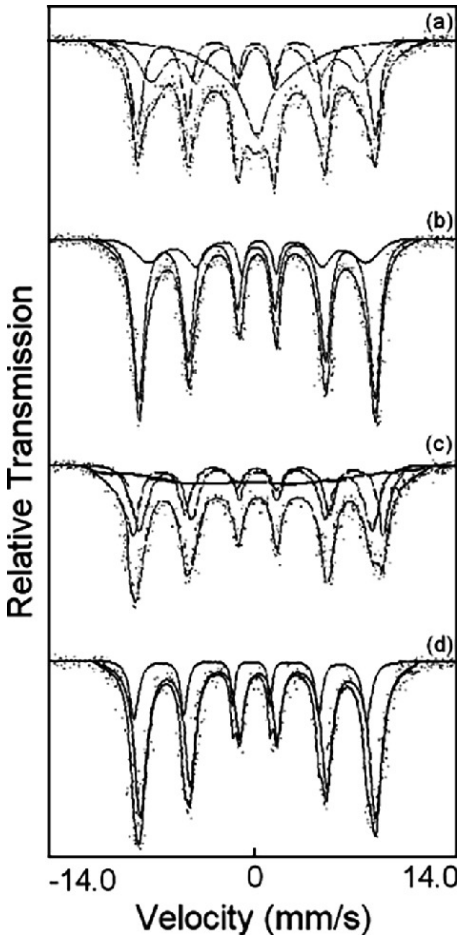

Fig. 3.29 Mössbauer spectra of $CoFe_2O_4$ particles: **a** 9 nm and **b** 30 nm and $NiFe_2O_4$ particles: **c** 9 nm and **d** 30 nm measured at room temperature. It is reproduced with permission from Elsevier Publishers (Gajbhiye et al. 2005)

3.13.2.1 Agglomerated Fe_3O_4 Particles Dispersed in a Medium

Agglomerated Fe_3O_4 particles (MN) with particle sized 10 nm show the superparamagnetic behaviour at room temperature in the magnetic study (M-H curves, $H_c \sim 0$ Oe), which is confirmed by observation of the superparamagnetic doublet in the Mossbauer study (Ghosh et al. 2011). Still, ferrimagnetic sextets (tetrahedral and octahedral sites of Fe) can be seen. It is suggested that agglomerated particles have magnetic dipolar interaction leading to ferrimagnetic character. The measurement time for Mossbauer is 10^{-7} s, whereas that for VSM/SQUID is 1 s. The relaxation of superparamagnetic

particles could not be determined by VSM/SQUID. However, it can be seen by the Mossbauer spectroscopy. This is shown in Fig. 3.30 (Ghosh et al. 2011). After dispersion in different mediums: PEG (polyethylene glycol, MN-PEG) and oleic acid (surfactant, OA-MN), the ferromagnetic fraction reduces drastically (Fig. 3.30) (Ghosh et al. 2011). It is suggested that with a decrease of agglomeration of nanoparticles, superparamagnetic fraction increases due to faster relaxation of spins.

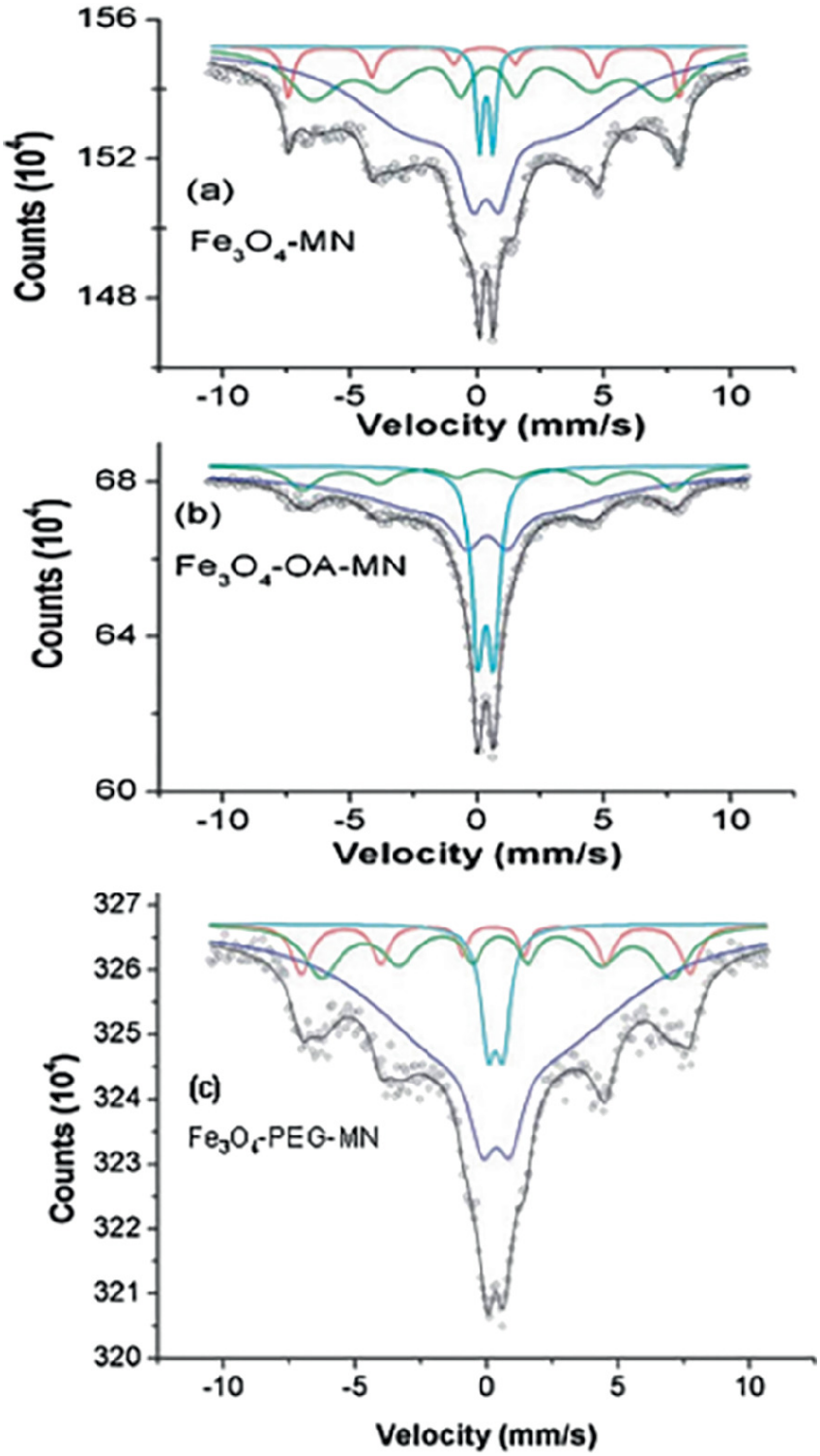

Fig. 3.30 Mossbauer spectra of **a** Fe_3O_4–MN, **b** Fe_3O_4–OA–MN, and **c** Fe_3O_4–PEG–MN. It is reproduced with permission from RSC Publishers (Ghosh et al. 2011)

3.14 Applications

Magnetic materials have been used in many applications from industry to environment to space to biology (Li et al. 2022; Di et al. 2020; Kritika 2022; Ali et al. 2021). Some are highly paramagnetic at room temperature. Some are ferromagnetic at room temperature. Some show magnetoresistance (negative or positive). Some are diamagnetic. Some compounds show a mixture of superconducting and ferromagnetic properties. When the size of particles changes from micron to nanometer, their intrinsic properties vary. Even when the dimension of particles changes from 3D to 2D to 1D to 0D, their magnetic properties change. Some molecules are magnetic. In low temperatures, metastable magnetic properties such as spin glasses properties are observed. Complexity of spins at low temperatures is observed in spin glasses.

In biological applications, the toxicity and biocompatibility of materials play an important role. In industry, magnetic nanoparticles, nanodots, hollows, and nanowires have been used. Development of data storage and read access memory are based on GMR and spintronic properties. MRI contrast agents and the development of SQUID, TEM, SEM, and VSM instruments are associated with magnetic materials. The direction of electric current, rays, or electrons can be controlled by the use of strong magnetic multipoles. In space research, many magnetic components are used. Many hybrids of the magnetic core and luminescent shell and magnetic nanoparticles functionalized with biocompatible ligands have been reported for potential applications in biology (Thorat et al. 2012; Khot et al. 2013; Thorat et al. 2013; Thorat et al. 2013; Jadhav et al. 2013; Shete et al. 2013; Soni et al. 2019; Perala et al. 2021; Perala et al. 2021; Joshi et al. 2022).

3.15 Conclusions

Fundamental concepts related to units and dimensions of magnetic materials are provided. The conversion factors

required during unit conversion from CGS to SI or MKS are given in the form of a Table. The diamagnetic, paramagnetic, ferromagnetic/ ferrimagnetic, and antiferromagnetic properties are discussed in detail. Heat generation from superparamagnetic nanoparticles under AC magnetic field is discussed. Identification of bulk, nanoparticles, and non-stoichiometric Fe_3O_4 are mentioned using the Mossbauer spectroscopy. Applications of magnetic materials are briefly mentioned.

Acknowledgements

One of the authors, M. Srivastava acknowledges the award through CSIR, New Delhi (CSIR-SRA; 9146-A). We highly acknowledge Dr. A. K. Tyagi and Dr. P. A. Hassan, Chemistry Division, BARC for their support and encouragement during this work.

References

Ali, A., Shah, T., Ullah, R., Zhou, P., Guo, M., Ovais, M., Tan, Z., Rui, Y.: Review on recent progress in magnetic nanoparticles: synthesis, characterization, and diverse applications. Front. Chem. **9**, 629054 (2021)

Chakraborty, S., Sharma, K.S., Rajeswari, A., Vimalnath, K.V., Sarma, H.D., Pandey, U., Jagannath, Ningthoujam, R.S. Vatsaand, R.K., Dash, A.: Radiolanthanide-loaded agglomerated Fe_3O_4 nanoparticles for possible use in the treatment of arthritis: formulation, characterization and evaluation in rats. J. Mater. Chem. B3, 5455–5466 (2015)

Cullity, B.D., Graham, C.D.: Introduction to Magnetic Materials. Wiley (2011)

Di, S., Ning, T., Yu, J., Chen, P., Yu, H., Wang, J., Yang, H., Zhu, S.: Recent advances and applications of magnetic nanomaterials in environmental sample analysis. TrAC Trends Analyt. Chem. **126**, 115864 (2020)
[Crossref]

Gajbhiye, N.S., Ningthoujam, R.S., Weissmuller, J.: Mössbauer study of nanocrystalline ε-$Fe_{3-x}Co_xN$ system. Hyperfine Interactions **156**, 51 (2004)
[Crossref]

Gajbhiye, N.S., Bhattacharyya, S., Balaji, G., Ningthoujam, R.S., Das, R.K., Basak, S., Weissmuller, J.: Mössbauer and magnetic studies of MFe_2O_4 (M = Co, Ni). Hyperfine Interact. **165**, 153 (2005)

[Crossref]

Gajbhiye, N.S., Ningthoujam, R.S., Bhattacharyya, S.: Magnetic properties of Co and Ni substituted ε-Fe_3N nanoparticles. Hyperfine Interact. **164**, 17 (2005)
[Crossref]

Gajbhiye, N.S., Sharma, S., Nigam, A.K., Ningthoujam, R.S.: Tuning of single to multidomain behavior for monodispersed ferromagnetic cobalt nanoparticles. Chem. Phys. Lett. **466**, 181 (2008)
[Crossref]

Gajbhiye, N.S., Sharma, S., Ningthoujam, R.S.: Synthesis of self-assembled monodisperse 3 nm FePd nanoparticles: phase transition, magnetic study and surface effect. J. Appl. Phys. **104**, 123906 (2008)
[Crossref]

Gajbhiye, N.S., Ningthoujam, R.S.: Structural, electrical and magnetic studies of nanocrystalline δ-MoN and γ-Mo_2N. Phys. Stat. Sol. (c) **1**, 3449 (2004)

Gajbhiye, N.S., Ningthoujam, R.S., Weissmuller, J.: Synthesis and magnetic studies of nanocrystalline nickel nitride material. Phys. Stat. Sol. (a) **189**, 691 (2002)

Gajbhiye, N.S., Panda, R.N., Ningthoujam, R.S., Bhattacharyya, S.: Magnetism of nanostructured iron nitride (Fe-N) systems. Phys. Stat. Sol. (c) **1**, 3252 (2004)

Ghosh, R., Pradhan, L., Devi, Y.P., Meena, S.S., Tewari, R., Kumar, A., Sharma, S., Gajbhiye, N.S., Vatsa, R.K., Pandey, B.N., Ningthoujam, R.S.: Induction heating studies of Fe_3O_4 magnetic nanoparticles capped with oleic acid and polyethylene glycol for hyperthermia. J. Mater. Chem. **21**, 13388 (2011)

Hah, H.Y., Gray, S., Johnson, C.E., Johnson, J.A., Kolesnichenko, V., Kucheryavy, P., Goloverd, G.: Mössbauer spectroscopy of superparamagnetic Fe_3O_4 nanoparticles. J. Magn. Magnet. Mater. **539**, 168382 (2021)

Jadhav, S.V., Nikam, D.S., Khot, V.M., Thorat, N.D., Phadatare, M.R., Ningthoujam, R.S., Salunkhe, A.B., Pawar, S.H.: Studies on colloidal stability of PVP-coated LSMO nanoparticles for magnetic fluid hyperthermia. New J. Chem. **37**, 3121 (2013)
[Crossref]

Jiao, F., Jumas, J.C., Womes, M., Chadwick, A.V., Harrison, A., Bruce, P.G.: Synthesis of ordered mesoporous Fe_3O_4 and γ-Fe_2 O_3 with crystalline walls using post-template reduction/oxidation. J. AM. CHEM. SOC. **128**, 12905–12909 (2006)
[Crossref][PubMed]

Joshi, R., Perala, R.S., Srivastava, M., Singh, B.P., Ningthoujam, R.S.: Heat generation from magnetic fluids under alternating currentmagnetic field or induction coil for hyperthermia-based cancer therapy: Basic principle. J. Radiat. Cancer Res. **10**, 156–164 (2019)
[Crossref]

Joshi, R., Singh, B.P., Ningthoujam, R.S.: Confirmation of highly stable 10 nm sized Fe_3O_4 nanoparticles formation at room temperature and understanding of heat-generation under AC magnetic fields for potential application in hyperthermia. AIP Adv. **10**, 105033 (2020)
[Crossref]

Joshi, R., Singh, B.P., Prajapat, C.L., Kashyap, Y., Nayak, C., Bhattacharyya, D., Ningthoujam, R.S.: Insights into the structural and microscopic origin of magnetic properties of the γ-Fe_2O_3@Mn_xO_y nanostructure. J. Phys. Chem. C **125**, 17971 (2021)
[Crossref]

Joshi, R., Shelar, S.B., Srivastava, M., Singh, B.P., Goel, L., Ningthoujam, R.S.: Development of core@Shell γ-Fe_2O_3@Mn_xO_y@SiO_2nanoparticles for hyperthermia, targeting, and imaging applications. ACS Appl. Bio Mater. **5**, 5386–5393 (2022)
[Crossref][PubMed]

Khot, V.M., Salunkhe, A.B., Thorat, N.D., Ningthoujam, R.S., Pawar, S.H.: Induction heating studies of dextran coated $MgFe_2O_4$ nanoparticles for magnetic hyperthermia. Dalton Trans. **42**, 1249–1258 (2013)
[Crossref][PubMed]

Kittel, C.: Introduction to Solid State Physics. Wiley (2005)

Kritika, I.R.: Therapeutic applications of magnetic nanoparticles: recent advances. Mater. Adv. **3**, 7425–7444 (2022)

Kumar, A.: NEET Obj Physics Vol. 1. Pearson Education India (2021)

Li, K., Xu, J., Li, P., Fan, Y.: A review of magnetic ordered materials in biomedical field: constructions, applications and prospects. Compos. Part B Eng. **228**, 109401 (2022)
[Crossref]

Lyubutin, I.S., Starchikov, S.S., Lin, C.-R., Gervits, N.E., Yu, N., Korotkov, Bukreeva, T.V.: Structural and magnetic properties of iron oxide nanoparticles in shells of hollow microcapsules designed for biomedical applications. Croat. Chem. Acta **88**, 1926 (2015)

Majeed, J., Pradhan, L., Ningthoujam, R.S., Vatsa, R.K., Bahadur, D., Tyagi, A.K.: Enhanced specific absorption rate in silanol functionalized Fe_3O_4 core—shell nanoparticles: study of Fe leaching in Fe_3O_4 and hyperthermia in L929 and HeLa cells. Colloids and Surfaces B:Biointerfaces **122**, 396–403 (2014)
[Crossref][PubMed]

Ningthoujam, R.S., Gajbhiye, N.S.: Magnetic study of single domain ε-Fe_3N nanoparticles synthesized by precursor techniques. Mater. Res. Bull. **43**, 1079 (2008)

[Crossref]

Ningthoujam, R.S., Gajbhiye, N.S., Sachil, S.: Reduction mechanism of Ni^{2+} into Ni nanoparticles prepared from different precursors: magnetic studies. Pramana J. Phys. **72**, 577 (2009)
[Crossref]

Ningthoujam, R.S., Panda, R.N., Gajbhiye, N.S.: Variation of intrinsic magnetic parameters of single domain Co-N interstitial nitrides synthesized via hexa-ammine cobalt nitrate route. Mater. Chem. Phys. **134**, 377–381 (2012)
[Crossref]

Ningthoujam, R.S., Gajbhiye, N. S.: Magnetization studies on ε-$Fe_{2.4}Co_{0.6}N$ nanoparticles. Mater. Res. Bull. **45**, 499 (2010)

Ningthoujam, R.S., Umare, S.S., Sharma, S.J., Shukla, R., Kurian, S., Vatsa, R.K., Tyagi, A.K., Tewari, R., Dey, G.K., Gajbhiye, N.S.: Magnetic and Mössbauer studies on nanocrystalline $Co_{1-x}Li_xFe_2O_4$ (x = 0, 0.2). Hyperfine Interact. **184**, 227 (2008)

Ningthoujam, R.S., Vatsa, R.K., Kumar, A., Pandey, B.N. Edited by S. Banerjee and A. K. Tyagi in Functional Materials Preparation, Functionalized magnetic nanoparticles: concepts, synthesis and application in cancer hypertherma Processing and Applications Publisher: Elsevier Inc., USA, Chapter 6, pages 229–260 (2012)

Perala, R.S., Singh, B.P., Putta, V.N.K., Acharya, R., Ningthoujam, R.S.: Enrichment of crystal field modification via incorporation of alkali K^+ions in YVO_4:Ho^{3+}/Yb^{3+}nanophosphor and its hybrid with superparamagnetic iron oxide nanoparticles for optical, advanced anticounterfeiting, uranyl detection, and hyperthermia applications. ACS Omega **6**, 19517–19528 (2021)
[Crossref][PubMed][PubMedCentral]

Perala, R.S., Joshi, R., Singh, B.P., Putta, V.N.K., Acharya, R., Ningthoujam, R.S.: Brilliant nonlinear optical response of Ho^{3+} and Yb^{3+} activated YVO_4 nanophosphor and its conjugation with Fe_3O_4 for smart anti-counterfeit and hyperthermia applications. ACS Omega **6**, 19471–19483 (2021)
[Crossref][PubMed][PubMedCentral]

Sharma, S., Gajbhiye, N.S., Ningthoujam, R.S.: Synthesis and self-assembly of monodisperse Co_xNi_{100-x} (x = 50, 80) colloidal nanoparticles by homogenous nucleation. J. Colloids Interface Science **351**, 323 (2010)
[Crossref]

Sharma, S., Gajbhiye, N.S., Ningthoujam, R.S.: Effect of annealing on magnetic properties of FePd and FePdPt nanoparticles. AIP Conf. Proc. **1313**, 125 (2010)
[Crossref]

Sharma, S., Ningthoujam, R.S., Gajbhiye, N.S.: Spin-glass-like behavior of surfactant capped $Co_{50}Ni_{50}$ nanoparticles. Chem. Phys. Lett. **558**, 48–52 (2013) [Crossref]

Sharma, K.S., Ningthoujam, R.S., Dubey, A.K., Chattopadhyay, A., Phapale, S., Juluri, R.R., Mukherjee, S., Tewari, R., Shetake, N.G., Pandey, B.N., Vatsa, R.K.: Synthesis and characterization of monodispersed water dispersible Fe_3O_4 nanoparticles and in vitro studies on human breast carcinoma cell line under hyperthermia condition. Scientific Reports **8**, 14766 (2018)

Shete, P.K., Patil, R.M., Ningthoujam, R.S., Ghosh, S., Pawar, S.H.: Magnetic core shell structures for magnetic fluid hyperthermia therapy application. New J. Chem. **37**, 3784–3792 (2013)
[Crossref]

Shukla, R., Ningthoujam, R.S., Umare, S.S., Sharma, S.J., Kurian, S., Vatsa, R.K., Tyagi, A.K., Gajbhiye, N.S.: Decrease of superparamagnetic fraction at room temperature in ultrafine $CoFe_2O_4$ particles by Ag doping. Hyperfine Interact. **184**, 217 (2008)
[Crossref]

Soni, A.K., Joshi, R., Singh, B.P., Naveen Kumar, N., Ningthoujam, R.S.: Near-infrared- and magnetic-field-responsive $NaYF_4$:Er^{3+}/Yb^{3+}@SiO_2@AuNP@Fe_3O_4 nanocomposites for hyperthermia applications induced by fluorescence resonance energy transfer and surface plasmon absorption. ACS Appl. Nano Mater. **2**, 7350−7361 (2019)

Srivastava, M., Joshi, R., Singh, B.P., Ningthoujam, R.S.: Edited by P.A. Hassan, Biji Balakrishnan and A.K. Tyagi in Engineered Biomaterials: Progress and Prospects, Advances on magnetic nanoparticles based cancer therapy through hyperthermia: Basic understanding and history, World Scientific Publishing Co Pvt Ltd, Singapore (2023)

Straumal, B.B., Protasova, S.G., Mazilkin, A.A., Goering, E., Schütz, G., Straumal, P.B., Baretzky, B.: Ferromagnetic behaviour of ZnO: the role of grain boundaries. Beilstein. J. Nanotechnol. **2016**(7), 1936–1947 (2016)
[Crossref]

Sudhakar, N., Ningthgoujam, R.S., Rajeev, K.P., Nigam, A.K., Weissmuller, J., Gajbhiye, N.S.: Effect of La, B doping on the electrical resistivity and magnetic susceptibility of nanocrystalline vanadium nitride. J. Appl. Phys. **96**, 688 (2004)
[Crossref]

Thorat, N.D., Shinde, K.P., Barick, K.C., Pawar, S.H., Betty, C.A., Ningthoujam, R.S.: Polyvinyl alcohol: an efficient fuel for synthesis of superparamagnetic LSMO nanoparticles for biomedical application. Dalton Trans. **41**, 3060 (2012)
[Crossref][PubMed]

Thorat, N.D., Khot, V.M., Salunkhe, A.B., Ningthoujam, R.S., Pawar, S.H.: Functionalization of $La_{0.7}Sr_{0.3}MnO_3$ nanoparticles with polymer: Studies on enhanced hyperthermia and biocompatibility properties for biomedical applications Colloids Surfaces B: Biointerfaces **104**, 40–47 (2013)

Thorat, N.D., Khot, V.M., Salunkhe, A.B., Prasad, A.I., Ningthoujam, R.S., Pawar, S.H.: Surface functionalized $La_{0.7}Sr_{0.3}MnO_3$nanoparticles with improved colloidal stability for hyperthermia applications. J. Phys. D **46**, 105003 (2013)

Umare, S.S., Ningthoujam, R.S., Sharma, S.J., Shrivastava, S., Kurian, S., Gajbhiye, N.S.: Mössbauer and magnetic studies on nanocrystalline $NiFe_2O_4$ particles prepared by ethylene glycol route. Hyperfine Interact. **184**, 235 (2008) [Crossref]

Verma, H.C.: Concepts of physics. Bharati Bhawan. (1993)

© The Author(s), under exclusive license to Springer Nature Singapore Pte Ltd. 2024
R. S. Ningthoujam, A. K. Tyagi (eds.), *Handbook of Materials Science, Volume 2*, Indian Institute of Metals Series
https://doi.org/10.1007/978-981-97-4646-0_4

4. Classification of Ferrites, Synthesis and Properties of Spinel Ferrite Nanoparticles and Their Applications

Vibha H. Ojha[1] ✉, Abha H. Oza[2], Ruchi Agrawal[3, 4] and Raghumani S. Ningthoujam[3, 4] ✉

(1) Solid State Physics Division, Bhabha Atomic Research Centre, Mumbai, 400085, India
(2) Department of Physics, R.T.M. Nagpur University, Nagpur, 440033, India
(3) Chemistry Division, Bhabha Atomic Research Centre, Mumbai, 400085, India
(4) Homi Bhabha National Institute, Mumbai, 400094, India

✉ **Vibha H. Ojha (Corresponding author)**
Email: ojha.vibha01@gmail.com

✉ **Raghumani S. Ningthoujam (Corresponding author)**
Email: rsn@barc.gov.in

Keywords Spinel ferrites – Superparamagnetism – Spin glass – Blocking temperature – Strain – Spin canting

4.1 Origin of the Work

Magnetism in magnetic materials is simply defined as the attractive or repulsive force exerted on the other material. However, the mechanism and principle working behind this is complex in nature. Most of the devices in recent technology depends on magnetic materials which includes radio, television, electric motors and power generators, computers, etc. Magnetism comes from the motion of electrons. Magnetism and electricity bring a natural phenomenon known as a force of electromagnetism. Among all the magnetic materials, ferrite nanomaterials are useful in nanotechnology, environmental and biomedical applications as their particle sizes are so small in dimension (nanometers) and chemically stable in pH = 4–10 and also, they have multi-functional properties in optical, electrical and magnetic behavior (Valenzuela 2012). The controlled dimension of magnetic nanoparticles limits the cation distribution in A and B sites of ferrite (AB_2O_4) that induces strain in nanocrystal which is responsible for the change in structural, optical and magnetic properties in the nanocrystal. Various investigations have been performed to study the effect of strain on magnetic properties of ferrite nanoparticles.

There were many reports on classification of ferrites. However, still, it has a scope to improve in term of easy explanation. There were many reports on preparation of ferrite nanoparticles and their characterization, but it is lacking behind understanding. In ferrite nanoparticles below the critical dimension, it is associated with strain induce in B site (Monalisa et al. 2021; Nikmanesh et al. 2017; Rodr´ıguezTorres et al. 2014). Characterization techniques to distinguish superparamagnetic and spin glass are not much mentioned in literature (Alzoubi et al. 2020).

4.2 Introduction of Ferrites

The ferrites are compounds formed by mixing of ferric oxide (Fe_2O_3) with metal oxides such as MO (e.g., M = Mg, Mn, Fe, Co, Ni, Cu, Zn, Ca, Sr, Ba) or Ln_2O_3 (e.g., Ln = Y, La, Gd, Dy). They have different lattices of Fe^{3+} ions known as sublattices such as tetragonal (FeO_4), octahedral (FeO_6) and trigonal bipyramid (FeO_6). In some compounds of ferrites, other ions such as Li^{+}, Ti^{4+}, Cr^{3+}, S^{2-}. B^{3+}, etc. are found as dopants. These can change intrinsic properties of parent ferrite compound in terms of electrical, optical and magnetic parameters. When particle size and shape of ferrites change, what will happen in properties? The study of materials having particle size in the range of 1–100 nm is known as nanoscience whereas nanotechnology refers to creation or generation of new devices using nanoparticles. The reason behind tremendous study of nanotechnology is the consequence of quantum size effect of nanomaterials which shows unique chemical, physical and magnetic properties. Based on magnetism, the materials are classified as diamagnetic, paramagnetic, ferromagnetic, antiferromagnetic and ferrimagnetic materials (Nisticò et al. 2020). This is provided in Table 4.1 with illustration. The elemental diamagnetic material has the fully paired or completely filled electrons in the orbitals of atoms. For example, Zinc is a diamagnetic material due to completely filled outermost shell as shown in the electronic configuration $1s^2\ 2s^2\ 2p^6 3s^2\ 3s^6 3d^{10} 4s^2$. It has a net zero magnetic moment, and the external magnetic field creates the induced magnetic field which is in the opposite direction of applied magnetic field. The compound ZnO is diamagnetic since Zn^{2+} has fully paired electrons.

Table 4.1 Behavior of magnetic materials with examples

Type of magnetism	Examples	Magnetic ordering	Magnetic behavior	
Diamagnetism	Zn, ZnO, Cu, Ag, Au, inert gases Small susceptibility and negative (-10^{-6} to -10^{-5})		Atoms have no magnetic moments	
Paramagnetic	Al, O_2, MnBi Small susceptibility and positive (10^{-3} to 10^{-5})	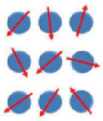	Atoms have randomly oriented magnetic moments	
Ferromagnetic	Fe, Ni, Co and Gd Large susceptibility and positive (>>1)	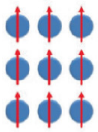	Atoms are arranged in domains with parallel alignment of magnetic moments	
Antiferromagnetic	Cr, MnO, FeO Small susceptibility and positive (1 to 10^{-5})	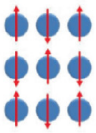	Atoms are arranged in domains with antiparallel alignment of magnetic moments	
Ferrimagnetic	Fe_3O_4, $MnFe_2O_4$, $NiFe_2O_4$ Large susceptibility and positive (>>1)	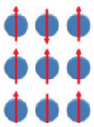	Atoms are arranged in domains with a mixture of unequal antiparallel alignment of magnetic moments	

The diamagnetic materials exhibit negative magnetic susceptibility $\chi \cong -10^{-6}$ to -10^{-5} and relative permeability of $\mu_r < 1$. The magnetic susceptibility χ is defined as ratio of magnetization (M) and applied magnetic field (H). In paramagnetic material, it has unpaired electrons. In

existence of magnetic field, the feeble magnetization is generated in the direction of magnetic field. The paramagnetic materials have magnetic susceptibility of $\chi \tilde{=}$ 10^{-3} to 10^{-5} and relative permeability of $\mu_r \geq 1$. For example, the elemental Na metal has unpaired electron in the outermost shell of atom and thus it becomes paramagnetic. The ferromagnetic materials exhibit the spontaneous magnetization in absence of external magnetic field. Examples of elemental ferromagnetic materials are Fe, Co, Ni. A ferromagnetic material can have single or multidomain structure. A domain has the parallel spins. In multidomain structure, there is a domain wall in between domains. In magnetic domains the magnetic moments are randomly oriented in the absence of external magnetic field. As the magnetic field is applied externally, the magnetic moment gets oriented in the direction of external magnetic field and it results in net magnetization. The magnetization remains in the materials after the removal of external magnetic field is called as remanent magnetization. These phenomena occur in ferromagnetic materials below Curie temperature (T_c). In case of antiferromagnetic materials, there is spontaneous magnetization below Neel temperature (T_N). Above T_c or T_N, the ferromagnetic or antiferromagnetic material behaves as paramagnetic material. The magnetic susceptibility is large $\chi >> 1$ and relative permeability is $\mu_r >> 1$ in case of ferromagnetic or ferrimagnetic materials. The magnetic materials such as magnetite (Fe_3O_4) and maghemite (γ-Fe_2O_3) are ferrimagnetic materials made of Fe and O atoms, occupying different lattice positions (tetrahedral and octahedral co-ordinations). In ferrimagnetic materials, the magnetic moments are oppositely directed with each other but having different magnitudes resulting in net spontaneous magnetization.

Magnetic moment increases with applied magnetic field. Nowadays, study of ferrites in nanoscale dimension has shown great importance in various areas of applications due to its novel chemical, physical and mechanical properties than bulk.

Ferrites are the semiconducting or insulating metal oxides which show low eddy current loss, low dielectric loss and low to high magnetization. Among various ferrites, the cobalt ferrite materials are of great importance due to its chemical stability, large coercivity (4.3 kOe), high saturation magnetization (80 emu/g) and high anisotropic constant (2.65×10^6–5.1×10^6 ergcm^{-3}) for bulk at room temperature and excellent magnetic properties (Sivakumar et al. 2007, 2008; Fu et al. 2010; Bharathi et al. 2011; Ren et al. 2006; Melikhov et al. 2006; Chinnasamy et al. 2003). Many applications of cobalt ferrites include the followings transducers, activators, recording media, permanent magnets, phase shifters, electrode material for lithium ion batteries, solid oxygen fuel cells, computer technology, magnetic fluids, drug delivery, environmental applications, gas sensors and humidity (Idrees et al. 2010; Chen et al. 2010; Gul et al. 2007; Pachpinde et al. 2014; Mallick et al. 2023). The ferrites exhibit dielectric properties and high electrical resistivity and hence these are used as an alternative for iron, nickel, cobalt metal magnets which conduct electricity easily (Mathew et al. 2007; Céspedes et al. 2014; Investigations of Properties of Spinel Ferrite Compound Doped with Rare Earth Ionsquot 2012).

4.3 Classifications of Ferrites

Ferrites exhibit various properties such as low electrical conductivity, UV–visible absorption, Curie temperature and magneto-crystalline anisotropy which make them important materials in various applications. The magnetic property in

ferrite mainly is result of the net spin moment of unpaired 3d electron of the transition metal ions in different lattices. Electrical conductivity in ferrites arises due to hoping of electrons of the metal ions (having different oxidation states) distributed in the sub-lattices. Otherwise, most ferrites are insulators. The Curie temperature of the ferrites measures the strength of A-B interaction of cations situated at A- site and B- site. Magneto-crystalline anisotropy is a result of spin–orbit coupling due to which the alignment of magnetic moment takes place along a preferred crystallographic direction.

The distribution of cations in spinel ferrites at tetrahedral and octahedral site is represented by the formula $(M^{2+}_{1-\delta}Fe^{3+}_{\delta})\ [M^{2+}_{\delta}Fe^{3+}_{2-\delta}]\ O_4$ (Valenzuela and Magnetic Ceramics 1996; Gignoux et al. 2006; Toksha et al. 2011; Cullity et al. 2012; Soliman et al. 2011; Chinnasamy et al. 2001; Kumar et al. 2017; Kittel 1946; Birajdar et al. 2012; Nikam et al. 2015). Spinel ferrite has A- and B- sites, represented by the round brackets and square brackets. O ions occupy ccp positions and metal ions occupy the interstitial positions.

Ferrites can be classified according to magnetic properties and crystal structures (Vedrtnam et al. 2020; Singh et al. 2018; Kumari et al. 2020). On the basis of magnetic properties, the ferrites are classified into 2: (i) soft and (ii) hard ferrites. Soft ferrites have low coercivity of magnetism ($H_c < 500$ Oe), whereas hard ferrites have high coercivity of magnetism ($H_c > 1000$ Oe). Examples of soft ferrites are Fe_3O_4, $NiFe_2O_4$, etc. Examples of hard ferrites are $CoFe_2O_4$, $SrFe_{12}O_{19}$, etc.

On basis of crystal structures, ferrites are broadly classified into 4: (i) spinel, (ii) garnet, (iii) hexagonal and (iv) orthorhombic ferrites (Table 4.2) (Vedrtnam et al. 2020).

Table 4.2 Classifications of ferrites on the basis of crystal structures with chemical formula and examples

S. N	Classifications	Chemical formulae	Molar ratio	Examples
1	Spinel	MFe_2O_4	Fe_2O_3-1MO (M = transition metal or metal ion having 2+)	$CoFe_2O_4$
2	Hexagonal	$MFe_{12}O_{19}$	$6Fe_2O_3$-1MO (M = alkali metal ion having 2+)	$CaFe_{12}O_{19}$
3	Garnet	$R_3Fe_5O_{12}$	½($5Fe_2O_3$–$3M_2O_3$) (M = rare earth ion having 3+)	$Y_3Fe_5O_{12}$
4	Orthorhombic	$MFeO_3$	½(Fe_2O_3–M_2O_3) (M = rare earth ion having 3+)	$DyFeO_3$

4.3.1 Spinel Ferrites

Spinel ferrites belong to cubic structure with space group Fd3m. There are 3 types of spinel ferrites or structures: normal, inverse and mixed spinel ferrites or structures. Its chemical formula is AB_2O_4 in which O^{2-} ions occupy the ccp lattice sites, A and B occupy octahedral and tetrahedral positions. In cubic unit cell, it consists of 8 fcc cells.

In a fcc cell, there are 4 anions (O^{2-}anions), 4 octahedral sites (cations) and 8 tetrahedral sites (cations). For 8 fcc cells, there are 32 anions (8×4), 32 octahedral sites and 64 tetrahedral sites. However, cations occupy the half of octahedral sites and 1/8 of tetrahedral sites.

Thus, number of oxygen anions in a cubic unit cell is 32.

Number of cations occupying octahedral sites is $½ \times 32 = 16$.

Number of cations occupying tetrahedral sites is $1/8 \times 64 = 8$.

In term of stoichiometry: A_T: B_O: $O = 8:16:32 = 1:2:4$ and therefore, the chemical formula will be AB_2O_4.

In normal spinel, tetrahedral sites are fully occupied by A, octahedral sites are fully occupied by B (Fig. 4.1)

(Vedrtnam et al. 2020). In inverse spinel, tetrahedral sites are fully occupied by one B, and octahedral sites are fully occupied by A and B. In mixed spinel, some of A and B are occupying tetrahedral and octahedral sites.

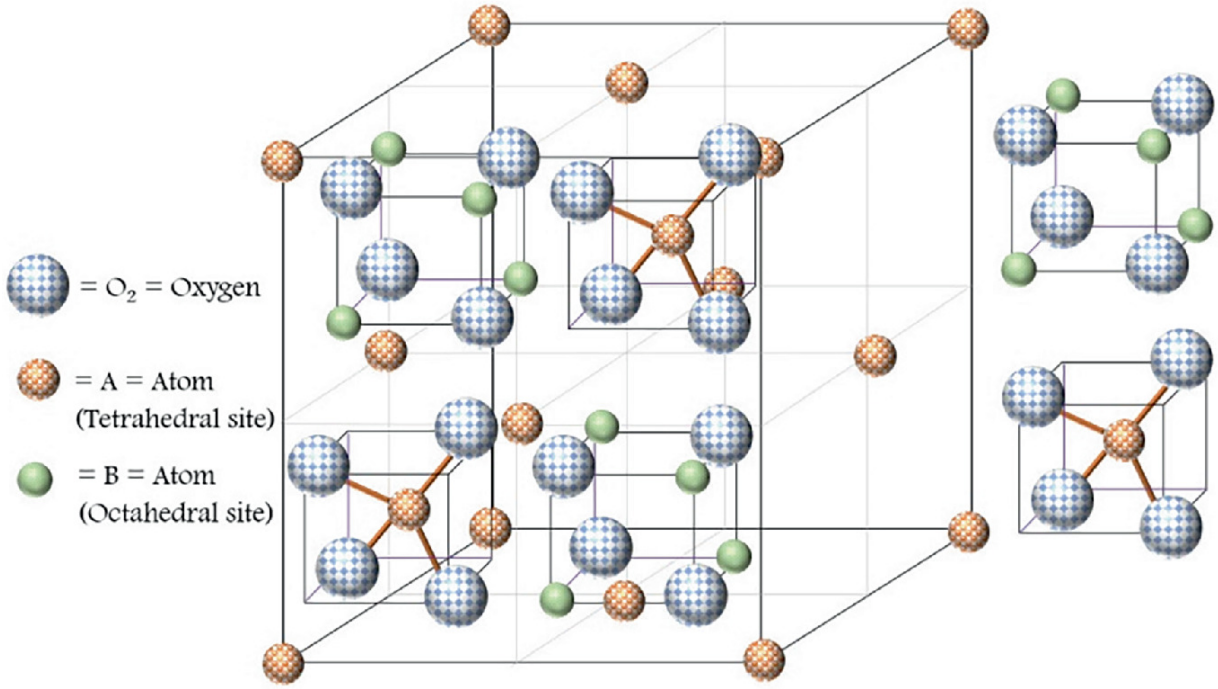

Fig. 4.1 Schematic diagram representing unit cell of ABO_4 spinel structure. It is reproduced with permission from AIMS Press (Vedrtnam et al. 2020)

Normal spinel is represented by $(A)[B]_2O_4$, in which round bracket is fully occupied by A cations (generally, A is having 2 + charge), square bracket is fully occupied by 2B cations (generally, B is having 3 + charge). One of the naturally found stable spinel structure is $MgAl_2O_4$ in which Al^{3+} and Mg^{2+} cations reside at the octahedral (B) and tetrahedral (A) sites, respectively and it is represented as $(Mg)[Al]_2O_4$. Another example is $ZnFe_2O_4$ (Cullity et al. 2012).

Inverse spinel is represented by $(B)[AB]O_4$, in which round bracket is fully occupied by B cations (generally, B is having 3 + charge), square bracket is occupied by A and B cations (generally, A is having 2 + charge). Examples are

Fe_3O_4, $CoFe_2O_4$, $NiFe_2O_4$ (Gajbhiye et al. 2005; Ningthoujam et al. 2008; Shukla et al. 2008; Umare et al. 2008, 2010; Khot et al. 2013; Bhattacharya et al. 2015; Dalal et al. 2017, 2018; Ningombam et al. 2018; Sharma et al. 2018; Joshi et al. 2021).

Mixed spinal is represented by $(A_{1-\delta}B_{\delta})[B\ B_{1-\delta}A_{\delta}]O_4$, in which tetrahedral and octahedral sites are occupied by A and B. Examples are $MnFe_2O_4$, $Zn_xNi_{1-x}\ Fe_2O_4$.

Among all the spinel ferrites, magnetite Fe_3O_4 ($FeFe_2O_4$) is one of the oldest natural oxides and one of the significant magnetic materials with various practical applications. The $CoFe_2O_4$ is hard magnetic material with formula $(Co^{2+}{}_{1-\delta}Fe^{3+}{}_{\delta})\ [Co^{2+}{}_{\delta}Fe^{3+}{}_{2-\delta}]\ O_4$, where $\delta = 1$ is degree of inversion (Dmowski et al. 2002; Kim et al. 2003; Laokul et al. 2015). The cations distributed over A and B sites vary with heat treatment, chemical environment and intrinsic strain in the crystal (Khorsand Zak et al. 2011; Yogamalar et al. 2009).

The existence of magnetism in $CoFe_2O_4$ arises due to super-exchange interaction. The super-exchange interaction is dependent upon the stronger interaction of Fe_A^{3+} and Fe_B^{3+} than Co_A^{2+} and Fe_B^{3+}. The superexchange interaction depends on the cations distributed over A and B sites which is effectively affected by the lattice constants, size of crystallite, bond angles, bond length and existence of crystalline strain (Yadav et al. 2017). While dealing with the materials of nanosized dimension, crystallite and lattice strain lead to variation in position and broadened X-ray diffraction peak (Bersani et al. 1998; Maria and Soler Fanyao 2012; Majetich et al. 2013; Lamouri et al. 2020; Burton et al. 2009). To get the accurate measurement of the crystallite with modifications in crystal structures, the evaluation of strain becomes essential for which Williamson- Hall (W–H) analysis which is a simplified

integral Breadth method is used. Figure 4.2 shows the crystal structure of $CoFe_2O_4$particles (Lamouri et al. 2020).

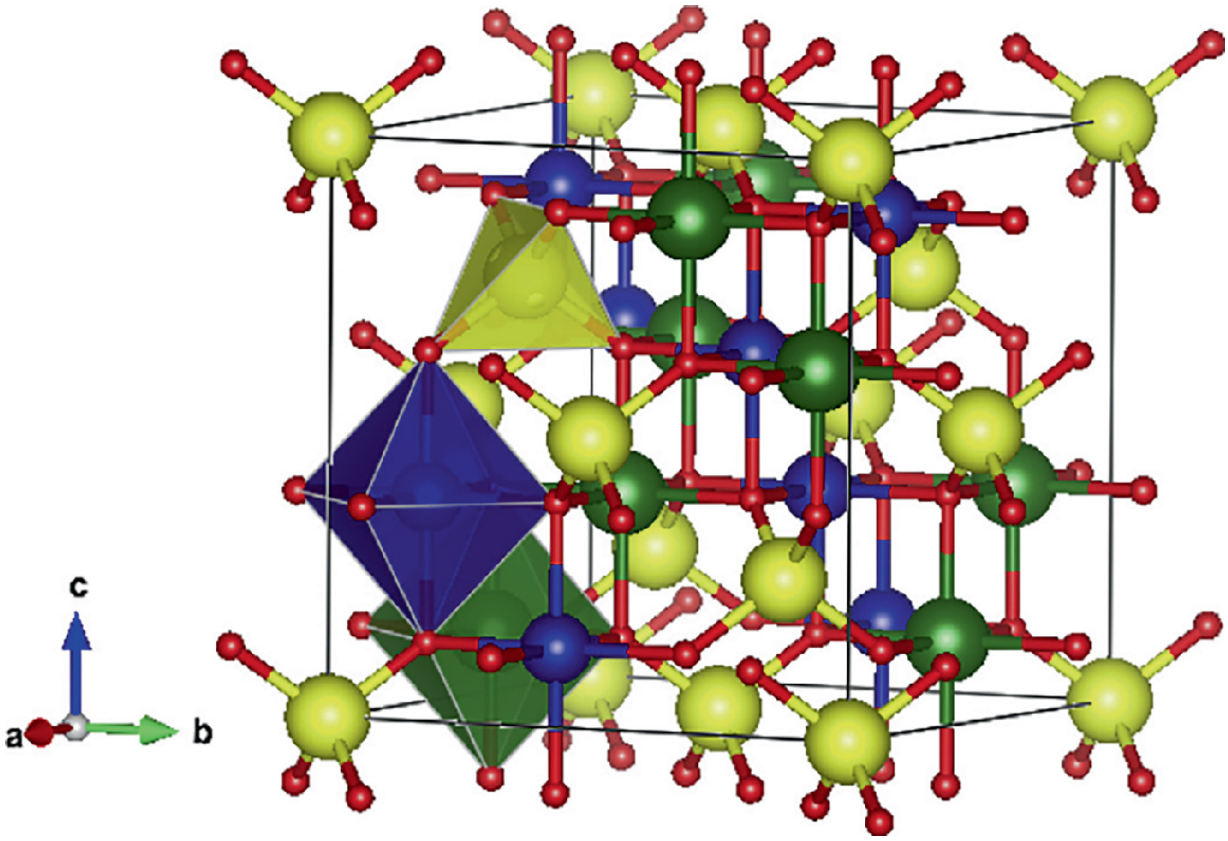

Fig. 4.2 Schematic diagram representing crystal structure of $CoFe_2O_4$inverse spinel structure. Red ball = Oxygen ions occupying ccp sites. Yellow ball: Fe^{3+} ions occupying tetrahedral sites. Green ball: Fe^{3+} ions occupying octahedral sites. Blue ball: Co^{2+} ions occupying octahedral sites. It is reproduced with permission from Elsevier (Lamouri et al. 2020)

$CoFe_2O_4$ is ferrimagnetic material that shows magnetization at 300 K which is dependent on Co^{2+} and Fe^{3+} interaction occurring at *A–A*, *A–B*, *B–B* sites with the strongest interaction between *A-B*. In inverse spinel $CoFe_2O_4$, the electronic spins ($3d^n$) of Fe^{3+}in A site and Co^{2+} in B site are antiparallel and also the electronic spins ($3d^n$) of Fe^{3+} in A site and Fe^{3+} in B site are antiparallel shown in above Fig. 4.3. The net moment is $3\mu_B$ per

molecule. Similarly, Fe_3O_4 and $NiFe_2O_4$ with inverse spinel structure can have net moment of 4 and 2 μ_B per molecule, respectively. Therefore, saturation magnetization decreases from Fe_3O_4 (90 emu/g) to $CoFe_2O_4$ (80 emu/g) to $NiFe_2O_4$ (55 emu/g) as net magnetic moment decreases.

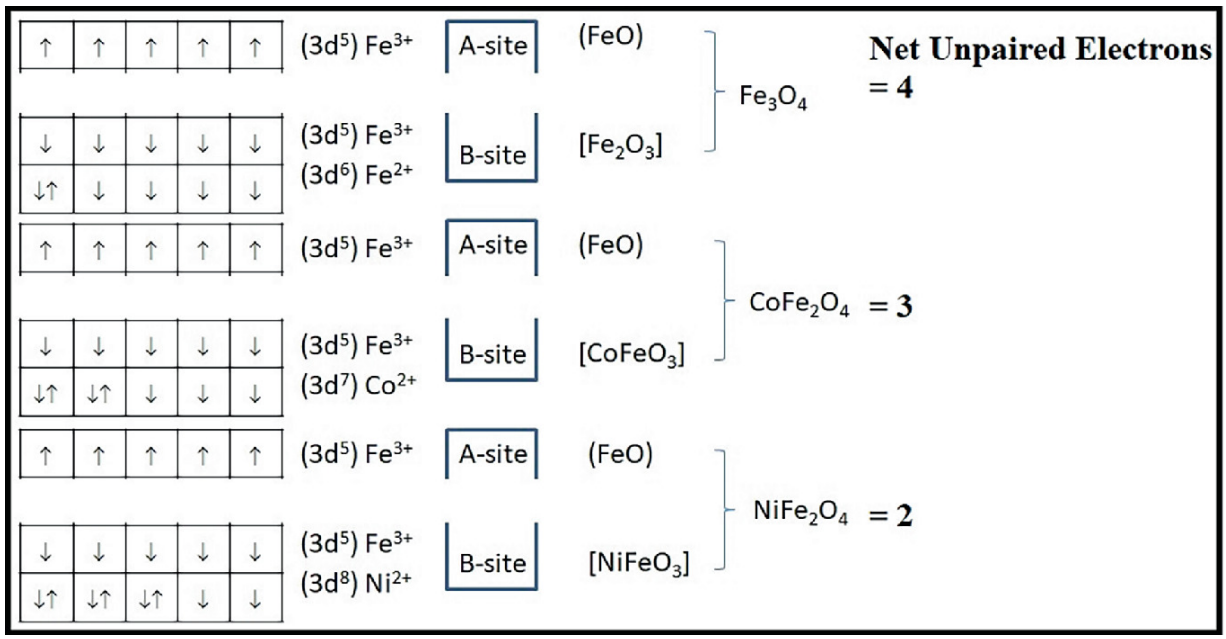

Fig. 4.3 Spin alignments of Fe^{3+} and Fe^{2+} or $Co^{2+}$of Ni^{2+}ions in respective inversed spinel structure of molecule Fe_3O_4 or $CoFe_2O_4$ or $NiFe_2O_4$

4.3.2 Hexaferrites

The hexaferrites are a type of ferrites having hexagonal crystal structure with unique c-axis (Vedrtnam et al. 2020; Singh et al. 2018; Vijayalakshmi and Gajbhiye 1998). Magnetic properties of the hexaferrites are dependent on their crystalline structures. Its magneto-crystalline anisotropy can be grouped in two: uniaxial hexaferrites and hexaplana ferrites. Uniaxial hexaferrite shows easy axis of magnetization, and ferroxplana or hexa-plana ferrites shows an easy plane (or cone) of magnetization.

In general, chemical formula is represented by $MFe_{12}O_{19}$, where M can be Sr, Ba, Pb, etc. The lattice of

hexaferrites and spinel structure are alike, with closely packed O^{2-} ions. Three types of interstitial sites such as tetrahedral, octahedral and trigonal bi-pyramid in hexagonal structure are found and metal ions occupy such interstitial sites. Depending on different metal ions present in this series, six types of hexaferrties are found: M, W, Y, X, Z, and U letters. Ratios of (MO + MeO) and Fe_2O_3 are 1:6, 3:8, 4:6: 5:12 and 6:18 for M, W, Y, X, Z, and U ferrites, respectively. M = Ca, Sr, Pb, Ba; Me = Zb, Mn; substation of Fe^{3+} can be possible with Al^{3+}, Sc^{3+}, Ga^{3+}, In^{3+}.

1. M-type ferrites, $BaFe_{12}O_{19}$ (BaM), $SrFe_{12}O_{19}$ (SrM),

2. Z-type ferrites ($Ba_3A_2Fe_{24}O_{41}$) such as $Ba_3Co_2Fe_{24}O_{41}$, or Co_2Z.

3. Y-type ferrites ($Ba_2A_2Fe_{12}O_{22}$), such as $Ba_2Co_2Fe_{12}O_{22}$, or Co_2Y.

4. W-type ferrites ($BaA_2Fe_{16}O_{27}$), such as $BaCo_2Fe_{16}O_{27}$, or Co_2W.

5. X-type ferrites ($Ba_2A_2Fe_{28}O_{46}$), such as $Ba_2Co_2Fe_{28}O_{46}$, or Co_2X.

6. U-type ferrites ($Ba_4A_2Fe_{36}O_{60}$), such as $Ba_4Co_2Fe_{36}O_{60}$, or Co_2U.

Hexagonal ferrites or hexaferrites, have become important material commercially and techno-logically (Vedrtnam et al. 2020; Singh et al. 2018; Vijayalakshmi and Gajbhiye 1998; Pullar 2012). M-type HFs have high uniaxial anisotropy, high coercivity, large saturation magnetization, high Curie temperature, exceptional chemical stability, high corrosion resistivity and high mechanical strength,

etc. M-type HFs, are used in several applications such as permanent magnet high density magnetic recording media, telecommunication, micro electromechanical system, microwave devices, and magneto optical recording. Unit cell of hexagonal ferrites has three fundamental structural units in general S, R and T blocks (Fig. 4.4) (Vedrtnam et al. 2020). The S-block has 2 spinel units ($A_2Fe_4O_8$, $A = M^{2+}$) that is equivalent to S_2 unit. S_2 consists of 4 octahedral sites and 2 tetrahedral sites. The R-block has 3 hexagonal packed layers of 4 oxygen atoms, but out of which 1 oxygen atom at the center layer is substituted by a similarly size atom (Ba) and unit formula is $CaFe_6O_{11}$. The T-block has unit formula of $Ba_2Fe_8O_{14}$ and is constituted of 4 oxygen layers and out of which oxygen atom in the middle two oxygen layers is substituted by Ba atom. M, W, X, Y, Z, and U letters (Figs. 4.5, 4.6, 4.7, 4.8, 4.9 and 4.10) (Vedrtnam et al. 2020).

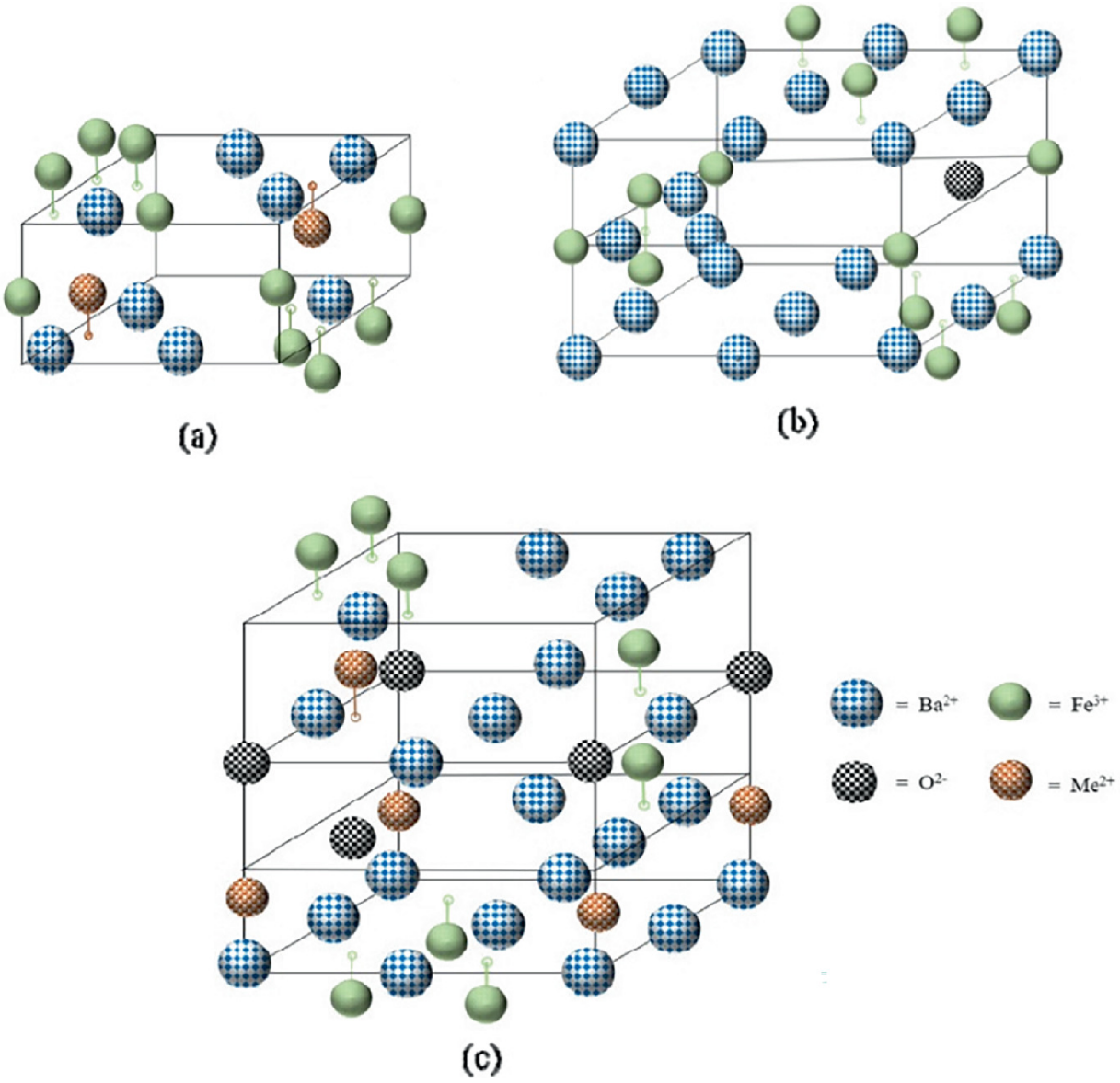

Fig. 4.4 Schematic diagram representing **a** S-, **b** R- and **c** T-blocks. It is reproduced with permission from AIMS Press (Vedrtnam et al. 2020)

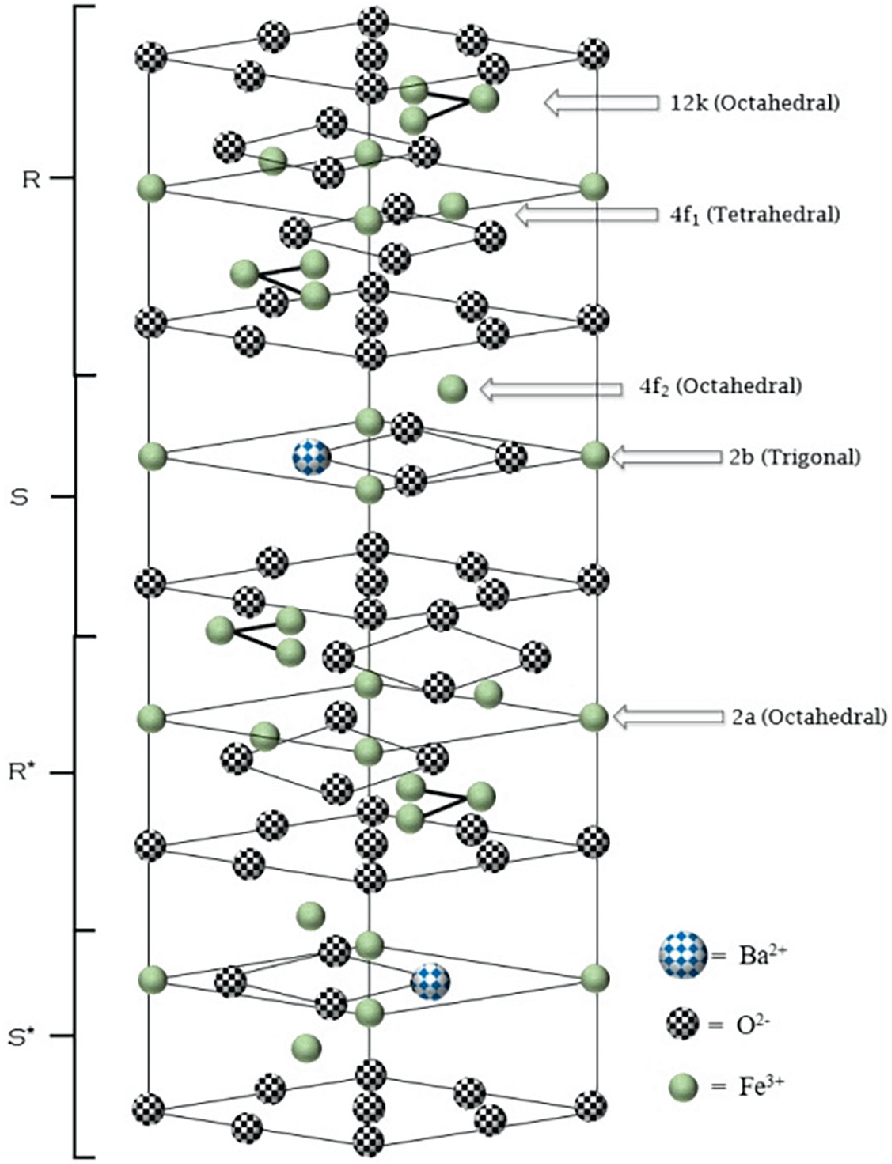

Fig. 4.5 Schematic diagram representing crystal structure of M-type hexaferrite. It is reproduced with permission from AIMS Press (Vedrtnam et al. 2020)

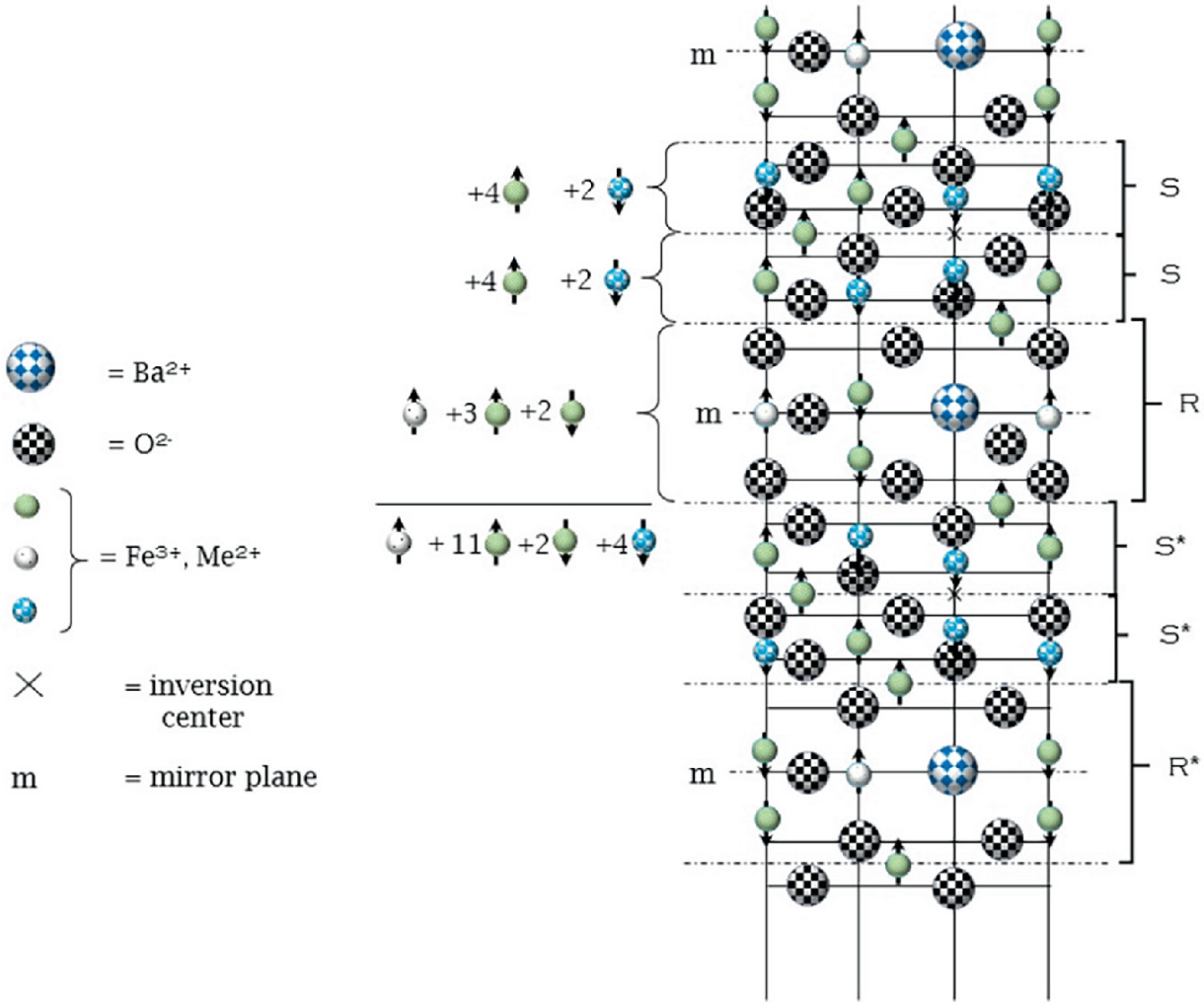

Fig. 4.6 Schematic diagram representing crystal structure of W-type hexaferrite. It is reproduced with permission from AIMS Press (Vedrtnam et al. 2020)

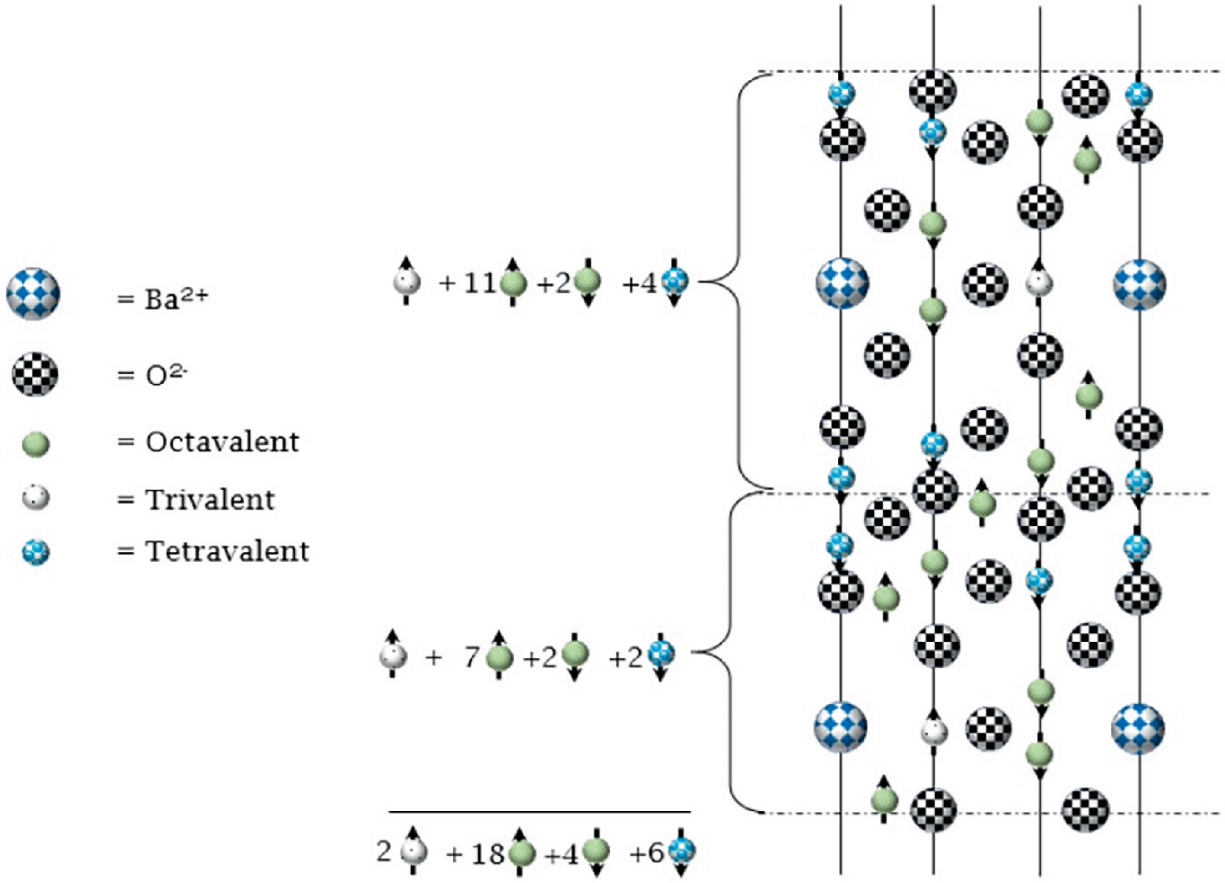

Fig. 4.7 Schematic diagram representing crystal structure of X-type hexaferrite. It is reproduced with permission from AIMS Press (Vedrtnam et al. 2020)

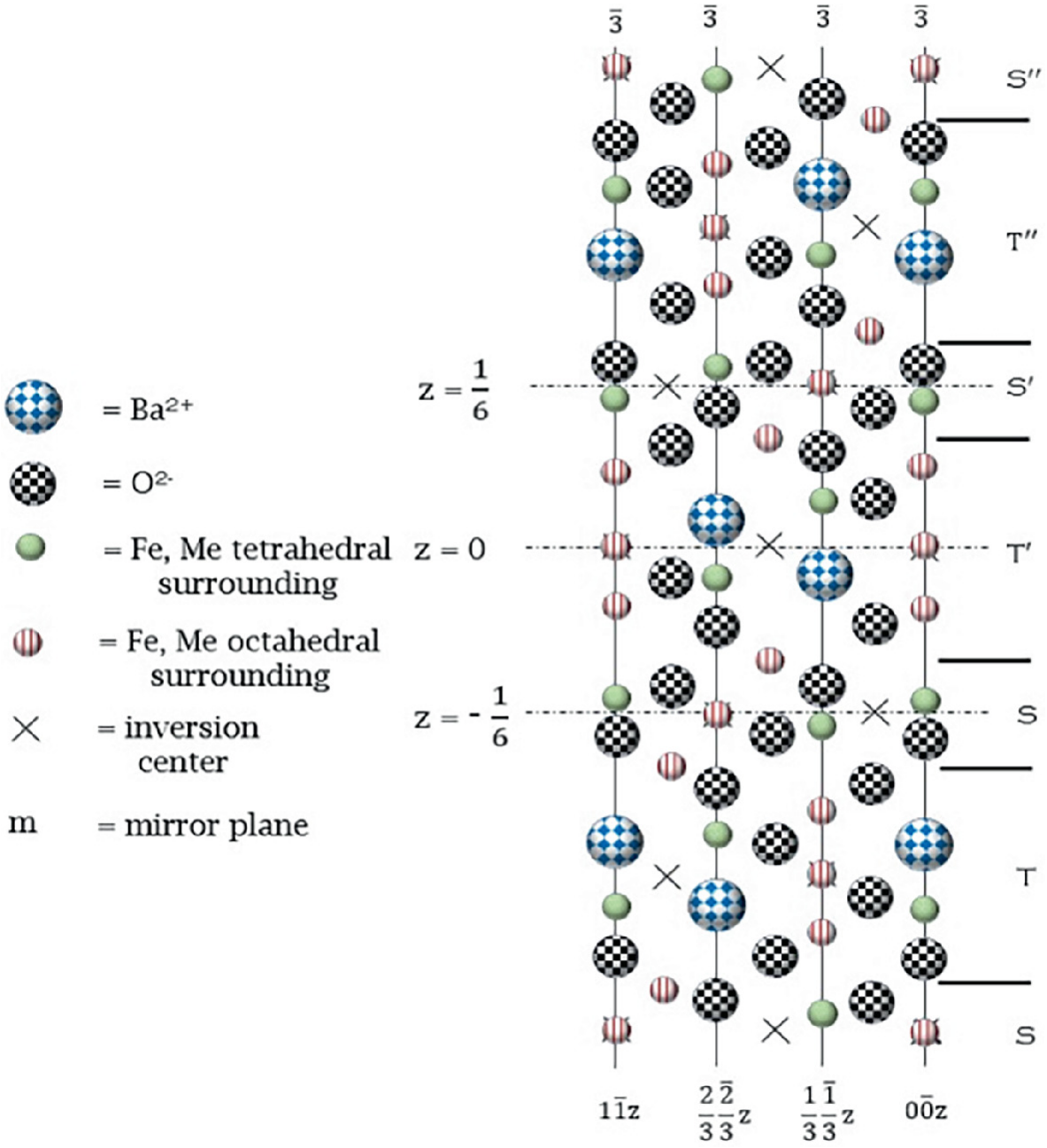

Fig. 4.8 Crystal structure of Y-type hexaferrite. It is reproduced with permission from AIMS Press (Vedrtnam et al. 2020)

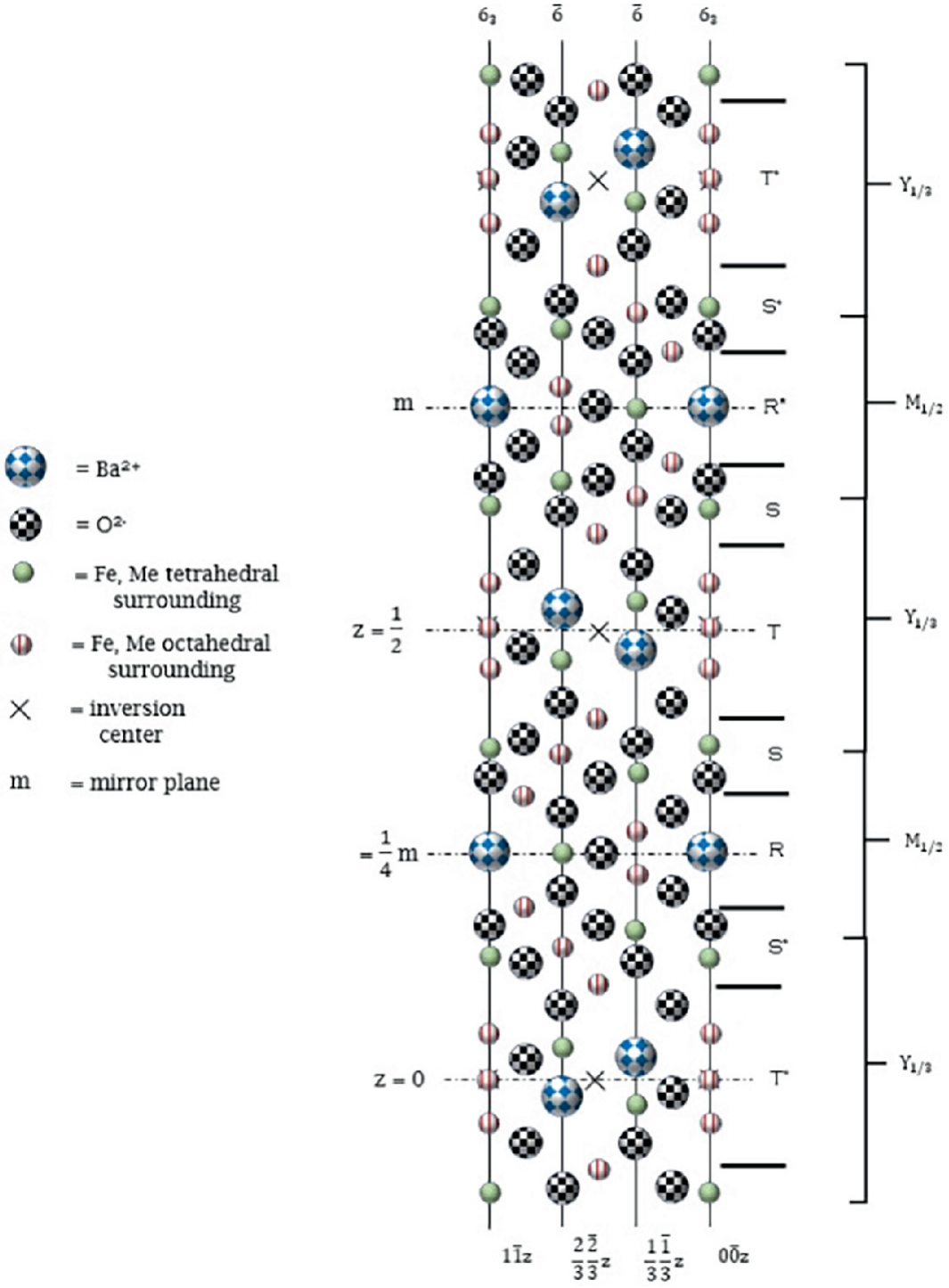

Fig. 4.9 Crystal structure of Z-type hexaferrite. It is reproduced with permission from AIMS Press (Vedrtnam et al. 2020)

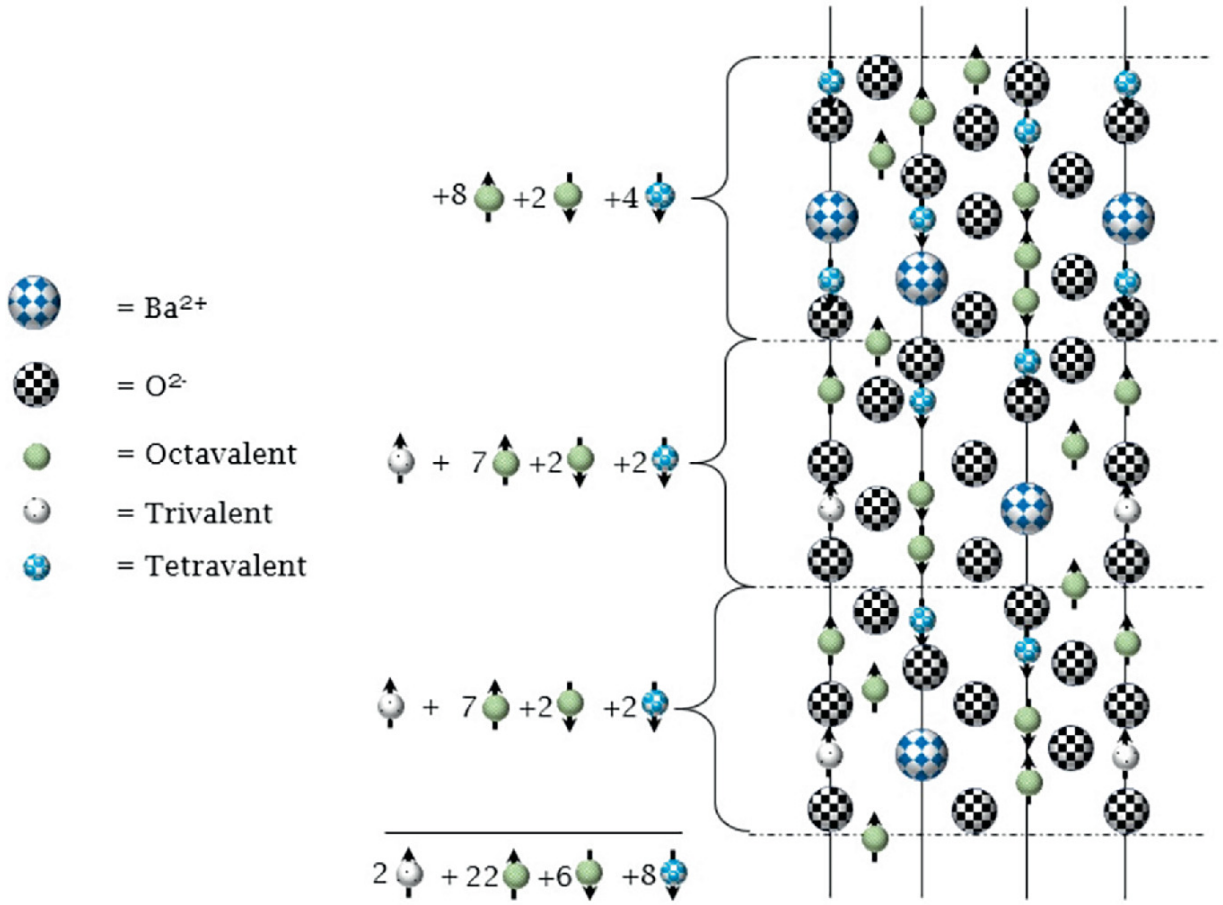

Fig. 4.10 Crystal structure of U-type hexaferrite. It is reproduced with permission from AIMS Press (Vedrtnam et al. 2020)

In case of M ferrite (e.g., $BaFe_{12}O_{19}$), unit cell has one S and one R blocks having cubically and hexagonally packed layers of oxygens. Its basal plane has Ba atom making a mirror plane. 2 S (spinel) blocks above and below R (hexagonal) block. The rotation of 180° at c-axis (the axis of easy magnetic polarization) of unit cell can generate S^* and R^* and thus construction of crystal structure can be done. It requires 2 formula units per unit cell. The crystallographic build up can be represented by RSR^*S^*. Similarly, crystal structures of W, Y, X, Z, and U ferrites can be generated by taking different combinations of S, R, T, S^*, R^*, T^*.Crystal structures of M, W, X, Y, Z, and U ferrites are shown in Figs. 4.5, 4.6, 4.7, 4.8, 4.9 and 4.10. Their crystallographic build ups are done by arrangement S, R, T, S^*, R^*, $T^*$with

Ba, Co, Fe and O atoms in a unit formula unit (Vedrtnam et al. 2020).

They are widely used as permanent magnets, magnetic recording, and data storage materials. Apart from this, hexaferrites can be used as a component in electrical devices, especially in high frequency devices operating at GHz frequencies.

4.3.3 Garnets

Garnets have been used as Gemstones and Abrasives since the Bronze age. The general formula is $X_3Y_2(SiO_4)_3$ in which X = Mn, Fe, Mg and Y = Al, Cr (Mallmann et al. 2013; Akhtar et al. 2018; Narayanan et al. 1987; Wan et al. 2020). Those are available in nature. Nowadays, synthesis garnets such as host ($Y_3Al_5O_{12}$, $La_3Al_5O_{12}$, $Lu_3Al_5O_{12}$) and host: Ln^{3+} (Ce^{3+}-Yb^{3+}) have been reported. They are used in opto-electronic applications.

Garnet ferrites were prepared in 1956 by taking precursors of ½($5Fe_2O_3$–$3M_2O_3$) (M = rare earth ion having 3+). In garnet, all Fe^{n+} ions are n = 3. The chemical formula is $R_3Fe_5O_{12}$ and its crystal structure exhibits body centred cubic with space group Ia-3d. It has 3 sub-lattices: tetrahedral (4 coordination), octahedral (6 coordination) and dodecahedral polyhedrons. The tetrahedral and octahedral sites are occupied by Fe^{3+} ions, whereas dodecahedral site (8 coordination) is occupied by R^{3+}ions (Y^{3+}, La^{3+}, Ce^{3+}, −Lu). Crystal structures are shown in Fig. 4.11 (Wan et al. 2020). The distribution of cations are expressed using different types of brackets as $\{R_3\}(Fe_3)[Fe_2]O_{12}$; {} for dodecahedral sites, () for tetrahedral site, and [] for octahedral sites. Examples are $Y_3Fe_5O_{12}$ (YFG), $Gd_3Fe_5O_{12}$ (GFG), $Sm_3Fe_5O_{12}$ (SFG).

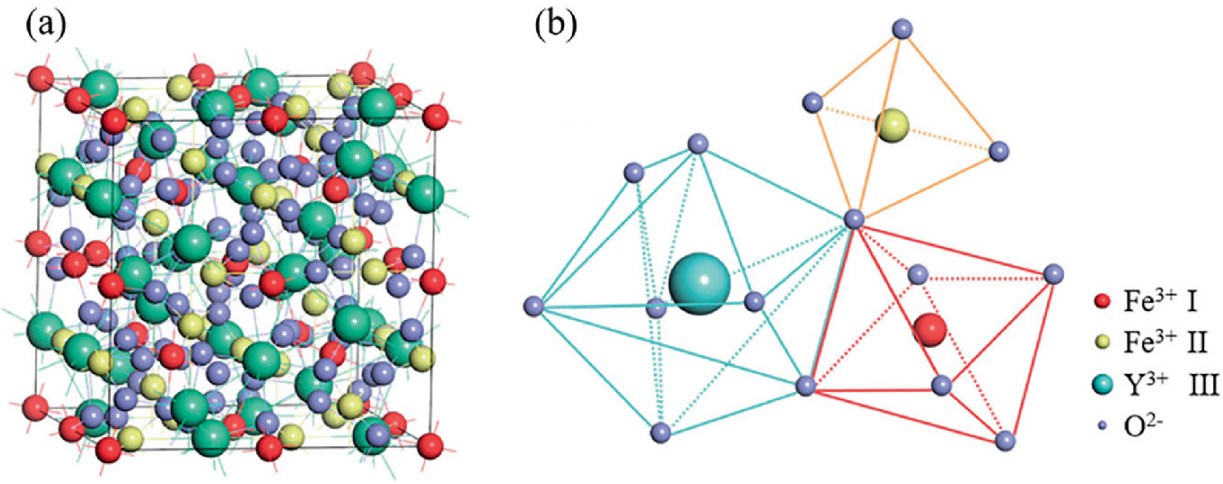

Fig. 4.11 Schematic diagram depicting **a** Lattice structure and **b** interstitial sites. It is reproduced with permission from AIP Advances publishers (Wan et al. 2020)

Ratio of tetrahedral to octahedral sites is 3:2. Fe^{3+} ions in both sites are antiparallel and net of 5 Fe^{3+} after cancellation of spins is one Fe^{3+} (5 unpaired electrons = 5 μ_β). One Fe^{3+} is interacted with R^{3+} ion. However, Y^{3+}, La^{3+} and Lu^{3+} do have no-electron or all paired electrons in f orbitals. Thus, their magnetic properties in general are depending on interaction between one Fe^{3+} and R^{3+}. There is no electron hopping mechanism in electron transport experiment as all Fe^{3+} and R^{3+} ions unlike Fe_3O_4 in which there is electron hopping from Fe^{2+} to Fe^{3+}. Therefore, garnets in general are insulator.

The garnet ferrites have wide applications in telecommunications and magneto-optic engineering. Garnets are observed to be useful in microwave applications. They exhibit high electrical resistivity and reduce the losses around microwave frequencies.

4.3.4 Orthorhombic Ferrites

Orthoferrites are a class of magnetic materials with antiferromagnetic ordering of the Fe^{3+} ions and its interaction with rare-earth ions (Tokunaga et al. 2009;

Wang et al. 2019; Pavarini et al. 2005). Its chemical formula is $RFeO_3$ and crystal structure in general exhibits orthorhombic with space group Pnma. This is of Perovskite type ABO_3in which A (R) atoms occupy the corner of orthorhombic structure, B (Fe) atom occupies the centre in cubic closed packing structure of oxygen atoms (ccp) (Fig. 4.12) (Pavarini et al. 2005). Spins of Fe^{3+} ion at one site with nearest neighboring Fe^{3+} ions are antiparallel and thus it exhibits G-type antiferromagnetic. There are 3 types of antiferromagnetic interactions (A, C and G) (Fig. 4.13) (Zhu et al. 2017). Depending on A (R) site say La, Sm, Gd, Dy, Ho, some of interaction may rise to ferromagnetic or ferrimagnetic properties. Example, $LaFeO_3$ shows the Neel temperature at $T_N \approx 740$ K (Lin et al. 2018). Even, the weak ferromagnetic is observed due to the partial Fe^{3+} ion spin tilt and anti-parallel interaction. This also shows ferroelectric property. In case of $DyFeO_3$, there are magnetic interactions of Fe–Fe and Fe-Dy and thus its exhibits many properties such Neel temperature, ferromagnetic or ferrimagnetic ordering, spin reorientations, etc. (Biswas et al. 2022). Bismuth ferrite ($BiFeO_3$) shows the multiferroic property with antiferromagnetic order at $T_N \sim 643$ K, spontaneous electric polarization (59.4 mC cm^{-2} up to Tc ~ 1100 K. $GdFeO_3$, has a Neel temperature ~ 661 K, possesses weak ferromagnetism and ferroelectricity (Tokunaga et al. 2009; Wang et al. 2019).

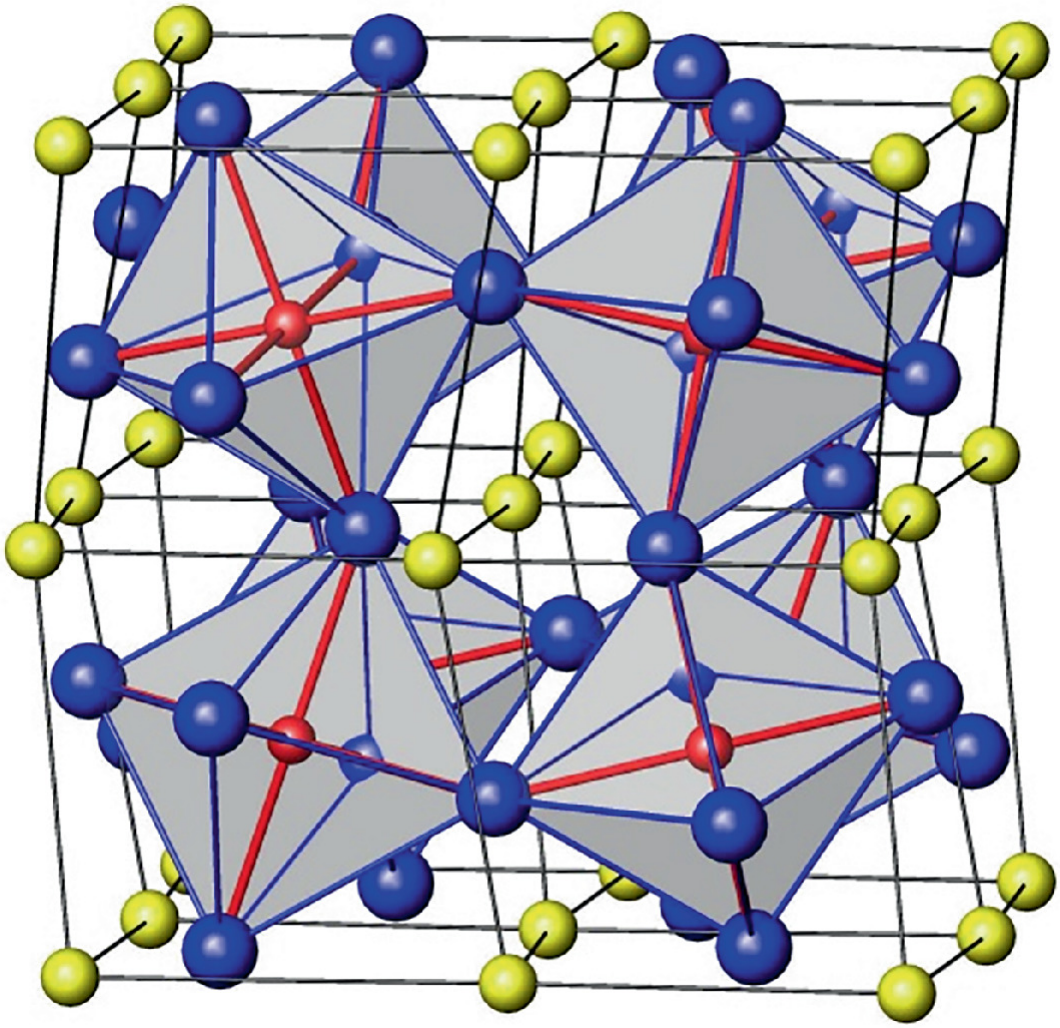

Fig. 4.12 Schematic diagram representing the crystal structure $GdFeO_3$, which is distorted ABO_3 perovskite ($YTiO_3$) in Pbnm symmetry. Yellow ball: oxygen atom, Blue ball: A site, Red ball = B site. It is reproduced with permission from New Journal of Physics (IOP Science) publishers (Pavarini et al. 2005)

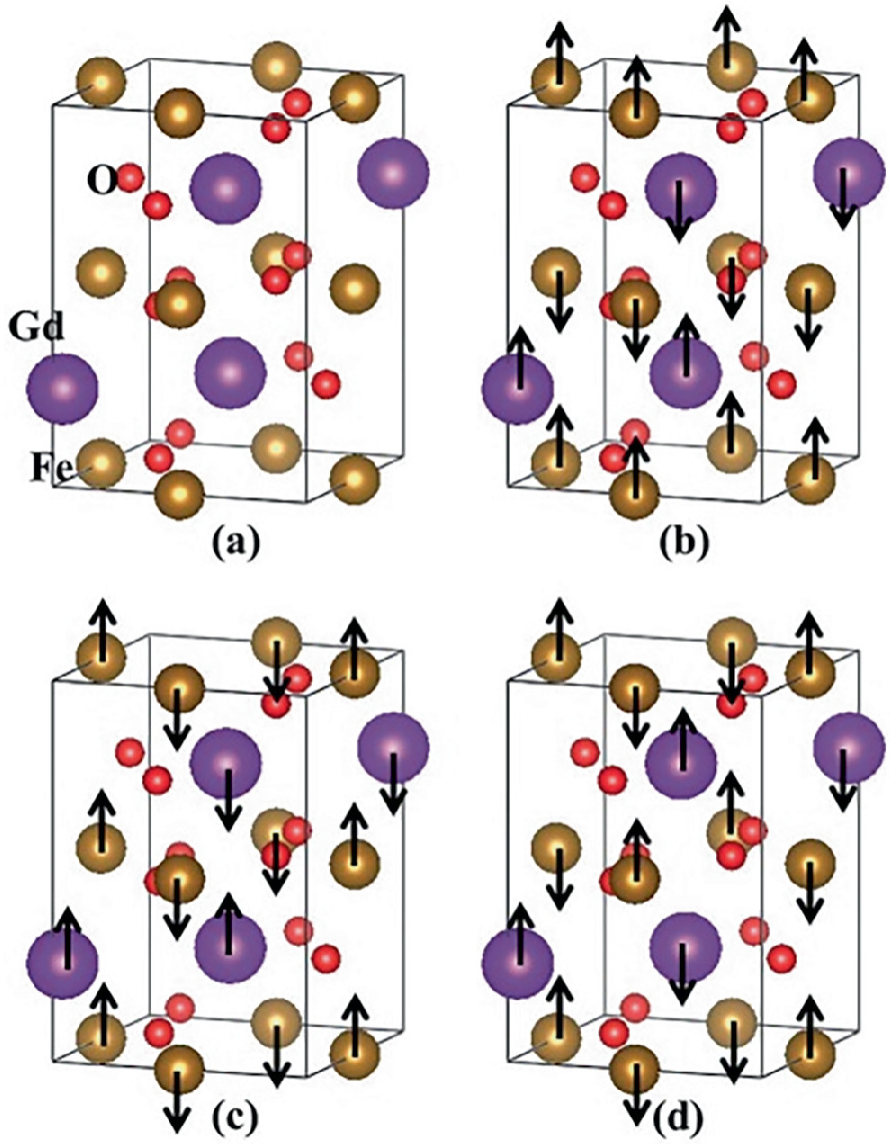

Fig. 4.13 Schematic diagram representing the crystal structure with all the magnetic moments of Gd and Fe being in the same direction (**a**) and three antiferromagnetic ordering configurations (b–d) in orthorhombic $GdFeO_3$: **b** A-AFM, **c** C- AFM and **d** G- AFM. The arrows indicate magnetic moment orientations on Gd and Fe atoms. It is reproduced with permission from RSC publishers (Zhu et al. 2017)

4.4 Particle Size Effects on Magnetism

What is it happened on magnetism when particle size decreases? In general, we are discussed about

classification of magnetism when sizes of particles of materials are in micron. There are a few compounds with single molecular magnets such as $[Mn_{12}O_{12}(CH_3COO)_{16}(H_2O)_4]0.2CH_3COOH.4H_2O$, $[Mn_{12}O_{12}(O_2CR)_{16}(H_2O)_4]$, $DySc_2N@C_{80}$ (metallo-fullerene). Organization of endohedral metallofullerenes in 1D, 2D, and 3D ordered structures are reported (Caneschi et al. 1991; Sessoli et al. 1993; Nakanishi et al. 2018). A molecule has many clusters of metal ions with magnetic spins. Such single molecular magnets are smaller than that of nanosized particles and thus are possible structural components for a quantum computer.

Evolution of magnetism in molecular magnets is different from bulk materials such as Au, Ni, Na, Co, ZnO, MnO, TiO_2, Fe_2O_3, Fe_3O_4.When size of particles having diamagnetic property decreases from micron to nanometer, their magnetic property can become either paramagnetic or ferromagnetic. For example, micro-sized ZnO particles are diamagnetic, whereas nanosized ZnO particles show the weak ferromagnetism (Straumal et al. 2016). In case of paramagnetic particles, particles can become antiferromagnetic or ferromagnetic with decrease of particle size. Antiferromagnetic particles can become paramagnetic or ferromagnetic. NiO is antiferromagnetic in case of bulk particles, whereas it becomes ferromagnetic in case of nanosized particles (Bi et al. 2004). Ferromagnetic or ferrimagnetic particles can become superparamagnetic or paramagnetic with decrease of particle size. Bulk Fe_3O_4 particles (micron size) show ferrimagnetic, whereas small sized nanoparticles (10 nm) become superparamagnetic (Joshi et al. 2020). Bulk cobalt and CoNi particles are ferromagnetic, whereas it become superparamagnetic in case of small sized nanoparticles (10 nm). Sometimes, materials having strong magnetic anisotropy can show ferromagnetic property even if size of particles is in nano-

range (10 nm). Examples are FePt, FePd, FePdPt (Sharma et al. 2010; Gajbhiye et al. 2008a; Sun et al. 2000, 2006; Stahl et al. 2002). FePd particles with size of 3 nm shows superparamagnetic properties, whereas that with size of 10 nm shows ferromagnetic property.

4.4.1 Superparamagnetism in Ferrite Nanoparticles

The magnetic property varies with changing the dimension of particles of the material from bulk to nano (Sharma and Singhal 2013). The magnetic moments per atom/formula, magnetic anisotropy, coercivity field (H_C) and Curie temperature (T_C) or Néel temperatures (T_N) of nanomaterials are different from those of bulk counterpart. A bulk ferromagnetic material is composed of a multidomain structure and domain walls. The magnetic domain arises due to balance of exchange energy, magneto-crystalline anisotropy, and the magnetostatic (or dipolar) energy (Fiorillo et al. 2006; Mody et al. 2013).

The exchange energy is responsible for the directional orientation of magnetic moments in uniform direction. The magneto-crystalline anisotropy is responsible for the alignment of magnetic moments in specific direction and magnetostatic energy is the potential energy stored in a static magnetic field. Each domain has the orientation of magnetic moments in a particular direction and its magnetic direction is different from neighboring domains. However, it has a net magnetic moment resulting from the sum of all individual domains. When the size of ferromagnetic material is reduced below the critical dimension (say 20 nm) it is difficult to split the domains as it becomes energetically unfavorable and results the formation of a single domain structure and the magnetic properties change drastically. The thermal energy plays essential role in single domain structure (Cullity et al.

2012). With decrease of particle size, thermal energy of surrounding can be comparable with anisotropy energy of particle at particular temperature (known as Blocking temperature, T_B). When temperature is less than T_B, direction of magnetic domain is blocked and thus ferromagnetic/ferrimagnetic property exists. On the other hand, when temperature is more than T_B, direction of magnetic domain is able to rotate from easy direction (0°) to opposite direction (180°). Time required to rotate from easy direction (0°) to opposite direction (180°) is so small $\sim 10^{-9}$ s. This is known as Neel' relaxation. In such condition, material behaves as paramagnetic (i.e. no coercivity in MH curve). However, individual domain has a large magnetic moment $\sim 10^2$–10^3 μ_B. Thus, such particle is called superparamagnetic. In this, the thermal energy is more than the anisotropy energy (Szotek et al. 2006; Gubin et al. 2005; A. P. 2009). Time taken to measure magnetic moment is much longer than that of relaxation time for superparamagnetic domain. In general, time taken to measure magnetic moment is 1 second to 60 seconds in most instruments (VSM, SQUID).

In nano-dimension range, the magnetic property of material strongly depends on the crystal structure, surface of particles, defects in lattice, size and shape of particles. When breaking of symmetry takes place at the surface of particle of nanomaterial due to dangling of bonds, strain in the crystal is generated that changes the chemical and physical properties and results in change in magnetic property as compared to bulk.

A bulk particle is consisting of large number of bunches of area of uniform magnetization known as domains. Each domain has different direction of magnetization from other and is bifurcated from each other by a wall called as domain wall. This domain wall arises due to magnetostatic energy (E_{ms}) and the domain-wall energy (E_{dw}). In bulk

material the external magnetostatic energy increases with volume, and enhancement in domain wall energy takes place due to the increment in interfacial area. In nanodimension a high amount of energy is required for the formation of further domain wall compared to external magnetostatic energy. As a result, below the critical size (varies with material to material) of nanomaterial the particle is restricted for the further formation of multiple domains and turned to be a single domain nanoparticle. In such a single domain, the orientation of all the spins is unidirectional resulting in uniform magnetization. Such a single domain nanoparticle exhibits high anisotropy value due to absence of domain walls, as reverse magnetization takes place due to rotation in spins only. Hence the high coercivity can be observed from single domain nanomaterials. This can be explained by result of two major factors such as spin rotation and shape anisotropy. In nanowire or nanorods (aspect ratio of length to diameter is more than 1.0), their coercivity (Hc) is more than that of spherical particles in the same material. This is known as shape anisotropy in magnetism (Cullity et al. 2012).

The interaction between spin and orbit of a material give rise to the magneto crystalline anisotropy energy (Cullity et al. 2012). Due to this magneto crystalline energy $(\mathrm{E_a})$ where $E_a = KVsin^2\theta$ with two energy minima at $\theta = 0^\circ \text{to } 180^\circ$ with energy barrier KV, in a single domain material all the spins are arranged in particular direction not necessarily in a direction parallel to external magnetic field. As per the Stonner–Wohlfarth model, $\mathrm{E_a}$ depends on volume of particle (V), anisotropy energy constant (K) and an angle between magnetization vector and easy axis of magnetization (θ). Anisotropy energy is responsible for the separation of the two directions of easy magnetization having equivalent energy and acts as an energy barrier to magnetic moment reversal. When the dimension of a bulk

material reduces to nano, the surface to volume ratio increases and it results in reduction of $\mathrm{E_a}$. At this stage the thermal energy is of great importance as it increases with increasing the temperature. Below a blocking temperature ($\mathrm{T_b}$), the anisotropy energy dominates over the thermal energy and it results in blocking of magnetic moment along the direction of easy axis. The system becomes ferromagnetic. When thermal energy dominates the anisotropy energy, there is a breaking of magnetic blocking. Instead, domain starts rotation from easy to other direction. The system becomes superparamagnetic. When both the energies are comparable ($E_T = k_B T$) at no external magnetic field, there is an equilibrium between ferromagnetism and superparamagnetism. The temperature at which the flipping of spins from the easy axis starts is called as the blocking temperature $(\mathrm{T_B})$. This temperature varies with the dimension of nanoparticles and depends on many factors. Above blocking temperature $(\mathrm{T_B})$ the material behaves as superparamagnetic (SPM) material and below it the material remains ferromagnetic or ferrimagnetic in nature.

In SPM state of nanoparticles, the nature of magnetic moments acts similar to single domain, like paramagnet but shows large magnitude. The mean time taken between the flipping in spins of magnetic moment is called as Neel relaxation time (τ_N) given by the Neel–Arrhenius relation $\tau_\mathrm{N} = \tau_0 \exp\left(\frac{\mathrm{KV}}{\mathrm{k_B T}}\right)$, where KV is the height of energy barriers, τ_0 is the length of time in the range from 10^{-9} to 10^{-11} seconds and τ_N is Neel relaxation time $\tau_\mathrm{N} = (2\pi \mathrm{f})^{-1}$. The measurement time (τ_m) decides the SPM and blocked state of the magnetic nanoparticles and considered to be constant for the determination of transition between SPM and blocking state as a function of temperature. At $\tau_\mathrm{m} > \tau_\mathrm{N}$, magnetic moments flip multiple times whereas at $\tau_\mathrm{m} < \tau_\mathrm{N}$,

no flipping of magnetic moments occur. At the blocking temperature $T_B = \frac{KV}{k_B \ln(\tau_m/\tau_0)}$, τ_m and τ_N becomes comparable where $\ln(\tau_m/\tau_0) = 25$ for laboratory measurement (Chinnasamy et al. 2001). The Néel relaxation time $\tau_N = \tau_0 \exp\left(\frac{KV}{k_B T}\right)$ feebly depends on the temperature. The evaluation of blocking temperature is dependent on many factors as the dimension of nanoparticles, distance between particles, size distribution, effective anisotropy constant (K_{eff}), external magnetic field and experimental measurement time. There is a reduction in magnetization with decrease of particle size is due to decrease of exchange interaction among spins. Two main sources for decrease of magnetization are rotation of domain from easy axis to other and surface spin canting. These are observed in many materials including nitrides, carbides, oxides and metal nanoparticles (Ningthoujam and Gajbhiye 2015; Ningthoujam and Joshi 2021; Gajbhiye et al. 2002, 2004). The variation of coercivity (H_c) with particle size of ferromagnetic material is shown in Fig. 4.14. Such variation was obtained in many materials including Co nanoparticles (Gajbhiye et al. 2008b).

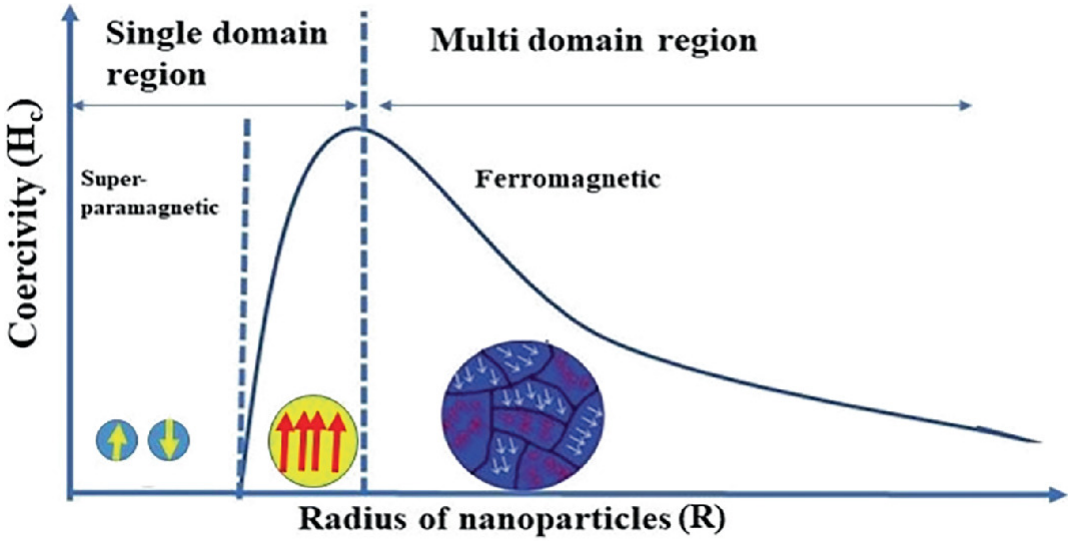

Fig. 4.14 Relation between coercivity and size of small particles

4.4.2 Spin Glass

A spin glass in general refers to a material in which a few magnetic spins (ppm) are randomly interacting in conducting or non-conducting medium with a large number of metastable states, which restrict reaching equilibrium. This is sometimes known as dilute magnetic material or disordered magnetic states. This concept was started in 1960s and explained in 1980s. Prof. G. Parisi, Sapienza University of Rome, Italy was awarded Nobel Prize in Physics in 2021 *"for the discovery of the interplay of disorder and fluctuations in physical systems from atomic to planetary scales"*. Freezing of spin at a particular temperature is spin glass transition (T_g). For example, Fe in Cu matrix, Mn in Au matrix (Nigam et al. 1983; Parisi 2006). Above T_g, system acts as paramagnetic. T_g can be determined by low temperature study of magnetization versus temperature using AC magnetic field. In AC magnetic field, frequency can be varied. Real and imaginary components in magnetic susceptibility can be derived. This is different from ferromagnetic material, in which spontaneous magnetization (parallel spins) takes place. Figure 4.15a shows difference between Spin glass and Ferromagnet, (B) Frustration of spins and (C) example of spin glass is dilute magnetic Fe atoms in Cu matrix (https://en.wikipedia.org/wiki/Spin_glass) (https://www.nobelprize.org/prizes/physics/2021/press-release/).

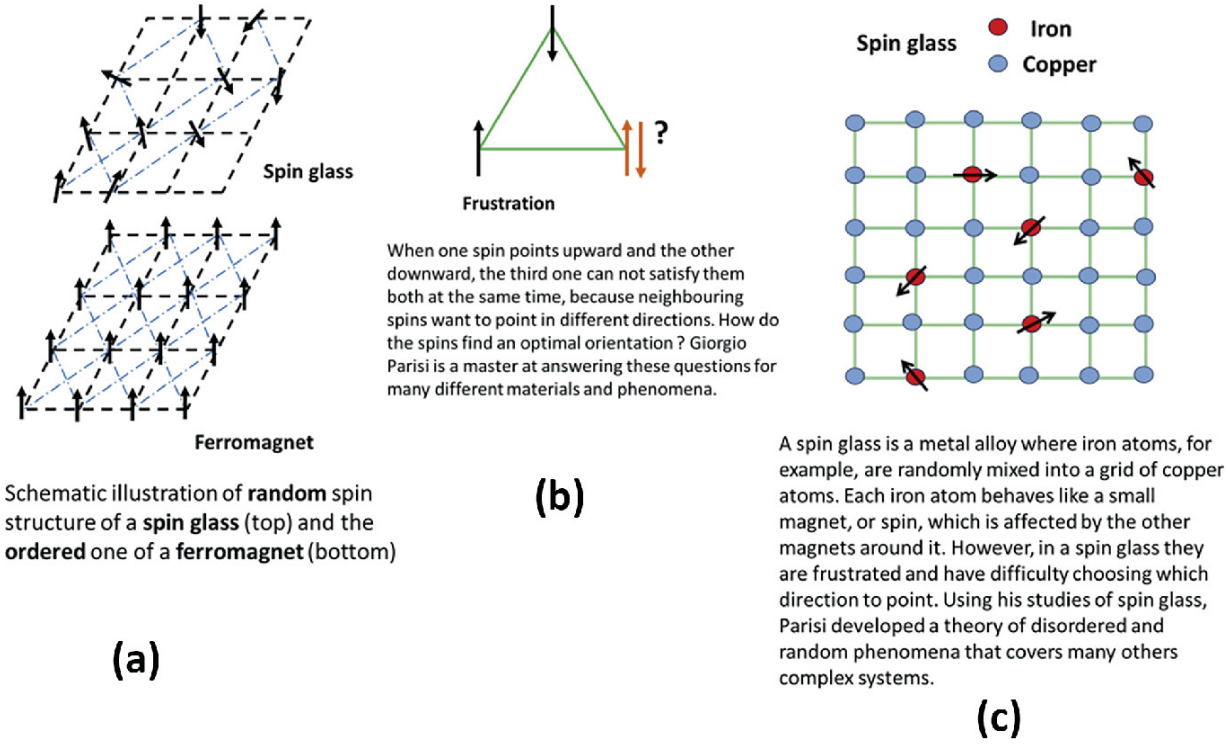

Fig. 4.15 **a** Difference between Spin glass and Ferromagnet. **b** Frustration of spins. **c** Example of Spin glass is dilute magnetic Fe atoms in Cu matrix. It is redrawn by the authors (https://en.wikipedia.org/wiki/Spin_glass) (https://www.nobelprize.org/prizes/physics/2021/press-release/)

Nowadays, the similar disordered spins are observed in many systems such as magnetic nanomaterials, including mixed phase oxide materials, dilute magnetic alloys, intermetallics and frustrated magnets (Alzoubi et al. 2020; Topkaya et al. 2012). The spin glass properties are also observed in various ferrite nanomaterials. The randomness, magnetic frustration, competing interaction and surface disordered spins give rise to spin glass state in nanomagnetic materials. Due to reduced size in magnetic nanomaterials, the core and surface are exposed to different kind of environments. The increased surface area in magnetic nanomaterials results in various surface defects like dangling bonds and atomic vacancies. The defects present at the surface give rise to uncompensated disordered spins which are randomly oriented and the state is referred as spin -glass like state. Zero-field-cooled (ZFC) and field-cooled (FC) magnetization measurements are

generally used to detect spin glass properties in magnetic nanomaterials. The best method to identify spin glass from superparamagnetic transition (T_B) is AC susceptibility. Spin glass transition varies with frequency applied, whereas superparamagnetic transition does not vary much with frequency applied.

The spin glass behavior results from dipolar interaction in nanomaterials, which is called super spin- glass (Tiwari et al. 2023). The spin glass behavior results from disordered surface spin in nanomaterials is called as surface spin glass. It is difficult to differentiate between the super and surface spin glass behavior in nanomaterials. The interaction type of super exchange interaction is in general stronger than the dipolar interaction.

$MnFe_2O_4$ nanoparticles are unique when compared to other spinel ferrite nanomaterials, as they show magnificent chemical stability with temperature and time, exhibit properties like dimensional dependent saturation magnetization, excellent magneto-crystalline anisotropy and mechanical hardness. In $MnFe_2O_4$ nanoparticles, the core has well-ordered magnetic structure compared to a surface as the crystalline symmetry breaking at the surface results in disordered spins. Core and surface of $MnFe_2O_4$ nanoparticles affects the magnetic properties. The AC susceptibility characterization of $MnFe_2O_4$ nanoparticles at lower temperature with varying frequencies shows strong interparticle interactions resulting in spin glass state (Aslibeiki et al. 2010). There is report on CoNi nanoparticles that shows spin-glass nature (Sharma et al. 2013).

4.5 Synthesis Methods

For the synthesis of the magnetic ferrite nanomaterials, numerous synthesis routes can be used. Particles can be in

either powder or thin films. Here, particles with powder form will be mentioned. These powder particles can be prepared by various chemical routes such as co-precipitation, sol–gel, reverse micelles and micro-emulsion technology, hydrothermal reactions, hydrolysis and thermolysis of precursors, and electrospray synthesis, etc. (Nisticò et al. 2020; Pullar 2012; Kefeni et al. 2017a) For different applications the surface modification of the magnetic nanomaterials is important factor concerning to selectivity and aqueous stability of the nanomaterials. The followings are some synthesis methods of magnetic ferrite nanomaterials:

4.5.1 Co-precipitation

The precipitation of any ions occurs only when their ionic product is more than that of solubility product. Example is the formation of AB in which ions [A^+] and [B^-] in aqueous solution come closer as concentration of their respective ions increases. There is a particular concentration at which the formation of [AB] can take place. At initial stage, the formation of [AB] and dissociation to [A^+] and [B^-] takes place. There will be an equilibrium. As concentration of their respective ions increases further, dissociation reduces, instead, the formation of [AB] increases. This is a stage of nucleation. Then size of particle of [AB] increases. This is a growth of particle. If there are more than a positive type [A^+], the precipitation can take place. This is known as co-precipitation. In other word, the precipitation of metal ions having different elements is known as co-precipitation. Examples are the formation of $Fe(OH)_3$, $Ni(OH)_2$, FeS, $FePO_4$, YPO_4, YVO_4, PbSe, etc. and these are formed by one metal ion and one negative species such as OH^-, S^{2-}, PO_4^{3-}, VO_4^{3-}, Se^{2-}. This is known as precipitation. Whereas you can come the formation of

$CoFe_2O_4$, $NiFe_2O_4$, $MnFe_2O_4$, $BaFe_{12}O_{19}$,$Y_3Fe_5O_{12}$. This formation is of co-precipitation type because 2 metal ions having different elements are used. In the formation of $CoFe_2O_4$, 2 metal ions such as Co^{2+} and Fe^{3+} ions are used.

This is one of the best cost effective and easy methods of synthesis of magnetic ferrite nanoparticles. In this method, an aqueous precursor salt solution is prepared by dissolving metal precursors in H_2O or acids (HCl, HNO_3). One of the respective negative species OH^-, VO^{3-}, PO^{3-}, S^{2-}, Se^{2-} is added. In this way, precipitation occurs only when ionic product is more than respective solubility product. In some cases, heat-treatment temperature, pH and surfactant, ligand molecules are provided to get better yield, better crystallinity, shape and size control (Chen et al. 2010; Gul et al. 2007).

Schematic diagram representing synthesis procedure for magnetic nanoparticles by co-precipitation route is shown in Fig. 4.16. In this way, superparamagnetic Fe_3O_4 and $CoFe_2O_4$ nanoparticles are prepared. In some cases, the magnetite nanomaterials are unstable under ambient conditions as they get easily oxidized. Thus, water adsorbed or absorbed in or on particles must be removed by washing with acetone. It can be stored in a glass ampoule with vacuum. Sometimes, it can be stored in hexane medium as hexane is hydrophobic as ambient air could not contact ferrite materials. Fe_3O_4 nanoparticles are prepared by coprecipitation of $FeSO_4$ and $Fe(NO_3)_3$with ammonia or NaOH in aqueous medium. The particles are highly agglomerated and agglomeration of such magnetic nanoparticles can be reduced by using capping agents such as polyethylene glycol (PEG) and oleic acid or oleate (Ghosh et al. 2011).

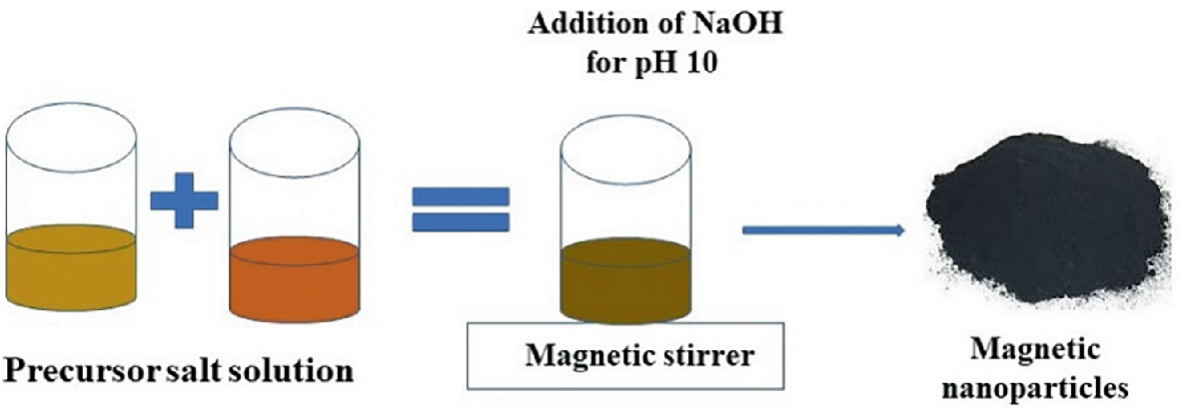

Fig. 4.16 Schematic diagram representing synthesis procedure for magnetic nanoparticles by co-precipitation route

4.5.2 Reverse Micelles and Micro-emulsion Method

In this method, stable isotropic dispersion of two immiscible liquids and the microdomain of both the liquids are stabilized by an interfacial film of surfactant molecules. The formation of nanodroplets of smallest dimension takes place spontaneously by surfactant molecules, micelles (1–10 nm) or water-in-oil emulsions (10–100 nm) (Sivakumar et al. 2007, 2008). Figure 4.17 shows the scheme for micelle and reverse micelle. In case of water-in-oil microemulsions (reversed micelle formation), a small amount of water is added in a system containing oil (hexane). Both are immiscible as water is hydrophilic and oil is hydrophobic in nature. Surfactant (oleic acid, sodium dodecyl sulphate (SDS), or cetyltrimethylammonium bromide (CTAB) is added to it. The surfactant has a long chain hydrocarbon with hydrophobic and hydrophilic groups. This can interact with water as well as oil parts. When concentration of surfactant increase, miscibility of water and oil increases. At a particular concentration of surfactant known as critical micelle concentration, the stable micelle is formed. Here water droplet size is formed inside micelle and surfactant molecules are surrounding water core region; and oil is in large medium. Metal ions

can be stored in water droplet region of micelle in a beaker. The negative species OH^-, VO^{3-}, PO^{3-}, S^{2-}, Se^{2-} can be stored in water droplet region of micelle in another beaker. By bringing 2 micelles having metal ions and negative ions, the precipitation can occur. Here, micelles are interacted each other in oil medium and fusion of two or more micelles takes place. In this way, many compounds such as $Fe(OH)_3$, Fe_3O_4, $Ni(OH)_2$, FeS, $FePO_4$, YPO_4, YVO_4, PbSe are prepared. With increase of size of water droplet, particle size increases. The formation of monodispersed nanoparticles can be achieved.

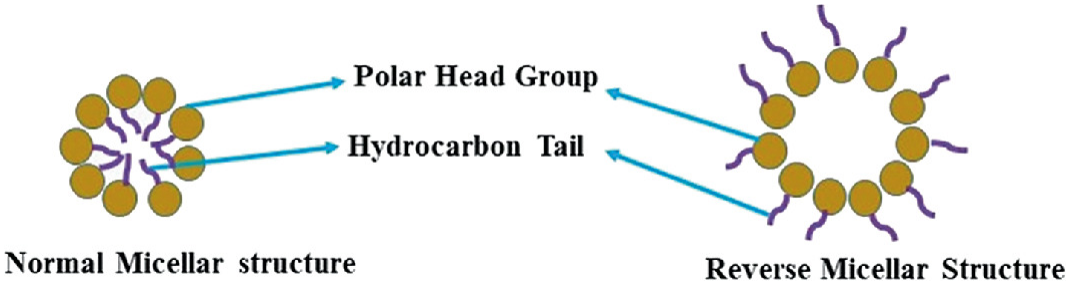

Fig. 4.17 Schematic diagram representing normal and reverse micelles

4.5.3 Sol–gel Technique

In sol–gel method, fine particles of materials can be prepared. Here, sol is defined as colloidal form dispersed in a medium. Medium can be liquid or solid. Size of sol varies from a few nanometers to sub-microns. One example is a formation of iron hydroxide ($Fe(OH)_3$) after mixing of NH_4OH and $FeCl_3$ in water medium. Gel is a polymeric network with semi-solid. One example is silica gel.

Many years back, sol–gel technique has been used. The formation of TiO_2 fine particles (nm size) is done at 100–120 °C after dispersion of Titanium tetra-isopropoxides or Titanium tetra-butoxides in water (Dubey et al. 2019). SiO_2 nanoparticles are prepared through hydrolysis of tetra-ethyl orthosilicates. Many ferrite particles are prepared by sol–gel method. It needs 2 steps: hydrolysis of the metal

precursor in the presence of citric acid or polyvinyl alcohol takes place and followed by polycondensation of the hydrolyzed products. During hydrolysis, sols are formed at room temperature and finally it is heated at 100–120 °C with slow heating rate (1 °C/s). Condensation takes place and a polymeric network is framed. Upon heating at 500 °C, fine particles of ferrites are formed. Uniform size particles can be prepared (Fig. 4.18).

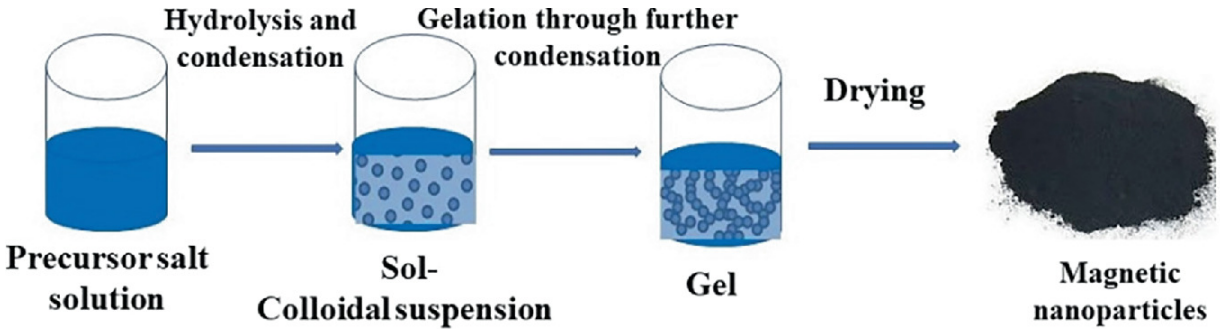

Fig. 4.18 Schematic diagram representing synthesis procedure for magnetic nanoparticles by Sol–gel technique route

4.5.4 Thermolysis of Precursors

Thermolysis is a process of breakdown of molecules or precursors in a liquid medium using heat (Fig. 4.19) (Soni et al. 2019, 2021). In the preparation of highly crystalline nanoparticles, it requires to heat metal precursors above 100 °C for a few hours. To get highly crystalline nanoparticles in a liquid medium, liquid medium must have a high boiling points (say, $T > 250$ °C). Examples having high boiling point solvents are 1-Octadecence (315 °C), diphenyl ether (258 °C), dibenzyl ether (298 °C), etc. To get highly crystalline as well as monodispersed nanoparticles at higher temperature, it needs to have capping agents with high boiling points. Capping agents with high boiling points will have a large hydrocarbon chain with hydrophilic group. In this direction, surfactants can be one of molecules having a large hydrocarbon chain with hydrophilic group. Examples of surfactants are oleic

acid (b.p. = 360 °C; $CH_3-(CH_2)_7-CH=CH-(CH_2)_7-COOH$), oleyl amine (b.p. = 364 °C; $CH_3-(CH_2)_7-CH=CH-(CH_2)_7-CH_2\text{-}NH_2$), triphenyl phosphine (b. p. = 377 °C; $P(C_6H_5)_3$), Triphenylphosphine oxide (b. p. = 360 °C; $(C_6H_5)_3PO$)). The metal precursors are generally in the form of acetate or acetyl acetonate.

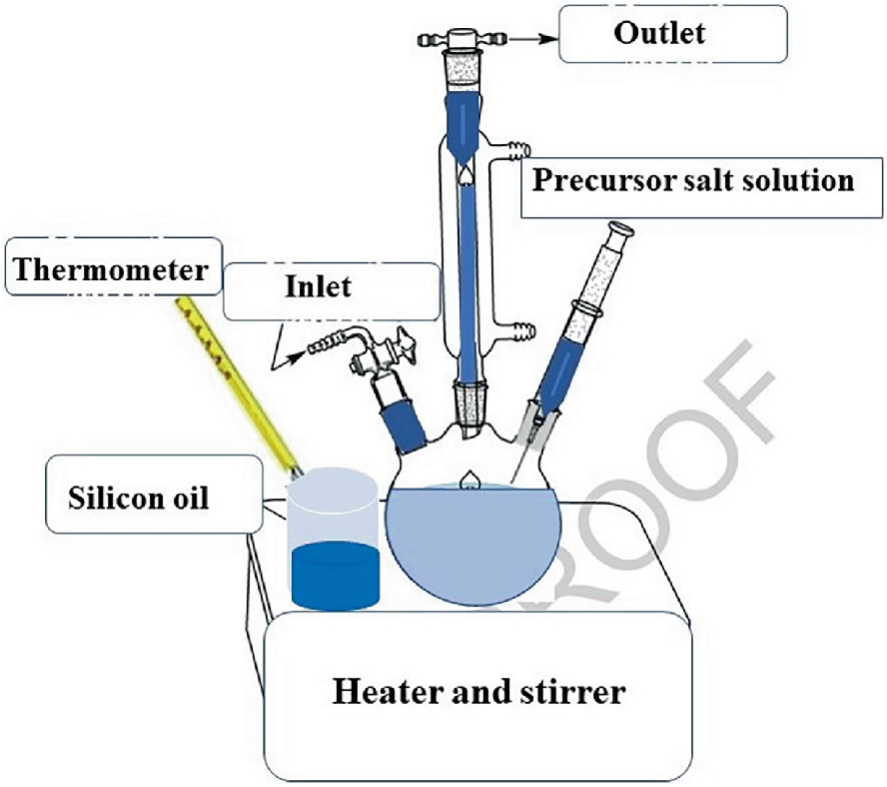

Fig. 4.19 Schematic diagram representing synthesis procedure for magnetic nanoparticles by thermolysis of precursors

For preparation of Fe_3O_4 highly crystalline monodispersed nanoparticles, 1 mmol from metal precursor (Fe acetate) is dissolved in 5 ml oleic acid and 15 ml 1-octadecence in 50 ml volumetric flask. It is heated slowly upto 300 °C for 1 h to 5 h under stirring. The heating rate will be 1 °C per minute. Fe_3O_4 nanoparticles are recovered through centrifugation. Ethanol is used as coagulating agent and washing solvent. TEM images of Fe_3O_4, $\gamma\text{-}Fe_2O_3$ and $\gamma\text{-}Fe_2O_3@Mn_xO_y$ are shown in Fig. 4.20 (Sharma et al.

2018; Joshi et al. 2021). Similarly, $CoFe_2O_4$, $MnFe_2O_4$ and $ZnFe_2O_4$ can be prepared.

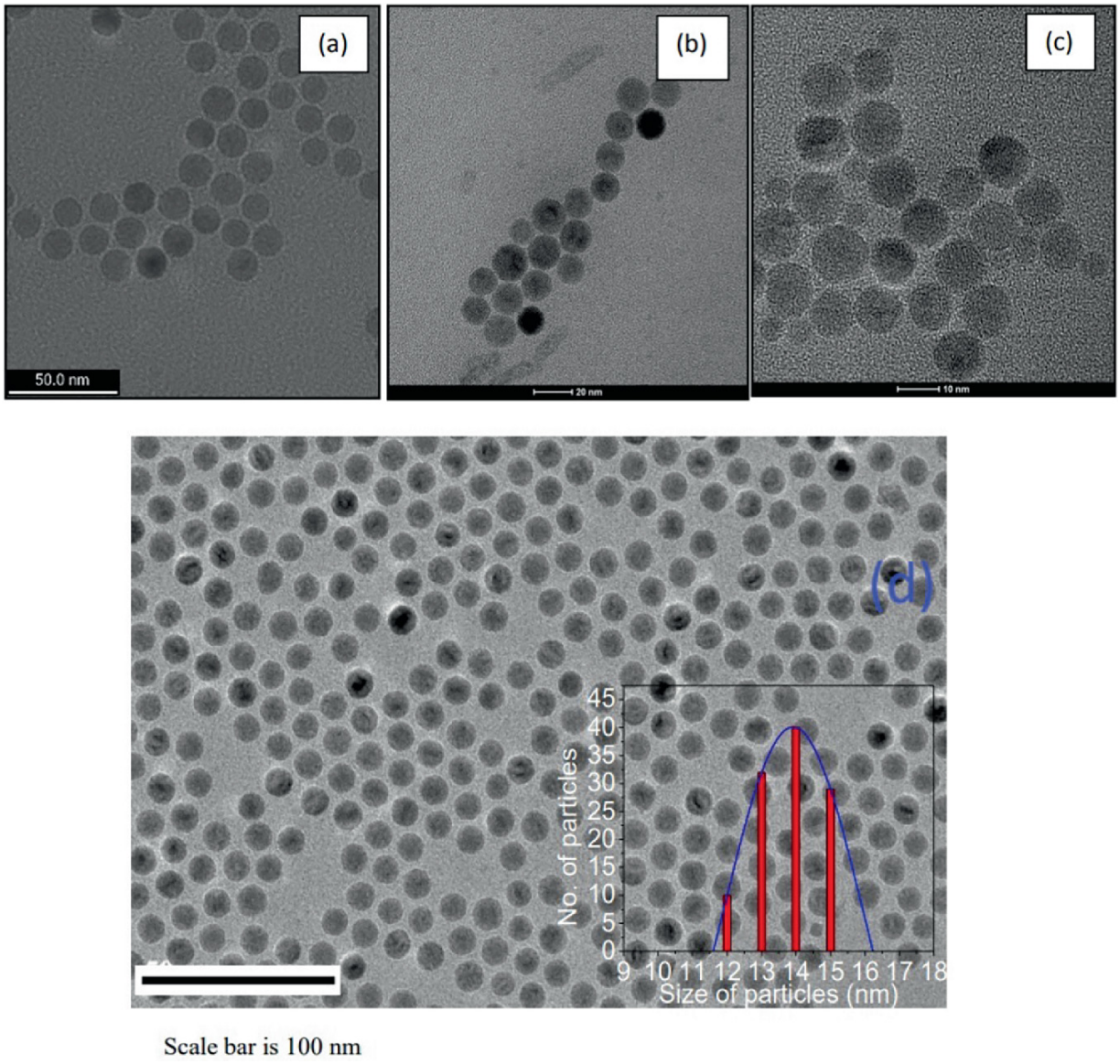

Fig. 4.20 TEM images of **a** γ-Fe_2O_3, **b** γ-Fe_2O_3@Mn_xO_y (Mn6), **c** γ-Fe_2O_3@Mn_xO_y (Mn12) (Joshi et al. 2021) **d** TEM image of Fe_3O_4 monodispersed nanoparticles prepared by thermolysis method. It is reproduced with permission from ACS Publishers (Sharma et al. 2018)

4.5.5 Hydrothermal Reaction

Hydrothermal reaction is preparation of particles from metal precursor under pressure and temperature above

room temperature in aqueous medium (Pullar 2012; Kefeni et al. 2017a). The pressure can be maintained in closed vessel. The Teflon vessel was kept inside stainless-steel vessel. Here, Teflon vessel is used because chemical reactions occurred during heating do not affect Teflon layer much. Chemical precursors including metal ions, surfactant, oxidizing agent or reducing agent were kept inside Teflon vessel. Volume of chemical precursors in water must be 1/3 capacity of reaction vessel of Teflon. After adding precursors in Teflon vessel, it was closed with Teflon cap. Finally, closed vessel of Teflon is inserted inside stainless steel vessel. Stainless steel vessel is closed tightly. It is kept in temperature-controlled furnace (200 °C or less) for a few hours to days. As temperature is maintained at 200 °C, pressure is developed inside Teflon vessel. In this method, highly crystalline particles are prepared. The shape and size of particles can be controlled. It is to be noted that dielectric constant of water is 78 at ambient atmosphere and this value decreases as pressure and temperature increases. Thus, some precursors could not be dissolved in water, but can be dissolved in this reaction condition. If solvent water is replaced by other solvent, this technique is known as solvo-thermal reaction. A liquid NH_3 can be used. This is known as ammono-thermal method. In this way, many particles including ferrites can be prepared (Fig. 4.21).

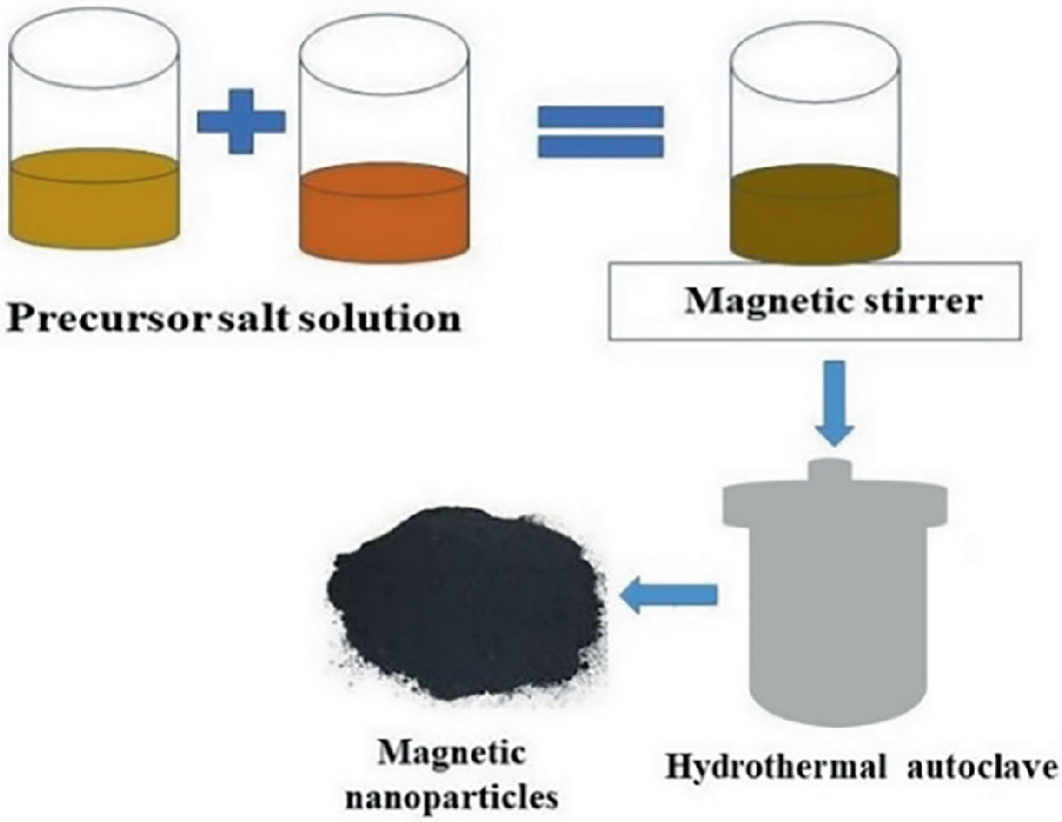

Fig. 4.21 Schematic diagram representing synthesis procedure for magnetic nanoparticles by hydrothermal reactions route

4.5.6 Solution Combustion Technique

The solution combustion technique is a self-propagating high temperature synthesis (SHS) method which is highly efficient and cheap (Pullar 2012; Kefeni et al. 2017a; Ningthoujam et al. 2009). The high purity and homogeneity of the nanoparticles can be prepared using this method. This method is heat-initiated self-sustained reaction which takes place between the oxidizer and the fuel resulting in formation of fine powders of nanoparticles. In this method the dimension and surface area of the nanoparticles can be controlled by varying heat and temperature. Solution combustion technique is a high temperature synthesis method of nanoparticles which results in thermodynamically stable phase (Fig. 4.22). Metal precursors are initially dissolved in HNO_3 (acting as

oxidizing agent), and citric acid, Polyvinyl alcohol (PVA) (acting as fuel agent) are added. These are slowly heated at 300 °C and finally it was heated at 500–600 °C for a few hours. Pure compounds can be prepared.

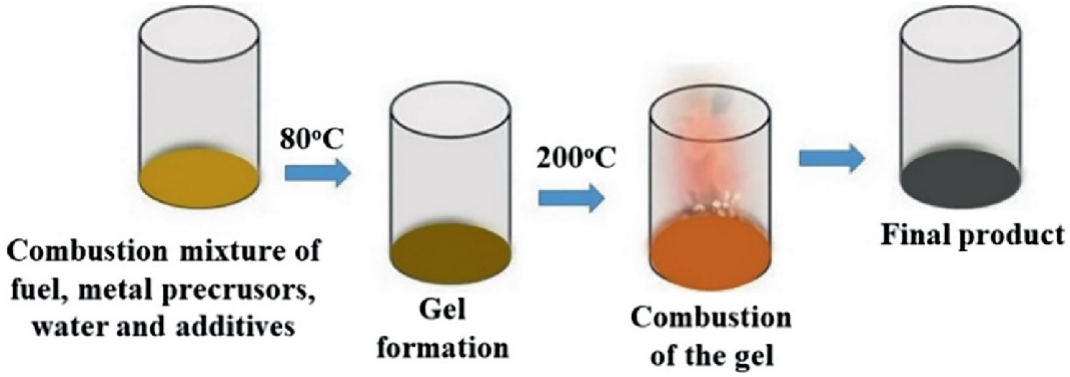

Fig. 4.22 Schematic diagram representing synthesis procedure for magnetic nanoparticles by solution combustion technique

4.6 Effect of Surface on Magnetic Properties of Ferrites

As the size of the particle decreases to nano-dimension, the surface area gets enhanced and the contribution of the surface area plays vital role in magnetization studies (Ing and Heck 1974). In a single domain nanoparticle, there exists a uniaxial anisotropy and the orientation of magnetic moments results in up or down position at the easy axes at zero field. The interaction of the environment at the surface of nanoparticle behaves in different way than the volume (ferromagnetic core) of the material. The different environmental behavior of the surface is observed as compared to the core due to presence of defects/dangling bonds on surface of particles as size decreases to nanometers. These defects result in randomization of the spins on surface and it leads to spin canting or antiferromagnetism. Even, the materials which are not magnetic in nature such as cerium oxide and aluminum

oxide show hysteresis loop at 300 K indicating weak ferromagnetism due the local ordering of unpaired electrons arising from defects in lattice or surface (Sundaresan and Rao 2009). At the surface of the nanoparticles, the reoriented irreversible spins are observed. A nonuniform strain at the surface is observed while studying the structural relaxation in spinel ferrite nanomaterials with molecular dynamic modeling by the author Nunes et al. (Nunes et al. 1998). Using Molecular dynamic model, it is observed that with decrease of the dimension of the nanoparticles, magnetization decreases with the significant irreversibility and time dependent magnetic moment in high fields. In nanomagnetic materials due to finite size effects, there exist uncompensated spins at the surface and spin-glass like nature is observed which results in increased magnetic anisotropy due to enhanced surface anisotropy.

The surface effects lead to a decrease or increase in the value of magnetization of nanoparticles. In case of some metal oxides the value of magnetization is reported to be reduced compared to some metallic nanoparticles (cobalt). When the size of the nano-dimension material is reduced below critical dimension, the surface of the material gets spin canted and it shows a spin –glass behavior; and sometimes increased magnetic anisotropy is observed. The computational studies show the difference in anisotropy and magnetic moment at the surface of magnetic clusters, while the Synchrotron radiation studies shows difference in spin and orbital moments at the surface of nano and bulk material.

In case of preparation of iron metal magnetic nanoparticles, many reducing agents such as ethylene glycol, poly-ethylene glycol and $NaBH_4$ have been used. However, storage of iron metal magnetic nanoparticles is one of challenges because always, it tries to oxidize. At

initial stage, surface oxidation occurs. It is like core@shell nanostructures. Surface canting structure occurs arising from iron oxide, which is antiferromagnetic. With time, whole nanoparticles become iron oxide, which is purely antiferromagnetic. In case of preparation of nickel nanoparticles, effect of surface canting is very less (almost negligible for particle size more than 100 nm). In case of metal oxide magnetic nanoparticles such as Fe_3O_4, $CoFe_2O_4$, and $NiFe_2O_4$, their saturation magnetization measured at 1 T is less than bulk value. Here surface defects in nanoparticles generate spin canting, which is one of reasons to reduce magnetization in addition to spin relaxation of single domain.

4.7 Functionalization of Magnetic Nanoparticles

The magnetic nanomaterials show higher surface area and moderate magnetic properties and thus they are used in many applications including higher adsorption efficiency, high toxic element removal from water, quick separation of adsorbent from liquid using external magnetic field (Pullar 2012; Kefeni et al. 2017a). For use of a specific purpose, a proper surface functionalization using capping agents is required. The functionalization with organic, inorganic or polymer functional group onto superparamagnetic nanoparticles can improve their functionality for various applications. Some of capping ligands for use of functionalization are citric acids, ascorbic acids, polyethylene glycol or diacids, chitosan, chitin, glucose, mannose, etc. Such surface ligands have different properties; and surface charges developed in nanoparticles are different from one capping ligand to another. Various synthesis routes such as hydrothermal method, electrospinning, sol–gel route, co-precipitation route, auto-

combustion route, reversed micelle formation, thermolysis, and evaporation method have been used for the formation of the controlled size and shape of ferrite nanoparticles. The cheapest and easiest method is the chemical co-precipitation route due to easy handle in aqueous medium in a beaker.

To get more stability of nanoparticles, core–shell nanostructures have been developed. SiO_2 coating over nanoparticles has been developed using tetraethyl orthosilicate (TEOS), APTMS molecules have been used to get NH_2 functional group. Such nanostructures are found to be improved for their bio-compatibility toward cells. From this NH_2 functional group, many important molecules can be linked such as Folic acid (targeting to a particular cancer cells), FITC (imaging, internalization), DAPI (internalization), drug molecules, DNA (repairing), antibody (targeting).

In some cases, different models such as core@shell, hollow, rotation/floating of magnetic nanoparticles inside hollows, dendrimers, composites/hybrids have been developed by many scientists till date. Coating of mesoporous substances including SiO_2 over magnetic nanoparticles has extended its applications in high drug delivery and control release of drug, removal of unwanted ions such as toxic ions, industrial applications, and energy storage.

Core–shell magnetic nanomaterials are functionalized with appropriate capping agents; and these are used in catalysis and biomedical fields. The shell coating onto the core material gives the particles disperse-ability and makes them chemically stable in a liquid solvent. The further functionalization is carried out onto the shell with various organic/ polymeric materials and allows a controlled release of drug delivery and hyperthermia applications. Magnetic nanoparticles of core shell structure exhibits

ordered core and disordered shell showing broken chemical bonds at the interfaces. The exchange bias (EB) properties are exhibited in such core shell magnetic materials (Ferromagnetic@Antiferromagnetic) when the magnetic coupling occurs at the interfaces. The exchange bias property of magnetic materials is useful to convert electromagnetic energy into heat in biomedical field such as hyperthermia application and in energy storage applications.

4.8 Characterization Techniques

4.8.1 Structural and Morphological Studies

The crystal structure of the prepared nanoparticles can be determined by using XRD (X-ray diffraction) technique. There are seven crystal systems:—Cubic, tetrahedral, hexagonal, monoclinic, orthorhombic, triclinic, and trigonal systems.

Till now XRD is an imperative experimental technique that has been used to discuss all the issues correlated to the crystal structure of solids, including its geometry and lattice constants, recognition of unknown materials, orientation of single crystals, polycrystals preferred orientation, defects presence in crystal structure, strain etc. In magnetic nanomaterials, neutron diffraction techniques can give information about crystal structure as well as magnetic structure as neutron has no charge. The neutron diffraction has advantage over X-ray diffraction in crystal structure determination of compounds having light atoms such as hydrogen (e.g. UH_3), different atomic isotopes, similar number of electrons in both negative and positive charge ions (e.g. K^+Cl^-) and in the studies of lattice vibrations (West 2007; Bacon 1966). UH_3 crystallizes in tetragonal $P4_2/mmc$ space group. Its crystal

structure can be identified by use of neutron diffraction, but could not be verified by XRD.

The Powder Diffractometer or Debey-Scherrer Diffractometer is commonly used to study the properties of the crystal structure of magnetic nanomaterials. For the determination of physical properties of the magnetic nanomaterials, the study of the crystal structure including the distribution of atoms is essential. The X-ray diffraction is very useful and nondestructive technique for the determination of lattice constant, crystallite/particle/grain size and strain. Rietveld refinement is used to refine the X-ray diffraction data and to determine the lattice constants, position of atom, occupancy and micro structural parameters such as crystallite size and strain of the crystals. To determine the morphology of small magnetic nanomaterials, electron microscopic techniques such as transmission electron microscope (TEM), Scanning electron microscope (SEM) and Atomic force microscope (AFM) are used (West 2007). Transmission electron microscope is referred due to its high resolution (better than 0.1 nm). In TEM, the electrons of higher energy > 100 keV are made to pass through a series of magnetic lenses and finally pass through sample loaded over a carbon coated copper grid. The positions of the atoms can be examined using TEM in which selected area electron diffraction (SAED) pattern is used to evaluate the interplanar spacing values. Using Fast Fourier Transformation (FFT), atomic positions can be determined.

To observe the modes of molecular vibration, rotational and other low-frequency modes of the nanomaterial, the Raman spectroscopy and FTIR spectroscopy are used (West 2007). Raman spectroscopy is on the basis of polarizability of molecules in the presence of a particular wavelength of light (laser light). The intensity vs. frequency shift plot is expressed. The frequency shift is the difference between the original frequency of light and Raman scattered light.

The frequency shift is known as the Raman shift. The monochromatic laser light in the visible or near infrared range interacts with molecular vibrations; excitation of phonons takes place in the material due to which the energy of scattered lights gets increased or decreased. This is an inelastic process. This shift in the energy gives the information about modes of vibration. IR spectroscopy is on the basis of absorption of light by dipole moment of molecules/ions through stretching and bending vibrations of molecules. The plot of intensity vs. wavenumber corresponding to frequency of vibration of molecule is expressed.

4.8.2 Techniques to Measure Magnetization of Ferrite Nanoparticles

4.8.2.1 Vibrating Sample Magnetometer (VSM)

For the magnetic measurement studies of magnetic nanoparticles, a vibrating sample magnetometer (VSM) is frequently used which works on Faraday's Law of Induction (Fig. 4.23) (Cullity et al. 2012). As per this law, varying magnetic field generates an electric field that gives the information about magnetic moment. The magnetic properties of the materials can be determined by vibrating a magnetic sample in VSM which creates an oscillatory magnetic field. In first step the magnetic field is applied which generates magnetism in the material. In VSM, electromagnet having magnetic field of 0 to 2.5 Tesla is generally used.

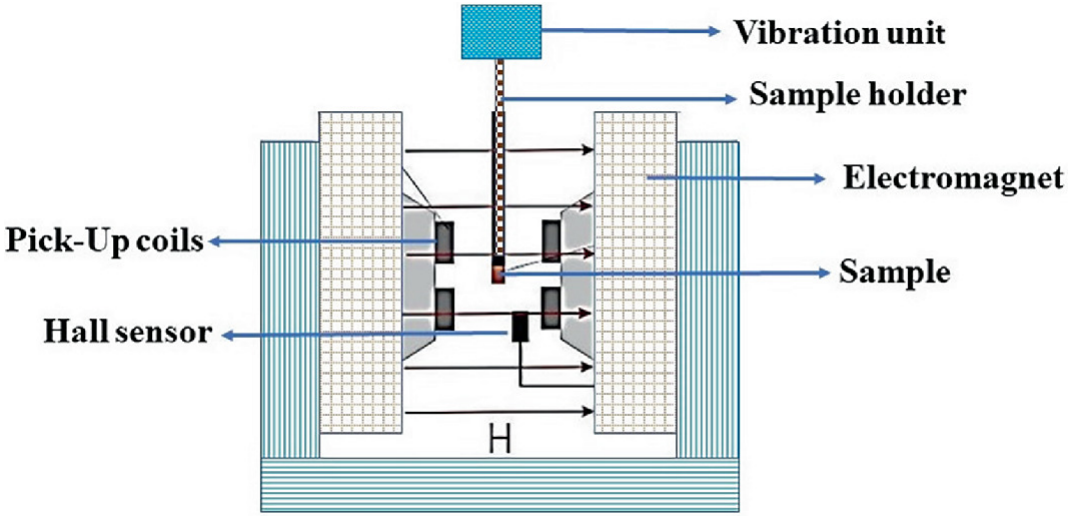

Fig. 4.23 Schematic representation of Vibrating Sample Magnetometer (VSM)

To operate VSM, first the sample to be studied is placed in a uniform magnetic field. When the magnetic field is applied to the material, the magnetic moments get align themselves in the direction of applied magnetic field and generates magnetism. The oscillating magnetic field as a function of time is generated with up and down movement of the sample and sensed by a set of pick-up coils. It is converted to electric current or moment (emu).

The VSM is used to study the magnetic behavior of the paramagnetic, diamagnetic, ferromagnetic, ferrimagnetic, superparamagnetic and other bulk and nanomaterials. A graph is plotted between the magnetization versus applied magnetic field of the material. The transition of the magnetic phase can be carried out by giving heating or cooling to the material during magnetic measurements. Some of VSM, temperature up to 900 °C can be used so that the Curie temperature (T_c) of ferromagnetic materials is measured.

4.8.2.2 Superconducting Quantum Interference Device (SQUID)

SQUID is superconducting Quantum Interference Device (Kittel et al. 1946). This device is used to measure small

magnetic field of the sample, voltage and current. Superconducting quantum interference device is widely used over vibrating sample magnetometer due to its higher sensitivity and higher resolution of the order of 10^{-8} emu. The smaller magnetic moments of the synthesized ferrites can be measured using this magnetometer. The working principle of SQUID is based on the tunneling of superconducting electrons known as the Cooper pairs through a thin insulating gap between two superconductors (Josephson junction). In SQUID, a superconducting loop is used with one or more Josephson junctions. A schematic diagram of Superconducting Quantum Interference Device is shown in Fig. 4.24. As shown in the figure, a DC super current I enters the SQUID device from the port C. The DC current then differentiated in two ports where the currents are I_1 and I_2. These currents pass through a thin insulating gap between two superconductors i.e. the two identical Josephson junctions. The currents I_1 and I_2 undergo a phase shift due to applied magnetic field, when they pass through the Josephson junctions P and Q and become I_1' and I_2' respectively. The super currents I_1' and I_2'interface at port D. In the absence of any applied magnetic field the phase shift and phase difference are measured to be zero. The resultant current is measured at the port D. This current oscillates between maxima (when the magnetic flux enhances by one quantum) and minima. Generally, the voltage is measured in place of current which oscillates with varying the magnetic field. SQUID is known as flux-to-voltage transducer that used to converts small change in magnetic flux to voltage. Due to high sensitivity to magnetic field SQUIDS are used in many fields like geology, medicine, engineering, etc. When the magnetic material is placed in the loop of a Josephson junction, an emf is induced in the loop. This results in induced current with a frequency estimated by the Josephson equations.

Using SQUID, the variation in currents or frequency can be detected to reduce the magnetic moment of the sample.

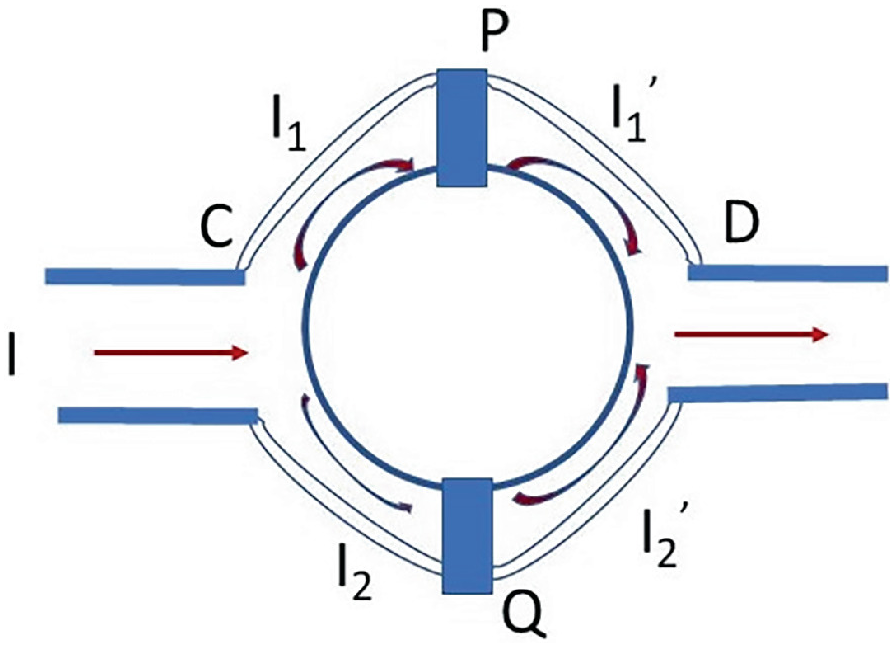

Fig. 4.24 Schematic representation of Superconducting Quantum Interference Device (SQUID)

4.9 Magnetic Measurement of Superparamagnetic Ferrite Nanoparticles

4.9.1 Field Cooled (FC) and Zero Field Cooled (ZFC) Measurement

The zero-field-cooled (*ZFC*) and the field-cooled (*FC*) measurements are used for the evaluation of blocking temperature in DC magnetic field (Fig. 4.25) (Joshi et al. 2021). For zero-field-cooled (*ZFC*) measurement, at the very beginning, the sample is cooled to lower temperature (say 5 K) and then temperature is increased with application of external small magnetic field (10–50 *Oe*) and as a result, the magnetic moments get oriented along the direction of magnetic field. As the temperature increases,

the thermal energy increases which results in alignment of magnetic moments along the direction of applied magnetic field. At $T < T_B$, the magnetic moments are blocked and system becomes ferromagnetic. The more and more magnetic moments get oriented along the direction of applied magnetic field as the temperature increases to its maximum blocking temperature. At the temperature higher than T_B, the increment of thermal energy, which overcome over the anisotropy energy of particles and results in random flipping of the magnetic moments due to which reduction in magnetization occurs. A graph plotted between the magnetization versus increment in the temperature of zero-field-cooled (*ZFC*) and the field-cooled (*FC*) measurement gives the value of blocking temperature (T_B). A peak observed in the curve of *ZFC* shows the value of T_B. A sharp peak observed for a narrow size distribution of nanoparticles gives the value of blocking temperature. In a broad size distribution of nanoparticles, a broadening in peak is observed and this maximum broad peak temperature is known as maximum temperature (T_m). In field-cooled (*FC*) measurements, the cooling of sample is carried out from higher temperature in presence of an external small magnetic field. When the temperature is larger than the blocking temperature, the high thermal energy causes the random alignment of the magnetic moments resulting in less magnetization. When the temperature is less than the blocking temperature the less thermal energy causes freezing of large number of magnetic moments along the applied magnetic field direction and results in the increased magnetization of nanoparticles at the lowest temperature. The shape of *ZFC* and *FC* curves gives qualitative data of the particle size distribution and interaction of the nanoparticles. Monodispersed and non-interacting nanoparticles show T_B at T_{irr}. i.e., both coincide. If there is an interaction among

the nanoparticles (magnetic dipolar interaction), $T_B < T_{irr}$ occurs. It is to noted that T_{irr} is a temperature at which ZFC and FC coincide. Thus, polydispersed nanoparticles exhibit T_B, which is much below T_{irr}. However, T_B will be average of all particles. For non-interacting magnetic nanoparticles, narrow curve/ peak is examined in ZFC curve. At lower temperature, the anisotropy energy barrier (KV) is more than thermal energy (k_BT).

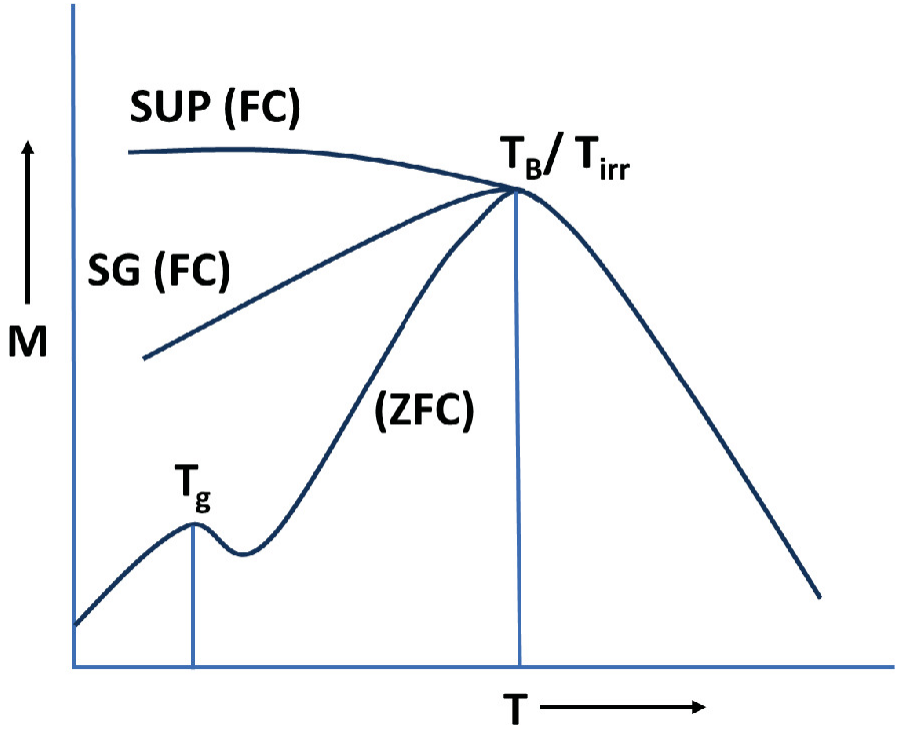

Fig. 4.25 Magnetization (M) versus Temperature (T) curve of superparamagnetic and spin glass ferrites

Above blocking temperature, the magnetic moments get freed from the direction of easy axes results in lower magnetization. The time between the flip of magnetic moments is called as Neel relaxation time and depends on temperature. The irreversibility arises in ZFC and FC curves because of blocking and unblocking of the magnetic moment of nanoparticles. When the FC curve is nearly become constant, it resembles the presence of magnetic interaction in the ensemble of nanoparticles. The average

blocking temperature T_B, is demonstrated by performing temperature dependence $dM\left(T\right)/dT$. It is reported that superparamagnetic behavior of the magnetic nanoparticles is exhibited above T_B below which the nanoparticle ensemble shows ferrimagnetic behavior with non- zero M_r and H_c. To determine the distribution of T_B denoted by $f(T_B)$ the magnetic moments are depending on the temperature.

$$f\left(T_B\right) = \frac{3k_B}{H\mu_S^2}\frac{d\left(M_{ZFC} - M_{FC}\right)}{dT} \qquad [44, 45]$$

The Curie temperature can be obtained by fitting the magnetization as a function of temperature using modified Bloch's law $M_s = M_0\left[1 - \left(\frac{T}{T_0}\right)^{\alpha}\right]$. When the size of the magnetic nanoparticles decreases below the critical dimension, the surface of particles gets covered with the non-magnetic layer of canted spins, known as a dead layer which results in decrease in M_s value. The canted spin layer thickness (t) can be evaluated by $M_S = M_b\left(1 - \frac{6t}{d_P}\right)$ (Ningombam et al. 2018; Sharma et al. 2018; Ojha and Kant 2021, 2022), where d_P is the average dimension of the nanoparticle and M_b is the saturation magnetization of the bulk magnetic material.

For the study of superparamagnetism of nanoparticles, the superparamagnetic moments per particle $(\mu_{SP}\left(\mu_B\right))$ at different temperature is essential. The determination of $\mu_{SP}\left(\mu_B\right)$ can be determined by the following relation:

$$\mu_{SP}\left(\mu_B\right) = \frac{3k_B}{M_s\mu_B}.\frac{d\left(1/\chi\right)}{dT} \qquad [44, 45],$$

where the values of M_s is measured at different temperatures and $\frac{d1/\chi}{dT}$ is the slope of an inverse of susceptibility at different temperature.

4.9.2 Spin Canting

The effect of strain is observed to affect the saturation magnetization (M_s) due to distributed cations at A and B sites. The redistribution of cations modifies the dominant super-exchange interaction that changes spin canted angle (Φ) between B site spins. The net magnetization of ferrites can be obtained using the relation $M = M_B cos\Phi$- M_A, where M_A and M_B are net magnetic moments at A and B site, respectively and Φ is the canted spins angle at B site which increases as Co^{2+} distributed from B to A site in $CoFe_2O_4$. The change in bond length and angle confirm existence of strain in the crystal and hence there are the dependence of the spin canting angle (Φ) on M_s on relative population of Co^{2+} at the A and B sites that result in strain in the crystal given by the $M_s = M_s^0 \cos(\gamma.\varepsilon)$, where γ is constant, ε is strain, and M_s^0 is saturation magnetization of bulk ferrite where no spin canting at B site is present (Ojha and Kant 2021, 2022, 2019; Ojha and Mohan Kant 2019).

4.9.3 Spin Glass Behavior

To study spin glass (SG) behavior of ferrite nanoparticles, low field ZFC and FC magnetization studies are performed (Nigam et al. 1983; Parisi 2006; https://en.wikipedia.org/wiki/Spin_glass; https://www.nobelprize.org/prizes/physics/2021/press-release/; Topkaya et al. 2012; Tiwari et al. 2023; Aslibeiki et al. 2010). In the graph of temperature dependence DC magnetization, a sharp cusp at lower temperature is observed which is known as the spin freezing temperature (T_f). The FC-ZFC difference observed at lower temperatures shows spin-glass or spin-glass-like nanomaterial. AC susceptibility measurements (χ) are needed to study the dynamics of freezing of the spin-glass systems in which the temperature associated with the maxima of χ' (real part) changes slowly with the measuring frequency. Spin-glass behavior of the spinel material is

characterized by the AC susceptibility and from which T_f is evaluated using the position of the cusp of the real part of AC susceptibility (χ'). In the real part of AC susceptibility (χ'), a small shifting of the peak position of χ' towards high temperature is generally observed for high driving frequency and the peak intensity is observed to increase for lower measuring frequencies. In χ'-T graph, the different measuring frequencies overlap for temperatures higher than the peak temperature. This behavior is reported in many spin-glass and disordered magnetic system. Whereas these type of shifting in frequencies is not observed in antiferromagnetic or ferromagnetic long-range-ordered system. This result implies a transition from paramagnetic phase (PM) to spin glass phase (SG). As compared to spin glass system, superparamagnetic system does not change much peak position with frequency. In general, spin glass in nanosized particles is observed in high concentrations or agglomerated particles in which surface spins can interact each other, whereas superparamagnetic behavior is observed in non-interacting nano-sized particles. Even, due to surface spin interaction, powder or agglomerated nanoparticles of antiferromagnetic NiO show the spin glass (Tiwari et al. 2005).

4.10 Applications of Ferrites

Among the all ferrites, the spinel ferrites (soft magnetic material) are of special interest due to its various applications from telecommunication, catalysts, magnetic core, water purifier, drug delivery, and radar systems due to its phenomenal properties, as moderate saturation magnetization, high electrical resistivity, low electrical losses, and excellent chemical stability to the biomedical field (Kefeni et al. 2017b; Amiri et al. 2019). Spinel ferrites are used for Alternating Current (AC) and Direct Current

(DC) purpose also where, a high permeability is necessary for the two of them. In DC applications, for the flux is channeled inside the ferrite material for the shielding purpose. In DC application, permeability is the primary consideration for the selected ferrite material and the ferrite is selected to generate a magnetic field.

Ferrites also have applications in various electronic devices as home appliances, military communication, equipment and data processing devices. The magnetic ferrites with higher saturation magnetization values, moderate electrical properties and high resistivity are used as core material for inductors and transformers. Catalysis magnetic separation of ferrite catalysts is dominant over filtration and centrifugation as they have high catalytic efficiency and easy separation for expensive reactants. Generally, magnetite and hematite are used as catalysts in ferrites. Ferrites are also applicable in medicinal field as magnetic resonance imaging (MRI), magnetic extraction, hyperthermia and targeted drug delivery due to their phenomenal magnetic properties.

The superparamagnetic ferrite nanomaterials are also useful as sealants, lubricants and coolants which can be used in medicinal purpose in MRI, hyperthermia, targeted drug delivery, biosensors, gene transfer, cell separation and magnetically mediated separation of bio-molecules (Ningthoujam et al. 2012; Rajan et al. 2022; Srivastava et al. 2023; Joshi et al. 2019). Ferrites are also useful in water purification and toxic metal ion removal applications from waste water. The hierarchical porous structure, narrow sized distribution, large surface to volume ratio and high magnetization properties are needed for the ferrite nanomaterials to be used for adsorption of pollutants, toxic metal ions from waste water. The ferrite nanoparticles exhibiting superparamagnetic behavior at room temperature which makes them useful for biomedical applications after suitable coating and subsequent

functionalization. In this context, the encapsulation of synthesized magnetic nanoparticles within a biocompatible polymer is essential during or after the preparation process to prevent agglomeration.

4.11 Conclusions

Ferrites are compounds of ferric oxide and metal oxides. They are classified into two: soft and hard ferrites. On basis of crystal structures, they are further classified as spinel, hexaferrites, garnets and orthoferrites. Spinel crystal structure can have 3 distinct structures: normal, inverse and mixed spinel structures. Fe^{3+} ions can occupy different sites such as tetrahedral, octahedral and trigonal bipyramid. With decrease of particle size, system can change from ferromagnetic to superparamagnetic phase. The transition is known as the blocking temperature (T_b). This T_b can be identified from the zero-field cooled curve at low magnetic field (10–50 Oe). The synthesis of spinel ferries can be prepared by many techniques and their characterization techniques namely VSM and SQUID are mentioned. The spin glass arose from normal dilute magnetic system and magnetic nanoparticles are provided. Spin canting from surface spin as well as non-stoichiometry in B-site of spinel structure are explained.

Acknowledgements

Vibha Ojha thanks Bhabha Atomic Research Centre, Mumbai for providing “Research Associate Fellowship”.

References

Akhtar, M.N., Saleem, M., Khan, M.A.: Al doped spinel and garnet nanostructured ferrites for microwave frequency C and X- band applications. J. Phys. Chem. Solids **123**, 260–265 (2018)
[Crossref]

Alzoubi, G.M., Alsmadi, A.M.: Alna'washi, coexistence of super-paramagnetism and spin-glass like behavior in zinc-substituted cobalt ferrite nanoparticles. Appl. Phys. A **126**, 512 (2020).https://doi.org/10.1007/s00339-020-03655-7

Amiri, M., Niasari, M.S., Akbari, A.: Magnetic nanocarriers: evolution of spinel ferrites for medical applications. Adv. Coll. Interface. Sci. **265**, 29–44 (2019) [Crossref]

Aslibeiki, B., Kameli, P., Salamati, H., Eshraghi, M., Tahmasebi, T.: Superspin glass state in $MnFe_2O_4$ nanoparticles. J. Magn. Magn. Mater. **322**, 2929–2934 (2010)
[Crossref]

Bacon, E.: Neutron diffraction and its applications in inorganic chemistry. Editor(s): H.J. Emeléus, A.G. Sharpe in Advances in Inorganic Chemistry and Radiochemistry. Academic Press, Volume 8, 225–256 (1966)

Bersani, D., Lottici, P.P., Ding, X.Z.: Phonon confinement effects in the Raman scattering by TiO_2 nanocrystals. Appl. Phys. Lett. **72**, 73–75 (1998)

Bharathi, K.K., Tackett, R.J., Botez, C.E., Ramana, C.V.: Coexistence of spin glass behavior and long-range ferrimagnetic ordering in La- and Dy-doped Co ferrite. J. Appl. Phys. **109**, 2012–2015 (2011)

Bhattacharya, S., Roychowdhury, A., Tiwari, V., Prasad, A.I., Ningthoujam, R.S., Patel, A.B., Das, D., Nayar, S.: Effect of biomimetic templates on the magneto-structural properties of Fe_3O_4 nanoparticles. RSC Adv. **5**, 13777–13786 (2015)
[Crossref]

Bi, H., Li, S., Zhang, Y., Du, Y.: Ferromagnetic-like behavior of ultrafine NiO nanocrystallites. J. Magn. Magn. Mater. **277**, 363–367 (2004)
[Crossref]

Birajdar, A.A., Shirsath, S.E., Kadam, R.H., Patange, S.M., Mane, D.R., Shitre, A.R.: Rietveld structure refinement and cation distribution of substituted nanocrystalline Ni–Zn ferrites. ISRN Ceram **2012**, 1–5 (2012)
[Crossref]

Biswas, B., Michel, V.F., Fjellvåg, Ø.S., Bimashofer, G., Döbeli, M., Jambor, M., Keller, L., Müller, E., Ukleev, V., Pomjakushina, E.V., Singh, D., Stuhr, U., Vaz, C.A.F., Lippert, T., Schneider, C.W.: Role of Dy on the magnetic properties of orthorhombic $DyFeO_3$. Phys. Rev. Mater. **6**, 074401 (2022)

Burton, A.W., Ong, K., Rea, T., Chan, I.Y.: On the estimation of average crystallite size of zeolites from the Scherrer equation: a critical evaluation of its application to zeolites with one-dimensional pore systems. Microporous Mesoporous Mater. **117**, 75–90 (2009)

[Crossref]

Caneschi, A., Gatteschi, D., Sessoli, R., Barra, A.L., Brunel, L.C., Guillot, M.: Alternating current susceptibility, high field magnetization, and millimeter band EPR evidence for a ground S = 10 state in $[Mn_{12}O_{12}(CH_3COO)_{16}(H_2O)_4].2CH_3COOH.4H_2O$. J. Am. Chem. Soc. **113**, 5873–587 (1991)

Céspedes, E., Byrne, J.M., Farrow, N., Moise, S., Coker, V.S., Bencsik, M., Lloyd, J.R., Telling, N.D.: Bacterially synthesized ferrite nanoparticles for magnetic hyperthermia applications. Nanoscale **6**, 12958–12970 (2014) [Crossref][PubMed]

Chen, W., Zhu, W., Tan, O.K., Chen, X.F.: Frequency and temperature dependent impedance spectroscopy of cobalt ferrite composite thick films. J. Appl. Phys. **108**, 034101 (2010)

Chinnasamy, C., Jeyadevan, B., Shinoda, K., Tohji, K., Djayaprawira, D., Takahashi, M., Joseyphus, R.J., Narayanasamy, A.: Unusually high coercivity and critical single-domain size of nearly monodispersed $CoFe_2O_4$ nanoparticles. Appl. Phys. Lett. **83**, 2862–2864 (2003) [Crossref]

Chinnasamy, C.N., Narayanasamy, A., Ponpandian, N., Chattopadhyay, K., Shinoda, K., Jeyadevan, B., Tohji, K., Nakatsuka, K., Furubayashi, T. Nakatani, I.: Mixed spinel structure in nanocrystalline $NiFe_2O_4$. Phys. Rev. B Condens. Matter Mater. Phys. **63**, 2–7 (2001)

Cullity, B.D., Graham, C.D.: Introduction to Magnetic Materials. Wiley (2012)

Dalal, M., Greneche, J.M., Satpati, B., Ghzaiel, T.B., Mazaleyrat, F., Ningthoujam, R.S., Chakrabarti, P.K.: Microwave absorption and the magnetic hyperthermia applications of $Li_{0.3}Zn_{0.3}Co_{0.1}Fe_{2.3}O_4$ nanoparticles in multiwalled carbon nanotube matrix. ACS Appl. Mater. Interfaces **9**, 40831–40845 (2017)

Dalal, M., Das, A., Das, D., Ningthoujam, R.S., Chakrabarti, P.K.: Studies of magnetic, Mössbauer spectroscopy, microwave absorption and hyperthermia behavior of Ni–Zn–Co-ferrite nanoparticles encapsulated in multi-walled carbon nanotubes. J. Magn. Magn. Mater. **460**, 12–27 (2018)

Dmowski, W., Egami, T., Swider-Lyons, K.E., Love, C.T., Rolison, D.R.: Local atomic structure and conduction mechanism of nanocrystalline hydrous RuO_2 from X-ray scattering. J. Phys. Chem. B. **106**, 12677–12683 (2002)

Dubey, R.S., Krishnamurthy, K.V., Singh, S.: Experimental studies of TiO_2 nanoparticles synthesized by sol-gel and solvothermal routes for DSSCs

application. Results Phys. **14**, 102390 (2019)

Fiorillo, A.F., Appino, C., Pasquale, M.: Hysteresis in Magnetic Materials. Elsevier Inc. pp 1–190 (2006)

Fu, Y.P., Hu, S.H.: Electrical and magnetic properties of magnesium-substituted lithium ferrite. Ceram. Int. **36**, 1311–1317 (2010)

Gajbhiye, N.S., Ningthoujam, R.S., Weissmuller, J.: Synthesis and magnetic studies of nanocrystalline nickel nitride material. Phys. Stat. Sol. (a) **189**, 691 (2002)

Gajbhiye, N.S., Ningthoujam, R.S., Weissmuller, J.: Mössbauer study of nanocrystalline ε-$Fe_{3-x}Co_xN$ system. Hyperfine Interactions 156, 51 (2004)

Gajbhiye, N.S., Bhattacharyya, S., Balaji, G., Ningthoujam, R.S., Das, R.K., Basak, S., Weissmuller, J.: Mössbauer and magnetic studies of MFe_2O_4 (M = Co, Ni). Hyperfine Interact. **165**, 153 (2005)

Gajbhiye, N.S., Sharma, S., Ningthoujam, R.S.: Synthesis of self-assembled monodisperse 3 nm FePd nanoparticles: phase transition, magnetic study and surface effect. J. Appl. Phys. **104**, 123906 (2008)

Gajbhiye, N.S., Sharma, S., Nigam, A.K., Ningthoujam, R.S.: Tuning of single to multidomain behavior for monodispersed ferromagnetic cobalt nanoparticles. Chem. Phys. Lett. **466**, 181 (2008)

Ghosh, R., Pradhan, L., Devi, Y.P., Meena, S.S., Tewari, R., Kumar, A., Sharma, S., Gajbhiye, N.S., Vatsa, R.K., Pandey, B.N., Ningthoujam, R.S.: Induction heating studies of Fe_3O_4 magnetic nanoparticles capped with oleic acid and polyethylene glycol for hyperthermia. J. Mater. Chem. **21**, 13388 (2011)

Gignoux, D., Schlenker, M., Lacheisserie, E.T.: Magnetism Materials and Applications, 2005th edn. Springer (2006)

Gubin, S.P., Koksharov, Y.A., Khomutov, G.B., Yurkov, G.Y.: Magnetic nanoparticles: preparation, structure and properties. Usp. Khim. **74**, 539–574 (2005)

Gul, I.H., Maqsood, A.: Influence of Zn-Zr ions on physical and magnetic properties of co-precipitated cobalt ferrite nanoparticles. J. Magn. Magn. Mater. **316**, 13–18 (2007)

Guimaraes, A.P.: Principles of Nanomagnetism. Springer, Berlin, Heidelberg (2009)

https://en.wikipedia.org/wiki/Spin_glass

https://www.nobelprize.org/prizes/physics/2021/press-release/

Idrees, M., Nadeem, M., Hassan, M.M.: Investigation of conduction and relaxation phenomena in $LaFe_{0.9}Ni_{0.1}O_3$ by impedance spectroscopy. J. Phys. D. Appl. Phys. **43**, 155401 (2010)

Ing., D., Heck, C.: Magnetic Materials and their Applications. London Butterworth and Co. Publication (1974)

Investigations of properties of spinel ferrite compound doped with rare earth ionsquot (2012). http://shodhganga.inflibnet.ac.in:8080/jspui/bitstream/10603/13720/7/07_chapter 1. 1–6

Joshi, R., Perala, R.S., Srivastava, M., Singh, B.P., Ningthoujam, R.S.: Heat generation from magnetic fluids under alternating current magnetic field or induction coil for hyperthermia-based cancer therapy: basic principle. J. Radiat. Cancer Res **10**, 156–164 (2019)

Joshi, R., Singh, B.P., Ningthoujam, R.S.: Confirmation of highly stable 10 nm sized Fe_3O_4 nanoparticles formation at room temperature and understanding of heat-generation under AC magnetic fields for potential application in hyperthermia. AIP Adv. **10**, 105033 (2020)

Joshi, R., Singh, B.P., Prajapat, C.L., Kashyap, Y., Nayak, C., Bhattacharyya, D., Ningthoujam, R.S.: Insights into the structural and microscopic origin of magnetic properties of the γ-Fe_2O_3@Mn_xO_y nanostructure. J. Phys. Chem. C **125**, 17971 (2021)

Kefeni, K.K., Msagati, T.A.M., Mamba, B.B.: Ferrite nanoparticles: Synthesis, characterisation and applications in electronic device. Mater. Sci. Eng., B **215**, 37–55 (2017a)
[Crossref]

Kefeni, K.K., Mamba, B.B., Msagati, T.A.M.: Application of spinel ferrite nanoparticles in water and wastewater treatment: a review. Sep. Purif. Technol. **188**, 399–422 (2017b)
[Crossref]

Khorsand Zak, A., Abd. Majid, W.H., Abrishami, M.E., Yousefi, R.: X-ray analysis of ZnO nanoparticles by Williamson-Hall and size-strain plot methods. Solid State Sci. **13**, 251–256 (2011)

Khot, V.M., Salunkhe, A.B., Thorat, N.D., Ningthoujam, R.S., Pawar, S.H.: Induction heating studies of dextran coated $MgFe_2O_4$ nanoparticles for magnetic hyperthermia. Dalton Trans. **42**, 1249–1258 (2013)
[Crossref][PubMed]

Kim, Y.I., Kim, D., Lee, C.S.: Synthesis and characterization of $CoFe_2O_4$ magnetic nanoparticles prepared by temperature-controlled coprecipitation

method. Phys. B Condens. Matter. **337**, 42–51 (2003)

Kittel, C.: Theory of the structure of ferromagnetic domains in films and small particles. Phys. Rev. **70**, 965–971 (1946)

Kumar, G., Kotnala, R.K., Shah, J., Kumar, V., Kumar, A., Dhiman, P., Singh, M.: Cation distribution: a key to ascertain the magnetic interactions in a cobalt substituted Mg–Mn nanoferrite matrix. Phys. Chem. Chem. Phys. **19**, 16669–16680 (2017)

Kumari, N., Kour, S., Singh, G., Sharma, R.K.: A brief review on synthesis, properties and applications of ferrites. AIP Conf. Proc. **2220**, 020164 (2020)

Lamouri, R., Mounkachi, O., Salmani, E., Hamedoun, M., Benyoussef, A., Ez-Zahraouy, H.: Size effect on the magnetic properties of $CoFe_2O_4$ nanoparticles: a Monte Carlo study. Ceramics Int. **46,** 8092–8096 (2020)

Laokul, P., Arthan, S., Maensiri, S., Swatsitang, E.: Magnetic and optical properties of $CoFe_2O_4$ nanoparticles synthesized by reverse micelle Microemulsion method. J. Supercond. Nov. Magn. **28**, 2483–2489 (2015)

Lin, Q., Yang, X., Lin, J., Guo, Z., He, Y.: The structure and magnetic properties of magnesium-substituted $LaFeO_3$ perovskite negative electrode material by citrate sol-gel. Int. J. Hydrogen Energy **43**, 12720–12729 (2018)
[Crossref]

Majetich, S.A., Wen, T., Mefford, O.T.: Magnetic nanoparticles. MRS Bull. **38**, 899–903 (2013)
[Crossref]

Mallick, A., Dey, C.C., Sadhukhan, S., Das, S., Ningthoujam, R.S., Greneche, J.-M., Chakrabarti, P.K.: Microwave absorption and hyperthermia properties of titanium dioxide–nickel zinc copper ferrite nanocomposite. J. Magn. Magn. Mater. **587**, 171373 (2023)

Mathew, D.S., Juang, R.S.: An overview of the structure and magnetism of spinel ferrite nanoparticles and their synthesis in microemulsions. Chem. Eng. J. **129**, 51–65 (2007)

Mallmann, E.J.J., Sombra, A.S.B., Goes, J.C., Fechine, P.B.A.: Antennas, ferrites, magnetic ceramics, yttrium iron garnet. Solid State Phenom. **202**, 65–96 (2013)
[Crossref]

Maria, A.G., SolerFanyao, Q.: Raman Spectroscopy of Iron Oxide Nanoparticles. Springer Materials (2012)

Melikhov, Y., Snyder, J.E., Jiles, D.C., Ring, A., Paulsen, J., Lo, C.C., Dennis, K.W.: Temperature dependence of magnetic anisotropy in Mn-substituted cobalt ferrite. J. Appl. Phys. **99**, 08R102 (2006)
[Crossref]

Mody, V.V., Singh, A., Wesley, B.: Basics of magnetic nanoparticles for their application in the field of magnetic fluid hyperthermia. Europ. J. Nanomed. **5**, 11–21 (2013)
[Crossref]

Monalisa, S., Sharma, H.K., Satyapal, R.K.: Singh, correlation between lattice strain and magnetic properties enhancement of nanocrystalline cobalt ferrite with controlled annealing. J. Mater. Sci. Mater. Electron. **32**, 23843–23853 (2021)
[Crossref]

Nakanishi, R., Satoh, J., Katoh, K., Zhang, H., Breedlove, B.K., Nishijima, M., Nakanishi, Y., Omachi, H., Shinohara, H., Yamashita, M.: $DySc_2N$@C80 single-Molecule magnetic Metallofullerene encapsulated in a single-walled carbon nanotube. J. Am. Chem. Soc. **140**, 35 (2018)

Narayanan, V.K.S., Gajbhiye, N.S., Bahadur, D.: Characterization of dysprosium and samarium iron garnets synthesized by the citrate gel process. J. Mater. Sci. Lett. **6**, 281–284 (1987)
[Crossref]

Nigam, A.K., Majumdar, A.K.: Magnetoresistance in canonical spin-glasses. Phys. Rev. B **27**, 495 (1983)

Nikam, D.S., Jadhav, S.V., Khot, V.M., Bohara, R.A., Hong, C.K., Mali, S.S., Pawar, S.H.: Cation distribution, structural, morphological and magnetic properties of $Co_{1-x}Zn_xFe_2O_4$ (x = 0–1) nanoparticles. RSC Adv. **5**, 2338–2345 (2015)
[Crossref]

Nikmanesh, H., Kameli, P., Asgarian, S.M., Karimi, S., Moradi, M., Kargar, Z., Ventura, J., Bordalo, B., Salamati, H.: Positron annihilation lifetime, cation distribution and magnetic features of $Ni_{1-x}Zn_xFe_{2-x}Co_xO_4$ ferrite nanoparticles. RSC Adv. **7**, 22320 (2017)

Ningombam, G.S., Ningthoujam, R.S., Kalkura, S.N., Singh, N.R.: Induction heating efficiency of water dispersible $Mn_{0.5}Fe_{2.5}O_4$@YVO_4:Eu^{3+} magnetic-luminescent nanocomposites in acceptable AC magnetic field: haemocompatibility and cytotoxicity studies. J. Phys. Chem. B **122**, 6862–6871 (2018)

Ningthoujam, R.S., Joshi, R.: Synthesis and applications of borides, carbides, nitrides and phosphides. Edited by A.K. Tyagi and R.S. Ningthoujam; Publisher: Springer Nature, Singapore. Chapter 9, 307–366 in Handbook on Synthesis Strategies for Advanced Material: Volume-III: Materials specific synthesis strategies (2021)

Ningthoujam, R.S., Umare, S.S., Sharma, S.J., Shukla, R., Kurian, S., Vatsa, R.K., Tyagi, A.K., Tewari, R., Dey, G.K., Gajbhiye, N.S.: Magnetic and Mössbauer studies on nanocrystalline $Co_{1-x}Li_xFe_2O_4$ (x = 0, 0.2). Hyperfine Interact. **184**, 227 (2008)

Ningthoujam, R.S., Shukla, R., Vatsa, R.K., Duppel, V., Kienle, L., Tyagi, A.K.: Gd_2O_3:Eu^{3+} particles prepared by glycine-nitrate combustion: Phase, concentration, annealing, and luminescence studies. J. Appl. Phys. **105**, 084304 (2009)

Ningthoujam, R.S., Vatsa, R.K., Kumar, A., Pandey, B.N.: Functionalized magnetic nanoparticles: concepts, synthesis and application in cancer hyperthermia. Edited by S. Banerjee and A.K. Tyagi in Functional Materials Preparation, Processing and Applications. Publisher: Elsevier Inc., USA. Chapter 6, 229–260 (2012)

Ningthoujam, R.S., Gajbhiye, N.S.: Synthesis, electron transport properties of transition metal nitrides and applications. Prog. Mater Sci. **50**, 50–154 (2015) [Crossref]

Nisticò, R., Cesano, F., Garello, F.: Magnetic materials and systems: domain structure visualization and other characterization techniques for the application in the materials science and biomedicine. Inorganics **8**(1) 1–59 (2020)

Nunes, A.C., Yang, L.: Calculated ferrite nanocrystal relaxation and its magnetic implications. Surf. Sci. **399**, 225–233 (1998)

Ojha, V.H., Kant, K.M.: Investigation of structural and magnetic properties of strained $CoFe_2O_4$ nanoparticles. J. Phys. Chem. Solids **148**, 109655 (2021)

Ojha, V.H., Kant, K.M.: Strained $CoFe_2O_4$—amorphous SiO_2 nanocomposites: Evaluation of structural and magnetic properties. J. Magn. Magnet. Mater. **544**, 168448 (2022)

Ojha, V.H., Mohan Kant, K.: Structural and magnetic properties of single domain $CoFe_2O_4$ magnetic nanoparticles dispersed in SiO_2 matrix. Mater. Res. Express **6**, 105087 (2019)

Ojha, V.H., Kant, K.M.: Temperature dependent magnetic properties of superparamagnetic $CoFe_2O_4$nanoparticles. Physica B **567**, 87–92 (2019) [Crossref]

Pachpinde, A.M., Langade, M.M., Lohar, K.S., Patange, S.M., Shirsath, S.E.: Impact of larger rare earth Pr^{3+} ions on the physical properties of chemically derived $Pr_xCoFe_{2-x}O_4$ nanoparticles. Chem. Phys. **429**, 20–26 (2014)

Parisi, G.: Spin glasses and fragile glasses: statics, dynamics, and complexity. PNAS **103**, 7948–7955 (2006) [Crossref][PubMed][PubMedCentral]

Pavarini, E., Yamasaki, A., Nuss, J., Andersen, O.K.: How chemistry controls electron localization in 3d1 perovskites: a Wannier-function study. New J. Phys. **7**, 188 (2005)

Pullar, R.C.: Hexagonal ferrites: a review of the synthesis, properties and applications of hexaferrite ceramics. Prog. Mater Sci. **57**, 1191–1334 (2012) [Crossref]

Rodr´ıguezTorres, C.E., Pasquevich, G.A., Mendoza Z´elis, P., Golmar, F., Heluani, S.P., Nayak, S.K., Adeagbo, W.A., Hergert, W., Hoffmann, M., Ernst, A., Esquinazi, P., Stewart. S.J.: Oxygen-vacancy-induced local ferromagnetism as a driving mechanism in enhancing the magnetic response of ferrites. Phys. Rev. B **89**, 104411 (2014)

Rajan, A., Chandunika, R.K., Raju, F., Joshi, R., Sahu, N.K., Ningthoujam, R.S.: Synthesis and processing of magnetic based nanomaterials for biomedical applications. Edited by A. K. Tyagi and R. S. Ningthoujam. Publisher: Springer Nature, Singapore. Chapter 16, pp. 659–714 in Handbook on Synthesis Strategies for Advanced Material: Volume-II: Processing and functionalization of materials (2022)

Ren, P., Guan, J.G., Cheng, X.D.: Influence of heat treatment conditions on the structure and magnetic properties of barium ferrite $BaFe_{12}O_{19}$ hollow microspheres of low density. Mater. Chem. Phys. **98**, 90–94 (2006)

Sessoli, R., Tsai, H.L., Schake, A.R., Wang, S., Vincent, J.B., Folting, K., Gatteschi, D., Christou, G., Hendrickson, D.N.: High-spin molecules: $[Mn_{12}O_{12}(O_2CR)_{16}(H_2O)_4]$. J. Am. Chem. Soc. **115**, 5, 1804–1816 (1993)

Sharma, R., Singhal, S.: Structural, magnetic and electrical properties of zinc doped nickel ferrite and their application in photo catalytic degradation of methylene blue. Phys. B Condens. Matter. **414**, 83–90 (2013)

Sharma, S., Gajbhiye, N.S., Ningthoujam, R.S.: Effect of annealing on magnetic properties of FePd and FePdPt nanoparticles. AIP Conf. Proc. **1313**, 125 (2010)

Sharma, S., Ningthoujam, R.S., Gajbhiye, N.S.: Spin-glass-like behavior of surfactant capped $Co_{50}Ni_{50}$ nanoparticles. Chem. Phys. Lett. **558**, 48–52 (2013)

Sharma, K.S., Ningthoujam, R.S., Dubey, A.K., Chattopadhyay, A. Phapale, S., Juluri, R.R., Mukherjee, S., Tewari, R., Shetake, N.G., Pandey, B.N., Vatsa, R.K.: Synthesis and characterization of monodispersed water dispersible Fe_3O_4 nanoparticles and in vitro studies on human breast carcinoma cell line under hyperthermia condition. Scientific Reports **8**, 14766 (2018)

Shukla, R., Ningthoujam, R.S., Umare, S.S., Sharma, S.J., Kurian, S., Vatsa, R.K., Tyagi, A.K., Gajbhiye, N.S.: Decrease of superparamagnetic fraction at room temperature in ultrafine $CoFe_2O_4$ particles by Ag doping. Hyperfine Interact. **184**, 217 (2008)

Singh, A.K., Zaidi, M.G.H., Sah, P.L., Saxena, R.: A review on classification of various ferrite particles on the basis of crystal structure. European J. Adv. Eng. Technol. **5**(5), 350–435 (2018)

Sivakumar, N., Narayanasamy, A., Ponpandian, N., Govindaraj, G.: Grain size effect on the dielectric behavior of nanostructured $Ni_{0.5}Zn_{0.5}Fe_2O_4$. J. Appl. Phys. **101,** 0–6 (2007)

Sivakumar, N., Narayanasamy, A., Jeyadevan, B., Joseyphus, R.J., Venkateswaran, C.: Dielectric relaxation behaviour of nanostructured Mn-Zn ferrite. J. Phys. D. Appl. Phys. **41**, 245001 (2008)

Soliman, S., Elfalaky, A., Fecher, G.H., Felser, C.: Electronic structure calculations for $ZnFe_2O_4$. Phys. Rev. B Condens. Matter Mater. Phys. **83**, 2–7 (2011)

Soni, A.K., Joshi, R., Singh, B.P., Naveen Kumar, N., Ningthoujam, R.S.: Near-infrared- and magnetic-field-responsive $NaYF_4$:Er^{3+}/Yb^{3+}@SiO_2@AuNP@Fe_3O_4 nanocomposites for hyperthermia applications induced by fluorescence resonance energy transfer and surface plasmon absorption. ACS Appl. Nano Mater. **2**, 7350−7361 (2019)

Soni, A.K., Joshi, R., Ningthoujam, R.S.: Hot injection method for nanoparticle synthesis: basic concepts, examples and applications. Edited by A.K. Tyagi and R.S. Ningthoujam; Publisher: Springer Nature, Singapore. Chapter 13, pp. 383–434 in Handbook on Synthesis Strategies for Advanced Material: Volume-I: Techniques and fundamentals (2021)

Srivastava, M., Joshi, R., Singh, B.P., Ningthoujam, R.S.: Advances on magnetic nanoparticles based cancer therapy through hyperthermia: Basic understanding and history. Edited by P. A. Hassan, B.

Balakrishnan and A.K. Tyagi in Engineered Biomaterials: Progress and Prospects. Publisher: World Scientific Publishing Co Pvt Ltd, Singapore (2023)

Stahl, B., Gajbhiye, N.S., Wilde, G., Kramer, D., Ellrich, J., Ghafari, M., Hahn, H., Gleiter, H., Weißmüller, J., Würschum, R., Schlossmacher, P.: Electronic and magnetic properties of monodispersed FePt nanoparticles. Adv. Mater. **14**, 24–27 (2002)

Straumal, B.B., Protasova, S.G., Mazilkin, A.A., Goering, E., Schütz, G., Straumal, P.B., Baretzky, B.: Ferromagnetic behaviour of ZnO: the role of grain boundaries. Beilstein J. Nanotechnol. **7**, 1936–1947 (2016)
[Crossref][PubMed][PubMedCentral]

Sun, S., Murray, C.B., Weller, D., Folks, L., Moser, A.: Monodisperse FePt nanoparticles and ferromagnetic FePt nanocrystal superlattices. Science **287**, 1989–1992 (2000)
[Crossref][PubMed]

Sun, S.: Recent advances in chemical synthesis, self-assembly, and applications of FePt nanoparticles. Adv. Mater. **18**, 393–403 (2006)

Sundaresan, A., Rao, C.N.R.: Ferromagnetism as a universal feature of inorganic nanoparticles. Nano Today **4**, 96–106 (2009)
[Crossref]

Szotek, Z., Temmerman, W.M., Ködderitzsch, D., Svane, A., Petit, L., Winter, H.: Electronic structures of normal and inverse spinel ferrites from first principles. Phys. Rev. B Condens. Matter Mater. Phys. **74**, 1–12 (2006)

Tiwari, S.D., Rajeev, K.P.: Signatures of spin-glass freezing in NiO nanoparticles. Phys. Rev. B **72**, 104433 (2005)

Tiwari, S., Lal, G., Bhoi, H., Punia, K., Meena, S.S., Kumar, S.: Coexistence of superparamagnetism and superspin glass in non-stoichiometric $Zn_{0.5}Ca_{0.5}Fe_2O_4$ nanoferrite. J. Magn. Magnet. Mater. **570**, 170466 (2023)

Toksha, B.G., Shirsath, S.E., Mane, M.L., Patange, S.M., Jadhav, S.S., Jadhav, K.M.: Autocombustion high-temperature synthesis, structural , and magnetic properties of $CoCr_x$ Fe $_{2-x}O_4$ (x= 0 to 1). J. Phys. Chem. C. **115**, 20905–20912 (2011)

Tokunaga, Y., Furukawa, N., Sakai, H., Taguchi, Y., Arima, T.H., Tokura, Y.: Composite domain walls in a multiferroic perovskite ferrite. Nature Mater **8**, 558–562 (2009)
[Crossref]

Topkaya, R., Akman, O., Kazan, S., Aktaş¸ B., Durmus, Z., Baykal, A.: Surface spin disorder and spin-glass-like behaviour in manganese-substituted cobalt

ferrite nanoparticles. J. Nanopart. Res. **14**, 1156 (2012)

Umare, S.S., Ningthoujam, R.S., Sharma, S.J. Shrivastava, S., Kurian, S., Gajbhiye, N.S.: Mössbauer and magnetic studies on nanocrystalline $NiFe_2O_4$ particles prepared by ethylene glycol route. Hyperfine Interact. **184**, 235 (2008)

Umare, S.S., Shambharkar, B.H., Ningthoujam, R.S.: Synthesis and characterization of polyaniline–Fe_3O_4 nanocomposite: electrical conductivity, magnetic, electrochemical studies. Synthetic Metals **160**, 1815 (2010)

Valenzuela, R.: Novel Applications of Ferrites. Hindawi Publishing Corporation Physics Research International, Volume 2012, Article ID 591839, 9 p. https://doi.org/10.1155/2012/591839

Valenzuela, R.: Magnetic ceramics. J. Am. Chem. Soc. **118**, 5–6 (1996)

Vedrtnam, A., Kalauni, K., Dubey, S., Kumar, A.: A comprehensive study on structure, properties, synthesis and characterization of ferrites. AIMS Mater. Sci. **7**(6), 800–835 (2020)
[Crossref]

Vijayalakshmi, A., Gajbhiye, N.S.: Magnetic properties of single-domain $SrFe_{12}O_{19}$ particles synthesized by citrate precursor technique. J. Appl. Phys. **83**, 400 (1998)

Wan, Y., Xue, M., Cheng, X., Peng, Y., Li, P., Yang, S., Liu, M., Kan, E., Yang, J., Dai, L.: Surface-sensitive magnetic characterization technique for ultrathin ferromagnetic film with perpendicular magnetic anisotropy. AIP Adv. **10**(6), 065019 (2020)

Wang, W., Sun, W., Zhang, G., Cheng, Z., Wang, Y.: Magnetic domain-wall induced ferroelectric polarization in rare-earth orthoferrites $AFeO_3$ (A = Lu, Y, Gd): first-principles calculations. J. Mater. Chem. C **7**, 10059–10065 (2019)

West, A.R.: Solid State Chemistry and Its Applications Paperback, 2nd Edn. Wiley (2007)

Yadav, R.S.: Impact of grain size and structural changes on magnetic, dielectric, electrical, impedance and modulus spectroscopic characteristics of $CoFe_2O_4$ nanoparticles synthesized by honey mediated sol-gel combustion method. Adv. Nat. Sci: Nanosci. Nanotechnol. **8**, 045002 (2017)

Yogamalar, R., Srinivasan, R., Vinu, A., Ariga, K., Bose, A.C.: X-ray peak broadening analysis in ZnO nanoparticles. Solid State Commun. **149**, 1919–1923 (2009)
[Crossref]

Zhu, X.H., Xiao, X.B., Chen, X.R., Liu, B.G.: Electronic structure, magnetism and optical properties of orthorhombic $GdFeO_3$ from first principles. RSC Adv. **7**, 4054–4061 (2017)
[Crossref]

© The Author(s), under exclusive license to Springer Nature Singapore Pte Ltd. 2024
R. S. Ningthoujam, A. K. Tyagi (eds.), *Handbook of Materials Science, Volume 2*, Indian Institute of Metals Series
https://doi.org/10.1007/978-981-97-4646-0_5

5. Applications of Magnetic Materials

Ruchi Agrawal[1, 2], Manas Srivastava[1] and Raghumani S. Ningthoujam[1, 2] ✉
(1) Chemistry Division, Bhabha Atomic Research Centre, Mumbai, 400085, India
(2) Homi Bhabha National Institute, Anushaktinagar, Mumbai, 400094, India

✉ **Raghumani S. Ningthoujam**
Email: rsn@barc.gov.in

Keywords Magnetic materials – Applications – Types of magnetic materials – Nanoparticles – Superparamagnetic materials

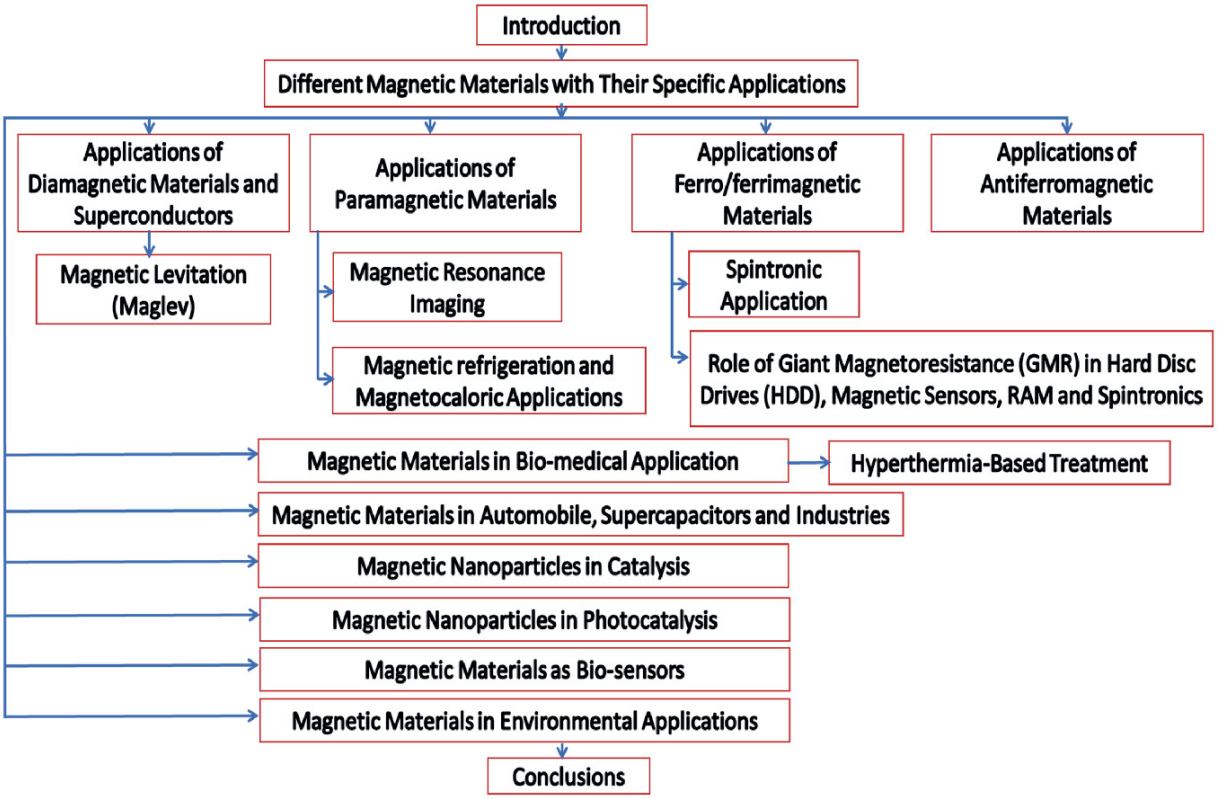

5.1 Introduction

Magnetic materials are those materials that exert a force of attraction or repulsion under the influence of external magnetic field. Magnetic materials possess magnetism, which occurs due to the orbital motion and spin motion of electrons present in the atoms of the elemental materials or alloys. Elemental ferromagnetic materials are Fe, Co, Ni. Metal nitrides, carbides and phosphides show the ferromagnetic properties (Gajbhiye et al. 2002, 2004a, 2004b, 2005; Ningthoujam and Joshi 2021; Ningthoujam and Gajbhiye 2008, 2010a; Cullity and Graham 2009). In general, addition of N/C/P in Fe/Co/Ni lattice reduces magnetization and sometimes, antiferromagnetic or paramagnetic property is observed. In exception, $Fe_{16}N_2$ phase is having higher moment comparable with pure α-Fe.

Metal oxides show various properties such as ferromagnetic, antiferromagnetic or paramagnetic or diamagnetic behaviours. In case of metal oxides, fluorides or sulphides, a super-exchange or double exchange mechanism such as M^{n+}–X–M^{n+} or M^{n+}–X–$M^{(n-1)}$ (X = O, F or S) or mixture gives rise to magnetism. In general, elemental metal has higher moment that of respective metal oxide. Fe and Fe_3O_4 have saturation magnetizations at 217 and 90 emu/g, respectively at room temperature (Achievements and Therapeutic Potential 2012). The double exchange mechanism gives raised to the ferromagnetism, whereas super-exchange mechanism gives raise to anti-ferromagnetism in general. Ferromagnetism and paramagnetic properties in $La_{0.7}Sr_{0.3}MnO_3$ arise due to association of double exchange mechanism (Mn^{4+}-O-Mn^{3+}). Anti-ferromagnetism in $LaMnO_3$ and $SrMnO_3$ arises due to association of super-exchange mechanism (Mn^{3+}-O-Mn^{3+} or Mn^{4+}-O-Mn^{4+}) (Sudhakar et al. 2007; Thorat et al. 2013a; Jadhav et al. 2013). Exchange interaction depends on angle of M–O–M. When dimension of particle in a material changes from 3D to 2D to 1D to 0D, their magnetic properties vary. Sometimes, due to association of defects, magnetic properties of a material vary. Due to the different behaviour of magnetic materials in the presence of magnetic field, they are classified into five categories. This is decided by magnetic susceptibility ($\chi = M/H$, M = magnetization and H = applied magnetic field):

(i) Diamagnetic materials (negative susceptibility)

(ii) Paramagnetic materials (positive susceptibility)

(iii) Ferromagnetic materials (positive susceptibility)

(iv) Ferrimagnetic materials (positive susceptibility)

(v) Antiferromagnetic materials (positive susceptibility).

Examples of diamagnetic materials are H_2, He, Ar, Ne, Au and superconductors below transition and they show negative moment in the presence of applied magnetic moment, i.e., induced magnetic moment developed is opposite to applied magnetic field (Achievements and Therapeutic Potential 2012). The examples of paramagnetic materials are O_2, Na, VN, MoN and their net spin is oriented towards applied magnetic field, but net moment is low (Ningthoujam et al. 2002; Sudhakar et al. 2004; Gajbhiye and Ningthoujam 2004; Ningthoujam and Gajbhiye 2010b). The examples of ferromagnetic materials are Fe, Co, Ni and alloys FePt, CoPd, CoPt, CoNi at room temperature and have spontaneous magnetization even in absence of magnetic field (Achievements and Therapeutic Potential 2012; Ningthoujam et al. 2009, 2012; Gajbhiye et al. 2008a, 2008b; Sharma et al. 2010a, 2010b, 2013). Their magnetic properties can be explained by the presence of magnetic domains and domain walls. Magnetic domain is a region in which all spins are aligned in one direction. Domain wall is a boundary which separate neighbouring domains having different directions. They exhibit the saturation magnetization (M_s), Curie temperature (T_c), coercivity (H_c) and retentivity (M_r). Similarly, ferrimagnetic materials are Fe_3O_4, ɣ-Fe_2O_3, $CoFe_2O_4$, $BaFe_{12}O_{19}$, $Y_3Fe_5O_{12}$ and they exhibit similar to ferromagnetic properties such as M_s, T_c, H_c and M_r, but their magnetic property arises from the net spins from Fe^{3+} or Fe^{2+} or mixture occupying 2 or more sub-lattices (tetrahedral or octahedral or trigonal bipyramidal or dodecahedral polyhedron). Antiferromagnetic materials have Neel

temperature (T_N), below which they are antiferromagnetic and above this they are paramagnetic. Examples are MnO, NiO, $LaFeO_3$, $SrFeO_3$, Fe_2N, Fe_3N (Joshi et al. 2021; Kittel 2005). Ferromagnetic/Antiferromagnetic proximity systems exhibit the exchange biased phenomenon such as having different coercivity values in positive and negative magnetic fields.

Ferromagnetic and ferrimagnetic materials are divided into 2: soft and hard magnetic materials depending on coercivity. If coercivity is more than 1000 Oe, they are considered as hard magnetic materials, otherwise, they are considered as soft magnetic materials. Examples of hard magnetic materials are $BaFe_{12}O_{19}$, $SrFe_{12}O_{19}$, FePt, CoPt, CoPd, $Nd_2Fe_{14}B$, $Nd_2Fe_{14-x}Co_xB$, $Sm_2Fe_{17}C$, $Sm_2Fe_{17}N$, where soft magnetic materials are Fe, Co, Ni, Fe_3O_4, $NiFe_2O_4$, Fe_4N, Co_4N, Ni_3N, Fe–Co–N, etc. (Ningthoujam and Joshi 2021; Vedrtnam et al. 2020; Sharma et al. 2018; Wang et al. 1995; Majeed et al. 2014; Umare et al. 2008). Some of magnetic materials exhibit ferromagnetic and ferroelectric properties (multi-ferroic property) and their examples are $BiFeO_3$, $LaFeO_3$.

These magnetic materials have interesting and unique physical and chemical properties on subjecting magnetic field which takes them a way towards a large number of applications around the globe.

These magnetic materials play an important role in the progress of industrial (automotive industry), technical, biomedical development and scientific growth. They are constantly used in transformers, power generation, magnetic tape recording, spintronics, electronic devices (computer, mobile phones, toys, loud speaker, printer, etc.), data storage devices, medical devices, biomedical field (magnetic therapy through hyperthermia, magnetic resonance imaging (MRI), drug delivery, etc.),

environmental studies (wastewater treatment, sorption of radioactive nuclides), catalysis, biosensors and scientific equipment, etc. as shown in Fig. 5.1 (https://www.dingcimagnet.com/blog/what-are-the-applications-and-types-of-magnets-in-industry_b46).

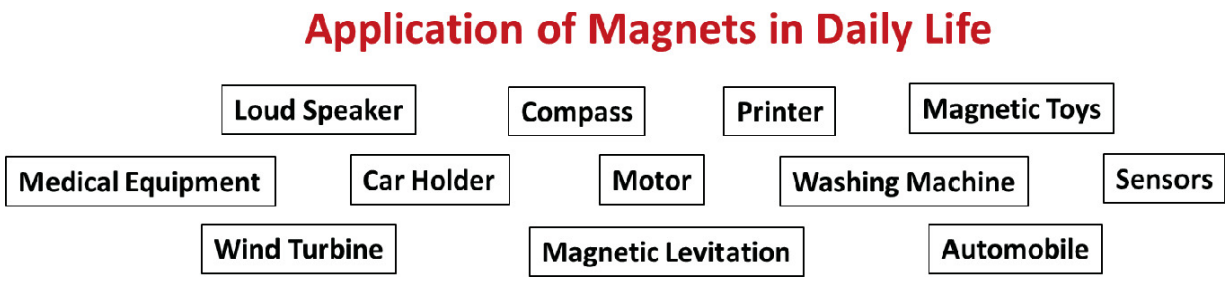

Fig. 5.1 Application of magnets in daily life. It is adapted (https://www.dingcimagnet.com/blog/what-are-the-applications-and-types-of-magnets-in-industry_b46)

The magnetic materials are in the form of metal oxides (e.g., iron oxide, cobalt oxide, nickel oxide, etc.) or metal ferrites (e.g. cobalt ferrites, nickel ferrites, copper ferrites, etc.), suphides, nitrides, borides, carbides, phosphides, metals, alloys, composites, core@shell, thin films, etc. There are several methods to prepare the magnetic materials such as solid-state method, co-precipitation, thermal decomposition, hydrothermal, polyol method, sol–gel method, microemulsion method, physical vapour deposition, chemical vapour deposition and molecular beam epitaxy.

5.2 Different Magnetic Materials with Their Specific Applications

5.2.1 Applications of Diamagnetic Materials and Superconductors

Diamagnetic materials are materials which have no unpaired electrons in atom (as the atomic orbitals are completely filled) due to which they have very weak magnetism and zero net magnetic moment. The magnetic

moment of diamagnetic materials is opposite to the applied magnetic field and independent of temperature. Also, they have small, negative magnetic susceptibility ($\chi < 0$) and their magnetic permeability is less than 1 ($\mu_r < 1$). The examples of diamagnetic substances are Au, Ag, Bi, NaCl, Sb, Zn, Pb, Si, Ge, H_2O, C (graphite and diamond), etc. Most of the polymers and organic compounds are diamagnetic in nature. Even these materials are considered as non-magnetic in nature; these have their own advantages in today's world.

The diamagnetic materials are used for electromagnetic shielding to protect the sensitive electronic devices, scientific and medical equipment from the strong magnetic field interference as they absorb the high-frequency radiations. The electromagnetic shielding materials act as radiation barriers as they have the tendency to shield radio wave and microwave radiations. These materials are basically used in telecommunication and wireless facilities like Wi-Fi, GPS, radio, cell phones, Bluetooth, etc. Typically, composites of ferro/ferrimagnetic material and non-magnetic conducting carbon-based materials (like, flexible graphite, carbon nanotubes and reduced graphene oxide) are reported (Chung 2020; Guan and Chung 2020; Wang et al. 2019; Yu et al. 2019).

A perfect diamagnetic material is known as "Superconductor". Superconductors have the capability to carry high current densities and zero resistance in the presence of high magnetic fields. The Superconductors came into existence in 1911 as engineering materials, but after 1960 they were started to be used in laboratory purpose, in high-energy particle accelerators and then later in magnetic resonance imaging for biomedical application. The Superconductors are based on the concept of "Meissner effect", which states that they have zero magnetic flux density, due to which these are very

important for scientific community (Meissner and R. 1933; Geim et al. 1998). The concept of Meissner effect is shown in Fig. 5.2a, b (Yaghoubi 2013).

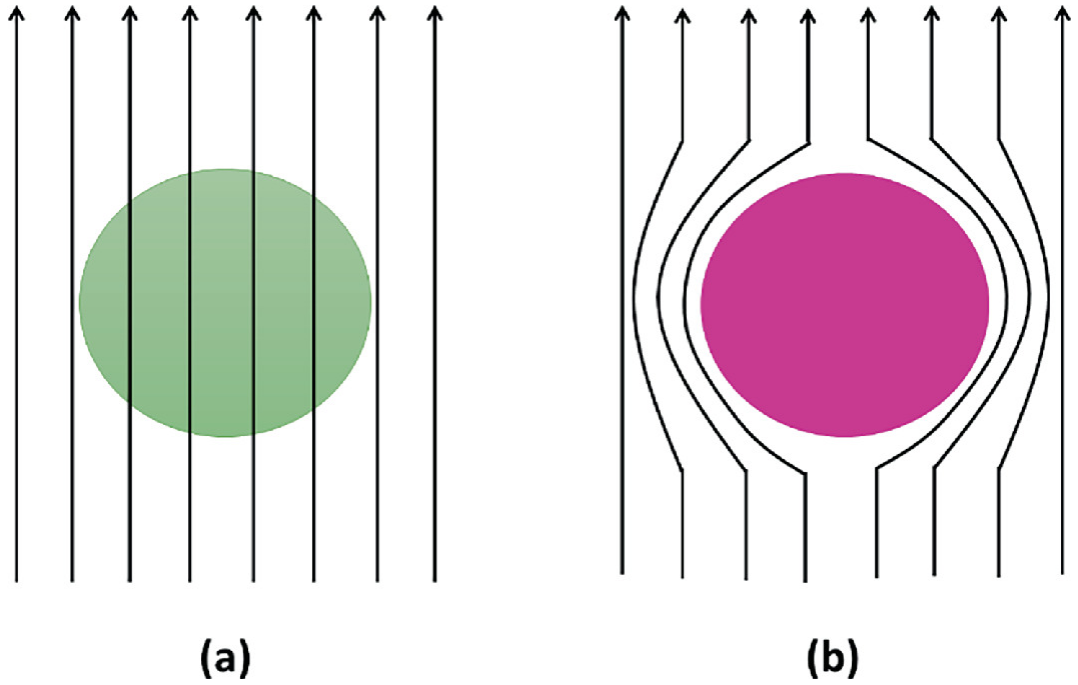

Fig. 5.2 **a** Magnetic field lines pass through a superconductor at a temperature above its critical transition temperature ($T > T_C$), **b** Magnetic field lines are repelled from the superconductor due to Meissner effect, when the temperature of superconductor reaches below its transition temperature ($T < T_C$). It is redrawn and adapted with permission under Creative Common License (Open Journal) from Hindawi Publishers (Yaghoubi 2013)

Various applications of superconductor and magnetic materials in different technologies include cables, induction heaters, motors, generators, maglev, electric aircraft, MRI, NMR, accelerator, etc. with their operating fields are represented in Fig. 5.3 (Yao and Ma 2021). The growth of various temperature superconductors with time is depicted in Fig. 5.4 (Yao and Ma 2021).

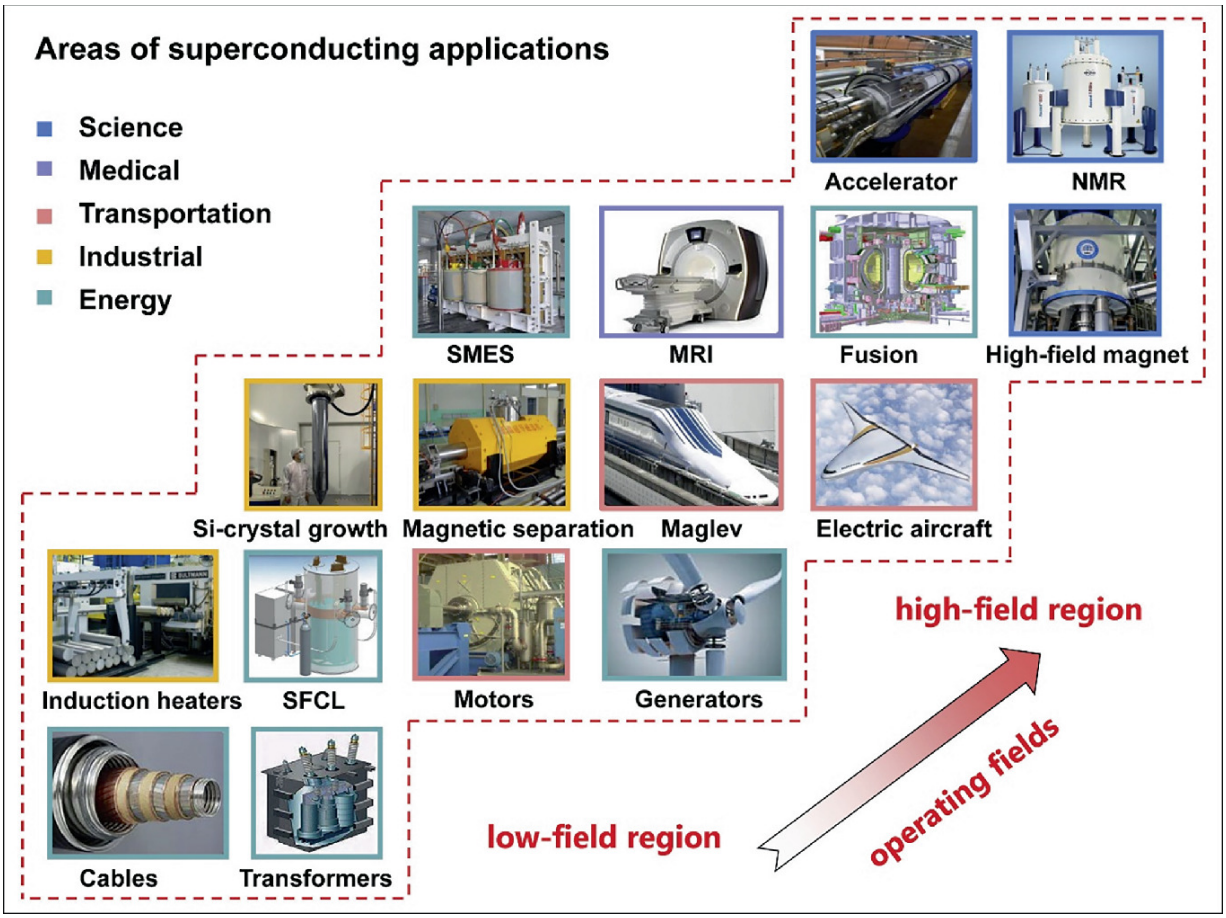

Fig. 5.3 Applications of superconductor and magnetic materials in different technologies with their operating fields. It is reproduced with permission from Elsevier Publishers (Yao and Ma 2021)

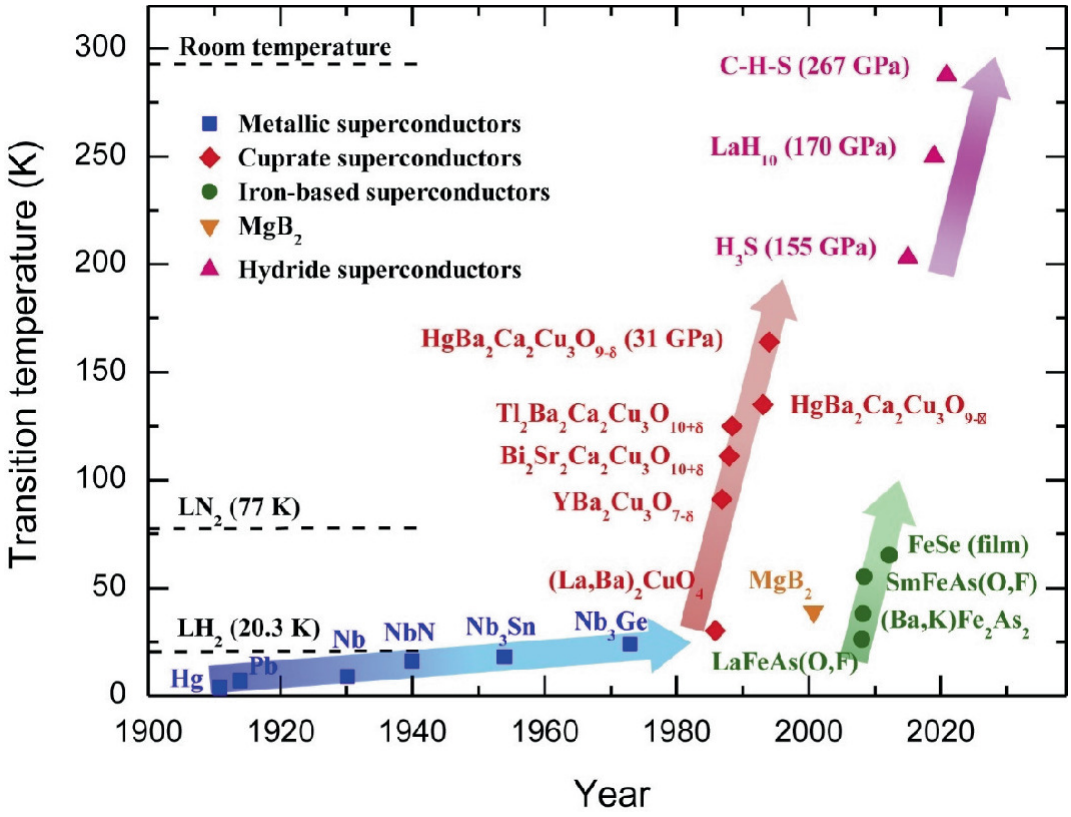

Fig. 5.4 Development of superconductors at different temperatures over time. It is reproduced with permission from Elsevier Publishers (Yao and Ma 2021)

5.2.1.1 Magnetic Levitation (Maglev)

The Maglev trains running in China, Japan, South Korea and United States for last 30 years are based on the principle of diamagnetism. The maglev is high speed train that floats frictionless over the electromagnetic tracks having superconducting property, which is known as magnetic levitation. They cooled down by using liquid N_2 to produce 10 times stronger magnetic fields than conventional trains, which leads to frictionless propelling of trains. For example, if a neodymium magnet is placed on the surface of Ytterium Barium Copper Oxide $YBa_2Cu_3O_7$ (YBCO) and cooled down to its critical temperature of YBCO, the magnetic field of a neodymium magnet is repelled by YBCO (superconductor). These superconducting materials suspend a train above a U-

shaped concrete guideway. The magnets will repel each other when they are placed in opposite face. The magnetic fields generated will interact with the conducting metallic loops (made of Aluminium) and create an electric current to produce another magnetic field (thekidshouldseethis.com n.d.). This leads to floating the train above the tracks without touching each other and move in faster rate and low noise than the ordinary trains.

Also, diamagnetic levitation is used to levigate light objects like live organisms, organic molecules and water droplets. In 2000, frogs were levigated by using diamagnetic materials, which requires very high magnetic fields of ~16 Tesla (Beaugnon and Tournier 1991; Motokawa et al. 2001; Simon and Geim 2000; Kaur et al. 2021).

Generally, low temperature Superconductors include Ni–Ti and Nb_3Sn which are commercially applied in electric power industry, generators, NMR machines, scientific research and Magnetic Resonance Imaging machines. Copper coils and high temperature superconductors are used in motors. High temperature superconducting material like Ytterium Barium Copper Oxide $YBa_2Cu_3O_7$ (YBCO) is used in SQUID (Superconducting Quantum Interference Device). The typical images of these superconductors are given in Fig. 5.5 (Yao and Ma 2021; Lee 2018; Osabe et al. 2019; Jiang et al. 2019; Zhang 2019; Li et al. 2013; Braccini et al. 2007; Yao et al. 2015). Solenoid magnets with high-field based on cuprate HTS (High temperature superconductor) materials are shown in Fig. 5.6 (Yao and Ma 2021; Hahn et al. 2019; Juarez et al. 2018; Liu et al. 2020; Yoon et al. 2016; Yanagisawa et al. 2016; Awaji et al. 2017).

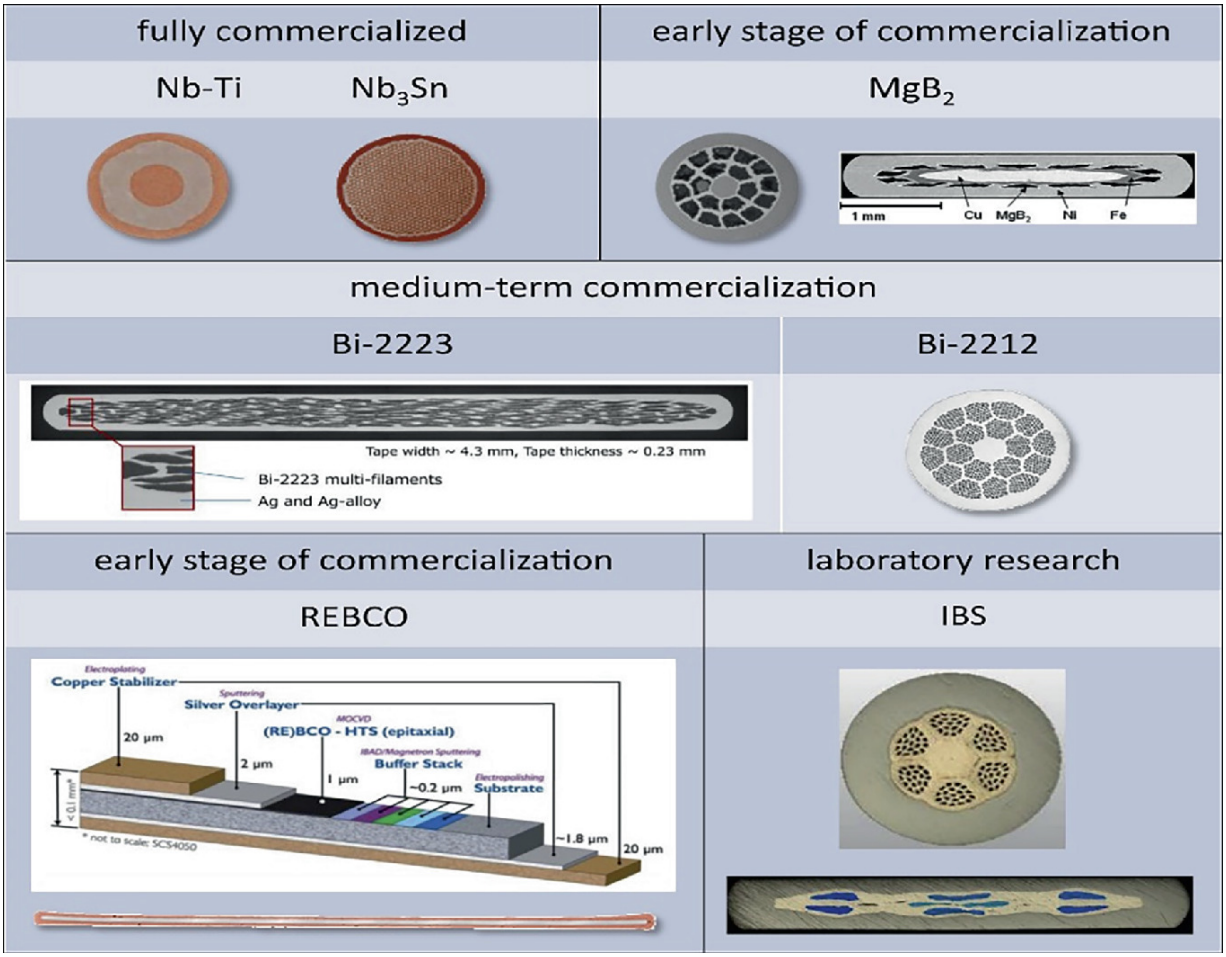

Fig. 5.5 Upper conducting materials such as niobium-based superconductors (Nb–Ti and Nb_3Sn), copper-based oxides (Bi-2223), Bi-2212, REBCO, MgB_2 and iron-based superconductors (IBS). It is reproduced with permission from Elsevier Publishers (Yao and Ma 2021; Lee 2018; Osabe et al. 2019; Jiang et al. 2019; Zhang 2019; Li et al. 2013; Braccini et al. 2007; Yao et al. 2015)

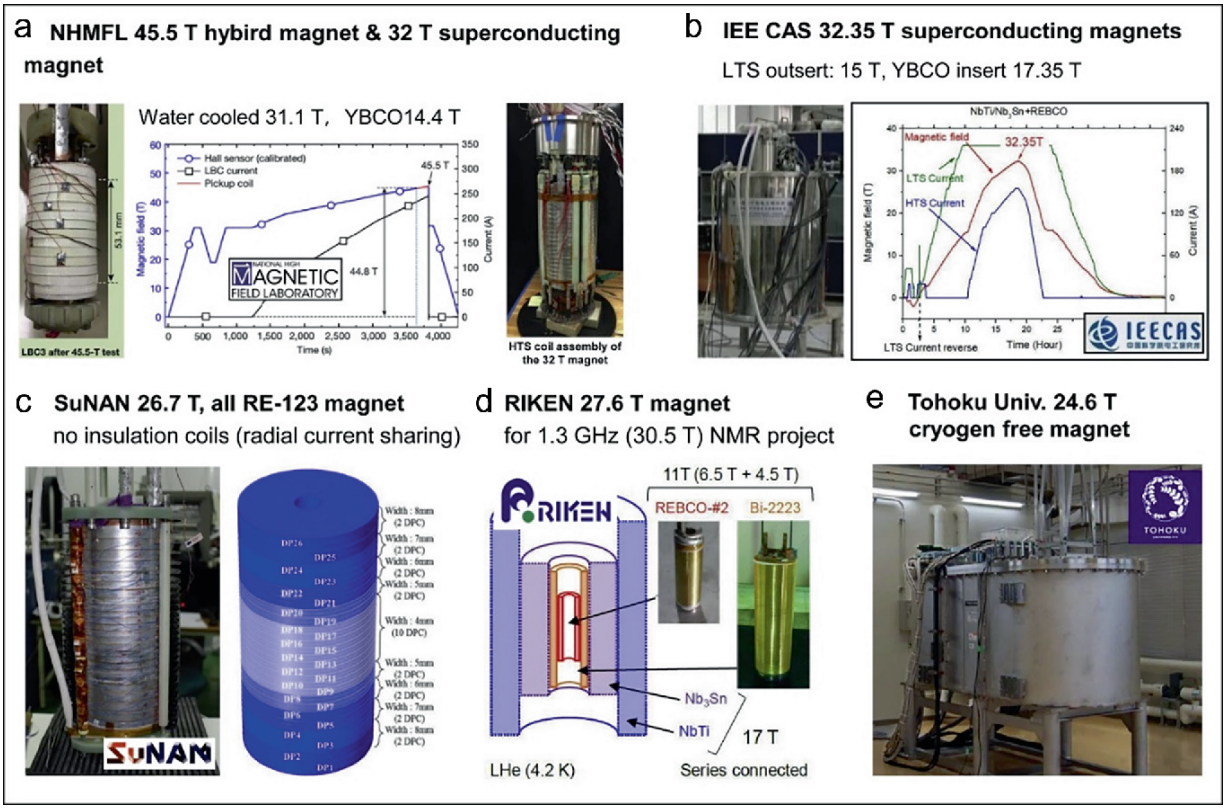

Fig. 5.6 State-of-the-art high-field solenoid magnets based on cuprate HTS materials. It is reproduced with permission from Elsevier Publishers (Yao and Ma 2021). **a** a 45.5 T hybrid magnet with a 14.4 T REBCO insert in a 31.1 T resistive magnet and a 32 T magnet with a 15 T LTS oursert and a 17 T REBCO insert; **b** a 32.35 T magnet with a 15 T LTS oursert and a REBCO insert; **c** a 26.7 T all-REBCO magnet; **d** a 27.6 T magnet with a Bi-2223 coil and a small REBCO test coil in a 17 T LTS background magnet; **e** a 24.6 T cryogen free magnet with a Bi-2223 insert and an Nb_3Sn outsert (Yao and Ma 2021; Hahn et al. 2019; Juarez et al. 2018; Liu et al. 2020; Yoon et al. 2016; Yanagisawa et al. 2016; Awaji et al. 2017)

In 1911 at the University of Leiden, Netherlands, Heike Kammerlingh Onnes discovered the zero resistance for mercury below 4 K. This was the first demonstration among superconducting materials. In 1913, he was awarded Nobel Prize in Physics. After this, discovery of many materials had been reported. In 1933, Meissner effect (repulsion of magnet or expulsion of a magnetic field by superconducting material below its T_c) was observed for the first time by the German physicists Walther Meißner (anglicized Meissner) and Robert Ochsenfeld. New observation of electron

tunnelling between superconductor and metal or insulator in 1960s by Brian Josephson and later he was awarded Nobel Prize in Physics in 1973. Theoretical model known as BCS theory was established to explain superconductivity in 1957s and its long form is Bardeen, Cooper and Schrieffer and Nobel Prize in Physics was awarded to them in 1972. This is based on the formation of the pair electrons with parallel spins mediated by phonons below superconducting transition. This is sometimes called Cooper pair. J. Georg Bednorz and K. Alexander Müller in 1986 discovered Cu–O ceramic materials having Tc ~ 30 K. Because of this, both were awarded Nobel Prize in 1987. Hg containing Cu–O material with T_c ~ 136 K in 1993 and Tc ~ 150 K under pressure in 1993, MgB_2(39 K) in 2001, Iron-containing material with T_c at 5 K in 2006 and many other superconductors were reported. Figure 5.7 (Ningthoujam and Gajbhiye 2015). shows the evolution of superconducting materials with years (Ningthoujam and Gajbhiye 2015). The superconducting materials have been used in development of many instruments/devices such as SQUID, MRI and levitation in train.

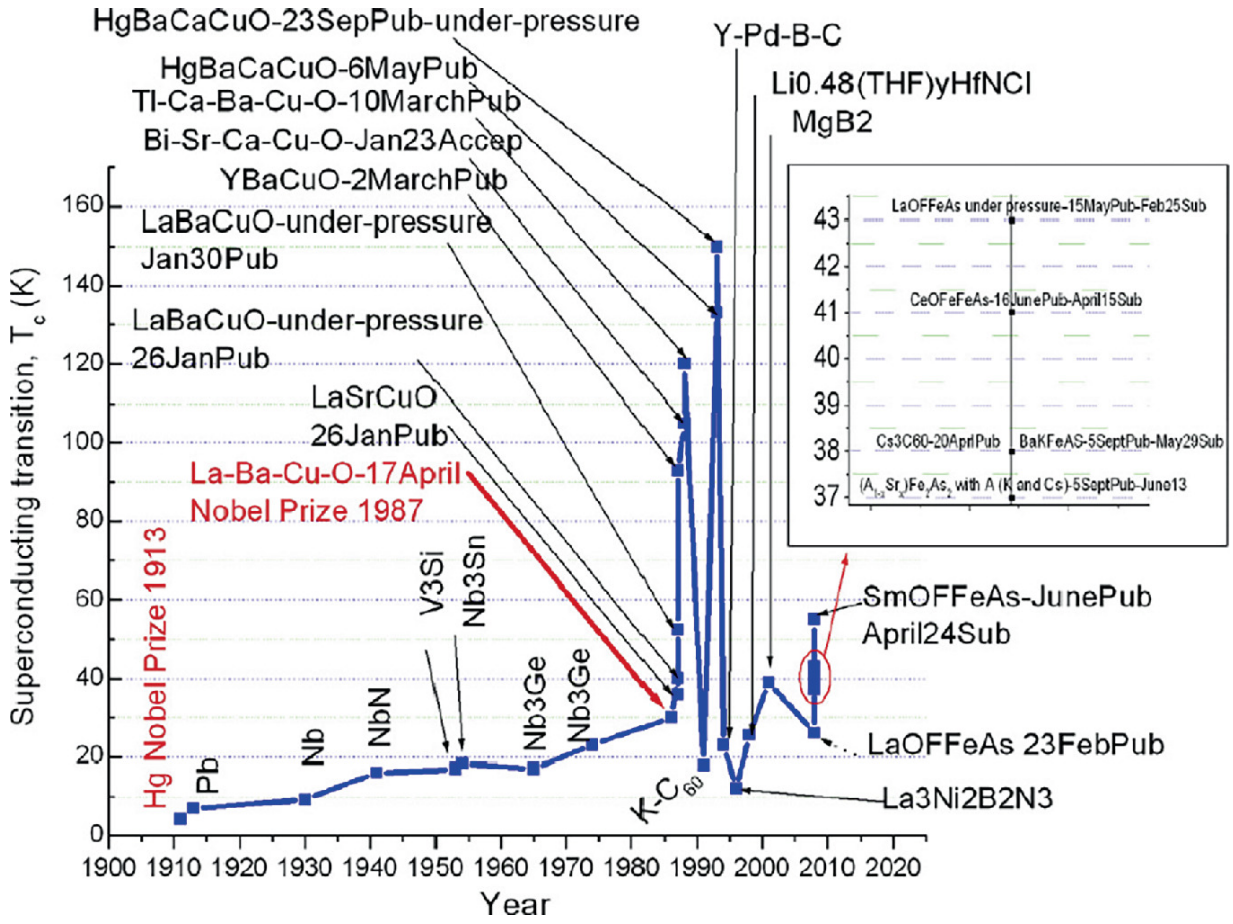

Fig. 5.7 Development of superconductors. It is taken permission from Ningthoujam and Gajbhiye (2015)

5.2.2 Applications of Paramagnetic Materials

Paramagnetic materials are materials which contain an unpaired electron having partially filled orbitals due to which they have small magnetic moment. The magnetic moment of paramagnetic materials is aligned in the direction of the applied magnetic field. After removal of magnetic field, it does not retain magnetization and hence no permanent magnetization in absence of magnetic field. Also, they have small, but positive magnetic susceptibility ($\chi > 0$) and magnetic permeability is greater than 1 ($\mu_r > 1$). The susceptibility of paramagnetic substances depends on the temperature according to Curie's Law ($\chi_m = C/T$, C is curie constant and T is temperature). The examples of

paramagnetic substances are O_2, Al, Pt, Gadolinium (Gd), Mn, Cr, Li, Na, Ca, $CuSO_4$, etc. Due to these unique properties of paramagnetic materials, they are used in various applications.

5.2.2.1 Magnetic Resonance Imaging

MRI is a technique which is used for the diagnosis of diseases by using radiofrequency in medical modalities. For this, paramagnetic contrast agents, i.e. Gadolinium-based contrast agents (GBCA), which have good water solubility, non-toxic in nature, targeting property, stable, more retention time in blood and quick excretion from body are preferred (Kang and Zhao 2022). So, they give strong signals in various tissues leading to better visualization/images with high resolution for diagnostic purpose. For example, Gd(III) and Fe(III) compounds are considered as T_1-based paramagnetic contrast agents. Gadolinium (Gd) is a silvery-white f-block inner transition element (rare earth element) that occurs naturally in the earth crust with an atomic number of 64, common oxidation state (+3) and an ionic radius of 0.99 Å. Gadolinium ions can coordinate with many ligands (CN = 6–12) to form strong compounds that can serve as contrast agent for MRI. For high contrast ability, it has shorter T_1 and more relaxation time R_1 (as, $R_1 = 1/T_1$). Examples of GBCA are (gadoterate meglumine) Gd-DOTA, (gadopentetate dimeglumine) Gd-DTPA, (gadoxetate disodium) Gd-EOB-DTPA, (gadodiamide) Gd-DTPA-BMA, (Gadoversetamide) Gd-DTPA-BMEA, (Gadobutrol) Gd-DO3A-butrol, (gadobenatedimeglumine) Gd-BOPTA, (gadoteridol) Gd-HP-DO3A, etc. which are studied by the researchers in the world. Some of them are represented in Fig. 5.8 (Bi et al. 2022; Grueber et al. 2021; Kanda et al. 2016; Iyad et al. 2023).

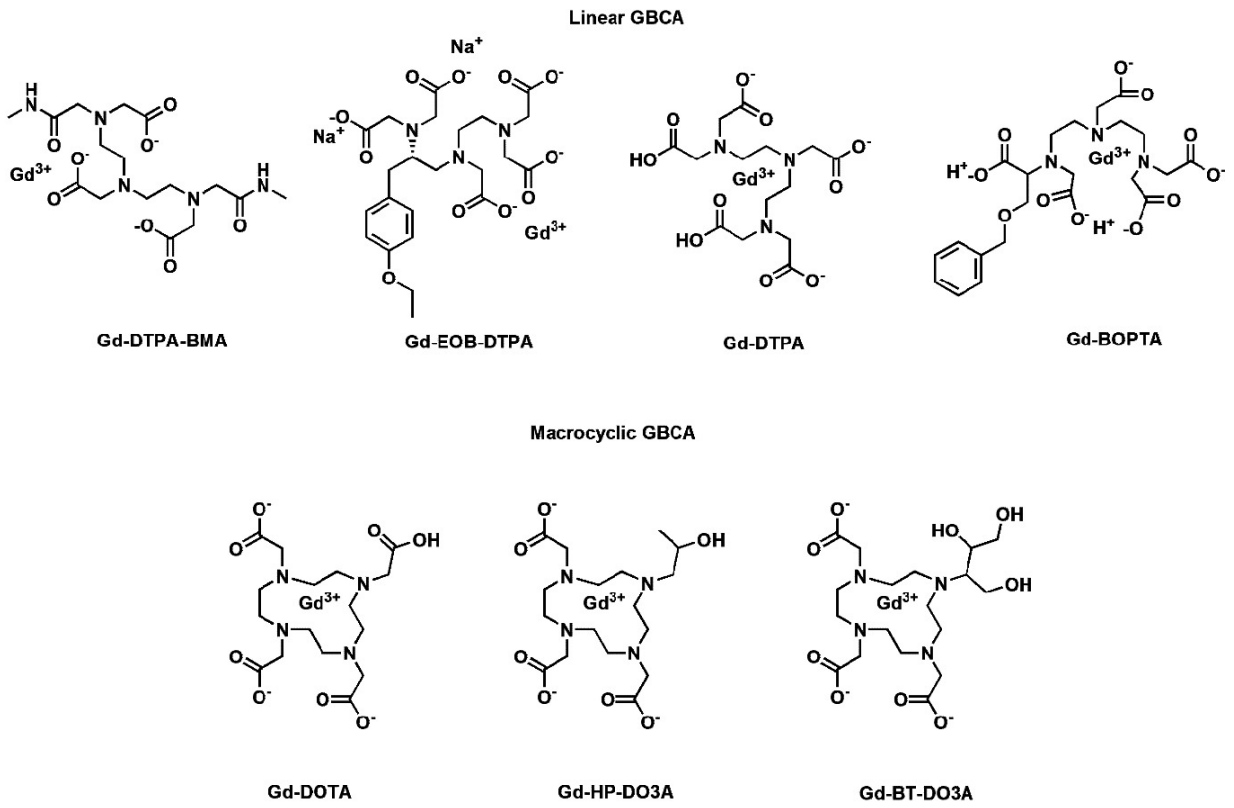

Fig. 5.8 Linear and macrocyclic gadolinium-based ligands used for MRI contrast agents. It is adapted and redrawn from Elsevier Publishers (Iyad et al. 2023)

Some compounds are utilized for the drug delivery as well as specific targeting in the disease site for the early detection of tumours (Huang et al. 2021).

5.2.2.2 Magnetic Refrigeration and Magnetocaloric Applications

Nowadays, a lot of paramagnetic materials are used in adiabatic demagnetization refrigeration (ADR), cryogenics and magnetocaloric cooling systems (Mellari 2023). One can demagnetize the materials by using their temperature dependence behaviour to achieve very low temperature (in milli Kelvin range) by varying their magnetic field. But the question is why to demagnetise the material, so the devices we use in our daily life like magnetic tape or some storage device, so before discarding it is important to demagnetize it for security reasons. Both the applications are based on

the principle of adiabatic demagnetization, which includes the combination of magnetic and heating behaviour of paramagnetic materials. The cooling and heating tendency depends on the entropy of the system. In the case of paramagnetic materials, entropy/randomness is very low in the presence of magnetic field, which results in the cooling of substances below 1 K. According to the studies, the cooling efficiency with Gadolinium base materials can reach up to 60% of theoretical limit as compared to gas-compressed refrigerators (45%). Conventionally, chlorofluorocarbons (CFCs), hydrofluorocarbons (HFCs) and ammonia are used in gas-compressed refrigerators which are actually harmful for food preservation (Zimm et al. 1998).

In view of that, a polycrystalline $La_{0.5}Gd_{0.2}Sr_{0.3}MnO_3$ oxide is reported in the literature having very good performance in magnetic refrigeration at room temperature. This compound shows large change in magnetic entropy with peak at 270.5 K near its Curie temperature (Sun et al. 2002). Moreover, a lot of single crystals, alloys, Perovskite type substances are also highly used above room temperature. Examples are MnFe(P,*X*) (*X* = As, Ge, Si), La (Fe, Co)$_{13-x}Si_x$, $MnAs_{1-x}Sb_x$, $Mn_5Ge_{3-x}Sb_x$, $CoMnSi_{1-x}Ge_x$, $Ni_{2+x}Mn_{1-x}Ga$, $La_{1-x}K_xMnO_3$, $Pr_{0.63}Sr_{0.37}MnO_3$, RMn_2O_5, etc. (Yibole et al. 2014; Balli et al. 2007, 2015; Wada and Tanabe 2001; Songlin et al. 2002; Sandeman et al. 2006; Cherechukin et al. 2004; Das and Dey 2007; Phan et al. 2005).

Paramagnetic materials are separated from the mixture of materials by incorporating strong magnetic field. Magnetic separation is used to isolate contaminants or some materials in different purposes like in mineral processing, waste management industries, sewage treatment, in recycling process, food production, nuclear industry, etc.

5.2.3 Applications of Ferro/Ferrimagnetic Materials

Ferromagnetic materials are materials which have spontaneous magnetization in absence of magnetic field. They have magnetic domains and domain walls. Domain is a region in which unpaired electrons are aligned in one direction. Also, they have high and positive magnetic susceptibility ($\chi > 0$) and magnetic permeability is much greater than 1 ($\mu_r >> 1$). The susceptibility of ferromagnetic substances depends on the temperature according to Curie–Weiss Law ($\chi_m = C/(T–T_c)$, C is Curie constant, T is temperature, which is more than T_c(Curie temperature). The examples of ferromagnetic substances are Fe, Co, Ni, Gadolinium (Gd), Dysprosium (Dy), rare earth magnets ($Nd_2Fe_{14}B$), etc. The main applications of ferromagnetic materials are in electromagnets, transformers, inductors, magnetic storage devices, etc.

Ferrimagnetic materials are those materials which have 2 or more sub-lattices of Fe^{3+}/Fe^{2+} ions with anti-parallel spins, but they have spontaneous magnetization in absence of magnetic field. These materials have very large magnetization even on subjecting low magnetic field. These materials have high d.c. resistivity in comparison to ferromagnetic materials. That is why, ferrimagnetic materials are used in high-frequency applications like computers, memory devices (magnetic tape and hard disc), data storage, magnetic field sensors, microwave devices, etc. Examples of ferrimagnetic materials are nickel ferrites, Iron ferrites like Fe_3O_4 (magnetite), yttrium iron garnet (YIG, $Y_3Fe_5O_{12}$), $MnZnFe_2O_4$, $NiZnFe_2O_4$, strontium hexaferrite ($SrFe_{12}O_{19}$), etc. Both ferromagnetic and ferrimagnetic materials are based on domain theory by exhibiting spontaneous magnetization, coercivity, retentivity and hysteresis loss. There are two types of

ferromagnetic/ferrimagnetic materials on the basis of coercivity (H_c): soft and hard magnetic materials.

Soft magnetic materials have high value of permeability and low value of coercivity ($H_c < 700$ Oe). It can be easily magnetized and demagnetized. Its area of hysteresis loop is small. In case of hard magnetic materials, they have low permeability and high coercivity ($H_c > 1000$ Oe) and also show high residual magnetism. Its area of hysteresis loop is large. They are also considered as permanent magnetic materials.

Examples of soft magnetic materials are silicon steel (in transformer cores), soft ferrites like Mn–Zn and Ni–Zn (transformers, inductors, chokes and filters for energy storage), amorphous Fe-based materials, Co-based alloys (used to build wound cores of transformers), and iron-nickel alloys (like mu-metal and permalloy for magnetic shielding in electronic devices), like Fe–Si, Fe–Ni, Fe–Co and their composites are useful materials for manufacturing items of electrical machine (Sai Ram et al. 2021; Rodriguez-Sotelo et al. 2020; Metglas n.d.; Valenzuela 2012; Warlimont and Boll 1982).

Mu-metal (Fe–Ni alloys, high permeability and low magnetic loss) with multilayer structures is used in atomic sensors, magnetometers, atomic clocks. SQUID systems use mu-metal layers in order to shield the thick walls for eliminating noise or interference in scientific equipment like magnetometers, geophysics instruments, etc. (Fang et al. 2022; Fan et al. 2020; Ma et al. 2022).

Different hard materials include KS-steel, MK-steel, Alnico, $SmCo_2$, Sm_2TM_{17}, Nd–Fe–B, Ba–Sr-ferrites, $Sm_2Co_{17}$are most common and widely studied by the researchers (Hinz et al. 2004; Hai-Peng Chen et al. 2937).

Superparamagnetic materials have very large magnetic moment in the presence of magnetic field, and they lose their magnetization on the removal of magnetic field. This

property of superparamagnetic materials leads to lot of attractive applications like magnetic separation, hyperthermia and drug delivery. Superparamagnetic character is a size dependent property, which only exists in nano-size particles. For example, iron oxide nanoparticles (NPs) show superparamagnetism in the range of ~5–20 nm particle size. Due to the small size and large particle surface area, these nanoparticles have numerous advantageous magnetic properties than the bulk material. Iron oxide nanoparticles can exist in different forms according to their synthesis procedure. For example, Fe_3O_4(magnetite) nanoparticles can be synthesized by heating the iron precursors below 200 °C, and heating up to 300 °C leads to the production of γ-Fe_2O_3 (maghemite) nanoparticles, while heating above 500 °C results in the formation of α-Fe_2O_3 (hematite) nanoparticles given in Fig. 5.9 (Cardoso et al. 2018). In control H_2/Ar atmosphere, transformation of α-Fe_2O_3 to γ-Fe_2O_3 to Fe_3O_4 takes place. These nanoparticles have different magnetic property as Fe_3O_4 (ferrimagnetic), γ-Fe_2O_3 (ferrimagnetic) and α-Fe_2O_3 (antiferromagnetic material) in nature. As nanoparticles have a large surface area, surface functionalization with other ligands (citric acid, ascorbic acid) is easy and has hydroxyl (OH) groups after contact with atmosphere, which make system easily dispersible in water. The –OH group on the surface of particle gets de-protonated in water leading to $–O^-$ ion and thus surface charge becomes negative.

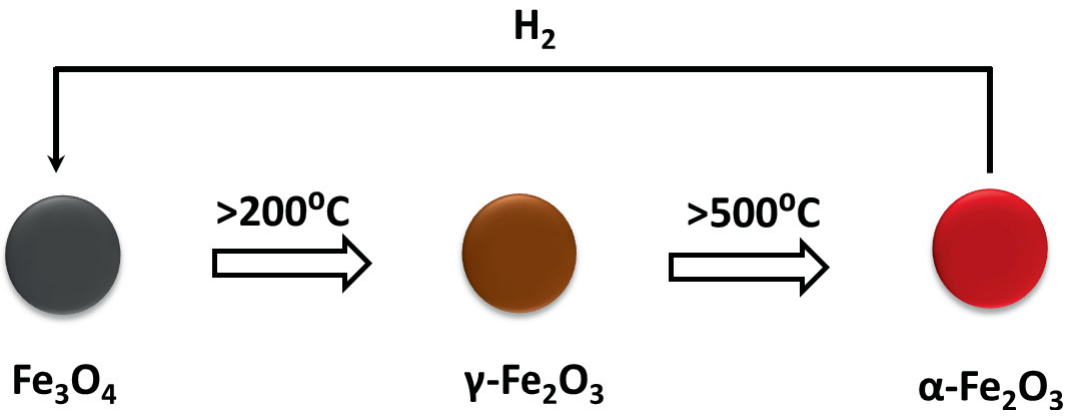

Fig. 5.9 Transformation of Fe_3O_3 to γ-Fe_2O_3 to α-Fe_2O_3. It is adapted and redrawn from RSC Publishers (Cardoso et al. 2018)

The property of superparamagnetism depends on several parameters like size, temperature, method of preparation, surface modification of the nanomaterial, mostly seen in the ferromagnetic materials. The nano-size of superparamagnetic particles exhibits single domain behaviour. Generally, in the presence of magnetic field, the superparamagnetic nanoparticles can get agglomerated, while in the absence of magnetic field the particles can get separated. Superparamagnetic materials show ON–OFF switching behaviour which is used for the sensor-based systems (Hu et al. 2019).

5.2.3.1 Spintronic Application

Spintronics is based on the interaction between spins of electrons/holes with conduction electrons (spin-polarized electrical injection), which lead to be utilized for the nano-electronic devices as they consume less power and enhance the magnetic storage capacity. A single spin can have up or down state (+ ½ (↑) or -½ (↓)). Conduction electrons can interact with spins. Utilization of spintronics concepts has been applied to hard disc drives (HDD), magnetic field sensors and semiconductor devices (http://zfmezo.home.amu.edu.pl/images/research/Spintronics_v2.png; Hirohata et al. 2020). Figure 5.10 (Hirohata et al. 2020) gives an introduction to spintronics and its application in different

devices. It is divided into two types (Mott type and Dirac type), where they are categorized into spin memories and spin transistors.

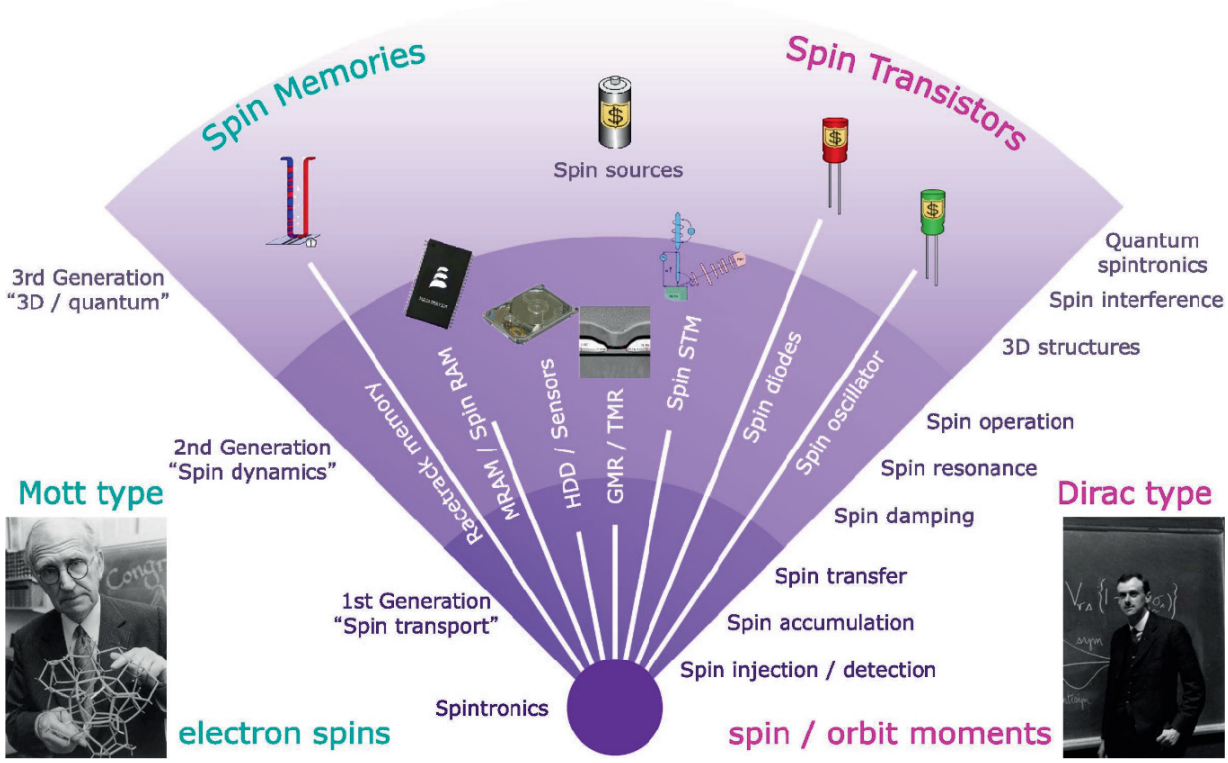

Fig. 5.10 Applications of spintronics in different devices. It is reproduced with permission under Creative Common License (Open Journal) from Elsevier Publishers (Hirohata et al. 2020)

All the spintronic devices work on the phenomenon of different spin polarized current generation like mechanical rotation of spins, spin–orbit effects, electrical spin generation, electric field application on spins, influence of thermal gradient on spins, spin band splitting, electromagnetic wave application and their geometrical phase as depicted in Fig. 5.11 (Hirohata et al. 2020).

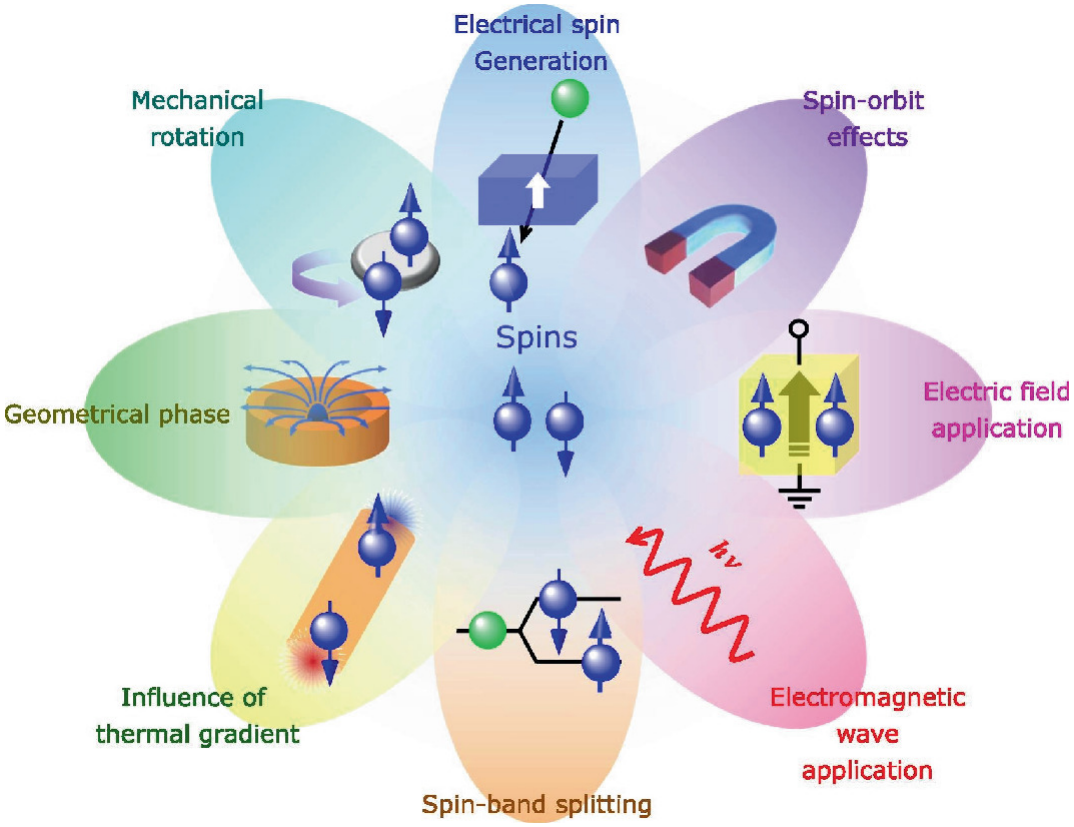

Fig. 5.11 Different methods of spin polarized current generation in spintronics. It is reproduced with permission under Creative Common License (Open Journal) from Elsevier Publishers (Hirohata et al. 2020)

These methods include different magnetic systems such as Lateral spin-valve: $Co_2FeSi/Cu/Co_2FeSi$, Spin Hall: $Pt_{0.85}Hf_{0.15}$ (5.5)/Pt (0.5)/Co (1) (nm), Topological insulator: $(Bi_{1-x}Sb_x)_2Te_3$ thin films, Quantum spin Hall: HgTe/(Hg,Cd)Te, Spin pumping: $Y_3Fe_5O_{12}$/Pt, $Pt/Ni_{0.2}Zn_{0.3}Fe_{2.5}O_4$ film, etc. (Kimura et al. 2012; Nguyen et al. 2016; Kondou et al. 2016; Konig et al. 2007; Tashiro et al. 2015; Kirihara et al. 2016).

MRAM (Magnetic random-access memory) is a solid-state memory, which is made up of several layers of patterned MTJs of few thicknesses, due to which it stores the data. Figure 5.12 (Hirohata et al. 2018) represents the correlation between magnetoresistance (MR) and resistance-area product (*RA*) of magnetic tunnel junctions (MTJs) in different magnetic materials which are used in

hard disc drives (HDD) and MRAM (Magnetic random-access memory).

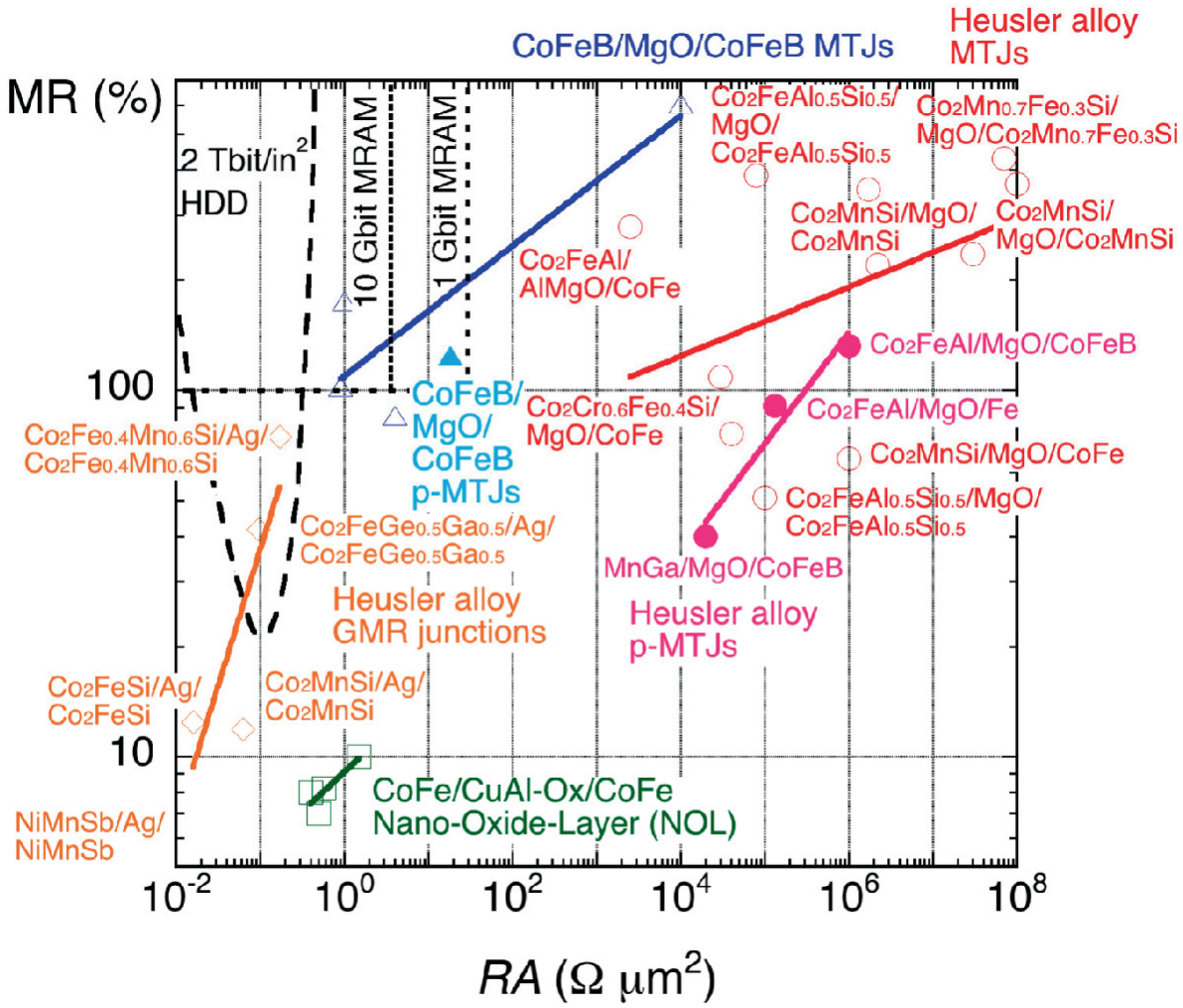

Fig. 5.12 The study focuses on the correlation between the resistance-area product (RA) and magnetoresistance (MR) of magnetic tunnel junctions (MTJs) with CoFeB/MgO/CoFeB (blue triangles), nano-oxide layers (NOL, green squares) and Heusler alloys (red circles). The MTJs' MR and RA values are compared with that of giant magneto resistive (GMR) junctions with Heusler alloys, as well as between the two scenarios (orange rhombus). The purple and yellow shaded zones, respectively, represent the target requirements for 1 and 10 Gbit magnetic random-access memory (MRAM) applications and 2 Tbit/in2 hard disc drive (HDD) read heads. It is reproduced with permission under Creative Common License (Open Journal) from materials Publishers (Hirohata et al. 2018)

5.2.3.2 Role of Giant Magnetoresistance (GMR) in Hard Disc Drives (HDD), Magnetic Sensors,

RAM and Spintronics

Giant magnetoresistance (GMR) is defined as the large changes observed in the electrical resistance under the influence of external magnetic field. This effect occurs when the two or more ferromagnetic material layers were separated by any thin antiferromagnetic layer or a non-magnetic material. The system looks like Ferromagnetic-Antiferromagnetic-Ferromagnetic (F-A-F) sandwich. The ferromagnetic spins are aligned in presence of magnetic field and also spins at the interface are oriented towards magnetic field; thereby its electrical resistivity drops drastically as compared to those without magnetic field, which leads to the generation of GMR.

Generally, Fe is separated by different magnetic elements to give the giant magneto resistive effect. Spin valve uses copper and alloys of iron and nickel. Albert Fert and Peter Grünberg were two physicists, who got Nobel Prize in Physics in 2007 for the revolutionary discovery of GMR. Both worked independently on Fe–Cr–Fe system at Germany and France in 1988. The evolution of GMR makes a huge development in the field of electronic devices. Spin valve GMR plays a very important role in hard disc drive, which are used as large data storage devices in gigabytes/cm^2 (density) and magnetic sensors. One more important application of GMR is in magneto resistive random-access memory (MRAM) and in spintronics applications (http://simple.wikipedia.org/wiki/Giant_magnetoresistance; https://www.nobelprize.org/prizes/physics/2007/popular-information/; Hinchey and Mills 1986; Grünberg et al. 1986; Carbone and Alvarado 1987; Baibich et al. 1988; Binasch et al. 1989; Berkowitz et al. 1992; Xiao et al. 1992; https://www.collegesidekick.com/study-guides/boundless-physics/applications-of-magnetism).

Magnetoresistance is the collective term of magnetism and resistance, which states resistance created in the magnetic material, where the rotation and scattering of electrons in the interface of two magnetic materials induces magnetic moment under the influence of magnetic field. The direction of those magnetic moments is either aligned or opposite to the applied magnetic field. Generally, in the magnetic materials, large number of spins is aligned in the same direction to magnetic field, while some are in different directions, which gives rise to the scattering. The irregularity mostly occurs in interface of the magnetic materials. So, the presence of more anti-parallel spins gives rise to more scattering of electrons and high resistance is observed (case B), while when the spins are aligned in the direction of magnetic field, then the scattering of electrons will be less and also the resistance is also less (case A) as represented in Fig. 5.13 (http://simple.wikipedia.org/wiki/Giant_magnetoresistance) and Fig. 5.14 (https://www.nobelprize.org/prizes/physics/2007/popular-information/).

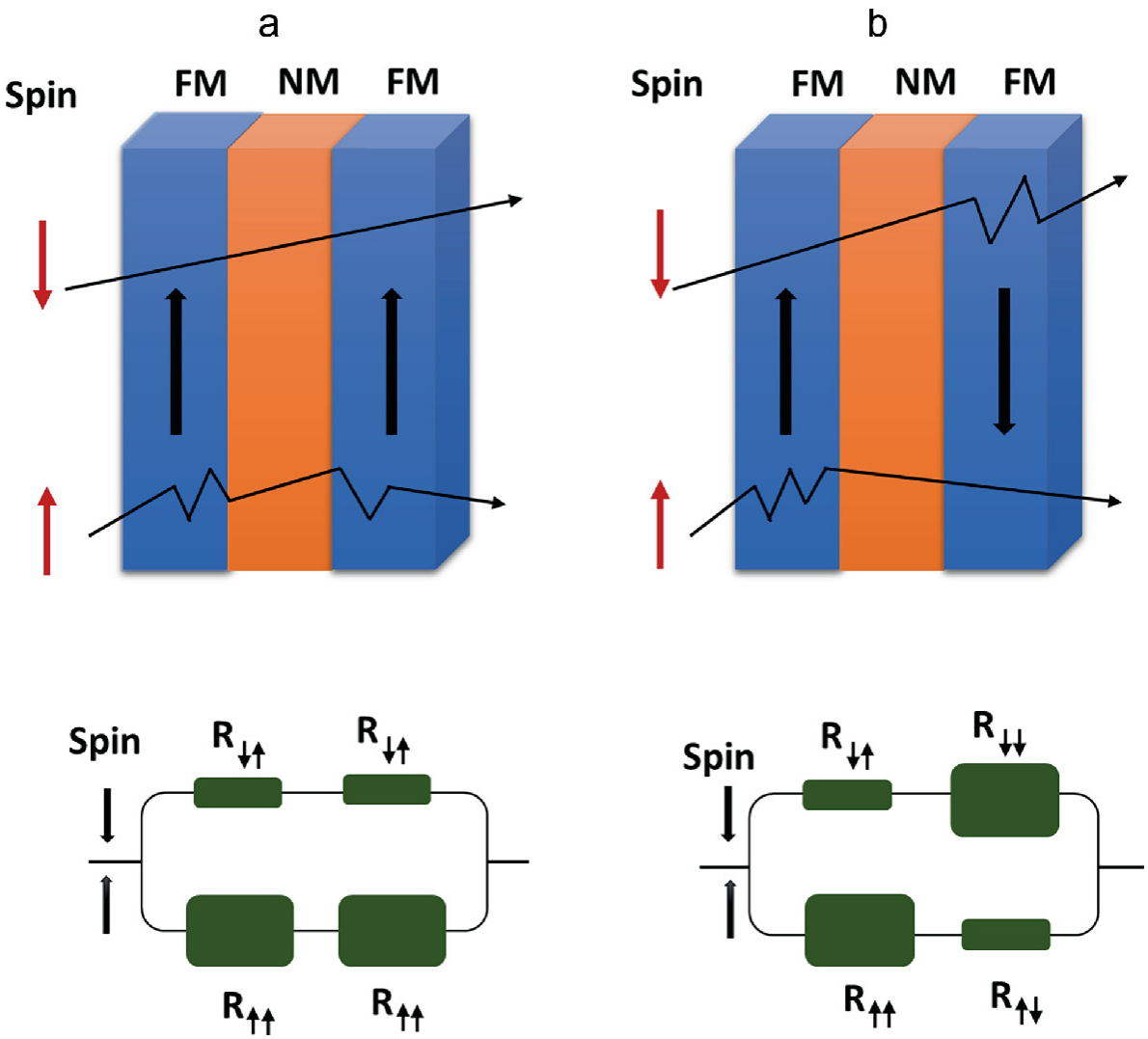

Fig. 5.13 **a** represents the low resistance due to the same spin direction of both the layers without any scattering, **b** represents the high resistance due to the opposite spin direction of both the layers with scattering. It is redrawn by author (http://simple.wikipedia.org/wiki/Giant_magnetoresistance)

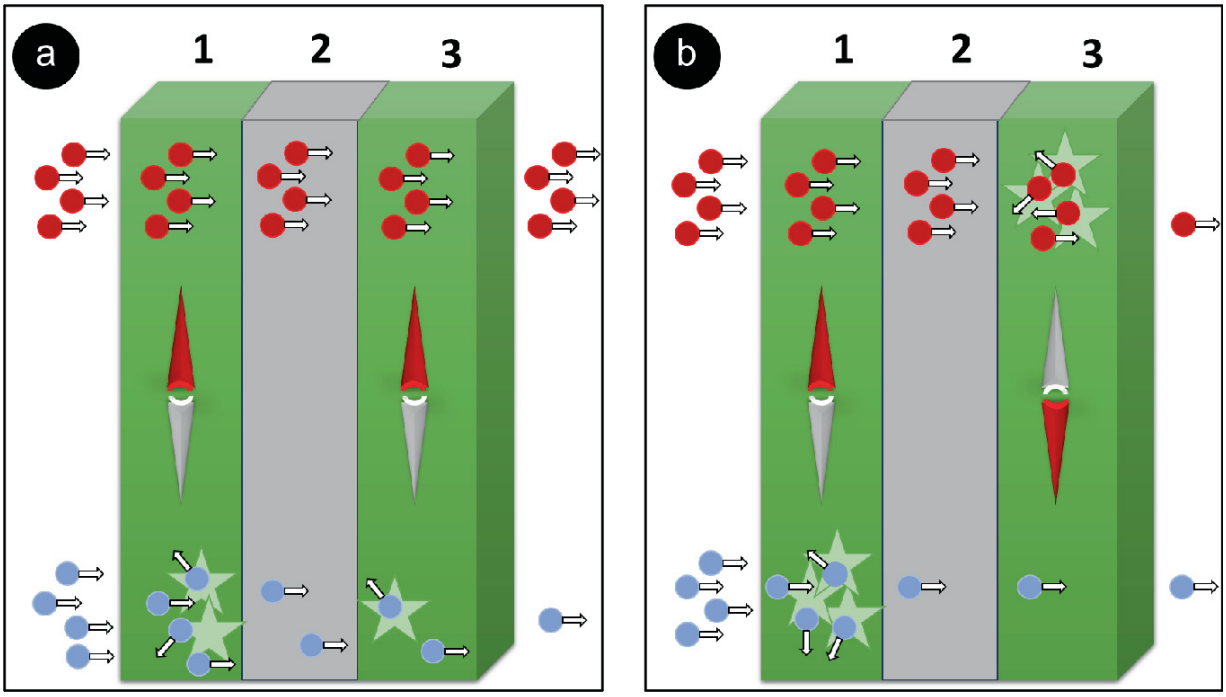

Fig. 5.14 **a** When the magnetization of both the magnetic layers are in the similar direction than that of the applied field, it is easy for the electrons to move through the structure due to their parallel spins. So, the total resistance will hence be low. This can be possible only when high magnetic field is applied. **b** When the magnetizations of the both the magnetic layers are in opposite direction then that of the applied field, so all electrons will be in the state of anti-parallel spin in one of the two layers. So, many electrons cannot move easily through the system and the total resistance will therefore be high. This can be possible only when no magnetic field is applied. It is redrawn by authors (https://www.nobelprize.org/prizes/physics/2007/popular-information/)

5.2.4 Applications of Antiferromagnetic Materials

Antiferromagnetic materials are the materials where the magnetic spins are anti-parallel to each other, resulting in small net magnetic moment. But they have small and positive magnetic susceptibility ($\chi > 0$) due to the presence of magnetic exchange interaction.

Traditionally some antiferromagnetic materials like $IrMn_3$ are used in magnetization along with the neighbouring ferromagnetic layers by interexchange mechanism, but Ir being a metal of platinum group has

criticality issues (Kohn et al. 2013). So, some different antiferromagnetic materials were developed. As, most of the antiferromagnetic materials have their Neel temperature (T_N) less than the room temperature, while some antiferromagnetic materials such as NiO, $CuFeS_2$, $NiMn_3$ and $PtMn_3$ and $MnSiN_2$ have Neel temperature greater than the room temperature, but these materials exhibit very poor corrosion resistance due to which they are not suitable for spintronic devices (Nayak et al. 2017).

In view of that, antiferromagnetic Heusler alloys are developed, which are classified into two parts: (a) full-Heusler alloys and (b) half-Heusler alloys (Gao 2013). These alloys are devoid of rare, expensive and toxic elements, which make them extremely important in the field of spintronic application. The antiferromagnetic Heusler alloys have huge application in storage materials for read/write heads and also for ultra-low damping MRAM.

A tetragonal Heusler alloy $Mn_{1.4}Pt_{0.9}Pd_{0.1}Sn$ (D_{2d} symmetry), which is antiferromagnetic skyrmions, was reported to be used as memory and logic elements for traditional and neuromorphic computing applications (Li et al. 2014).

5.3 Magnetic Materials in Biomedical Application

Magnetic materials specifically nanoparticles (MNPs) are utilized in various areas such as catalysis, biosensing, cancer theranostics, bacterial theranostics, agriculture and environment applications as shown in Fig. 5.15 (Ali et al. 2021). Among all the magnetic materials, superparamagnetic materials are preferred in biomedical application, as they do not retain the magnetization after

the removal of the external alternating magnetic field at room temperature. Generally, Fe_3O_4 (magnetite) and γ-Fe_2O_3 (maghemite) being non-toxic, biocompatible, inert, thermally stable and superparamagnetic in nature can be used for biomedical applications. Nowadays, a lot of surface functionalized magnetic nanoparticles are used as drug carriers in order to act as multifunctional material for the synergistic kind of treatment. Also, these magnetic nanoparticles were conjugated with some antibodies or targeting agents or lipid bilayers and fluorescing probes in order to target the specific disease site and bio-imaging purpose.

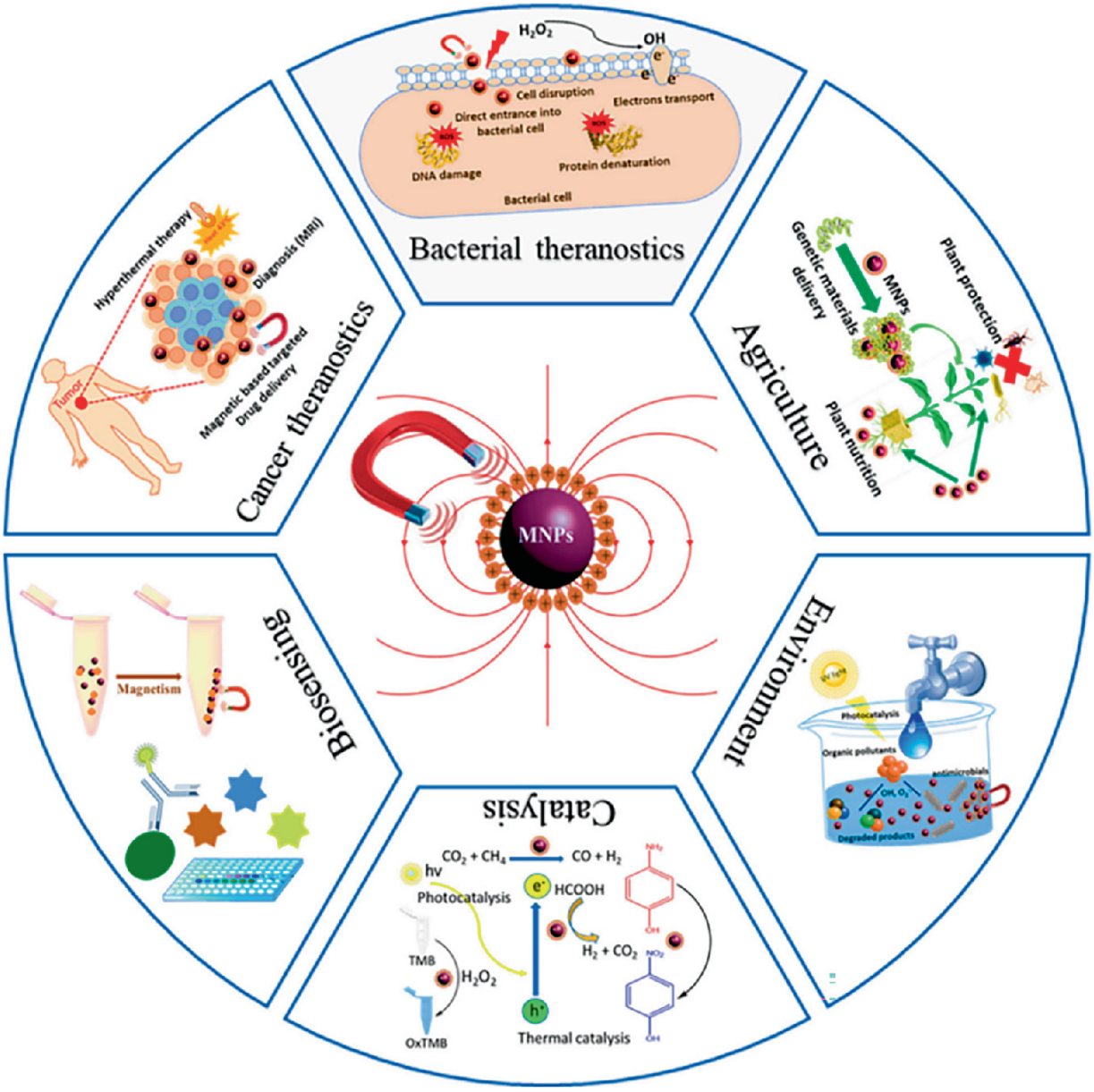

Fig. 5.15 Applications of magnetic nanoparticles in various fields. It is reproduced with permission under Creative Common License (Open Journal) from Frontiers Publishers (Ali et al. 2021)

In the case of agglomerated nanoparticles, they are only useful in the localized injection therapy, so monodispersed-based magnetic core@shell-based nanoparticles are also in great demand as individual particle has the tendency to target the disease site. As, these magnetic nanoparticles are hydrophobic in nature, in order to utilize them in

hyperthermia and biomedical application, it is important to make them water dispersible.

So, we can say that the magnetic nanoparticles have tailorable multifunctional applications such as MRI contrast agent, tissue engineering, magnetic hyperthermia, phot-thermal therapy (PTT), Photodynamic therapy (PDT), chemotherapy (drug-delivery agent), etc. as depicted in Fig. 5.16 (Martins et al. 2021; Kritika 2022).

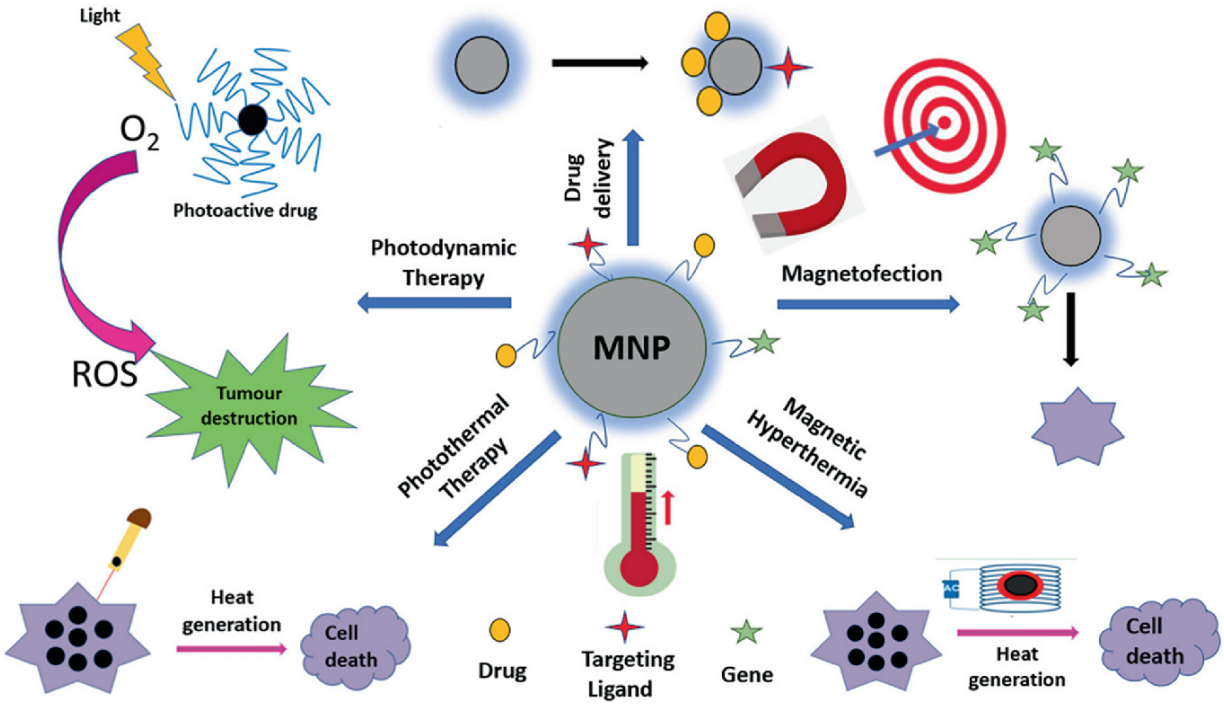

Fig. 5.16 Magnetic nanoparticles in biological applications. It is reproduced with permission under Creative Common License (Open Journal) from RSC Publishers (Kritika 2022)

There are various reports available in literature for converting the hydrophobic nanoparticles into hydrophilic substances, where mesoporous silica coating using CTAB (Cetyltrimethylammonium bromide) as template by reverse micro emulsion method or well-known Stober's method, or by normal silica amine coating using TEOS (Tetraethyl orthosilicate) and APTMS ((3-Aminopropyl) trimethoxysilane) by ligand exchange method, or by phase

transfer mechanism and so on. Also, polymer-coated nanoparticles play important role in biomedical application due to its morphology, size and biocompatibility. There are several strategies are present in literature for theranostics (therapy + diagnosis) application of magnetic materials for better performance. These magnetic nanoparticles are conjugated with some antibody or targeting agent like folic acid, loaded with drugs for chemotherapy, combined with some fluorescing probe or quantum dot for bio-imaging, so that on exciting with external alternating magnetic field, it also produces heat for the synergistic effect in the cancer cells as shown in Fig. 5.17 (Wu et al. 2020).

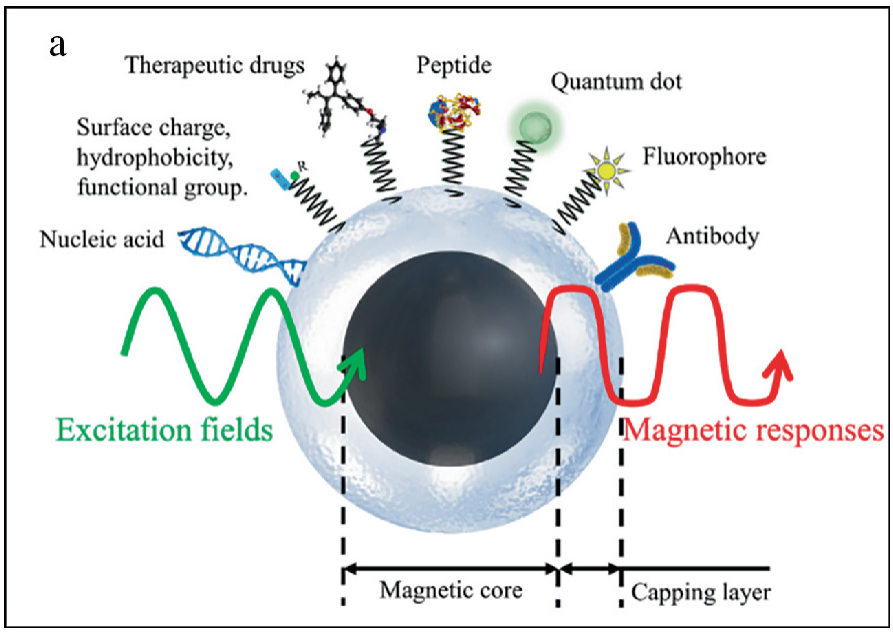

Fig. 5.17 Conjugation of magnetic materials with different molecules for multifunctional applications. It is reproduced with permission from ACS Publishers (Wu et al. 2020)

Various magnetic nanostructures are conjugated with nanophosphors such as Fe_3O_4@$NaYF_4$:Ho,Yb which shows multifunctional behaviour as hyperthermia treatment, bio-imaging and anticounterfeiting applications (Joshi et al. 2021, 2020, 2019; Perala et al. 2021a; Soni et al. 2021) $NaYF_4$:Er^{3+}/Yb^{3+}@SiO_2@AuNP@Fe_3O_4 is a well-reported

nanocomposite that is used for bio-imaging, cancer treatment by hyperthermia as well as photothermal therapy (Soni et al. 2019).

The effect of the size of the nanoparticles on the cellular uptake and liver MRI were investigated with PVP coated iron oxide nanoparticles, according to which 100 nm sized nanoparticles exhibit the greatest enhancement in the efficacy of the treatment (Huang et al. 2010).

There are different strategies for the conjugation of targeting agents and drugs in the magnetic nanoparticles, which are depicted in Fig. 5.18 (Ulbrich et al. 2016).

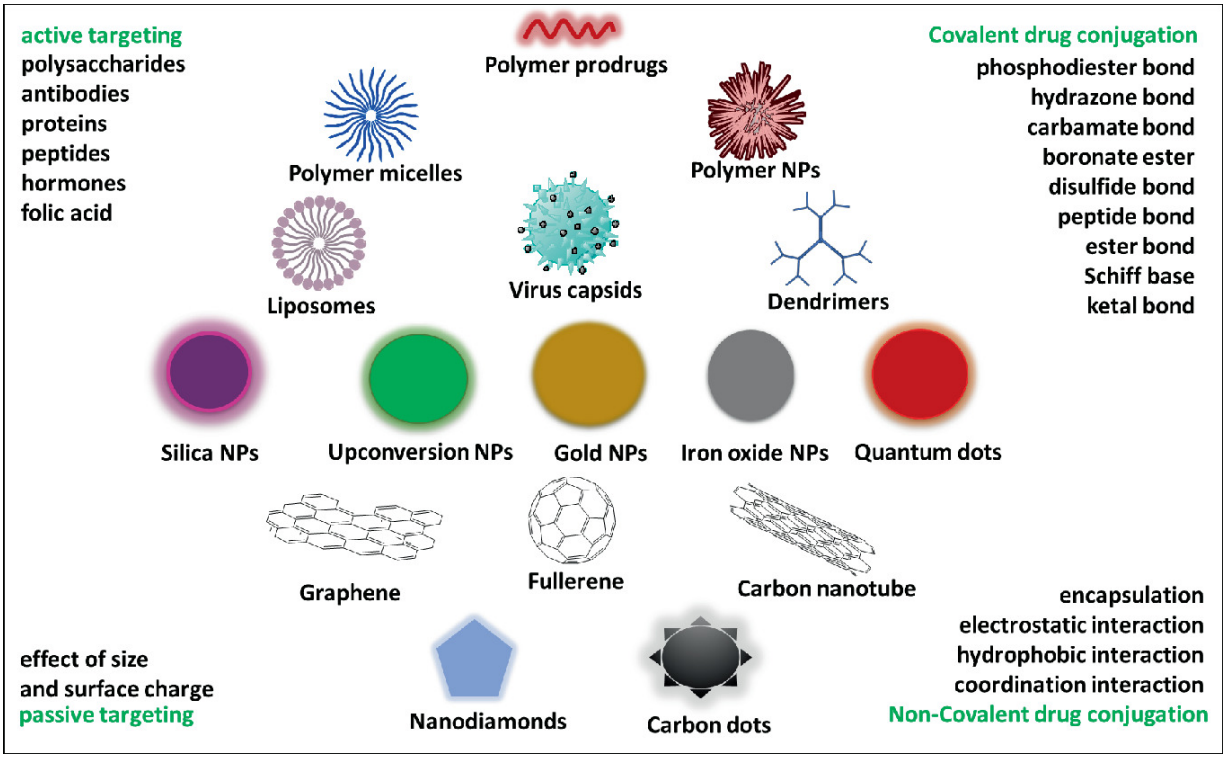

Fig. 5.18 Different strategies of conjugation of targeting and drug in the nanoparticles for biomedical application. It is redrawn and adapted with permission under Creative Common License (Open Journal) from ACS Publishers (Ulbrich et al. 2016)

There are various strategies for surface engineering are implied, where magnetic nanoparticles exhibit different models such as core–shell (includes single, reverse core–

shell, multicore, yolk-shell and decorated), core-shell$_a$-shell$_b$, dumbbell and janus and brush-like models as shown in Fig. 5.19 (Wu et al. 2016) for biomedical application (Wu et al. 2016).

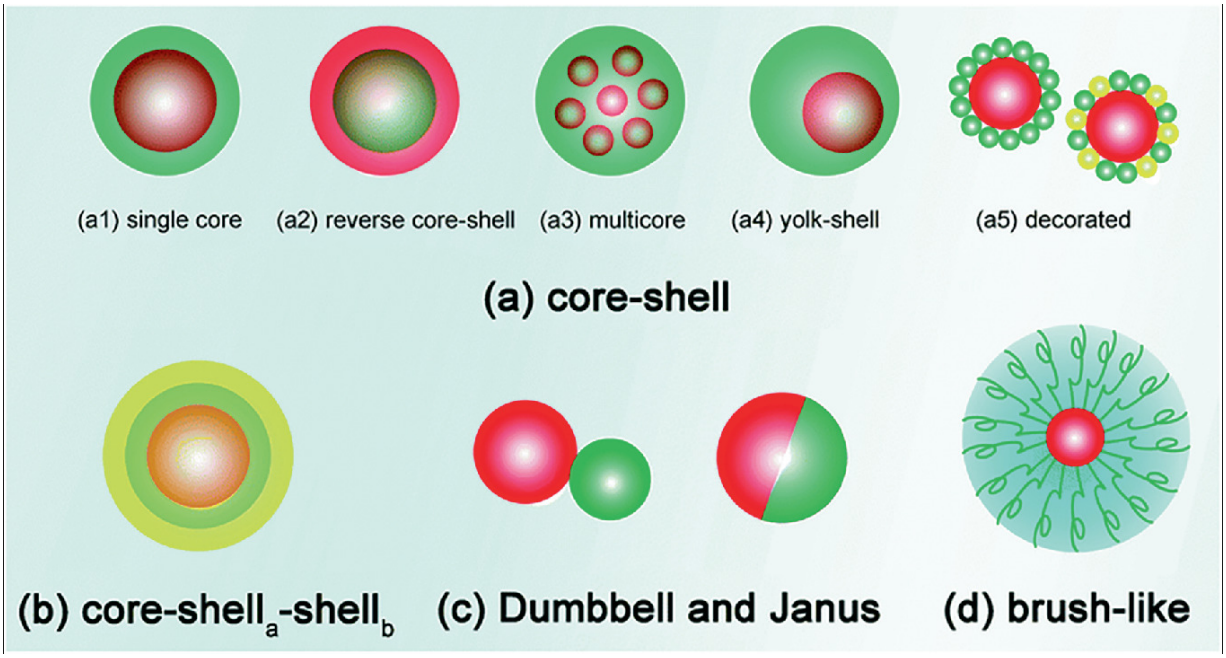

Fig. 5.19 Different models of magnetic materials in the form of core–shell. It is reproduced with permission under Creative Common License (Open Journal) from RSC Publishers (Wu et al. 2016)

The $MgFe_2O_4$ superparamagnetic nanoparticles were synthesized by co-precipitation method to be used as both produce aqueous and solid magneto-liposomes, for chemotherapy and hyperthermia treatment (Cardoso et al. 2018). An environmentally benign and versatile approach was adapted for the synthesis of γ-Fe_2O_3 nanoparticles coated with hydrophobic polymeric shell of poly(methyl methacrylate) (PMMA) and hydrophilic shell of chitosan shell, without using any surfactants, emulsifiers, or toxic organic solvents. Their synthesis procedure is represented in Fig. 5.20 (Ho and Li 2008).

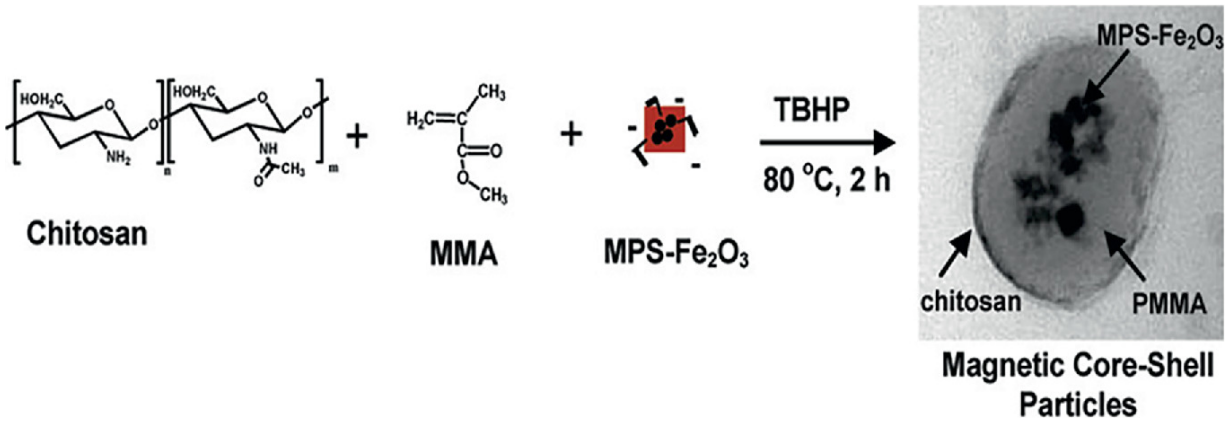

Fig. 5.20 Synthesis procedure of magnetic core–shell polymeric particles. It is reproduced with permission from ACS publishers (Ho and Li 2008)

Also, magnetic nano-micelles was prepared by chemical conjugation procedure, which is based on superparamagnetic iron oxide nanoparticles and the biocompatible polymer-Pluronic F127 or its copolymer with poly(DL-lactic acid) (F127–PLA) and it can also be used as drug carrier for combined therapy (Huang et al. 2011). The schematic illustration of different nano-sized magnetic composites in biomedical application is shown in Fig. 5.21 (Hervaultab and Thanh 2014).

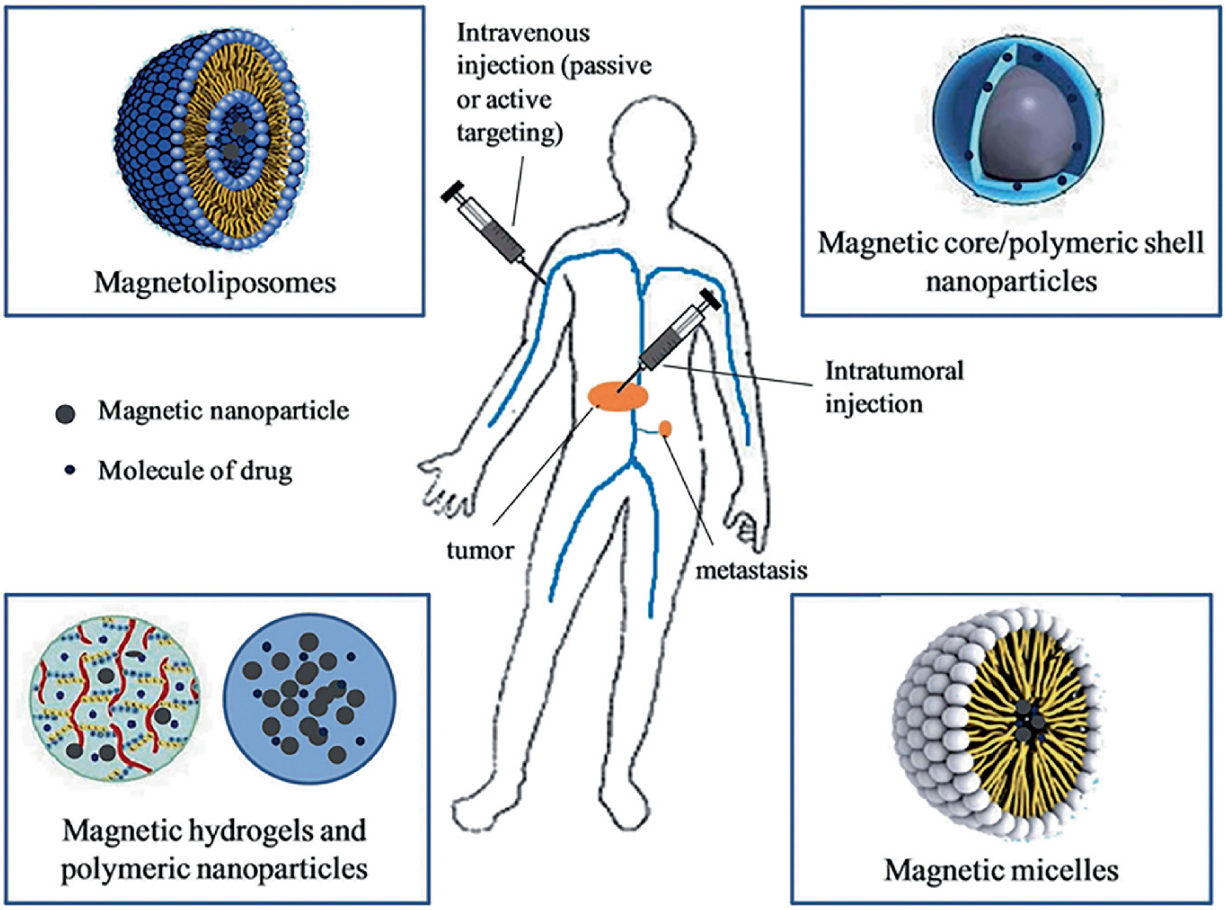

Fig. 5.21 The schematic illustration of different nano-sized magnetic composites in biomedical application. It is reproduced with permission under Creative Common License (Open Journal) from RSC Publishers (Hervaultab and Thanh 2014)

5.3.1 Hyperthermia-Based Treatment

Hyperthermia is a medical treatment which utilizes magnetic materials (ferromagnetic/ferrimagnetic materials) to kill the tumour cells by raising the temperature 40–42 °C under the influence of AC magnetic field. Now, the question is whether all the magnetic nanoparticles can be used for hyperthermia treatment? Commonly, the magnetic nanoparticles having hysteresis loss undergo hyperthermia like Fe_3O_4, γ-Fe_2O_3, Mn, Co, Ni doped ferrite and their core@shell-based models because of high magnetic moment (70–80 emu/g) under the influence of external magnetic field.

Hyperthermia is more advantageous over chemotherapy because it specifically targets the disease site and does not have any adverse effect on the healthy cells of the body, as the cancer cells are more sensitive to heat than the normal cells. The main cause of heat generation (known as thermal ablation) in hyperthermia is the dissipation of energy in the form of heat when ferro/ferrimagnetic materials come under the influence of external magnetic field. Although some materials became ferromagnetic in nature on decrease in particle size but not be used for hyperthermia purpose due to their low magnetic moments (e.g., ZnO). Also, FePd, FePt, CoPt, CoPd having tetragonal phase are some of the magnetic nanoparticles which lead to the generation of heat to kill the tumour cells. Some ferromagnetic metal carbides, nitrides, borides and phosphides have been used in hyperthermia (Ningthoujam and Joshi 2021). There are various mechanisms which are responsible for heat generation by applying alternating magnetic fields, through converting magnetic energy into thermal energy (Joshi et al. 2020, 2019; Srivastava et al. 2023; Singh et al. 2014; Ningombam et al. 2018; Dalal et al. 2018). It includes.

(1) Hysteresis loss,

(2) Eddy current,

(3) Néel's relaxations (single domain spin relaxation), and

(4) Brownian relaxations (particle–particle collision relaxation).

Generally, the generation of heat in the case of ferro/ferrimagnetic materials is due to the dissipation of energy in the form of heat in the hysteresis loop during the magnetization cycle. In a multi-domain system, all the

magnetic domains tend to align in the direction of the external magnetic field. When all the magnetic moments of each domain align in same direction under external high magnetic field, that state is known as saturation magnetization (Ms). When the magnetic field is lowered, the magnetization does not become zero, that state is known as remanent magnetization (Mr). The magnetic field required to attain the demagnetized state is known as coercivity (Hc). The whole magnetization curve continues to form a hysteresis loop and the integrated area under this loop gives the hysteresis loss in the thermal energy, which is required for hyperthermia as given in Fig. 5.22 (Hervaultab and Thanh 2014). The magnetic curve for superparamagnetic materials is shown in Fig. 5.23 (Hervaultab and Thanh 2014).

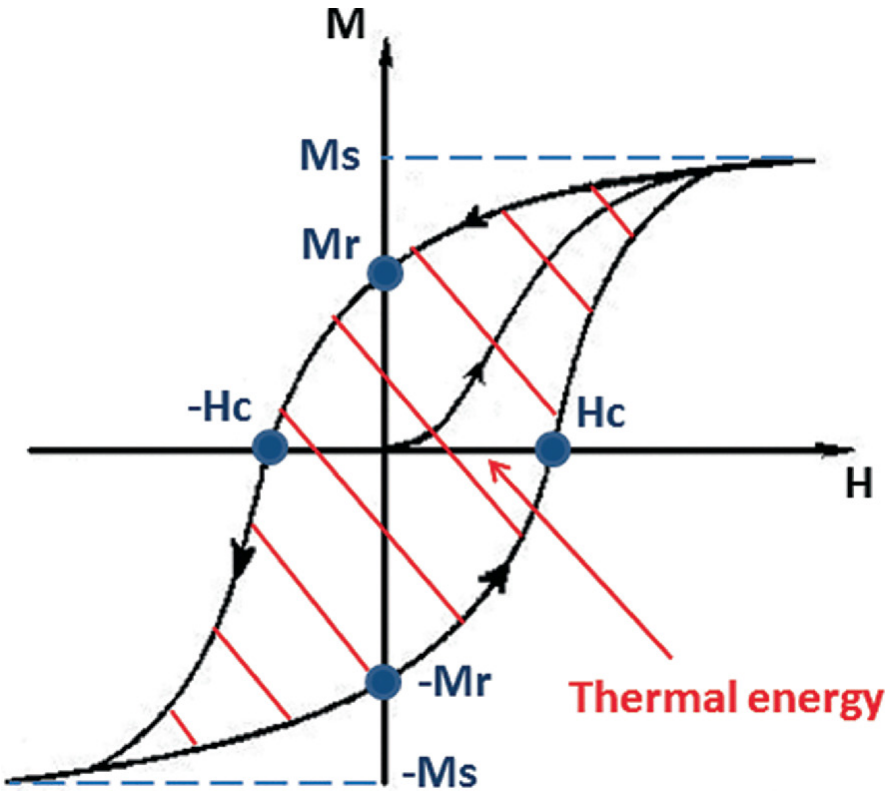

Fig. 5.22 Hysteresis loop of a ferromagnetic material. The area under the hysteresis loop represents the thermal energy dissipated during a magnetization cycle. It is reproduced with permission under Creative Common License (Open Journal) from RSC Publishers (Hervaultab and Thanh 2014)

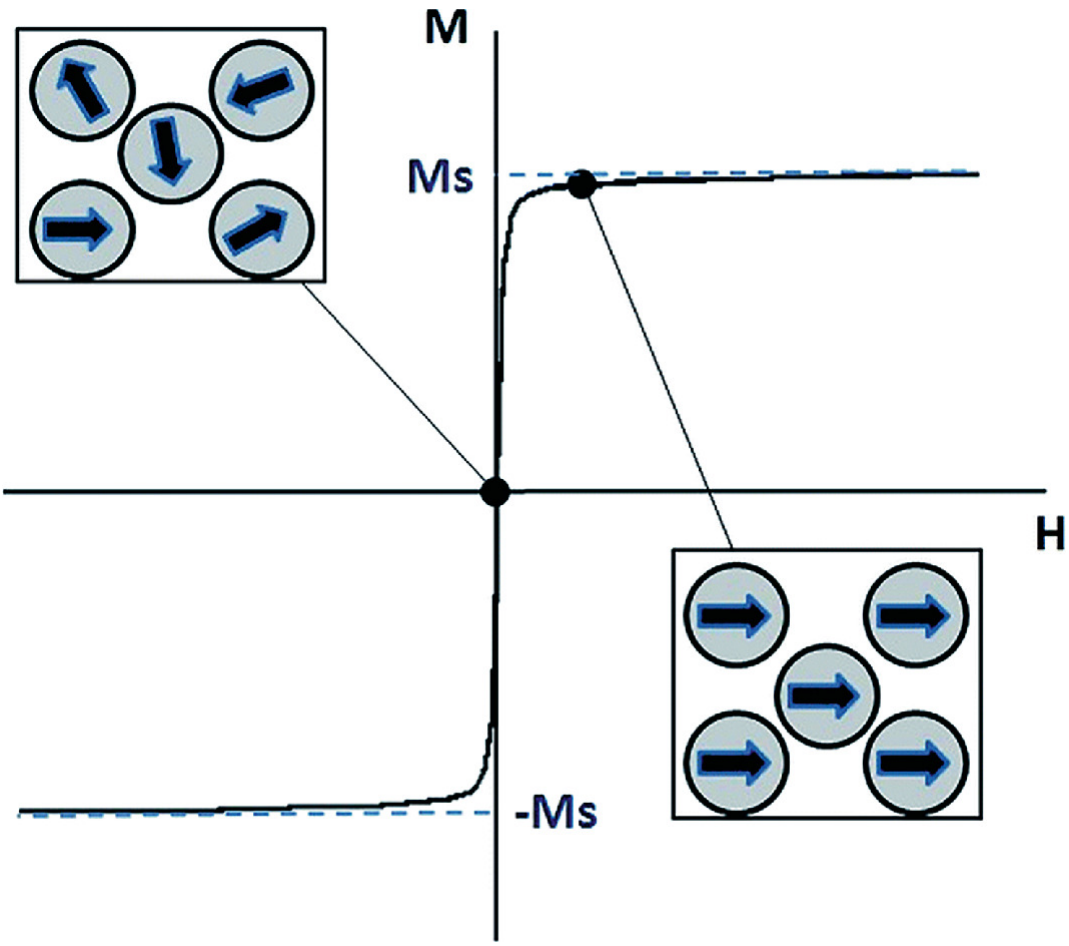

Fig. 5.23 The magnetic curve for superparamagnetic material. It is reproduced with permission under Creative Common License (Open Journal) from RSC Publishers (Hervaultab and Thanh 2014)

The hysteresis loss during the magnetization cycle under external alternating magnetic field is given by Eq. (5.1)

$$Area = f \int MdH \tag{5.1}$$

where f is the frequency of the alternating magnetic field.

The resonance frequency (f_0) in the LCR circuit is given by Eq. (5.2)

$$f_0 = \frac{1}{2\pi\sqrt{LC}} \tag{5.2}$$

where M, H, L and C are magnetization, applied magnetic field, inductor and capacitor, respectively.

Bulk magnetic materials have multi-domain system due to their large size, but the nano-size particles of ferro/ferrimagnetic materials behave as superparamagnetic material and regarded as single domain system. In case of single domain systems, the spin relaxation is very fast (10^{-9} s). So, the nanoparticles give rise to heat generation by relaxation phenomenon, which depends on the size of the particle and its anisotropic properties are basically of two types: Neel's relaxation (single domain spin relaxation) and Brownian relaxation (particle–particle collision relaxation). Neel's relaxation occurs due to the reorientation of the spins in the direction of external magnetic field with each field oscillations through an activation barrier, which is given by Eq. (5.3)

$$\tau_N = \tau_0 exp \frac{KV}{K_B T} \tag{5.3}$$

where τ_0 is the pre-exponential factor (10^{-9} to 10^{-13} s), $\tau_N$is Neel's relaxation time, K_B is the Boltzmann constant, K is the anisotropic constant of magnetic particles, V is volume of individual particle and T is temperature. Particles with smaller size need less energy for the rotation, hence the flipping of spins is fast.

Brownian relaxation is caused by the collision between two particles as friction arises during the rotation of the particle in the medium, which is given by Eq. (5.4)

$$\tau_B = \frac{3\eta V_H}{K_B T} \tag{5.4}$$

where η is the viscosity of the medium, V_H is hydrodynamic volume of particle. The rotation of spins is faster in low viscous medium.

In case of superparamagnetic materials, Neel's relaxation dominates over the Brownian relaxation, so the heat generation is due to Neel's relaxation which is

efficient for hyperthermia, because due to Brownian relaxation in the cells the viscous medium will restrict the rotation of the spins of the particles. The total relaxation (τ) due to the combination of both the phenomenon is given by Eq. (5.5)

$$\frac{1}{\tau} = \frac{1}{\tau_N} + \frac{1}{\tau_B} \tag{5.5}$$

The overall heat dissipated (P) is given by Eq. (5.6)

$$P = \mu_0 \chi'' f H^2 \tag{5.6}$$

where μ_0 is the permeability of free space, $\chi^{//}$ is the imaginary term for magnetic susceptibility. Magnetic susceptibility (χ) is expressed as M/H, where two real ($\chi^{/}$) and imaginary ($\chi^{//}$) terms are included. Now, the specific absorption rate (SAR) is used to quantify the heat loss by the magnetic nanoparticles, which is given by Eq. (5.7).

$$SAR = C\frac{\Delta T}{\Delta t}\frac{1}{m} \tag{5.7}$$

where C is the specific heat capacity of the sample, m is considered as ratio of the amount of magnetic particles to total amount of magnetic particles and solvent. It has not unit. ΔT/Δt is the slope of the time-dependent temperature. SAR has unit of J/s/Kg or W/Kg (Huang et al. 2011).

There are reports where core@shell-based magnetic nanoparticles are developed for therapy through AC magnetic field, as these materials are highly biocompatible and non-toxic to the body. For example, γ-Fe_2O_3@Mn_xO_y@SiO_2 nanoparticles are reported where they can behave as a single entity for therapy by AC magnetic field, imaging by FITC and targeting by folic acid simultaneously (Joshi 2022). The cytotoxicity of magnetic nanoparticles with hyperthermia and imaging in the presence of FITC is shown in Fig. 5.24 (Joshi 2022).

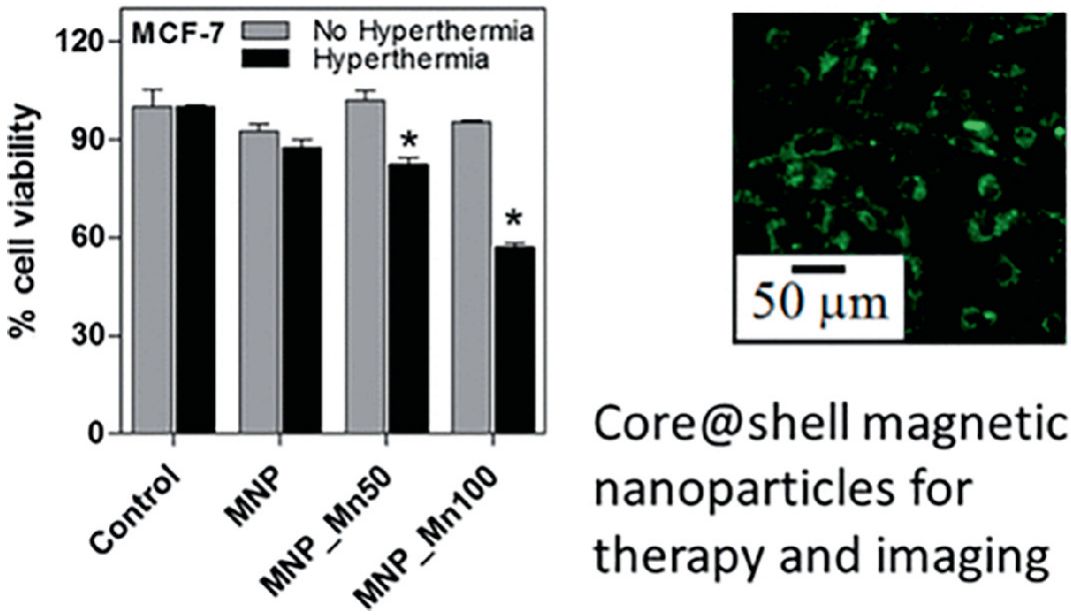

Fig. 5.24 γ-Fe_2O_3@Mn_xO_y@SiO_2core@shell magnetic nanoparticles for therapy and imaging. It is reproduced with permission from ACS Publishers (Joshi 2022)

The magnetic nanoparticles are covalently or non-covalently conjugated with drug molecules in order to achieve synergistic behaviour (magnetic hyperthermia + chemotherapy) for the treatment of cancer is represented in the scheme Fig. 5.25 (Hervaultab and Thanh 2014), and its effect is illustrated in Fig. 5.26 (Wu et al. 2016).

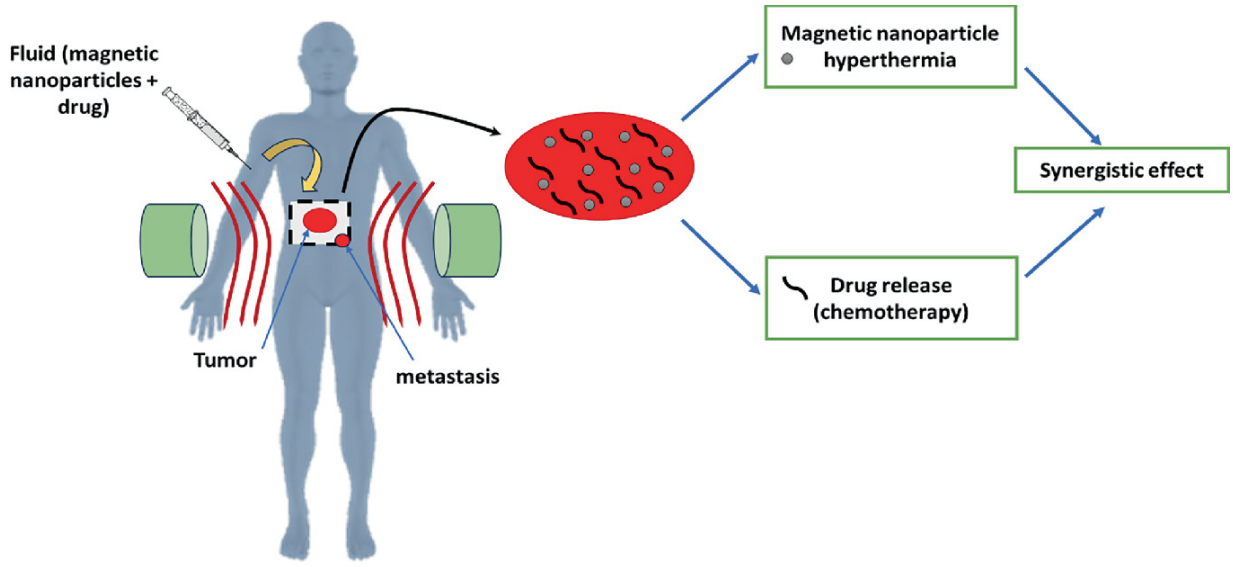

Fig. 5.25 Synergistic role of magnetic nanoparticles loaded with drug molecules leading to hyperthermia and chemotherapy, simultaneously. It is redrawn and adapted with permission under Creative Common License (Open Journal) from RSC Publishers (Hervaultab and Thanh 2014)

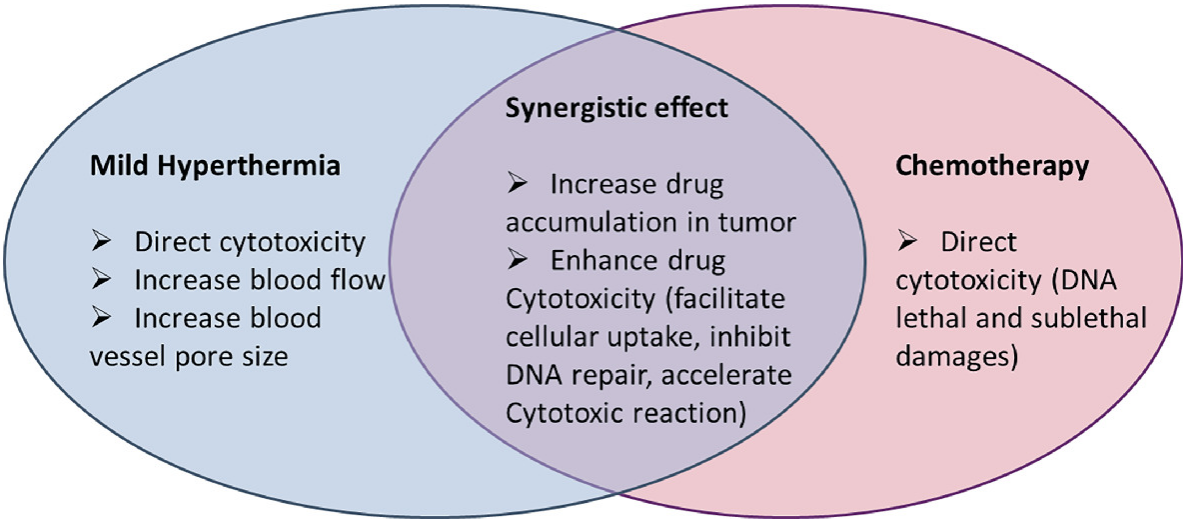

Fig. 5.26 Synergistic effect of magnetic nanoparticles in biomedical field. It is adapted and redrawn from RSC Publishers (Wu et al. 2016)

It is investigated that Co or Zn dopant on metal ferrite NPs tend to show improved SAR value. $(Zn_{0.4}Mn_{0.6})Fe_2O_4$ NPs having 15 nm size synthesized by thermolysis method exhibit four times higher SAR value than that of iron oxide NPs along with increased anisotropy and a saturation magnetization of 175 emu g^{-1}, which are useful as MRI agent as well as in hyperthermia (Jang et al. 2009).

Many ferrites such as Magnetite, Zn-ferrite, $LaSrMnO_3$, and many hybrids with luminescence and functionalized nanoparticles have been reported (Dalal et al. 2024, 2017; Dey et al. 2021; Fatima et al. 1203; Perala et al. 2021b; Mallick et al. 2018; Shetake et al. 2015; Barick et al. 2015; Thorat et al. 2014a, 2014b, 2733, 2013b, 2013c; Nikam et al. 2014; Parchur et al. 2014; Shete et al. 2013) for hyperthermia applications.

5.4 Magnetic Materials in Automobile, Supercapacitors and Industries

Several magnetic materials are used for automobile and industrial purpose such as in the vehicle systems, in transmission and oil chip collectors, steering sensors, power window motors, loudspeakers of car systems, power seat motors, actuators, generators (wind turbine), etc. So, mainly neodymium iron boron magnets are high energy materials, while samarium cobalt magnets are used as corrosion resistant materials. Also, ceramic magnets are economically fit, while alnico magnets are highly durable. Neodymium magnets are very light weight magnets so, suitable for vehicle systems as shown in Fig. 5.27 (https://www.hsmagnets.com/blog/examples-applications-using-neodymium-magnets/). Also, rare earth magnets are used in the automotive parts of trains as they are environment friendly in nature. These magnetic materials provide good performance, easy convenience and safety in the vehicles.

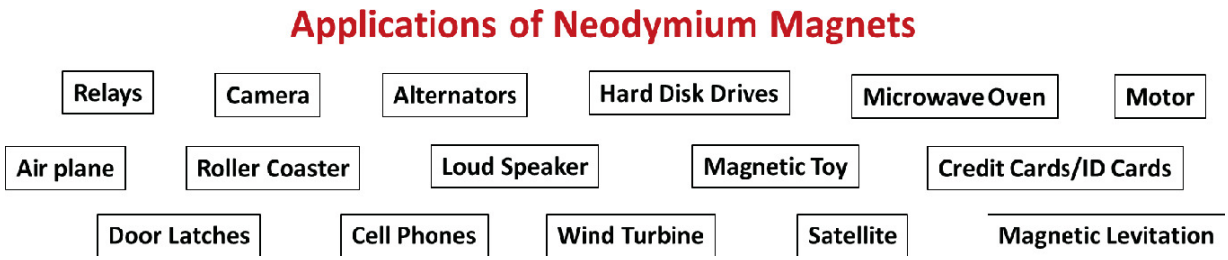

Fig. 5.27 Applications of Neodymium magnets in daily life. It is redrawn by author (https://www.hsmagnets.com/blog/examples-applications-using-neodymium-magnets/)

Electronics includes Sensors, hard disc drives, switches, etc. Automobile industry includes electricity motors (both hybrid and electric), power steering, etc. Medical includes MRI equipment and checking products. These are also used as magnetic separators which are useful for recycling

purpose, waste removal, quality control checking of foods and beverages, etc.

Also, N-doped graphene quantum dots (N-GQDs) grafted on Fe_3O_4-halloysite nanotubes (Fe_3O_4-HNTs) were reported as active anode materials which are used for supercapacitor applications as shown in Fig. 5.28 (Ganganboina et al. 2017). These N-GQD@Fe_3O_4-HNTs have excellent electrochemical property and high specific capacity. It is a low-cost electrode material with energy and power densities of 10.4–29 W h kg^{-1} and 0.25–5.2 kW kg^{-1} which is efficient for energy storage devices (Ganganboina et al. 2017).

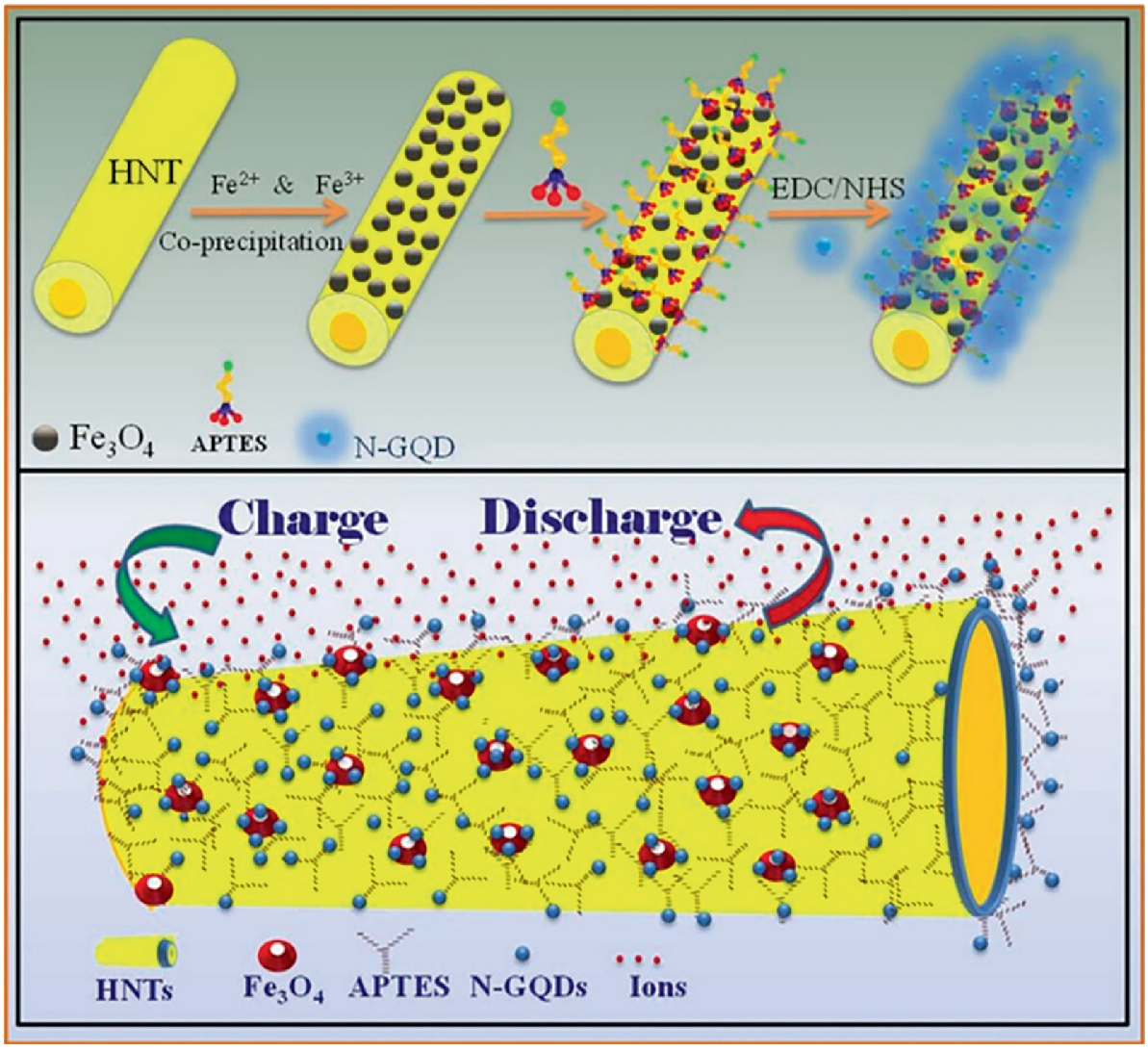

Fig. 5.28 Synthesis procedure of N-GQD@Fe_3O_4-HNTs and their applications in supercapacitor. It is reproduced with permission from Elsevier Publishers (Ganganboina et al. 2017)

5.5 Magnetic Nanoparticles in Catalysis

Magnetic separation by using magnetic catalyst proved to be a highly efficient tool, as the recovery and reusability of the catalyst without loss in its activity is the pre-requisite requirement for the sustainable development. The recovery of magnetic catalyst is easy as they only require external magnetic field as shown in Fig. 5.29 (Kumara and Gupta 2023). Halloysite nanotubes (HNTs) play important role on construction of surface functionalized nanocomposites for magnetic separation, drug delivery, microwave adsorption, etc. (Kumara and Gupta 2023).

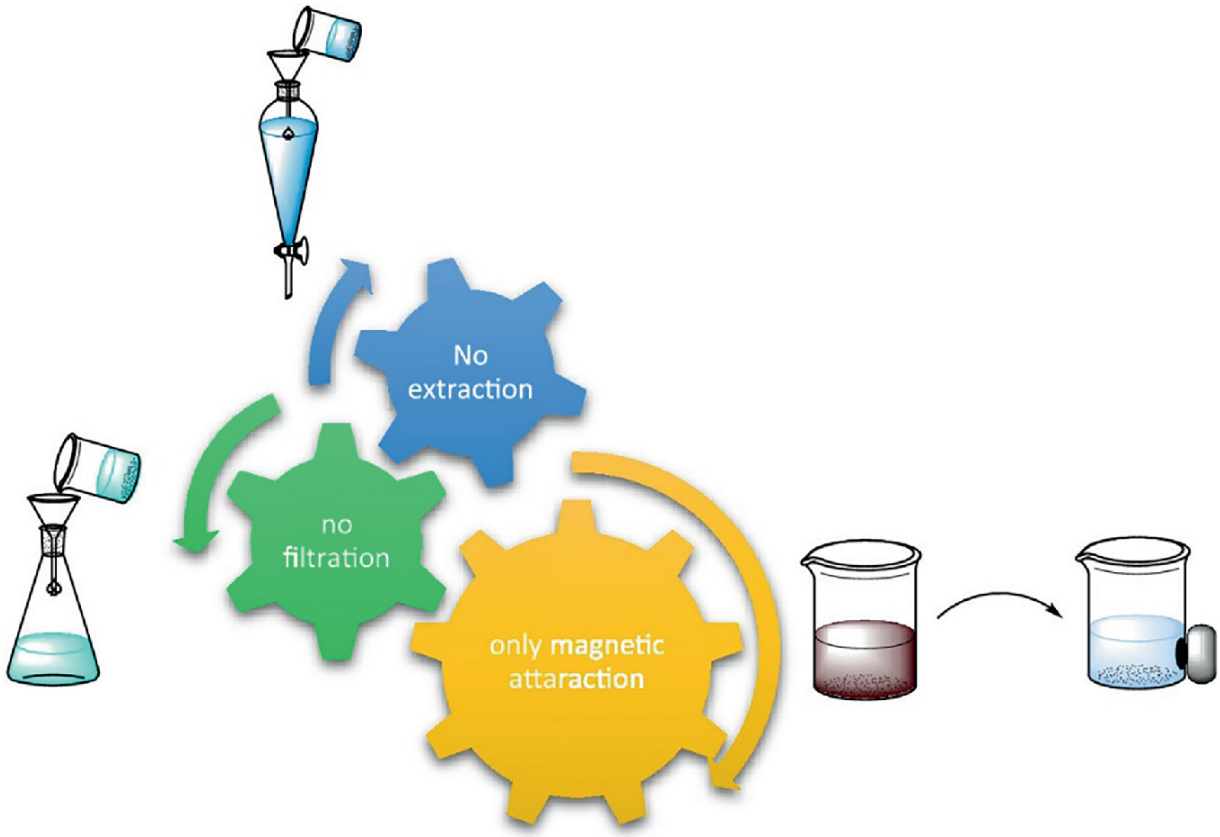

Fig. 5.29 Schematic representation of Catalytic separation by magnetic attraction. It is reproduced with permission from ACS Publishers (Kumara and Gupta 2023)

The various magnetic catalyst based on HNTs were synthesized for catalyzing various reactions like multi-component reactions, reduction and oxidation process, bio catalysis, etc. For instance, a new magnetic halloysite-based catalyst was synthesized by incorporating Fe_3O_4 nanoparticles into HNTs along with the covalent conjugation of 3-mercaptopropyl(trimethoxy)silane, which is further oxidized from thiol to sulphonic acid group using hydrogen peroxide to produce M-Fe_3O_4@HAL-SO_3H as shown in Fig. 5.30 (Kumara and Gupta 2023; Kumar et al. 2021). This Fe_3O_4@HAL-SO_3H catalyst has the tendency to efficiently accelerate the rate of reaction for the synthesis of bis-amides with solvent-free approach, while synthesis of 4H-pyrans with aqueous ethanol as shown in Fig. 5.31 (Kumara and Gupta 2023; Kumar et al. 2021).

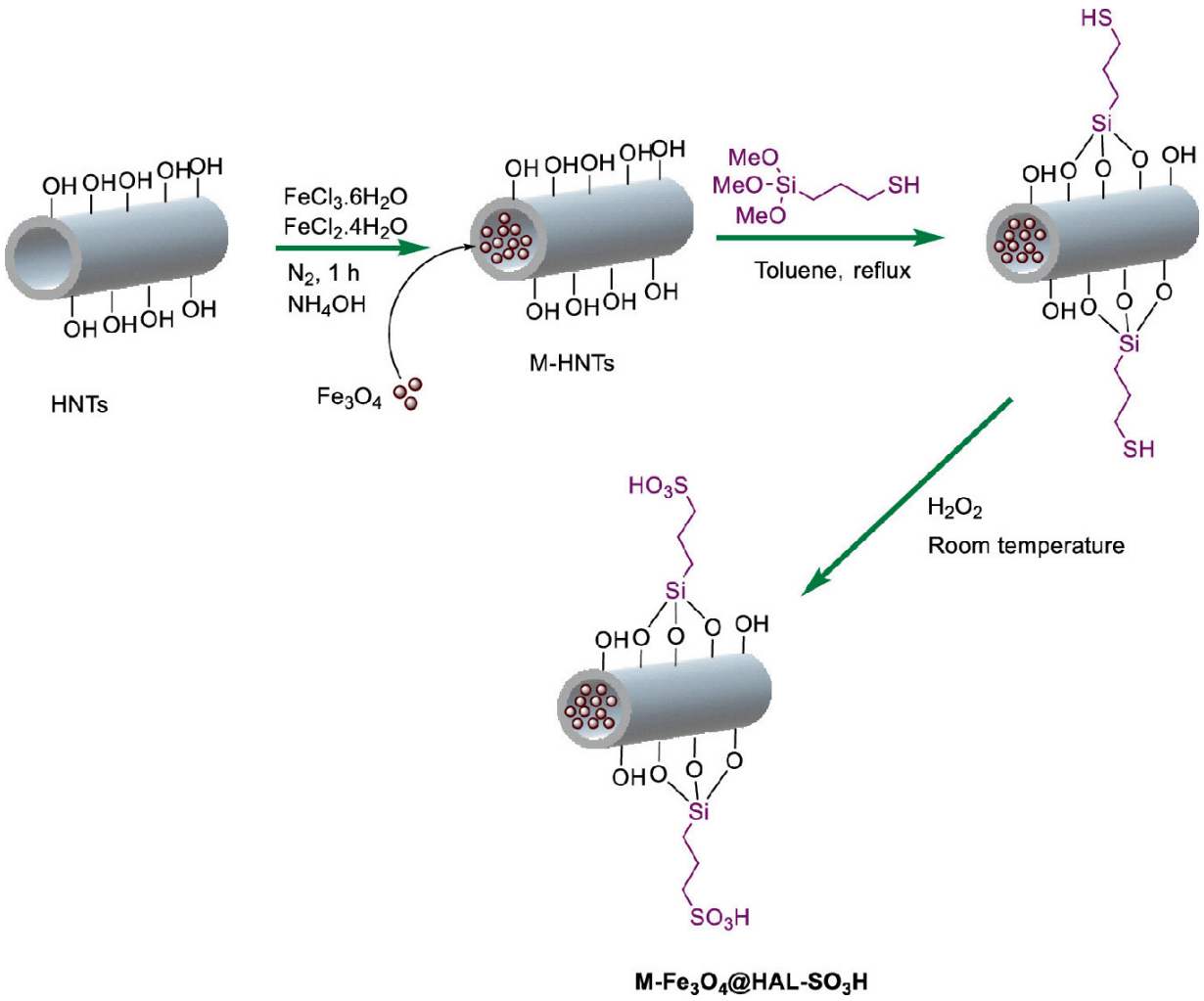

Fig. 5.30 Schematic Representation for the preparation of M-Fe_3O_4@HAL-SO_3H. It is reproduced with permission from ACS Publishers (Kumara and Gupta 2023)

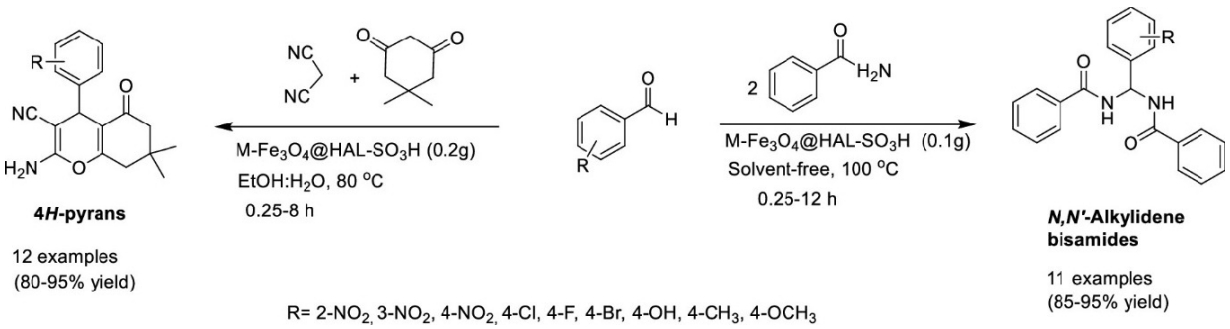

Fig. 5.31 Synthesis of Bis-amides and 4H-Pyrans using M-Fe_3O_4@HAL-SO_3H. It is reproduced with permission from ACS Publishers (Kumara and Gupta 2023)

Also, for the reduction of 4-nitrophenol to the corresponding aminophenol in presence of $NaBH_4$, a sandwich structured silver/HNT-based superparamagnetic nanocomposite catalyst (Ag/HNTs/Fe_3O_4) was synthesized, where Fe_3O_4 nanoparticles are loaded in silver nanorods containing HNTs as shown in Figs. 5.32 and 5.33 (Kumara and Gupta 2023; Mu et al. 2014).

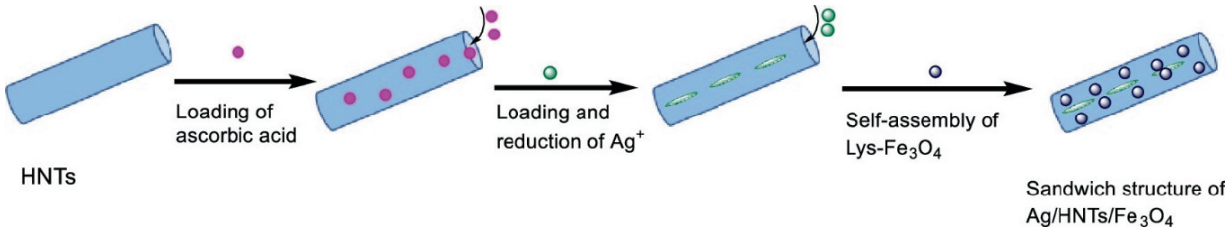

Fig. 5.32 Synthesis of Sandwich-Structured Ag/HNTs/Fe_3O_4 Catalyst. It is reproduced with permission from ACS Publishers (Kumara and Gupta 2023)

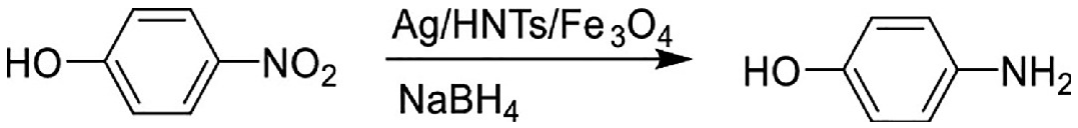

Fig. 5.33 Reduction reaction of 4-Nitrophenol to Aminophenol. It is reproduced with permission from ACS Publishers (Kumara and Gupta 2023)

A selective, efficient and cost-effective Fe_2O_3-HNTs photocatalyst was prepared for the oxidation of benzyl alcohols to aldehydes and 2-naphthol to BINOL, where O_2 and hydrogen peroxide (H_2O_2) are oxidants. It was synthesized by loading of Fe_2O_3 in ethylenediaminetetraacetic acid (EDTA) mediated HNTs (Baruah et al. 2021) as shown in Figs. 5.34 and 5.35 (Kumara and Gupta 2023).

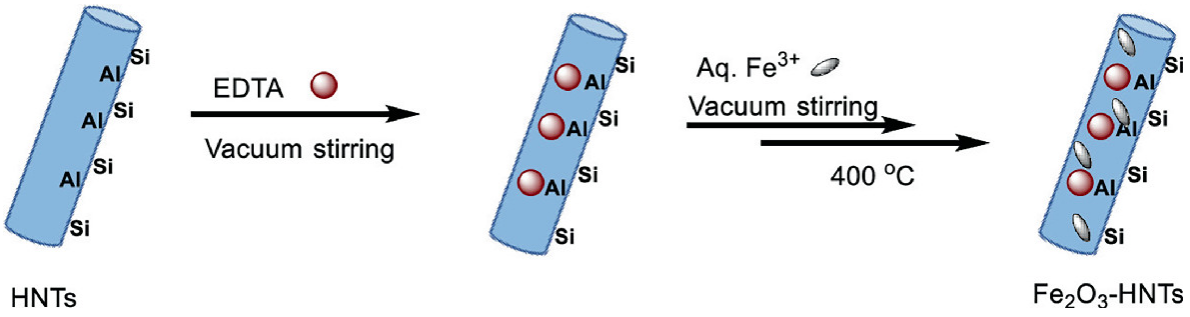

Fig. 5.34 Preparation of Fe_2O_3-HNTs. It is reproduced with permission from ACS Publishers (Kumara and Gupta 2023)

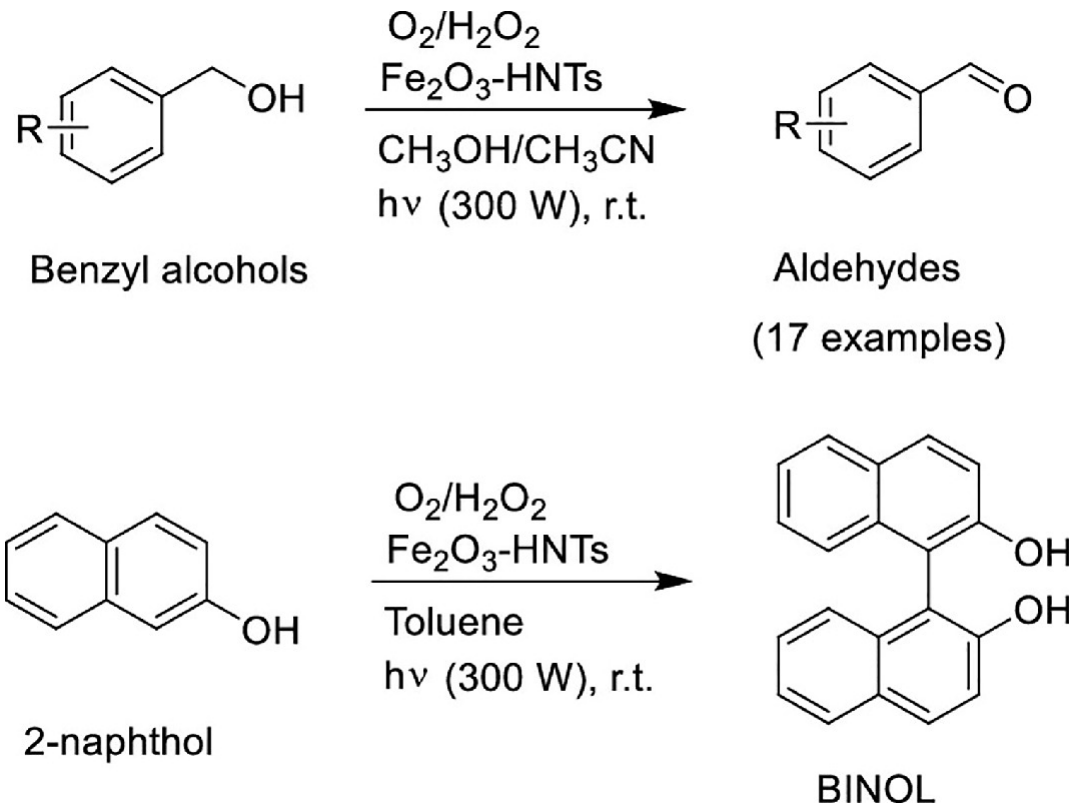

Fig. 5.35 General route for visible-Light-Assisted Oxidation of Benzyl Alcohol and Oxidative C–C Coupling of 2-Naphthol. It is reproduced with permission from ACS Publishers (Kumara and Gupta 2023)

An environmentally benign biocatalyst having superparamagnetic Fe_3O_4 nanoparticle loaded in HNTs and surface functionalized with γ-aminopropyltriethoxysilane (APTES)-linked glutaraldehyde (GTA) nanocomposite for the degradation of micropollutants like SMX by the immobilization of laccase as shown in Fig. 5.36 (Kumara and Gupta 2023). The obtained A-M-HNTs-GTA-Lac

composite has high thermal stability, good storage ability and reusability (Kumara and Gupta 2023; Kadam et al. 2017).

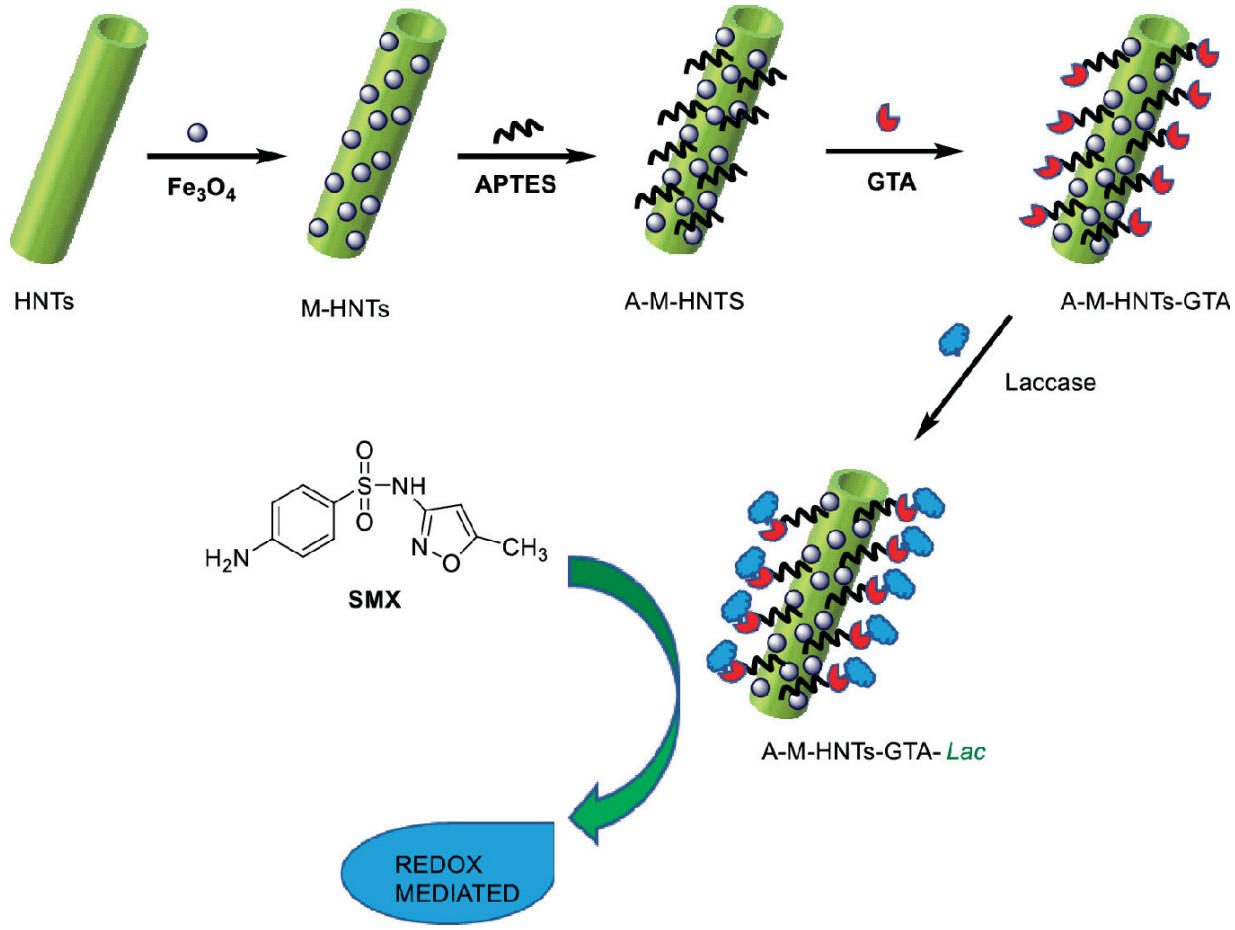

Fig. 5.36 Procedure of the Immobilization of Laccase and degradation of Sulfamethoxazole. It is reproduced with permission from ACS Publishers (Kumara and Gupta 2023)

5.6 Magnetic Nanoparticles in Photocatalysis

For sustainable development of energy and environment, the solar energy is converted into chemical energy through photocatalysis. The solar energy is considered as a natural, eco-friendly and abundant source of energy, which is useful for the photocatalytic and catalysis process. Photocatalysis

is considered as promising approach for the storage and conversion of solar energy into chemical energy in the form of fuels so that they can be useful in various solar-driven reactions, like CO_2 reduction and photocatalytic overall water splitting. Also, the degradation of organic molecules such as dyes and other contaminants through photocatalysis improves the quality of air and water by purifying them. Figure 5.37 (Wang et al. 2012) represents the effects of magnetic field on photocatalytic driven reactions.

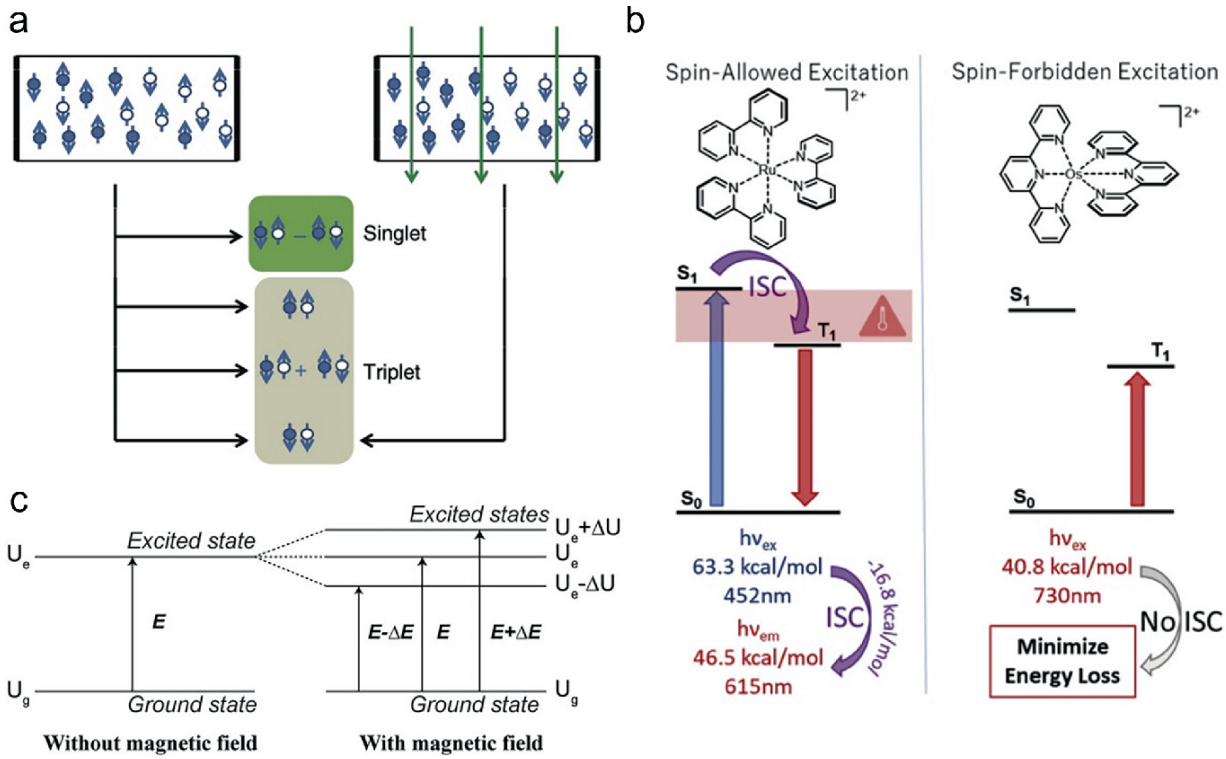

Fig. 5.37 Effect of magnetic field in photocatalysis after light absorption. **a** Spin-polarization effect in an organic optoelectronic device. It is reproduced with permission from Springer Nature Publishers (Wang et al. 2012). **b** Jablonski diagram for $[Ru(bpy)_3]^{2+}$ and a schematic diagram of the S_0 to T_1 excitation in Os(II) polypyridyl complex. It is reproduced with permission under Creative Common License (Open Journal) from ACS Publishers (Ravetz et al. 2020). **c** Schematic diagram for the splitting of energy levels by Zeeman effect. It is reproduced with permission from Elsevier Publishers (Wang et al. 2022)

The absorption of light by magnetic semiconductor photocatalysts increases due to the presence of external

magnetic field. According to Fig. 5.37a (Wang et al. 2012), the orientation of electrons and holes spins are randomly aligned in the absence of magnetic field, where singlet and triplet excitons exist in a ratio of 1:3, while the orientation of electrons and holes are in the same direction of magnetic field in the presence of external magnetic field. Due to the change in the electronic structure of photocatalysts, the light absorption increases. This type of spin-polarization effect occurs in an organic optoelectronic device. The presence of magnetic field changes the spin multiplicity of the system by aligning the spins with from singlet (less stable, high energy) to triplet state (more stable, less energy) (Wang et al. 2012).

It is reported that the presence of external magnetic field has remarkably increased the absorption wavelength of Os(II) polypyridyl complex, which absorbs the light and changes the spins from singlet to triplet state and consequently allows the forbidden singlet-to-triplet excitation with minimum energy loss as shown in Fig. 5.37b (Wang et al. 2012).

In the case of extended solid systems, the influence of external magnetic field leads to the Zeeman splitting by changing the amount of energy required for the excitation of electrons, which ultimately changes the band structure of photocatalysts. Due to Zeeman splitting, excited state splits into different states, which enables the excitation of ground state electrons of different energies. As the Zeeman energy is directly proportional to the magnetic field strength, the Zeeman splitting energy is smaller than Gibb's free energy of photocatalytic reactions as shown in Fig. 5.37c (Wang et al. 2022). For Zeeman splitting, large magnetic field is required, which changes the band structure of the solid photocatalysts and is called the Paschen-Back effect (Wang et al. 2022).

The presence of magnetic fields affects the catalytic systems by changing the magnetoresistance behaviour, by

introducing electromotive force, Lorentz force and spin polarization. According to Fig. 5.38, change in magnetoresistance (MR) is given as in Eq. (5.8)

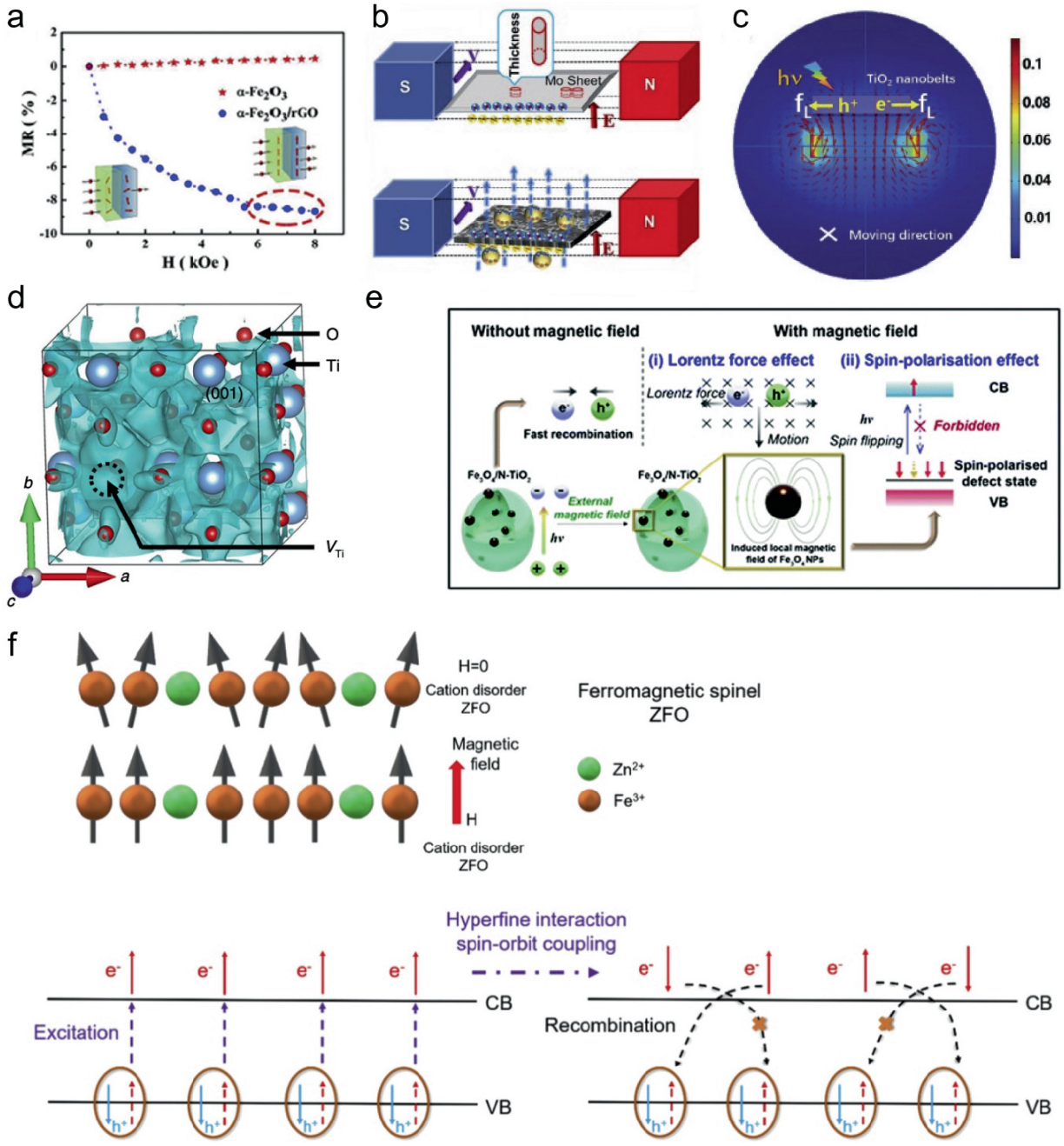

Fig. 5.38 Effect of magnetic field in separation of charge carrier in catalysis. **a** Negative Magnetoresistance occurred in α-Fe_2O_3/rGO composite as compared to α-Fe_2O_3. It is reproduced with permission from ACS Publishers (Li et al. 2018). **b** Negative magnetoresistance in $CoFe_2O_4/MoS_2$ hybrid structure. It is

reproduced with permission from Elsevier Publishers (Zhao et al. 2021). **c** Schematic diagram of the Lorentz force effect on holes and electrons. It is reproduced with permission under Creative Common License (Open Journal) from Wiley Publishers (Gao et al. 2019). **d** (001)-Planar 3D spatial distributions of spin polarization of the Ti-defected $Ti_{15}O_{32}$system. It is reproduced with permission under Creative Common License (Open Journal) from Springer Nature Publishers (Pan et al. 2020). **e** Representation of carrier separation with and without magnetic field in Superparamagnetic Fe_3O_4/N-TiO_2 photocatalyst. It is reproduced with permission under Creative Common License (Open Journal) from RSC Publishers (Li et al. 2022). **f** Mechanism for spin polarization enhancing the suppression of photoinduced carrier recombination for ferromagnetic $ZnFe_2O_4$. It is reproduced with permission from ACS Publishers (Gao et al. 2021)

$$MR\% = \frac{R_H - R_0}{R_0} \tag{5.8}$$

where R_H and R_0 are the resistance in the presence and absence of external magnetic field, respectively.

If the change in magnetoresistance is negative, it means that the resistance in the presence of magnetic field is less than the resistance in the absence of the magnetic field, which subsequently facilitates the easy migration of charge carriers to the reaction sites and improves the photocatalytic activity. It is reported that such kind of negative magnetoresistance can be easily seen in the α-Fe_2O_3/reduced graphene oxide (rGO) catalyst in comparison to the α-Fe_2O_3. In the presence of external magnetic field, the migration of the charge carriers increases from α-Fe_2O_3 to rGO, which leads to faster decomposition of rhodamine B as shown in Fig. 5.38a (Li et al. 2018).

The negative magnetoresistance is also reported in the $CoFe_2O_4$/MoS_2 hybrid structure, where the charge transfer increases on the influence of magnetic field by 89% across the interface for the efficient degradation of Congo red as shown in Fig. 5.38b (Zhao et al. 2021).

Another factor that occurs in the presence of magnetic field is described in the terms of the Lorentz force which occurs on the charge carriers. It is reported that the Lorentz force affects the photocatalytic degradation in TiO_2 and rGO/TiO_2 catalysts under the influence of magnetic field Fig. 5.38c (Wang et al. 2013; Bian et al. 2021; Gao et al. 2019). Also, it is reported that the spin polarization of TiO_2 occurs in the presence of magnetic field, which increases the photocatalytic performance by the use of Ti vacancies, as it limits the recombination of charge carriers. The rate of reaction increases by 54% due to the effect of spin polarization in TiO_2 system Fig. 5.38d (Pan et al. 2020).

The introduction of superparamagnetic nanoparticles like Fe_3O_4 and γ-Fe_2O_3 as support for photocatalysis increases the spin polarization effect with stronger magnetic field. Superparamagnetic Fe_3O_4/N-TiO_2 photocatalyst is designed with efficient photocatalytic activity and increased spin polarization from 8.9% to 22.6% for water splitting reaction. Figure 5.38e illustrates the Lorentz as well as spin polarization effect in the absence and presence of magnetic field (Li et al. 2022).

A similar kind of spin-polarization effect is seen in the ferromagnetic $ZnFe_2O_4$ material Fig. 5.38f (Gao et al. 2021).

5.7 Magnetic Materials as Bio-sensors

Superparamagnetic materials are used as bio-sensors for various analyte detection. These particles have ability to increase the sensitivity of the device for the detection of analytes even in very dilute concentrations of biological samples like in saliva or urine, for touch-free and

instantaneous magnetic sensing. Some materials are also used for immunoassay as analyte detection. The working mechanism of these nanoparticles is shown in Fig. 5.39 (Ha et al. 2018).

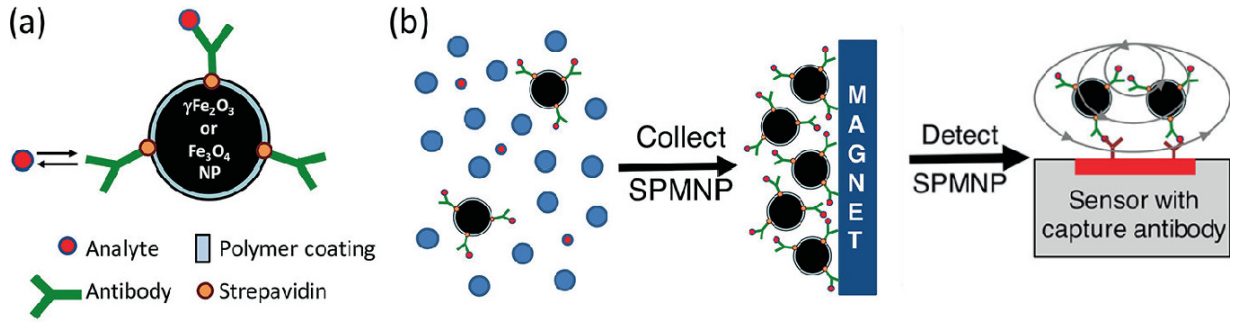

Fig. 5.39 Different modifications of superparamagnetic particles are possible for analyte detection. **a** These superparamagnetic materials are conjugated with different antibodies for specific binding of analyte under magnetic field for immunoassays. **b** Collection and detection of the analyte under magnetic field. It is reproduced with permission under Creative Common License (Open Journal) from ACS Publishers (Ha et al. 2018)

The combination of magnetic separation and magnetic relaxation switching is reported for the one step detection of pathogens and viruses. The magnetic of 0.01 T helps to separate the large magnetic beads (250 nm diameter) from small magnetic beads (30 nm diameter) with use of transverse relaxation time of water molecules as the signal for the immunoassay, with high sensitivity and reproducibility than the traditional methods as shown in Fig. 5.40 (Chen et al. 2015a).

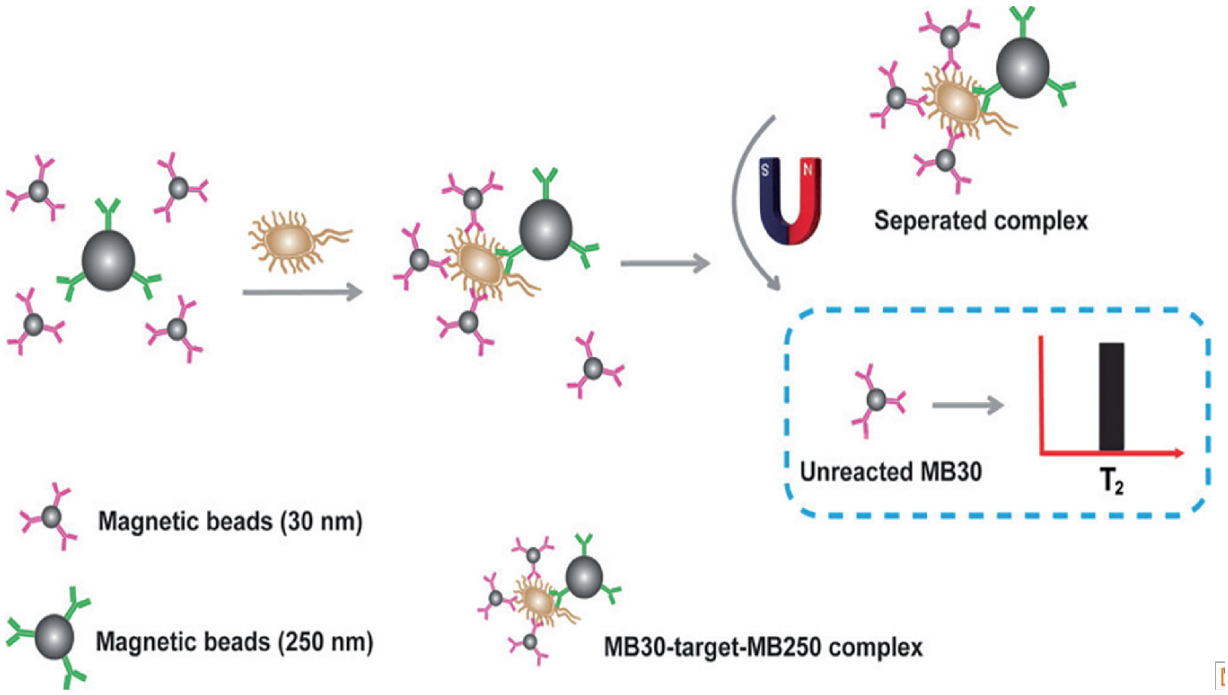

Fig. 5.40 Schematic representation of magnetic separation and magnetic relaxation switching. It is reproduced with permission from ACS publishers (Chen et al. 2015a)

Not only surface functionalization of superparamagnetic nanoparticles passivates the surface of the nanoparticles, but also increases its dispersion ability in solvents. The shell of different polymeric materials such as poly(ethylene glycol) [PEG], and poly(vinyl acetate) [PVA], inorganic materials such as silica and gold and carbon-based materials such as glucose are utilized to stabilize the nanoparticles. The coating with different materials prevents aggregation by creating the repulsion between the nanoparticles to overcome the attractive van der Waals forces. It is reported that PEG coated superparamagnetic nanoparticles are stable for one month in the cell culture media (Torrisi et al. 2014).

Diabetes is considered as a worldwide disease that occurs due to the high sugar concentration in the blood in human bodies. The rapid diagnosis of sugar level in the body is very important as it leads to many dangerous

diseases. A lot of glucose biosensors were widely developed for the detection of glucose level in the blood.

Magnetic nanocomposites based glucose biosensors have more advantages over the traditional biosensors such as large surface area low toxicity, biocompatibility and high absorption capacity. Over the past decades, a lot of reports are available on graphene-based nanocomposites as glucose biosensors, as it increases the sensitivity and detection limits. For this, an in situ deposition approach of Fe_3O_4 in graphene oxide sheet-based nanocomposite for the immobilization of glucose oxidase in the glassy carbon electrode for the fast electron transfer and good catalytic activity as shown in Fig. 5.41 (Wang et al. 2018). A facile one step procedure of poly (styrene-glycidyl methacrylate)-Fe_3O_4nanocomposite is reported for glucose biosensing (Hossain et al. 2023).

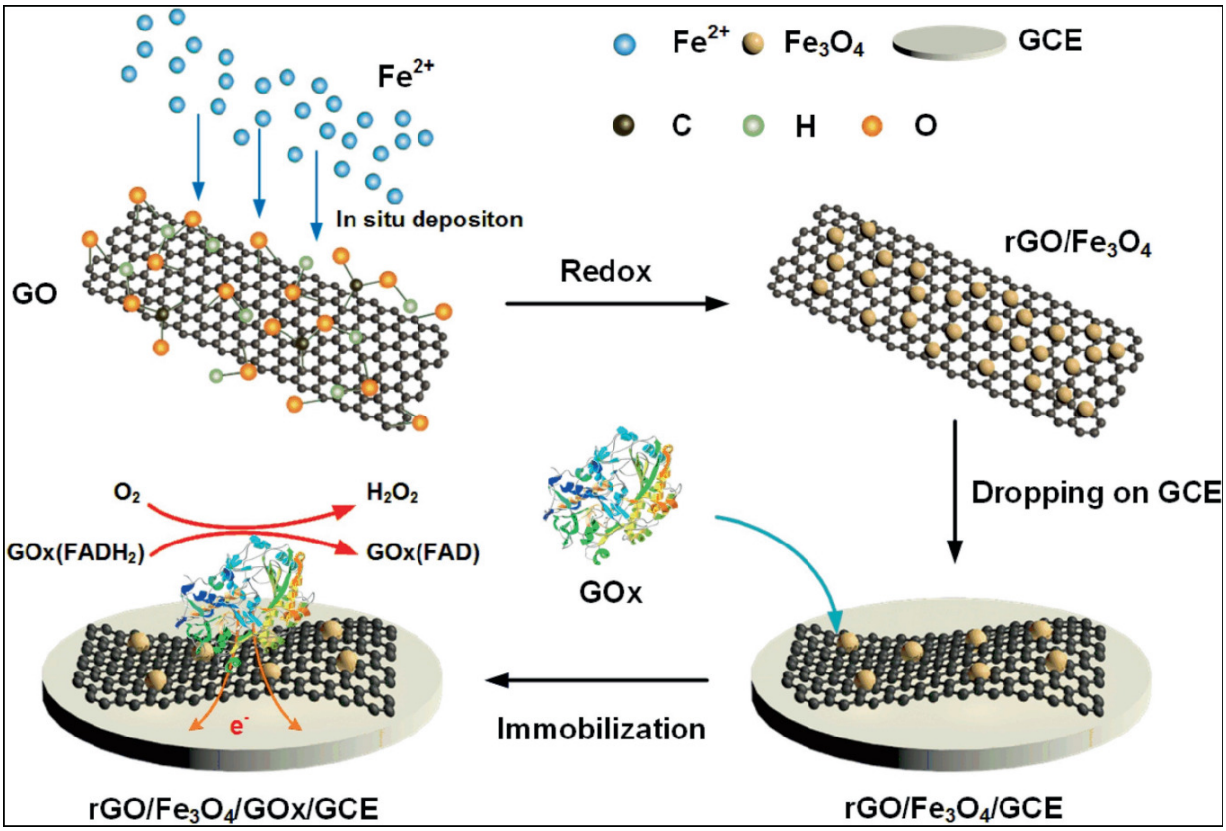

Fig. 5.41 Schematic illustration of synthesis and fabrication of $rGO/Fe_3O_4/GO_x/GCE$. It is reproduced with permission from Elsevier Publishers (Wang et al. 2018)

Also, a lot of magnetic nanocomposites were reported for the nucleic acid-based biosensors. The surfaces of magnetic nanocomposites are functionalized by specific molecules such as aptamers, antibodies, proteins, viruses and nucleic acids. The transducer converts the chemical signal into physical signal in the form of optical, electrochemical, piezoelectric and magnetic field for further signal analysis. This is the fundamental scheme for the isolation of specific analytes using magnetic nanocomposites for biosensing as shown in Fig. 5.42 (Popova et al. 2023).

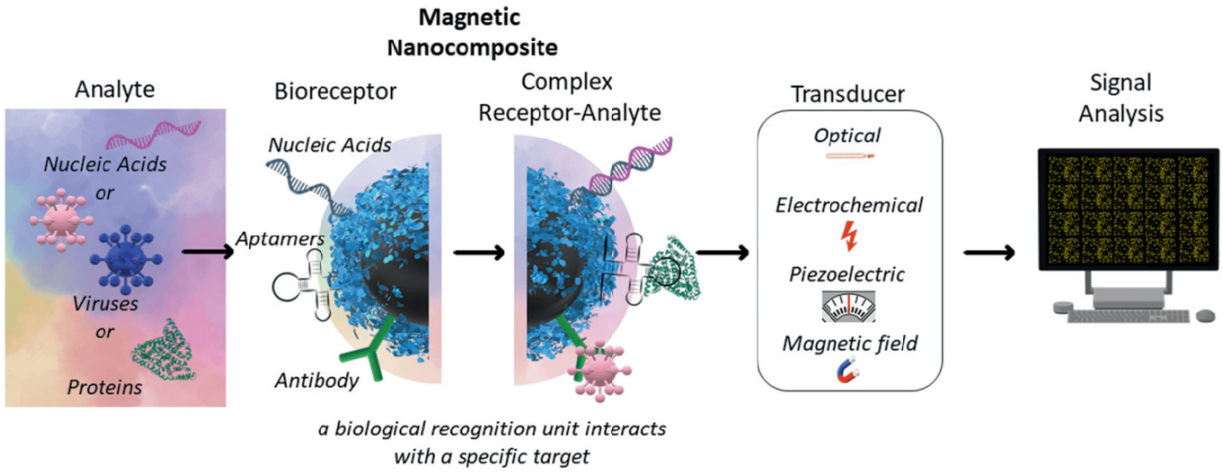

Fig. 5.42 The scheme for the isolation of specific analytes using magnetic nanocomposites for biosensing. It is reproduced with permission under Creative Common License (Open Journal) from MDPI Publishers (Popova et al. 2023)

According to literature, a simple, versatile, inexpensive geo-sensor is reported for the detection of oligonucleotides which is a part of HTLV-I (Human T-lymphotropic virus type 1 is known as retrovirus, which causes cancer). For this, carbon dots are functionalized with the probes, and the fluorescence of carbon dots is quenched in presence of

the magnetic nanoparticles coated by a gold (Fe_3O_4@Au) as shown in Fig. 5.43 (Ghobadi et al. 2018).

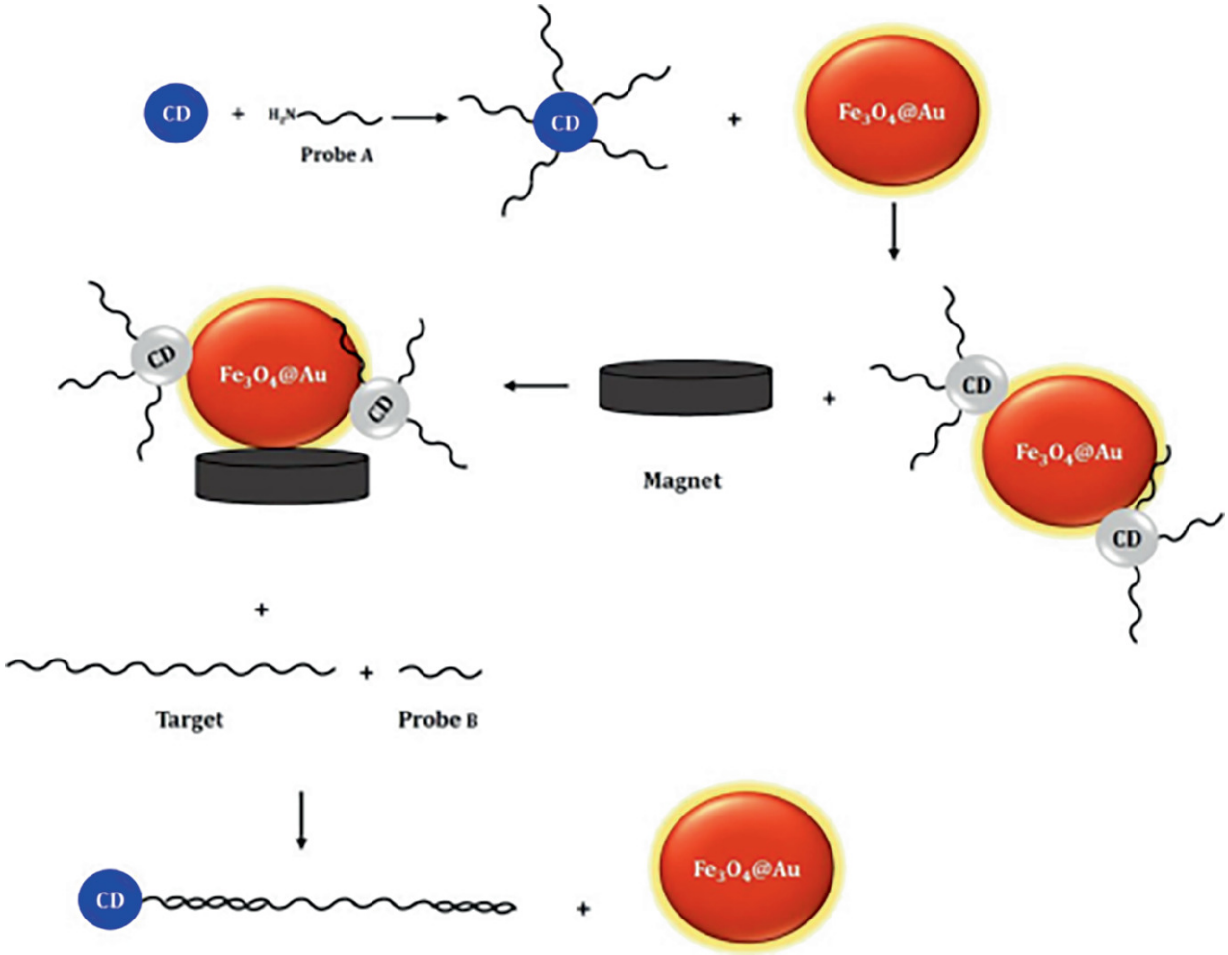

Fig. 5.43 Detection steps of geo-sensor for DNA target. It is reproduced with permission under Creative Common License (Open Journal) from Scientific reports (Ghobadi et al. 2018)

Also, there are various reports available where the magnetic materials can be used as biosensors for different viruses like influenza virus, jaundice (Wu et al. 2017; Su et al. 2019; Pan et al. 2019) and also detection of different pathogenic bacteria in food (Zhao et al. 2017).

5.8 Magnetic Materials in Environmental Applications

Various magnetic materials specifically superparamagnetic particles are reported, which are useful in the environmental applications like in waste water treatment by removing toxic ions and soil remediation to increase the fertility of the soil. Several toxic ions and heavy metals (like arsenic, fluoride, lead, sulphates, phosphates, etc.) are present in aqueous environments, which causes a lot of acute and chronic effects in the body, which are removed by various methods such as filtration, adsorption, precipitation, ion-exchange and electrochemical methods.

Arsenic is a toxic element present in groundwater, which is big problem of several countries. Fe_3O_4 nanoparticles have potential application because of their easy production. Fe_3O_4 nanoparticles are also used for the removal of arsenic from drinking water and also for the treatment of oilfield water (Yavuz et al. 2010). But, the removal of arsenic is not easy from water and also it requires high magnetic field. To avoid this problem anisotropic barium hexaferrite (BHF)$BaFe_{12}O_{19}$ acts as fridge magnets as they are permanent magnets, and it is reported that BHF has high magnetism, low cost and more effective towards arsenic removal (75%) from water than Fe_2O_3 nanoparticles of similar size. They are also used for fixed bed type cartridge applications (Patel et al. 2012).

Also, the $Fe_3O_4@Al(OH)_3$ nanoparticles are used as adsorbents. They exhibit high adsorption capacity with high surface area than the bulk magnetic materials. Also, these nano-size particles exhibit strong superparamagnetic nature which leads to the faster waste water treatment even in larger volumes due to the presence of external magnetic field (Zhao et al. 2010).

The nuclear power station produces a large amount of radioactive waste and spent fuels in water, which leads to environmental pollution and affects the human health. For example, radionuclides ^{60}Co are released from pressurized

water nuclear power reactors. ^{60}Co is non-degradable, so it is necessary to remove radio cobalt from water. As sorption technique is easy to operate and cost effective, it can be appropriate for the removal of radionuclides from aqueous solutions. For this, titanate/graphene oxide-based composites are reported to remove the radioactive cobalt from aqueous solutions, with efficient results. Figure 5.44 (Chen et al. 2015b) represents the SEM images of titanate (inset shows the SEM image of graphene oxides) and titanate/graphene oxide composites. The interaction of Co(II) on solid particle surface depends on the reaction conditions, such as if pH is low, adsorption occurs by outer-sphere complexation, or by ion-exchange mechanism, while if pH is high, it occurs via inner-sphere complexation, or by co-precipitation (Chen et al. 2015b; Wang et al. 2017).

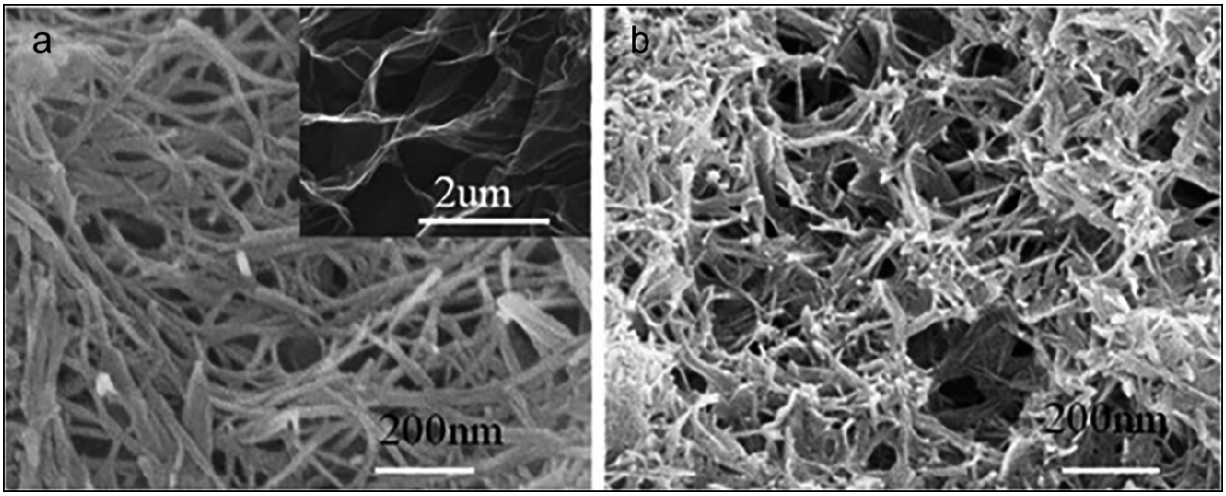

Fig. 5.44 **a** SEM images of titanate, the inset shows the SEM image of graphene oxides, **b** titanate/graphene oxide composites. It is reproduced with permission from Elsevier Publishers (Chen et al. 2015b)

A double layer magnetic nanocomposite having metal organic framework type of structure is reported. Fe_3O_4@ZIF-8@ZIF-67 are reported for the removal of tetracycline from the water for the treatment of waste water by using the phenomena of adsorption and Fenton-like oxidation. The highly porous structure of the

Fe_3O_4@ZIF-8@ZIF-67 provides high adsorption capacity along with high removal efficiency (Song et al. 2022).

Phenoxy acid herbicides are one of the derivatives of phenoxy-acetic acid which are basically used in agriculture in order to control annual and perennial weeds in several crops. These herbicides are highly selective and specifically strong in activity. As these herbicides are soluble in water and low soil sorption, they can easily permeate in the ground water. It is important to remove these herbicides from water as they have irreversible impact in the environment including animals and humans. These are present in trace amount in the ecosystem and traditionally removed by various kinds of chromatographic techniques, which makes this procedure laborious and time-consuming. So, there are some reports for the treatment of ground water by the use of selective magnetic molecularly imprinted polymer (MMIP) as sorbent material with high extraction capacity, good selectivity and excellent reusability. For this, magnetic molecularly imprinted polymer (MMIP) was formed where 4-chloro-2-methylphenoxyacetic acid acts as a template and 4-vinylpiridine acts as monomer along with vinylized magnetite nanoparticles are reported. The determination of the acid was done by using HPLC–DAD method as shown in Fig. 5.45 (Meseguer-Lloret et al. 2022).

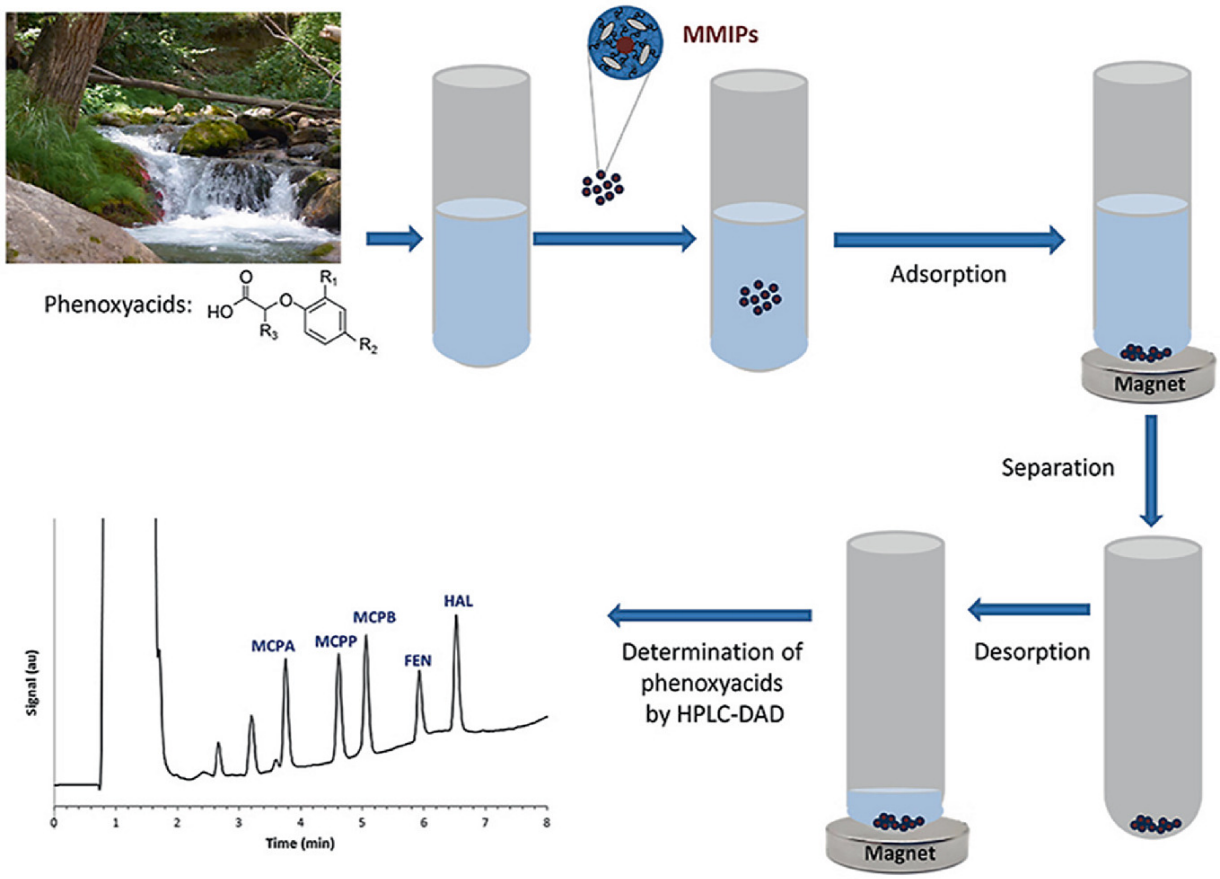

Fig. 5.45 The determination of the acid was done by using HPLC–DAD method using MMIP. It is reproduced with permission from Elsevier Publishers (Meseguer-Lloret et al. 2022)

Also, magnetic bifunctional nanocomposite having two building blocks by hydrothermal method (MOF-metal organic framework having Co and Ni as coordination ions, and graphene to form CoNi–MOFs–GR) are reported with excellent electro-catalytic activity as electrochemical sensor and also removes environmental pollutants like organic dyes from water. The nanocomposite was utilized as a sensing marker for glucose detection in human blood serum and also the removal of organic dyes (methylene blue (MB), congo red (CR) and neutral red (NR)) from water as shown in Fig. 5.46 (Lei et al. 2023).

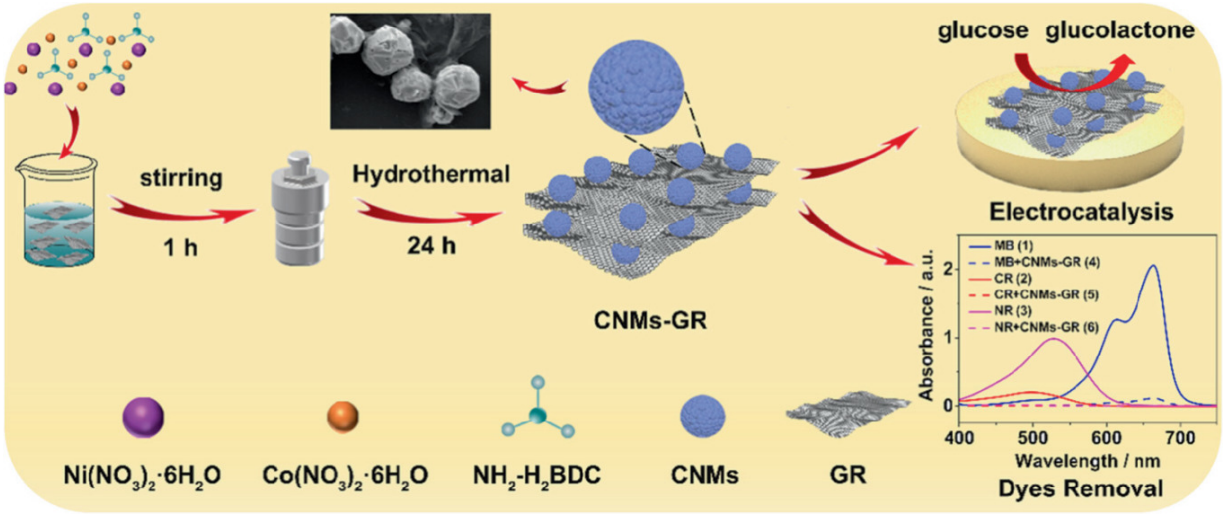

Fig. 5.46 The synthesis procedure and application of bifunctional magnetic nanocomposite in electrocatalysis and adsorption. It is reproduced with permission from ACS Publishers (Lei et al. 2023)

Also, silica–amine coated superparamagnetic γ-Fe_2O_3-NH_4OH@SiO_2(APTMS) nanoparticles are reported to adsorb one of the most critical rare earth elements, i.e. dysprosium ions $Dy^{3+}$from the aqueous solution with the maximum adsorption efficiency 90% at pH 7, which is useful for magnetic separation as represented in Fig. 5.47 (Kegl et al. 2019).

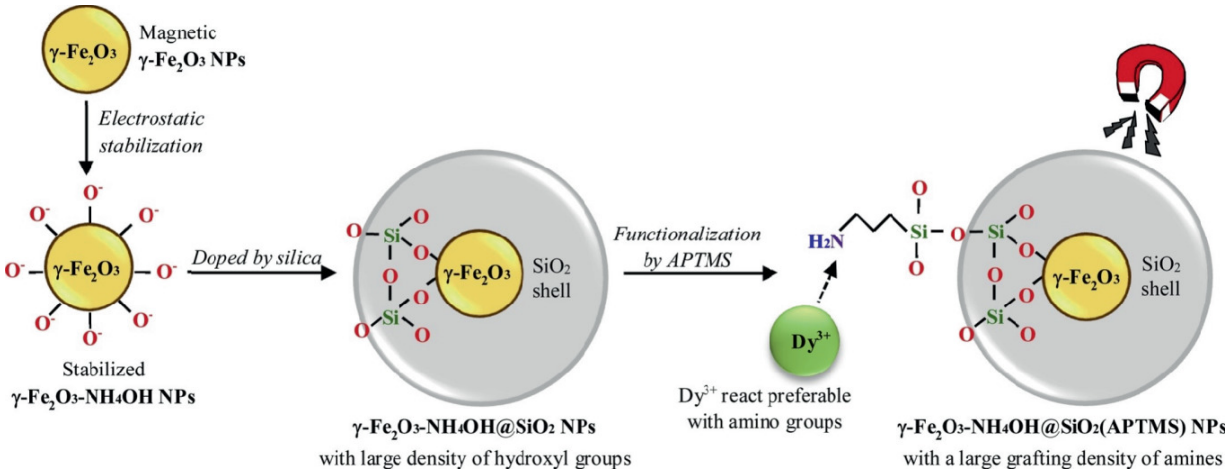

Fig. 5.47 Superparamagnetic γ-Fe_2O_3-NH_4OH@SiO_2(APTMS) nanoparticles used for adsorption of Dy^{3+} from water. It is reproduced with permission from Elsevier Publishers (Kegl et al. 2019)

Fe_3O_4 covered with SiO_2 (Fe_3O_4@SiO_2) along with chitosan (CHT)/sodium alginate (ALG) hydrogel beads based on magnetic hybrid materials were synthesized for the sorption of Pb (II) ions from water. These CHT/ALG/Fe_3O_4@SiO_2hydrogel beads were developed for the treatment of a battery effluent to reduce the Pb(II) content and turbidity (Facchi et al. 2018). Figure 5.48 shows schematic diagram for the removal of toxic contaminants from the wastewater using magnetic hydrogels.

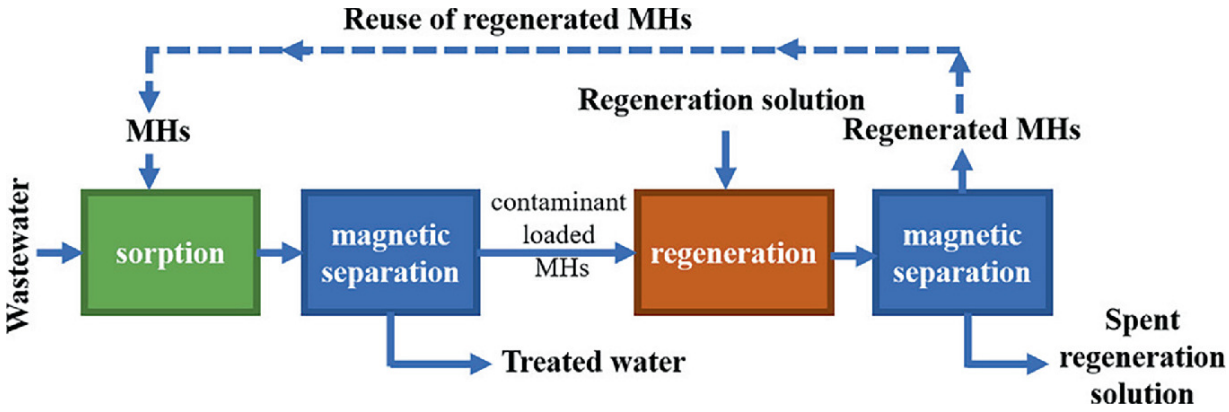

Fig. 5.48 Scheme for the removal of contaminants from waste water using magnetic hydrogels. It is reproduced with permission under Creative Common License (Open Journal) from Wiley Publishers (Gang et al. 2021)

5.9 Conclusions

Many examples of magnetic materials useful in various areas are mentioned. Depending on the types of magnetic materials such as diamagnetic, paramagnetic, ferromagnetic, ferromagnetic and antiferromagnetic materials, their utilization in different applications is provided. When size of ferromagnetic or ferromagnetic particles decreases to nanometers, they can generate different properties such as lower magnetization and zero coercivity as compared to their bulk counterparts. One property shown by small-sized magnetic particles are

superparamagnetic nature. Such superparamagnetic nanoparticles have been used in many fields such as catalysis, sensors, magnetic-based separation of toxic ions from water and biological areas (hyperthermia and carrier for drug).

References

Ali, A., Shah, T., Ullah, R., Zhou, P., Guo, M., Ovais, M., Tan, Z., Rui, Y.: Review on recent progress in magnetic nanoparticles: synthesis, characterization, and diverse. Front. Chem. **9** (2021)

Awaji, S., Watanabe, K., Oguro, H., Miyazaki, H., Hanai, S., Tosaka, T., Ioka, S.: First performance test of a 25 T cryogen-free superconducting magnet. Supercond. Sci. Technol. **30**, 065001 (2017)

Baibich, M.N., Broto, J.M., Fert, A., Nguyen Van Dau, F., Petroff, F., Eitenne, P., Creuzet, G., Friederich, A., Chazelas, J.: Giant Magnetoresistance of (001)Fe/(001)Cr Magnetic Superlattices. Phys. Rev. Lett. **61**(21), 2472–2475 (1988)
[PubMed]

Balli, M., Fruchart, D., Gignoux, D.: Optimization of La $(Fe, Co)_{13-x}Si_x$ based compounds for magnetic refrigeration. J. Phys.: Condens. Matter **19**(23), 236230 (2007)

Balli, M., Mansouri, S., Jandl, S., Fournier, P., Dimitrov, D.Z.: Analysis of the Anisotropic magnetocaloric effect in RMn_2O_5 single crystals.
Magnetochemistry **3**(4), 36 (2015)

Barick, K.C., Sharma, A., Shetake, N.G., Ningthoujam, R.S., Vatsa, R.K., Babu, P.D., Pandey, B.N., Hassan, P.A.: Covalent bridging of surface functionalized $Fe_3O_4$and YPO_4: Eu nanostructures for simultaneous imaging and therapy.
Dalton Trans. **44**, 14686–14696 (2015)
[PubMed]

Baruah, M.J., Bora, T.J., Dutta, R., Roy, S., Guha, A.K., Bania, K.K.: Fe(III) superoxide radicals in halloysite nanotubes for visible-light-assisted benzyl alcohol oxidation and oxidative C-C coupling of 2-naphthol. Mol. Catal. **515**, 111858 (2021)

Beaugnon, E., Tournier, R.: Levitation of organic materials. Nature **349**, 470 (1991)

Berkowitz, A.E., Mitchell, J.R., Carey, M.J., Young, A.P., Zhang, S., Spada, F.E., Parker, F.T., Hutten, A., Thomas, G.: Giant magnetoresistance in heterogeneous Cu–Co alloys. Phys. Rev. Lett. **68**(25), 3745–3748 (1992) [PubMed]

Bi, Q., Li, H., Du, J., Li, H., Li, Q., Wang, J., Huang, Y., Gong, X.: Gadolinium deposition in the brain is related to various contrast agents: a matched case–control study. Clin. Radiol. **77**(4), 299–306 (2022) [PubMed]

Bian, Y., Zheng, G., Ding, W., Hu, L., Sheng, Z.: Magnetic field effect on the photocatalytic degradation of methyl orange by commercial TiO_2 powder. RSC Adv. **11**, 6284–6291 (2021) [PubMed][PubMedCentral]

Binasch, G., Grünberg, P., Saurenbach, F., Zinn, W.: Enhanced magnetoresistance in layered magnetic structures with antiferromagnetic interlayer exchange. Phys. Rev. B **39**(7), 4828–4830 (1989)

Braccini, V., Nardelli, D., Penco, R., Grasso, G.: Development of ex situ processed MgB_2 wires and their applications to magnets. Physica C **456**, 209–217 (2007)

Carbone, C., Alvarado, S.F.: Antiparallel coupling between Fe layers separated by a Cr interlayer: dependence of the magnetization on the film thickness. Phys. Rev. B **36**(4), 2433–2435 (1987)

Cardoso, B.D., Rio, I.S.R., Rodrigues, A.R.O., Fernandes, F.C.T., Almeida, B.G., Pires, A., Pereira, A.M., Araújo, J.P., Castanheira, E.M.S., Coutinho, P.J.G.: Magnetoliposomes containing magnesium ferrite nanoparticles as nanocarriers for the model drug curcumin. R. Soc. Open Sci., 5181017 (2018)

Chen, Y., Xianyu, Y., Wang, Y., Zhang, X., Cha, R., Sun, J., Jiang, X.: One-step detection of pathogens and viruses: combining magnetic relaxation switching and magnetic separation. ACS Nano **9**(3), 3184–3191 (2015a) [PubMed]

Chen, L., Lu, S., Wu, S., Zhou, J., Wang, X.: Removal of radiocobalt from aqueous solutions using titanate/graphene oxide composites. J. Mol. Liq. **209**, 397–403 (2015b)

Cherechukin, A.A., Takagi, T., Matsumoto, M., Buchel'nikov, V.D.: Magnetocaloric effect in $Ni_{2+x}Mn_{1-x}Ga$ Heusler alloys. Phys. Lett. A **326**(1–2), 146–151 (2004)

Chung, D.D.L.: Materials for electromagnetic interference shielding. Mater. Chem. Phys. **255**, 123587 (2020)

Cullity, B.D., Graham, C.D.: Introduction to Magnetic Materials. Wiley (2009)

Dalal, M., Das, A., Das, D., Ningthoujam, R.S., Chakrabarti, P.K.: Studies of magnetic, Mössbauer spectroscopy, microwave absorption and hyperthermia behavior of Ni-Zn-Co-ferrite nanoparticles encapsulated in multi-walled carbon nanotubes. J. Magn. Magn. Mater. **460**, 12–27 (2018)

Dalal, M., Greneche, J.-M., Satpati, B., Ghzaiel, T.B., Mazaleyrat, F., Ningthoujam, R.S., Chakrabarti, P.K.: Microwave absorption and the magnetic hyperthermia applications of $Li_{0.3}Zn_{0.3}Co_{0.1}Fe_{2.3}O_4$ nanoparticles in multiwalled carbon nanotube matrix. ACS Appl. Mater. Interfaces **9**, 40831–40845 (2017)

Dalal, M., Greneche, J.-M., Ningthoujam, R.S., Chakrabarti, P.K.: Study of magnetic induction heating of $Li_{0.25}Zn_{0.3}Co_{0.15}Fe_{2.3}O_4$ nanoparticles. Mater. Chem. Phys. **313**, 128756 (2024)

Das, S., Dey, T.K.: Magnetic entropy change in polycrystalline $La_{1-x}K_xMnO_3$ perovskites. J. Alloy. Compd. **30**(1–2), 30 (2007)

Dey, C.C., Mallick, A., Mahapatra, A.S., Dalal, M., Bajorek, A., Greneche, J.-M., Ningthoujam, R.S., Chakrabarti, P.K.: Mössbauer analysis and induction heating evaluation of grapes like FZ@MWCNT towards cancer treatment. Solid State Sciences **122**, 106756 (2021)

Facchi, D.P., Cazetta, A.L., Canesin, E.A., Almeida, V.C., Bonafé, E.G., Kipper, M.J., Martins, A.F.: New magnetic chitosan/alginate/Fe_3O_4@SiO_2 hydrogel composites applied for removal of Pb (II) ions from aqueous systems. Chem. Eng. J. **337**, 595–608 (2018)

Fan, W., Quan, W., Liu, F., Pang, H., Xing, L., Liu, G.: Performance of low-noise ferrite shield in a K-Rb-$_{21}$Ne Co-magnetometer. IEEE Sens. J. **20**(5), 2543–2549 (2020)

Fang, X., Ma, D., Sun, B., Xu, X., Quan, W., Xiao, Z., Zhai, Y.: High-performance magnetic shield with MnZn ferrite and mu-metal film combination for atomic sensors. Materials **15**(19), 6680 (2022) [PubMed][PubMedCentral]

Fatima, H., Charinpanitkul, T., Kim, K.S.: fundamentals to apply magnetic nanoparticles for hyperthermia therapy. Nanomaterials (Basel) **11**, 1203 (2021)

Gajbhiye, N.S., Ningthoujam, R.S., Bhattacharyya, S.: Magnetic properties of Co and Ni substituted ε-Fe_3N nanoparticles. Hyperfine Interact. **164**, 17 (2005)

Gajbhiye, N.S., Sharma, S., Ningthoujam, R.S.: Synthesis of self-assembled monodisperse 3 nm FePd nanoparticles: phase transition, magnetic study and surface effect. J. Appl. Phys. **104**, 123906 (2008a)

Gajbhiye, N.S., Sharma, S., Nigam, A.K., Ningthoujam, R.S.: Tuning of single to multidomain behavior for monodispersed ferromagnetic cobalt nanoparticles. Chem. Phys. Lett. **466**, 181 (2008b)

Gajbhiye, N.S., Ningthoujam, R.S.: Structural, electrical and magnetic studies of nanocrystalline δ-MoN and γ-Mo_2N. Phys. Stat. Sol. (c) **1**, 3449 (2004)

Gajbhiye, N.S., Ningthoujam, R.S., Weissmuller, J.: Synthesis and magnetic studies of nanocrystalline nickel nitride material. Phys. Stat. Sol. (a) **189**, 691 (2002)

Gajbhiye, N.S., Ningthoujam, R.S., Weissmuller, J.: Mössbauer study of Nanocrystalline ε-$Fe_{3-x}Co_xN$ system. Hyperfine Interactions **156** (2004)

Gajbhiye, N.S., Panda, R.N., Ningthoujam, R.S., Bhattacharyya, S.: Magnetism of nanostructured iron nitride (Fe-N) systems. Phys. Stat. Sol. (c) **1**, 3252 (2004)

Gang, F., Jiang, L., Xiao, Y., Zhang, J., Sun, X.: Multi-functional magnetic hydrogel: design strategies and applications. Nano Select **2**(12), 2291–2307 (2021)

Ganganboina, A.B., Chowdhury, A.D., Doong, R.-A.: Nano assembly of N-doped graphene quantum dots anchored Fe_3O_4/halloysite nanotubes for high performance supercapacitor. Electrochim. Acta **245**, 912–923 (2017)

Gao, G.Y.: Kai-Lun Yao, Antiferromagnetic half-metals, gapless half-metals, and spin gapless semiconductors: the D03-type Heusler alloys. Appl. Phys. Lett. **103**, 232409 (2013)

Gao, W., Peng, R., Yang, Y., Zhao, X., Cui, C., Su, X., Qin, W., Dai, Y., Ma, Y., Liu, H., Sang, Y.: Electron spin polarization-enhanced photoinduced charge separation in ferromagnetic $ZnFe_2O_4$. ACS Energy Lett. **6**, 2129–2137 (2021)

Gao, W., Lu, J., Zhang, S., Zhang, X., Wang, Z., Qin, W., Wang, J., Zhou, W., Liu, H., Sang, Y.: Suppressing photoinduced charge recombination via the Lorentz force in a photocatalytic system. Adv. Sci. (Weinh) **6**, Article 1901244 (2019)

Geim, A.K., Dubonos, S.V., Lok, J.G.S., Henini, M., Maan, J.C.: Paramagnetic Meissner effect in small superconductors. Nature **396**, 144–146 (1998)

Ghobadi, M.Z., Mozhgani, S.H., Dashtestani, F., Yadegari, A., Hakimian, F., Norouzi, M., Ghourchian, H.: A geosensor for detection of HTLV-I based on

photoluminescence quenching of fluorescent carbon dots in presence of iron magnetic nanoparticle-capped Au. Scientific Reports **8** (2018)

Grueber, H.P., Helbling, A., Joerg, L.: Skin test results and cross-reactivity patterns in IgE- And T-cell-mediated allergy to gadolinium-based contrast agents. Allergy, Asthma Immunol. Res. **13**(6), 933–938 (2021)

Grünberg, P., Schreiber, R., Pang, Y., Brodsky, M.B., Sowers, H.: Layered magnetic structures: evidence for antiferromagnetic coupling of Fe layers across Cr interlayers. Phys. Rev. Lett. **57**(19), 2442–2445 (1986) [PubMed]

Guan, H., Chung, D.D.L.: Radio-wave electrical conductivity and absorption-dominant interaction with radio wave of exfoliated-graphite-based flexible graphite, with relevance to electromagnetic shielding and antennas. Carbon **157**, 549–562 (2020)

Gutfleisch, O., Müller, K.H., Khlopkov, K., Wolf, M., Yan, A., Schäfer, R.: Evolution of magnetic domain structures and coercivity in high-performance Sm Co 2:17-type permanent magnets. Acta Mater. **54**, 997 (2006)

Ha, Y., Ko, S., Kim, I., Huang, Y., Mohanty, K., Huh, C., Maynard, J.A.: Recent Advances Incorporating Superparamagnetic Nanoparticles into Immunoassays. ACS Appl. Nano Mater. **1**(2), 512–521 (2018) [PubMed][PubMedCentral]

Hahn, S., Kim, K., Kim, K., Hu, X.B., Painter, T., Dixon, I., Kim, S., Bhattarai, K.R., Noguchi, S., Jaroszynski, J., Larbalestier, D.C.: 45.5-tesla direct-current magnetic field generated with a high-temperature superconducting magnet. Nature **570**, 496–499 (2019)

Hai-Peng Chen, C., Lee, D., Liu, S., Walmer, M., Zhang, Y., Hadjipanayis, G.C.: Fully dense bulk nanocomposites of $(Sm_{1-x}Gd_x)_2(Co_{1-y}Fe_y)_{17}$+(Co, Fe) with high coercivity and high Curie temperature. IEEE Trans. Magn. **40**, 2937 (2004)

Hervaultab, A., Thanh, N.T.K.: Magnetic nanoparticle-based therapeutic agents for thermo-chemotherapy treatment of cancer. Nanoscale **6**, 11553 (2014)

Hinchey, L.L., Mills, D.L.: Magnetic properties of superlattices formed from ferromagnetic and antiferromagnetic materials. Phys. Rev. B **33**(5), 3329–3343 (1986)

Hinz, D., Lyubina, J., Fuchs, G., Brown, D., Ma, B.M., Gutfleisch, O., Müller, K.-H.: Hot deformed (Nd,Pr)(Fe,Co)B magnets for low-temperature applications. J. Magn. Magnet. Mater. **272** (2004)

Hirohata, A., Frost, W., Samiepour, M., Kim, J.-Y.: Perpendicular magnetic anisotropy in Heusler alloy films and their Magnetoresistive junctions.

Materials **11**, 105 (2018)
[PubMed][PubMedCentral]

Hirohata, A., Yamada, K., Nakatani, Y., Prejbeanu, I.L., Diény, B., Pirro, P., Hillebrands, B.: Review on spintronics: principles and device applications. J. Magn. Magn. Mater. **509**, 166711 (2020)

Ho, K.M., Li, P.: Design and synthesis of novel magnetic core−shell polymeric particles. Langmuir **24**(5), 1801–1807 (2008)
[PubMed]

Hossain, M.K., Sharafat, M.K., Minami, H., Suzuki, T., Alam, M.A., Rahman, M.M., Ahmad, H.: Facile one-step synthesis of poly(styrene-glycidyl methacrylate)-Fe_3O_4 nanocomposite particles and application potency in glucose biosensors. J. Polymer Res. **30**(3) (2023)

http://simple.wikipedia.org/wiki/Giant_magnetoresistance.

http://zfmezo.home.amu.edu.pl/images/research/Spintronics_v2.png.

https://www.collegesidekick.com/study-guides/boundless-physics/applications-of-magnetism.

https://www.dingcimagnet.com/blog/what-are-the-applications-and-types-of-magnets-in-industry_b46.

https://www.hsmagnets.com/blog/examples-applications-using-neodymium-magnets/.

https://www.nobelprize.org/prizes/physics/2007/popular-information/.

Hu, M., Butt, H.J., Landfester, K., Bannwarth, M.B., Wooh, S., Aubin, H.T.: Shaping the assembly of superparamagnetic nanoparticles. ACS Nano **13**(3), 3015–3022 (2019)
[PubMed][PubMedCentral]

Huang, J., Bu, L., Xie, J., Chen, K., Cheng, Z., Li, X., Chen, X.: Effects of nanoparticle size on cellular uptake and liver MRI with Polyvinylpyrrolidone-coated iron oxide nanoparticles. ACS Nano **4**(12), 7151–7160 (2010)
[PubMed][PubMedCentral]

Huang, C., Zhou, Y.B., Jin, Y., Zhou, X., Tang, Z.M., Guo, X., Zhou, S.B.: Preparation and characterization of temperature-responsive and magnetic nanomicelles. J. Mater. Chem. **21**, 5660–5670 (2011)

Huang, Z., Wang, Y., Wu, M., Li, W., Zuo, H., Xiao, B., Zhang, X., Wu, J., He, H., Xia, Q.: Sericin-based gadolinium nanoparticles as synergistically enhancing contrast agents for pH-responsive and tumor targeting magnetic resonance imaging. Mater. Des. **203**, 109600 (2021)

Iyad, N., Ahmad, M.S., Alkhatib, S.G., Hjouj, M.: Gadolinium contrast agents-challenges and opportunities of a multidisciplinary approach: literature review. Eur. J. Radiol. Open, 100503 (2023)

Jadhav, S.V., Nikam, D.S., Khot, V.M., Thorat, N.D., Phadatare, M.R., Ningthoujam, R.S., Salunkhe, A.B., Pawar, S.H.: Studies on colloidal stability of PVP-coated LSMO nanoparticles for magnetic fluid hyperthermia. New J. Chem. **37**, 3121 (2013)

Jang, J.T., Nah, H., Lee, J.H., Moon, S.H., Kim, M.G., Cheon, J.: Critical enhancements of MRI contrast and hyperthermic effects by dopant-controlled magnetic nanoparticles. Angew. Chem., Int. Ed. Engl., **48**, 1234–1238 (2009)

Jiang, J., Bradford, G., Hossain, S.I., Brown, M.D., Cooper, J., Miller, E., Huang, Y., Miao, H., Parrell, J.A., White, M.: High-performance Bi-2212 round wires made with recent powders. IEEE Trans. Appl. Supercond. **29**, 6400405 (2019) [PubMed][PubMedCentral]

Joshi, R.: Sandeep Balu Shelar, Manas Srivastava, Bheeshma Pratap Singh, Lokesh Goel, Raghumani Singh Ningthoujam, Development of Core@Shell γ-Fe_2O_3@Mn_xO_y@SiO_2 nanoparticles for hyperthermia, targeting, and imaging applications. ACS Appl. Bio Mater. **5**(11), 5386–5393 (2022) [PubMed]

Joshi, R., Perala, R.S., Srivastava, M., Singh, B.P., Ningthoujam, R.S.: Heat generation from magnetic fluids under alternating current magnetic field or induction coil for hyperthermia-based cancer therapy: basic principle. J. Rad. Cancer Res. **10**, 156–164 (2019)

Joshi, R., Singh, B.P., Ningthoujam, R.S.: Confirmation of highly stable 10 nm sized Fe_3O_4 nanoparticle formation at room temperature and understanding of heat generation under AC magnetic fields for potential application in hyperthermia. AIP Adv. **10**, 105033–105038 (2020)

Joshi, R., Singh, B.P., Prajapat, C.L., Kashyap, Y., Nayak, C., Bhattacharyya, D., Ningthoujam, R.S.: Insights into the structural and microscopic origin of magnetic properties of the γ-Fe_2O_3@Mn_xO_y nanostructure. J. Phys. Chem. C **125**, 17971 (2021)

Juarez, E.B., Zermeno, V.M.R., Trillaud, F., Gavrilin, A.V., Grilli, F., Abraimov, D.V., Hilton, D.K., Weijers, H.W.: Estimation of losses in the (RE)BCO two-coil insert of the NHMFL 32 T all-superconducting magnet. IEEE Trans. Appl. Supercond. **28**, 4602005 (2018)

Kadam, A.A., Jang, J., Lee, D.S.: Super-magnetically tuned halloysite nanotubes functionalized with amino silane for covalent laccase immobilization. ACS Appl. Mater. Interfaces **9**, 15492–15501 (2017)

[PubMed]

Kanda, T., Oba, H., Toyoda, K., Kitajima, K.: Brain gadolinium deposition after administration of gadolinium—based contrast agents. Jpn. J. Radiol. **34**(1), (2016)

Kang, Y., Zhao, Y.: Preparation of magnetic resonance contrast agent gadolinium-containing organic nanoparticles and their electrochemical behavior investigation. Int. J. Electrochem. Sci. **17**, 1–10 (2022)

Kaur, H., Kaur, H., Sharma, A.: Materials today proceeding. a review of recent advancement in superconductors. Mater. Today Proc. **37**(2), 3612–3614 (2021)

Kegl, T., Ban, I., Lobnik, A., Košak, A.: Synthesis and characterization of novel γ-Fe_2O_3-NH_4OH@SiO_2(APTMS) nanoparticles for dysprosium adsorption. J. Hazard. Mater. **378**, 120764 (2019)
[PubMed]

Kimura, T., Hashimoto, N., Yamada, S., Miyao, M., Hamaya, K.: Room-temperature generation of giant pure spin currents using Co_2FeSi spin injectors, NPG Asia Mater. **4**, Article 9 (2012)

Kirihara, A., Kondo, K., Ishida, M., Ihara, K., Iwasaki, Y., Someya, H., Matsuba, A., Uchida, K., Saitoh, E., Yamamoto, N., Kohmoto, S., Murakami, T.: Flexible heat-flow sensing sheets based on the longitudinal spin Seebeck effect using one-dimensional spin-current conducting films. Sci. Rep. **6**, 23114 (2016)
[PubMed][PubMedCentral]

Kittel, C.: Introduction to Solid State Physics. Wiley (2005)

Kohn, A., Kovács, A., Fan, R., McIntyre, G.J., Ward, R.C., Goff, J.P.: The antiferromagnetic structures of $IrMn_3$ and their influence on exchange-bias. Sci. Rep. **3**, 2412 (2013)
[PubMed][PubMedCentral]

Kondou, K., Yoshimi, R., Tsukazaki, A., Fukuma, Y., Matsuno, J., Takahashi, K.S., Kawasaki, M., Tokura, Y., Otani, Y.: Fermi-level-dependent charge-to-spin current conversion by Dirac surface states of topological insulators Nat. Phys. **12**, 1027–1031 (2016)

Konig, M., Wiedmann, S., Brüne, C., Roth, A., Buhmann, H., Molenkamp, L.W., Qi, X.-L., Zhang, S.-C.: Quantum spin hall insulator state in HgTe quantum wells. Science **318**, 766–770 (2007)
[PubMed]

Kritika, I.: Roy, Therapeutic applications of magnetic nanoparticles: recent advances. Mater. Adv. **3**, 7425 (2022)

Kumar, P., Gupta, P., Sharma, C.: Surface modified novel magnetically tuned halloysite functionalized sulfonic acid: synthesis, characterization, and catalytic activity. Catal. Sci. Technol. **11**, 3775 (2021)

Kumara, P., Gupta, P.: Halloysite-based magnetic nanostructures for diverse applications: a review. ACS Appl. Nano Mater. **6**(15), 13824–13868 (2023)

Lee, P.: Engineering critical current density vs. Applied field for superconductors, nationalmaglab.org/magnet-development/applied-superconductivity-center/plots (2018)

Lei, P., Zhou, Y., Dong, C., Liu, Y., Shuang, S.: CoNi–MOF–graphene magnetic nanocomposites for the electrocatalytic detection of glucose and the efficient removal of organic dyes. ACS Appl. Nano Mater. **6**(11), 9369–9375 (2023)

Li, G.Z., Sumption, M.D., Zwayer, J.B., Susner, M.A., Rindfleisch, M.A., Thong, C.J., Tomsic, M.J., Collings, E.W.: Effects of carbon concentration and filament number on advanced internal Mg infiltration-processed MgB_2 strands. Supercond. Sci. Technol. **26**, 095007 (2013)

Li, J., Liu, H., Zhang, Z., et al.: Obtaining half-metallic ferrimagnetism and antiferromagnetism by doping Mn and Fe for D03-type Heusler compound Cr_3Si. J. Alloys Compd. **597**, 8 (2014)

Li, J., Pei, Q., Wang, R., Zhou, Y., Zhang, Z., Cao, Q., Wang, D., Mi, W., Du, Y.: Enhanced photocatalytic performance through magnetic field boosting carrier transport. ACS Nano **12**, 3351–3359 (2018)
[PubMed]

Li, Y., Wang, Z., Wang, Y., Kovács, A., Foo, C., Dunin-Borkowski, R.E., Lu, Y., Taylor, R.A., Wu, C., Tsang, S.C.E.: Local magnetic spin mismatch promoting photocatalytic overall water splitting with exceptional solar-to-hydrogen efficiency. Energy Environ. Sci. **15**, 265–277 (2022)

Liu, J.H., Wang, Q.L., Qin, L., Zhou, B.Z., Wang, K.S., Wang, Y.H., Zhang, Z.L., Dai, Y.M., Liu, H., Hu, X.N.: World record 32.35 tesla direct-current magnetic field generated with an all-superconducting magnet, Supercond. Sci. Technol. **33** (2020)

Ma, D., Fang, X., Lu, J., Wang, K., Sun, B., Gao, Y., Xu, X., Han, B.: Analysis and measurement of differential-mode magnetic noise in Mn–Zn soft ferrite shield for ultra-sensitive sensors. Materials **15**(23), 8704 (2022)
[PubMed][PubMedCentral]

Majeed, J., Pradhan, L., Ningthoujam, R.S., Vatsa, R.K., Bahadur, D., Tyagi, A.K.: Enhanced specific absorption rate in silanol functionalized Fe_3O_4 core—

shell nanoparticles: study of Fe leaching in Fe_3O_4 and hyperthermia in L929 and HeLa cells. Colloids Surf. B **122**, 396–403 (2014)

Mallick, A., Mahapatra, A.S., Mitra, A., Greneche, J.M., Ningthoujam, R.S., Chakrabarti, P.K.: Magnetic properties and bio-medical applications in hyperthermia of lithium zinc ferrite nanoparticles integrated with reduced graphene oxide. J. Appl. Phys. **123**, 055103 (2018)

Martins, P.M., Lima, A.C., Ribeiro, S., Mendez, S., Martins, P.: Magnetic nanoparticles for biomedical applications: from the soul of the earth to the deep history of ourselves. ACS Appl. Bio Mater. **4**(8), 5839–5870 (2021)
[PubMed]

Meissner, W., Ochsenfeld, R.: Ein neuer Effekt bei Eintritt der Supraleitfähigkeit Naturwissenschaften, Scientific Res. **21**, 787–788 (1933)

Mellari, S.: Introduction to magnetic refrigeration: magnetocaloric materials. Int. J. Air-Conditioning Refrigeration **32**, 5 (2023)

Meseguer-Lloret, S., Torres-Cartas, S., Gómez-Benito, C., Herrero-Martínez, J.M.: Magnetic molecularly imprinted polymer for the simultaneous selective extraction of phenoxy acid herbicides from environmental water samples. Talanta **239**, 123082 (2022)
[PubMed]

Metglas, Learn about magnetic materials from metglas, inc., https://metglas.com/magnetic-materials/.

Motokawa, M., Hamai, M., Sato, T., Mogi, I., Awaji, S., Watanabe, K., Kitamura, N., Makihara, M.: Magnetic levitation experiments in Tohoku University. Phys. B Condens. Matter. **294–295**, 729–735 (2001)

Mu, B., Wang, W., Zhang, J., Wang, A.: Superparamagnetic sandwich structured silver/halloysite nanotube/Fe_3O_4 nanocomposites for 4-nitrophenol reduction. RSC Adv. **4**, 39439–39445 (2014)

Nayak, A.K., Kumar, V., Ma, T., Werner, P., Pippel, E., Sahoo, R., Damay, F., Rößler, U.K., Felser, C., Parkin, S.S.P.: Magnetic antiskyrmions above room temperature in tetragonal Heusler materials. Nature **548**(7669), 561–566 (2017)
[PubMed]

Nguyen, M.-H., Zhao, M., Ralph, D.C., Buhrman, R.A.: Enhanced spin Hall torque efficiency in $Pt_{100-x}Al_x$ and $Pt_{100-x}Hf_x$ alloys arising from the intrinsic spin Hall effect. Appl. Phys. Lett. **108**, Article 242407 (2016)

Nikam, D.S., Jadhav, S.V., Khot, V.M., Ningthoujam, R.S., Hong, C.K., Mali, S.S., Pawar, S.H.: Colloidal stability of polyethylene glycol functionalized

$Co_{0.5}Zn_{0.5}Fe_2O_4$ nanoparticles: effect of pH, sample and salt concentration for hyperthermia application. RSC Adv. **4**, 12662 (2014)

Ningombam, G.S., Ningthoujam, R.S., Kalkura, S.N., Singh, N.R.: Induction heating efficiency of water dispersible $Mn_{0.5}Fe_{2.5}O_4$@YVO_4:Eu^{3+} magnetic-luminescent nanocomposites in acceptable AC magnetic field: Haemocompatibility and cytotoxicity studies. J. Phys. Chem. B, **122**, 6862–6871 (2018)

Ningthoujam, R.S., Gajbhiye, N.S.: Magnetic study of single domain ε-Fe_3N nanoparticles synthesized by precursor techniques. Mater. Res. Bull. **43**, 1079 (2008)

Ningthoujam, R.S., Gajbhiye, N.S.: Electron-electron interaction effect and resistivity maximum in nanocrystalline and ordered superconducting γ-Mo_2N. Int. J. Nanotechnol. **7**, 932 (2010b)

Ningthoujam, R.S., Gajbhiye, N.S.: Synthesis, electron transport properties of transition metal nitrides and applications. Prog. Mater Sci. **50**, 50–154 (2015)

Ningthoujam, R.S., Sudhakar, N., Rajeev, K.P., Gajbhiye, N.S.: Electrical resistivity study of La, B doped nanocrystalline superconducting vanadium Nitride. J. Appl. Phys. **91**, 6051 (2002)

Ningthoujam, R.S., Gajbhiye, N.S., Sachil, S.: Reduction mechanism of Ni^{2+} into Ni nanoparticles prepared from different precursors: magnetic studies Pramana. J. Phys. **72**, 577 (2009)

Ningthoujam, R.S., Panda, R.N., Gajbhiye, N.S.: Variation of intrinsic magnetic parameters of single domain Co–N interstitial nitrides synthesized via hexa-ammine cobalt nitrate route. Mater. Chem. Phys. **134**, 377–381 (2012)

Ningthoujam, R.S., Gajbhiye, N.S.: Magnetization studies on ε- $Fe_{2.4}Co_{0.6}N$ nanoparticles. Mater. Res. Bull. **45**, 499 (2010)

Ningthoujam, R.S., Joshi, R.: Synthesis and applications of borides, carbides, nitrides and phosphides publisher. In: Tyagi, A.K., Ningthoujam, R.S. (Eds.), Handbook on Synthesis Strategies for Advanced Material: Volume-III: Materials specific synthesis strategies, pp. 307–366. Springer Nature, Singapore (2021)

Osabe, G., Kobayashi, S., Kato, T., Hayashi, K., Ueno, E., Yamade, S., Saito, T., Kikuchi, M., Nakashima, T., Minamino, T.: Recent developments of Ag-sheath Bi-2223 wire, presentation at the 28th International Superconductivity Industry Summit, Beijing, China (2019)

Pan, X., Li, L., Lin, H., Tan, J., Wang, H., Liao, M., Chen, C., Shan, B., Chen, Y., Li, M.: A Graphene oxide-gold nanostar hybrid based-paper biosensor for label-

free SERS detection of serum bilirubin for diagnosis of jaundice. Biosens. Bioelectron. **145**, 111713 (2019)
[PubMed]

Pan, L., Ai, M., Huang, C., Yin, L., Liu, X., Zhang, R., Wang, S., Jiang, Z., Zhang, X., Zou, J.J., Mi, W.: Manipulating spin polarization of titanium dioxide for efficient photocatalysis. Nat. Commun. **11**, 418 (2020)
[PubMed][PubMedCentral]

Parchur, A.K., Ansari, A.A., Singh, B.P., Hasan, T.N., Syed, N.A., Rai, S.B., Ningthoujam, R.S.: Enhanced luminescence of $CaMoO_4$: Eu by core@shell formation and its hyperthermia study after hybrid formation with F_e3_O4: cytotoxicity assessing on human liver cancer cells and mesanchymal stem cells. Integr. Biol. **6**, 53–64 (2014)

Patel, H.A., Byun, J., Yavuz, C.T.: Arsenic removal by magnetic nanocrystalline barium Hexaferrite. J. Nanopart. Res. **14**, 881 (2012)

Perala, R.S., Joshi, R., Singh, B.P., Putta, V.N.K., Acharya, R., Ningthoujam, R.S.: Brilliant nonlinear optical response of Ho^{3+} and Yb^{3+} activated YVO_4 nanophosphor and its conjugation with Fe_3O_4 for smart anticounterfeit and hyperthermia applications. ACS Omega **6**, 19471–19483 (2021a)
[PubMed][PubMedCentral]

Perala, R.S., Singh, B.P., Putta, V.N.K., Acharya, R., Ningthoujam, R.S.: Enrichment of crystal field modification via incorporation of alkali K^+ ions in YVO_4:Ho^{3+}/Yb^{3+} nanophosphor and its hybrid with superparamagnetic iron oxide nanoparticles for optical, advanced anticounterfeiting, uranyl detection, and hyperthermia applications. ACS Omega **6**, 19517–19528 (2021b)
[PubMed][PubMedCentral]

Phan, M.H., Peng, H.X., Yu, S.C.: Large magnetocaloric effect in single crystal $Pr_{0.63}Sr_{0.37}MnO_3$. J. Appl. Phys. **97**,10M306–10M301 (2005)

Popova, V., Dmitrienko, E., Chubarov, A.: Magnetic nanocomposites and imprinted polymers for biomedical applications of nucleic acids. Magnetochemistry **9**, 12 (2023)

Ravetz, B.D., Tay, N.E.S., Joe, C.L., Sezen Edmonds, M., Schmidt, M.A., Tan, Y., Janey, J.M., Eastgate, M.D., Rovis, T.: Development of a platform for near-infrared photo-redox catalysis, ACS Cent. Sci. **6**, 2053–2059 (2020)

Rodriguez-Sotelo, D., Rodriguez-Licea, M.A., Soriano-Sanchez, A.G., Espinosa-Calderon, A., Perez-Pinal, F.J.: Advanced ferromagnetic materials in power electronic converters: a state of the art. IEEE Access **8**, 56238–56252 (2020)

Sai Ram, B., Paul, A.K., Kulkarni, S.V.: Soft magnetic materials and their applications in transformers. J. Magn. Magnet. Mater. **537**, 168210 (2021)

Sandeman, K., Daou, R., Ozcan, S., Durrell, J., Mathur, N., Fray, D.: Negative magnetocaloric effect from highly sensitive metamagnetism in $CoMnSi_{1-x}Ge_x$. Phys. Rev. B **74**(22), 224436–224441 (2006)

Schwerdt, J.I., Goya, G.F., Pilar Calatayud, M., Hereñú, C.B., Reggiani, P.C., Goya1, R.G.: Magnetic field-assisted gene delivery: achievements and therapeutic potential. Current Gene Therapy **12**, 116–126 (2012)

Sharma, S., Gajbhiye, N.S., Ningthoujam, R.S.: Effect of annealing on magnetic properties of FePd and FePdPt nanoparticles. AIP Conf. Proc. **1313**, 125 (2010a)

Sharma, S., Gajbhiye, N.S., Ningthoujam, R.S.: Synthesis and self-assembly of monodisperse Co_xNi_{100-x} (x = 50, 80) colloidal nanoparticles by homogenous nucleation. J. Colloids & Interface Sci. **351**, 323 (2010b)

Sharma, S., Ningthoujam, R.S., Gajbhiye, N.S.: Spin-glass-like behavior of surfactant capped $Co_{50}Ni_{50}$ nanoparticles. Chem. Phys. Lett. **558**, 48–52 (2013)

Sharma, K.S., Ningthoujam, R.S., Dubey, A.K., Chattopadhyay, A., Phapale, S., Juluri, R.R., Mukherjee, S., Tewari, R., Shetake, N.G., Pandey, B.N., Vatsa, R.K.: Synthesis and characterization of monodispersed water dispersible Fe_3O_4 nanoparticles and in vitro studies on human breast carcinoma cell line under hyperthermia condition. Sci. Rep. **8**, 14766 (2018) [PubMed][PubMedCentral]

Shetake, N.G., Kumar, A., Gaikwad, S., Ray, P., Desai, S., Ningthoujam, R.S., Vatsa, R.K., Pandey, B.N.: Magnetic nanoparticle-mediated hyperthermia therapy induces tumour growth inhibition by apoptosis and Hsp90/AKT modulation. Int. J. Hyperthermia **31**, 909–919 (2015) [PubMed]

Shete, P.K., Patil, R.M., Ningthoujam, R.S., Ghosh, S., Pawar, S.H.: Magnetic core shell structures for magnetic fluid hyperthermia therapy application. New J. Chem. **37**, 3784–3792 (2013)

Simon, M.D., Geim, A.K.: Diamagnetic levitation: Flying frogs and floating magnets (invited). J. Appl. Phys. **87**, 6200–6204 (2000)

Singh, L.P., Srivastava, S.K., Mishra, R., Ningthoujam, R.S.: Multifunctional hybrid nanomaterials from water dispersible CaF_2:Eu^{3+}, Mn^{2+} and Fe_3O_4 for

luminescence and hyperthermia application. J. Phys. Chem. C **118**, 18087–18096 (2014)

Song, X., Mo, J., Fang, Y., Luo, S., Xu, J., Wang, X.: Synthesis of magnetic nanocomposite Fe_3O_4@ZIF-8@ZIF-67 and removal of tetracycline in water. Environ. Sci. Pollut. Res. **29**, 35204–35216 (2022)

Songlin, D., Tegus, O., Brück, E., de Boer, F.R., Buschow, K.H.J.: Magnetic and magnetocaloric properties of $Mn_5Ge_{3-x}Sb_x$. J. Alloy. Compd. **337**(1–2), 269–271 (2002)

Soni, A.K., Joshi, R., Singh, B.P., Kumar, N.N., Ningthoujam, R.S.: Near-infrared- and magnetic-field-responsive $NaYF_4:Er^{3+}/Yb^{3+}$@SiO_2@AuNP@Fe_3O_4 nanocomposites for hyperthermia applications induced by fluorescence resonance energy transfer and surface Plasmon absorption. ACS Appl. Nano Mat. **2**, 7350–7361 (2019)

Soni, A.K., Yadav, K.K., Singh, B.P., Joshi, R., Chakraborty, S., Chakravarty, R., Nagaraja, N.K., Singh, D.K., Kain, V., Dash, A., Ningthoujam, R.S.: Smart YPO_4:Er-Yb nanophosphor for optical heating, hyperthermia, security ink, cancer Endoradiotherapy, and uranyl recovery. ACS Appl. Nano Mater. **4**, 850–860 (2021)

Srivastava, M., Joshi, R., Singh, B.P., Ningthoujam, R.S.: Edited by P.A. Hassan, Biji Balakrishnan, A.K. Tyagi in Advances on magnetic nanoparticles based cancer therapy through hyperthermia: Basic understanding and history in Engineered Biomaterials: Progress and Prospects: Publisher: World Scientific Publishing Co Pvt Ltd, Singapore (2023)

Su, D., Wu, K., Krishna, V., Klein, T., Liu, J., Feng, Y., Perez, A.M., Cheeran, M.C., Wang, J.-P.: Detection of influenza a virus in swine nasal swab samples with a wash-free magnetic bioassay and a handheld giant magnetoresistance sensing system. Front. Microbiol. **10**, 1077 (2019) [PubMed][PubMedCentral]

Sudhakar, N., Ningthgoujam, R.S., Rajeev, K.P., Nigam, A.K., Weissmuller, J., Gajbhiye, N.S.: Effect of La, B doping on the electrical resistivity and magnetic susceptibility of nanocrystalline vanadium nitride. J. Appl. Phys. **96**, 688 (2004)

Sudhakar, N., Ningthoujam, R.S., Gajbhiye, N.S., Rajeev, K.P.: Structural, magnetic and electron transport studies on nanocrystalline layered manganite $La_{1.2}Ba_{1.8}Mn_2O_7$ system. J. Nanosci. Nanotech. **7**, 965 (2007)

Sun, Y., Tong, W., Liu, N., Zhang, Y.: Magnetocaloric effect in polycrystalline $(La_{0.5}Gd_{0.2})Sr_{0.3}MnO_3$. J. Magn. Magnet. Mater. **238**(1), 25–28 (2002)

Tashiro, T., Matsuura, S., Nomura, A., Watanabe, S., Kang, K., Sirringhaus, H.: Kazuya Ando, Spin-current emission governed by nonlinear spin dynamics. Sci. Rep. **5**, 15158 (2015)
[PubMed][PubMedCentral]

thekidshouldseethis.com, The Meissner Effect: How to levitate a neodymium magnet

Thorat, N.D., Otari, S.V., Patil, R.M., Bohara, R.A., Yadav, H.M., Koli, V.B., Chaurasia, A.K., Ningthoujam, R.S.: Synthesis, characterization and biocompatibility of chitosan functionalized superparamagnetic nanoparticles for heat activated curing of cancer cells. Dalton Trans. **43**, 17343–17351 (2014a)
[PubMed]

Thorat, N.D., Otari, S.V., Bohara, R.A., Yadav, H.M., Khot, V.M., Salunkhe, A.B., Phdatre, M.R., Prasad, A.I., Ningthoujam, R.S., Pawar, S.H.: Structured superparamagnetic nanoparticles for high performance mediator of magnetic fluid hyperthermia: synthesis, colloidal stability and biocompatibility evaluation. Mater. Sci. Eng., C **42**, 637–646 (2014b)

Thorat, N.D., Khot, V.M., Salunkhe, A.B., Prasad, A.I., Ningthoujam, R.S., Pawar, S.H.: Surface functionalized $La_{0.7}Sr_{0.3}MnO_3$ nanoparticles with improved colloidal stability for hyperthermia applications. J. Phys. D **46**, 105003 (2013)

Thorat, N.D., Otari, S.C., Patil, R.M., Khot, V.M., Prasad, A.I., Ningthoujam, R.S., Pawar, S.H.: Enhanced colloidal stability of polymer coated $La_{0.7}Sr_{0.3}MnO_3$ nanoparticles in physiological media for hyperthermia application. Colloids and Surfaces B: Biointerfaces **111**, 264 (2013)

Thorat, N.D., Khot, V.M., Salunkhe, A.B., Ningthoujam, R.S., Pawar, S.H.: Functionalization of $La_{0.7}Sr_{0.3}MnO_3$ nanoparticles with polymer: Studies on enhanced hyperthermia and biocompatibility properties for biomedical applications. Colloids Surfaces B Bio Interfaces **104**, 40–47 (2013)

Thorat, N.D., Patil, R.M., Khot, V.M., Salunkhe, A.B., Prasad, A.I., Barick, K.C., Ningthoujam, R.S., Pawar, S.H.: Highly water dispersible surface functionalized LSMO nanoparticles for magnetic fluid hyperthermia application. New J. Chem. **37**, 2733 (2013)

Torrisi, V., Graillot, A., Vitorazi, L., Crouzet, Q., Marletta, G., Loubat, C., Berret, J.F.: Preventing corona effects: multiphosphonic acid Poly(Ethylene Glycol) copolymers for stable stealth iron oxide nanoparticles. Biomacromol **15**, 3171–3179 (2014)

Ulbrich, K., Hola, K., Subr, V., Bakandritsos, A., Tucek, J., Zboril, R.: Targeted drug delivery with polymers and magnetic nanoparticles: covalent and noncovalent approaches, release control, and clinical studies. Chem. Rev. **116**, 5338–5431 (2016)
[PubMed]

Umare, S.S., Ningthoujam, R.S., Sharma, S.J., Shrivastava, S., Kurian, S., Gajbhiye, N.S.: Mössbauer and magnetic studies on nanocrystalline $NiFe_2O_4$ particles prepared by ethylene glycol route. Hyperfine Interact. **184**, 235 (2008)

Valenzuela, R.: Novel applications of ferrites. Phys. Res. Int., 591839 (2012)

Vedrtnam, A., Kalauni, K., Dubey, S., Kumar, A.: A comprehensive study on structure, properties, synthesis and characterization of ferrites. AIMS Mater. Sci. **7**, 800–835 (2020)

Wada, H., Tanabe, Y.: Giant magnetocaloric effect of $MnAs_{1-x}Sb$ x. Appl. Phys. Lett. **79**(29), 3302–3304 (2001)

Wang, J.L., Li, W.Z., Zhong, X.P., Gao, Y.H., Qin, W.D., Tang, N., Lin, W.G., Zhang, J.X., Zhao, R.W., Yan, Q.W.: Fu-ming Yang, Study on high performance $Sm_2Fe_{17}N_x$ magnets. J. Alloy. Compd. **222**, 23–26 (1995)

Wang, J., Chepelianskii, A., Gao, F., Greenham, N.C.: Control of exciton spin statistics through spin polarization in organic optoelectronic devices. Nat. Commun. **3**, 1191 (2012)
[PubMed]

Wang, Y.-H., Zhao, J.-L., Liang, Y.: Photocatalytic degradation of phenol in aqueous solution by titanium dioxide coupled with magnetic field. J. Adv. Oxid. Technol. **16**, 173–178 (2013)

Wang, Q., Prigiobbe, V., Huh, C., Bryant, S.L.: Alkaline earth element adsorption onto PAA-coated magnetic nanoparticles. Energies **10**, 223 (2017)

Wang, Y., Liu, X., Xu, X., Yang, Y., Huang, L., He, Z., Xu, Y., Chen, J., Feng, Z.: Preparation and characterization of reduced graphene oxide/Fe_3O_4 nanocomposite by a facile in-situ deposition method for glucose biosensor applications. Mater. Res. Bull. **101**, 340–346 (2018)

Wang, L., Qiu, H., Liang, C., Song, P., Han, Y., Han, Y., Gu, J., Kong, J., Pan, D., Go, Z.: Electromagnetic interference shielding MWCNT-Fe_3O_4@Ag/epoxy nanocomposites with satisfactory thermal conductivity and high thermal stability. Carbon **141**, 506–514 (2019)

Wang, Z., Li, Y., Wu, C., Tsang, S.C.E.: Electric-/magnetic-field-assisted photocatalysis: mechanisms and design strategies. Joule **6**(8), 1798–1825 (2022)

Warlimont, H., Boll, R.: Applications of amorphous soft magnetic materials. J. Magn. Magn. Mater. **26**(1), 97–105 (1982)

Wu, W., Jiang, C.Z., Roy, V.A.: Designed synthesis and surface engineering strategies of magnetic iron oxide nanoparticles for biomedical applications. Nanoscale **8**, 19421–19474 (2016)
[PubMed]

Wu, K., Klein, T., Krishna, V.D., Su, D., Perez, A.M., Wang, J.-P.: Portable GMR handheld platform for the detection of influenza A virus. ACS Sens. **2**, 1594–1601 (2017)
[PubMed]

Wu, K., Su, D., Saha, R., Liu, J., Chugh, V.K., Wang, J.: Magnetic particle spectroscopy: a short review of applications using magnetic nanoparticles. ACS Appl. Nano Mater. **3**(6), 4972–4989 (2020)

Xiao, J.Q., Jiang, J.S., Chien, C.L.: Giant magnetoresistance in nonmultilayer magnetic systems. Phys. Rev. Lett. **68**(25), 3749–3752 (1992)
[PubMed]

Yaghoubi, H.: The most important maglev applications. Hindawi, 537986 (2013)

Yanagisawa, Y., Kajita, K., Iguchi, S., Xu, Y., Nawa, M., Piao, R., Takao, T., Nakagome, H., Hamada, M., Noguchi, T.: 27.6 T generation using Bi-2223/REBCO superconducting coils. IEEE/CSC & ESAS Supercond News Forum **10** (2016)

Yao, C., Lin, H., Zhang, Q.J., Zhang, X.P., Wang, D.L., Dong, C.H., Ma, Y.W., Awaji, S., Watanabe, K.: Critical current density and microstructure of iron sheathed multifilamentary $Sr_{1-x}K_xFe_2As_2$/Ag composite conductors. J. Appl. Phys. **118**, 203909 (2015)

Yao, C., Ma, Y.: Superconducting materials: challenges and opportunities for large-scale applications, iScience **24**(6), 102541 (2021)

Yavuz, C.T., Mayo, J.T., Suchecki, C., Wang, J., Ellsworth, A.Z., D'Couto, H., Quevedo, E., Prakash, A., Gonzalez, L., Nguyen, C., Kelty, C., Colvin, V.L.: Pollution magnet: nano-magnetite for arsenic removal from drinking water. Environ. Geochem. Health **32**, 327–334 (2010)
[PubMed]

Yibole, H., Guillou, F., Zhang, L., van Dijk, N.H., Brück, E.: Direct measurement of the magnetocaloric effect in MnFe(P, X)(X = As, Ge, Si) materials. J. Phys. D Appl. Phys. **47**(7), 075002 (2014)

Yoon, S., Kim, J., Lee, H., Hahn, S., Moon, S.H.: 26 T 35 mm all-$GdBa_2Cu_3O_{7-x}$ multi-width no-insulation superconducting magnet. Supercond. Sci. Technol. 29 (2016)

Yu, K., Zeng, Y., Wang, G., Luo, X., Li, T., Zhao, J., Qian, K., Park, C.B.: RGO/Fe_3O_4 hybrid induced ultra-efficient EMI shielding performance of phenolic-based carbon foam. RSC Adv. **9**(36), 20643–20651 (2019) [PubMed][PubMedCentral]

Zhang, Y.F.: 2G HTS wire production at Super Power for emerging magnet applications, presentation at the 28th International Superconductivity Industry Summit, Beijing, China (2019)

Zhao, X., Wang, J., Wub, F., Wang, T., Cai, Y., Shi, Y., Jiang, G.: Removal of fluoride from aqueous media by Fe_3O_4 @$Al(OH)_3$ magnetic nanoparticles. J. Hazard. Mater. **173**, 102–109 (2010) [PubMed]

Zhao, Y., Li, Y., Jiang, K., Wang, J., White, W.L., Yang, S., Lu, J.: Rapid detection of listeria monocytogenes in food by biofunctionalized magnetic nanoparticle based on nuclear magnetic resonance. Food Control **71**, 110−116 (2017)

Zhao, X., Gao, W., Liu, Q., Cui, C., Zhou, W., Wang, X., Zhang, X.L., Zhao, L., Sang, Y., Liu, H.: Enhanced photo-induced carrier separation of CdS/MoS_2 via micro-potential of Mo microsheet derived from electromagnetic induction. Chem. Eng. J. **404**, Article 126972 (2021)

Zimm, C., Jastrab, A., Sternberg, A., Pecharsky, V., Jr. Geschneidner, K., Anderson, M.I.: Description and performance of a near-room temperature magnetic refrigerator. Adv. Cryogenic Eng. **43**, 1759–1766 (1998)

© The Author(s), under exclusive license to Springer Nature Singapore Pte Ltd. 2024
R. S. Ningthoujam, A. K. Tyagi (eds.), *Handbook of Materials Science, Volume 2*, Indian Institute of Metals Series
https://doi.org/10.1007/978-981-97-4646-0_6

6. Defects-Induced Multifunctional Properties in $BiFeO_3$

Subhajit Nandy[1, 3], Pavana S. V. Mocherla[2, 3] and C. Sudakar[3] ✉

(1) Advanced Analysis Center, Korea Institute of Science and Technology, Seoul, 02792, Republic of Korea
(2) Centre for Automotive Energy Materials (CAEM), International Advanced Research Centre for Powder Metallurgy and New Materials (ARCI), Chennai, 600113, India
(3) Multifunctional Materials Laboratory, Department of Physics, Indian Institute of Technology Madras, Chennai, 600036, India

✉ **C. Sudakar**
Email: csudakar@iitm.ac.in

Keywords $BiFeO_3$ – Multiferroics – Magnetoelectric coupling – Spin cycloid – Magnetism – Defects – Oxygen vacancies

Subhajit Nandy and Pavana S. V. Mocherla these authors contributed equally to this work.

6.1 Introduction

Defects in a material are localized deviations from an otherwise perfectly ordered crystal structure. Based on the extent of their influence in a crystal lattice, defects are broadly categorized into planar defects (stacking faults, twin boundaries), line defects (edge and screw dislocations), and point defects (interstitials and vacancies). Defects prevailing in the interfaces and grain boundaries are of significant importance as well. Even the surface of a material is treated as a defect due to the truncated bonds and associated local disruption it hosts. Dopants in a lattice are also categorized as substitutional defects. Defects are not always undesirable—they play a crucial role in bringing out novel properties that cannot be realized in an otherwise pristine material. Regardless of the fact that the point defects limit their influence to a few unit cells in their vicinity, their distribution and concentration in the lattice decide the physical properties of a material. Manipulation of a material structure for its defect concentration and thereby its physical properties have gradually evolved into an exclusive field of research under the title defect engineering. Concurrently, several works emerged on how engineering strain, an associated parameter, can be used to regulate the properties of materials, particularly oxides (Tsutsui et al. 2019; Schlom et al. 2014). This has opened up new possibilities in the fields of spintronics (Nenno et al. 2019), ferroelectrics (Nataf et al. 2020; Dong et al. 2022), thermoelectrics (Zheng et al. 2021), energy storage (Liu et al. 2022; Liu and Fan 2023), memristors (Banerjee et al. 2020), photovoltaics (Wang et al. 2022), photocatalytics (Zhang et al. 2019), sensors (Liang et al. 2021), etc. Sophisticated characterization techniques such as surface-enhanced Raman spectroscopy, x-ray photoelectron spectroscopy,

high-resolution transmission electron microscopy, electron paramagnetic resonance spectroscopy, etc., have been used to detect the defects and the structural modifications caused by them.

These studies have been amply substantiated by a multitude of theoretical calculations on the kinetics of defect formation using several approaches. Freysoldt et al. (2014) in their comprehensive review on the modeling of point defects in solids highlighted the accuracy and reliability of modern first-principles simulations, which when analyzed with sufficient care, corroborate well with the experimental results. It is reported that theoretical methods can provide a deeper insight into many properties of defects which cannot be probed otherwise using experiments. Their formalism includes using first-principles density functional theory for estimating the formation energy of a point defect as a function of thermodynamic variables like chemical potential, temperature, and pressure. The formation energy $E_f\,[X^q]$ of a defect X in charge state q is defined as

$$E_f\,[X^q] = E_{\text{tot}}\,[X^q] - E_{\text{tot}}\,[\text{bulk}] - \sum_i n_i\mu_i + qE_f + E_{\text{corr}}$$

where $E_{\text{tot}}\,[X^q]$ is the total energy derived from a supercell calculation containing the defect X and E_{tot}[bulk] is the total energy for the perfect crystal using an equivalent supercell, n_i is the number of atoms added or removed to the supercell to form the defect and μ_i is the corresponding chemical potential of these atoms. A recent review article by Hamidreza et al. (Arandiyan et al. 2021) surveys the role of defect-engineering in the design, fabrication, modification, and application of oxide perovskites for photocatalysis and energy storage applications. This work, comprehensively summarizes the studies on various oxides

and how examining the mechanism of defects from various sources can be used, in combination with the theoretical and experimental findings, to address the challenges currently faced in utilizing these materials for device applications. Such studies also justify the need for a comprehensive understanding of the defect-induced tailoring of functional properties of different oxide materials.

Generally, the formation of defects in solids is unavoidable due to the fact that almost all the processes take place away from the equilibrium and that they occur at finite temperatures well above 0 K. Defects, either individually or through a collective interaction with the other defects of similar type, greatly influence the physical properties of a material. Understanding the structure–property relationship in defect-engineered systems enables the application of materials in advanced technologies. The following sections of this chapter set off to provide a more specific extension to the prologue on defects in materials—bismuth ferrite, a classic room temperature multiferroic. The first part of the chapter covers the general description of multiferroic materials, broad classification, and the structure of bismuth ferrite. The latter part of the chapter runs into the details of how various types of defects, and strain influence the magnetic ordering, ferroelectricity, and magnetoelectric coupling in bismuth ferrite. Additionally, a brief note on the role of defects in altering the electronic structure, photoconductivity, and photovoltaic properties of bismuth ferrite is also given.

6.1.1 Multiferroic Materials

Multifunctional materials are those which exhibit multiple functions in a single material. Multiferroics is one such class of multifunctional materials that shows promising potential for a multitude of device applications in various fields. Ferroic is a term given to the intrinsic physical

property of a material that is capable of retaining a spontaneous and switchable parameter. Multiferroics are those materials that exhibit more than one primary ferroic order parameter in a single phase. The most common ferroic (order parameter) properties are ferromagnetism (magnetic moment), ferroelectricity (electric dipole moment), and ferroelasticity (strain). Ferroelectrically-induced ferromagnetism in an otherwise antiferromagnetic material was first discovered in 1958. Significant works by Smolensky and Agranovskaya (1958), Smolensky et al. (1958), Ascher et al. (1966), and Schmid (1969) have incited global research toward comprehending the microscopic phenomena responsible for coupling between polarization and magnetization in these materials alongside the potential device applications (Fox and Scott 1977). Schmid in 1994 established the concept of multiferroism as co-existence of two or all three of ferromagnetism, ferroelectricity and ferroelasticity in single phase (Schmid 1994). Few multiferroics exhibit magnetoelectric coupling in the same phase, giving us an additional degree of freedom—the ability to tune magnetization with an applied electric field and vice versa.

The study of magnetoelectric multiferroics is fascinating because the requirements of a material to be singly magnetic or ferroelectric are not just different but also negating. A remarkable study by Nicola Hill (2000), explaining the criterion for the co-existence of otherwise mutually exclusive magnetic and ferroelectric phenomena is an upshot in this field. For example, the *d* orbital electrons required to produce ferromagnetism reduce the tendency for ferroelectric distortion in perovskite structures of type ABO_3. Paucity in magnetoelectric multiferroics, particularly in perovskites, was attributed to the interplay of several competing factors with the *d* electron configuration of the transition metal being a

critical variable. These multiferroics are much anticipated to bear potential applications in devices like ferroelectric memories, terahertz radiation sources, switches, etc. The chief application of these multiferroics is magnetoelectric random access memory (MERAM) which can be written using voltage and read by magnetic field. This has the core advantages of implementing in a solid-state circuit without mobile parts, low-energy requirement, the possibility of scaling down voltage with dimensions, and non-destructive reading with magnetic field unlike ferroelectric reading based on polarization switching (Catalan and Scott 2009). Multiferroic materials are classified into three categories based on the origin of ferroelectricity (Fig. 6.1). In Type-I, the sources of ferroelectricity and magnetism are distinct and the coupling between these parameters is weak. The mechanism of multiferroism in such magnetic perovskite structure oxides and related materials is most commonly achieved by the stereochemical activity of the lone pair on the large A-site cation to provide a ferroelectric nature, while the small B-site cation serves as a magnetic source. $BiFeO_3$ is a well-known example of Type-I multiferroics. Type-II multiferroics are also called geometric multiferroics that exhibit ferroelectric instability from the topology of the chemical environment and ionic size effects. $YMnO_3$ is a good example of Type-II multiferroics wherein ferroelectricity originates from the rotation of MnO_5 bi-pyramids. In Type-III multiferroics, ferroelectricity comes from long-range ordering of an electronic degree of freedom like orbital, charge, or spin. These are also called magnetically-induced ferroelectricity and $TbMnO_3$ is a good example of this class. Long-familiar ferroelectrics, the perovskite oxides of type ABO_3 with transition metal cations have been the subjects of pursuit over the past two decades. Enhancing the magnetoelectric coupling to better suit the storage requirements and other related

applications via defect control, microstructural modulations, and physical property manipulation has been the core objective of this multiferroic research. The following sections present more details on $BiFeO_3$—the most extensively studied Type-I room temperature multiferroic. The emphasis is laid on how defects, both intrinsic and caused by doping, influence the multiferroic properties. Also, a brief discussion along similar lines is provided about the other multifunctional properties of $BiFeO_3$.

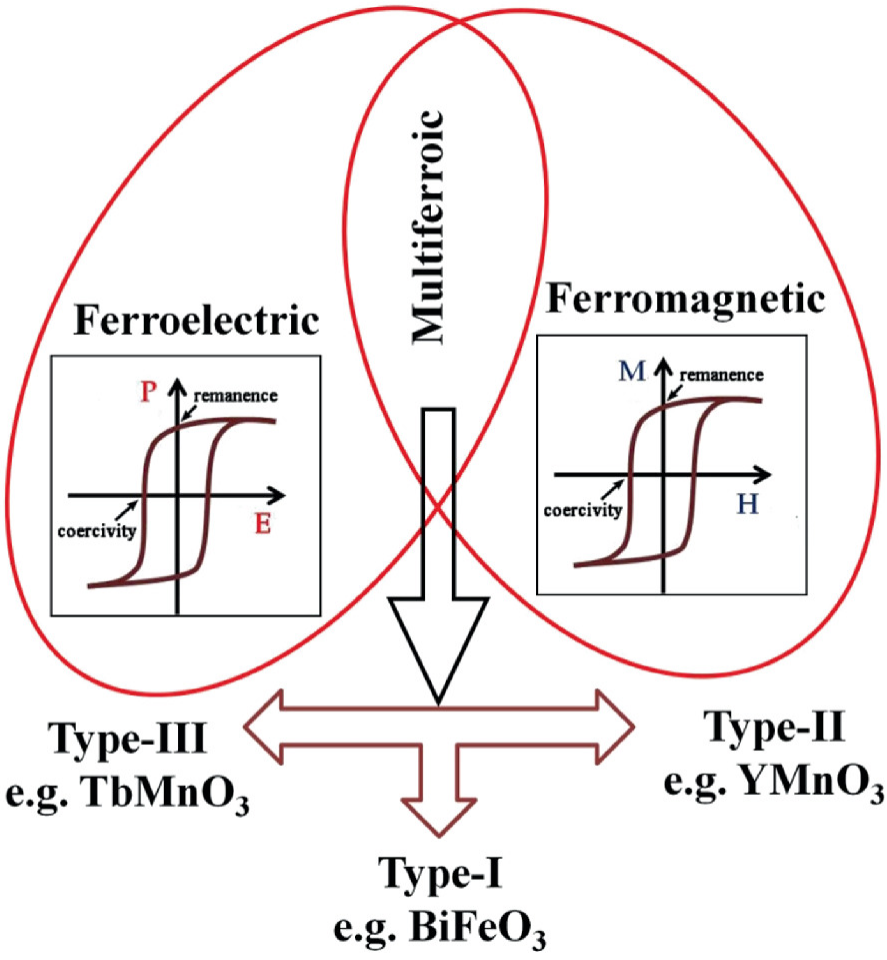

Fig. 6.1 Different types of multiferroic materials

6.1.2 Bismuth Ferrite

$BiFeO_3$ is a Type-I multiferroic material, wherein the ferroelectricity and magnetism have distinct sources. The crystal structure of $BiFeO_3$ deviates from an ideal cubic perovskite of ABO_3 belonging to $Pm\bar{3}m$ space group (a_C = 3.965 Å; $\alpha_C \sim 89.3°$). The stereochemical activity of the lone pair in Bi $6s^2$ orbital introduces the distortion in FeO_6 octahedral alignment. The extent of structural distortion possible in perovskite structure can be indicated by the Goldschmid tolerance factor, $t = (r_A + r_O)/\sqrt{2}\ (r_B + r_O)$; where r_X is the ionic radius of the respective X ion; $t = 1$ represents an ideal cubic perovskite. $BiFeO_3$ composed of Bi^{3+} (117 pm), Fe^{3+} (78.5 pm), and O^{2-} (126 pm) ions have $t = 0.88$. $BiFeO_3$ usually crystallizes in rhombohedrally distorted perovskite structure of $R3c$ space group (S.G.) with $a_R = 5.636$ Å, $\alpha_R \sim 59.34º$ (Fig. 6.2). Equivalently, it is also represented in a hexagonal frame of reference with unit cell constants $a_H = b_H = 5.5876$ Å, $c_H = 13.867$ Å, $\alpha = \beta = 90º$, and $\gamma = 120º$ (Fig. 6.2) (Moreau et al. 1971). Adjacent octahedra in $BiFeO_3$ are rotated by an angle of 13.8°, as opposed to 0° in cubic perovskite (Kubel and Schmid 1990).

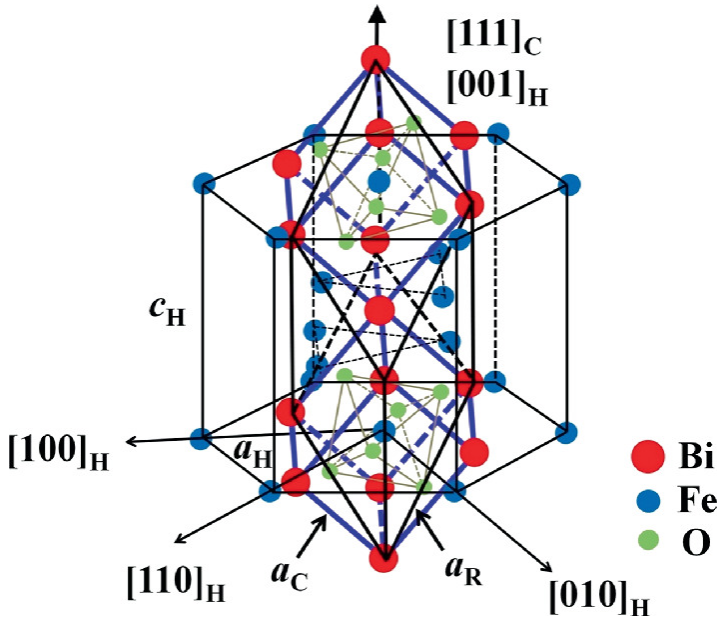

Fig. 6.2 Structure of $BiFeO_3$: hexagonal, rhombohedral (S.G. *R*3*c*) and pseudo-cubic (S.G. $Pm\bar{3}m$) unit cells are shown overlapped

The off-center displacement of FeO_6 octahedra with respect to Bi^{3+} ions, resulting from the hybridization of O 2*p* orbitals with Bi 6*s* causes ferroelectric polarization. The direction of the spontaneous polarization in $BiFeO_3$ is along $[111]_{PC}$ for a pseudo-cubic (PC) unit cell which is equivalent to the direction $[001]_H$ for a hexagonal (H) perovskite unit cell. In the case of $BiFeO_3$ single crystal, a spontaneous polarization of 6.1 μC/cm^2 was reported in the direction $[111]_{PC}$ for a pseudo-cubic unit cell (Teague et al. 1970). Later, a large polarization of 100 μC/cm^2 was observed in $BiFeO_3$ single crystal (Lebeugle et al. 2007). The observed spontaneous polarization was found to match well with the theoretically calculated polarization in the range of 90–100 μC/cm^2 from the first principle studies (Neaton et al. 2005*)*. In $BiFeO_3$, ferroelectric domains are oriented in eight different directions, separated by three possible domain walls named 71°, 109°, and 180° (Streiffer et al. 1998).

Magnetism, on the other hand, is solely due to Fe^{3+} ions ordered in a G-type antiferromagnetic structure (Fig. 6.3a and b). The opposite Fe sublattices do not exactly compensate, leaving a net moment (0.39 μ_B) per each rhombohedral unit cell. These residual local moments constitute a cycloidal spin structure of period length ~62 nm (Fig. 6.3c) (Catalan and Scott 2009). Beyond this length scale, these net moments compensate totally making the bulk $BiFeO_3$ antiferromagnetic. Disrupting the cycloidal spin structure was conceived to be a route to enhance magnetization and strengthen the magnetoelectric coupling in $BiFeO_3$. Researchers considered size reduction of $BiFeO_3$ as an avenue to achieve the desired enhancement. Several reports discuss the size-dependent magnetic and ferroelectric properties in $BiFeO_3$ nanoparticles as well as thin films. However, size reduction in $BiFeO_3$, as in many other oxide systems, comes along with several other challenges and any observable change in the physical properties below a size scale is an aggregate of multiple competing factors. These include the dimensions (particle size or film thickness), morphology, cation and anion defects, and strain. These factors are most often tuned by altering the synthesis/processing conditions and elemental composition. A few theoretical works probing the role of point defects and strain on the physical properties of $BiFeO_3$ were reported in the early 2000s. Alongside, there have been experimental studies exploring the size-dependence of magnetism and ferroelectricity in $BiFeO_3$. Since then, a multitude of theoretical and experimental studies have emerged and size-defects-strain-local structure-physical property correlation is still an ongoing topic of interest with respect to $BiFeO_3$.

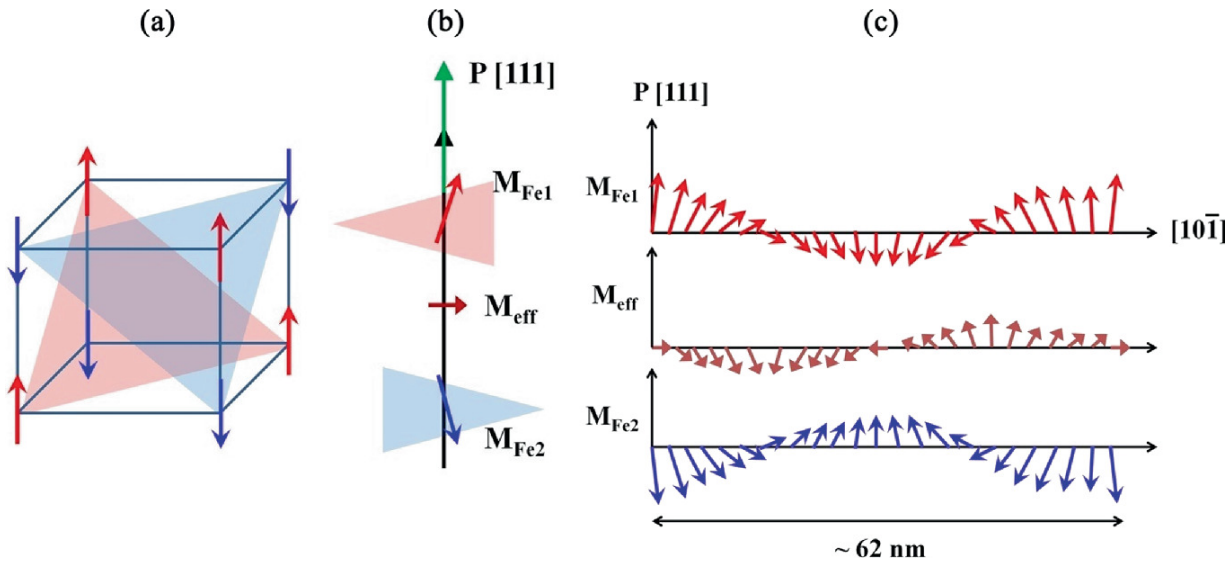

Fig. 6.3 **a** Schematic of G-type antiferromagnetic spins in a cubic lattice. **b** Weak ferromagnetism is produced from the spin canting of adjacent Fe ions perpendicular to [111]. (Adapted with permission from Heron et al. Appl. Phys. Rev., 1, 021303, 2014 (Heron et al. 2014). Copyright (2014) American Institute of Physics). **c** Schematic of spin cycloid in $BiFeO_3$. Red and blue arrows represent the magnetic moments of Fe ions in the unit cell. The brown color shows the net magnetization in a unit cell. Net magnetic moment moves along [$10\bar{1}$] perpendicular to [111]

6.2 Defects and Strain in Bismuth Ferrite

Defects and strain can alter the electronic structure of $BiFeO_3$ and hence influence the properties significantly. Various point defects such as Bi vacancy (V_{Bi}), Fe vacancy (V_{Fe}), O vacancy (V_O) along with the substitutional (X_{Bi} or Y_{Fe}) and interstitial (Z_i) dopants in $BiFeO_3$ and the strain (compressive and tensile) resulting to the structural changes are summarized in Fig. 6.4. The significance of defects and strain in $BiFeO_3$ has been explored by many researchers and umpteen reports related to both anion (V_O) and cation (V_{Bi} and V_{Fe}) vacancies exist to date. Substitutional (X_{Bi} or Y_{Fe}) and interstitial dopant (Z_i)

defects are also shown to alter the structure and properties of $BiFeO_3$. The substitution of the Bi site strongly affects the ferroelectric property of $BiFeO_3$ as the polarization is mainly dependent on the Bi site. Bi site of $BiFeO_3$ is already substituted by alkaline earth metals (Ca, Sr, Ba) and rare earth metals (La, Ce, Pr, Nd, Sm, Eu, Gd, Dy, Ho). Substitution at the Bi site can modify the electronic structure and indirectly influence the band structure. Fe site in $BiFeO_3$ is usually substituted by transition metals like Ti, Cr, Mn, Co, Ni, Zn, and Cu. Since the 3*d* orbital of Fe^{3+} constitutes the conduction band, doping at the Fe site strongly influences the electronic structure near the Fermi level and thereby the physical properties. Strain can be categorized into longitudinal, shearing, and volumetric based on the distortion produced in the structure. Strain alters the lattice parameters and affects the physical properties. There has been an adequate number of reports on how defects and strain influence the properties of $BiFeO_3$ in various contexts (Zeches et al. 2009). In this section, the emphasis is laid on how researchers construed the role of defects and strain in altering the physical properties of $BiFeO_3$ ever since the concept of multiferroicity was formulated. The following discussion is confined to those works which presented an explicit study on defects and strain in $BiFeO_3$, for brevity.

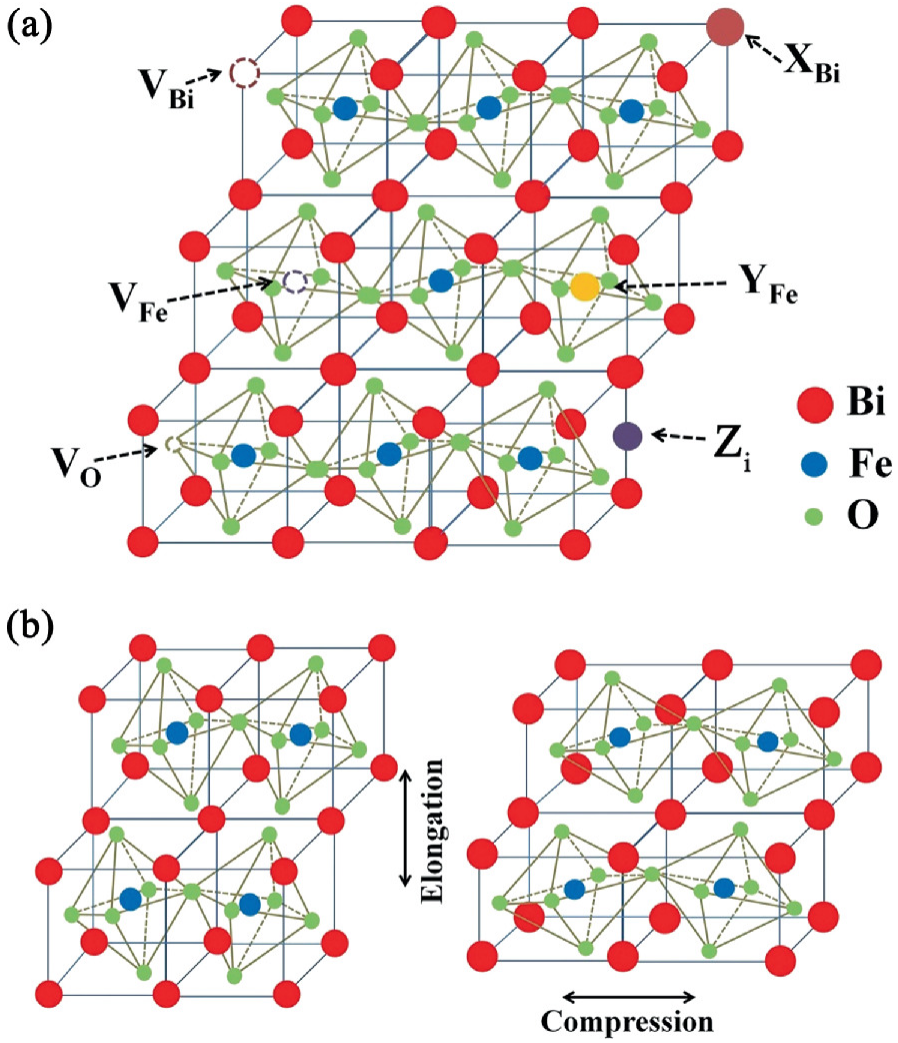

Fig. 6.4 Schematic illustration of **a** different point defects, **b** compressive and tensile strain-induced changes in $BiFeO_3$ structure

6.2.1 Magnetic and Ferroelectric Properties

Initial first principle density functional calculations carried out by Ederer and Spaldin suggested that, unlike any conventional perovskite, neither oxygen vacancies nor strain showed any effect on the ferroelectric polarization (Ederer and Spaldin 2005). The strain does not influence the magnetization, but they reported that a slight alteration in the magnetization and generation of Fe^{2+} is possible in the presence of oxygen vacancies.

Modulation of magnetization by size control: Size dependence of magnetism and ferroelectricity were first explored in 2007. A few seminal reports which highlighted the definite influence of material dimensions on the physical properties of $BiFeO_3$ are mentioned here. Thickness-dependent (40–500 nm) studies on $BiFeO_3$ films by Rana et al. (2007) observed a structural transformation from rhombohedral to tetragonal for films of thickness less than 75 nm, and a fully relaxed rhombohedral phase above 110 nm. Interestingly, the strained phase in an otherwise relaxed structure, just by changing the pressure of O_2 during post-synthesis annealing, was realized. Weak magnetism of the order of 0.1 μ_B (per Fe ion) in these films is attributed to the epitaxial strain. Park et al. (2007) reported a linear increase in magnetization with a reduction in the size of $BiFeO_3$ nanoparticles from 245 to 41 nm. This is in line with Neel's model of antiferromagnetic single-domain particles. Such an increase is explained by considering these nanoparticles to be made of antiferromagnetic core and ferromagnetic surface. Further reduction in size to 14 nm displayed a considerable deviation from this linearity, mostly attributed to the permeation of surface strain into the entire particle volume randomizing the spin structure.

Finite-size effects in $BiFeO_3$ nanoparticles were also reported by Selbach et al. (2007). Below a critical size of 30 nm, the rhombohedral distortion gradually disappears nearing the ideal cubic structure of a perovskite. The magnetic transition temperature reduces with a decrease in particle size and gets increasingly diffused. On extrapolation, they estimated the critical size of the ferroelectric phase in the compound to be around 8 to 10 nm. Huang et al. (2013) reported a peculiar behavior of sudden rise in the magnetization and ferroelectricity for

$BiFeO_3$ nanoparticles of size close to 62 nm, the spin cycloid length. They attribute this deviation from monotonic increase to the structural anomalies that set in around this size scale.

Modulation of magnetic property by strain control: Compressively strained $BiFeO_3$ films grown by Cheng et al. (2011) exhibited spin-glass behavior at low temperatures, asserting the presence of spin frustration in the strained films. Films of thickness around 38 nm exhibited a maximum magnetization of ~28 emu/cm^3 and coercivity of 130 Oe. Rondinelli and Spaldin in their extensive report on transition metal oxide heterostructures pointed out that interface chemistry and strain caused due to the mismatch influences the macroscopic properties of a heteroepitaxy significantly (Rondinelli and Spaldin 2011). Sando et al. (2013) using a combination of Raman and Mössbauer spectroscopies, Landau-Ginzberg theories, and effective Hamiltonian calculations demonstrated that the cycloidal spin structure exists in a phase with low compressive strain and changes into pseudo-collinear antiferromagnetism with high strain of both compressive and tensile type. Raman studies in this work suggested that strain quenches high-energy magnon modes. Also, it was reported that a spin reorientation from in-plane to out-of-plane takes place as the strain changes from compressive to tensile.

Modulation of magnetic property by defect and dopant control: Paudel et al. in 2012 presented that cation defects, i.e., Bi and Fe vacancies dominate in oxygen-rich conditions, and O and Bi vacancies dominate in oxygen deficient conditions (Paudel et al. 2012). Their first-principles calculations suggested that Bi and Fe vacancies produce magnetic moments of ~1 μ_B and ~5 μ_B per vacancy, respectively for p-type $BiFeO_3$. These cation

vacancies do not affect the magnetic moment in insulating $BiFeO_3$. According to Paudel et al., oxygen vacancies, on the other hand, do not seem to alter the magnetic moment in $BiFeO_3$ in either case, quite contrasting to all the above studies discussed.

Complex interplay of defects, strain, and dopants: Reports on strain in $BiFeO_3$ discussed so far referred to the lattice strain in thin films. Early size-dependent studies mentioned the increased surface effects on the physical properties of $BiFeO_3$. However, Mocherla et al. (2014) discussed microstrain as an averaged effect of local structural deviations observed in nanoparticles. Their study involved discussing the local structure variation and its effect on the physical properties of $BiFeO_3$ nanoparticles of size less than 65 nm. It was shown that the average microstrain increases as the size reduces below a critical value of ~30 nm. X-ray diffraction studies showed that the double peak at $2\theta \sim 32^{\circ}$ which is characteristic of the rhombohedral distortion in the structure suffers a gradual change in its profile with a reduction in size from 65 nm (Fig. 6.5a). Around this critical size value, which is almost half the spin-cycloid length, the local structure partially transforms from rhombohedral to pseudo-cubic symmetry. Raman shift in two phonon mode as a function of crystallite size also substantiates these structural changes (Figs. 6.5b, c and 6.7d). Existence of both the symmetries in highly strained nanoparticles was confirmed from the high-resolution transmission electron microscopy images (Fig. 6.6). X-ray photoelectron spectral studies confirmed that the oxidation states of Bi and Fe are predominantly 3+, suggesting the presence of oxygen defects.

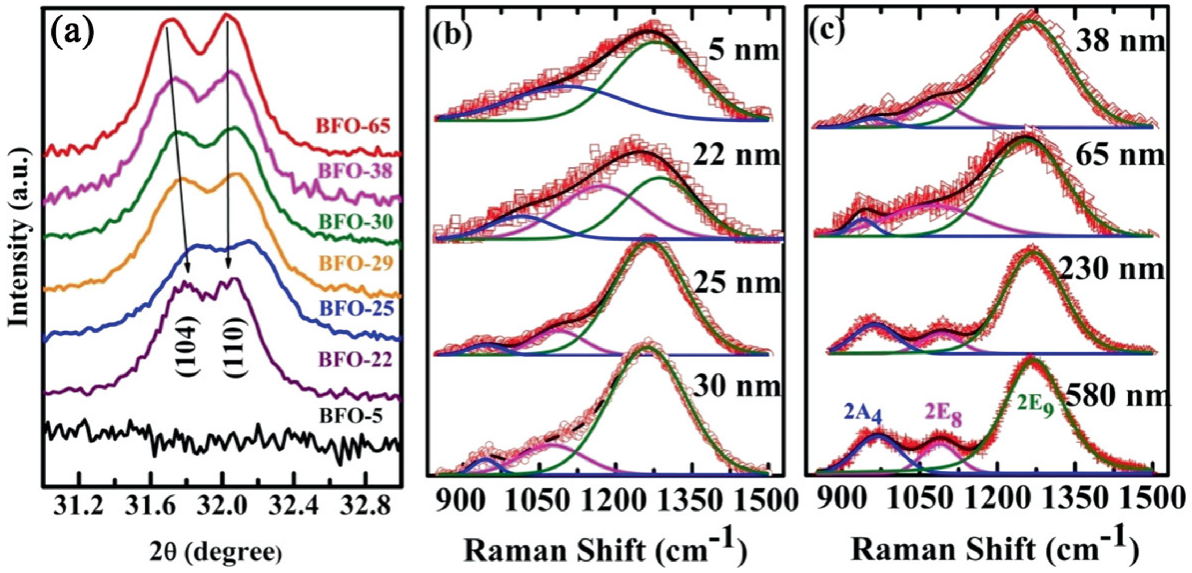

Fig. 6.5 **a** X-ray diffraction patterns showing the (104) and (110) reflections of $BiFeO_3$ nanoparticles with crystallite sizes vary from 5 to 65 nm (Reprinted with permission from Mocherla et al. Appl. Phys. Lett., 103, 022,910, 2013 (Mocherla et al. 2013). Copyright (2013) American Institute of Physics). **b**, **c** Variation of two phonon modes ($2A_4$, $2E_8$ and $2E_9$) of $BiFeO_3$ nanoparticles with crystallite sizes vary from 5 to 580 nm (Reprinted with permission from Mocherla et al. Appl. Phys. Lett., 105, 132,409, 2014 (Mocherla et al. 2014). Copyright (2014) American Institute of Physics)

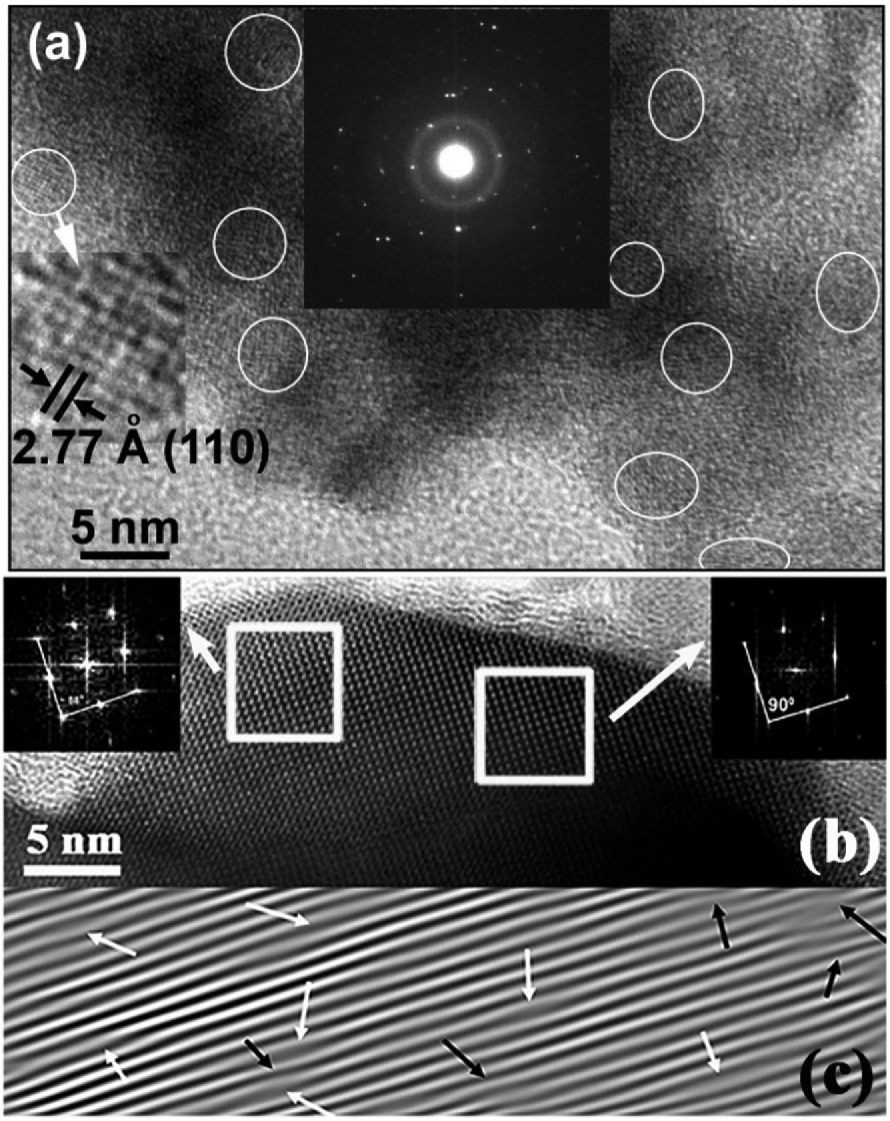

Fig. 6.6 **a** HRTEM image and SADP (inset) of $BiFeO_3$ nanoparticle with crystallite size of 5 nm. Regions of local crystallization are marked by white circles and a magnified region is marked by (110) lattice planes (Reprinted with permission from Mocherla et al. Appl. Phys. Lett., 103, 022910, 2013 (Mocherla et al. 2013). Copyright (2013) American Institute of Physics). **b** HRTEM image of $BiFeO_3$ nanoparticles with crystallite size of 22 nm. Left inset shows the FFT exhibits a rhombohedral distortion with 88° and right FFT shows cubic symmetry with 90° suggesting local structural changes in highly strained $BiFeO_3$ nanoparticles. **c** FFT of the same crystallite showing the compressive (black arrows) and tensile (white arrows) strains (Reprinted with permission from Mocherla et al. Appl. Phys. Lett., 105, 132409, 2014 (Mocherla et al. 2014). Copyright (2014) American Institute of Physics)

Generally, according to Néel's behavior of antiferromagnetic systems, a linear increase in the

magnetization is expected with the decrease in size. By contrast, the magnetic moment in these nanoparticles showed a sudden dip around the critical size of 30 nm, deviating largely from the ideal antiferromagnetic behavior (Fig. 6.7c). These results were discussed in combination with the altered Raman spectral profile of modes related to Fe–O bond activity (Fig. 6.7). Presence of microstrain in the nanoparticles, particularly of size less than 30 nm is reasoned to be the cause of the magnetic property variation. The Raman spectral modes at high frequency (450–650 cm^{-1}) are due to the Fe–O bond vibration in $BiFeO_3$. Overtones of these modes constitute a wide band centered around 1200 cm^{-1}. Both the position and relative intensity of the modes constituting this band alter systematically with size, particularly around the critical value where the microstrain is maximum. These results established that size reduction is not a straightforward solution to enhance the magnetization in $BiFeO_3$. Oxygen defects and microstrain play a critical role in deciding the magnetic properties of $BiFeO_3$ (Fig. 6.7).

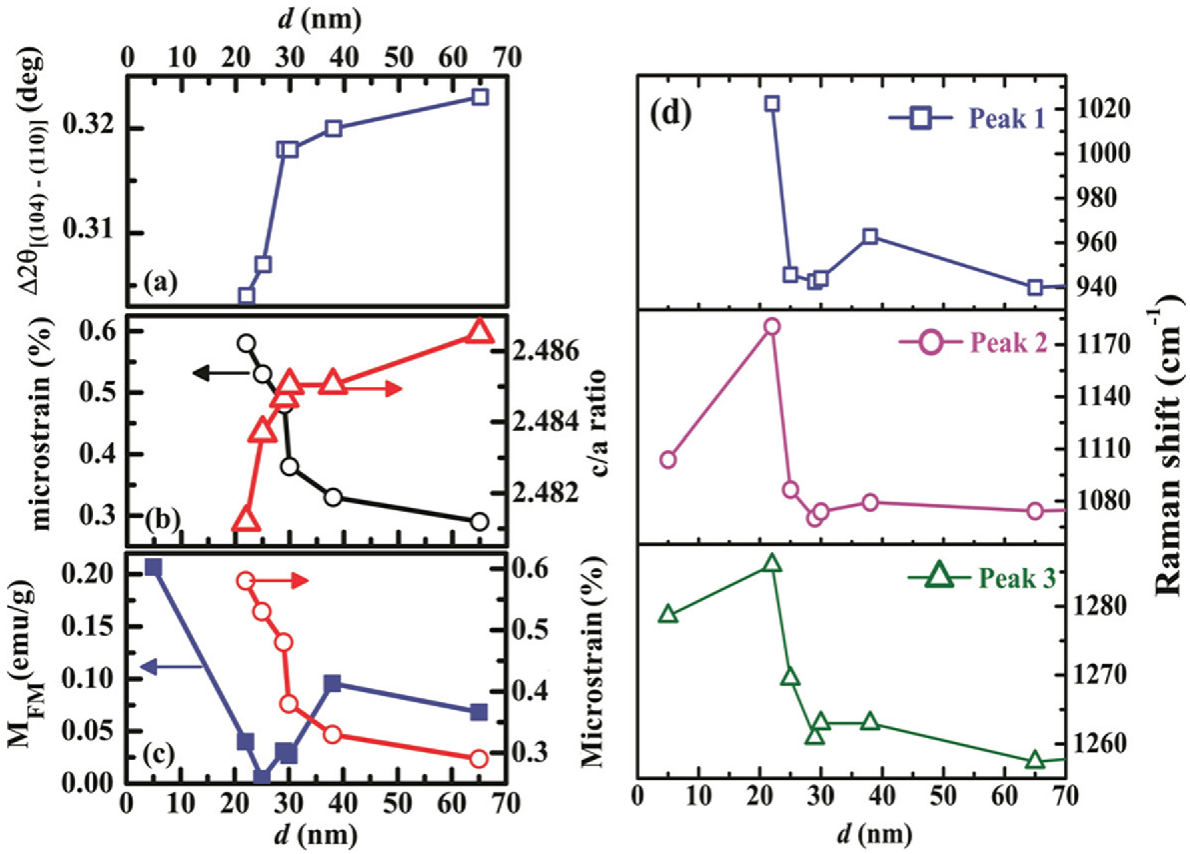

Fig. 6.7 Variation of **a** Δ2θ [(104)−(110)] **b** microstrain (%) and c/a ratio **c** magnetization (M_{FM}) at 2 T and microstrain (%) with increasing crystallite sizes of $BiFeO_3$ nanoparticles. **d** Raman shift in two phonon modes as a function of crystallite size (Reprinted with permission from Mocherla et al. Appl. Phys. Lett., 105, 132409, 2014 (Mocherla et al. 2014). Copyright (2014) American Institute of Physics)

Having observed that the oxygen vacancies play a dominant role in altering the magnetic structure, Mocherla et al. (2017) worked to increase the oxygen concentration by way of aliovalent doping at the cation sites in $BiFeO_3$. A comparative analysis between the properties of two sets of nanoparticles, viz., $Bi_{1-x}Ca_xFeO_{3-\delta}$ and $Bi_{1-x}Ca_xFe_{1-y}Ti_yO_{3-\delta}$ $(x = y)$ was presented. A complex interplay of size, defect concentration, temperature, and microstrain was discussed. Increasing oxygen vacancy concentration via aliovalent Ca^{2+} doping at Bi^{3+} site sets in a complex scenario of spin cycloid propagation in strained $BiFeO_3$ nanoparticles. Oxygen vacancy formation was found

to be suppressed when Ti^{4+} was substituted at the Fe^{3+} site in an equal amount as Ca^{2+} at the Bi^{3+} site. The oxygen-rich Ca-doped $BiFeO_3$ nanoparticles showed a mix of rhombohedral and orthorhombic structures, whereas the rhombohedral distortion is mostly preserved in the Ca^{2+}-Ti^{4+} co-doped $BiFeO_3$. Near-edge X-ray absorption spectroscopy was used to confirm the oxidation states of the cations and the presence of oxygen vacancies. High-resolution transmission electron microscopy studies and electron diffraction revealed the ordering of oxygen vacancies above a certain temperature.

Microstrain in Ca-doped $BiFeO_3$ is found to be an aggregate of deviations caused by oxygen vacancies within the particle core and surface disorder. Clearly, Ca-Ti co-doped nanoparticles showed a predominant surface strain component due to an insignificant number of oxygen vacancies (Fig. 6.8). It was interesting that for the same doping concentration, the particle size of Ca-doped and Ca-Ti co-doped $BiFeO_3$ differs considerably. Accordingly, possible differences in spin cycloid propagation in oxygen-deficient and near-stoichiometric conditions were elucidated (Fig. 6.9a). A deviation from the Néel's linear increase of magnetization with inverse particle size is observed in Ca-doped nanoparticles. For a given range of particle size, an empirical relationship between microstrain and magnetization is deduced (Fig. 6.9b). Thermomagnetic studies on oxygen-deficient nanoparticles showed a bifurcation of the magnetic Néel transition temperature, confirming the presence of mixed magnetic ordering due to coexistence of rhombohedral and orthorhombic phases. On the contrary, the near-stoichiometric system showed only a single transition. More interestingly, $BiFeO_3$ nanoparticles, irrespective of their composition and oxygen stoichiometry commonly exhibited a sharp Hopkinson-like effect at high

temperature (Mocherla et al. 2018). This sharp feature is attributed to the competing magnetocrystalline anisotropy and thermal randomization of spins in nanoparticles.

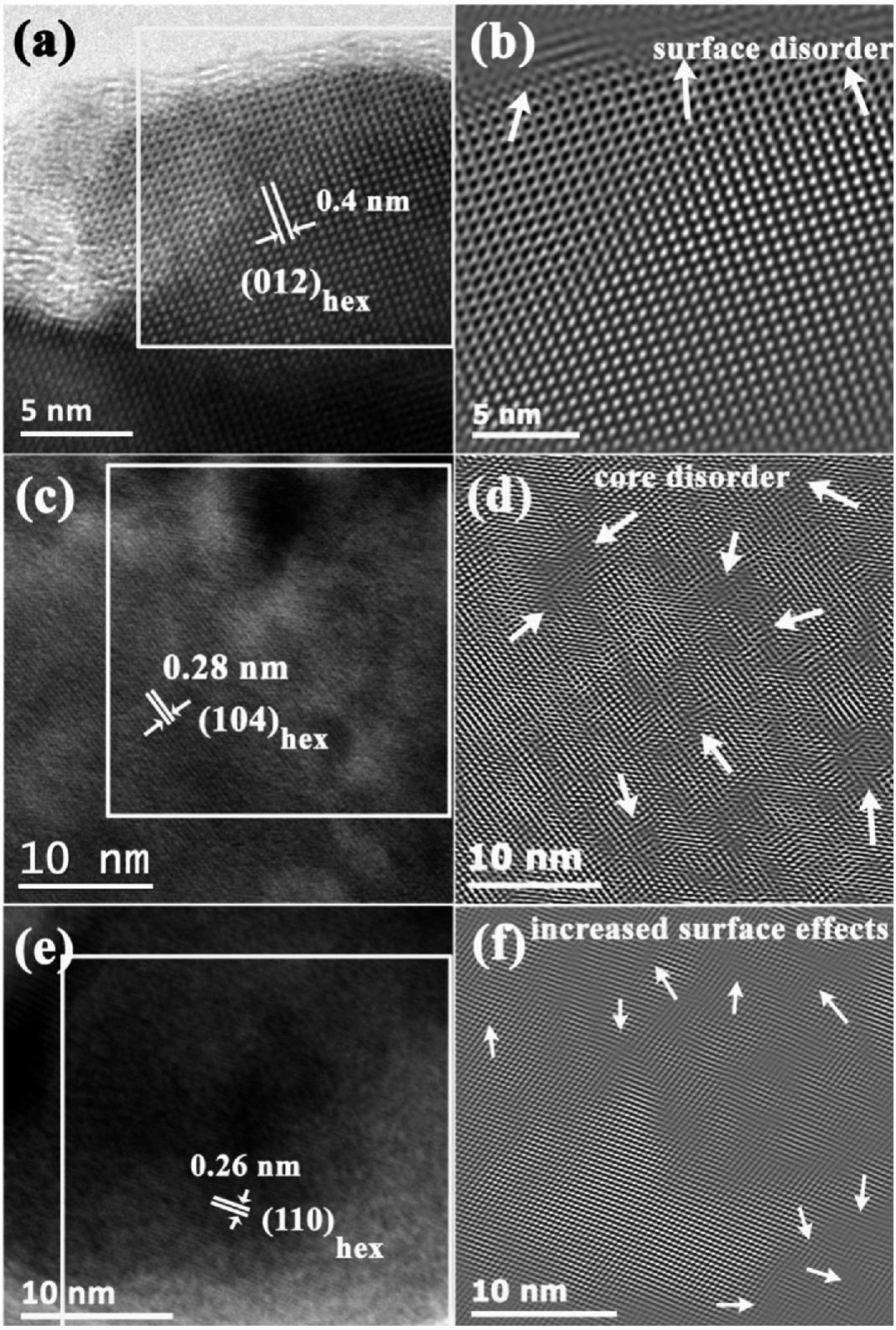

Fig. 6.8 HRTEM strain contrast and strained lattice images of **a**, **b** $BiFeO_3$, **c**, **d** $Bi_{1-x}Ca_xFeO_{3-\delta}$ ($x = 0.1$), and **e**, **f** $Bi_{1-x}Ca_xFe_{1-y}Ti_yO_{3-\delta}$ ($x = y$). Squares

in the left panel HRTEM images are the selected areas for obtaining filtered FFT. Arrows in the right panel show the strained regions (Reprinted with permission from Mocherla et al. Mater. Res. Express, 4 (10), 106106, 2017 (Mocherla et al. 2017). Copyright (2017) Institute of Physics)

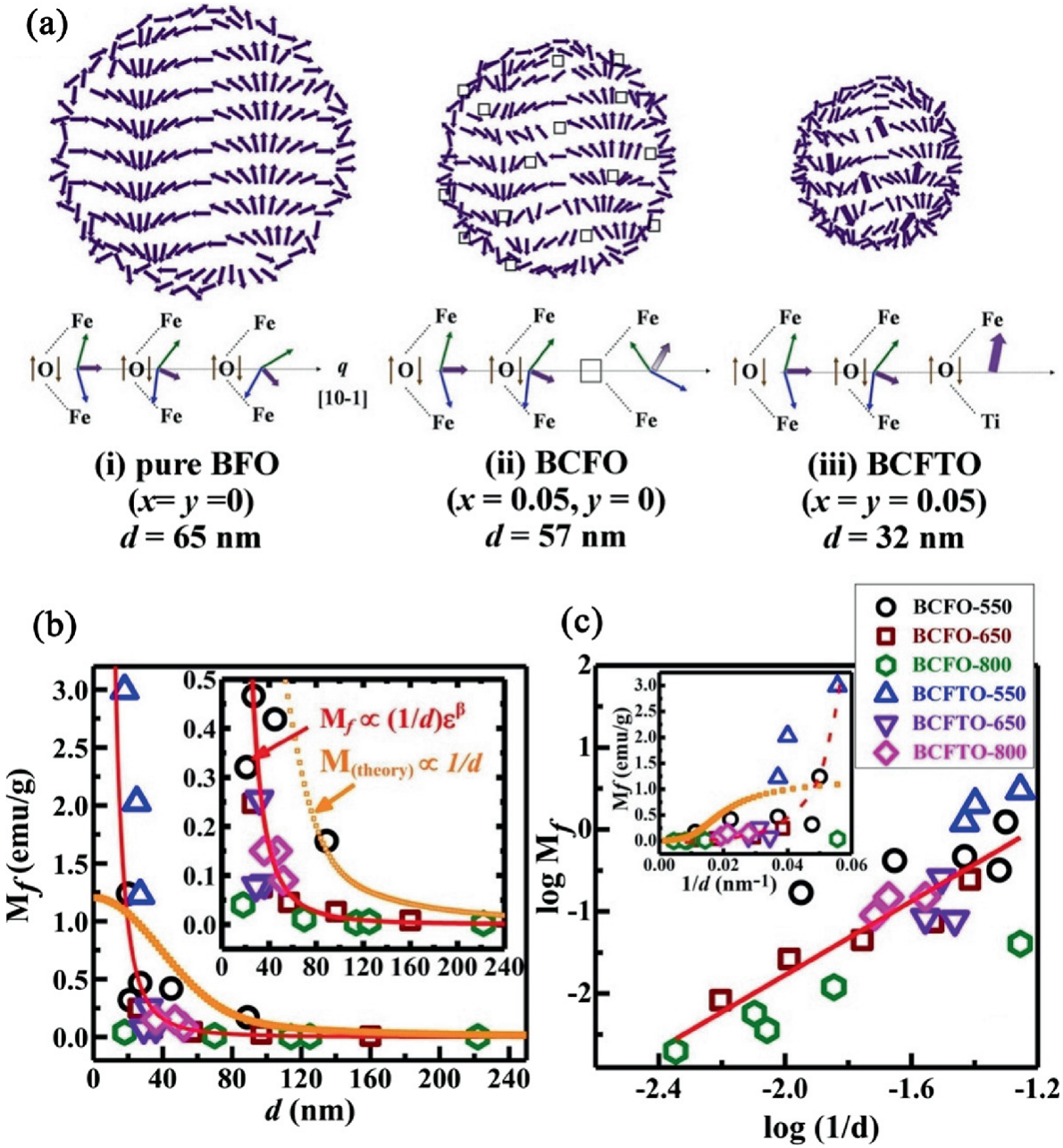

Fig. 6.9 **a** Schematic representation of spin structure in pure and substituted $BiFeO_3$ nanoparticles. **b** Ferromagnetic magnetization (M_f) of Ca-substituted $BiFeO_3$ (BCFO) and Ca-Ti co-substituted $BiFeO_3$ (BCFTO) nanoparticles as a function of crystallite size (d). Inset shows experimental data with the theoretical estimation of magnetization as a function of $1/d$ and $(1/d)\ \varepsilon^{\beta}$. **c** log

(M_f) vs log ($1/d$) plots for BCFO and BCFTO nanoparticles (Reprinted with permission from Mocherla et al. Mater. Res. Express, 4 (10), 106106, 2017 (Mocherla et al. 2017). Copyright (2017) Institute of Physics)

Defects and ferroelectricity: Defect engineering in $BiFeO_3$ films via ion bombardment was demonstrated by Saremi et al. (2018). Both the type and concentration of intrinsic defects could be controlled by altering the ion dosage. The ion bombardment helped in reducing the leakage current density by almost 4 orders by creating deep defect levels arresting free carrier transport. However, they indicated the risk of losing resistive switching due to the defect-polarization coupling and suggested using an appropriate ion dosage to maintain an optimum combination of leakage current and ferroelectric switching. The as-grown $BiFeO_3/SrRuO_3/DyScO_3$ (110) thin films show an unsaturated ferroelectric hysteresis loop with a high leakage current density of $\sim 10^{-2}$ A/cm^2 at an external applied electric field of 400 kV/cm. He^{2+} ions with an energy of 3 MeV are bombarded on these heterostructures with the variation of dosages from 10^{14} to 10^{16} cm^{-2}. A systematic decrease in leakage current and an enhancement in the coercivity values from the ferroelectric hysteresis loop are observed with increasing the dosages of ions bombardment (Fig. 6.10). Interestingly, the polarization is found to reduce from 85 to 65 μC/cm^2 and does not change further upon increasing ion dosage.

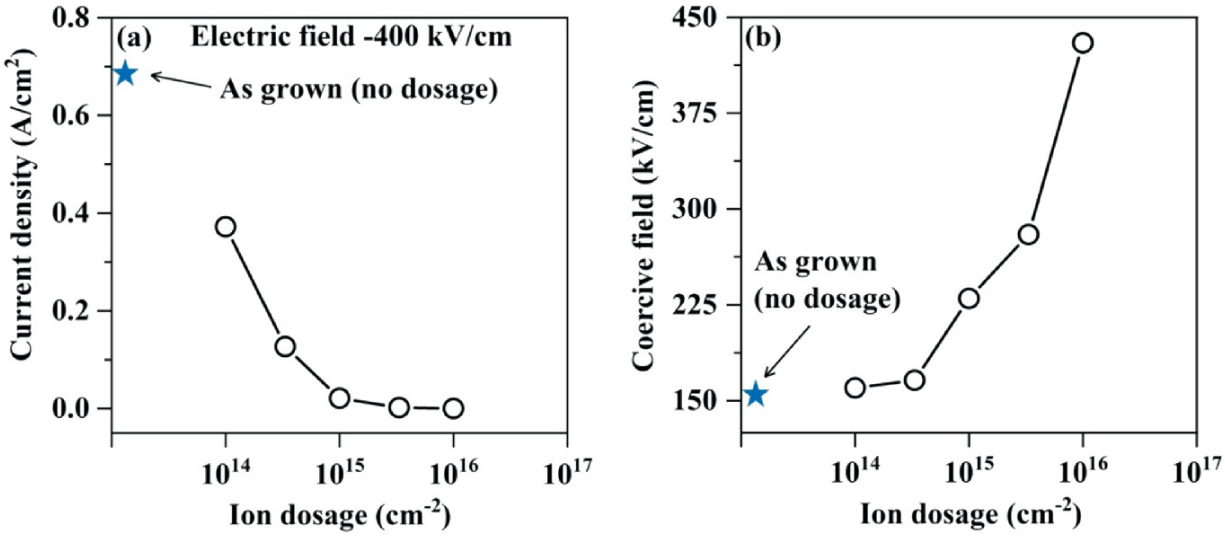

Fig. 6.10 **a** Leakage current density and **b** coercive field of $BiFeO_3/SrRuO_3/DyScO_3$ (110) thin films as a function of He^{2+} ion dosage with an energy of 3 MeV. Leakage current density values as observed at an electric field of −400 kV/cm are plotted (Data for the plots are obtained from Saremi et al. Advanced Materials Interfaces 5, 1700991 (2018) (Saremi et al. 2018))

Improved ferroelectric properties and domain switching are reported in Nd^{3+} and V^{5+} co-substituted $BiFeO_3$ thin films by suppressing the oxygen vacancy defects. Piezo force microscopy images show an improved domain switching in co-substituted thin films indicating the improvement in ferroelectric properties (Agarwal et al. 2018). Oxygen vacancy distribution is controlled in Mn^{3+}-substituted $BiFeO_3$ thin films where partially or fully occupied e_g states trap oxygen vacancies that lead to a robust polarization switching (Noguchi et al. 2019). Nandy et al. (2020) have demonstrated the effect of lattice oxygen vacancy defects on the ferroelectric nature in pure and aliovalent-substituted $BiFeO_3$ thin films. It is shown that the presence of lattice oxygen vacancies in Ca^{2+}-substituted $BiFeO_3$ thin films suppresses the ferroelectric nature of pure $BiFeO_3$ thin films. On the contrary, the suppressed ferroelectric nature can be negated when Bi^{3+} and Fe^{3+} sites are co-substituted with Ca^{2+} and Ti^{4+}, respectively.

The method of co-substitution reduces the lattice oxygen vacancies thereby retaining the ferroelectric nature. The ferroelectric hysteresis loop measured at room temperature at a fixed frequency of 100 kHz, shows polarization of ~10 $\mu C/cm^2$ at an electric field of 600 kV/cm for pure $BiFeO_3$ thin films (Fig. 6.11). This value reduces to 6 $\mu C/cm^2$ for Ca-substituted $BiFeO_3$ thin films and enhances to 15 $\mu C/cm^2$ for Ca-Ti co-substituted $BiFeO_3$ thin films. Ferroelectric domain switching images captured on these films using piezo force microscopy also confirm the ferroelectric nature of these films. Studies on K-Ti co-substituted and Cs-Ti co-substituted $BiFeO_3$ thin films show a similar dependency of ferroelectric polarization on lattice oxygen vacancy defects. The saturation polarization decreases to 4 $\mu C/cm^2$ and 5 $\mu C/cm^2$ in the case of K and Cs-substituted $BiFeO_3$ thin films, respectively, compared to the pure $BiFeO_3$ (~10 $\mu C/cm^2$). These results suggest the reduction in ferroelectric nature due to the formation of lattice oxygen vacancies. The polarization enhances to 9 and 7 $\mu C/cm^2$ for K^+-Ti^{4+} and Cs^+-Ti^{4+} co-substituted $BiFeO_3$ thin films. These results suggest the partial charge compensation by Ti^{4+} co-doping which suppresses the oxygen vacancies (Nandy et al. 2021a).

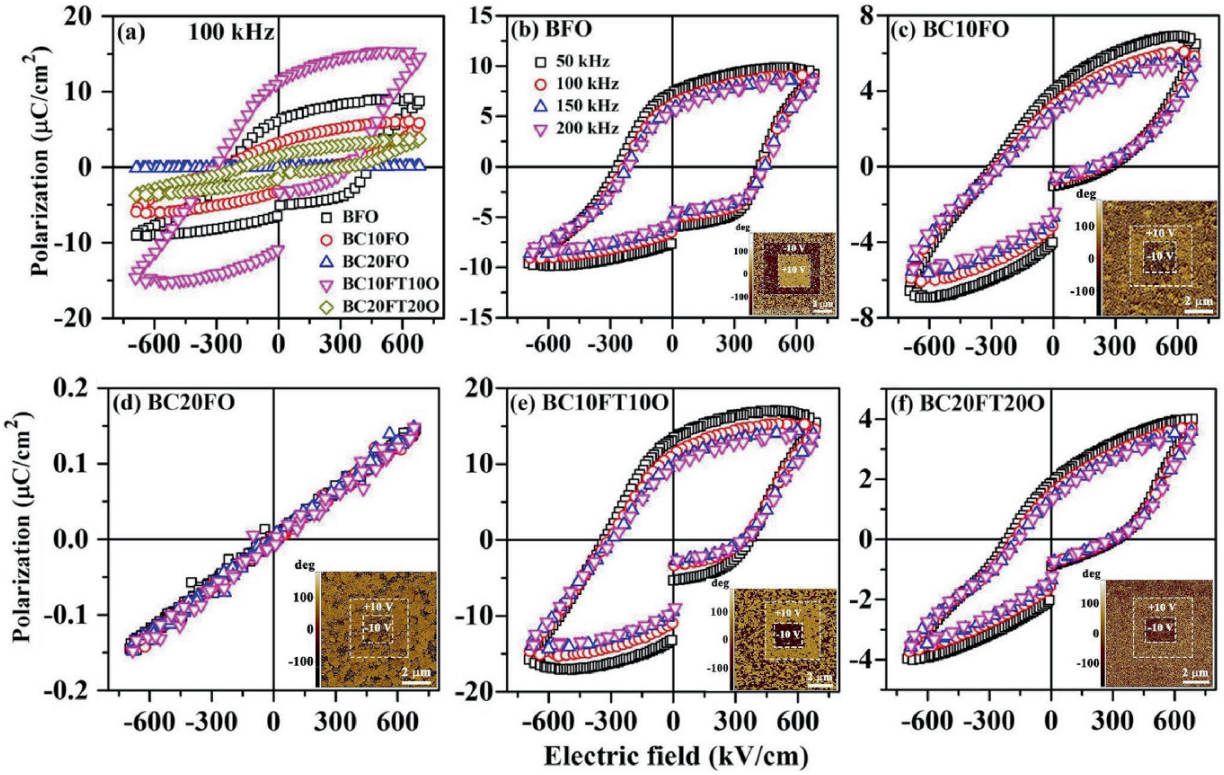

Fig. 6.11 **a** Polarization vs electric field curves of pure $BiFeO_3$ (BFO), Ca-substituted (10 wt.% (BC10FO); 20 wt.% (BC20FO)), and Ca-Ti co-substituted $BiFeO_3$ (Ca^{2+} and Ti^{4+} 10 wt.% each (BC10FT10O); Ca^{2+} and Ti^{4+} 20 wt.% each (BC20FT20O)) thin films at a frequency of 100 kHz. **b**–**f** Frequency dependent Polarization vs electric field curves of pure $BiFeO_3$, Ca-substituted and Ca-Ti co-substituted $BiFeO_3$ thin films (Reprinted with permission from Nandy et al. ACS Appl. Mater. Interfaces, 12 (12), 14105–14118, 2020 (Nandy et al. 2020). Copyright (2020) American Chemical Society)

Defects and electrical property: Yang et al. (2019a) have demonstrated the effect of strain gradient on local photoelectric properties by separating the photo-excited electron–hole pairs in $BiFeO_3$ thin films. This study is carried out by doing a systematic analysis on local conduction at morphotropic phase boundaries using a nanometer resolution conducting atomic force microscopy during both dark and illuminated conditions. A giant strain gradient in $BiFeO_3$ films, originated at morphotropic phase boundaries, resulted in an enhanced photoconduction in the R-phase and a negative photoconduction in the T′

phase. The effect of defects on electrical conductivity and Seebeck coefficient of high quality and polycrystalline pure $BiFeO_3$ and Ca-substituted $BiFeO_3$ ceramics is reported (Schrade et al. 2017). This shows the formation of V_O defects by compensating the charge imbalance in Ca-substituted $BiFeO_3$ ceramics. Undoped $BiFeO_3$ shows similar conductivity and a small change in the Seebeck coefficient with changing partial pressure of O_2. This indicates a small number of ionic defects which is very close to the intrinsic nature of $BiFeO_3$. Two regions with different compositions contribute to the charge transport in pure $BiFeO_3$. These two regions are agglomeration of V_{Bi} at the domain walls and the defect free undoped bulk. A recent study by Bencan et al. (2020) provides insight into atomic and nanoscale defects in $BiFeO_3$. Advanced characterization techniques like atomic resolution microscopy, piezo-force microscopy, and conducting atomic force microscopy are used to confirm the existence of coupling between the domain walls and charged point defects in polycrystalline $BiFeO_3$. Accumulation of charged defects at the domain walls in polycrystalline $BiFeO_3$ was confirmed in the studies done by Rojac et al. (2017). These defects identified as Fe^{4+} and Bi vacancies induce *p*-type hopping conduction. It was further shown that the local domain wall conductivity can be regulated by altering the atmosphere during high-temperature annealing.

X-ray absorption studies carried out by Ravalia et al. (2014) present a strong influence of defects in modifying the local electronic structure of Fe $L_{2,3}$ and O K-edges thereby influencing the magnetic as well as electric transport properties in $BiFeO_3$ films. Defects-induced by high-energy Ag ion irradiation below a certain fluence increased the structural strain and resulted in an enhancement of resistive and polarization switching

behavior. Further increase in the fluence created a local annealing-like effect releasing the strain caused due to the oxygen defects.

6.2.2 Magnetoelectric Coupling

Multiferroic materials that exhibit a strong coupling between ferromagnetic and ferroelectric order parameters are known as magnetoelectric coupling. In magnetoelectric coupling, the changes in ferroelectric polarization with an applied magnetic field and the variation of magnetization with an applied electric field are examined. $BiFeO_3$, a single-phase multiferroic material has been studied for magnetoelectric coupling that can be altered with the presence of various defects and strain in the system. This is done primarily by substituting Bi or Fe sites or both of them with appropriate metal cations. In many cases, the dielectric constant of a multiferroic material is investigated in the presence and absence of a magnetic field to understand magnetoelectric coupling also known as magnetodielectric coupling. Magnetodielectric studies on as-grown and air-annealed Ba-substituted $BiFeO_3$ bulk with and without V_O suggest the importance of V_O for enhancing the coupling (Singh and Jung 2010). The linear increase of magnetodielectric constant with increasing applied magnetic field indicates the existence of a positive magnetoelectric coupling in Ba-substituted $BiFeO_3$ bulk sample. On the other hand, the magnetodielectric constant is found to be decreased with increasing the magnetic field in $BiFe_{1-x}Ni_xO_3$ nanoceramics showing a negative magnetoelectric coupling (Kumar and Yadav 2010). This is shown to get enhanced with increasing Ni content in $BiFeO_3$. A maximum magnetodielectric constant of 6.5% noticed for $BiFe_{0.75}Ni_{0.25}O_3$ nanoceramics is attributed to the formation of V_O in the system. In the case of Sm^{3+} (at

Bi^{3+} sites) and Zr^{4+} (at Fe^{3+} sites) co-substituted $BiFeO_3$ nanoceramics, a maximum positive magnetodielectric constant of 6% is reported (Dutta and Tyagi 2018). The magnetodielectric coupling is attributed to the greater structural distortion which enhances the ferroelectric order parameter and change in lattice parameters because of the dissimilar size of substitute ions. So, the strain introduced into the system by co-substitution plays a dominant role in determining the coupling rather than the influence of V_O defects. To show the role of V_O defects present in the lattice and surfaces on the magnetodielectric coupling, pure $BiFeO_3$, Ca-substituted $BiFeO_3$, and Ca-Ti co-substituted $BiFeO_3$ ceramics prepared by spark plasma sintering were studied (Nandy et al. 2021b). The as-prepared sintered pure $BiFeO_3$ ceramics host grain boundary surface V_O defects due to the presence of nanoparticle $BiFeO_3$ along the boundaries of bulk grains of $BiFeO_3$. On the other hand, air annealing of these $BiFeO_3$ ceramics results in the disappearance of the nanoparticles on the grain boundaries and merges with the larger grains reducing the surface V_O defects. Lattice V_O defects are introduced by substituting 5 *at.* % and 10 *at.* % aliovalent Ca^{2+} at Bi^{3+} sites in $BiFeO_3$, respectively. These ceramics are also found to be surface V_O defect-rich due to the formation nanoparticle grains. Surface V_O defects are suppressed due to the air-annealing of these ceramics. In as-prepared 5 at.% and 10 at.% Ca-Ti co-substituted $BiFeO_3$ ceramics, lattice V_O defects are absent due to the charge compensation by the co-substitution. Only surface V_O defects are present in these ceramics due to the presence of nanoparticle grains. Air-annealing of these ceramics reduces the surface V_O defects. The magnetodielectric

constant of these ceramics as function of applied magnetic field is shown in Fig. 6.12. At low temperature, both as-prepared and air-annealed ceramics showed negative magnetodielectric effect. As-prepared and air-annealed samples of pure $BiFeO_3$ showed a small magnetodielectric response ($\sim -0.06\%$ at $H = 5$ T) at low temperature (10 K). In Ca and Ca-Ti-substituted $BiFeO_3$ ceramics, this response increases significantly suggesting the dominant role of V_O defects present into the system. The highest magnetodielectric response around -10% at $H = 5$ T is seen for Ca and Ca-Ti doped $BiFeO_3$ samples with 5 at.% doping concentration (Fig. 6.12a). With further increase in the concentration of Ca and Ca-Ti to 10 at.%, magnetodielectric response reduces to $\sim -1\%$. This decrease could be due to the deterioration of ferroelectricity with the enhancing V_O defects above an optimum concentration. At low temperature (10 K), air-annealed ceramics show reduced magnetodielectric response compared to their as-prepared counterpart. This is attributed to the reduction of surface V_O defects (Fig. 6.12b). At high temperature (300 K), as-prepared and air-annealed $BiFeO_3$ show a small negative and positive magnetodielectric response, respectively. As-prepared $BiFeO_3$ samples with 5 at.% of Ca and Ca-Ti doping show the positive response at low field ($<\pm 2$ T) and switch to negative response at higher field ($>\pm 2$ T) while their corresponding 10 at.% doped samples show a complete positive response of around 3.5% (Fig. 6.12c). After air-annealing, all these samples show a positive response, with a maximum of 3% for 10 at.% co-doping of Ca-Ti in $BiFeO_3$ ceramics, due to the reduction of surface V_O defects (Fig. 6.12d).

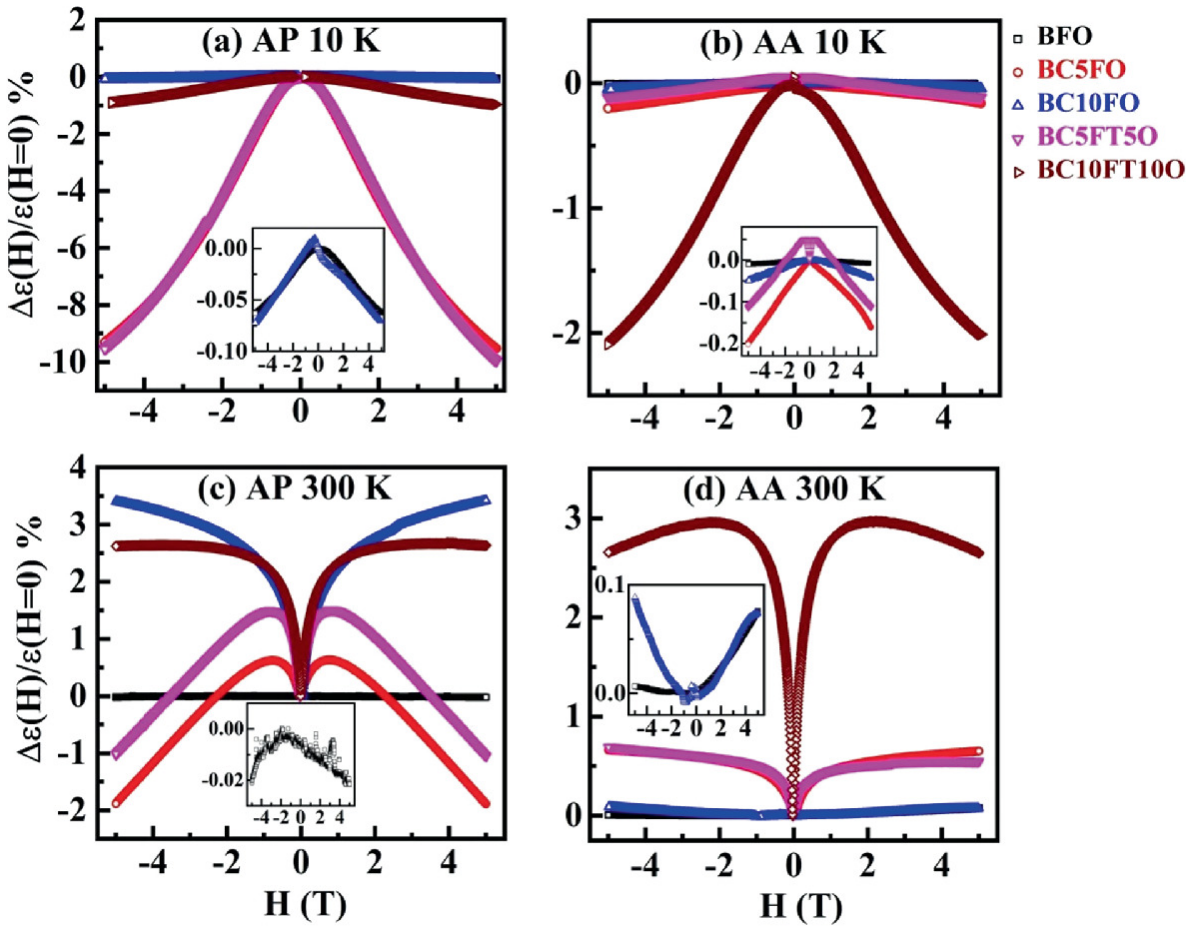

Fig. 6.12 Magnetodielectric response of as-prepared (AP) and air-annealed (AA) ceramics of pure $BiFeO_3$, Ca-substituted $BiFeO_3$, and Ca-Ti co-substituted $BiFeO_3$ at temperatures 10 K and 300 K (Reprinted with permission from Nandy et al. Phys. Rev. B, 103, 184406, 2021 (Nandy et al. 2021b). Copyright (2021) by the American Physical Society)

6.2.3 Electronic Structure and Optical Properties

Defects, specifically oxygen vacancies in $BiFeO_3$ influence the electronic and optical properties as well. UV–visible absorption and cathodoluminescence studies on highly strained $BiFeO_3$ thin films by Hauser et al. (2008) showed the presence of sub-bandgap transitions at 2.2 and 2.46 eV, apart from the band-edge at 2.7 eV. The transition at 2.46 eV, slightly lower than the bandgap is attributed to the oxygen vacancies. Clark and Robertson (2009) through

density functional calculations confirmed the above experimental results. Energy levels of oxygen vacancies in 0, +1, and +2 charge states were estimated to be 0.6 eV below the conduction band (Fig. 6.13a). Interestingly, the oxygen vacancy-related defect states are localized on the Fe *d* states rather than on the vacant site itself, and they do not affect the Bi orbitals (Fig. 6.13b and c) (Clark and Robertson 2009). The presence of oxygen vacancies influences the absorption edge and reduces the strength of the linear optical magnetoelectric effect (Ju and Cai 2009). Hence, good quality $BiFeO_3$ are recommended for optical and optoelectronic applications.

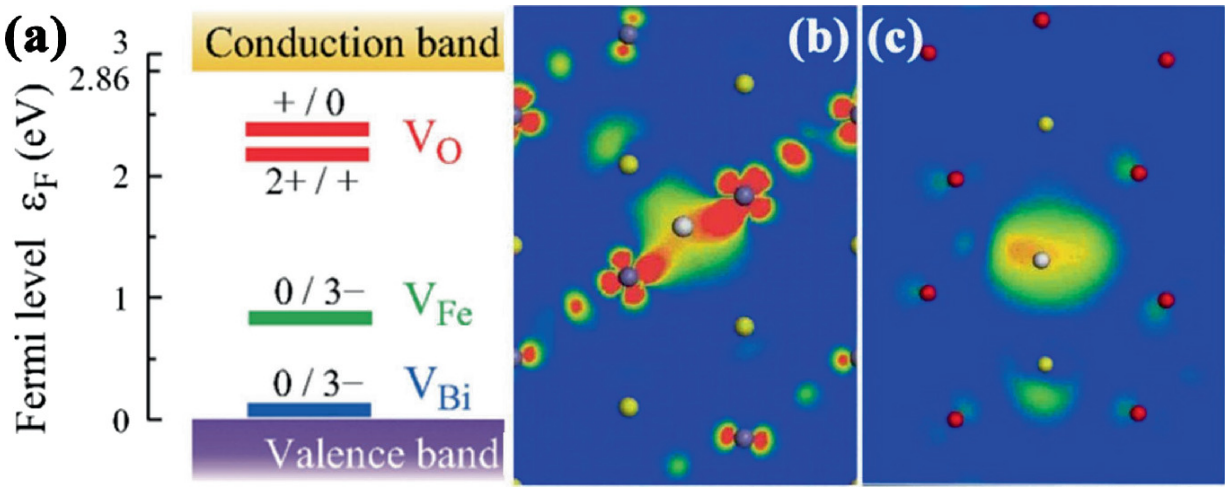

Fig. 6.13 **a** Defect states due to O, Bi, and Fe vacancies along with their charge states in between valence and conduction band (Adapted with permission from Shimada et al. Phys. Rev. B, 93, 174107, 2016 (Smolenskii and Agranovskaya 1958) Copyright (2016) by the American Physical Society). Charge density of the O vacancy defect level **b** through a plane containing Fe atoms and **c** a plane containing the vacancy and Bi atoms. The white sphere is the vacancy. Fe is gray, Bi is yellow, and O is red (Reprinted with permission from Clark et al. Appl. Phys. Lett., 94, 022902, 2009 (Clark and Robertson 2009). Copyright (2009) American Institute of Physics)

Shimada et al. (2016) through hybrid Hartree–Fock density functional theories showed that the effect of oxygen vacancies depends on their charge state. In oxygen-deficient conditions, neutral vacancies reduce the moment of neighboring Fe ions, while the charged vacancies aid in

inducing polarization. In oxygen-rich conditions, Bi vacancies suppress the polarization, while Fe vacancies act on both electric and spin polarization. The position of defect states corresponding to O, Bi, and Fe vacancies with their charge states are indicated in Fig. 6.13. Oxygen vacancy shows two transitions at 0.68 and 0.48 eV below the conduction band for different charge states. Bi and Fe vacancy states are seen at 0.08 and 0.83 eV, respectively above the valence band. O vacancy states act as a donor and Bi and Fe vacancy states work as acceptors which can trap electrons.

To demonstrate the particle size-dependent bandgap tunability, $BiFeO_3$ nanoparticles are prepared in sizes ranging from 5 to 65 nm by controlling the calcined temperature from 350 to 550 °C. The Tauc plot using the Kubelka–Munk function shows a sharp transition in the range 2–2.4 eV which corresponds to the electronic transition involving from O 2*p* states valence band to Fe 3*d* states conduction band (Fig. 6.14). This transition shows a blue shift with increasing particle sizes of $BiFeO_3$ nanoparticles. Bandgap values obtained using the Tauc relation $(\alpha h\nu)^n = (h\nu - E_g)$ with $n = 2$ for direct bandgap is shown in Fig. 6.14b with respect to the particle sizes. The changes in bandgap values are linear, varying from 2.13 eV for BFO-22 nm to 2.3 eV for BFO-38 nm. The decrease in bandgap with decreasing particle sizes is attributed to the presence of defect-induced mid bandgap energy levels originating from oxygen vacancies and microstrain. These mid-bandgap energy levels mostly situated near the conduction band can reduce the effective bandgap for smaller particles. The non-uniform microstrain present at the particle surfaces influences the absorption band edge by modifying the energy levels. The microstrain in $BiFeO_3$ originates from the oxygen vacancy defects and unsaturated bonds on the surface of the nanoparticles. The

bandgap of $BiFeO_3$ nanoparticles reduces back to ~2.1 eV for the larger particle sizes in the range of 200–600 nm (Mocherla et al. 2013).

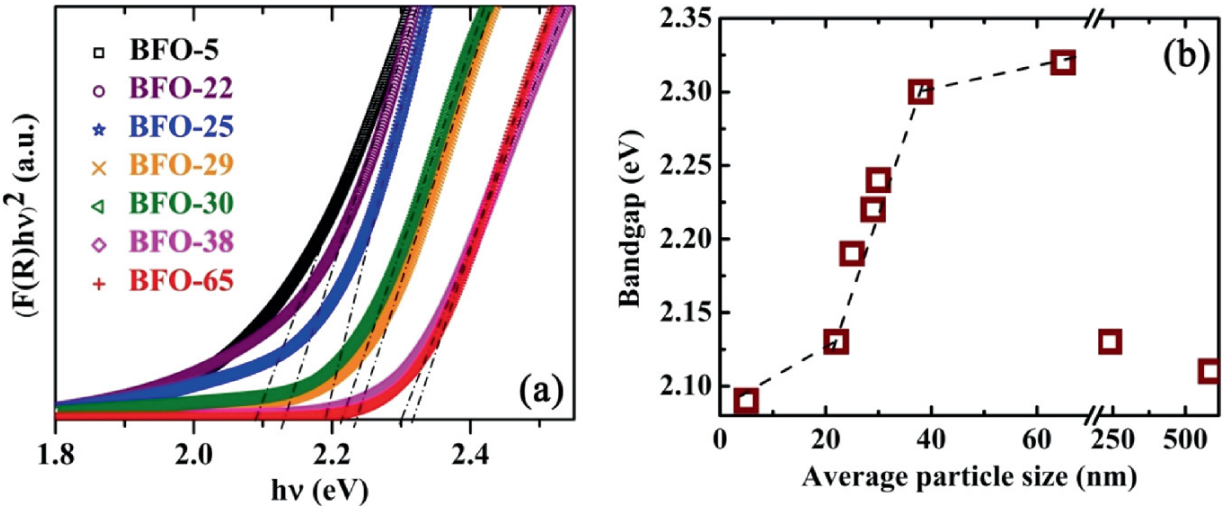

Fig. 6.14 **a** Tauc plot using Kubelka–Munk function for $BiFeO_3$ nanoparticles of sizes ranging from 5 to 65 nm. **b** The estimated band gap from (**a**) is shown as a function of the average particle size of $BiFeO_3$ nanoparticles (Reprinted with permission from Mocherla et al. Appl. Phys. Lett., 103, 022910, 2013 (Mocherla et al. 2013). Copyright (2013) American Institute of Physics)

The effect of oxygen vacancy defects and microstrain on the optical properties is demonstrated by considering pure $BiFeO_3$, Ca-substituted $BiFeO_3$, and Ca-Ti co-substituted $BiFeO_3$ nanoparticles. The variation of the direct bandgap of these nanoparticles depending on the Ca substitution concentration (x), crystallite size (d), microstrain (ε), and calcination temperature (T) is shown in Fig. 6.15. The bandgap remains almost unchanged in BCFO and BCFTO nanoparticles except a linear increase in bandgap values is observed for BCFO calcinated at 800 °C (Fig. 6.15a). On the other hand, bandgap values increase sharply up to a critical crystallite size of 60 nm and then decreases with further increase of d (Fig. 6.15b). Microstrain plays a dominant role in changing the bandgap only below the critical crystallite sizes and beyond this value the effect of microstrain fades out (Fig. 6.15c). The bandgap changes in

a narrow region between 2.1 and 2.3 eV with the variation of size-induced microstrain irrespective of the concentration of the substitution, and calcination temperature. Only the BCFO nanoparticles calcinated at 800 °C show a different behavior. Particularly these nanoparticles display a bandgap variation from 1.5 to 2 eV inversely with crystallite size and microstrain. A systematic decrease in the bandgap is seen in BCFO nanoparticles upon increasing the calcination temperature (Fig. 6.15d). On the other hand, BCFTO nanoparticles do not show any variation with the changing calcination temperature (Mocherla et al. 2015).

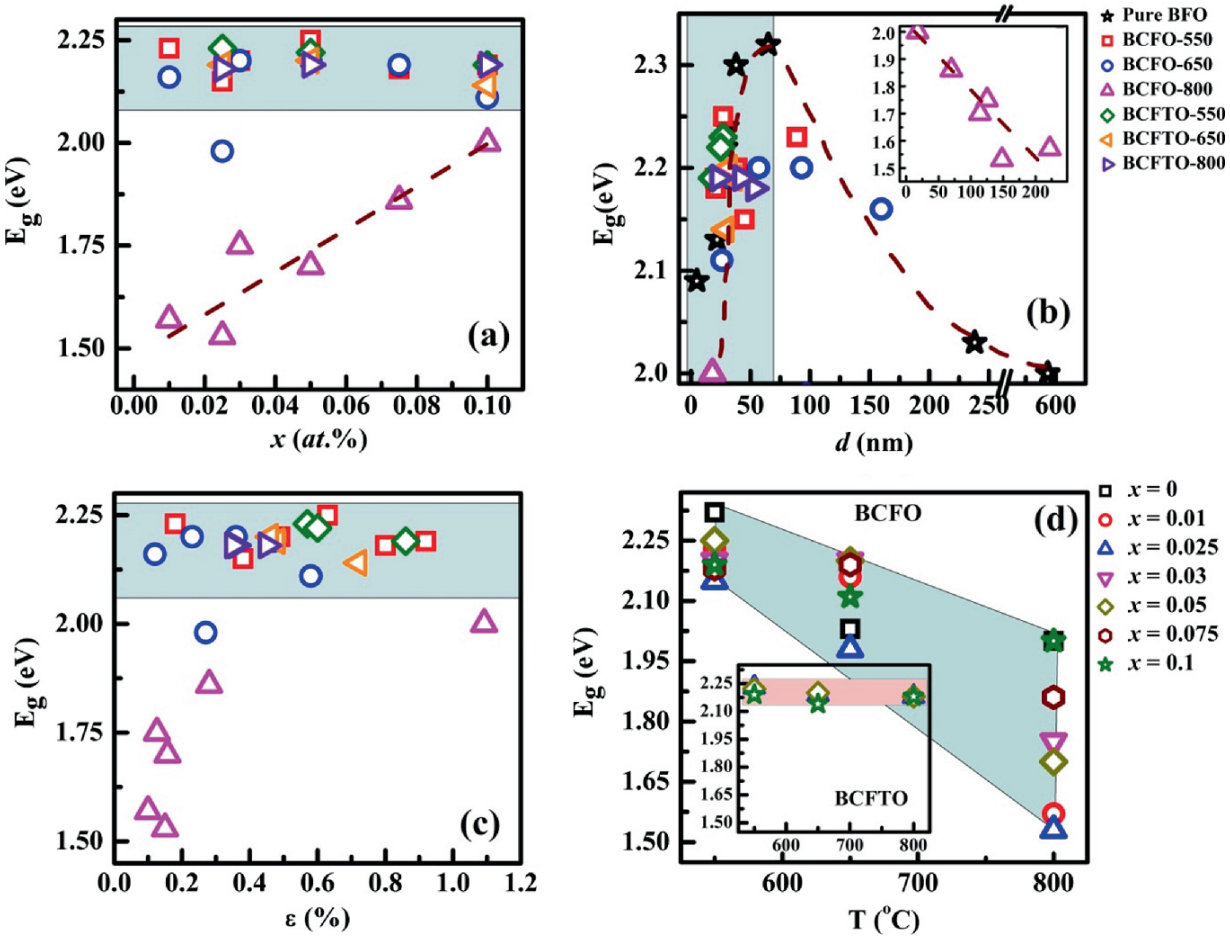

Fig. 6.15 Bandgap variation in pure $BiFeO_3$, Ca-substituted $BiFeO_3$, and Ca-Ti co-substituted $BiFeO_3$ nanoparticles with **a** the concentration of substitution (*x* at.%), **b** crystallite size (*d nm*), **c** microstrain (ε %), and **d** calcination

temperature (T ºC) (Reprinted with permission from Mocherla et al. Mater. Res. Express, 2 (9), 095012, 2015 (Mocherla et al. 2015). Copyright (2015) Institute of Physics)

To demonstrate the electronic states of these oxygen vacancy defects and the effect of Ca and Ca-Ti substitution in $BiFeO_3$, band structure calculated from density functional theory is shown in Fig. 6.16. In the case of bulk $BiFeO_3$ (Fig. 6.16a), band structure and density of states of pristine samples are seen. In Ca-substituted $BiFeO_3$ structure, where V_O defects are formed, mid-bandgap defect states are also observed (Fig. 6.16b). On the other hand, V_O defects present at the surface or at the grain boundaries increase the mid-bandgap density of states (Fig. 6.16c). In the case of Ca-Ti substitution, charge compensation reduces the probability of V_O formation when Ca and Ti lie close to each other. The electronic structure, in this case, does not show mid-bandgap defect states (Fig. 6.16d). However, the bandgap reduces due to the presence of electronic states due to Ti-*d* and Ca-*s* near the conduction band minimum and valence band maximum, respectively. When substituent Ca and Ti sit far from each other in the lattice, the formation of V_O cannot be ruled out. In this case, V_O defect states are present at the middle of the conduction and valence bands, in addition, the defect states originating from Ti-*d* and Ca-*s* are present (Fig. 6.16e). But dense mid-bandgap defect states are present in the case of Ca-Ti co-substituted $BiFeO_3$ with V_O defect at the surface or grain boundaries (Nandy et al. 2020).

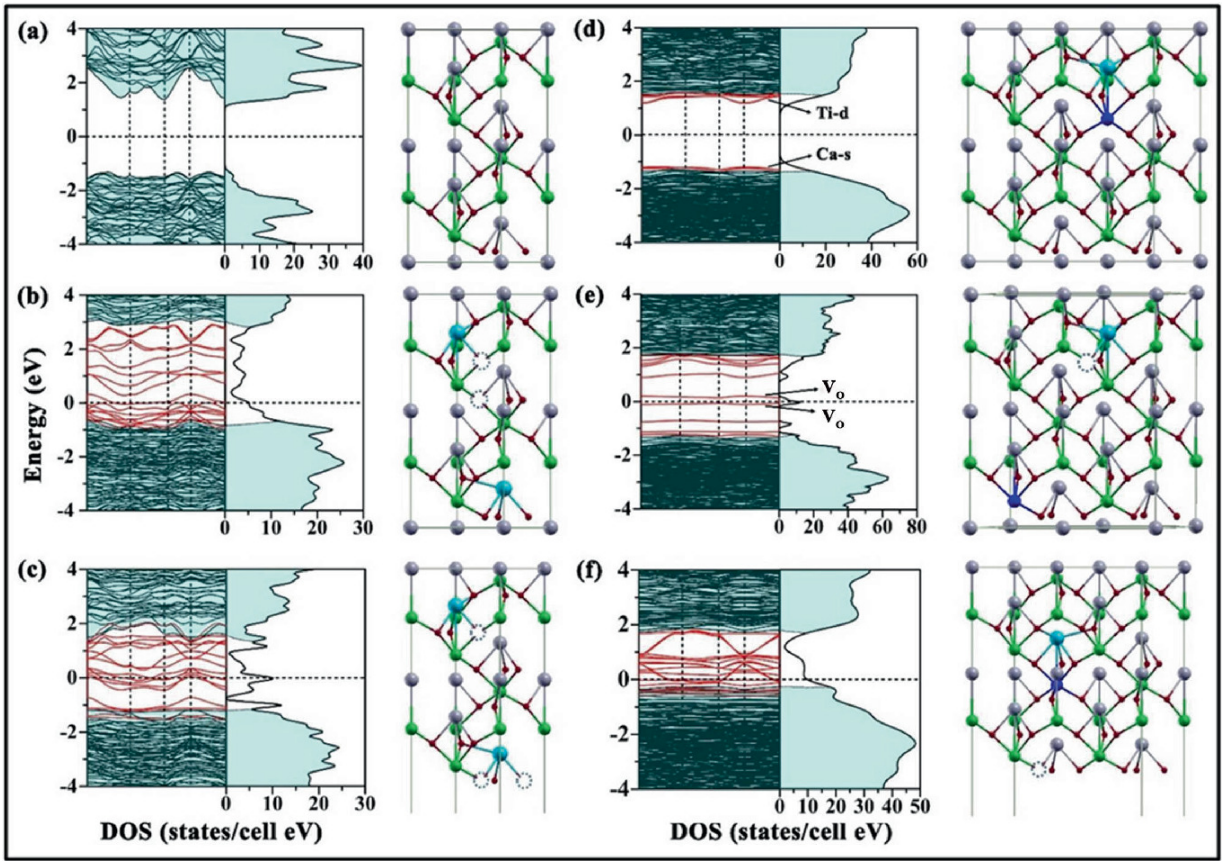

Fig. 6.16 Band structure and density of states for Ca-substituted $BiFeO_3$ (left panel) and Ca-Ti co-substituted $BiFeO_3$ (right panel). **a** Pure bulk, **b** Ca substitution with lattice V_O, **c** Ca substitution with lattice and surface V_O, **d** Ca and Ti co-substitution residing close to each other, **e** Ca and Ti co-substitution residing away from each other with the coexisting lattice V_O, **f** Ca and Ti co-substitution with V_O at the surface (Reprinted with permission from Nandy et al. ACS Appl. Mater. Interfaces, 12 (12), 14105–14118, 2020 (Nandy et al. 2020). Copyright (2020) American Chemical Society)

A much-diffused band edge is observed in the case of as-prepared Ca and Ti-substituted $BiFeO_3$ ceramics that host mid-band gap defects. On the other hand, these ceramics, after air-annealing, show a sharper band edge indicating a reduction in the mid-bandgap defect states. The first principle density functional calculation shows that the mid-bandgap defect states are not produced due to the presence of Ca and Ti co-substituents, but rather originated from unsaturated bonds and oxygen vacancies residing at the grain boundaries (Nandy et al. 2019). The effect of

vacuum annealing on the optical properties of $BiFeO_3$ thin films is demonstrated by showing the variation in the bandgap and photoluminescence spectra. The oxygen vacancy-related mid-band gap defect states present in vacuum-annealed $BiFeO_3$ films cause a bandgap reduction to 2 eV from 2.12 eV in air-annealed $BiFeO_3$ films. The photoluminescence studies confirmed the defects in vacuum-annealed $BiFeO_3$ films by showing a broad peak around 715 nm (Nandy and Sudakar 2019).

6.2.4 Photoconductivity and Photovoltaic Properties

Photoconductivity is another relevant property to be understood for photovoltaic and photodetector applications. This method is used to know the generation and recombination lifetime of photogenerated electron–hole pairs. So, realizing the controlled photoconductivity in $BiFeO_3$, specifically when defects are present in the nanoscale, is a big challenge. Photovoltaic properties based on ferroelectric materials have attracted scientific interest due to their unusual polarization-driven photo-excited electron–hole pairs separation mechanism. Recent research findings on photo-ferroelectrics suggested that $BiFeO_3$ is a suitable candidate because of its higher ferroelectric polarization (100 $\mu C/cm^2$) and lower bandgap (~2.7 eV in bulk). However, the presence of defects in the nanoscale can alter the photovoltaic nature by tuning these physical properties of $BiFeO_3$. This is found to be interesting for solar cell applications. Hence, the studies on photoconductivity and photovoltaic properties of $BiFeO_3$ in the form of ceramics and thin films are crucial. Photoconductivity, in $BiFeO_3$, is shown to be greatly influenced by the grain boundary oxygen vacancy (V_O) defects. This is demonstrated by studying two samples: (i) a

spark plasma sintered pellet with $BiFeO_3$ nanoparticles (100–200 nm) predominantly present at the grain boundary regions of large $BiFeO_3$ grains (1–2 μm), that results due to the short sintering time performed during sintering process (Fig. 6.17a), and (ii) the second with sharp grain boundary region obtained by performing annealing process in air which lets the grains to complete the growth and removing the nanoparticles at the grain boundary region (Fig. 6.17b) (Nandy et al. 2017). A larger photoconductivity results in as-prepared ceramics, where the nanoparticles are present along the grain boundaries (Fig. 6.17c). On the other hand, the absence of these nanoparticles results in a decrease in photoconduction (Fig. 6.17d). The V_O defects present at the nanoparticle surfaces along the grain boundaries in as-prepared $BiFeO_3$ provide an extra channel for photoconduction (Fig. 6.17e). These defects known as nanoparticle surface vacancy (NPSV) are situated just below the conduction band. Such conduction channels are not present in the ceramics with sharp grain boundary regions as the V_O defect states are absent in air-annealed samples suggesting poor photoconductivity (Fig. 6.17f). A decrease in photoconduction during the illumination is seen in air-annealed ceramics due to the absence of these NPSV and the dominance of photo-induced trap states (PITS). These studies on plasma-sintered phase pure $BiFeO_3$ ceramics revealed a significant influence of morphology and V_O on photoconductivity response. Hence, the V_O defects are incorporated into a lattice by substituting aliovalent substituent Ca^{2+} at Bi^{3+} sites in the $BiFeO_3$ structure. Further, the V_O defects are increased by reducing the grain sizes to 100–200 nm in Ca-substituted $BiFeO_3$ ceramics. The photoconductivity enhances two to four orders in plasma sintered $Bi_{0.95}Ca_{0.05}FeO_{3-\delta}$ and

$Bi_{0.9}Ca_{0.1}FeO_{3-\delta}$ ceramics (Fig. 6.18). This enhancement in photoconductivity is due to the lattice and surface V_O defects which allow the conduction through grains and grain boundaries. Air annealing of these ceramics results in the reduction of photoconductivity due to the suppression of grain boundary defects that limit the conduction along the grain boundaries. These results conclude that nanoparticle grain boundary defects play a dominant role in photoconduction (Nandy et al. 2018). Further, to confirm the nanoparticle grain boundaries conductivity, Ca-Ti-substituted $BiFeO_3$ ceramics with nanosized grains are investigated for photoconduction (Fig. 6.18).

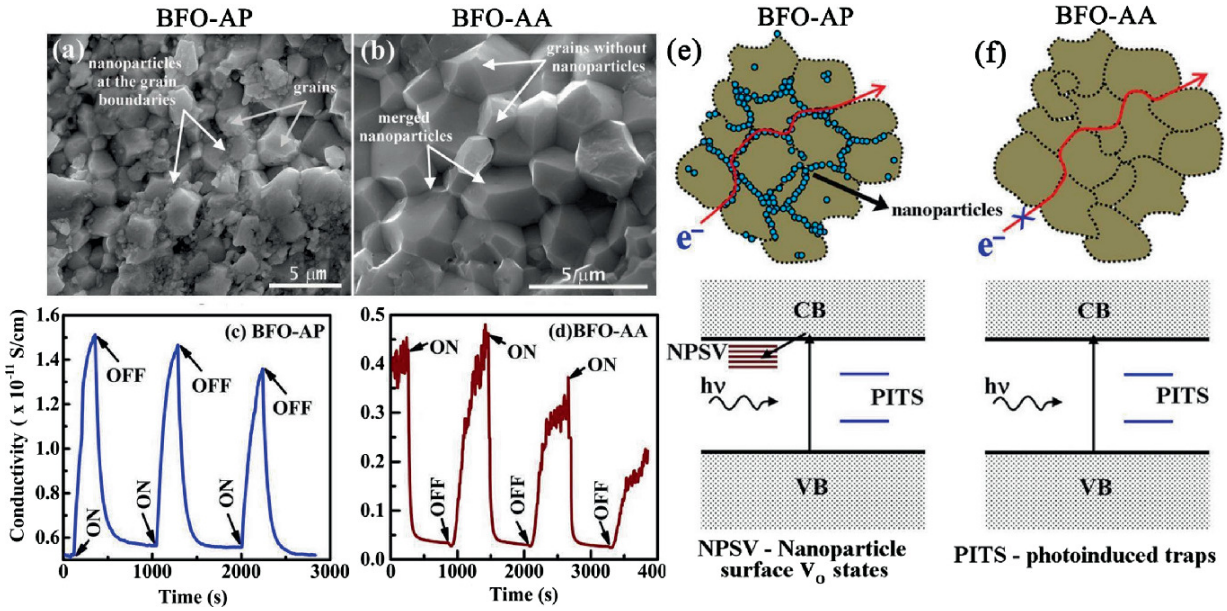

Fig. 6.17 FESEM images of **a** BFO-AP and **b** BFO-AA ceramics. In BFO-AP, nanoparticles are present at grain boundaries while grain boundaries are clear in BFO-AA. Photoconductivity response of **c** BFO-AP and **d** BFO-AA ceramics under the ON and OFF conditions of the light source (AM 1.5). **e** Nanoparticle segregated grain boundaries showing the conduction path through the oxygen vacancy defect states on nanoparticle surfaces and the associated band structure. **f** Clear grain boundaries showing the absence of photoconduction and related band structure (Reprinted with permission from Nandy et al. J. Appl. Phys., 121, 203102, 2017 (Nandy et al. 2017). Copyright (2017) American Institute of Physics)

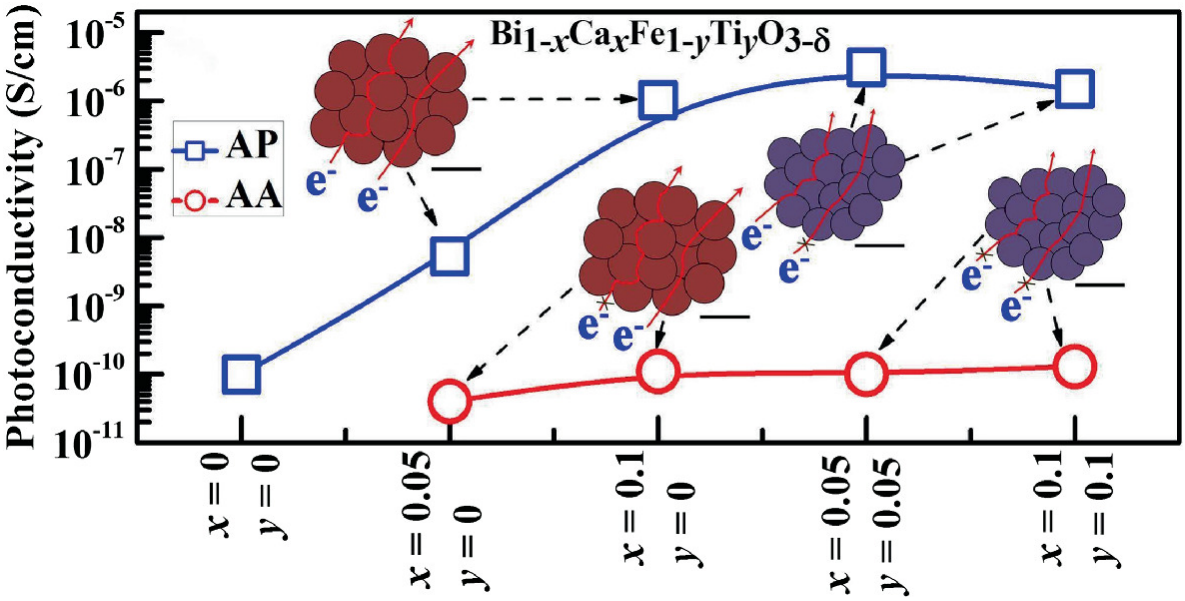

Fig. 6.18 Photoconductivity response of as-prepared (AP) and air-annealed (AA) ceramics for pure $BiFeO_3$, Ca, and Ca-Ti-substituted $BiFeO_3$ ceramics. Schematics show the possibilities of conduction through grains and grain boundaries (Reprinted with permission from Nandy et al. J. Appl. Phys., 126, 235101, 2019 (Nandy et al. 2019). Copyright (2019) American Institute of Physics)

In Ca-Ti-substituted as-prepared (AP) ceramics, lattice V_O defects are absent due to the charge compensation by these aliovalent substituents (Ca^{2+} at Bi^{3+} sites and Ti^{4+} at Fe^{3+} sites). The photoconductivity observed in Ca-Ti-substituted as-prepared ceramics is almost similar to the photoconduction observed in Ca-substituted as-prepared ceramics suggesting the dominant role of surface conduction. The air-annealing (AA) of these ceramics reduced the conductivity by two to four orders due to the suppression of V_O defects at the grain boundaries (Nandy et al. 2019).

The V_O-defects-controlled photoconduction demonstrated in the ceramics can also be extended to thin films for photovoltaic applications. Photovoltaic properties of Ca and Ca-Ti-substituted $BiFeO_3$ thin films were studied by preparing thin films on FTO-coated glass substrates (Fig. 6.19a). The effect of lattice and surface V_O defects on

short circuit current density (J_{SC}) and open circuit voltage (V_{OC}) from a vast number of FTO/$Bi_{1-x}Ca_xFe_{1-y}Ti_yO_{3-\delta}$/Au thin film devices fabricated are summarized in Fig. 6.19b. It is found that J_{SC} increased with increasing V_O defects, while V_{OC} started decreasing. A high J_{SC} of 2.6 mA/cm^2 is obtained in Ca-substituted BFO thin film devices which have a large concentration of V_O defect. J_{SC} in these devices is five orders of magnitude higher than the J_{SC} (0.3 μA/cm^2) observed for pure BFO devices (Fig. 6.19b). The V_{OC} reduced from 0.7 V in pure BFO devices to 0.15 V in V_O-rich Ca-substituted BFO devices. Ca-Ti-substituted BFO devices, wherein the lattice V_O concentration gets suppressed, exhibit higher V_{OC}~8 V. These studies contrastingly bring out the importance of V_O to increase the conductivity while the detrimental effect on the photovoltaic property as it kills the ferroelectric nature that is required to enhance the V_{OC}. But it is quite possible to control them independently. The optimization of lattice and grain boundaries V_O shows an enhancement in both J_{SC} and V_{OC} for a particular concentration of Ca-Ti substitution (Nandy et al. 2020).

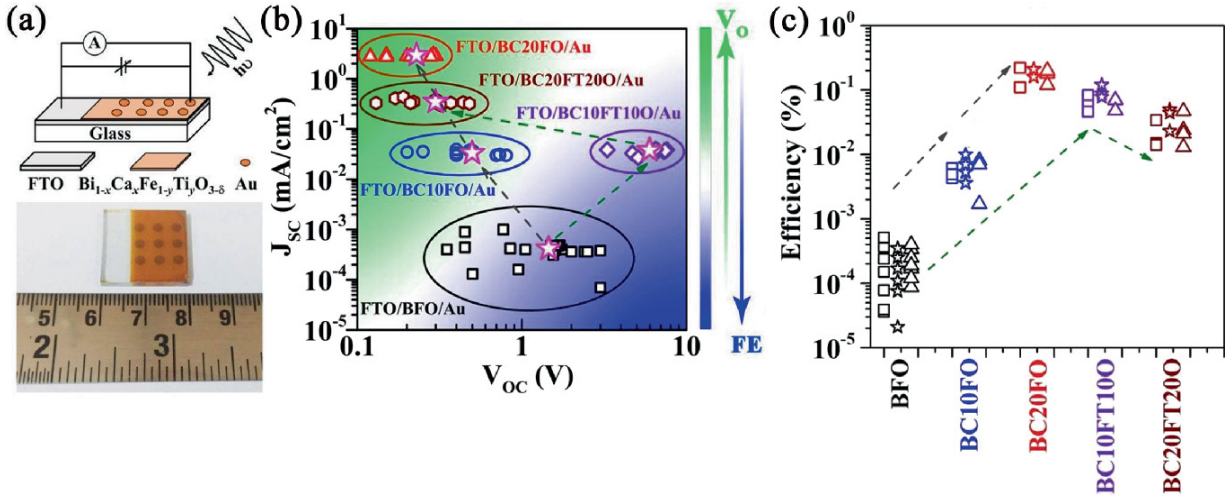

Fig. 6.19 **a** Schematic of the Glass/FTO/$Bi_{1-x}Ca_xFe_{1-y}Ti_yO_{3-\delta}$/Au devices and the picture of a real device with a scale showing the dimension of the device fabricated. **b** The changes in short circuit current density (J_{SC}) and open circuit voltage (V_{OC}) with changing oxygen vacancy defects (V_O) and ferroelectricity (FE) in a large number of devices. **c** The efficiency of these solar cell devices in three batches is shown (Reprinted with permission from Nandy et al. ACS Appl. Mater. Interfaces, 12 (12), 14105–14118, 2020) (Nandy et al. 2020). Copyright (2020) American Chemical Society)

The effect of V_O defects on the band structure of these devices is depicted in Fig. 6.20, which illustrates the band diagram of Au/$Bi_{1-x}Ca_xFe_{1-y}Ti_yO_{3-\delta}$/FTO devices. These band diagrams establish a connection between V_O, ferroelectric polarization, $V_{OC,}$ and J_{SC} observed in these devices. Since the work function of Au (5.1 eV) is larger than the work function of $BiFeO_3$ (4.7 eV), a Schottky barrier is formed at Au/$BiFeO_3$ interfaces. On the other hand, an Ohmic contact is formed at $BiFeO_3$/FTO interfaces as the work function of FTO (4.4 eV) is smaller than the work function of $BiFeO_3$ (4.7 eV). So, a maximum V_{OC} that can be obtained from these devices is around 0.7 V, combining the effect of the Schottky and Ohmic barriers. However, the V_{OC} is found to be more than 0.7 V in these devices due to the presence of a ferroelectric domain oriented in a particular direction. The direction of ferroelectric polarization can be switched by reversing the direction of applied bias. In Fig. 6.20a, band diagrams are shown for less V_O defect systems where strong ferroelectric polarization arises and a large band bending results in a high V_{OC}. However, these devices show a smaller J_{SC} because of having less V_O defects in the systems. On the other hand, band diagrams with more V_O defect systems, that weaken the ferroelectric polarization, result in a lesser band bending as shown in Fig. 6.20b. These systems show a larger J_{SC} but lesser V_{OC} due to the smaller band bending

across the devices. Hence, it is established that the V_O defects significantly influence the device's properties.

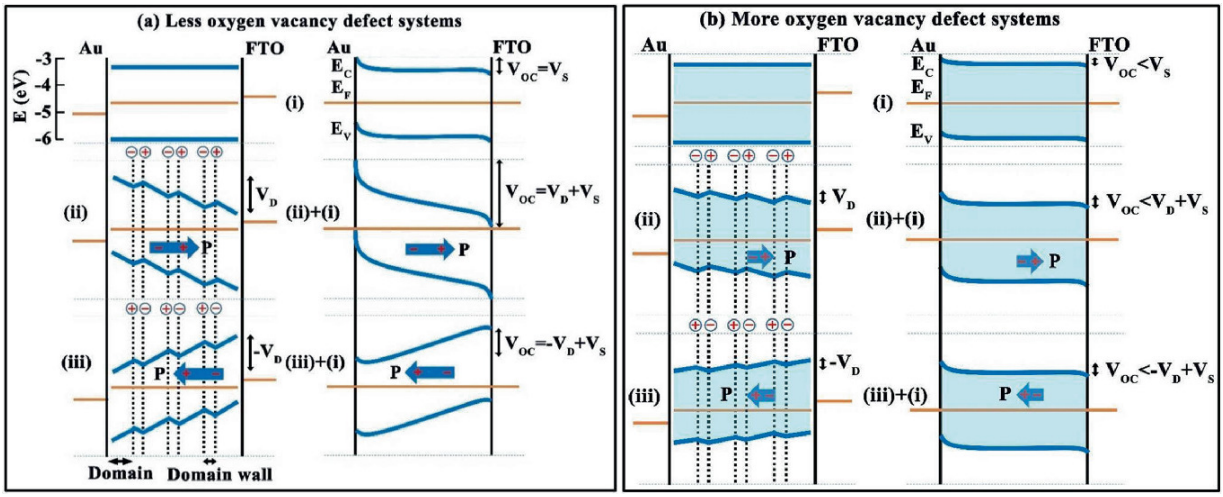

Fig. 6.20 Schematics show the band diagram of Glass/FTO/$Bi_{1-x}Ca_xFe_{1-y}Ti_yO_{3-\delta}$/Au devices having **a** less and **b** more V_O defects. The shaded region in (**b**) represents the V_O defects in between the valence and conduction bands. The role of defects on the ferroelectric polarization and the band structure are shown (Reprinted with permission from Nandy et al. ACS Appl. Mater. Interfaces, 12 (12), 14105–14118, 2020 (Nandy et al. 2020). Copyright (2020) American Chemical Society)

One of the ways of manipulating the V_O concentration is by altering the Bi content in $BiFeO_3$ thin films. This V_O concentration is shown to be an effective way to enhance the photovoltaic performance of the devices. Moreover, V_O migration plays a major role in determining the switchable photovoltaic effects. The J_{SC} and V_{OC} are found to be ~66 $\mu A/cm^2$ and ~89 mV, respectively in $Bi_{1.05}FeO_3$ devices. This current density is 13 times higher than that of $Bi_{0.95}FeO_3$ devices and about 6 times higher than that of $BiFeO_3$. Similarly, the output voltage of $Bi_{1.05}FeO_3$ devices is significantly higher than $Bi_{0.95}FeO_3$ and $BiFeO_3$ devices (Yang et al. 2019b).

6.3 Current Challenges and Future Scope

Regardless of numerous attempts to strengthen the innate multiferroic coupling in bismuth ferrite, a lot remains to be explored. A multitude of reports on various morphologies of bismuth ferrite exists in the literature. Thin films and nanostructures are of special importance in view of device applications. In general, magnetoelectric coupling in $BiFeO_3$ can be altered by regulating factors that affect the cycloidal spin structure of Fe^{3+} ions in the compound. The most common and widely accepted approach to enhance the coupling between magnetic and ferroelectric order parameters is to substitute either or both Bi^{3+} and Fe^{3+} sites with suitable alternatives. However, the influence of doping at the cation sites manifests along with other allied phenomena—defects and strain. Conventional applications of $BiFeO_3$ are centered on the magnetoelectric and spintronic properties of the material. Realizing memory devices in which information can be electrically stored and magnetically read is still a major challenge. While electrical switching is relatively easier to achieve, reading the relatively weak magnetic changes is challenging. One possible solution is to synthesize hybrid structures comprising both ferromagnetic and antiferromagnetic ordering. Another possibility is to adopt techniques that enhance the ferromagnetic component in $BiFeO_3$ to the extent of enabling magnetic readability. Both these approaches hold a strong interdependence on the defects and strain, which if not regulated may not yield desirable results (Arandiyan et al. 2021; Gulati et al. 2022; Wang et al. 2020; Seyfouri and Wang 2021; Ma et al. 2019).

In spite of the whopping research work carried out for more than two decades (Arandiyan et al. 2021; Gulati et al.

2022; Wang et al. 2020; Seyfouri and Wang 2021; Ma et al. 2019), bismuth ferrite still receives attention not only for conventional applications based on its multiferroic nature, but also for many other functionalities this material offers. This includes photocatalytic activity, water cleaning, electrocatalysts, photovoltaics, photo ferroelectrics, etc. Several review articles in the last few years reiterate the multifunctional nature of bismuth ferrite and derived compounds. Most of these applications are yet again based on playing with the occupancy of the cations and associated phenomena. Taking a perspective through the lens of defects and their influence on physical properties showcases a holistic idea of the material and enables a pathway to control the intricate structure–property correlations. Thus, gaining a deeper insight into the underlying defect physics is an indispensable part of the endeavor to alleviate the challenges and explore bismuth ferrite to the best of its potential.

6.4 Summary

The chapter provides a panoptic summary on how defects and associated strain influence the physical properties of $BiFeO_3$—a well-known room-temperature multiferroic material. Preluding the central theme, a short note on the definitions and different types of multiferroic materials, significant outcomes in the field, and crystal structure of $BiFeO_3$ is provided. Following this general discussion, the rest of the chapter focuses on the important results that highlight the role of defects in altering the physical properties of $BiFeO_3$. These results were categorized based on the end properties investigated—magnetic, ferroelectric, magnetodielectric, optical/electronic, photovoltaic, photocatalytic, and photoferroelectric properties of $BiFeO_3$. Specific results on various forms of $BiFeO_3$, viz.,

nanoparticles, bulk, and thin films in both pristine and doped conditions are included. Particularly, the study of defects and strain in nano $BiFeO_3$ gained attention for its wide applicability in technologically relevant areas of memory devices, magnetoelectric sensors, spintronics, photocatalytic, photodetectors, and photovoltaics. Finally, current challenges and the future scope of using defects as a tool to control the multifunctional properties in the $BiFeO_3$ and related compounds are highlighted. Through this report, the importance of defect and strain engineering in multifunctional oxides, based primarily on understanding the defect-structure–property correlations in these compounds, is emphasized. Defect engineering in oxides is an exciting and deserving endeavor for material scientists and offers an additional route to control and enhance material properties.

Acknowledgements

C.S. acknowledges the support from SERB-SUPRA (Science and Engineering Research Board-Scientific and Useful Profound Research Advancement) through Grant No. SPR/2021/000499-G. C.S. acknowledges IIT Madras for the support of research initiatives for establishing the Research Center of Excellence on Center for Advanced Materials and Microscopy (CAMM) vide project # SB20210844MMMHRD008277. This initiative is supported by the Ministry of Human Resource and Development, India, through the Institutes of Eminence (vide SP20210777DRMHRDDIRIIT).

Author Contributions

“The manuscript was written through the contributions of all authors. All authors have given approval to the final version of the manuscript.”

References

Agarwal, R., Sharma, Y., Hong, S., Katiyar, R.S.: J. Phys. D Appl. Phys. **51**, 275303 (2018)

Arandiyan, H., Mofarah, S.S., Sorrell, C.C., Doustkhah, E., Sajjadi, B., Hao, D., Wang, Y., Sun, H., Ni, B.-J., Rezaei, M.: Chem. Soc. Rev. **50**, 10116–10211 (2021)
[PubMed]

Arandiyan, H., Mofarah, S., Sorrell, C.C., Doustkhah, E., Sajjadi, B., Hao, D., Wang, Y., Sun, H., Ni, B.-J., Rezaei, M., Shao, Z., Maschmeyer, T.: Chem. Soc. Rev. **50,** 10116–10211 (2021)

Ascher, E., Rieder, H., Schmid, H., Stössel, H.: J. Appl. Phys. **37**, 1404–1405 (1966)

Banerjee, W., Liu, Q., Hwang, H.: J. Appl. Phys. **127** (2020)

Bencan, A., Drazic, G., Ursic, H., Makarovic, M., Komelj, M., Rojac, T.: Nat. Commun. **11**, 1762 (2020)
[PubMed][PubMedCentral]

Catalan, G., Scott, J.F.: Adv. Mater. **21**, 2463–2485 (2009)

Cheng, C.-J., Lu, C., Chen, Z., You, L., Chen, L., Wang, J., Wu, T.: Appl. Phys. Lett. **98**, 242502 (2011)

Clark, S.J., Robertson, J.: Appl. Phys. Lett. **94**, 022902 (2009)

Dong, W., Xiao, H., Jia, Y., Chen, L., Geng, H., Bakhtiar, S.U.H., Fu, Q., Guo, Y.: Adv. Sci. **9**, 2105368 (2022)

Dutta, D.P., Tyagi, A.K.: Appl. Surf. Sci. **450**, 429–440 (2018)

Ederer, C., Spaldin, N.A.: Phys. Rev. B **71**, 224103 (2005)

Fox, D.L., Scott, J.F.: J. Phys. C: Solid State Phys. **10**, L329–L331 (1977)

Freysoldt, C., Grabowski, B., Hickel, T., Neugebauer, J., Kresse, G., Janotti, A., Van de Walle, C.G.: Rev. Mod. Phys. **86**, 253–305 (2014)

Gulati, S., Goyal, K., Arora, A., Kumar, S., Trivedi, M., Jain, S.: Environ. Sci.: Water Res. Technol. **8**, 1590–1618 (2022)

Hauser, A.J., Zhang, J., Mier, L., Ricciardo, R.A., Woodward, P.M., Gustafson, T.L., Brillson, L.J., Yang, F.Y.: Appl. Phys. Lett. **92**, 222901 (2008)

Heron, J.T., Schlom, D.G., Ramesh, R.: Appl. Phys. Rev. **1**, 021303 (2014)

Hill, N.A.: J. Phys. Chem. B **104**, 6694–6709 (2000)

Huang, F., Wang, Z., Lu, X., Zhang, J., Min, K., Lin, W., Ti, R., Xu, T., He, J., Yue, C., Zhu, J.: Sci. Rep. **3**, 2907 (2013)
[PubMed][PubMedCentral]

Ju, S., Cai, T.-Y.: Appl. Phys. Lett. **95**, 231906 (2009)

Kubel, F., Schmid, H.: Acta Crystallogr. B **46**, 698–702 (1990)

Kumar, A., Yadav, K.L.: Physica B **405**, 4650–4654 (2010)

Lebeugle, D., Colson, D., Forget, A., Viret, M.: Appl. Phys. Lett. **91**, 022907 (2007)

Liang, Q., Zhang, Q., Zhao, X., Liu, M., Wee, A.T.S.: ACS Nano **15**, 2165–2181 (2021)
[PubMed]

Liu, F., Fan, Z.: Chem. Soc. Rev. **52**, 1723–1772 (2023)
[PubMed]

Liu, X., Cao, Y., Sun, J.: Adv. Energy Mater. **12**, 2202532 (2022)

Ma, C.-J., Chen, Y., Zhu, C., Chen, Q., Song, W.-L., Jiao, S., Chen, H., Fang, D.: J. Mater. Chem. A **7**, 12176–12190 (2019)

Mocherla, P.S.V., Karthik, C., Ubic, R., Rao, M.S.R., Sudakar, C.: Appl. Phys. Lett. **103**, 022910 (2013)

Mocherla, P.S.V., Gautam, S., Chae, K.H., Rao, M.S.R., Sudakar, C.: Mater. Res. Express **2**, 095012 (2015)

Mocherla, P.S.V., Prabhu, D., Sahana, M.B., Hebalkar, N.Y., Gopalan, R., Rao, M.S.R., Sudakar, C.: J. Appl. Phys. **124**, 073904 (2018)

Mocherla, P.S.V., Karthik, C., Ubic, R., Rao, M.S.R., Sudakar, C.: Appl. Phys. Lett. **105**, 132409 (2014)

Mocherla, P.S.V., Sahana, M.B., Gopalan, R., Ramachandra Rao, M.S., Nanda, B.R.K., Sudakar, C.: Mater. Res. Express **4**, 106106 (2017)

Moreau, J.M., Michel, C., Gerson, R., James, W.J.: J. Phys. Chem. Solids **32**, 1315–1320 (1971)

Nandy, S., Sudakar, C.: J. Appl. Phys. **126**, 135303 (2019)

Nandy, S., Mocherla, P.S.V., Kaur, K., Gautam, S., Nanda, B.R.K., Sudakar, C.: J. Appl. Phys. **126**, 235101 (2019)

Nandy, S., Kaur, K., Gautam, S., Chae, K.H., Nanda, B.R.K., Sudakar, C.: ACS Appl. Mater. Interfaces **12**, 14105–14118 (2020)
[PubMed]

Nandy, S., Hegde, M., Sudakar, C.: Thin Solid Films **733**, 138804 (2021a)

Nandy, S., Mocherla, P.S.V., Abdelhamid, E., Nadgorny, B., Naik, R., Sudakar, C.: Phys. Rev. B **103**, 184406 (2021b)

Nandy, S., Mocherla, P.S.V., Sudakar, C.: J. Appl. Phys. **121**, 203102 (2017)

Nandy, S., Kaur, K., Mocherla, P.S.V., Nanda, B.R.K., Sudakar, C.: J. Appl. Phys. **124**, 195108 (2018)

Nataf, G.F., Guennou, M., Gregg, J.M., Meier, D., Hlinka, J., Salje, E.K.H., Kreisel, J.: Nat. Rev. Phys. **2**, 634–648 (2020)

Neaton, J.B., Ederer, C., Waghmare, U.V., Spaldin, N.A., Rabe, K.M.: Phys. Rev. B **71**, 014113 (2005)

Nenno, D.M., Scheuer, L., Sokoluk, D., Keller, S., Torosyan, G., Brodyanski, A., Lösch, J., Battiato, M., Rahm, M., Binder, R.H., Schneider, H.C., Beigang, R., Papaioannou, E.T.: Sci. Rep. **9**, 13348 (2019)
[PubMed][PubMedCentral]

Noguchi, Y., Matsuo, H., Kitanaka, Y., Miyayama, M.: Sci. Rep. **9**, 4225 (2019)
[PubMed][PubMedCentral]

Park, T.-J., Papaefthymiou, G.C., Viescas, A.J., Moodenbaugh, A.R., Wong, S.S.: Nano Lett. **7**, 766–772 (2007)
[PubMed]

Paudel, T.R., Jaswal, S.S., Tsymbal, E.Y.: Phys. Rev. B **85**, 104409 (2012)

Rana, D.S., Takahashi, K., Mavani, K.R., Kawayama, I., Murakami, H., Tonouchi, M., Yanagida, T., Tanaka, H., Kawai, T.: Phys. Rev. B **75**, 060405 (2007)

Ravalia, A., Vagadia, M., Solanki, P.S., Gautam, S., Chae, K.H., Asokan, K., Shah, N.A., Kuberkar, D.G.: J. Appl. Phys. **116**, 153701 (2014)

Rojac, T., Bencan, A., Drazic, G., Sakamoto, N., Ursic, H., Jancar, B., Tavcar, G., Makarovic, M., Walker, J., Malic, B., Damjanovic, D.: Nat. Mater. **16**, 322–327 (2017)
[PubMed]

Rondinelli, J.M., Spaldin, N.A.: Adv. Mater. **23**, 3363–3381 (2011)
[PubMed]

Sando, D., Agbelele, A., Rahmedov, D., Liu, J., Rovillain, P., Toulouse, C., Infante, I.C., Pyatakov, A.P., Fusil, S., Jacquet, E., Carrétéro, C., Deranlot, C., Lisenkov, S., Wang, D., Le Breton, J.M., Cazayous, M., Sacuto, A., Juraszek, J., Zvezdin, A.K., Bellaiche, L., Dkhil, B., Barthélémy, A., Bibes, M.: Nat. Mater. **12**, 641–646 (2013)
[PubMed]

Saremi, S., Xu, R., Dedon, L.R., Gao, R., Ghosh, A., Dasgupta, A., Martin, L.W.: Adv. Mater. Interfaces **5**, 1700991 (2018)

Schlom, D.G., Chen, L.-Q., Fennie, C.J., Gopalan, V., Muller, D.A., Pan, X., Ramesh, R., Uecker, R.: MRS Bull. **39**, 118–130 (2014)

Schmid, H.: Growth Crystals **7**, 25–52 (1969)

Schmid, H.: Ferroelectrics **162**, 317–338 (1994)

Schrade, M., Masó, N., Perejón, A., Pérez-Maqueda, L.A., West, A.R.: J. Mater. Chem. C **5**, 10077–10086 (2017)

Selbach, S.M., Tybell, T., Einarsrud, M.-A., Grande, T.: Chem. Mater. **19**, 6478–6484 (2007)

Seyfouri, M.M., Wang, D.: Crit. Rev. Solid State Mater. Sci. **46**, 83–108 (2021)

Shimada, T., Matsui, T., Xu, T., Arisue, K., Zhang, Y., Wang, J., Kitamura, T.: Phys. Rev. B **93**, 174107 (2016)

Singh, P., Jung, J.H.: Physica B **405**, 1086–1089 (2010)

Smolenskii, G.A., Agranovskaya, A.I.: Zhur. Tekh. Fiz. **28**, 1491 (1958)

Smolensky, G.A., Agranovskaya, A.I., Popov, S.N., Isupov, V.A.: Zh. Tekh. Fiz. **28**, 2152 (1958)

Streiffer, S.K., Parker, C.B., Romanov, A.E., Lefevre, M.J., Zhao, L., Speck, J.S., Pompe, W., Foster, C.M., Bai, G.R.: J. Appl. Phys. **83**, 2742–2753 (1998)

Teague, J.R., Gerson, R., James, W.J.: Solid State Commun. **8**, 1073–1074 (1970)

Tsutsui, G., Mochizuki, S., Loubet, N., Bedell, S.W., Sadana, D.K.: AIP Adv. **9** (2019)

Wang, N., Luo, X., Han, L., Zhang, Z., Zhang, R., Olin, H., Yang, Y.: Nano-Micro Lett. **12**, 81 (2020)

Wang, Z., Xiao, M., You, J., Liu, G., Wang, L.: Acc. Mater. Res. **3**, 1127–1136 (2022)

Yang, M.-M., Iqbal, A.N., Peters, J.J.P., Sanchez, A.M., Alexe, M.: Nat. Commun. **10**, 2791 (2019a)
[PubMed][PubMedCentral]

Yang, T., Wei, J., Guo, Y., Lv, Z., Xu, Z., Cheng, Z.: ACS Appl. Mater. Interfaces **11**, 23372–23381 (2019b)
[PubMed]

Zeches, R.J., Rossell, M.D., Zhang, J.X., Hatt, A.J., He, Q., Yang, C.-H., Kumar, A., Wang, C.H., Melville, A., Adamo, C., Sheng, G., Chu, Y.-H., Ihlefeld, J.F., Erni, R., Ederer, C., Gopalan, V., Chen, L.Q., Schlom, D.G., Spaldin, N.A., Martin, L.W., Ramesh, R.: Science **326**, 977–980 (2009)
[PubMed]

Zhang, N., Gao, C., Xiong, Y.: J. Energy Chem. **37**, 43–57 (2019)

Zheng, Y., Slade, T.J., Hu, L., Tan, X.Y., Luo, Y., Luo, Z.-Z., Xu, J., Yan, Q., Kanatzidis, M.G.: Chem. Soc. Rev. **50**, 9022–9054 (2021)
[PubMed]

© The Author(s), under exclusive license to Springer Nature Singapore Pte Ltd. 2024
R. S. Ningthoujam, A. K. Tyagi (eds.), *Handbook of Materials Science, Volume 2*, Indian Institute of Metals Series
https://doi.org/10.1007/978-981-97-4646-0_7

7. Basic Concepts of Nitride Magnetic Materials and Their Applications

Pragnya P. Mishra[1] and Rabi N. Panda[1] ✉
(1) Department of Chemistry, Birla Institute of Technology and Science Pilani, K K Birla Goa Campus, Zuarinagar, Goa, 403726, India

✉ **Rabi N. Panda**
Email: rnp@goa.bits-pilani.ac.in

Keywords Nitrides – Nano-magnetism – Size and surface effects – Solid–gas reaction – Citrate precursor route

7.1 Introduction

7.1.1 General Introduction

Recently, much attention has been rendered to studies of metal nitrides because of their potential technological applications. Several nitrides are refractory in addition to their metallic nature. Among several applications, some of them are notably known for hard materials, catalytic properties, magnetic recording, permanent magnets, etc. (Flores-Livas et al. 2019; Wojciechowski and Lewandowski 2022; Panda and Gajbhiye 1997a; Oyama 1996). However,

investigations on metal nitrides are not wide spread because of the lack of the mechanistic approaches involved in their formation. Many of the processes in the literature involve temperature programme reactions (TPR) using metal oxide as precursors and the processes are case sensitive having different elements and involving different reaction pathways. In certain cases, surface oxidation of the materials involving oxy-nitride materials renders difficulties in synthesizing pure nitride products (Bem et al. 1993).

7.1.2 Different Classes of Nitride Ceramics

In metal nitride ceramics, metal atoms are bonded to N atoms in a variety of ways. The oxidation states of N can vary from 0 to −3. One of the considerations which is based on chemical bonding indicates the fact that binary nitrides can be classified as follows: (i) ionic nitrides, (ii) covalent nitrides and (iii) semi-metallic or molecular compounds (Tareen et al. 2019). Apart from the 3 types of nitrides mentioned above, interstitial nitrides are also important in classification (Tareen et al. 2019). For ternary nitrides, structure and bonding are complicated and the classification scheme is not adopted.

7.1.2.1 Ionic Nitrides

In ionic nitrides, metal ion (M) possesses a positive charge, and nitride ion (N), a negative charge to form $M^{n+}N^{n-}$, where n is the number of charge carriers. These are usually soluble in acids and alkalis. Examples of these kinds of nitrides are Li_3N, Mg_3N_2, Zn_3N_2, Cu_3N, etc.

7.1.2.2 Covalent Nitrides

In covalent nitrides, the orbitals of nitrogen atoms are bonded to the hybrid orbitals of atoms of Group III–VI A to form nitrides. Examples include BN, CN_x, $(SN)_x$, AlN, GaN,

etc. These nitrides are very hard and refractory or ceramic materials except in a few cases. These are resistant to weak acids and alkalis and usually show semiconducting or insulating properties; while $(SN)_x$ shows the superconducting property.

7.1.2.3 Metallic Nitrides

In metallic nitrides, metal–metal bond strengths are comparable with metal-nonmetal bond strengths. Sometimes, metal–metal bonds are stronger than metal-nonmetal bonds (Toth 1971). These can be subdivided into hard and soft nitrides. Hard nitrides include the Group III–VI B nitrides and lanthanide and actinide nitrides. These are hard, refractory and ceramic materials. These possess a metallic nature in electrical resistivity studies. Most are superconducting materials, e.g., LaN, TiN, VN, WN. Soft nitrides include the Group VII-VIII B nitrides. They are soft and decompose to non-stoichiometric nitrides easily because of less affinity between nitrogen and metal atoms, e.g., MnN, Mn_4N, FeN, Fe_3N, Fe_4N, CoN, Co_2N, Co_3N and Ni_3N. Usually, the melting points of non-stoichiometric soft nitrides are less than the respective elements because metal–metal bonding is stronger than metal-nonmetal bonds. However, some of the hard nitrides are superconductors, semiconductors, or insulators, e.g., ScN, TaN (Gall et al. 2001; Yu et al. 2002).

7.1.2.4 Interstitial Nitrides

The term, interstitial means vacant interstitial sites present in the host lattice. It is in the tetrahedral, octahedral and/or trigonal prism form. Atoms with small atomic radii, e.g., C (0.77 Å), N (0.71 Å), B (0.91 Å) and H (0.46 Å) are potential interstitial atoms. Depending on the amount of interstitial atoms, these can be divided into two types: (1) interstitial solid solutions and (2) interstitial compounds. If

the crystal structure of the host lattice after the insertion of an interstitial atom is not changed, these belong to interstitial solid solutions. Here, the amount of interstitial atoms is low, e.g., C present in steel is very small in amount (<2%), and the crystal structure of the host alloy is not changed. It forms the second phase that increases the hardness of the steel (Narula et al. 1988). Another example is the $FeNi_xN_y$ system where the amount of nitrogen is low, 0.03% (Panda and Gajbhiye 1999). The bonding between interstitial atoms and metal is very weak. When the crystal structure of the host metal atom is changed, then these nitrides belong to interstitial compounds. The amount of interstitial atoms can be more and the bonding among metal and N atoms is strong, e.g., VN, MoN.

7.1.2.5 Structure and Bonding in Transition Metal Nitrides

Transition metal nitrides are produced by dissolving nitrogen atoms into the metal lattice. These nitride materials have unique physical and chemical properties, which combine characteristic properties of covalent solids, ionic crystals and transition metals (Oyama 1996, 1992; Toth 1971; Schnitzke et al. 1990). Nitrogen atoms enter the 3d transition metals in interstitial positions and are bonded to metal atoms in a covalent way, majorly. This reduces the number of unpaired d-electrons in the metal. Distinct magnetic behaviours are observed based on the magnetic structures of the materials. Some examples of magnetic behaviours (ferromagnetic/paramagnetic and antiferromagnetic) for various selected nitride materials are presented in Table 7.1. Furthermore, it is observed that the crystal lattice gets expanded. The altered structure due to nitrogen insertion results in modification of the original properties of the transition metals and remains in accordance with the desired structure–property

correlation. The presence of interstitial nitrogen modifies the properties of Fe lattice in a useful manner. For instance, α′′-$Fe_{16}N_2$ shows a giant magnetic moment compared to α-Fe at room temperature and hence is a very suitable candidate for high-density magnetic recording media (Gajbhiye et al. 2004a).

Table 7.1 Examples of selected nitride materials with various magnetic behaviours

Sl no	Magnetic behaviour	Nitride materials
1	Ferromagnetic	Fe_4N, Mn doped GaN, Co_3N
2	Paramagnetic	$FeMoN_2$, Co doped Mo_2N
3	Antiferromagnetic	Fe_6W_6N, Mn_3NiN

The early transition metal nitrides adopt rock salt structure, whereas the late transition metal nitrides adopt zinc blende structure with the crossover at MnN. Crystal structure and magnetic behaviour are studied and results have been published (Lambercht et al. 2005; Coey and Smith 1999; Sifkovits et al. 1999; Matar 2002). It has been found that the tendency towards magnetism is stronger in the rock salt (RS) phase than in the zinc blende (ZB) phase. The lattice constant of the zinc blende (ZB) structure is always larger than that of the rock salt (RS) structure. FeN has a high magnetic moment in the RS structure, while in ZB, it becomes magnetic at a very large lattice expansion. CoN stays nonmagnetic in the ZB structure. MnN also becomes magnetic above a certain lattice constant in the ZB structure. CrN has a gradually increasing magnetic moment as a function of the lattice constant. VN shows a very weak magnetism and TiN and ScN are nonmagnetic. Studies on Fe_xN_y type interstitials indicate that magnetization increases with a decrease in nitrogen content for the compounds (Matar 2002). In magnetism, maximum interest is focussed on iron and iron-based alloys

because these materials are of the greatest practical use and the cheapest magnetic element by far (Coey and Smith 1999).

The presence of Nitrogen in the crystal lattice is an important factor for the modification of magnetic properties in 3d transition metals/alloys (Ma et al. 2009; Sun et al. 1990). In fact, several magnetic parameters such as saturation magnetization (M_s), Curie temperature (T_c), coercivity (H_c), blocking temperature (T_B), etc. change upon insertion of atomic nitrogen in the host crystal structure. The presence of nitrogen in the interstitial positions provokes the expansion of the lattice, majorly. The influence of nitrogen on the tailoring of magnetic properties can be well understood from the fact that certain iron-based alloys can change their magnetic states from weak ferromagnet to strong ones (Coey and Smith 1999).

In this book chapter, we will discuss preparation, characterization and magnetic property studies of a few binary and ternary transition metal nitrides (interstitial and ternary nitrides) along with their structure–property correlation.

7.2 Synthesis of Materials

7.2.1 Synthesis of Nitride Using Solid–Gas Reactor

7.2.1.1 General Introduction of Materials Synthesis

Difficulty in synthesizing nitride materials lies in the fact that it has to overcome large thermodynamic barriers towards the formation of the product(s) (Balogun et al. 2015). This is primarily due to the high bond dissociation energy of nitrogen (N_2). Therefore, many transition metal

nitrides can be synthesized only at very high temperatures (say >1500 °C). In addition, most of the nitrides are air-sensitive. Besides being non-oxide ceramics, there is a chance of surface oxidation of the materials in fine particle form in the air atmosphere. For example: synthesis difficulty for γ′-Fe_4N can be understood by its existence as a narrow region in the Fe–N phase diagram Fig. 7.1 (Wetzel et al. 2021). However, various synthetic routes are available for nitride materials, such as passing of N_2(g) over metal powder/ thin film, passing of NH_3(g) over metal powder/ thin film/oxide/ halide/sulphide, chemical vapour deposition method to form thin films of nitride, magnetron sputtering method to form coatings and films, molecular beam epitaxy method to produce nanowires and interfaces, etc. (Balogun et al. 2015; Ningthoujam and Gajbhiye 2015; Mazumder and Hector 2009; Parkin and Elwin 2001; Caicedo et al. 2011; Pak et al. 2010; Choi and Gilan 2009). Other synthesis methods include metathesis reaction, solvothermal process, metal azide precursor, sol–gel processing, etc. (Balogun et al. 2015; Ningthoujam and Gajbhiye 2015; Choi and Gilan 2009). Before we proceed to describe synthesis strategies for a few selected transition metal-based interstitial and compound-based nitrides, the fabrication of a nitridation reactor will be addressed in the following Sect. 7.2.1.2.

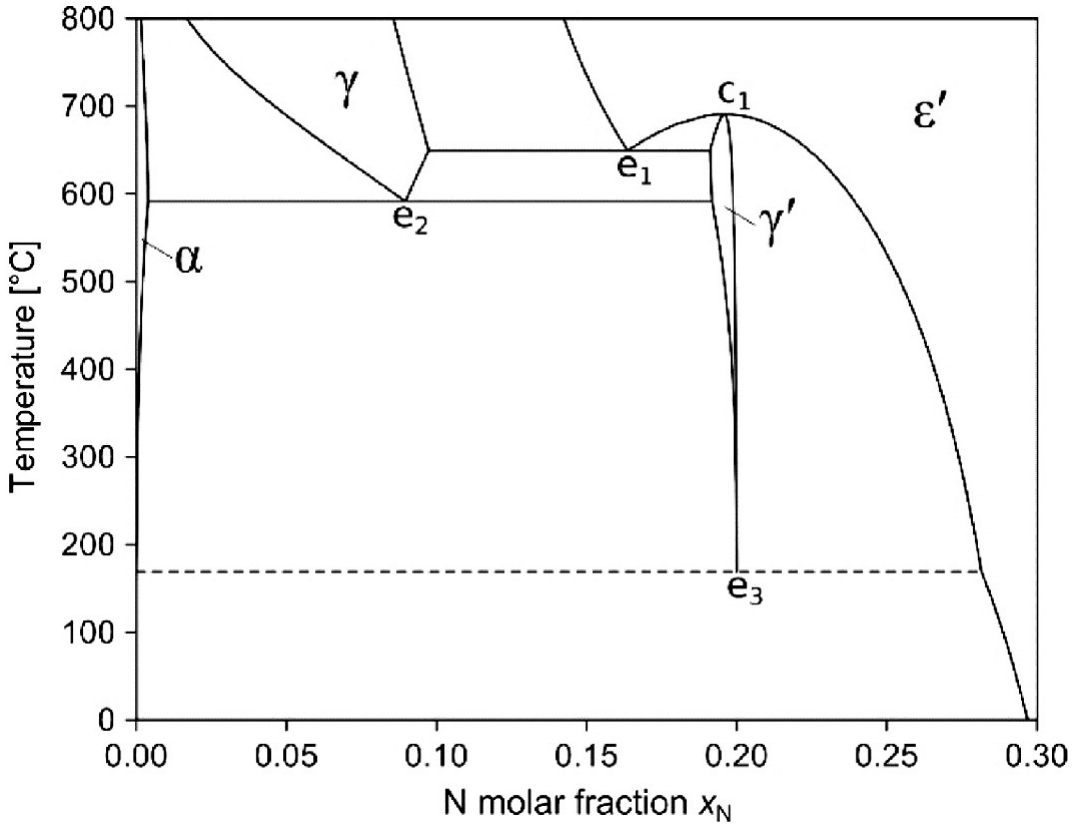

Fig. 7.1 Phase diagram of iron–nitrogen system. Reprinted from Ref. (Wetzel et al. 2021).

Copyright © 2021, MDPI, Basel, Switzerland (CC BY). c_1 and e_1, e_2 and e_3 represent congruent reactions and eutectoid decompositions, respectively

7.2.1.2 Solid–Gas Nitridation Reactor

Nitridation reactions can be carried out using one of the following ways; such as: (i) nitridation of oxide precursors using NH_3(g), (ii) nitridation of metal and alloys using N_2(g), (iii) nitridation of oxide precursors using a mixture of H_2(g) and NH_3(g), (iv) heating oxide or organometallic precursors with N containing compounds (say urea) in inert gas atmosphere, etc. Nitridation using N_2(g) requires high temperatures and materials prepared using this method are rarely nanostructured. It is known that nitrides prepared using organometallic or organic compounds contain carbon as an impurity and are mostly non-stoichiometric. However, the nitridation of oxide precursors using ammonia gas to

produce nitride is known for its pure phase formation with a homogeneous distribution of N atoms, nanocrystalline nature and high-surface areas.

Two different methods have been adopted for the nitridation process, using two different reactors for the materials described in this chapter. These nitridation methods include: (1) passing NH_3(g) over powdered metal oxide precursors and (2) passing N_2(g) over a mixture of precursor and urea in fixed ratios. The additional advantages of using both routes are described here. In oxides, the fractional difference in M–O and M′–O bond strength is much smaller. Therefore, it is possible to prepare complex nitride phases (M-M′-N) at lower temperature from the oxide precursors (Bem et al. 1993). The urea route involves preparation of the metal-urea complex precursor, which is a chemically stable and inexpensive compound, compared to other precursors such as organometallic materials or anhydrous. Finally, the complex transforms into metal nitride at elevated temperatures under a flowing N_2(g) atmosphere.

The schematic diagrams of nitridation reactors are described in the following subsections. The former was used for nitridation using gaseous ammonia while the later for nitridation using urea under nitrogen gas flow. In case of nitridation reactions using ammonia, samples were suspended vertically inside the quartz reactor tube. On the contrary, while carrying out the nitridation reactions using urea as a nitridation source, a horizontal gas flow reactor was employed. The details of the experimental approach have been described in the following sub-sections.

Nitridation Using Gaseous NH_3(g)

The typical sketch of the nitridation reactors, used for the nitridation using ammonia gas in order to synthesize nitride material, is shown in Fig. 7.2. The reactor employs

ammonia gas, which passes through a vertical quartz glass tube of 1 cm diameter. The flow of the gas is controlled by a flow controller. The precursor powder is suspended in the middle of the quartz tube with the help of a quartz wool plug, which allows through passage of NH_3(g). The vertical alignment of the reactor facilitates the homogeneous distribution of NH_3(g) molecules through the precursor powder which leads to qualitative product formation. The furnace controller is programmed to heat the precursor in different heating regimes and time intervals. The gas from the outlet is ventilated to the fume hood. The nature and quality of the product can be controlled by adjustment of operating conditions; such as temperature, precursor concentration and residence time inside the reactor (Volpe and Baudart 1985).

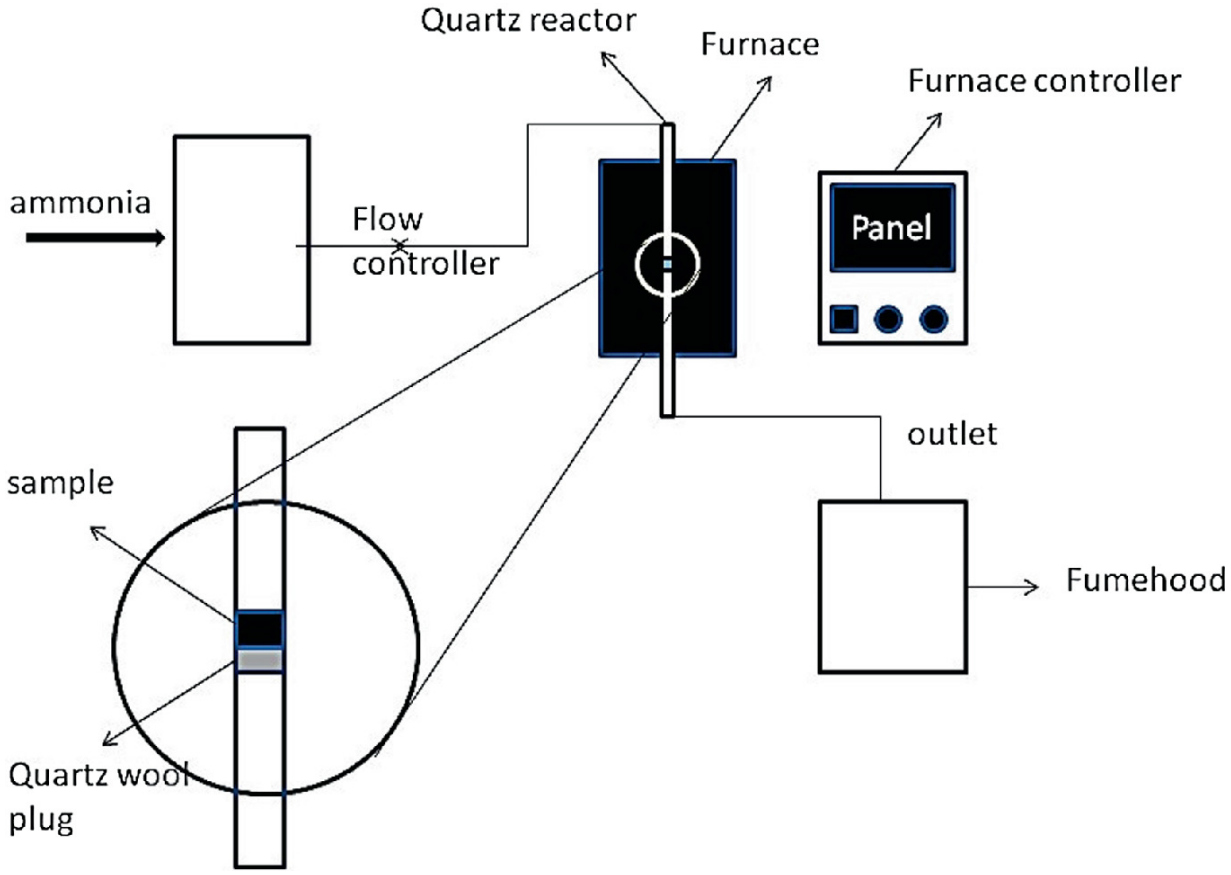

Fig. 7.2 Schematic block diagram of vertical nitridation reactor (sample chamber is enlarged for clarity reason)

The ammonolysis of oxides is one of the commonest routes for the synthesis of nanocrystalline and high surface area nitrides. Volpe and Boudart (1985) developed temperature-programmed reactions to facilitate nitridation reactions. In this process, often a topotactic relationship between the reactants and the products exists and the product can be pseudomorphic with the reactant, i.e. crystallographic orientations, particle size and geometry are retained from the reactant solid. The replacement of oxygen atoms by nitrogen during this transformation can also generate porous, lower-density nitride materials. Depending upon the N content (i.e. z) in the nitride materials, different phases (stable and metastable) can be synthesized.

Nitridation Using Solid Urea in N_2(g) Atmosphere

Typical sketch of the solid–gas reactor used for nitridation of solid-state precursors using urea as a nitrogen source in the presence of N_2(g) gas flow atmosphere is shown in Fig. 7.3. A quartz tube of 10 cm diameter is placed horizontally inside the furnace, which is connected with N_2(g) inlet and outlet. The precursor material (about 1 gm) is placed in an alumina boat placed horizontally inside towards the middle of the reactor tube. N_2(g) enters through the reactor tube passes over the solid precursor material and comes out through the outlet. The arrangement allows the final product to cool down under the flow of N_2(g) until the furnace is cooled down to room temperature.

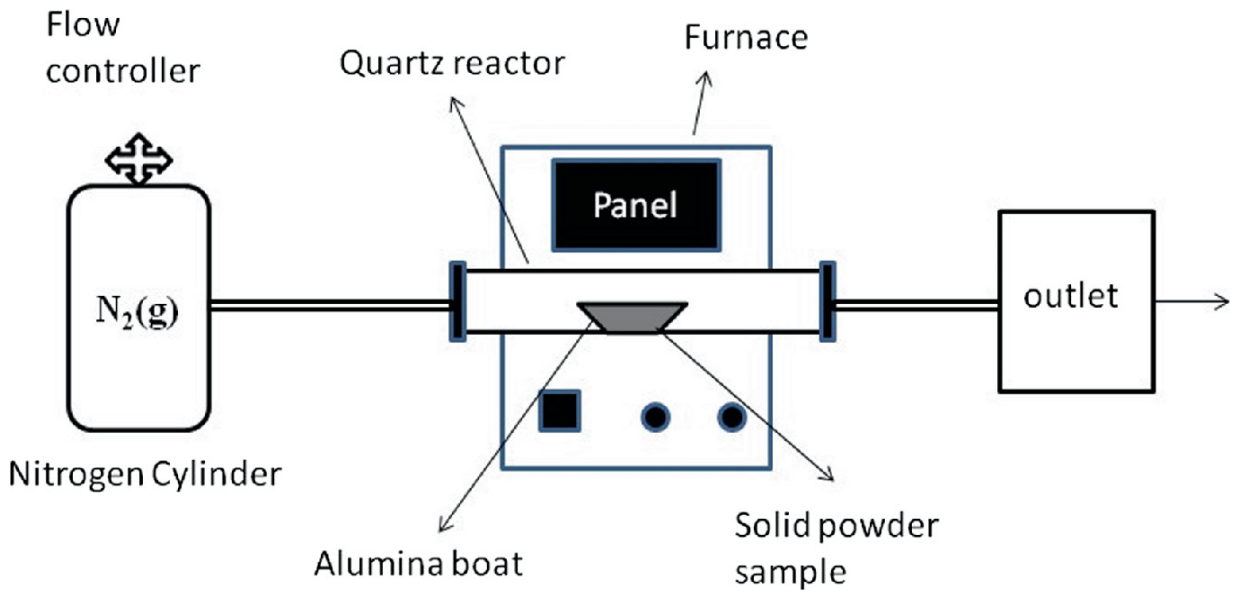

Fig. 7.3 Schematic block diagram of horizontal nitridation reactor

The use of nitrogen and chlorine-containing compounds instead of oxide precursors as nitrogen sources, has been known in the literature (Ningthoujam and Gajbhiye 2015; Mazumder and Hector 2009; Parkin and Elwin 2001). Urea ($(NH_2)_2CO$) can form a metal–urea complex in the form of a gel. The gel can be isolated as solid-state precursors by simple materials processing techniques, such as washing with suitable solvent, and drying in air/inert gas at room temperature or moderate temperature. The resulting gel is subjected to heat treatment using nitrogen/argon gas, nano-structured nitrides/carbides are produced at relatively lower temperature. In this procedure, urea acts as a stabilizing agent in addition to its role as a nitrogen source (Mazumder and Hector 2009; Giordano et al. 2008).

7.2.2 Synthesis of Some Important Ferromagnetic Iron-Based Binary and Ternary Nitrides

A two-step synthetic methodology has been adopted for the synthesis of Co and Ni substituted iron nitride. The first step involves the synthesis of nano-dimensional oxide precursor by a citrate method, and the second one is the

nitridation of the oxide powder using ammonia gas $NH_3(g)$ as a gas vector.

7.2.2.1 Synthesis of Co/(Ni)-Fe-Based Mixed Oxide via Citrate Precursor Route

The flow diagram for the synthesis of Co/(Ni)-Fe-based mixed oxide precursor is shown in Fig. 7.4. The methodology includes the thermal decomposition of metal (or mixed metal)—citrate complex having desired metal atom ratios in the air atmosphere. Metal ions are taken in stoichiometric proportion and anhydrous citric acid, $C_6H_8O_7$, was used to chelate them in an aqueous solution. pH is adjusted appropriately to the acidic value of 2–3. The solution is homogenized by refluxing for several hours below 100^o C. The resulting sol is evaporated to get a viscous gel which in turn dried at 90–100^o C for several hours. The mixed metal citrate precursors are obtained as solid fluffy mass heat treated at various temperatures in order to synthesize Co–Fe or Ni–Fe-based mixed metal citrate complexes.

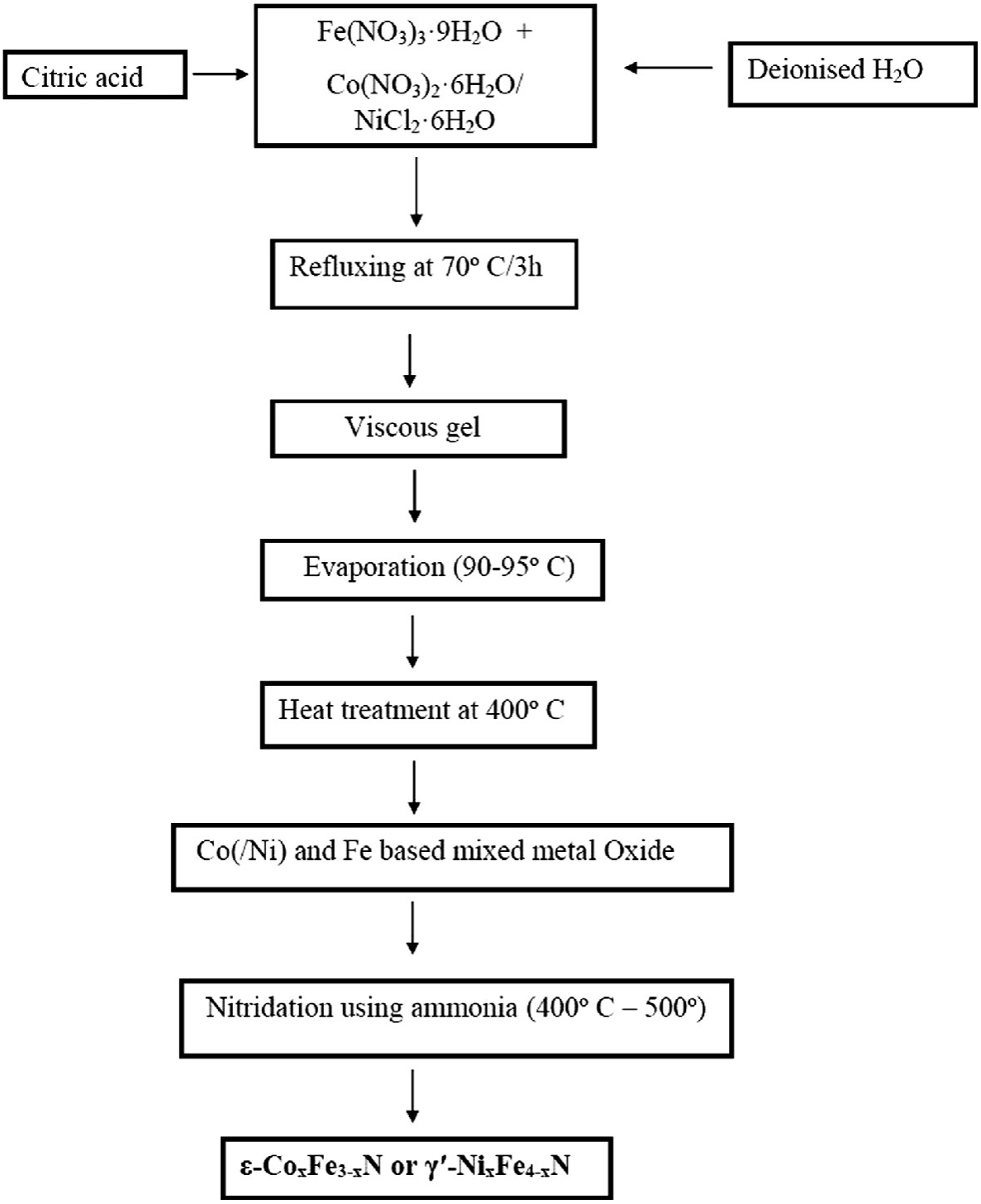

Fig. 7.4 Flow diagram for synthesis and subsequent nitridation of Co(/Ni)–Fe-based mixed oxide precursors to produce Fe–Co(/Ni) nitrides

7.2.2.2 Nitridation of Co/(Ni)–Fe Based Mixed Oxides to Form ε-$Co_xFe_{3-x}N$ ($0 \leq x \leq 0.4$) and γ′-

$Ni_xFe_{4-x}N$ ($0 \leq x \leq 0.8$)

Low-temperature chemical routes are preferably used for the synthesis of nitride products. The formation of nitrides using finely divided metal (mixed metal) oxides as precursors for nitridation is known (Gajbhiye et al. 2004a). Following the above-mentioned procedure, topotactic transformation of the oxide precursors and nitride product takes place. Crystallographic orientations, geometry, particle dimensions, etc. are retained from the reactant (Volpe and Baudart 1985). Several reports are found where metal oxalate precursors are directly nitrided in order to obtain nitride products with an elongated shape. The use of metal citrate has the advantage of being capable of providing both amorphous and nano-structured oxide powders which on subsequent nitridation can produce nitride products at relatively lower temperature (Panda and Gajbhiye 1998a).

Formation of ε-$Co_xFe_{3-x}N$ ($0 \leq x \leq 0.4$)

Nitridation of iron oxide precursor was carried out in a vertical tubular furnace using a quartz reactor of 1 cm diameter under flowing NH_3(g) in the temperature range 823–973 K for a duration of 2 h. After asserting the formation of pure phase ε-Fe_3N at 973 K, the mixed metal oxide precursors containing Co and Fe atoms in desired stoichiometry were nitrided at the same temperature in order to get ε-$Co_xFe_{3-x}N$ ($0 \leq x \leq 0.4$) material. The heating ramp was moderately high and kept at 3.8 K/min. The furnace was allowed to cool down naturally until room temperature (298 K) was reached. During cooling, constant NH_3(g) flow rate was maintained. The resulting grey/black coloured nitride products were removed from the quartz reactor after completion of the experiment and exposed to an air atmosphere. The summary of the materials

synthesized is listed in Table 7.2 along with other synthesis and processing parameters.

Table 7.2 Materials, stoichiometric amount of reagents, nitridation temperature and heating ramp ε for various ε-Co-Fe-N phases

Materials	**Stoichiometric amount of reagents used (g)**		**Nitridation temperature (K)/nitridation time (h)**	**Heating ramp ($Kmin^{-1}$)**
	$Fe(NO_3)_3 9H_2O$	**$Co(NO_3)_2 6H_2O$**		
ε-Fe_3N	6	–	973/2	3.8
ε-$Co_{0.1}Fe_{2.9}N$	5.819	0.145	973/2	3.8
ε-$Co_{0.2}Fe_{2.8}N$	5.656	0.291	973/2	3.8
ε-$Co_{0.3}Fe_{2.7}N$	5.417	0.433	973/2	3.8
ε-$Co_{0.4}Fe_{2.6}N$	5.20	0.580	973/2	3.8

Formation of γ′-$Ni_xFe_{4-x}N$ ($0 \leq x \leq 0.8$)

Similarly, all compositions of varying Ni substituted oxide precursors were nitrided at the same temperature, i.e. 973 K in order to get γ′-$Ni_xFe_{4-x}N$ ($0.2 \leq x \leq 0.8$) materials. In short, every experimental parameter being similar, $Fe(NO_3)_3 \cdot 9H_2O$ and $Ni(NO_3)_2 \cdot 6H_2O$ were used for Fe and Ni source, respectively. The summary of the materials synthesized is listed in Table 7.3 along with the synthesis and processing parameters. The material γ′-Fe_4N ($x = 0$) could not be synthesized in pure phase by using the present methodology and experimental parameters therein.

Table 7.3 Materials, stoichiometric amount of reagents, nitridation temperature and heating ramp for various γ′-Ni-Fe-N phases

Materials	Stoichiometric amount of Reagents used (g)		Nitridation TEMPERATURE (K)/nitridation time (h)	Heating ramp ($Kmin^{-1}$)
	$Fe(NO_3)_3 \cdot 9H_2O$	$Ni(NO_3) \cdot 6H_2O$		
γ′-$Ni_{0.2}Fe_{3.8}N$	5.656	0.166	973/2	3.8
γ′-$Ni_{0.4}Fe_{3.6}N$	5.400	0.353	973/2	3.8
γ′-$Ni_{0.6}Fe_{3.4}N$	5.099	0.530	973/2	3.8
γ′-$Ni_{0.8}Fe_{3.2}N$	4.799	0.706	973/2	3.8

7.2.3 Synthesis of Some Important W or Mo-Based Paramagnetic/antiferromagnetic Binary and Ternary Nitrides

Several synthesis methods have been adopted in literature for the synthesis of W and Mo-based ceramics. Chen et al. have tried to synthesize nano-size W–N particles with 3–12 nm size (Chen et al. 2020). A non-toxic source, dicyandiamide (C_2N_4 H_4), is used as a nitrogen source for synthesis during the nitridation of W-containing precursors. In another development, the synthesis and characterization of W_2N from nitridation of oxide precursors (i.e. WO_3/H_2WO_4) is reported (Villaseca et al. 2015). While synthesizing, NH_3(g) is used as a nitrogen source at elevated temperatures. Single-phase products with moderately high surface area are obtained. Synthesis of Mo_2N using molybdenum precursors ((MoO_3, $(NH_4)_6$ Mo_7O_{24}. 4 H_2O, $(NH_4)_6$ Mo_7O_{24}) in ammonia atmosphere are reported (Roy et al. 2015; Sidana et al. 2018). For bimetallic nitrides (Fe_3Mo_3N, Co_3Mo_3N, Co_3W_3N),

amorphous metastable precursors containing multiple metal ions are nitrided (Wang et al. 2012). Synthesis of ternary nitrides can also be possible by nitridation of metal(s) tungstate(s) and metal(s) molybdate(s) using a mixture of H_2(g) and N_2(g) at elevated temperature (Zhang et al. 2006). From the above-mentioned literature reports, it is clear that along with oxide-based precursors, several other N-based compounds are profitably used for the preparation of nitride products. In the following subsections, we will describe the synthesis of Mo_2N, W_2N, Co-Mo–N, $FeMoN_2$ and $CoWN_2$.

7.2.3.1 Synthesis of Some Important W or Mo-Based Paramagnetic/antiferromagnetic Binary and Ternary Nitrides

In this subsection, synthesis methodologies for Mo and W-based binary and ternary nitrides; such as γ-Mo_2N, β-W_2N, γ-$Co_{0.25}$ $Mo_{1.75}$ N, $FeMoN_2$, $CoWN_2$, etc. will be described. In such kind of material systems, owing to the lack of proper correlation lengths between the magnetic ions in their crystalline state, exchange interactions are not found. In several ternary transition metal nitrides, antiferrimagnetic orderings are observed at lower temperatures. The details regarding the magnetic properties will be elaborated in Sect. 7.3.

Synthesis of γ-Mo_2N and γ-$Co_{0.25}$ $Mo_{1.75}$ N Nitrides

We will describe the synthesis of γ-Mo_2N and γ-$Co_{0.25}$ $Mo_{1.75}$ N nitrides using different precursors and nitridation routes (Mishra and Panda 2017). Two different precursors have been used for the synthesis of γ-Mo_2N such as molybdenum oxide via hydrazine route for ammonia route and molybdenum ethylene diamine organometallic complex precursor for urea route. Co–Mo bimetallic oxide precursor

has been prepared via the borohydride route for the synthesis of γ-$Co_{0.25}$ $Mo_{1.75}$ N nitride.

Synthesis of MoO_3 Precursors

(a) Via Hydrazine Route

For the preparation of oxide precursor, 5 g of ammonium paramolybdate, $(NH_4)_6Mo_7O_{24}{\cdot}4H_2O$, was dissolved in 50 ml of distilled water and stirred with a magnetic stirrer. After the complete dissolution of the solid, 7.5 ml of 15% hydrazine hydrate ($NH_2NH_2{\cdot}H_2O$) solution was added dropwise at room temperature (298 K) until the colour of the solution became brown. The resulting solution was refluxed at 70 °C for 30 min in an air atmosphere. The resulting coarse precipitate was filtered out, washed with distilled water and ethanol several times, and air-dried at 298 K for 12 h. The dried precipitate was heated under N_2(g) flow at 300 °C for 2 h duration in order to get precursor powder.

(b) via Molybdenum-Ethylenediamine Complex

We have tried to synthesize ethylenediammonium trioxomolybdate (VI)-μ-oxotrioxoethylenediaminemolybdate(VI) (enH_2)[O_3Mo-O–Mo(en)O_3]) precursor which has been known in the literature via developing newer synthetic strategy (Roman et al. 1991). The procedure adopted may be summarized as follows: commercially available molybdenum trioxide (MoO_3) (Molychem 99.5%) and ethylenediamine ($NH_2CH_2CH_2NH_2$) were taken in 1: 25 equivalence of molar ratios in a 500 ml beaker. In real practice, approximately, 4 g of MoO_3 was taken in a beaker and

120 ml of distilled water was added. 4.6 ml of ethylenediamine was added to the resulting suspension in order to obtain a clear solution. After stirring for 5 min at room temperature, conc. HCl (aq) was added dropwise till a white precipitate was formed. This is heated at 100 °C for 5 h with constant stirring and reflux in an oil bath. The precipitate formed is then filtered out using filter paper and dried at room temperature for 48–72 h. The white-coloured dried precipitate was then collected, crushed properly and used as the precursor for nitridation.

Synthesis of Co-Mo Based Bimetallic Oxides via Borohydride Route

In a typical synthesis of γ-$Co_{0.25}Mo_{1.75}N$, stoichiometric amounts of Co and Mo sources (i.e. $NH_4)_6Mo_7O_{24}.4H_2O$ and Co $(NO_3)_2.6H_2O$) were taken and dissolved in 40 ml of distilled water followed by stirring (Mishra and Panda 2017). 10 ml of 0.1N aq. ammonia was gradually added in order to make the solution basic. After that, 15 ml of 0.04 M KBH_4 was added to the solution and agitated using a magnetic stirrer for 1 h at 298 K resulting in a pinkish white solid precipitate. The collected precipitate was washed with aqueous ammonia and ethanol and cooled down to 298 K followed by drying at 80 °C in the air for a duration of 72 h, approximately. The resulting solid was heated at 200 °C for 2 h duration under N_2(g) flow. After cooling down to 298 K, the resulting solid was crushed well and used for nitridation experiments.

Synthesis of γ-Mo_2N and γ-$Co_{0.25}Mo_{1.75}N$ via Ammonia Route

For the nitride synthesis, approximately, 0.6 g of oxide precursors (obtained by the procedure described above) were loaded in the middle of a 1 m long quartz reactor with the help of quartz wool (Mishra and Panda 2017). The

reactor containing the precursor is placed inside a vertical tubular furnace. NH_3(g) is then purged for 1 h to remove any residual oxygen present in the reactor. Then a furnace is programmed to heat the precursor from room temperature to 700 °C in 4 h with the heating ramp at 2.9 °C/min and maintained at 700 °C for 2 h (Mishra and Panda 2017). The furnace was switched off, and allowed to cool down naturally under the flow of NH_3(g) till room temperature was reached. The resulting final product was subjected to characterization studies.

Synthesis of γ-Mo_2N Nitrides via Nitridation Using Solid Urea

The organometallic precursor (0.7 g) (as described in Sect. 2.3.1.1.1) and solid urea (1.057 g) were taken in 1:9 molar equivalences and mixed well using a mortar and pestle. The mixture was taken in an alumina boat and placed inside the tubular furnace. Initially, N_2(g) was purged for 1–2 h to remove any residual oxygen content present in the sample chamber and to make the reaction in an inert atmosphere. Next, the furnace was programmed to heat the reactant mixture in a controlled manner under the flow of N_2(g). The precursor was heated up to 650 °C inside the furnace in 3 h duration with a heating rate of 3.6 °C/min. The furnace was maintained at the final temperature for the reaction to take place for 3 h duration. After that, the reactor was allowed to cool down naturally under N_2(g) flow until room temperature was reached. The sample was removed from the reactor and exposed to air at room temperature.

Synthesis of β-W_2N Nitrides

The synthesis of β-W_2N involves two steps: (1) synthesis of precursor and (2) nitridation of precursor. The details of

the synthetic procedure adopted have been described below.

(a) **Precursor Synthesis**

For the synthesis, 2.44 g of ammonium tungsten oxide hydrate ($(NH_4)_6W_{12}O_{39}\cdot$ x H_2O) (Alfa Aesar) and 1.92 g of anhydrous citric acid ($C_6H_8O_7$) (Fisher Scientific) were taken in 1:1 molar ratio and dissolved in 300 ml of distilled water in order to get a clear solution. Next, the solution was taken in a round bottom flask and refluxed at 80 °C for 1 h. The resulting clear solution was dried at 90 °C for 3 h duration. The resulting greenish-coloured gel was heat treated again at 90 °C in an air atmosphere for 24 h. The dried crystal gel was then prefired at a temperature of 150 °C for 30 min in order to obtain precursor for nitridation.

(b) **Nitridation of Precursor via Urea Route**

The prefired precursor, obtained after heat treatment at 150 °C, was used for nitridation to yield β-W_2N using urea as a nitrogen source. For the nitridation experiment, the precursor and solid urea were taken in a molar ratio of 1:12 and crushed well mechanically using an agate mortar and pestle for 15–20 min. The solid mixture was placed inside the middle of a horizontal reactor of the furnace and taken in an alumina boat. The furnace was programmed to heat the reactants in N_2(g) atmosphere up to a temperature range of 700–750 °C for a duration of 3 h–4 h. The reaction temperature was held for 2 h duration, followed by natural cooling of the product in the flow of N_2(g). The resulting nitride product was removed from the furnace at room temperature.

Synthesis of $FeMoN_2$ and $CoWN_2$

(a) Synthesis of $FeMoN_2$

In order to synthesize Fe_3Mo_3N interstitial compound chemically synthesized $FeMoO_4$ is taken as a precursor for nitridation at 773 K using ammonia gas (Panda and Gajbhiye 1997b). When Fe_3Mo_3N is nitrided again (tempered) at much lower temperature of 573 K under vigorous NH_3(g) flow, $FeMoN_2$, ternary nitride having WC structure results (Panda and Gajbhiye 1998b). To be noted, $FeMoN_2$ contains a larger nitrogen content compared to Fe_3Mo_3N and is majorly ionic in nature.

(b) Synthesis of $CoWN_2$

The two-step synthetic methodology for the preparation of ternary $CoWN_2$ has been adopted in this study. The first step involves the synthesis of $CoWO_4$ precursor, while the second step is the nitridation of the synthesized precursor. The details of the experimental procedure are described as follows:

(I) Synthesis of Cobalt Tungstate, $CoWO_4$, Precursor

In a typical synthesis of precursor, i.e. $CoWO_4$, 0.8162 g of ammonium tungsten oxide hydrate ($(NH_4)_6W_{12}O_{39}\cdot xH_2O$) (Alfa Aesar, United States) and 0.9701 g of cobalt nitrate ($Co(No_3)_2\cdot 6H_2O$)) (Molychem, India) were taken in 1:1 molar ratio. Cobalt and tungsten salts were dissolved separately in distilled water and added to an aqueous solution containing 5 g of citric acid. The resulting solution was taken in a 500 ml round bottom flask and diluted to

300 ml using distilled water. Next, the solution was stirred and refluxed at 80˚C for 3 h duration using a magnetic stirrer. At the end, a pink-coloured solution was obtained. This solution was placed in the fume hood for evaporation using a hot plate. The evaporation was continued until approximately 5–10 ml of the viscous gel was left. The gel was collected and heated in an air atmosphere at 90 °C overnight. After drying, it was scratched, crushed, freed from moisture and heated again at 400 °C in an air atmosphere for 3 h to yield $CoWO_4$ precursor.

(II) **Nitridation of $CoWO_4$ Precursor Using Ammonia**

The synthesized $CoWO_4$ precursor was nitrided using NH_3(g) as a nitrogen source to produce $CoWN_2$ nitride material. The quartz reactor containing the precursor material is placed inside the tubular furnace vertically. Then, the furnace was programmed to heat the precursor up to 700 °C in a 4 h duration with a heating ramp of 2.9 K/min. The reaction temperature of 700 °C was maintained for 2 h duration inside the furnace, followed by natural cooling under a continuous flow of NH_3(g). The product was removed after 24 h when the reactor temperature reached 298 K. The resulting product was characterized for further study.

7.2.4 Characterization of the Synthesized Products

An X-ray diffractometer was used to record X-ray powder diffraction (XRD) patterns using Cu Kα radiation (λ = 0.154 nm). The X-ray diffraction confirms the phase purity of the product. The crystallite size of the product was calculated using the Scherrer equation, $t = 0.9l\ \lambda/B\cos\theta$, where t is the crystallite size, λ is the wavelength of X-ray

radiation, B is the full width at half maximum (FWHM) in radian and θ is the diffraction angle (Panda and Gajbhiye 1997a; Mishra and Panda 2017). Scanning electron microscopy (SEM) and transmission electron microscopy (TEM) techniques were used to examine the shape and morphology of the products. SEM–EDX and AAS were used for the composition analysis of the materials. Magnetization measurements (M Vs H characteristics) at room temperature (298 K) were carried out on solid powdered material using a vibrating sample magnetometer which can provide a magnetic field of up to 20 kOe.

7.3 Introduction to Fine Particle Magnetism

Nanomagnetic materials exhibit interesting magnetic behaviour that is distinct from those of the bulk form of the same substance (Wu et al. 2006; Yuan et al. 2009). In the fine particle form, the dimensions of the materials are comparable to the critical length of one or more of various phenomena, one such example being the size of magnetic domains. Critical length is the maximum length below which, at given temperature the particle is single domain in nature and behaves as superparamagnetic (Ce et al. 2014). The details of the specific magnetic phenomena occurring in the nano-magnetic systems are presented as follows.

Based on the theory of magnetism, the total energy of an ellipsoid is contributed by three types of energies, i.e. exchange, anisotropy and magnetostatic energy (Kittel 1946). As the size of the magnet increases, the number of domain walls also increases. This results in a reduction of magnetostatic energy. On the other hand the presence of numerous domain walls increase the exchange and anisotropic energies. Therefore, the size of a magnet has a great influence on the magnetic behaviour (popularly

known as size effect). In addition, due to large volume to surface ratio because of small size of the nano materials surface effects get pronounced. The size and surface effects are described as follows (Ce et al. 2014).

(I) **Size Effect in Nanomaterials: Superparamagnetism**

A single domain particle is uniformly magnetized with all the spins aligned in the same direction. The magnetization is reversed by spin rotation as there are no domain walls to move. This is the reason for very high saturation magnetization in nanomagnetic systems. In such a system coercivity increases from the bulk value, attains a maximum and then reduces further to zero value with the decrease of particle size. However, another source for the high coercivity in nanoparticles is the shape anisotropy which may result from particulate shape (Lu et al. 2007).

Magnetic crystallites below the threshold size or critical diameter at a particular temperature show superparamagnetism. The temperature is referred as blocking temp (T_B), above which a particle is superparamagnetic (Ce et al. 2014). The thermal energy (K_BT) overcomes the magnetic energy barrier ($K_{eff}V$) with decreasing particle size and the system behaves like a paramagnet. Instead of atomic magnetic moments, there is now a giant (super) moment inside each particle. This system is named as super-paramagnet. Such a system has no hysteresis (Figs. 7.5a and b) (Ce et al. 2014; Lu et al. 2007).

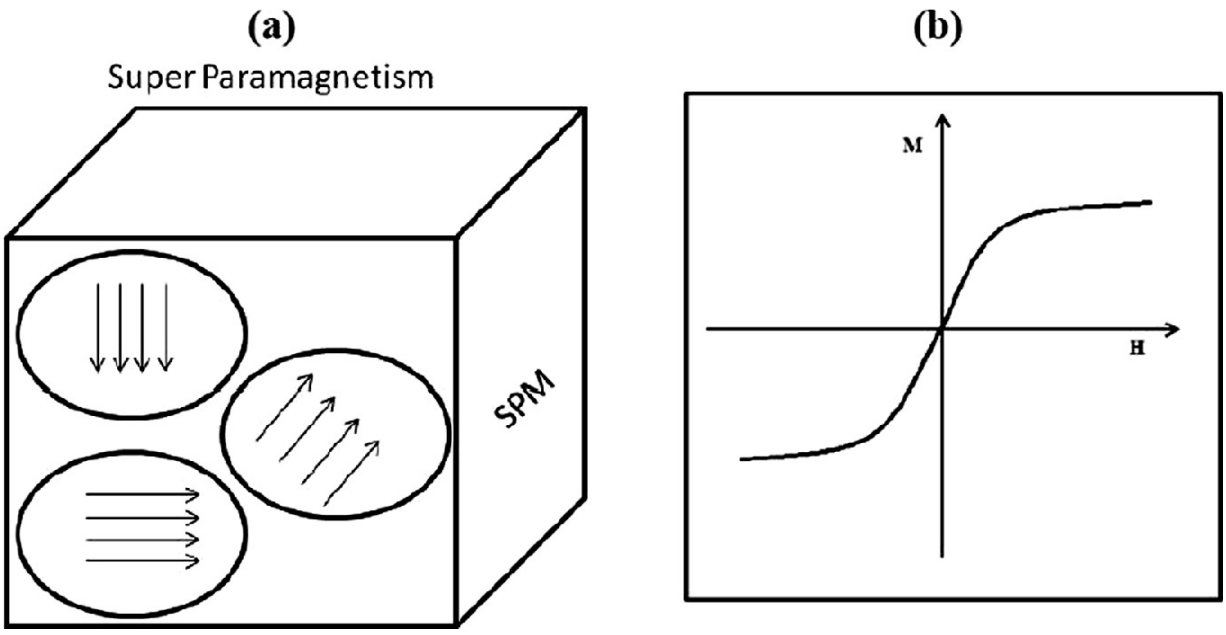

Fig. 7.5 **a** and **b** Representation of superparamagnetic domains (**a**) and hysteresis loop (**b**) showing zero coercivity of a superparamagnetic assembly of nanoparticles

(II) **Surface Effects in Nanomaterials**:

As the particle size decreases, a large percentage of all the atoms in a nanoparticle are surface atoms, which implies that surface and interface effects become more important. Due to the large surface atoms to bulk atoms ratio, the surface signs contribute more towards the magnetizations. The local breaking of symmetry might lead to changes in the band structure, lattice constant and atom coordination (Lu et al. 2007).

7.3.1 Magnetic Properties of Binary Transition Metal Nitrides

7.3.1.1 Ferromagnetism in Binary Transition Metal Nitrides

One of the interesting properties of transition metals and transition metal compounds is the occurrence of magnetism due to the establishment of a spontaneous (local) spin

polarization of the electrons. Electrons occupying 3d and 4f orbitals are highly localized on the atoms and correlations between electronic spins are very important for magnetic phenomenon to occur. Late transition metal elements, i.e. Fe, Co, and Ni, show ferromagnetic behaviour due to the parallel alignment of magnetic moments in terms of exchange interaction between neighbouring moments (Morin-Lopez and Bennemann 1981). This argument is also extended while explaining magnetism in metal nitrides, such as Fe_4N, Mn_4N, Fe_3N, etc. except the contribution from N spin pairing with 3d states of transition metal (Panda and Gajbhiye 1997a). The origin of ferromagnetic phenomena in transition metal nitride can be understood by considering the structure and bonding in nitride. Therefore, we will describe studies on selected ferromagnetic binary nitrides, i.e. Fe_3N and Fe_4N binary nitrides in the following subsections.

Magnetic Properties of Fe_4N and Fe_3N Nitrides

Introduction

Nitridation of Fe-based precursors using NH_3(g) at higher temperatures leads to varieties of phases; such as ζ-Fe_2N, ε-Fe_3N, γ′-Fe_4N, α′-(Fe–N), α″-$Fe_{16}N_2$, etc. Among these phases, the magnetic properties of ε-Fe_3N and γ′-Fe_4N are studied in more detail in the literature (Chen et al. 2015; Liu et al. 2020; Kantar and Ertas 2016). In fact, understanding the origin of ferromagnetism in these interstitial nitrides has become a matter of interest (Leineweber et al. 2017). As the magnetic properties of ε-Fe_3N and γ′-Fe_4N are closely related to their corresponding crystal structures, we will focus on the crystal structure of these nitrides.

Crystal Structure of γ′-Fe_4N and ε-Fe_3N

(I) Crystal Structure of γ′-Fe_4N

The simplest ordered Fe–N compound is cubic γ′-Fe_4N. This is a cubic antiperovskite which can be described as a face centred cubic lattice of iron metal (γ-Fe) with N atom located at the body centre site (Fig. 7.6). γ′-Fe_4N structure crystallizes in *Pm3m* space group (Gajbhiye et al. 2004a; Coey and Smith 1999; Bhattacharyya 2015). The FCC lattice of γ-Fe is expanded by 33% by interstitial nitrogen in the 1b body centre position, giving a value of lattice parameter of 3.795 Å against the value of 3.450 Å for γ-Fe. There are two non-equivalent iron sites; the corner 1a site with cubic symmetry having 12 iron neighbours at 2.68 Å and the 3c face centre site with two nitrogen neighbours at 1.90 Å and 12 iron second neighbours at 2.68 Å.

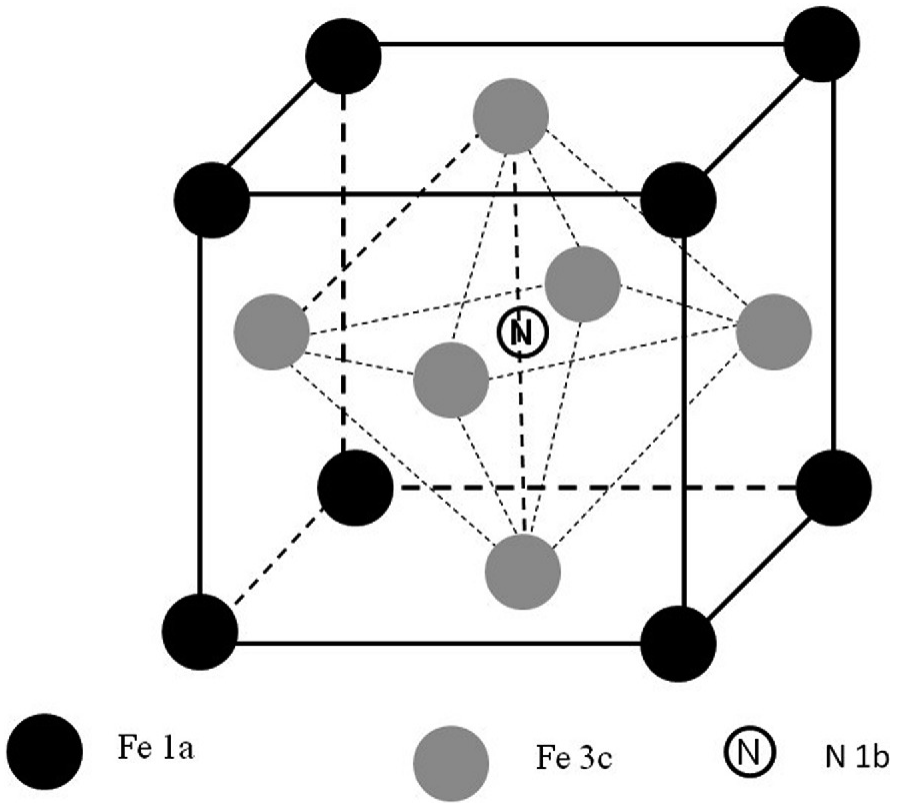

Fig. 7.6 Crystal structure of γ′-Fe_4N. The specific site occupancies of Fe and N are mentioned

(II) Crystal Structure of ε-Fe_3N

Similarly, the ε-Fe_3N phase crystallizes with a hexagonal close packed (hcp) structure with alternate stacking of Fe and N layers (Fig. 7.7). The epsilon phase exists over a wide range of compositions in the iron–nitrogen phase diagram ranging from 25 to 33 at.% N. The upper limit of the nitrogen concentration for the ε phase is 49.3 N atoms/100 Fe atoms (Jack 1952). In this hexagonal lattice, all Fe sites are equivalent as are the N sites. In ε-Fe_3N, Fe atoms form an hcp arrangement with N atoms occupying voids inside Fe_6 octahedra. One-third of the octahedral voids in an hcp arrangement of Fe are occupied by N in the ideal structure of ε-Fe_3N resulting in NFe_6 octahedra sharing only common vertices. The structure can be regarded as optimized in terms of avoiding close N–N contacts that correspond to NFe_6 octahedra sharing common edges and faces (Sifkovits et al. 1999).

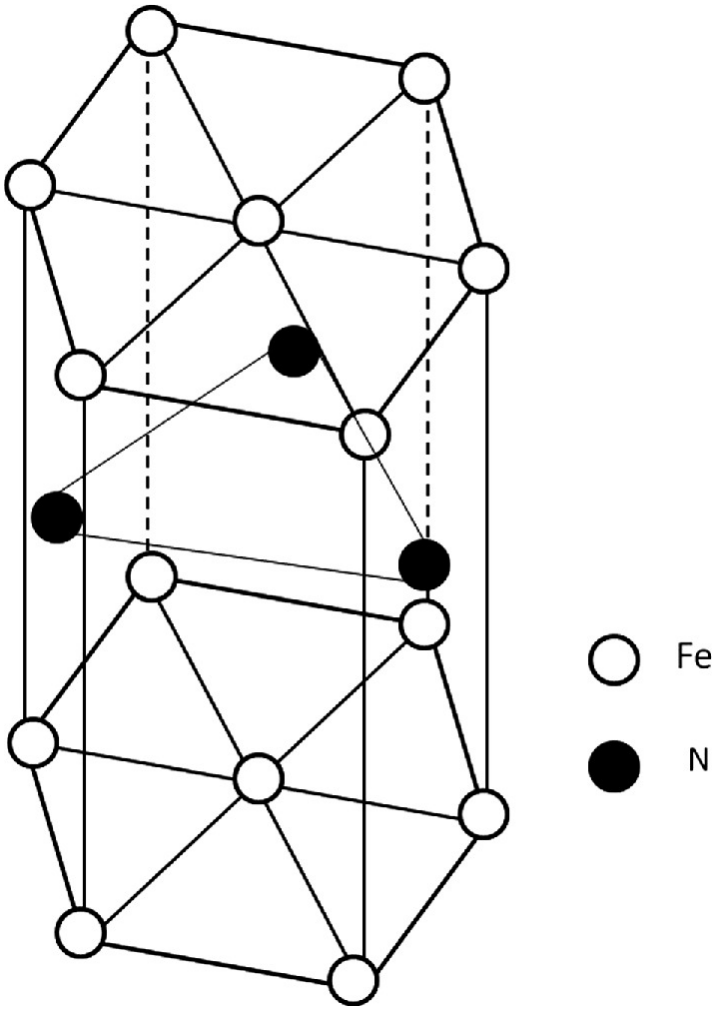

Fig. 7.7 Hexagonal structure of ε-Fe_3N indicating arrangements of Fe and N atoms in hcp lattice

Origin of Ferromagnetism in γ′-Fe_4N and ε-Fe_3N

γ′-Fe_4N is an important magnetic material with high M_r/M_s ratios and saturation magnetization. In a typical thin film system of γ′-Fe_4N, a best value of 0.52 is obtained for M_r/M_s ratios (Wang et al. 2009). A very high value of saturation magnetization, i.e. $M_s = 196$ emu/g, is reported for micron size γ′-Fe_4N particles (Yu et al. 2016). Magnetic properties of γ′-Fe_4N obtained by various groups are sensitive towards the synthesis methodology used. A detailed study on the stabilization of γ′-Fe_4N and ε-Fe_3N

nitride in nanoparticle form by a novel citrate route has been investigated by Panda et al. (Panda and Gajbhiye 1997a, 1998a).

M versus H plots of γ′-Fe_4N and ε-Fe_3N are shown in Fig. 7.8. Very high saturation magnetization of 183.5 emu/g (298 K) has been reported for γ′-Fe_4N having a particle size of 22 nm (Panda and Gajbhiye 1998a). For ε-Fe_3N nitride (particle size, 18 nm) systems, reduced magnetization of 59 emu/g is noted at room temperature. This reduction can be majorly due to the presence of superparamagnetic fractions in the materials (see Sect. 7.3). These results indicate the nanocrystalline nature of the materials with significant size and surface effects.

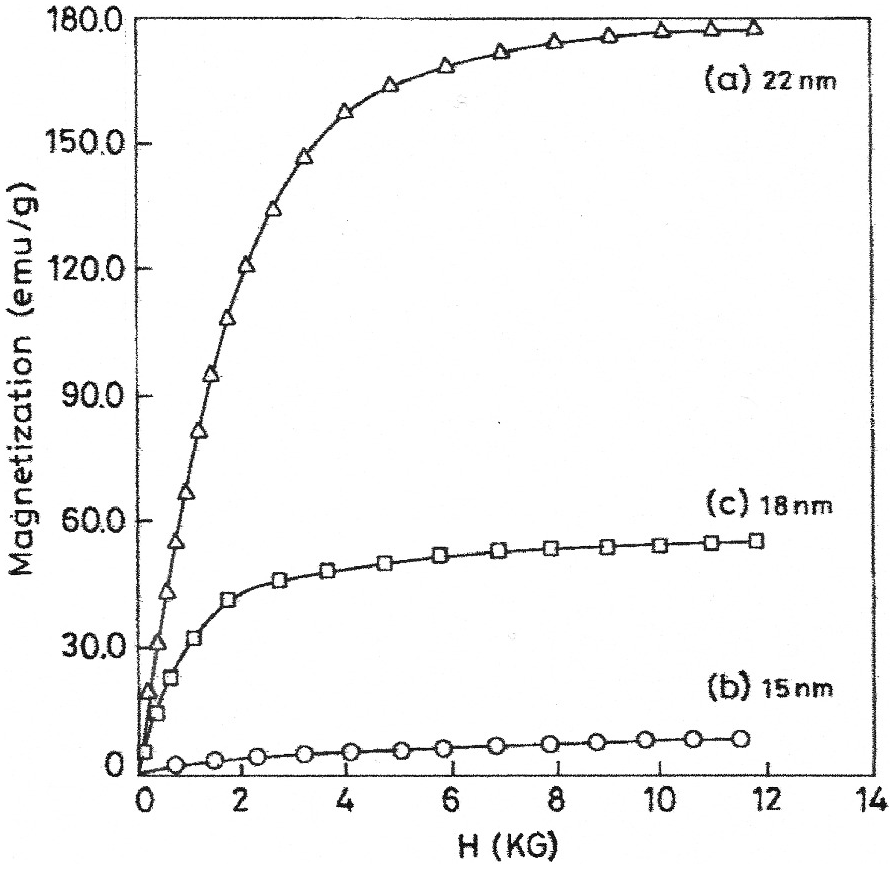

Fig. 7.8 Plot of Magnetization as a function of field for γ′-Fe_4N and ε-Fe_3N nitrides. Observed crystallite sizes for the materials are indicated against the

plot in nm unit. Reprinted with permission from Ref. (Panda and Gajbhiye 1998a).

Copyright © 1998, IEEE

The origin of magnetism in ε-Fe_3N can be explained via the spin-up and spin-down concept. Intrinsic magnetic moments possessed by Fe atoms in the lattice of ε-Fe_3N is affected by the spin pairing effect of N atoms. This is because of similarities in the density of states (DOS) of Fe-3d and N-2p levels (Panda and Gajbhiye 1997a; Matar et al. 2992). All the N atoms sites are not completely occupied in ε-Fe_3N. The occurrence of non-stoichiometry in ε-Fe_3N may also be a reason for the alteration of magnetic parameters. The variation of magnetic parameters as a function of particle sizes of stoichiometric ε-Fe_3N is shown in Fig. 7.9 (Panda and Gajbhiye 1998c). In a similar way, N atoms located at the central positions of the cubic FCC lattices of Fe atoms interact very strongly with Fe atoms located at FCC positions. Thus, intrinsic magnetic moments of Fe atoms located at FCC positions are reduced. In addition, there will be lattice expansion due to the insertion of N atoms, and giant magnetic moments are observed for Fe atoms located at corner positions (Kurian and Gajbhiye 2008).

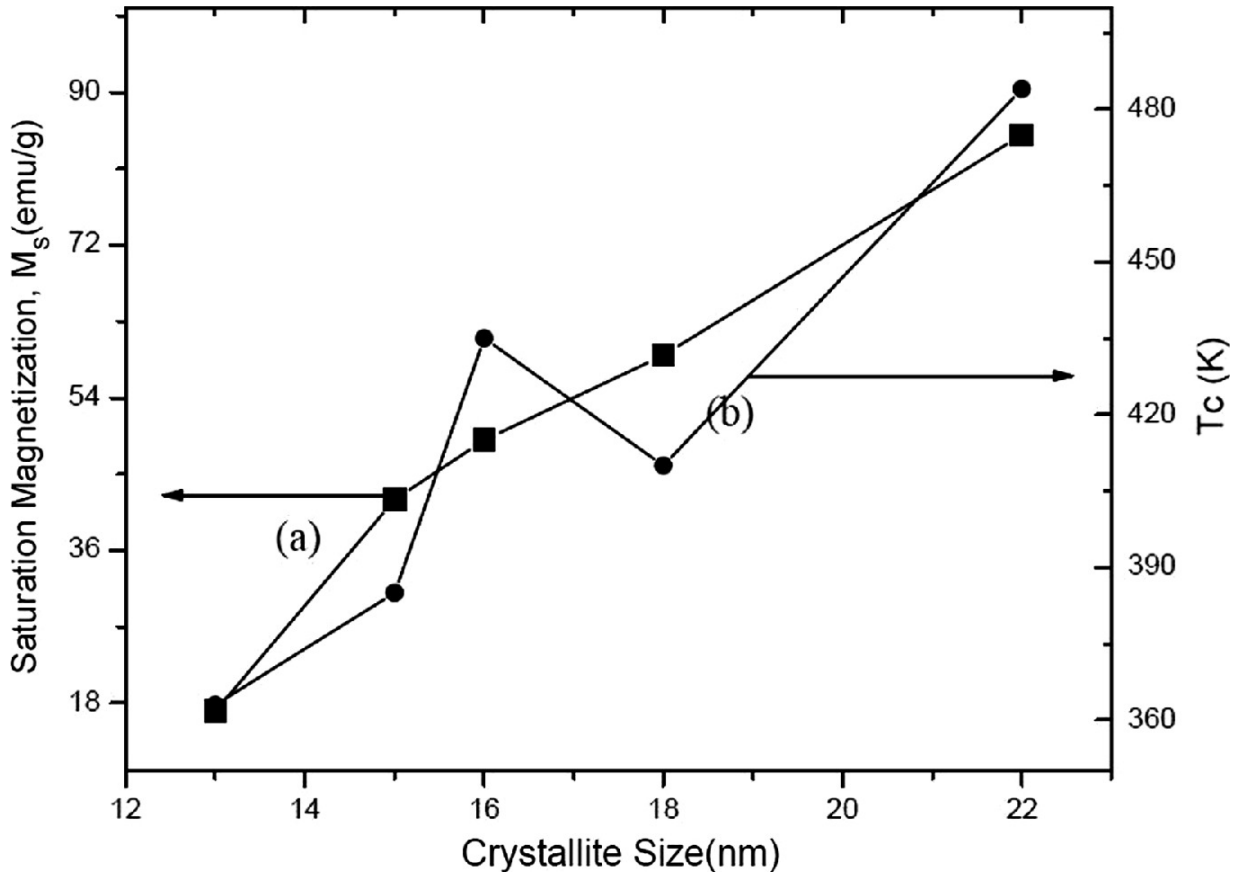

Fig. 7.9 Variation of **a** M_S and **b** T_C as a function of particle sizes for ε-Fe_3N nitrides (Panda and Gajbhiye 1998c)

7.3.1.2 Para/Antiferromagnetism in Binary Transition Metal Nitrides

Apart from ferri- or ferromagnetically ordered phases, paramagnetic/antiferromagnetic nitride materials are well known in the literature. Some examples include Cr–N, Co–N, V–N, etc. (Feng et al. 2006; Suzuki et al. 1995; Huber et al. 2016). The magnetic properties of W_2N and Mo_2N will be described in this subsection.

Magnetic Properties of B-W_2N

The room temperature field-dependent magnetization plot of β-W_2N material has been presented in Fig. 7.10. The hysteresis plot shows a gradually increasing trend of specific magnetization with the increase in applied

magnetic field and does not get saturated up to 15 kOe, also. The values of saturation magnetization and coercivity are estimated to be 0.031 emu/g and 759 Oe for β-W_2N nitride. This result indicates the origin of ferromagnetism in addition to the expected paramagnetism.

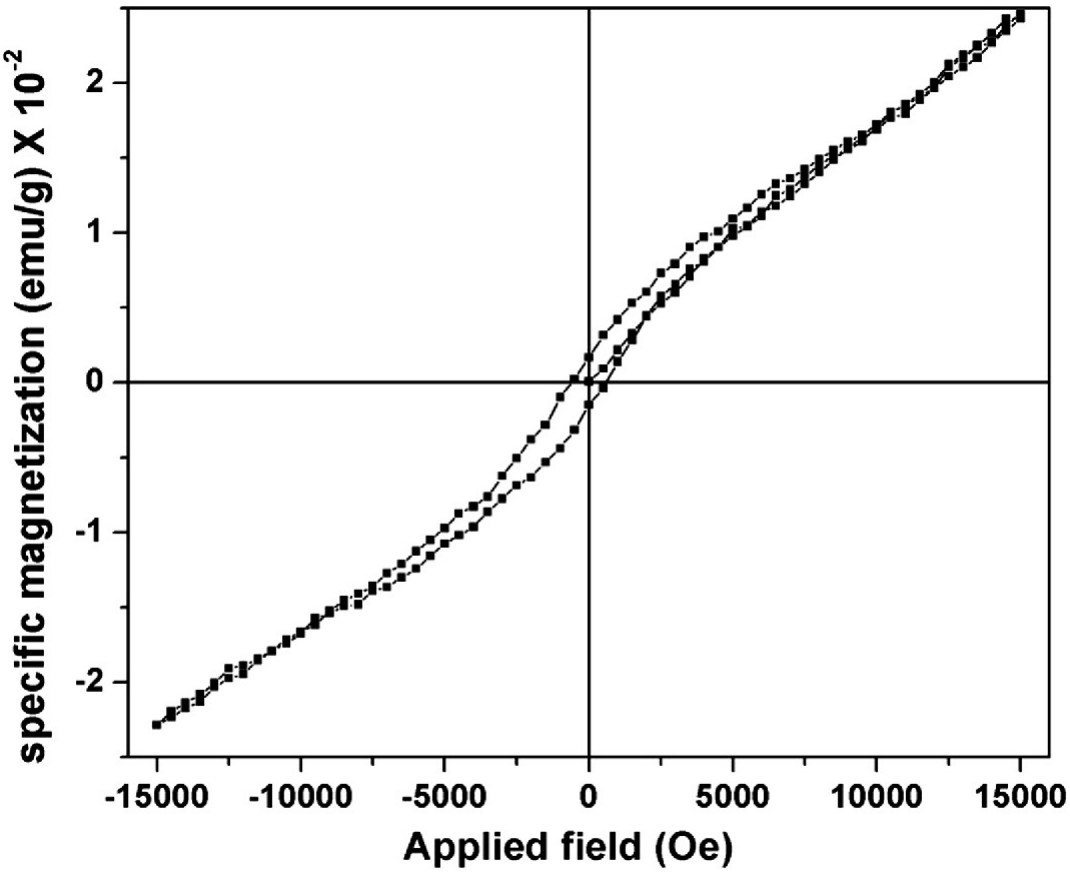

Fig. 7.10 M versus H plot of nanocrystalline β- W_2N nitride

Magnetic Properties of Γ- Mo_2N

The field-dependent magnetization (hysteresis) plot of γ-Mo_2N has been shown in Fig. 7.11. M versus H characteristic plot shows ferromagnetic behaviour with specific magnetizations in the order of 10^{-2} emu/g with a faster increase in magnetization in the lower field region ($0 < H < 2$ kOe) with finite coercivities. The specific magnetization of γ-Mo_2N at the field strength of 5 kOe is estimated to be 0.03 emu/g. The magnetic parameters

obtained for synthesized γ-Mo_2N in our study are well supported by the literature-reported results of Sidana et al. (2018).

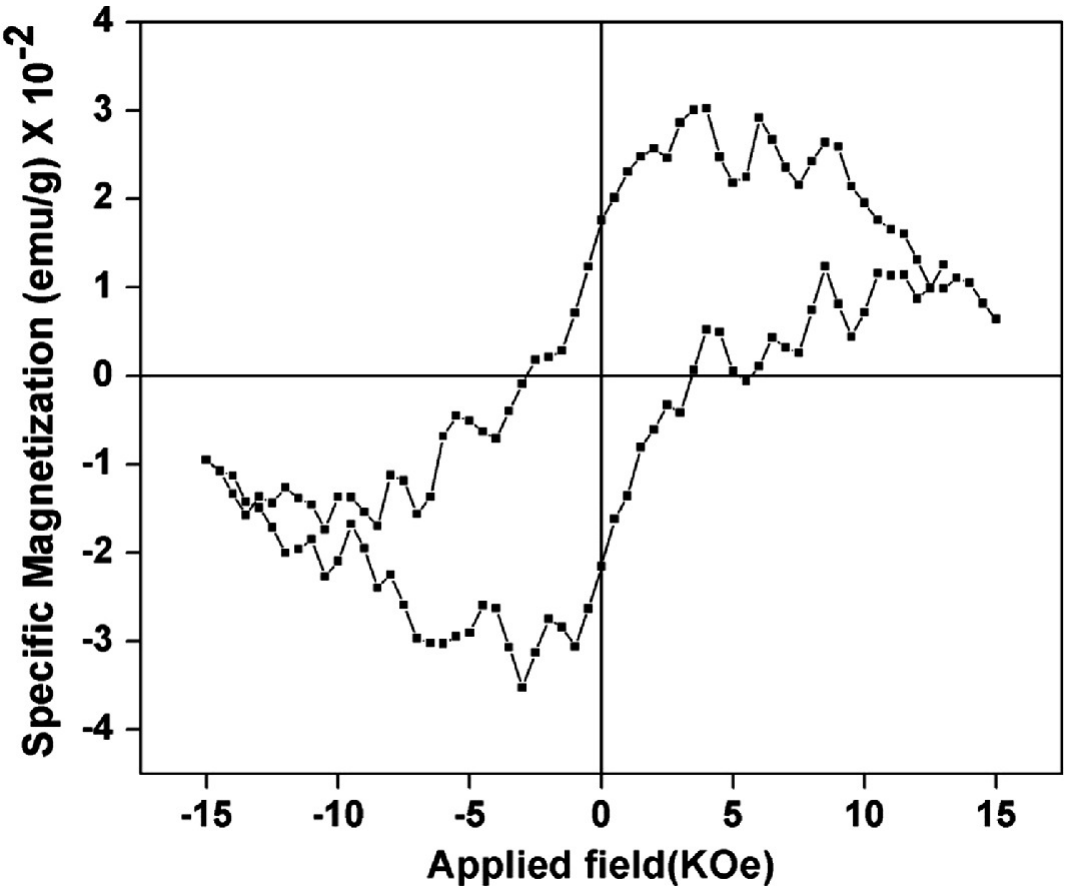

Fig. 7.11 Plot of specific magnetization versus field of γ-Mo_2N measured at 298 K. Adopted (Replotted a portion of figure) with permission from Ref. (Mishra and Panda 2017). Copyright
© 2017, Elsevier

7.3.2 Magnetic Properties of Selected Ternary Transition Metal Nitrides

The magnetic properties of ε-$Co_xFe_{3-x}N$ ($0 \leq x \leq 0.4$) and γ′-$Ni_xFe_{4-x}N$ ($0 \leq x \leq 0.8$) materials were studied and the results were analysed in order to correlate with various structural parameters. The doping of Co and Ni in these ternary nitrides is important due to their corrosion resistance properties. Furthermore, the ferromagnetic

magnetic nature of Co and Ni does not reduce the magnetization of the ternary materials drastically.

7.3.2.1 Magnetic Properties of ε-$Co_xFe_{3-x}N$ ($0 \leq x \leq 0.4$)

The field-dependent magnetization plots for ε-$Co_xFe_{3-x}N$ ($0 \leq x \leq 0.4$) have been presented in Fig. 7.12a–d. The saturation magnetization (M_s) and coercivities (H_c) of the synthesized ε-$Co_xFe_{3-x}N$ ($0 \leq x \leq 0.4$) are in the range of 8–39 emu/g and 199–219 Oe, respectively. These measured values of M_s and H_c are presented in Table 7.3.

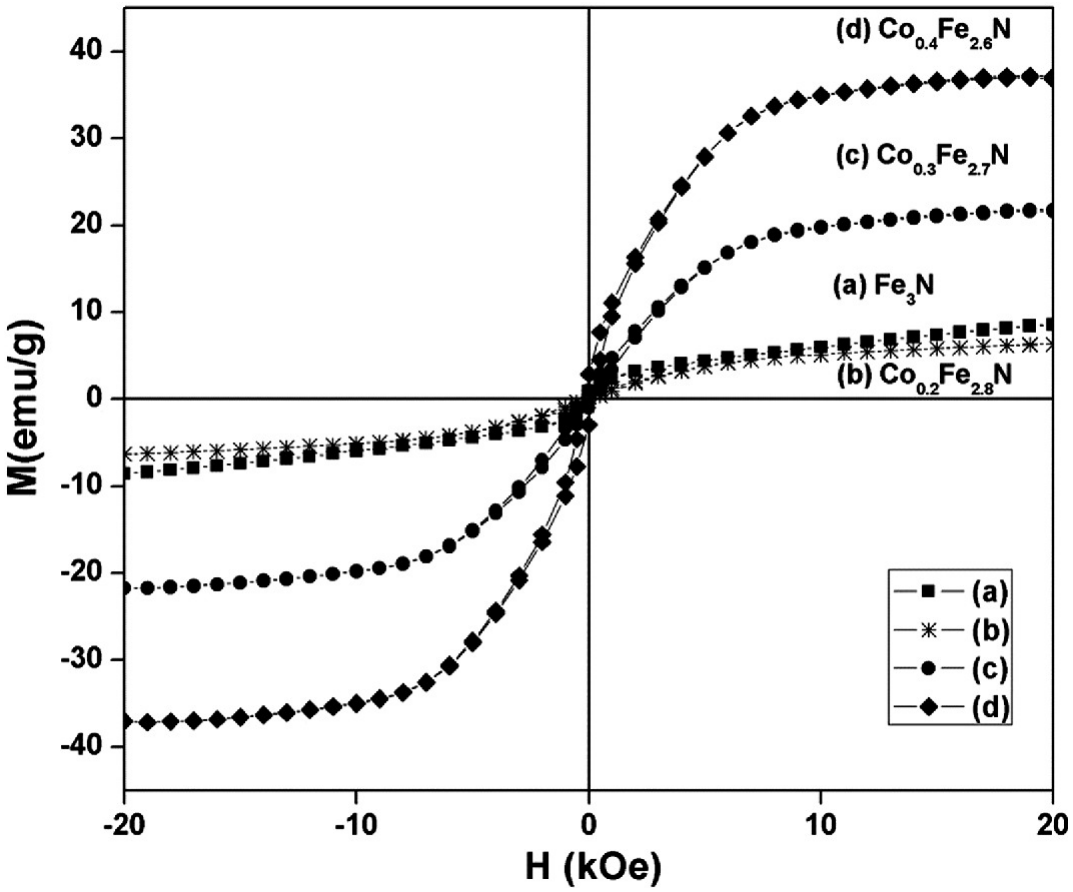

Fig. 7.12 Plot of specific magnetization versus field for **a** ε-Fe_3N and ε-$Co_xFe_{3-x}N$ ($0.2 \leq x \leq 0.4$) materials; **b** $x = 0.2$, **c** $x = 0.3$ and **d** $x = 0.4$ (Mishra and Panda 2017). Reprinted with permission from Ref. (Mishra and Panda 2017). Copyright

© 2016, Elsevier

The magnetization plots indicate that the synthesized materials are superparamagnetic in nature at room temperature. X-ray diffraction analysis shows an expansion in lattice volume of synthesized ε-Fe_3N (101 $Å^3$) compared to the stoichiometric composition of ε-$Fe_3N_{1.37}$ (96.75 $Å^3$). This finding confirms that the nitrogen content in our product ε-Fe_3N is excess. This excessive nitrogen content in the product leads to a decrease in magnetization value, 11 emu/g as compared to the theoretical reported value of magnetization of 123 emu/g for bulk ε-Fe_3N (Robbins and White 1964). For Co content, $x = 0.2$ at wt%, the value of saturation magnetization (M_s) is slightly less than that of pure ε-Fe_3N, i.e. 8 emu/g. However, with an increase in Co substitution amount, enhancement of magnetization was observed up to 39 emu/g for $x = 0.4$ in ε-$Co_xFe_{3-x}N$ ($0 \leq x \leq 0.4$) system, which is evident from Table 7.4. This observation is quite consistent with the results obtained by Gajbhiye et al. (Gajbhiye et al. 2004a, b). This result can be explained on the basis of structural alteration in the lattice due to Co atoms leading to high moment Fe atoms. The coercivity of the materials in ε-Fe_3N and ε-$Co_xFe_{3-x}N$ ($0.2 \leq x \leq 0.4$) almost remains constant with a gradual increase in the values of Co at %.

Table 7.4 Material, Co at.wt%, Saturation magnetization (M_S) and Coercivity (H_C) of ε-$Co_xFe_{3-x}N$ nitrides

Material	Co at.wt%	Saturation magnetization (emu/g)	Coercivity (Oe)
ε-$Co_xFe_{3-x}N$	0	11	219
	0.2	8	204
	0.3	24	206
	0.4	39	199

7.3.2.2 Magnetic Properties of γ′-$Ni_xFe_{4-x}N$ ($0 \leq x \leq 0.8$) Materials

The room temperature magnetic hysteresis plots for γ′-$Ni_xFe_{4-x}N$ ($0.2 \leq x \leq 0.8$) materials are presented in Fig. 7.13. The values of saturation magnetization for γ′-$Ni_xFe_{4-x}N$ ($0.2 \leq x \leq 0.8$) materials are found to be in the range of 144–181 emu/g. The coercivities of the materials are estimated to be in the range of 76–106 Oe. The values of M_s and H_c of the corresponding material phases have been presented in Table 7.5.

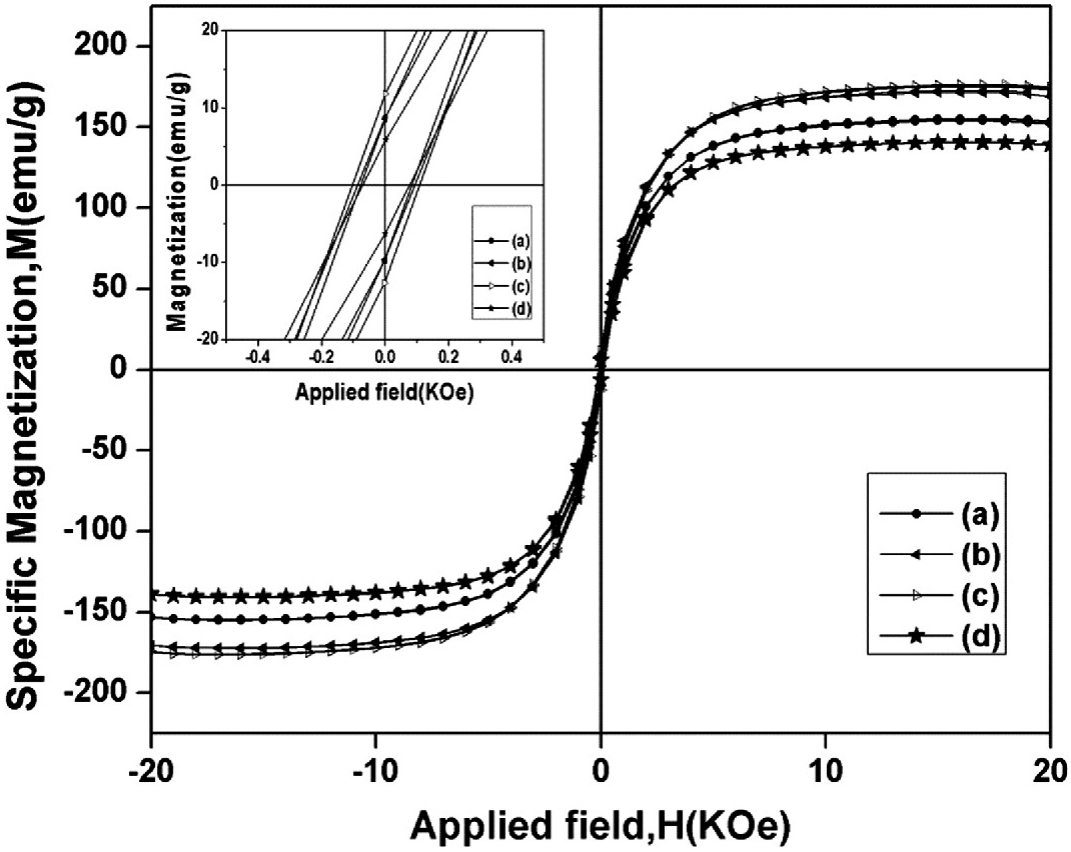

Fig. 7.13 Plot of specific magnetization as a function of field for γ′-$Ni_xFe_{4-x}N$ ($0 \leq X \leq 0.8$) materials for **a** $x = 0.2$, **b** $x = 0.4$, **c** $x = 0.6$, **d** $x = 0.8$ materials. Inset shows zoom in plots near 0 KOe. Reprinted with permission from Ref. (Mishra et al. 2016). Copyright
© 2016, Springer

Table 7.5 Materials, Ni at.wt%, saturation magnetization (M_S) and coercivity (H_C) of γ′-$Ni_xFe_{4-x}N$ nitrides

Material phase	Ni at.wt% (x)	Saturation magnetization (M_S) (emu/g)	Coercivities (H_C) (Oe)
γ′-$Ni_xFe_{4-x}N$	0.2	158	95
	0.4	176	82
	0.6	181	109
	0.8	144	76

With progressive Ni substitution in the γ′-Fe_4N lattice, the value of saturation magnetization was found to increase from 158 emu/g for $x = 0.2$ to 181 emu/g for $x = 0.6$. The value of M_s decreased thereafter to 144 emu/g for $x = 0.8$. However, there is no significant alteration in the values of coercivities with the change in wt % of Ni(x). The M_s values for γ′-$Ni_xFe_{4-x}N$ ($0.2 \leq x \leq 0.8$) are larger but quite smaller than the reported M_s value of bulk γ′-Fe_4N, i.e. 208 emu/g at 0 K (Panda and Gajbhiye 1998a; Li et al. 1995). These observations can be correlated to the nano size and surface effect along with Ni substitution.

There are several factors responsible for this kind of unusual trend in saturation magnetization with progressive Ni substitution. It has been well known that the addition of Ni in γ′-Fe_4N structure, induces magnetic dilution as the magnetic moment of Ni (55 emu/g) is considerably less than that of α-Fe (222 emu/g) (Theerthagiri et al. 2013; Hwang et al. 1997). The second effect may be correlated to a change in lattice volume leading to an alteration of exchange interactions in the lattice, thereby marginal change in overall magnetization. The combined effect of both the factors explained above leads to an overall decrease in magnetic moments with a progressive increase in Ni wt % and has been reported by several investigators with different synthesis and processing of the materials (Panda 1999; Wang et al. 2010). In addition, with the

progressive addition of Ni, the generation of high-moment Fe atoms in the corner position of the FCC lattice has been reported (Li et al. 1995). The magnitude of this enhanced magnetic moment may be dependent on particle size and lattice strain (Li et al. 1995).

7.3.2.3 Para/Antiferromagnetism in Some W and Mo-Based Ternary Transition Metal Nitrides

Ternary nitrides where one of the metal is transition metal and other being alkali/alkaline earth metal, are well known. However, Studies on magnetic properties of ternary transition metal nitrides are rare. In this subsection, we will describe magnetic properties of γ-$Co_{0.25}$ $Mo_{1.75}$ N, $CoWN_2$ and $FeMoN_2$ in detail.

The M versus H plot of field-dependent magnetization of γ-$Co_{0.25}$ $Mo_{1.75}$ N has been shown in Fig. 7.14. The hysteresis plot shows ferromagnetic behaviour with a higher value of M_s, i.e. 0.268 emu/g, and a finite value of coercivity of 296 Oe (Mishra and Panda 2017; Panda and Gajbhiye 1997b). The origin of weak ferromagnetism in the crystal lattice may be due to the presence of intrinsic magnetic moments which are susceptible to long-range ordering in the crystal structure. The coercivity for γ-$Co_{0.25}Mo_{1.75}N$ material is in the soft ferromagnetic range.

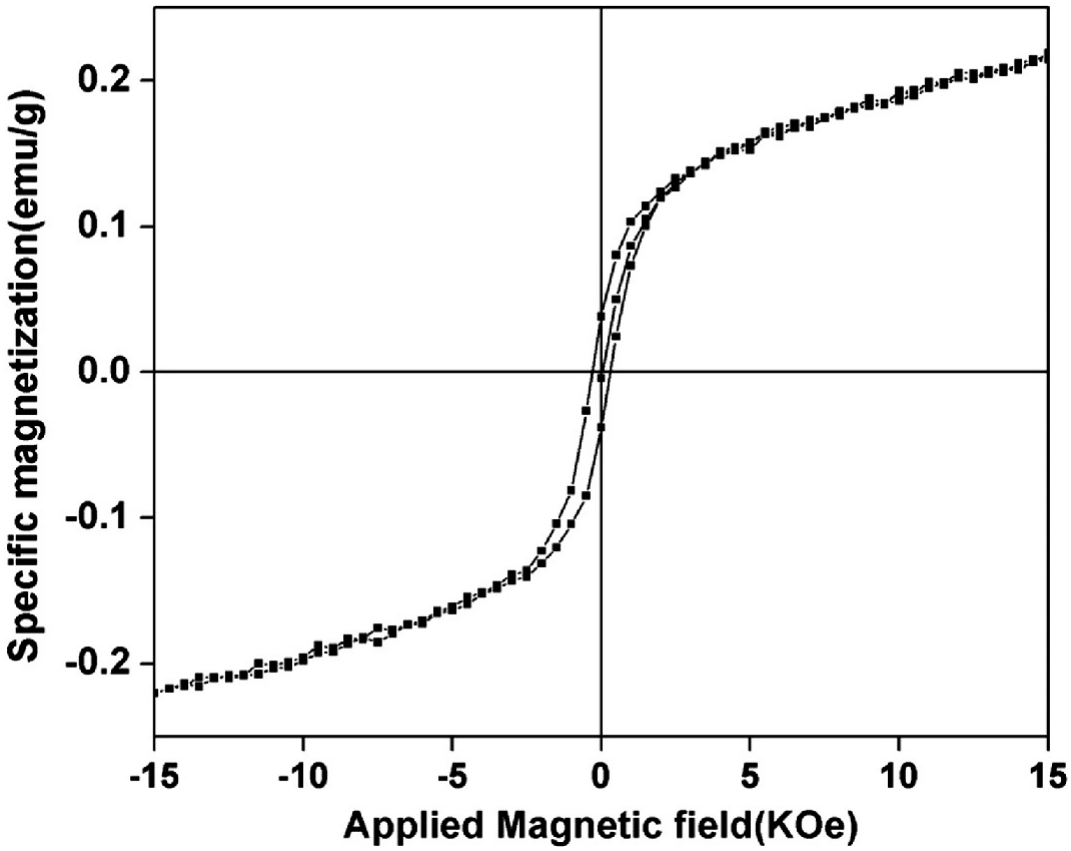

Fig. 7.14 Plot of specific magnetization vs. applied field of γ-$Co_{0.25}Mo_{1.75}N$ materials synthesized at 700 °C. Adopted (Replotted a portion of figure) with permission from Ref. (Mishra and Panda 2017). Copyright © 2017, Elsevier

The room temperature field-dependent magnetization plot of $CoWN_2$ nitride materials synthesized at 750 °C has been presented in Fig. 7.15. The values of M_s and H_c are estimated to be 1.71 emu/g and 375Oe, respectively. The hysteresis plot shows ferromagnetic behaviour. Insertion of Co atoms having intrinsic magnetic moments might be a reason for enhanced values of saturation magnetization, i.e. $M_s = 1.71$ emu/g, in $CoWN_2$ nitride. However, ferromagnetic couplings are considered to be weak which may be understood as lack of effective distance required for coupling of Co^{2+} ions in the lattice structure. Observation of finite coercivity, i.e. 375 Oe, in the magnetic

study for $CoWN_2$ confirms our interpretation (Mazumder and Hector 2009).

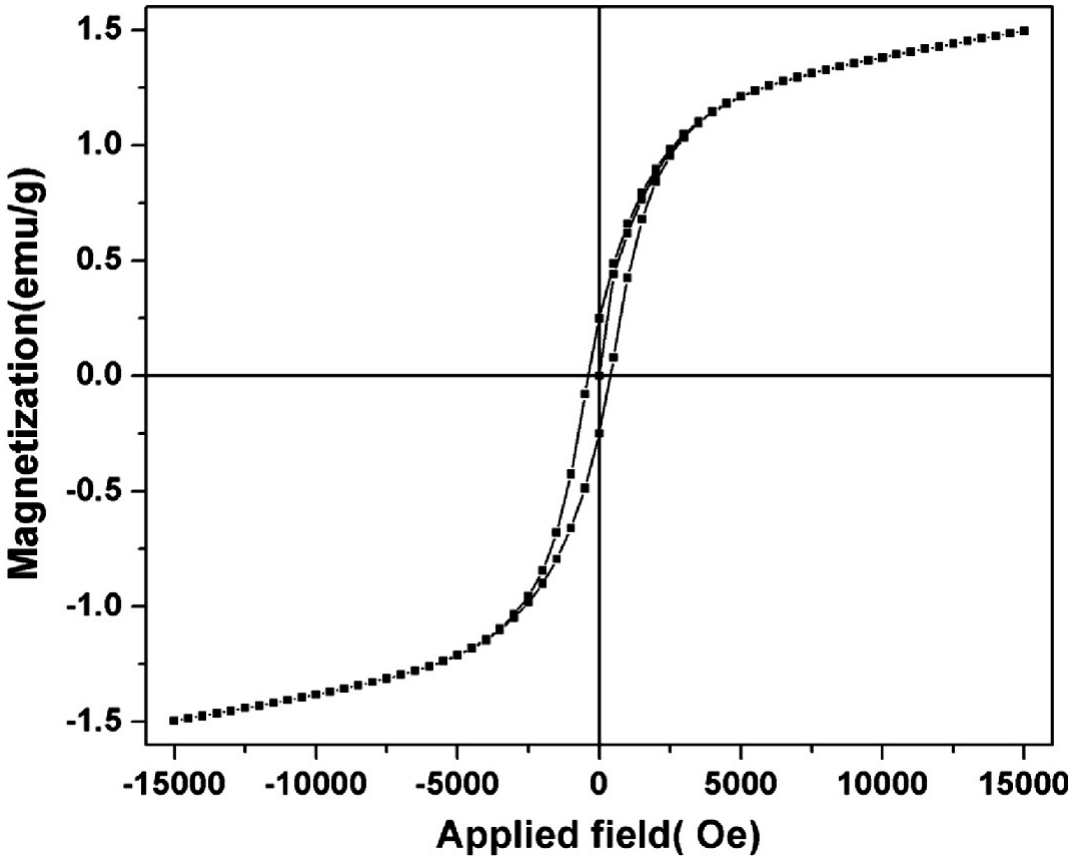

Fig. 7.15 Field-dependent magnetization plot of $CoWN_2$ measured at room temperature

M versus H characteristics of $FeMoN_2$ nitride are shown in Fig. 7.16. The field-dependent characteristics show the presence of the small amount of ferromagnetic contamination (Fe–N type) in the materials. (Inset) Fig. 7.16 shows the susceptibility versus H^{-1} plot and the true susceptibility (230×10^{-6} emu/g) is calculated from the intercept at $H^{-1} = 0$ (Panda and Gajbhiye 1998b). This kind of magnetism has its origin from Pauli paramagnetism.

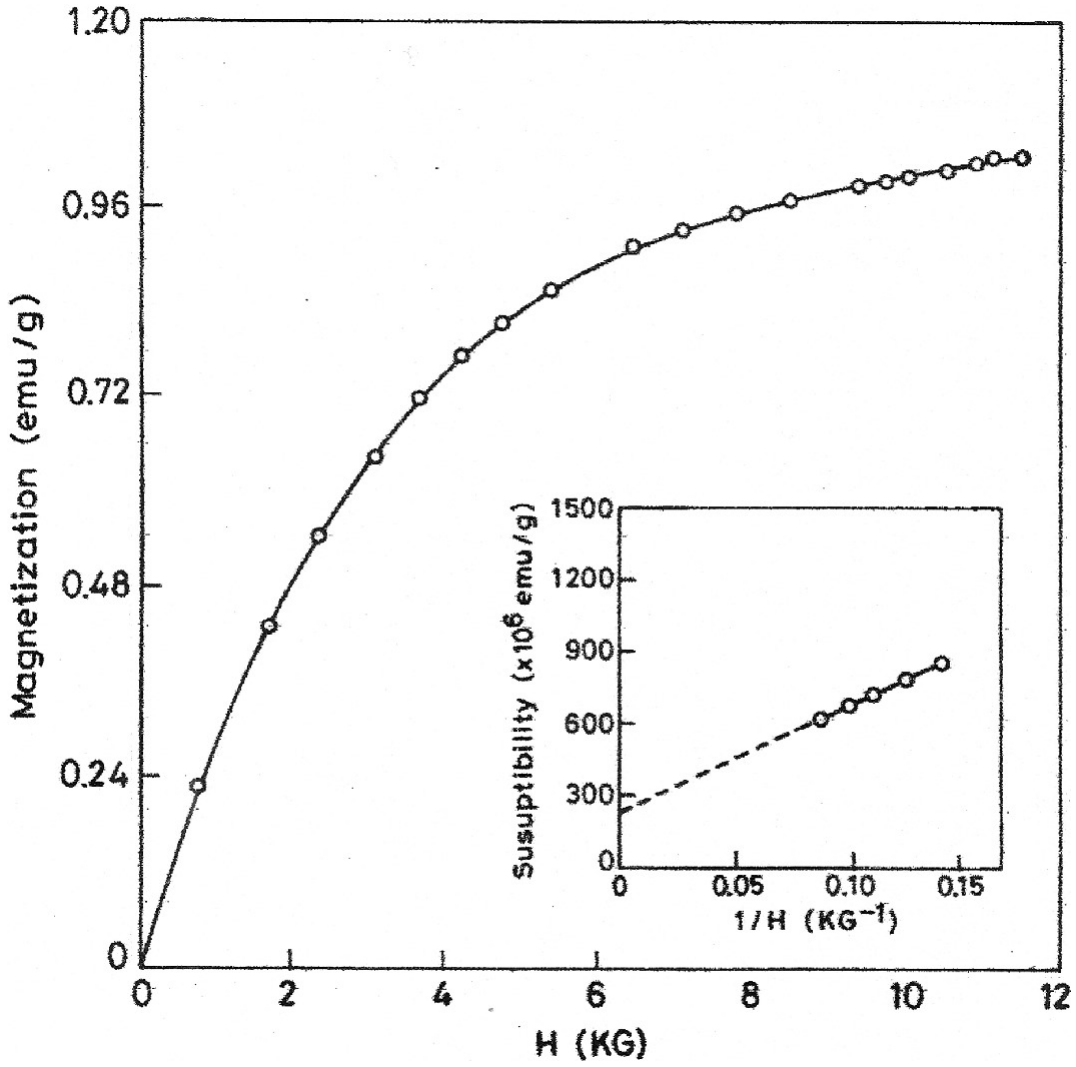

Fig. 7.16 Plot of M versus H and (inset) susceptibility as a function of inverse H of $FeMoN_2$ nitride. Reprinted with permission from Ref. (Panda and Gajbhiye 1998b). Copyright
© 1998, Elsevier

7.3.3 A Comparison of Magnetic Parameters of Various Nitride Materials

Magnetic parameters obtained for various magnetic nitrides used in this study have been summarized in Table 7.6. As it can be seen from Table 7.6, both ferromagnetic and paramagnetic behaviours are seen for various binary and ternary nitride systems. Saturation magnetization as high as 183.5 emu/g is obtained for γ′-Fe_4N, whereas an

extremely low value of 0.03 emu/g is noted for β-W_2N. Similarly, moderate to high coercivities are obtained for various nitrides. It should be noted that the magnetic parameters of the nanostructured nitride materials can be tailored by inserting nonmagnetic elements and varying nitrogen contents in the lattice structure.

Table 7.6 Materials, magnetic behaviours, saturation magnetizations and Coercivities of the various materials presented in the current chapter

Material	Magnetic behaviour	Saturation magnetization, Ms (emu/g)	Coercivity, Hc (Oe)
ε-Fe_3N	Ferromagnetic	11	219
ε-$Co_{0.2}Fe_{2.8}N$		8	204
ε-$Co_{0.3}Fe_{2.7}N$		24	206
ε-$Co_{0.4}Fe_{2.6}N$		39	199
γ′-$Ni_{0.2}Fe_{3.8}N$	Ferromagnetic	158	95
γ′-$Ni_{0.4}Fe_{3.6}N$		176	82
γ′-$Ni_{0.6}Fe_{3.4}N$		181	109
γ′-$Ni_{0.8}Fe_{3.2}N$		144	76
γ- Mo_2N (urea route)	Paramagnetic	–	880
γ- Mo_2N (ammonia route)		–	2838
γ-$Co_{0.25}Mo_{1.75}$			296
$CoWN_2$		1.71	375
β-W_2N		0.031	759

7.4 Selected Potential Applications of Metal Nitride Ceramics

Potential applications of binary and ternary nitrides are mainly based on their properties. In some cases, binary nitrides prove better for applications compared to the ternary ones or vice versa. In some cases, binary nitrides (for instance, silicon nitride) are extremely important for device applications. On the other hand, RE-Fe–N (RE represents rare-earth) ternary nitrides are very important for hard permanent applications. Mo–N and W–N nitrides are good catalysts and have electrochemical applications.

In recent years, different phases of ferromagnetic iron nitride compounds have attracted great attention over pure iron by virtue of their excellent magnetic properties that include high saturation magnetization, low coercivity over pure iron and good corrosion and wear resistance (Fratczak et al. 2014; Matar et al. 1990). Iron nitride has received much attention as a promising material for high-density magnetic recording, hard and wear-resistant material. The metastable and unstable group VII and VIII nitrides, mainly those of iron, are of extreme importance in steel hardening. Acicular γ'-Fe_4N particles are regarded as potential candidates for magnetic recording applications (Panda and Gajbhiye 1998a). Iron nitride can also be used as a magnetic fluid active damper, spintronic device and magnetic sensor (Kamiyama et al. 2002; Loloee 2012). γ'-Fe_4N has an antiperovskite crystal structure, where the iron atoms occupy the two non-equivalent sites, namely, the corner (c) sites and face-centred (f) sites, while the nitrogen atoms sit at the body-centred (b) positions (Ma et al. 2009). The main role of nitrogen is to enhance the iron moment and to raise the curie temperature (Coey and Smith 1999). In order to improve the corrosion resistance and magnetic properties of γ'-Fe_4N, various elements, e.g. Mn, Ni, Ir, Rh, etc. are used as a substitution for Fe (Chen 2006; Appen and Dronskowski 2005). It is observed that Mn is a valuable substitution for Fe in γ'-Fe_4N because of

its control over particle size during the processing (Panda 1999). The interest of Ni lies primarily in its improved corrosion resistance over pure γ′-Fe_4N. Also, the substitution of Ni for Fe does not change the saturation magnetization significantly compared to the other substituents such as Mn, Sn, Ru, Os, Nd, etc. and exhibits better magnetic and electrical properties over pure iron (Siberchicot et al. 1990).

The catalytic activity of binary and ternary metal nitrides is very promising. The nitrides include those of molybdenum, vanadium, uranium, rhenium and cerium nitrides. These interstitial nitrides are often found to exhibit group VIII noble metal-like properties. Early transition metal nitrides are a possible alternative for Pt-group metal catalysts. Like the Pt-group metals, nitride-based catalysts are capable of catalyzing isomerization, dehydrogenation, hydrogenation, water gas shift, and amination reactions with competitive rates. There are reports on selective catalytic activities of molybdenum nitride in various reactions such as hydrogenation of aromatic nitro-compounds and dehydrogenation of aromatic alcohols (Cárdenas-Lizana et al. 2011; Li et al. 2014). Cobalt molybdenum nitride has been used as a highly active and stable electrocatalyst for hydrogen evolution reaction (Cao et al. 2013). The tungsten nitride-supported Pt catalysts exhibit significantly improved performance towards methanol electrooxidation in acidic aqueous solutions in comparison with other catalysts (Yin et al. 2013). The nitrides VN, Mo_2N and W_2N have been successfully used as catalysts for NO reduction with hydrogen (Shi et al. 2004).

7.5 Conclusions and Future Scopes

7.5.1 Conclusions

Transition metal nitrides are an important class of materials because of their unique physical and chemical properties. However, there is intrinsic difficulty in the synthesis of the nitride products in nano form due to the making and breaking of strong bonds associated with N≡N. Further, many nitrides are moisture and air-sensitive. Therefore, those are synthesized in bulk form in micron size or as protected/coated thin films. Based on the above-mentioned facts, the development of alternative, cost-effective, novel chemical synthetic routes, useful in fine-tuning the important properties of nanocrystalline transition metal nitrides, merits further investigation. The present study involves the development of novel synthetic routes for various transition metal nitrides, binary, substituted binary, and ternary nitrides such as ε-$Co_xFe_{3-x}N$, γ′-$Ni_xFe_{4-x}N$, γ-Mo_2N, γ-$Co_xMo_{2-x}N$, β-W_2N, $FeMoN_2$, $CoWN_2$ and investigations on their magnetic properties study.

This chapter contains a general introduction to transition metal nitrides, their classification, structure and types of bonding. The origin of magnetism in Fe, Co, Ni and their corresponding binary and ternary nitrides have been presented. For the proper understanding of the magnetic behaviour of particles in bulk and nano form, a discussion on various forms of magnetism has been presented. The effects of fine particle magnetism such as size and surface effects on various magnetic properties (M_s, H_c, K and T_c) have been specifically emphasized. Magnetic phenomena like superparamagnetism and spin canting at the nanoscale have been described in this chapter. An overview of available synthetic methods for transition metal nitrides is presented. The observed magnetic parameters are correlated to structural parameters.

Citric acid-assisted sol–gel method for the synthesis of a precursor followed by nitridation using ammonia gas has

been adopted for the synthesis of ε-$Co_xFe_{3-x}N$ ($0 \leq x \leq 0.4$) and γ′-$Ni_xFe_{4-x}N$ ($0 \leq x \leq 0.8$) nitride materials. Also, magnetic properties are investigated in detail and correlated to structural parameters. Magnetic studies reveal the superparamagnetic nature of the synthesized products having coercivity in the range of 76–109 Oe. A maximum value of M_s, i.e. 181 emu/g, was achieved for Ni content, $x = 0.6$, in γ′-$Ni_xFe_{4-x}N$ ($0.2 \leq x \leq 0.8$) materials system. The unusual increasing trend in M_s for γ′-$Ni_xFe_{4-x}N$ materials has been explained on the basis of size and surface effects in addition to lattice strain effects. The existence of finite values of coercivities indicates either deformed structures or the presence of bigger crystallites well beyond the superparamagnetic size limit. In this study, the achievement of high saturation magnetization with low coercivity and reduced particle size is particularly useful for soft magnetic applications.

Synthesis of Mo and Co-Mo-based precursors through various synthetic routes and their transformation into nitrides using different nitrogen sources have been presented. This study involves the use of hydrazine ($NH_2NH_2{\cdot}H_2O$) and potassium borohydride (KBH_4) as reducing agents and ethylenediamine ($NH_2CH_2CH_2NH_2$) as an organic source for the synthesis of different precursors. Ammonia gas and solid urea have been used for the nitridation experiment as nitrogen sources. The effect of various precursor routes and nitridation sources on the magnetic properties of nitrides has been studied in detail. Room temperature VSM study indicates weak ferromagnetic behaviour of γ-Mo_2N and γ-$Co_{0.25}Mo_{1.75}N$ (ammonia route) and γ-Mo_2N (urea route) materials having coercivity values of 2838 Oe, 880 Oe and 296 Oe, respectively.

Binary β-W_2N and ternary $CoWN_2$ materials are synthesized using a citric acid-assisted sol–gel route for the precursors. Solid urea and NH_3(g) gas are used as vectors for the nitridation of the precursors, separately. The values of the saturation magnetization, M_s and coercivity, H_c, are estimated to be 0.031 emu/g and 759 Oe, respectively for crystalline β-W_2N synthesized at 750 °C. The values of M_s and H_c of $CoWN_2$ synthesized at 750 °C are estimated to be 1.71 emu/g and 375Oe, respectively.

In summary, the present chapter describes various novel chemical synthesis routes for the preparation of nanocrystalline transition metal nitrides. The structural, microstructural, surface and magnetic properties of the synthesized nitride products have been investigated in detail. Substitution of transition metals into the binary nitride system has been attempted successfully and its effect on various physical properties has been studied. The use of various nitridation routes and varieties of precursors for the synthesis of nitride products has been explored in this study. Magnetic material systems such as ε-Fe_3N and γ′-Fe_4N have been synthesized and the effect of transition metal substitution into the lattice has been studied in detail. Highly magnetic Ni substituted γ′-Fe_4N material having magnetization 181 emu/g has been achieved.

7.5.2 Future Prospects

Transition metal nitrides have received increasing attention as an important class of functional materials. These materials are mainly important having unique physical and chemical properties, which can be useful for varied applications: as high-temperature ceramics, magnetic materials, superconductors, optoelectronic devices or catalysts and so on. Despite the very interesting and unique properties of transition metal nitrides, there are several

issues that still need to be investigated. The development of novel synthetic methods for the binary and ternary nitrides has become significant as the properties of the nitrides are dependent on the synthetic route employed and the nature of the precursor. For example, for catalytic applications, the nitride powders with high specific surface area need to be synthesized at moderate temperature conditions. However, a facile route to metal nitrides on a large scale is still a challenge and should be developed in order to meet the increasing demands of nitrides from a variety of fields of potential application. Ternary nitrides have not been studied much in the literature because of their challenges in synthesis, which involve low decomposition temperatures. Therefore, research on nitrides has become more intensive focusing mainly on new ternary and higher order transition metal nitrides. In future, research on innovative low-temperature synthetic routes, solid-state reactivity of phase formation and kinetics may provide more information into nitride chemistry. The optimization of reaction parameters for different sizes and shapes of the material is of significance in fine-tuning various structure-dependent properties of nitride materials in nanoscale. Research on structure-dependent properties of nanocrystalline nitrides is an interesting future scope. The production of hybrid or composite nitrides is considered the next important step in the field of these nanomaterials systems. Further, more detailed structural characterization using advanced characterization techniques is crucial for understanding the relationship among structural, electronic and catalytic properties of the nitride materials.

Although many nitrides in the iron nitride family are well studied, some of the metastable pure phases are still not produced in bulk form due to fundamental difficulties. The large magnetization or the giant magnetic moment of α′′-$Fe_{16}N_2$ is incompatible with band theory. Because of the

controversy upon the widely different observations of magnetic properties in terms of thin films and bulk form, it seems desirable to measure the magnetic properties of pure bulk α′′-$Fe_{16}N_2$. Doping of other elements like Ga, Cr, Mn, Ni and Cu in the ferromagnetic Fe–N lattice breaks the long-range ordering and introduces localized nonmagnetic or antiferromagnetic interactions. These mixed magnetic phases give rise to short-range ordering like spin glass with alteration in magnetic and exchange anisotropy. Extensive research on the magnetic property of binary and substituted binary nitrides may lead to the development of candidates for high-density magnetic recording, biomedical and catalytic applications.

Acknowledgements

The authors acknowledge the financial support in part from Birla Institute of Technology, Pilani, Goa campus, India. We acknowledge Department of Science and Technology, India, and CSIR, India, for financial support during the execution of this work. Also, the authors acknowledge the valuable support including suggestions during these investigations from Dr. R. S. Ningthoujam, BARC, Dr. Manivel Raja, DMRL Hyderabad, Prof. N. S. Gajbhiye, IIT Kanpur, Prof. G. Balaji, BITS Hyderabad and Prof. Sayan Bhattacharya, IISER Kolkata, India. Technical assistance in the laboratory received from Dr. Shankar B. Dalavi is also acknowledged. We acknowledge sophisticated instrumental facilities located at IIT Kanpur, BITS Pilani, Karunya University, Anna University, IIT Madras and IIT Mumbai, India, for data procurement. The current paper is also based on some findings in the PhD thesis work of one of the authors (Dr. Pragnya Paramita Mishra) which is available in the Sodhganga repository.

Author Contributions

“The manuscript was written through the contributions of all authors. All authors have given approval to the final version of the manuscript.”

References

Appen, J.V., Dronskowski, R.: Angew. Chem. Int. Ed. **44**, 1205–1210 (2005)

Balogun, M.S., Qiu, W., Wang, W., Fang, P., Lu, X., Tong, Y.: J. Mater. Chem. A **3**, 1364–1387 (2015)

Bem, D.S., Gibson, C.P., Loye, H.Z.: Chem. Mater. **5**, 397–399 (1993)

Bhattacharyya, S.: J. Phys. Chem. C **119**, 1601−1622 (2015)

Caicedo, J.C., Zambrano, G., Aperador, W., Escober-Alarcon, L., Camps, E.: Appl. Surf. Sci. **258**, 312–320 (2011)

Cao, B., Veith, G.M., Neuefeind, J.C., Adzic, R.R., Khalifah, P.G.: J. Am. Chem. Soc. **135**, 19186–19192 (2013)
[PubMed]

Cárdenas-Lizana, F., Lamey, D., Gómez-Quero, S., Perret, N.: Catal. Today **173**, 53–61 (2011)

Ce, Y., Yang-Long, H., Song, G.: Chin. Phys. B **23**, 057505-(1–8) (2014)

Chen, L.: J. Magn. Magn. Mater. **303**, 266–269 (2006)

Chen, J.S., Yu, C., Lu, H.: J. Alloys Compd. **625**, 224–230 (2015)

Chen, Q., Lib, X., Xiec, R., Xub, L., Lie, L.: Ceram. Int. **46**, 2580–2584 (2020)

Choi, J., Gilan, E.G.: Inorg. Chem. **48**, 4470–4477 (2009)
[PubMed]

Coey, J.M.D., Smith, P.A.I.: J. Magn. Magn. Mater. **200**, 405–424 (1999)

Feng, W.J., Li, D., Li, W.F., Ma, S., Li, Y.B., Xiong, D.K., Zhang, W.S., Zhang, Z.D.: J. Alloys Compd. **425**, 4–9 (2006)

Flores-Livas, J.A., Sarmiento-Perez, R., Botti, S., Goedecker, S., Marques, M.A.L.: J. Phys. Mater. **2**, 025003 (2019)

Fratczak, E.Z., Prieto, J.E., Moneta, M.E.: J. Alloys Compd. **586**, 375–379 (2014)

Gajbhiye, N.S., Panda, R.N., Ningthoujam, R.S., Bhattacharyya, S.: Phys. Status Solidi (c) **1**, 3252–3259 (2004a)

Gajbhiye, N.S., Ningthoujam, R.S., Weissmüller, J.: Hyperfine Interact. **156**(157), 51–56 (2004b)

Gall, D., Petrov, I., Greene, J.E.: J. Appl. Phys. **89**, 401–409 (2001)

Giordano, C., Erpen, C., Yao, W., Antonietti, M.: Nano Lett. **8**, 4659–4663 (2008)
[PubMed]

Huber, S., Jankovsky, O., Sedmidubsky, D., Lux, J., Klimova, K., Hejtmanek, J., Sofer, Z.: Ceram. Int. **42**, 18779–18784 (2016)

Hwang, J.H., Dravid, V.P., Teng, M.H., Host, J.J., Elliott, B.R., Johnson, D.L., Mason, T.O.: J. Mater. Res. **12**, 1076–1082 (1997)

Jack, K.H.: Acta Cryst. **5**, 404–411 (1952)

Kamiyama, S., Okamoto, K., Oyama, T.: Energy Convers. Manage. **43**, 281–287 (2002)

Kantar, E., Ertas, M.: J. Supercond. Nov. Magn. **29**, 2319–2326 (2016)

Kittel, C.: Phys. Rev. **70**, 965–971 (1946)

Kurian, S., Gajbhiye, N.S.: Hyperfine Interact. **183**, 147–153 (2008)

Lambercht, W.R.L., Miao, M.S., Lukashev, P.: J. Appl. Phys. **97**, 10D306(1)–(3) (2005)

Leineweber, A., Hickel, T., Azimi-Manavi, B.: Acta Mater. **140**, 433–442 (2017)

Li, F., Yang, J., Xue, D., Zhou, R.: Appl. Phys. Lett. **66**, 2343–2345 (1995)

Li, Z., Chen, C., Zhan, E., Ta, N., Shen, W.: Catal. Commun. **51**, 58–62 (2014)

Liu, Y., Qie, Y., Kong, F., Yang, Z., Yang, H.: Mater. Today Commun. **30**, 1–6 (2020)

Loloee, R.: J. Appl. Phys. **112**, 023902(1)–(6) (2012)

Lu, A.H., Salabas, E.L., Schuth, F.: Angew. Chem. Int. Ed. **46**, 1222–1244 (2007)

Ma, X.G., Jiang, J.J., Liang, P., Wang, J., Ma, Q., Zhang, Q.K.: J. Alloys Compd. **480**, 475–480 (2009)

Matar, S.F.: J. Alloys Compd. **345**, 72–76 (2002)

Matar, S.F., Demazeau, G., Siberchicot, B.: IEEE Trans. Magn. **26**, 60–62 (1990)

Matar, S., Siberchicot, B., Penicaud, M., Demazeau, G.: J. Phys. I France **2**, 1819–1831 (1992)

Mazumder, B., Hector, A.L.: J. Mater. Chem. **19**, 4673–4686 (2009)

Mishra, P.P., Panda, R.N.: Mater. Res. Bull. **86**, 241–247 (2017)

Mishra, P.P., Raja, M.M., Panda, R.N.: J. Supercond. Nov. Magn. **29**, 1347–1356 (2016)

Morin-Lopez, J.L., Bennemann, K.H.: Phys. Rev. B **23**, 5978–5981 (1981)

Narula, G.K., Narula, K.S., Gupta, V.K.: Materials Science. Tata McGraw-Hill Publishing Co., Ltd., New Delhi (1988)

Ningthoujam, R.S., Gajbhiye, N.S.: Prog. Mater. Sci. **70**, 50–154 (2015)

Oyama, S.T.: Catal. Today **15**, 179–200 (1992)

Oyama, S.T.: The Chemistry of Transition Metal Carbides and Nitrides. Blackie Academic & Professional, New York (1996)

Pak, J., Lin, W., Wang, K., Chinchore, A., Shi, M., Ingram, D.C., Smith, A.R.: J. Vac. Sci. Technol. A **28**, 536–540 (2010)

Panda, R.N., Gajbhiye, N.S.: J. Magn. Magn. Mater. 195, 396–405 (1999)

Panda, R.N., Gajbhiye, N.S.: J. Magn. Soc. Jpn. **22S1**, 209–211 (1998)

Panda, R.N., Gajbhiye, N.S.: J. Appl. Phys. **81**, 335–339 (1997a)

Panda, R.N., Gajbhiye, N.S.: J. Alloy. Compd. **256**, 102–107 (1997b)

Panda, R.N., Gajbhiye, N.S.: IEEE Trans. Magn. **34**, 542–548 (1998a)

Panda, R.N., Gajbhiye, N.S.: J. Cryst. Growth **191**, 92–96 (1998b)

Panda, R.N., Gajbhiye, N.S.: J. Appl. Phys. **86**, 3295–3302 (1999)

Parkin, I.P., Elwin, G.S.: J. Mater. Chem. **11**, 3120–3124 (2001)

Robbins, M., White, J.: J. Phys. Chem. Solids **25**, 717–720 (1964)

Roman, P., Luque, A., Gutierrez-Zorrilla, J.M., Garcia-Granda, S.: Polyhedron **10**, 2057–2064 (1991)

Roy, A., Serov, A., Artyushkova, K., Brosha, E.L., Atanassov, P., Ward, T.L.: J. Solid State Chem. **228**, 232–338 (2015)

Schnitzke, K., Schultz, L., Wecker, J., Katter, M.: Appl. Phys. Lett. **57**, 2853–2855 (1990)

Shi, C., Zhu, A.M., Yang, X.F., Au, C.T.: Appl. Catal. A -Gen **276**, 223–230 (2004)

Siberchicot, B., Matar, S.F., Fournes, L., Demazeau, G., Hagenmuller, P.: J. Solid State Chem. **84**, 10–15 (1990)

Sidana, H.K., Mir, R.A., Pandey, O.P.: J. Alloys Compd. **736**, 255–265 (2018)

Sifkovits, M., Smolinski, H., Hellwig, S., Weber, W.: J. Magn. Magn. Mater. **204**, 191–198 (1999)

Sun, H., Coey, J.M.D., Otani, Y., Hurley, D.P.F.: J. Phys. Condens. Matter **2**, 6465–6470 (1990)

Suzuki, K., Kaneko, T., Yoshida, H., Morita, H., Fujimori, H.J.: J. Alloys Compd. **224**, 232–236 (1995)

Tareen, A.K., Priyanga, G.S., Behara, S., Thomas, T., Yang, M.: Prog. Solid State Chem. **53**, 1–26 (2019)

Theerthagiri, J., Dalavi, S.B., Raja, M.M., Panda, R.N.: Mater. Res. Bull. **48**, 4444–4448 (2013)

Toth, L.E.: Transition Metal Carbides and Nitrides. Academic Press, New York (1971)

Villaseca, L., Moreno, B., Lorite, I., Jurado, J.R., Chinarro, E.: Ceram. Int. **41**, 4282–4288 (2015)

Volpe, L., Baudart, M.: J. Solid State Chem. **59**, 332–347 (1985)

Wang, L.L., Zheng, W.T., Gong, J., Li, H.B., Wang, X., Ma, N., Cao, P.J., Ma, X.C.: J. Alloys Compd. **467**, 1–5 (2009)

Wang, L.L., Zheng, W.T., Ana, T., Mab, N., Gong, J.: J. Alloys Compd. **495**, 265–267 (2010)

Wang, H., Wu, Z., Kong, J., Wang, Z., Zhang, M.: J. Solid State Chem. **194**, 238–244 (2012)

Wetzel, M.H., Rabending, T.T., Friak, M., Vsianska, M., Sob, M., Leineweber, A.: Materials **14**(3963), 1–27 (2021)

Wojciechowski, P., Lewandowski, M.: Cryst. Growth Des. **22**, 4618–4639 (2022) [PubMed][PubMedCentral]

Wu, C., Yin, P., Zhu, X., Yang, C.O., Xie, Y.: J. Phys. Chem. B **110**, 17806–17812 (2006)
[PubMed]

Yin, S., Yang, L., Luo, L., Huang, F., Qiang, Y.: New J. Chem. **37**, 3976–3980 (2013)

Yu, M.J., Xu, Y., Mao, Q., Li, F.Z., Wang, C.G.: J. Alloys Compd. **656**, 362–367 (2016)

Yu, L., Stampfl, C., Marshall, D., Eshrich, T., Narayanan, V., Rowell, J.M., Newman, N., Freeman, A.J.:Phys. Rev. B **65,** 245110(1)–245110(5) (2002)

Yuan, Z.M., Liu, B., Zhou, T., Goh, C.K., Ong, C.L., Cheong, C.M., Wang, L.: IEEE Trans. Magn. **45**, 5038–5043 (2009)

Zhang, H., Zhao, Z., Xu, C., Duan, A., Lin, W., Tian, H., Wachs, I.E.: Mater. Res. Bull. **41**, 2334–2340 (2006)

© The Author(s), under exclusive license to Springer Nature Singapore Pte Ltd. 2024
R. S. Ningthoujam, A. K. Tyagi (eds.), *Handbook of Materials Science, Volume 2*, Indian Institute of Metals Series
https://doi.org/10.1007/978-981-97-4646-0_8

8. Fundamental Aspects of Nanomagnetism and Its Versatile Applications

Asnit Gangwar[1, 2], P. A. Hassan[1, 3] and K. C. Barick[1, 3] ✉
(1) Chemistry Division, Bhabha Atomic Research Centre, Trombay, Mumbai, 400 085, India
(2) Dept. of Mechanical Engineering, Shri Vishnu Engineering College for Women, West Godavari, 534 202, Andhra Pradesh, India
(3) Homi Bhabha National Institute, Anushaktinagar, Mumbai, 400 094, India

✉ **K. C. Barick**
Email: kcbarick@barc.gov.in

Keywords Nanomagnets – Superparamagnetism – Nanomagnets synthesis – Nanomagnets applications

8.1 Introduction

In the last few decades, nanotechnology has achieved significant advancement in various fields, especially in medical science for cancer diagnosis and treatment (Pradhan et al. 2007; He et al. 2013; Sadighian et al. 2014; Duman et al. 2005). Nevertheless, “cancer” remained a global and significant public health concern of research scientists. The uncontrolled growth of the cancerous cells caused a high

mortality rate worldwide. It is anticipated that, by 2040, the cancer incidence and mortality will rise to 29.5 million and 16.3 million, respectively, which is a matter of grim concern for humanity. Thus, the treatment of cancer or malignant tumors is the foremost priority of the World Health Organization (WHO). The traditional approaches for the treatment of these malignant tumors include surgical treatment, radiation therapy, and chemotherapy. These treatment approaches exhibited less efficiency in targeting the tumors precisely which can cause severe collateral destruction to the normal cells of the patients. Yet another approach utilizes heat for the destruction of malignant tumor tissues to raise the temperature of the localized region from 42 to 43 °C and the term is especially given as “Hyperthermia”. The malignant tumors are found to be more sensitive to the conduction heat than that of the normal tissues due to their hypoxic nature, disorganized vasculature that overflows with blind ends, and abnormal bulges; these can be preferentially destroyed in the 42 to 46 °C temperature range. Conventionally, hyperthermia treatment was administered through electromagnetic waves, e.g. ultrasound, radiofrequency, microwaves, and infrared radiation, generated by some external devices. Hot water tubes and baths were also in tradition for hyperthermic treatment. A major drawback of these conventional modalities is heating of the tumor site via different ways to the therapeutic temperature range of approximately 42 to 43 °C without damaging the normal cells. However, increasing beyond the therapeutic temperature range can kill a larger number of tumor cells through thermal ablations and necrosis. The tumor-specific hyperthermia overcomes the above drawbacks due to its lesser side effects and localized heating. Among several strategies, MNP-mediated localized hyperthermia treatment modalities have shown the most promising domino effect during clinical and various in vivo and in vitro studies. In the present-day nanoscale era, the localized magnetic hyperthermia approach utilizes the heat

which is generated by MNPs in the presence of an AC magnetic field. Nevertheless, these MNPs are also implemented for diagnosis, bioimaging, and treatment in healthcare industries, i.e. magnetic resonance imaging, advanced targeted drug delivery as nanocarriers, immunoassays, and cell separation. In addition, these MNP_S with appropriate structural, microstructural, optical, electrical, and magnetic properties have been explored for electronics industries: (i.e. magnetic data storage, sensors, and xerography), as a magnetically separable catalyst for wastewater treatment and as an electrode for energy storage in battery/supercapacitors. Nanomagnetism in magnetic nanoparticles refers to the study and manipulation of magnetic ordering at the nanoscale (<100 nm) and making them for specific applications based on their physical properties (He et al. 2012; Gazeau et al. 2008). Thus, let's explore in this chapter the fundamental aspects of nanomagnetism and its versatile applications in detail.

8.1.1 Fundamental Aspects of Nanomagnetism

At the nanometric scale, materials exhibit unique magnetic properties that are completely distinct from their bulk counterparts. The nanometric size of the $MNP_{S,}$ known as single domain particles, can exhibit superparamagnetic behavior (Gajbhiye et al. 2005; Kaźmierczak et al. 2007; Ganesan et al. 2019). In this range, most of the magnetic moments are aligned in the direction of the field and give the giant magnetization termed saturation magnetization. Specifically, the nanomagnets have different magnetic behavior than their bulk counterparts, such as changes in magnetic anisotropy, coercivity, and magnetization. Interestingly, the dimension of the MNP particles reduced from bulk to nanoscale, and significant changes in the structural and magnetic properties were observed. Moreover, as materials are scaled down to the nanoscale, their crystalline structure can lead to different magnetic

orientations or anisotropy. Magnetic anisotropy is the entirely direction-dependent property which is necessary for the permanent magnets. This anisotropy affects the stability of the magnetic state and is crucial for controlling and manipulating nanomagnetic systems. The dynamics of electron spins become prominent at the nanoscale. Understanding and controlling spin dynamics are essential for applications like spintronics, where the spin of electrons is used for information processing. Nanomagnetic structures can exhibit exchange coupling, where neighboring magnetic moments influence each other. This phenomenon plays a crucial role in creating spintronics devices and magneto-optical applications. These properties are exploited in various applications, including magnetic storage and biomedical imaging. Similarly, the saturation magnetization (M_S) of small particles is lower than the bulk magnetization caused by the formation of magnetically dead layers over their surface. The magnetically dead layer is made of disordered magnetic dipoles having directions different from the core magnetic moment and acts as a negative force to reduce the magnetization.

8.1.2 Origin of Magnetism

Magnetism is a virtue of a material by which it attracts or repels another one. The source of magnetic behavior comes due to either the movement of electrically charged particles revolving around the nucleus in planetary motion or its own spin’s direction of motion and their interactions with one another. Based on this all materials have spinning electrons, so each material should exhibit a magnet. But this is not true due to two reasons that are explained in detail. According to Pauli exclusion rules, two electrons have the same energy but the directions of spins are opposite causing the cancelation of magnetic moments. Another one is that the orbital motion of electrons also cancels out each other (Yang et al. 2012; Zarrin et al. 2016). Hence, no net magnetic moments were obtained if there were no unpaired electrons in the orbital.

Based on the electronic configuration, the number of unpaired electrons that will cause the net magnetic moments can be identified. Some examples that include no unpaired electrons are Cu, Zn, etc. Thus, the origin of magnetism is mainly associated with orbital motion and spin of the electrons.

8.1.3 Classification of Magnetic Materials

Materials can be classified by their magnetic response toward the applied magnetic field. Magnetic moment orientation in the orbital of an atom helps to categorize the different types of magnetism that exist. Magnetic materials are substances that can generate and respond to magnetic fields. They can be categorized into various types based on their magnetic properties like magnetic susceptibility, coercivity, remanence, magnetization, and their behavior toward the applied external field. There are three kinds of magnetic materials such as diamagnetic, paramagnetic, and ferromagnetic, whereas antiferromagnetic and ferrimagnetic are considered as subclasses of ferromagnetic (Kim and Zhao 2022).

8.1.3.1 Diamagnetism

Diamagnetic materials exert repulsive force because their atomic moments are aligned oppositely in the presence of magnetic fields, and they do not retain magnetic properties in the absence of a field. The electronic configurations of diamagnetic materials are filled with electronic subshells where all the spins are paired, resulting in no net magnetization. These materials exhibited a negligible negative susceptibility ($\chi < 0$), and it is defined by the slope of magnetization versus the applied field. The value of diamagnetic susceptibility is independent of temperature and applied magnetic field. They act as a perfect superconductor because of zero resistance to forming current loops (Kim and Zhao 2022). Most of the elements in the periodic table show diamagnetic nature. Examples include hydrogen, carbon, gold, copper, quartz, etc.

8.1.3.2 Paramagnetism

Paramagnetic materials have unpaired electrons causing a stronger effect to overcome diamagnetism. The orbital electrons form the current loops that don't cancel out each other and contribute a net magnetic moment. But, the magnetic moments of these unpaired electrons do not have long-range order causing weak attraction in the presence of the external magnetic field. Although this weak attraction is also not permanent, it disappears on the removal of the external field. Thus, the net magnetizations of these materials are linearly proportional to the strength of the applied field. Due to weak attraction, these materials show a small positive magnetic susceptibility ($\chi > 0$), and it is often dominated by thermal energy (Kim and Zhao 2022; Kong et al. 2018). The susceptibility of paramagnetic materials is independent of the magnetic field and depends on temperature. Examples of paramagnetic materials include pyrite, lithium, oxygen, sodium, magnesium, molybdenum, uranium, etc.

8.1.3.3 Ferromagnetism

Ferromagnetic materials possess strong attraction toward the applied external magnetic field and conserve the magnetic behavior even after the removal of the field. The electronic configuration of these materials shows the number of unpaired electron shells that give the ultimately strong net magnetization. The direction of magnetic moments of each domain is randomly oriented in the absence of a field and when the field is applied, the magnetic moments of each domain get aligned in the direction of the field and give a high magnetization value. On removal of the external magnetic field, again the materials get demagnetized due to the random orientation of magnetic domains. Interestingly, an applied external magnetic field makes many domains' magnetic moments aligned in the same direction even after the removal of the field. It is worth saying that these materials have strong intrinsic magnetic moment ordering in the absence of an external field causing the permanent

magnetization known as hard magnets (Kim and Zhao 2022; Kong et al. 2018). These kinds of permanent magnets are utilized extensively in various applications such as electric motors, transformers, magnetic data storage, and many more places. Examples of ferromagnetic materials include iron, cobalt, nickel, etc.

8.1.3.4 Ferrimagnetism

Ferrimagnetic materials have atomic magnetic moments that are aligned in opposite directions but with an unequal strength, resulting in a net magnetization even though it's not as strong as in ferromagnetic materials. The ferrimagnetism phenomenon observed in those complex systems has two types of ions at different sites known as sublattices. These two types of ions at sublattices, influence each other through negative exchange interaction and form the antiparallel alignment. The antiparallel unequal magnetic moments of these ions at different sites cause some net magnetization. In the presence of an external magnetic field, the net magnetization behavior of these materials lies in between the antiferromagnetic and ferromagnetic materials. Similar to ferromagnetic materials, ferrimagnetic materials also break down into several magnetic domains. A ferrimagnetic material also shows the transition of phase from ferrimagnetic to paramagnetic above the Curie temperature and revives its behavior on cooling. Generally, ferrimagnetism is observed chiefly in ferrites (Kim and Zhao 2022; Kong et al. 2018). Examples include Magnetite (Fe_3O_4), $NiFe_2O_4$, (Mn, Mg)Fe_2O_4, $PbFe_{12}O_{19}$, $BaFe_{12}O_{19}$, yttrium iron garnet ($Y_3Fe_5O_{12}$), etc.

8.1.3.5 Antiferromagnetism

In antiferromagnetic materials, the alignment of the spin moments of neighboring atoms or ions is in exactly opposite directions. The opposing magnetic moments cancel one another, and, as a consequence, the solid as a whole

possesses no net magnetic moment. The spontaneous antiferromagnetic coupling is disrupted entirely upon heating called Néel temperature. Above the Néel temperature, the transition of the antiferromagnetic nature of the material to paramagnetic behavior occurred. Above Néel temperature, thermal energy progressively assisted the alignment of the atomic moments with the field, and a weak magnetism was exerted by the materials as the temperature increased. Despite this lack of macroscopic magnetization, antiferromagnetic materials play a significant role in various magnetic technologies, especially in the field of spintronics (Kim and Zhao 2022; Kong et al. 2018). Examples include MnO, Mn, Cr, NiO, CoO, FeS, etc. The classification of magnetic materials and their behavior in the presence of external magnetic fields are shown in Table 8.1.

Table 8.1 Classification of magnetic materials and their behavior in presence of external magnetic field

Types	Examples	Susceptibility	Permeability	Atomic/Magnetic moment behavior
Diamagnetic	SiO_2, Ag, Cu	Small and negative $-1 < \chi < 0$	$\mu < 1$	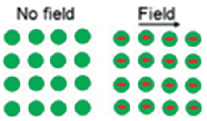
Paramagnetic	Mg, Cs	Small and positive $0 < \chi < \varepsilon$	$\mu > 1$	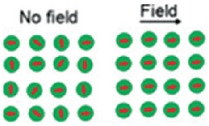
Ferromagnetic	Fe, Co, Ni, Gd	Large and positive $\chi > > 0$	$\mu > > 1$	
Ferrimagnetic	Fe_3O_4, $BaFe_{12}O_{19}$	Large and positive $\chi > > 0$	$\mu > > 1$	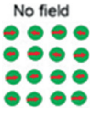
Antiferromagnetic	Cr, Mn, MnO	Small and positive $0 < \chi < \varepsilon$	$\mu > 1$	

As discussed above, the classification of magnetic materials, ferromagnetic or ferrimagnetic materials are

considered as magnetic on behalf of their magnetization behavior and response to an applied field. On behalf of the magnetic properties, ferro and ferrimagnetic materials are subdivided into three categories: soft magnetic, hard magnetic, and superparamagnetic materials. The major difference among these three types of magnetic materials can be described qualitatively based on their magnetization versus field curves (M–H) (Kim and Zhao 2022; Kong et al. 2018; Eshaghi et al. 2021).

8.1.4 Classification of Ferro/Ferrimagnetic Materials and Their Uses

8.1.4.1 Soft Magnetic Materials

Soft magnetic materials such as iron oxides/carbides/nitrides exhibited high magnetic susceptibility and saturation magnetization along with low remanence and coercivity. As a result of these properties, soft magnetic materials are strongly attracted toward a permanent magnet. By this, these materials are referred to as soft magnets which are easy to magnetize and demagnetize in the relatively weak magnetic field and, hence, these materials show temporary magnetism. For these materials, the area of the hysteresis loop (area of M vs. H plot) is very small; due to this hysteresis losses are observed to be low (Fig. 1a). Generally, soft magnetic materials such as iron and nickel ferrites have high resistivity. Consequently, the eddy current loss occurring in these materials is also low. These soft magnets have several important industrial applications such as electromagnets, electrical rotating machines, transformers cores, communication equipment, audio transformers, recording heads, magnetic modulators, magneto-mechanical sensors, magnetostrictive transducers, switches, and in the medical field (Eshaghi et al. 2021).

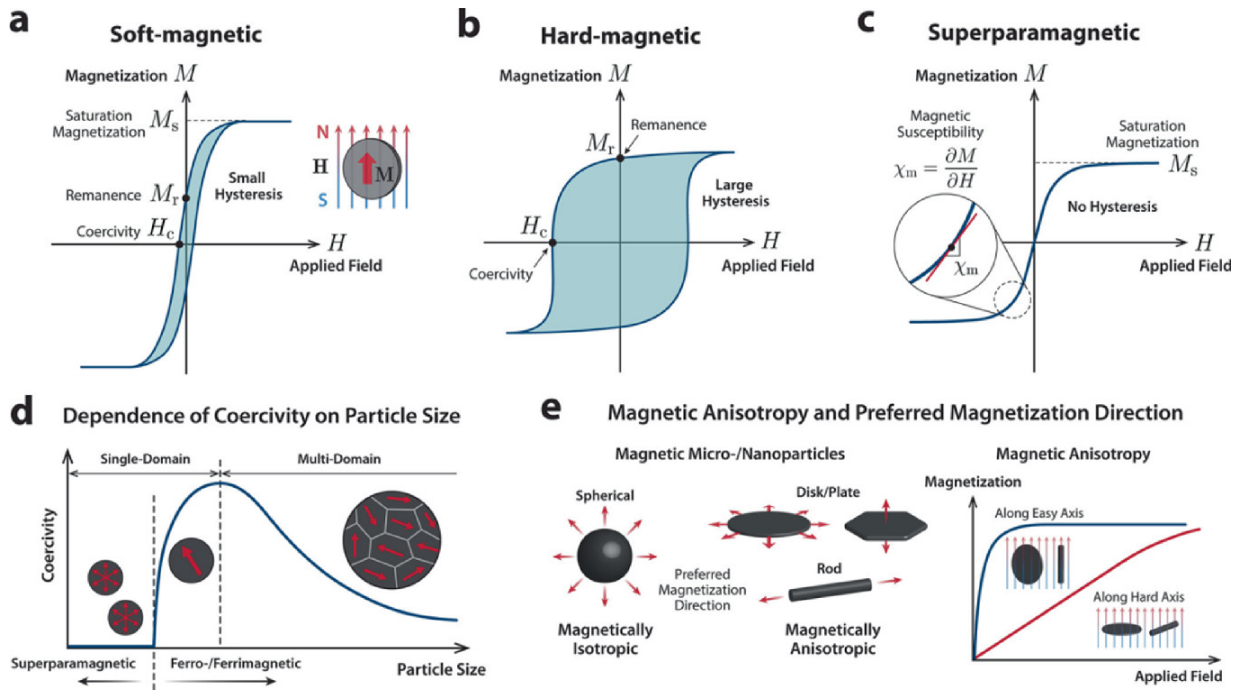

Fig. 8.1 Schematic representation of size-dependent coercivity and magnetization behavior: **a** hysteresis for the soft magnetic materials, **b** hard magnetic materials, **c** superparamagnetic materials (SPM), **d** size-dependent coercivity, and **e** shape-dependent anisotropy of the particles. Reprinted with permission from Kim et al. (2022) Chem. Rev. 2022, 122, 5317–5364.

Copyright © 2022, American Chemical Society

8.1.4.2 Hard Magnetic Materials

Hard magnetic materials consist of large magnetic hysteresis loops due to large coercivity and remanence (Fig. 1b). For example, the coercivity of AlNiCo ranges 30–150 kA/m, comparatively much higher than for soft magnetic materials. Similarly, the hexagonal ferrites ($BaFe_{12}O_{19}$) and strontium hexaferrite ($SrFe_{12}O_{19}$) exhibited high coercivity ~ 300 kA/m. The coercivity can be obtained even more than 1000 kA/m in the case of rare-earth doped magnets such as samarium-cobalt ($SmCo_5$ or Sm_2Co_{17}) or neodymium-iron-boron ($Nd_2Fe_{14}B$). The relatively higher magnitude of the coercivity renders greater resistance to them for demagnetization as compared to the soft magnetic materials. Permanent magnets are utilized widely in the automotive industry (i.e. motor drivers for fans, wipers, injection pumps, starter motors, and

control of seats and windows), telecommunication industries (i.e. microphones, loudspeakers, and telephone ringers), data processing industries (i.e. printers, stepping motors, disk drives, and actuators), and biosurgical industries (i.e. NMR/MRI body scanner and wound closures) (Kim and Zhao 2022; Kong et al. 2018; Eshaghi et al. 2021).

8.1.4.3 Superparamagnetic Materials

A single domain ferri/ferromagnetic nanoparticle in the presence of an external magnetic field exhibited giant magnetization along with zero coercivity and zero remanence value and did not retain any magnetization upon removal of the field. Owing to these properties, a single domain ferri/ferromagnetic nanoparticle is known as superparamagnetic material and the phenomenon is superparamagnetism. This is possible when the diameter of nanoparticles is in the range of 3–50 nm, depending on the materials. Thus, it is one of the useful size-dependent properties that appears with the introduction of nanomagnets. The external magnetic field is sufficient to magnetize the nanoparticles like a paramagnet. However, the magnetic susceptibility of these nanoparticles is much higher than that of paramagnetic materials. The superparamagnetic materials has numerous attractive applications in biomedical fields such as magnetic hyperthermia, magnetic separation, and drug delivery etc. Nevertheless, the superparamagnetism phenomenon strongly relies on the size of the MNP_S. In the case of magnetite (Fe_3O_4), superparamagnetism behavior was noticed below 30 nm. An experimental analysis of the size-dependent magnetic coercivity is shown in Fig. 1c.

Superparamagnetism occurs due to the small size of the particles. In general, the ferromagnetic particles exhibited a hysteresis loop. When ferromagnetic particles increase in size, the magnetic moment increases, which in turn increases the magnetization till saturation. This translates to a thinner hysteresis loop. On the other hand, the hysteresis loop widens

on decreasing the particle size until a certain nanoparticle size, called the critical diameter (D_c). Once this size is reached, the hysteresis loop starts to narrow further decreasing the size until a threshold of superparamagnetic size is reached. When the nanoparticles reach superparamagnetic sizes, the magnetization curve retains the sigmoidal shape of a ferromagnetic response without a hysteresis loop (Fig. 1d). The critical diameter D_C for the different materials may differ based on several parameters like shape, temperature, crystallinity of material, magneto isotropy, etc. The magnetic anisotropy-dependent magnetization and preferred magnetization direction of magnetic particles are shown in Fig. 1e.

8.2 Synthesis Methods of Nanomagnets

Researchers have extensively focused on the synthesis of uniformed size and highly crystalline nanomagnets using various methods that allow for precise control over their size, shape, composition, and magnetic properties. Some common preparation methods for nanomagnets are co-precipitation, sol–gel, thermal decomposition, microemulsion, mechanical ball milling, and hydrothermal methods to attain desired structural and magnetic properties (Anik et al. 2021). A brief overview of the synthesis methods is as follows.

8.2.1 Co-Precipitation

The co-precipitation technique is an easy and cost-effective bottom-up synthesis method, which is utilized for the production of nanoparticles with uniform size (Fig. 8.2). This process involves the metal precursors mixed in an aqueous medium under constant stirring to form the metal hydrous oxides or oxalates under an inert atmosphere above room temperature. For the precipitation, some precipitating agents like NaOH, KOH and NH_3 etc. are utilized during the

reaction. The major benefit of the co-precipitation route is that it gives a crystalline particle through nucleation and growth process. Moreover, the crystallite size and morphological structure of the nanoparticles can be controlled using different capping agents to allow growth in a specific direction (Anik et al. 2021).

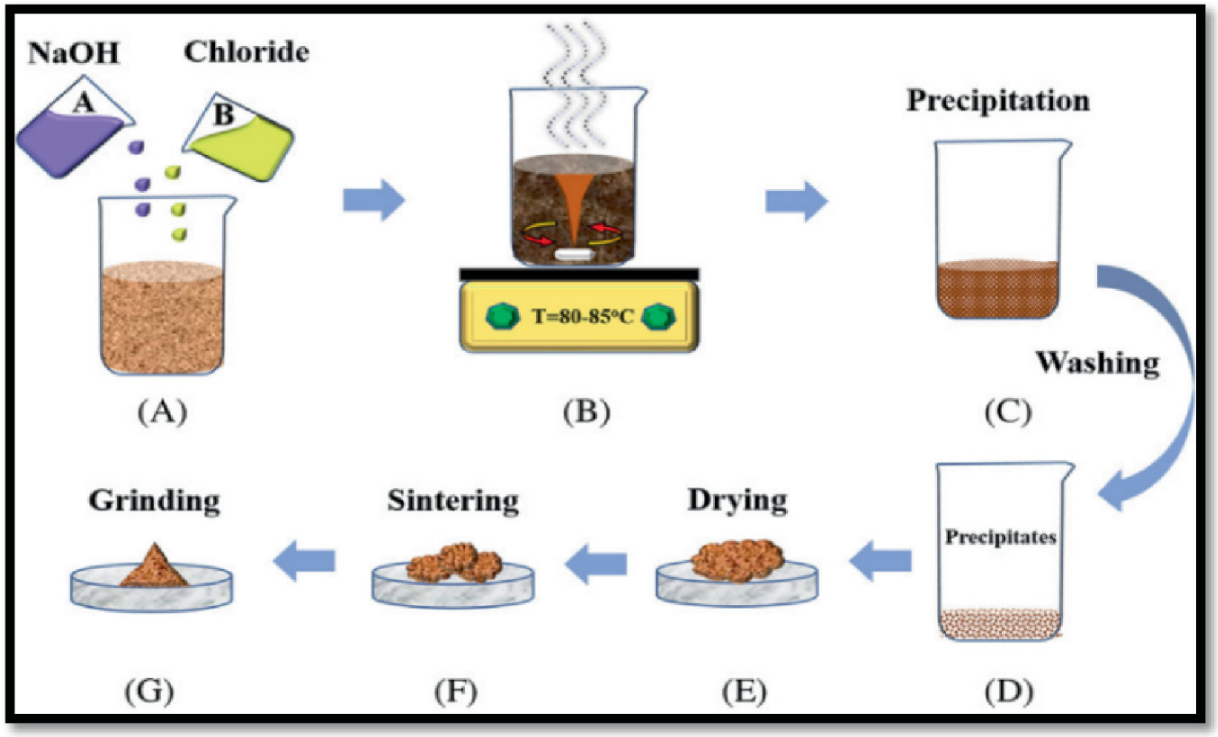

Fig. 8.2 The general process involved in a Co-precipitation method. 2021 Reproduced with permission from Anik et al. (2021) Nano Select 2021, 2, 1146–1186. Copyright © 2021, The Authors. Nano Select published by Wiley-VCH GmbH. An open access article distributed under the terms of the Creative Commons CC BY license

8.2.2 Sol–Gel Method

The sol–gel process is a wet chemical method for the synthesis of nanomagnets, particularly for metal oxide/carbide/nitride-based nanomagnets and composites. Sol–gel method consists of several stages to the formation of nanomagnets (Fig. 8.3). These stages are hydrolysis, polymerization, condensation, and gelation. Initially, the metal precursor dissolves in the solvent like water and alcohol to form the metal hydroxides through hydrolysis

(breaking of complex structures into simple), i.e. called “Sol”. Furthermore, some long-chain organic materials such as urea, citric acid, and cetyltrimethylammonium bromide ($C_{19}H_{42}BrN$) are utilized for the polymerization reaction to form the semi-solid foam-like structures known as “Gel”. Afterward, the gel is dried in different conditions to form aerogel, xerogel, and cryogel. Finally, the obtained gel can be calcined at a phase transition temperature to get the powder of the desired phase. Thus, it is worth saying that the sol–gel process is a cost-effective method to achieve high-quality products even at a relatively low temperature. It can be used for making ceramic products and thin films of metal oxides. Sol–gel process is used at conventional and industrial levels for the synthesis of nanomagnets. The obtained final qualitative product is used for versatile fields such as optical, electronic, energy, surface engineering, biosensors, and pharmaceutical and separation technologies (Gangwar et al. 2020a).

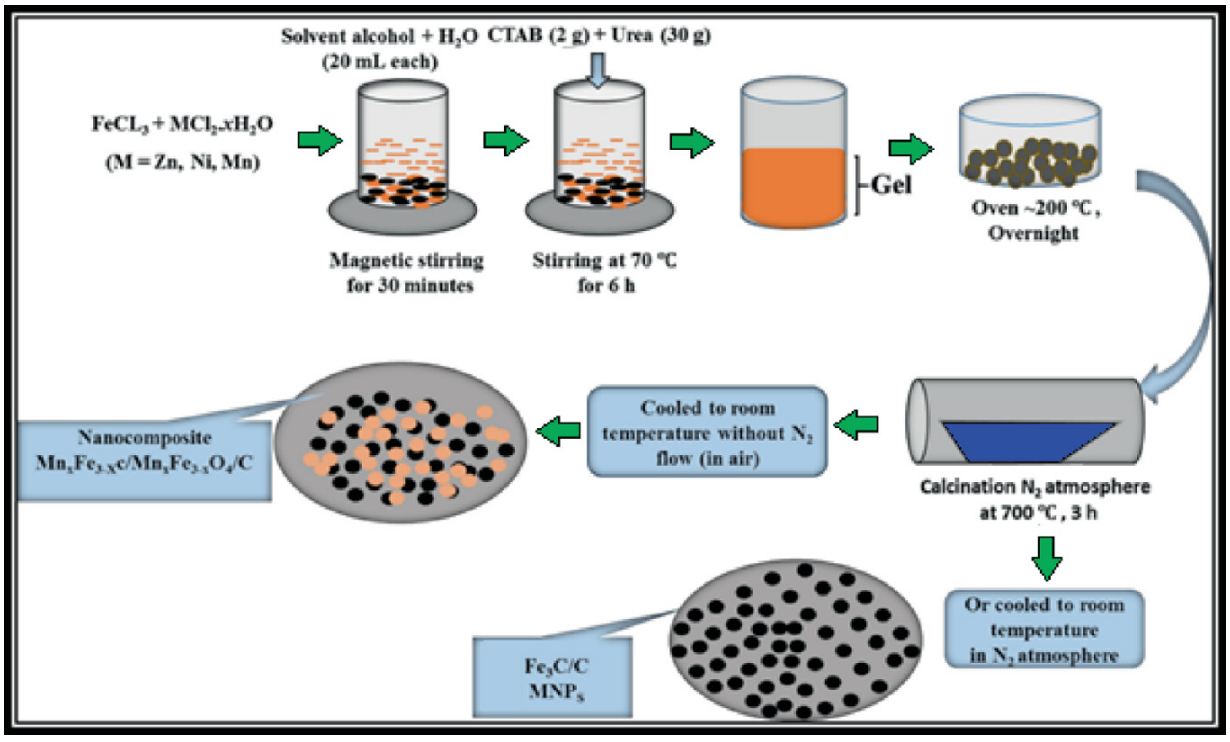

Fig. 8.3 Schematic representation of the sol–gel process followed by calcination

8.2.3 Thermal Decomposition

The thermal decomposition process consists of the decomposition of the chemical bonds due to heat supplied (Fig. 8.4). Thus, it is an endothermic process to synthesize the nanomagnets with uniform size distribution. Sometimes, the decomposition of a chemical reaction is found to be a significant liberation of heat called an exothermic reaction which may cause the explosion of the reaction. Thus, it is a temperature-dependent kinetic process that is significantly based on the initial reaction temperature of the experimental setup conditions and sensitivity. These processes are also utilized to obtain uniform sizes of nanomagnets for various medical and industrial applications (Anik et al. 2021).

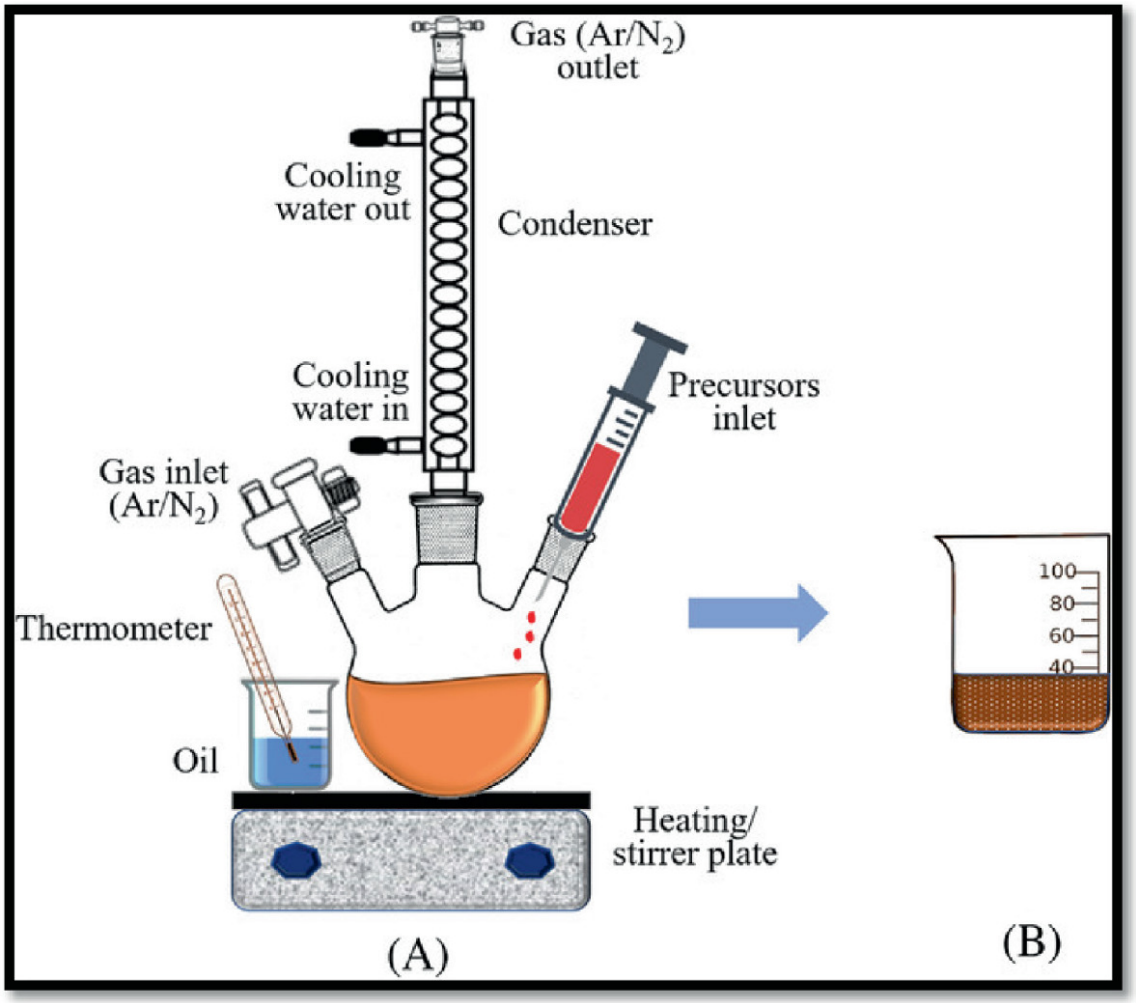

Fig. 8.4 Setup for the synthesis of MNP_S via thermal decomposition process. 2021

Reproduced with permission from Anik et al. () Nano Select 2021, 2, 1146–1186. Copyright © 2021, The Authors. Nano Select published by Wiley-VCH GmbH. An open access article distributed under the terms of the Creative Commons CC BY license

8.2.4 Microemulsion and Emulsion Techniques

Magnetic nanoparticles are formed within small droplets of a microemulsion system (Fig. 8.5). The size and properties of the nanoparticles can be controlled by adjusting the microemulsion composition. Magnetic nanoparticles can be synthesized by incorporating magnetic precursors within polymerizing droplets in an emulsion system. The definition of emulsion is based on the mixing of the two different densities of liquids like water and oil which are completely immiscible and form separate phases. Thus, the mixing of two liquids required the energy input and established the connections between water instead of replacing water-water and oil-oil. The interface can be formed between water by reducing the interfacial tension through surfactants containing both hydrophilic and lipophilic properties. Generally, emulsions are classified into three categories such as micro, mini, and macro emulsions based on the size of droplets. Moreover, for the production of inorganic nanomagnets, the microemulsion route is used extensively in laboratories and industries (Dhand et al. 2015).

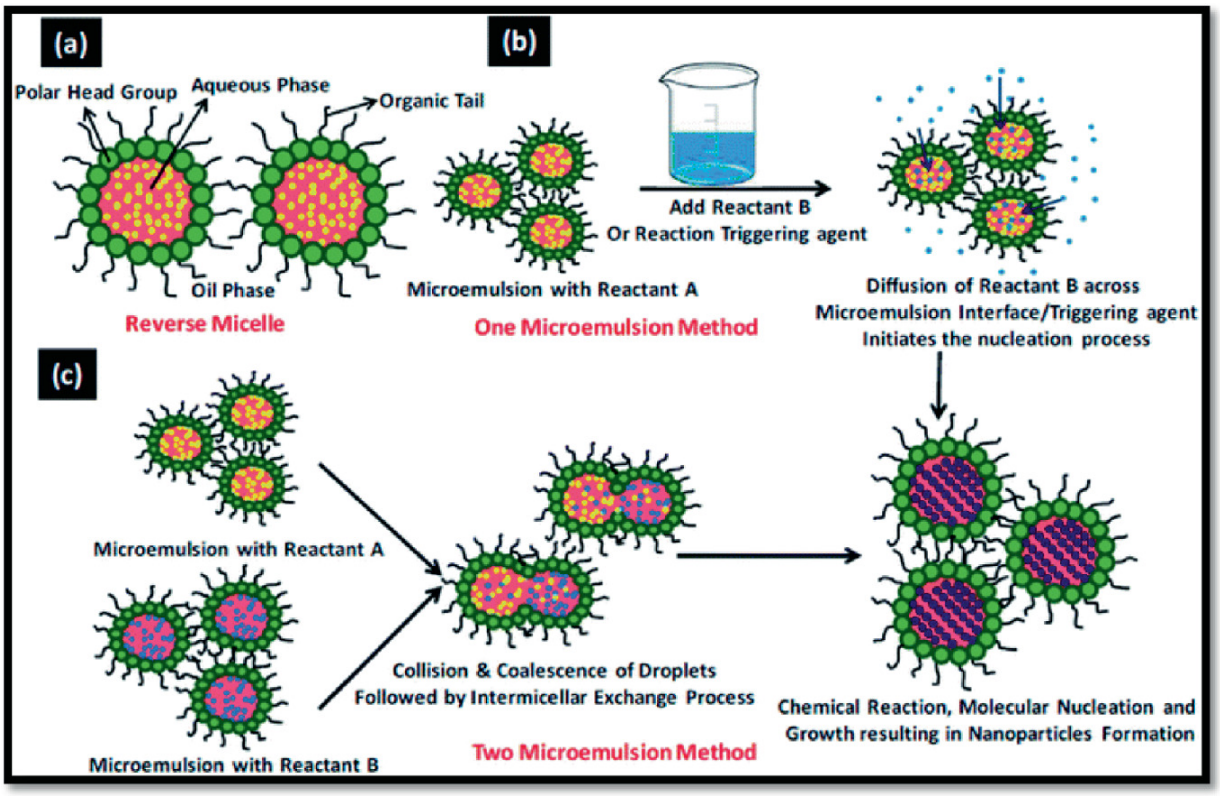

Fig. 8.5 Schematic representation of a revered microemulsion method: **a** A reverse micellar system, **b** one microemulsion method, and **c** two microemulsion method.

Reproduced from Dhand et al. (2015) RSC Adv., 2015, 5, 105,003 with permission from The Royal Society of Chemistry

8.2.5 Mechanical Ball Milling

Ball milling process is a kind of top-down approach for synthesizing the MNPs from the bulk/micron size of material (Fig. 8.6). The working principle of mechanical ball milling is quite simple, but it takes time to get the nano-dimensional material. In this process, precursors are kept inside a small hollow cylindrical jar having hundreds of steel balls as a grinding medium. Mechanical energy is applied to bulk magnetic materials to reduce their size to the nanoscale. The crystal size of the final product depends on several parameters such as the ratio of the weight of the ball to material, size of the balls, vibration speed, and time duration of milling time. It is suitable for preparing various morphologies of magnetic nanostructures like nanoparticles,

nanowires, rods, hexagonal plates, disks, etc. It is extensively used for grinding bulk macro-size materials to fine particles of nanometric range using high-energy balls. In the mechanical ball milling process, size reduction of the particles due to impact/collision between two balls so that intermolecular bonds can be broken. Several kinds of solvents are also used to prevent aggregation of the neighbor particles again (Dhand et al. 2015; Ramya et al. 2019). The only disadvantage of the ball milling process is the wide size distribution of particles comparable to other chemical synthesis routes.

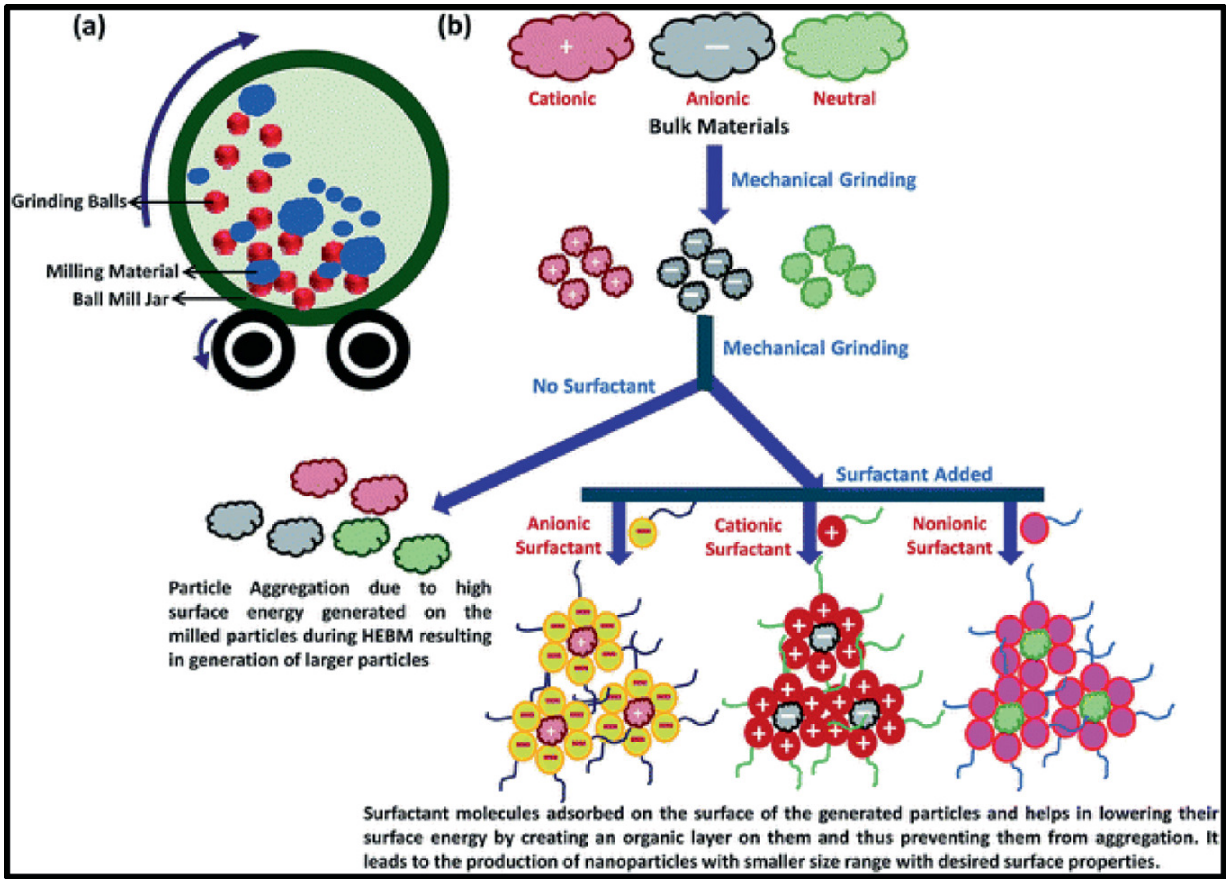

Fig. 8.6 Typical steps involved in the Mechanical ball milling process. Reproduced from Dhand et al. (2015) RSC Adv., 2015, 5, 105,003 with permission from The Royal Society of Chemistry

8.2.6 Hydrothermal Synthesis

The MNP_S has been synthesized through the hydrothermal method using Teflon-lined autoclave at a high-temperature and high-pressure aqueous solution using a Teflon-lined autoclave (Fig. 8.7). It is a versatile and cost-effective method to produce a wide range of nanomagnets. The morphology of the nanomagnets can be controlled through variations of pressure, temperature, and depending upon the vapor pressure of the chemical reaction. The major advantage of the hydrothermal method over others is to synthesize such controlled morphologies as well as compositions of the nanomagnets which are unstable at high temperatures with minimal loss of the precursors. To date, researchers obtained various morphologies such as nanoparticles, nanorods, nanotubes, hollow nanosphere, and graphene nanosheets using the hydrothermal method. Similar to the hydrothermal process, the solvothermal method was also opted for by many researchers to synthesize controlled sizes and morphologies of the nanostructures. The major difference between hydrothermal and solvothermal is the solvent used during the reaction. Some common organic solvents used in the solvothermal process include dimethylformamide (DMF), acetone, diethyl formamide, ethylene glycol, methanol, acetonitrile, and ethanol (Anik et al. 2021; Gangwar et al. 2019a).

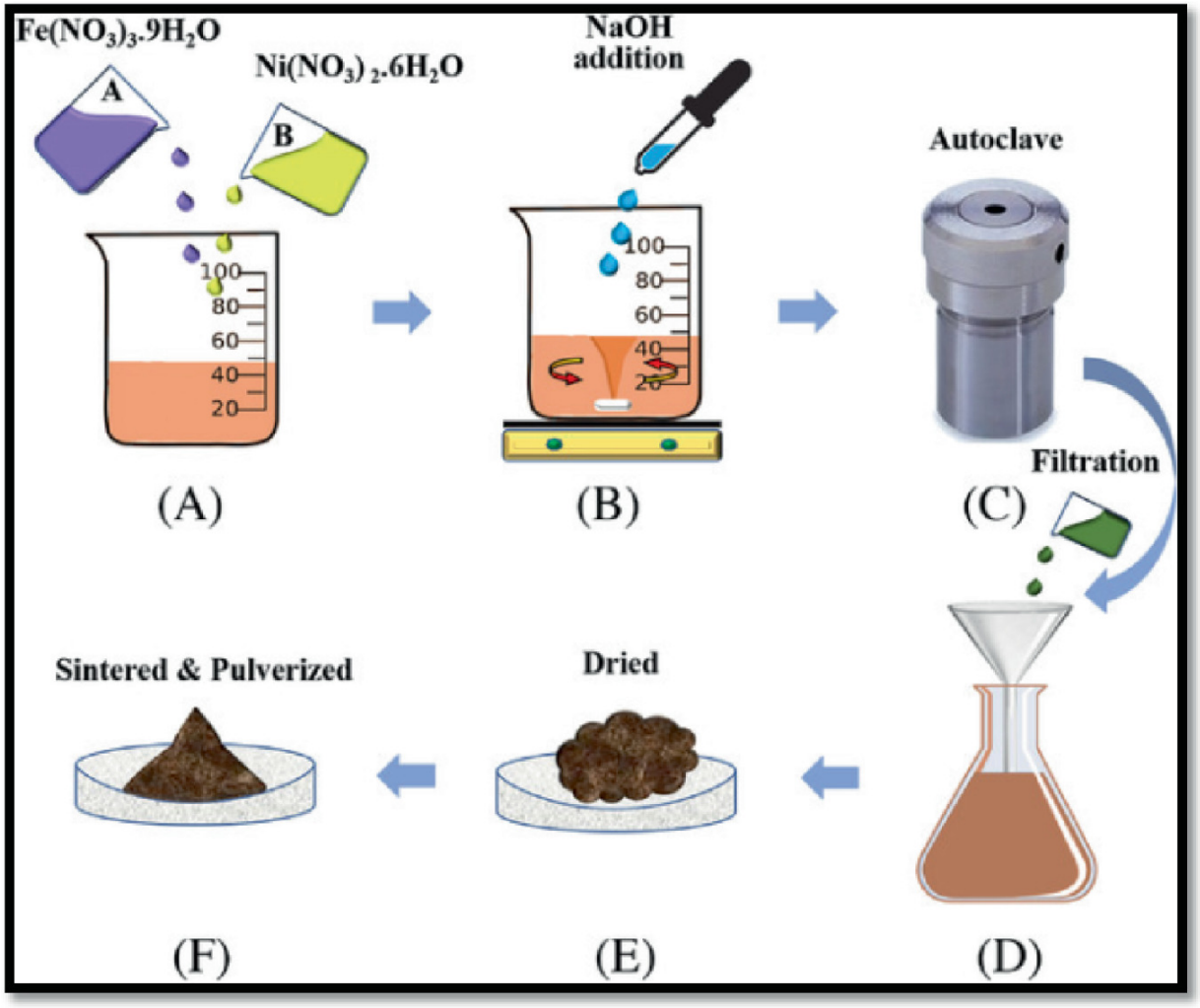

Fig. 8.7 The general steps involved in a hydrothermal method.
Reproduced with permission from Anik et al. (2021) Nano Select 2021, 2, 1146–1186. Copyright © 2021, The Authors. Nano Select published by Wiley-VCH GmbH. An open access article distributed under the terms of the Creative Commons CC BY license

8.3 Applications of Nanomagnets

Nanomagnets have achieved significant popularity and possible advancement in the electronics, catalysis, electrochemical sensors, optics, and biomedical fields due to their unique surface and physical as well as chemical properties. Nanomagnets' interaction with the AC magnetic field makes them more prominent for a specific application. Here are some prominent applications of nanomagnets.

8.3.1 Magnetic Data Storage

Nanomagnets play a crucial role in magnetic data storage technologies. They are used in hard disk drives (HDDs) and magnetic random-access memory (MRAM) to store and retrieve data by changing the orientation of nanoscale magnetic domains. Nanomagnets are essential components of spintronic devices, which utilize the spin of electrons for information processing. Spintronic devices include spin valves, magnetic tunnel junctions, and domain-wall-based devices, all of which rely on controlled nanomagnetic structures. The key aspect of magnetic data storage is a technology that is used to store digital information by encoding it as magnetic patterns on a medium. This technology is widely used in various forms, including hard disk drives (HDDs), magnetic tape, and magnetic stripe cards. Magnetic data storage relies on the fundamental property of magnetism, where data is represented as tiny magnetic domains that can be polarized in different directions to represent binary information. Magnetic data storage requires a suitable magnetic medium to store data. Common media include hard disk platters, magnetic tapes, and magnetic stripes on cards. Data is written to the magnetic medium using a write head, which generates a magnetic field. This field aligns the magnetic domains on the medium to represent the desired data. To retrieve data, a read head detects the changes in the magnetic field on the medium and converts them into electrical signals that can be processed by a computer. Data is typically represented in binary form, where each binary digit (bit) is stored as either a magnetic north or south pole. For example, a north pole might represent a 1, and a south pole might represent a 0. Advances in technology have led to higher data storage densities. This means that modern storage devices can store more data in smaller physical spaces. Magnetic data storage has been a reliable and widely used technology for several decades, but it faces competition from newer storage technologies like solid-state drives (SSDs) and optical

storage. SSDs, in particular, have gained popularity due to their speed and durability, although magnetic storage continues to be a cost-effective option for large-scale data storage and backup solutions (Ma et al. 2023; Chiolerio and Allia 2012).

8.3.2 Biomedical Applications

MNPS (especially superparamagnetic, ferrimagnetic, and ferromagnetic, 1–100 nm) are utilized in the biomedical field because they can be guided in the presence of an external field (Kumar et al. 2021). These MNPS are used as a carrier in advanced targeted drug delivery, and as a contrast agent in magnetic resonance imaging (MRI) to enhance the visibility of specific tissues, extraction of biomolecules, and diagnosis and treatment of the cancer, i.e. magnetic hyperthermia. The surface morphology of these MNPS has drawn great interest from researchers in the biomedical field. The unique morphological structure provides adequate surface chemistry to show the biocompatibility at a specific area for better diagnostic accuracy. Functionalized nanomagnetic particles can be used to deliver drugs to specific locations in the body. Magnetic targeting allows for improved delivery efficiency and reduced side effects. Nanomagnetic particles are employed in magnetic hyperthermia therapy, where they generate heat in response to an alternating magnetic field (Ito et al. 2005; Lu et al. 2007; Gangwar et al. 2016, 2019b, b, c, 2021; Suthar et al. 2023; Salkar et al. 2019; Singh et al. 2019; Alla et al. 2021; Krishnan 2010; Liu et al. 2011; Wust et al. 2006; Thiesen and Jordan 2008; Sun et al. 2008; Sung et al. 2020; Mahmoudi et al. 2018; Ortega and Pankhurst 2013; Tran and Webster 2010; Kumar and Mohammad 2021; therapy and controlled drug delivery 2011). Barick et al. have reported the carboxyl and amine decorated Fe_3O_4 MNP_S as a high-efficiency T_2 contrast agent in MRI and as a part of diagnosis (Gupta and Sharma 2019). Furthermore, Barick et al. reported the

glycine passivated Fe_3O_4 nanoparticles for magnetic thermal therapy for the treatment of cancer (Johannsen et al. 2005). Moreover, Gangwar et al. also reported the surface functionalized Fe_3C-, Fe_3O_4-, and $Fe_3N@Fe_3O_4$-based superparamagnetic nanoparticles as efficient magnetic hyperthermia applications (Gangwar et al. 2019a, 2016, 2019b, 2020b, 2020c, 2021; Barick et al. 2013). Shaw et al. have utilized the ɣ-Fe_2O_3, $MnFe_2O_4$, and exchange-coupled $MnFe_2O_4$/ɣ-Fe_2O_3 nanoflowers as efficient magnetic hyperthermia (Barick and Hassan 2012; Gangwar et al. 2020d). The schematic representation of the uses of MNPs in various biomedical applications is shown in Fig. 8.8 (Shaw et al. 2021).

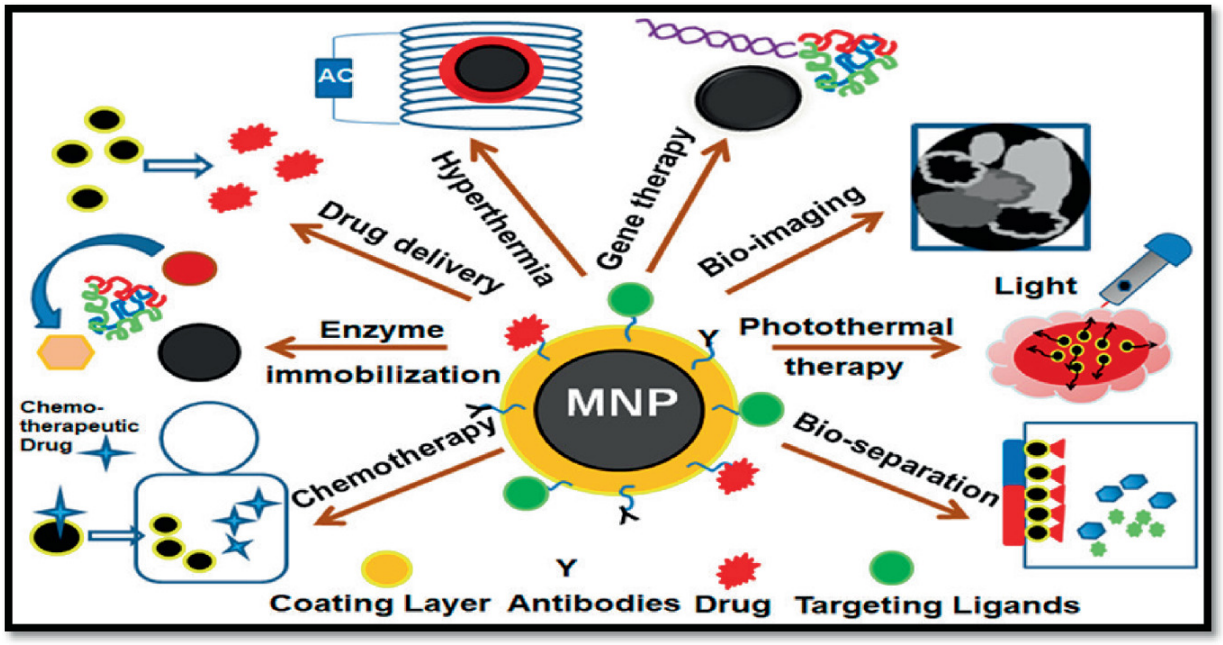

Fig. 8.8 Schematic representation of uses of MNPs in various biomedical applications. Reprinted with permission from Khizar et al. (2021) ACS Appl. Nano Mater. 2021, 4, 42,844,306.

Copyright © 2021, American Chemical Society

8.3.3 Sensors Application

In the past few years, it has been found that “Nanomagnets” are widely utilized in the field of sensing due to the most obvious magnetic properties shown by the nanomagnets.

Nanomagnet-based sensors allow fast response, are highly selective, and their long life makes them suitable candidates for the sensor application. These nanomagnets can achieve optimal performance for a wide range of sensing applications if the nanomagnets have high saturation magnetization (M_S), low coercivity and remanence values, high magnetic stability, and surface morphological properties that are essential for sensing-specific applications. Nanomagnets with a high (M_S) enable a fast response in the presence of the small external applied magnetic field. This feature enables the quick assemblage of the analyte, and provides a fast response time for a sensor. Thus, nanomagnets with high M_S can create a strong magnetic signal for detection and imaging. Nanomagnets in sensors are used in food industries, and water quality inspection to identify the presence of various organic species (Shaw et al. 2019; Khizar et al. 2021; Elaissari 2021). The schematic representation of MNP_S as electrochemical sensors is shown in Fig. 8.9.

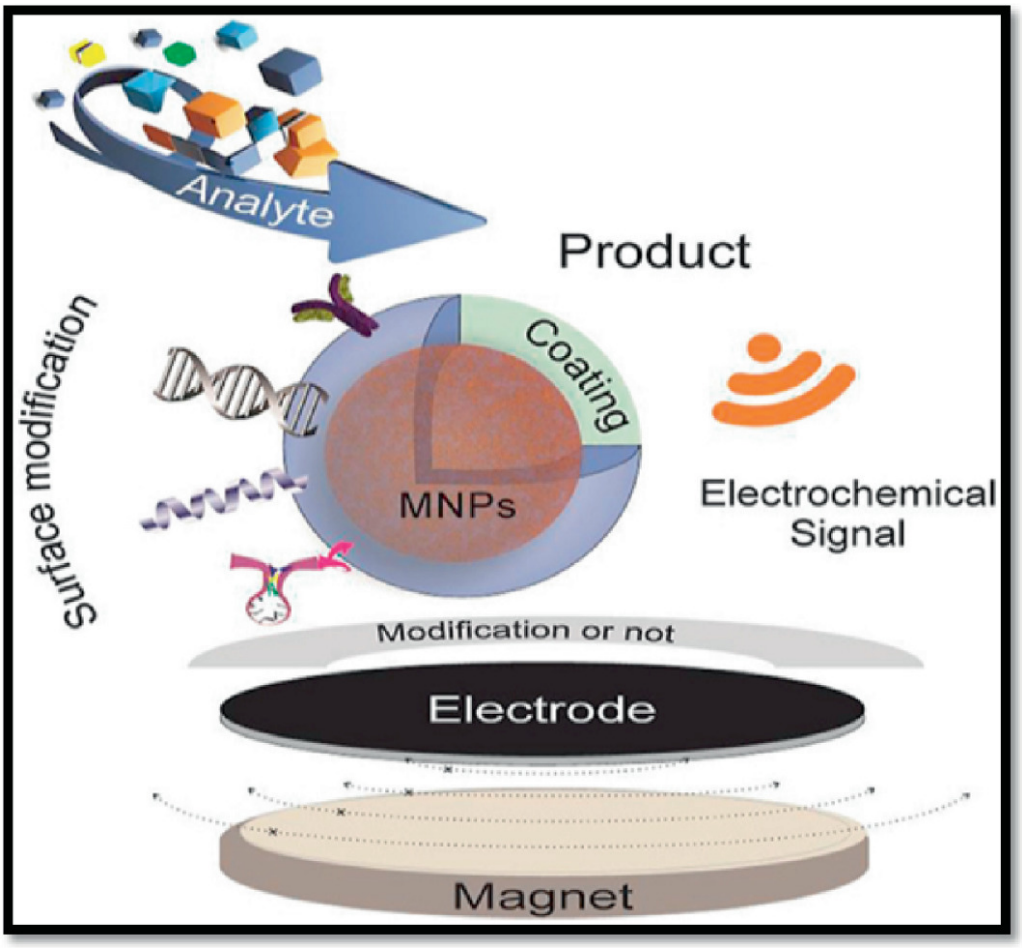

Fig. 8.9 Schematic representation of MNP_S as electrochemical sensors. Reproduced from Mollarasouli et al. (2021) Talanta, 2021, 226, 122,108. Copyright © 2021 Elsevier B.V

8.3.4 Environmental Remediation

MNPs can serve as catalysts for chemical reactions, enhancing reaction rates and selectivity. Their easy separation using an external magnetic field simplifies the catalyst recovery process. Nanomagnets can be used to remove pollutants and contaminants from water and soil through photocatalytic processes efficiently. In the past few decades, researchers have exploited several magnetically separable magnetic nanocomposite photocatalysts such as γ-Fe_2O_3@SnO_2, Fe_3O_4@TiO_2@Ag, Fe_3C/Fe_3O_4/C, Fe_3O_4@TiO_2, bean-like core/shell Fe_3O_4@C@Cu_2O_{35}, (Mn_3O_4/MnO)@rGO α-Fe_2O_3@TiO_2, and α-Fe_2O_3/Ag/SnO_2. Gangwar et al. have

reported the nanomagnetic composite of Ni-substituted $Fe_3C/Fe_3O_4/C$ as excellent catalytic degradation of organic pollutant dyes under Fenton and Photo Fenton conditions (Mollarasouli et al. 2021). Shaw et al. have examined a magnetic high entropy oxide $(Mn_{0.2}Fe_{0.2}Co_{0.2}Ni_{0.2}Zr_{0.2})_3O_4$ as an efficient catalyst for environmental remediation (Pradeep et al. 2022). Nanomagnets with significant saturation magnetization value, electrical resistivity, and optical (i.e. narrow bandgap) properties make them suitable candidates for environmental remediation. The stable phase of these nanomagnets enhances the recycling efficacy along with the low recombination effects of photogenerated electron–hole pairs (Koh and Josephson 2009). The schematic representation of the degradation of pollutants through an advanced oxidation process using MNPs as a catalyst is shown in Fig. 8.10.

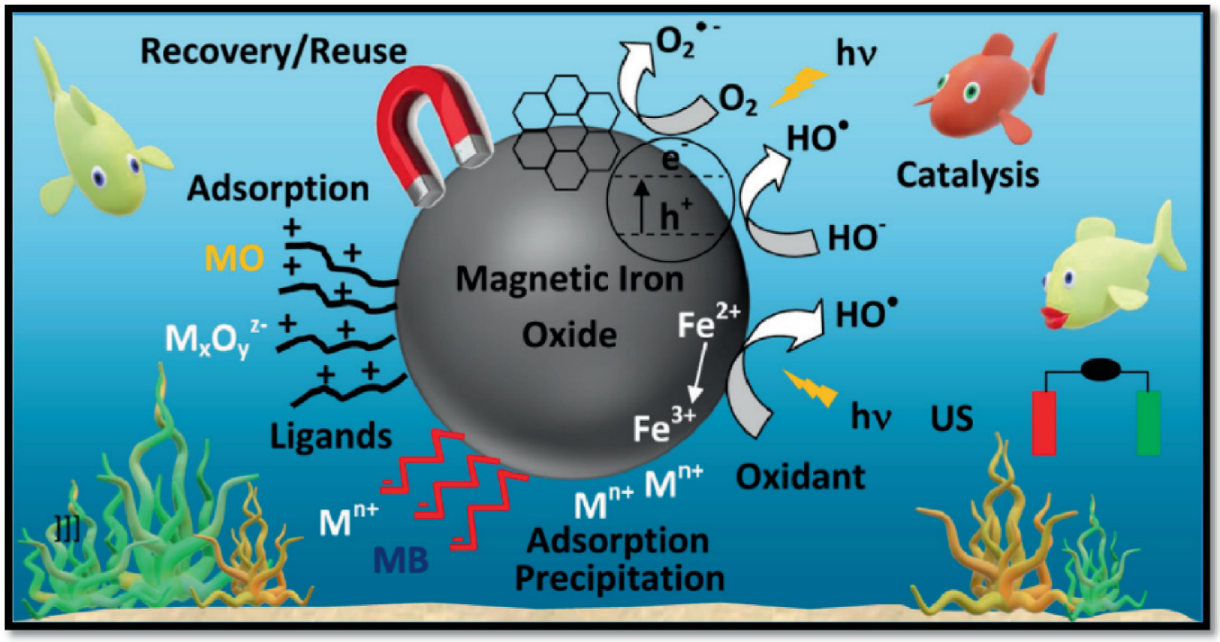

Fig. 8.10 Schematic representation of degradation of pollutants through advanced oxidation process.

Reproduced from Leonel et al. (2021) Water Res. 2021, 190, 116,693. Copyright © 2020 Elsevier B.V

8.3.5 Energy Conversion and Storage

In recent years, nanomagnets have been explored as potential energy conversion and storage applications due to their high theoretical specific capacity. Researchers have shown a remarkable interest in magnetic nanomaterials as energy storage devices such as electrodes for batteries and supercapacitors. Researchers found the impacts on the capacitive performances of the magnetic electrodes upon the external magnetic field, and it depends on the characteristics of the magnetic properties of the nanomagnets. MNP_S with adequate M_S value help in improving the electrochemical performances due to magnetoresistance. Recently, Gangwar et al. reported the Mn-substituted Fe_3C/Fe_3O_4 with carbon magnetic nanocomposites as a potential and highly stable electrode material for Li-ion batteries (Gangwar et al. 2020a). Similarly, Xu et al. also have reported the excellent electrochemical performance of $CNT/Fe_3O_4@C$ for Li-ion batteries (Gangwar et al. 2019c). In addition, Miao et al. have synthesized the heterogeneous interface of $Fe_3C@C@CNT$ as a potential electrode material for carrying high energy density in Li-ion batteries (Shaw et al. 2023). It is observed that $Fe_3C@C@CNTs$-based heterogeneous interface anode exhibited a high reversible capacity of 1027 mAh/g even after 150 cycles at 0.1 A/g along with excellent cycling stability after 1000 cycles at 1 A/g (Shaw et al. 2023).

8.4 Summary and Future Scope

Nanomagnetism is a field that explores the behavior and manipulation of magnetic properties at the nanoscale. It involves the study of magnetic materials and structures with dimensions on the order of nanometers. The unique properties exhibited by nanomagnetic materials, such as enhanced magnetization, size-dependent behavior, and tunability, have led to a wide range of applications in various domains. These applications include magnetic data storage, spintronics, biomedical imaging, drug delivery, sensors,

energy conversion, and more. Nanomagnetism has revolutionized industries, enabling advancements in electronics, medicine, energy, and materials science. The future of nanomagnetism holds exciting possibilities for both scientific research and technological innovation. Nanomagnetism will continue to drive innovations in magnetic data storage technologies, enabling higher capacity and more energy-efficient memory devices. Research in nanomagnetism will likely lead to the discovery of novel magnetic materials with tailored properties, and it will open new avenues for applications and device design in the future. The field of spintronics will advance further, with nanomagnets playing a central role in creating faster, more efficient, and low-power electronic devices. Nanomagnetic materials will find expanded use in biomedical applications, from targeted drug delivery to highly sensitive imaging techniques. Nanomagnetism could contribute to advancements in energy conversion and storage technologies, including thermoelectric devices and efficient waste heat recovery systems. Nanomagnets might play a role in quantum computing and quantum information processing due to their potential for encoding and manipulating quantum states. Highly sensitive nanomagnetic sensors will become more prevalent in various fields like environmental remediation, healthcare diagnostics, and industrial quality control. Nanomagnetism will continue to intersect with various fields, including materials science, chemistry, physics, biology, and engineering, leading to cross-disciplinary breakthroughs. Nanomagnetic applications could contribute to more sustainable technologies, such as efficient energy harvesting and cleaner water purification. In essence, the future of nanomagnetism promises a continuous stream of discoveries, innovations, and applications that will reshape various industries and contribute to solving some of the world's most pressing challenges. As researchers uncover new phenomena and techniques, the potential for transformative impact on technology and society remains significant.

References

Pradhan, P., Giri, J., Banerjee, R., Bellare, J., Bahadur, D.: Cellular interactions of lauric acid and dextran-coated magnetite nanoparticles. J. Magn. Magn. Mater. 311, 1 SPEC. ISS., 282–287 (2007)

He, H., David, A., Chertok, B., Cole, A., Lee, K., Zhang, J., Wang, J., Huang, Y., Yang, V.C.: Magnetic nanoparticles for tumour imaging and therapy: a so-called theranostic system. Pharm. Res. 30, 2445–2458 (2013)

Sadighian, S., Rostamizadeh, K., Hosseini-Monfared, H., Hamidi, M.: Doxorubicin-conjugated core-shell magnetite nanoparticles as dual-targeting carriers for anticancer drug delivery. Colloids Surf. B **117**, 406–413 (2014)

Duman, E., Acet, M., Wassermann, E.F., Itié, J.P., Baudelet, F., Mathon, O., Pascarelli, S.: Magnetic Instabilities in Fe_3C Cementite Particles Observed with Fe K-Edge X-Ray Circular Dichroism under Pressure. Phys. Rev. Lett. **94**(7), 075502 (2005)
[PubMed]

He, X., Wu, X., Cai, X., Lin, S., Xie, M., Zhu, X., Yan, D.: Functionalization of magnetic nanoparticles with dendritic–linear–brush-like triblock copolymers and their drug release properties. Langmuir **28**(32), 11929–11938 (2012)
[PubMed]

Gazeau, F., Lévy, M., Wilhelm, C.: Optimizing magnetic nanoparticle design for nanothermotherapy. Nanomed. **3**, 831–844 (2008)

Gajbhiye, N.S., Ningthoujam, R.S., Bhattacharyya, S.: Magnetic properties of Co and Ni substituted ε-Fe_3N nanoparticles. Hyperfine Interact. **2005**(164), 17–26 (2005)

Kaźmierczak, J., Ślawska-Waniewska, A., Pełech, I., Lachowicz, H., Lipert, K., Narkiewicz, U.: Magnetic properties of cementite (Fe_3C) nanoparticle agglomerates in a carbon matrix. Mater. Sci. Pol. **25**, 399–404 (2007)

V. Ganesan, B. B. Lahiri, C. Louis, J. Philip, and S. P. Damodaran, Size-controlled synthesis of superparamagnetic magnetite nanoclusters for heat generation in an alternating magnetic field, J. Mol. Liq., 2019, 281. 315–323.

Yang, C., Zhao, H., Hou, Y., Ma, D.: Fe_5C_2 Nanoparticles: A Facile Bromide-Induced Synthesis and as an Active Phase for Fischer-Tropsch Synthesis. J. Am. Chem. Soc. **134**, 15814–15821 (2012)
[PubMed]

A. Zarrin, S. Sadighian, K. Rostamizadeh, O. Firuzi, M. Hamidi, S. Mohammadi-Samani, S. and R. Miri, Design, preparation, and in vitro characterization of a

trimodally-targeted nanomagnetic onco-theranostic system for cancer diagnosis and therapy. Int. J. Pharm., 2016, 500(1–2), 62–76.

Kim, Y., Zhao, X.: Magnetic Soft Materials and Robots. Chem. Rev. **122**(5), 5317–5364 (2022)
[PubMed][PubMedCentral]

L. B. Kong, Liu, Z. yang, S. Li, T. Zhang, C. Wang, 15- Theory of ferrimagnetism and ferrimagnetic metal oxides, Metal Oxides, 2018, 8, 287–311.

Eshaghi, M., Ghasemi, M., Khorshidi, K.: Design, manufacturing and applications of small-scale magnetic soft robots. Extreme Mech. Lett. **44**, 101268 (2021)

Anik, M.I., Hossain, M.K., Hossain, I., Mahfuz, A.M.U.B., Rahman, M.T., Ahmed, I.: Recent progress of magnetic nanoparticles in biomedical applications: A review. Nano Select **2**, 1146–1186 (2021)

Gangwar, A., Sharma, A., Shaw, S.K., Meena, S.S., Prasad, N.K.: Structural and electrochemical performance studies for nanocomposites of carbon with Fe_3C or Mn-Substituted (Fe_3C/Fe_3O_4) as anodes for Li-batteries. Appl. Surf. Sci. **533**, 147474 (2020a)

C. Dhand, N. Dwivedi, X. J. Loh, A. N. Jie Ying, N. K. Verma, R. W. Beuerman, R. Lakshminarayanan and S. Ramakrishna, Methods and strategies for the synthesis of diverse nanoparticles and their applications: a comprehensive overview. RSC Adv., 2015, 5, 105003–105037.

Ramya, V., Gangwar, A., Shaw, S.K., Mukhopadhyay, N.K., Prasad, N.K.: Fe/Fe_3O_4 nanocomposite powders with giant high magnetization values by high energy ball milling. Bull. Mater. Sci. **42**, 1–7 (2019)

Gangwar, A., Varghese, S.S., Meena, S.S., Prajapat, C.L., Gupta, N., Prasad, N.K.: Fe_3C nanoparticles for magnetic hyperthermia application. J. Magn. Magn. Mater. **481**, 251–256 (2019a)

Z. Ma, J. Mohapatra, K. Wei, J. Ping Liu, and S. Sun, Magnetic Nanoparticles: Synthesis, Anisotropy, and Applications, Chem. Rev. 2023, 123, 7, 3904–3943.

A. Chiolerio, P. Allia, Magnetic Nanostructures and Spintronics BT. Encyclopedia of Nanotechnology, Bhushan, B., Ed.; Springer: Dordrecht, The Netherlands. 2012:1248–56.

Kumar, N., Shukla, A., Kumar, N., Choudhary, R.N.P.: Studies of structural, ferroelectric, magnetic and electrical characteristics of multiferroics. J. Mater. Sci. Mater. Electron. **32**, 5870–5885 (2021)

Ito, A., Shinkai, M., Honda, H., Kobayashi, T.: Medical application of functionalized magnetic nanoparticles. J. Biosci. Bioeng. **100**, 1–11 (2005)
[PubMed]

Lu, H., Salabas, E.L., Schüth, F.: Magnetic nanoparticles: synthesis, protection, functionalization, and application. Angew. Chem. Int. Ed. Engl. **46**(8), 1222–1244 (2007)
[PubMed]

Gangwar, A., Alla, S.K., Srivastava, M., Meena, S.S., Prasadrao, E.V., Mandal, R.K., Prasad, N.K.: Structural and magnetic characterization of Zr-substituted magnetite ($Zr_xFe_{3-x}O_4$, $0 \leq x \leq 1$). J. Magn. Magn. Mater. **401**, 559–566 (2016)

A. Gangwar, G. Singh, S. K. Shaw, R. K. Mandal, A. Sharma, S. S. Meena, N. K. Prasad, Synthesis and structural characterization of $Co_xFe_{3-x}C$ ($0 \leq x \leq 0.3$) magnetic nanoparticles for biomedical applications, New J Chem 2019, 43 (8), 3536–3544.

Gangwar, A., Kumar, S., Meena, S.S., Sharma, A., Viswanadh, M.K., Neogi, K., Prasad, N.K.: Structural and in-vitro assessment of $Zn_xFe_{3-x}C$ ($0 \leq x \leq 1$) nanoparticles as magnetic biomaterials. Appl. Surf. Sci. **509**, 144891 (2020b)

Suthar, M., Khare, D., Gangwar, A., Banerjee, S., Prasad, N.K., Dubey, A.K.: Structural, magnetic, and biocompatibility evaluations of chromium substituted barium hexaferrite (Co_{2-Y}) for hyperthermia application. Mater. Chem. Phys. **296**, 127348 (2023)

Salkar, K.Y., Tangsali, R.B., Gad, R.S., Gangwar, A., Prasad, N.K.: Electrical properties of Zn(1–x)CoxO dilute magnetic semiconductor nanoparticles. J. Mater. Sci. Mater. Electron. **30**, 18374–18383 (2019)

Gangwar, A., Varghese, S.S., Meena, S.S., Viswanadh, M.K., Neogi, K., Prasad, N.K.: Physical and in vitro evaluation of ultra-fine cohenite particles for the prospective magnetic hyperthermia application. J. Mater. Sci. Mater. Electron. **31**, 10772–10782 (2020c)

Singh, P., Bharti, P., Gangwar, A., Prasad, N.K., Upadhyay, C.: Janus shaped plasmonic-magnetic silver-magnetite nanostructures for multimodal applications. Jpn. J. Appl. Phys. **58**(10), 105001 (2019)

Gangwar, A., Alla, S.K., Prasad, N.K.: RF induction heating and in-vitro study of citrate functionalized Zr-substituted Fe_3O_4 nanoparticles with human lung adenocarcinoma (A549) cell. Phys. b: Condens. Matter. **611**, 412970 (2021)

S. K. Alla, A. Gangwar, S. K. Shaw, M. K. Viswanadh, K. Neogi, M. S. Muthu, N. K. Prasad, Physical and in-vitro evaluation of pure and substituted $M_xCe_{1-x}O_2$ (M= Co, Fe or Ti and x= 0.05) magnetic nanoparticles, Ceram. Int. 2021, 47 (7), 8812–8819.

Krishnan, K.M.: Biomedical nanomagnetics: a spin through possibilities in imaging, diagnostics, and therapy. IEEE Trans. Magn. **46**, 2523–2558 (2010)
[PubMed][PubMedCentral]

Liu, F., Laurent, S., Fattahi, H., Elst, L.V., Muller, R.N.: Superparamagnetic nanosystems based on iron oxide nanoparticles for biomedical imaging. Nanomedicine **6**, 519–528 (2011)
[PubMed]

Wust, P., Gneveckow, U., Johannsen, M., Böhmer, D., Henkel, T., Kahmann, F.: Magnetic nanoparticles for interstitial thermotherapy-feasibility, tolerance and achieved temperatures. Int J Hyperther. **22**, 673–685 (2006)

Thiesen, B., Jordan, A.: Clinical applications of magnetic nanoparticles for hyperthermia. Int J Hyperther. **24**, 467–474 (2008)

Sun, C., Lee, J.S.H., Zhang, M.: Magnetic nanoparticles in MR imaging and drug delivery. Adv Drug Deliver Rev **60**, 1252–1265 (2008)

H. Sung, J. Ferlay, R. L. Siegel, M. Laversanne, I. Soerjomataram, A. Jemal and F. Bray, Global Cancer Statistics 2020: GLOBOCAN Estimates of Incidence and

Mortality Worldwide for 36 Cancers in 185 Countries, CA: A Cancer Journal for Clinicians,

2021, 71, 209–249.

Mahmoudi, K., Bouras, A., Bozec, D., Ivkov, R., Hadjipanayis, C.: Magnetic hyperthermia therapy for the treatment of glioblastoma: a review of the therapy's history, efficacy and application in humans. Int. J. Hyperthermia **34**, 1316–1328 (2018)
[PubMed][PubMedCentral]

Ortega, D., Pankhurst, Q.A.: Magnetic hyperthermia. Nanoscience **1**(60), 60–88 (2013)

Tran, N., Webster, T.J.: Magnetic nanoparticles: Biomedical applications and challenges. J. Mater. Chem. **20**, 8760–8767 (2010)

C. S. S. R. Kumar and F. Mohammad, Magnetic nanomaterials for hyperthermia-based

therapy and controlled drug delivery: Adv. Drug Deliv. Rev. **63**, 789–808 (2011)

Gupta, R., Sharma, D.: Evolution of Magnetic Hyperthermia for Glioblastoma Multiforme Therapy. ACS Chem. Neurosci. **10**, 1157–1172 (2019)
[PubMed]

Johannsen, M., Gneveckow, U., Eckelt, L., Feussner, A., Waldöfner, N., Scholz, R., Deger, S., Wust, P., Loening, S.A., Jordan, A.: Clinical hyperthermia of prostate cancer using magnetic nanoparticles: presentation of a new interstitial technique. Int. J. Hyperthermia **21**, 637–647 (2005)
[PubMed]

Barick, K.C., Singh, S., Bahadur, D., Lawande, M.A., Patkar, D.P., Hassan, P.A.: Carboxyl decorated Fe_3O_4 nanoparticles for MRI diagnosis and localized hyperthermia. J. Colloid Interface Sci. **418**, 120–125 (2013)
[PubMed]

Barick, K.C., Hassan, P.A.: Glycine passivated Fe_3O_4 nanoparticles for thermal therapy. J. Colloid Interface Sci. **369**, 96–102 (2012)
[PubMed]

A. Gangwar, S. S. Varghese, S. S. Meena, C. L. Prajapat, M. K. Viswanadh, N. K. Prasad Physical and in-vitro evaluation of ϵ-Fe_3N@Fe_3O_4 nanoparticles for bioapplications, Ceram. Int. 2020, 46 (8), 10952–10962.

Shaw, S.K., Kailashiya, J., Gangwar, A., Alla, S.K., Gupta, S.K., Prajapat, C.L., Prasad, N.K.: γ-Fe_2O_3 nanoflowers as efficient magnetic hyperthermia and photothermal agent. Appl. Surf. Sci. **560**, 150025 (2021)

Shaw, S.K., Biswas, A., Gangwar, A., Maiti, P., Prajapat, C.L., Meena, S.S., Prasad, N.K.: Synthesis of exchange coupled nanoflowers for efficient magnetic hyperthermia. J. Magn. Magn. Mater. **484**, 437–444 (2019)

S. Khizar, N. M. Ahmad, N. Zine, N. Jaffrezic-Renault, A. Errachid-el-salhi, and A. Elaissari, Magnetic Nanoparticles: From Synthesis to Theranostic Applications, ACS Appl. Nano Mater. 2021, 4, 4284−4306.

F. Mollarasouli, E. Zor, G. Ozcelikay, A. Sibel Ozkan, Magnetic nanoparticles in developing electrochemical sensors for pharmaceutical and biomedical applications, Talanta, 2021, 226, 122108.

Pradeep, V., Alla, S.K., Sharma, A., Arun, B., Vasundhara, M., Gangwar, A.: Synthesis and characterization of $Fe_xCo_{3-x}O_4$ nanoparticles for sensor applications. Inorg. Chem. Commun. **142**, 109698 (2022)

Koh, I., Josephson, L.: Magnetic Nanoparticle Sensors. Sensors **9**(10), 8130–8145 (2009)
[PubMed][PubMedCentral]

A. Gangwar, A. Singh, Shaili Pal, I. Sinha, S. S. Meena, and N. K. Prasad, Magnetic nanocomposites of Fe_3C or Ni-substituted (Fe_3C/Fe_3O_4) with carbon for degradation of methylene orange and p-nitrophenol, J. Clean. Prod. 2019, 309, 127372.

Shaw, S.K., Kumari, P., Sharma, A., Jatav, N., Gangwar, A., Anuraag, N.S., Rajput, P., Kavita, S., Meena, S.S., Vasundhara, M., Sinha, I.: Assessment of ionic site distributions in magnetic high entropy oxide of $(Mn_{0.2}Fe_{0.2}Co_{0.2}Ni_{0.2}Zr_{0.2})_3O_4$ and its catalytic behaviour, Phys. B: Condens. Matter. 2023, 652, 414653.

Leonel, A.G., Mansur, A.A., Mansur, H.S.: Advanced Functional Nanostructures based on Magnetic Iron Oxide Nanomaterials for Water Remediation: A Review, Water Res. 190, 116693 (2021)

Xu, L., Zhu, A.: Preparation and electrochemical performance of CNT/Fe_3O_4@C for lithium-ion battery. J. Solid State Electrochem. **27**, 2199–2206 (2023)

Miao, Z., Li, D., Zhao, L., Gao, K., Sun, W., Zhao, W., Yuan, L., Zhang, H., Li, Z., Wang, Y., Li, Z., Zhang, M., Sun, C.: Domain-limited growth strategy to construct Fe_3C@C@CNTs heterogeneous interfaces for multi-functional high-performance lithium-ion storage and microwave absorption. J. Alloys Compd. **967**, 171650 (2023)

© The Author(s), under exclusive license to Springer Nature Singapore Pte Ltd. 2024
R. S. Ningthoujam, A. K. Tyagi (eds.), *Handbook of Materials Science, Volume 2*, Indian Institute of Metals Series
https://doi.org/10.1007/978-981-97-4646-0_9

9. Ferromagnetic Functional Materials

A. P. Srivastava[1, 2] ✉
(1) Materials Science Division, Bhabha Atomic Research Centre, Mumbai, 400085, India
(2) Homi Bhabha National Institute, Anushaktinagar, Mumbai, 400094, India

✉ **A. P. Srivastava**
Email: apsri@barc.gov.in

Keywords Ferromagnetism – Soft magnetic materials – Hard magnetic materials – Permanent magnets

9.1 Introduction

The use of magnetic materials in industry and our daily life is indispensable as magnets are a basic need for conversion of electrical energy to mechanical energy and vice versa. Fascination towards magnetism started with the discovery of a natural iron-oxide-rich rock magnetite (Fe_3O_4), known as lodestone which could attract other pieces of same rock or iron. In ancient time, a huge deposit of magnetite was known to exist in a district called Magnesia, which is in Turkey now. The word magnet is supposed to originate from this district name or by the name of a Greek shepherd

Magnes who first noticed the attractive property of this rock. Exact time of discovery of Lodestone is not known, but surely identified for centuries before Christ. In the iron age itself, magnetism found its application as in compasses wherein a shaped lodestone or magnetized iron bar would direct itself in a particular direction of the Earth's magnetic field. Understanding of the interaction of lodestone pieces or magnetised iron bars is the subject of magnetism. The first book on this subject, 'De Magnete' was published in 1600 by William Gilbert (Ball David 2011). The concept of magnetic field to describe such magnetic interactions was proposed in the seventeenth century by René Descartes. In 1820, Oersted discovered that the magnetic field can also be generated by electric current and electromagnets were discovered where the source of magnetism was electric current (Ball David 2011). Now electromagnets are used in telephones, computers, door bells, mobiles, tape recorders etc.

9.2 Basic Concepts and Definition in Magnetism

In order to appreciate advance development in this field, it is important to describe in brief a few important terminologies used in this chapter. Understanding of magnetic interaction requires consideration of the magnetic field which is generated either by a current or by an entity (atoms, molecules or materials) having a net magnetic moment ($\overrightarrow{\mu}$). Magnetic field ($\overrightarrow{B}$) produced due to a current segment ($_d\overrightarrow{l}$) carrying a constant current (I) at a position vector ($\overrightarrow{r}$) is given by the famous Bio-Savart law.

$$d\overrightarrow{B} = \frac{\mu_0}{4\pi}\left(\frac{Id\overrightarrow{l} \times \overrightarrow{r}}{\overrightarrow{r}^3}\right) \tag{9.1}$$

Primarily there are two sources of magnetic moment, electric current and spin of electrons, protons and neutrons, the constituent fundamental particles of an atom. Atomic nucleus which is made up of proton and neutron gives rise to what is known as the nuclear magnetic moment. It turns out that this nuclear magnetic moment is very small when compared to that produced by electrons in an atom. The magnetic properties of a material are entirely dictated by the magnetic moment produced due to electrons. An electron is known to do orbital motion and this may be equated to a current loop which contributes a magnetic moment

$$\overrightarrow{\mu} = g\mu_B \overrightarrow{L}, \tag{9.2}$$

where L is the angular momentum associated with the orbital motion of electrons in an atom. The natural unit of the magnetic moment is Bohr magneton μ_B and it is equal to the electron's magnetic moment in the 1st orbit i.e., $e\hbar/2\ m$. The magnetic moments are quantized in units of Bohr magneton. The spin of electrons in an atom contributes to a magnetic moment

$$\overrightarrow{\mu} = -g_s\mu_B \overrightarrow{S}, \tag{9.3}$$

where S is the total spin of electrons in an atom and its origin is quantum mechanical in nature with no classical analogue. The g-factor, which represents a dimensionless correction factor with respect to classical theory, is equal to ~2 for spin quantum number and 1 for the angular quantum number. The total angular momentum of an atom can be estimated in the purview of Hund's law. For a material, the net magnetic moment per unit volume is

known as Magnetization ($\overrightarrow{M}$). In the presence of an external magnetic field $\overrightarrow{B}$, the magnetic interaction of magnetic moment with the field is described by the potential energy known as Zeeman Energy which is equal to $-\overrightarrow{\mu}.\overrightarrow{B}$. Thus, magnetic moments will try to orient themselves in the direction of the applied field to minimize this energy. The response of a material in a magnetic field depends on the magnetic moments possessed by atoms in that material. If the atoms have completely filled electronic shell or subshell, they show very weak response to a magnetic field which is described as diamagnetic behaviour. All materials will have such response as inner shells of most atoms are completely filled. For practical purpose diamagnetic materials are treated as nonmagnetic materials. However, in the presence of partially filled shells/subshells, atoms have a finite magnetic moment due to an incomplete cancelation of spins or orbital angular momentum and they can show magnetic behaviour which is often described under the categories of paramagnet, ferromagnet, ferrimagnet or antiferromagnet. In paramagnetic materials, the magnetic moments of individual magnetic atoms/ions are oriented randomly. These magnetic moments do not interact with each other and show no net magnetization, except in the presence of an external field. In the presence of an external field, magnetic moment tries to orient itself in the direction of the external field to minimize the Zeeman energy, whereas thermal energy opposes this. Depending on the balance of these two energies, there exists a net magnetization in the presence of an external field. On the other hand, it is also possible that the magnetic moments in a material, themselves interact with each other giving rise to another energy known as exchange energy which may depend on the distance between magnetic ions, density of states etc. The nature of this exchange interaction along with Zeeman

interaction and thermal energy decides whether the material will show ferromagnetic, ferrimagnetic, antiferromagnetic or some complicated behaviour. Some of such materials (ferromagnet or ferrimagnet) may give rise to a finite magnetization even in the absence of an externally applied magnetic field, which is known as spontaneous magnetization. This property of possessing spontaneous magnetization in ferromagnetic materials is very useful for their various applications.

Such magnetic materials are further classified into soft and hard magnetic material. The term “soft” is used to describe the class of ferromagnetic metals or alloys which can be easily magnetized and demagnetized, whereas the term “hard” magnetic material is used for materials which are difficult to demagnetize.

To improve our understanding on soft and hard magnets, it is necessary to revisit technical terms viz. coercivity, magnetocrystalline anisotropy, magnetostriction and exchange length. The field at which the magnetization of any ferro- or ferri-magnetic material reduces to zero is known as coercive field and this is very sensitive to microstructural features such as defects and grain size.

It has been observed that along certain crystallographic directions, it is easy to magnetize a crystal. Such directions are known as the easy axis of magnetization and along others it is harder and known as hard axis. This anisotropy leads to an energy E which varies depending on the crystallographic direction of magnetization. For example, in hcp Co or any system with uniaxial anisotropy, this additional energy can be expressed as

$$E = K_1 \sin^2 \phi + K_2 \sin^2 \phi, \tag{9.4}$$

K_1 and K_2 represent anisotropy constants, while φ denotes the angle between magnetization and the

preferred axis. In symmetrical cubic systems e.g., Fe and Ni, this energy has the form of

$$E = K_1\left(m_x^2 m_y^2 + m_z^2 m_y^2 + m_z^2 m_x^2\right) + K_2 m_x^2 m_y^2 m_z^2;\ \overrightarrow{m} = \frac{\overrightarrow{M}}{|M|}, \quad (9.5)$$

where, $\vec{M}$ is the magnetization vector. The anisotropy constant K_1 at room temperature is 48×10^3 J/m^3 for Fe, 50×10^4 J/m^3 for Co and -5.7×10^3 J/m^3 for Ni (Blundell 2001). Whereas, in the 4f transition metals namely the rare earths, the constant K_1 is very high ~10^6 J/m^3. Lower value of anisotropy constants results in lower coercivity and hence favours soft magnetic properties. The anisotropy constants are also known to be strongly dependent on temperature, crystalline structure and spin–orbit coupling. Clearly, the anisotropy energy will favour smaller width of the domain walls, whereas the exchange energy will favour larger width to accommodate smoother transitions between domains. Balance of these two energies determines the width of a domain wall.

Magnetostriction refers to the alteration in the shape of ferromagnetic materials during the process of magnetization, occurring due to interactions involving magnetoelastic interactions; magnetoelastic interactions result in straining of ferromagnetic material during the process of magnetization. Magnetostriction is quantified by magnetostrictive strain or magnetostriction coefficient, defined as the strain attained at saturation magnetization and is given by $\lambda = \delta\lambda/l$; where l is the initial length and $\delta\lambda$ is the change in length due to magnetization. For a typical ferromagnetic transition metal, the magnetostriction is of the order of 10^{-5}. Magnetostriction poses a disadvantageous characteristic in the context of utilizing soft magnetic materials, as it contributes to losses in transformers, often accompanied by the humming sound of

the transformer. The strain in a magnetostrictive material increases with the magnetic field and it saturates at higher value. In general, the contribution of magnetostriction is much smaller compared to magnetocrystalline anisotropy. Therefore, in the presence of magnetocrystalline anisotropy, magnetostriction is often neglected.

The ferromagnetic exchange length, denoted as L_{ex}, signifies the smallest distance scale over which magnetic moments are compelled to align in a parallel fashion due to exchange interactions.

It is defined as

$$L_{ex} = \sqrt{\frac{A}{K}} \tag{9.6}$$

where A is exchange stiffness. For example, the exchange length, $L_{ex,}$ for $Fe_{80}Si_{20}$ is ~35 nm, ($A = 10^{-11}$ J/m^3 and $K =$ 8 kJ/m^3) (Krishnan Kannan 2016). The width of the domain wall is estimated using the exchange length typically by πL_{ex}.

9.3 Soft Magnetic Materials and Their Applications

Having learned about the technical terms, a soft magnet can be defined as a ferromagnetic material having coercivity value typically less than 1000 A/m whereas, if coercivity is in excess of 10 kA/m, the magnet is referred as a hard magnetic material. Other distinguishing properties of interest for soft magnetic materials are the following:

1. High permeability: Permeability, denoted as (= B/H), is a characteristic of a material that defines the flux density, B, generated in response to a specified applied field strength, H. Therefore, it refers to a material's ability to absorb magnetic flux. In high permeability

materials, one can produce large magnetic flux density with the application of a small magnetic field.

2. Low hysteresis loss: Hysteresis loss is the area under the B-H loop in the hysteresis curve of a ferromagnetic material. The energy dissipation of an AC device comprises of a component that is the product of the frequency and the hysteric loss per cycle.

3. Low eddy current loss: Another type of energy loss that becomes significant at high frequencies is eddy current loss, which is closely connected to the electrical resistivity of the material.

4. Large saturation magnetization: Saturation magnetization is the maximum magnetization that can be achieved under application of the magnetic field. Figure 9.1 shows a typical hysteresis loop from a ferromagnetic material which shows coercivity and saturation magnetization. In applications involving soft magnetic materials, having a high saturation magnetization (M_s) is advantageous.

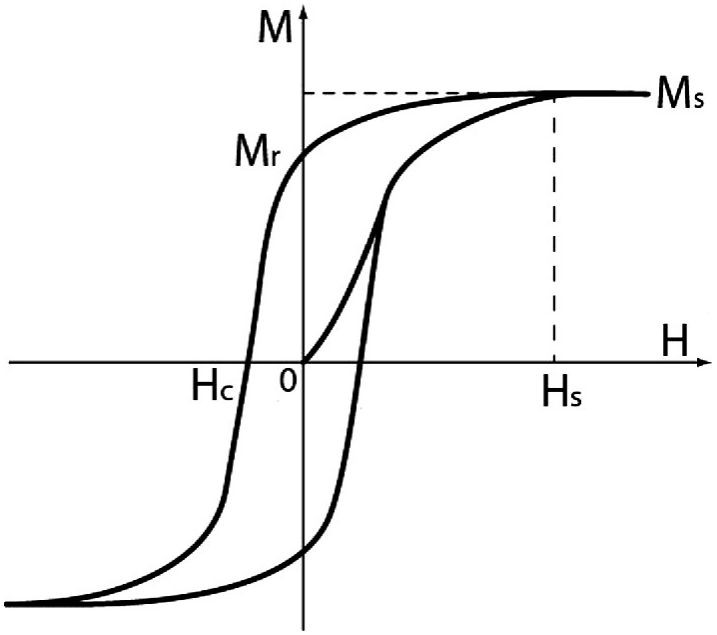

Fig. 9.1 A typical hysteresis curve of a ferromagnetic material, demonstrating the concept of saturation magnetization, M_S, coercivity H_C and field required for magnetic saturation H_S. The area under the curve represents hysteresis loss in on cycle

5. High Curie temperature: The Curie temperature is the temperature at which a ferromagnetic material transitions from being ferromagnetic to paramagnetic upon heating. The practicality of utilizing soft magnetic materials at higher temperatures hinges significantly on the Curie temperature of the material.

The most common applications of soft magnetic materials are as heavy-duty flux multipliers, light-duty flux multipliers in special purpose transformers and in microwave system components. Heavy duty high flux multiplier application refers to their use as core of big size transformers, motors and generators. High permeability of soft magnetic materials makes it possible to reduce the size and weight of the core and hence make it cost effective.

9.3.1 Energy Losses

Before considering the materials for soft magnetic applications, it is important to emphasize that soft magnetic materials show huge energy losses at higher frequency operation. First important energy loss is the hysteresis loss which is defined as the inside area under the full cycle of a magnetization curve of a ferromagnetic material. This energy loss is managed by controlling the coercivity of the material (Fig. 9.1). At higher frequencies, losses associated with low coercivity materials also become important. Another consideration in designing of low loss soft magnet is eddy current losses. Eddy currents refer to closed loops or paths of electrical current that form on the surface of a conductive material in response to a magnetic field that varies over time. These circulating current loops generate a magnetic field that opposes the alteration in

magnetic flux. Power losses due to eddy current roughly varies as the square of the frequency and it increases with increase in conductivity. Additionally, there is an anomalous loss associated with the movement of domain walls within the material and this can be controlled by microstructure tailoring. Mitigating these losses is the core idea in designing the materials with superior soft magnetic properties.

9.3.2 Fe or Fe–C Alloys

Coming back to the development of soft magnets, most inexpensive choice for a ferromagnet was iron. Earlier low carbon steels were used for these applications with a carbon content less than 0.03 wt%. It can be thought of as pure iron with some impurity in the form of iron carbide Fe_3C. They may show very high saturation magnetization (~2.15 T), permeability ~5000 and a small coercivity (~70 A/m) (McHenry et al. 1999). These properties depend on the purity of iron and microstructure particularly the crystal orientation. However, these materials have high power losses and low efficiencies and therefore, they are now used only in the cores of small motors for home appliances such as vacuum cleaner and washing machines, where energy loss is not a main concern because of their limited use.

9.3.3 Fe–Si Alloys

Sir Robert Hadfield introduced Fe–Si alloys in the early 1900s, which exhibited significantly higher permeability and notably reduced losses compared to earlier low carbon steels (Yoshihiko et al. 2008). This turned out to be the first major improvement in materials used for transformers. The most popular alloy was 3–4% Si in Fe. Addition of Si was found to increase the resistivity and hence to reduce the eddy current losses. Silicon addition also results in reduced

magnetization and Curie temperature. These are referred to as silicon steel. Alloys having Si up to 6.5% in Fe were investigated but could not be used because these materials were very brittle (Yoshihiko et al. 2008). Later in 1933, N. P. Goss introduced grain-oriented iron silicon alloy. These materials have large grain size which resulted in reduced coercivity. They are only suitable for the power and distribution transformers, which are used at lower frequency. These materials, i.e., low-carbon steel containing up to approximately 3% silicon or without any alloying additions are commonly referred as electrical steel, and they are mostly used at low frequencies i.e., 50 or 60 Hz power frequency. Another very famous alloy Fe–Si–Al in the family is commonly known by the brand name “Sendust” (Abshinova 2014). This shows very high permeability and low coercivity and in this alloy, it is possible to achieve nearly zero magnetocrystalline anisotropy as well magnetostriction. Therefore, it finds its applications in low audible noise devices because of nearly vanishing magnetostriction and in inductors, chokes and filters. However, they are very hard and brittle and hence have limited applications.

9.3.4 Fe–Ni and Fe–Co Alloys

However, since Fe based alloys have high conductivity it restricts their use for low frequency applications as at high frequency the eddy current losses will be very high. This is due to the fact that these losses are proportional to the square of the operating frequency. Therefore, for the cases where frequency may go up to megahertz and cost is secondary, Fe–Ni and Fe–Co based alloys and ferrites are used. For example, application of light-duty flux multiplier in special purpose transformers, or inductors used in electronic equipment uses such ferrites. The Fe–Ni alloys, often called permalloys, show good soft magnetic properties (Arnold and Elmen 1923). Fe–Ni alloys

containing 30% and 80% Ni have high ductility, allowing one to fabricate materials of reduced thicknesses which could be annealed to achieve larger grain sizes. These alloys are being used for special purpose applications such as transducers, magnetic audio recording heads, computer peripherals etc. Some alloys which have compositions close to 80% Ni, like mumetal (77%Ni–16%Fe–5%Cu–2%Cr) and 78-permalloy (alloy with 78% Ni) have shown high permeability around 3×10^5 and the coercive field as low as 0.4 A/m. The first magnetocrystalline anisotropy constant K is found to reduce to zero for Fe–Ni alloy having composition close to 75% Ni. This is responsible for showing high permeability and low coercivity in these polycrystalline alloys. Lower K value causes lowering of energy associated with the domain-wall and an increase in the thickness of the domain wall. Therefore, inclusions become less-effective in the impeding of the motion of the domain wall. In the same family addition of a small wt% of Mo and Mn to Permalloy resulted in much higher permeability. This alloy is referred as “Supermalloy” and find applications in pulse transformers magnetic amplifiers (‘Supermalloy 1948; Wieserman et al. 2002).

However, these alloys show lower values of saturation magnetization and Curie temperature. For applications, where higher saturation magnetization and higher operating temperature are needed, Fe–Co based alloys may be considered because the addition of Co helps in increasing both saturation magnetization and Curie temperature. The alloy $Fe_{50}Co_{50}$ (wt%) shows very high permeability and saturation magnetization. It can endure very high permeability and is known as “Permendur”. The addition of 2%V results in better mechanical properties in 49Fe–49Co–2 V (at%) alloy known as “Supermendur” or Hiperco 50A which is its commercial name (Gould and Wenny 1957). Of course, best magnetic properties could be

reached only after optimization of microstructure. The drawback of these alloys is their price. However, these properties led to the several applications of Fe–Co alloys such as in the electromagnets' pole pieces, in aircraft motors, generators, in beam-focusing lenses for electron microscopes.

9.3.5 Soft Ferrites

Soft ferrites are another class of soft magnets having low saturation magnetization and permeability compared to magnetic metals and alloys discussed above and are extensively used in practice. They show ferrimagnetic behaviour have a general formula given as MO. Fe_2O_3 where M is a divalent metal Cu, Zn, Mn, or Ni (or their combination known as mixed ferrite) and its crystal structure is cubic. Ferrites are not suitable for use in static or low (power) frequency fields. However, since their electrical resistivity is high with decent magnetic properties, they show very low eddy current loss and hence they are extensively used in high frequency applications, such as cores for special transformers, pulsed transformers or inductors, switched mode power supply (SMPS) and radio-frequency transformers. Most commonly used soft ferrites are Mn–Zn and Ni–Zn ferrites. Mn–Zn ferrites show higher saturation magnetization and permeability, lower electrical resistivity and lower Curie temperature than those of Ni–Zn ferrites. For frequencies up to 1 MHz, Mn–Zn Ferrites having permeability of the order of 1000–2000 are used. For very high frequencies ~100 MHz or more, Ni–Zn Ferrites having an initial permeability of 10–1000 are used. For applications involving frequencies in the range of GHz, ferrites such as Mg–Mn, Ni–Zn–Al and hexagonal ferrites based on $BaFe_{12}O_{19}$ are preferred. The cost effectiveness of ferrites and simple fabrication favours its use in intermediate frequency and high frequency fields,

particularly in household appliances' power supply where compact size may not be of major concern. However, they find limited applications in large size equipment because of diminishing saturation magnetization and a reduced yield ratio of the larger-sized device (Silveyra et al. 2018). After silicon steel, these ferrites are the second most produced soft magnetic material in the world.

9.3.6 Ferromagnetism in Non-Crystalline Materials

Till now all the soft magnetic materials that have been discussed were crystalline materials. An essential advancement in soft magnetic materials over the past three decades has been the synthesis of metallic glass or amorphous soft magnetic alloys produced by the method of planar flow casting. A planar flow casting equipment, namely a melt spinning unit is shown in Fig. 9.2a and a schematic is shown in Fig. 9.2b. In this unit metallic melt obtained by induction melting of an alloy is allowed to fall on a rotating copper wheel in a controlled manner. A very high cooling rate of $\sim 10^6$ K/s can be achieved in such units. This high cooling rate makes it possible to kinetically arrest the liquid structure which is non-crystalline. A transmission electron micrograph and a selected area electron diffraction (SAED) pattern from an amorphous metallic glass of composition $Co_{64.5}Fe_{3.5}Si_{16}B_{14}Ni_2$ is shown in Fig. 9.3a. Unlike a crystalline material, TEM micrographs are featureless and SAED pattern shows a diffuse halo. These are typical of an amorphous structure. Gubanov in 1960 was the first to theoretically predict the potential existence of amorphous ferromagnetism (Gubanov 1960). He based this prediction on the argument that the electronic band structure of crystalline materials does not fundamentally alter when transitioning to a liquid or amorphous state (Gubanov 1960, 1965). Hence, the

amorphous materials that lack any long-range ordering of atoms may also exhibit ferromagnetism, i.e., long-range ordering of atoms is not an essential criterion for a material to be ferromagnetic. It should be noted that in case of amorphous materials magnetocrystalline anisotropy exists due to short range ordering. Harris introduced a model to address the issue of averaging over randomly oriented local anisotropy axes, which he termed the random anisotropy model (Alben et al. 1978). This model was proposed to explain the small effective magnetic anisotropy resulting from the statistical averaging, essentially through a random walk process, of the magnetocrystalline anisotropy (Alben et al. 1978). In amorphous alloys, the traditional idea of a crystal field that determines the anisotropy constant (K) in crystalline materials is substituted with the concept of a short-range local field operating on a length scale of several angstroms. The symmetry of this local field defines the local magnetic anisotropy and is influenced by factors such as local coordination and chemical short-range order. The local anisotropy might indeed possess significant magnitude, but it is averaged out due to fluctuations in the orientation of easy axes. This statistical averaging of the local anisotropy occurs over a length scale that is equivalent to the ferromagnetic exchange length, denoted as L_{ex}.

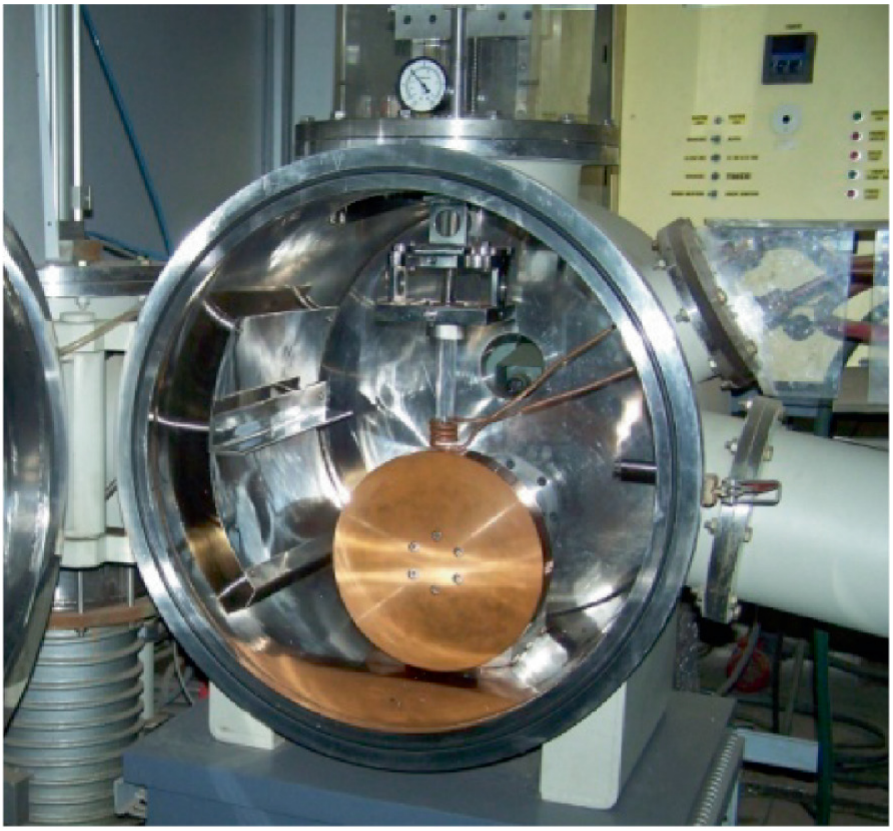

a

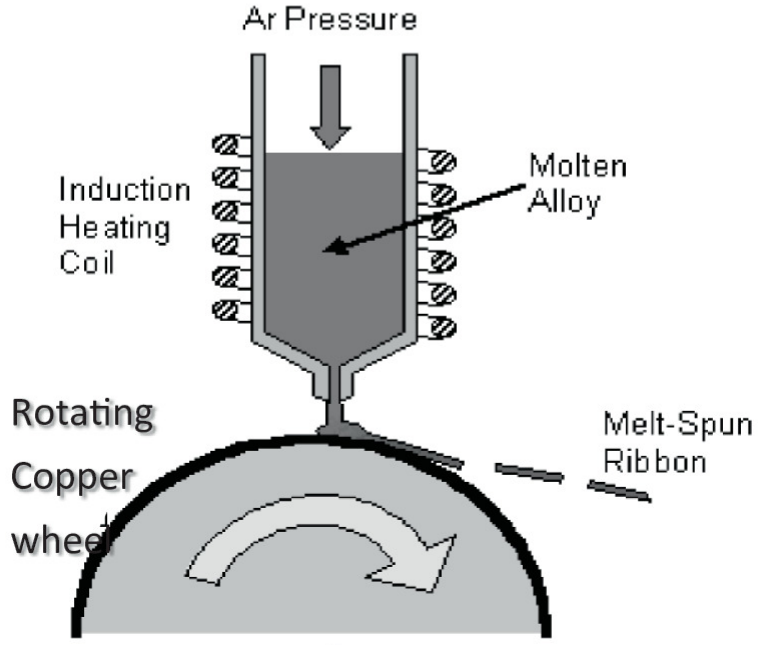

b

Fig. 9.2 **a** Photograph of planar flow casting unit used for synthesis of amorphous ribbons. **b** Schematic diagram of the melt spinning technique

showing metallic melt being forced by Ar gas to fall on the rotating copper wheel, which results in melt spun ribbon

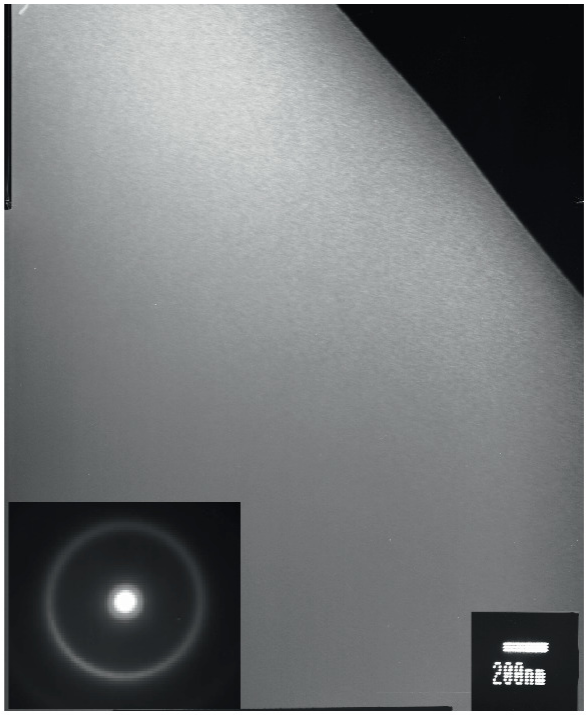

a

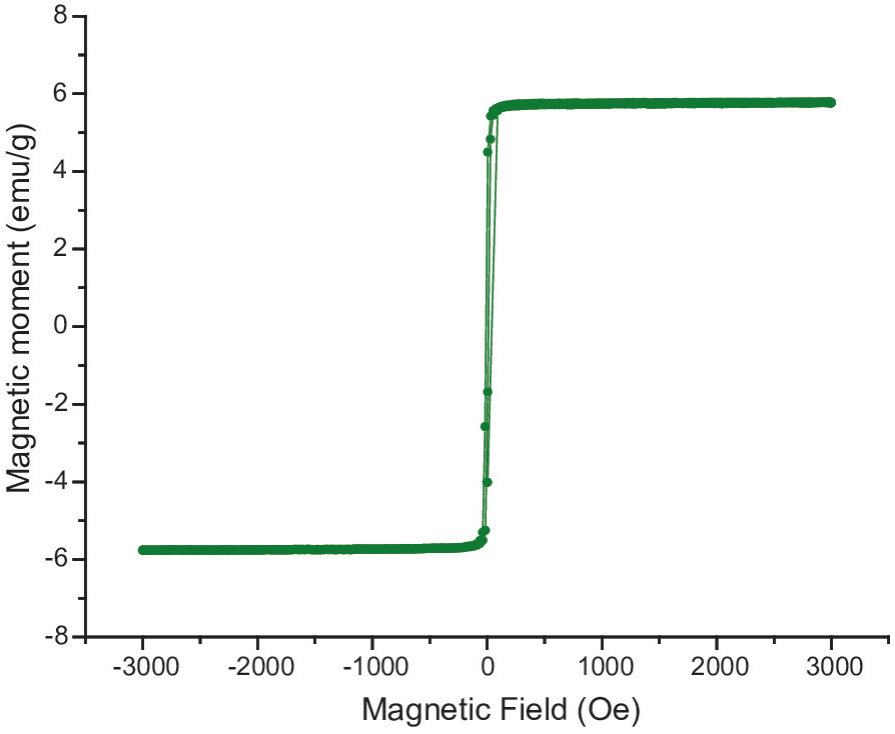

b

Fig. 9.3 **a** TEM Micrograph and SAED pattern obtained from amorphous metallic glass of composition $Co_{64.5}Fe_{3.5}Si_{16}B_{14}Ni_2$. **b** Hysteresis loop obtained from amorphous metallic glass of composition $Co_{64.5}Fe_{3.5}Si_{16}B_{14}Ni_2$

The first magnetic amorphous metallic glass of Fe–P–C alloy made by rapid solidification by Duwez and Lin (Duwez and Lin 1967) activated the research on magnetism of amorphous alloys because this exhibited moderate saturation magnetization (~0.68 T), small coercivity (~240 A/m), Curie temperature of 320 °C and reasonable stability at room temperature against crystallization and this also confirmed the prediction of Gubanov. In 1995, for the first time a bulk form of amorphous material of composition $Fe_{73}Al_5Ga_2P_{11}C_5B_4$ could be produced (Inoue et al. 1995) which had a high value of $M_s \sim 1.26$ T and thereafter search of better composition having good glass forming ability, magnetic properties and mechanical properties has been a hot topic in the field of soft magnetic materials. Amorphous materials are being used in small distribution transformers.

It has been also used for a 16-kVA unit which has shown only 20% of the loss of normal oriented silicon steels. Earlier, amorphous materials could not be used in large power transformers due to their low saturation induction and high price. Saturation magnetization of magnetic metallic glasses may vary in the range of 1.5 T to 1.9 T, with a low magnetic anisotropy and magnetostriction values, usually in the range of approximately $\sim 20–30 \times 10^{-6}$. Metallic glasses show relatively high electrical resistivity generally over 100 $\mu\Omega \cdot$ cm. These amorphous materials show very good soft magnetic properties as there are no microstructural discontinuities such as grain boundaries or precipitate to pin the domain wall motion as well as they have negligible magnetocrystalline anisotropy due to microstructural homogeneity. The soft magnetic properties can be further improved by low temperature annealing in

the presence of the magnetic field so that these materials can have performance better than the permalloys. The quest for achieving high magnetic inductions often restricts the selection to transition metal elements possessing the largest atomic dipole moments, namely, iron (Fe), nickel (Ni), and cobalt (Co). Iron (Fe) and cobalt (Co) exhibit substantial Curie temperatures of 770 °C and 1100 °C, respectively, making them prime candidates, especially in high-temperature applications. Numerous crucial soft magnetic alloy systems can be designed by exploiting the feature of zero crossings in their magnetocrystalline anisotropy or magnetostriction coefficients with compositions. Presently, three groups of metal-metalloid amorphous alloys are found to be suitable as soft magnetic materials. The first category consists of iron-rich magnetic alloys composed of cost-effective raw materials like iron (Fe), silicon (Si), carbon (C), and boron (B). These alloys showcase the highest values of saturation magnetization and remarkable soft magnetic characteristics (Lu et al. 2020; Lingxiang and Kefu 2020). For example, a well-known commercial $Fe_{78}Si_{13}B_9$ alloy recognized by the trade name METGLAS 2605™ has high M_s of 1.56 T, high permeability, and extremely low core loss (Hasegawa and Azuma 2008). The second category includes amorphous alloys primarily composed of iron (Fe) and nickel (Ni), with each metal making up roughly 40 atomic percent. These alloys demonstrate a saturation magnetization ranging from 0.7 to 1.0 Tesla. The inclusion of nickel enhances the ability to form a glassy amorphous structure and improves ductility, thereby simplifying the manufacturing process and subsequent processing steps. A well-known commercial alloy is METGLAS 2826 MB with elements Fe, Ni, Mo and B. This has a M_s value of 0.88 T, coercivity of 4 A/m and Curie temperature of 353 °C (Srivastava et al. 2006). The third group comprises of Co based alloys having very low to

zero magnetostrictive that exhibit the best soft magnetic properties with moderate saturation magnetization. These alloys are also suitable for high temperature applications. A very famous such alloy known by trade name METGLAS 2714A contains Co, Fe, Ni, Si and B. It shows an Ms value of 0.57 T, coercivity of 0.4 A/m and Curie temperature of 225 °C. A typical hysteresis loop obtained from a cobalt based amorphous metallic glass is shown in Fig. 9.3b, which shows a rectangular loop, a characteristic of a good soft magnet. Amongst these groups, most widely used are iron based alloys. Few other compositions that are seen as potential candidate for new materials are $Fe_{80}Si_5B_{10}P_5$, $Fe_{83}B_{8.5}Si_{4.5}P_3Nb_{0.67}Cr_{0.33}$ and $(Fe_{0.8}Co_{0.2})_{85}B_{14}Si_1$ (Zhang et al. 2012; Kong et al. 2016; Wang et al. 2017). Recently developed bulk metallic glass compositions known under trade name SENNTIX are of type Fe–Nb-(P, B, Si) and Fe–Nb–Cr-(P, B) and exhibit very small core losses because eddy current losses are very low due to their high electrical resistance (Suryanarayana and Inoue 2013). These are being used as DC converters and in the circuits of CPU or GPU power supply for laptops and mobile phones (Matsumoto et al. 2007, 2011). All these amorphous metallic glasses are formed in the form of ribbons or rods. Recently, magnetic metallic glasses in the form of nanowires have attracted research for their potential application in miniaturized sensor and spintronic applications.

9.3.7 Nanocrystalline Soft Magnetic Materials: Emerging Area of Research

Conventional methods within the realm of physical metallurgy focus on enhancing the characteristics of soft ferromagnetic materials by fine-tuning the chemical composition and refining the microstructure. Prior to 1988, fine-particle systems with sizes surpassing the

superparamagnetic limit were predominantly recognized for exhibiting hard-magnetic properties. In these cases, fine particles are single domain. The reduction of the particle (grain) size is a well-recognised method to increase the coercivity following 1/D law where *D* is the grain size. This is because with an increase in the grain boundary area, domain wall motion becomes difficult and hence an increase in coercivity is observed.

As mentioned in the previous section, amorphous metallic glasses show very good soft magnetic properties. It was shown that coercivity can be further reduced in amorphous metallic glasses by controlled microstructural tailoring to achieve partial nanocrystallization of amorphous soft magnetic materials. If such a heat treatment is devised so that amorphous matrix contains nanocrystalline particles of magnetic phases such as α-Fe, in the size range less than the ferromagnetic exchange length (~50 nm) and particles are close enough to exchange couple with each other and volume fraction of nanocrystalline particles in amorphous matrix is such that net magnetostriction of nanoparticles (which should have opposite sign of magnetostriction compared to that of amorphous matrix) and amorphous matrix is nearly zero, then an improvement in soft magnetic properties takes place (Srivastava et al. 2013). A typical transmission electron micrograph showing such a microstructure is shown in Fig. 9.4a and selected area electron diffraction from nanoparticle is shown in Fig. 9.4b (Srivastava et al. 2013). In this case, the primary phase that appears after heat treatment is Fe_3Si which is magnetic and the particle size and their distribution are favourable. Therefore, right composition is also necessary. If heat treatment is not controlled and timed properly, the secondary non-magnetic phase may appear or particle size may increase which increases coercivity. Figure 9.5 shows the micrograph

wherein secondary particles Fe_2B have appeared and average particle size of both the phases has increased (Srivastava et al. 2013). This resulted in deterioration of soft magnetic properties. These conditions restrict the number of alloy systems in which magnetic amorphous or nanocrystalline metallic glass formation is likely.

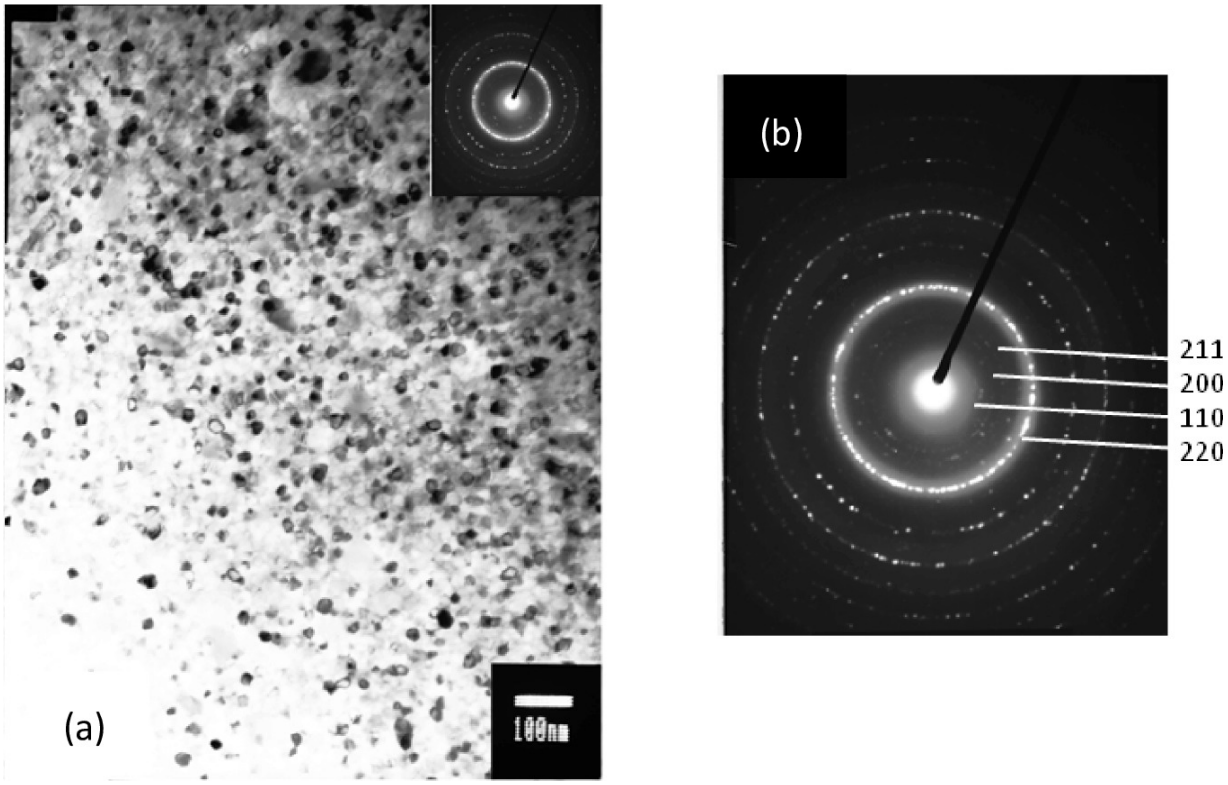

Fig. 9.4 **a** Bright field TEM image obtained from a nanocrystalline $Fe_{68.5}Cu_1Nb_3Si_{18.5}B_9$ metallic glass **b** Electron diffraction pattern from magnetic nanoparticles

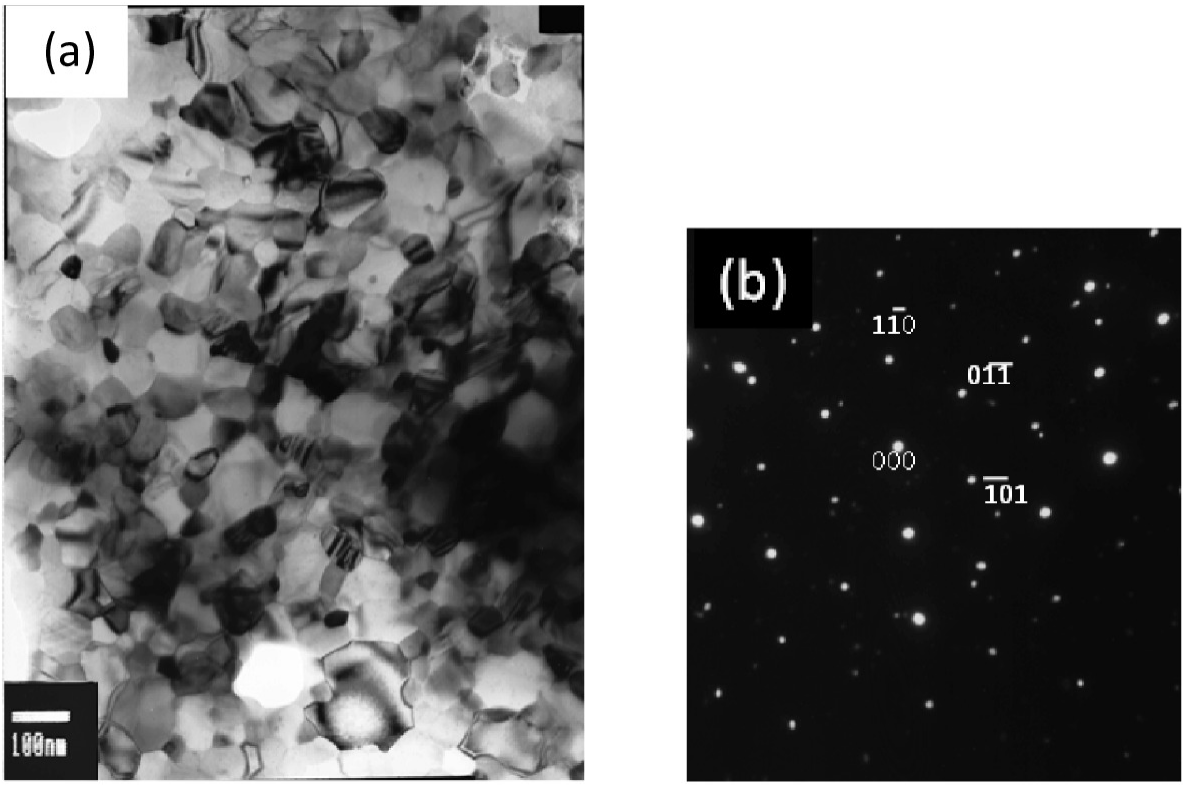

Fig. 9.5 **a** Bright field TEM image obtained from a nanocrystalline $Fe_{68.5}Cu_1Nb_3Si_{18.5}B_9$ metallic glass showing the appearance of nonmagnetic bigger size undesirable particles **b** Electron diffraction pattern from a nonmagnetic nanoparticle

A new area of research interest started with the invention of FINEMET materials ($Fe_{74}Si_{15}B_7Cu_1Nb_3$) by Yoshizawa in 1988, where nanocrystallization of an amorphous precursor resulted in a decrease of coercivity following a D^6 law and an increase in permeability (Yoshizawa et al. 1988). In this composition, addition of Cu enhances the nucleation of nanocrystalline particles (Fe_3Si). The element Nb is added to inhibit the growth of crystalline particles. Herzer emphasized that when the size of nanocrystals within nanocomposites falls below the ferromagnetic exchange length (approximately 50 nm), the neighbouring grains can no longer align with their randomly oriented anisotropies K. A schematic shown in Fig. 9.6 depicts this. As a result, the effective anisotropy is diminished to the statistical mean of the anisotropies within

the magnetically correlated grains. This reduction in effective anisotropy significantly lowers the coercivity as the grain size decreases (Herzer 1989).

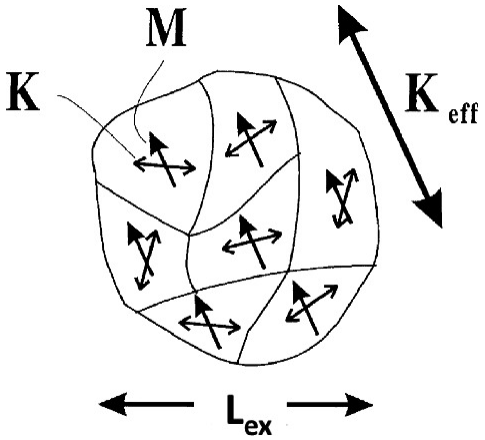

Fig. 9.6 Schematic explaining mechanism of improvement in soft magnetic properties after nanocrystallization. Within a subvolume V having a diameter of Lex, the magnetizations M of the grains aligned parallel to each other, countering the random anisotropies K of the individual grains

This FINEMET nanocrystalline material has saturation magnetization ~1.24 T, low coercivity of ~0.53 A/m, and permeability of ~100,000 @1 kHz. The saturation magnetostriction coefficient is also nearly zero (Yoshizawa et al. 1988). In terms of saturation induction and permeability, amorphous and nanocrystalline magnetic materials have now reached a level of competitiveness with conventionally utilized materials like Fe-3%Si bulk alloys, Fe–Co alloys, and Permalloy. Since the cost is low and its performance is excellent, FINEMET type materials with minor additions of other elements are replacing Permalloy, soft ferrites and Co-based amorphous alloys in many fields.

Over the past few decades, amorphous and nanocrystalline alloys have undergone significant development in terms of their soft magnetic properties, which now surpass those of traditional iron (Fe) and cobalt (Co) bulk alloys based. More recently, nanocrystalline alloys like (Fe,Co)MBCu (M = Nb, Hf, or Zr), known as HITPERM, and FeMBCu (M = Nb, Hf, or Zr), referred to as

NANOPERM, have demonstrated compelling characteristics, including high magnetic inductions ranging from 1.6 to 2.1 Tesla, along with elevated permeability and Curie temperature. Maximum saturation magnetization can be achieved in HITPERM (slightly more than 2 T) followed by NANOPERM and then FINEMET. On the other hand, maximum permeability is achieved in FINEMET followed by NANOPERM and HITPERM (Transactions on Magnetics n.d.; Miglierini et al. 2015; Parsons et al. 2021, Rama et al. 2021). Performance wise, these nanocrystalline materials outperform conventional materials like soft ferrites and silicon steel. Current research on soft magnetic materials mainly focuses on finding out new nanocrystalline composites which are cost effective. Fe based nanocrystalline alloy compositions are being explored on a wide scale as they have the potential of replacing bulk steels. One such example is Fe–Si–B–P–Cu nanocrystalline soft magnetic alloys that can show saturation magnetization similar to that of Si steel, but it has advantage of having very low coercivity when compared with silicon steel. Other systems under considerations are Fe–B–C–Cu, Fe–Co–B and system containing elements Nb, Ta, Zr, and Hf having high melting points. Few researchers have shown interest in magnetic high entropy alloys, however, this still requires active research before it can show competitive magnetic properties (Zhang et al. 2013a).

9.4 Hard Magnetic Materials

Materials that show coercivity in between soft and hard magnets are termed as semi-hard magnets and they are typically used as analog and digital magnetic recording media. Another important class of ferromagnetic material is hard magnetic materials which are also commonly described as permanent magnets. They have large coercivity, and they should possess maximum remnant

magnetization. The figure of merit to characterize the grade of a permanent magnet is the energy product BH_{max} which is the maximum value of the product of magnetic induction, B and H in the second quadrant of the hysteresis loop where B and H are in opposite directions (demagnetizing part). The energy associated with the stray magnetic field generated by a magnet in its surrounding space is equivalent to half of its energy product. Consequently, the energy product of a magnet serves as a measure of its capacity to store magnetostatic energy. Another important parameter in the context of permanent magnet is the dimensionless magnetic hardness defined as

$$\kappa = \sqrt{\left(\frac{K_1}{\mu_o M_s^2}\right)}, \tag{9.7}$$

where K_1, $\mu_{0,}$ and M_s are magnetocrystalline anisotropy constant, the vacuum permeability and the saturation magnetization, respectively. This parameter signifies if a magnet having adequate magnetization M_s can be made in any shape without demagnetizing itself, i.e., ability to resist self-demagnetization (Skomski and Coey 2016). A rule of thumb that is used to qualify a permanent magnet is $\kappa \geq 1$ with the rider of adequate magnetization for practical uses. The importance of this rider can be understood by considering the case of α-$Fe_2O_{3,}$ which can have very large hardness parameters (~eight times greater than a very good permanent magnet $SmCo_5$) but $\mu_0 M_s$ of only 3 mT and hence this Hematite may be a hard magnetic material, but it cannot be used as a permanent magnet.

Permanent magnets are used to produce the magnetic field in a particular open space. The same can be done using electric current in a conductor of suitable shape, however, permanent magnet does the same without any expenditure on electricity. Since the aim of a permanent

magnet is to produce a magnetic field in an open space, it must have a free pole (open circuit). A magnet making a closed magnetic circuit will have no free poles and hence of no practical use as a permanent magnet. In a ferromagnetic material with a pole at the free surface, magnetization has to suddenly vanish (i.e. divergence of M), but to make the divergence of $B = 0$, the magnetic poles act as a source of additional field inside the material known as demagnetizing field H_d which opposes the magnetization and its value depends on the shape of the magnet. Now we shall consider the materials that are used for permanent magnets.

9.4.1 Steel Magnets

Very early design of permanent magnets used this demagnetizing field to their advantage and made permanent magnets only in selected shapes such as bars, needles and horseshoe. For centuries, high-carbon steel magnets were used as compass needles. The best steel magnet contained tungsten, chromium and nearly 40% cobalt with the best energy product of 8 kJ/m^3. All the magnetic steels have energy products of a few kJ/m^3. Magnet steels are no more used. In 1930s, an alloy of $Fe_{58}Ni_{30}Al_{12}$ was discovered which had coercivity twice of the coercivity of the best magnet steel. Several modifications of this alloy have been developed and they are commonly referred as alnicos based on the presence of aluminium, nickel, and cobalt, albeit the measure component is iron in these alloys. Other elements such as Cu, Nb or Ti are also added in the family of alnico alloys (Rehman et al. 2022). A typical alnico magnet consists of elongated/ acicular (contributing towards shape anisotropy) ferromagnetic FeCo phase of nano-size embedded in a nonmagnetic NiAl matrix. However, they are very brittle so often they are cast and imparted

magnetic annealing to develop the required oriented nanostructure by spinodal decomposition. The energy products of different alnico alloys range from 40 to 80 kJ/m^3. Nonetheless, discovery of rare earth magnets and ferrites have replaced alnico in most of the magnetic applications. Since alnico have very high Curie temperatures, they are used in applications where the operating temperature is high or excellent thermal stability of the Fe–Co at room temperature is valued and hence still they are produced in significant amount. It should be noted that the permanent magnetic properties of these alloys resulted because of the shape anisotropy of the single domain particles.

9.4.2 Ferrites

The discovery of $L1_o$ compound CoPt and a ferrimagnetic hexagonal ferrite $BaO.6Fe_2O_3$ broke this barrier of a few selected shapes (shape anisotropy) by utilizing magnetocrystalline anisotropy and thereafter bulk size magnets of any shape are being produced. Now-a-days a family of $SrFe_{12}O_{19}$ hexagonal ferrites are produced extensively being one of the cheapest options available (Breton 2021; Maltoni et al. 2021). Strontium ferrites are generally costlier than Barium ferrites and generally have better properties, especially in terms of coercivity. These ferrite magnets are also referred to as ceramic magnet or hexa-ferrite. However, since these ferrites are ferrimagnetic in nature and include a good fraction of non-magnetic oxygen atoms, they show very small magnetization. At room temperature theses ferrites have saturation magnetization less than that of iron. The commercial ferrites offer energy product of up to 30 kJ/m^3 with a maximum reported value of ~40 kJ/m^3 (Maltoni et al. 2021).

9.4.3 Rare Earth Magnets

In the development of permanent magnets, a breakthrough came with the invention of rare earth magnets which include rare earth elements with either Iron or Cobalt. These magnets show decent magnetization and very high anisotropy so that the magnetic material can be given any shape and still maintain their magnetization. It is known that in the case of Fe, Co, Ni or Mn (3d metals), 3d-orbits have larger spatial extent resulting in the stronger orbital-lattice interaction which causes quenching of orbital angular momentum. Hence, their magnetism is governed by pure spin contribution. On the other hand, single-electron spin–orbit interaction becomes stronger with increasing atomic number Z. Therefore, rare earth elements can provide strong spin–orbit coupling which is required for high magnetocrystalline anisotropy, even though they possess small spontaneous magnetization that is not suitable for any practical use on their own. Therefore, rare-earth magnets encompass elements from both the rare earth group and 3d transition metals, which contribute to their remarkable spontaneous magnetization and notable Curie temperatures. A typical rare earth permanent magnet will have a uniaxial crystal structure (tetragonal, rhombohedral, hexagonal) that produces a large uniaxial anisotropy and its magnetization follows a crystallographic symmetry axis. Most powerful known rare earth magnets contain metals such as Nd and Sm, along with Tb and Dy, and 3d metals such as iron and cobalt.

The first such rare earth magnet $SmCo_5$ was made in 1966. It is an intermetallic and has the hexagonal structure which contributes massive uniaxial anisotropy resulting in an energy product of 160 kJ/m^3 which was much higher than ferrites or alnico. In $SmCo_5$ family energy product of up to 190 kJ/m^3 has been achieved (Koshkaki et al. 2022; Collocott 2016). These magnets can be easily fabricated in

any shape and they have a very high magnetic hardness κ = 4.3 (Koshkaki et al. 2022). Thereafter, another family Sm_2Co_{17} magnet was discovered which could provide energy product up to 260 kJ/m^3. The microstructure of these magnets consists of fine bands of $SmCo_5$ separating the regions of Sm_2Co_{17}. The Sm_2Co_{17} phase has either hexagonal or rhombohedral structures. In case of SmCo5, coercivity is nucleation controlled, whereas in case of Sm_2Co_{17} family, coercivity is due to domain wall pinning. Sm_2Co_{17} magnets show higher magnetization. These magnets are also referred as 2:17 magnets (Yang et al. 2022). Since Co price was high, the magnet was costly and researchers started developing a magnet which would be based on the combination of rare earth elements and iron, as iron is inexpensive and available with ease.

Croat et al. (1984) could produce a new magnetic ternary alloy NdFeB using melt spinning also known as rapid solidification technique followed by annealing to get nanocrystalline material famously recognised as MAGNEQUENCH. Another group Sagawa et al. produced the same ternary hard magnet by traditional methods of intermetallic synthesis (Sagawa et al. 1987). It is recognized as NEOMAX. This new ternary compound $Nd_2Fe_{14}B$ established itself as one of the best high-performance magnet, particularly useful in the laptop computers and compact servers, where small size is the requirement. This composition has Fe and Nd which are cheaper than Co and Sm, respectively, and rare earth content is also lower in this new compound. It has the tetragonal phase and κ was 1.54 (Koshkaki et al. 2022). It has a Curie temperature of ~588 K comparatively lower than SmCo magnets. Extensive study on the control of microstructure and the processing of this magnet to optimize the coercivity led to an achievement of the highest

value of energy product of 474 kJ/m^3 for any laboratory magnet (Matsuura 2006). Till now it is the best hard magnet available. The anisotropy of the ternary compound $Nd_2Fe_{14}B$ is increased by the substitution (2–10 wt%) of heavy rare earth terbium (Tb) or dysprosium (Dy) in place of Nd, though at the cost of slightly reduced magnetization; Mostly Dy because it is cheaper. Co is also sometimes added to increase its Curie temperature and thermal stability. The typical energy product of this family of magnet varies from 160 to 350 kJ/m^3.

9.4.4 Rare Earth Lean or Rare Earth Free Permanent Magnets

The rare earth magnets are very compact and powerful, whereas Ferrites are cheaper, and alnico have the advantage of higher Curie temperature. There is a wide gap in terms of performance and price between rare earth magnet and ferrite/alnico magnets. There is also a risk of supply constraint for Dy and Tb rare earth elements. Therefore, to fill this gap and lower the reliability on rare earth elements, extensive research is being carried out to develop new magnetic materials. Some of the potential candidate materials for permanent magnets will be discussed in the following sections.

The addition of N_2 in $SmCo_{17}$ resulted in improved properties. Active research is being carried out on $Sm_2Co_{17}N_3$, $Sm_2Fe_{17}N_3$ and $NdFe_{11}TiN_x$ based magnets especially towards scaling up, as these are not stable at conventional sintering temperatures because nitrogen is driven off at the required high temperatures (Takagi et al. 2020; Hirayama et al. 2015; Sato et al. 2017). Nevertheless, some oriented and polymer bonded magnets have been used for niche applications (Takagi et al. 2020; Hirayama et al. 2015; Sato et al. 2017). Substituting Nd by Ce in NdFeB magnet to reduce the cost of the magnet has

also attracted scientific interest (Yongxiang and Walton 2017; Hussain et al. 2020).

Development of several rare earth free magnets is also under serious consideration. Mn based magnets such as carbon stabilized $L1_0$-MnAl and hexagonal MnBi compound have shown promising properties (Gabay and Hadjipanayis 2020; Zhao et al. 2019). Magnet made from MnBi ball-milled powders has shown the energy product of 62 kJ/m^3 but its thermal stability above 473 K is still a problem (Cui et al. 2014).

Cost consideration of the magnet has directed the research towards development of iron based magnets such as L10-FeNi and L10-FePt (Obeidat et al. 2022; Rani et al. 2020). Tetragonal FeNi (tetrataenite) is known to have a high magnetization and an artificially produced chemically ordered hard magnetic L10-FeNi phase which has been developed having better property than cosmic meteorites, which is one of the best magnet (Makino et al. 2015). Tetragonal interstitial nitride α''-$Fe_{16}N_2$ are known for high magnetization in thin films. However, in the synthesis of bulk magnet by powder route, achieving good coercivity is challenging (Jian-Ping 2020).

Cobalt based permanent magnets are also being explored. Cobalt nanowires produced via chemical route and then aligned have shown the energy product of 165 kJ/m^3 and with better optimization it may tend towards 350 kJ/m^3 which is expected for 100% density (Anagnostopoulou et al. 2016; Gandha et al. 2014). YCo_5 is another potential candidate for permanent magnet having large anisotropy. Magnet based on this compound prepared using ball milling has shown the energy product of 140 kJ/m^3 (Tozman et al. 2015). Other serious contenders for permanent magnets are based on Co are Zr_2Co_{11} and $HfCo_7$ as they have magnetization comparable to $SmCo_5$

(Zhang et al. 2013b; Balamurugan et al. 2012; Rao et al. 2019; Jun et al. 2018).

9.5 Novel Magnets by Nanoscale Engineering

A new approach of realizing next-generation permanent magnets is also being explored by developing better understanding to engineer magnetism at the nanoscale. In this approach, a two-phase magnetic composite material is designed by combining a soft ferromagnetic phase with large magnetization to a hard ferromagnetic phase with high coercivity at nanoscale. When the size of the soft phase equals or exceeds twice the estimated domain wall thickness of the hard magnetic phase, the nucleation of reversed domains and the formation of domain walls within the soft phase is impeded and hence coercivity increases. This results in the composite with the higher energy product $(BH)_{max}$ than individual soft and hard phases. Such magnetic nanocomposites are referred to as exchange spring magnets. For better results, the hard magnetic phases should be crystallographically aligned. Clearly, the magnetic correlation length which is in nanoscale, controls the desired properties and it is still a challenge to engineer a bulk composite of soft and hard phases on a nanoscale. Researchers are involved in developing composites of rare earth magnets such as $Nd_2Fe_{14}B$ and SmCo with soft magnetic phases such as α–Fe or FeCo phase in the hope of developing a magnet with lower cost and better energy product (Poudyal and Liu 2013; Ngo et al. 2021)

In the context of nanoscale engineering of magnetic nanocomposite material, it is important to mention exchange-biased magnets. When a ferromagnetic layer (FM) is exchanged coupled to an antiferromagnetic layer at the interfaces, a displacement in the hysteresis loop along

the field axis is observed, which is termed as Exchange bias. The exchange interaction at the interface pins the ferromagnetic moments during the reversal process, and hence coercivity increases and an increased $(BH)_{max}$ is observed. In multilayer systems, another interesting phenomenon is Giant Magnetoresistance (GMR), recognized with the Nobel Prize awarded to Fert and Gruenberg in 2007. This GMR effect, initially identified in 1988 within Fe (ferromagnetic)/Cr (nonmagnetic)/Fe (ferromagnetic metal) multilayers, manifests in the thin films with alternating ferromagnetic and non-magnetic layers with the non-magnetic layer being very thin of the order of a few nanometers (Dey and Roy 2021). At specific thicknesses of the non-magnetic layer and in the absence of an external magnetic field, the indirect Ruderman-Kittel-Kasuya-Yosida (RKKY) interaction between adjacent ferromagnetic layers results in an energetically favorable alignment of magnetizations in an anti-parallel configuration. That is the successive ferromagnetic layers exhibit an ordered antiparallel orientation of magnetizations. In such a system, when a magnetic field is applied, a significant change in resistivity (ranging from 10 to 80%) is observed and this is known as GMR. The unique properties of GMR find practical applications, particularly in the hard disk technology. Magnetic materials based on thin films may be useful in spin electronics and magnetic recording applications, but they are not of any practical use as permanent magnets, where one needs to generate stray field as in the gap magnets. Even if bulk magnet could be made based on exchange bias, antiferromagnetic material reduces the magnetization and Curie temperature as the antiferromagnetic phase is mostly based on Manganese. Therefore, most of the research in the development of nanoscale magnetic composite is restricted to the concept of exchange spring magnets.

Till now we have considered bulk magnets. In addition to these magnets, there are possibilities of using low dimensional magnets or molecular magnets as functional materials.

9.6 Low-Dimensional Magnetic Materials

Low-dimensional magnetic materials characterized by their constrained dimensionality and localized magnetic moments, have introduced a wealth of intriguing phenomena that challenge conventional understanding of magnetism and hence offer a fascinating opportunity to explore unique magnetic behaviours and their potential applications. In insulating materials, the magnetic moment is confined to specific atomic sites, and the interactions between these moments are limited to short ranges. This characteristic allows us to create low-dimensional magnetic materials, even if the crystals housing the magnetic atoms possess a three-dimensional structure.

It all began with the Mermin-Wagner theorem, a foundational concept that underlines the limitations of long-range magnetic order in one or two dimensions considering isotropic exchange interactions (Mermin and Wagner 1966). This theorem has initiated extensive investigations into how anisotropy, originating from factors like crystalline structure and dipolar interactions, governs the behaviour of magnetic moments in these confined systems. Unlike ferromagnetism, anti-ferromagnetic interactions exhibit the potential for multiple ground states representing configurations of minimal energy. In a one-dimensional context, the anti-ferromagnetic ground state manifests as an alternating sequence of spins: up, down, up, down, and so forth. However, in two dimensions, the existence of multiple ground states becomes feasible. This

distinctive magnetic behaviour has been identified in minerals possessing crystal stacking arrangements, such as the Kagome lattice or hexagonal lattice showcasing the fascinating complexity inherent to low-dimensional magnetism (Néel 1948).

On the experimental front, the controlled synthesis of artificially layered magnetic materials has led to significant advancements, revealing a wide range of captivating phenomena from a technological perspective, particularly in the fields of communication devices and storage media. In contrast to the conventional ferromagnetic, antiferromagnetic, and ferrimagnetic domains commonly found in bulk magnetic materials, two-dimensional magnetic systems have unveiled intricate domain structures such as stripes, labyrinths, and vortices. These structures have been extensively studied due to their complex magnetic interactions, which result from the interplay of exchange, long-range dipolar, and magneto-crystalline anisotropic interactions (Huang and Clark 2017; Seul and Andelman 1995; Whitehead and De'Bell 1994). For instance, stripe domains emerge as a result of a balance between the increase in exchange energy associated with the formation of domain walls and the reduction in dipolar energy attributed to the interactions of magnetization currents generated at these domain walls (Booth et al. 1995; Ng and Vanderbilt 1995). The discovery of 2D antiferromagnetic behaviour in high-temperature superconductors, such as the compound LaCuO4, has spurred a surge of interest in the realm of two-dimensional magnetism (Huang and Clark 2017). In certain instances, it is feasible to precisely compute the ground state energy, excitation spectra, and thermodynamic properties of magnetic systems that exist in one- and two-dimensional space. The intricate interplay of magnetic interactions within quasi-2D structures has led to the exploration of exotic spin structures like skyrmions, bubbles, and merons,

which show unique properties (Yu et al. 2018; Nagaosa and Tokura 2013). Owing to the inherent stability provided by defects and pinning sites in their topology, skyrmions can be manipulated using a current density that is nearly hundred times lower than what is required for conventional magnetic domains. This remarkable characteristic renders them highly appealing for energy-efficient spintronic applications, including but not limited to ultra-dense storage based on skyrmions, magnetic random-access memory and race track memory (Zhang et al. 2015; Fert et al. 2013).

9.7 Molecular Magnets

Molecular magnetism is another fascinating and rapidly evolving field of research that explores the design, synthesis and the magnetic properties of molecules and molecular complexes. The origins of molecular magnetism can be traced back to the late 1970s when efforts were initiated to develop organic ferromagnetic materials, driven by the notion that organic substances might exhibit metal-like electrical conductivity properties. Unfortunately, these early endeavours yielded only limited success. Consequently, the quest for room-temperature organic ferromagnets remains ongoing (Pokhodnya et al. 2007) with limited success till date. While the prospect of robust ferromagnetic interactions among organic molecules is not inconceivable, the primary challenge lies in arranging them within three-dimensional structures, an essential prerequisite for achieving spontaneous magnetization. Over the past few years, significant progress has been made in understanding and controlling molecular magnetism, which has both fundamental scientific implications and potential applications in areas such as information storage and quantum computing.

One of the most exciting developments in this field is the study of Single-Molecule Magnets (SMMs) or zero-dimensional magnets. These are individual molecules or compounds that can retain spin information over extended durations at very low temperatures, primarily due to the energy barrier hindering their spin reversal. This results in the measurement of a noticeable slow magnetic relaxation (Sessoli et al. 1993; Gatteschi et al. 2006; Woodruff et al. n.d.; Benelli and Gatteschi 2015). The investigation on lanthanide-based Single Molecule Magnets has shown the potential of practical applications for SMMs in fields such as molecular spintronics, data storage devices, and quantum computing (Jiang et al. 2015; McAdams et al. 2017). The long coherence times of certain SMMs make them attractive candidates for qubit storage and manipulation. The tunability of molecular magnets allows for the design of spintronic devices with unique properties. These can revolutionize quantum information processing.

There has been active research on single chain magnets (SCM), a one-dimensional magnet. Similar to Single-Molecule Magnets, the spins tend to align preferentially in one specific direction in SCM displaying Ising-type magnetic anisotropy (Cornia et al. 2006). As mentioned earlier, a 1D system cannot show long range magnetic order at finite temperature. Nonetheless, as the temperature decreases, progressively lengthier sections of the chains experience spin alignment, thus making the relaxation slower and slower (reversal of magnetization becomes difficult). Since this Ising-type magnetic anisotropy can be quite substantial, single-chain magnets (SCM) present a clear advantage over Single-Molecule Magnets (SMM) when it comes to attaining elevated blocking temperatures. This has instigated active research in this field. Molecular magnets are being also explored for their potential use in enhancing MRI contrast agents.

In conclusion, the field of molecular magnetism continues to advance rapidly, driven by interdisciplinary collaborations between chemists, physicists, and materials scientists. The ability to design and manipulate molecular magnets at the nanoscale opens up exciting possibilities for both fundamental research and practical applications, from quantum computing to medical imaging.

9.8 Conclusion

Functional soft magnetic materials are being used in many appliances and in advance devices and equipment in our daily life. Electronic steel and soft ferrite which have been in use extensively over a century now are being replaced by the newest type of soft magnets which are either amorphous or partially nanocrystalline materials. The technological advancement has made these materials to be more efficient, cost effective and less noisy. Current researchers are actively involved in developing cost effective amorphous and nanocrystalline alloy compositions that can be used in wide frequency range and show better soft magnetic properties than existing materials. Permanent magnets are extensively used in power generators and electric motors. Rare earth magnets and ferrites are currently fulfilling all the requirements and related technologies are also quite matured. However, due to uncertainty in the supply of rare earth elements such as Dy and Nd due to geopolitical reasons, researchers are now developing rare earth lean or free magnets which shall be cost effective and compete with existing rare earth magnets. These magnets are aiming to fill the gap between cost-effective hard ferrite magnet and the expensive rare earth permanent magnets. Another focus has been towards making composite magnets using existing rare earth magnet and soft magnets which could perform better than the existing magnets using nanoscale engineering.

Apart from activities towards bulk magnets, low dimensional magnets have shown their importance in understanding the intricates of basics of magnetism. These low-dimensional magnetic materials present intriguing prospects for technological advancement and pave the way for additional exploration and progress. In addition to this, the domain of molecular magnetism is rapidly progressing, fuelled by collaborative efforts across various disciplines, including chemistry, physics, and materials science. The capability to engineer and control molecular magnets at the nanoscale unlocks thrilling opportunities for both foundational research and real-world applications, spanning from quantum computing to medical imaging.

References

Abshinova, M.: Factors affecting magnetic properties of Fe–Si–Al and Ni–Fe–Mo alloys. Procedia Eng. **76**, 35–44 (2014)

Alben, R., Becker, J.J., Chi, M.C.: Random anisotropy in amorphous magnets. J. Appl. Phys. **49**, 1653–1658 (1978)

Anagnostopoulou, E., Grindi, B., Lacroix, L.M., Ott, F., Panagiotopoulos, I., Viau, G.: Dense arrays of cobalt nanorods as rare-earth free permanent magnets. Nanoscale **8**, 4020–4029 (2016)
[PubMed]

Arnold, H.D., Elmen, D.G.W.: Permalloy: an alloy of remarkable magnetic properties. J. Franklin Inst. **195**, 621–632 (1923)

Balamurugan, B., Das, B., Shah, V.R., Skomski, R., Li, X.Z., Sellmyer, D.J.: Assembly of uniaxially aligned rare-earth-free nanomagnets. Appl. Phys. Lett. **101**, 122407–122415 (2012)

Ball David, W.: Maxwell's equations, part I: history. Spectroscopy **26**(4), 16–23 (2011)

Benelli, C., Gatteschi, D.: SMM past and present. In: Introduction to Molecular Magnetism, Wiley-VCH Verlag GmbH & Co. KGaA, pp. 195–215 (2015)

Blundell, S.: Magnetism in Condensed Matter 1st den. Oxford University Press, New York, USA (2001)

Booth, I., MacIsaac, A.B., Whitehead, J.P., De'Bell, K.: Domain structures in ultrathin magnetic films. Phys. Rev. Lett. **75**, 950–953 (1995) [PubMed]

Breton, J.M.L.: Ferrite magnets: properties and applications. Encyclopedia Mater. Techn. Ceramics Glasses **3**, 206–216 (2021)

Collocott, S.J.: Magnetic materials: domestic applications. In: Reference Module in Materials Science and Materials Engineering (2016)

Cornia, A., Fabretti, A.C., Zobbi, L. et al.: In: Winpenny, R. (Ed.), Single-Molecule Magnets and Related Phenomena, Structure and Bonding Book Series, vol. 122, Springer, Berlin, Heidelberg (2006)

Croat, J.J., Herbst, J.F., Lee, R.W., Pinkerton, F.E.: Pr–Fe and Nd–Fe based magnets: a new class of high-performance permanent magnets. J. Appl. Phys. **55**, 2079–2082 (1984)

Cui, J., Choi, J.P., Li, G., Polikarpov, E., et al.: Thermal stability of MnBi magnetic materials. J. Phys. Condens. Matter **26**, 064212–064311 (2014) [PubMed]

Dey, P., Roy, J.N.: Giant Magnetoresistance (GMR). In: Spintronics. Springer, Singapore (2021). https://doi.org/10.1007/978-981-16-0069-2_3

Duwez, P., Lin, S.C.H.: Amorphous ferromagnetic phase in iron-carbon-phosphorus alloys. J. Appl. Phys. **38**, 4096–4097 (1967)

Fert, A., Cros, V., Sampaio, J.: Skyrmions on the track. Nature Nanotech. **8**, 152–156 (2013)

Gabay, A.M., Hadjipanayis, G.C.: MnBi-based magnets prepared from melt-spun alloys: effect of α → β phase transformation during field annealing. J. Magn. Magn. Mater. **516**, 167340–167347 (2020)

Gandha, K., Elkins, K., Poudyal, N., Liu, X., Liu, J.P.: High energy product developed from cobalt nanowires. Sci. Rep. **4**, 5345 (2014) [PubMed][PubMedCentral]

Gatteschi, D., Sessoli, R., Villain, J.: (2006) Molecular Nanomagnets. Oxford University Press, Oxford

Gould, H.L.B., Wenny, D.H.: Supermendur: a new rectangular-loop magnetic material. Electr. Eng. **76**, 208–211 (1957)

Gubanov, A.: Calculation of the energy spectrum for strongly anisotropic crystals. Sov. Phys. Sol. State **2**, 1253–1262 (1960)

Gubanov, A.: Quantum Electron Theory of Amorphous Conductors, pp. 247–257. Springer, Boston, MA (1965)

Hasegawa, R., Azuma, D.: Impacts of amorphous metal-based transformers on energy efficiency and environment. J. Magn. Magn. Mater. **320**, 2451–2456 (2008)

Herzer, G.: Grain structure and magnetism of nanocrystalline ferromagnets. IEEE Trans. Magn. **25**, 3327–3329 (1989)

Hirayama, Y., Takahashi, Y.K., Hirosawa, S., Hono, K.: $NdFe_{12}N_x$ hard-magnetic compound with high magnetization and anisotropy field. Scr. Mater. **95**, 70–72 (2015)

Huang, B., Clark, G., et al.: Layer-dependent ferromagnetism in a van der Waals crystal down to the monolayer limit. Nature **546**, 270–273 (2017) [PubMed]

Hussain, M., Liao, X., Akram, R., Milyutin, G., Khan, M., Liu, Z.: Elevated temperature behavior of rapidly quenched La/Ce substituted nanocrystalline NdFeB alloys with various compositions. J. Alloy. Comp. **845**, 156292–156297 (2020)

Inoue, A., Shinohara, Y., Gook, J.S.: Thermal and magnetic properties of bulk Fe-based glassy alloys prepared by copper mold casting. Mater. Trans. JIM **36**, 1427–1433 (1995)

Jiang, S.D., Wang, B.W., Gao, S.: Advances in lanthanide single-ion magnets. In: Gao, S. (ed.) Molecular Nanomagnets and Related Phenomena, pp. 111–141. Springer, Berlin Heidelberg, Berlin, Heidelberg (2015)

Jian-Ping, W.: Environment-friendly bulk Fe16N2 permanent magnet: Review and prospective. J. Magn. Magn. Mater. **497**, 165962 (2020)

Jun, C., Matthew, K., Lin, Z., Fei, L., Alexander, G., George, H., Balasubramanian, B., Sellmyer, D.: Current progress and future challenges in rare-earth-free permanent magnets. Acta Mater. **158**, 118–137 (2018)

Kong, F.L., Han, Y., Wang, X.H., et al.: SENNTIX-type amorphous alloys with high Bs and improved corrosion resistance. J. Alloy. Compd. **707**, 195–198 (2016)

Koshkaki, S.R., Allahyari, Z., Oganov, A.R., et al.: Computational prediction of new magnetic materials. J. Chem. Phys. **157**, 124704 (2022)

Krishnan Kannan, M.: ‘Hard and Soft Magnets’ in Fundamentals and Applications of Magnetic Materials, Oxford, online end, Oxford Academic, 476–518 (2016)

Lingxiang, S., Kefu, Y.: Composition design for Fe-based soft magnetic amorphous and nanocrystalline alloys with high Fe content. Mater. Des. **189**, 108511 (2020)

Lu, Z., Chen, X., Liu, X. et al.: Interpretable machine-learning strategy for soft-magnetic property and thermal stability in Fe-based metallic glasses. npj Comput. Mater **6**, 187 (2020)

Makino, A., Sharma, P., Sato, K., Takeuchi, A., Zhang, Y., Takenaka, K.: Artificially produced rare-earth free cosmic magnet. Sci. Rep. **5**, 16627 (2015) [PubMed][PubMedCentral]

Maltoni, P., Sarkar, T., Barucca, G., et al.: Tuning the magnetic properties of hard−Soft SrFe12O19/$CoFe_2O_4$ nanostructures via composition/interphase coupling. J. Phys. Chem. C **125**, 5927–5936 (2021)

Matsumoto, H., Urata, A., Yamada, Y., et al.: “MPCG” for large-current using ultra low loss dust material “SENNTIX” formed by one-piece construction. NEC Tech. J. **2**, 66–70 (2007)

Matsumoto, H., Urata, A., Yamada, Y., et al.: Novel FePBNbCr glassy alloys “SENNTIX” with good soft-magnetic properties for high efficiency commercial inductor cores. J. Alloy. Compd. **509**, S193–S196 (2011)

Matsuura, Y.: Recent developments of Nd–Fe–B sintered magnets and their applications. J. Magn. Magn. Mater. **303**, 344–347 (2006)

McAdams, S.G., Ariciu, A.M., Kostopoulos, A.K., Walsh, J.P.S., Tuna, F.: Molecular single-ion magnets based on lanthanides and actinides: design considerations and new advances in the context of quantum technologies. Coord. Chem. Rev. **346**, 216–239 (2017)

McHenry, M.E., Willard, M.A., Laughlin, D.E.: Amorphous and monocrystalline materials for applications as soft magnets. Prong. Mater. Sci. **44**, 291–433 (1999)

Mermin, N.D., Wagner, H.: Absence of ferromagnetism or Antiferromagnetism in One- or Two-dimensional isotropic heisenberg models. Phys. Rev. Lett. **17**, 1133–1136 (1966)

Miglierini, M., Pavlovič, M., Procházka, V., et al.: Evolution of structure and local magnetic fields during crystallization of HITPERM glassy alloys studied by in situ diffraction and nuclear forward scattering of synchrotron radiation. Phys. Chem. Chem. Phys. **17**, 28239–28249 (2015) [PubMed]

Nagaosa, N., Tokura, Y.: Topological properties and dynamics of magnetic skyrmions. Nature Nanotech **8**, 899–911 (2013)

Néel, L.: Propriétées magnétiques des ferrites; Férrimagnétisme et antiferromagnétisme. Annales De Physique (Paris) **3**, 137–198 (1948)

Ng, K.-O., Vanderbilt, D.: Stability of periodic domain structures in a two-dimensional dipolar model. Phys. Rev. B **52**, 2177–2183 (1995)

Ngo, H.M., Lee, G., Haider, S.K., Pal, U., Hawari, T., Kim, K.M., Kim, J., Hae-Woong, K., Soo, K.Y.: Chemical synthesis of Nd2Fe14B/Fe–Co nanocomposite with high magnetic energy product. RSC Adv. **11**, 32376–32382 (2021) [PubMed][PubMedCentral]

Obeidat, A., Aladerah, B., Qaseer, M.K.: Computational study of magnetic properties of L10 ordered FeNi and FePt binary alloys. J. Magn. Magn. Mater. **559**, 169501–169509 (2022)

Parsons, R., Ono, K., Li, Z., Kishimoto, H., Shoji, T., Kato, A., Hillde, M.R., Suzukia, K.: Prediction of density in amorphous and nanocrystalline soft magnetic alloys: a data mining approach. J. Alloy. Comp. **859**, 157845–157848 (2021)

Pokhodnya, K.I., Lefler, B., Miller, J.S.: A Methyl Tricyanoethylenecarboxylate-based room-temperature magnet. Adv. Mater. **19**, 3281–3285 (2007)

Poudyal, N., Liu, J.P.: Advances in nanostructured permanent magnets research. J. Phys. D Appl. Phys. **46**, 043001–043023 (2013)

Rama, B.S., Paul, A.K., Kulkarni, S.V.: Soft magnetic materials and their applications in transformers. J. Magn. Magn. Mater. **537**, 168210–168213 (2021)

Rani, P., Kashyap, M.K., Singla, R., Thakur, J., Reshak, A.H.: Magnetism and magnetocrystalline anisotropy of tetragonally distorted L10-FeNi: N alloy. J. Alloy. Comp. **835**, 155325–155326 (2020)

Rao, N.V.R., Nagendra, M.V., Ninawe, P., Babu, D.A., Chary, V.R., Mathur, R.P.: Structural and magnetic properties of nanocrystalline Zr–Co–Nb–Si–B rare earth free permanent magnets fabricated by spark plasma sintering. J. Magn. Magn. Mater. **476**, 329–333 (2019)

Su, R., Chen, W., Ruibiao, Z., Haihua, L., Shaoxiong, L., Zhong, M., Munan, Y., Qingzheng, J., Jun, W., Zhenchen, Z.: Tailoring the magnetic properties and microstructure of Alnico 8 magnets by various Ti contents and processing conditions. Intermetallics **143**, 107486-7 (2022)

Sagawa, M., Hirosawa, S., Yamamoto, H., Fujimura, S., Matsuura, Y.: Nd–Fe–B permanent magnet materials. Jpn. J. Appl. Phys. **26**, 785–802 (1987)

Sato, T., Ohsuna, T., Yano, M., Kato, A., Kaneko, Y.: Permanent magnetic properties of $NdFe_{12}N_x$ sputtered films epitaxially grown on V buffer layer. J. Appl. Phys. **122**, 053903–053905 (2017)

Sessoli, R., Gatteschi, D., Caneschi, A., Novak, M.A.: Magnetic bistability in a metal-ion cluster. Nature **365**, 141–143 (1993)

Seul, M., Andelman, D.: Domain shapes and patterns: the phenomenology of modulated phases. Science **267**, 476–483 (1995)
[PubMed]

Silveyra, J.M., Ferrara, E., Huber, D.L., Monson, T.C.: Soft magnetic materials for a sustainable and electrified world. Science **362**, eaao0195 (2018)

Skomski, R., Coey, J.M.D.: Magnetic anisotropy -How much is enough for a permanent magnet? Scr. Mater. **112**, 3–8 (2016)

Srivastava, A.P., Srivastava, D., Dey, G.K.: A study on microstructure, magnetic properties and kinetics of the nanocrystallization of $Fe_{40}Ni_{38}B_{18}Mo_4$ metglass. J. Magn. Magn. Mater. **306**, 147–155 (2006)

Srivastava, A.P., Srivastava, D., Sharma, S.K., et al.: Understanding microstructural evolution and soft magnetic properties in nanocrystallized metallic glass Fe68.5Cu1Nb3Si18.5B9. J. Nanopart. Res. **15**, 1357–1414 (2013)

Supermalloy: A new magnetic alloy. Nature **161**, 554 (1948)

Suryanarayana, C., Inoue, A.: Iron-based bulk metallic glasses. Int. Mater. Rev. **58**, 131–166 (2013)

Takagi, K., Soda, R., Jinno, M., Yamaguchi, W.: Possibility of high-performance $Sm_2Fe_{17}N_3$ sintered magnets by low-oxygen powder metallurgy process. J. Magn. Magn. Mater. **506**, 166811–166817 (2020)

Tozman, P., Venkatesan, M., Zickler, G., Fidler, J., Coey, J.M.D.: Enhanced energy product in Y–Co–Fe magnets intermediate between Nd–Fe–B and ferrite. Appl. Phys. Lett. **107**, 032405–032415 (2015)

Wang, F., Inoue, A., Han, Y., et al.: Soft magnetic Fe–Co-based amorphous alloys with extremely high saturation magnetization exceeding 1.9 T and low coercivity of 2 A/m. J. Alloy. Compd. **723**, 376–384 (2017)

Whitehead, J.P., De'Bell, K.: Stability of striped phases in two-dimensional dipolar systems. J. Phys. Matter. **6**, L731–L734 (1994)

Wieserman, W.R., Schwarze, G.E., Niedra, J.M.: Magnetic and electrical characteristics of Supermalloy thin tape toroidal cores. 37th Intersociety

Energy Conversion Engineering Conference, pp. 311–312 (2002)

Woodruff, D.N., Winpenny, R.E.P., Layfield, R.A.: Lanthanide single-molecule magnets. Chem. Rev. **113**, 5110–5148

Yang, Q., Liu, Z., Gao, X., Wu, H., Zhu, C., Cheng, W., Ma, Y., Chen, R., Yan, A.: Prolonged ordering process induced higher segregation of copper in 2:17 type SmCo magnets. J. Alloy. Comp. **924**, 166463 (2022)

Yongxiang, Y., Walton, A., et al.: REE recovery from end-of-life NdFeB permanent magnet scrap: a critical review. J. Sustain. Metall. **3**, 122–149 (2017)

Yoshihiko, O., Masaaki, K., Atsuhito, H.: Recent development of non-oriented electrical steel sheet for automobile electrical devices. J. Magn. Magn. Mater. **320**, 2430–2435 (2008)

Yoshizawa, Y., Oguma, S., Yamauchi, K.: New Fe-based soft magnetic alloys composed of ultrafine grain structure. J. Appl. Phys. **64**, 6044–6046 (1988)

Yu, X.Z., Koshibae, W., Tokunaga, Y., et al.: Transformation between meron and skyrmion topological spin textures in a chiral magnet. Nature **564**, 95–98 (2018)
[PubMed]

Zhang, J., Chang, C., Wang, A., et al.: Development of quaternary Fe-based bulk metallic glasses with high saturation magnetization above 1.6 T. J. Non-Cryst. Solids **358**, 1443–1446 (2012)

Zhang, Y., Zuo, T., Cheng, Y., et al.: High-entropy alloys with high saturation magnetization, electrical resistivity, and malleability. Sci. Rep. **3**, 1455 (2013a)
[PubMed][PubMedCentral]

Zhang, W.Y., Li, X.Z., Volloppolly, S., et al.: Magnetism of rapidly quenched rhombohedral Zr2Co11-based nanocomposites. J. Phys. D Appl. Phys. **46**(2013), 135004–135005 (2013b)

Zhang, X.C., Ezawa, M., Zhou, Y.: Magnetic skyrmion logic gates: conversion, duplication and merging of skyrmions. Sci. Rep. **5**, 9400–9408 (2015)
[PubMed][PubMedCentral]

Zhao, S., Wu, Y., Wang, J., Jia, Y., Zhang, T., Zhang, T., Chengbao, J.: Realization of large coercivity in MnAl permanent-magnet alloys by introducing nanoprecipitates. J. Magn. Magn. Mater. **483**, 164–168 (2019)

© The Author(s), under exclusive license to Springer Nature Singapore Pte Ltd. 2024
R. S. Ningthoujam, A. K. Tyagi (eds.), *Handbook of Materials Science, Volume 2*, Indian Institute of Metals Series
https://doi.org/10.1007/978-981-97-4646-0_10

10. Origin of Magnetism, Synthesis, Characterization and Perspective Application of Magnetic Graphene

Mohit Kumar Singh[1], Sunil Kumar[1] and Ranjan K. Sahu[1] ✉
(1) CSIR-National Metallurgical Laboratory, Jamshedpur, 831007, India

✉ **Ranjan K. Sahu**
Email: rksahu@nmlindia.org

Keyword Graphene – Magnetic graphene – Magnetism

10.1 Introduction

Graphene is a novel carbon allotrope with two dimensions, an atomic scale, and a honeycomb crystal lattice. The structural units of graphene and other crystalline carbon allotropes like graphite, carbon nanotubes, and fullerenes are quite similar to one another. Graphene can be viewed as a single sheet of graphite based on its structure. In other words, graphite is formed by parallel stacking graphene sheets with an inter-planner distance of 0.335 nm. Similarly, with the discovery of graphene, it was determined that carbon nanotubes are made by rolling

graphene into 1D cylinders and fullerene is formed by wrapping graphene into zero dimensions (Fig. 10.1). All of these allotropes have covalent bonds connecting the carbon atoms, and sp^2 hybridization creates sigma (σ) and pi (π) bonds between the carbon atoms. These allotropes demonstrate a wide variety of variations in their physical properties despite having similar bonds. In fact, graphene has several qualities that are far superior to those of the parent substance from which it is extracted. For instance, graphene exhibits isotropic qualities while graphite exhibits anisotropic electrical properties (Novoselov et al. 2004, 2005; Castro Neto et al. 2009; Lee et al. 2008; Ezawa 2007). In addition, graphite is a soft substance, whereas graphene is the strongest substance ever discovered, being 300 times stronger than steel. Additionally, at room temperature, graphene has 100 times greater heat conductivity than graphite. The research community is extremely interested in unravelling the secret of graphene's disparate features, understanding the underlying mechanism, and utilizing it for cutting-edge uses of carbon allotropes. Contrary to graphite allotrope, graphene does not naturally occur; as a result, it is a synthetic allotrope. In order to attain the improved qualities, a number of ways have been documented in the literature to synthesize graphene allotrope and optimize the process. Despite the outstanding qualities of graphene, all of its outside electrons are exactly coupled to form σ and π bonds, making it naturally nonmagnetic. In order to use graphene for cutting-edge applications, every effort is made to break the symmetric bonds in graphene. It will release unpaired electrons and produce net spins. When the periodic spins on the graphene plane are close enough to interact with one another, magnetic clusters or magnetic ordering can occur. In fact, it has been shown by certain researchers that the magnetic state may be manipulated by

applying an external magnetic field that is aligned either in the plane of the graphene or out of it. In contrast, the intrinsic magnetism of magnetic materials without spin–orbit coupling can only be controlled when the external magnetic field is oriented in the same direction as the magnetism. This finding suggests that graphene does indeed have spin–orbit coupling. As a result, prior discussing the formation of magnetism in graphene, we briefly covered the underlying theory for magnetism in any kind of material.

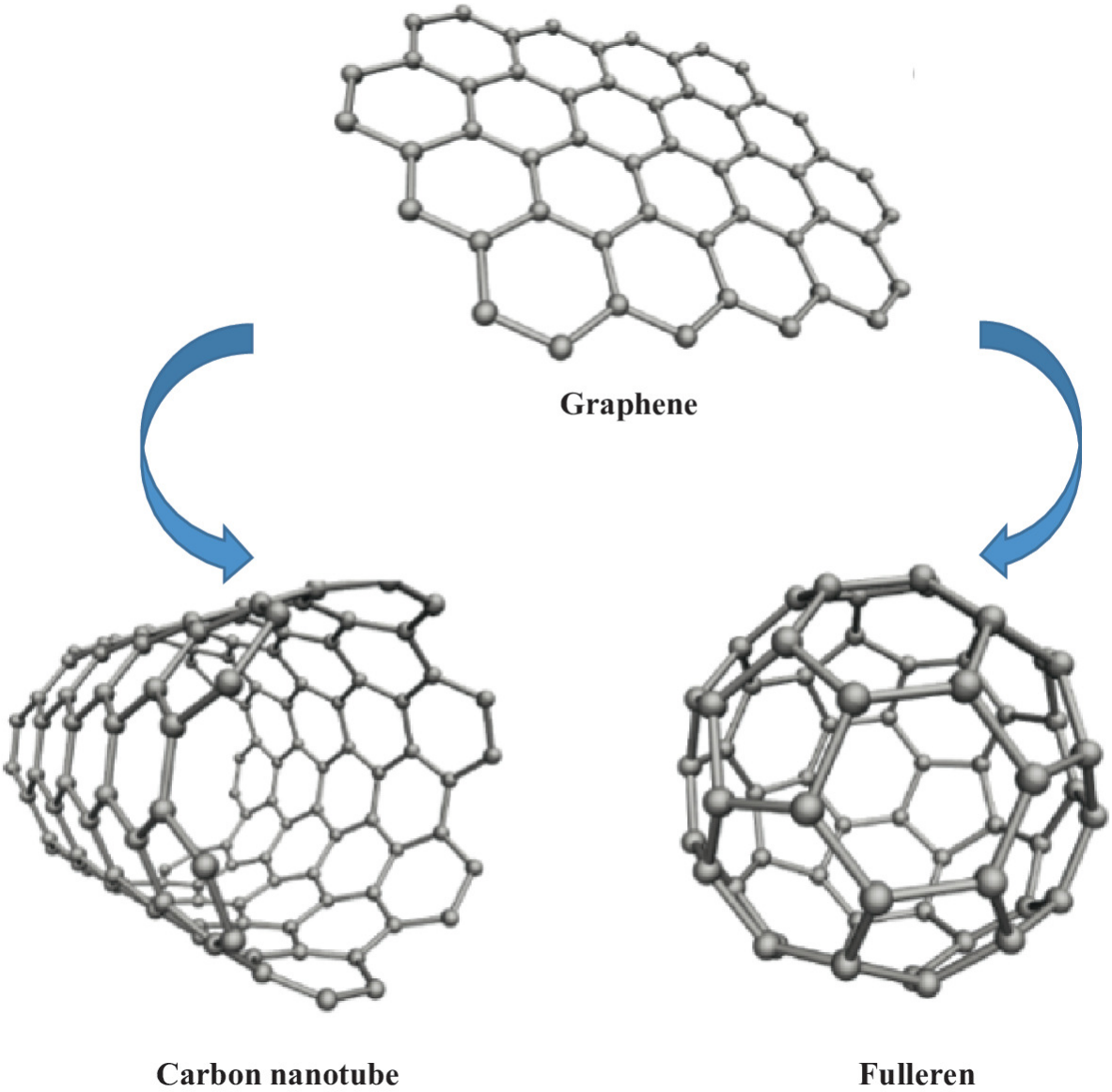

Fig. 10.1 Schematic diagram representing production of the structures of other carbon allotropes such as carbon nanotube and fullerene through rolling and wrapping of graphene's structure

10.2 Basic of Magnetism

In a magnetic substance, unpaired electrons are the primary source of magnetism. The electron's rotation around its own axis is what generates the spin magnetic moment. Additionally, the orbital motion of the electron results in an orbital magnetic moment. As a result, the net magnetic moment of the atom is influenced by both the spin magnetic moment and the orbital magnetic moment (Fig. 10.2). The quantity of unpaired electrons directly affects the magnitude of the spin magnetic moment. However, the orbital magnetic moment is quenched in some materials, its contribution in those situations is negligible. Again, the sort of exchange interactions between the magnetic moments of atoms determines the macroscopic magnetic properties. The positive exchange interaction favours magnetic moment parallel alignment, while the negative exchange interaction favours magnetic moment anti-parallel alignment. Furthermore, the degree of magnetic moment alignment is determined by the magnitude of the interaction. In ferro and para magnetic materials, the sign of exchange interaction is positive. However, in the case of anti-ferromagnetic materials, it is negative. The empirical relationship $E = -J_{12}\ S_1.S_2$ can also be used to illustrate how the exchange interaction depends on the type of magnetic material. The two nearby magnetic moments tend to align anti-parallel for energy minimization when the J value is negative, increasing the potential energy. The potential energy decreases when J is positive, which tends to align the magnetic moments parallel. So, unpaired electrons can be utilized to explain the magnetic characteristics of all materials, including organic materials.

The use of band theory has also been frequently used to discuss materials' magnetic properties (Fig. 10.3). This model was developed by Stoner. An atom's magnetic moment is entirely controlled by the amount of overlap between the spin-up and spin-down bands, which is entirely controlled by exchange energy. For instance, the two bands totally overlap in diamagnetic materials, whereas they only partially overlap in ferro and paramagnetic materials. In fact, polarization is used to determine how much of these two bands overlap. Therefore, temperature has an impact on the degree of polarization, which in turn has an impact on the magnetization of the material.

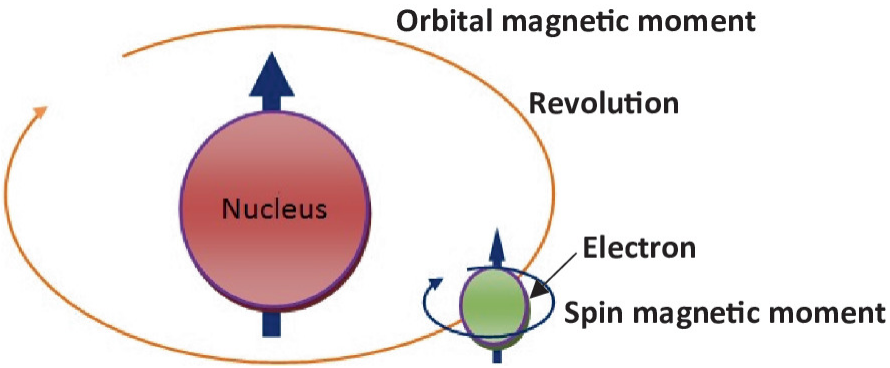

Fig. 10.2 A schematic representation of the origin of an atom's spin and orbital magnetic moment

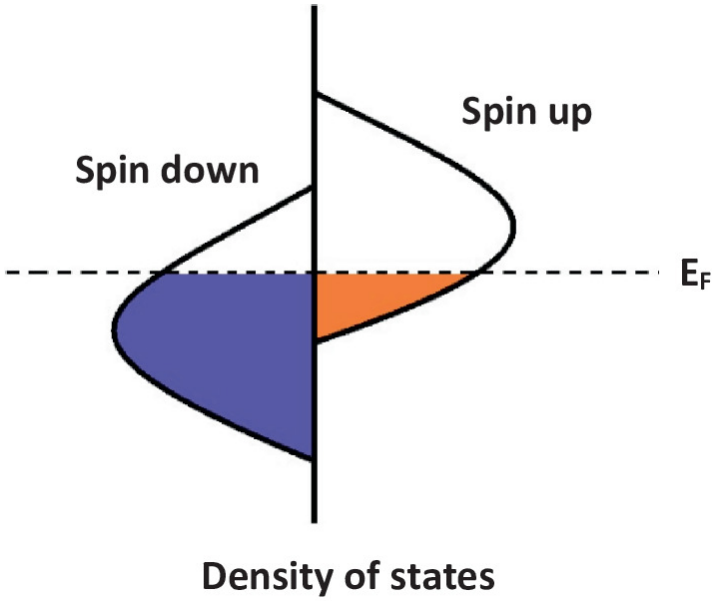

Fig. 10.3 A diagrammatic representation of magnetism's origin by band theory

The three basic types of exchange interactions that are used to characterize a material's magnetism are direct exchange, super-exchange, and double exchange interactions. The super-exchange and double exchange interactions mediate magnetism when an anion separates the atomic orbitals of two metal centres, whereas the direct exchange interaction mediates magnetism when the atomic orbitals of two metal centres are directly overlapping. The exchange integral can result in ferromagnetic, antiferromagnetic, or ferromagnetic outcomes depending on the symmetry and occupancy number of the overlapped orbitals. The Goodenough-Kanamori-Andorson (GKA) empirical rule states (Goodenough 1963) that (a) interactions of 180° with partially two filled d orbitals are anti-ferromagnetic, and (b) interactions of 180° with one partially filled orbital and another empty orbital or filled orbital with another half-filled orbital initiate ferromagnetic interaction (Fig. 10.4).

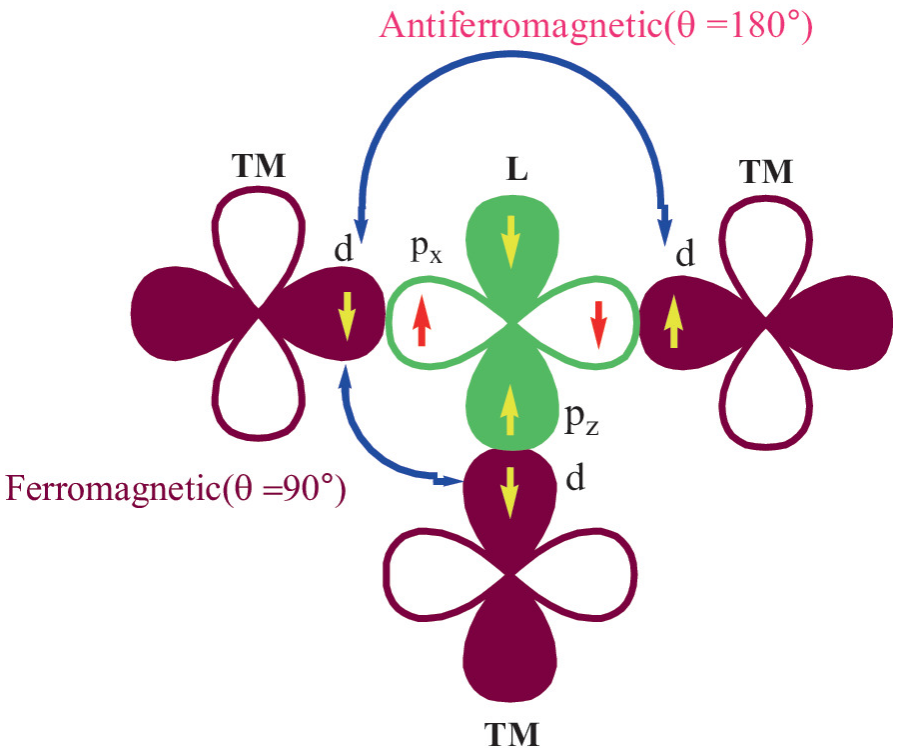

Fig. 10.4 A representation of the magnetic interaction between two cations that are 180° and 90° separated due to anion. The cation's magnetic moment is aligned antiparallel at an angle of 180° and parallel at a 90° angle

Furthermore, the extent of orbital overlaps and the degree of electron hopping determine the strength of super-exchange. In other words, as the angle between the cation and the anion decreases from 180°, the strength of the anti-ferromagnetic interaction weakens and shifts toward the ferromagnetic interaction. Contrarily, one can consider super-exchange interaction to be a subset of double exchange interaction. In order for the super-exchange interaction to mediate magnetism through double exchange, the following requirements must be satisfied: (a) two separate metal centres must have different oxidation states; (b) two different oxidation states must have equivalent oxidation and reduction potentials; and (c) the spin of the delocalized electron and the local atomic magnetic moment must have the same sign. As a result, materials having a twofold exchange interaction induce ferromagnetic interaction (Fig. 10.5). A material can, in

fact, have both super-exchange and double-exchange interactions. Which interaction dominates the others ultimately determines the macroscopic magnetic properties of super-exchange and double-exchange mediated materials.

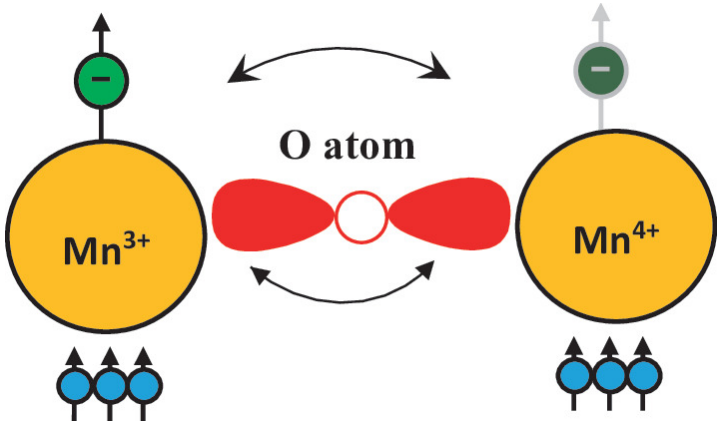

Fig. 10.5 A schematic representation of the double exchange magnetic interaction model between Mn^{+3} and Mn^{+4} ions

10.3 Origin of Magnetism in Graphene

Carbon atoms with sp^2 connections arranged hexagonally in a honeycomb lattice build up the single atomic layer known as graphene. However, according to the most recent report, graphite with up to ten layers can be referred to as graphene. Graphene can be represented as a structure of fused benzene rings with nearby carbon atoms replacing the hydrogen atoms. Each sp^2 hybridized carbon atom in the plane overlaps head-to-head to produce a strong covalent π-bond that provides strength to the graphene structure (Fig. 10.6). The π-bond is formed when half-filled p orbitals perpendicular to the plane of sp^2 hybridized carbon atoms overlap laterally. Because all of the valence electrons are involved in bond formation and there are no unpaired electrons, magnetism in graphene is not

expected. However, under some conditions, theπ -electrons can be disrupted, allowing magnetism to be induced in graphene. Some of the conditions that cause graphene to induce magnetism are listed below (Fig. 10.7).

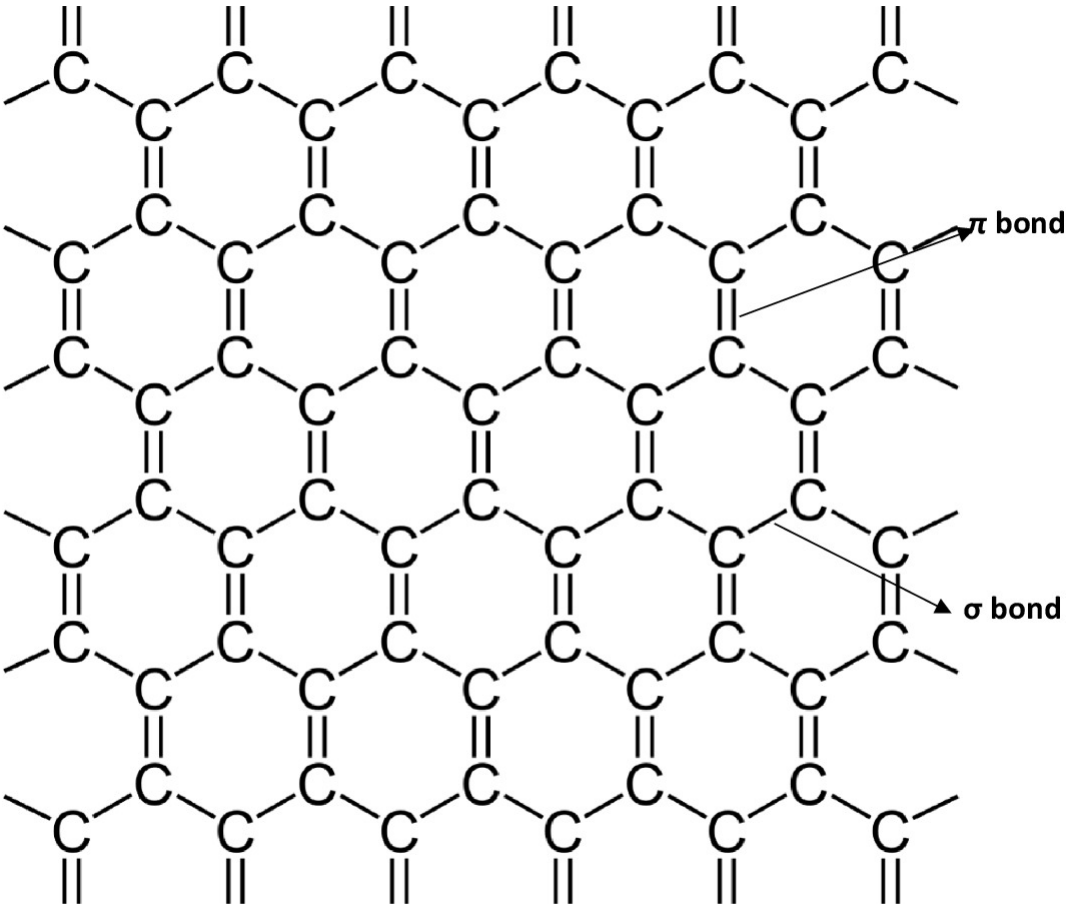

Fig. 10.6 A diagram illustrating graphene's chemical bonding

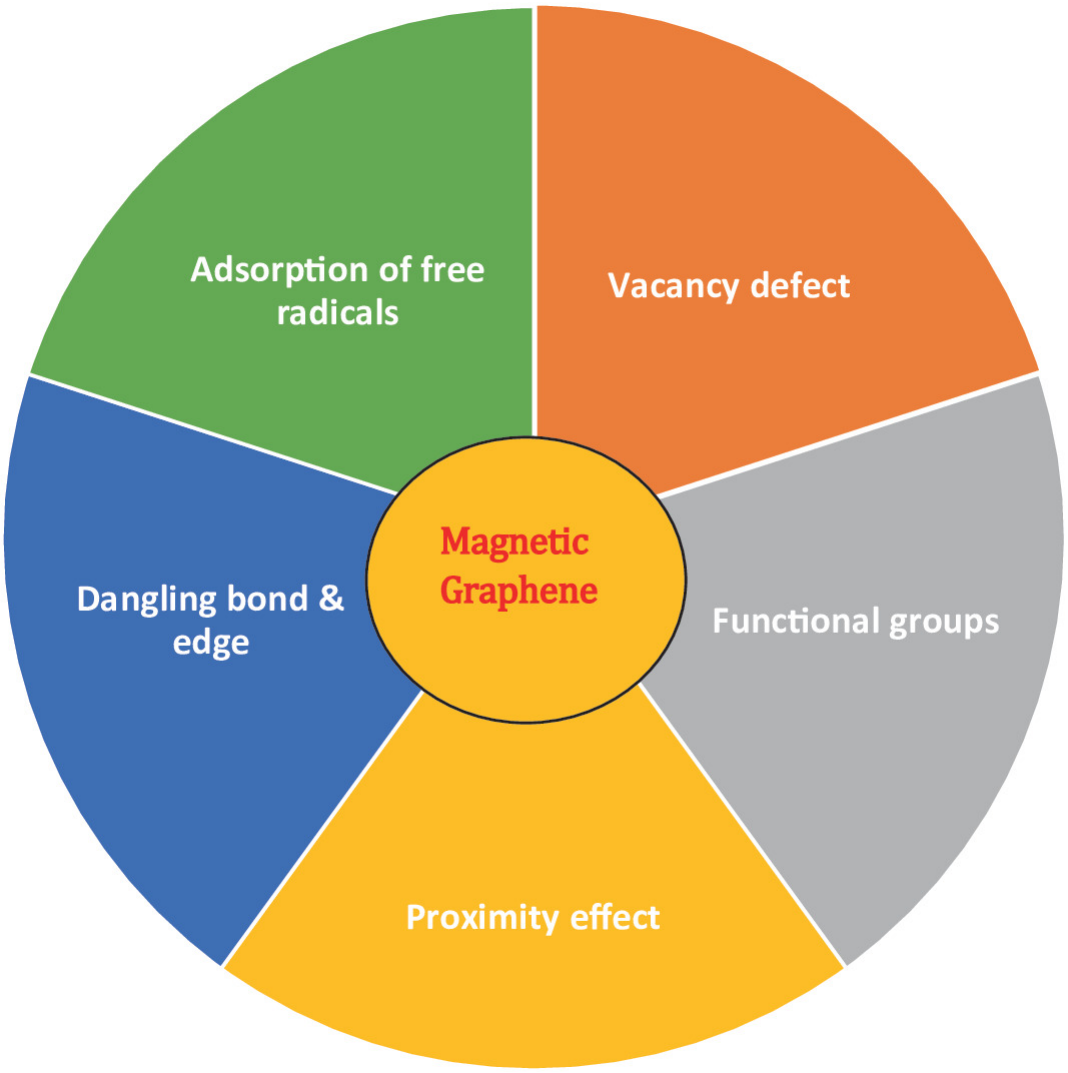

Fig. 10.7 A schematic representation of the entities that make graphene magnetic

10.3.1 Magnetism of Graphene by Adsorption of Free Radicals

Lin et al. theoretically investigated the effect of aromatic radicals on the magnetism of graphene. They conducted a theoretical investigation of the low-coverage adsorption of aromatic radicals onto graphene. The pure graphene is covered in the adsorbed aromatic radicals like.

methoxyphenyl, phenyl, or nitrophenyl. The reason for choosing these radicals is because the nitryl group in nitrophenyl serves as an electron acceptor, whilst the

methoxy group in methoxyphenyl functions as an electron provider. Phenyl, however, is situated between two electron donor–acceptor systems. Graphene is a material with a zero bandgap. However, radical adsorption results in a band gap and two spin-dependent midgap states. The location is both below and above pure graphene's Fermi energy level. The occurrence of two spin bands at two different locations produces a net magnetic moment (Lin et al. 2015a). Additionally, using density functional theory, Pan et al. investigated the magnetism of armchair graphene nanoribbons attached with O, CH_2, or NH radical groups. CH_2 has the strongest magnetism of the three radical groups evaluated, with a magnetic moment of $2\mu_B$per group. Magnetism is shown to be obtained from unsaturated states on C atoms towards the edges and in radical groups. On the other hand, no spin polarization occurs in the ribbons with NH radicals (Pan and Yang 2011). According to these studies, the induction of magnetism in graphene is very selective to radicals that have been adsorbed.

10.3.2 Magnetism of Graphene by Vacancy Defect

The vacancy defect is caused by atoms missing from the crystal lattice, and the number of absent atoms determines the size of the defect. In some situations, the crystal structure may collapse due to the instability of surrounding atoms produced by defects. Furthermore, the formation of defects in crystal lattices results in imperfections in the surrounding atoms, resulting in magnetism in the material. Yazyev et al. investigated into the origins of graphene magnetism induced by single carbon atom defects (Yazyev and Helm 2007). They investigated two types of defects: hydrogen chemisorption and vacancy defects. Depending on the defect concentration, calculated magnetic moments

correspond to 1 μ_B for each hydrogen chemisorption defect and 1.12–1.53 μ_B for each vacancy defect (Fig. 10.8). Furthermore, depending on whether the defects correspond to one or more hexagonal sublattices of the graphene lattice, the interaction between the magnetic moments is either ferromagnetic or antiferromagnetic. Indeed, Lehtinen et al. showed that additional hydrogen adsorption on the vacancy can destroy the magnetism (Lehtinen et al. 2004).

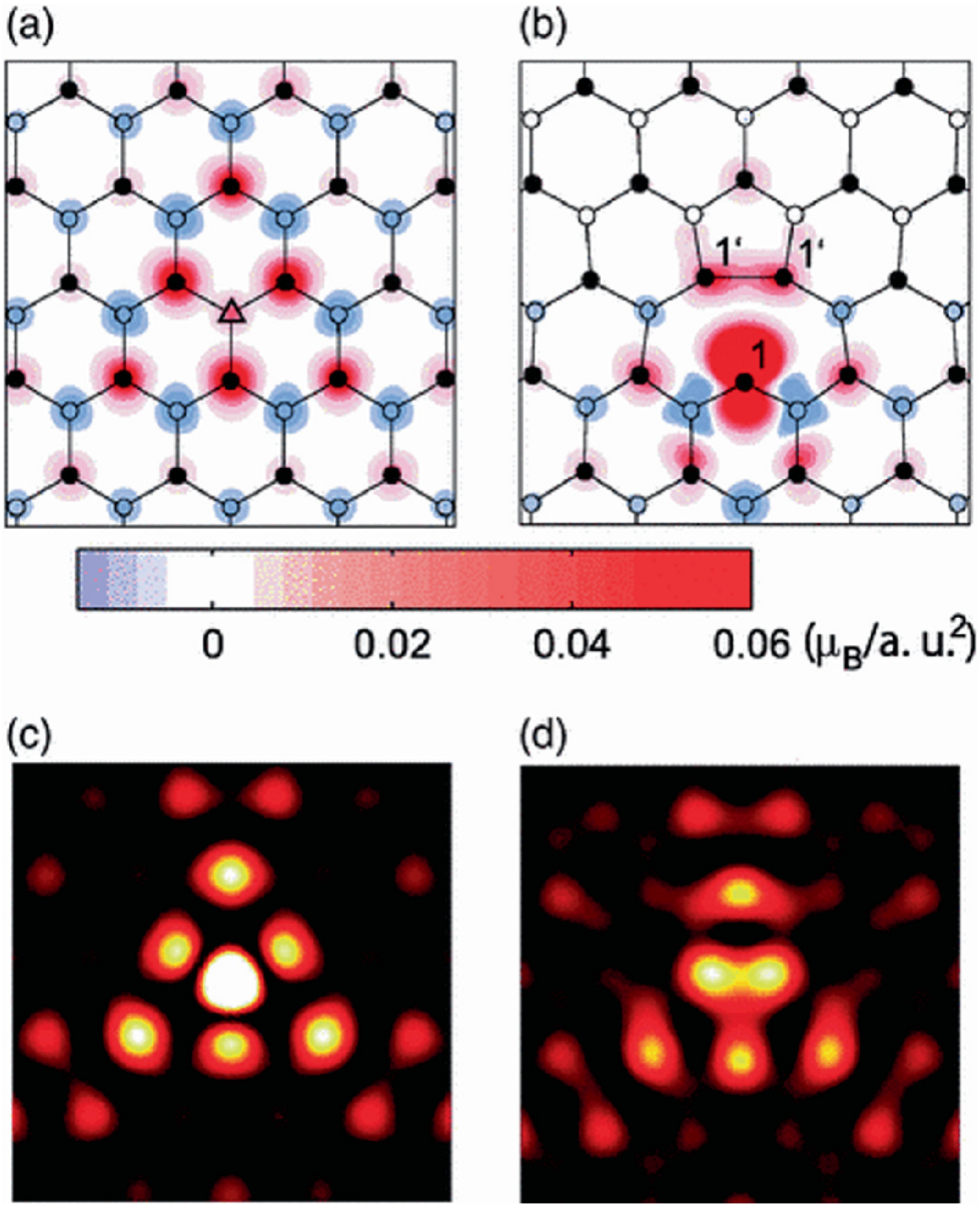

Fig. 10.8 The schematic representation of the spin density projections of **a** the hydrogen chemisorption defect and **b** the vacancy defect in the sublattice on the graphene plane is shown. **c**, **d** illustrate simulated STM images of the defect structure, respectively.

Reproduced from Ref. (Yazyev and Helm 2007)

In contrast, Zhang et al. demonstrated that the presence of nitrogen around a vacancy can produce larger macroscopic magnetic signals than a single carbon vacancy (Zhang et al. 2007). Additionally, the carbon vacancies

formed during the adsorption of foreign elements provide a highly helpful method for controlling the magnetic properties of graphene. According to Nair et al., the magnetic of defect graphene can also be altered by the application of voltage. Utilizing molecular doping, they altered the carrier concentration using aniline as an electron dopant and nitric acid (HNO_3) or NO_2 gas as hole dopants. They found that an electric field can modify the magnetic properties of graphene that has been doped with holes. They also underlined the finding of a dual genesis for vacancy magnetism. Defect graphene's magnetic properties are governed by both dangling bonds and itinerant magnetism (Nair et al. 2013).

10.3.3 Magnetism of Graphene by Dangling Bond, Edge and Surface Morphology

By creating nanoholes, Li et al. looked at how dangling bonds affected the magnetic properties of graphene oxide (GO) nanosheets. GO with more nanoholes (MHGO) and fewer nanoholes (LHGO) were generated on graphene oxide nanosheets. The number of dangling bonds in GO increased as the number of nanoholes increased. As the density of nanoholes on GO rose, GO's magnetic property also increased. In addition, more dangling connections led to magnetic interaction between spin units, which changed paramagnetism GO into ferromagnetism (Li et al. 2020a). Joly et al. revealed spin magnetism for chemical vapour deposition-produced few-layer graphene nanoribbons after characterizing them using electron-spin resonance and near-edge x-ray absorption fine structure. For the clean sample, the acquired data indicate a prepeak below the peak near the Fermi level, indicating the presence of additional electronic states near the Fermi level. Furthermore, the strength of this prepeak decreased with increasing annealing temperature and disappeared after

annealing above 1500 °C. The annealing-temperature-dependent behaviour of the prepeak was closely paralleled by the electron-spin resonance spectra, which confirmed the presence of localized spins. This study backs up the presence of a magnetic edge state produced by open nanographene edges (Joly et al. 2010). Singhbabu et al. demonstrated the magnetic properties of bubble decorated graphene oxide generated by heating a shellac biopolymer coated quartz substrate at 900 °C in an Ar atmosphere (Singhbabu et al. 2015). These findings show that controlling the surface morphology of graphene oxide can induce magnetic properties.

10.3.4 Magnetism of Graphene by Functional Groups

Spin polarized density functional theory was used by Li et al. to investigate the mechanism of magnetic coupling of monovalent and divalent adsorbates decorated graphene (Li et al. 2009). They discussed that monovalent adsorbate introduce localized states due to the breaking of π-bond and then the electron transfers to adatoms. The π-electron system become polarized due to the electron–electron interaction. The two adjacent sublattices orient oppositely. According to Lieb's theorem, the unsymmetric values of spin up and spin down of two adjacent sublattices make the system ferromagnetic. Experimental results also reveal that the magnetism in graphene is originated from the π-electrons. They also conclude that the monovalent adatoms introduce local magnetic moment at high adsorption concentration. On the other hand, the addition of divalent adatoms are capable to induce room temperature ferromagnetic ordering in graphene. Additionally, Lee et al. have demonstrated that epoxy (-O-) groups can produce the magnetic in graphene (Fig. 10.9) (Lee et al. 2015). They employed first-principles calculations and correlated with

the experimental data to comprehend the origin of magnetism. They also varied the epoxy content from 17 to 34% and observed that the magnetic moment increases as the epoxy content increases. They also presented the first-principles theoretical data considering low content and high content of epoxy groups on the graphene structures. They argued that the C–C bond length gets decreased to 1.47 Å, which is smaller than the C–C bond length (1.52 Å) when the graphene sheet contains low percentage of epoxy groups. Therefore, more unpaired spins reside over the oxygen atoms of epoxy groups. The Hund's coupling mediates the spins alignment that leads to long range ferromagnetic ordering. Density functional theory was used by Langer et al. to investigate the impact of the functional groups F, –SH, $–NH_2$, $–CH_3$, $–BH_3$, and $–BH_2$ on the magnetic properties of graphene (Langer et al. 2019). They observed that the size and propensity of the functional groups to form hydrogen bonds affect the stability of the graphene derivative. For instance, due to hydrogen bonding, graphene with -OH and -NH attachments are far more stable than graphene with -SH attachments. Magnetic ordering is produced by super-exchange contact, which is mediated by these functional groups. They also used the relationship $k_BT/|J| = 0.3797$, where $J = \Delta E/2z$, z is coordination number, to compute the magnetic transition temperature. It was noted that the ΔE value is higher for those derivatives had greater overlap between the orbitals as the super-exchange coupling becomes effective. According to Tang et al., the -OH functional group can provide a stable magnetic moment of up to 217 μ_B for every 1000 OH groups (Tang et al. 2015). Additionally, they have demonstrated that even at 900 °C, this magnetic moment is sustained. They discussed about potential magnetism-generating mechanisms. One of the causes of the magnetic moment in the basal plane of the graphene sheet could be

the cluster formation $(OH)_7$. According to the theoretical prediction, the $(OH)_7$ cluster has the capacity to produce a magnetic moment of 5 μ_B. As a result, it is hypothesized that cluster formation is what causes the magnetism in the basal plane. They also noticed that the measured maximal magnetic moment is still less than the theoretical value of 1 μ_B per single OH group. This could be because some of the −OH groups do not contribute to the net magnetic moment of the graphene sheet. Sun et al. showed that magnetism can be induced in graphene by substituting the functional groups SH, OH, COOH, and NH_2. They also showed that diamagnetism, paramagnetism, and ferromagnetism coexist at $T = 5$ K in graphene substituted by SH, OH, and COOH. At room temperature, the magnetic moment is observed to be in the order $SH > OH > COOH$, showing that the induced magnetic moment is dependent on the kind of substituted functional group (Sun et al. 2014). Tuek et al. investigated the magnetic properties of sp^3 functionalized graphene with F and OH groups at ambient temperature (Tuček et al. 2017). They analyzed the density of states using spin-polarized DFT to better understand the origins of ferromagnetism and to support the experimental evidence. They concluded that OH groups are essential in establishing and sustaining a magnetically ordered state up to room temperature.

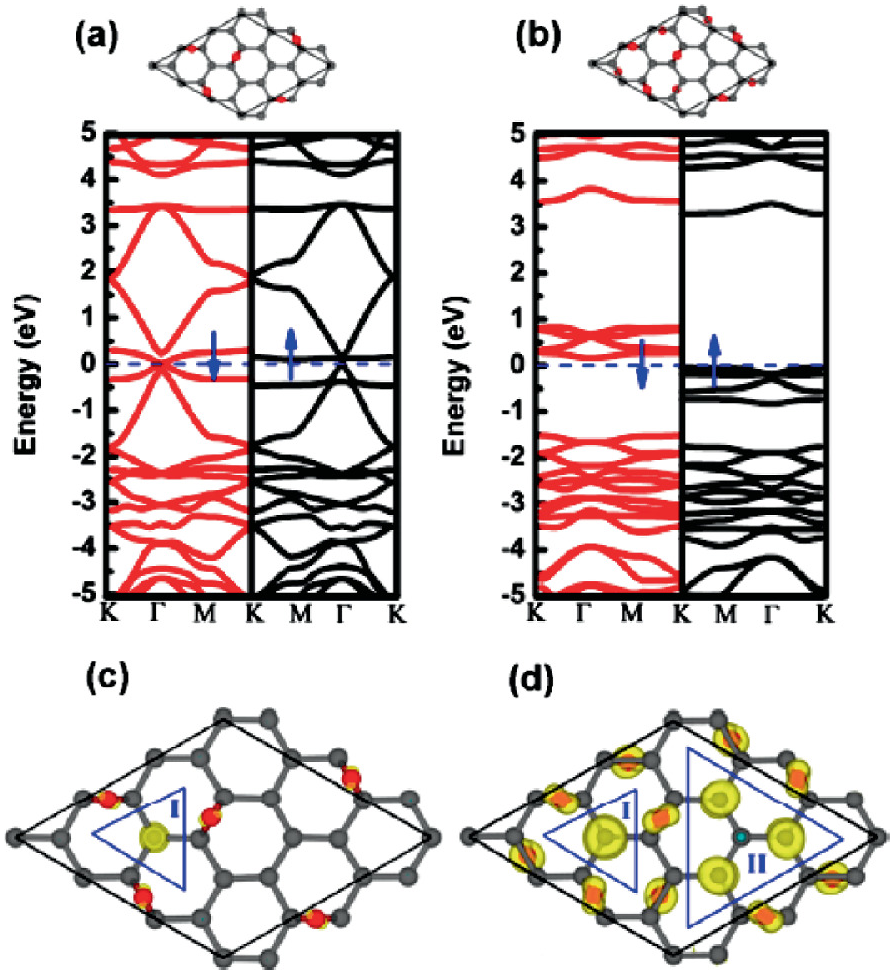

Fig. 10.9 **a** Two GO structures with epoxy functional groups have different band structures and spin densities. The magnetic moments calculated for **a**, **b** are 0.02 and 4 μ_B, respectively. Spin densities are plotted with yellow coloured regions in (**c**) and (**d**). The atoms of carbon and oxygen are grey and red, respectively.

Reproduced from Ref. (Lee et al. 2015)

10.3.5 Magnetism of Graphene by Proximity Effect

A graphene and chromium tribromide ($CrBr_3$) heterostructure's magnetic proximity effect was studied by Behera et al. using first-principles simulations (Behera et al. 2019). The electronic structure of sandwiched materials controls the proximity effect brought on by spin-dependent interlayer coupling. Such an action leads to up to a 63.6% increase in the spin polarization of the graphene orbital

and an increase of 8% in the magnetic moment in the heterostructure. Spin–orbit interactions caused by proximity have also been seen during the integration of graphene with the ferromagnetic semiconductor EuO. The results suggest a magnetic transition at $T_C \sim 220$ K, which is much higher than EuO's Curie temperature of 69 K (Averyanov et al. 2018). Furthermore, Karpiak et al. studied the effect of magnetic proximity on the heterostructure of the magnetic insulator $Cr_2Ge_2Te_6$ and graphene (Karpiak et al. 2020). The ferromagnetic exchange interaction is induced between two graphene layers, according to this study. The results suggest that long-range ferromagnetic ordering is caused by the interaction of spin-polarized d orbitals and graphene's orbitals. Furthermore, adding a gate to the Co/Pt/Gr system improves proximity-induced spin polarization in graphene and its gate control (Bosnar et al. 2020). It has been also demonstrated that the magnetic features of graphene can be improved by placing it over a multiferroic substrate. Furthermore, first principles simulations with and without spin–orbit coupling show that the spin-dependent electronic structure of graphene is heavily influenced by both magnetic order and electric polarization in the underlying $BiFeO_3$ (Wu et al. 2017).

10.4 Methods to Produce Magnetic Graphene

10.4.1 By Ion-Irradiation Method

Irradiation is an efficient method for producing defect-induced magnetic graphene (Ney et al. 2011; Sepioni 2013). When intense radiations collide with graphene, target atoms are displaced, resulting in interstitial sites. Furthermore, the "knock-on" collision removes a carbon

atom from the graphene lattice, resulting in a vacancy in the graphene sheet. As a result, collision of intense radiation has the potential to generate both vacancies and interstitials. Those interstitials that form around the vacancy combine to form a Frenkel pair. The energy, on the other hand, allows the void to migrate far away from the impact location. As a result, a vacancy forms in the non-collided region. It may generate multi-vacancies defects under high irradiation. The electronic properties of graphene are unaffected by interstitial carbon atoms. Therefore, only interstitials do not induce magnetic properties. However, the magnetic properties are induced by vacancies caused by unsaturated bonds in the neighbouring carbon atoms. The atoms near the vacancy reconstructs for stabilization of the graphene lattice, called Jahn–Teller distortion. The reconstructed structure's C–C bond distance is 2.1 Å, which is lower than the unconstructed structure's (2.46 Å). The rearranged structure results in the formation of a pentagon with one unsaturated bond, which creates a magnetic moment of $\sim 1 \mu_B$ around the vacancy. In this method, the number density and dimension of defects in the graphene sheet can be controlled by choosing the right irradiation parameters such as ion type, ion dosage, energy and temperature.

10.4.2 Chemical Method

Magnetic graphenes can also be chemically produced using covalent and non-covalent functionalization methods.

10.4.2.1 Non-covalent Approach

Non-covalent modification refers to the attachment of small molecules or large molecules to the surface of graphene and GO through noncovalent forces like the π–π-interaction, electrostatic interaction, hydrogen bonding, and hydrophobic interaction. Because these interactions

are generally weak, molecules tend to cluster or may be eliminated during functionalized material processing. The noncovalent modification, as opposed to covalent modification, will reinforce the original physical and chemical properties of graphene and GO, as well as expand their new physical and chemical qualities. It will also protect the structure of graphene or GO from damage. Furthermore, non-covalent modification is more promising than covalent modification since the resulting products are easier to handle and the modification can do a lot to preserve the desirable features of graphene. The several associated forces involved for non-covalent functionalization are discussed below.

Hydrogen Bonding

Hydrogen bonding arises from the attraction between the positively charged hydrogen nucleus and the negatively charged atom with lone pair electrons. It’s a strong type of bond that doesn’t involve sharing electrons, known as a noncovalent bond. Graphene oxide (GO) has oxygen-containing groups on its surface, like hydroxyl, epoxy, and carboxyl groups. These groups easily interact with other substances that have polar groups, forming hydrogen bonds. This property makes it easy to modify GO’s properties. For instance, by utilizing hydrogen bonding, we can functionalize GO, enhancing its abilities for various applications. Additionally, the oxygen-containing groups on GO can interact with polar polymers such as polyaniline, polyurethane, polyamide, and inorganic metal oxide nanoparticles. This interaction allows for the creation of magnetic graphene without needing to form chemical bonds, providing a straightforward approach to tailor graphene’s properties.

Electrostatic Interaction

The oxygen-based groups in graphene oxide (GO) make its water solution carry a charge, and this charge varies depending on the pH level. To modify GO's properties, it needs to interact with substances that have an opposite charge through electrical attraction. Additional modifications typically occur after this initial interaction. For instance, Wang et al. decorated Fe_3O_4/rGO magnetic composite by in situ polymerization process by polypyrrole, a conducting polymer having positively charged N atoms (Wang et al. 2015). They added pyrrole monomers to a solution containing Fe_3O_4/rGO magnetic composite and cetyltrimethylammonium bromide (CTAB). The monomers were quickly attracted to the composite's surface by electrostatic forces which was accompanied by a type of interaction called "π-π" interactions.

π–π Stacking Interaction

Graphene has a six-membered carbon ring as its basic structure. Each carbon atom's three electrons make a σbond, and the outermost electron produces a largeπ bond. For the magnetic graphene, large conjugated GO can interact with molecules containing benzene, pyridine, or imidazole rings to achieve noncovalent modification of GO via π–πstacking interaction.

10.4.2.2 Covalent Approach

The term "covalent approach of GO" primarily refers to the chemical reaction that occurs when organic small molecules or macromolecules are combined with oxygen-containing groups (hydroxyl, epoxy, and carboxyl groups) on the surface of GO to form covalent bonds. Furthermore, the GO structure comprises conjugated C=C double bonds, and the molecule can be attached to the GO's base plane via addition reaction. Because covalent bond modification

is linked by covalent bond, the resulting product has relatively stable chemical characteristics and is difficult to remove. Graphene, on the other hand, is resistant of covalent bonding with other molecules. As a result, reactive species such as diazonium salts, nitrenes, diazirines, and others are required for covalent functionalization of pristine graphene. This section examines briefly the involvement of these species in the covalent functionalization of pristine graphene.

Diazonium Salts

One of the widely used techniques for covalently functionalizing conductive and semiconducting materials is diazonium chemistry. Free radicals are believed to play a role in the functionalization reaction. After the nitrogen gas is removed, the graphene functions as an electron transfer agent, giving an electron to the aryl diazonium ion to create an aryl radical. It is thought that the production of aryl radicals close to the graphene is caused by the strong reactivity of diazonium salts in conjunction with concerted N_2 cleavage. This ensures that the radical reacts with the graphene quickly rather than diffusing into the solution. Because the diazonium compounds break down quickly, it is advised that they be newly made and used right away.

Nitrene

When exposed to light or heat, the azide group breaks down into nitrogen compounds and a reactive singlet nitrene molecule. Researchers have extensively investigated the behaviour of singlet nitrene and related nitrenes, such as phenyl nitrene, over several decades. Interestingly, singlet phenyl nitrenes don’t readily form bimolecular adducts with alkenes; instead, they isomerize into benzazirine solutions at room temperature, eventually

converting into cyclic ketenimines. This conversion process can be hindered by using substances like ethanethiol or diethyl amine. In the absence of an amine, cyclic ketenimines combine with phenyl azides to form tar-like macromolecules. Nitrene chemistry has become a powerful tool for chemically modifying carbon nanotubes, graphene, and fullerenes, and it has found effective application in graphene modification. The literature reports various azides' capability to functionalize graphene.

Diazirines

Three-membered heterocyclic rings called azirines contain an sp^3 carbon atom linked to an azo group. Similar to azides, diazirines break down when heated or exposed to radiation, producing the electron-deficient carbene species and molecular nitrogen. If there are no opposing reaction pathways, the highly reactive carbene can perform high yielding insertion reactions to CH bonds and [1 + 2] cycloaddition reactions to C=C bonds. Due to the lack of intramolecular rearrangement of the matching carbene, 3-Aryl 3(trifluoromethyl)diazirine becomes one of the most common diazirine compounds. Diazirines were initially created as photo-affinity labels for proteins, but they have since found use in surface modification and the creation of useful materials. It should come as no surprise that diazirines are also used to functionalize diamond, fullerene, carbon nanotubes, and, more recently, reduced graphene oxide.

10.4.2.3 In-Situ Reduction Method

Majority magnetic graphene was produced through in-situ metal precursor reduction on the surface of GO. Electrostatic interactions are used to bind the functional groups of GO with metal precursors like $FeCl_2$, $Fe(acac)_3$,

$FeCl_3$, etc. The metal precursors are then reduced by agents like NaOH, hydrazine hydrate, amines, ascorbic acid, citric acid, and $NaBH_4$ into magnetic nanoparticles on the surface of GO. For instance, Fe_3O_4-Pd/RGO nanocomposites were created by in situ reducing $FeCl_2$ and $PdCl_2$ with NaOH at pH 13.0 (Li et al. 2020b). By combining magnetic nanoparticles with graphene oxide by a high-temperature synthesis of ferric triacetylacetonate with GO in 1-methyl-2-pyrrolidone, Shen et al. developed a one-step method for producing GO- magnetic nanoparticle composites (Shen et al. 2010).

10.5 Some Important Techniques to Characterize Graphene and Its Derivatives

10.5.1 Raman Spectroscopy

The G, D, and 2D peaks distinctive characteristics serve as the Raman spectrum's fingerprint for identifying graphene and its derivatives. These peaks are the result of inelastic light scattering brought on by interactions between electrons and phonons. It is crucial to understand the phonon dispersion in graphene in order to comprehend the scattering phenomenon (Saito et al. 2002; Mafra et al. 2007; Piscanec et al. 2007). In graphene, there are two atoms per unit cell, resulting in six phonon dispersion branches; three of these branches are optical and the remaining three are acoustic modes. These vibrational modes can also be separated into in-plane and out-of-plane groups. Since the out of plane vibrations in graphene and a derivative of it are not Raman active, they are not covered in this article. Once more, longitudinal and transverse types are used to categorize the in-plane vibrational modes. These divisions are based on the atomic vibrational

directions, which are parallel and perpendicular to the vector connecting two carbon atoms in the unit cell (Maultzsch et al. 2004; Malard et al. 2009; Ferrari and Basko 2013). The E_{2g} mode of vibrations, which are two active in-plane modes of vibration in the point, come from the TO and LO modes of vibrations, respectively. The A_1 mode is a further mode seen in the K point (Ferrari 2007; Dresselhaus et al. 2008; Casiraghi et al. 2007). The observed peaks in the spectra of graphene and its derivatives are caused by these modes of vibration in the Γ and K points. Due to the in-plane stretching vibration of C=C, the scattering from the E_{2g} mode of vibration results in the G peak. The Raman spectrum's D peak is caused by the breathing mode of vibration of six carbon atoms in a hexagonal ring, which scatters light from A-symmetry. The overtones are represented by the additional peaks 2D, D + D, and D + D. In the subsequent section, the origin and significance of individual peaks are discussed.

10.5.1.1 G Peak

As was previously mentioned, the G peak results from the scattering of the E_{2g} mode of vibration. If the molecule belongs to the sp^2 bonded carbon allotrope, the G peak in the Raman spectroscopy will be seen. The G peak for graphene can be found at 1580 cm^{-1} (Saito et al. 2002; Mafra et al. 2007; Piscanec et al. 2007; Maultzsch et al. 2004; Malard et al. 2009; Ferrari and Basko 2013; Ferrari 2007; Dresselhaus et al. 2008; Casiraghi et al. 2007). However, in defects-containing graphene, the G peak shifts to a longer wavelength and becomes saturated at 1600 cm^{-1}. In addition, when the remaining aliphatic chains are connected with graphene derivatives, the G peak shifts past 1600 cm^{-1} and rises as high as 1690 cm^{-1}. As a result, a careful examination of the G peak can reveal

important details about the synthesis of graphene and its derivative as well as details about defects.

10.5.1.2 D Peak

The D peak is produced by scattering from the A_1 mode of vibration (Maultzsch et al. 2004; Malard et al. 2009; Ferrari and Basko 2013; Ferrari 2007; Dresselhaus et al. 2008; Casiraghi et al. 2007). The D peak is caused by the six membered rings' breathing mode of vibrations. In the Raman spectra, the D peak is located at 1350 cm^{-1}. However, because there are no defects in perfect graphene, the responsible modes are inactive and the D peak does not show up. The nature of the defect is revealed by the D peak's shape and FWHM. As a result, the analysis of the D peak provides information on the nature and extent of defects. A defect related peak at 1620 cm^{-1}, which is known as the D peak, also appears in the spectra. Because the D peak is close to the G peak, the two peaks overlap, and the D peak appears as a shoulder of the G peak (Ferrari and Basko 2013).

10.5.1.3 2D Peak

The 2D peak is an overtone of the D peak, and its spectral features are critical in distinguishing graphite, graphene, and their derivatives. In fact, the 2D peak's notable characteristics, such as FWHM, position, and intensity with respect to the G peak of the spectrum, provide information about the quality of graphene and its derivatives in terms of number of layers and defects. In the case of graphene, for example, the intensity of the 2D peak is four times that of the G peak. However, in the case of doped and chemically synthesized graphene, the intensity of the 2D peak is significantly reduced, and a broad peak appears at this position (Ferrari and Basko 2013; Yang et al. 2009; Guoxiu et al. 2008; Kudin et al. 2008). Other complementary

techniques are used in this case to confirm the formation of graphene. Table 10.1 summarizes the Raman peak position of G, D and 2D peaks.

Table 10.1 Summarizes the position of G, D and 2D peaks in the Raman spectrum of graphene and its derivative

Peak	Position (cm^{-1})
G	1580–1600
D	1350
2D	2700

10.5.2 UV–Vis Spectroscopy

UV–Vis spectroscopy provides useful information about the extent of oxidation and reduction during graphene and its derivatives synthesis (Williams et al. 2008; Li et al. 2008; Choi et al. 2002; Stankovich et al. 2007; Guo et al. 2011; Xu et al. 2011; Zhuo et al. 2013). The absorption peak of GO appears at 229 nm. When GO is reduced, the absorption maximum shifts to a longer wavelength region due to an increase in conjugation length. When all of the attached functional groups of GO are removed completely, the absorption maximum appears at 279 nm. As a result, the absorption maximum position is used as a reference data to identify the functional groups and their content in graphene derivatives. Table 10.2 summarizes the peak positions of GO and rGO.

Table 10.2 Summarizes the UV–Vis peak position of GO and rGO

Sample	Peak position (nm)
GO	229–230
r-GO	235–279

10.5.3 X-ray Diffractometer

According to the XRD data of graphene, the most intense graphite peak corresponding to the (002) plane appears around 26°. Furthermore, in the case of GO, the peak shifts to a lower 2θ value, and the position of the (002) peak shifts close to 26° upon reduction (Moon et al. 2010; Cote et al. 2009; Pei et al. 2010). Because the introduction of oxygen functional groups increases the interlayer spacing between the layers, the d spacing increases and thus the 2θ value shifts to a lower angle in GO. The extent of oxidation in the oxidized sample can also be quantified by the amount of shifting in the peak position. Because the oxygen functional groups are removed during reduction, the peak shifts from the lower 2θ angle to the higher 2θ angle. The peak position of the (002) peak appeared nearly at the same position as that of graphite with a broadened peak in the case of few layers graphene. As a result, XRD is a very useful technique for characterizing graphene and its derivative production. Table 10.3 summarizes the characteristic peak position of graphite, GO, and rGO for the Cu Kα X-ray source.

Table 10.3 Summarizes the 2θ value of graphite, GO and rGO recorded using Cu K_{α} X-ray source

Sample	2θ (in degree)	Peak feature
Graphite	26–27	Sharp peak
GO	9–10	Broad
rGO	24–27	Broad

10.5.4 X-ray Photoelectron Spectroscopy

The spectral characteristics of the C1s and O1s XPS peaks are used to determine the type and quantity of oxygen functional groups present in the graphene network. Furthermore, it provides useful information for understanding the extent of doping and the type of networking structure formed with the dopants. When

oxygen functional groups are attached to the carbon network, the binding energy positions of the C1s peak shift towards higher binding energy. Table 10.4 summarizes the change in C1s binding energy caused by the attachment of functional groups such as double bonds (C=C), hydroxyl (-OH), epoxy (-O-), carbonyl (>C=O), and carboxylic (-COOH) (Ganguly et al. 2011; Yang et al. 2015; Stankovich et al. 2006; Bai et al. 2010; Yu et al. 2011; Liu et al. 2013). These data are used as a reference to determine the type of oxygen functional groups that exist during the synthesis of graphene and its derivatives. Furthermore, the peak intensity can be used to calculate the content of each oxygen functional group. Furthermore, the position, intensity, and width of the C1s peak have been widely used to deduce the mechanism involved in the formation of graphene and its derivatives from their sources. Furthermore, the characteristics of the O1s peak are used to supplement the conclusions drawn from the C 1 s peak. Furthermore, the C1s/O1s peak ratio is used to discuss the quality of graphene produced in the synthesis method.

Table 10.4 Summarizes the B.E position of C1s when the different functional groups are attached to the carbon atom

Sample	C=C (eV)	C–OH(eV)	C–O–C(eV)	>C=O(eV)	-COOH(eV)
Graphite	284.6	–	–	–	–
GO	284.6	285.8	285.8	287.5	288.9
r-GO	284.6	285.8	285.8	287.5	288.9

10.5.5 Transmission Electron Microscopy

To understand the quality, number of layers, type of defects, and morphology of graphene and its derivatives, TEM study is crucial (Bai et al. 2010; Yu et al. 2011; Liu et al. 2013). The interplanar spacing, which is used to verify the formation of graphene or its derivatives, is measured by the distance between two atomic fringes. Selected area

diffraction pattern (SADP) also provides useful information regarding the type of material, such as whether it is crystalline or amorphous. When it comes to crystalline material, the SADP shows a spot pattern, whereas when it comes to amorphous material, it shows a diffuse ring pattern. Additionally, the SADP data is used to distinguish between single and multilayered graphene. In the case of single layered graphene, a clear six spot pattern is seen, whereas two six spot patterns are seen side by side in the case of multilayered graphene.

10.6 Specialized Techniques to Characterize Magnetic Properties of Graphene

10.6.1 Magneto Optical Kerr Effect (MOKE)

In the realm of magneto-optics, the interaction between light and magnetic materials is termed the magneto-optic effect, which can induce changes in the spectrum, polarization state, phase, and intensity of transmitted light passing through a magnetic substance. This phenomenon has provided a crucial experimental basis for understanding classical matter theory, electromagnetic wave theory, and quantum theory, contributing significantly to the history of electromagnetics. In 1845, Michael Faraday and his research team observed a slight rotation in the polarization of light passing through a glass medium when subjected to a magnetic field. Subsequently, in 1876, John Kerr discovered that the polarization plane of light reflected from a magnetic material’s surface also undergoes rotation, leading to the development of the magneto-optic Kerr effect (MOKE). MOKE exhibits an exceptionally high sensitivity, capable of detecting subatomic layer magnetism, making it an ideal tool for

investigating the magnetism of low-dimensional systems, particularly atomically thin 2D materials like graphene and its derivatives (Mertins et al. 2018, reference (Lan et al. 2020)). Mertins et al. measured Faraday rotation angles of 2.9×10^5 deg/mm due to the carbon 1 s edge of single-layer graphene on cobalt (Co), comparable to those observed at the Co 3p and 2p edges. Through element-selective magnetic hysteresis curves, they discovered ferromagnetic order in graphene on Co, where the magnetism is transferred and significantly enhanced by aligned carbon atom orbitals, resulting from hybridization with the Co 3dz2 orbitals, while carbon bonds show little magnetism due to minimal hybridization with Co.

10.6.2 Magnetic Force Microscopy (MFM)

Using MFM, magnetic domains on a sample surface can be spatially mapped using scanning probe microscopy. Magnetic force microscopy was used by Alimohammadian et al. to detect magnetic domains in graphene (Fig. 10.10) (Alimohammadian and Sohrabi 2020). This method, which is based on cantilever oscillations, is comparable to atomic force microscopy (AFM). At different distances, the magnetic needle probes the surface of the materials. Each line is scanned twice: the first time with the tip close to the surface to get topographical data, and the second time with the tip far from the surface to gather magnetic data. At flight modes, parallel magnetic domains are shown by the amplitude of visible magnetic lines.

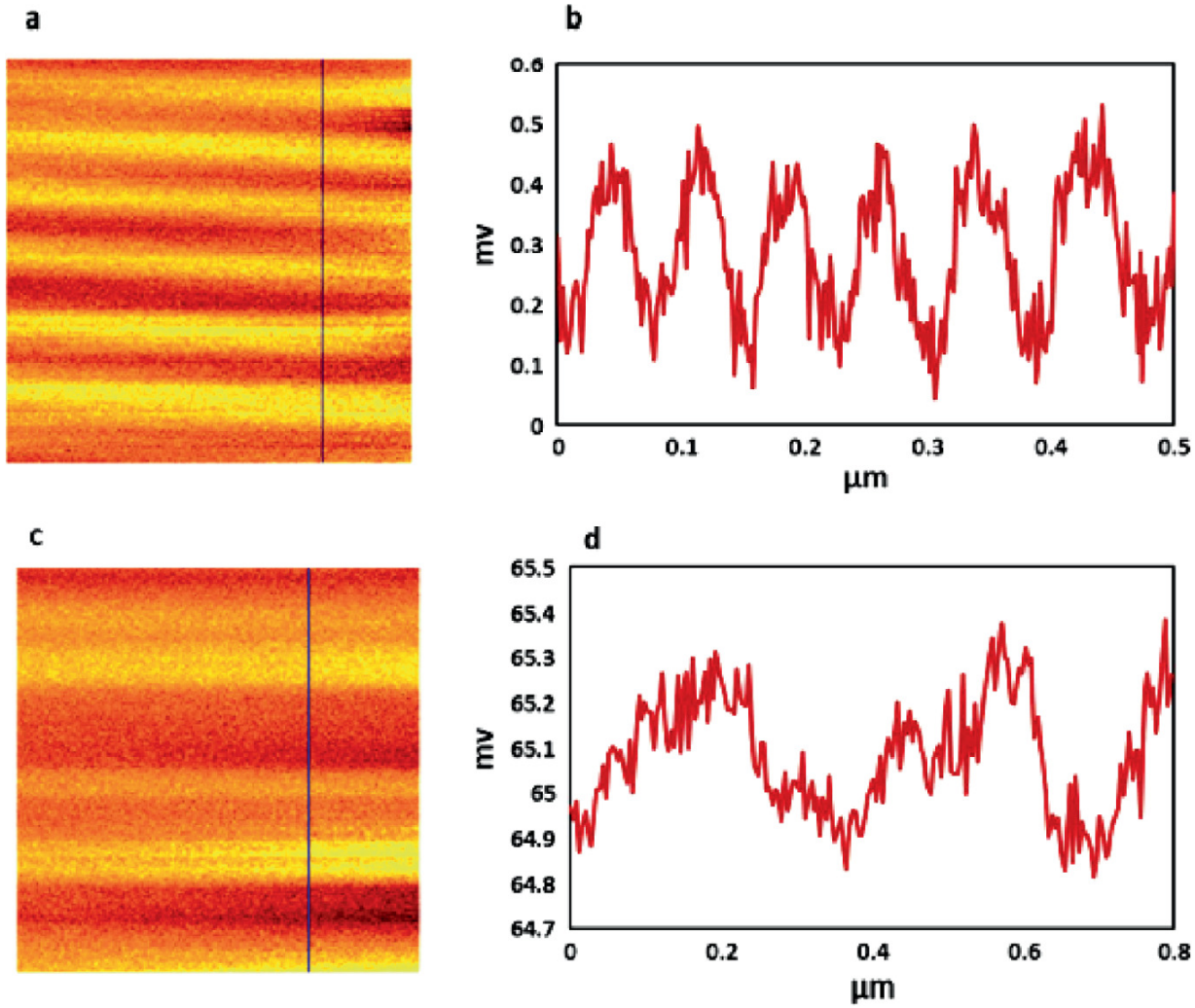

Fig. 10.10 Magnetic domains of LFE- and Autoclave-samples and their domain size. Amplitude images and profile of blue line (**a, b**) LFE-method. (**c, d**) Autoclave-method.

Reproduced from Ref. (Alimohammadian and Sohrabi 2020)

10.6.3 Scanning Tunneling Microscopy (STM)

Due to its incredibly high resolution, scanning tunneling microscopy is frequently used to image the surface of graphene. It does not allow for quantitative magnetic measurements but it does allow for atomic-level analysis of materials. In terms of numbers, it has a lateral resolution of 0.1 nm and a depth resolution of 0.01. There is no need for an extremely high vacuum for the STM measurements. Almost any environment, including one with air, water, or

gas, can be simply The versatility of measurements in scanning tunneling microscopy (STM) extends to various temperatures. However, the main limitations of STM revolve around surface roughness, stability, and cleanliness requirements for the sample. STM operates by scanning a probe-tip across a surface while adjusting the distance between them to maintain a constant tunnel current. This tunneling current is influenced by the applied voltage, tip height, and local density of states. STM also allows for differential conductance calculations (dI/dV), where the signal strength correlates with the sample's local density of states, and the sample bias corresponds to a shift relative to the Fermi level. This method holds significance for studying magnetism in graphene derivatives due to its ability to measure electronic structure at specific locations. As the emergence of magnetism in carbon materials is linked to the spin-split density of states near the Dirac points, STM enables the direct detection of magnetism even at a single vacancy by probing its electronic structure. By applying an external magnetic field, visualization techniques like magnetic force microscopy can be employed, as demonstrated in nitrophenyl-functionalized graphene as shown in Fig. 10.11 (Wang et al. 2022).

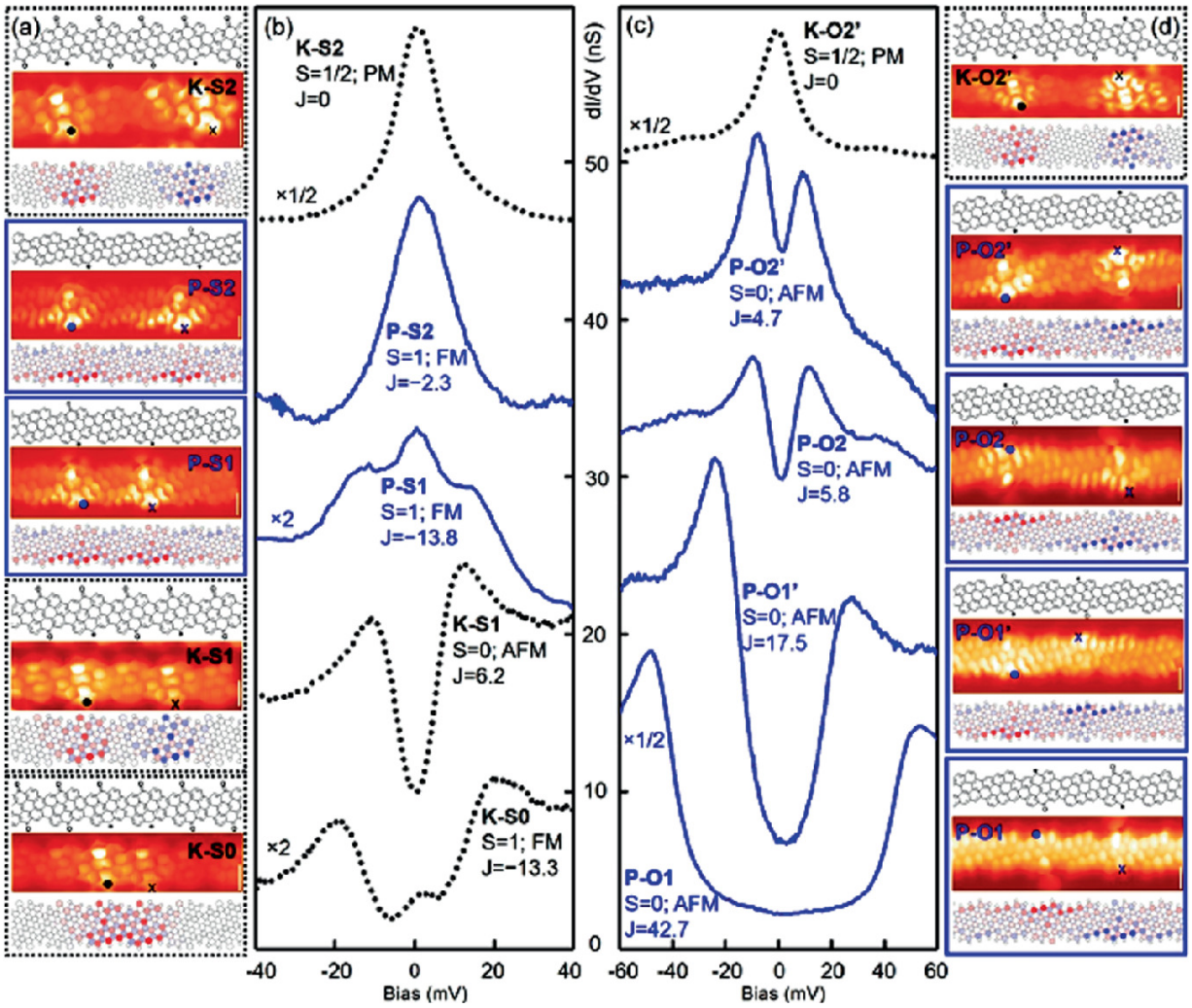

Fig. 10.11 Characterizations of radical pairs. **a**, **d** BR-STM images ($V = 5$ mV) of experimentally obtained radical pairs at the same (**a**) and opposite sides (**d**) on P- and K-chGNRs, together with the chemical structure and DFT calculated spin-polarized LDOS for each case (ground states). **b**, **c** dI/dV spectra measured at the marked positions in STM images. The blue solid and black dotted curves refer to radical pairs on P- and K-chGNRs, respectively. P-O1 shows the original signal and other spectra were vertically shifted to match the positions of STM images. Some of the spectra were additionally scaled as marked. Total spin and coupling strength are shown for each case, where PM, FM, and AFM stand for paramagnetic, ferromagnetic and antiferromagnetic coupling, respectively. Lock-in amplitude: 2 mV for P-O1, 1.5 mV for K-S0, 1 mV for other cases. Scale bars: 0.5 nm.

Reproduced from Ref. (Wang et al. 2022)

10.6.4 Electron Spin-Resonance Spectroscopy (ESRS)

In the study of carbon nanomagnetism, electron spin resonance (ESR) is a valuable technique that specifically addresses the paramagnetic aspect of susceptibility, allowing for the differentiation of various paramagnetic contributions to a sample's overall magnetic response. Conduction electrons, edge states, and molecular states are commonly identified as sources of paramagnetic signals in carbon materials, with the latter particularly relevant for graphene flakes when the system is well described by molecular states. The principle behind ESR involves the splitting of electron energy levels by an external magnetic field, known as Zeeman splitting, induced by the presence of a paramagnetic atom. This splitting enables resonance absorption of external electromagnetic radiation, with resonance conditions dictated by the equation $h\nu = g\mu BB$, where $h\nu$ represents the energy required to transition between energy levels, g is the dimensionless g-factor, μB is the Bohr magneton, and B is the applied magnetic field. Typically, ESR experiments involve fluctuating the frequency or magnetic field to achieve resonance conditions, with calculations commonly performed under fixed frequencies using an alternating magnetic field. Tampieri et al. conducted investigations into the magnetic properties of graphene using EPR techniques (Tampieri et al. 2014). They analyzed EPR spectra to identify different paramagnetic centers contributing to the spectrum, and through temperature-dependent EPR spectra and pulsed techniques, they successfully distinguished and characterized the contributions of free conduction electrons from localized edge states and molecular-type paramagnetic states.

10.7 Perspective Application of Magnetic Graphene

10.7.1 Biomedical

A reusable biosensor made of magnetic graphene oxide (MGO) over Au electrode was proposed by Lin et al. for cancer diagnosis (Lin et al. 2015b). Avastin is used as the accurate bio-recognition component in this biosensor and is placed onto the MGO carrier. The additional benefit of employing MGO due to its magnetic nature is that it allows quick purification and reduces bioactivity loss. Furthermore, the biosensor may be made rapidly and without the requirement for drying, which is advantageous for moving on to detection. In comparison to enzyme-linked immunosorbent *assay* (ELISA) analysis, this biosensor offers an ideal level of sensitivity for disease diagnosis as well as a wide range of linear detection, extending from 31.25–2000 pg mL^{-1}. The repeatability relative standard deviation for the Au-MGO biosensor was 2.36%. This MGO-based biosensor shows potential as a diagnostic tool by not only improving detection efficiency but also cutting costs and response times by a factor of 10. Magnetic graphene was also utilized to create electrochemical sensors for harmful microbes such as bacteria and norovirus-like particles (NoV-LP). The Au-magnetic nanoparticles decorated graphene (Au/MNP-GRPs) composite has been shown to be effective for detecting NoV-LP (Li et al. 2020b). He et al. looked into the cellular behaviours, osteogenesis, and mechanisms of bone marrow-derived mesenchymal stem cells (BMSCs) treated with magnetic graphene oxide (MGO) and a static magnetic field (SMF) (He et al. 2021). As shown by mRNA and protein expression levels, the synthetic MGO particles were found to be biocompatible and capable of significantly boosting BMSC osteogenesis in the presence of SMFs. Graphene oxide added to Fe_3O_4 at the same intensity as SMF may boost BMSC osteogenic potential. The Wnt/β-catenin signalling pathway has been linked to MGO-driven

osteogenic activity of BMSCs in SMF. According to the findings, MGO in the presence of an SMF could induce osteogenesis in BMSCs via the Wnt/β-catenin pathway.

10.7.2 Water Treatment

According to Abdi et al., covalent functionalization was used to graft functional groups of biguanide onto the GO surface in order to create a magnetic graphene-based composite (MMGO) (Abdi et al. 2018). The phase inversion precipitation technique was then used to insert the produced MMGO hybrid into the polyethersulfone (PES) polymer. The developed MMGO embedded PES membranes underwent tests to determine their capability for water purification. The effects of the MMGO composite on the cross-sectional morphology, hydrophilicity, and roughness of the PES membrane were also studied. By inserting MMGO composite, the membranes' surface roughness and hydrophilicity were altered, which considerably boosted the flow of pure water. The capacity of the synthesized membranes to remove copper and dye was also significantly enhanced by the hydrophilic active groups of the MMGO composite. The most effective nano-filtration membrane for removing copper ions was one that contained 0.5 wt % of MMGO hybrid (92%). Dye rejection was nearly identical (about 99%) at different MMGO hybrid concentrations, whereas the bare PES membrane had a value of 91%. Using magnetic field aided casting and a phase-inversion technique, Xu et al. reported a novel Fe_3O_4/GO-poly vinylidene fluoride (PVDF) based ultra-filtration membrane (Xu et al. 2016). During this procedure, the Fe_3O_4/GO nanocomposites could move towards the membrane upper layer due to magnetic attraction, making the surface very hydrophilic and fouling resistant. In terms of hydrophilicity and water flux, the new membranes consistently outperformed those generated

without the use of a magnetic field. Furthermore, the novel membranes displayed significant flux recovery ratios (up to 86.4%) and high bovine serum albumin rejection rates (> 92%).Ultrafiltration membranes (UF) have also been employed for water treatment in a variety of industrial wastes. The biggest concern with UF membrane is fouling. To avoid this issue, Aldawsari et al. created the PVDF-co-PAAm/MGO nanocomposite membrane by synthesizing the PVDF-co-PAAm copolymer blended with magnetic graphene oxide (MGO) using a non-solvent induced phase separation (NIPS) method (Aldawsari et al. 2022). To examine the effectiveness of the membranes, four different types of PVDF were used: PVDF, PVDF-co-PAAm, PVDF-co-PAAm/GO, and PVDF-co-PAAm/MGO. Permeation, antifouling, and antibacterial properties of synthetic membranes were evaluated. The results of the characterization show that both porosity homogeneity and membrane hydrophilicity were increased. When PVDF-co-PAAm and MGO were mixed, pure water flux increased by 60%, flux recovery ratio increased by 10%, and rejection percentage increased by 12%. While the R_{ir} could fall from 53.53 to 42.16%, the R_r could rise from 6.05 to 39.81%. The modified membrane also demonstrated strong antibacterial activity, with a maximum antibacterial ratio. Zhan et al. reported on a magnetic Fe_3O_4/graphene composite created utilizing the solvothermal approach that successfully eliminated both bacteriophage and bacteria in water (Zhan et al. 2015). The Fe_3O_4-graphene composite was demonstrated to be effective in removing a wide range of pathogens, including bacteriophage ms2, as well as other bacteria such as S. aureus, Salmonella, E. coli, E. faecalis, E. faecium, and Shigella. In comparison to pure Fe_3O_4 nanoparticles, which have a removal rate of just 54.97% for E. coli, Fe_3O_4-graphene composites have a

removal rate of 93.09%. Additionally, the Fe_3O_4-graphene composite can eliminate 94.8% of germs from real water samples, according to the results of a detailed verification test that was also conducted using actual water samples. Chang et al. described magnetic graphene oxide-TiO_2 (MGO–TiO_2) composites. MGO-TiO_2 had significant antibacterial activity against E. coli. MGO–TiO_2 was found to practically completely inactivate E. coli when exposed to sunlight after 30 min (Chang et al. 2015). Li et al. described a novel adsorbent for removing methylene blue (MB) from wastewater, a magnetic humic acid/graphene oxide composite (MHAGO). MHAGO has a maximal MB adsorption of approximately 59.00 mg/g at 45 °C. The thermodynamic data further indicated that the adsorption is endothermic. The primary processes for MB adsorption on the MHAGO surface were electrostatic attraction, and hydrogen bonding. Furthermore, the MHAGO shows good capability for removing pollutants from industrial dyeing effluent (Li et al. 2021). Zarenezhad et al. demonstrated the removal of Pb^{2+} from water using magnetic graphene oxide (MGO) nanocomposites functionalized with various amine ligands. The effects of pH, adsorbent mass, exposure duration, and lead concentration on adsorption efficacy were investigated, and the best conditions for Pb^{2+} removal were 20 mg/L beginning Pb^{2+} concentration, $pH = 4$, 40 mg adsorbent mass, and a reaction time of 10 min. Pb^{2+} adsorption efficiency was compared for adsorbents functionalized with ethylenediamine (EDA), melamine, and monoethanolamine. The effectiveness of Pb^{2+} adsorption for these three adsorbents was determined to be 98%, 96.34%, and 97.65%, respectively. The EDA functionalized MGO (EDA-MGO) adsorbent showed an 8.8% decrease in Pb^{2+} adsorption efficiency after 5 cycles of adsorption and desorption (Zarenezhad et al. 2021). Liang et al. used

assembly and a chemical bubble to make a macroporous 3D GO hydrogel (MGOH). Based on the properties, 3D MGOH indicated As(III) and As(V) sorption capacities of 25.1 mg g^{-1} and 74.2 mg g^{-1}, respectively. Because of the average pore width of 26.3 nm and good hydrophilicity, the ultrafast sorption equilibriums were achieved in 2 min. It has also been demonstrated that MGOH has good As (V) adsorption capabilities under neutral environments (Liang et al. 2019).

10.7.3 Chemical Sensor

In order to make an imprinted electrochemical sensor to detect sunset yellow, Li et al. developed an electrode made of cyclodextrin, ionic liquid and gold nanoparticles functionalized magnetic graphene oxide (Li et al. 2016). The suggested sensor demonstrated a quick rebinding kinetics under optimal conditions, and it was effective for detecting sunset yellow, with a range of 5.0×10^{-9} to 2.0×10^{-6} and a sensitivity limit of 2.0×10^{-9} mol. L^{-1}. In order to determine sunset yellow in spiked water samples and mirinda drink, the electrochemical sensor has been successfully used. The added-standards recoveries range from 97 to 105%. For the detection of tryptophan (Trp), Wang et al. reported the creation of a unique, ultra-sensitive, and selective sensing platform based on β-cyclodextrin (CD) modifiedmagnetic graphene oxide (MGO) nanocomposites (Wang et al. 2016). A straightforward co-precipitation procedure was used to create magnetically modified graphene oxide (MGO), which was then used to conjugate CD using a strong hydrogen bond and hydrophobic contact. The interactions between graphene oxide (GO) and Fe_3O_4 could raise the surface area and accelerate the electron transfer rate, the sensitivity was undoubtedly enhanced. Additionally, the graft of CD showed high recognition properties that allowed Trp to

form persistent host–guest inclusion complexes, hence enhancing selectivity. The electrochemical sensor showed a broad linear range from 5.0×10^{-7} M to 7.5×10^{-4} M under optimal conditions, with a low detection limit of 3.1×10^{-7} M. The suggested approach demonstrated high stability and excellent reproducibility. Li et al. reported a simple one-step method for synthesizing NH_2-MIL-88B(Fe) and Fe_3O_4 modified reduced graphene oxide magnetic composite as enzyme mimics. This composite has a greater affinity for hydrogen peroxide and consequently has significant peroxidase-mimic activity. Under optimal conditions, this composite has excellent glucose detection performance in the 20–800 µM range, with a detection limit of 3.16 µM (Li et al. 2022). Pathan et al. created magnetic graphene quantum dots-based highly sensitive and selective As^{3+} ion sensors (Fe-GQDs). Over a broad pH range, Fe-GQDs were found to exhibit good sensitivity for As^{3+} ions. As-prepared fluorescent Fe-GQDs had an achieved limit of detection (LOD) value of 5.1 ppb, which is significantly less than the allowable limit for arsenic in drinking water (Pathan et al. 2019).

10.7.4 Gas Sensor

Zou et al. demonstrated the fabrication of a sensing device utilizing a uniform three-dimensional (3D) structure composed of γ-Fe_2O_3 nanoparticles embedded in reduced graphene oxide (RGO) film. This sensor, prepared through in-situ thermal reduction and drop-coating supported by a magnetic field, exhibited remarkable selectivity and sensitivity to NO_2, with a sensitivity of 3.43 towards 50 ppm NO_2, approximately 2.5 times higher than that of a pure RGO sensor. The enhanced performance can be attributed to the larger surface area, reduced aggregation, and well-developed heterostructures, which facilitate

efficient charge transfer. Moreover, the magnetic properties of γ-Fe_2O_3 enabled stable and repeatable sensing performance using the magnetic-field assisted drop-coating method (Zou et al., reference (Zou et al. 2020)). Ma et al. presented multichannel gas sensors composed of 3D core–shell structures consisting of Fe_3O_4 nanoparticles encapsulated in SiO_2 and then coated with RGO, aligned by a magnetic field. By adjusting the magnetic field and sphere concentration, the sensing channels based on these spheres could be tailored. Experimental results by Ma et al., indicated that the multichannel sensor exhibited a sensitivity 7.96 times higher than a random RGO sensor, with a sensitivity of 34.41 towards 5 ppm of NO_2 at room temperature (Ma et al. 2020).

10.7.5 Spin-Dependent Electronics

Rameshti et al. investigated magnetic graphene's spin-dependent thermoelectric properties in both the diffusive and ballistic regimes. Using the Boltzmann and Landauer formalisms, they estimated the Seebeck coefficient values in magnetic graphene by varying the spin splitting and temperature of the junction. It has been observed that magnetic graphene generates a larger spin current than normal graphene because of its innate magnetism (Rameshti and Moghaddam 2015).

10.7.6 Microwave Absorption

Xu et al. developed 3D porous N-doped magnetic graphene-supported Ni nanoparticles (MGF@Ni) with a bulk density of 0.027 g cm^{-3} (Xu et al. 2019a). The performance results show that at 13.9 GHz, the minimal reflection loss can approach 58.7 dB with a thickness of 2.3 mm, and the maximum absorption bandwidth (EAB) can exceed 10 dB. Surprisingly, the 3D porous N-doped MGF@Ni composites

outperform the 2D hybrids in terms of microwave absorption (MA) and corrosion resistance. Furthermore, 3D porous MGF@Ni retains outstanding MA performance after one month of treatment in hydrochloric acid, demonstrating that 3D porous MGF@Ni can be employed as an efficient MA material in humid environments. The improved MA capabilities are attributed to specific porous architectures and synergistic loss mechanisms, according to the results. According to these results, 3D porous graphene-based composites could be an effective approach for lightweight, corrosion-resistant microwave absorption materials. Sun et al. observed significant differences in the electromagnetic characteristics of magnetic graphene over pure graphene. Furthermore, microwave absorption measurements show that the as-prepared composite has a reflection loss of less than 10 dB (90% absorption) at 10.4–13.2 GHz with a coating layer thickness of 2.0 mm (Sun et al. 2013). Wang et al. developed two-dimensional (2D) composite material of PEDOT: PSS-Fe_3O_4-rGO (P-GF) via molecular-atomic deposition processes (Wang et al. 2018). The electromagnetic characteristics and microwave absorption (MA) performance of composite materials can be successfully controlled by adjusting the atom and molecule deposition and hybrid ratios. The MA has been greatly improved, and the absorption bandwidth (BW) has been increased by 140%. The greatest reflection loss is 61.4 dB, with a maximum BW of 6.4 GHz (10 dB). The deposition of PEDOT: PSS, which rearranges a conductive network for aggregation-controlled charge transport and is the result of the new interface's contribution to multiple relaxation, is responsible for the improved MA performance. Furthermore, covalently grafting Co@C polyhedrons onto magnetic N-doping reduced graphene oxide (NRGO) made from MOF using the amino reaction is a novel technique Wang et al. proposed (Wang et al. 2020).

The study showed that Co@C polyhedrons could be effectively esterified to the magnetic graphene using a variety of reaction techniques. According to the results of the microwave absorption experiments, Co@C@NRGO can achieve a maximum RL of 73.4 dB at 12.1 GHz with an absorber thickness of 2 mm, and its absorption bandwidth (90% absorption efficiency) can be as high as 5.3 GHz (from 9.9 to 15.2 GHz) with a 20% weight content. The Co@C@NRGO hybrid's preferred impedance matching, strong attenuation capabilities, and different interfacial polarization all work together to increase its EM wave absorption capacity. In addition, Xu et al. revealed three-dimensional hydrophobic graphene aerogels adorned with ultra-fine Fe_3O_4 nanocrystal composites synthesized through chemical self-assembly and in situ pyrolysis (Xu et al. 2022). Surprisingly, composites with only 5% filling exhibit great microwave absorption performance (MAP) in respect of both minimum reflection loss (RL_{min}) and effective absorption bandwidth (EAB), outperforming the most often reported microwave absorbers. Furthermore, the magnetic graphene aerogels composites have a high hydrophobicity, making them appealing for self-cleaning, waterproofing, anti-icing, and corrosion resistance. Importantly, practical and theoretical studies show that improved MAP can be achieved by controlling the electromagnetic parameters. Wu et al. described a simple one-pot chemical reduction process for forming amorphous-Fe/rGO magnetic nanocomposites from surface-oxidized amorphous Fe nanoparticles on reduced graphene oxide (rGO) sheets (Wu et al. 2019). These magnetic graphene-based nanosheets supported by evenly dispersed amorphous Fe nanoparticles attain a comparatively low coercivity of 60.2 Oe. Appropriate rGO additions successfully modify the dielectric characteristics of amorphous-Fe/rGO nanocomposites. Improved impedance

matching can be obtained in the Fe/5 wt% rGO nanocomposites due to balanced magnetic and dielectric loss, resulting in good wave absorption performance with a high maximum reflection loss (72.8 dB at 4.48 GHz) for a 3.26 mm thickness and a wide absorption bandwidth (5.90 GHz, 10 dB). Amorphous-Fe/rGO nanocomposites have substantial potential uses in lightweight electromagnetic microwave absorbers due to their facile synthesis, great structural stability, low density, and outstanding wave absorption capabilities.

10.7.7 Catalyst

Xu et al. investigated the use of magnetic graphene oxide as a catalyst for reducing the viscosity of heavy oils and aiding in oil displacement using microwaves (Xu et al. 2019b). They found that magnetic graphene oxide, supported by nano-sized ferro-ferric oxide particles (referred to as nano-Fe_3O_4), exhibited good load-ability and dispersibility in water. However, as the duration of microwave radiation increased, its dispersibility in water decreased, leading to the formation of magnetic-reduced graphene oxide (MRGO), which displayed higher lipophilicity and microwave absorption capability compared to magnetic graphene oxide. Magnetic graphene oxide was effective in heavy oils with low viscosity when supplemented with microwaves, and the addition of a hydrogen donor to the heavy oil resulted in a 43.61% reduction in viscosity after 10 min of microwave treatment, leading to an increase in the percentage of light components in the heavy oil. In addition, magnetic graphene oxide fluid flooding showed improved recovery efficiency compared to water flooding under microwave irradiation. Doustkhah et al. described a multi-step synthesis method for covalently sulfonated magnetic graphene oxide, beginning with the production of graphene

oxide (GO) using Hummer's method for the chemical oxidation of graphite (Doustkhah and Rostamnia 2016). Fe_3O_4 nanoparticles were then supported on graphene oxide nanosheets (Fe_3O_4@GO) during co-precipitation, resulting in the formation of homogeneous Fe_3O_4 particles on the surface of GO sheets. The material was subsequently sulfonated (Fe_3O_4@GO-Pr-SO_3H) by treatment with 3-mercaptopropyltrimethoxysilane (MPTMS) and oxidation with hydrogen peroxide (H_2O_2). Compared to graphene oxide sulfonic acids, covalently bonded propyl sulfonic acid groups were found to be more dominant. The resulting catalyst exhibited high activity and recyclability for at least 11 cycles. Furthermore, Feng et al. utilized a co-precipitation method to synthesize graphene-Fe_3O_4 nanocomposites (G-Fe_3O_4) (Feng et al. 2013). This compound served as an effective catalyst for the reduction of nitroarenes using hydrazine hydrate, achieving yields ranging from 75 to 92% across various compounds. The graphene-supported Fe_3O_4 catalyst could be recycled and reused up to five times without significant loss of catalytic activity. Tamoradi et al. developed a magnetically reusable nanocatalyst with basic properties for producing biodiesel through the trans-esterification of waste corn oil and rapeseed oil with methanol (Tamoradi et al. 2021). In the catalyst preparation process, magnetic $CuFe_2O_4$ nanoparticles were combined with graphene oxide (GO) using pistachio leaf extract, followed by the impregnation of MgO nanoparticles. Response Surface Methodology (RSM) was utilized to optimize reaction parameters such as reaction time, methanol-to-oil molar ratio, and catalyst loading using a Box-Behnken experimental design. Moreover, the catalysts could be magnetically recovered and reused up to five times without experiencing

significant loss of reactivity in the transesterification reaction.

10.7.8 Adsorption of Heavy Metal

Huang et al. observed Cd(II) and As (V) adsorption onto magnetic graphene oxide (MGO), magnetic chemically-reduced graphene (MCRG), and magnetic annealing-reduced graphene (MARG). The adsorption was pH-dependent, and the order of adsorption capabilities was MGO > MCRG > MARG. MGO had highest adsorption capabilities of 234 mg/g for Cd(II) and 14 mg/g for As (V). High dispersibility, thin sheets, and different oxygen functional groups were primarily identified as the merits of MGO (Huang et al. 2019). Zhang et al. produced composites of graphene oxide and Fe_3O_4 (GO–Fe_3O_4) using a copper-catalyzed azide-alkyne cycloaddition procedure. After additional processing with polyacrylic acid, magnetic graphene nanocomposites that are water soluble were produced (PAA). Cu^{2+}, Cd^{2+}, and Pb^{2+} ions have been demonstrated to be easily removed by PAA-GO-Fe_3O_4 nanocomposites. The PAA-GO-Fe_3O_4 composites may also separate these ions due to the superparamagnetism of Fe_3O_4, and the composite can be recycled. The removal efficiency for Cu^{2+}, Cd^{2+}, and Pb^{2+} ions is greater than 85% after five cycles of reused composite (Zhang et al. 2013). Molaei et al. developed a composite from SiO_2-coated magnetic graphene oxide and a pyrrole-thiophene (mGO/SiO_2@coPPy-Th) copolymer. This composite's highest sorption capacity for Cu^{+2}, Pb^{+2}, Zn^{+2}, Cr^{+3}, and $Cd^{+2}$was 201, 230, 125, 98, and 80 mg g^{-1}, respectively (Molaei et al. 2017). Guo et al. demonstrated an efficient adsorbent based on few-layered magnetic graphene oxide (FLMGO) for the removal of aqueous Cd^{+2} and Cu^{+2}. FLMGO was found to have a greater absorption efficiency

than GO or Fe_3O_4. For example, absorbed 401.14 and 1114.22 mg/g Cd^{+2} and Cu^{+2} in 5 and 7 min, respectively. FLMGO can also be magnetically separated using a hand-held magnet for easy recovery. These heavy ions can be successfully separated due to the formation of coordination bonds between lone pair electrons of C-O and C-O-related groups and Cd^{+2} and Cu^{+2} (Guo et al. 2021). Cui et al. showed that EDTA embedded magnetic graphene oxide (EDTA-mGO) is an efficient adsorbent for Pb^{+2}, Hg^{+2}, and Cu^{+2}. The metal chelation EDTA and the electrostatic attractions of many groups on the GO surface are the primary determinants of absorption. Furthermore, the high magnetic properties of EDTA-mGO facilitate solid–liquid separation. The magnetic separation process only takes 25 s. According to the Langmuir isotherm, the maximum adsorption capacity for Pb^{+2} was 508.4 mg g^{-1}, 268.4 mg g^{-1} for Hg^{+2}, and 301.2 mg g^{-1} for Cu^{+2} (Cui et al. 2015a). Cui et al. shown that xanthate functionalized magnetic graphene oxide (Fe_3O_4-xGO) is a superior Hg^{+2} adsorbent. Magnetic separation at a modest magnetic field may separate Fe_3O_4-xGO from water in 1 min. The capacity for Hg^{2+} adsorption was determined to be 118.55 mg/g (contact time of 180 min, pH of 7, and temperature of 25 °C) (Cui et al. 2015b).

10.7.9 Photocatalysis

Mardiroosi et al. reported a nanocomposite of ZnO/NiO/magnetic graphene oxide (ZNMG). ZNMG outperformed pure ZnO/NiO, ZnO, and NiO in the removal of Congo Red (CR) dye under visible light irradiation, which was attributed to the extended light absorption range and the reduction of electron–hole pair recombination in ZnO with the formation of p-n hetrojunction ZNMG (Mardiroosi et al. 2017). Piranshahi et

al. demonstrated an efficient photodegradation of crystal violet (CV) using a magnetized nano-photocatalyst based on TiO_2/magnetic graphene (Piranshahi et al. 2018). Graphene incorporation increased the activity of the produced magnetic nano-photocatalyst. Using an external magnetic field, TiO_2/magnetic graphene may be easily isolated from an aqueous solution. Under optimal conditions, efficient photodegradation (>98%) of the specified dye was accomplished in 25 min employing the produced nano-photocatalyst under UV light irradiation. The produced magnetic nano-photocatalyst can be employed to degrade CV in a wide pH range (4–10).

10.7.10 Energy Storage

Magnetic graphene nanocomposites (MGNCs) were produced by Zhu et al. using a simple thermal decomposition technique. To assess the capacitor performance of graphene, its Fe_2O_3 nanocomposites are made as electrochemical electrodes. Due to their higher particle loading (52.5 wt%), which results in a higher internal resistance and impedes effective electron transportation within the electrodes, MGNCs exhibit poorer capacitance than graphene under normal circumstances (i.e., without the presence of a magnetic field). However, compared to the results obtained under normal circumstances, both graphene and MGNC electrodes exhibit dramatically increased capacitance in the presence of an external magnetic field. At sweeping rates of 2 mV s^{-1} and 10 mV s^{-1}, respectively, the capacitance of graphene is enhanced by 67.1 and 26.8%, respectively. At the same sweeping rates of 2 and 10 mV s^{-1}, MGNCs showed even greater increases of 154.6 and 98.2%, respectively. In the presence of a magnetic field, the energy density and power density of electroactive materials are greatly increased. The magnetic field played a significant role in constraining

the interfacial relaxation process and therefore increasing the electrode capacitance, as demonstrated by equivalent circuit modelling of impedance spectra. These results have the potential to revolutionize standard electrochemical capacitors by simply adding an external magnetic field to greatly increase capacitance (potentially doubling it depending on the electroactive materials) without the need of any material (Zhu et al. 2013). Ahmed et al. described a magnetic graphene composite made from $FeCl_3$-graphite intercalation compounds and thermally treated for up to 75 min at 400 °C or 2 min at high temperatures up to 900 °C. These heat treatments of the magnetic graphene composite resulted in cubical expansion of graphene and an increase in inter-graphene distances. After being heated for two minutes at 900 °C, the magnetic graphene composite's specific capacitance reached 42 F g^{-1} at a scan rate of 5 mV s^{-1} in 1.0 M NaCl. In comparison to the pure magnetic graphene composite before heat treatment, this number represents an 840% increase in capacitance activity. The rise in surface area that occurred during the non-defective inter-graphene exfoliation, which increased to 17.2 m^2 g^{-1}, may have been significantly influenced by this capacitance improvement. Additionally, to achieve a specific capacitance of 253 F g^{-1} at 5 mV s^{-1}, polyaniline was hybridized with the magnetic graphene composite heated at 900 °C. The current heat-treatment and hybridization with a conductive polymer approach can be employed to make a magnetic graphene composite with improved electrochemical activity, a reasonably high energy density (141 W h kg^{-1} in 1.0 M NaCl), and outstanding stability (99% after 9000 cycles of 20 A g^{-1}) (Ahmed and Imae 2016). Ahmed et al. investigated the cyclic voltammetric performance of magnetic graphene composites expanded at 90, 900, and 2000 °C, as well as their composites with polyaniline and carbon dots, under

external magnetic fields of up to 1191 Gauss supplied by a 7 A current source. These composites demonstrated improved performance as the magnetic field strength increased. When iron oxide nanoparticles were added to magnetic graphene composites, polyaniline was in-situ coupled with magnetic graphene composites, or carbon dot was hydrothermally loaded on magnetic graphene composites, capacitance was increased even further. These findings provide light on the extraordinary effect of an external magnetic field on the electrochemical performance of magnetic graphene composites (Ahmed and Imae 2019). Ahmed et al. investigated the effect of an external magnetic field on the performance of cobalt oxide/magnetic graphene composite supercapacitors. The composites were created by combining cobalt nitrate with iron oxide-incorporated magnetic graphene in a hydrothermal reaction. Cobalt oxide nanoparticles were placed on graphene sheets and contributed to increasing electrochemical capacitance because cobalt oxide might function as a pseudo-capacitance material distinct from the graphene sheet due to the electric double-layer capacitance effect. Additional amplification was noticed when the external magnetic field was enhanced using a home-made electric circuit. The specific capacitances of the composite materials were found to be 11 times higher in the presence of an external magnetic field of 1191 Gauss than in the absence of the magnetic field. It was also proposed that the rise in specific capacitance under the magnetic field follows the magnetic field's power law due to a magneto-hydrodynamic effect. These findings highlight the significance of the external magnetic field in the development of new technologies for magnetic materials with energy-related applications (Ahmed et al. 2021).

10.8 Conclusions and Future Scope

In summary, we discussed recent developments and knowledge in magnetic graphene and its composites. Magnetic graphene has a promising future in a wide range of sectors, including electronics, catalysis, absorbents, sensors, medicinal applications, and many others. The development of simple, cost-effective, and environmentally friendly procedures for producing high-quality magnetic graphene remains a problem for researchers. One approach is to find effective techniques to lessen and overcome van der Waals forces in order to create high magnetization graphene layers with minimal effort. It is also critical to use non-toxic chemical reagents in conjunction with a highly integrated and efficient production line. Furthermore, the cost-to-performance ratio is an important component in determining the commercial worth of a product. Products with low cost-to-performance ratios are more likely to catch the market's attention and thus succeed. Because of the unique properties and numerous possible uses of magnetic graphene, 'application-oriented' manufacturing should be developed. This is similar to the case of certain semiconductor manufacturers, where a few tens or hundreds of different items can be manufactured on a few manufacturing lines, and the production volume of each product is determined by customer and market demand. It is critical to have effective consumer communication and a marketing strategy. Furthermore, the progressive improvement of the entire industrial chain is strongly desired. The gap between industry demand and laboratory research substantially impedes graphene industrial advancement, which, in turn, dampens interest in graphene research, creating a vicious cycle. Given the foregoing, more attention and finances should be directed into research that promotes high-value products as well as cost-effective and sustainable production. Meanwhile, the majority of graphene R & D is being done at research institutions and universities, which

rely on government financing because businesses lack the requisite funds. Because high-impact journal papers mostly focus on cutting-edge research with potential applications only many years later, market demand-driven and applied research become less appealing. The major issue that all graphene manufacturers are now experiencing is that most businesses are still unable to create a reliable business plan and profit model.

References

Abdi, G., Alizadeh, A., Zinadini, S., Moradi, G.: Removal of dye and heavy metal ion using a novel synthetic polyethersulfone nanofiltration membrane modified by magnetic graphene oxide/metformin hybrid. J. Memb. Sci. **552**, 326–335 (2018)

Ahmed, M.M.M., Imae, T.: Electrochemical properties of a thermally expanded magnetic graphene composite with a conductive polymer. Phys. Chem. Chem. Phys. **18**, 10400–10410 (2016)
[PubMed]

Ahmed, M.M.M., Imae, T.: Effect of external magnetic field on cyclic voltammetry of exfoliated graphene-based magnetic composites with conductive polymer and carbon dots. J. Magn. Magn. Mater. **491**, 165604 (2019)

Ahmed, M.M.M., Imae, T., Ohshima, H., Ariga, K., Shrestha, L.K.: External magnetic field-enhanced supercapacitor performance of cobalt oxide/magnetic graphene composites. Bull. Chem. Soc. Jpn **94**, 2245–2251 (2021)

Aldawsari, A.M., Hassan, H.M.A., Alrashidi, A.N., Alsohaimi, I.H., Moustafa, S.M.N., Youssef, H.M., Hamdi, R., Azzam, M.A.: Preparation of PVDF-co-PAAm membrane with robust antifouling, and antibacterial performance by blending with magnetic graphene oxide. J. Environ. Chem. Eng. **10**, 108093 (2022)

Alimohammadian, M., Sohrabi, B.: Observation of magnetic domains in graphene magnetized by controlling temperature, strain and magnetic field. Sci. Rep. **10**, 21325 (2020)
[PubMed][PubMedCentral]

Averyanov, D.V., Sokolov, I.S., Tokmachev, A.M., et al.: High-temperature magnetism in graphene induced by proximity to EuO. ACS Appl. Mater. Interfaces **10**, 20767–20774 (2018)
[PubMed]

Bai, J., Zhong, X., Jiang, S., Huang, Y., Duan, X.: Graphene nanomesh. Nat. Nanotechnol. **5**, 190–194 (2010)
[PubMed][PubMedCentral]

Behera, S.K., Bora, M., Paul Chowdhury, S.S., Deb, P.: Proximity effects in graphene and ferromagnetic CrBr 3 van der Waals heterostructures. Phys. Chem. Chem. Phys. **21**, 25788–25796 (2019)
[PubMed]

Bosnar, M., Lončarić, I., Lazić, P., Belashchenko, K.D., Žutić, I.: Proximity-induced magnetization in graphene: towards efficient spin gating. Phys. Rev. Mater **4**, 1–9 (2020)

Casiraghi, C., Pisana, S., Novoselov, K.S., Geim, A.K., Ferrari, A.C.: Raman fingerprint of charged impurities in graphene. Appl. Phys. Lett. **91**, 233108–233113 (2007)

Castro Neto, A.H., Guinea, F., Peres, N.M.R., Novoselov, K.S., Geim, A.K.: The electronic properties of graphene. Rev. Mod. Phys. **81**, 109–162 (2009)

Chang, Y.N., Ou, X.M., Zeng, G.M., Gong, J.L., Deng, C.H., Jiang, Y., Liang, J., Yuan, G.Q., Liu, H.Y., He, X.: Synthesis of magnetic graphene oxide-TiO_2 and their antibacterial properties under solar irradiation. Appl. Surf. Sci. **343**, 1–10 (2015)

Choi, H.C., Shim, M., Bangsaruntip, S., Dai, H.: Spontaneous reduction of metal ions on the sidewalls of carbon nanotubes. J. Am. Chem. Soc. **124**, 9058–9059 (2002)
[PubMed]

Cote, L.J., Cruz-Silva, R., Huang, J.: Flash reduction and patterning of graphite oxide and its polymer composite. J. Am. Chem. Soc. **131**, 11027–11032 (2009)
[PubMed]

Cui, L., Wang, Y., Gao, L., Hu, L., Yan, L., Wei, Q., Du, B.: EDTA functionalized magnetic graphene oxide for removal of Pb(II), Hg(II) and Cu(II) in water treatment: adsorption mechanism and separation property. Chem. Eng. J. **281**, 1–10 (2015a)

Cui, L., Guo, X., Wei, Q., Wang, Y., Gao, L., Yan, L., Yan, T., Du, B.: Removal of mercury and methylene blue from aqueous solution by xanthate functionalized magnetic graphene oxide: Sorption kinetic and uptake mechanism. J. Colloid Interface Sci. **439**, 112–120 (2015b)
[PubMed]

Doustkhah, E., Rostamnia, S.: Covalently bonded sulfonic acid magnetic graphene oxide: Fe_3O_4@GO-Pr-SO_3H as a powerful hybrid catalyst for

synthesis of indazolophthalazinetriones. J. Colloid Interface Sci. **478**, 280–287 (2016)
[PubMed]

Dresselhaus, M.S., Dresselhaus, G., Hofmann, M.: Raman spectroscopy as a probe of graphene and carbon nanotubes. Phil. Trans. R. Soc. A **366**, 231–236 (2008)
[PubMed]

Ezawa, M.: Metallic graphene nanodisks: electronic and magnetic properties. Phys. Rev. B **76**, 245415 (2007)

Feng, C., Zhang, H.Y., Shang, N.Z., Gao, S.T., Wang, C.: Magnetic graphene nanocomposite as an efficient catalyst for hydrogenation of nitroarenes. Chin. Chem. Lett. **24**, 539–541 (2013)

Ferrari, A.C.: Raman spectroscopy of graphene and graphite: Disorder, electron-phonon coupling, doping and nonadiabatic effects. Solid State Commun. **143**, 47–57 (2007)

Ferrari, A.C., Basko, D.M.: Raman spectroscopy as a versatile tool for studying the properties of graphene. Nat. Nanotechnol. **8**, 235–246 (2013)
[PubMed]

Ganguly, A., Sharma, S., Papakonstantinou, P., Hamilton, J.: Probing the thermal deoxygenation of graphene oxide using high-resolution in situ X-ray-based spectroscopies. J. Phys. Chem. C **115**, 17009–17019 (2011)

Goodenough, J.B.: Magnetism and the chemical bond. Interscience Monographs on Chemistry, Vol I, Publisher, John Wiley and Sons, USA (1963)

Guo, J., Ren, L., Wang, R., Zhang, C.: Water dispersible graphene noncovalently functionalized with tryptophan and its poly(vinyl alcohol) nanocomposite. Compos. B **42**, 2130–2135 (2011)

Guo, T., Bulin, C., Ma, Z., Li, B., Zhang, Y., Zhang, B., Xing, R., Ge, X.: Mechanism of Cd(II) and Cu(II) adsorption onto few-layered magnetic graphene oxide as an efficient adsorbent. ACS Omega **6**, 16535–16545 (2021)
[PubMed][PubMedCentral]

Guoxiu, W., Juan, Y., Jinsoo, P., Gou, X., Wang, B., Liu, H., Yao, J.: Facile synthesis and characterization of graphene nanosheets. J. Phys. Chem. C **112**, 8192–8195 (2008)

He, Y., Chen, G., Li, Y., Li, Y., Yi, C., Zhang, X., Li, H., Zeng, B., Wang, C., Xie, W., Zha, W., Yu, D.: Effect of magnetic graphene oxide on cellular behaviors and osteogenesis under a moderate static magnetic field. Nanomedicine **37**, 1–15 (2021)

Huang, D., Wu, J., Wang, L., Liu, X., Meng, J., Tang, X., Tang, C., Xu, J., et al.: Novel insight into adsorption and co-adsorption of heavy metal ions and an organic pollutant by magnetic graphene nanomaterials in water. Chem. Eng. J. **358**, 1399–1409 (2019)

Joly, V.L.J., Kiguchi, M., Hao, S.J., et al.: Observation of magnetic edge state in graphene nanoribbons. Phys. Rev. B Condens Matter Mater. Phys. **81**, 1–6 (2010)

Karpiak, B., Cummings, A.W., Zollner, K. et al.: Magnetic proximity in a van der Waals heterostructure of magnetic insulator and graphene. 2d Mater 7: 015026 (2020)

Kudin, K.N., Ozbas, B., Schniepp, H.C., Prud'homme, R.K., Aksay, I.A., Car, R.: Raman spectra of graphite oxide and functionalized graphene sheets. Nano Lett. **8**, 36–41 (2008)
[PubMed]

Lan, T., Ding, B., Liu, B.: Magneto-optic effect of two-dimensional materials and related applications. Nano Select **1**, 298–310 (2020)

Langer, R., Błoński, P., Otyepka, M.: Tuning the magnetic properties of graphene derivatives by functional group selection. Phys. Chem. Chem. Phys. **21**, 12697–12703 (2019)
[PubMed]

Lee, C., Wei, X., Kysar, J.W., Hone, J.: Measurement of the elastic properties and intrinsic strength of monolayer graphene. Science **321**, 385–388 (2008)
[PubMed]

Lee, D., Seo, J., Zhu, X., et al.: Magnetism in graphene oxide induced by epoxy groups. Appl. Phys. Lett. **106**, 172402–172405 (2015)

Lehtinen, P.O., Foster, A.S., Ma, Y., et al.: Irradiation-induced magnetism in graphite: a density functional study. Phys. Rev. Lett. **93**, 1–4 (2004)

Li, D., Müller, M.B., Gilje, S., Kaner, R.B., Wallace, G.G.: Processable aqueous dispersions of graphene nanosheets. Nat. Nanotechnol. **3**, 101–105 (2008)
[PubMed]

Li, W., Zhao, M., Xia, Y., et al.: Covalent-adsorption induced magnetism in graphene. J. Mater. Chem. **19**, 9274–9282 (2009)

Li, J., Wang, X., Duan, H., Wang, Y., Bu, Y., Luo, C.: Based on magnetic graphene oxide highly sensitive and selective imprinted sensor for determination of sunset yellow. Talanta **147**, 169–176 (2016)
[PubMed]

Li, J., Cui, R., Chang, Y., et al.: Preparing dangling bonds by nanoholes on graphene oxide nanosheets and their enhanced magnetism. RSC Adv. **10**, 36378–36385 (2020a)
[PubMed][PubMedCentral]

Li, F., Huang, Y., Huang, K., Lin, J., Huang, P.: Functional magnetic graphene composites for biosensing. Int. J. Mol. Sci. **21**, 390 (2020b)
[PubMed][PubMedCentral]

Li, D., Hua, T., Yuan, J., Xu, F.: Methylene blue adsorption from an aqueous solution by a magnetic graphene oxide/humic acid composite. Colloids Surf. A Physicochem. Eng. Asp. **627**, 127171 (2021)

Li, Y., Wang, Q., Ding, Z., Wan, D., Nie, X., Zhong, C.: A functionalized magnetic graphene-based MOFs platform as the heterogeneous mimic enzyme sensor for glucose detection. Catal Lett. **152**, 2375–2385 (2022)

Liang, J., He, B., Li, P., Yu, J., Zhao, X., Wu, H., Li, J., Sun, Y., Fan, Q.: Facile construction of 3D magnetic graphene oxide hydrogel via incorporating assembly and chemical bubble and its application in arsenic remediation. Chem. Eng. J. **358**, 552–563 (2019)

Lin, H., Fratesi, G., Brivio, G.P.: Graphene magnetism induced by covalent adsorption of aromatic radicals. Phys. Chem. Chem. Phys. **17**, 2210–2215 (2015a)
[PubMed]

Lin, C.W., Wei, K.C., Liao, S.S., Huang, C.Y., Sun, C.L., Wu, P.J., Lu, Y.J., Yang, H.W., Ma, C.C.M.: A reusable magnetic graphene oxide-modified biosensor for vascular endothelial growth factor detection in cancer diagnosis. Biosens. Bioelectron. **67**, 431–437 (2015b)
[PubMed]

Liu, Z., Ma, L., Shi, G., Zhou, W., Gong, Y., Lei, S., Yang, X., Zhang, J., Yu, J., Hackenberg, K.P., Babakhani, A., Idrobo, J.C., Vajtai, R., Lou, J., Ajayan, P.M.: In-plane heterostructures of graphene and hexagonal boron nitride with controlled domain sizes. Nat. Nanotechnol. **8**, 119–124 (2013)
[PubMed]

Ma, D., Su, Y., Tian, T., Yin, H., Zou, C., Huo, T., Hu, N., Yang, Z., Zhang, Y.: Multichannel room-temperature gas sensors based on magnetic-field-aligned 3D Fe_3O_4@SiO_2@reduced graphene oxide spheres. ACS Appl. Mater. Interfaces **12**, 37418–37426 (2020)
[PubMed]

Mafra, D.L., Samsonidze, G., Malard, L.M., Elias, D.C., Brant, J.C., Plentz, F., Alves, E.S., Pimenta, M.A.: Determination of LA and TO phonon dispersion

relations of graphene near the Dirac point by double resonance Raman scattering. Phys. Rev. B Condens. Matter Mater Phys. **76**, 233407–233414 (2007)

Malard, L.M., Pimenta, M.A., Dresselhaus, G., Dresselhaus, M.S.: Raman spectroscopy in graphene. Phys. Rep. **473**, 51–87 (2009)

Mardiroosi, A., Mahjoub, A.R., Fakhri, H.: Efficient visible light photocatalytic activity based on magnetic graphene oxide decorated ZnO/NiO. J. Mater Sci. Mater Electron. **28**, 11722–11732 (2017)

Maultzsch, J., Reich, S., Thomsen, C., Requardt, H., Ordejón, P.: Phonon dispersion in graphite. Phys. Rev. Lett. **92**, 075501–075504 (2004) [PubMed]

Mertins, H.C., Jansing, C., Krivenkov, M., Varykhalov, A., Rader, O., Wahab, H., Timmers, H., Gaupp, A., Sokolov, A., Tesch, M., Oppeneer, P.M.: Giant magneto-optical Faraday effect of graphene on Co in the soft x-ray range. Phys. Rev. B **98**, 064408–064409 (2018)

Molaei, K., Bagheri, H., Asgharinezhad, A.A., Ebrahimzadeh, H., Shamsipur, M.: SiO_2-coated magnetic graphene oxide modified with polypyrrole–polythiophene: a novel and efficient nanocomposite for solid phase extraction of trace amounts of heavy metals. Talanta **167**, 607–616 (2017) [PubMed]

Moon, I.K., Lee, J., Ruoff, R.S., Lee, H.: Reduced graphene oxide by chemical graphitization. Nat. Commun. **1**, 73 (2010) [PubMed]

Nair, R.R., Tsai, I.L., Sepioni, M., et al.: Dual origin of defect magnetism in graphene and its reversible switching by molecular doping. Nat. Commun. **4**, 1–6 (2013)

Ney, A., Papakonstantinou, P., Kumar, A., Shang, N., Peng, N.: Irradiation enhanced paramagnetism on graphene nanoflakes. Appl. Phys. Lett. **99**, 102504–102513 (2011)

Novoselov, K.S., Geim, A.K., Morozov, S.V., Jiang, D., Zhang, Y., Dubonos, S.V., Grigorieva, I.V., Firsov, A.A.: Electric field in atomically thin carbon films. Science **306**, 666–669 (2004) [PubMed]

Novoselov, K.S., Jiang, D., Schedin, F., Booth, T.J., Khotkevich, V.V., Morozov, S.V., Geim, A.K.: Two-dimensional atomic crystals **102**, 10451–10453 (2005)

Pan, Y., Yang, Z.: Exploration of magnetism in armchair graphene nanoribbons with radical groups. Chem. Phys. Lett. **518**, 104–108 (2011)

Pathan, S., Jalal, M., Prasad, S., Bose, S.: Aggregation-induced enhanced photoluminescence in magnetic graphene oxide quantum dots as a fluorescence probe for As(III) sensing. J. Mater Chem. A **7**, 8510–8520 (2019)

Pei, S., Zhao, J., Du, J., Ren, W., Cheng, H.: Direct reduction of graphene oxide films into highly conductive and flexible graphene films by hydrohalic acids. Carbon **48**, 4466–4474 (2010)

Piranshahi, Z.A., Behbahani, M., Zeraatpisheh, F.: Synthesis, characterization and photocatalytic application of TiO_2/magnetic graphene for efficient photodegradation of crystal violet. Appl. Organomet. Chem. **32**, e3985 (2018)

Piscanec, S., Lazzeri, M., Mauri, F., Ferrari, A.C.: Optical phonons of graphene and nanotubes. Europ. Phys. J. Special Topics **148**, 159–170 (2007)

Rameshti, B.Z., Moghaddam, A.G.: Spin-dependent Seebeck effect and spin caloritronics in magnetic graphene. Phys. Rev. B **91**, 155407–155409 (2015)

Saito, R., Jorio, A., Souza Filho, A.G., Dresselhaus, G., Dresselhaus, M.S., Pimenta, M.A.: Probing phonon dispersion relations of graphite by double resonance Raman scattering. Phys. Rev. Lett. **88**, 027401–027404 (2002) [PubMed]

Sepioni, M.: Magnetic properties of graphene, Thesis, School of Physics and Astronomy, University of Manchester (2013)

Shen, J., Hu, Y., Shi, M., Li, N., Ma, H., Ye, M.: One step synthesis of graphene oxide-magnetic nanoparticle composite. J. Phys. Chem. C **114**, 1498–1503 (2010)

Singhbabu, Y.N., Choudhary, S.K., Shukla, N., et al.: Observation of large positive magneto-resistance in bubble decorated graphene oxide films derived from shellac biopolymer: a new carbon source and facile method for morphology-controlled properties. Nanoscale **7**, 6510–6519 (2015) [PubMed]

Stankovich, S., Piner, R.D., Chen, X., Wu, N., Nguyen, S.T., Ruoff, R.S.: Stable aqueous dispersions of graphitic nanoplatelets via the reduction of exfoliated graphite oxide in the presence of poly(sodium 4-styrenesulfonate). J. Mater. Chem. **16**, 155–158 (2006)

Stankovich, S., Dikin, D.A., Piner, R.D., Kohlhaas, K.A., Kleinhammes, A., Jia, Y., Wu, Y., Nguyen, S.T., Ruoff, R.S.: Synthesis of graphene-based nanosheets via chemical reduction of exfoliated graphite oxide. Carbon **45**, 1558–1565 (2007)

Sun, X., He, J., Li, G., Tang, J., Wang, T., Guo, Y., Xue, H.: Laminated magnetic graphene with enhanced electromagnetic wave absorption properties. J. Mater. Chem. C **1**, 765–777 (2013)

Sun, P., Wang, K., Wei, J., et al.: Magnetic transitions in graphene derivatives. Nano Res. **7**, 1507–1518 (2014)

Tamoradi, T., Kiasat, A.R., Veisi, H., Nobakht, V., Besharati, Z., Karmakar, B.: MgO doped magnetic graphene derivative as a competent heterogeneous catalyst producing biofuels via transesterification: Process optimization through Response Surface Methodology (RSM). J. Environ. Chem. Eng. **9**, 106009 (2021)

Tampieri, F., Silvestrini, S., Riccò, R., Maggini, M., Barbon, A.: A comparative electron paramagnetic resonance study of expanded graphites and graphene. J. Mater Chem. C **2**, 8105–8112 (2014)

Tang, T., Tang, N., Zheng, Y., et al.: Robust magnetic moments on the basal plane of the graphene sheet effectively induced by OH groups. Sci. Rep. **5**, 18–23 (2015)

Tuček, J., Holá, K., Bourlinos, A.B., Błoński, M., Bakandritsos, A., Ugolotti, J., Dubecký, M., Karlický, F., Ranc, V., Čépe, K., Otyepka, M., Zbořil, R.: Room temperature organic magnets derived from sp^3 functionalized graphene. Nat. Commun. **8**, 14525 (2017)
[PubMed][PubMedCentral]

Wang, H., Yuan, X., Wu, Y., Chen, X., Leng, L., Wang, H., Li, H., Zeng, G.: Facile synthesis of polypyrrole decorated reduced graphene oxide-Fe_3O_4 magnetic composites and its application for the Cr(VI) removal. Chem. Eng. J. **262**, 597–606 (2015)

Wang, C., Li, T., Liu, Z., Guo, Y., Li, C., Dong, C., Shuang, S., et al.: An ultra-sensitive sensor based on β-cyclodextrin modified magnetic graphene oxide for detection of tryptophan. J. Electroanal. Chem. **781**, 363–370 (2016)

Wang, X., Shu, J.C., He, X.M., Zhang, M., Wang, X.X., Gao, C., Yuan, J., Cao, M.S.: Green approach to conductive PEDOT: PSS decorating magnetic-graphene to recover conductivity for highly efficient absorption. ACS Sustain. Chem. Eng. **6**, 14017–14025 (2018)

Wang, Y., Di, X., Gao, X., Wu, X., Wang, P.: Rational construction of Co@C polyhedrons covalently-grafted on magnetic graphene as a superior microwave absorber. J. Alloys Compd. **843**, 156031 (2020)

Wang, T., Sanz, S., Castro-Esteban, J., Lawrence, J., Berdonces-Layunta, A., Mohammed, M.S.G., Vilas-Varela, M., Corso, M., Pena, D., Frederiksen, T., de Oteyza, D.G.: Magnetic interactions between radical pairs in chiral graphene nanoribbons. Nano Lett. **22**, 164–171 (2022)
[PubMed]

Williams, G., Seger, B., Kamat, P.V.: TiO_2-graphene nanocomposites. UV-assisted photocatalytic reduction of graphene oxide. ACS Nano **2**, 1487–1491 (2008)
[PubMed]

Wu, Y.F., Song, H.D., Zhang, L., Yang, X., Ren, Z., Liu, D., Wu, H.C., Wu, J., Li, J.G., Jia, Z., Yan, B., Wu, X., Duan, C.G., Han, G., Liao, Z.M., Yu, D.: Magnetic proximity effect in graphene coupled to a $BiFeO_3$ nanoplate. Phys. Rev. B **95**, 195426–195427 (2017)

Wu, Y., Pan, W., Li, Y., Yang, B., Meng, B., Li, R., Yu, R.: Surface-oxidized amorphous Fe nanoparticles supported on reduced graphene oxide sheets for microwave absorption. ACS Appl. Nano Mater **2**, 4367–4376 (2019)

Xu, Y., Sheng, K., Li, C., Shi, G.: Highly conductive chemically converted graphene prepared from mildly oxidized graphene oxide. J. Mater. Chem. **21**, 7376–7380 (2011)

Xu, Z., Wu, T., Shi, J., Wang, W., Teng, K., Qian, X., Shan, M., Deng, H., Tian, X., Li, C., Li, F.: Manipulating migration behavior of magnetic graphene oxide via magnetic field induced casting and phase separation toward high-performance hybrid ultrafiltration membranes. ACS Appl. Mater. Interfaces **8**, 18418–18429 (2016)
[PubMed]

Xu, D.W., Yang, S., Chen, P., Yu, Q., Xiong, X.H., Wang, J.: 3D nitrogen-doped porous magnetic graphene foam-supported Ni nanocomposites with superior microwave absorption properties. J. Alloys Compd. **782**, 600–610 (2019a)

Xu, Z., Li, Z., Jing, A., Meng, F., Dang, F., Lu, T.: Synthesis of magnetic graphene oxide (MGO) and auxiliary microwaves to enhance oil recovery. Energy Fuels **33**, 9585–9595 (2019b)

Xu, D., Ren, Y., Guo, X., Feng, D., Yang, R., Zhao, B., Zhang, R.: Synthesis of super-hydrophobic and self-cleaning magnetic graphene aerogel with excellent microwave absorption properties. Diam. Relat. Mater. **126**, 109045 (2022)

Yang, D., Velamakanni, A., Bozoklu, G., Park, S., Stoller, M., Piner, R.D., Stankovich, S., Jung, I., Field, D.A., Ventrice, C.A., Ruoff, R.S.: Chemical analysis of graphene oxide films after heat and chemical treatments by X-ray photoelectron and Micro-Raman spectroscopy. Carbon **47**, 145–152 (2009)

Yang, Z.Z., Bin, Z.Q., Qiu, H.X., Li, J., Yang, J.: A simple method for the reduction of graphene oxide by sodium borohydride with $CaCl_2$ as a catalyst. New Carbon Mater. **30**, 41–47 (2015)

Yazyev, O.V., Helm, L.: Defect-induced magnetism in graphene. Phys. Rev. B **75**, 1–5 (2007)

Yu, Q., Jauregui, L.A., Wu, W., Colby, R., Tian, J., Su, Z., Cao, H., Liu, Z., Pandey, D., Wei, D., Chung, T.F., Peng, P., Guisinger, N.P., Stach, E.A., Bao, J., Pei, S.S., Chen, Y.P.: Control and characterization of individual grains and grain boundaries in graphene grown by chemical vapour deposition. Nat. Mater. **10**, 443–449 (2011)
[PubMed]

Zarenezhad, M., Zarei, M., Ebratkhahan, M., Hosseinzadeh, M.: Synthesis and study of functionalized magnetic graphene oxide for Pb^{2+} removal from wastewater. Environ. Technol. Innov. **22**, 101384 (2021)

Zhan, S., Zhu, D., Ma, S., Yu, W., Jia, Y., Li, Y., Yu, H., Shen, Z.: Highly efficient removal of pathogenic bacteria with magnetic graphene composite. ACS Appl. Mater. Interfaces **7**, 4290–4298 (2015)
[PubMed]

Zhang, Y., Talapatra, S., Kar, S., et al.: First-principles study of defect-induced magnetism in carbon. Phys. Rev. Lett. **99**, 1–4 (2007)

Zhang, W., Shi, X., Zhang, Y., Gu, W., Li, B., Xian, Y.: Synthesis of water-soluble magnetic graphene nanocomposites for recyclable removal of heavy metal ions. J. Mater Chem. A **1**, 1745–1753 (2013)

Zhu, J., Chen, M., Qu, H., Luo, Z., Wu, S., Colorado, H.A., Wei, S., Guo, Z.: Magnetic field induced capacitance enhancement in graphene and magnetic graphene nanocomposites. Energy Environ. Sci. **6**, 194–204 (2013)

Zhuo, Q., Gao, J., Peng, M., Bai, L., Deng, J., Xi, Y., Ma, Y., Zhong, J., Sun, X.: Large-scale synthesis of graphene by the reduction of graphene oxide at room temperature using metal nanoparticles as catalyst. Carbon **52**, 559–564 (2013)

Zou, C., Hu, J., Su, Y., Zhou, Z., Cai, B., Tao, Z., Huo, T., Hu, N., Zhang, Y.: Highly repeatable and sensitive three-dimensional γ-Fe_2O_3@reduced graphene oxide gas sensors by magnetic-field assisted assembly process. Sens. Actuators B Chem. **306**, 127546 (2020)

© The Author(s), under exclusive license to Springer Nature Singapore Pte Ltd. 2024
R. S. Ningthoujam, A. K. Tyagi (eds.), *Handbook of Materials Science, Volume 2*, Indian Institute of Metals Series
https://doi.org/10.1007/978-981-97-4646-0_11

11. Externally Driven Interface in 3D Ising Model: A Monte Carlo Study

Manish K. Sahai[1, 2] ✉ and A. K. Bakshi[1, 2]
(1) Homi Bhabha National Institute, Anushaktinagar, Mumbai, 400094, India
(2) Radiological Physics and Advisory Division, Bhabha Atomic Research Center, Mumbai, 400094, India

✉ **Manish K. Sahai**
Email: mksahai@barc.gov.in

Keywords Ising model – Monte Carlo – Dynamical transitions – Devil's staircase

11.1 Introduction

In our daily lives, we frequently come across moving interfaces. Ignite a horizontally held piece of paper that burns without a flame. Observe the interface between the burnt and unburnt parts. Dip a part of a paper towel in a colored fluid. One can observe a moving interface. In a snowfall, the surface of ice is a growing 2D interface. Flux lines in a superconductor tend to get proximity to impurity sites. Hence, the flux lines which would have been smooth become tortuous (rough), just like a fire front or fluid

interface although there is a difference between flux lines and the case of fire fronts or fluid interfaces. Fire front or fluid interfaces are 1D interfaces moving on 2D surfaces, whereas flux lines are 1D in 3D spaces. The growth of bacterial colonies is an example of biology where moving interfaces are involved. Molecular Beam Epitaxy (MBE) is technologically important in manufacturing chips and semiconductor devices (Barabasi and Stanley 1995). It also involves growing surfaces/interfaces. Here we are more interested in magnetism. Acquiring, storage and retrieval of data in magnetic recording devices requires the fabrication of material which involves surfaces/interfaces. It is technologically important to fabricate smooth surfaces/interfaces in these devices as roughness drastically reduces the quality (Falicov et al. 1990). Extensive investigation of surfaces/interfaces in connection with magnetism has been carried out because of its technological concerns (Hellman et al. 2017). Zao et al. (2000) established a correlation between surface roughness and surface magnetization. Real interfaces are complex. So it is better to model them using the Ising model with an external magnetic field. The field is positive on one side and negative on the other side. Thus a magnetization interface is induced. The field moves with an externally applied velocity and tries to drag the magnetization interface with it. Mostly such studies have been in two dimensions (Rikvold and Kolesik 2002a, 2003, 2000; Chaudhuri et al. 2002, 2004), and studies in three dimensions are limited (Sahai and Sengupta 2008; Sahai and Bakshi 2022).

The direct impact of the presented work is in the semiconductor industry (Barabasi and Stanley 1995) where MBE is used to grow surfaces/interfaces. Another domain is of magnetic recording devices (Hellman et al. 2017) where the smoothness of the surface is the most important technological concern. But the purpose of this article is to

make the reader acquainted with a simulation methodology. This methodology has the potential of being exploited in various frontier problems, and articles on it are limited (Cheimarios et al. 2021). Clubbing this methodology with ab initio results can make the approach more practical. Hence, further reading should be done with this perspective.

11.2 Theoretical Background

In this section, we will be mapping the problem of surface/interface growth to the Ising model and describe how its dynamics can be simulated using the Metropolis algorithm. We would start with an introduction to the Ising model and develop the methodology in a step-by-step process.

11.2.1 Ising Model

In bulk magnetic material, major components of energy are (a) exchange interaction, (b) spin–orbit coupling and (c) magnetic dipolar interaction (Fulde 1995; Wahle et al. 1998; Coey 2010). Exchange interaction is the interaction of orbital wave function with crystal field. It is basically a manifestation of charge-charge interaction. In solids, compared to s and p shells, d and f shells are less spatially localized. The degree of hybridization is dependent on the detailed nature of chemical bonding. This degree of hybridization decides either the local moment model or band model of magnetism appropriate to work with.

In the local moment model, the reason behind magnetic ordering is the exchange interaction between electrons on different atoms. In the absence of this interaction, paramagnetic ordering is expected with susceptibility following Curie law. The inter-atomic exchange couples

total spin **S** of two nearby atoms (labeled further as i and j). This interaction is complex due to the overlap of wave functions. But it can be established to have a relatively simple form with major terms $-J_{ij}S_iS_j$, where J_{ij} is the exchange integral or the exchange constant. For positive J_{ij}, ferromagnetic ordering is favored and with negative J_{ij} antiferromagnetic ordering is favored.

It is a consequence of spin–orbit coupling that the magnetization direction is connected to the crystal lattice. The preferred direction of magnetization is a result of spin–orbit coupling and crystal field. This phenomenon is known as magneto crystalline anisotropy (Neel 1954; Jhonson et al. 1996). In the case of material having a large number of symmetry axes such as cubic lattice, this effect is weak. But it is quite strong in material with uniaxial symmetry. In the local moment model be it ferromagnetic or antiferromagnetic ordering, there is no preferred direction without spin–orbit coupling (as explained in the previous paragraph). This model is known as the Heisenberg model. If magneto crystalline anisotropy exists, and spins are restricted to an axis, then the model is known as the Ising model.

As stated in the previous paragraph, the Ising model is a set of spins (usually arranged on a lattice), which has two preferred orientations of spins. The two orientations are symbolized by +1 and −1. Lattice can be 1D, 2D or 3D leading to 1D, 2D or 3D Ising model, respectively. The spin–spin interaction is only with nearest neighbors. Interaction can be ferromagnetic (positive J_{ij}) or antiferromagnetic (negative J_{ij}). In the presence of an external magnetic field, an additional term is added to the Hamiltonian. Thus the Hamiltonian for Ising model is represented by Eq. (11.1):

$$H = -J_{ij}\sum_i\sum_j S_iS_j + \sum_i H.S_i \tag{11.1}$$

where j runs over the nearest neighbors and i runs over all the lattice sites.

In this chapter, the Ising model is discussed in the context of magnetism, which is its basic origin. But the Ising model is applied to many branches of science like bioscience (Shi and Duke 1998; Vtyurina et al. 2016), neurosciences (Schneidman et al. 2006) and many more.

Here we are interested in applying the Ising model to the Solid-on-Solid model of surface growth (Barabasi and Stanley 1995). This is technologically important in MBE which is used in the fabrication of chips and semiconductor devices. Further, we shall digress and discuss the phenomenon of deposition and further we will discuss how the Ising model can be used to simulate the phenomenon.

11.2.2 Deposition Processes

The objective of any deposition process is to deposit material on a surface by any physical or chemical technique. In physical processes, the material to be deposited is injected as a gas/vapor. The injected material sticks on the surface with a probability (or rate). Physical vapor deposition (PVD) is an example of this category. Other deposition processes are chemical vapor deposition (CVD), atomic layer deposition (ALD) and electrochemical deposition.

Depending on the physical or chemical technique of interest, the number and type of processes that occur in the proximity of the lattice site differ. Accordingly, the steps of Monte Carlo/Kinetic Monte Carlo simulation also get modified. In the phenomenon of deposition, adsorption, desorption, surface diffusion and surface reaction events are used. The physical or chemical mechanism which is unique to each deposition process is designed to achieve a balance between this phenomenon and to get the desired parameters for a film. The objective of using the Monte

Carlo (MC)/Kinetic Monte Carlo (KMC) technique is to derive the growth rate and to predict the morphology of the growing surface. Simulation using MC/KMC is very useful in this domain as the snapshots of simulation can be directly correlated to the images from scanning tunneling microscopy (Cheimarios et al. 2021).

11.2.3 Mapping of Deposition Process Using Ising Model and Metropolis Algorithm

To map a growing surface/interface using the Ising model, we apply the following methodology. We start with all up, all down or paramagnetic state set of spin arranged on a lattice. An external step-shaped magnetic field is applied to the set of spins and is evolved using MC/KMC techniques (Cheimarios et al. 2021). For the sake of completeness, an example of an update rule (for the evolution of the spin set in a particular field condition) using the Metropolis algorithm (Bhanot 1988) is explained. In the Metropolis algorithm, the spins are flipped in the evolution according to the probability given below

$$P\left(\chi \rightarrow \chi'\right) \alpha \exp\left(-\frac{E\left(\chi'\right) - E\left(\chi\right)}{K_B T}\right) \tag{11.2}$$

where

χ is the original state of the system.

$\chi\prime$ is the state of system obtained by flipping the site under consideration.

$E\left(\chi\prime\right)$ is the energy of system in $\chi\prime$ state.

$E\left(\chi\right)$ is the energy of system in χ state.

K_B is Boltzmann constant.

T is temperature in Kelvin.

so that the system moves from state χ to $\chi\prime$ if $\triangle E(= E(\chi\prime) - E(\chi)) <$ 0. If $\triangle E$ > 0 system moves from state χ to $\chi\prime$ with a probability $\exp(-\triangle E/K_B T)$. For doing this in simulation, we generate a standard random number between 0 and 1 and compare it with a probability of spin flip to make a decision.

There are other update rules also (Rikvold and Kolesik 2002b). By flipping the randomly chosen spins a large number of times, the system equilibrates in that field and temperature condition. In the limit where the temperature is low and the field is high, an interface in the magnetization profile is developed corresponding to the field interface. By moving the field, the magnetization interface translates on the lattice. This simulates the growing surface.

11.3 Simulation Details

11.3.1 System Specifications

In the simulation work, two separate systems are considered. The first system (system I) of our simulation consists of $14 \times 14 \times 30$ spins. The lattice on which the spins are arranged is simple cubic. The interaction is ferromagnetic only with nearest neighbors. When an external field is applied, the spins interact with the external field as well. The profile of the external field is shown in Figs. 11.1 and 11.2. It is step-shaped. On the left, the field is oriented toward the -Y axis. On the right, it is oriented toward the +Y axis. Clearly, there would be an interface, where the field would change sign. Further, this interface is not perpendicular to the Z axis. It has an inclination to the X axis (=θ) and with the Y axis (=φ) as illustrated in Fig. 11.3. The field is also not static. It translates toward

the +Z direction. Its velocity is controlled externally. We are interested in low temperature, and high field limits. Under this assumption, only in the vicinity of the interface interesting dynamics of spins is observed. The spins far off from the interface are fixed along the field at that location. Accordingly, boundary conditions are applied in the simulation. In X and Y directions, to ensure the periodic image of each spin has the same value of the magnetic field, shifted periodic boundary conditions are applied. Along the Z axis we have open boundary conditions. The exact nature of boundary conditions along the Z direction is irrelevant as in any way spins are fixed along the magnetic field at their respective locations. Due to this, left extreme spins will always be oriented toward the -Y axis and spins of extreme right will be oriented toward the +Y axis. We will refer to this field interface as a planar field interface in further text.

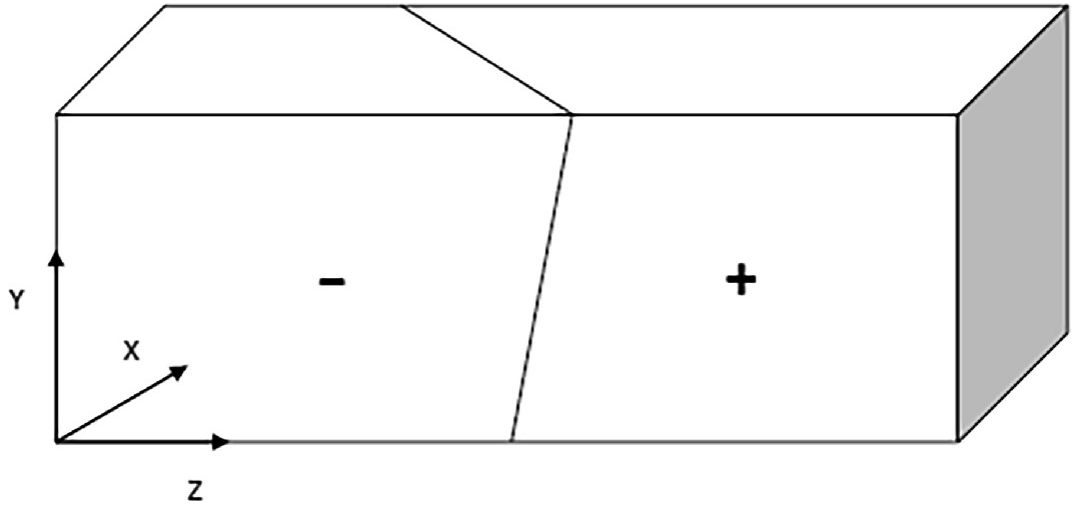

Fig. 11.1 The orientation of external field in system I. On left side, field is oriented along (−)ve Y axis and on right side along (+)ve Y axis. Figure has been redrawn by author

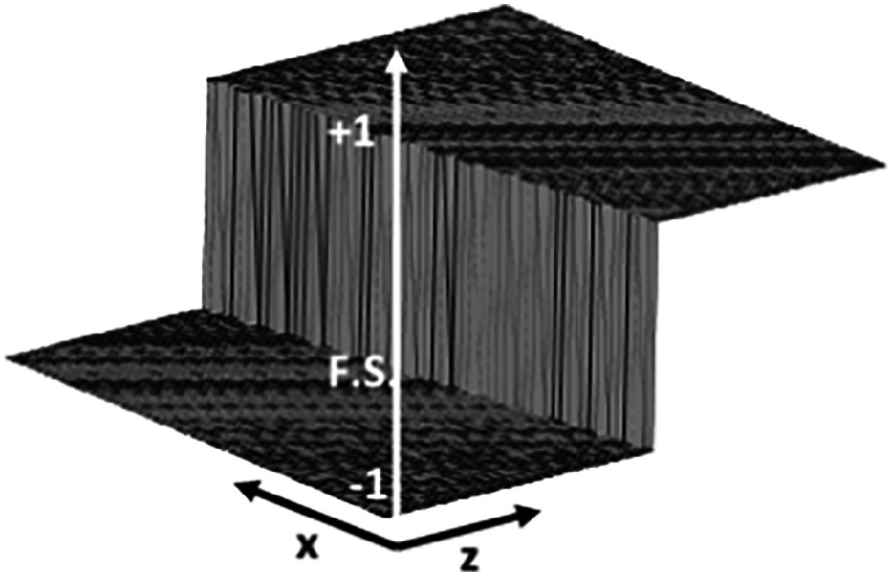

Fig. 11.2 The profile of external magnetic field on a horizontal cross section of lattice. It illustrates step shape of field strength. F.S. stands for field strength. Figure has been redrawn by author

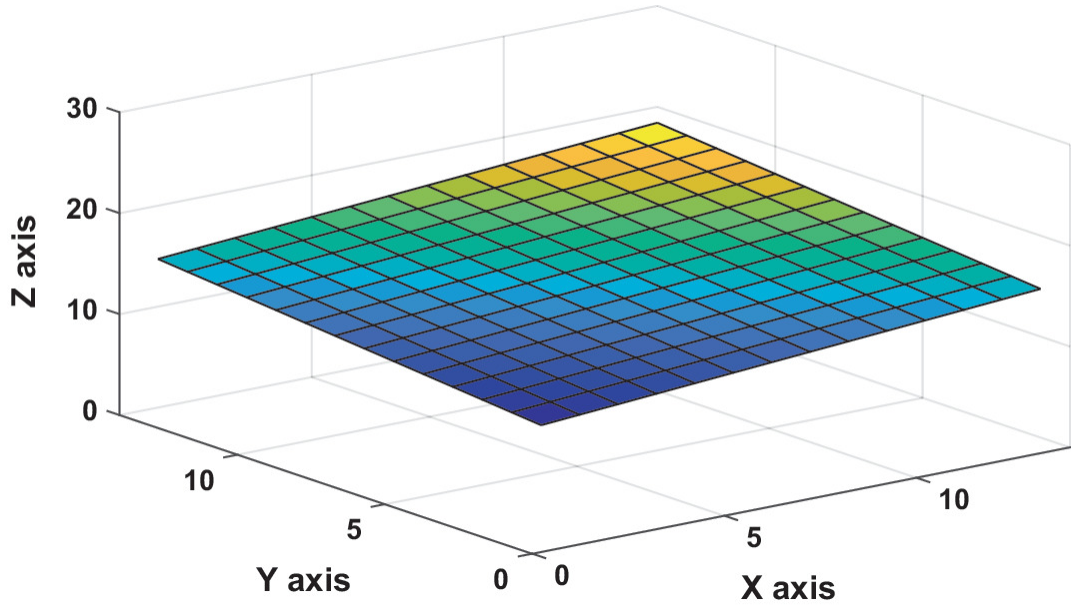

Fig. 11.3 A snapshot of field interface in system I. Figure has been redrawn by author

This system has two limitations.

(a) It does not allow large inclinations of field interface.

(b) It is better to have a spatially large magnetization interface, so that reasonable histograms are

generated (the need to generate histograms will be explained later in the text).

Considering the above two constraints, it was decided to consider a modified system (system II) along with this system (system I). Only increasing size along the Z axis will allow larger inclinations but the surface area of the magnetization interface will not be enhanced considerably. Taking a very large system has its own constraints of increased computational time. Looking into all the aspects, it was decided to double the system in X and Y orientations and to fold the field interface giving it a shape as shown in Fig. 11.4. The obtained field interface will be called folded field interface, and the corresponding field profile folded field profile. The folded field interface can be obtained from the planar field interface by taking mirror images about the $x = 0$ plane in and about the $y = 14$ plane respectively in the first system. On the left side, same as system I, system II has a field oriented toward the -Y axis and on the right toward the +Y axis. A folded field profile has its own additional advantage. It answers the question, what happens if the field interface has curvature! In both systems field strength is unity (−1 on the negative side and +1 on the positive side) (Fig. 11.5).

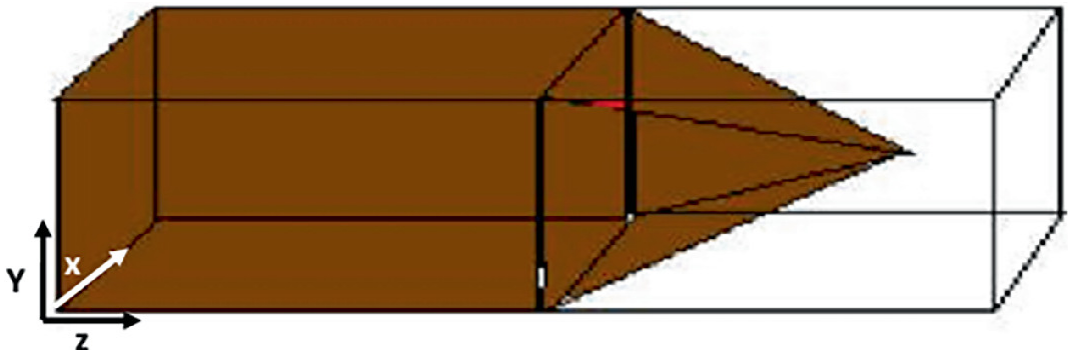

Fig. 11.4 System II. It illustrates the field orientation in system II. Shaded part has field toward (-)ve Y axis and rest toward (+)ve Y axis. This field profile is obtained from field profile of Fig. 11.1 by taking mirror images about $x = 0$ and $y = 14$ planes of Fig. 11.1 respectively. Origin is relocated. Figure has been redrawn by author

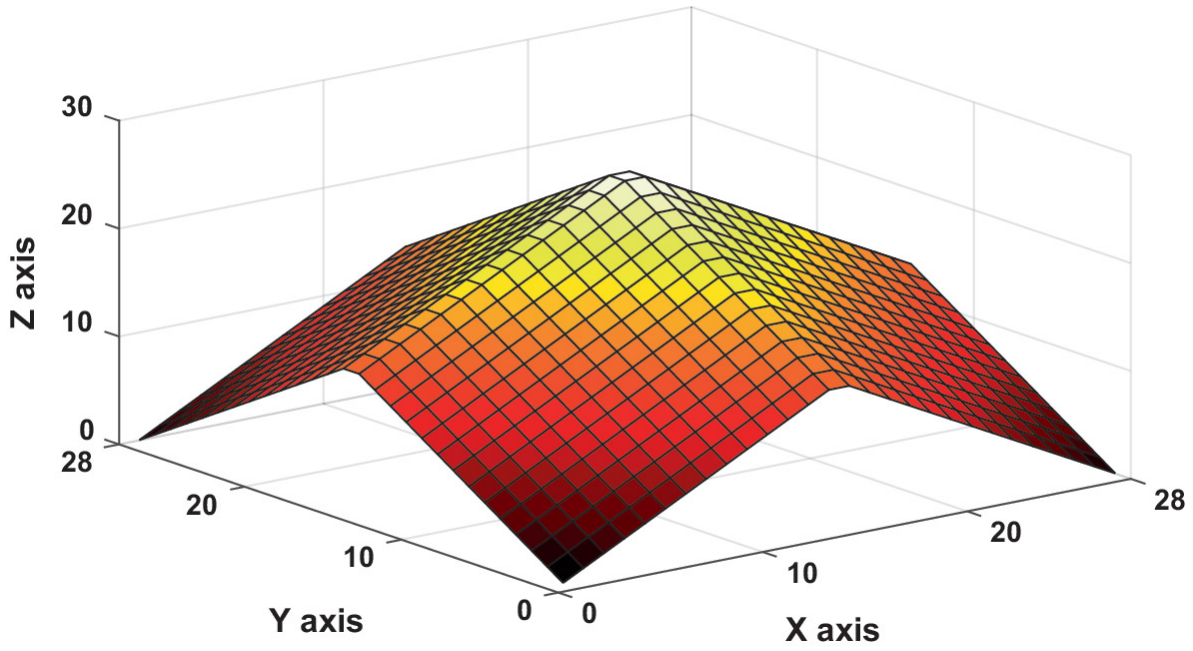

Fig. 11.5 Field interface with folded field profile (System II). Figure has been redrawn by author

11.3.2 Nomenclature

It would be good to clarify the nomenclature used in the text at this stage. The symbol **H**(**r**, t) stands for the magnetic field applied (and) and the symbol **B**(**r**, t) for the field interface (and). The applied field will magnetize the underlying spins and will generate a moving magnetization interface. The symbol **M** (**r**, t) stands for the magnetization profile and the S(**r**, t) for the magnetization interface. To observe the mutual positions of magnetization and field interfaces, we introduce a fluctuation profile which is calculated as F(**r**, t) = S(**r**, t)-B(**r**, t). The orientation of B with respect to the X and Y axes is parameterized by m_x (=tanθ) and m_y (=tan φ). Our interest is in the local orientation of the magnetization interface to understand the local surface morphology. For this, a window of 5 spins × 5 spins is considered. This window is moved on the whole magnetization interface. The spatial orientation of this window is m'_x (=tan φ′) and m'_y (=tan φ′) θ′ and φ′ are

orientations of this window with respect to the X and Y axes respectively. The symbols m'_x and m'_y are denoted as the local slope of the magnetization interface. It is worth noting that (m'_x, m'_y) is an independent symbol and in no way is a derivative of (m_x, m_y).

11.3.3 Equilibrating System in a Particular Field Condition

We start with a randomly oriented set of spins and apply the magnetic field. Further, our target is to equilibrate the system in this particular field condition. For this, the procedure is to locate spin sites randomly and flip them according to the Metropolis algorithm mentioned previously. The following section give the details of the ensemble-averaged magnetization profile in a particular field condition in a step-by-step process.

The first step is to locate the spin site randomly. Standard random number generators generate random numbers between 0 and 1. The rule for generating arbitrary random numbers between 'a' and 'b' from standard random numbers between 0 and 1 is as follows:

$$\eta = \mathrm{a} + (\mathrm{b} - \mathrm{a})\,\xi$$

where

η is a random number between 'a' and 'b'.

ξ is a random number between 0 and 1.

Depending on the system size which is $N_x\,(=14)\,xN_y\,(=14)\,xN_z\,(=30)$ in system I and $N_x\,(=28)\,xN_y\,(=28)\,xN_z\,(=30)$ in system II, we generate random numbers to locate the spin site. Let us take system I as an example. First, a random number is generated between 0 and 14 which is denoted as η_x. Again we generate a random number between 0 and 14 which is

denoted as η_y. Further, a random number is generated between zero and 30, which is denoted as η_z. The set of random numbers (η_x, η_y, η_z) is the location of the arbitrary spin site. In the second step, randomly located spin site is required to flip as per the Metropolis algorithm discussed previously. For this purpose, the Hamiltonian used is as mentioned below

$$H = -J_{ij} \sum_j S_i S_j + H_i S_i \tag{11.3}$$

where j runs over the nearest neighbors of i.

S_i is the spin at the randomly located site.

S_j is the spins at the nearest neighbor sites of located spin.

H_i is the local magnetic field at the located site.

As per the Hamiltonian energy, difference in the state χ and χ' is calculated. Accordingly, the system remains in the state χ or migrates to the state χ'. The process of randomly locating the spin sites and updating the flip of spin is done for large number of times depending on the system size. It was done 10^6 times for a system size $N_x\,(=14)\,xN_y\,(=14)\,xN_z\,(=30)$.

In this way, the final configuration of spins in that field condition and at that temperature is obtained. This is the procedure for first initial condition. Subsequently, a fresh initial condition is taken and the whole process is repeated. In this way, repetition is done 250 times. An independent initial condition is taken every time.

From this, an ensemble-averaged magnetization profile in a particular field condition is obtained.

11.3.4 Dynamics of the Field

Further, the field location is incremented as per the externally controlled velocity (V_f). Again, ensemble-averaged magnetization profile is obtained. Similarly, a large number of initial runs are taken. In our case 10^2 independent runs are taken. In each configuration of field independent run averaged magnetization profile **M** (**r**, t) is obtained. For each field configuration, we have to find the magnetization interface. To find the magnetization interface in a particular field configuration (at any instant of time), the following procedure is followed.

At any instant **M**(**r**, $t = t'$) is taken. In this magnetization configuration, each 1D thread in the direction of the Z axis is fitted with $\tanh(\frac{z-z_0}{d})$. The value of z_0 provides a position of the magnetization interface for the considered 1D thread **M** ($x = x'$, $y = y'$, z, $t = t'$). By repeating this procedure for all sets of (x', y'), we obtain the magnetization interface for that instant of time **S**(**r**, $t = t'$). We repeat this process for all field conditions and obtain **S**(**r**, t). F (**r**, t) is obtained in each field condition. Algorithm 1 explains the above procedure using a flowchart. The algorithm for Metropolis update is illustrated in Algorithm 2. Temperature is taken to be unity in units of K_BT. In Metropolis update while calculating $\exp(-\Delta E/(K_BT))$, K_BT is taken to be unity.

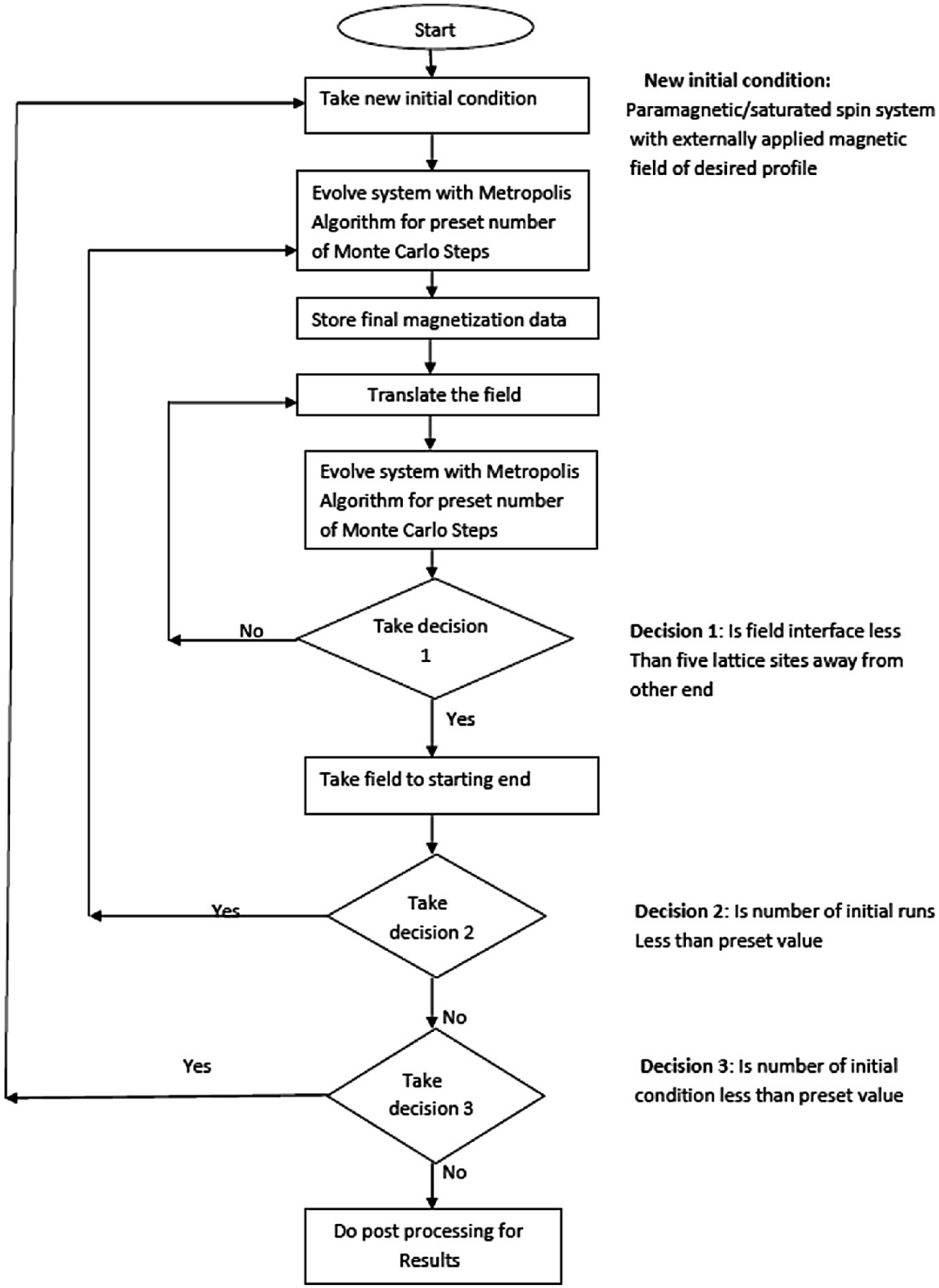
Start
Take new initial condition
Evolve system with Metropolis Algorithm for preset number of Monte Carlo Steps
Store final magnetization data
Translate the field
Evolve system with Metropolis Algorithm for preset number of Monte Carlo Steps
Take decision 1
No
Yes
Take field to starting end
Take decision 2
Yes
No
Take decision 3
Yes
No
Do post processing for Results
New initial condition: Paramagnetic/saturated spin system with externally applied magnetic field of desired profile
Decision 1: Is field interface less Than five lattice sites away from other end
Decision 2: Is number of initial runs Less than preset value
Decision 3: Is number of initial condition less than preset value

Algorithm 1 Flow chart of algorithm for generating data base

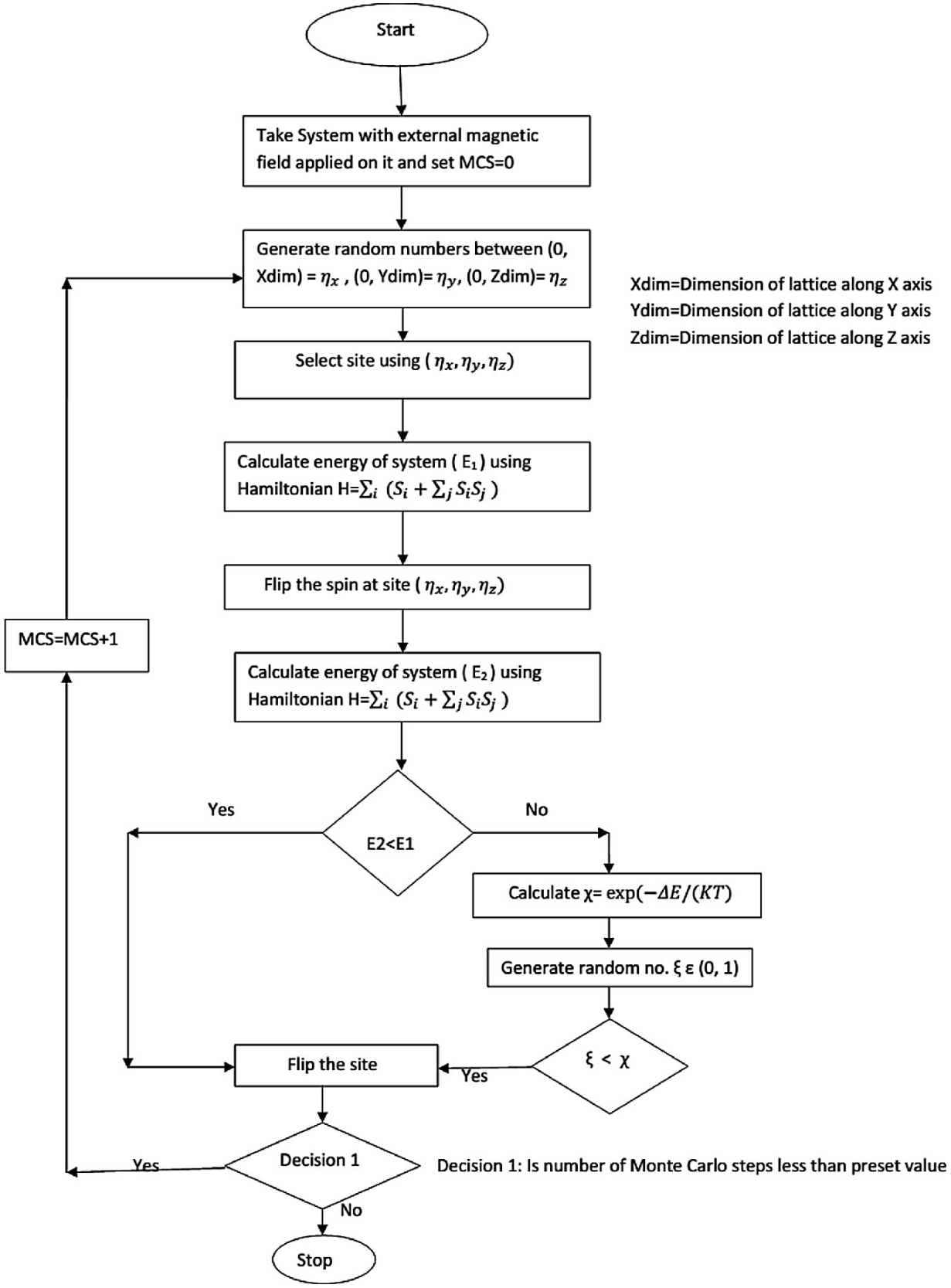
Start
Take System with external magnetic field applied on it and set MCS=0
Generate random numbers between (0, Xdim) = η_x , (0, Ydim)= η_y, (0, Zdim)= η_z
Xdim=Dimension of lattice along X axis
Ydim=Dimension of lattice along Y axis
Zdim=Dimension of lattice along Z axis
Select site using (η_x, η_y, η_z)
Calculate energy of system (E_1) using Hamiltonian H=$\sum_i$ ($S_i + \sum_j S_i S_j$)
Flip the spin at site (η_x, η_y, η_z)
MCS=MCS+1
Calculate energy of system (E_2) using Hamiltonian H=$\sum_i$ ($S_i + \sum_j S_i S_j$)
Yes
E2<E1
No
Calculate χ= exp($-\Delta E/(KT)$
Generate random no. ξ ε (0, 1)
ξ < χ
Yes
Flip the site
Yes
Decision 1
Decision 1: Is number of Monte Carlo steps less than preset value
No
Stop

Algorithm 2 Flow chart of algorithm for evolution of system using Metropolis algorithm

11.3.5 Morphology of Magnetization Interface

For analysis of (m'_x, m'_y), a window of 5×5 spins is taken on the magnetization interface at a particular instant of time. The orientation of this window is obtained. This gives us the first set of (m'_x, m'_y). A wealth of data is obtained by moving this window on the whole magnetization interface (only the rippled part in the case of system II to remove the effect of curvature in the field profile) and further temporally in all field configurations. The histogram of this data set is obtained. We expect the local slope of the magnetization interface from 0.0 to 1.0 ($m'_x = 0.0$ to 1.0 & $m'_y. = 0.0$ to 1.0). This range is divided into 100 × 100 equal divisions. Hence, the bin size of the histogram is 0.01 × 0.01. A rational fraction is assigned to each bin corresponding to the lowest fraction: For example, if bin from (0.28–0.29), (0.28–29)} is assigned a fraction (2/7, 2/7). A magnetization interface is denoted by the parameters of the field interface that has generated it. Hence, such statements will be found in further text “The most probable local slopes of magnetization interface (2/7, 2/7) is {(1/4, 1/4) & (1/3, 1/3)}”.

11.4 Results

11.4.1 Pinned-Lagging Transition of Magnetization Interface

The flowchart for obtaining pinned-lagging transition is given in Algorithm 3. The locus of all the points where the field changes sign is referred to as the field interface, B(**r**, t). The method of finding the magnetization interface is explained in Sect. 3.4. S(**r**, t) is the locus of all the points where magnetization changes sign. In this section, our

results on the movement of S(**r**, t) along with B(**r**, t) are discussed. The velocity of S(**r**, t) in unit lattice per MCS is determined by finding the location of center of mass of S(**r**, t) with respect to time. MCS is Monte Carlo steps.

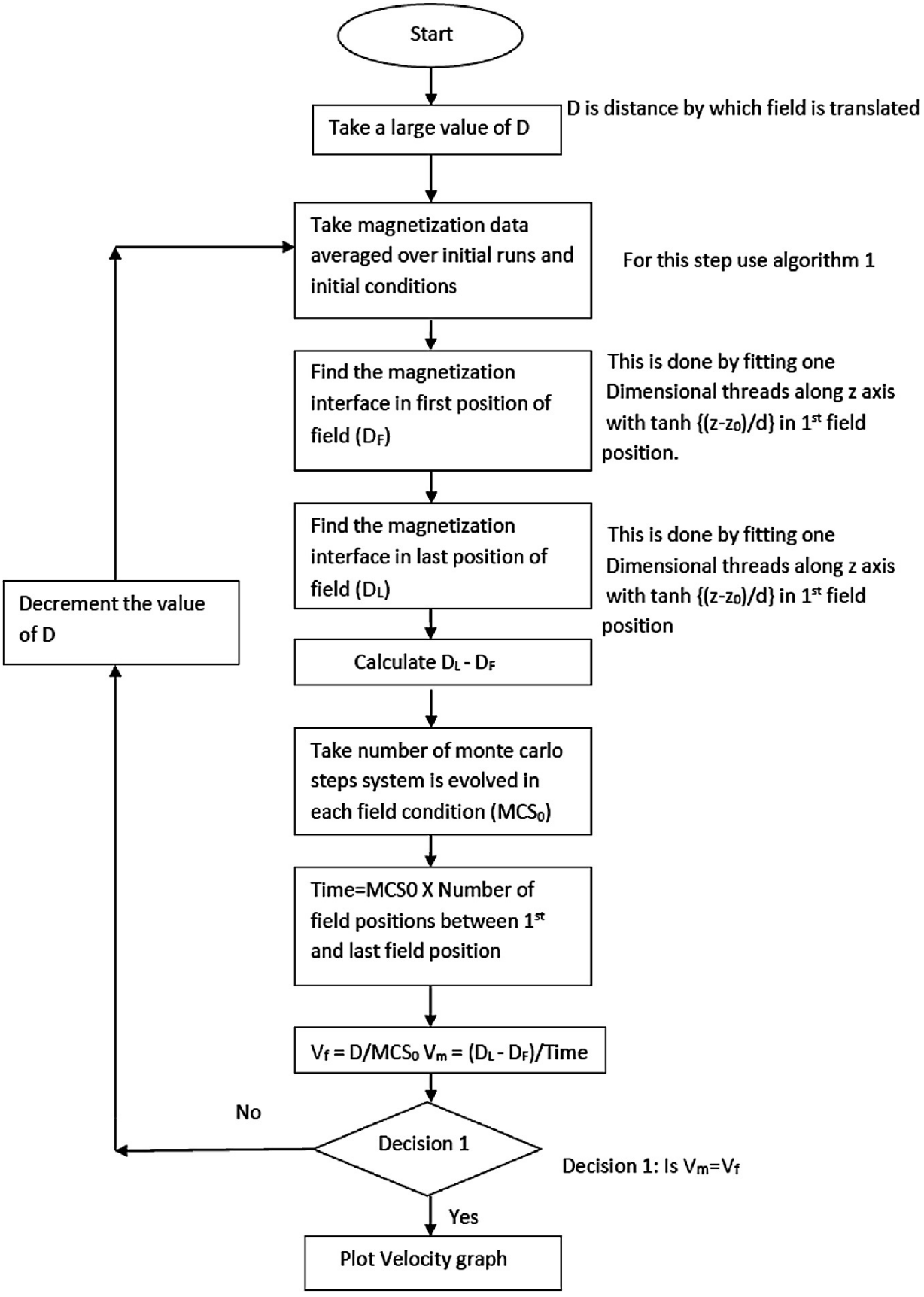
Start
Take a large value of D
D is distance by which field is translated
Take magnetization data averaged over initial runs and initial conditions
For this step use algorithm 1
Find the magnetization interface in first position of field (D_F)
This is done by fitting one Dimensional threads along z axis with tanh {(z-z0)/d} in 1st field position.
Find the magnetization interface in last position of field (D_L)
This is done by fitting one Dimensional threads along z axis with tanh {(z-z0)/d} in 1st field position
Calculate D_L - D_F
Take number of monte carlo steps system is evolved in each field condition (MCS_0)
Time=MCS0 X Number of field positions between 1st and last field position
$V_f = D/MCS_0$ $V_m = (D_L - D_F)/Time$
No
Decision 1
Decision 1: Is $V_m=V_f$
Yes
Plot Velocity graph
Decrement the value of D

Algorithm 3 Flow chart of algorithm for pinned—lagging transition (Result in Sect. 11.4.1)

This is symbolized as V_m. The value of V_f is already known as it is externally applied. We drive B(**r**, t) with various velocities and find the velocity of S(**r**, t) in each case. It is observed that for low V_f, the value of V_m is the same as V_f. This is the phase when S(**r**, t) moves pinned with B(**r**, t). This phase is called the pinned phase (phase I). But, as V_f is increased slowly S(**r**, t) starts lagging B(**r**, t). This phase is called the lagging phase (phase II). Finally, the value of V_m saturates. This means whatever be the velocity of B(**r**, t), S(**r**, t) moves with a saturated velocity. Figure 11.6 shows the V_m-V_f graph for system I. It is evident from Fig. 11.6 that there is a transition from phase I to phase II. The orientation of the field interface effects this transition. This transition is less sharp in 3D case (Sahai and Sengupta 2008) as compared to 2D (Chaudhuri et al. 2002, 2004). This is attributed to the finite size effect (Landau and Binder 2000).

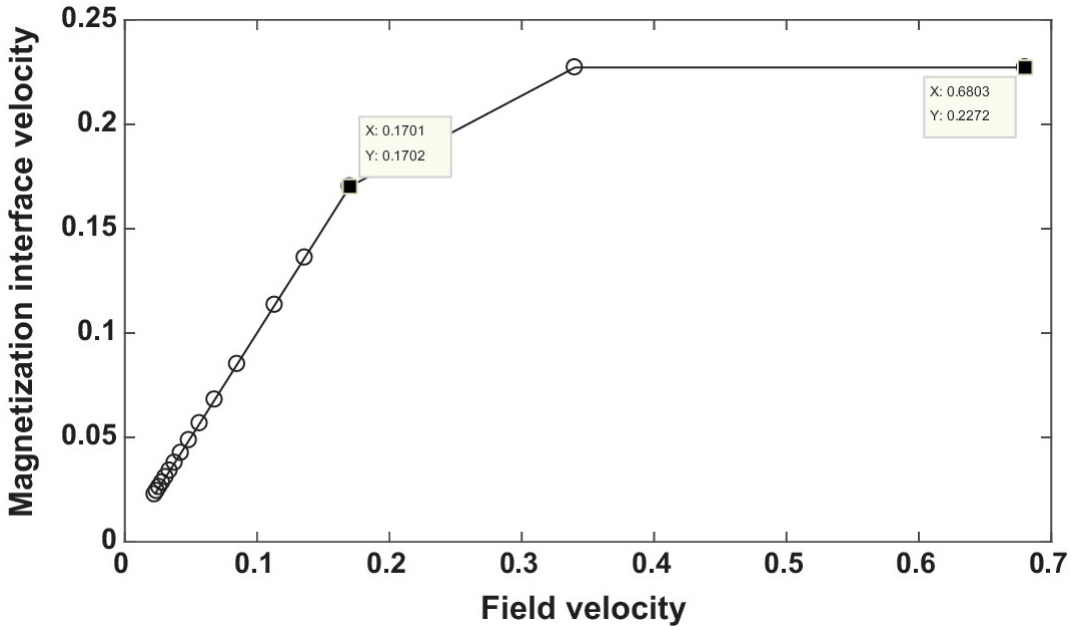

Fig. 11.6 Graph between field interface velocity (V_f) and magnetization velocity (V_m). It illustrates pinned-lagging transition. Figure has been redrawn by author

11.4.2 Structure of Magnetization Interface

The morphology of system I is discussed in this section. The flowchart for obtaining results reported in 4.2, 4.3 and 4.4 is given in Algorithm 4.

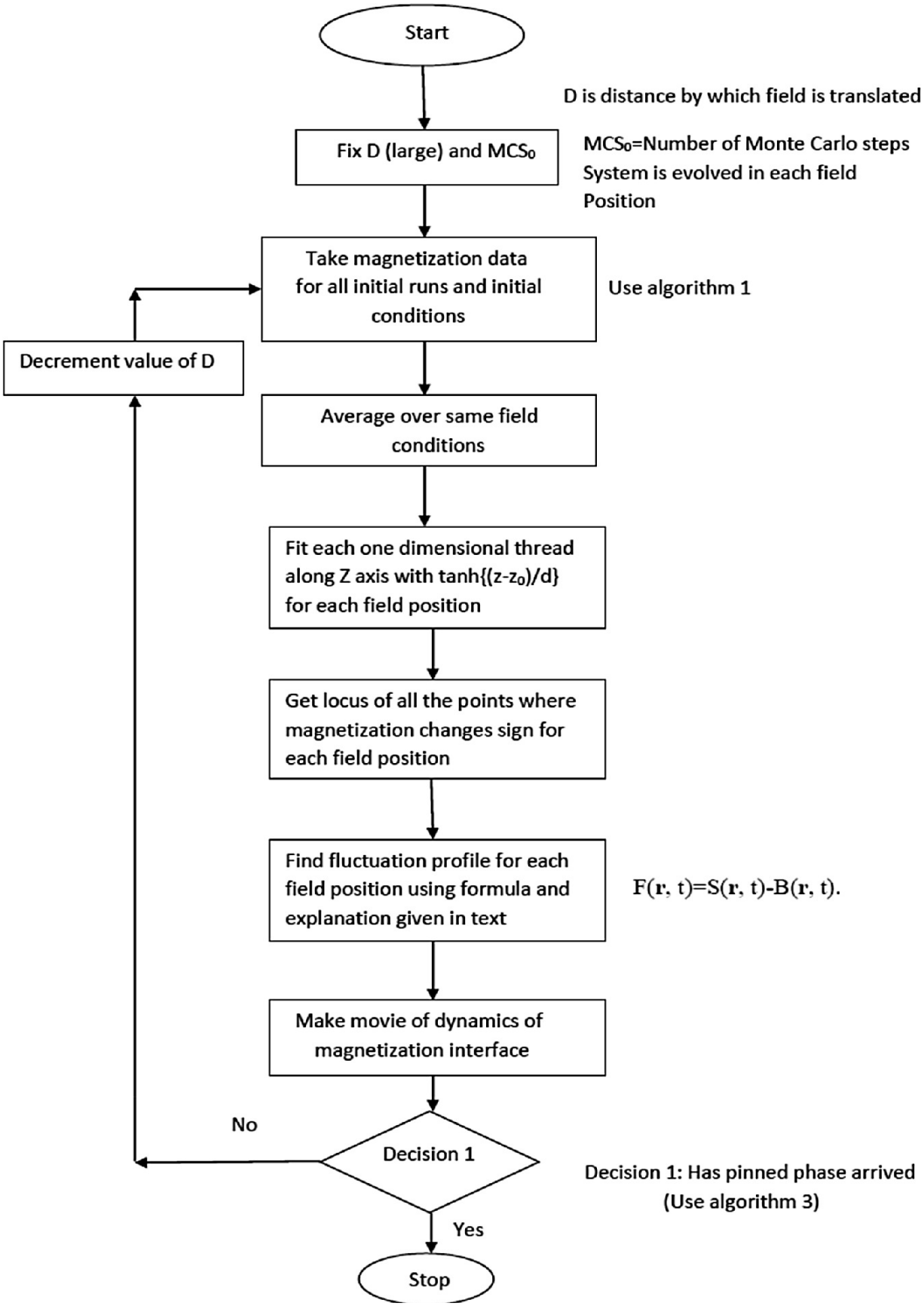
Start
D is distance by which field is translated
Fix D (large) and MCS0
MCS0=Number of Monte Carlo steps System is evolved in each field Position
Take magnetization data for all initial runs and initial conditions
Use algorithm 1
Decrement value of D
Average over same field conditions
Fit each one dimensional thread along Z axis with tanh{(z-z0)/d} for each field position
Get locus of all the points where magnetization changes sign for each field position
Find fluctuation profile for each field position using formula and explanation given in text
F(r, t)=S(r, t)-B(r, t).
Make movie of dynamics of magnetization interface
No
Decision 1
Decision 1: Has pinned phase arrived (Use algorithm 3)
Yes
Stop

Algorithm 4 Flow chart of algorithm for structure of magnetization interface (Result of Sects. 11.4.2, 11.4.3 and 11.4.4)

In pinned phase, the S(**r**, t) is rippled as illustrated in Fig. 11.7c. Figure 11.7 shows the magnetization interface for $m_x = m_y = 2/7$. As V_f is increased, the ripples start melting, making the surface smoother on average. Figure 11.7b shows the morphology of the magnetization interface at a higher field velocity. It is evident from Fig. 11.7 that there is the smoothing of the magnetization interface as the value of field velocity increases.

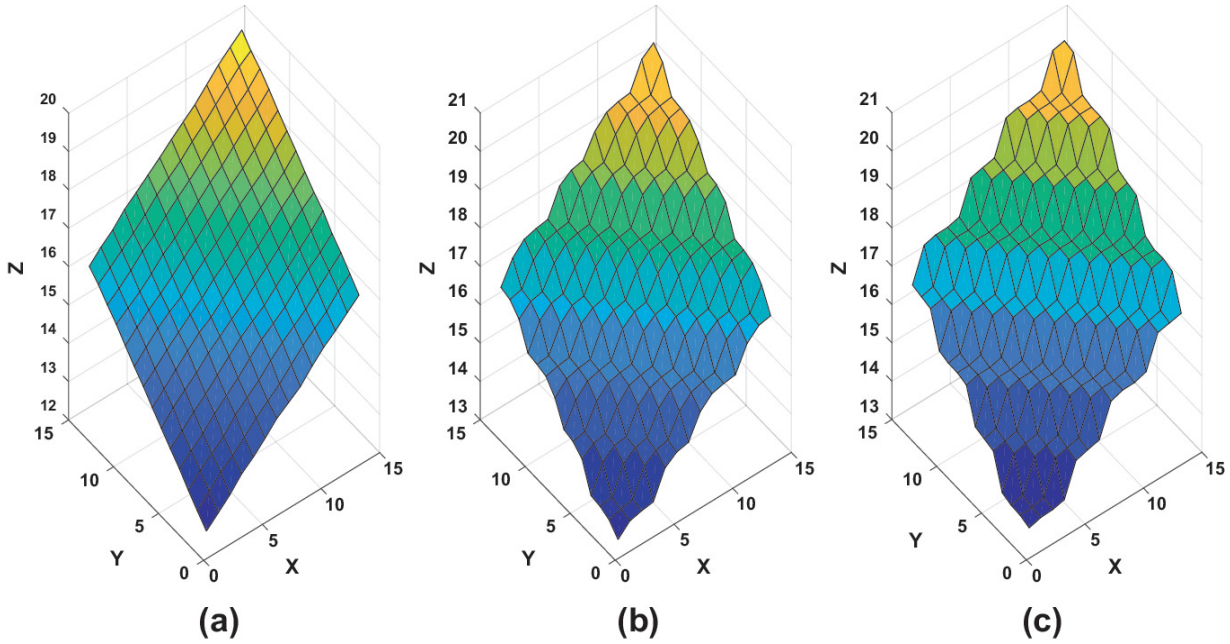

Fig. 11.7 Morphology of magnetization interface at three different velocities. The velocity is decreasing from (**a**) to (**c**). It illustrates the effect of pinned-lagging transition on the morphology of magnetization interface. Figure has been redrawn by author

11.4.3 Curvature's Effect

In the case of system II, S(**r**, t) has two regions as far as morphology is concerned. There is a central smooth region and a peripheral rippled region. The behavior of the peripheral rippled region is similar to that of the planar magnetization interface. The ripples melt and the surface

becomes smoother on average as the value of V_f is increased.

Meanwhile, there is a central region which is microscopically smooth and macroscopically flat. This region is perpendicular to the velocity. Figure 11.8 shows S(**r**, t) for the folded field profile clearly illustrating the rippled and smooth parts.

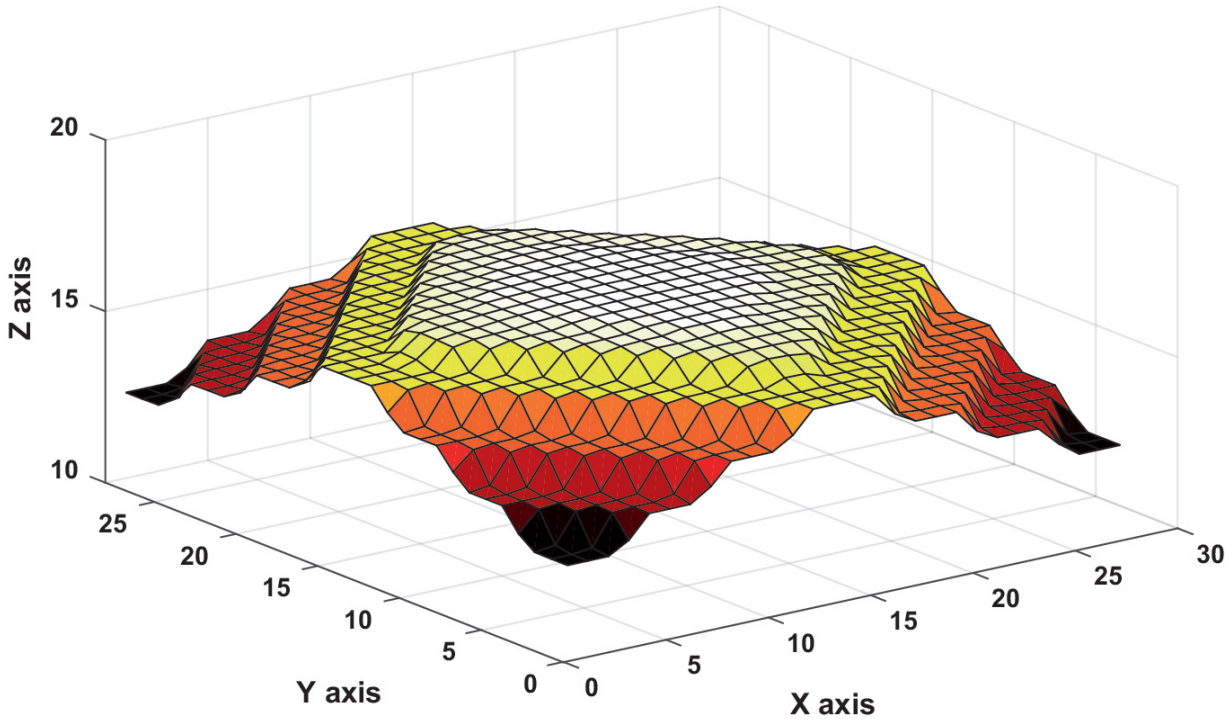

Fig. 11.8 Snapshot of magnetization interface with folded field profile (System II) in pinned phase. It illustrates the smooth and rippled parts in the magnetization interface in the pinned phase. Figure has been redrawn by author

Superficially thinking, one may contend that the central smooth region in the magnetization interface is due to a sharp point in the field interface. But, detailed analysis has been performed with a hemisphere-shaped field interface also and it is verified that the central smooth part continues to exist. Hence, it is concluded that the central smooth part is a result of curvature in the field interface and not due to the sharp point.

11.4.4 The Fluctuation Profile

The magnetization interface fluctuates in space and time about the field interface during the dynamics of the field interface.

The spatial location of different parts of S(**r**, t) with respect to B(**r**, t) for the case of folded field profile using the fluctuation profile is shown in Fig. 11.9. It is generated as per the explanation given in the simulation details (Sect. 11.3). From the fluctuation profile, it is observed that the central smooth part of the magnetization interface lags the field interface, and the rippled part leads the field interface.

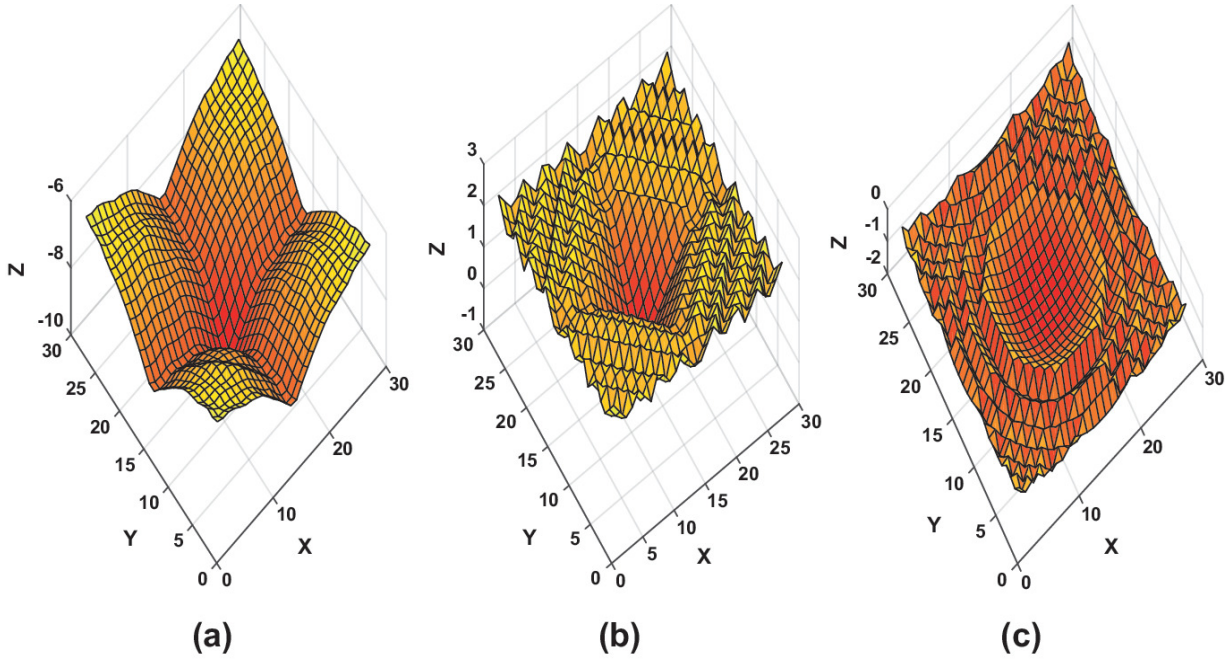

Fig. 11.9 Spatial location of different parts of S(**r**, t) with respect to B(**r**, t) using fluctuation profile, F(**r**, t) = S(**r**, t)-B(**r**, t). **a** lagging phase in system II, **b** pinned phase in system II and **c** pinned phase with hemispherical field profile. Figure has been redrawn by author

11.4.5 Kinematic Waves

As the field interface moves, there is an apparent flow of waves on the magnetization interface. These are known as Kinematic Waves. The physics behind Kinematic Waves is

explained below. The algorithm for results reported in Sects. 4.5 and 4.6 is given in Algorithm 5.

In the pinned phase, S(**r**, t) is forced to follow B(**r**, t) as closely as possible. But B(**r**, t) is smooth whereas the lattice on which it is applied is discrete. Hence, S(**r**, t) cannot coincide with B(**r**, t). So it settles fluctuating about it in space and time during the dynamics of the field.

As B(**r**, t) moves, the environment of the lattice around S(**r**, t) continuously changes. This causes structural changes in S(**r**, t). It appears like waves flowing on the surface S(**r**, t).

In the case of a folded field profile, these waves continuously converge and diverge temporally. The period of convergence and divergence is slope-dependent. For the case of $m_x = -2/7$, $m_y = -2/7$ waves diverge slowly followed by fast convergence. With $m_x = 2/7$, $m_y = 2/7$ waves converge slowly followed by fast divergence. This sequence of converging and diverging waves is continuous during the dynamics of the field.

With a hemispherical field profile, a qualitatively similar phenomenon is observed, but, with a signature of field geometry.

11.4.6 Microstructure of Magnetization Interface

As explained previously in simulation details (Sect. 11.3) in order to probe the microstructure of the magnetization interface, a 5×5 spin window is taken. The whole magnetization interface (rippled part) is scanned by this window. The scanning is done continuously as the S(**r**, t) translates on the lattice. This gives a set of data on the window's orientation. The orientation is parameterized by

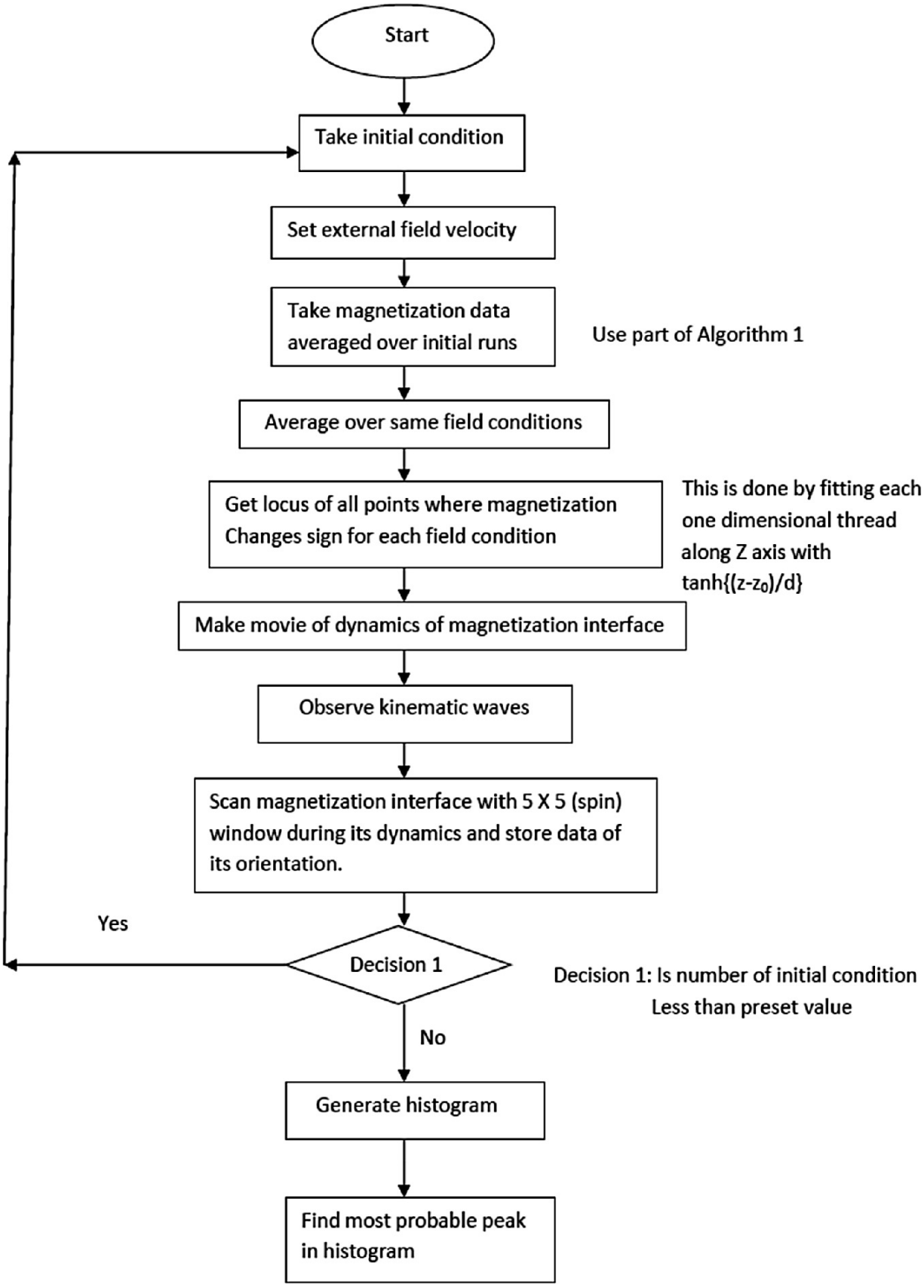
Start
Take initial condition
Set external field velocity
Take magnetization data averaged over initial runs
Use part of Algorithm 1
Average over same field conditions
Get locus of all points where magnetization Changes sign for each field condition
This is done by fitting each one dimensional thread along Z axis with tanh{(z-z0)/d}
Make movie of dynamics of magnetization interface
Observe kinematic waves
Scan magnetization interface with 5 X 5 (spin) window during its dynamics and store data of its orientation.
Yes
Decision 1
Decision 1: Is number of initial condition Less than preset value
No
Generate histogram
Find most probable peak in histogram

Algorithm 5 Flow chart of algorithm for kinematic waves and histograms (Result of Sects. 4.5 and 4.6)

$m_{x'} = \tan\Theta'$ and $m_{y'} = \tan\Phi'$, and Θ' and Φ' are the orientations of the window with respect to the X and Y axes. The parameters ($m_{x'}$, $m_{y'}$) are called the local orientations or slopes of $S(\mathbf{r}, t)$. From this data we generate a histogram using 2D bin (0.01×0.01). Each bin is assigned a rational fraction as exemplified in the previous section.

11.4.6.1 Effect of Velocity on Microstructure of Magnetization

In the previous section, it is seen that there is a smoothening of the magnetization interface with increasing field velocity.

Hence, it is observed that histograms are dependent on field velocity. It is expected that the pinned-lagging transition will be reflected in the histogram of the local slope. Figure 11.10 shows the joint probability distribution and histograms in transition between the two phases, namely pinned and lagging. As expected we can observe a series of transitions.

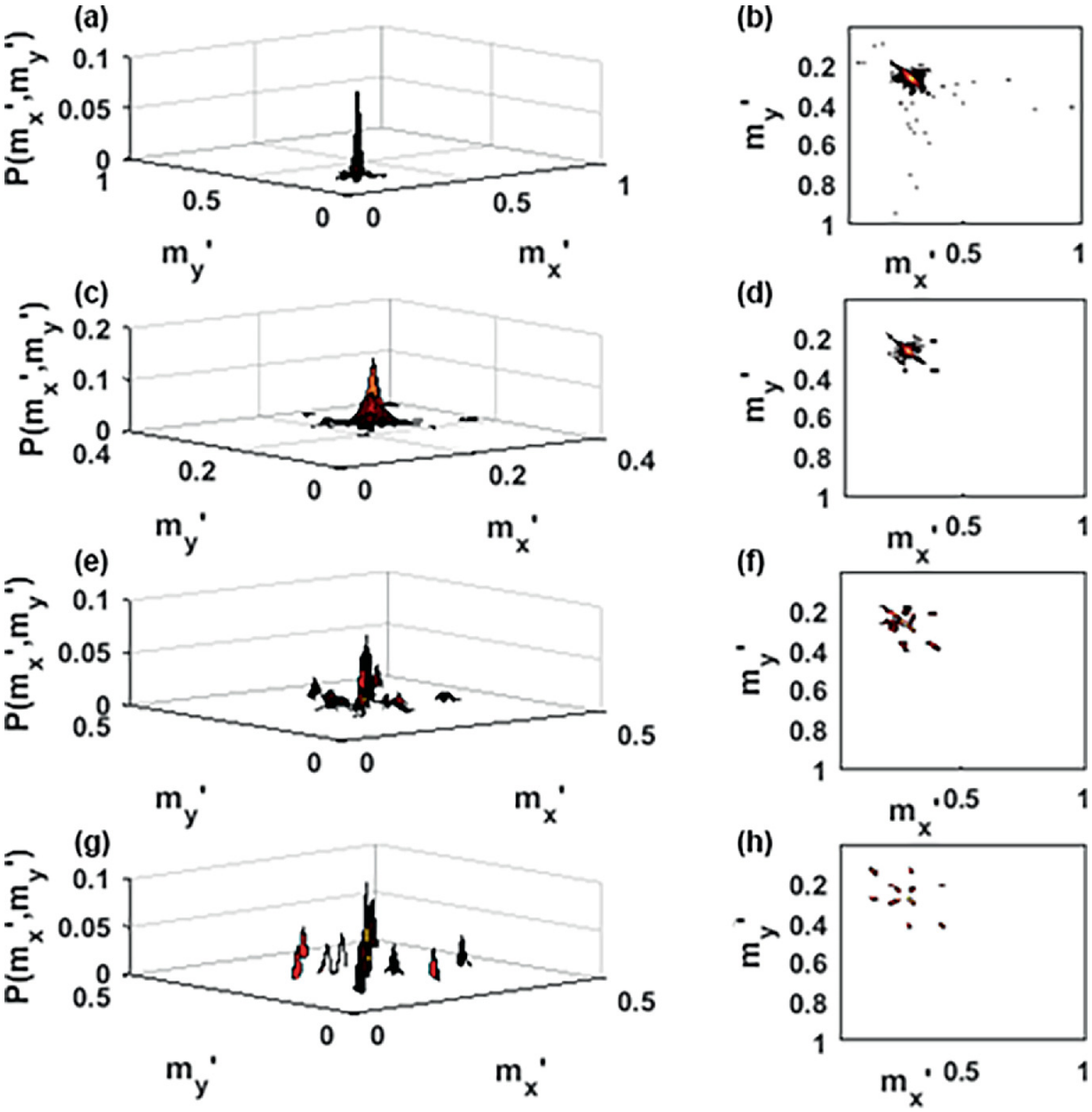

Fig. 11.10 The joint probability distribution (**a**, **c**, **e**, **g**) and histograms (**b**, **d**, **f**, **h**) at four different velocities. The velocity decreases as we move from top to bottom. It illustrates that a number of phases exist between lagging and pinned phases. Figure has been redrawn by author

As S(**r**, t) continuously fluctuates in space and time about B(**r**, t), there are considerable weights of nearby slopes. As an example for (2/7, 2/7) interface in pinned phase, the most prominent local slopes are combinations of many rational fractions. This is illustrated in Fig. 11.10g, h.

With an increase in field velocity, histograms are observed to be close to Gaussian with a maxima nearly at the orientation of the field interface. This is shown in Fig. 11.10a, b.

Figures 11.11 and 11.12 show the histograms for different field interface inclinations in lagging and pinned phases, respectively. X axis of each histogram is m'_x and Y axis is m'_y. From the histograms, it can be observed that peaks are more sharp in the pinned phase as compared to the lagging phase. It can be correlated to the morphology of the magnetization interface (Fig. 11.7) where the ripples are sharper in the pinned phase as compared to the magnetization interfaces at larger field velocities.

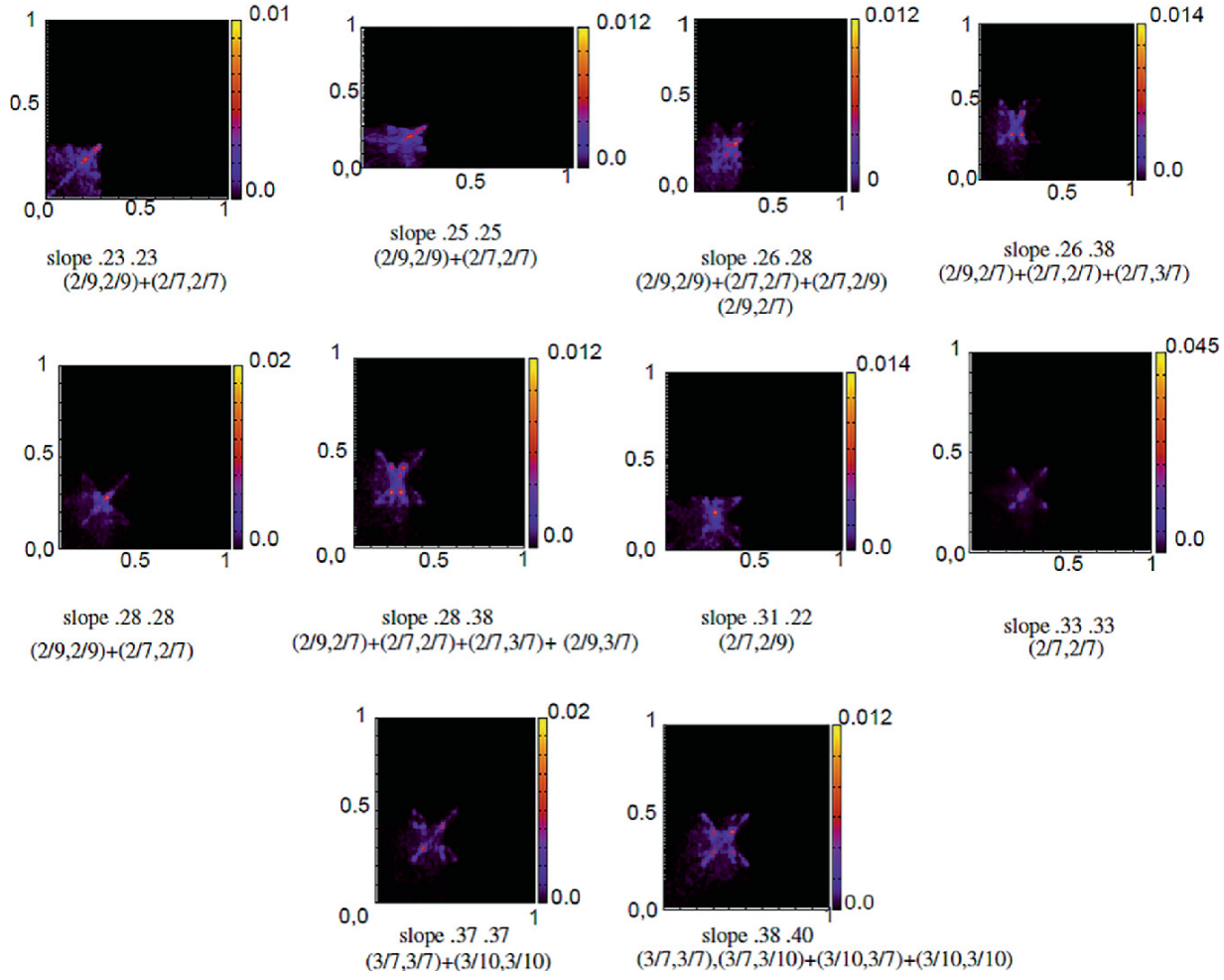

Fig. 11.11 The histograms for different field inclinations in the lagging phase. The average inclination of the external field interface is mentioned as slope (e.g. slope 0.38.40 means $m_x = \tan\theta = 0.38$ and $m_y = \tan\varphi = 0.40$). In the bracket below the slope shows the rational values of most probable peaks (e.g. (3/7, 3/7) + (3/10,3/10) means most probable peaks are at $m'_x = \tan\theta' = 3/7$, $m'_y = \tan\varphi' = 3/7$ and $m'_x = \tan\theta' = 3/10$, $m'_y = \tan\varphi' = 3/10$). Figure has been redrawn by author

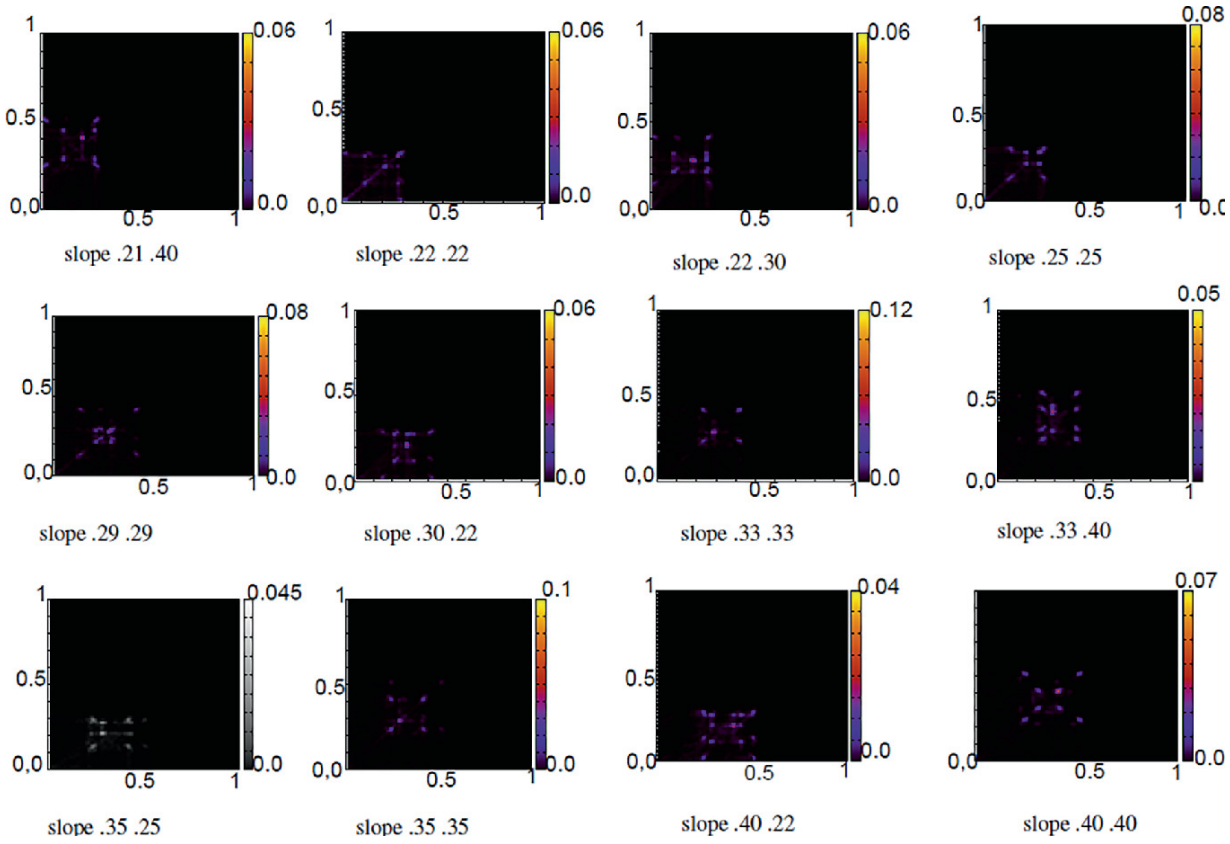

Fig. 11.12 Figure shows the histograms for different field inclinations in the pinned phase. The average inclination of the external field interface is mentioned as slope (e.g. slope 0.40.40 means $m_x = \tan\theta = 0.40$ and $m_y = \tan\varphi = 0.40$). Figure has been redrawn by author

A comparison with 2D case is worth doing. As compared to the case of the 2D Ising model (Chaudhuri et al. 2002, 2004), the 3D Ising model histogram is richer. There are many local orientations coming up as secondary peaks.

11.4.6.2 Many Histograms Are Superpositions

We refer to S(**r**, t) by the orientations of corresponding B(**r**, t). For example, a magnetization interface that originates

from the field interface of slopes $m_x(=\tan\theta) = 2/7$ and $m_y(=\tan\varphi) = 2/7$ will be referred to as (2/7, 2/7). Figure 11.13a, b shows the histogram for a magnetization interface (1/4, 1/4). Figure 11.13c, d shows the histogram for (1/3, 1/3). Similarly, Fig. 11.13e, f is corresponding to (2/7, 2/7).

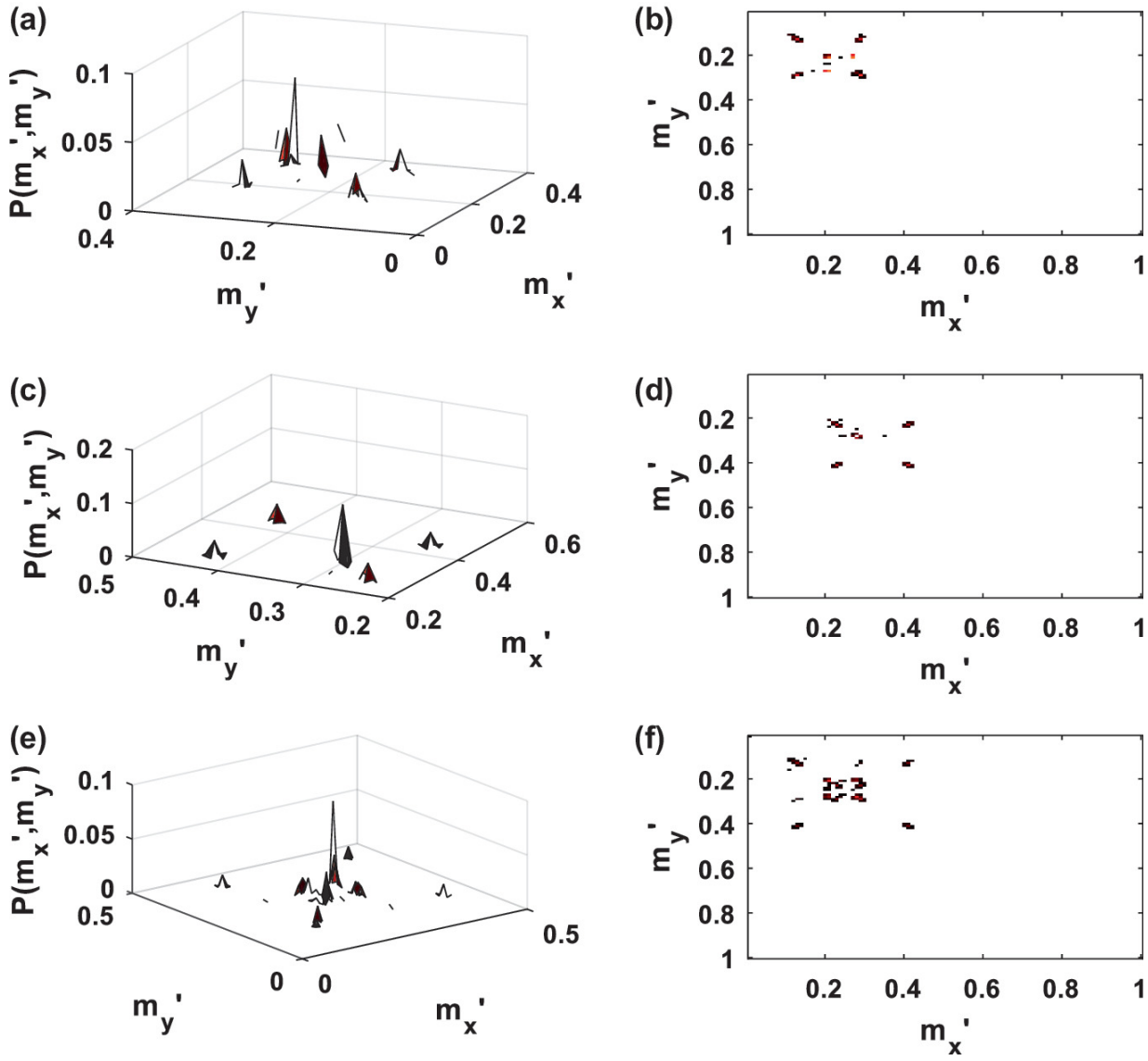

Fig. 11.13 Joint probability distribution (A, C, E) and histogram (B, D, F) in the pinned phase for (1/4, 1/4), (1/3, 1/3) and (2/7, 2/7) (top to bottom). Figure illustrates that most probable peaks in higher rational fractions are combination peaks in lower fractions (though many peaks are suppressed and many are elevated). Figure has been redrawn by author

The histograms and joint probability distribution are generated, and rational fractions are assigned by the procedure explained before. In the histogram of (1/4, 1/4), most probable peaks correspond to a combination of rational fractions 2/7, 2/9, 3/10, 3/14 and 1/7. For the case of (1/3, 1/3), the most prominent peaks are combinations of 5/17, 3/10, 3/7, 6/25, 1/4.

Upon analysis of the histogram of (2/7, 2/7), most of the prominent peaks are either from (1/3, 1/3) or from (1/4, 1/4). However, many combinations are suppressed and many are relatively elevated. The most prominent peaks are $\{m_x' = (\tan\theta') = 2/7,\ m_y'\ (=\tan\varphi') = 2/7\}$ and $\{m_x' = (\tan\theta') = 5/17,\ m_y'\ (=\tan\varphi') = 5/17\}$, one being from (1/4, 1/4) and other from (1/3, 1/3).

11.4.7 The Dynamical Phase Diagram

As the magnetization interface moves fluctuating in space and time about the field interface, its rippled part locks into one of many possible rational fractions. This fraction approximates the local field orientation at that point with the constraint of the local crystal (which is discrete) environment at that point. It can be widely different from the average orientation of magnetization or field interface. In the 2D case, the plot of the most probable local slope against the slope of the field interface has a stepped structure called Devil's staircase. The steps of the Devil's staircase structure shrink and expand with the translational velocity of the external field.

In the 3D case, a qualitatively similar phenomenon occurs. The interface in the 3D case is parameterized by two parameters m_x and m_y. Hence, the steps of the Devil's staircase manifest themselves as patches/domains in the planes of m_x and m_y. Different color patches/domains correspond to different most probable peaks. These patches/domains shrink and expand with velocity.

Figure 11.14 shows the patch/domain structure for the pinned case, and Fig. 11.15 shows the patch/domain structure for a higher velocity (but not in an extreme lagging case).

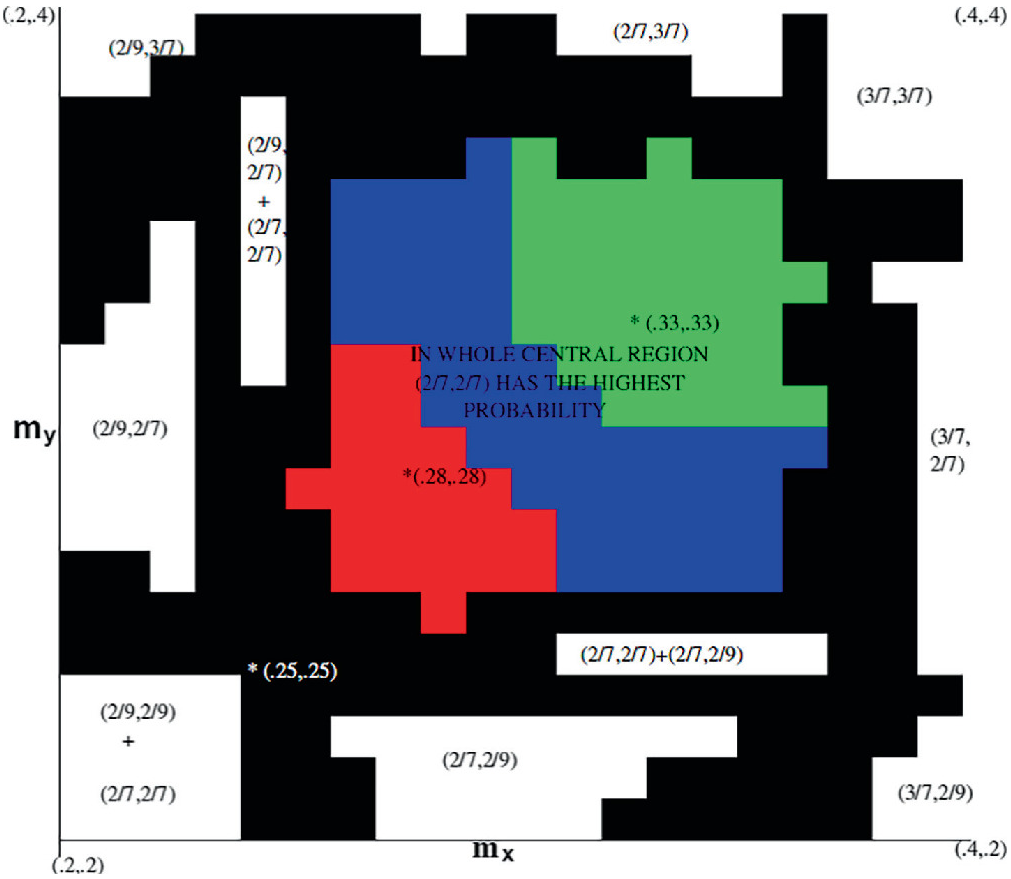

Fig. 11.14 The dynamical phase diagram for the system in phase I. X axis is m_x and Y axis is m_y. Patches of same color illustrate areas of same most probable local orientation. The entries in the bracket tell the ration value of most probable local orientation (e.g. (2/9, 2/9) + (2/7, 2/7) means that in this area there are two most probable local slopes (i) $m'_x = 2/9$, $m'_y = 2/9$ (ii) $m'_x = 2/7$, $m'_y = 2/7$). Figure has been redrawn by author

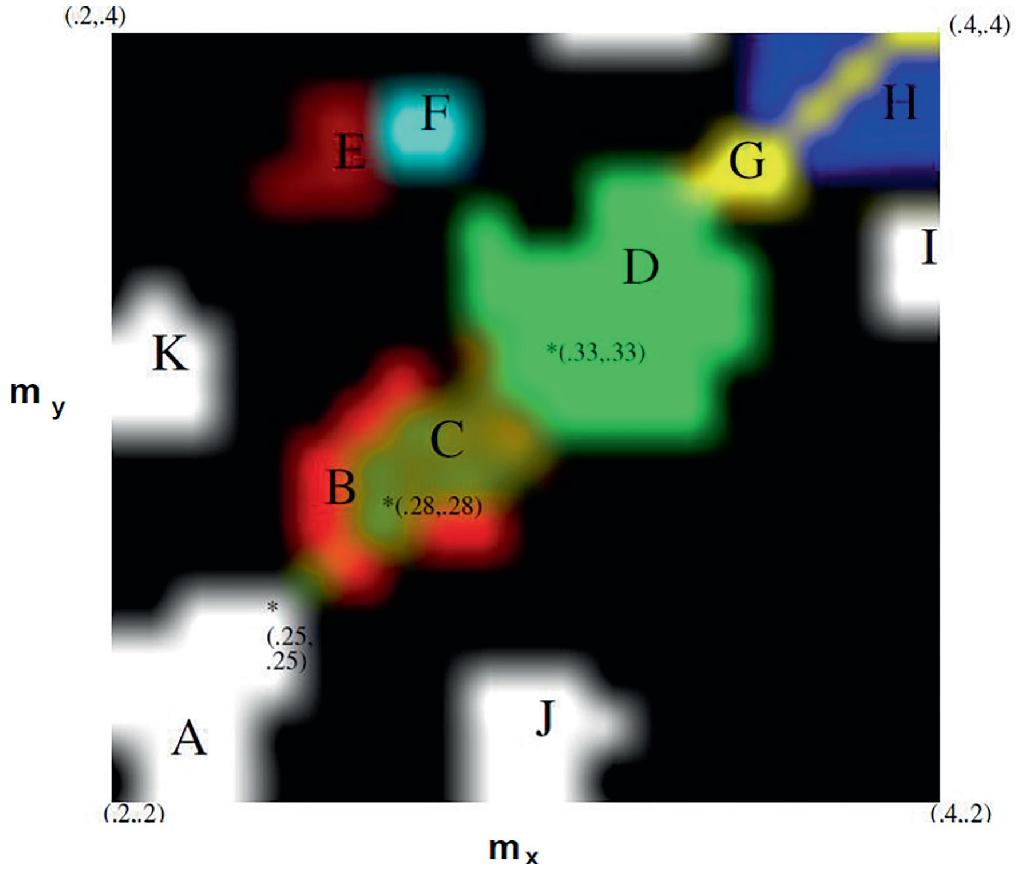

Fig. 11.15 The dynamical phase diagram for the system at a higher velocity as compared to Fig. 11.11. X axis is m_x and Y axis is m_y. Patches of same color illustrate areas of same most probable local slope. Figure has been redrawn by author

Looking at both diagrams together (Figs. 11.14 and 11.15) a transition is evident. Many such transitions take place with increasing velocity. The flowchart for this result is given in Algorithm 6.

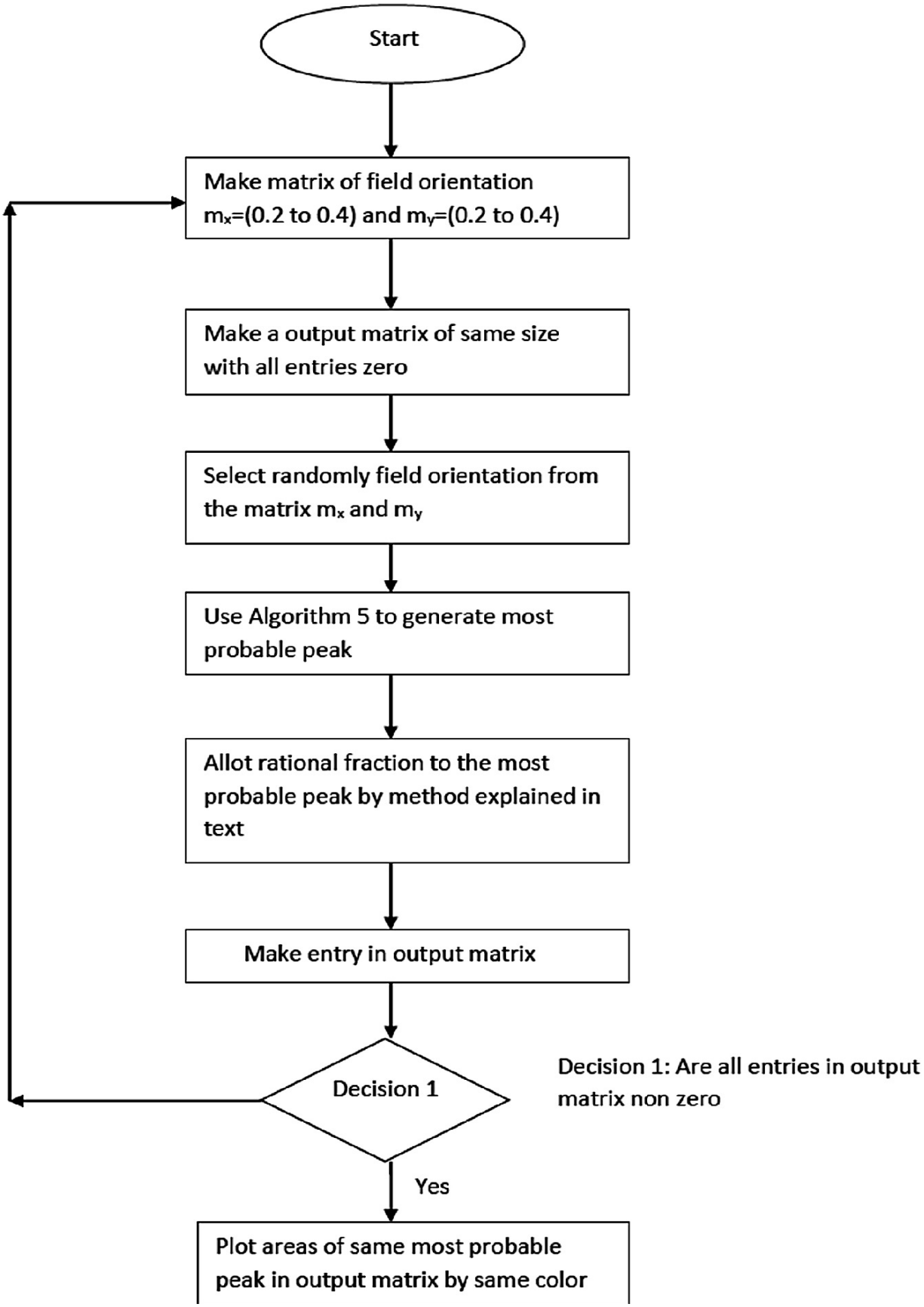
Start
Make matrix of field orientation m_x=(0.2 to 0.4) and m_y=(0.2 to 0.4)
Make a output matrix of same size with all entries zero
Select randomly field orientation from the matrix m_x and m_y
Use Algorithm 5 to generate most probable peak
Allot rational fraction to the most probable peak by method explained in text
Make entry in output matrix
Decision 1
Decision 1: Are all entries in output matrix non zero
Yes
Plot areas of same most probable peak in output matrix by same color

Algorithm 6 Flow chart of algorithm for dynamical phase disgram (Result of Sect. 4.7)

11.5 Applications and Emerging Areas

In this section, we will be discussing applications of magnetic thin films. Both areas of scientific fascination and technological importance would be our domain of interest. In no way do we claim to be comprehensive as applications of magnetic thin film are very vast. The motivation is to give a glimpse of the importance of the study of magnetic thin films.

11.5.1 Data Storage Media

Magnetic thin films are the base of hard disk drives (HDD). They are important both as soft underlayer and high anisotropy (hard) storage layers in data storage media. This field is continuously being probed like exchange springs with perpendicular anisotropy have found their place in data storage in HDD (Victora and Shen 2005a, 2005b). There is a need for trade between thermal stability (which is the basic requirement for data retention) and the capacity to switch magnetization by controlling of link between anisotropy and reversal. This trade-off is allowed by exchange springs. Thin film exchange springs are expected to allow data storage densities close to 1 Tbit/inch^2.

With continuous research in paradigms of data storage, e.g. bit patterned media, solid state spintronic devices, energy-assisted recording and discrete track media, exchange springs materials are expected to gain more importance.

Thin films with anisotropy perpendicular to the plane of the film are not only important in storage but as sensors

and spin transfer torque devices as well. Some technologically important alloys and multilayer systems are CoCrPt-based alloys, ordered alloys of FePt, FePd and CoPt, Co/X (X = Pt, Pd, Ni) with perpendicular anisotropy, CoFeB with perpendicular anisotropy, etc.

11.5.2 Spin Manipulative Devices

Exploitation of manipulation of electronic spin is the basis of spin manipulation devices. Broadly, there are two categories:

(A) Spin senses the state of the magnetic layer (an example is the Giant Magnetoresistance effect)

(B) Spin is used to change the magnetic state via spin transfer torque.

Spintronic devices include spin torque oscillators, vortex oscillators and many more.

Magnetic tunnel junctions (MTJs) based on tunneling magneto resistance (TMR) are important for sensing as well as generating spin-polarized currents.

TMR sensors are spintronic devices.

11.5.3 Spin Seeback Effect (Spin Caloritronics)

Spin Seeback effect (SSE) also known as spin caloritronics converts heat current into spin current. This is presently more of scientific curiosity than a technology.

11.5.4 Write Heads

For the recording of data, a high spatially localized magnetic field with very sharp gradients is required. High moment soft magnetic thin films are strong contenders for refinement of material for write heads in magnetic recording.

11.5.5 Sensors

Many sensors use magnetic thin films.

- A much larger anomalous (extraordinary) Hall effect is utilized in Hall devices incorporating a magnetic material.
- Magnetostrictive sensors utilize strains and generate change in permeability, which, in turn, can be recorded by spin resonance measurements.
- Magnetoresistive: Anisotropic magnetoresistance (AMR), Giant magnetoresistance (GMR) and tunneling magnetoresistance (TMR) are examples.

11.6 Conclusions

It is concluded that a transition from a phase where two interfaces (field and magnetization) move together to a phase where they are separated. This depends on the velocity of the externally driven field. There is a strong effect of the velocity of the external field on the microstructure of S(**r**, t). The flow of kinematic waves on S(**r**, t) is also discussed. Devil's staircase structure of the 2D Ising model is successfully extended to a 3D model, though the interface in the 3D model is richer in terms of its microstructure as compared to the 2D model.

The primary motivation of the chapter is to introduce the reader to a method of simulation relevant to thin films. By clubbing the methodology with ab inito results from software like VASP and Quantum Expresso, the approach can be made more realistic and practical. Many upcoming domains of magnetic thin films can be simulated using the approach given in the chapter.

Acknowledgements

The authors are thankful to Dr. Surajit Sengupta for explaining the basic framework of the problem. The authors

are also thankful to Dr. Saibal Basu for giving reference material for the development of this manuscript.

References

Barabasi, A.L., Stanley, H.E.: Fractal Concept in Surface Growth. Cambridge University Press (1995)
[Crossref]

Bhanot, G.: Rep. Prog. Phys. **51**, 429–457 (1988)
[Crossref]

Chaudhuri, A., Sreeram, P.A., Sengupta, S.: Phys. Rev. Lett. **89**, 176101 (2002)
[Crossref][PubMed]

Chaudhuri, A., Sreeram, P.A., Sengupta, S.: Phase Transitions **77**, 691 (2004)
[Crossref]

Cheimarios, N., To, D., Kokkoris, G., Memos, G., Boudouvis, A.G.: Frontiers Phys. **9**, 631918 (2021)
[Crossref]

Coey, J.M.D.: Magnetism and Magnetic Materials. Cambridge University Press, Cambridge, England (2010)

Falicov, L.M., Daniel, T.P., Bader, S.D., Gronsky, R., Hathaway, K.B., Hopster, H.J., Lambeth, D.N., Parkin, S.S.P., Prinz, G., Salamon, M., Schuller, I.K., Victora, R.H.: J. Mater. Res. **5**, 1299–1340 (1990)
[Crossref]

Fulde, P.: Electron Correlations in Molecules and Solids. Springer, New York (1995)
[Crossref]

Hellman, F., Hoffmann, A., Tserkovnyak, Y., Beach, G.S.D., Fullerton, E.E., Leighton, C., MacDonald, A.H., Ralph, D.C., Arena, D.A., Durr, H.A., Fischer, P., Grollier, J., Heremans, J.P., Jungwirth, T., Kimel, A.V., Koopmans, B., Krivorotov, I.N., May, S.J., Petford-Long, A.K., Rondinelli, J.M., Samarth, N., Schuller, I.K., Slavin, A.N., Stiles, M.D., Tchemyshyov, O., Thiaville, A., Zink, B.L.: Rev. Mod. Phys. **89**, 025006 (2017)
[Crossref][PubMed][PubMedCentral]

Jhonson, M.T., Bloemen, P.J.H., den Broeder, F.J.A., de Vries, J.J.: Rep. Prog. Phys. **59**, 1409 (1996)
[Crossref]

Landau, D.P., Binder, K.: Monte Carlo Simulation in Statistical Physics. Cambridge University Press, Cambridge, England (2000)

Neel, L.: J. Phys. Radium **15**, 225 (1954)
[Crossref]

Rikvold, P.A., Kolesik, M.: J. Stat. Phys. **100**, 377 (2000)
[Crossref]

Rikvold, P.A., Kolesik, M.: Phys. Rev. E **66**, 066116 (2002a)
[Crossref]

Rikvold, P.A., Kolesik, M.: J. Phys. A: Math. Gen. **35**, L117 (2002b)
[Crossref]

Rikvold, P.A., Kolesik, M.: Phys. Rev. E **67**, 06611 (2003)

Sahai, M.K., Bakshi, A.K.: Int. J. Theoret. Phy. **61**, 141 (2022)
[Crossref]

Sahai, M.K., Sengupta, S.: Phys. Rev. E **77**, 032601 (2008)
[Crossref]

Schneidman, E., Berry, M.J., Segev, R., Bialek, W.: Nature **440**, 1007 (2006)
[Crossref][PubMed][PubMedCentral]

Shi, Y., Duke, T.: Phys. Rev. E **58**, 6399 (1998)
[Crossref]

Victora, R.H., Shen, X.: IEEE Trans. Magnet. **41**, 2828–2833 (2005)

Victora, R.H., Shen, X.: IEEE Trans. Magnet. **41**, 537–542 (2005)

Vtyurina, N.N., Dulin, D., Docter, M.W., Meyer, A.S., Dekker, N.H., Abbondanzieri, E.A.: Proc. Nat. Acad. Sci. **113**, 4982 (2016)

Wahle, J., Blumer, N., Schlipf, J., Held, K., Vollhardt, D.: Phys. Rev. B **58**, 12749 (1998)
[Crossref]

Zhao, D., Liu, F., Huber, D.L., Lagally, M.G.: Phys. Rev. B **62**, 11316 (2000)
[Crossref]

© The Author(s), under exclusive license to Springer Nature Singapore Pte Ltd. 2024
R. S. Ningthoujam, A. K. Tyagi (eds.), *Handbook of Materials Science, Volume 2*, Indian Institute of Metals Series
https://doi.org/10.1007/978-981-97-4646-0_12

12. Selected Examples of Iron and Cobalt Complexes Exhibiting Spin-Crossover Behavior

Monika Rana[1], Venkata Nikhil Raj Mothikari[1] and Anuj Kumar Sharma[1] ✉
(1) Department of Chemistry, School of Chemical Sciences and Pharmacy, Central University of Rajasthan, NH-8, Bandarsindri, Ajmer Distt., Rajasthan, 305817, India

✉ **Anuj Kumar Sharma**
Email: aks.iitk@gmail.com

Keywords Spin crossover – Iron – Cobalt – Magnetism – High-spin (HS) – Low-spin (LS)

12.1 Introduction

In the field of molecular magnetism, rational design and synthesis of coordination compounds with predictable magnetic properties requires a deep understanding of the underlying mechanisms that decides their overall magnetic behavior. In last about four decades, a lot of efforts have been made to make molecules that can display magnetic properties which are usable for real applications. As a

result, literature is now quite rich in terms of availability of molecular systems with desired properties. However, designing single molecule magnets or molecules with bistability in their magnetic properties is still a great challenge for synthetic inorganic chemists (Gütlich and Goodwin 2004a; Gómez et al. 2015; Chen et al. 2014; Jureschi et al. 2014). Spin crossover phenomenon (SCO) is a very fascinating and dynamic research field for synthetic inorganic chemists. The design of such molecules in which metal exists in two stable spin states and can be switched reversibly under the influence of external stimulus like temperature, pressure, light etc. is of huge interest in the domain of molecular magnetism and is the focus of this chapter. By far, the SCO phenomenon is majorly reported in Fe(II) and Co(II) complexes (Scheme 1). The highest studied system is Fe(II) (d^6 system). It exhibits the largest possible change in magnetic moment during SCO. It switches from a diamagnetic system in low-spin (LS) to a highly paramagnetic system with four unpaired electrons in high-spin (HS). Hence, it is simple to observe the spin state by routine spectroscopic techniques (detailed discussion in Sect. 12.4). SCO is well characterized for Co(II) (d^7 system) also; although it is relatively less common than for Fe(II), the possible reason might be the higher spin pairing energy and the destabilizing effect of the single e_g electron in low spin six-coordinate complexes (Kahn and Martinez 1998; Dugay et al. 2015; Shatruk et al. 2015; Brooker 2015; Halcrow 2013).

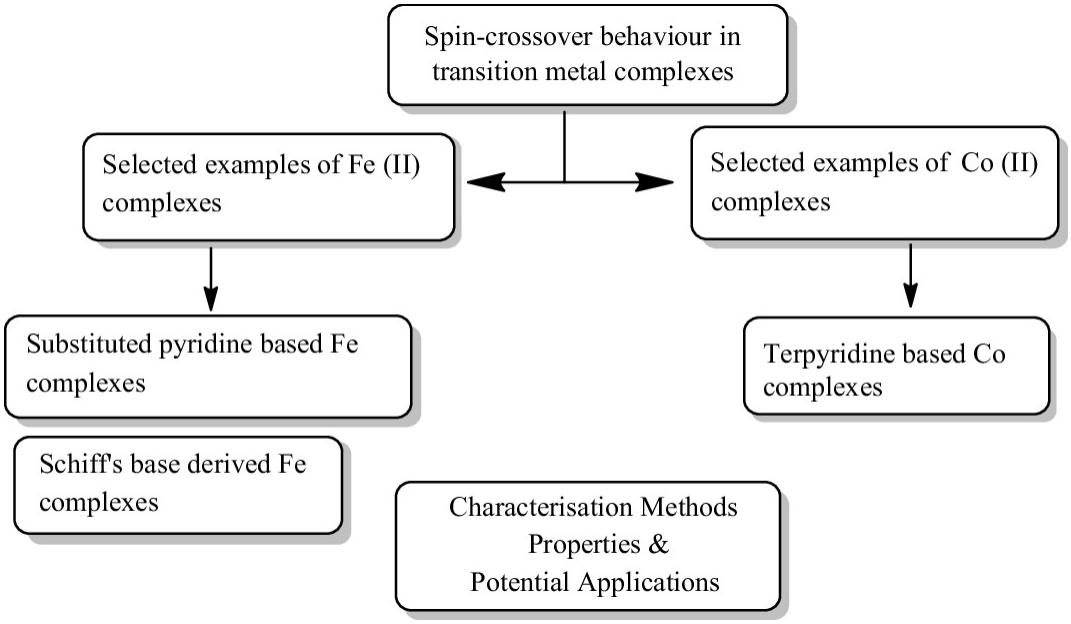

Scheme 1 Schematic flow of the work discussed in the chapter

However, discussing all the examples is out of scope of this chapter. So, here, we are primarily focusing on selected examples of Fe(II) and Co(II) systems that display spin crossover behavior. The chapter is organized with an emphasis on the structural features of SCO complexes, methods used for characterization and their potential applications towards design and development of molecular switches in industry. Before a detailed discussion on some distinct examples of this class, few basic information is presented here like (a) background of spin crossover, (b) spin transition curves and cooperative effect and followed by the effect of the ligand on the temperature dependent SCO behavior in both Fe(II) and Co(II) metal complexes. The chosen ligands act as potential candidates that are able to generate suitable intermediate ligand field that can balance the crystal field splitting and pairing energy under the influence of external perturbation. The generation of spin crossover switch molecules through such ligands is the real challenge in the field of material science.

12.2 Theoretical Background

12.2.1 Background of Spin Crossover (SCO)

Octahedral metal complexes with configurations of d^4 to d^7 electrons may exist in either the high-spin (HS) or low-spin (LS) states. The metal ion surrounded by weak field ligand forms HS complex with maximum multiplicity while strong field ligand forms LS complex with minimum multiplicity. There is the third situation where certain ligands provide intermediate ligand field able to change the spin state of the complex from LS state to HS state and *vice-versa* under the external perturbation. In this case, the ligand field strength is approximately close to cross over energy between HS and LS states. Here, the reversible change of spin state from LS $\leftrightarrow$ HS occurs when the electrons move from t_{2g} orbitals to e_g orbitals or vice versa. It is induced by the influence of external stimuli like pressure, temperature and light. This spin transition phenomenon is termed classically as "**Spin Crossover**". This is also referred to as Spin Transition (ST) and less frequently Spin Equilibrium. The change in the spin state is accompanied by the change in magnetic and optical behavior of the metal complexes. The actual physicochemical properties of the metal complexes were influenced by the ligand field present around the metal ion (Gütlich and Goodwin 2004a; Gómez et al. 2015; Chen et al. 2014; Jureschi et al. 2014). The changes in spin state behavior of the metal complexes at the molecular level attracted the researchers to utilize these molecular magnetic materials in the field of storage and display devices (Kahn and Martinez 1998; Dugay et al. 2015; Shatruk et al. 2015; Brooker 2015; Halcrow 2013). As the situation where certain ligands provide intermediate ligand field is able to change the spin state of the complex from LS state to HS state occurs primarily in octahedral

complexes, only octahedral complexes are considered here for the discussion.

In definition, molecular bistability is the property of molecules exhibiting two stable electronic states in a given range of external perturbation factors (Kahn and Martinez 1998; Dugay et al. 2015; Shatruk et al. 2015; Brooker 2015; Halcrow 2013). Normally, one of the states is the ground state, and the other is a metastable state. The molecules exhibiting bistability property at room temperature are expected to have greater applications in the electronics industry (Létard and Guionneau 2004; Halcrow 2011, 2009). One of the most astonishing examples of the molecular bistability phenomenon is the SCO which occurs mainly in the octahedral complexes. The SCO phenomenon was majorly reported with Fe(II) and Co(II) metal complexes. However, very few reports based on Fe(III) SCO complexes were published (Hayami et al. 2011a; Molnár et al. 2014; Harding et al. 2016). However, the first SCO phenomenon was discovered in Fe(III)tris(*N*,*N*-dialkyl-dithiocarbamates) complexes by Cambi and Szego in 1931, in which change in electronic states was observed with increase in temperature and *vice-versa* (Gütlich and Goodwin 2004b), with spin transition of low spin $^{2}T_{2g}(t_{2g}^{5})$ to high spin $^{6}A_{1g}(t_{2g}^{3}e_{g}^{2})$ as shown in Fig. 12.1. After three decades, White et al. explained the SCO mechanism using ligand field theory in Fe(III) complexes (Gütlich et al. 2013). The first Fe(II) (d^6 system) SCO system $[Fe(phen)_2(NCS)_2]$ was synthesized by Madeja et al. in 1963 with the spin transition from the low spin $^{1}A_{1g}(t_{2g}^{6})$ to high spin $^{5}T_{2g}(t_{2g}^{4}e_{g}^{2})$ state (Madeja and König 1963; König et al. 1966; Nihei et al. 2007). Stouffer et al. first reported the Co(II)(d^7 system) tridentateamine ligand SCO system in 1961 with the spin transition occurring from the low spin $^{2}E_{g}(t_{2g}^{6}e_{g}^{1})$ to high spin $^{4}T_{1g}(t_{2g}^{5}e_{g}^{2})$ state

(Gütlich et al. 2002). In the SCO phenomenon, the alteration of the spin state in the complex corresponds to variations in bond length, crystal volume, and color. In this chapter, we have highlighted primarily SCO phenomenon in mononuclear six coordinated Fe(II) and Co(II) metal complexes. The bistability phenomenon of the molecules should occur around the room temperature associated with response function like change in color or magnetism (Kahn and Martinez 1998; Dugay et al. 2015; Shatruk et al. 2015; Brooker 2015; Halcrow 2013).

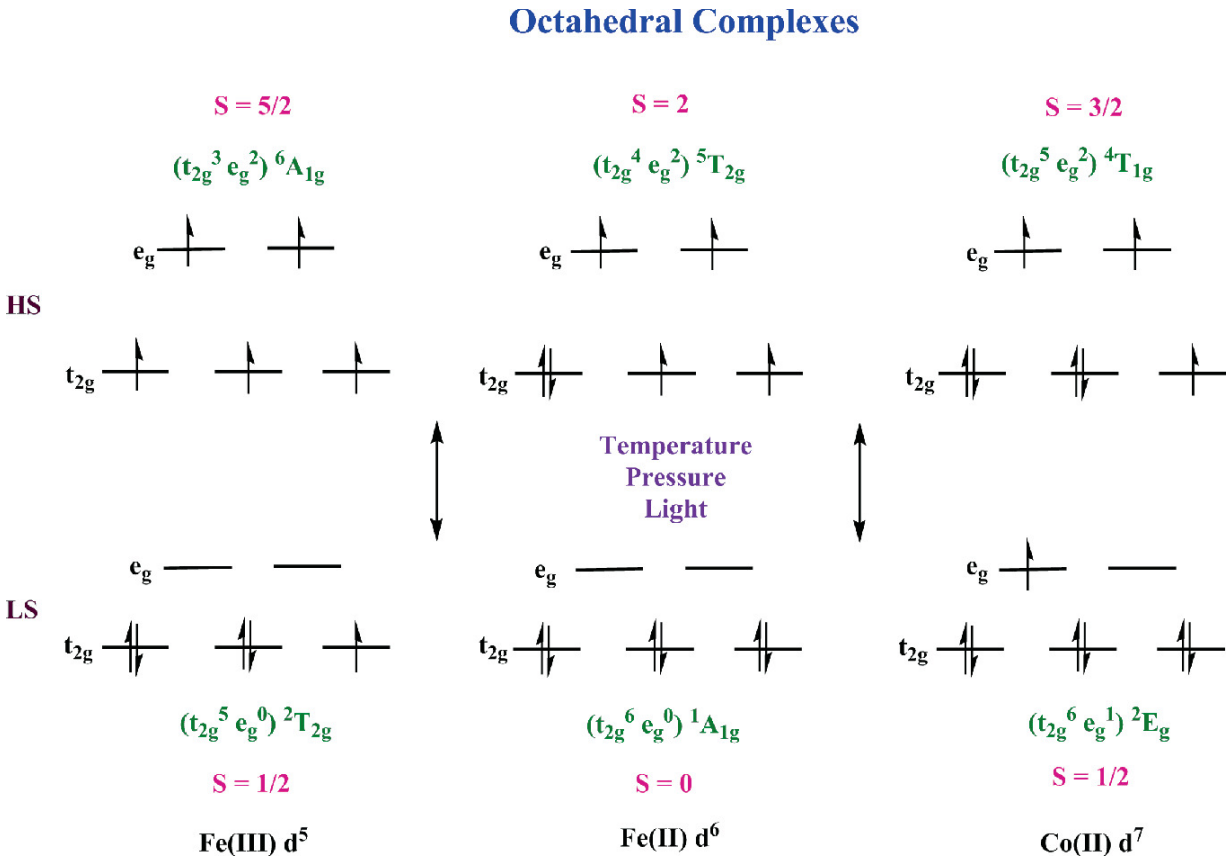

Fig. 12.1 HS and LS states for octahedral complexes of d^5, d^6 and d^7 configurations showing SCO phenomenon which were labeled with respective term symbols

The detectable responses like color change associated with a change in magnetic properties have potential applications in the development of display and sensor devices (Létard and Guionneau 2004; Halcrow 2011, 2009;

Gamez et al. 2009). The light irradiation as external stimuli in changing the spin state of the molecule provides promising applications in the development of optical storage devices. Utilizing alterations in spin state induced by applied pressure could be harnessed for sensor development with a change in color for the remote sensing (Gamez et al. 2009). Kröberet al. documented the first example showing bistability feature with abrupt hysteresis behavior at the room temperature (295 K) of a Fe(II)/triazole coordination polymer (Krober et al. 1993). A few number of substituted Fe(II)/triazole coordination polymer of this class were synthesized and reported in the literature (Kahn and Martinez 1998; Dugay et al. 2015; Shatruk et al. 2015; Brooker 2015; Halcrow 2013). In these polymeric compounds, the change in spin state was accompanied by a color change from violet (LS) to colorless (HS). The Fe(II) coordination polymer was used to develop as thermochromic display devices (Kahn and Martinez 1998; Dugay et al. 2015; Shatruk et al. 2015; Brooker 2015; Halcrow 2013; Gütlich et al. 2000). However, polymeric structures are not considered as molecular forthwith, because in polymeric structures the metal centers are communicated through chemical bridges, whereas, in molecular materials metal centers are communicated via spatial interactions. The challenge arises to develop mononuclear molecules which show spin transition with wide thermal hysteresis around room temperature (Kahn and Martinez 1998; Dugay et al. 2015; Shatruk et al. 2015; Brooker 2015; Halcrow 2013). Over the few past decades, lot of efforts were made in design and development of large number of mononuclear Fe(II) and Co(II) complexes with wide variety class of ligands having nitrogen donor atoms. Large number of ligands have been designed covering from mono- to hexadentate for the development of Fe(II) and Co(II) SCO complexes. We sincerely apologize to those authors whose work could not be included or mentioned.

12.2.2 Spin Transition Curves and Cooperativity Effect

A spin transition curve is obtained by plotting the graph between molar high spin fraction vs. temperature (γ_{HS} vs. T) or between the product of temperature and molar magnetic susceptibility vs. temperature (χ_M.T vs T). The spin transition curve gives the information about the population of the LS and HS state of the metal with respect to the temperature and also about spin transition temperature ($T_{1/2}$). $T_{1/2}$ is defined as a state where the half fraction of low spin and a half fraction of high spin coexists at the same point of temperature denoted as $\gamma_{LS} = \gamma_{HS} = 0.5$. Different forms of spin transition curves are illustrated below in Fig. 12.2a–e.

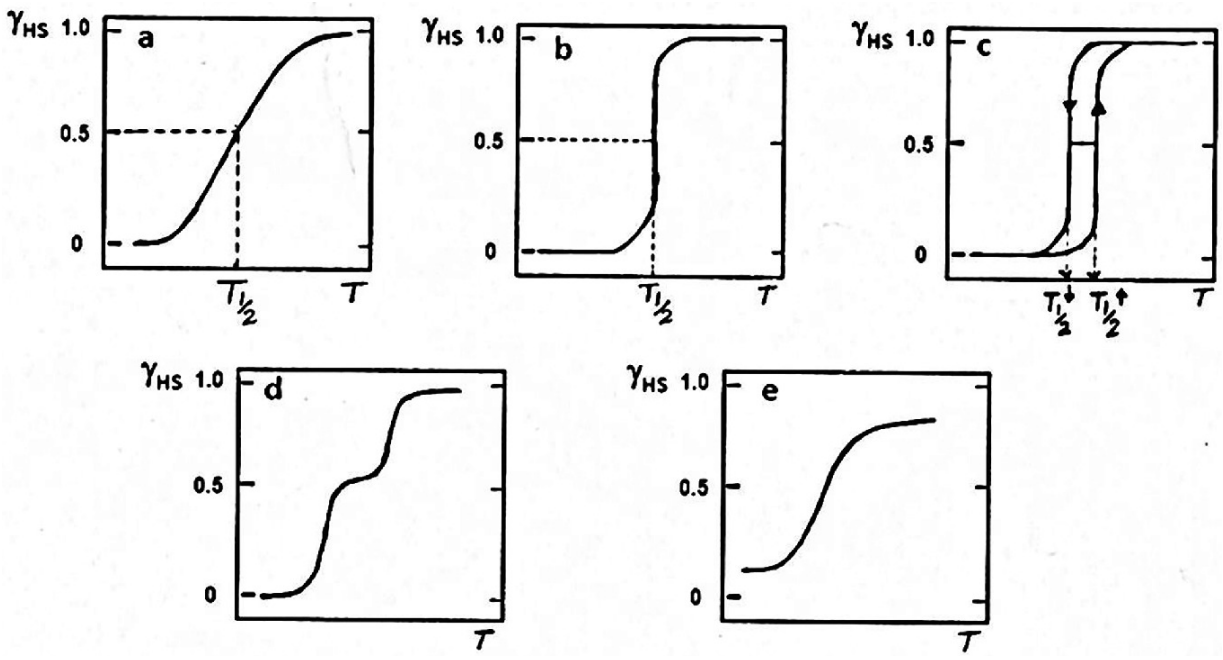

Fig. 12.2 Illustration of main types of spin transition as γ_{HS} (high spin fraction) versus temperature curves **a** gradual; **b** abrupt; **c** hysteresis and **d** two-step; **e** incomplete

The nature of the spin transition curve depends on the cooperativity between the molecules present in the crystal

matrix through the ligand framework. In general, cooperativity is the degree to which magnetic and structural properties change in a molecule when it goes through the spin transition affecting its neighbouring molecules. As cooperativity strengthens, the spin transition curve transitions from a gradual to a sudden shift, occasionally leading to hysteresis (Fig. 12.2c). Hysteresis is defined as the dependence of the state of a system on its history. For instance, a magnet may have more than one possible magnetic moment in a given magnetic field, which is dependent on how the field changed in the past. Thermal hysteresis refers to a delay in the magnetic reaction when the temperature undergoes a change. Hysteresis curves depict the plots of a specific moment component, showcasing a loop that varies with the direction of change in another variable. This historical dependence observed in the loop forms the foundation for memory in storage devices. In the hysteresis curve, two different $T_{1/2}$ temperatures are obtained; one from the cooling curve ($T_{1/2}\downarrow$) and another from the heating curve ($T_{1/2}\uparrow$). The difference between the two $T_{1/2}$ s is termed as hysteresis width ($\Delta T_{1/2}$) (Fig. 12.2c). The two curves create two stable/metastable states in the particular range of temperature depicting a bistability phenomenon which is desirable for the memory applications. In other case, two-step transitions were observed when the metal ions occupy two different crystallographic sites or exist in the polymeric complex. As the temperature increases, the metal ion in one crystallographic site changes from 2LS → [LS-HS] followed by the other metal ion changes from [LS-HS] → 2HS. Sometimes, incomplete or partial transitions occur where the molecules does not undergo complete spin state change or remained in LS/HS (Gütlich and Goodwin 2004a; Gómez et al. 2015; Chen et al. 2014; Jureschi et al. 2014). At the macroscopic level, cooperative effect depends on the

metal-atom bond lengths, π–π stacking, hydrogen bonding network of ligand-ligand, ligand counteranion or with the solvent which influences the lattice properties of the molecule. In other words, they depend on intermolecular or intramolecular interactions between neighbouring molecules which in turn influence the electron–phonon coupling. The level of cooperation among molecules can be enhanced through (i) establishment of a robust network of hydrogen bonds involving ligands, counterions, and solvent molecules; (ii) incorporation of extended aromatic rings to increase the degree of π–π stacking between the ligands (Gamez et al. 2009; Zhong et al. 1998). To illustrate, three Fe(II) complexes were discussed following with the molecular formula 1,10-phenanthroline (phen), $[Fe(L)_2(NCS)_2]$ [L = 2,2-bithiazoline (btz), and dipyrido[3,2-*a*:2_3_-*c*]phenazine (dppz)] (Fig. 12.3) (Brooker 2015; Gütlich et al. 2000). The ligand *phen* is aromatic compound*, btz* is aliphatic compound, and *dppz* has extended aromatic ligand. The *btz* showed less or no significant inter or intramolecular interactions but *phen* complex shows the number of C–C contacts and π–π interactions. These interactions become more prominent in the *dppz* derivative with extended conjugation and planar structure. As the ligand changes from *btz* to *dppz* the SCO behavior of the complexes also changes from gradual, abrupt and hysteresis (width 40 K).

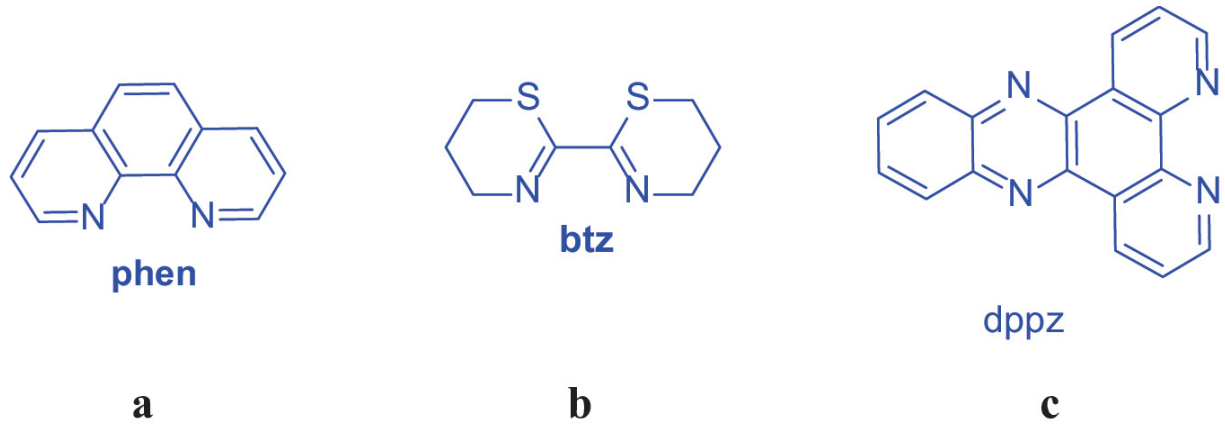

Fig. 12.3 Structure of the ligand **a** 1,10-phenanthroline (phen); **b** 2,2-bithiazoline (btz); **c** dipyrido[3,2-a:2_3_-c]phenazine (dppz)

12.3 Classification/Types

12.3.1 Fe(II) Spin Crossover (SCO) Complexes

During SCO, the spin transition from $t_{2g} \leftrightarrow e_g$, the metal–ligand bond length increases and influences the adjacent molecules by phonon interactions which lead to the expansion of other molecules in the crystal lattice like a chain reaction (Gamez et al. 2009). The most widespread SCO examples were studied in Fe(II) complexes. However, few SCO examples were also reported with the Fe(III) and Co(II) complexes. Majorly, the SCO molecules are reported with nitrogen donor ligands with N_6 environment. In some cases, the Co(II) exhibit spin transition through the valence tautomerism with N,O-donor ligands (Tezgerevska et al. 2014). Most of the SCO compounds synthesized were reported with the nitrogen ligands having a strong π-acceptor character mainly pyridine containing ligands. During spin transition from LS ↔ HS appreciable changes were observed in the crystal lattice like the elongation of bond lengths followed by an increase in volume. The average difference between M–N bond lengths in the two spin states in Fe(II) is 0.2 Å, Fe(III) is 0.15 Å and Co(II) is 0.1 Å (Brooker 2015; Hayami et al. 2011a; Molnár et al.

2014; Gütlich et al. 2000). The elongation of bond lengths was more pronounced in Fe(II/III) due to the transfer of two electrons from t_{2g} to e_g, whereas, in Co(II) one electron transfer takes place from the t_{2g} to e_g. The magnetic behavior changes from diamagnetic to paramagnetic in Fe(II). However, in Fe(III) and Co(II) unpaired electrons remain in both the energy levels and only the extent of paramagnetism changes (Kahn and Martinez 1998; Dugay et al. 2015; Shatruk et al. 2015; Brooker 2015; Halcrow 2013). In most of the systems other than Fe(II), a chemical change prevails which limits the spin-crossover examples in these systems. Therefore, to explore the Fe(II) SCO molecules preferably compared to other metal ions have remained more encouraging. A great deal of effort is being made in the design, synthesis and development of mononuclear Fe(II) SCO complexes with a hope to display electronic properties for information storage/processing in the electronic industry. In literature, temperature induced Fe(II) SCO complexes are reported more common when compared to other external stimuli like light and pressure. In addition to external stimuli, other factors involved in the Fe(II) SCO compounds are ligand design, counter anions, co-ligands and solvent molecules of crystallization.

12.3.1.1 Design and Synthesis of N-Donor Based Fe(II) SCO

The ligand design plays a key role in the development of Fe(II) SCO complexes. In the literature, the major share of Fe(II) SCO complexes were reported with ligands containing nitrogen donor atoms. The Fe(II) SCO complexes were reported with monodentate ligands like oxazoles and tertrazoles using different anions BF_4^-, ClO_4^-, PF_6^- and $CF_3SO_3^-$ and their $T_{1/2}$ exhibited variations within a range of 91 K to 213 K across various spin transition curves (Hibbs et al. 2003). The Fe(II) SCO complexes were

reported with different types of nitrogen donor containing ligands conjugated pyridines, pyridine conjugated triazoles, imidazole/benzimidazole, and thiazole/benzathiazole (Fleisch et al. 1977; König and Ritter 1976; Onggo et al. 1990, 2000; Onggo and Goodwin 1991; Craig et al. 1988; Figg et al. 1991; Stupik et al. 1988, 1986; Sugiyarto et al. 1995; Sugiyarto and Goodwin 1987; Baker et al. 1984, 1987; Baker and Goodwin 1984; Sams and Tsin 1976). A large portion of Fe(II) SCO complexes were reported with the bidentate ligands in the literature. The very first report of Fe(II) SCO complex was reported in sample dependent *cis*-$[Fe(phen)_2(NCS)_2]$ complex by Madejaet al. in 1966 (Madeja and König 1963; König et al. 1966; Nihei et al. 2007). Further, researchers studied the effect of substituents over the **phen** ligand which led to alter $T_{1/2}$ temperature of Fe(II) complexes. Fleisch et al. documented the SCO behavior of $[Fe(\mathbf{phen})_3]^{2+}$ complexes derived from the 2-methyl and 2-methoxy substituted **phen** ligand (Table 12.1 entry 2). The complexes showed gradual SCO behavior with $T_{1/2}$ of ~150 and 205 K in the temperature range of 2–320 K. Though the complexes were synthesized with different counter anions, the changes in the $T_{1/2}$ values were explained by the inductive effect and steric hindrance offered by the ligands (Fleisch et al. 1977; König and Ritter 1976). In the case of *cis*-$[Fe(\mathbf{phen})_2(NCS)_2]$ complexes, authors documented that the methyl substituents on **phen** ligand alter the spin transition curve in Fe(II) thiocyanato complexes (Table 12.1 entry 3–4). The methyl groups at 5,6 and 4,7 positions on **phen** ligand changes the spin transition temperature ($T_{1/2}$) from 121 to 221 K (Fleisch et al. 1977; König and Ritter 1976; Figg et al. 1991). In case of bipyridine (**bipy**) ligands, Onggo et al. documented the methyl substitutions at different positions on bipyridyl ligand in $[Fe^{II}(\mathbf{bipy})_3]^{2+}$ complexes (Table 12.1

entry 6–7) (Onggo and Goodwin 1991; Craig et al. 1988; Figg et al. 1991). The complexes showed gradual SCO behavior with varied $T_{1/2}$ temperature range from 89 K > $T_{1/2}$ < 345 K. The methyl substituents at 2-position next to the nitrogen donor imparted distortion in the octahedral geometry of the complex due to inter ligand repulsions which enabled a close approach to the metal atom (Onggo et al. 1990; Onggo and Goodwin 1991). The variation of methyl and methyl carboxylate substituents at 6-position on bipyridyl ligand not only imparted strong steric effect but also leads to distortion in the complex by disrupting the planarity of the ligand. Due to the above reasons, the ligands affected the quintet state ($^5T_{2g}$) of Fe(II) at room temperature and acts as a barrier to approach close to the metal center (Onggo et al. 1990; Onggo and Goodwin 1991).

Table 12.1 List of some conjugated pyridine ligands and their corresponding mononuclear Fe(II) SCO complexes

S. no	Ligands	Comments	References
1.	L	$[Fe(\mathbf{L})_6](BF_4)_2$ $[Fe(\mathbf{L})_6](ClO_4)_2$ 91 K ($T_{1/2}$), 192 K ($T_{1/2}$), two steps, gradual (BF_4^-) 213 K ($T_{1/2}$), abrupt (ClO_4^-) LS:HS 2:1, X-ray structure (BF_4^-, ClO_4^-) Absorption, Mössbauer spectra	Hibbs et al. (2003)
2.	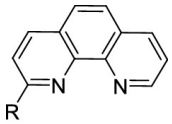 R = CH_3, L R = OCH_3, L1	$[Fe(\mathbf{L})_3](BF_4)_2$, ~ 150 K ($T_{1/2}$), Gradual $[Fe(\mathbf{L_1})_3](ClO_4)_2$, 205 K ($T_{1/2}$), Gradual	Fleisch et al. (1977); König and Ritter (1976)

S. no	Ligands	Comments	References
		Mössbauer spectra, IR	
3.	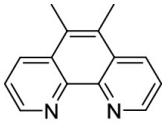 5,6-dmphen	*Cis*-[Fe(**5,6-dmphen**)$_2$(NCS)$_2$] 221 K ($T_{1/2}$), Gradual HS, X-ray structure, Mössbauer spectra, IR, LIESST	Figg et al. (1991)
4.	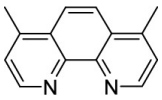 4,7-dmphen	*Cis*-[Fe(**4,7-dmphen**)$_2$(NCS)$_2$] 118 K ($T_{1/2}\downarrow$), 121 K ($T_{1/2}\uparrow$), Abrupt, Hysteresis ($\Delta T_{1/2} = 3$ K) Mössbauer spectra, IR	Fleisch et al. (1977); König and Ritter (1976)
5.	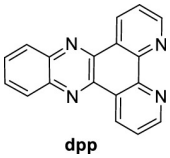 dpp	Cis-[Fe(**dpp**)$_2$(NCS)$_2$].C_5H_5N 123 K ($T_{1/2}\downarrow$), 163 K ($T_{1/2}\uparrow$), Abrupt hysteresis($\Delta T_{1/2} = 40$ K) HS, X-ray structure, Mössbauer spectra	Zhong et al. (1998)
6.	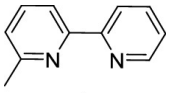 L	[Fe(**L**)$_3$](BF$_4$)$_2$ [Fe(**L$_1$**)$_3$](ClO$_4$)$_2$ Gradual (BF_4^-, ClO_4^-) HS, X-ray structure (ClO_4^-) UV–Visible absorption, Mössbauer spectra	Onggo et al. (1990); Onggo and Goodwin (1991)
7.	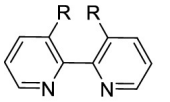 R = CH_3, L R = CO_2CH_3, L1	[Fe(**L**)$_3$](ClO$_4$)$_2$ [Fe(**L**)$_3$](PF$_6$)$_2$ 310–345 K ($T_{1/2}$), Gradual (ClO_4^-, PF_6^-) [Fe(**L$_1$**)$_3$](BPh$_4$)$_2$, > 313 K ($T_{1/2}$), Gradual HS:LS (1:1), X-ray structure (ClO_4^-) Mössbauer spectra	Onggo et al. (1990); Onggo and Goodwin (1991); Craig et al. (1988)

S. no	Ligands	Comments	References
8.	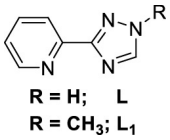	$[Fe(\mathbf{L})_3](X)_2$ ($X = PF_6^-$, ClO_4^-, Cl^-, SO_4^{2-}) $[Fe(\mathbf{L})_3](BF_4)_2 \cdot 2H_2O$ $[Fe(\mathbf{L_1})_3](X)_2 \cdot nH_2O$ ($X = BF_4^-$, ClO_4^-, PF_6^-) 140–180 K ($T_{1/2}$), Gradual (all) ($\mathbf{L}$) 135 K ($T_{1/2}$), Gradual ($\mathbf{L}$) 89–245 K ($T_{1/2}$), Gradual (all) ($\mathbf{L_1}$) HS, X-ray structure, (BF_4^-) ($\mathbf{L}$), Mössbauer spectra, UV–Visible absorption	Stupik et al. (1986, 1988)
9.	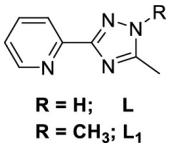	$[Fe(\mathbf{L})_3](PF_6)_2 \cdot H_2O$ $[Fe(\mathbf{L_1})_3](BF_4)_2$ $[Fe(\mathbf{L_1})_3](ClO_4)_2$ $[Fe(\mathbf{L_1})_3](PF_6)_2$ 250 K ($T_{1/2}$), Gradual 150–170 K ($T_{1/2}$), Gradual (BF_4^-, ClO_4^-, PF_6^-) HS, X-ray structure, (BF_4^-), ($\mathbf{L_1}$), Mössbauer spectra	Stupik et al. (1986, 1988); Sugiyarto et al. (1995); Sugiyarto and Goodwin (1987)
10.	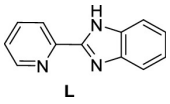	$[Fe(\mathbf{L})_3](X)_2 \cdot nH_2O$ ($X = Br^-$, I^-, NO_3^-, PF_6^-, BPh_4^-) $[Fe(\mathbf{L})_3](ClO_4)_2 \cdot nH_2O$ ($n = 1, 2$) 80–250 K ($T_{1/2}$), Gradual (Br^-, I^-, NO_3^-, PF_6^-, BPh_4^-) 140 K ($T_{1/2}$) ($n = 1$), 210 K ($T_{1/2}$) ($n = 2$), Gradual (both) (ClO_4^-)	Sams and Tsin (1976)

S. no	Ligands	Comments	References
		HS ($n = 2$), X-ray structure, (ClO_4^-), Mössbauer spectra	
11.	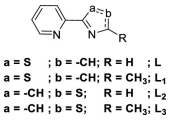 a = S ; b = -CH; R = H ; L a = S ; b = -CH; R = CH_3; L_1 a = -CH ; b = S; R = H ; L_2 a = -CH ; b = S; R = CH_3; L_3	$[Fe(\mathbf{L})_3](ClO_4/BF_4)_2$ $[Fe(\mathbf{L_1})_3](ClO_4/BF_4)_2$ $[Fe(\mathbf{L_2})_3](ClO_4/BF_4)_2{\cdot}H_2O$ $[Fe(\mathbf{L_3})_3](ClO_4/BF_4)_2{\cdot}nH_2O$ (BF_4^-, n = 0; ClO_4^-, n = 1) LS ($\mathbf{L}$, $\mathbf{L_2}$); 180–230 K ($T_{1/2}$), Abrupt (ClO_4^-), Gradual (BF_4^-)($\mathbf{L_1}$); 230–270 K ($T_{1/2}$), Gradual ($\mathbf{L_3}$) HS, LS (ClO_4^-) ($\mathbf{L_1}$); LS (BF_4^-) ($\mathbf{L_3}$) X-ray structure, Mössbauer spectra, UV–Visible absorption	Onggo et al. (2000); Baker et al. (1987)
12.	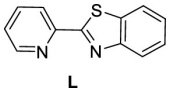 L	$[Fe(\mathbf{L})_3](BPh_4)_2.H_2O$ 180 K ($T_{1/2}$), Gradual UV–Visible absorption	Baker et al. (1984); Baker and Goodwin (1984)

Other research groups studied the SCO behavior of the Fe(II) complexes by substituting one pyridine ring of bipyridine moiety with five-membered heterocycle ring triazole which decreases the ligand field near to the crossover junction. Stupiket al. and Sugiyarto et al. synthesized and characterized different methyl substituted or unsubstituted triazoles appended with pyridine ring i.e., 3-(pyridin-2-yl)-1,2,4-triazole ligands (Table 12.1, entries 8–9) and their corresponding Fe(II) complexes (Fig. 12.4) (Stupik et al. 1986, 1988; Sugiyarto et al. 1995; Sugiyarto and Goodwin 1987). The unsubstituted triazole derived Fe(II) complexes showed gradual SCO behavior due to the hydrogen bonding network formed with the help of counter anion and solvent molecules (Stupik et al. 1986, 1988). The complex containing 2-substituted 3-(pyridin-2-yl)-1,2,4-

triazole ligand showed HS behavior above room temperature due to two high spin species and, as temperature decreased the third species (LS) started to emerge. This abnormal behavior was explained by the ordered and disordered transitions in the crystal lattice or the possibility of formation of *facial* and *meridional* isomers. The complex containing 4-substituted 3-(pyridin-2-yl)-1,2,4-triazole ligand showed LS state throughout the temperature scan due to the strong ligand field (Nihei et al. 2007; Gütlich et al. 2002). In case of tris-2-(1,5-dimethyl-1H-1,2,4-triazol-3-yl)pyridine Fe(II) tetrafluoroborate complex, the change in spin state was evidenced with color change, in which yellow colour (HS) of the complex at room temperature changed to bright orange (LS) at low temperatures (Sugiyarto et al. 1995; Sugiyarto and Goodwin 1987). The striking color changing feature in such SCO materials may be utilized in the development of thermochromic switches.

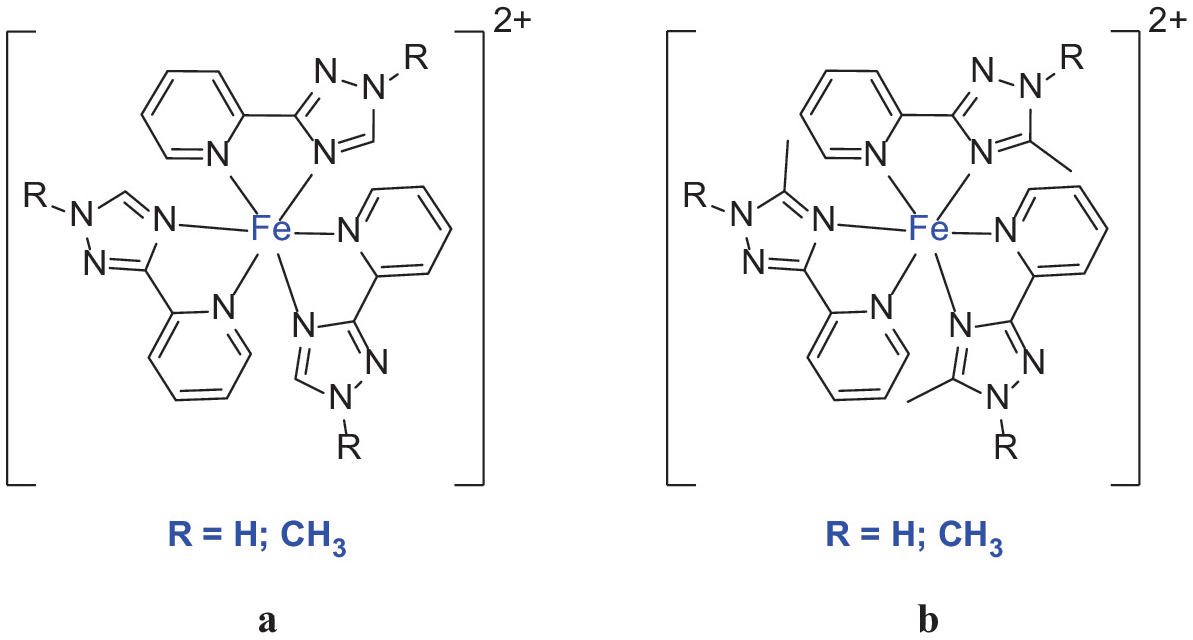

Fig. 12.4 Structure of the Fe(II) complex synthesized by **a** Stupiket al. (1986, 1988) and **b** Sugiyarto et al. (1995), Sugiyarto and Goodwin (1987)

From the above bidentate ligand system, the triazole moiety attached to the pyridine ring was replaced with un/substituted benzimidazole to synthesize and study the SCO behavior of the Fe(II) complexes. Samset al. documented the synthesis of unsubstituted tris 2-(2′-pyridyl)benzimidazole Fe(II) complexes with varied counter anions (Br^-, I^-, NO_3^-, ClO_4^-, PF_6^-, BPh_4^-) Table 12.1 (entry 10). From the structural studies, the complexes showed distorted octahedral geometry with *meridionial* configuration (Fig. 12.5a) (Sams and Tsin 1976). The complexes showed gradual SCO behavior in all the cases with the $T_{1/2}$ in the range of 80–250 K. The presence of acidic –NH in the benzimidazole was responsible for the formation of hydrogen bond network and also contributed to the strength of the nitrogen-metal bond. The chelating strength of the N–M σ-bond depends upon the acidity of the hydrogen present on the nitrogen atom. To prevent the accumulation of charge on the metal, an increase in N→M σ donation was probably accompanied by the π-back donation from the t_{2g} orbital of metal. The presence of a hydrogen bonding network involving water molecules diminishes the acidity of the -NH hydrogen and affects the N → M bond. The Bronsted acidity of the –NH group in the complex decides the net HS ↔ LS conversion (Sams and Tsin 1976). Sugiyatro et al. replaced the hydrogen on the –NH with the methyl group (Fig. 12.5b), as it knocked out the Bronsted acidity effect on the ligand and imparted better donation capability to the nitrogen donor atom through + I effect. The presence of methyl substituents on the pyridine ring exerts steric effects more than the methyl substitution adjacent on the imidazole ring due to the difference in geometry of the six-membered ring to the five-membered ring (Sugiyarto et al. 1995; Sugiyarto and Goodwin 1987). Besides the influence of steric effects, the employment of methyl group also strengthened the ligand

field which shifted the $T_{1/2}$ to the higher temperature. In case of the benzimidazole ligand, the benzene ring acted as a steric barrier in binding to the metal which affected the spin pairing at low temperatures.

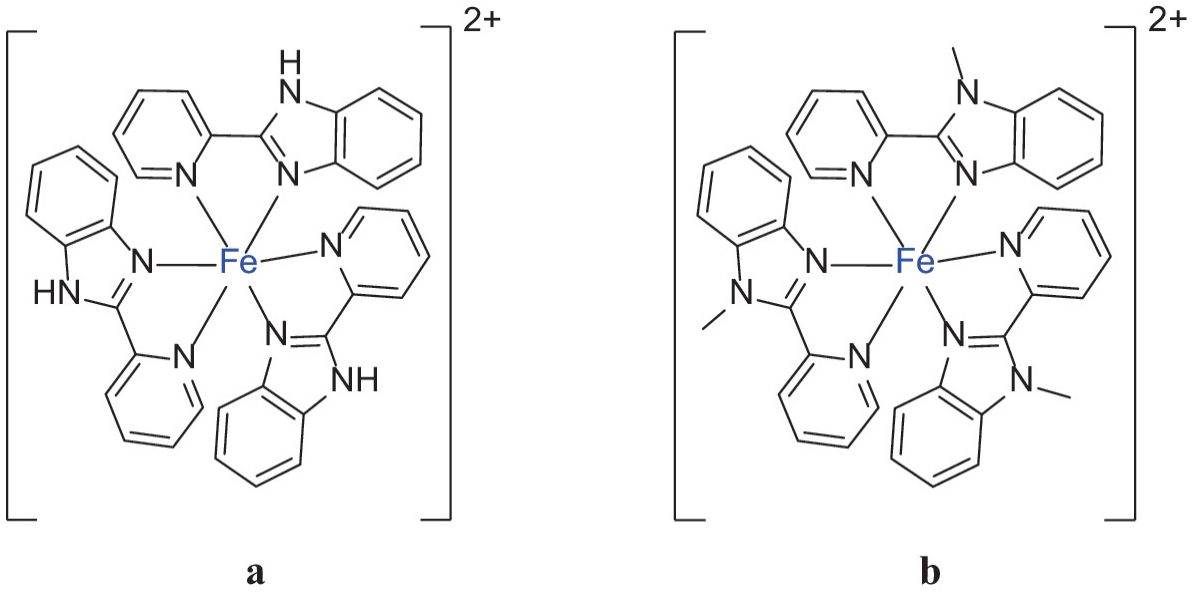

Fig. 12.5 Structure of the Fe(II) complex synthesized by **a** Sams and Tsin (1976) and **b** Sugiyatro et al. (Gütlich et al. 2002)

Goodwin et al. replaced the benzimidazole with the thiazole moiety and synthesized 4-(pyridin-2-y1)thiazole and 2-(pyridin-2-y1)thiazole ligands Table 12.1 (entry 11) (Onggo et al. 2000; Baker et al. 1984; Baker and Goodwin 1984). The ligands were utilized to synthesize Fe(II) complexes with perchlorate and tetrafluoroborate as counter anions (Fig. 12.6a). The magnetic studies of the complexes showed LS state throughout the temperature range. The structural studies of tris(4-(pyridin-2-y1)thiazole) Fe(II) tetrafluoroborate showed octahedral geometry with the average bond distance between Fe–N to be 2.02 Å which was very near to the value of 1.96 Å (average Fe–N distance in [Fe(**bipy/phen**)$_3$](X)$_2$] showed that Fe(II) was in the LS state (Onggo et al. 2000)). Later, Baker et al. documented the synthesis of ligands 4-methyl-2-(pyridin-2-yl)thiazole, 2-methyl-4-(pyridin-2-yl)thiazole

(Table 12.1 entry 11) and their corresponding Fe(II) complexes with ClO_4^- as counter anion. In both cases, they also studied the effect of methyl substitution on the SCO behavior when there is methyl susbtitution located in close proximity to the nitrogen donor atom of thiazole in both cases. The structural studies showed that the Fe(II) complexes occupy *facial* configuration. In this case, the presence of methyl substituent next to the nitrogen donor atom in thiazole showed a less steric effect. The steric hindrances exerted by inter ligand repulsions in the complex caused distortion in octahedral geometry (Baker et al. 1987). Further, Baker et al. documented the synthesis of tris-[2-(pyridin-2-yl)benzothiazole] Fe(II)tetraphenylborate (Table 12.1 entry 12) (Fig. 12.6b). The complex showed gradual SCO behavior within the given range of temperature 2–320 K with the $T_{1/2}$ value 180 K. In all benzo fused five-membered heterocyclic systems such as benzimidazole, benzthiazole etc., the effect of fused benzene was to destabilize the singlet ($^1A_{1g}$) ground state of Fe(II) due to the strong steric hinderance offered by the same (Baker et al. 1984; Baker and Goodwin 1984).

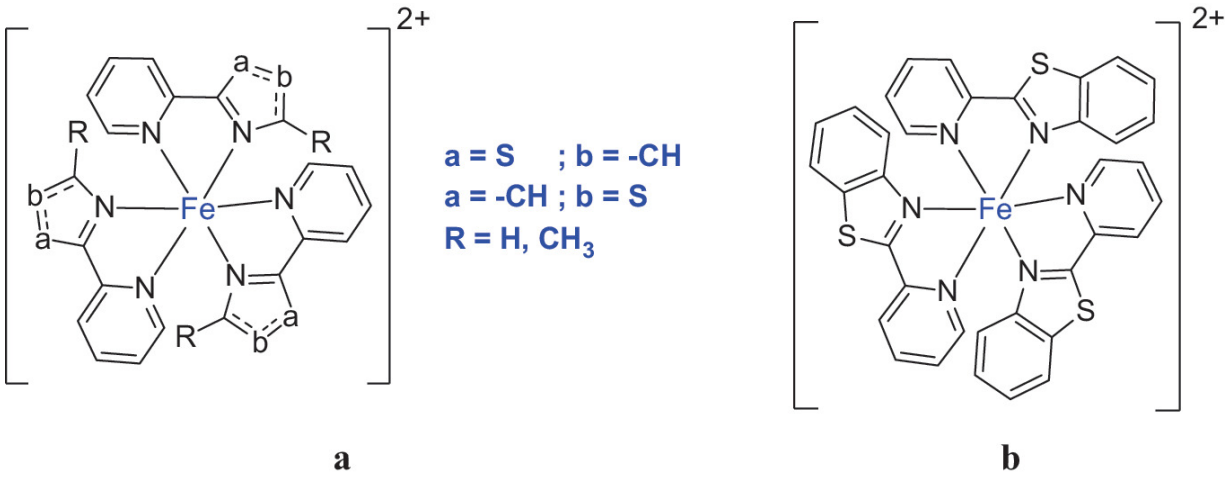

a **b**

Fig. 12.6 Structure of the Fe(II) complex synthesized by **a** Goodwin et al. (Onggo et al. 2000; Baker et al. 1984; Baker and Goodwin 1984) and **b** Baker et al. (1984), Baker and Goodwin (1984)

12.3.1.2 Design and Synthesis of Schiff Base Derived Fe(II) SCO

In the series of polypyridyl ligands, instead of any heterocyclic rings, the Schiff base was introduced in conjunction with pyridine ring. Schiff bases are derived from the condensation of aldehydes and amines and contain N-donor atoms. From literature, the Schiff base based *cis*-$[Fe^{II}(\textbf{diimine})_2(NCS)_2]$ SCO complexes are mostly reported with substituted N-(2′-pyridylmethylene) aniline (**PM-L**) (**L**: subunit). The **PM-L** ligands are produced through the condensation reaction between pyridine-2-carboxaldehyde and aromatic amines (Fig. 12.7). From the structural point of view, the Schiff bases of pyridine-2-carboxaldehyde can be correlated with the 2,2′-bipyridine, 1,10-phenanthroline etc., because the azomethine group has structure similarity in conjugation –N = C–C = N which can coordinate with the metal ion. These **PM-L** Schiff bases were used to develop mononuclear Fe(II) SCO complexes of type *cis*-$[Fe^{II}(\textbf{diimine})_2(NCS)_2]$. The SCO behavior of the central metal ion was dependent on cooperativity between the molecules. To increase the cooperativity in *cis*-$[Fe^{II}(\textbf{PM-L})_2(NCS)_2]$ complexes, two approaches were followed in the literature. One approach was to vary substituents at different positions on the **PM-L** ligand. Different research groups studied SCO behavior of *cis*-$[Fe^{II}(\textbf{PM-L})_2(NCS)_2]$ complexes with varied substituents like extended aromatic ring, alkyl chains and other functional groups at the *para* position of phenyl ring (Oso and Ishida 2009).

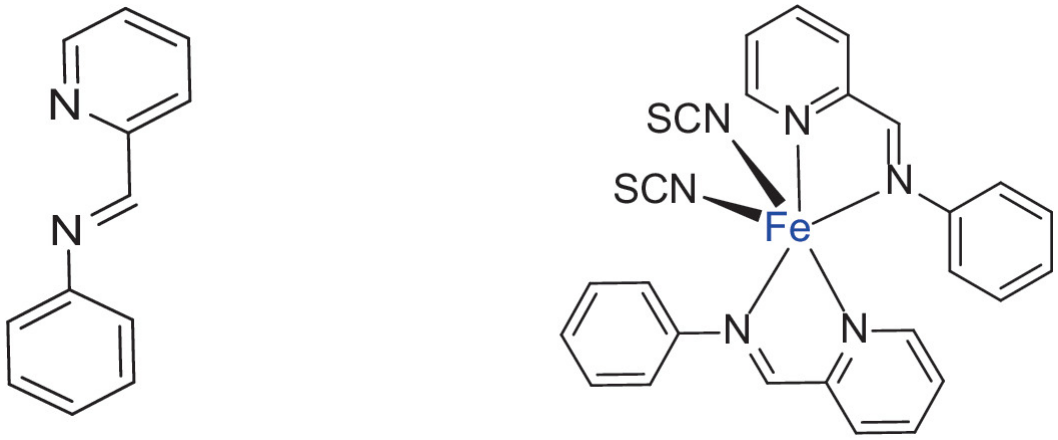

Fig. 12.7 **a** Structure of the *N*-(2′-pyridylmethylene) aniline ligand (**PM-L**) and their corresponding *cis*-[Fe^{II}(**PM-L**)$_2$$(NCS)_2$] complex

Very recently, Sharma and coworkers reported a family of molecular *cis*-[Fe^{II}(**X-PPMA**)$_2$$(NCS)_2$]·$H_2O$ [4-X-*N*-(phenyl(pyridin-2-yl)methylene)aniline; **X-PPMA** complexes that exhibit spin crossover behavior above room temperature (Table 12.2, entry 1). The authors discussed the interesting spin crossover features of complexes which are drastically dependent on the nature of the substituent (Cl/Br → CH_3).The relatively strong ligand field of the Schiff bases stabilizes the low spin state of iron(II) up to 300 K with complexes **1** (**X = Cl**) and **2** (**X = Br**) exhibiting complete, gradual and slightly irreversible spin crossover behavior over the temperature range of 300–500 K with equilibrium temperatures ($T_{1/2}$) 375 K (**1**) and 380 K (2). Complex **3** (**X = CH_3**) shows a complete and gradual spin crossover in the temperature range 10–475 K with strong irreversible features. The equilibrium temperatures obtained upon first warming ($T_{1/2}$↑) and second cooling ($T_{1/2}$↓) are 375 K and 200 K, respectively (Bhar et al. 2022). Guionneau et al. documented the SCO behavior in mononuclear *cis*-[Fe^{II}(**PM-L**)$_2$$(NCS)_2$] complexes by varying the substituents at the *para* position with biphenyl, phenyl-azo, phenyl, phenylethylene (Table 12.2, entry 2–4).

The $T_{1/2}$ of the complexes varied in the range of 165–212 K giving rise to different SCO behaviors like gradual, abrupt and hysteresis. The difference in the spin transition curve and $T_{1/2}$ was explained by intra- and inter-sheet interactions between the molecules through structural analysis (Guionneau et al. 1999; Capes et al. 2000). The other approach was replacement of NCS^- to $NCSe^-$ which creates a stronger ligand field and causes subtle structural changes in the crystal lattice network which eventually shifts the spin transition curve to higher temperature (Gütlich and Goodwin 2004a; Gómez et al. 2015; Chen et al. 2014; Jureschi et al. 2014). Letard et al. and Tailleur et al. documented the SCO behavior of *cis*-[Fe^{II}(**PM-CC-C_6H_5**)$_2$$(NCE)_2$] (E = S, Se) showing thermal hysteresis width 42 K ($\Delta T_{1/2}$) (Table 12.2 entry 5). The replacement of S to Se shifted the $T_{1/2}$ from 194 to 286 K which was below room temperature. From the literature survey, all the **PM-L** based *cis*-[Fe^{II}(**diimine**)$_2$$(NCE)_2$] (E = S, Se) complexes showed $T_{1/2}$ in the range of 165–270 K (for S) and 255–286 K (for Se). In both the cases, the desired $T_{1/2}$ does not show around the room temperature (Létard et al. 1997; Tailleur et al. 2017). But the challenge is still incomplete in designing the Fe(II) SCO complexes in which $T_{1/2}$ should occur around room temperature. Recently, Osoet al. documented *cis*-[Fe^{II}(**DPM-L**)$_2$$(NCS)_2$] (L = –H, $–C_4H_9$) derived from the condensation of *p*-alkylated aniline with di-2-pyridyl ketone. In **DPM-L** ligand imine hydrogen of **PM-L** ligand was replaced with a pyridine ring. The *cis*-[Fe^{II}(**DPM-H**)$_2$$(NCS)_2$] compound show the $T_{1/2}$ = 270 K with gradual transition, whereas, *cis*-[Fe^{II}(**DPM-C_4H_9**)$_2$$(NCS)_2$] compound shows thermal hysteresis with $T_{1/2}$ = 320 K which was above the room temperature (Table

12.2, entry 7). A wider hysteresis loop with ca. $\Delta T_{1/2} = 40$ K ($T_{1/2}\uparrow = 290$ K; $T_{1/2}\downarrow = 250$ K) was observed upon the introduction of longer alkyl chain ($-C_{14}H_{29}$). The introduction of long alkyl chains has improved the cooperativity and induces phase transition from solid to mesophase, which can be explored in the field of liquid crystals for display devices (Oso et al. 2008). The list of a few related Fe(II) complexes derived from conjugated pyridines and Schiff base ligands are given in the Tables 12.1 and 12.2.

Table 12.2 List of some Schiff base ligands and their corresponding mononuclear Fe(II) SCO complexes

S. no	Ligands	Comments	References
1.	X-PPMA X=Cl, Br, CH_3	*cis*-$[Fe^{II}(X\text{-}PPMA)_2(NCS)_2]\cdot H_2O$ X = Cl,375 K ($T_{1/2}$), Gradual X = Br, 380 K ($T_{1/2}$), Gradual X = CH_3, 375 K ($T_{1/2}\uparrow$), 200 K $T_{1/2}\downarrow$, Gradual X-ray Structure, UV–Visible absorption,Mössbauer spectra	Bhar et al. (2022)
2.	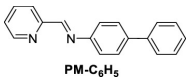 PM-C_6H_5	*Cis*-[Fe(**PM-C_6H_5**)$_2$(NCS)$_2$] 168 K ($T_{1/2}\downarrow$), 173 K ($T_{1/2}\uparrow$), Abrupthysteresis ($\Delta T_{1/2} = 5$ K) HS, LS, X-ray Structure, LIESST, UV–Visible absorption, Mössbauer spectra	Guionneau et al. (1999)
3.	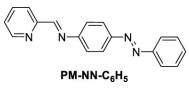 PM-NN-C_6H_5	*Cis*-[Fe(**PM-NN-C_6H_5**)$_2$(NCE)$_2$] E = S, Se 186 K ($T_{1/2}\downarrow$), 192 K ($T_{1/2}\uparrow$), Abrupt Hysteresis ($\Delta T_{1/2} = 6$ K) (S) 255 K ($T_{1/2}$), Gradual (Se) HS, LS, X-ray Structure, LIESST	Guionneau et al. (1999); Capes et al. (2000)

S. no	Ligands	Comments	References
4.	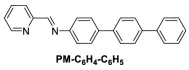 PM-C_6H_4-C_6H_5	*Cis*-[Fe(**PM-C_6H_4-C_6H_5**)$_2$(NCS)$_2$] Gradual, Incomplete HS, X-ray Structure, LIESST, UV-Visibleabsorption	Guionneau et al. (1999)
5.	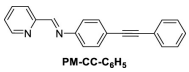 PM-CC-C_6H_5	*Cis*-[Fe(**PM-CC-C_6H_5**)$_2$(NCE)$_2$] (E = S, Se) 194 K ($T_{1/2}\downarrow$), 231 K ($T_{1/2}\uparrow$), Abrupt hysteresis ($\Delta T_{1/2} = 37$ K) (S) 256 K ($T_{1/2}\downarrow$), 306 K ($T_{1/2}\uparrow$), Hysteresis ($\Delta T_{1/2} = 50$ K) (Se) HS, LS, X-ray Structure, LIESST	Guionneau et al. (1999); Létard et al. (1997); Tailleur et al. (2017)
6.	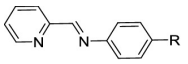 R = H, (PM-H) R = C_6H_{13}, (PM-C_6H_{13}) R = $C_{16}H_{33}$, (PM-$C_{16}H_{33}$)	Cis-[Fe(PM-H)2(NCS)2] Cis-[Fe(PM-C6H13)2(NCS)2] Cis-[Fe(PM-C16H33)2(NCS)2] HS (PM-C6H13) 117 K (T1/2), Abrupt(PM-C6H13) 176 K (T1/2), Gradual(PM-C16H33)	Oso and Ishida (2009)
7.	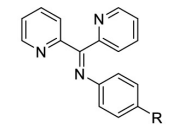 R = H, (DPM-H) R = C_4H_9, (DPM-C_4H_9) R = $C_{14}H_9$, (DPM-$C_{14}H_{29}$) R = $C_{16}H_{33}$, (DPM-$C_{16}H_{33}$)	*Cis*-[Fe(**DPM-H**)$_2$(NCS)$_2$] *Cis*-[Fe(**DPM-C_4H_9**)$_2$(NCS)$_2$] *Cis*-[Fe(**DPM-$C_{14}H_{28}$**)$_2$(NCS)$_2$] *Cis*-[Fe(**DPM-$C_{16}H_{33}$**)$_2$(NCS)$_2$] 270 K ($T_{1/2}$), Gradual (**DPM-H**) 290 K ($T_{1/2}\downarrow$), 250 K ($T_{1/2}\uparrow$), Hysteresis ($\Delta T_{1/2} = 40$ K) (**DPM-$C_{14}H_{28}$**) 300 K ($T_{1/2\ intial}$), 210 K ($T_{1/2}$), irreversible thermal cycle (**DPM-$C_{16}H_{33}$**) LS, X-ray Structure (**DPM-H**)	Oso et al. (2008)

Note HS: High Spin; LS: Low Spin; LIESST: Light induced excited spin state trapping; IR: Infrared spectroscopy; $T_{1/2}$ = Spin transition temperature; $T_{1/2}\downarrow$ = Spin transition temperature of cooling curve; $T_{1/2}\uparrow$ = Spin transition temperature of heating curve; $\Delta T_{1/2}$ = Hysteresis width

12.3.2 Co(II) Spin Crossover(SCO) Complexes

In the mononuclear octahedral Co(II) SCO complexes, the change in spin state occurs from LS ($S = \frac{1}{2}$) to HS ($S = \frac{3}{2}$) by the transfer of one electron from $t_{2g} \leftrightarrow e_g$ orbital. During the spin transition of Co(II) complex appreciable change has been observed in the coordination bond lengths by 0.1 Å (Hayami et al. 2011a; Molnár et al. 2014). All Co(II) SCO complexes (d^7 system) exhibited Jahn–Teller distortion (tetrahedral compression) due to the presence of odd electron in the e_g orbital (Hayami et al. 2011a; Molnár et al. 2014). The Co(II) SCO complexes were reported with the polypyridyl ligands like terpyridine, terpyridone and Schiff bases. The major share of Co(II) SCO complexes was reported with terpyridine ligands (Fig. 12.8). Firstly, the anomalous magnetic behavior in the Co(II) complexes was observed by Hoggset al. and Wilkins et al. without extensive magnetic studies which were later confirmed by EPR spectroscopic studies by Stouferet al. (1966). Majority of the Co(II) complexes showed gradual SCO behavior, however, it exhibited abrupt and hysteresis provided with increased cooperativeness by the substitution on ligands and counter anions. Different research groups investigated the effect of change of counter anions like $X = Cl^-$, Br^-, I^-, ClO_4^-, BF_4^-, PF_6^-, $CF_3SO_3^-$, NO_3^-, SCN^- in $[Co^{II}(\mathbf{terpy})_2](X)_2.nH_2O$ (n = 0–5) SCO complexes (Table 12.3 (entry 1)) (Kilner and Halcrow 2010). Krivokapicet al. documented the SCO behavior of mononuclear $[Co^{II}(\mathbf{terpy})_2](X)_2$ (X =

ClO_4^-, PF_6^-) in which counter anions were varied. The structural analysis revealed that the Co(II) metal ion occupied pseudo-octahedral geometry with N6 environment. The $[Co^{II}(\mathbf{terpy})_2](ClO_4)_2$ showed gradual spin transition with $T_{1/2}$ around 190 K, whereas, $[Co^{II}(\mathbf{terpy})_2](PF_6)_2$ showed mostly HS state in the given range of temperature 300–5 K. But, the complex showed little dip in the magnetic curve around 100–5 K which exhibited the presence of small population of LS of Co(II). Later, Kilner et al. documented the gradual SCO behavior in $[Co^{II}(\mathbf{terpy})_2](BF_4)_2$ with $T_{1/2}$ around 270 K. The temperature-dependent structural studies showed that the average change in Co–N donor bond was 0.1 Å. The change in $T_{1/2}$ does not depend on the size of counter anion but depends on the nature of molecular interactions between the cations and surrounding molecules (Kilner and Halcrow 2010). In addition, Gasper et. al documented influence of counter anions (BF_4^-, SiF_6^{2-}, $[Co(NCS)_4]^{2-}$, Cl^-, I^-, PF_6^-, NO_3^-, SO_4^{2-}, ClO_4^-) and solvent molecules (H_2O and CH_3OH) on the SCO behavior of Co(II) complexes derived from the terpyridone ligand (Table 12.3 entry 2). The complexes having counter anions SiF_6^{2-}, $[Co(NCS)_4]^{2-}$, PF_6^-, SO_4^{2-} showed HS state and I^- showed the LS state throughout the temperature range 300–2 K. The anions BF_4^-, NO_3^- and ClO_4^- showed SCO behavior, while the Cl^- showed gradual incomplete spin transition at 350 K. The Co(II) SCO complex with BF_4^- anion forms two polymorphs which convert irreversibly (I → II) above 340 K. The two polymorphs structurally differed in arrangement of anions and solvent molecules (H_2O) in the crystal lattice. Agusti et al. also documented formation of two polymorphs in Co(II) triflate SCO complexes derived from the terpyridone ligand

(Table 12.3 entry 2). One of the polymorphs showed gradual with $T_{1/2}$ around 220 K in the given temperature range of 300–2 K. Other polymorph showed abrupt 'reverse' SCO behavior with thermal hysteresis width ca. 33 K (Agustí et al. 2009).

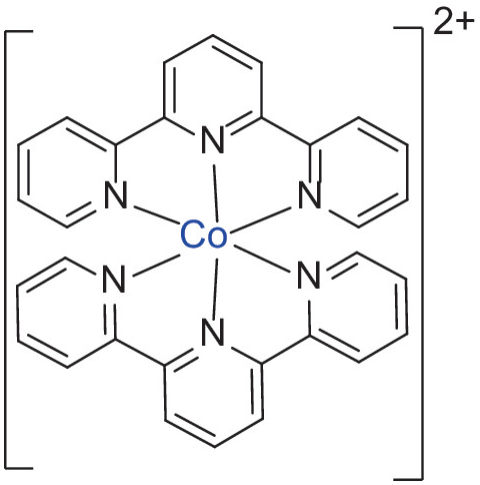

Fig. 12.8 Structure of Co(II) *bis*-terpyridine complex

Table 12.3 List of some substituted terpyridine ligands and their mononuclear Co(II) complexes

S. no	Ligands	Comments	References
1.	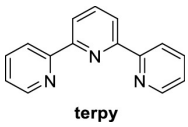 terpy	[Co(**terpy**)$_2$]I$_2$, ~ 150 K ($T_{1/2}$), Gradual [Co(**terpy**)$_2$]I$_2$·H$_2$O, ~ 200 K ($T_{1/2}$), Gradual [Co(**terpy**)$_2$](SCN)$_2$·H$_2$O, ~ 190 K ($T_{1/2}$), Gradual [Co(**terpy**)$_2$](NO$_3$)$_2$, ~ 340 K ($T_{1/2}$), Gradual [Co(t**erpy**)$_2$](BF$_4$)$_2$, 270 K ($T_{1/2}$), Gradual [Co(**terpy**)$_2$](ClO$_4$)$_2$·0.5H$_2$O, 190 K ($T_{1/2}$), Gradual [Co(**terpy**)$_2$](PF$_6$)$_2$, HS	Kilner and Halcrow (2010)

S. no	Ligands	Comments	References
		LS, HS, X-ray structure (BF_4^-) LS, X-ray Structure ($CF_3SO_3^-$), UV–Visible absorption	
2.	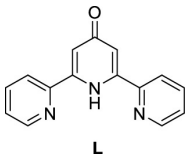 L	$[Co(\mathbf{L})_2](BF_4)_2 \cdot 2H_2O$ (Polymorph I and II) $[Co(\mathbf{L})_2](SiF_6) \cdot 3CH_3OH \cdot H_2O$ $[Co(\mathbf{L})_2][Co(NCS)_4] \cdot 0.5CH_3OH$ $[Co(\mathbf{L})_2]Cl_2 \cdot H_2O$ $[Co(\mathbf{L})_2]I_2 \cdot 5H_2O$ $[Co(\mathbf{L})_2](PF_6)_2$ $[Co(\mathbf{L})_2](NO_3)_2$ $[Co(\mathbf{L})_2](ClO_4)_2 \cdot H_2O$ $[Co(\mathbf{L})_2](CF_3SO_3)_2 \cdot H_2O$ (Polymorph I and II) ~270 K ($T_{1/2}$), (Polymorph I), ~175 K ($T_{1/2}$), (Polymorph II), Gradual (both), (BF_4^-) HS (SiF_6^{2-}, $[Co(NCS)_4]^{2-}$, PF_6^-, SO_4^{2-}); LS (I^-), Incomplete, gradual (Cl^-, NO_3^-); 172 K ($T_{1/2}$), Gradual (ClO_4^-) ~225 K ($T_{1/2}$), Gradual ($CF_3SO_3^-$) (Polymorph I) 155 K ($T_{1/2}\downarrow$), 188 K ($T_{1/2}\uparrow$), Hysteresis ($\Delta T_{1/2} = 33$ K) ($CF_3SO_3^-$) (Polymorph II) HS, X-ray structure (Polymorph I and II)	Agustí et al. (2009)

S. no	Ligands	Comments	References
3.	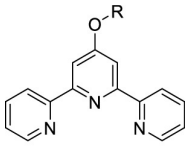 R = $C_5C_{12}C_{10}$, L R = $C_2C_8C_{10}$, L1 R = $C_2C_{10}C_{12}$, L2	$[Co(\mathbf{L})_2](BF_4)_2$ $[Co(\mathbf{L_1})_2](BF_4)_2$ $[Co(\mathbf{L_2})_2](BF_4)_2$ 284 K ($T_{1/2}\downarrow$), 288 K ($T_{1/2}\uparrow$), Hysteresis ($\Delta T_{1/2} = 4$ K) (**L**) 250 K ($T_{1/2}\downarrow$), 275 K ($T_{1/2}\uparrow$), Hysteresis ($\Delta T_{1/2} = 25$ K) (**L_1**) 296 K ($T_{1/2}\downarrow$), 307 K ($T_{1/2}\uparrow$), Hysteresis ($\Delta T_{1/2} = 11$ K) (**L_2**)	Hayami et al. (2009)
4.	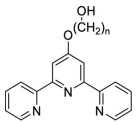 n = 6 (**HO-C_6-O-terpy**) 8 (**HO-C_8-O-terpy**) 10 (**HO-C_{10}-O-terpy**) 12 (**HO-C_{12}-O-terpy**) 14 (**HO-C_{14}-O-terpy**)	$[Co(\mathbf{HO\text{-}C_6\text{-}O\text{-}terpy})_2](BF_4)_2 \cdot H_2O$ $[Co(\mathbf{HO\text{-}C_8\text{-}O\text{-}terpy})_2](BF_4)_2$ $[Co(\mathbf{HO\text{-}C_{10}\text{-}O\text{-}terpy})_2](BF_4)_2$ $[Co(\mathbf{HO\text{-}C_{12}\text{-}O\text{-}terpy})_2](BF_4)_2$ $[Co(\mathbf{HO\text{-}C_{14}\text{-}O\text{-}terpy})_2](BF_4)_2 \cdot H_2O$ ~295 K ($T_{1/2}$), Gradual (**HO-C_6-O-terpy**) ~205 K ($T_{1/2}$), Gradual (**HO-C_8-O-terpy**) 295 K ($T_{1/2}\downarrow$), 316 K ($T_{1/2}\uparrow$), Hysteresis ($\Delta T_{1/2} = 21$ K) (**HO-C_{10}-O-terpy**) 308 K ($T_{1/2}\downarrow$), 348 K ($T_{1/2}\uparrow$), Abrupt, Hysteresis ($\Delta T_{1/2} = 40$ K) (**HO-C_{12}-O-terpy**) 214 K ($T_{1/2}\downarrow$), 231 K ($T_{1/2}\uparrow$), Hysteresis ($\Delta T_{1/2} = 17$ K) (**HO-C_{14}-O-terpy**) LS, X-ray structure	Komatsu et al. 2012)
5.	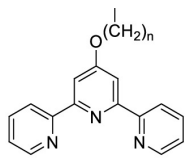 n = 11 (**C_{12}-O-terpy**) 13 (**C_{14}-O-terpy**) 15 (**C_{16}-O-terpy**)	$[Co(\mathbf{C_{12}\text{-}O\text{-}terpy})_2](BF_4)_2$ $[Co(\mathbf{C_{14}\text{-}O\text{-}terpy})_2](BF_4)_2 \cdot MeOH$ $[Co(\mathbf{C_{16}\text{-}O\text{-}terpy})_2](BF_4)_2$ 145 K ($T_{1/2}$), Gradual (**C_{12}-O-terpy**)	Hayami et al. (2011b, c)

S. no	Ligands	Comments	References
		217 K ($T_{1/2}\downarrow$), 260 K ($T_{1/2}\uparrow$), Hysteresis ($\Delta T_{1/2} = 43$ K) (**C_{14}-O-terpy**) 184($T_{1/2}\downarrow$), 206($T_{1/2}\uparrow$), Hysteresis ($\Delta T_{1/2} = 22$ K) (**C_{16}-O-terpy**) HS, X-ray structure (**C_{12}-O-terpy**) HS, X-ray structure (**C_{14}-O-terpy**, **C_{16}-O-terpy**)	
6.	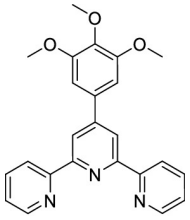 L	$[Co(\mathbf{L})_2](BF_4)_2 \cdot CH_3CN \cdot 0.5H_2O$ Gradual LS, X-ray Structure	Lee et al. (2013a)
7.	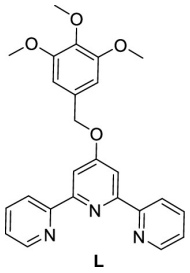 L	$[Co(\mathbf{L})_2](BF_4)_2$ ~220 K ($T_{1/2}$), Gradual LS, X-ray Structure	Lee et al. (2013a)
8.	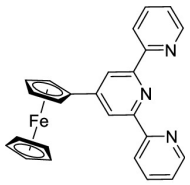 L	$[Co(\mathbf{L})_2](ClO_4)_2$ $[Co(\mathbf{L})_2](PF_6)_2$ $[Co(\mathbf{L})_2](BF_4)_2$ $[Co(\mathbf{L})_2](BPh_4)_2$ Incomplete, Gradual LS, X-ray Structure (ClO_4^-, PF_6^-)	Takami et al. (2015)
9.	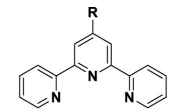 R = C_6H_4-C_6H_4-C_6H_5 C_6H_4-C_6H_4-C_6H_4-C_6H_5 **C_6H_5-C_6H_4-C_6H_4-terpy** **C_6H_5-C_6H_4-C_6H_4-C_6H_4-**	$[Co(\mathbf{C_6H_5\text{-}C_6H_4\text{-}C_6H_4\text{-}terpy})_2]$ $(BF_4)_2 \cdot MeOH$ $[Co(\mathbf{C_6H_5\text{-}C_6H_4\text{-}C_6H_4\text{-}C_6H_4\text{-}terpy})_2]$ $(BPh_4)_2 \cdot 3.5DMF \cdot 2H_2O$ ~350 K ($T_{1/2}$), Gradual (**C_6H_5-C_6H_4-C_6H_4-terpy**)	Lee et al. (2013b)

S. no	Ligands	Comments	References
		Gradual (**C_6H_5-C_6H_4-C_6H_4-C_6H_4-terpy**) HS, X-ray structure (**C_6H_5-C_6H_4-C_6H_4-terpy**) LS, X-ray structure (**C_6H_5-C_6H_4-C_6H_4-C_6H_4-terpy**)	
10.	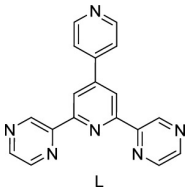 L	$[Co(\mathbf{L})_2](BF_4)_2 \cdot 2.5H_2O$ ~273 K ($T_{1/2}$), Gradual HS, X-ray Structure	Miller and Brooker (2015)
11	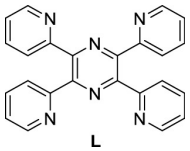 L	$[Co(\mathbf{L})_2](C_2N_3)_2$ Gradual LS, X-ray Structure	Palion-Gazda et al. (2017)
12.	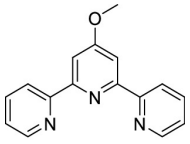 L	$[Co(\mathbf{L})_2](BF_4)_2 \cdot H_2O$ $[Co(\mathbf{L})_2](BF_4)_2$ $[Co(\mathbf{L})_2](BF_4)_2 \cdot CH_3COCH_3$ 163 K ($T_{1/2}1$), 231 K ($T_{1/2}2$), Gradual, Two steps (H_2O) Gradual (desolvated), HS (CH_3COCH_3) LS, X-ray Structure (H_2O)	Hayami et al. (2015)
13.	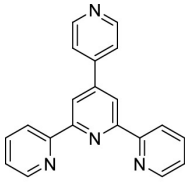 pyterpy	$[Co^{II}(\mathbf{pyterpy})_2](PF_6)_2 \cdot 2CH_3OH$ $[Co^{II}(\mathbf{pyterpy})_2](PF_6)_2 \cdot 2CH_2Cl_2 \cdot CH_3OH$ 182 K ($T_{1/2}\downarrow$), 191 K ($T_{1/2}\uparrow$), Hysteresis ($\Delta T_{1/2} = 9$ K) ($2CH_3OH$) Incomplete, Gradual ($2CH_2Cl_2 \cdot CH_3OH$) HS, LS X-ray structure ($2CH_3OH$)	Guo et al. (2015)

Note HS: High Spin; LS: Low Spin; $T_{1/2}$ = Spin transition temperature; $T_{1/2}\downarrow$ = Spin transition temperature of cooling

curve; $T_{1/2}\uparrow$ = Spin transition temperature of heating curve; $\Delta T_{1/2}$ = Hysteresis width

12.3.2.1 Effect of Substituents on Terpyridine Ligand in Co(II) SCO

The spin transition curve of the Co(II) SCO complexes has been influenced by varying substituting ligands on the terpyridine ligand. The substituents were varied like alkyl/alkoxy, aromatic at 4′-position of the terpyridine, in addition, Schiff bases were used to synthesize Co(II) SCO complexes (Stoufer et al. 1966; Kilner and Halcrow 2010; Agustí et al. 2009; Hayami et al. 2009; Komatsu et al. 2012; Hayami et al. 2011b, c, 2015; Lee et al. 2013a, b; Takami et al. 2015; Miller and Brooker 2015; Palion-Gazda et al. 2017; Guo et al. 2015). Hayami et al. documented the Co(II) SCO complexes derived from varied alkyl chain ($C_xC_yC_z$ = 4′-5′″-Alkyl-1′″-alkoxy-2,2′:6′,2″-terpyridine) appended terpyridine ligands (Table 12.3 entry 3 and Fig. 12.9). The $\chi_M T$ *vs* T plot of all complexes show hysteresis SCO behavior with $T_{1/2}$ temperatures in the range of 250–307 K just above liquid crystalline temperature (Hayami et al. 2009). Further, Komatsu et al. and Hayami et al. documented varied length of alkyl chain appended terpyridine ligands with presence/absence of terminal hydroxyl groups in Co(II) complexes. The change in SCO behavior of complexes was observed to change from gradual to hysteresis with an increased length of the alkyl chains which was explained by fastener effect and intermolecular interactions by the substituents. In the complexes, the spin transition was associated with the phase transition from solid → mesophase which is the property of metallomesogens (Hayami et al. 2011a; Molnár et al. 2014; Komatsu et al. 2012). Complexes exhibiting such type of property are likely candidates for the development of display devices.

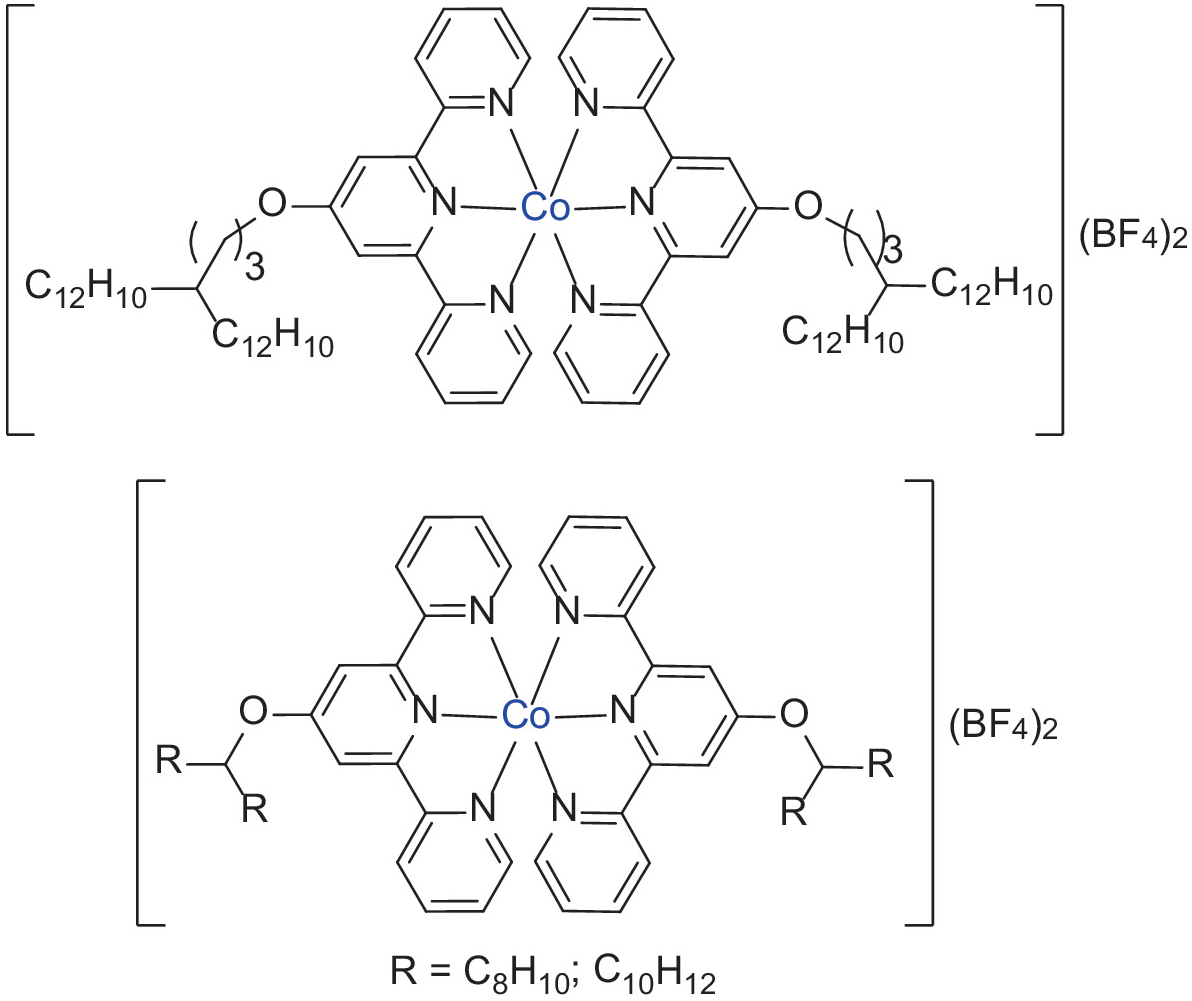

Fig. 12.9 Structure of the Co(II) complexes synthesized by Hayami et al. (2009)

Komatsu et al. documented the SCO behavior of Co(II) complexes derived from the hydroxyl appended alkyl chains on terpyridine to synthesize $[Co^{II}(\mathbf{HO\text{-}C_n\text{-}O\text{-}terpy})_2](BF_4)_2$ ($n = 6$, 8, 10, 12, 14) (Table 12.3 entry 4). The SCO behavior of Co(II) complexes changes from gradual, abrupt and wide hysteresis with the varied alkyl chains in $\mathbf{HO\text{-}C_n\text{-}O\text{-}terpy}$ ($n = 6$–12) except in $\mathbf{HO\text{-}C_{14}\text{-}O\text{-}terpy}$. The $T_{1/2}$ of the $[Co^{II}(\mathbf{HO\text{-}C_n\text{-}O\text{-}terpy})_2](BF_4)_2$ complexes shown in the range of 205 K to 348 K which was above or below the temperature. The changes in SCO behavior was explained by the fastener effect, where the shorter alkyl chains ($n = 6$,

8) do not form strong end-to-end intermolecular interactions than long alkyl chains ($n = 10$, 12). Except in $[Co^{II}(\mathbf{HO\text{-}C_{14}\text{-}O\text{-}terpy})_2](BF_4)_2$, the hysteresis width was decreased due to thermal movement of the alkyl chain in crystal lattice leading to structural deformation eliminating strong end-to-end intermolecular interactions between molecules (Komatsu et al. 2012). In the same way, Hayamiet al. also reported similar kind of 'reverse' SCO behavior in other Co(II) complexes containing alkyl chain appended terpyridine ligand of type $[Co^{II}(\mathbf{C_n\text{-}O\text{-}terpy})_2](BF_4)_2$ ($n = 12$, 14, 16) complexes (Table 12.3 entry 4). The $[Co^{II}(\mathbf{C_n\text{-}O\text{-}terpy})_2](BF_4)_2$ complexes showed $T_{1/2}$ in the range of 145–260 K. Terminal hydroxyl groups were absent in these compounds (Hayami et al. 2011b, c). Komatsu et al. documented the influence of intermolecular interactions formed by alkyl chains with the presence and absence of terminal OH group in the Co(II) SCO complexes. They explained that the complexes having terminal OH group in long alkyl chains do not form any intermolecular interactions with the solvent and counter anions, yet the alkyl chain appended Co(II) complexes show 'reverse' SCO behavior through the fastener effect (Komatsu et al. 2012).

In extension, researchers substituted extended aromatic groups like phenyl rings and heterocyclic ring at different positions on the terpyridine ligand. Lee et al. documented the effect of trimethoxy phenyl substituents on the terpyridine in Co(II) SCO complexes (Table 12.3 entry 6–7). The magnetic studies of the complexes showed that the progressive SCO behavior with given $T_{1/2}$ nearly about 220 K. The structural studies of the complex were measured at different temperatures 100 K and 293 K showing average metal donor distance Co–N: 2.02 (LS) and Co–N: 2.09 (HS) respectively. The subtle changes observed in the bond distances were explained by compact packing

due to increased cooperativity through hydrogen bonding between solvent-anions, anions-cations, solvent-cations. In addition, the methoxy group participated in C–H–π interactions and phenyl ring involved in face-to-face interactions (Lee et al. 2013a). Later, Takamiet al. documented the ferrocene appended terpyridineCo(II) SCO complexes with varied counter anions BF_4^-, ClO_4^-, PF_6^- and BPh_4^- (Table 12.3 entry 8). The variable temperature magnetic studies showed the gradual and incomplete SCO behavior in the given range of temperature 5–400 K (Takami et al. 2015). On the other hand, Lee et al. documented SCO behavior of Co(II) bis-terpyridine complexes derived from the extended aromatic rings appended terpyridine to synthesize $[Co^{II}(\mathbf{C_6H_5\text{-}C_6H_4\text{-}C_6H_4\text{-}terpy})_2](BF_4)_2.MeOH$ and $[Co^{II}(\mathbf{C_6H_5\text{-}C_6H_4\text{-}C_6H_4\text{-}C_6H_4\text{-}terpy})_2](BPh_4)_2.3.5DMF.2H_2O$ complexes (Table 12.3 entry 9). The Co(II) complexes showed gradual SCO behavior with $T_{1/2}$ value ~350 K (**C_6H_5-C_6H_4-C_6H_4-terpy**) and incomplete at >370 K (**C_6H_5-C_6H_4-C_6H_4-terpy**) which was above the room temperature. The structural studies of complexes show strong CH–π (edge-to-face), π–π interactions involving terminal phenyl rings and remote segment of pyridine rings, along with the H-bonding formed between anions, solvent and cation. The gradual SCO behavior of the complexes was explained through the intermolecular interactions with respect to the Co–Co separation in the crystal lattice (Lee et al. 2013b).

Different research groups observed the SCO behavior of Co(II) complexes when the central/distal pyridines are replaced with pyrazine. Miller et al. documented the SCO behavior of the Co(II) complex derived from pyridine appended terpyridine analogue where distal pyridines were replaced with pyrazine moiety (Table 12.3 entry 10). The complex showed very gradual and incomplete SCO

behavior in the given range of temperature 50–350 K. The structural studies recorded at 100 K reveal the Jahn–Teller distortion with the average bond lengths $Co{-}N_{py} = 1.900$ Å versus $Co{-}N_{pz} = 2.072$ Å comparable to the parent $[Co(\mathbf{terpy})_2](BF_4)_2$ complex in its LS state showing $Co{-}N_{pycentral}$ 1.909 versus $Co{-}N_{pydistal}$ 2.092 Å (Miller and Brooker 2015). In another case, Palion-Gazdaet al. documented the SCO behavior of the Co(II) complex derived from the terpyridine analogue where central pyridine was replaced with pyrazine moiety (Fig. 12.10) and has dicyanmide ($C_2N_3^-$) as a counter anion (Table 12.3 entry 11). The complex showed gradual incomplete SCO behavior in the given range of temperature 2–400 K. The structural data recorded at two temperatures (125 K and 330 K) revealed a change in average bond length in Co–N was 2.114 (HS) and 2.009 Å (LS) of Co(II) respectively. But the change in the angular distortion parameter (Σ) was not varied much 82.6° and 84.0° at 125 and 330 K respectively (Palion-Gazda et al. 2017).

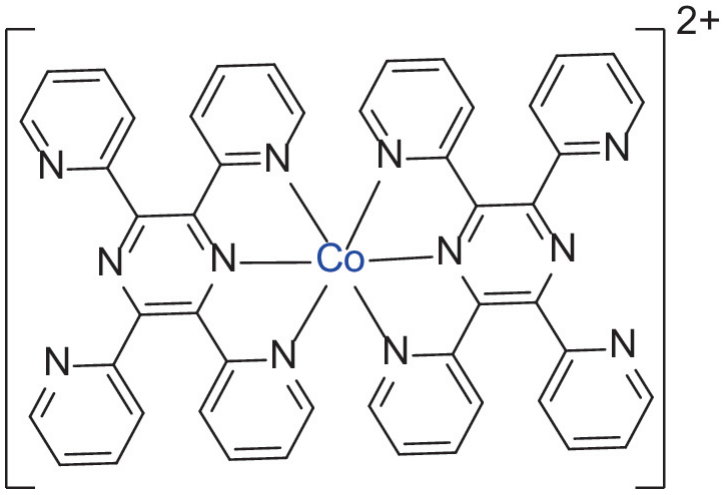

Fig. 12.10 Structure of the Co(II) complexes synthesized by Palion-Gazdaet al. (2017)

Furthermore, change of solvent molecule(s) in crystal lattice tends to alter the intermolecular interactions

between molecules. The solvent molecules are more likely involved in the formation H-bonding network between $[Co(\mathbf{terpy})_2]_2^+$ and counter anions which form the foundation of cooperativity between the molecules (Šalitroš et al. 2009). Hayamiet al. documented the SCO behavior of three mononuclear Co(II) complexes (Table 12.2 entry 12). Initially, the magnetic behavior of the aqua complex showed two-step gradual transition showing $T_{1/2}$ of 163 and 231 K. After the annealing process, the complexes showed gradual SCO behavior with given $T_{1/2}$ value around ~235 K. However, the complex having acetone as crystal solvent showed HS state in the given range of temperature 2–320 K. After the annealing process, the complex showed 'reverse' spin transition due to the structural phase transition. The difference in magnetic behavior was explained by the disruption of face-to-face intermolecular interactions between ligand motifs by CH_3COCH_3 which unlikely present in H_2O (Hayami et al. 2015). Guoet al. documented the SCO behavior in $[Co^{II}(\mathbf{pyterpy})_2](PF_6)_2{\cdot}2CH_3OH$ derived from the pyridine appended terpyridine ligand (Table 12.2 entry 13). The complex showed abrupt SCO behavior with hysteresis width of 9 K due to the strong cooperative effect in the givenrange of temperature 100–300 K. The strong cooperative effect was explained by the formation of strong hydrogen bonding and edge-to-face C–H–π interactions. The structural studies of the complex, recorded at different temperatures exhibited different space groups originated due to order–disorder phase transition. In contrast, $[Co^{II}(\mathbf{pyterpy})_2](PF_6)_2.2CH_2Cl_2{\cdot}CH_3OH$ showed gradual and incomplete SCO behavior in the given temperature range of 2–380 K (Guo et al. 2015). From the above, the SCO behavior of the Co(II) bis-terpyridine complexes is sensitive to the changes caused by the metal centre. The compilation of substituted

terpyridine ligands and their mononuclear Co(II) complexes are given in the Table 12.3.

12.4 Characterization

Transition metal ions with d^4–d^7 configurations adopt either a high-spin (HS) or a low-spin (LS) electronic arrangement in octahedral ligand fields. This depends upon whether the crystal field energy is lower or higher than the mean spin pairing energy. If the two energies are comparable (i.e. favorable ligand field strength), different external perturbations like temperature, pressure, irradiation etc. can bring about transitions between the two spin states. The disparity between the HS and LS states arises from their distinct occupancy of anti-bonding (e_g) orbitals. Notably, the distance between the metal and donor atom is significantly influenced by the spin state. Another significant parameter which varies upon the spin transition is change in the magnetic property. The transition from low spin to high spin results in a pronounced increase in the paramagnetism of the system and hence the measurement of this change remains the most common way of observing a spin transition (Gütlich and Goodwin 2004a; Gómez et al. 2015; Chen et al. 2014; Jureschi et al. 2014; Kahn and Martinez 1998; Dugay et al. 2015; Shatruk et al. 2015; Brooker 2015; Halcrow 2013; Gamez et al. 2009; Gütlich et al. 2000). Various spectroscopic techniques are frequently utilized to observe the transition and generate a ST (spin transition) curve. The routine techniques used to monitor SCO are temperature dependent magnetic susceptibility measurement, optical spectroscopy, Mossbauer spectroscopy, vibrational spectroscopy, single crystal diffraction technique and Differential Scanning Calorimetry technique etc.

12.4.1 Magnetic Susceptibility Measurements

Considering the marked difference in magnetic moments of high spin and low spin states, the measurement of magnetic susceptibility as a function of temperature has always been a standard technique to characterize a ST. The change in the number of unpaired electrons between the strongly paramagnetic HS and weakly paramagnetic or diamagnetic LS states is readily reflected in a drastic change of $\chi(T)$ as the mole fraction of the high-spin species (χHS) is a temperature-dependent quantity. The magnetic susceptibility; $\chi(T)$ for a SCO material is determined by the temperature dependent contributions χHS and χLS according to equation $\chi(T) = \gamma HS(T) \cdot \chi HS + (1-\gamma HS(T)) \cdot \chi LS$. Knowing the susceptibilities of the pure HS and LS states, the mole fraction of the HS state (or LS state), χHS, at any temperature can be readily derived and is plotted to produce the spin transition curve. Transition curves related to spin can take a number of forms including gradual or abrupt changes, single or multiple steps, varying widths of hysteresis, and positions on the temperature scale. Additionally, these curves may appear incomplete at both higher and lower temperatures. The variety in these curves stems from various factors, with cooperative interactions linked to spin state transitions being the primary contributor (Gütlich and Goodwin 2004b; Madeja and König 1963; König et al. 1966; Nihei et al. 2007; Gütlich et al. 2002; Gütlich 2013; Šalitroš et al. 2009).

12.4.2 ^{57}Fe Mössbauer Spectroscopy

Since, SCO phenomenon has been dominantly observed for either iron(II) or iron(III) complexes, ^{57}Fe Mössbauer spectroscopy has become a powerful tool for investigating the ST behavior of iron compounds. Electron density at the nucleus is significantly different for the LS and HS states, so the isomer shift and quadrupole splitting observed in the

Mössbauer spectra are very different for the two states. It provides details regarding oxidation and spin states, magnetic properties, molecular symmetry, distortions, etc. The characteristics of the absorption depend on the chemical environment of the ^{57}Fe nucleus and the velocity of the cobalt source. Isomer shift (δ) and electric quadrupole splitting (ΔE_Q) are the two crucial parameters in Mössbauer spectroscopy. The isomer shift (δ), arises from interaction of nucleus with s electrons and thus is proportional to the s-electron population at the nucleus. The parameters give information on oxidation state, spin state and allow valuable insight into bonding properties. The quadrupole splitting (ΔE_Q) is based upon the interaction between the quadrupole moment of the iron nucleus and the electric field of the s electron cloud. It gives us an idea of the spin state and oxidation number of iron. There are significant differences in the spectral parameters linked to the HS and LS states. Usually, Mössbauer spectra of high-spin iron(II) exhibit a noticeable quadrupole splitting, ($\Delta E_Q \approx 2–3$ mm/s) and isomer shift, (δ≈ 1 mm/s). For a Low Spin iron(II), these characteristics are normally smaller ($\Delta E_Q \leq 1$ mm/s, $\delta \leq 0.5$ mm/s) (Halcrow 2009). The technique's temporal resolution enables the identification and assessment of individual spin states during the transition. By analyzing the resonance signals' area fractions, which are roughly correlated with the iron concentrations of coexisting spin states, spin transition curves, denoted as γHS(T) can be readily generated (Gütlich and Goodwin 2004b; Gütlich et al. 2013, 2002; Madeja and König 1963; König et al. 1966; Nihei et al. 2007; Gütlich 2013).

12.4.3 Measurement of Electronic Spectra

Thermal switching of spin states is generally accompanied by a color change too. The LS state is usually strongly

coloured (e.g. purple or dark red), whereas the HS state is typically pale (e.g. white or yellow). As a result, optical spectroscopy within the UV/Vis range is frequently utilized for the characterization of SCO. This provides a very convenient means of detecting the probable occurrence of a transition by simple observation of the colour at different temperatures. For example, SCO complexes of iron(II) with tetrazole and triazole ligands are generally weakly colored or nearly white in the HS state but purple in the LS. Ligand field transitions (d-d transitions) which are parity-forbidden but spin-allowed give rise to rather intense color, particularly in the LS state. If the colour imparted is majorly attributed by the ligand field bands, then for iron(II) a striking change from colourless in the high spin state to violet in the low spin state will be observed which can be readily observed by monitoring the temperature dependent optical spectra of the samples. Sometimes, the ligand based transitions are masked by charge transfer bands occurring in the same region. In that case, a pronounced effect in increase in intensity of colour with slight change in frequency to lower side is observed when transition occur from high spin to low spin. For iron(II), the UV–Vis spectrum for the HS ion shows one ligand field band in the near-infrared region arising from the $^5T_2 \rightarrow {}^5E$ transition, while for LS iron(II) two ligand field bands occur, $^1A_1 \rightarrow {}^1T_1$ and $^1A_1 \rightarrow {}^1T_2$, the former appearing in the visible and the latter in the ultra-violet region (Brooker 2015; Gütlich and Goodwin 2004b; Gütlich et al. 2000; Gütlich 2013).

12.4.4 Measurement of Vibrational Spectra

Due to changes in the vibrational states of the coordination polyhedron in spin transition process, bond vibrations differ for the two spin states i.e. LS and HS. Temperature-dependent far-infrared vibration spectroscopy is another

useful tool for the investigation of ST compounds. In the course of spin transition from high-spin to low spin, there is a decrease in electron density in antibonding e_g orbitals (d^4, d^5 and d^6 species) with an increase in electron density in bonding t_{2g} orbitals. This leads to considerable strengthening of metal to ligand bond which can be observed with a change in stretching frequency of metal-donor bond in vibrational spectrum. As the temperature increases, the intensity of the LS vibrations decrease and the HS peaks increase. For example, the stretching frequency detected in the far infrared region typically shifted from 300 cm^{-1} in the HS state to about 450 cm^{-1} in the LS state. Certain ligand based vibrations are characteristically monitored to observe the change in spin state. For instance, N-coordinated ligands NCS^- and $NCSe^-$, which are commonly used in the synthesis of classical iron(II) SCO complexes. In high spin state, the C–N stretching bands of NCS^- and $NCSe^-$ are seen as strong doublet near 2060–2070 cm^{-1}. Upon cooling, near transition temperature i.e. 176 K the intensity of the doublet decreases with the appearance of a new doublet at 2100–2110 cm^{-1}, attributed to the presence of LS state. Considering the cumbersome nature of vibrational spectra, it is not normally practiced though, the spin conversion curves, denoted as $\gamma_{HS}(T)$ can be traced by graphing the temperature-dependent area fractions of distinctly identifiable HS or LS bands (Brooker 2015; Gütlich and Goodwin 2004b; Gütlich et al. 2013, 2002, 2000; Madeja and König 1963; König et al. 1966; Nihei et al. 2007; Gütlich 2013).

12.4.5 X-Ray Diffraction Method

The rearrangement of valence electrons due to spin transition brings about fundamental changes in the crystal

lattice. Drastic electron rearrangement between bonding t_{2g} orbitals antibonding e_g orbitals in HS and LS cause changes in metal–ligand bond angles and lengths which are reflected with a change in molecular dimension of crystal lattice. Therefore, it is essential to incorporate structural examinations in the exploration of SCO in solids, primarily through X-ray diffraction on either single crystals or polycrystalline materials. In the case of continuous spin transition, only bond length and angle are affected, whereas discontinuous transition with hysteretic behavior causes a shift in the space group, signaling the occurrence of a first-order phase transition accompanied by substantial lattice reorganization. It is observed that metal ligand bond is high in case of HS state as compared to LS state. The change in bond length is particularly large for SCO complexes of Fe(II), $\Delta = 2$; which is ($\Delta r_{HL} = r_{HS} - r_{LS} \approx 220$–200 pm ≈ 20 pm).It brings an approximate change of 3–4% in elementary cell volumes. In comparison, about 10–13 pm change in bond lengths is observed in iron(III) spin-crossover (SCO) systems, transitions with $\Delta = 2$ occur, while in cobalt(II) systems, transitions with $\Delta = 1$ have a range of less than or equal to 10 pm. Therefore, crystal structure determination at various temperatures above and below the transition temperature ($T_{1/2}$, temperature of half-way spin transition, where 50% of the “SCO-active” molecules have changed their spin state) becomes essential to gain insights about ST phenomenon. In case where, suitable single crystals are not accessible, temperature dependent X-ray powder diffraction data can also help to provide details about the changes in the lattice parameters and nature of the ST (gradual or abrupt) (Gütlich et al. 2013; Šalitroš et al. 2009).

12.4.6 Light-Induced Excited Spin State Trapping (LIESST) Effect

The classical LIESST phenomenon has remained a major topic of interest for the design of optical switches. The switching of SCO compound from LS configuration to HS configuration upon irradiation with light (specifically green) is termed as Light-Induced Excited Spin State Trapping (LIESST) Effect. This photo-physical effect was first observed in $[Fe(ptz)_6](BF_4)_2$ SCO compound by Mainz group in 1984. The molecule undergoes thermal ST behavior which has been demonstrated by temperature dependent Mössbauer spectra. In thermal ST, the phase change occurs at a temperature $T_{1/2}$ of ca. 135 K with hysteresis of ca. 7 K width. For the first time, it was observed that LS to HS conversion can also be induced in solid compounds upon irradiation with green light. The irradiation produced a metastable HS state with long lifetimes even up to days below ca. 20 K. Later on the phenomenon was further studied by Houser and it was proved that red light switches the metastable HS back to LS and referred to as reverse-LIESST. Today, the LIESST effect as well as inverse-LIESST has been studied for numerous iron(II) systems and a few iron(III) systems. Though, it has been well studied, however the main limitation is its time domain. The photoinduced metastable HS has a normally long lifetime i.e. around weeks at 20 K for $[Fe(ptz)_6](BF_4)_2$, but at high temperatures of above 50 K, the thermally activated relaxation process takes place leading to decay of HS to LS within seconds. At present, the studies on iron(II) complexes involve the LIESST and reverse LIESST processes with the aim of obtaining suitable materials for technical applications such as displays, information storage and sensors. The normal lifetimes of photo-excited LIESST states in SCO complexes have been found to be in the range of minutes to hours, or even days, below ca. 20 K. For the real applications, a system with thermal hysteresis of 100 K is desired. A few

SCO systems of iron (II) have been designed in literature with lifetimes reaching to 100 K which is highly motivating. Efforts are continued in this direction and it has been observed that cooperative interactions play a crucial role in the interpretation of photo-magnetic behavior when a large increase in metal–ligand bond lengths takes place during the light-induced population of the HS state at low temperatures. In systems where the intermolecular cooperative interaction in the solid is weak, the HS → LS relaxation is single exponential whereas in strongly cooperative systems the curves follow a sigmoidal behavior (Brooker 2015; Gütlich et al. 2013, 2000; Létard 2006). Apart from the above discussed techniques, other methods such as calorimetric measurements, magnetic resonance spectroscopy (EPR, NMR), X-ray absorption spectroscopy (EXAFS, XANES) etc. are also employed to get details of spin transition behavior (Gütlich and Goodwin 2004b; Gütlich et al. 2002; Šalitroš et al. 2009).

12.5 Emerging Areas and Applications

As discussed above that SCO complexes exhibit a dynamic change in their basic properties with the change of spin transition. The spin state transition is accompanied by a change in electronic structure of the central ion and the complex molecule on the whole, which significantly changes the physical and chemical properties of the material. Spin-crossover has a large impact on the physical properties of a solid material, including its magnetic moment, color, molecular structure, dielectric constant, and electrical resistance. Strong temperature dependence of various properties is manifested in SCO materials as in correspondence to spin transition. With the change in electronic arrangements upon spin transition, a drastic

effect is observed in magnetic properties. For example, system changes behavior from a highly paramagnetic to diamagnetic system when it undergoes transition from high spin to low spin. Similarly, vibrant colored systems changes to colorless with change in temperature. Moreover some spin-crossover materials show pronounced hysteresis, which often reflects a structural phase change during the transition. Within the hysteresis loop, the materials are bistable switches that can be either high or low spin depending on their history. Metal complexes with spin-crossover (SCO) behavior serve as classic instances of molecular switches. Their color, magnetic features, conductivity, and other physicochemical properties can be reversibly altered through external stimuli, such as changes in temperature, pressure, or exposure to light. The SCO materials of d^4-d^7 systems are also important compounds as which can be widely and deeply investigated as potentially smart materials with multifunctional properties. The significant aspects such as transitions occurring at nanoscale, molecular switching at room temperature and very fast changes in electronic states makes these molecules a highly potential system for future molecular and electronic devices (Gütlich and Goodwin 2004a, 2004b; Gómez et al. 2015; Chen et al. 2014; Jureschi et al. 2014; Kahn and Martinez 1998; Dugay et al. 2015; Shatruk et al. 2015; Brooker 2015; Halcrow 2013; Gütlich et al. 2013, 2002, 2000; Gütlich 2013). The switching properties of SCO materials driven by external factors make these molecules highly attractive for several practical applications, e.g., as switching devices and sensors. This include display and memory devices, electrical and electroluminescent devices, temperature and pressure sensors, MRI contrast agent, switchable liquid crystals, nanoparticles and thin films of spin crossover materials etc. The possible future applications of this class

of substances are temperature or pressure sensors with an easy optical readout (Létard and Guionneau 2004; Halcrow 2011, 2009). Coordination complexes of Fe(II) have remained largest number of the systems showing the spin-crossover phenomenon, that is displaying an entropy driven transition from a low-spin (LS) at low temperatures to a high-spin (HS) state at higher temperatures (Kahn and Martinez 1998; Dugay et al. 2015; Shatruk et al. 2015; Brooker 2015; Halcrow 2013).

Though the progress of research in SCO field reflects a lot of potential for the application of these materials in fabrication of various devices still, instances of their incorporation into functional devices are still limited. Several groups around the world have worked in a direction into incorporation of nanoparticles showing spin-crossover behavior and thin films into electronic, photonic, and mechanical devices through utilizing the remarkable alterations in physicochemical characteristics linked to the SCO. While the present status of research focuses mainly on the device functionalities and little is known about long-term stability, reproducibility, and scalability etc. Fernandez et al. has explored the spin crossover (SCO) polymer of $[Fe(NH_2trz)_3](BF_4)$employing various organic polymers as host. Here, the authors have investigated the application of the nanocomposites in colorimetric temperature sensor for the rapid visually detecting alterations in temperature. Gentili et al. reported the Fe (II) SCO complex $[Fe(L)_2]$ (L = (2-(pyrazol-1-yl)-6-(1Htetrazol-5-yl)pyridine)), for the selective multi-modal sensing of ethanol and methanol. The authors showed that the system exhibits a simultaneous change of colour, birefringence and Raman spectra corresponding to the spin transition which has been explored for its utility in a multi-modal sensor. Bousseksou et al. reported the lithographically patterned gold nanorod arrays, coated by

thin films of an iron(II)–triazole spin crossover for plasmonic resonance properties. The results showed that active, even synergistic, modulation of plasmonic properties can be efficiently achieved by molecular spin state switching which allows for an active tuning of the plasmon resonance (Hayami et al. 2011a; Molnár et al. 2014, 2018; Lapresta-Fernández et al. 2014).

Matsuda et al. reported a spin-crossover complex $[Fe(dpp)_2](BF_4)_2$ (dpp = 2,6-di(pyrazol-1-yl)pyridine) to build an organic light-emitting diode doped with chlorophyll-a luminophores. The complex showed temperature dependence of the EL Spectrum. The EL spectrum was observed at 300 K, while the spectrum could not be observed below 260 K which is the spin-transition temperature of $[Fe(dpp)_2](BF_4)_2$ suggesting the EL quenching accompanied by spin transition (Hayami et al. 2011a; Molnár et al. 2014, 2018; Lapresta-Fernández et al. 2014; Masaki et al. 2008; Chen et al. 2015).

For application in memory devices, the existence of bistability should be correlated with a response function. Atypical molecular switch is characterized with bistability domain with an “ON” and an “OFF” position. In its “ON” position, the molecular switch either perform some function or allow another device to perform a function while in its “OFF” position, it remain inactive. The bistability phenomenon of the molecules should occur around the room temperature associated with response function like change in color or magnetism (Létard and Guionneau 2004; Halcrow 2011, 2009; Hayami et al. 2011a; Molnár et al. 2014). The detectable responses by the naked eye like color change associated with a change in magnetic properties have potential applications in the development of display and sensor devices (Harding et al. 2016; Zhong et al. 1998). Particularly, micro- and nanoparticles of $[Fe(Htrz)_2(trz)]$ (BF_4) have been commonly used. This

compound has garnered interest due to its resilient spin transition occurring above room temperature, coupled with conductivity dependent on the spin state. This behaviour has been utilized for making electronic switches, though the ON-to-OFF current ratio is very less than the preferred electronic switch parameter (Molnár et al. 2018; Lapresta-Fernández et al. 2014).

SCO materials have also been recently investigated in the effective incorporation of SCO materials into microelectromechanical systems (MEMS) and muscle-mimicking actuator technologies. MEMS technology in microelectronics has attained wide attention over the last few decades; MEMS have been extensively utilized across various applications in data communication, sensors, and actuation technologies. Notably, MEMS can offer exceptionally high sensitivity for chemical and biochemical sensing purposes. Various silicon MEMS cantilevers were built recently based on SCO compounds of Fe ([Fe(H_2B(pz)$_2$)$_2$(phen)], [Fe(HB(tz)$_3$)$_2$] (tz = 1,2,4-triazol-1-yl),[Fe(H_2B(pz)$_2$)$_2$(dmbpy) etc.). These devices have demonstrated that thermal and light-induced SCO phenomena can be easily identified by monitoring the alteration in the resonance frequency (fr) of the MEMS (Hayami et al. 2011a; Molnár et al. 2014; Létard 2006). Different Fe based SCO compounds have also been explored in Muscle-like actuator technologies. This technology mimics the human motion to provide soft, smooth, noiseless movement and has been of significant importance in medical implants, surgical and diagnostic tools, human assist devices, lightweight robots, and aerospace applications. Chen et al. created a polymer device that incorporated a piezoresistive detection system. This system transformed the bistable mechanical output of the SCO material into a bistable voltage signal (Hayami et

al. 2011a; Molnár et al. 2014, 2018; Lapresta-Fernández et al. 2014; Masaki et al. 2008; Chen et al. 2015).

The light irradiation as external stimuli in changing the spin state of the molecule provides promising applications in the development of optical storage devices. The alteration in spin state when pressure is applied can be utilized in the development of pressure sensors, leading to a color change suitable for remote sensing. (Gamez et al. 2009; Tezgerevska et al. 2014).

Another important parameter which has been of prime importance is the stability of the chemical properties and the consistency of the behavior after cycling through the hysteresis loop. The main advantage of using such molecule-based materials is that even at the nanometric scale, the spin-crossover (SCO) switching event can be achieved. Therefore, it is crucial to interface the switching molecular entity with a micro-scaled device for potential applications. With the fine tuning in the design of SCO, switching can even occur at room temperature which is of prime significance for the application of SCO in potential applications. The very fast transitions due to change in electronic states (at leaston the molecular level) provide a wide range of flexibility to design new materials. Certain data generated by a spin-crossover (SCO) switching event is detectable only at the nanometric scale. Consequently, it is crucial to connect the switching molecular entity with a microscaled device for potential applications. In contemporary times, there is a significant focus on the micro- and nanopatterning of functional materials based on molecules with switching properties. This is aimed at advancing the development of information storage devices or sensors and has become a leading area of research (Gütlich and Goodwin 2004a; Gómez et al. 2015; Chen et al. 2014; Jureschi et al. 2014; Létard and Guionneau 2004; Halcrow 2011, 2009; Gamez et al. 2009; Gütlich 2013;

Molnár et al. 2018; Lapresta-Fernández et al. 2014; Masaki et al. 2008; Chen et al. 2015).

12.6 Conclusion

The study of molecular spin cross over is though old, it remains an attractive and challenging task among the coordination chemists. Since the first observation of spin transition in 1931, a lot of progress has been made in this field. In this chapter, a detailed account of the spin transition phenomenon, its history and theoretical background is presented. For making it easy for the reader, scope of this chapter was kept limited to the selected spin crossover complexes of Fe(II), and Co(II) and the effect of ligand environment on the spin crossover phenomenon in these system is presented. The SCO complexes of Fe(II) with pyridine and Schiff base ligands, while the synthesis, properties and magnetic behavior of terpyridine based Co(II) complexes have been thoroughly covered in this article. The challenge in the field is to obtain systems where spin transition phenomenon can be observed at ambient conditions which may be suitable for real applications. The design of SCO compounds which exhibits large cooperativity remain one of the major concern of the field. Understanding the cooperative behavior is the primary motivation for investigating the impact of intermolecular interactions in spin transition complexes which plays a significant role in observed hysteresis behaviour of SCO compounds. In this direction, a variety of Fe(II) and Co(II) based systems have been developed having spin transition temperature around room temperature which exhibit a wide hysteresis behaviour. Amongst the few examples exhibiting remarkable SCO behavior, the systems based on the Fe(II) complexes of 1,2,4-triazole ligands remain among the promising materials. Few of these, particularly the coordination 1D-

polymers show wide thermal hysteresis loops around room temperature. A wide array of cobalt complexes have also been explored with emphasis on terpyridine based ligands. Most of the Co(II) complexes showed gradual SCO behavior, however, they exhibited abrupt spin transition and hysteresis loops when the cooperativeness is increased by the substitution on ligands and counter anions. The substitution of the 4-position in the skeleton of terpy ligand allows diverse magnetic behavior of Co(II) complexes by enhancing intermolecular interactions in the solid state. The change in SCO behavior of complexes was observed to change from gradual to hysteresis with an increased length of the alkyl chains which was explained by fastener effect and intermolecular interactions by the substituents.

In the recent years, notable progress has been witnessed in the production of spin-crossover (SCO) nanomaterials, taking diverse forms like nanoparticles, thin films, nanopatterns, nano-heterostructures, and nanocomposites. The focus has primarily been on investigating the device applications of this remarkable phenomenon. The development of SCO materials is attracting a huge deal of scientific attention due to their potential application in fabrication of memory devices. The ever increasing need of electronic data retrieval and storage has played a key role in the growth of the field. Continuous efforts are needed in direction towards further understanding of the molecular level phenomenon. Nevertheless, the current status of the field indicates significant advancements in the pursuit; the utilization of spin-crossover (SCO) compounds is still in its early stages, and the scientific community must address various practical challenges to reach new frontiers.

Acknowledgements

AKS acknowledges the project grant from CSIR, India (Ref.: 01(3084)/21/EMR-II). The chapter is dedicated to Prof. R.

N. Mukherjee for his contribution in Indian Science.

References

Agustí, G., Bartual, C., Martínez, V., Muñoz-Lara, F.J., Gaspar, A.B., Muñoz, M.C., Real, J.A.: New J. Chem. **33**, 1262–1267 (2009)

Baker, A.T., Goodwin, H.A.: Aust. J. Chem. **37**, 1157–1162 (1984)

Baker, A.T., Goodwin, H.A., Rae, A.D.: Aust. J. Chem. **37**, 2431–2440 (1984)

Baker, A.T., Goodwin, H.A., Rae, A.D.: Inorg. Chem. **26**, 3513–3519 (1987)

Bhar, K., Guo, W., Gonidec, M., Sharma, A.K.: Dalton Trans. **51**, 9302–9313 (2022)
[PubMed]

Brooker, S.: Chem. Soc. Rev. **44**, 2880–2892 (2015)
[PubMed]

Capes, L., Létard, J.F., Kahn, O.: Chem. Eur. J. **6**, 2246–2255 (2000)
[PubMed]

Chen, M.-Y., Chen, X.-R., Ning, W.-H., Ren, X.-M.: RSC Adv. **4**, 39126–39131 (2014)

Chen, Y.-C., Meng, Y., Ni, Z.-P., Tong, M.-L.: J. Mater. Chem. C **3**, 945–949 (2015)

Craig, D.C., Goodwin, H., Onggo, D.: Aust. J. Chem. **41**, 1157–1169 (1988)

Dugay, J., Giménez Marqués, M., Kozlova, T., Zandbergen, H.W., Coronado, E., van der Zant, H.: S. J. Adv. Mater. **27**, 1288–1293 (2015)

Figg, D., Felner, I., Herber, R.: Inorg. Chem. **30**, 2535–2540 (1991)

Fleisch, J., Gütlich, P., Hasselbach, K.: Inorg. Chem. **16**, 1979–1984 (1977)

Gamez, P., Costa, J.S., Quesada, M., Aromí, G.: Dalton Trans. 7845–7853 (2009)

Gómez, V., Sáenz de Pipaón, C., Maldonado-Illescas, P., Waerenborgh, J.-C., Martin, E., Benet-Buchholz, J., Galán-Mascarós, J.-R.: J. Am. Chem. Soc. **137**, 11924−11927 (2015)

Guionneau, P., Létard, J.-F., Yufit, D.S., Chasseau, D., Bravic, G., Goeta, A.E., Howard, J.A., Kahn, O.: J. Mater. Chem. **9**, 985–994 (1999)

Guo, Y., Yang, X.-L., Wei, R.-J., Zheng, L.-S., Tao, J.: Inorg. Chem. **54**, 7670–7672 (2015)
[PubMed]

Gütlich, P., Goodwin, H.A.: Top. Curr. Chem. **233**, 1–47 (2004b)

Gütlich, P., Garcia, Y., Goodwin, H.A.: Chem. Soc. Rev. **29**, 419–427 (2000)

Gütlich, P., Gaspar, A.B., Garcia, Y.: Beilstein J. Org. Chem. **9**, 342–391 (2013)
[PubMed][PubMedCentral]

Gütlich, P.: Eur. J. Inorg. Chem. 581–591 (2013)

Gütlich, P., Goodwin, H.A.: Spin Crossover in Transition Metal Compounds I, p. 1. Springer (2004)

Gütlich, P., Garcia, Y., Spiering, H.: Magnetism: Molecules to Materials IV: Spin Transition Phenomenon, pp. 271–344. Wiley (2002)

Halcrow, M.A.: Coord. Chem. Rev. **253**, 2493–2514 (2009)

Halcrow, M.A.: Chem. Soc. Rev. **40**, 4119–4142 (2011)
[PubMed]

Halcrow, M.A.: Spin-Crossover Materials: Properties and Applications. John Wiley & Sons (2013)

Harding, D.J., Harding, P., Phonsri, W.: Coord. Chem. Rev. **313**, 38–61 (2016)

Hayami, S., Komatsu, Y., Shimizu, T., Kamihata, H., Lee, Y.H.: Coord. Chem. Rev. **255**, 1981–1990 (2011a)

Hayami, S., Kato, K., Komatsu, Y., Fuyuhiro, A., Ohba, M.: Dalton Trans. **40**, 2167–2169 (2011b)
[PubMed]

Hayami, S., Komastu, Y., Shimizu, T., Kamihata, H., Lee, Y.: H Coord. Chem. Rev. Chem. **255**, 1981–1990 (2011c)

Hayami, S., Nakaya, M., Ohmagari, H., Alao, A.S., Nakamura, M., Ohtani, R., Yamaguchi, R., Kuroda-Sowa, T., Clegg, J.K.: Dalton Trans. **44**, 9345–9348 (2015)
[PubMed]

Hayami, S., Kojima, Y., Inoue, K.: Mol. Cryst. Liquid Cryst. **509**, 309/[1051] (2009)

Hibbs, W., Van Koningsbruggen, P.J., Arif, A.M., Shum, W.W., Miller, J.S.: Inorg. Chem. **42**, 5645–5653 (2003)

[PubMed]

Jureschi, C.M., Rusu, I., Codjovi, E., Linares, J., Garcia, Y., Rotaru, A.: Phys. B **449**, 47−51 (2014)

Kahn, O., Martinez, C.J.: Science **279**, 44–48 (1998)

Kilner, C.A., Halcrow, M.A.: Dalton Trans. **39**, 9008–9012 (2010)
[PubMed]

Komatsu, Y., Kato, K., Yamamoto, Y., Kamihata, H., Lee, Y.H., Fuyuhiro, A., Kawata, S., Hayami, S.: Eur. J. Inorg. Chem. 2769–2775 (2012)

König, E., Madeja, K.: Chem. Commun. (Lond.) **61** (1966)

König, E., Ritter, G.: Solid State Commun. **18**, 279–282 (1976)

Krober, J., Codjovi, E., Kahn, O., Groliere, F., Jay, C.: J. Am. Chem. Soc. **115**, 9810–9811 (1993)

Lapresta-Fernández, L., Cuéllar, M.P., Herrera, J.M. et al.: J. Mater. Chem. C **2**, 7292–7303 (2014)

Lee, Y.H., Harrowfield, J.M., Shin, J.W., Won, M.S., Rukmini, E., Hayami, S., Min, K.S., Kim, Y.: Int. J. Mol. Sci. **14**, 20729–20743 (2013a)
[PubMed][PubMedCentral]

Lee, Y.H., Won, M.S., Harrowfield, J.M., Kawata, S., Hayami, S., Kim, Y.: Dalton Trans. **42**, 11507–11521 (2013b)
[PubMed]

Létard, J.-F., Guionneau, P., Codjovi, E., Lavastre, O., Bravic, G., Chasseau, D., Kahn, O.: J. Am. Chem. Soc. **119**, 10861–10862 (1997)

Létard, J.-F.: J. Mater. Chem. **16**, 2550–2559 (2006)

Létard, J.-F., Guionneau, P., Goux-Capes, L.: Spin Crossover in Transition Metal Compounds III, p. 221. Springer (2004)

Madeja, K., König, E.J.: Inorg. Nucl. Chem. **25**(4), 377–385 (1963)

Masaki, M., Hikaru, I., Hiroyuki, T.: Chem. Lett. **37**, 374–375 (2008)

Miller, R.G., Brooker, S.: Inorg. Chem. **54**, 5398–5409 (2015)
[PubMed]

Molnár, G., Rat, S., Salmon, L., Nicolazzi, W., Terki, F., Bousseksou, A.J.: Mater. Chem. C **2**(8), 1360–1366 (2014)

Molnár, G., Rat, S., Salmon, L., Nicolazzi, W., Bousseksou, A.: Adv. Mater. **30**, 17003862 (2018)

Nihei, M., Sigha, T., Maeda, Y., Oshio, H.: Coord. Chem. Rev. **251**, 2606–2621 (2007)

Onggo, D., Goodwin, H.: Aust. J. Chem. **44**, 1539–1551 (1991)

Onggo, D., Hook, J.M., Rae, A.D., Goodwin, H.A.: Inorg. Chim. Acta **173**, 19–30 (1990)

Onggo, D., Scudder, M.L., Craig, D.C., Goodwin, H.A.: Aust. J. Chem. **53**, 153–158 (2000)

Oso, Y., Ishida, T.: Chem. Lett. **38**, 604–605 (2009)

Oso, Y., Kanatsuki, D., Saito, S., Nogami, T., Ishida, T.: Chem. Lett. **37**, 760–761 (2008)

Palion-Gazda, J., Machura, B., Kruszynski, R., Grancha, T., Moliner, N.S., Lloret, F., Julve, M.: Inorg. Chem. **56**, 6281–6296 (2017)

Šalitroš, I., Madhu, N.T., Boča, R., et al.: Monatsh. Chem. **140**, 695–733 (2009)

Sams, J.R., Tsin, T.B.: Inorg. Chem. **15**, 1544–1550 (1976)

Shatruk, M., Phan, H., Chrisostomo, B.A., Suleimenova, A.: Coord. Chem. Rev. **289–290**, 62–73 (2015)

Stoufer, R.C., Smith, D.W., Clevenger, E.A., Norris, T.E.: Inorg. Chem. **5**, 1167–1171 (1966)

Stupik, P., Zhang, J., Kwiecien, M., Reiff, W., Haasnoot, J., Hage, R., Reedijk, J.: Hyperfine Interact. **28**, 725–727 (1986)

Stupik, P., Reiff, W., Hage, R., Jacobs, J., Haasnoot, J., Reedijk, J.: Hyperfine Interact. **40**, 343–346 (1988)

Sugiyarto, K.H., Goodwin, H.A.: Aust. J. Chem. **40**, 775–783 (1987)

Sugiyarto, K.H., Craig, D.C., Rae, A.D., Goodwin, H.A.: Aust. J. Chem. **48**, 35–54 (1995)

Tailleur, E., Marchivie, M., Daro, N., Chastanet, G., Guionneau, P.: Chem. Commun. **53**, 4763–4766 (2017)

Takami, K., Ohtani, R., Nakamura, M., Kurogi, T., Sugimoto, M., Lindoy, L.F., Hayami, S.: Dalton Trans. **44**, 18354–18359 (2015)
[PubMed]

Tezgerevska, T., Alley, K.G., Boskovic, C.: Coord. Chem. Rev. **268**, 23–40 (2014)

Zhong, Z.J., Tao, J.-Q., Yu, Z., Dun, C.-Y., Liu, Y.-J., You, X.-Z.: J. Chem. Soc. Dalton Trans. 327–328 (1998)

© The Author(s), under exclusive license to Springer Nature Singapore Pte Ltd. 2024
R. S. Ningthoujam, A. K. Tyagi (eds.), *Handbook of Materials Science, Volume 2*, Indian Institute of Metals Series
https://doi.org/10.1007/978-981-97-4646-0_13

13. Magnetism in Bulk and Thin Film Metallic Glass Systems

Debarati Bhattacharya[1, 2] ✉
(1) Solid State Physics Division, Bhabha Atomic Research Centre, Mumbai, 400085, India
(2) Homi Bhabha National Institute, Anushaktinagar, Mumbai, 400094, India

✉ **Debarati Bhattacharya**
Email: debarati@barc.gov.in

Keywords Thin film metallic glass – Ferromagnetic thin films and multilayers – Magnetic metallic glassy alloys – Metallic glassy alloy films

13.1 Introduction

Multifunctional materials are all the rage now and will certainly continue to be so in the future with extensive research being pursued to meet growing demands in widespread fields. The emphasis on development of new age materials has caused concomitant research to foray into distant domains. Desirable characteristics of an applicable material which are sought include sustainability, ability to withstand harsh environmental conditions, and various functional capabilities which aim to bring about

improvement in quality of life. Metallic glasses, a form of amorphous alloys, come close to being an ideal choice in this regard given the synergistic combination of their structural and functional (i.e., optical, electrical, magnetic, thermal) properties (Glasses 2020). They can be prepared over a wide composition range which allows significant scope of tailoring their properties for various applications. By virtue of their amorphous nature governed by a characteristic glass-forming ability (GFA), these materials exhibit high wear and corrosion resistance and good mechanical strength. Magnetic metallic glasses, which incorporate ferromagnetic elements (Fe, Co, or Ni) in their composition, in addition to having the useful properties associated with metallic glasses also possess high saturation magnetization and low coercivity. These soft magnetic properties being available at high temperatures and high frequencies make them very useful in power electronics and high-frequency applications (Jiang et al. 2023). They are also potentially useful in energy transfer devices owing to their exceptional soft magnetism. The non-magnetic component of these metallic glass systems responsible for maintaining the GFA of the material can be chosen from a range of alloying elements such as metallic (Cr, Zr, Mn, Nb, Al, Ga, Mo, and Ta), rare-earth (Y, Gd, Er, and Tm), and also metalloid (B, C, Si, and P) ones. The use of a magnetic metallic glass in nano-patterning is limited due to its inherent size and poor deformability although current research trends seek to improve upon this aspect (Wang et al. 2020; Nano-imprinting Potential of Magnetic FeCo-based Metallic Glass 2019). In thin film form such an amorphous alloy is termed as Thin Film Metallic Glass (TFMG), characterized by properties which are distinctly superior to their bulk counterparts. TFMGs are known to possess elevated mechanical strength and structural stability (Yu et al. 2016), high elastic strain limit (Jiang et al. 2012), better machinability (Abboud et al. 2019; Liang

et al. 2022), remarkably high corrosion and wear resistance (Chu et al. 2020). These features form the basis of their wide-ranging applicability in diverse fields (PakmanYiu et al. 2020) as in biomedical instrumentation (Thanka Rajan and Arockiarajan 2021) and wastewater treatment (Hubert et al. 2021). TFMGs with a ferromagnetic component combine the aforementioned aspects with excellent soft magnetic properties of high saturation magnetization and low coercivity, which leads to desirably low hysteretic and eddy current losses. This enables them to be model candidates for the development of materials for spintronics and miniaturized device applications using ferromagnetic shape-memory alloys and in micro- and nano-electro-mechanical systems (Phan et al. 2011).

In this chapter, the phrase “metallic glass systems” used is meant to include both bulk metallic glass and TFMG.

The amorphous nature of metallic glass systems provides them with unique properties like elevated mechanical strength and good corrosion resistance. This is because in these materials the absence of long-range order precludes the existence of grain boundaries, along which any strain can propagate. Notwithstanding their disordered nature, metallic glass systems have very uniform and defect-free structures. Their structural homogeneity is dictated by a characteristic chemical short-range order (CSRO) originating from the chemistry of intermolecular interactions within a composition, which responds to external stimuli like temperature (Bhattacharya et al. 2022a). The stability of the amorphous structure intrinsically depends on its compositional conformity (Ghaemi et al. 2022). The coordination of atomic pairs defining CSRO forms local structural units, which comprise the metallic glass system. CSRO can lower the driving force for nucleation of crystalline phases thus enhancing the GFA of the material, but it can also favor the tendency to stabilize the system toward crystallization with the

formation of intermetallic compounds corresponding to the appropriate stoichiometry of components (Debarati Bhattacharya et al. 2019). GFA of a material thus forms the cornerstone in creation and development of a metallic glass system. Current interest in metallic glasses is apparent from recent literature reports on the use of artificial intelligence to predict new compositions in view of GFA of the system (Dasgupta et al. 2019). GFA can be correlated with various structural properties of a metallic glass system like its mechanical strength (Li et al. 2023) and elasticity (Apreutesei et al. 2017). Most interestingly it can aid in the design and development of new alloys by being linked with tuning of magnetic properties of a ferromagnetic metallic glass system, as evinced by very recent reports (Jiang et al. 2022; Li et al. 2022; Nam 2023). Magnetic properties can thus be correlated with disorder in the atomic arrangement in metallic glass systems. This aspect becomes all the more important in the nanoscale region wherein compositional variations can govern magnetic ordering temperature in metallic glasses (Thórarinsdóttir et al. 2022).

Since the origin of magnetism in a simple ferromagnetic film lies in the exchange interactions between spins of unpaired electrons, it is obvious that an increase in ferromagnetic content can be correlated with the exchange coupling among magnetic components growing stronger. However, in a ferromagnetic metallic glass system, a rise of ferromagnetic content would indicate a concomitant decrease in the non-ferromagnetic or glass-forming components of the system. These elements are usually relatively larger in size and with lesser mobility, which makes them play a vital role in the development of GFA by delaying crystallization rates. A decrease in these components negatively impacts the stability of the amorphous phase by reducing the GFA. On the other hand, an increase in GFA would mean redistribution of the magnetic component among the excess non-magnetic

components and consequent dilution of magnetic signature of the metallic glass. Hence, optimization of GFA can lead to improvement in magnetic properties of the metallic glass system. Modulation in the metallic glass constituents must be balanced by the role of glass-forming elements in order to maintain soft magnetic properties while not compromising the inherent GFA of the material (Krimer et al. 2020). This is the inherent challenge in making metallic glass systems viable for various applications as in magnetic recording devices, inductors, and sensors. It also underlines the importance of parameters used in their preparation methods. The design of a ferromagnetic metallic glass film with specific composition can be made while balancing saturation magnetization and GFA. This is aided by the fact that TFMGs, like their bulk analogues, can accommodate a high degree of chemical substitution (Obeydavi et al. 2019). The dependence of magnetic properties of TFMGs on their thickness has also been studied (Rauf et al. 2019; Prasanna Kumari et al. 2014). Thickness defines magnetism as it is related to coercivity of the material. Low coercivity, which is a hallmark of ferromagnetic TFMGs, is a consequence of higher packing density (CSRO) defined by the structural homogeneity of the glassy material.

The introduction of nanostructures within metallic glasses has been seen to produce dramatic changes in their structural, mechanical, and magnetic properties, favoring their use in advanced functional materials (Fu and Ma 2023; Li et al. 2022). One of the generally used methods for this purpose is annealing; more details about the effects created by annealing of metallic glass systems are given in one of the following sections in this chapter. Annealing of magnetic metallic glasses causes structural relaxation which can improve mechanical properties and enhance magnetic softness of the material (Pang et al. 2019). Thin film metallic glasses with a magnetic component

undergoing devitrification (gradual transformation from amorphous-to-crystalline state) can create partially crystallized or completely crystallized materials with desirably tuned magnetic properties (Pookat et al. 2013). The generation of such properties motivates the need to understand the underlying mechanism of thermal evolution of these systems (Bhattacharya et al. 2022a). This chapter gives a brief overview of classifications, preparation methods, and annealing effects of (magnetic) TFMGs.

13.2 Classification and Properties of Magnetic TFMGs

The base metal defines the main characteristics of the ferromagnetic TFMG which can be Fe-, Co- or Ni-based. During the design and synthesis processes of any alloy, the selection of components is decided such that each one contributes in a way to enhance certain properties of the alloy. Along similar lines, in case of magnetic TFMGs, the magnetic elements impart specific properties to the alloy. The various properties and applications associated with magnetic metallic glass systems are summarized in Table 13.1.

Table 13.1 Properties and applications of magnetic TFMGs

Base metal in MG/TFMG	Properties	Applications
Fe	Magnetic softness, good corrosion resistance, high mechanical strength and durability, high electrical resistivity, and thermal stability. Fe is abundantly available	• Materials for transformer cores, magnetic switches, and transducers • Improvement in cutting tools though hard surface layers • Spintronic devices

Base metal in MG/TFMG	Properties	Applications
Co	High magnetic induction and permeability, good corrosion resistance, high resistance to mechanical deformation, and low hysteresis loss. Co is expensive	• Materials for magnetic recording and amplifiers • Magnetic shielding • Magneto-optoelectronics • Corrosion protection
Ni	Magnetic softness, good corrosion resistance, high ductility/hardness, and hydrogen permeability. Ni is cost-effective	• Hydrogen storage/separation • Shape memory alloys • Precision motors, gears • Nuclear fuel reprocessing

Fe-based metallic glass systems with outstanding soft magnetic properties (Suryanarayana and Inoue 2013; Inoue et al. 2018; Ansar Masood et al. 2014) can be gainfully used in energy transfer and spintronic device applications. The exploitation of the corresponding TFMGs as efficient core materials for transformers and in inductors for magnetic switches and transducers is a profitable choice. This is because among the ferromagnetic elements Fe is a low cost option and is readily available as well. The high mechanical strength, sustainability, and durability offered by Fe-based TFMGs promote their use as hard protective coatings for surgical cutting tools (Chu et al. 2019) and their superior wear resistance property is employed in biomaterial applications (Ibrahim et al. 2020). In addition to their magnetic behavior and applications (Rauf et al. 2019; Ansar Masood et al. 2014), Fe-based TFMGs also exhibit high electrical resistivity, favorable mechanical properties (Tayyebi et al. 2022), good corrosion resistance (Obeydavi et al. 2020), and biocompatibility (Bih-Show et al. 2019).

Co-based metallic glasses are characterized by high permeability along with low hysteresis loss, which earns

them vital integration into magnetic recording and magnetic shielding applications (Taghvaei and Eckert 2020). The magnetic properties of these useful materials are well documented (Jaworski et al. 2011). In keeping with the trend of developing advanced functional materials inherent drawbacks of metallic glasses are now being challenged to provide a breakthrough (Wang et al. 2020). Co-based TFMGs are also useful in magneto-optoelectronic applications (Shauyenova et al. 2021). However, Co being the most expensive of the ferromagnetic elements, this limits the widespread usage of these films.

TFMGs incorporating Ni possess remarkably good strength (Apreutesei et al. 2017), high impact resistance (Dong et al. 2021), and display resilience to deformation (Jia et al. 2014) which can be related to film thickness (Jiang et al. 2013). Ni-TFMGs are also quite cost-effective and portray diverse properties (PakmanYiu et al. 2020). The corrosion resistance property is common to the magnetic TFMGs and originates from their inherent passivity. It has been studied in Ni-based metallic glass systems (Wu et al. 2014) and also effectively utilized in nuclear fuel reprocessing applications (Poddar et al. 2020).

It has been observed that a combination of magnetic elements in TFMGs can give rise to improved properties while practically mitigating the costs involved. One such example is that of Co–Fe alloys (Liang et al. 2022; Pookat et al. 2013). Among their non-magnetic properties, Fe–Co-based TFMG has been demonstrated as a catalyst material for wastewater treatment (Hubert et al. 2021). Fe–Ni-based alloys, being a cheaper option than Co-based alloys, have also been explored (Krimer et al. 2020) for their potential magnetic properties (Chen et al. 2022).

The study of TFMGs is not restricted to alloys; they have also been studied in multilayer and composite forms (Marimuthu et al. 2023; Jhou et al. 2018; Zhou et al. 2019).

The scheme in Fig. 13.1 gives an overall view of various aspects of the magnetic TFMGs.

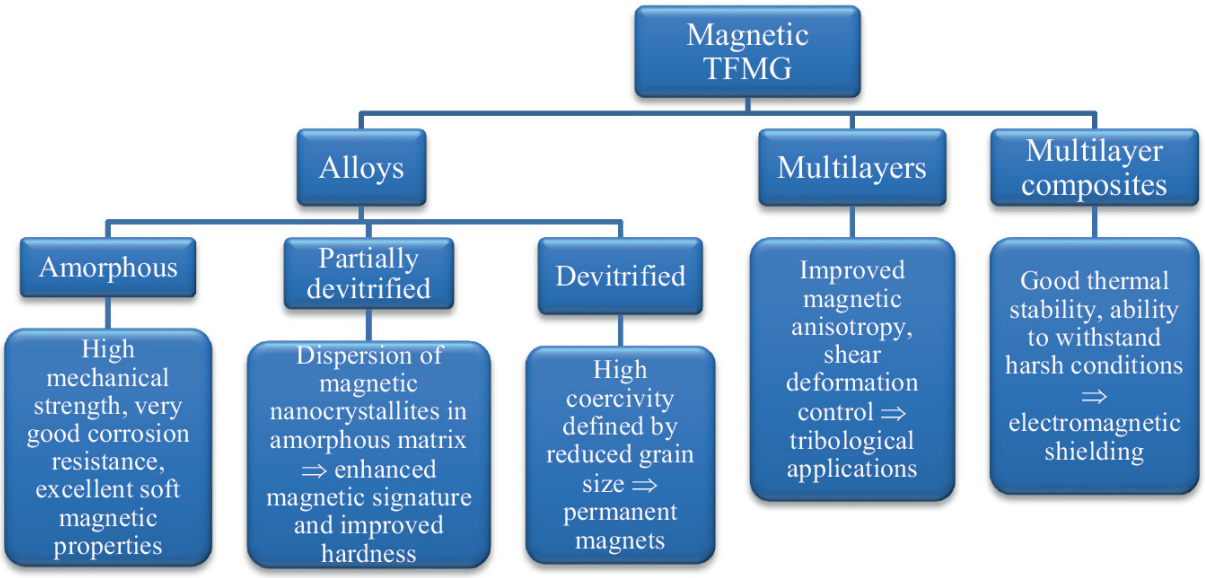

Fig. 13.1 A scheme depicting the various forms of TFMG systems: alloys, multilayer, and composite structures, along with some characteristic properties

Devitrification of amorphous alloys has often been explored to enhance the magnetic properties of the amorphous material. This was found to be inimitably linked to the changes in their nanostructure. Layered structures of metallic glass materials have also been observed to improve soft magnetic properties. A further extension in this regard comprises metallic glass composites with layered structure, incorporating magnetic components (Monson et al. 2019). The strong thermal stability and high corrosion resistance of these materials make them invaluable in scenarios involving harsh environments as in electromagnetic shielding applications (Zhang et al. 2017; Ma et al. 2021).

13.3 Synthesis of TFMG Materials

Careful preparation of a TFMG is important since the parameters of a chosen methodology can strongly influence

its structure and properties (Sharma and Gupta 2005). Unlike the formation of bulk metallic glasses wherein the amorphous state is obtained through rapid quenching of the liquid state, deposition techniques for TFMGs bypass the liquid state but can create all the thermodynamic conditions required to inhibit crystallization. TFMGs have been deposited by thermal evaporation (Pookat et al. 2013), combinatorial arc-plasma deposition (Sakurai et al. 2007), and pulsed laser deposition (Thanka Rajan et al. 2021). However, the most popular deposition technique for TFMGs by far remains sputtering, which affords the appropriate conditions required to form stable amorphous structures. Sputtering for this purpose has been employed using various modes such as ion beam sputtering (Thanka Rajan et al. 2017), magnetron sputtering through co-sputtering of individual targets (Debarati Bhattacharya et al. 2019), or by using an alloy target (Obeydavi et al. 2020) and high-power impulse magnetron sputtering (PakmanYiu et al. 2020). Tuning of sputtering process parameters like sputter power, substrate temperature, target-substrate distance, gas flow, etc. can be used for structure–property studies (Liu et al. 2019). Due to its versatile approach, in some cases, sputtering can also facilitate TFMGs being deposited in crystalline form (Ketov et al. 2017), which can provide interesting details with respect to the thermal stability of the system under study (Debarati Bhattacharya et al. 2015). Several investigations regarding the composition and structure of the alloy sputter target used for deposition of TFMGs have also been reported. The formation of a composite target for TFMG deposition through sputtering is schematically shown in Fig. 13.2 (Yoon et al. 2020). In this work, it was found that a crystalline target gave better results than an amorphous one with respect to TFMG formation. On the other hand, it has also been reported that the composition of high-entropy

TFMGs was basically unaffected by the amorphous or crystalline nature of the target used (Liu et al. 2012).

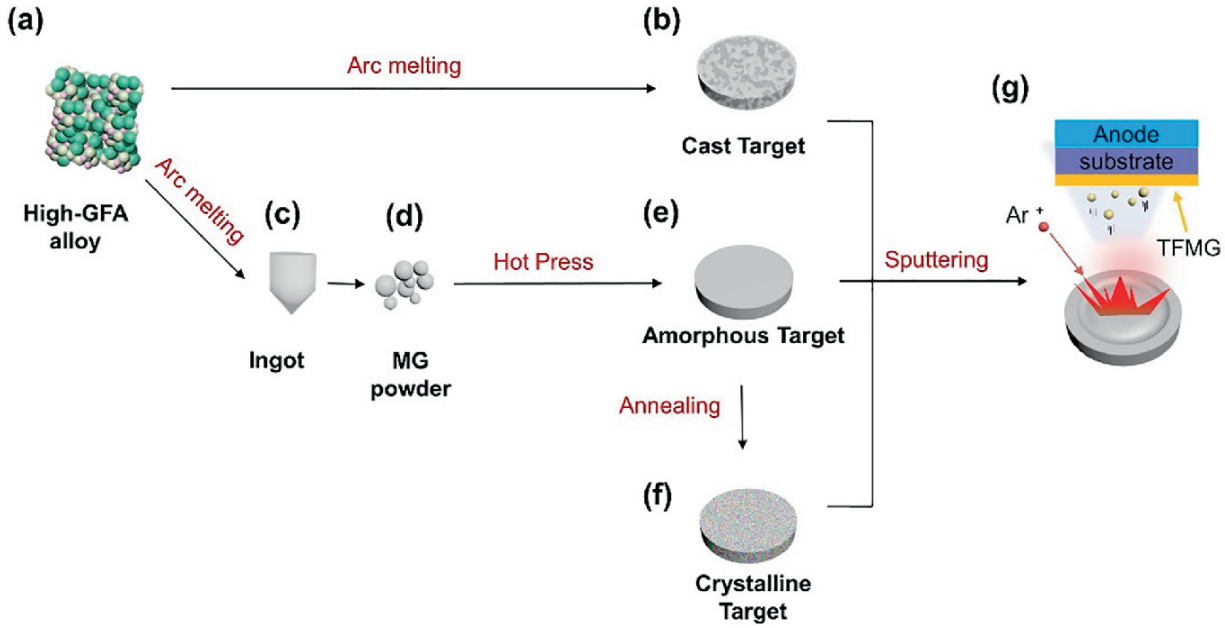

Fig. 13.2 Schematic of target manufacture. **a** Preparation of alloys with high GFA. **b** Manufacture of cast targets by arc melting. **c** Manufacture of ingots by arc melting. **d** Metallic glass powder preparation via an atomizer. **e** Creation of amorphous targets using spark plasma sintering. **f** Preparation of crystalline target through annealing of the amorphous target. **g** TFMG deposition using the fabricated sputter target. Reproduced in accordance with the Creative Commons Attribution license (Open Access) from MDPI Publishers (Yoon et al. 2020)

13.4 Characterization of Ferromagnetic Metallic Glass Systems: Effects of Annealing

Annealing of ferromagnetic metallic glass systems can induce interesting changes in their structural, electrical, and magnetic properties. The temperature range of annealing which is most effective in creating such novel structures lies between the crystallization temperature and glass-transition temperature of the material. This is called the super-cooled liquid region which is targeted to cause

variation in metallic glass properties since the material exhibits lower viscosity in this regime, making it viable to effect changes. Figure 13.3 depicts the increasing trends of electrical resistivity and hardness obtained on annealing a Fe-based TFMG within such a temperature range (Chu et al. 2006).

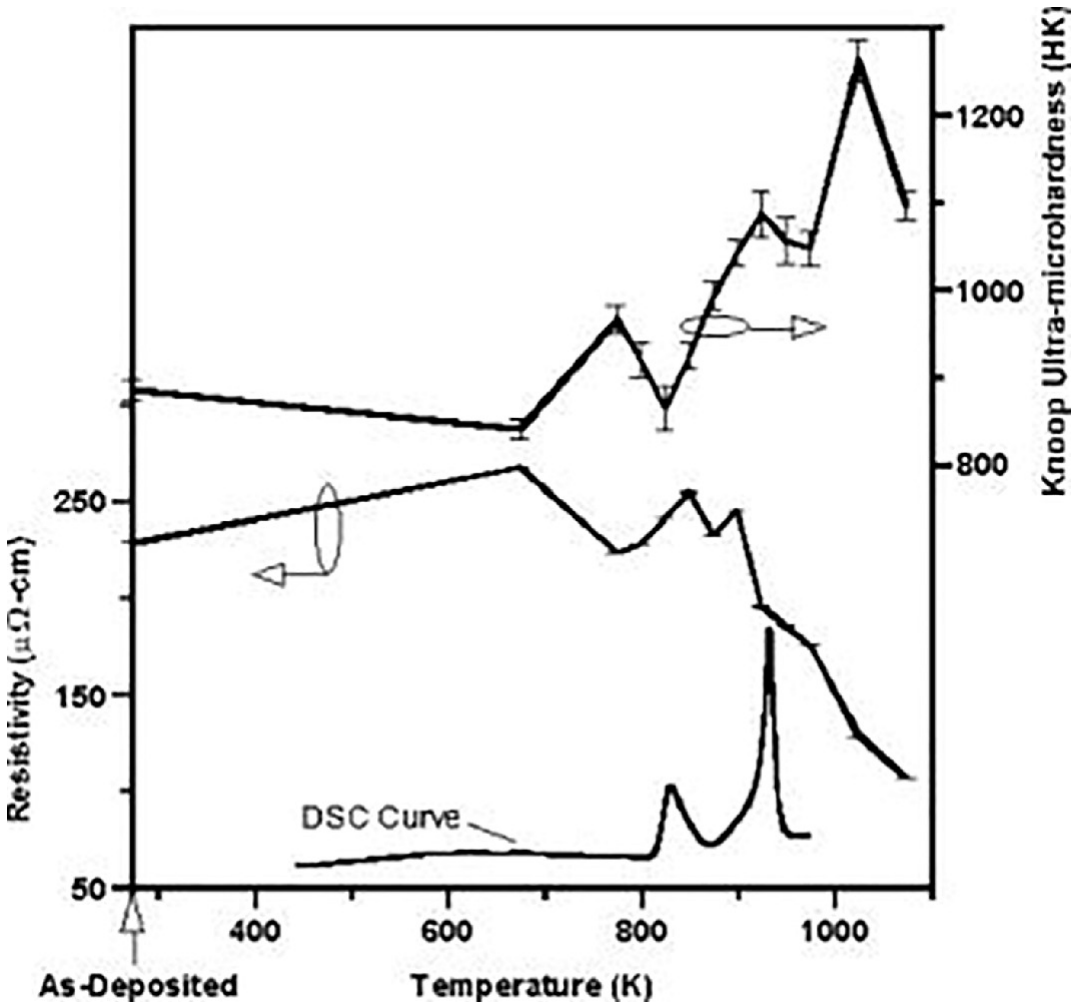

Fig. 13.3 Variations of electrical resistivity and hardness of Fe-based TFMG with annealing temperature. DSC scan shows glass-transition and super-cooled liquid region. Reproduced from Chu et al. (2006), with the permission of AIP Publishing

Metallic glass systems respond to thermal energy provided by annealing to undergo devitrification and can thereby produce partially crystallized or fully crystallized forms. By virtue of their amorphicity, metallic glass systems

are not associated with grain boundaries and hence do not possess a fixed anisotropy direction as seen in crystals. This implies that they can be magnetized in any direction. However, annealing can improve their magnetic properties sufficiently to be used in high-frequency applications. Small crystallites can be introduced in the material which can cause refinement in domain size, development of an anisotropy direction, and partial pinning of domain walls, thus reducing excess eddy current loss. Magnetic metallic glasses can act as precursors for fully crystallized permanent magnets. Annealing of magnetic metallic glass systems also produces popular nanocrystalline soft magnetic alloys, which have been widely commercialized under various brands, e.g., FINEMET (of the type Fe–Si–B–Nb–Cu) and studied in detail for their useful properties (Gheiratmand and Madaah Hosseini 2016). The soft magnetic properties of these functional materials have also been studied in TFMG form (Sharma and Gupta 2005). Partially crystallized forms indicate that both amorphous and crystalline structures co-exist in the material rendering the composite unique. Nanostructured composites of metallic glass systems are formed when nanocrystalline particles are embedded in an amorphous glassy matrix. The resultant material beneficially combines magnetic properties from both constituents, such as soft magnetic properties like low coercivity originating from the amorphous part and a particular easy direction of magnetization contributed by the crystalline part. The grain size and distribution of the dispersed nanocrystals directly contribute to the special properties associated with these structures. These amorphous-crystalline composite structures invariably display homogeneous grain distribution, compact structural arrangement, and consequently higher hardness values. In tribological applications it is known that hardness is directly proportional to wear resistance. It has been seen in case of

metallic glasses that this paradigm appears to be reversed with respect to the effect of crystallinity (Yoon et al. 2007), which leads to an increase in hardness but is accompanied by a decrease in wear resistance. For more practical applicability of the metallic glass structure, the wear resistance should be improved by controlling the plastic deformation. Metallic glass multilayers offer a model solution in this regard (Zhou et al. 2019) wherein shear deformation is suppressed due to the layered structure incorporating high-density layers. This results in improved wear resistance. TFMGs display higher hardness after annealing as seen in several devitrified binary Ni-based films (Huang and Ramirez 2009; Bhattacharya et al. 2018) and in some cases can also display a shape-memory effect after crystallization (Sakurai et al. 2010). Structural relaxation through devitrification in ferromagnetic TFMGs is seen to strongly influence their magnetic properties (Debarati Bhattacharya et al. 2019; Pookat et al. 2013). These properties are invariably linked to the arrangement of magnetic nanostructures in the composite material.

Crystallization of metallic glass systems can lead to the formation of desirably fine-grained nanostructured materials. Investigation of devitrification in TFMGs can provide important insight into the growth process of the crystalline state via local atomic structure analysis. Further it can offer comprehensive understanding of thermal stability of the glassy material with regard to film thickness, which can be used to engender potential applications. The stages of devitrification in a magnetron sputter deposited Ni–Zr TFMG annealed from room temperature to 800 °C were examined with respect to the changes of its atomic scale structure through detailed structural characterization studies (Bhattacharya et al. 2022a). The study demonstrated that devitrification of the glassy alloy film proceeded through a polymorphous transformation to a final nanocrystalline state, wherein its

phase was identified as Ni7Zr2. Figure 13.4 compares grazing incidence X-ray diffraction data and correspondingly derived structure factors, for the as-deposited and final annealed states.

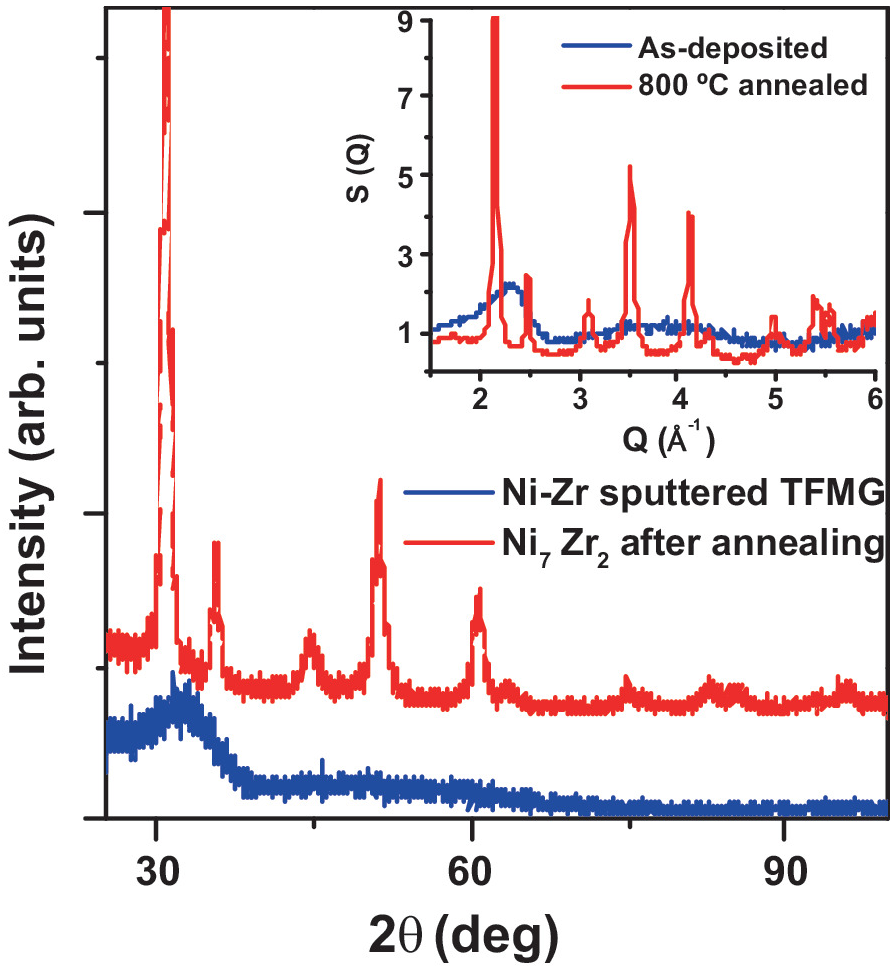

Fig. 13.4 Grazing incidence X-ray diffraction patterns of amorphous Ni–Zr TFMG sputter deposited at room temperature (blue line) and after annealing at 800 °C to form Ni_7Zr_2 nanocrystalline alloy (red line). Inset compares corresponding structure factors computed for these films. Adapted and redrawn from Elsevier (Bhattacharya et al. 2022a)

The process was accompanied by an increase in densification much higher than that achieved in bulk alloys, thereby affecting an increase in the CSRO of the system with a reduction in residual entropy. The bonding of unlike pairs of atoms (Ni–Zr) took precedence over that of like atoms (Ni–Ni, Zr–Zr) while the films developed structural

order in the amorphous-to-crystalline transition. The average crystallite size derived for the nanocrystalline alloy film was reported in another study (Debarati Bhattacharya et al. 2019) to be of the order of 9.7 nm. The increase in magnetic signature after devitrification was suitably correlated with the rise in Ni coordination number around Ni atoms. The soft magnetic properties of the annealed film were seen to be much better than those of the as-deposited Ni–Zr TFMG as a result of the disorder-to-order transformation.

The influence of annealing-induced structural rearrangement of atoms on magnetic ordering has been recently reported for Fe-based bulk metallic glass (Zhao et al. 2023). The magnetic signature evolves through the exchange coupling interactions between magnetic nanocrystallites through the amorphous matrix they are present in. The corresponding grain sizes obtained after annealing must be below the exchange correlation length in order to maintain the magnetic properties (e.g., coercivity) of the system. This condition is called the exchange-softening effect. A higher percentage of the magnetic components vis-à-vis the non-magnetic entities would therefore ensure a higher saturation magnetization. However, the latter play a pivotal role in the retention of GFA of the material and thereby ensuring its reliable mechanical properties. On the other hand, the annealing-induced growth of regions in the metallic glass system enriched with non-magnetic components could adversely affect the interaction between the magnetic nanostructures thus diminishing magnetic softness (Zhai et al. 2018). Hence, a balance must be maintained in these composites so that the functional properties of magnetic softness and mechanical strength can co-exist at optimal levels. Soft magnetic properties of these materials in conjunction with reliably high strength and high elasticity are desirable for various ferromagnetic sensor applications. In order to

overcome annealing-induced embrittlement in metallic glasses while retaining soft magnetic properties, compositional changes can be made to enhance their GFA or composite structures are sought to improve their plasticity (Evaluation of the Effect of Minor Additions 2021; Zheng et al. 2020). The relaxation of internal stresses in annealed metallic glass systems ultimately leads to their magnetic softening. Composite structures can combat the inherent plasticity failure in amorphous systems (Adit Sharma and Vladislav Zadorozhnyy 2021). Annealing of multilayers of metallic glass systems which are composed of the early-late transition metal binary couples (e.g., Ni–Zr system) also gives rise to interesting properties. Herein the asymmetric diffusion kinetics of the strongly miscible components of the precursor multilayer can be exploited to engender magnetic properties of the resultant composite material (Bhattacharya et al. 2022b). Further, the interdiffusional strain built up due to unbalanced diffusional flow during rapid intermixing of the multilayer components is related to the mechanical strength of these materials. The utility of TFMGs in high-strength structural applications is affected by shear band instability restricting plastic flow and causatively limiting their ductility. This can be overcome by alternating amorphous and crystalline layers in a multilayer structure applicable for potential engineering applications. Figure 13.5 compares the magnetic measurements made on as-deposited and 400 °C annealed crystalline-Ni/amorphous-Zr multilayer. It was observed that the effect of annealing on the metallic glass multilayer was to enhance the value of saturation magnetization while lowering both coercivity and magnetic anisotropy. Furthermore, the magnetic correlations arising from the interaction of nanocrystalline particles followed a single-domain particle model. The improvement in the soft magnetic properties could be attributed to the asymmetric diffusion occurring across the two interfaces consisting of

crystalline-on-amorphous layers and amorphous-on-crystalline layers. The thermally induced interfacial behavior in such magnetic/non-magnetic multilayers can tailor the formation of novel materials with technologically appropriate magnetic properties.

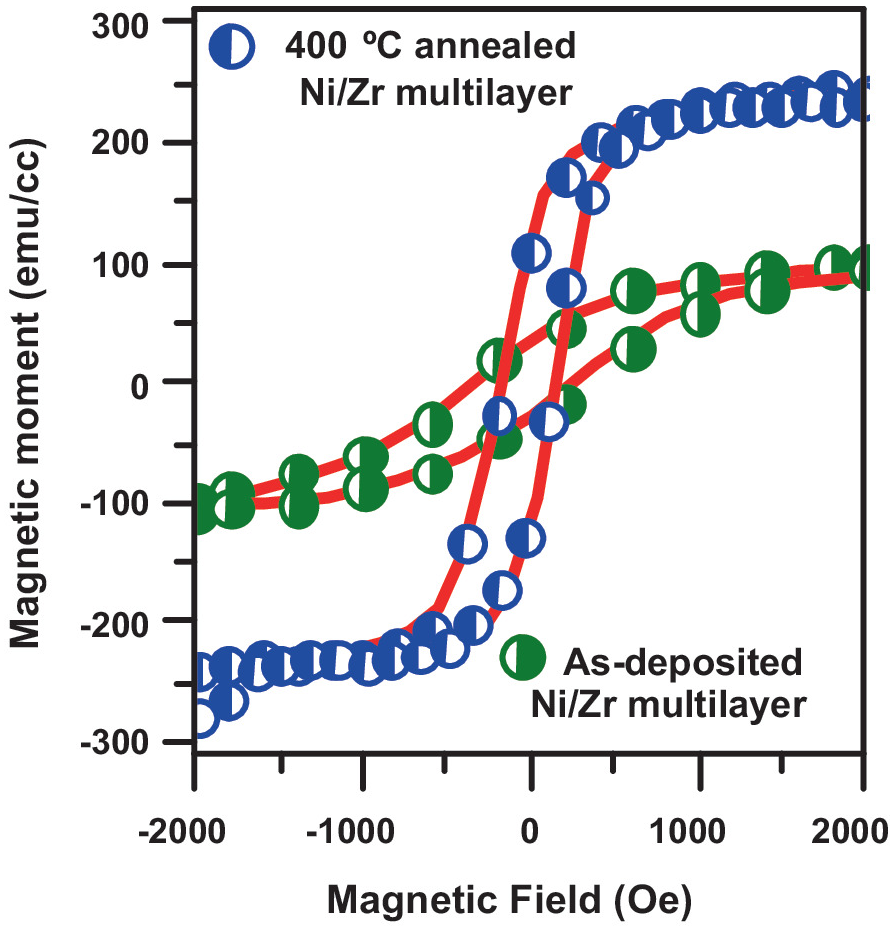

Fig. 13.5 Comparison of SQUID measurements on as-deposited and 400 °C annealed Ni/Zr multilayers. Langevin fits to both sets of data are shown as red lines. Adapted and redrawn from Elsevier (Bhattacharya et al. 2022b)

It may be mentioned here in passing that although it is known that annealing directly affects the magnetic anisotropy, several reports have also demonstrated that ion beam irradiation can also be used to alter the magnetic anisotropy of metallic glass systems (Marcel Miglierini and Mariusz Hasiak 2015; Dubey et al. 2007).

The rate of annealing used to transform metallic glass systems is a critical aspect which can ensure that grain

refinement be realized with sizes relating to magnetic softening in the material. This is because magnetic properties of the annealed system show a strong dependence on both size and distribution of the nanocrystalline entities. In this context, rapid annealing offers advantages over conventional annealing since it is desirable to form homogeneous nanostructures (Zhu et al. 2019). This process does not require the addition of extra non-magnetic components normally required to ensure the formation of nanostructures above the glass-transition temperature. Therefore, this eliminates the occurrence of heterogeneous nucleation. The proportion of magnetic components can be raised in absence of extra non-magnetic additives, which results in increase in the saturation magnetization of the nanocomposite formed after annealing (Suzuki et al. 2018). However, it has also been observed in some materials with a specific composition that a very high annealing rate is not recommended, since it leads to redistribution of the magnetic components such that their mutual interaction decreases (Zhai et al. 2018).

An effective method used to promote variations in magnetic anisotropy in metallic glass systems is through magnetic field annealing. In this method of thermal annealing, a strong uniform magnetic field is externally applied during the annealing process. The underlying principle is to symmetrically orient magnetic domains of the ferromagnetic metallic glass under study such that they are aligned along the direction of the applied field. This minimizes the spin–orbit coupling energy and gives rise to directional anisotropy in the system. The advantage of using magnetic field annealing is to provide control over the uniformity of this uniaxial magnetic anisotropy in the material so that its properties can be tuned to suit various applications. The strength of the magnetic field applied during the process is sufficient to achieve the desired magnetized state. There is a pronounced effect on magnetic

anisotropy by this process as compared to annealing without the presence of a magnetic field. Apart from this aspect, magnetic field annealing can also positively influence the soft magnetic properties of the material. It can affect variation in domain structure thereby creating relief of internal stress and reduction of core loss. The factors responsible for the formation of anisotropy are also linked to the thermal stability of the magnetic properties of the material. Magnetic field annealing applied to metallic glass systems has been observed to create nanocrystallites with larger grains than that obtained with zero field annealing (i.e., conventional annealing) (Jiang et al. 2023; Miglierini et al. 2015). The nanocrystalline alloys derived from metallic glass systems undergoing magnetic field annealing also exhibit superior magnetic properties (Miglierini and Matúš 2015).

It is now clear that many metallic glass applications use the advantage of both mechanical and magnetic properties of these materials being at favorable levels. Metallic glass systems have large reserves of elastic energy which can be effectively used in applications like mechanical windings used in high technology springs for watches, or for magnetic cores of electrical equipment like transformers. The potential of plastic deformation of metallic glass systems enables them to undergo thermomechanical processing required to attain the right shapes for these applications. However, ferromagnetic metallic glasses are often prone to thermal embrittlement, associated with reduction in their free volume. In order to overcome this deficiency, mechanical stress annealing has also been applied to metallic glass systems in order to attain desirable magnetic properties while exercising control over the inherent brittleness (Bruno et al. 2023; Kozikowski et al. 2020; Aljerf et al. 2011). In this method, annealing of the material is carried out when a mechanical load imposes a particular shape to the material. Annealing under these

conditions induces structural relaxation (rejuvenation) in the glassy material, which causes it to get locked in the forced shape.

Some of the techniques commonly used to detect magnetic signatures of annealed metallic glass systems include magnetic force microscopy (Pookat et al. 2013; Chu et al. 2006, 2012), analyzing M-H patterns from a vibrating sample magnetometer (Liang et al. 2022; Rauf et al. 2019) and measurements using a SQUID device (Monson et al. 2019; Debarati Bhattacharya et al. 2015; Bhattacharya et al. 2022b). There are also nuclear-based analytical methods applied to probe magnetic metallic glass systems. Polarized neutron reflectivity is one such neutron scattering technique which offers good depth resolution of layered structures (Debarati Bhattacharya et al. 2019, 2015; Bhattacharya et al. 2022b). Another useful technique which examines hyperfine interactions in these materials is Mössbauer spectrometry (Marcel Miglierini and Mariusz Hasiak 2015; Dubey et al. 2007). Investigation into the evolution of crystallization in magnetic metallic glass systems has been seen to provide useful information with regard to the structural rearrangement and magnetic transformations in the material during annealing (Bhattacharya et al. 2022a). More in-depth information regarding the variation of magnetic structures with respect to time has been reported through a combined in situ study of nuclear forward scattering of synchrotron radiation and Mössbauer spectroscopy (Smrčka et al. 2019).

13.5 Conclusions and Future Scope of TFMGs

The expansion of functional capabilities of magnetic TFMGs is seen to be proceeding in the right direction, coloring a bright future for these versatile materials. Their properties

are efficiently being utilized for both magnetic and non-magnetic applications. Some of the advantages pertaining to the use of these resilient TFMGs in various applications stem from their: cost-effectiveness—increasing their manifold practical uses; ability to withstand exposure to harsh environmental conditions—which makes them very useful in magnetic shielding; and excellent soft magnetic properties along with elevated mechanical strength, ductility, and stability—aiding their effective miniaturization apt for nanoscale magnetic device applications. Innovative trends are developing in the versatile applicability of magnetic TFMGs, primarily arising from their wide compositional tunability. However, the pace of progression needs to be expedited in order to meet the growing demands of multifunctional device advancement. High-density magnetic data storage technology being currently much sought after offers a novel platform for the utility of magnetic TFMGs in high-capacity magnetic-based memory devices, especially as in resistive random access memory systems. A further insight into annealing-induced crystallization of TFMGs through model-based approach is highly desired. This can be achieved with the development of more growth models which can predict pathways of diffusion-controlled nanostructures during annealing, thus paving the way for more promising applications of these useful materials.

References

Abboud, M., Motallebzadeh, A., Verma, N., Özerinç, S.: Nanoscratch behavior of metallic glass/crystalline nanolayered composites. J. Miner. Met. Mater. Soc. **71**, 593–601 (2019)

Adit S., Zadorozhnyy, V.: Review of the recent development in metallic glass and its composites. Metals **11**, 1933 (2021)

Aljerf, M., Georgarakis, K., Yavari, A.R.: Shaping of metallic glasses by stress-annealing without thermal embrittlement. Acta Mat **59**, 3817–3824 (2011)

Apreutesei, M., Djemia, P., Belliard, L., Abadias, G., Esnouf, C., Billard, A., Steyer, P.: Structural-elastic relationships of Zr–TL (TL =Cu Co, Ni) thin films metallic glasses. J. Alloy. Compd. **707**, 126–131 (2017)

Bhattacharya, D., Chatterjee, A., Jana, S.: Mechanical properties of amorphous and devitrified Ni–Zr alloy thin films: a cyclic nanoindentation study. AIP Conf. Proc. **1942**, 080033 (2018)

Bhattacharya, D., Nidhi Tiwari, P.S.R., Krishna, D.B.: Evolution of local atomic structure accompanying devitrification of amorphous Ni–Zr alloy thin films. Thin Solid Films **762**, 139544 (2022a)

Bhattacharya, D., Karki, V., Singh, S., Chandrasekhar Rao, T.V.: Thermal stability of interfacial mixed layers in c-Ni/a-Zr multilayer during annealing: structural and magnetic properties. Appl. Surface Sci. **572**, 151300 (2022)

Bih-Show, L., Tzu-Yao, L., Wei-Ting, C., Jyh-Wei, L.: Corrosion property and biocompatibility evaluation of Fe–Zr–Nb thin film metallic glasses. Thin Solid Films **691**, 137615 (2019)

Bruno, N.M., Adoo, N.A., Meakins, E., Keylin, V., Feichter, G.E., Noebe, R.D.: The effect of stress-annealing on the mechanical and magnetic properties of several Fe-based metal-amorphous nano-composite soft magnetic alloys. J. Non-Cryst. Solids **600**, 122037 (2023)

Chen, Z., Kang, S., Zhu, Q., Zhang, K., Hu, J., Jiang, Y.: Effect of Fe/Ni ratio on amorphization, crystallization kinetics, andmagnetic properties of FeNiSiBCuNb alloys. J. Non-Cryst. Solids **595**, 121842 (2022)

Chu, J.P., Lo, C.-T., Fang, Y.-K., Han, B.-S.: On annealing-induced amorphization and anisotropy in a ferromagnetic Fe-based film: a magnetic and property study. Appl. Phys. Lett. **88**, 012510 (2006)

Chu, J.P., Jang, J.S.C., Huang, J.C., Chou, H.S., Yang, Y., Ye, J.C., Wang, Y.C., Lee, J.W., Liu, F.X., Liaw, P.K., Chen, Y.C., Lee, C.M., Li, C.L., Rullyani, C.: Thin film metallic glasses: unique properties and potential applications. Thin Solid Films **520**, 5097–5122 (2012)

Chu, J.P., Diyatmika, W., Tseng, Y.-J., Liu, Y.-K., Liao, W.-C., Chang, S.-H., Chen, M.-J., Lee, J.-W., Jang, J.S.C.: Coating cutting blades with thin-film metallic glass to enhance sharpness. Sci. Rep. **9**, 15558 (2019) [PubMed][PubMedCentral]

Chu, J.P., Lai, B.-Z., PakmanYiu, Y.-L., Chang, C.-W.: Metallic glass coating for improving diamond dicing performance. Sci. Rep. **10**, 12432 (2020) [PubMed][PubMedCentral]

Dasgupta, A., Broderick, S.R., Mack, C., Kota, B.U., Subramanian, R., Setlur, S., Govindaraju, V., Rajan, K.: Probabilistic assessment of glass forming ability rules for metallic glasses aided by automated analysis of phase diagrams. Sci. Rep. **9**, 357 (2019)
[PubMed][PubMedCentral]

Debarati Bhattacharya, T.V., Chandrasekhar Rao, K.G., Bhushan, K.A., Debnath, A., Singh, S., Arya, A., Bhattacharya, S., Basu, S.: Thermal evolution of nanocrystalline co-sputtered Ni–Zr alloy films: Structural, magnetic and MD simulation studies. J. Alloy. Compd. **649**, 746–754 (2015)

Debarati Bhattacharya, S., Rayaprol, K.A., Chandrasekhar Rao, T.V., Krishna, P.S.R., Tokas, R.B., Singh, S., Prajapat, C.L., Arya, A.: Structure-property relations characterizing the devitrification of Ni–Zr glassy alloy thin films. J. Appl. Phys. **125**, 205305 (2019)

Dong, J.L., Song, X., Wang, Z.J., Xiao, K.L., Liu, Y.H., Wilde, G., Wu, X.Q., Jiang, M.Q.: Impact resistance of single-layer metallic glass nanofilms to high-velocity micro-particle penetration. Extreme Mech. Lett. **44**, 101258 (2021)

Dubey, R., Gupta, A., Sharma, P., Darowski, N., Schumacher, G.: Tailoring of magnetic anisotropy in amorphous and nanocrystalline soft magnetic alloys using swift heavy ions. J. Magn. Magn. Mater. **310**, 2491–2493 (2007)

Fu, J., Ma, J.: Nanoengineering of metallic glasses. Adv. Eng. Mater. **25**, 2200659 (2023)

Ghaemi, M., Jafary-Zadeh, M., Khoo, K.H., Gao, H.: Chemical affinity can govern notch-tip brittle-to-ductile transition in metallic glasses. Extreme Mech. Lett. **52**, 101651 (2022)

Gheiratmand, T., Madaah Hosseini, H.R.: Finemet nanocrystalline soft magnetic alloy: Investigation of glass forming ability, crystallization mechanism, production techniques, magnetic softness and the effect of replacing the main constituents by other elements. J. Magn. Magn. Mater. **408**, 177–192 (2016)

Huang, X., Ramirez, A.G.: Structural relaxation and crystallization of NiTi thin film metallic glasses. Appl. Phys. Lett. **95**, 121911 (2009)

Hubert, B., PakmanYiu, C.-C., Chu, J.P.: Fe-based thin film metallic glass as an activator of peroxymonosulfate for azo dye degradation. Surf. Coat. Technol. **412**, 127031 (2021)

Ibrahim, M.Z., Sarhan, A.A.D., Kuo, T.Y., Yusof, F., Hamdi, M., Lee, T.M.: Developing a new laser cladded FeCrMoCB metallic glass layer on nickel-free stainless-steel as a potential superior wear-resistant coating for joint replacement implants. Surf. Coat. Technol. **392**, 125755 (2020)

Inoue, A., Kong, F.L., Han, Y., Zhu, S.L., Churyumov, A., Shalaan, E., Al-Marzouki, F.: Development and application of Fe-based soft magnetic bulk metallic glassy inductors. J. Alloys Compd. **731**, 1303–1309 (2018)

Jaworski, J., Dryzek, E., Fleury, E.: Cobalt: Characteristics, Compounds and Applications, Editor: Lucas J. Vidmar, Nova Science Publishers, Inc., Chapter 5, Magnetic Properties of Co-Based Metallic Glasses (2011)

Jhou, W.T., Wang, C., Ii, S., Hsueh, C.H.: Nano scaled superelastic behavior of shape memory alloy/metallic glass multi-layered films. Compos. B Eng. **142**, 193–199 (2018)

Jia, H., Liu, F., An, Z., Li, W., Wang, G., Chu, J.P., Jang, J.S.C., Gao, Y., Liaw, P.K.: Thin-film metallic glasses for substrate fatigue-property improvements. Thin Solid Films **561**, 2–27 (2014)

Jiang, Q.K., Liu, P., Ma, Y., Cao, Q.P., Wang, X.D., Zhang, D.X., Han, X.D., Zhang, Z., Jiang, J.Z.: Super elastic strain limit in metallic glass films. Sci. Rep. **2**, 852 (2012)
[PubMed][PubMedCentral]

Jiang, Q.K., Liu, P., Cao, Q.P., Wang, C., Li, X.L., Gao, X.Y., Wang, X.D., Zhang, D.X., Han, X.D., Zhang, Z., Jiang, J.Z.: The effect of size on the elastic strain limit in Ni 60Nb 40 glassy films. Acta Mater. **61**, 4689–4695 (2013)

Jiang, M., Cai, M., Zhou, J., Di, S., Li, X., Luo, Q., Shen, B.: Superior high-frequency performances of Fe-based soft-magnetic nanocrystalline alloys. Mater. Today Nano **22**, 100307 (2023)

Jiang, Y., Jia, S., Chen, S., Li, X., Wang, L., Han, X.: Theoretical prediction and experimental validation of the glass-forming ability and magnetic properties of Fe–Si–B metallic glasses from atomic structures. Materials **15**, 3149 (2022)

Ketov, S.V., Joksimovic, R., Xie, G., Trifonov, A., Kurihara, K., Louzguine-Luzgin, D.V.: Formation of nanostructured metallic glass thin films upon sputtering. Heliyon **3**, e00228 (2017)
[PubMed][PubMedCentral]

Kozikowski, P., Ohnum, M., Hashimoto, R., Takano, K., Herzer, G., Kuhnt, M., Polak, C.: Temperature memory effect of stress annealing-induced anisotropy in metallic glasses. Phys. Rev. Mater. **4**, 095604 (2020)

Krimer, Y., Aronhime, N., Ohodnicki, P., McHenry, M.E.: Prediction of good glass forming ability in amorphous soft magnetic alloys by thermocalc simulation with experimental validation. J. Alloy. Compd. **814**, 152294 (2020)

Leila Panahi, S., Ramasamy, P., Masdeu, F., Stoica, M., Torrens-Serra, J., Bruna, P.: Evaluation of the effect of minor additions in the crystallization path

of $[(Fe_{0.5}Co_{0.5})_{0.75}\ B_{0.2}\ Si_{0.05}]_{100-x}M_x$ metallic glasses by means of Mössbauer spectroscopy. Metals **11**, 1293 (2021)

Li, H., Zhang, J.-C., Branicio, P.S., Sha, Z.-D.: Composition-dependent fracture energy in metallic glasses. Phys. Rev. Mater. **7**, 035602 (2023)

Li, N., Pan, J., Liu, Z., Liu, L.: Metallic glass nanostructures: forming strategies and functional applications. Mater. Today Adv. **15**, 100253 (2022)

Li, X., Shan, G., Shek, C.H.: Machine learning prediction of magnetic properties of Fe-based metallic glasses considering glass forming ability. J. Mater. Sci. Technol. **103**, 113–120 (2022)

Liang, X., Sharma, P., Zhang, Y., Kato, H.: Nanoimprinting of magnetic FeCo-based metallic glass thin films. J. Magn. Magn. Mater. **542**, 168455 (2022)

Liu, Y.H., Fujita, T., Hirata, A., Li, S., Liu, H.W., Zhang, W., Inoue, A., Chen, M.W.: Deposition of multicomponent metallic glass films by single-target magnetron sputtering. Intermetallics **21**, 105 (2012)

Liu, S.Y., Cao, Q.P., Yu, Q., Wang, X.D., Zhang, D.X., Jiang, J.Z.: Substrate temperature effect on growth behavior and microstructure-properties relationship in amorphous Ni–Nb thin films. J. Non-Cryst. Solids **510**, 112–120 (2019)

Masood, A., Tamaki, T., Ström, V., Borgenstam, A. Ågren, J., Rao, K.V.: A new class of materials for magneto-optical applications: transparent amorphous thin films of Fe–B–Nb and Fe–B–Nb–Y metallic glassy alloys. IEEE Trans. Magn. **50**, 4004005 (2014)

Ma, Z., Li, J., Zhang, J., He, A., Dong, Y., Tan, G., Ning, M., Man, Q., Liu, X.: Ultrathin, flexible, and high-strength Ni/Cu/metallic glass/Cu/Ni composite with alternate magneto-electric structures for electromagnetic shielding. J. Mater. Sci. Technol. **81**, 43–50 (2021)

Miglierini, M., Hasiak, M.: Impact of ion irradiation upon structure and magnetic properties of NANOPERM-type amorphous and nanocrystalline alloys. J. Nanomaterials, Article ID 175407, 19 p. (2015)

Marimuthu, K.P., Han, G., Lee, H.: Multilayer thin film metallic glasses under nanoscratch: deformation and failure characteristics. J. Non-Cryst. Solids **601**, 122047 (2023)

Miglierini, M., Matúš, P.: Surface features of nanocrystalline alloys. Croat. Chem. Acta **88**, 539–545 (2015)

Miglierini, M., Vit Procházka, R., Rüffer, R.Z.: In situ crystallization of metallic glasses during magnetic field annealing. Acta Mater. **91**, 50–56 (2015)

Minić, D., Vasić, M., (eds.).: Metallic Glasses. IntechOpen (2020). https://doi.org/10.5772/intechopen.77589.

Monson, T.C., Zheng, B., Delany, R.E., Pearce, C.J., Langlois, E.D., Lepkowski, S.M., Stevens, T.E., Zhou, Y., Atcitty, S., Lavernia, E.J.: Soft Magnetic Multilayered FeSiCrB–Fe_xN metallic glass composites fabricated by spark plasma sintering. IEEE Magn. Lett. **10**, 7102505 (2019)

Nam, C.: Convolutional neural network guided prediction of saturation magnetic flux density of Fe-based metallic glasses. Comput. Mater. Sci. **225**, 112198 (2023)

Obeydavi, A., Rezaeian, A., Shafyei, A., ParvizKameli, J.-W.: Prediction of amorphous phase formation by thermodynamic and kinetic analysis, a Fe-based thin film metallic glass deposited by direct current magnetron sputtering. Mater. Res. Express **6**, 096407 (2019)

Obeydavi, A., Shafyei, A., Rezaeian, A., Kameli, P., Lee, J.-W.: Microstructure, mechanical properties and corrosion performance of Fe44Cr15Mo14Co7C10B5Si5 thin film metallic glass deposited by DC magnetron sputtering. J. Non-Cryst. Solids **527**, 119718 (2020)

PakmanYiu, W.D., NiklasBönninghoff, Y.-C., Lai, B.-Z., Chu, J.P.: Thin film metallic glasses: properties, applications and future. J. Appl. Phys. **127**, 030901 (2020)

Pang, L.L., Inoue, A., Zanaeva, E.N., Wang, F., Bazlov, A.I., Han, Y., Kong, F.L., Zhu, S.L., Shull, R.B.: Nanocrystallization, good soft magnetic properties and ultrahigh mechanical strength for $Fe_{82–85}B_{13–16}Si_1Cu_1$ amorphous alloys. J. Alloy. Compd. **785**, 25–37 (2019)

Phan, T.A., Lee, S.M., Makino, A., Oguchi, H., Kuwano, H.: Fe-B-Nb-Nd Magnetic metallic glass thin film for MEMS/NEMS structure. In: Proceedings of the IEEE 24th International Conference on Micro Electro Mechanical Systems (MEMS), pp 428–431 (2011). https://doi.org/10.1109/MEMSYS.2011.5734453.

Poddar, C., Ningshen, S., Jayaraj, J.: Corrosion assessment of Ni60Nb30Ta10 metallic glass and its partially crystallized alloy in concentrated nitric acid environment. J. Alloy. Compd. **813**, 152172 (2020)

Pookat, G., Thomas, H., Thomas, S., Al-Harthi, S.H., Raghavan, L., Al-Omari, I.A., Sakthikumar, D., Ramanujan, R.V., Anantharaman, M.R.: Evolution of structural and magnetic properties of Co–Fe based metallic glass thin films with thermal annealing. Surf. Coat. Technol. **236**, 246–251 (2013)

Prasanna Kumari, T., Manivel Raja, M., Atul Kumar, S., Srinath, S.V.K.: Effect of thickness on structure, microstructure, residual stress and soft magnetic properties of DC sputtered Fe65Co35 soft magnetic thin films. J. Magn. Magn. Mater. **365**, 93–99 (2014)

Rauf, A., Fang, Y., Zhang, H., Peng, G., Feng, T.: Thickness effects on microstructure, mechanical and soft magnetic properties of sputtered Fe–Zr thin film metallic glass. J. Non-Cryst. Solids **521**, 119500 (2019)

Sakurai, J., Hata, S., Yamauchi, R., Shimokohbe, A.: Combinatorial arc plasma deposition search for Ru-based thinfilm metallic glass. Appl. Surf. Sci. **254**, 720–724 (2007)

Sakurai, J., Aono, Y., Ishida, Y., Hata, S.: Characteristics of Ti–Ni–Zr thin film metallic glasses exhibiting a shape memory effect after crystallization. Mater. Sci. Forum **654–656**, 1066–1069 (2010)

Sharma, P., Gupta, A.: Effect of preparation condition on the soft magnetic properties of FeCuNbSiB thin films. J. Magn. Magn. Mater. **288**, 347–353 (2005)

Shauyenova, D., Jung, S., Yang, H., Yim, H., Ju, H.: Electrical and optical properties of Co75Si15B10 metallic glass nanometric thin films. Materials **14**, 162 (2021)

Smrčka, D., Procházka, V., Vrba, V., Miglierini, M.B.: On the formation of nanocrystalline grains in metallic glasses by means of in-situ nuclear forward scattering of synchrotron radiation. Nanomaterials **9**, 544 (2019) [PubMed][PubMedCentral]

Suryanarayana, C., Inoue, A.: Iron-based bulk metallic glasses. Int. Mater. Rev. **58**, 131–166 (2013)

Suzuki, K., Parsons, R., Zang, B., Onodera, K., Kishimoto, H., Shoji, T., Kato, A.: Nano-crystallization of amorphous alloys by ultra-rapid annealing: an effective approach to magnetic softening. J. Alloy. Compd. **735**, 613–618 (2018)

Taghvaei, A.H., Eckert, J.: Development and characterization of new Co–Fe–Hf-B bulk metallicglass with high thermal stability and superior soft magnetic performance. J. Alloy. Compd. **823**, 153890 (2020)

Tayyebi, A., Rastgoo, A., Osgouie, K.G.: The manufacture and study of the microstructure, mechanical properties, and corrosion behavior of Fe31Cr15Mo14C10B10Si5Ti15 metallic glass thin film, prepared by the magnetic sputtering method. J. Non-Cryst. Solids **595**, 121805 (2022)

Thanka Rajan, S., Arockiarajan, A.: Thin film metallic glasses for bioimplants and surgical tools: a review. J. Alloy. Compd. **876**, 159939 (2021)

Thanka Rajan, S., Mitun Das, P., Sasi Kumar, A., Arockiarajan, B.S.: Biological performance of metal metalloid (TiCuZrPd:B) TFMG fabricated by pulsed laser deposition. Colloids Surf. B **202**, 111684 (2021)

Thanka Rajan, S., Nandakumar, A.K., Hanawa, T., Subramanian, B.: Materials properties of ion beam sputtered Ti–Cu–Pd–Zr thin film metallic glasses. J. Non-Cryst. Solids **461**, 104–112 (2017)

Thórarinsdóttir, K.A., Strandqvist, N., Sigurjónsdóttir, V.V., Thorsteinsson, E.B., Hjörvarsson, B., Magnus, F.: Finding order in disorder: magnetic coupling distributions and competing anisotropies in an amorphous metal alloy. APL Mater. **10**, 041103 (2022)

Wang, Q., Zhou, J., Zeng, Q., Zhang, G., Yin, K., Liang, T., Yang, W., Stoica, M., Sun, L., Shen, B.: Ductile Co-based bulk metallic glass with superhigh strength and excellent soft magnetic properties induced by modulation of structural heterogeneity. Materialia **9**, 100561 (2020)

Wu, Z.F., Cao, Q.P., Ma, Y., Wang, C., Liu, S.Y., Qian, X., Wang, X.D., Jiang, J.Z.: Thickness-dependent pitting corrosion behavior in Ni–Nb thin film metallic glass. Thin Solid Films **564**, 294–298 (2014)

Xiaoyu, L., Sharma, P., Zhang, Y., Makino, A., Kato, H.: Nano-imprinting potential of magnetic FeCo-based metallic glass. Nanotechnology **30**, 305302 (12pp) (2019)

Yoon, S., Lee, C., Choi, H.: Evaluation of the effects of the crystallinity of kinetically sprayed Ni–Ti–Zr–Si–Sn bulk metallic glass on the scratch response. Mater. Sci. Eng. A **449–551**, 285–289 (2007)

Yoon, H.W., Lee, H.C., Shin, S.Y., Kwon, S.H., Moon, K.I.: Preparation of Zr–Al–Mo–Cu single targets with glass forming ability and deposition of thin film metallic glass. Coatings **10**, 398 (2020)

Yu, C.-C., Lee, C., Chu, J.P., Greene, J., Liaw, P.K.: Fracture-resistant thin-film metallic glass: ultra-high plasticity at room temperature. APL Mater. **4**, 116101 (2016)

Zhai, X.B., Wang, Y.G., Zhu, L., Cao, C.C., Dai, Y.D., Chen, J.K., Pan, F.M.: Effect of heating rate on atom migration, phase structure and magnetic properties of the $Fe_{82}Si_2B_{11}P_4Cu_1$ alloy. J. Non-Cryst. Solids **499**, 337–343 (2018)

Zhang, J., Li, J., Tan, G., Hu, R., Wang, J., Chang, C., Wang, X.: Thin and flexible Fe–Si–B/Ni–Cu–P metallic glass multilayer composites for efficient electromagnetic interference shielding. ACS Appl. Mater. Interfaces **9**, 42192-42199 (2017)

Zhao, X., Lan, S., Hu, L., Wu, Z., Dong, Y., Ren, Y., Wang, X.-L.: Features of relaxation modes in soft magnetic metallic glasses and their correlation with magnetic ordering. J. Non-Cryst. Solids **602**, 122087 (2023)

Zheng, H., Zhu, L., Jiang, S.S., Wang, Y.G., Liu, S.N., Lan, S., Chen, F.G.: Role of Ni and Co in tailoring magnetic and mechanical properties of $Fe_{84}Si_2B_{13}P_1$ metallic glass. J. Alloy. Compd. **816**, 152549 (2020)

Zhou, Q., Du, Y., Ren, Y., Kuang, W., Han, W., Wang, H., Huang, P., Wang, F., Wang, J.: Investigation into nanoscratching mechanical performance of metallic glass multilayers with improved nano-tribological properties. J. Alloys Compounds **776**, 447–459 (2019)

Zhu, L., Zheng, H., Jiang, S.S., Wang, Y.G.: Modulating the crystallization process of Fe82B12C6 amorphous alloy via rapid annealing. J. Alloy. Compd. **785**, 328–334 (2019)

© The Author(s), under exclusive license to Springer Nature Singapore Pte Ltd. 2024
R. S. Ningthoujam, A. K. Tyagi (eds.), *Handbook of Materials Science, Volume 2*, Indian Institute of Metals Series
https://doi.org/10.1007/978-981-97-4646-0_14

14. Recent Developments in Magnetic Nanocrystalline Metal Oxides and Their Biomedical Applications

Kashmiri Deka[1] and Vikas L. Mathe[1] ✉
(1) Plasma Nanomaterials Laboratory, Department of Physics, Savitribai Phule Pune University, Pune, Maharashtra, 411007, India

✉ **Vikas L. Mathe**
Email: vlmathe@physics.unipune.ac.in

Keywords Nanomaterials – Metal oxides – Magnetic materials – Biomedical uses

14.1 Introduction

The union of nanoscience with life science and health science has shown the way to the dynamic progress of the discipline of nano-biotechnology offering fascinating prospects to develop new materials, methods, and theories (Anik et al. 2021). Particularly, magnetic nanoparticles (MNPs) have gathered augmented interest because of their structure and properties with tunable dimension, elevated chemical stability, greater surface area, easy

functionalization, cell viability, etc. Their worth is evident in a range of areas, including drug release process, magnetic hyperthermia-based therapy, magnetic resonance imaging (MRI) contrast agents, gene release, tissue engineering, antibacterial study, lab-on-a-chip devices, etc. (Anik et al. 2021; Siafaka et al. 2021; Rahban et al. 2020; Lim et al. 2020; Etemadi and Plieger 2020; Varma et al. 2017; Dadfar et al. 2019; Fu et al. 2018; Mai et al. 2019; Bhardwaj et al. 2021; Sharma and Javed 2020).

In the recent past, a great number of investigations have been conducted in the direction of using metal oxides for biomedical applications based on their suitable physicochemical properties, biocompatibility, and chemical stability. It has been stated that specific metal oxides can combine with the surface of a transporter to develop monolayer structures of oxide for drug release.

Based on the above information, it is inferred that magnetic metal oxide nanomaterials are of immense importance in therapeutic study especially due to the fact that they get easily biased by an externally applied magnetic effect (Murthy et al. 2020). In the previous few years, several reviews have reported biomedical uses of magnetic nanomaterials. However, consolidated information and analysis, particularly related to the magnetic metal oxide nanomaterials for biomedical applications, are majorly missing. There are certain challenges in the route of research of these nanomaterials as therapeutic agents. Hence, it is very important to develop a detailed account with comprehensive information on different fabrication approaches of magnetic metal oxide nanomaterials and their relevance in medical science. This chapter attempts a comprehensive analysis of the progress in the field of application of magnetic metal oxide nanomaterials in theranostics. It is worth mentioning that an emphasis is given on magnetic metal oxides viz. spinel ferrites, in this book chapter as any metal ferrite can be

considered as a mixture of iron oxide and other 3d metal oxide(s). This book chapter gives a significant addition to the existing literature on prospective features of magnetic nanosized chemicals appropriate for biomedical applications. Figure 14.1 provides a flowchart illustrating the scope of the book chapter.

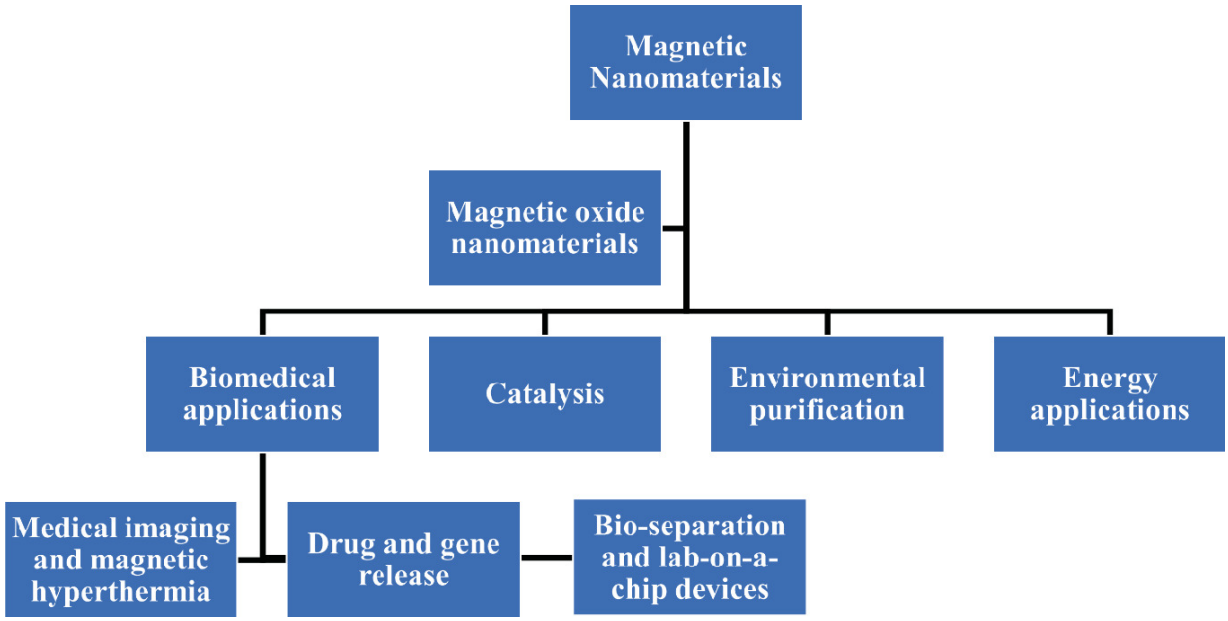

Fig. 14.1 Flowchart of the main topics covered in the chapter

14.2 Structures of Magnetic Oxides

The most significant structures of magnetic oxides associated with their magnetic performance are spinel, garnet, and magnetoplumbite. All of them are described briefly below (Srdic et al. 2018; Jain et al. 2013).

14.2.1 Spinel

Spinel structure typically appears in ferrites and various other binary oxides having a common chemical formula AB_2O_4, where A indicates ions present at a tetrahedral site, whereas B indicates ions present at an octahedral site. Generally, Fe^{3+} (in the case of ferrite) is at the position B

(Fig. 14.2). However, several other transition metal ions like Fe^{2+}, Co^{2+}, Ni^{2+}, Cu^{2+}, Mn^{3+}, etc. are also observed in B position. Position A is filled with a cation like Fe^{3+}, Zn^{2+}, Cd^{2+}, or occasionally with the Li^{+} ion or with vacancies, if this lack of positive charge is balanced by extra iron cations (Fe^{3+}). (O^{2-}) anions assume a close-packed cubic structure, whereas the metal ions fill two interstitial sites: tetrahedral A site and octahedral B site (Srdic et al. 2018; Jain et al. 2013).

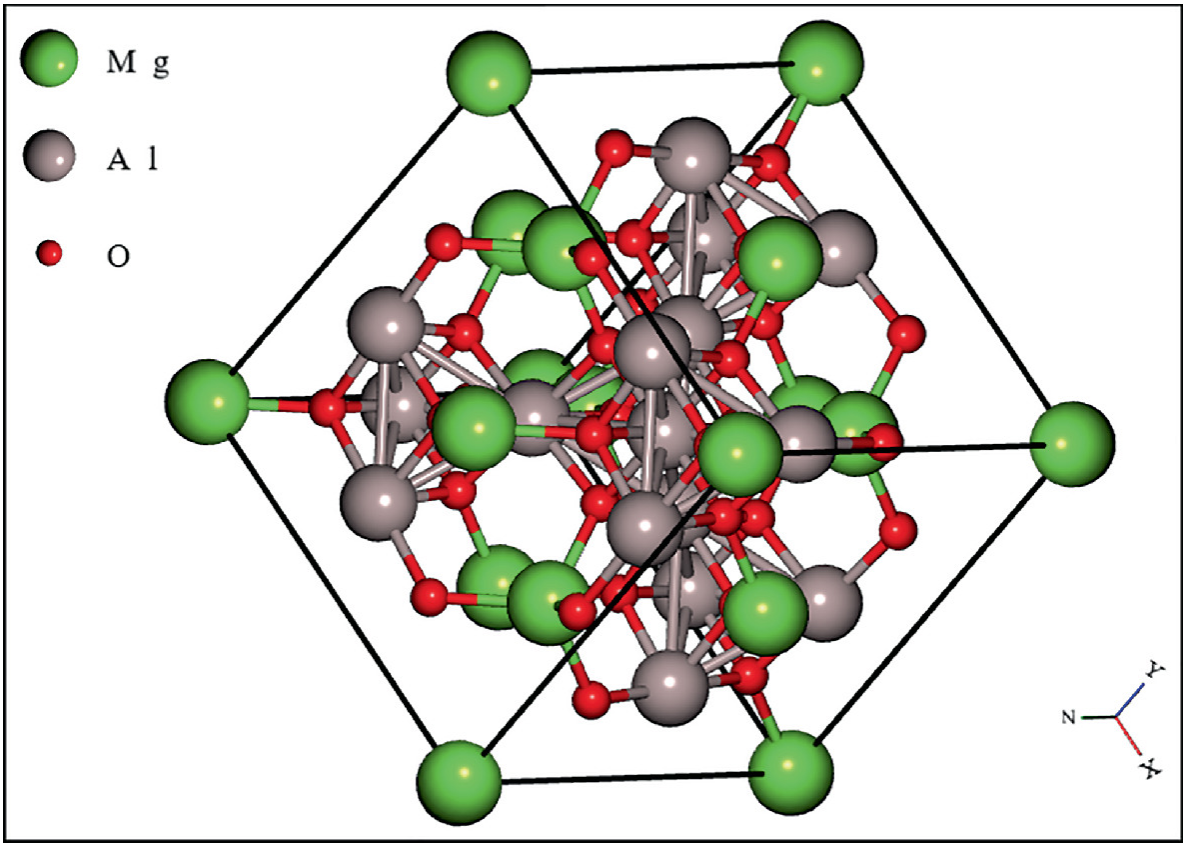

Fig. 14.2 Spinel structure. Developed by BURAI 1.3 software using CIF data from The Materials Project (Jain et al. 2013)

14.2.2 Garnet

Garnets have a cubic structure, with a common $A_3B_2(XO_4)_3$ formula where A is divalent and B is trivalent (Fig. 14.3). Cations A, B, and X are located on the dodecahedral,

octahedral, and tetrahedral sites, respectively (Srdic et al. 2018; Jain et al. 2013).

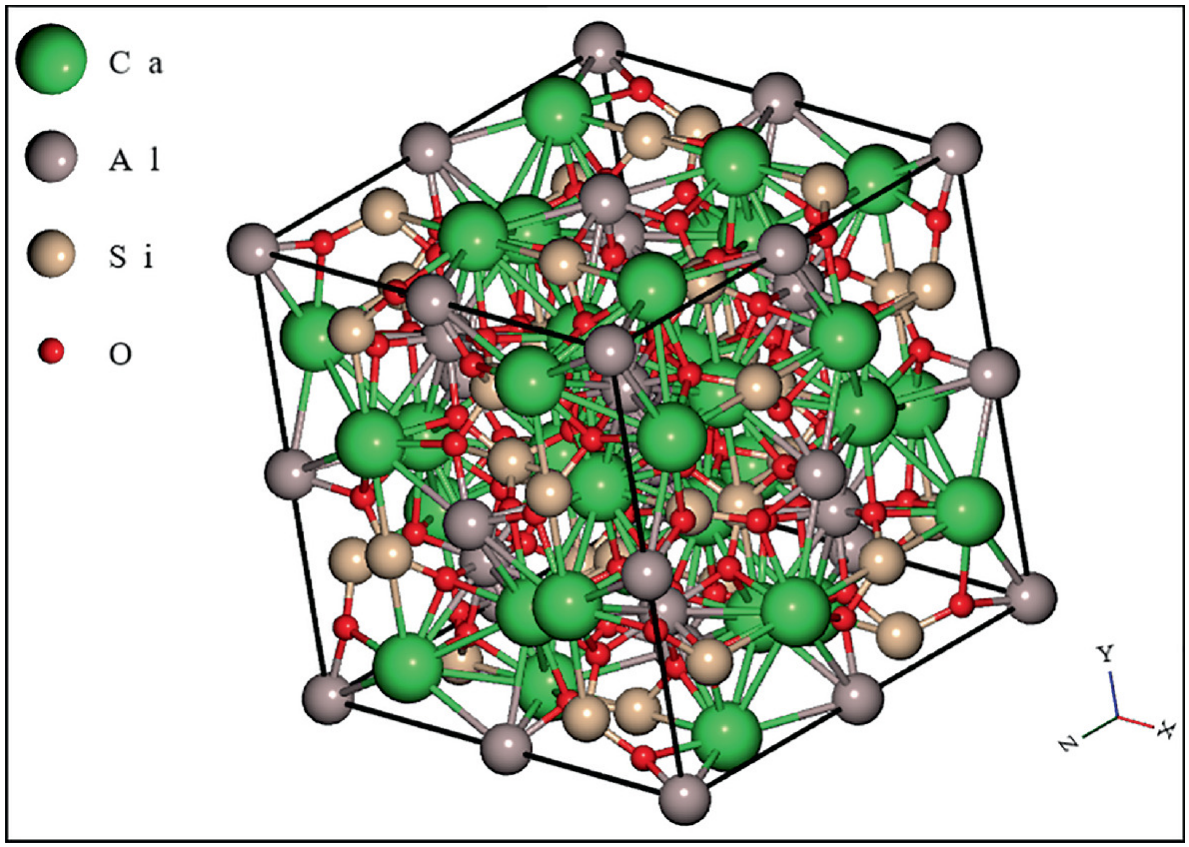

Fig. 14.3 Garnet structure. Developed by BURAI 1.3 software using CIF data from The Materials Project (Jain et al. 2013)

14.2.3 Magnetoplumbite

Hexagonal ferrites assume a magnetoplumbite structure. This structure is quite similar to the inverse spinel structure except for the fact that it has a hexagonal symmetry and spinel has a cubic structure (Fig. 14.4). The chemical formula of magnetoplumbite is $AB_{12}O_{19}$, where A and B are metal cations which are divalent and trivalent, respectively (Srdic et al. 2018; Jain et al. 2013).

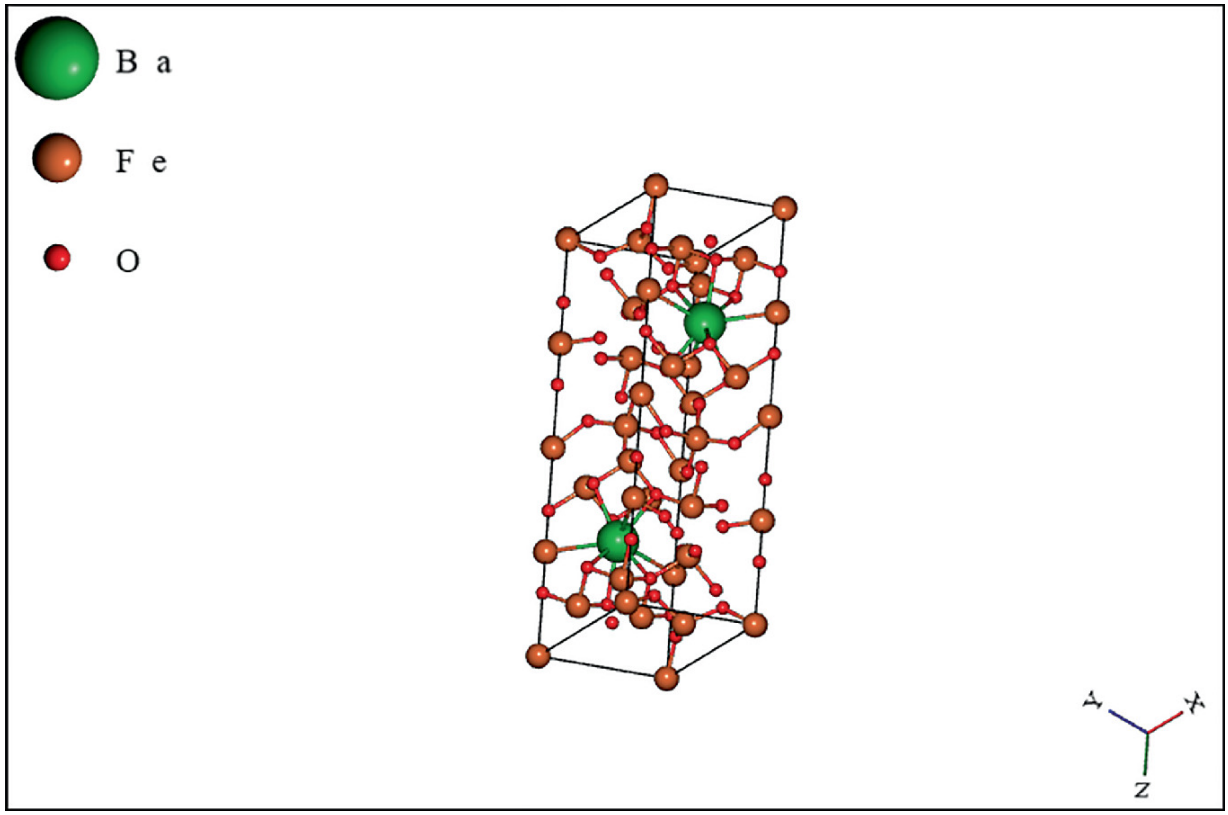

Fig. 14.4 Magnetoplumbite structure. Developed by BURAI 1.3 software using CIF data from The Materials Project (Jain et al. 2013)

14.2.4 Additional Magnetic Oxide Structures

In addition to the above-mentioned structures, magnetic oxides assume certain other structures for example halite, corundum, rutile, and perovskite. All of them are concisely elucidated below.

14.2.4.1 Halite

This structure can be looked upon as two interpenetrating face-centred cubic sublattices, having cations and anions alternating along the [100] directions (Fig. 14.5). Cations are coordinated by anions octahedrally and vice versa (Srdic et al. 2018; Jain et al. 2013).

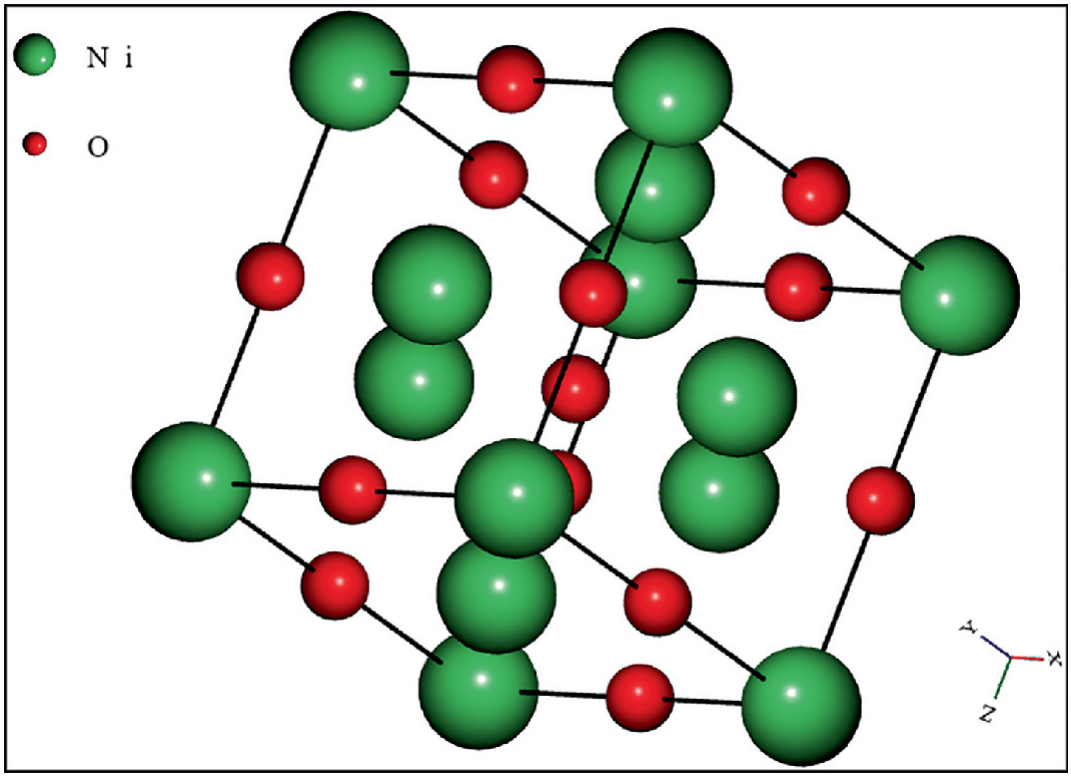

Fig. 14.5 Halite structure. Developed by BURAI 1.3 software using CIF data from The Materials Project (Jain et al. 2013)

14.2.4.2 Corundum

In this structure, the oxygen ions develop a distorted hexagonal close packing having two-thirds of the octahedral interstices occupied by metal cations (Fig. 14.6). Hematite (α-Fe_2O_3) is an example of a magnetic oxide having a corundum structure (Srdic et al. 2018; Jain et al. 2013).

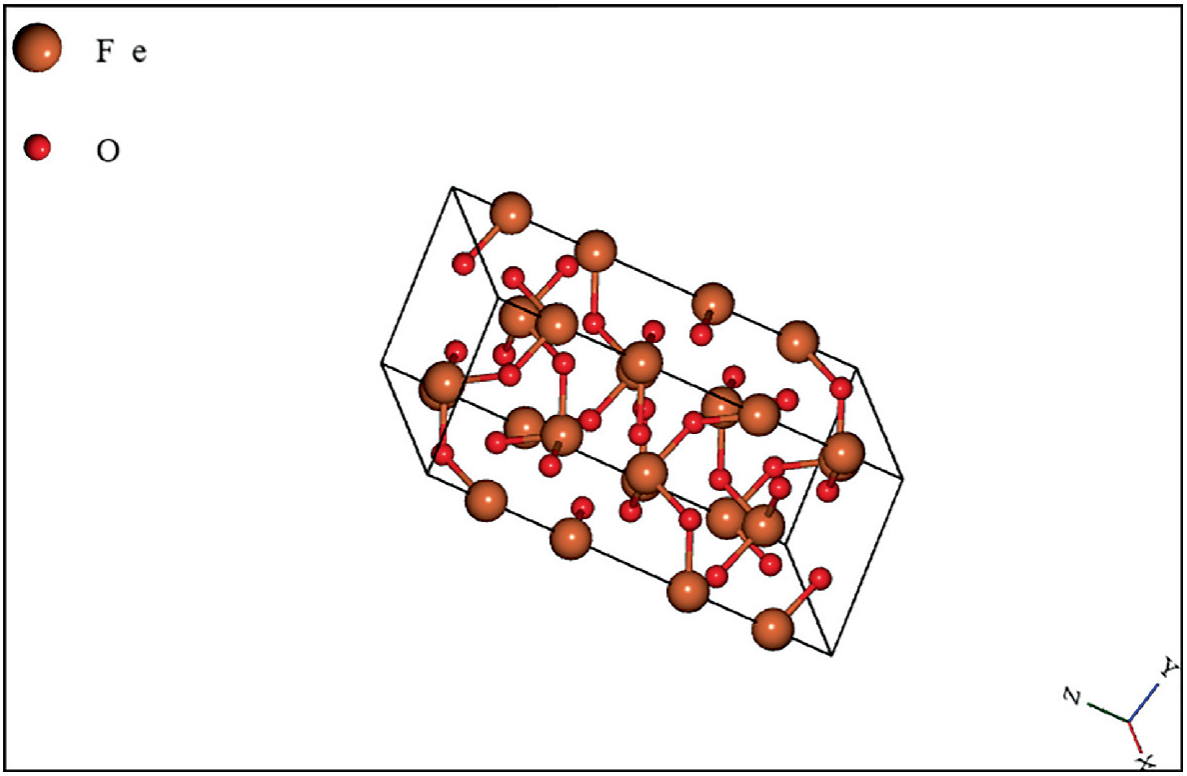

Fig. 14.6 Corundum structure. Developed by BURAI 1.3 software using CIF data from The Materials Project (Jain et al. 2013)

14.2.4.3 Rutile

The structure of rutile can be looked upon as a distorted hexagonal close-packed oxygen array, where cations fill half of the octahedral interstices (Fig. 14.7). CrO_2 possesses a rutile structure where the Cr^{4+} ions are situated at the corners of each unit cell, and a distorted CrO_6 octahedron is present at the centre (Srdic et al. 2018; Jain et al. 2013).

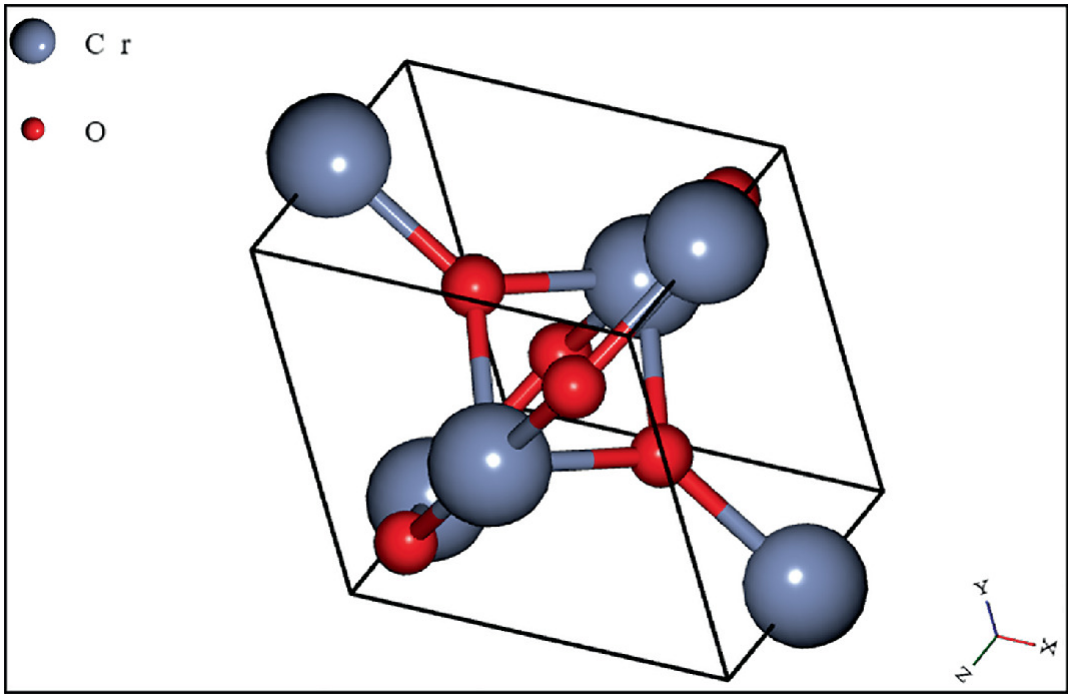

Fig. 14.7 Rutile structure. Developed by BURAI 1.3 software using CIF data from The Materials Project (Jain et al. 2013)

14.2.4.4 Perovskite

This structure has the formula of ABO_3, where A indicates a large cation site having 12-fold dodecahedral oxygen coordination, generally occupied by a trivalent lanthanide or other rare-earth element, and B is at the octahedral site where B mostly implies a 3d transition metal ion (Fig. 14.8) (Srdic et al. 2018; Jain et al. 2013). Many of the oxide ferroelectric such as $BaTiO_3$ and $PbTiO_3$ possess perovskite structures.

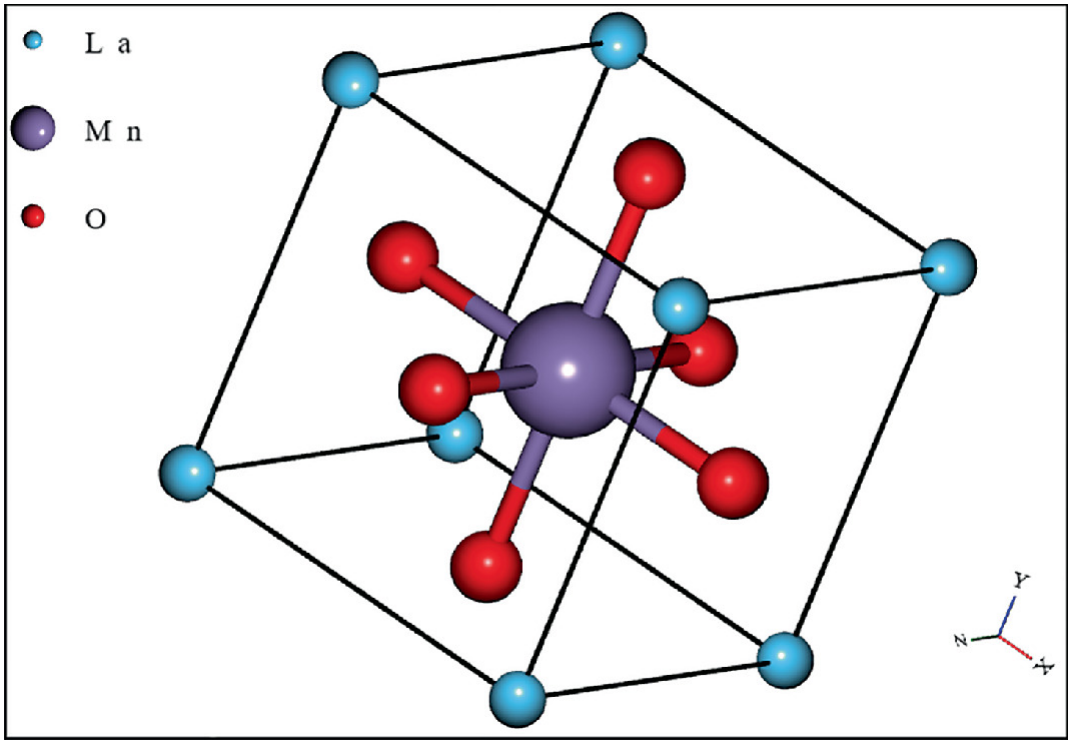

Fig. 14.8 Perovskite structure. Developed by BURAI 1.3 software using CIF data from The Materials Project (Jain et al. 2013)

14.3 Synthesis of Magnetic Metal Oxide Nanomaterials

Design of the nanomaterials according to the use requires knowledge of the synthesis measures. From the biomedical application point of view, there are quite a few significant characteristics of magnetic substances such as dimension, morphology, surface activity, and colloidal strength in a hydrophilic atmosphere. Hydrophilicity is required because water-soluble medicines get dissolved completely in water, and they remain in the bloodstream for an extended time. Other key advantages of these drugs include high solubility, limited side-effects, and increased bioavailability and effectiveness. These characteristics can be considered in the selection of the synthesis approach. The typically employed techniques for the synthesis and surface

functionalization of magnetic metal oxide nanomaterials are discussed below (Hussain and Patankar 2022).

14.3.1 Coprecipitation Method

The most extensively utilized, easiest, and well-organized process for getting magnetic metal oxide nanomaterials is the Chemical Coprecipitation (CCPT) technique (Mittal et al. 2022). Primarily two stages are included in this technique viz. nucleation and subsequent growth. As the concentration of constituents comes close to a threshold supersaturation juncture, burst nucleation occurs. When the nucleation finishes, sluggish growth of the nucleated particles takes place by the diffusion method of solute to crystal. In order to attain monodispersed particles, both these processes need to happen in dissimilar periods. Fundamentally, to get a narrow size distribution, the growth needs to take place after the nucleation is accomplished from the supersaturated solution. The number of particles varies based on the number of nuclei produced. Particles of dissimilar dimensions can be created by small changes in the factors like pH, ionic strength, temperature, etc. The common restriction of the CCPT technique is the enormous quantity of factors to be dealt with to get particles with a narrow size distribution. The reaction situation should be critically checked for a precise outcome that originates from a varied phase diagram and multifaceted aqueous chemistry (Hussain and Patankar 2022).

14.3.2 Hydrothermal Synthesis Technique

Hydrothermal synthesis is usually explained as the production of nanomaterials in water as the medium under intense circumstances like elevated pressure and temperature from materials that are generally insoluble at room temperature and normal pressure conditions. Under hydrothermal circumstances, quite a few kinds of

nanostructured substances have been synthesized by different researchers globally. Generally, the dimension of the nanoparticles upsurges with the lengthening of the synthesis period. The nucleation and growth steps mainly rule the dimension of particles shaped by the procedure. At elevated temperatures, the speed of nucleation becomes a lot quicker than the growth which causes a reduction of nanoparticle dimension (Hussain and Patankar 2022). If any solvent other than water is used in this method, then it is known as the solvothermal process (Li et al. 2016).

14.3.3 Thermal Decomposition Process

Thermal breakdown of organic starting materials, accompanied by surfactants in organic solvents at elevated temperatures, also shapes nanoparticles of great crystallinity as well as monodispersity. Solvents with high boiling points are employed for the creation of low-dimension nanoparticles with regularity via the disintegration of organometallic chemicals. The preliminary proportions of the starting materials, surfactant, and solvent along with the synthesis time happen to be the important factors contributing to the dimension, morphology, and geometry of the synthesized nanoparticles. Usually, the nanomaterials developed by the thermal decomposition process are hydrophobic and therefore extremely steady in a variety of organic solvents. So, a succeeding surface functionalization via either ligand addition or ligand exchange must be carried out for their water dispersibility. There are a few restrictions to this technique although it creates greatly crystalline magnetic metal oxide nanomaterials. Particularly, the thermolysis procedure happens at very elevated temperatures in this scheme, and it applies expensive organometallic starting materials (Hussain and Patankar 2022).

14.3.4 Microemulsion Formation

Microemulsions are known as thermodynamically steady macroscopically isotropic solutions containing at least three constituents viz. oil, water, and surfactant. Water-in-oil (W/O) or the reverse micelle gets extensively engaged to synthesize nanoparticles of ferrites and their substituted structures. The aqueous part stays in the form of microdroplets present in water-in-oil emulsion enclosed by surfactants present in the oil phase shaping water pools. Such pools are fundamentally the nanoreactors facilitating the precipitation of organic and inorganic materials to produce even-sized nanomaterials. The concentrations of surfactant and water largely dominate the dimension of these reverse micelles. Slight changes to the reaction scheme produce dissimilar dimensions of nanomaterials. As two alike W/O emulsions having required reacting agents are combined, the droplets bump into each other, unite, and at last get precipitated out. Although a variety of magnetic metal oxide nanomaterials have been synthesized in a properly regulated way by this process, however, this approach is, at times, not advantageous due to the very small yield of production in comparison to other techniques. It turns out to be costly too because of the necessity of a huge quantity of solvents. This technique is extremely hard to scale up since it usually involves the use of organic solvents which are not eco-friendly (Hussain and Patankar 2022).

14.3.5 Sonochemical Approach

Ultrasound with elevated intensity can be used as a significant means for producing a lot of inorganic, organic, and organometallic chemicals. It also finds extensive use in the field of synthesis of nanomaterials. The physical and chemical modifications occurring because of the ultrasound happen owing to acoustic cavitation which brings together the nucleation, growth, and disintegration of bubbles. Any fluid senses a vibrant pressure when a particular sound

wave with enough amplitude spreads throughout it. As a consequence, the density of the fluid goes through vigorous variation with alternative broadening and narrowing of the wave. Owing to the pre-existent contamination, bubbles get produced that begin swinging along with the used sound vibration. At first, a swinging bubble is grown from the bulk liquid. As it arrives at a crucial dimension, it effectively combines with the acoustic field and then gets expanded. Lastly, the bubble goes through an implosive breakdown. The extremely temporary circumstances created throughout the sonolysis via acoustic cavitation cause this method to look exceptional to develop a number of chemicals on the bench top in a room temperature arrangement which is otherwise extremely difficult because of the necessity of massively elevated temperatures, pressure, and lengthy duration. However, large-scale production of magnetic metal oxide nanomaterials is not easy to attain by the above-explained sonochemical technique (Hussain and Patankar 2022).

Evidently, the methods that offer the best control over the shapes of nanoparticles are the hydrothermal method, microemulsion method, and thermal decomposition.

14.3.6 Thermal Plasma: An Upcoming Alternative for the Development of Magnetic Nanosystems

Plasma can be produced by delivering a sufficiently strong electric current via a gas medium. The plasma technologies used for material processing broadly can be categorized as thermal plasma and cold plasma. Thermal plasmas exist at high pressure (generally >10 kPa) and exhibit high temperatures of about 2000–20,000 K. Such plasmas are produced using direct current/alternating current/radio frequency (RF)/microwave radiations. On the other hand, cold plasmas are basically low-pressure plasmas indicated

by low ion and neutral particle temperatures and high electron temperatures, and energy is usually expressed in terms of temperatures. The former one, i.e., thermal plasma technology is evolving as one of the utmost effective procedures in the discipline of materials processing (Hussain and Patankar 2022). Commercial companies like TEKNA produce turnkey plasma systems to yield powders fabricated to meet various requirements.

Thermal plasma technology is extensively utilized for special material development. The extraordinary thermal flux associated with the plasma plume improves its usability (Hussain and Patankar 2022). Direct current (DC) thermal plasmas are produced between two electrodes separated from each other, and a gaseous medium between them is made to ionize by applying a suitable electrical signal. Such plasma species are characterized by local thermodynamic equilibrium and enormous thermal flux. The precursors to be used for the synthesis are placed on the anode which get evaporated by the high temperature of the thermal plasma plume. The electrons emitted from the cathode reach the anode and during this journey, the electrons encounter collision with atoms and molecules causing excitation, ionization, etc. Electrons released during ionization are augmented to the anode triggering further collision along with additional ionization. Consequently, extremely conducting gas produces an electric spark. Collisions among electrons and neutrals (atoms, molecules) turn out to be more recurrent. The ions, electrons as well as neutral particles in plasma attain local thermodynamic equilibrium. All the plasma species attain almost the same energy as that of the electrons. The temperature inside the plasma plume may attain a magnitude of the order of 10^3 to 10^4 K with maximum temperature in the core region which decreases radially. At such a high temperature, chemical reactions are facilitated

among the precursors in their vapourized state to form the desired products. Contrary to the usual thermal sources which can reach temperature only to an extent of 3000 K, plasma can aid in chemical reactions involving high temperatures and in the field of extractive metallurgy. A sharp temperature gradient exists between the localized plasma and the nearby gas or ambient that lets quenching of product vapours, and the quenching limits the growth resulting in the formation of nanoparticles. The remarkable benefit of a plasma arc device over the orthodox systems is that it facilitates delivery of energy to the reactants via a regulated technique (Hussain and Patankar 2022).

These days, thermal plasma is emerging as a tool employed for the production of magnetic nanoparticles. As plasma consists of electrically charged travelling particles, it can susceptibly respond to outside magnetic and electric fields. Thermal plasmas are being explored for the production of a huge amount of scientifically significant magnetic materials based on nickel, cobalt, iron, and their oxides (Hussain and Patankar 2022). It is noteworthy that low-pressure plasmas (cold plasma) have also been explored for the synthesis of nanomaterials, where typically metallo-organic precursors are made to enter into plasma so as to get the desired product at optimal operating conditions. However, the yield of synthesis products using cold plasmas is comparatively lower than that of thermal plasma (Vollath 2007).

14.3.7 Functionalization of Magnetic Metal Oxide Nanomaterials

Although there are a lot of notable developments that have been realized for the synthesis of magnetic metal oxide nanomaterials, the chemical and colloidal stability of these materials is a vital topic. Because of this fact, investigators followed a range of approaches for the surface

functionalization of these nanomaterials by numerous kinds of small molecules, inorganic materials, polymers, and targeting agents. Several encapsulating agents have been launched onto the exterior of the nanoparticles to provide them colloidal stability to make them equipped for the applications they are meant to be used for. Several functionalization methods being exercised by scientists globally are discussed below (Hussain and Patankar 2022). The right functionalization is selected based on the requirement of colloidal stability, biocompatibility, or target specificity.

Small molecules holding phosphate, carboxylate, and amine groups are popular for acquiring elevated pull in the direction of the metal oxide nanomaterial surface. The structure of these molecules must be tailored for the stability of the dispersions of the nanomaterials both in water as well as hydrocarbon-based solvents.

Polymers are too often exploited for effective passivation of nanomaterials to evade clustering by means of steric hindrance or electrostatic repulsion. They are easily conjugated chemically or adsorbed physically on the surface of magnetic metal oxide nanomaterials. At times, the polymer coating is not sufficient to avoid aerial oxidation of the nanomaterials due to which they lose their magnetic properties.

Inorganic encapsulating agents like gold and silica are too widely engaged for providing colloidal stability to magnetic metal oxide nanomaterials by the creation of core–shell arrangements, which facilitates the coordination of various biomolecules and healing agents to the exterior of particles. Generally, the encapsulation by unreactive silica on the surface of magnetic metal oxide nanoparticles reduces the formation of agglomeration of nanoparticles in liquid medium or blood and offers biocompatibility to the materials. Other than bringing about the colloidal stability of these nanomaterials in water, surface adjustment

generates sites for attachment to various biomolecules, like proteins, antibodies, and enzymes. Several moieties such as proteins, antibodies, aptamers, and peptides are attached to the exterior of magnetic metal oxide nanomaterials as targeting agents.

The consequence of some selected synthesis methods on the size distribution and morphology of the magnetic nanomaterials is presented in Table 14.1 (Khizar et al. 2021).

Table 14.1 Size distribution and morphology commonly observed in magnetic nanomaterials obtained by various chemical synthesis procedures (Khizar et al. 2021)

Synthesis procedure	Size (nm)	Morphology
Coprecipitation	10–50	Spherical
Microemulsion	4–15	Cubic or spherical
Thermal decomposition	5–60	Spherical

14.4 Characterization Methods of Magnetic Nanomaterials

Material characterization techniques like X-ray diffraction, scanning electron microscopy, and transmission electron microscopy are engaged for structural analysis, as well as investigation of microstructural details of nanomaterials. Furthermore, Fourier transform infrared (FTIR) and Raman spectroscopy are engaged for the examination of the vibrational energy of the functional group present at the surface. X-ray photoemission spectroscopy (XPS), and Raman and IR spectroscopy are popularly used to investigate the surface of a given material. UV–visible and photoluminescence (PL) photospectrometry are also utilized to investigate the optical bands of nanoparticles (NPs). Thermal analysis of NPs is carried out by thermogravimetric analysis. Magnetic properties of

samples are inspected using vibrating sample magnetometry (VSM) and physical property measurement system (PPMS).

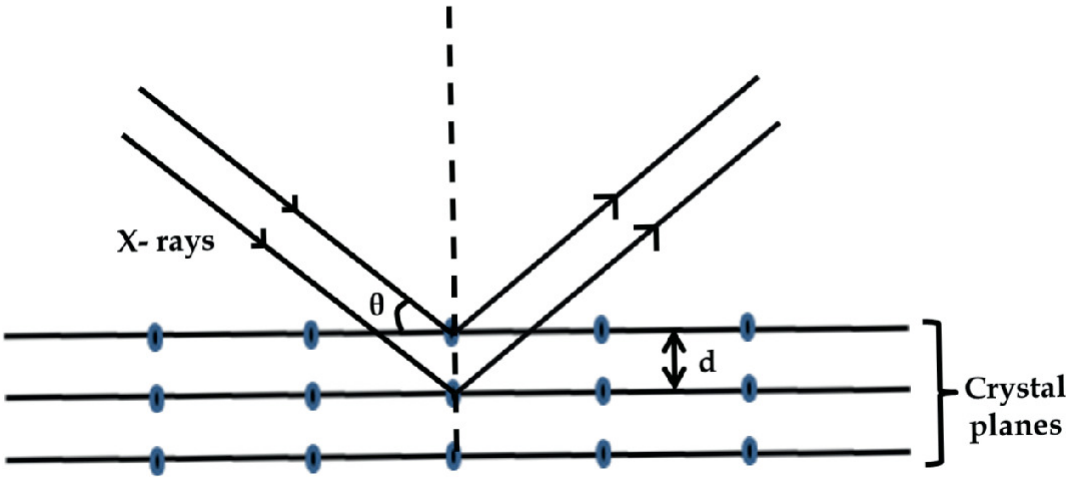

Fig. 14.9 X-ray diffraction.
Reproduced with permission from Deka and Deb (2018)

14.4.1 X-Ray Diffraction

X-ray diffraction (XRD) is a method mostly exercised for ascertaining the phase of a crystalline substance. The instrument engaged for this analytical method is known as a Goniometer. The X-rays are produced using an X-ray tube, which is then aimed at the sample as a monochromatic collimated radiation (Deka and Deb 2018).

A crystal structure is characterized by a regular and periodic array of atoms and molecules in three dimensions. The unit cell contains atoms or molecules arranged in a specific manner. When X-rays fall onto a particular material which consists of atoms and molecules as a scattering centre, they get scattered in all directions. If the object is crystalline, the scattering results in a constructive or destructive pattern depending on the diffraction angle (Deka and Deb 2018) (Fig. 14.9). In accordance with the geometrical understanding using XRD associated with constructive interference, W. L. Bragg put forth the condition

$$n\lambda = 2d_{hkl}\sin\theta, \ldots \quad (14.1)$$

where n implies the order of diffraction, λ implies the incident X-ray wavelength, d_{hkl} denotes the interplanar spacing, and θ is the diffraction angle (Deka and Deb 2018). XRD plot demonstrates the diffraction intensity distribution as a function of 2θ. Analysis of the XRD pattern, i.e., diffraction peak position and relative intensity is used to identify the crystal structure of the material under investigation. This allows uncovering of the crystal structure, lattice parameters, crystallite size, micro-strain, etc. It is noteworthy that the motive of using X-rays for the construction of diffraction patterns is that the scale of their wavelength is in a comparable range with the lattice spacing between planes in crystal structures (Deka and Deb 2018).

Every material generates a “fingerprint” XRD pattern attributed to its crystal structure. A chemically manufactured material can be scrutinized by matching its XRD profile to a collection of established patterns. The region under a peak connected to different planes is directly proportional to their abundance in the substance (Deka and Deb 2018).

14.4.2 Fourier Transform Infrared (FTIR) Spectroscopy

Infrared spectroscopy is applied to find out the structures of molecules founded on their distinctive infrared radiation absorption property. When molecules are subjected to infrared radiation, they particularly absorb radiation of definite wavelengths if there is a frequency match and net change in the dipole moment of the molecules. As a consequence, their vibrational energies reallocate from the ground state to the excited state. The frequency of the absorption relies upon the vibrational energy difference

(Deka and Deb 2018). In a characteristic infrared spectrum, intensity of light transmittance or absorbance percentage is plotted against the wavenumber (in cm^{-1}) of incident radiation. The quantity of peaks attained for a molecule is found out by the number of its vibrational freedom. The peak intensities are linked to the dipole moment change and the likelihood of the change of energy states. Each chemical structure delivers a fingerprint infrared profile. Therefore, it is extremely suitable to characterize a molecule by examining its infrared spectrum. Most infrared absorption spectra are recorded within the wavenumber range of 400–4000 cm^{-1}, as organic and inorganic compounds usually display their characteristic infrared peaks in this range (Deka and Deb 2018).

In an infrared spectroscopic examination, an interferometer is employed to adjust the wavelength from a broadband infrared supply. The intensity of transmitted or reflected radiations corresponding to the wavenumber is gauged by a detector. The use of Fourier Transform Infrared spectrometer gives an improved signal-to-noise ratio (Deka and Deb 2018). For FTIR, one can use both transmission and Attenuated Total Reflectance (ATR) mode. ATR is more suitable for biomedical applications as it travels only to the surface of the particle without transmitting through it.

14.4.3 Scanning Electron Microscopy (SEM)

It is an electron microscope where sample images are obtained by scanning its surface with a focused electron beam of sufficiently high energy typically a few tens of kV. From the signals gained due to the interaction of the electrons with the sample atoms, the structure of the surface, and composition of the sample can be identified. Since the de Broglie wavelength associated with an

electron is quite less in comparison to light wavelength, the resolution of SEM is, to a great extent, superior to an optical microscope. The scanning area by a usual SEM instrument may differ from approximately a few mm to a few microns in width while the magnification span varies in the range of 20X–30000X (Deka and Deb 2018).

When the electron beam is impinged upon the sample, the electrons which are bounced back are recognized as backscattered electrons. On the other hand, the electrons generated from the sample atoms due to the interaction with the applied electron beam are named secondary electrons. Secondary electrons give the information about morphology and topography of materials, whereas the backscattered electrons are used for representing composition contrasts of multiphase samples. In addition to electrons, X-rays have also evolved from inelastic collisions between the incident electrons and electrons in discrete orbitals of the sample atoms. Each substance emits X-rays of a specific energy. Consequently, these X-rays can function as the fingerprint to identify the elemental composition of the material under investigation detecting all the different elements present in it. For this reason, an Energy Dispersive X-ray Spectroscopy (EDX or EDS) is united with the SEM system which is used for elemental investigations. It is an investigative tool for chemical characterization established on the emission of element-dependent X-ray radiations. The EDX examination is obtained as a spectrum including peaks specific to different elements in the material. In addition to this qualitative information, the percentage concentration of every element can also be acquired (Deka and Deb 2018). The highest resolution achieved by the SEM is found by the spot size of the electron and the sample–electron beam interaction volume. SEM offers a resolution of the order of a few tens of 1 nm resolution (Deka and Deb 2018).

SEM has limitations mainly connected to the preparation of the sample, proficiency of the operator, high price, and attainable resolution. The high-energy ionizing electron beam can change the analysed sample by knock-on damage, heating, and radiolysis. Therefore, the operator should study the energy of the electron beam, rate of scan, and total experiment time while operating SEM. Samples which are sensitive to electron beams or which are non-conductive need the introduction of a conducting layer of carbon or gold by sputter coating, which can create artefacts (Lowell et al. 2004).

14.4.4 Transmission Electron Microscopy (TEM)

It is a different type of electron microscope like SEM where a highly energetic (hundreds of kV) electron beam is utilized. The dissimilarity between both techniques is that SEM images are produced by the electrons from the sample surface while in TEM, the electron beam is passed through the material to construct an image. TEM provides improved resolution than the SEM. The image is produced because of the interaction between the electron beam and the material when the electron beam is passed through the sample. The image so obtained is then magnified and focused on a fluorescent screen, photographic film, or a charge-coupled apparatus (Deka and Deb 2018). With the assistance of TEM, samples can be examined up to atomic level, i.e., less than 1 nm. TEM imaging gives information on morphology, crystal structure, dislocation, stress, grain boundaries, and even chemical composition (through TEM–EDX) (Deka and Deb 2018).

Depending on the energy of the electron beam, the wavelength can be tuned with interplanar spacing. As a result, a fingerprint pattern for a material system can be obtained. Consequently, a sequence of diffraction patterns

can be achieved and recognized as Selected Area Electron Diffraction (SAED).

The lattice spacing, d for different planes of a crystalline material, can be estimated from SAED by using the following equation:

$$d = \frac{\lambda l}{r}, \ldots \tag{14.2}$$

where λ denotes the wavelength of the electrons, l is the camera focal length, and r implies the distance between central and diffracted spots (Deka and Deb 2018).

This method is helpful for investigating the crystal structure of a substance. It is beneficial over XRD because of its relevance even in an extremely tiny region of inspection (nm range).

The diffraction pattern (reciprocal space) of a chosen zone can also be attained by the Fast Fourier Transform (FFT) study. These findings can be compared with the experimentally obtained SAED pattern for better insight into crystalline structures at the nanoscale (Deka and Deb 2018).

One noteworthy difficulty associated with the analysis of TEM is that it gives 2D images of a 3D specimen thereby creating confusion on various occasions. There has been improvement in overpowering this constraint by the development of electron tomography, which employs a sequence of images captured at diverse angles. Furthermore, there has been progress in specimen-holder design to allow full 360 rotation. As in SEM, the risk of specimen damage by the electron beam is there in TEM as well. The specimens under analysis have to be thin to receive good TEM results. While using both SEM and TEM for biological samples, one has to take care as the sample may get damaged due to high energy electron beam.

14.4.5 Raman Spectroscopy

Raman spectroscopy is associated with the inelastic scattering of a monochromatic laser light in the visible/near-infrared/near-ultraviolet region by Raman active vibrational, rotational, and other low-frequency modes of a given material (Deka and Deb 2018). When a monochromatic laser beam, which can be regarded as an oscillating electromagnetic wave possessing an electrical vector E, interacts with a material, it produces a change in its polarizability. Due to the interaction of the radiation with an electron cloud of an analyte bond, it induces a dipole moment P in the bond that is given by

$$P = \alpha E, \ldots \tag{14.3}$$

where α is the molecular polarizability. The dipole moment leads to periodical deformation of the molecules instigating them to vibrate with a typical frequency υ_m. Therefore, the molecules act similar to some oscillating dipoles after becoming energized by the laser light holding a specific frequency υ_0. These dipoles can produce light in three probable methods.

(a) If the sample molecules do not include any Raman-active modes, the excited molecules go back to their initial vibrational state producing light with unaltered frequency, i.e., υ_0. This is identified as the elastic Rayleigh scattering.

(b) A fraction of the energy of the incident beam is transmitted to the Raman-active mode of the material because of which the frequency of the released light is lower than υ_0. This observable fact is acknowledged as Stokes–Raman scattering.

(c) When the Raman active molecule is already at an energized vibrational state at the instance of interaction with the laser beam, the surplus energy is

discharged leading to a scattered light with a frequency more than υ_0. This is recognized as an Anti-Stokes–Raman occurrence (Deka and Deb 2018).

The dissimilarity between the frequencies of the scattered light and the incident laser beam is named as Raman shift which is the evidence of the vibrational, rotational, and additional low-frequency transitions in the sample material. A characteristic Raman spectrum is shown by plotting the intensity of Raman scattering against the Raman shift. Every peak stands for a specific vibrational mode associated with a molecular functional group in the material under examination. The peak location of the same vibrational mode may differ based on the nearby situation of the functional group. Hence, the Raman spectrum can be regarded as a molecular fingerprint of a Raman active substance. It can be employed to examine solid and liquid samples (Deka and Deb 2018). The degree of crystallinity in a given substance can also be determined from the width of its Raman peaks. Likewise, the direction and value of the Raman shift give knowledge about residual stress in a crystal structure (Deka and Deb 2018).

14.4.6 X-Ray Photoelectron Spectroscopy (XPS)

It is a surface-responsive spectroscopic method which is carried out by exciting the surface of a substance with monoenergetic Al Kα X-rays leading to the release of photoelectrons. The kinetic energy and quantity of the electrons getting discharged typically from the top 10 nm of a sample are calculated (Deka and Deb 2018). As the energy of X-rays used with definite wavelength is a known quantity, the binding energy of every discharged electron can be estimated by utilizing the equation below put forward by Ernest Rutherford:

$$E = E_{\text{photon}} - \left(E_{\text{kinetic}} + \Phi\right), \ldots \tag{14.4}$$

where E_{binding} and E_{kinetic} are the binding energy and kinetic energy of the electron, whereas X-ray photon energy is stated as E_{photon}. The term Φ, recognized as the work function, is an adaptable correction factor of the device (Deka and Deb 2018).

XPS is presented by plotting the number of electrons detected against the binding energy of the electrons. Every element shows typical XPS peaks at particular binding energies which aids in characterizing the elements present at the sample surface. The obtained peaks are indicative of the electron configuration of the atoms present in the material. The chemical environment of an atom influences the binding energy of the electrons emitted from it. The intensity of the peaks corresponding to a particular element is directly associated with the amount of that element in the scanned sample. XPS technique is employed to understand the surface chemistry of a material (Deka and Deb 2018).

XPS method can aid in learning the diverse oxidation states of metals in a metal oxide. The atoms of a greater positive oxidation state display a higher binding energy because of the extra Coulombic attraction of the photoelectron with the atomic core, in comparison to the binding energy of the elemental atom. For example, the mixed valence metal oxide Mn_3O_4 can be identified by deconvoluting the $Mn2p_{3/2}$ peak of its XPS, where peaks at 640.2 eV and 641.5 eV correspond to Mn^{2+} and Mn^{3+} oxidation states, respectively (Phys 2014).

14.4.7 UV Visible Spectrophotometry

It is a rapid investigative method that gauges the absorbance or transmittance of light. Though the wavelength of UV spans within 100–380 nm and the visible section extends up to 800 nm, the majority of the

spectrophotometers hold a functioning wavelength limit of 200–1100 nm.

Covalently unsaturated compounds having differences in electronic transition energy comparable to UV–visible light energy absorb at particular wavelengths. These materials are recognized as chromophores. When radiation of UV–vis strikes chromophores, electrons in the ground state jump to an energized state. This phenomenon is denoted as an excitation of electrons (Hussain and Patankar 2022).

UV–vis spectrophotometers guide a source of light via a material, and a detector on the reverse side notes the transmitted light. Usually, UV–vis plots state wavelength and absorbance (A) on the *x*-axis and the *y*-axis, respectively (Hussain and Patankar 2022).

The device operated in ultraviolet–visible spectroscopy is named UV–vis spectrophotometer. It determines the intensity of light after passing via a sample (I), and compares it with the light intensity before it passes via the sample (I_0). The ratio I/I_0 is termed as the transmittance, and is generally stated in percentage (%T). The absorbance, A, is derived from the transmittance via the following equation (Hussain and Patankar 2022):

$$A = \log_{10} \frac{I}{I_0} \ldots . \tag{14.5}$$

14.4.8 Photoluminescence (PL) Spectroscopy

It is a method of light emission spectroscopy where the light emission initiates from a procedure named photo-excitation. When the light is focused onto a chemical, the electrons inside the material reallocate to energized states. As the electrons come down from the excited states to their equilibrium states, the energy is emitted as light. The intensity of the light is plotted versus the wavelength of the spectrum. PL spectroscopy is valuable in defining the

electronic structure and properties of samples as it provides the peak light intensity that chemicals are capable of emitting for a particular wavelength (Hussain and Patankar 2022).

14.4.9 Thermogravimetric Analysis (TGA)

TGA is a technique of thermal study where the mass of a material is gauged over time with the variation of temperature. This experiment delivers data about physical as well as chemical occurrences. The thermogravimetric information gathered from a thermal reaction is expressed as a plot of mass or percentage of initial mass on the y-axis against temperature on the x-axis. A TGA can be employed for the characterization of chemicals via the examination of distinguishing decomposition patterns (Hussain and Patankar 2022).

14.4.10 Vibrating Sample Magnetometer

Magnetic characteristics of a given material are examined using a Vibrating Sample Magnetometer (VSM). In a VSM, the process involved is the oscillation of a magnetic material in a DC magnetic field, thus creating an alternating voltage in a pickup coil. After that, the resultant voltage is amplified and acquired in a voltmeter (Hussain and Patankar 2022). The signal produced in a pickup coil is associated with the magnetic properties of a given material.

14.4.11 BET Isotherm Analysis

The specific surface area of a material can be determined via an analytical technique founded on the Brunauer–Emmett–Teller (BET) theory dealing with the physical adsorption of gas molecules upon the surface of a solid. A chemically inert gas is usually employed as the adsorbate. The most common adsorbate is nitrogen gas due to which

BET experimentations are usually executed at 77 K, i.e., the boiling point of nitrogen (Lowell et al. 2004).

During BET analysis, Langmuir's theory dealing with the monolayer molecular adsorption model is accepted for multilayer adsorption. The adsorption phenomenon is studied by plotting the volume of adsorbate adsorbed on the surface of the adsorbent against the P/P_0 value at constant temperature. Here, P and P_0 are the equilibrium and saturation pressure of the adsorbates at the adsorption temperature, and the graph is known as the BET adsorption isotherm.

BET equation is expressed as

$$\frac{1}{v\left[\left(\frac{P_0}{P}\right)-1\right]}=\frac{c-1}{v_m c}\left(\frac{P}{P_0}\right)+\frac{1}{v_m c},\ldots \tag{14.6}$$

where v and v_m are the total adsorbed gas amount and monolayer adsorbed gas amount correspondingly, while c is considered as the BET constant.

Equation (14.6) displays linear characteristics when $0.05 < P/P_0 > 0.35$. A straight line can be gained from the equation plotting $1/[v(P_0/P)-1]$ versus P/P_0 (between 0.05 and 0.35) which is identified as the BET plot. The values of v_m and c can be estimated from the slope A and intercept I of the straight line based on the following equations:

$$v_m=\frac{1}{A+I},\ldots \tag{14.7}$$

$$c=1+\frac{A}{I}.\ldots \tag{14.8}$$

After receiving the values of v_m and c, the following two expressions are employed to ascertain the total surface area, $S_{\text{total,}}$ and specific surface area, S_{BET}:

$$S_{\text{total}} = \frac{v_m N_s}{v}, \ldots \tag{14.9}$$

where N is Avogadro's number, V is the molar volume of adsorbate, and s is the adsorption cross section:

$$S_{\text{BET}} = \frac{S_{\text{total}}}{a}, \ldots \tag{14.10}$$

where a is the mass of the adsorbent (Rouquerol et al. 2014).

14.5 Magnetic Properties of Nanomaterials

14.5.1 Types of Magnetic Materials

The magnetic materials are categorized on the basis of the alignment of magnetic moment at the atomic level with respect to the surroundings (Hussain and Patankar 2022). The following are categories of magnetic materials viz.

- Diamagnetic
- Paramagnetic
- Ferromagnetic
- Antiferromagnetic
- Ferrimagnetic
- Superparamagnetic.

The elementary definitions of all these categories of magnetic materials are provided below.

14.5.1.1 Diamagnetic Materials

Diamagnetic substances are characterized by negative magnetic susceptibility. The magnitude of the magnetic susceptibility governs the strength of the diamagnetic character of the material. Magnetic reaction of such materials opposes the externally applied magnetic field.

The arrangement of magnetic moments of electrons in these materials is present in such a way that their individual magnetic moments annul each other. Therefore, each atom produces nil magnetic moment.

14.5.1.2 Paramagnetic Materials

If these materials are left under the effect of an externally applied magnetic field, then it is observed that the magnetic moment grows a torque that attempts to direct the magnetic moments along the direction of that outer magnetic field and enhances the magnetic susceptibility.

14.5.1.3 Ferromagnetic Materials

Ferromagnetic materials are characterized by domain structure which exhibits net magnetic moment. The atoms of these materials, in their domain, possess permanent magnetic moments. The magnetic dipole moments of the domains of the ferromagnetic substance get positioned along the direction of any externally used magnetic field. An order at the atomic level prevailing over a long range is observed to be present in ferromagnetic materials which makes the magnetic spins of unpaired electrons align with respect to one another in a zone recognized as the domain. When there is an operative magnetic field, the atoms of the ferromagnetic materials are present in the form of a domain inside the material. All those domains possess dissimilar alignment directions of magnetic moments. Therefore, the ferromagnetic substance stays as a whole non-magnetized. On using an external magnetic field, the domains switch and line up along the outer magnetic field.

14.5.1.4 Antiferromagnetic Materials

In an antiferromagnetic material, the atomic dipole moments of adjacent magnetic sites arrange themselves antiparallel to one another producing a less net magnetization. Such a material retains this property up to a

magnetic transition temperature. Beyond that temperature, its domain structure disintegrates and the material transforms into a paramagnetic material.

14.5.1.5 Ferrimagnetic Materials

These materials own a domain structure where magnetic dipole moments of adjacent magnetic sites having unequal values are ordered in a way that they are directed in opposite directions. The unbalanced values of the magnetic moments preserve a certain quantity of magnetization within each domain.

14.5.1.6 Superparamagnetic Materials

When the size of a bulk magnetic material decreases to the nanometer level, severe changes are witnessed in its physical characteristics including magnetic properties, for example magnetic moment, magnetic ordering temperature, and coercive field. The synthesis route, chemical components, and structure are the most affecting features for the display of exceptional characteristics by magnetic nanoparticles. Thermal variations can also weaken the coercivity and hysteresis of magnetic nanoparticles. Magnetic nanoparticles possessing dimensions of a few nm to a few tens of nm display superparamagnetism. Superparamagnetism is shown by tiny ferromagnetic or ferrimagnetic nanomaterials. Typically, magnetic nanoparticles having dimensions of less than a hundred nanometers, possess a single domain, letting the magnetization of the nanoparticles be estimated as one massive magnetic moment by summing the separate magnetic moments of every component atom. This estimation is named the “macro-spin approximation.” When the sizes of the nanoparticles are sufficiently small, the energy barriers for magnetization reversal, which are related to grain volume, turn out to be somewhat small in comparison to thermal energy. With adequate thermal

energy, their magnetization can reverse direction arbitrarily over small durations, and the time between two reverses is termed the Neel relaxation time. In the case of superparamagnetic nanomaterials, the mean magnetization of the particles is almost zero when no external magnetic field is used and the measurement time for the magnetization of the nanoparticles is more than the Neel relaxation time. With an outer magnetic field operated, the nanoparticles are magnetized like paramagnets, but with far superior susceptibility.

14.5.2 Suitable Magnetic Materials for Biomedical Applications

The characteristics of superparamagnetism are useful compared to other magnetic effects for numerous medical uses, because superparamagnetic nanoparticles display great magnetic moment and function as one massive paramagnetic entity showing a quick reaction to outer magnetic fields having minor coercivity and remanence even at normal ambient temperature (Cardoso et al. 2018).

It is notable that pure metallic magnetic nanoparticles display greater magnetic moments in comparison to magnetic oxides. But, they have the drawback of being pyrophoric due to which they become reactive to oxidizing agents and difficult to produce taking water as the medium (Hussain and Patankar 2022).

Table 14.2 shows the magnetic properties reported for various magnetic metal oxide-based nanomaterials used for biomedical purposes (Martins et al. 2021).

Table 14.2 Magnetic properties of selected biomedically investigated metal oxide-based nanomaterials (Martins et al. 2021)

Magnetic nanomaterial	**Ms (emu g^{-1}); Saturation field (T)**
Gd doped Nickel Ferrite	50.3;7
$Co_{\chi}Fe_{3-\chi}C$	52;2

Magnetic nanomaterial	Ms (emu g^{-1}); Saturation field (T)
$CoFe_2O_4$	71;2
Fe_2O_3@PAA	70;0.05
Clustered Fe_3O_4 NPs	63.7;2
Fe_3O_4@Au	30;0.5
$CoFe_2O_3$@DMSA/DOX	107.81;4
FeCo@C-PEG	192;1.5
Fe_3O_4@ZrO_2	26.5;2
γ-Fe_2O_3	63;3.5
$Zn_xMn_{1-x}Fe_2O_4$	110;3
P(PEGMA-AA) @Fe_2O_3	10.2;4
Fe_3O_4/hydroxyapatite/chitosan	3.04;0.4
Fe_3O_4/PANI@Si	57;1
Fe_3O_4/cellulose	10;1
Fe_3O_4@SiO_2@PMIDA	60;1
Ag@Fe_3O_4-PEI NPs	50.5;1

14.6 Biomedical Applications of Magnetic Metal Oxide Nanomaterials

The performance of a magnetic material relies upon its structure particularly the electronic configuration and orientations of magnetic moment, if any. Each of the possible applications of magnetic nanomaterials needs special physical, chemical, and magnetic properties of the nanomaterials. These properties are governed by their synthesis method which controls their size, size-distribution, morphology, and magnetic properties. Additionally, the surface functionalization of magnetic

nanomaterials takes a significant part in their environmental and biomedical uses.

14.6.1 Medical Imaging

14.6.1.1 Magnetic Resonance Imaging (MRI)

MRI is a clinical method which works based on the theories of proton Nuclear Magnetic Resonance (NMR) and is employed to see interior structures of the body. MRI technology is implemented based on the fact that body tissues contain water molecules, and therefore protons (^{1}H nuclei) (Deka and Deb 2018). The image of the MRI instrument and a representative MR image are shown in Fig. 14.10.

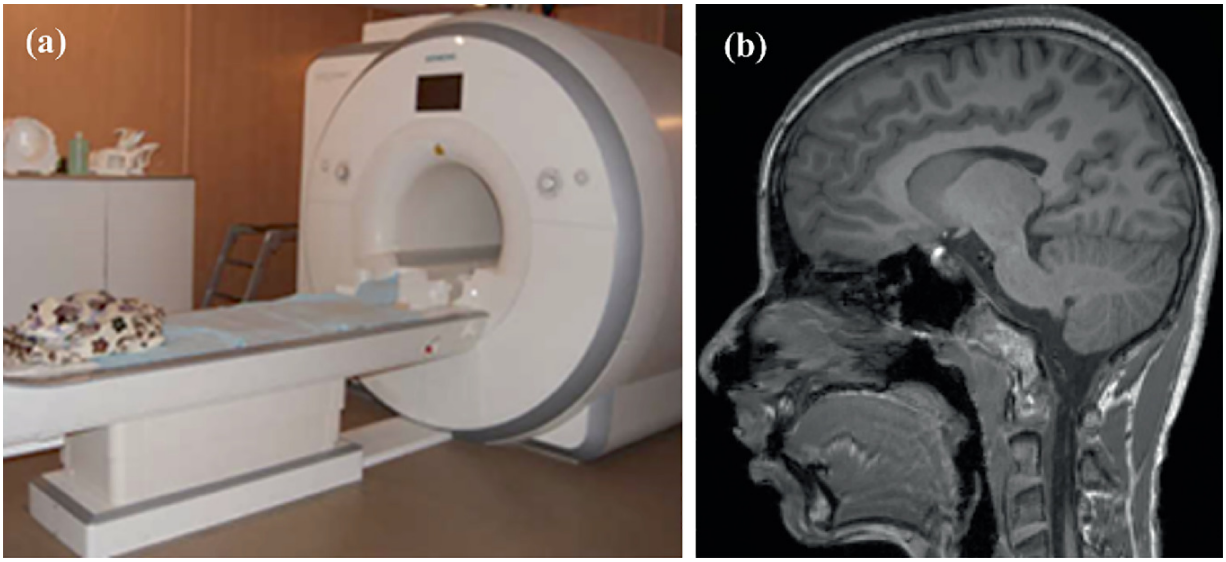

Fig. 14.10 **a** MRI machine; **b** MRI of brain.
Reproduced with permission from Deka and Deb (2018)

Proton (^{1}H) possesses a positive charge with two spin states $+\frac{1}{2}$ and $-\frac{1}{2}$. When there is a spinning charge, it produces a magnetic dipole. When a magnetic field B_0 is used on ^{1}H nuclei along the Z direction, two quantized spin states are obtained. A number of nuclei will precess along B_0 (α state) while the remaining precess in the opposite

direction (ß state) as demonstrated in Fig. 14.11 (Deka and Deb 2018).

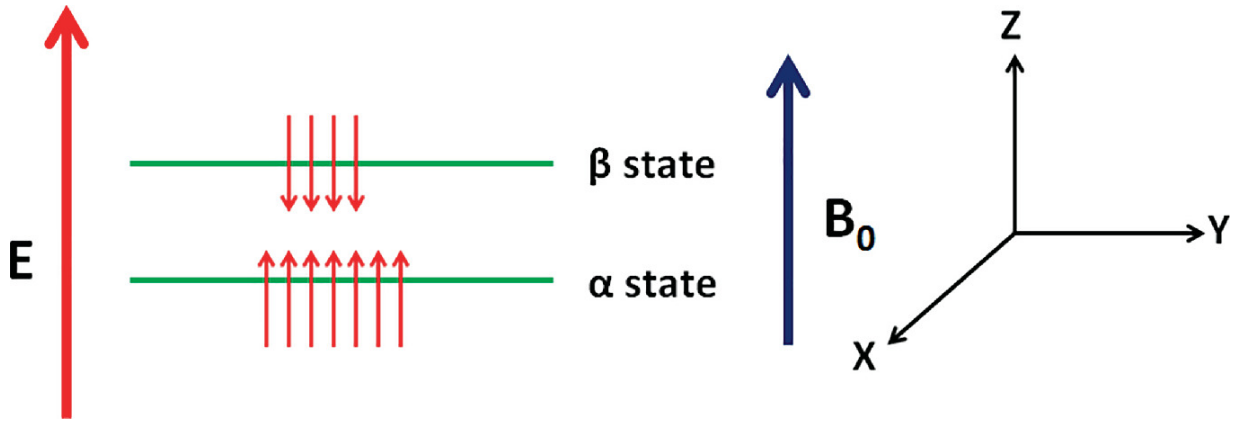

Fig. 14.11 Zeeman splitting of proton nuclei.
Reproduced with permission from Deka and Deb (2018)

The quantity of nuclei in the low energy state is greater compared to that in the elevated energy state. The differential population of nuclei with spin-up continues precessing along the direction of B_0. If the radio frequency (RF) pulse is used in the *X* direction, the vector along the *Z* direction starts rotating and the nuclei begin precessing in the *XY* plane as shown in Fig. 14.12 (Deka and Deb 2018).

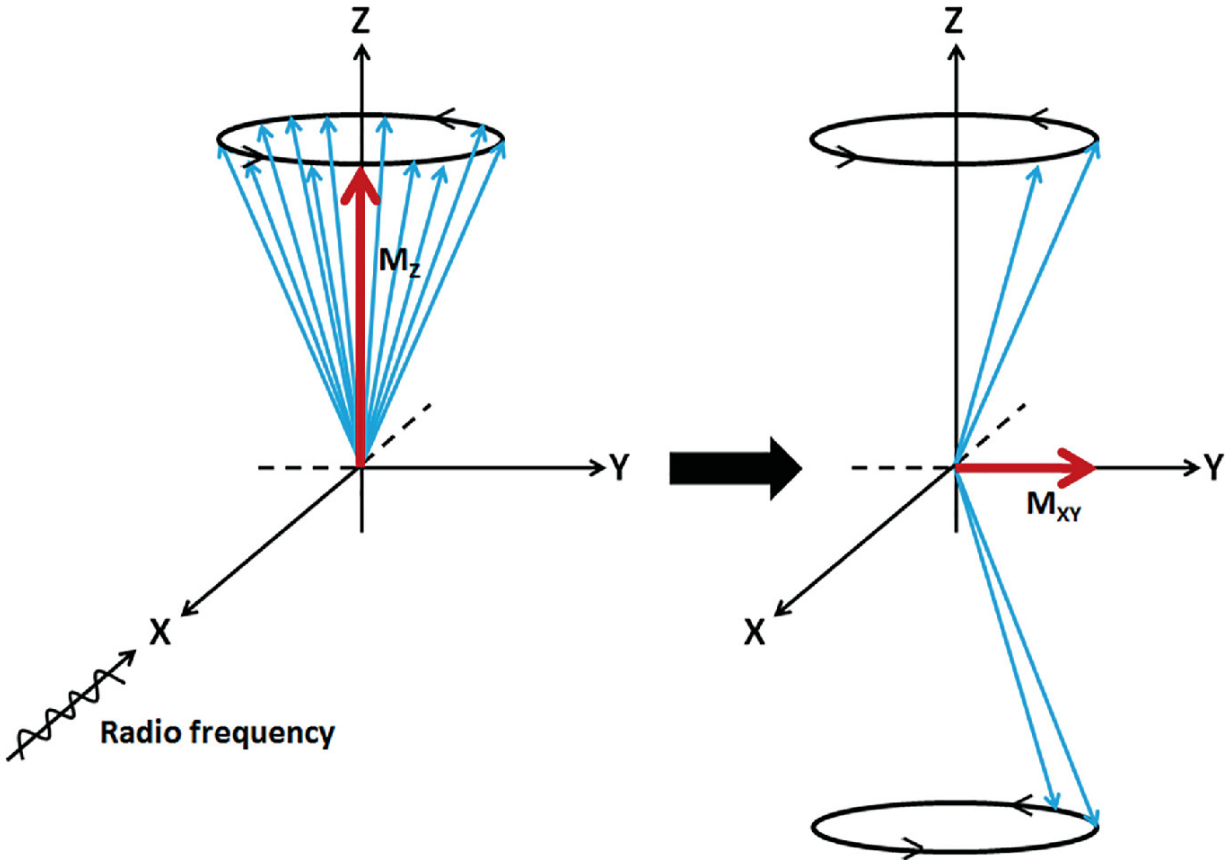

Fig. 14.12 Induction of RF pulse.
Reproduced with permission from Deka and Deb (2018)

Once the RF pulse is turned off, the spin of the protons gets realigned along the direction of B_0 by means of relaxation. During this relaxation, it produces radio-waves and MR images via Fourier Transform of those radio signals. The magnetic field employed in an MRI machine ranges from 0.2 to 9.4 T (Deka and Deb 2018).

The spin relaxation of protons occurs in two ways:

1. T_1 or Spin–lattice relaxation

2. T_2 or Spin–spin relaxation.

T_1 relaxation is the procedure of increase in net magnetization parallel to B_0, i.e., M_Z to its initial maximum value (M_0) (Fig. 14.13a). This takes place by the transport

of surplus energy of magnetic spins of the excited ^{1}H nuclei to the adjacent lattice, and therefore T_1 relaxation is also named spin–lattice relaxation. T_2 relaxation is the method of decay or dephasing of the transverse components of magnetization, i.e., M_{XY} (Fig. 14.13b). A dipole–dipole interaction between two protons leads to this dephasing and thus T_2 relaxation gets another name spin–spin relaxation.

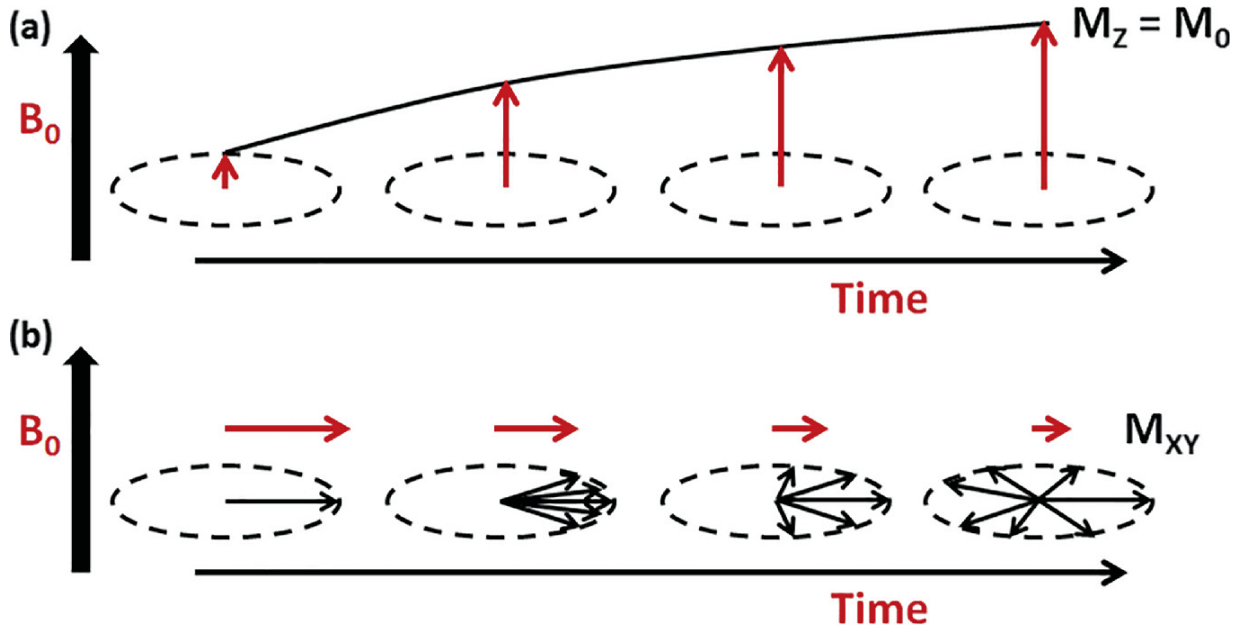

Fig. 14.13 **a** T_1 and **b** T_2 relaxation.
Reproduced with permission from Deka and Deb (2018)

The inverses of T_1 and T_2 relaxation time are recognized as relaxation rates R_1 and R_2, respectively (Deka and Deb 2018).

MR imaging frequently faces problems as healthy tissues and lesions show only minor dissimilarity in relaxation time. So, in many situations, while imaging a brain tumour with the help of an MRI scanner, the tumour fraction cannot be reliably distinguished from the ambiances. This can be confronted by using MRI Contrast Agents (CAs). Contrast agents improve the contrast of MR

images by interacting with the adjacent water protons. These agents are based on paramagnetic, superparamagnetic, or ferromagnetic compounds that shorten the relaxation times of water protons (Deka and Deb 2018). There are two major sets of CAs classified based on the relaxation procedure they mainly accelerate, i.e., T_1-CAs and T_2-CAs. While T_1-CAs bring about a positive contrast, i.e., a ^1H NMR signal of the concerned tissue rises, substances inducing the T_2 relaxation bring about a reduction of a local proton signal and, consequently, they show a “negative enhancement” (Deka and Deb 2018). Usually, paramagnetic metal-based compounds are regarded as positive MRI contrast agents, and superparamagnetic iron oxides are utilized as T_2-based contrast agents (Deka and Deb 2018).

Superparamagnetic iron oxide nanoparticles (SPIONs) have achieved substantial consideration as a class of T_2-based imaging agent during Magnetic Resonance Imaging (MRI) because of their exceptional magnetic properties. It is demonstrated that spherical magnetic iron oxide NPs show greater T_2 relaxation rates and high relaxivities. Because of this, after the delivery of SPIONs, MRI results display comprehensible and prominent signal intensity during tumour imaging, organ-specific imaging, and even during whole-body imaging (Siddique and Chow 2020). SPION-tagged macrophages are able to attack tissues via inflammatory procedures. This technique has been practiced on a model of inflammation in the central nervous system. Once the internalization of SPIONs occurred, microglial cells were noticed during an MRI scan (Siddique and Chow 2020). With the help of superparamagnetic iron oxide and perfluorocarbon nanoemulsions, quantitative checking of Tumour Associated Macrophages (TAM) is achievable with MRI-based TAM imaging (Siddique and Chow 2020). In a research work by Silva et al. on

multimodal imaging, a multifunctional targeting nanoparticle probe for pancreatic cancer has been presented based on 1,2 Distearoyl-sn-glycero-3-phosphoethanolamine-N-amino (polyethylene glycol)-modified SPIONs, attached with the plectin-1 antibody. Results of MRI and in vivo optical imaging confirmed that the NP probe was vastly gathered in MIAPaCa2 and XPA-1 carcinoma cells and, therefore, could be utilized as a theranostic probe for fluorescence and MRI to image pancreatic cancer (Siddique and Chow 2020). Regulation of the dimension of the iron oxide NPs within 1–100 nm scale guides to regulated magnetic properties varying from paramagnetic to ferrimagnetic, which considerably enhances their scientific execution and use as T_1- or T_2-based imaging agents. Though SPIONs are mostly known as T_2-based MRI contrast agents, however, zwitterion-coated SPIONs demonstrate T_1 contrast improvement similar to gadolinium-based contrast agents which are more popular as T_1-based MR imaging agents. In addition, these SPIONs show effective renal clearance (Singh and Amiji 2022). Manganese oxide nanoparticles also possess insignificant toxicity and decent T_1-based contrast effects (Siddique and Chow 2020).

14.6.1.2 Other Imaging Applications

In addition to MRI, magnetic metal oxide nanomaterials are applicable for other imaging techniques like Positron Emission Tomography (PET), Computed Tomography (CT), and Near-infrared fluorescence (NIRF) imaging. PET is an imaging method where a positron-releasing radiotracer is injected into a patient and allowed to get distributed physiologically within the body. The discharged positron generates two back-to-back 511 keV photons. These two photons are detected, and a 3D image is attained through analytical or statistical reconstruction algorithms (Guerra

et al. 2016). In CT, X-rays are passed through the patient and then allowed to fall onto X-ray detectors that can calculate the transmission or attenuation values. After that, the values gathered by the detectors are sent to a computer that employs special mathematical methods to reconstruct the CT image via image reconstruction algorithms. Nowadays, all innovative CT scanners employ iterative reconstruction algorithms (Seeram 2015). NIRF imaging is a promising medical technology that involves the delivery of a fluorescence-based imaging agent which is excited within the tissues at near-infrared region. The resultant fluorescence is detected to construct a two-dimensional (2D) image (Zhu and Sevick-Muraca 2015). For joint MRI and magnetomotive ultrasound PET/CT of sentinel lymph nodes, ^{68} Ga-labelled SPIONs were projected. The outcome of the research proved that the SPIONs delivered feasible contrast improvement (Fig. 14.14) (Evertsson et al. 2017).

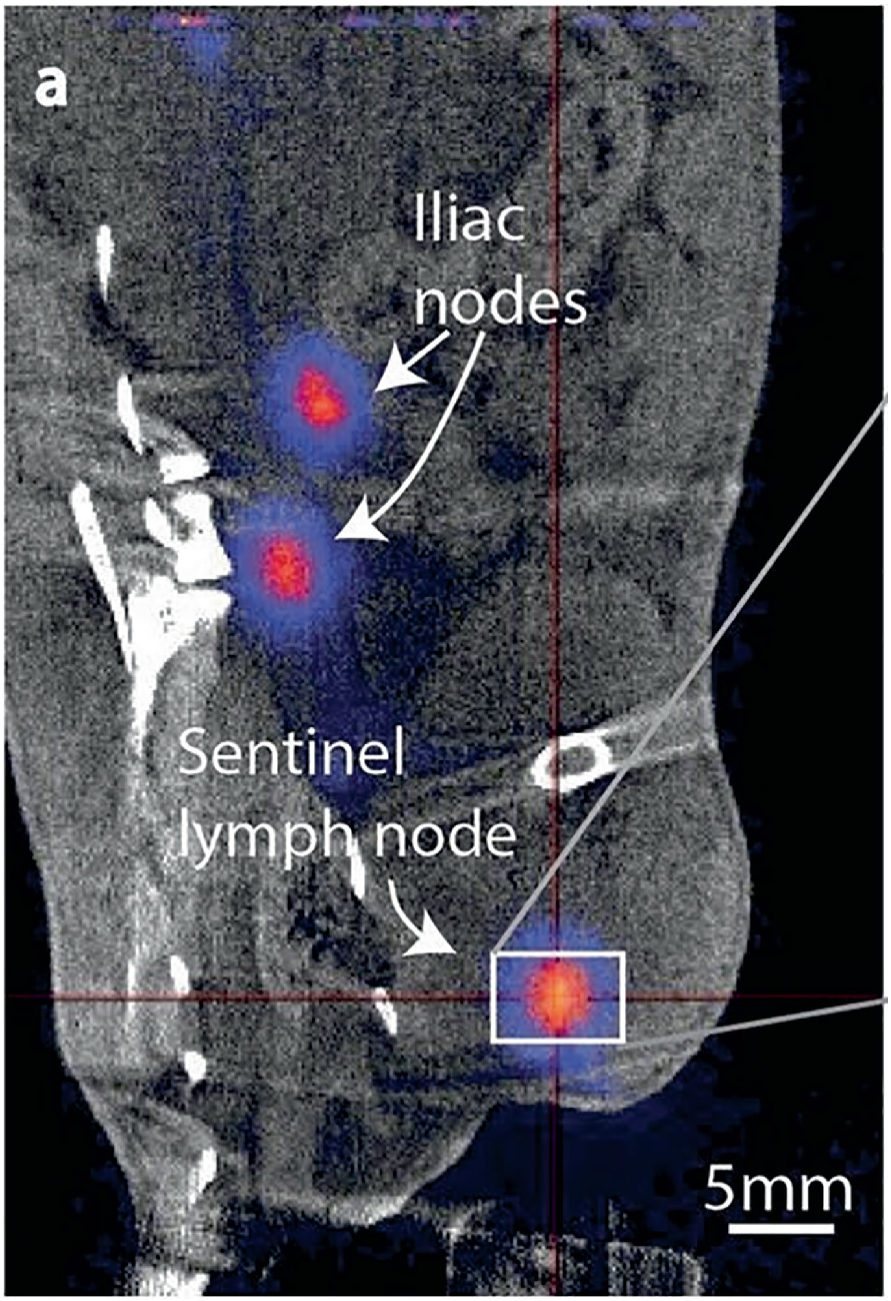

Fig. 14.14 Coronal PET/CT image of female Wistar rats showing ^{68}Ga-labelled superparamagnetic iron oxide nanoparticles gathering at sentinel lymph node and two iliac lymph nodes.

Reproduced with permission from Evertsson et al. (2017)

MnO-based nanoparticles, in combination with NIR fluorescence imaging and MRI, are able to aid in fighting in opposition to myocardial infarction (MI) (Fig. 14.15) (Zheng et al. 2018). MnO/SiO_2 core–shell can be employed for multimodal imaging. The localization of the core–shell

structure can be watched using MRI and polypropylene fumarate scaffolds (Siddique and Chow 2020).

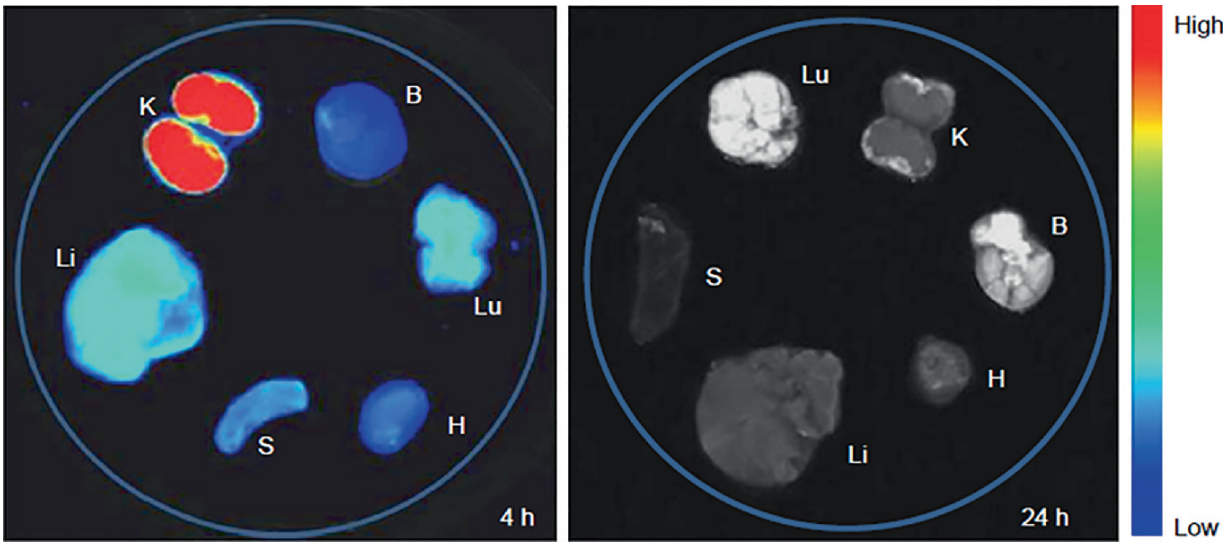

Fig. 14.15 NIRF images of organs of regular mice after 4 and 24 h of injecting MnO–PEG–Cy5.5 nanoparticles (Zheng et al. 2018). Originally published by and used with permission from Dove Medical Press Ltd.

Cerium oxide NPs coated with ^{89}Zr exhibited huge capability to be used in PET imaging (Siddique and Chow 2020).

14.6.2 Magnetic Hyperthermia (MHT)-Based Treatment

In clinical science, the word “hyperthermia” generally represents a remedial technique by which a selected area of the body of a patient is subjected to a temperature beyond 40 °C. A further recent type of this technique is magnetic hyperthermia (MHT), where the temperature rise is realized by using an alternating magnetic field (AMF) on a magnetic substance, mostly iron oxide (Fig. 14.16) (Périgo et al. 2015). This method can influence the role of cell membranes, proteins, nucleic acid repair enzymes, cellular structures, etc. and thus demolishes cells. Particularly, the tumour cells lack the endurance to abrupt alteration of temperature, and, therefore, they can be

damaged very easily (Peiravi et al. 2022). MNP-based magnetic hyperthermia is a proficient cancer healing method. The magnetic nanoparticles are sufficiently tiny so as to go through the biological walls for aiming the locations of the tumour exclusively. Usually, heat release by magnetic substances under the influence of a high-frequency magnetic field occurs via (i) eddy current loss, (ii) hysteresis loss, and (iii) relaxation loss. In spite of eddy currents being considerable in the case of bulk substances, their role in thermal dissipation in MNPs during MHT is trivial. The externally provided magnetic field frequency must be in the low radio-frequency span of 100–300 kHz for attaining the necessary remedial temperature for a successful cancer cell demolition. The number of magnetic nanoparticles to be administered must be at a nominal concentration preventing probable side-effects. During magnetic hyperthermia, magnetic nanoparticles are injected as colloids into the tumour region. Heat production heavily depends on the structure and magnetic behaviour of these nanoparticles. Furthermore, it relies upon the parameters related to the external field like amplitude and frequency (Rajan and Sahu 2020).

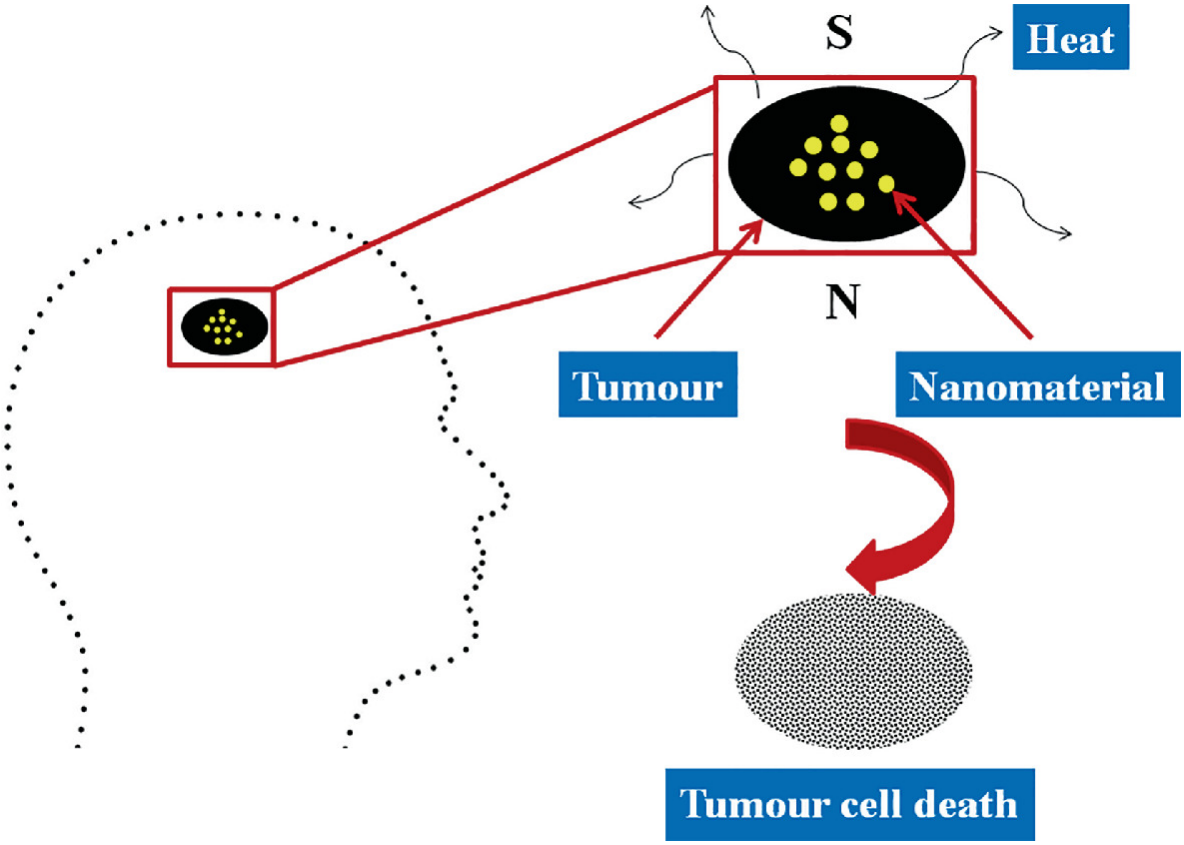

Fig. 14.16 Schematic representation of magnetic hyperthermia therapy

In magnetic transition metal oxides, the key process of production of heat is controlled by hysteresis losses, which intensely rely upon the dimension of the particles. Particularly, in the case of magnetic oxides having dimensions under the single-to-multidomain threshold, two processes make the nanoparticles proficiently convert the electromagnetic energy into heat: (i) Neél relaxation, centred on the particles' magnetic moment alignment along the externally employed magnetic field and their redirection to the equilibrium state in absence of magnetic field; (ii) Brownian relaxation, which is centred upon the friction between the nanoparticle surface and the solvent due to the torques produced during the alterable orientation of the magnetic moment by the magnetic field and the reorientation along the equilibrium state when the external magnetic effect is zero, which incites spin of the nanoparticles. Brownian and Neél fluctuations are

characterized by diverse magnetic relaxation periods, controlling the heat yield of the nanoparticles for particular intensity and frequency of the magnetic field employed. Both processes occur simultaneously, and the heating process is determined by the one with the smaller characteristic time. SAR or Specific Absorption Rate signifies standardized factors that lead to gauging and calculating the competence of a certain substance to convert electromagnetic energy into heat at definite magnitudes of amplitude and frequency of the magnetic field. Experimentally, SAR (expressed in units of Wg^{-1}) is estimated as stated by the equation given below

$$\mathrm{SAR} = \frac{C\Delta T}{m\Delta t}, \ldots \tag{14.11}$$

where C implies the specific heat capacity of the medium (usually, it is considered equal to that of water, which is 4185 JL^{-1} K^{-1}), m is the concentration of the relevant transition metal (expressed in the units of gL^{-1}) of the magnetic substance in solution, and $\Delta T/\Delta t$ is the slope of the initial linear segment of the temperature vs. time plot (Cardoso et al. 2018).

In the majority of the efforts centred on magnetic hyperthermia, Fe_3O_4 has been used as the magnetic NPs. Bai et al. demonstrated that the existence of graphene next to iron oxide nanoparticles enhances the magnetic hyperthermia performance, simultaneously maintaining the magnetism in the composite NPs (Farzin et al. 2022). Gupta and Sharma inspected Stevioside-Fe_3O_4 NPs to understand their biocompatibility, cellular uptake efficacy, and calorimetric MHT (Farzin et al. 2022). Albuquerque Reg et al. estimated the therapeutic property of magnetic hyperthermia by aminosilane-coated superparamagnetic Fe_3O_4 nanoparticles in animal glioblastoma (Farzin et al. 2022). Mamani et al. worked on MHT treatment in

glioblastoma tumour on-a-chip prototype by Fe_3O_4 nanoparticles coated with aminosilane (Farzin et al. 2022). Ramirez-Nunez et al. demonstrated in vitro MHT by polyphenol-coated Fe_3O_4@ɣFe_2O_3 NPs (Farzin et al. 2022). Salimi et al. stated that MHT of breast cancer cells with dendrimer-coated iron oxide (IONPs) (Farzin et al. 2022). Ling et al. employed a polymethylmethacrylate (PMMA)–Fe_3O_4 for extremely proficient MHT ablation of tumour (Farzin et al. 2022). Ma et al. used Fe_3O_4–Pd Janus nanoparticles for magnetic-photo hyperthermia (Farzin et al. 2022). Suleman and Riaz carried out 3D in silico investigation of magnetic fluid hyperthermia of breast tumour by Fe_3O_4 MNPs (Farzin et al. 2022). Murakami and co-workers used hyperthermia therapy for bone cancer by Fe_3O_4/hydroxyapatite nanocomposite (Farzin et al. 2022). Mondal and co-workers synthesized HAP-coated Fe_3O_4 NPs for MHT cancer healing (Farzin et al. 2022).

In addition to iron oxide NPs, a few other nanosystems have also been reported to be showing efficiency in magnetic hyperthermia-based treatment. Heidari et al. examined the consequence of magnetic fluid hyperthermia by dextrin-coated $Fe_{0.5}Zn_{0.5}Fe_2O_4$ ferrite nanoparticles on implanted melanoma in mouse models (Farzin et al. 2022). Bhardwaj et al. explored in vitro hyperthermic result of Mn–Zn ferrite nanoparticles on cervical and breast cancer cells (Farzin et al. 2022). Xie et al. produced multi-modal Mn–Zn ferrite nanomaterials for magnetically generated cancer-specific hyperthermia (Farzin et al. 2022). Albarqi and co-authors reported effective magnetic nanoclusters made up of Co- and Mn-doped, hexagonal iron oxide nanoparticles coated with biocompatible PEG–PCL (poly(ethylene glycol)-b-poly(ε-caprolactone))-based nanocarriers having improved heating competence for organized magnetic hyperthermia (Farzin et al. 2022).

Ahmad and co-workers demonstrated silica-coated gadolinium-doped lanthanum strontium manganite ($La_{0.54}Sr_{0.27}Gd_{0.19}MnO_3$) NPs for auto-regulated hyperthermia applications (Farzin et al. 2022). Melnikov et al. proposed Ag-doped manganite NPs ($La_{(1-x)}Ag_{(x)}MnO_3$) for temperature-regulated clinical hyperthermia (Farzin et al. 2022).

14.6.3 Drug and Gene Release

14.6.3.1 Drug Delivery

Magnetic nanoparticles can be influenced by the use of an outer magnetic field. This phenomenon leads to novel applications where drugs which are connected to a magnetic material can be delivered to particular regions inside the human body employing a magnetic field. Usually, targeting is attained by fixing a molecule that identifies another molecule that is specific to the preferred target spot (Bucak et al. 2012). Some of the reported research on the application of magnetic metal oxide nanomaterials for drug delivery are mentioned below.

Superparamagnetic iron oxide nanoparticles have been applied for exact tissue targeting during MRI scans. SPIONs can be administered intravenously into the blood and acquired by Reticuloendothelial System (RES). Once inside the cells, the nanoparticles can be checked by MRI. This method can prove to be extremely efficient for the observation of macrophages for the detection of the composition of Blood–Brain Barrier (BBB) in various ailments leading to inflammation (Sahu et al. 2021). Ferumoxtran-10, a dextran-coated iron oxide nanosystem, gives a steady imaging indicator to exclude brain tumours during surgical procedures and resides inside the brain for a considerably long time even after surgery aiding in the conduction of postoperative MRI study (Sahu et al. 2021). Aikawa et al. employed cross-linked iron oxide fluorescent

nanoparticles for immediate arrest of macrophages for evaluation of inflammatory reaction of atherosclerotic plaques (Sahu et al. 2021). SPIONs are also helpful for controlling and supervising of the remedial effect of stem cells on myocardial infarction by dint of their exceptional magnetic behaviour and suitable biocompatibility (Sahu et al. 2021). Another application of SPIONs is in the detection of Hepatocellular Carcinoma (HCC) during liver imaging where these nanoparticles are used as pre-treatment in the form of intravenous injection (Sahu et al. 2021). Sharifianjazi et al. (2021) modified iron oxide nanoparticles by attaching cyanine dye to them for optical imaging and subsequent cross-linking of green fluorescent protein-specific small interfering RNA for intracellular drug delivery. Sharifianjazi et al. (2021) reported the modification of iron oxide (Fe_3O_4) nanoparticles by attachment of doxorubicin (DOX) as a new drug release scheme. Another group (Sharifianjazi et al. 2021) examined the discharge performance of methotrexate (MTX) drug from MTX-loaded Fe_3O_4/PLA and MTX-loaded Fe_3O_4/PLA–PEG NPs. Subsequently, the competent anticancer action of biocompatible MTX-loaded Fe_3O_4/PLA–PEG to MCF-7 cells was achieved. Sharifianjazi et al. (2021) evaluated the performance of drug discharge of pH-responsive Fe_3O_4@PDA magnetic nanoparticles. In another research work carried out by Sharifianjazi et al. (2021), the novel nanotransporter of β-CDPDA magnetic nanoparticles was developed, which has dual advantages of (i) host–guest relations of hydrophobic medicines and cyclodextrins (CDs) and (ii) attractive superparamagnetic properties of Fe_3O_4 nanoparticles. Sharifianjazi et al. (2021) employed doxifluridine (DFUR) as an antitumour system to get core–shell Fe_3O_4@DFUR–LDH system with outstanding magnetization, indisputable drug discharge,

and targeted drug release. Hashemi- Sharifianjazi et al. (2021) utilized 3,4-dihydroxy-L-phenylalanine/Fe_3O_4 for target-specific release of the breast cancer medicine in mice in the presence as well as the absence of a magnetic field. Sharifianjazi et al. (2021) entrapped Fe_3O_4 nanoparticles and 5-fluorouracil in thermosensitive PNIPAM and attached chitosan and rhodamine 6G (baz) to their exterior to facilitate drug release for (i) intracellular imaging and (ii) thermo-chemotherapy of cancer.

Among the metal ferrites, cobalt ferrite ($CoFe_2O_4$) magnetic nanoparticles have been established as potential drug transporters. The internal magnetic field of $CoFe_2O_4$@$BaTiO_3$ nanoparticles employed for the transport of anti-HIV drugs across the BBB combats the outer field via the electric force of the bond between medicine and transporter that facilitates them to supply medicine in a measured way (Nair et al. 2013). Curcumin has been employed to cure a variety of tumour cells. Sharifianjazi et al. (2021) evaluated the effectiveness of curcumin drug loading in polyethylene glycol (PEG)/cobalt ferrite core–shell (PCC) nano-assembly to be 74.8% (w/w%). Sharifianjazi et al. (2021) applied a PEG shell on cobalt ferrite nanoparticles and attached folic acid (FA) to the exterior of the particles to enhance the internalization in HeLa cancer cells by receptor intervention. Sharifianjazi et al. (2021) produced $CoFe_2O_4$/PDA/ZIF-8 (CoPZ) NPs in which they distinguished two dissimilar types of discharge actions with pH or near-infrared stimulus for hydrophobic camptothecin (CPT) and hydrophilic DOX. Cobalt ferrite nanoparticles covered with tripolyphosphate (TPP) and chitosan polymer (Cs) were used as transporters for the antioxidant drug doxorubicin (DOX) (Ghanbari et al. 2021). Two types of magnetic core–shell substances, cobalt ferrite/chitosan (CFC) and manganese ferrite/chitosan (MFC), were employed as medicine transporters to

generate the synergistic result of the magnetic hyperthermia-cancer medicine. During the research, 5-Fluorouracil (5-FU) was chosen as a model tumour medicine (Yildirim and Ispirli 2022). Manganese oxide nanoparticles have been explored for brain cancer treatment. It is worth mentioning that additional investigation is essential to know the biodistribution, pharmacokinetics, harmfulness, and remedial applications of such nanoparticles. However, it must be acknowledged that they display a huge prospect in efficiently curing brain tumours by lessening the unfavourable results of old-style treatments (Ahamed et al. 2023).

14.6.3.2 Gene Delivery

Magnetic nanoparticle-based gene release or transfection is known as “magnetofection”. The competence of this transfection method is already established in a range of cells. The method is centred on the combination of genetic substances with magnetic nanomaterials. For in vitro magnetic nanomaterial-based transfection, the particle/DNA complex is brought into the cell culture where the magnetic field gradient formed by rare earth magnets located underneath the cell culture makes the complex get sedimented and improves the pace of transfection. On the other hand, in the case of in vivo transfection, magnetic fields applied on the objective location possess the capability to not just improve transfection but also aim the therapeutic gene at a definite organ or place inside the human body. In general, particles transporting the remedial gene are injected intravenously, and intense, high-gradient outer magnets are employed to arrest the particles when they run via the blood flow. When arrested by the magnetic field, the particles become bound to the target, where they are absorbed by the tissue. The remedial genes can be discharged either by means of charge exchanges, breakdown of the polymer matrix, or

enzymatic cleavage of the cross-linking molecules. On the other hand, if the DNA is entrenched inside the matrix, like with hydrogels, alternating fields can be used for heating the particles and liberating the genes from the magnetic transporter (Dobson 2006).

Magnetic metal oxide nanomaterials can also be used as gene carriers. Interestingly, MRI contrast can also be concurrently achieved using such systems along with superior gene transfection. It is well known that Polyethylenimine (PEI), consisting of several amino groups, is applicable for gene delivery. Core–shell structure of PEI-modified iron oxide nanoparticles effectively gets attached to siRNA to grow well-dispersed nanomaterials (Liu et al. 2011). BUCT–PGEA (ethanolamine functionalized poly(glycidyl methacrylate) introduced from the surface of Fe_3O_4@SiO_2 nanomaterials) utilized an outer magnetic field to show improved transfection efficacy (Wang et al. 2016). Stearic acid-modified PEI–SPIONs having low molecular mass PEI as the shell and SPIONs as the core can also efficiently get attached to DNA for efficient gene transfection (Wan et al. 2013).

An amalgamation of gene transfection with magnetic mediated hyperthermia (MMH) is also quite fruitful, particularly in terms of improved antitumour effectiveness. Tang et al. (2008) built a new heat-productive gene expression scheme, by modification of MnZn ferrite nanoparticles using PEI and then putting heterogonous genes. It is possible to raise the expression of heterogonous genes up to 10–500 folds over the background along with controlled hyperthermia. In that research, heat energy supported gene expression by aiding the transcription and translation of the genes. On the other hand, zinc ferrite ($ZnFe_2O_4$) nanoparticle-aided downregulating of heat shock proteins (HSP) expression is able to enhance the

antitumour efficiency of magnetic mediated hyperthermia (Yin et al. 2014).

Dextran-coated SPIONs can encourage autophagy of dendritic cells and thus protect them against apoptosis (Wu et al. 2017). Superparamagnetic iron oxide nanoparticles can also endorse autophagy through stimulation of the production of reactive oxygen species (ROS), consequently killing tumour cells (Khan et al. 2012; Du et al. 2017). Furthermore, superparamagnetic iron oxide nanoparticles can bring on temperature-sensitive autophagy, quickly breaking cell membranes and endorsing tumour apoptosis (Sadhukha et al. 2014). In another study, a coformulation complex of FGF2B-LK15-8R (FLR), DNA, and SPIONS was created for competent magnetically facilitated gene release of pDNA (Blokpoel et al. 2021). GregorSersa group demonstrated that surface-modified SPIONs combined with polyacrylic acid (PAA) and polyethylenimine (PEI) (SPIONs–PAA–PEI) showed to be reliable and effectual for the purpose of magnetoreception of cells and tumours in mice (Prijic et al. 2012). Another research venture employed the SPIONs–PAA–PEI complex for the transport of plasmid DNA encoding short hairpin RNA in opposition to the melanoma cell adhesion molecule (MCAM) for investigation of the in vivo antitumour and antiangiogenic properties on melanoma tumours of mice (Prosen et al. 2014), and for the survey of the accretion, distribution, uptake, and the resulting healing process (Prosen et al. 2016). Complexes made of bacterial magnetic particles, PEI, and DNA, in the presence of a magnetic field, can improve the gene expression of the pCMVβ plasmid in the muscles of the legs (Xiang et al. 2007). In a very recent study, iron oxide nanoparticles with considerably even shape and size distribution were functionalized with PEI, and the resultant system noticeably upgraded the gene release to bone marrow-derived mesenchymal stem cells

(BM-MSCs) with the help of magnetic force (Xu et al. 2022).

14.6.4 Bio-separation

The field of biotechnology has a serious requirement for easy, quick, and efficient procedures to remove biomolecules from suspensions. This removal can be performed with the help of a magnetic force by attaching the target biomolecules with MNPs. Magnetic bio-separation is an easy, reliable, and flexible technique, which has got great consideration in biomedical purposes because of the significant properties of magnetic nanomaterials like huge surface-to-volume ratios, biocompatibility, and low toxicity (Fatima and Kim 2017).

Zheng et al. developed phenylboronic acid-Fe_3O_4@polydopamine (Fe_3O_4@PDAPBA) magnetic microspheres to assess their target specificity and binding by employing standard glycoproteins and nonglycoproteins (Fatima and Kim 2017). Easy removal and separation of neural stem cells may result in new treatment procedures in regenerative medication. Therefore, Fe_3O_4 MNPs within a silica shell possessing amine terminal groups were attached with an anti-CD133 antibody, which is particular to the cluster of differentiation 133 biomarker (CD133) of the neural stem cells (Lui et al. 2013). Xu et al. (2011) produced iron oxide-based magnetic nanoparticles modified with polymer brushes of poly(2-hydroxyethyl methacrylate) which got connected to more proteins than typical commercial magnetic particles. Invertase is an industrially important enzyme. Therefore, it was attached to chitosan encapsulated ɣ-Fe_2O_3 magnetic nanoparticles to make its cyclic use possible by magnetic separation (Waifalkar et al. 2016). A new approach centred on the integration of the inverse emulsion cross-linking and colloidal assembly method was employed for synthesizing porous magnetic

Fe_3O_4/histidine (His) composite nanoclusters having an elevated saturation magnetization as well as extraordinary protein adsorption ability (Yang et al. 2015). Lan et al. stated magnetic nano rattles have a Fe_3O_4/polymethyl methacrylate (PMMA) composite nanospherical core and a mesoporous SiO_2 shell that showed an adsorption quantity of 400 mg g^{-1} of lysozyme (Lan et al. 2012). Fe_3O_4/carboxymethylated chitosan/poly (3-acrylaminophenylboronic acid) (Fe_3O_4/CMCS/PAAPBA) nanospheres were proven as capable of flexibly arresting and liberating glycoproteins with great target specificity and recovery inside a standard protein mixture, a pure protein solution, and a biological model (Yang et al. 2017). Guo et al. (2016) demonstrated magnetic nanospheres having a mesoporous copper oxide shell for selective separation of haemoglobin from thinned human blood.

14.6.5 Lab-on-a-Chip Devices

Lab-on-a-chip (LOC), frequently expressed as total micro analysis systems, is employed for the installation of various preferred operations within one chip in a region of a few centimeters having the capability to sense ailment indicators, toxins, and local medicine release (Anik et al. 2021). Sheng Lin et al. demonstrated controlled discharge of diclofenac with the help of iron oxide NPs (Anik et al. 2021). This led to fast drug delivery, and experiments on glioblastoma cell culture showed that such a microfluidic system can be utilized for tissue engineering purposes (Lin et al. 2012). $MnFe_2O_4$-based microfluidic system has been employed for detection of influenza virus (Hung et al. 2012). These magnetic nanoparticles possessed extremely elevated sensing capacity, low range of detection, and lasting thermal strength. The microfluidic chip has also been demonstrated in medical samples.

The past several years have seen an intense increase in the amount of research causing the development of Lab-on-a-Chip (LOC) devices for the synthesis of nanomaterials. A good number of these research works are concentrated on nanosized metal oxides. Developments in this area evidently highlight the prospect of pushing the boundaries of present medical procedures in the direction of tailored health care with a concept of automated LOC-based arrangement for execution of concurrent synthesis, bio-functionalization, and in vitro assessment of nanomaterials for their quicker medical translation.

Metal oxides like iron oxide have been produced by this method. Dextran-coated superparamagnetic iron oxide nanoparticles have been created via a steady passively driven capillary-based droplet reactor. These dextran-coated iron oxide nanoparticles showed a huge saturation magnetization of 58 emu/g and a high T_2 relaxivity at 4.7 T (Krishna et al. 2013).

14.7 Toxicity Aspect of Magnetic Nanomaterials

Cautious assessment of nanomaterials for any toxic effects is highly essential. The majority of the above-mentioned investigations are restricted to in vitro estimations, and only a section of research ventures has demonstrated investigation of in vivo analysis.

Possessing an impression of the characteristics of the nanomaterials is useful while forecasting or estimating their toxicity. The clearance of the nanomaterials employed for biomedical purposes from the body and their circulation are extremely dependent on their features and characteristics. When the dimension of the nanomaterials is reduced, their reactivity gets enhanced. As a result, their capability to enter inside the tissues and various cell

barriers gets boosted. The cellular uptake, delivery, and interaction processes are reliant on the dimension of nanomaterials. Moreover, the charge and morphology of the nanomaterials also affect their possible poisonous properties. The suitable charge and shape of the nanomaterials can fasten their translocation via cell membranes to a great extent. Other significant features adding to the toxicity of nanomaterials are stability, surface chemistry, and storage techniques (Sajid 2022).

Table 14.3 shows the toxic consequences on the various biological systems of magnetic metal oxide nanomaterials.

Table 14.3 Toxicity effect on physiological systems by magnetic metal oxide nanomaterials

Magnetic metal oxide nanomaterial	**Impacted physiological system**
Fe_2O_3	Liver and lung tissue (Sadeghi et al. 2015)
ZnO	Reproductive (Mozaffari et al. 2015)
$CoFe_2O_4$	Circulatory, reproductive (Anik et al. 2021)
TiO_2	Immune (Anik et al. 2021)
ZrO_2	Digestive (Anik et al. 2021)
Co_3O_4	Immune (Anik et al. 2021)
Fe_3O_4	Immune (Anik et al. 2021)
Mn_2O_3	Reproductive (Anik et al. 2021)

It has been reported that the addition of specialized kinds of surface coating is essential for numerous nanoparticles to be convenient for biomedical uses (Kang et al. 2022).

14.8 Summary and Conclusion

Because of their unique characteristics, magnetic metal oxide nanomaterials are getting widespread popularity in biomedical applications (Table 14.4). In this chapter, current uses of these materials in the biomedical discipline are furnished along with examples.

Table 14.4 Biomedical applications of some magnetic metal oxide nanomaterials

Magnetic metal oxides	Applications
Iron oxide	MRI contrast agent
	Hybrid PET–MRI
	Joint magnetomotive ultrasound PET/CT and MRI
	Magnetic hyperthermia
	Drug delivery
	Gene delivery
	Bio-separation
	Lab-on-a-chip devices
^{89}Zr labelled cerium oxide	PET imaging
$Fe_{0.5}Zn_{0.5}Fe_2O_4$	Magnetic hyperthermia
Mn–Zn ferrite	Magnetic hyperthermia
	Gene delivery
Co- and Mn-doped iron oxide	Magnetic hyperthermia
$La_{0.54}Sr_{0.27}Gd_{0.19}MnO_3$	Magnetic hyperthermia
$La_{(1-x)}Ag_{(x)}MnO_3$	Magnetic hyperthermia
Cobalt ferrite	Drug delivery
Zinc ferrite	Gene delivery and hyperthermia
Copper oxide	Bio-separation
Manganese ferrite	Lab-on-a-chip devices

Iron oxide is the most extensively utilized magnetic nanomaterial for biomedical purposes because it is

superparamagnetic, biocompatible, and less toxic. Additionally, it is comparatively easy and low-cost to prepare (Ansari et al. 2023).

Though the employment of magnetic metal oxide nanomaterials has been well accounted for, investigations on their toxicology and biocompatibility are not adequate. As particle dimension gets reduced, certain nanosystems may show amplified toxicity in comparison to the same material in its bulk state. The main challenge in connection with the synthesis of magnetic metal oxide nanosystems is to adjust these nanomaterials based on morphology, dimension, and exterior for appropriate biomedical applications without compromising on their non-toxicity. Aggregation of magnetic metal oxide nanosystems is a matter of concern which can influence their effectiveness and possible toxicity. Evaluation of the effects of dimension, morphology, substitution, and dosage of magnetic metal oxide nanomaterials has to be conducted prior to their extensive utilization. Mathematical modelling may as well be useful in tackling these questions. Proper synthetic techniques require to be employed, and the developed nanosystems should be examined to optimize their performance. Thermal plasma procedure may act as a solution in this scenario. The thermal plasma method is a magnificent practice to get the preferred nanomaterials in the form of metals, alloys, and oxides. It is pretty exciting to figure out the structure–property connection of nanomaterials varying the dominant factors of the thermal plasma-aided reaction. Computational approaches appear as an influential means for in-depth study of the development of materials exercising the thermal plasma technique.

In conclusion, there is a huge possibility of magnetic metal oxide nanosystems being applied extensively for biomedical purposes in future. Scrutiny of the exact activities of these promising materials in complex biological

conditions will let us have an in-depth perception of their healing efficiency and toxicology.

Author Contributions

The manuscript was written through the contributions of all authors. All the authors have given approval to the final version of the manuscript.

References

Ahamed, J., Gowda, B.H.J., Almalki, W.H., Gupta, N., Sahebkar, A., Kesharwani, P.: Eur. Polym. J. **193**, 112111 (2023)

Anik, M.I., Hossain, M.K., Hossain, I., Mahfuz, A.M.U.B., Rahman, M.T., Ahmed, I.: Nano Sel. **2**(6), 1146–1186 (2021)

Ansari, K., Ahmad, R., Tanweer, M.S., Azam, I.: Biomed. Mater. Devices, 1–19 (2023)

Bhardwaj, A., Jain, N., Parekh, K.: Cancer Nanotechnol. **12**, 7 (2021)

Blokpoel Ferreras, L.A., Chan, S.Y., Vazquez Reina, S., Dixon, J.E.: ACS Appl. Nano Mater. **4**(1), 167–181 (2021)

Bucak, S., Yavuzturk, B., Demir, A.: Magnetic nanoparticles: synthesis, surface modifications and application in drug delivery. In: Sezer, A.D. (ed.) Recent Advances in Novel Drug Carrier Systems, pp. 165–200. IntechOpen, UK, London (2012)

Cardoso, V.F., Francesko, A., Ribeiro, C., Bañobre-López, M., Martins, P., Lanceros-Mendez, S.: Adv. Healthc. Mater. **7**(5), 1700845 (2018)

Dadfar, S.M., Roemhild, K., Drude, N.I., von Stillfried, S., Knuchel, R., Kiessling, F., Lammers, T.: Adv. Drug Deliv. Rev. **138**, 302–325 (2019) [PubMed][PubMedCentral]

Deka, K., Deb, P.: Development of manganese based nanosystems as single and dual mode MRI contrast agents, PhD thesis, Tezpur University, Tezpur (2018). http://hdl.handle.net/10603/286712

Dobson, J.: Gene Ther. **13**(4), 283–287 (2006) [PubMed]

Du, S., Li, J., Du, C., Huang, Z., Chen, G., Yan, W.: Oncotarget **8**(6), 9410–9424 (2017)

[PubMed]

Etemadi, H., Plieger, P.G.: Advanced Therapeutics 2000061 (2020)

Evertsson, M., Kjellman, P., Cinthio, M., Andersson, R., Tran Thuy, A., Zandt, R., Grafström, G., Toftevall, H., Fredriksson, S., Ingvar, C., Strand, S., Jansson, T.: Sci. Rep. **7**, 4824 (2017)
[PubMed][PubMedCentral]

Farzin, L., Saber, R., Sadjadi, S., Mohagheghpour, E., Sheini, A.: J. Therm. Biol. **104**, 103201 (2022)
[PubMed]

Fatima, H., Kim, K.S.: Korean J. Chem. Eng. **34**(3), 589–599 (2017)

Fu, R., Yan, Y.Y., Roberts, C., Liu, Z.Y., Chen, Y.Y.: Sci. Rep. **8**, 4704 (2018)
[PubMed][PubMedCentral]

Ghanbari, M., Davar, F., Shalan, A.E.: Ceram. Int. **47**(7), 9409–9417 (2021)

Del Guerra, A., Belcari, N., Bisogni, M.: Riv del Nuovo Cim. **39**(4), 155–223 (2016)

Guo, Z.Y., Zhang, Y., Zhang, D.D., Shu, Y., Chen, X.W., Wang, J.H.: ACS Appl. Mater. Interfaces **8**(43), 29734–29741 (2016)
[PubMed]

Hung, L.Y., Cheng, F.Y., Huang, C.C., Tsai, Y.C., Yeh, C.S., Lei, H.Y., Lee, G.B.: Microfluidic system for rapid detection of influenza infection by utilizing magnetic $MnFe_2O_4$ nanoparticle based immunoassay. In: 7th IEEE International Conference on Nano/Micro Engineered and Molecular Systems, pp. 200–203 (2012)

Hussain, C.M., Patankar, K.K.: Fundamentals and Industrial Applications of Magnetic Nanoparticles, 1st edn. Elesevier (2022)

Jain, A., Ong, S.P., Hautier, G., Chen, W., Richards, W.D., Dacek, S., Cholia, S., Gunter, D., Skinner, D., Ceder, G., Persson, K.A.: APL Mater. **1**, 011002 (2013)

Kang, M.S., Kwon, M., Jang, H.J., Jeong, S.J., Han, D.W., Kim, K.S.: Emergent Mater. **5**, 1995–2029 (2022)

Khan, M.I., Mohammad, A., Patil, G., Naqvi, S.A.H., Chauhan, L.K.S., Ahmad, I.: Biomaterials **33**(5), 1477–1488 (2012)
[PubMed]

Khizar, S., Ahmad, N.M., Zine, N., Jaffrezic-Renault, N., Errachid-el-salhi, A., Elaissari, A.: ACS Appl. Nano Mater. **4**, 4284–4306 (2021)

Krishna, K.S., Li, Y., Li, S., Kumar, C.S.S.R.: Adv. Drug Deliv. Rev. **65**, 1470–1495 (2013)
[PubMed]

Lan, F., Hu, H., Jiang, W., Liu, K., Zeng, X., Wu, Y., Gu, Z.: Nanoscale **4**(7), 2264–2267 (2012)
[PubMed]

Li, J., Wu, Q., Wu, J.: Synthesis of nanoparticles via solvothermal and hydrothermal methods. In: Aliofkhazraei, M. (ed.) Handbook of Nanoparticles, pp. 295–328. Springer International Publishing, Switzerland (2016)

Lim, Z.W., Varma, V.B., Ramanujan, R.V., Miserez, A.: Acta Biomater. **110**, 221–230 (2020)
[PubMed]

Lin, Y.S., Huang, K.S., Yang, C.H., Wang, C.Y., Yang, Y.S., Hsu, H.C., Liao, Y.J., Tsai, C.W.: PLoS One **7**(3), e33184 (2012)

Liu, G., Xie, J., Zhang, F., Wang, Z., Luo, K., Zhu, L., Quan, Q., Niu, G., Lee, S., Ai, H., Chen, X.: Small **7**(19), 2742–2749 (2011)
[PubMed][PubMedCentral]

Lowell, S., Shields, J.E., Thomas, M.A., Thommes, M.: Characterization of Porous Solids and Powders: Surface area, Pore Size and Density. Springer Science & Business Media, New York (2004)

Lui, C.N.P., Tsui, Y.P., Ho, A.S.L., Shum, D.K.Y., Chan, Y.S., Wu, C.T., Li, H.W., Edman Tsang, S.C., Yung, K.K.L.: Angew. Chemie **125**(47), 12524–12528 (2013)

Mai, B.T., Balakrishnan, P.B., Barthel, M.J., Piccardi, F., Niculaes, D., Marinaro, F., Fernandes, S., Curcio, A., Kakwere, H., Autret, G., Cingolani, R., Gazeau, F., Pellegrino, T.: ACS Appl. Mater. Interfaces **11**, 5727–5739 (2019)
[PubMed][PubMedCentral]

Martins, P.M., Lima, A.C., Ribeiro, S., Lanceros-Mendez, S., Martins, P.: ACS Appl. Bio Mater. **4**, 5839–5870 (2021)
[PubMed]

Mittal, A., Roy, I., Gandhi, S.: Magnetochemistry **8**, 107 (2022)

Mozaffari, Z., Parivar, K., Roodbari, N.H., Irani, S.: Adv. Stud. Biol. **7**(6), 275–291 (2015)

Murthy, S., Effiong, P., Fei, C.C.: Metal oxide nanoparticles in biomedical applications. In: Al-Douri, Y. (ed.) Metal Oxide Powder Technologies, pp. 233–251. Elsevier (2020)

Nair, M., Guduru, R., Liang, P., Hong, J., Sagar, V., Khizroev, S.: Nat. Commun. **4**, 1707 (2013)
[PubMed]

Peiravi, M., Eslami, H., Ansari, M., Zare-Zardini, H.: J. Indian Chem. Soc. **99**(1), 100269 (2022)

Périgo, E.A., Hemery, G., Sandre, O., Ortega, D., Garaio, E., Plazaola, F., Teran, F.J.: Appl. Phys. Rev. **2**(4), 041302 (2015)

Phys, J.: Chem. C **118**, 14073–14081 (2014)

Prijic, S., Prosen, L., Cemazar, M., Scancar, J., Romih, R., Lavrencak, J., Bregar Vladimir, B., Coer, A., Krzan, M., Znidarsic, A., Sersa, G.: Biomaterials **33**(17), 4379–4391 (2012)
[PubMed]

Prosen, L., Markelc, B., Dolinsek, T., Music, B., Cemazar, M., Sersa, G.: Mol. Ther. Nucleic Acids **3**, e205 (2014)
[PubMed][PubMedCentral]

Prosen, L., Hudoklin, S., Cemazar, M., Stimac, M., Tratar, U.L., Ota, M., Scancar, J., Romih, R., Sersa, G.: Nanomedicine **11**(6), 627–641 (2016)
[PubMed]

Rahban, D., Doostan, M., Salimi, A.: Cancer Invest. **38**, 507–521 (2020)
[PubMed]

Rajan, A., Sahu, N.K.: J. Nanopart. Res. **22**, 319 (2020)

Rouquerol, J., Rouquerol, F., Llewellyn, P., Maurin, G., Sing, K.S.W.: Adsorption by Powders and Porous Solids: Principles, Methodology and Applications, 2nd edn. Elsevier, Oxford (2014)

Sadeghi, L., Babadi, V.Y., Espanani, H.R.: Bratisl. Lek. Listy **116**(6), 373–378 (2015)
[PubMed]

Sadhukha, T., Wiedmann, T.S., Panyam, J.: Biomaterials **35**(27), 7860–7869 (2014)
[PubMed][PubMedCentral]

Sahu, T., Ratre, Y.K., Chauhan, S., Bhaskar, L.V.K.S., Nair, M.P., Verma, H.K.: J. Drug Deliv. Sci. Technol. **63**, 102487 (2021)

Sajid, M.: Curr. Opin. Environ. Sci. Health **25**, 100319 (2022)

Seeram, E.: Computed Tomography: Physical Principles, Clinical Applications, and Quality Control, 4th edn. Elseveir, USA (2015)

Sharifianjazi, F., Irani, M., Esmaeilkhanian, A., Leila, B., Asl, M.S., Jang, H.W., Kim, S.Y., Ramakrishna, S., Shokouhimehr, M., Varma, R.S.: Mater. Sci. Eng. B Solid State Mater. Adv. Technol. **272**, 115358 (2021)

Sharma, S.K., Javed, Y.: Magnetic Nanoheterostructures: Diagnostic, Imaging and Treatment. Springer Nature, Switzerland (2020)

Siafaka, P.I., Okur, N.U., Karantas, I.D., Okur, M.E., Gundogdu, E.A.: Asian J. Pharm. **16**, 24–46 (2021)

Siddique, S., Chow, J.C.L.: Nanomaterials **10**(9), 1–41 (2020)

Singh, A., Amiji, M.M.: Curr. Opin. Biotechnol. **74**, 241–246 (2022)
[PubMed]

Srdic, V.V., Cvejic, Z., Milanovic, M., Stojanovic, G., Rakic, S.: Metal oxide structure, crystal chemistry, and magnetic properties. In: Stojanovic, B.D. (ed.) Magnetic, Ferroelectric, and Multiferroic Metal Oxides, pp. 313–332. Elsevier (2018)

Tang, Q., Zhang, D., Cong, X., Wan, M., Jin, L.: Biomaterials **29**(17), 2673–2679 (2008)

Varma, V.B., Wu, R.G., Wang, Z.P., Ramanujan, R.V.: Lab Chip **17**, 3514–3525 (2017)
[PubMed]

Vollath, D.: KONA Powder Part. J **25**, 39–55 (2007)

Waifalkar, P.P., Parit, S.B., Chougale, A.D., Sahoo, S.C., Patil, P.S., Patil, P.B.: J. Colloid Interface Sci. **482**, 159–164 (2016)
[PubMed]

Wan, Q., Xie, L., Gao, L., Wang, Z., Nan, X., Lei, H., Long, X., Chen, Z., He, C., Liu, G., Liu, X., Qiu, B.: Nanoscale **5**(2), 744–752 (2013)
[PubMed]

Wang, R., Hu, Y., Zhao, N., Xu, F.J.: ACS Appl. Mater. Interfaces **8**(18), 11298–11308 (2016)
[PubMed]

Wu, Q.H., Jin, R.R., Feng, T., Liu, L., Yang, L., Tao, Y.H., Anderson James, M., Ai, H., Li, H.: Int. J. Nanomed. **12**, 3993–4005 (2017)

Xiang, L., Bin, W., Jin, H., Wei, J., Jiesheng, T., Feng, G., Ying, L.: J. Gene Med. **9**(8), 679–690 (2007)
[PubMed]

Xu, F., Geiger, J.H., Baker, G.L., Bruening, M.L.: Langmuir **27**(6), 3106–3112 (2011)
[PubMed][PubMedCentral]

Xu, D., Su, Y., Xu, Q., Huang, T., Chen, Z., Zhang, T.: Nanotechnology **33**, 125101 (2022)

Yang, Q., Lan, F., Yi, Q., Wu, Y., Gu, Z.: Nanoscale **7**(42), 17617–17622 (2015)
[PubMed]

Yang, Q., Zhu, Y., Luo, B., Lan, F., Wu, Y., Gu, Z.: J. Mater. Chem. B **5**(6), 1236–1245 (2017)
[PubMed]

Yildirim, A., Ispirli Doğaç, Y.: Prep. Biochem. Biotechnol. (2022)

Yin, P.T., Shah, B.P., Lee, K.B.: Small **10**(20), 4106–4112 (2014)
[PubMed][PubMedCentral]

Zheng, Y., Zhang, H., Hu, Y., Bai, L., Xue, J.: Int. J. Nanomed. **13**, 6177–6188 (2018)

Zhu, B., Sevick-Muraca, E.M.: Br. J. Radiol. **88i**(1045), 20140547 (2015)

© The Author(s), under exclusive license to Springer Nature Singapore Pte Ltd. 2024
R. S. Ningthoujam, A. K. Tyagi (eds.), *Handbook of Materials Science, Volume 2*, Indian Institute of Metals Series
https://doi.org/10.1007/978-981-97-4646-0_15

15. Ferromagnetism in Two-Dimensional TMD Materials via Doping, Phase Transition and Defect Engineering

Rohini Sanikop[1], Bidisha Priyadarsini Jena[1], Vikasmita Samanta[1] and C. Sudakar[1] ✉
(1) Multifunctional Materials Laboratory, Department of Physics, Indian Institute of Technology Madras, Chennai, 600036, India

✉ **C. Sudakar**
Email: csudakar@iitm.ac.in

Keywords TMDs – 2D-ferromagnetism – Dopants – Defects – Phase control

These authors contributed equally to this work.

15.1 Introduction

Semiconductors form an important basis for the electronic devices. With the reduction in the size of electronic circuit components and efforts to exploit both the charge and spin characteristics of electrons, advanced semiconductor materials are being developed to tailor the functional

properties of electronic devices such as transistors. Spintronic devices require materials with both semiconductor and magnetic properties to control the charge and spin information of electrons. Diluted magnetic semiconductors (DMS) are potential candidates for spintronics applications. Extensive studies on III–V [e.g., (In, Mn) Se] and II–VI [e.g., (Zn, Cr) Te] based DMS and devices relevant to spintronics applications were explored in the last 2 decades. With the surge in 2D materials in recent years realizing the magnetic properties of 2D magnetic materials can provide an excellent platform for 2D spintronics (Khan et al. 2020; Han 2016). However, Mermin–Wagner theorem predicts the difficulty in establishing long-range magnetic ordering in 2D crystals due to enhanced thermal fluctuations (Mermin and Wagner 1966). According to this theorem, 2D magnetic materials cannot exhibit long-range magnetic ordering at $T > 0$ for the isotropic Heisenberg model. However, due to high magneto-crystalline anisotropy, spin–orbit coupling and dipolar interaction, magnetism is shown to exist in 2D materials.

The van der Waals layered structures are a class of 2D material in which individual layers are held together by weak van der Waals interaction. These layers could be separated into single or multilayer sheets. Exhaustive studies revealing interesting properties in 2D monoatomic layers like graphene have led to the exploration of other 2D layered materials including h-BN, MX_2 (M=Mo, W; X=S, Se, Te) and layered oxides (Jiang et al. 2021). Transition metal dichalcogenides (TMDs) with MX_2 chemical formulae, where M is a transition metal atom, and X is a chalcogen atom (S, Se or Te) form a large family of layered type materials. Among the family of 2D functional materials, 2D magnets are evolving as a promising candidate for next-generation information technology. Just

a few years before, these 2D magnetic materials were almost missing members of the emerging 2D family.

In 2017, intrinsic 2D magnetism was experimentally achieved in atomically thin layers of CrI_3 (Huang et al. 2017) and $Cr_2Ge_2Te_6$ (Gong et al. 2017) showing that the long-range magnetic ordering can be stabilized by magnetic anisotropy with an excitation gap opening. Traditional spintronics materials have poor spin–orbit interaction. This allows device operation only at low temperatures far below 300 K. Further, constructing long channel lengths and ultrahigh pure materials is challenging to avoid spin-flip scattering. 2D transition-metal dichalcogenides (TMDs) have strong spin–orbit coupling. This induces spin splitting of up to 0.4 eV at a valence-band maximum, thus enabling the feasibility of operating spintronics devices at room temperature. All these studies suggest that realizing high Curie temperature (T_C) and strong spin–orbit coupling will enable the use of 2D TMDs for novel spintronics applications such as spin-field-effect switches, spin valves, magnetic sensors, and ultrathin high-density data storage devices. Recently researchers have gained a significant lead by studying the room temperature long-range magnetic ordering in 2D systems like VSe_2, Fe_3GeTe_2, VS_2, VTe_2, $NbTe_2$, $MnSe_2$, $CrTe_2$, CrI_3, VI_3, $CrBr_3$, etc. (Jiang et al. 2021). The high-quality 2D magnetic monolayers/multilayers can be experimentally prepared by micromechanical cleavage, chemical vapour deposition (CVD) and molecular beam epitaxy (MBE) method. 2D TMDs are promising candidates in this sense and understanding the origin of magnetic properties in this system has been very challenging. The presence of defects including chalcogenide vacancies, and interstitials seems to significantly influence the magnetic properties. Likewise substituting the transition metal with appropriate magnetic ion dopants also enhances the magnetic properties. The

structural symmetry plays an important role in stabilizing long-range ordering. This book chapter will provide a review on several experimental strategies to make the TMDs ferromagnetic with Curie temperature T_C exceeding 300 K, along with theoretical studies which support the feasibility of such realization.

15.2 Transition Metal Dichalcogenides (TMDs)

Approximately 60 TMDs are known as MX_2 TMDs, with 'M' being a transition metal element from group IV to VII and X a chalcogen (S, Se or Te) (Samadi et al. 2018; Choi et al. 2017). Out of this, 40 TMDs form a layered structure. Unlike a single layer of carbon atoms forming graphene, the monolayer of TMDs consists of three layers: transition metal M layer is sandwiched between two chalcogen X (Samadi et al. 2018; Choi et al. 2017). Here M exists in 4+ oxidation state and X is in 2− oxidation state. In these layered structures, metals form strong covalent bonds with chalcogens in the intralayer, while weakly bonded van der Waals (vdW) interactions hold the adjacent MX_2 layers together. Due to the weak interactions between layers, TMDs offer a low coefficient of friction. As a result, they have been used as dry lubricants to reduce the friction since 1970s (Vazirisereshk et al. 2019). Large members of TMDs are semiconducting with bandgap ranging from visible to infrared.

A. **TMD Crystal Structure**:

TMDs exist in different structural phases depending on the coordination geometry of transition metals. Various phases of MX_2 known are 1T (tetragonal), 2H (hexagonal), and 3R

(rhombohedral). The structural arrangements in the top and side views of M and X atoms in these different phases are shown in Fig. 15.1. In the 2H and 3R phases, M exists in trigonal prismatic coordination. In 1T phase ligands are coordinated to transition metals in an octahedral geometry. The *d*-orbital in metal cations splits forming two degenerate states t_{2g} (d_{xy}, d_{yz}, d_{xz}) and e_g (d_{z^2}, $d_{x^2-y^2}$) as schematically presented in Fig. 15.2. In 1T′ phase, transition metal occupies distorted octahedral geometry. The structural difference among these phases is listed in Table 15.1. Among various TMDs, MoS_2 is widely explored due to its wide range of applications. MoS_2 forms a stable hexagonal crystal structure (2H phase) belonging to $P6_3/mmc$ space group. The hexagonal lattice constants are $a = b = 3.161$ Å and $c = 12.294$ Å, $\alpha = \beta = 90°$ and $\gamma = 120°$ (Schonfeld 1983). The thickness of each monolayer is 3.24 Å, with van der Waals gap of 2.90 Å. The comparison of lattice parameters in 1T, 2H, and 3R crystal structures of some of the well-known TMDs is given in Table 15.2.

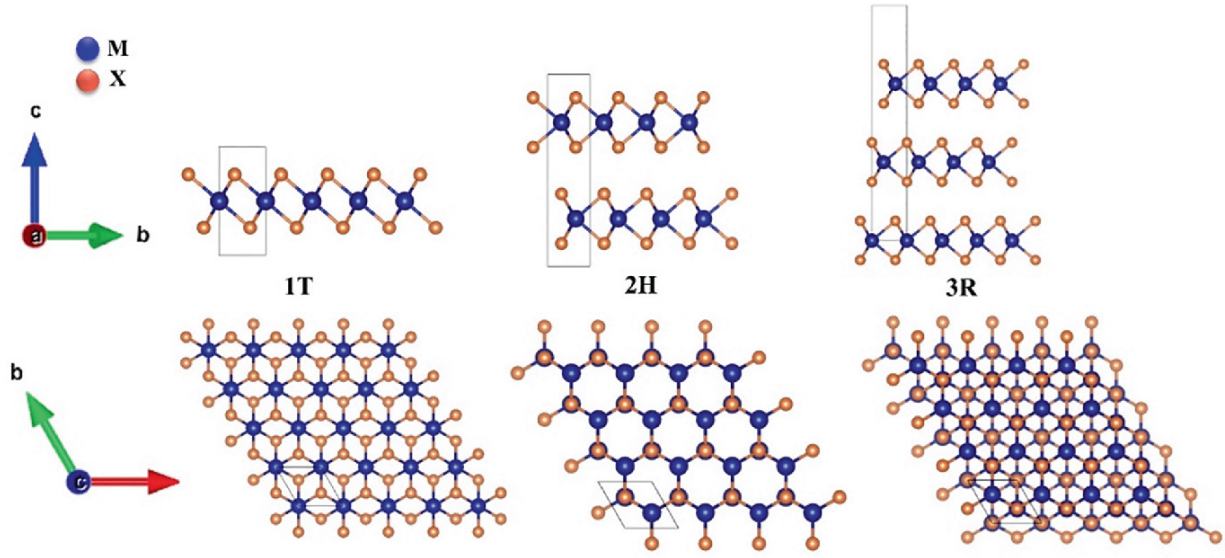

Fig. 15.1 Crystal structures of MX_2:1T, 2H, and 3R phases

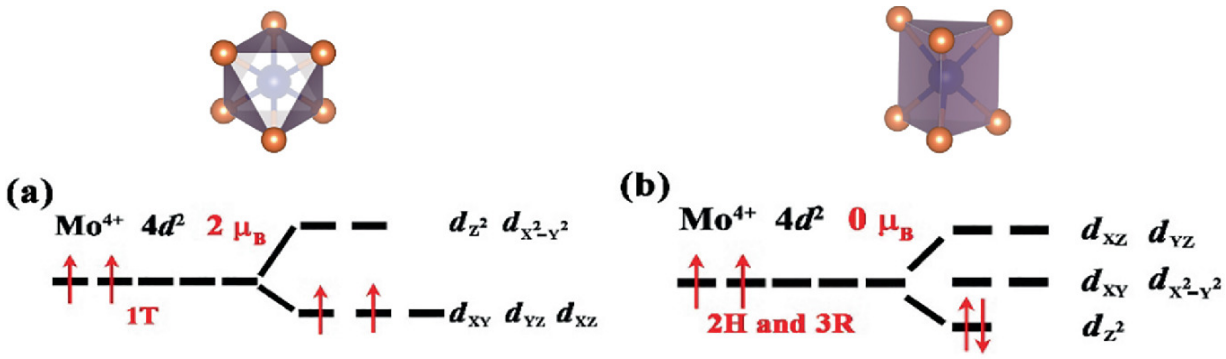

Fig. 15.2 Crystal field splitting in **a** octahedral and **b** trigonal prismatic geometry

Table 15.1 Details of 1T, 2H, and 3R MX_2 crystal structures

Structural phase	**2H**	**3R**	**1T**	**1T′**
Space group	$P6_3/mmc$	$R3m$	$P\bar{3}m1$	$P\bar{3}m1$
Geometry	Trigonal prismatic	Trigonal prismatic	Octahedral	Distorted Octahedra
Stacking of M and X layers	AbA BaB	AbABcBCaC	AbA	AbA

Table 15.2 Lattice parameters of 1T, 2H, and 3R phases of representative MX_2 compounds in different phases

MX_2 compound	**Lattice parameters (Å) of different of phases**		
	1T	**2H**	**3R**
MoS_2	***a*** = 3.160 ***c*** = 6.15	***a*** = 3.161 ***c*** = 12.294	***a*** = 3.163 ***c*** = 18.37
$MoSe_2$		***a*** = 3.288 ***c*** = 12.90	***a*** = 3.290 ***c*** = 19.29
$MoTe_2$		***a*** = 3.519 ***c*** = 13.964	
WS_2	***a*** = 3.21 ***c*** = 6.18	***a*** = 3.184 ***c*** = 12.978	
WSe_2		***a*** = 3.319 ***c*** = 13.737	

B. **Synthesis of 2D TMDs**:

The synthesis of single and few layered TMDs is done either by a top-down or bottom-up approach. Top-down methods include (i) mechanical cleavage, (ii) liquid-phase exfoliation, (iii) intercalation and exfoliation, and (iv) thinning. Bottom-up methods generally include (i) vapour deposition and (ii) solution-based methods (Samadi et al. 2018; Han et al. 2013, 2015).

1. **Top-down methodology**:

   (i) **Mechanical cleavage**: It is also known as the scotch-tape method and was first implemented in the exfoliation of graphene. This method is a low-cost and easy way to produce high-quality monolayer or few-layer nanosheets. Figure 15.3a shows steps followed for exfoliation. Initial exfoliation is carried out to get a fresh surface and this is followed by repeated folding and unfolding of the tape. This is performed until the desired number of layers is obtained. Finally, the nanosheets are transferred onto Si substrate coated with SiO_2 (90 nm or 285 nm thickness) by gently rubbing and peeling from the tape. Typical size of the flakes is in the range of 25–200 μm^2.

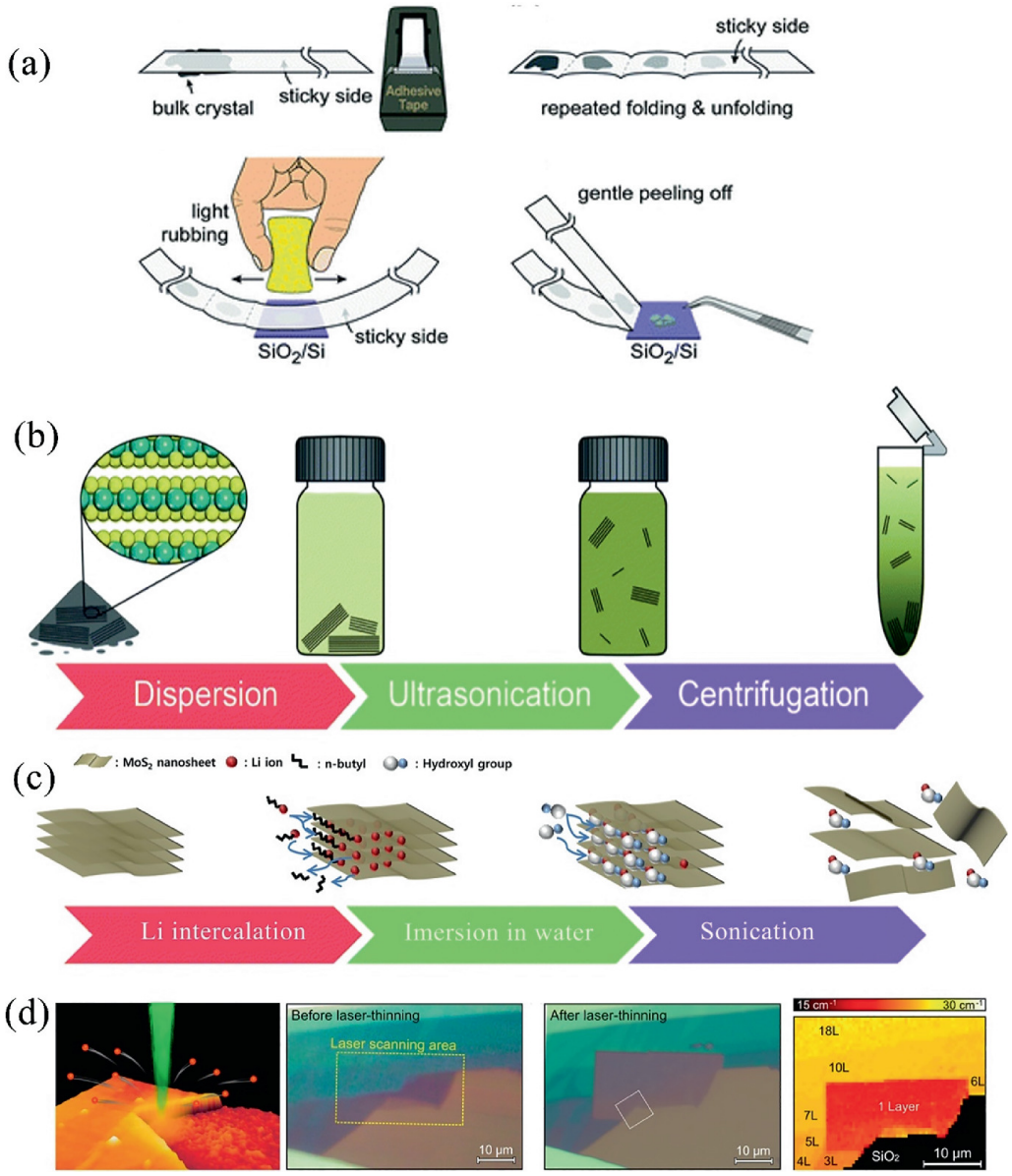

Fig. 15.3 **a** Mechanical exfoliation method, **b** Liquid exfoliation method, **c** Li intercalation and exfoliation. **a**–**c** is reproduced with permission from RSC publishers (Samadi et al. 2018). **d** Laser thinning: Optical microscope images of bulk MoS_2 before and after laser thinning process and spatial Raman map showing the difference between $E_{2g}{}^1$ and A_{1g}.

It is reproduced with permission from ACS Publishers (Castellanos-Gomez et al. 2012)

(ii) **Liquid-phase exfoliation (LPE)**: This process involves mainly three steps: (1) Dispersion of bulk layered materials in a suitable solvent, (2)

Exfoliation of the sample by sonication, and (3) Separation of nanosheets via centrifugation (Fig. 15.3b). By choosing a proper solvent, and suitable parameters (like time, RPM) large range of layered materials can be exfoliated. LPE is a prominent methodology for the commercial production of 2D materials. Dispersed nanosheets can be deposited on various substrates that find applications in thin-film transistors, inkjet-printed electronics, and conductive electrodes for photovoltaics. However, there is no control over the thickness and lateral size of the nanosheets.

(iii) **Intercalation and exfoliation**: Lamellar structure of TMDs with large interplanar spacing (~6 Å) allows a wide variety of species (alkali metals, polymers, organometallic species) to be intercalated into the space between layers held by van der Waals bond (Fig. 15.3c). In general, intercalating species have to be electron donors or reducing agents. After intercalation electron will be transferred to the metal *d*-orbital which reduces its oxidation from 4+ to 3+. The bulk sample is immersed in appropriate solvents for a few days in N_2/Ar atmosphere. The chemical reaction between intercalating agents and MX_2 brings electron transfer which expands the lattice along the *c*-direction. Further exfoliation is achieved by ultrasonication which forms a colloidal suspension. The resulting product obtained by centrifugation and filtration is called restacked MX_2 with enlarged interplanar spacing.

(iv) **Thinning**: It involves layer-by-layer peeling of bulk materials (Castellanos-Gomez et al. 2012). It can be carried out in various ways: (1)

Sublimation, local heating of the sample using the laser (Fig. 15.3d), (2) Plasma treatment with an external electric field as the driving force, and (3) Etching with highly oxidizing reagents. Mechanical exfoliation is performed initially to get few-layer flakes on which thinning is done.

2. **Bottom-up methodology**:

   (i) **Vapour deposition**: It can produce high-quality 2D nanosheets with controlled growth on layer thickness and lateral size. Hence it is the most promising methodology for device applications and provides an easy method for synthesizing doped, alloyed, lateral, and vertical heterostructures. This paves the way for tailoring optical, electrical, and magnetic properties. During the growth process, a metal precursor or a deposited metal film reacts with sulphur, selenium, or tellurium precursors on the surface of a substrate at high temperatures inside a tubular furnace, with either Ar (argon) or N_2 (nitrogen) serving as the carrier gas (Fig. 15.4) (Samadi et al. 2018). Some volatile by-products which are produced during the chemical reaction are removed by gas flow from the reaction chamber. Growth parameters like temperature, growth time, carrier gas flow rate, precursor ratio (M:X ratio) or substrate used show significant influence on the shape evolution of TMDs.

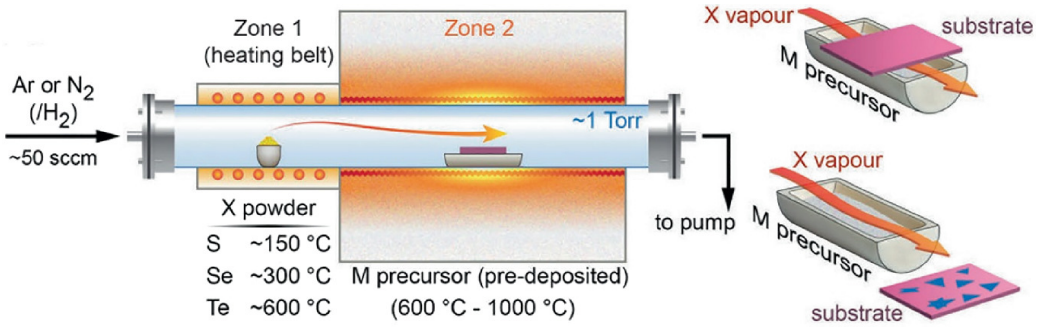

Fig. 15.4 Schematic of chemical vapour deposition method. It is reproduced with permission from RSC Publishers (Samadi et al. 2018)

(ii) **Solution-based synthesis**: The process involves chemical reactions at high temperature/pressure in a liquid medium. In addition to nanosheets, this method can also produce a variety of other morphologies, including nanoflowers, micro boxes, and core-shells (Samadi et al. 2018). In recent years this method has been used for incorporating graphene/graphene oxide in TMD nanosheets forming nanocomposites. It improves electrical conductivity in TMDs for exploring their electrochemical performances in catalysis and energy storage applications.

C. Origin of Magnetism in MX_2:

For the understanding of the magnetic properties of TMDs, the energy level splitting of *d*-orbitals based on the crystal field theory (CFT) due to the coordination of the surrounding atoms or ligands is very much important. CFT explains the splitting of *d* and *f* orbital energies of a central metal ion as the ligands (anions) approach (Cotton and Wilkinson 1972). The splitting of the *d*-orbital in the octahedral and trigonal prismatic geometry is shown in Fig. 15.2. The most common coordination is octahedral geometry with a transition metal at its center surrounded

by six ligands. Assuming there is only one valence electron present in the *d*-orbital (example Ti^{3+} or V^{4+}) and considering all the ligands in the octahedral geometry to be point charges, the electron involved in bonding will have an equal probability of occupying any one of the five *d* orbitals. But the *d*-orbitals in crystalline solids are not equivalent. More repulsion is experienced by *d*-orbitals of central metal cation lying on the axis joining anions. Hence the electron chooses to reside in those orbitals which have minimum repulsion from the anion. In the octahedral geometry lobes of d_{z^2}, $d_{x^2-y^2}$ lie along the line joining the metal and anion, thus experiencing maximum repulsion. While the remaining orbitals d_{xy}, d_{yz}, d_{zx} have lobes projecting between the charges. The first set of orbitals is equivalent but unfavourable as it requires more energy for bond formation. The latter three orbitals also have the same environment in the coordination and hence are equivalent. Therefore, the central metal ion with six surrounding ligands in octahedral coordination has two sets of *d* orbitals. The three *d*-orbitals with lower energy are referred to as t_{2g} and the other two with higher energy are called e_g. This division of *d* orbitals in central metal ion under the influence of surrounding charges is called crystal field splitting. As an example, due to the CFT Mo in 4+ oxidation states give a net magnetic moment of 2 μ_B in both 1T and 1T′ structure of MoS_2. Transition metals occupy a trigonal prismatic position in the case of 2H and 3R phases (Fig. 15.2b). Here *d*-orbital splits forming three degenerate levels that are *a*′, *e*′ and *e*″. The non-degenerate *a*′ corresponds to d_{z^2} orbital. Doubly degenerate *e*′ and *e*″ correspond to d_{xy}, $d_{x^2-y^2}$ and d_{yz}, d_{xz}, respectively. For 2H and 3R phases of MoS_2 electrons pair up in d_{z^2} orbital giving rise to a net magnetic moment of 0 μ_B. Thus 2H and

3R phases of MoS_2 are paramagnetic while 1T phase of MoS_2 is ferromagnetic.

The magnetism in 2D materials can be originating either due to the intrinsic nature or it can be induced by the influence of external factors including doping, phase transition, and defects. Accordingly, the magnetism in MX_2 can be classified as (i) intrinsic ferromagnetism (ii) extrinsic ferromagnetism.

1. **Intrinsic ferromagnetism**:

Intrinsic magnetism is greatly sought in materials and the promise of realizing it in 2D materials is already leading to a greater impact on 2D spintronics. This has important implications in increasing the efficiency of 2D spintronic devices, which can be improved by tweaking the charge and spin degrees of freedom. 2D materials with intrinsic ferromagnetism are promising in realizing such spintronics devices. Mechanically exfoliated $Cr_2Ge_2Te_6$ has shown intrinsic long-range FM order in bilayer by magneto-optic Kerr effect (MOKE) (Gong et al. 2017). While bulk $Cr_2Ge_2Te_6$ exhibits $T_C \sim 68$ K, the bilayer shows the $T_C \sim 30$ K. 2D $Cr_2Ge_2Te_6$ is shown to possess out-of-plane magnetic anisotropy with a magnetic moment of 2.4 μ_B per Cr atom. Realizing the intrinsic nature of ferromagnetism has been very challenging. In addition to the optical probe techniques like MOKE, anomalous Hall effect (AHE) has been used to detect 2D itinerant magnetism, caused by conduction electrons. AHE has been applied to check the ferromagnetic ordering of Fe_3GeTe_2 down to monolayer. On the contrary, few-layer $MnBi_2Te_4$ is shown to be antiferromagnetic. The layered flakes of Fe_3GeTe_2 have shown the T_C values to be 180 K and 130 K for bilayer and

monolayer, respectively, with strong out-of-plane magnetocrystalline anisotropy energy (MAE) ~0.92 meV (Chen et al. 2013).

Using SQUID magnetometer and magnetic force microscopy (MFM) studies, room-temperature FM ordering is also reported on the exfoliated 2D VSe_2 flakes (Bonilla et al. 2018). The unpaired electron in V^{4+} with $3d^1$ electronic configuration couple ferromagnetically because of the superexchange interactions mediated by Se atoms. Ferromagnetism in these systems exhibits a strong dependence on the layer numbers. Highest magnetization is found in monolayers ($M_S \sim 3 \times 10^3$ emu/cm^3 at ~300 K) and this decreases with increasing number of layers thus demonstrating magnetism tailorable by reducing the layer numbers. Upon increasing the layers beyond 10 the magnetization decreases further and the multilayered VSe_2 becomes predominantly paramagnetic. 2H VSe_2 also exhibit ferromagnetism when the thickness of 2D form is less than 50 nm. Owing to large structural anisotropy T_C is found to be 430 K for 8 nm thick VSe_2, whereas T_C decreases to 300 K as the thickness increases to 50 nm (Yu et al. 2019). 1T-phase of VX_2 (X=Se, Te, and S), grown by CVD, MBE or mechanically exfoliated layers, are most commonly investigated compared the 2H-phase. However, the role of defects and other interactions due to the interfaces and boundaries cannot be neglected for the origin of ferromagnetism in these systems (Memarzadeh et al. 2021).

1T phase of CrS_2 is believed to have ferromagnetic ordering though the 2H phase is non-magnetic. From first principle studies, antiferromagnetic monolayer has been predicted to undergo a magnetic phase transition to a ferromagnetic bilayer (Wang et al. 2018). Such a transition was attributed to the charge sharing of interlayer S atoms

and its resulting charge transfer from Cr e_g (d_{z^2} and $d_{x^2-y^2}$) orbitals to t_{2g} (d_{xy}, d_{yz}, and d_{xz}) orbitals (Khan et al. 2020). This brings a change in the oxidation state from 4+ to 3+ and enhances ferromagnetic ordering via double exchange mechanism. Besides these theoretical predictions on magnetic properties, CVD grown 2D CrS_2 flakes on mica substrates has shown room temperature ferromagnetism with coercive field of 28.7 Oe (Xiao et al. 2022). Also, the layer dependent magnetism of CrS_2 is consistent with the theoretical calculations. Atomically thin $CrSe_2$ grown by CVD process on WSe_2 substrate has shown ferromagnetism with $T_C \sim 110$ K. These layers also show excellent air stability (Li et al. 2021). Very recently, CVD-grown Cr-Te based binary 2D materials is attracting great interest for their excellent air stability and thickness dependent turnability of T_C. Tellurium (Te) has very strong spin–orbit coupling and as a result, chromium telluride (Cr_xTe_y) of different compositions and structures, like $CrTe_2$ (Meng et al. 2021), Cr_5Te_8 (Chen et al. 2022), Cr_2Te_3 (Wen et al. 2020), Cr_3Te_4 (Coughlin et al. 2021) and CrTe (Wang et al. 2020), should have strong magnetic anisotropy and the long-range magnetic order down to 2D limit. As an example, for $CrTe_2$, both MOKE and reflective magnetic circular dichroism (RMCD) measurements showed that T_C increases monotonically from 187 to 212 K with decreasing thickness from ~130.0 to ~7.5 nm associated with a change in magnetic easy axis from out-of-plane to in-plane (Meng et al. 2021).

Apart from these Cr, Fe and V based chalcogenides, MBE grown $MnSe_x$ monolayer on GaSe and $SnSe_2$ show room temperature ferromagnetism with a large saturation magnetization (M_S) of ~4 μ_B/Mn (O'Hara et al. 2018). Unlike most of the 1T- and 2H-phases of TMDs which

exhibit in-plane ferromagnetic ordering, $MnSe_2$ show out-of-plane magnetic anisotropy. Despite the experimental observation of interesting magnetic response from TMDs the exact origin is yet to be confirmed on most of these few layered vdW materials.

2. **Extrinsic ferromagnetism**:

Among the TMDs, mostly Fe, Cr and V based di-chalcogenides like $FeTe_2$, $CrTe_2$, VSe_2 show ferromagnetism intrinsically. On the other hand, TMDs such as MoX_2 (X=S, Se, Te), which have been extensively studied in various fields, are non-magnetic 2D semiconductor in their 2H- and 3R-phase. The non-magnetic nature arises due to the absence of unpaired electrons in the *d* orbitals of trigonal prismatically coordinated Mo in 4+ oxidation state. However, both experimental and theoretical investigations show the existence of diamagnetism, paramagnetism, and ferromagnetism under different conditions in the system. Theoretical studies reported two kinds of magnetic states depending on the existence of kind of edge terminations in MoS_2 namely zig-zag and arm-chair edges (Li et al. 2008; Gao et al. 2017; Tongay et al. 2012). Zig-zag edges are semiconducting and magnetic while arm-chair edges are metallic and non-magnetic. The experimental studies presented a dominating diamagnetic contribution in the MoS_2 sample as shown in Fig. 15.5 (Tongay et al. 2012). The plot shows a ferromagnetic loop in the low field region superimposed with a large diamagnetic background that is clearly visible in the high field region. This implies that the total observed magnetic signal has both diamagnetic and ferromagnetic contributions from MoS_2. Such weak ferromagnetism observed in pristine MoS_2 is attributed to

zig-zag edges and defects. Here the magnetization values are in the range of a few memu/g. These studies prompted that it is possible to enhance the intrinsic ferromagnetism in the MoS_2 by altering the structure and composition to enable these 2D materials for spintronics applications.

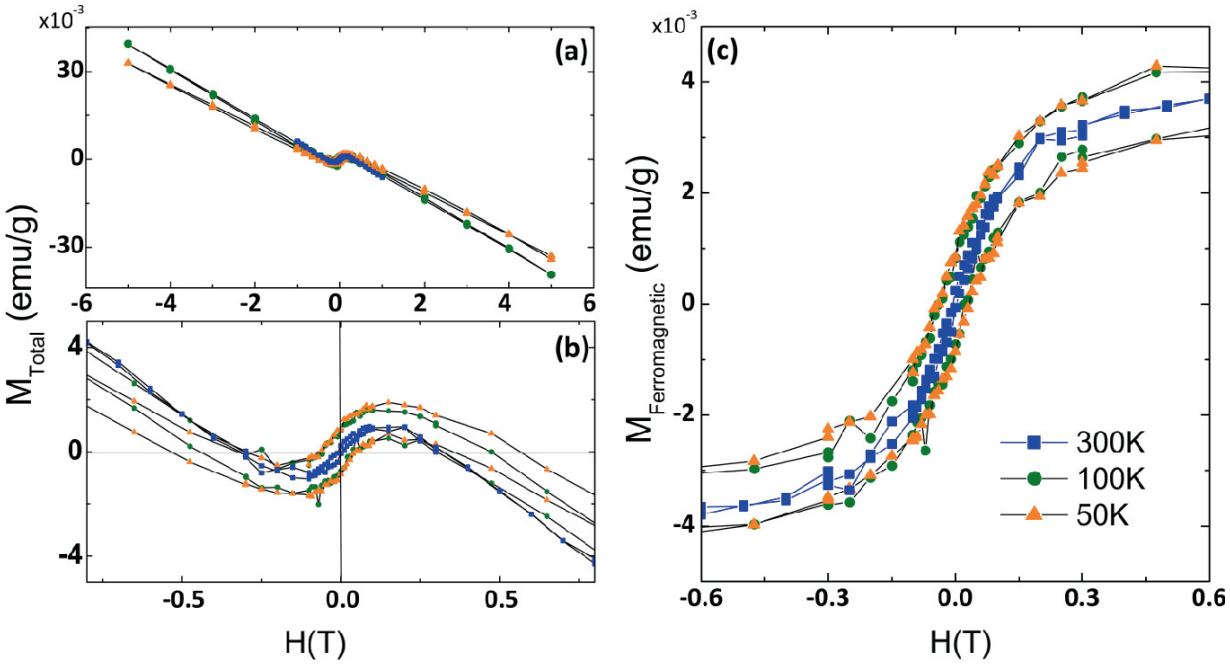

Fig. 15.5 M versus H plot of MoS_2 monolayer at different temperatures (**a**) and **b** as measured M versus H plots and magnified portion at low field region. And **c** M versus H plot obtained after subtracting diamagnetic background.
It is reproduced with permission from American Institute of Physics (Tongay et al. 2012)

TMDs 2D layers other than MoS_2, such as $MoSe_2$, WS_2, WSe_2, $SnSe_2$, etc. having a non-magnetic nature as MoS_2, are also examined by many researchers to induce the ferromagnetism. Most of the semiconducting TMDs have a non-magnetic ground state. However, to enable the injection of spins in the system and for it to be useful as 2D spintronics material, the TMDs should be made ferromagnetic.

Ferromagnetic interactions via Bound Magnetic Polarons:

Weak ferromagnetism in dilute magnetic semiconductors (DMS) is primarily elucidated by the bound magnetic polaron (BMP) Model. This model, initially proposed by Torrance et al. (1972), is widely used to elucidate ferromagnetic coupling in diluted magnetic semiconducting oxides (DMSO) (Ogale et al. 2010) and is currently being proposed for explaining weak ferromagnetism in TMDs (Sanikop and Sudakar 2020). A polaron, a quasiparticle introduced by Pekar (19651965), comprises an electron or hole surrounded by a polarization cloud. This concept of polaron was extended to describe the interactions of charge carriers with low concentrations of magnetic ions present in the lattice. When magnetic ions interact with an impurity site consisting of a loosely bound or trapped charge, the ferromagnetic exchange interaction between magnetic ions is mediated by this localized charge carrier, tending to the formation of BMPs.

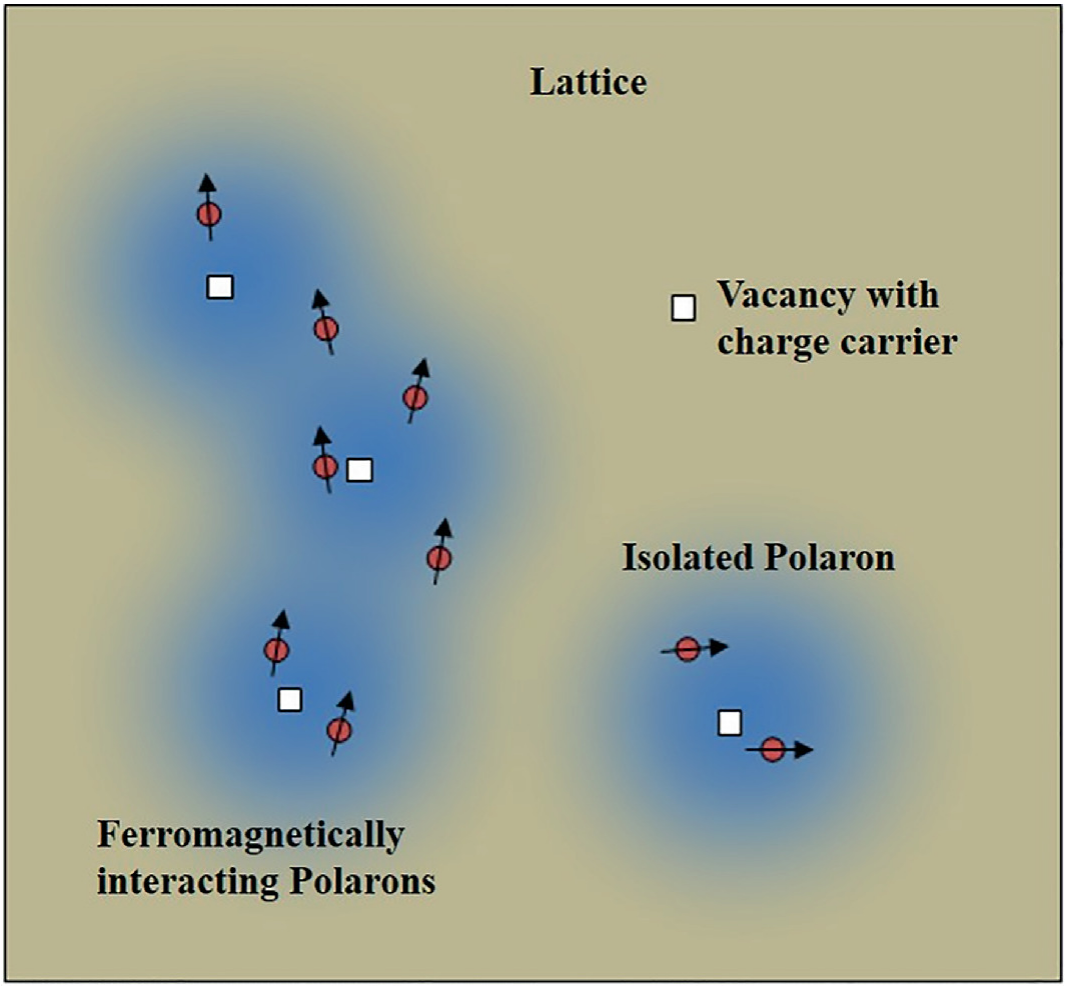

Fig. 15.6 Representation of BMPs (marked by large blue shades). Vacancies are marked by open squares, which donate carriers localized in a volume, allowing spins (black arrows) to couple with one another

According to BMP model, the ferromagnetic exchange interaction of magnetic ions in diluted magnetic oxides is facilitated by the donor electrons trapped due to the formation of oxygen vacancies within their hydrogenic orbits (Fig. 15.6). The trapped electron at the defect site has a Bohr radius r_H is given by,

$$r_H = \varepsilon(m/m^*)a_0$$

where ε is the high-frequency dielectric constant, m is the electron mass, m^* is the effective mass of the donor electrons and a_0 is the Bohr radius (53 pm). The exchange interaction ΔE_{ex}, between magnetic ion and trapped

electron, can be expressed in terms of the *s*-*d* exchange parameter J_{sd} as,

$$\Delta E_{ex} = -J_{sd} S \cdot s|\psi(r)|^2 \Omega$$

where *S* is the spin of the magnetic ion with a volume Ω, *s* is the spin of donor electron and $\psi(r)$ is the wave function of the trapped electron given by,

$$\psi(r) = (\pi r_H^3)^{-\frac{1}{2}} e^{-r/r_H}$$

where r_H is Bohr radius of the trapped electron and *r* is the distance from the nucleus. Increasing the density of trapped electrons enhances the exchange interaction. According to this BMP model, all the spins of the magnetic ions present inside the BMP align in the same direction leading to long-range ferromagnetism through the overlap of neighbouring BMPs. This same mechanism is envisaged for TMDs, where charges trapped within chalcogen vacancies interacting with the magnetic ions can lead to BMPs. Overlapping between the adjacent BMPs in TMDs, consisting of sufficient numbers of defect sites and magnetic ions, can lead to the long-range ferromagnetic ordering.

Inducing ferromagnetism by incorporating unpaired spins in these TMDs can be carried out in multiple ways, namely (Khan et al. 2020),

(a) by defect engineering,

(b) by transition metal cation doping,

(c) by structural phase transition.

In the following section we discuss various methods used to induce the magnetic properties of TMDs which are not intrinsically ferromagnetic. In addition to TMDs, magnetic

properties of other 2D materials including graphene, nitrides, and halides can be induced by these alterations. A summary of such an attempt is also provided in the end.

(a) **Ferromagnetism by defect engineering**:

Defects in TMDs widely influence their intrinsic properties and hence they are advantageous in many ways. The most commonly observed defects are vacancies, grain boundaries, dopants, dislocations, etc. (Lin et al. 2016). The defects are introduced in the system by different means like external doping, inducing strain, using reactive etchant, high energy electron/ion beam irradiation, etc. Sulphur vacancies (V_S) are most common in exfoliated layers, CVD grown and wet chemically synthesized TMD materials. In the following sub-sections, specific examples are presented on the ferromagnetism induced by defect engineering in TMDs.

(i) **MoS_2**:

Proton beam irradiation on MoS_2 with a fluence of 2×10^{18} ions/cm^2 is shown to enhance the ferromagnetic signal with observed $T_C = 895$ K (Fig. 15.7a) (Mathew et al. 2012). Such enhanced ferromagnetism is due to moments arising from the defects including vacancies, interstitials, deformation and partial destruction of the lattice structure, i.e., the formation of edge states and reconstructions of the lattice. The crystallinity of MoS_2 nanosheet can be improved with an increase in the processing temperature thus reducing defects in the system. MoS_2 nanosheets synthesized by hydrothermal method with processing temperatures ranging between 180 and 240 °C (Zhang et al. 2014) show such controlled improvement in the

crystallinity. This, in turn, has been shown to leave a strong impact on the magnetic properties (Fig. 15.7b), thus confirming the role of defect in influencing the ferromagnetic nature of MoS_2 nanosheets. Few-layered, bilayer, and monolayer MoS_2 obtained by mechanical exfoliation method is reported by Sarma et al. (2019). As the number of layers decreases the magnetic moment increases (Fig. 15.7c), thus exhibiting RT-FM. It has been attributed to arise from defect states such as zigzag edges in the grain boundary region or sulphur vacancies. The Weakening of S $2p_{1/2}$ peak in XPS upon exfoliation and a decrease in layer number is observed due to the dislocation of S atom from the edge state. The presence of defects and vacancies in the system was further confirmed from UPS spectra. From DFT theoretical studies it is also noted that the DOS of S 3*p*-derived states near E_f increased significantly with the decrease of the number of MoS_2-layers which can influence the RT-FM. Zhou et al. prepared bowl-like MoS_2 and bilayer MoS_2 flakes by chemical vapour deposition (CVD) (Zhou et al. 2020). In bowl-like MoS_2, vertical layer stacking of MoS_2 is shown to happen only at the edges with the central regions having a height of 0.87 nm and the edges showing a thickness of 15.5 nm. It is interesting to note that large edge defect sites resulting from this kind of stacking are shown to result in enhanced ferromagnetism compared to the diamagnetic nature observed in bilayer MoS_2. MoS_2 pyramids with zigzag-edge-rich layers grown by CVD show robust ferromagnetism compared to MoS_2 flakes and the presence of abundant zigzag edge defects was attributed to the existence of ferromagnetism in the system (Fig. 15.7d) (Zhou et al. 2018). However, the mechanism for defect-induced ferromagnetism is still under debate.

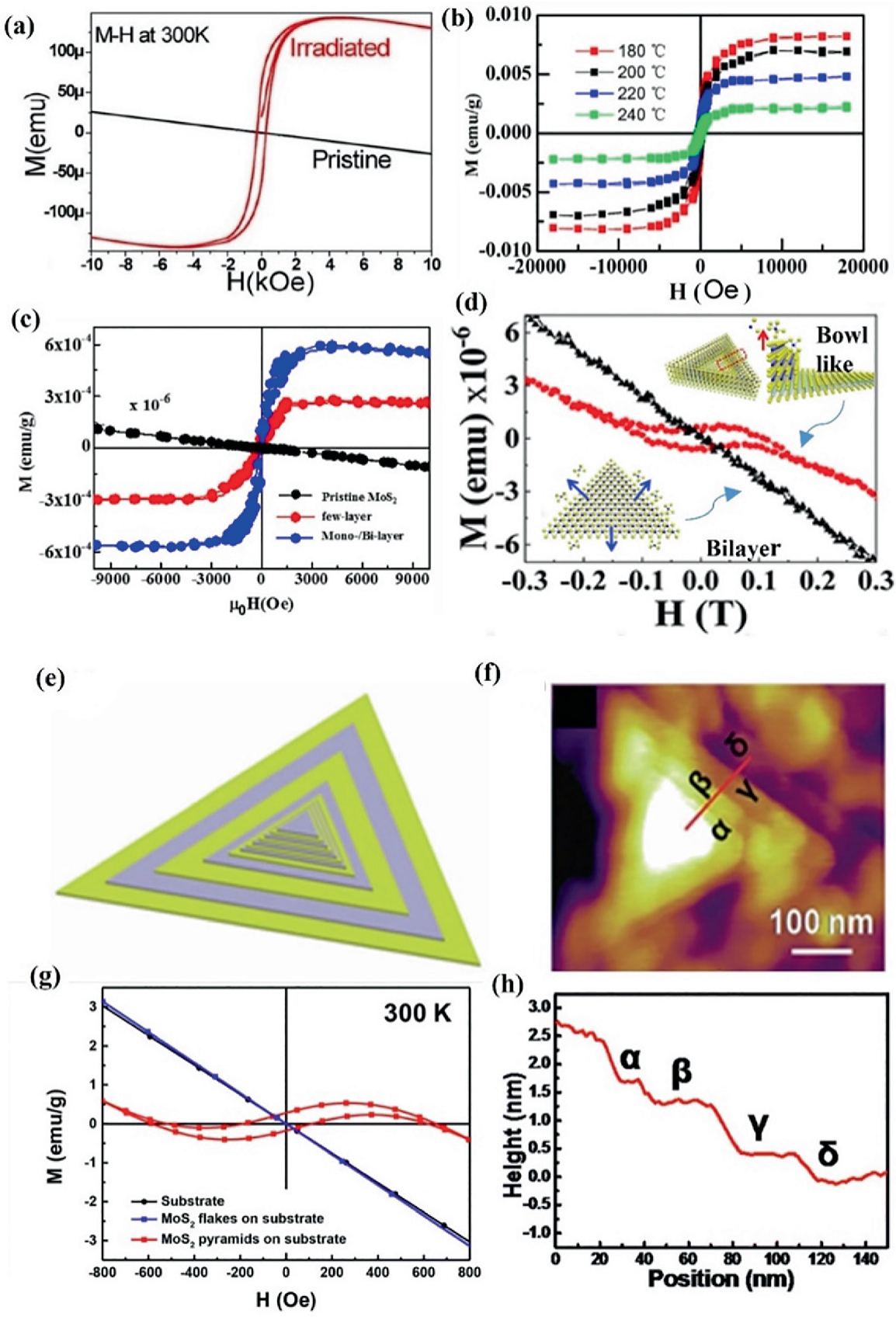
(a)
M-H at 300K
Irradiated
Pristine
M(emu)
H(kOe)
(b)
180 ℃
200 ℃
220 ℃
240 ℃
M (emu/g)
H (Oe)
(c)
x 10^-6
M (emu/g)
Pristine MoS2
few-layer
Mono-/Bi-layer
μ0H(Oe)
(d)
Bowl like
Bilayer
M (emu) x10^-6
H (T)
(e)
(f)
α
β
γ
δ
100 nm
(g)
300 K
M (emu/g)
Substrate
MoS2 flakes on substrate
MoS2 pyramids on substrate
H (Oe)
(h)
α
β
γ
δ
Height (nm)
Position (nm)

Fig. 15.7 **a** M versus H curve at 300 K for a pristine and proton beam irradiated MoS_2 after subtracting the substrate Si contribution. It is reproduced with permission from American Institute of Physics (Mathew et al. 2012). **b** M-H curves for the MoS_2 nanosheets synthesized at different temperatures. It is reproduced with permission under Creative Common License (Open Journal) from Springer Nature (Zhang et al. 2014). **c** Magnetic moment (*M*) versus magnetic field (*H*) curves, measured at room temperature for bulk MoS_2, few-layered MoS_2, and mono-bi layered MoS_2. It is reproduced with permission from IOP Publishing, Ltd. (Sarma et al. 2019). **d** Magnetic hysteresis loop at 5 K for bowl-like MoS_2 flakes and reference CVD-grown bilayer MoS_2 flakes. It is reproduced with permission from American Chemical Society (Zhou et al. 2020). **e** Schematic of MoS_2 pyramids, **f** AFM topography image, **g** M versus H curve at 300 K and **h** height profile across the red line shown in **f**.

e–**h** is reproduced with permission from Royal Society of Chemistry (Zhou et al. 2018)

In a recent work by Rohini et al., layer thickness and defect-density-controlled MoS_2 (2H-phase) nanosheets are obtained by annealing a wet-chemical precursor from 500 to 900 °C (Sanikop and Sudakar 2020). The diffraction peaks in XRD patterns are shown to become narrow as the annealing temperature increases, indicating an improvement in the crystallinity and an increase in the crystallite size of MoS_2 nanosheets. Very contrastingly the low temperature annealed MoS_2 nanosheets are found to be highly defect-rich and the interlayer spacing between the *c* planes (~6.351 Å) is larger. This is attributed to the presence of interlayer defects in the MoS_2 nanosheet. Nanosheets become more crystalline and devoid of defects upon annealing (Fig. 15.8). In MoS_2 nanosheets annealed at 500 °C, the edges of thin sheets are mostly curled up and agglomerated, resulting in the prominent features of bending, folding, curling, and tearing found in the high-resolution transmission electron microscopy images of the nanosheets (Fig. 15.9a–c). Upon annealing the sheets become straight and bending, folding, curling and tearing decrease.

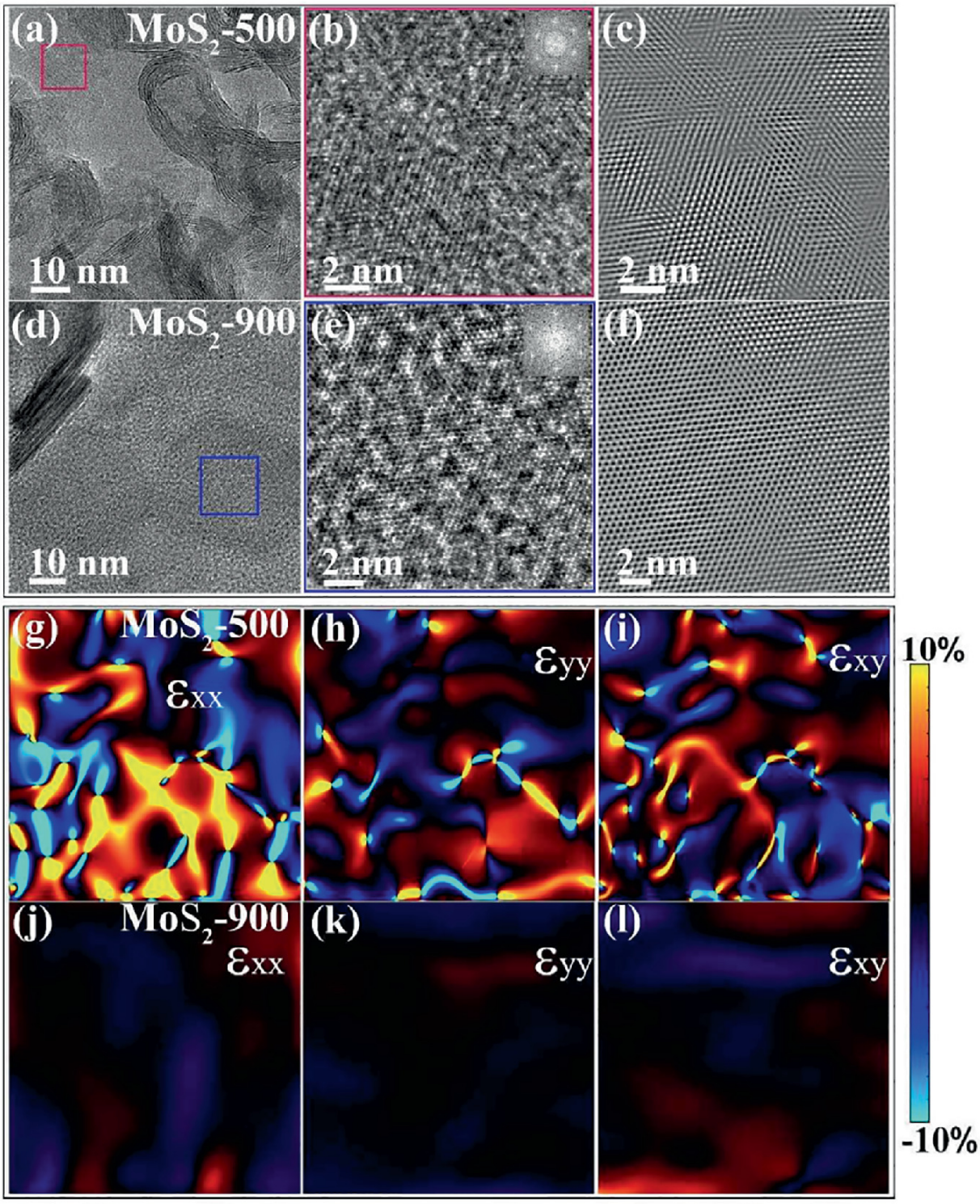

Fig. 15.8 **a** and **d** HRTEM images of MoS_2-500 and MoS_2-900, respectively. **b** and **e** Magnified HRTEM image of flat nanosheet (shown in the square box in **a** and **d**) on which strain mapping is carried out. Inset in **b** and **e** shows corresponding FFT pattern. **c** and **f** are filtered lattice images obtained by inverse FFT. Strain mapping obtained from **c** and **f** are shown in **g**–**i** and **j**–**l**,

respectively. Uniaxial strain ε_{xx} (**g** and **j**), ε_{yy} (**h** and **k**) and shear strain ε_{xy} (**i** and **l**) mapping are shown. The scale for the colour code referring to the strain in % is given.

It is reproduced with permission from ACS Publishers (Sanikop and Sudakar 2020)

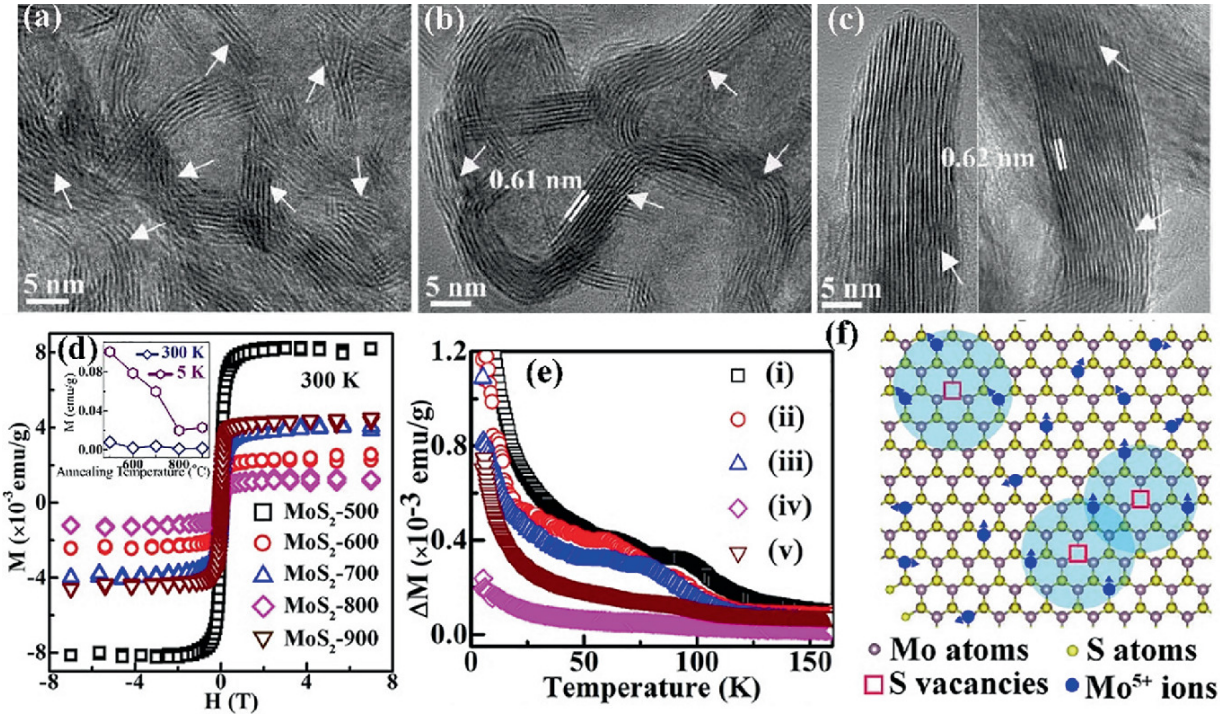

Fig. 15.9 HRTEM images of **a** 500 ºC (MoS_2-500), **b** 700 ºC (MoS_2-700), and **c** 900 ºC (MoS_2-900) annealed MoS_2 nanosheets. White arrows in the bottom panels indicate few representative planar dislocations (including bends, curls, folds and tearing). **d** M versus H curves measured at 300 K (diamagnetic moment subtracted) of MoS_2-T samples annealed at different temperatures (T = 500, 600, 700, 800 and 900 ºC). Inset in **d** shows M_S values versus annealing temperature plot at 5 K and 300 K. **e** $\Delta M = M_{FC}$-M_{ZFC} curves of MoS_2 nanosheets. Numbers (i)–(v) in **e** indicate data corresponding to MoS_2-500, MoS_2-600, MoS_2-700, MoS_2-800 and MoS_2-900, respectively. **f** Representation of bound magnetic polarons (BMPs) (marked by large, shaded circles) in MoS_2 nanosheets. Sulfur vacancies are marked by open pink squares, which donate carriers localized in a volume, allowing spins (blue arrows) on the magnetic sites from Mo^{5+} to couple one another.

It is reproduced with permission from ACS Publishers (Sanikop and Sudakar 2020)

Significant fraction of defect concentration present in the nanosheets can also be discerned from the strain

mapping shown in Fig. 15.8g–i. Defects present in MoS_2 activate the magnetic nature of the defect sites. These magnetically active defects gradually reduce as the annealing temperature is increased, where the nanosheets grow in a more orderly fashion and become well crystallized. The corresponding strain maps also show almost perfect ordering in the structure. Thus, smaller-sized MoS_2 nanosheets with few layers and large defect concentrations exhibit large saturation magnetization (0.10 emu/g at 10 K and 8×10^{-3} emu/g at 300 K) due to the defect-activated magnetic nature. Such samples also show clear ferromagnetic transition at ~120 K as shown in Fig. 15.9e. Magnetization at 5 K demonstrates a systematically higher variation with an order of magnitude greater M_S (~0.10 emu/g) observed in MoS_2 nanosheets produced at 500 °C compared to those synthesized at 900 °C. The systematic decrease in the magnetically active defects upon annealing can be clearly evidenced by the systematic fading of both the magnetization and the ferromagnetic transition shown in Fig. 15.8d. In defect-rich MoS_2 nanosheets, the prevalence of Mo^{5+} and sulphur vacancy point defects is prominent, as indicated by electron paramagnetic resonance and X-ray photoelectron spectra (Sanikop and Sudakar 2020). The ferromagnetic behaviour in MoS_2 is likely attributed to ferromagnetically interacting bound magnetic polarons (BMP). BMP formation arises from the interaction between sulphur vacancies with trapped electrons and the 4d Mo^{5+} magnetic moments within MoS_2 nanosheets, as depicted in Fig. 15.9f. Consequently, in nanosheets annealed at low temperatures, which exhibit a high concentration of sulphur vacancies and Mo^{5+} paramagnetic defects, there is a significant likelihood of overlapping bound magnetic polarons, resulting in an order of magnitude greater magnetization

compared to nanosheets annealed at high temperatures. This investigation by Rohini et al. thus presents an effective strategy for modulating the magnetic properties of MoS_2 by regulating magnetically active defect sites. Such magnetically enhanced 2D MoS_2 nanosheets hold promise for diverse applications in spintronic devices, including spin field-effect switches, spin valves, magnetic sensors, and ultrathin high-density data storage. In addition to these experimental results, the DFT calculations also prompted the ferromagnetic ground state of MoS_2 when TM and non-metal adsorbs on the monolayer and bilayer sheets (Zhou et al. 2020, 2018; Lin and Ni 2014; He et al. 2010; Xia et al. 2015; Mao et al. 2013; Li et al. 2016a). In the case of TM adsorption, calculations proposed interlayer adsorption to be more favourable than surface adsorption in monolayer MoS_2. He et al. explored the magnetic properties in MoS_2 monolayers when non-metallic elements such as H, B, C, N, and F are adsorbed (He et al. 2010). They considered stable configurations for calculation which include adsorption at the top of S atoms, top of Mo atoms, above the middle of the Mo-S bond, and above the center of MoS_2 hexagonal ring. Of these configurations, adsorption of C on top of Mo atom showed a maximum moment of 2 μ_B.

(ii) **$MoSe_2$**:

By getting inspired from the ferromagnetic properties of MoS_2 nanosheets due to zig-zag edges or defects, Xia et al. predicted that low dimensional materials with plenty of edges can be desirable to induce magnetism in 2D TMDs (Xia et al. 2015). To understand the effect of such edge defects, they chose $MoSe_2$ for their studies. A few layered flakes of $MoSe_2$ with a large number of edges were prepared by the CVD growth process. Films were grown on

Si/SiO_2 substrate at temperatures 860 °C. M-H hysteresis studies of this sample at several temperatures starting from 300 to 700 K (after subtracting the linear contribution due to substrate) indicated that the T_C is around 700 K. Though M_S and H_C decrease with increasing the temperature, ferromagnetism still exists up to 700 K which can make it as a potential candidate for next-generation spintronics. To validate the origin of ferromagnetic nature observed with high T_C, larger-sized flakes were synthesized at higher temperatures (900 and 940 °C). By increasing the growth temperature in CVD, the lateral dimension of the prepared flakes is found to get increased (Fig. 15.10a, b) and due to this, the number of edges defects get lowered. Consequent to this ferromagnetism is found to decrease rapidly with growth temperature (Fig. 15.10c) (Xia et al. 2015). This suggests that the main contribution to the ferromagnetic property of $MoSe_2$ flakes arises from the edge states of defects. Spin-polarized DFT simulations also support the contribution of strong spin polarization of the edge Se and Mo atoms on the ferromagnetic moments of $MoSe_2$ nanoflakes.

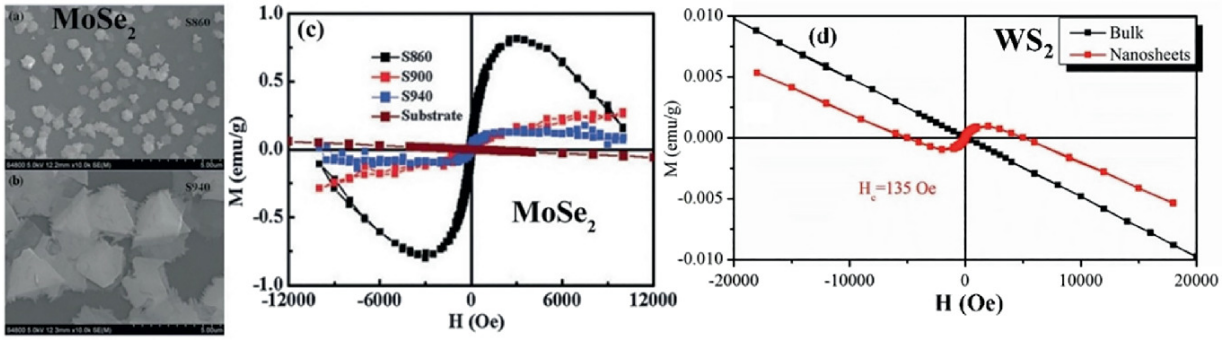

Fig. 15.10 SEM results for $MoSe_2$ nanoflakes grown on SiO_2/Si substrates synthesized at different temperatures. **a** 860 °C (S860), **b** 940 °C (S940). **c** The original M–H curves for $MoSe_2$ nanoflakes synthesized at different temperatures with SiO_2/Si substrates and the bare SiO_2/Si substrate. **a**–**c** is reproduced with permission from the RSC Publishers (Xia et al. 2015). **d** Magnetization versus applied field of bulk and nanosheet of WS_2.

It is reproduced with permission under Creative Common License (Open Journal) from Springer Nature (Mao et al. 2013)

(iii) **WS_2**:

Pristine bulk WS_2 is diamagnetic in nature and Li et al. had examined the effect of spin–orbit coupling in the WS_2 TMD membrane considering the most commonly present point defects. In this work the authors calculated the formation energies of typical point defects including monovacancies, interstitials and anti-sites (Fig. 15.11) and found that the S vacancy (V_S) and adatom S interstitials (S_i) have the lowest formation energies (Li et al. 2016a). Further, V_S as well as W_S and W_{S_2} anti-site defect states exhibit strong splitting when SOC is considered. The presence of point defects also exhibits stronger spin orbit coupling which is expected to alter the host materials properties drastically. The examination of spin orbit coupling for each type of vacancy had confirmed that this defect is responsible for the observation of magnetic state in monolayer WS_2. Experimental studies indeed proved that WS_2 nanosheet exhibit ferromagnetic behaviours in contrast to the diamagnetic nature found in the bulk WS_2 (Fig. 15.10d) (Li et al. 2018; Ahmed et al. 2017; Zhang et al. 2019). The presence of zig zag edge state and high density of sulphur vacancy are found to have a strong correlation to the magnetization. Thus, in WS_2 defects are found to be a strong source for the observation of ferromagnetic order.

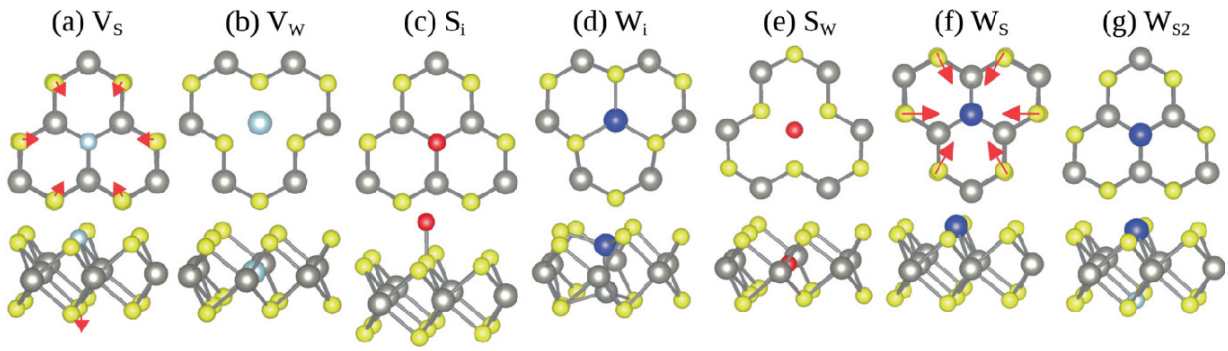

Fig. 15.11 The relaxed structures of all the defective monolayer WS_2 supercells. The vacancies are denoted by the light blue circles. The defect sulphur atoms are marked in red, and defect tungsten atoms in blue. The arrows indicate the directions and magnitudes of the relaxations. V_S and V_W are S and W monovacancies, S_i and W_i are S and W interstitials, S_W, W_S and W_{S_2} are anti-site defects.

It is reproduced with permission from American Physical Society Publishers (Li et al. 2016a)

(iv) $\mathbf{MoTe_2}$:

Transition metal dichalcogenide $MoTe_2$ exist in four different structural forms (1T, 2H, 1T′, 3R phases) similar to MoS_2. 2H phase is the most stable crystal structure in the monolayer. Molybdenum and tellurium atoms are arranged in a hexagonal crystal lattice in a monolayer of $MoTe_2$. $MoTe_2$ has a large excitonic binding energy which results in efficient light emission and high photoluminescence efficiency as well (Cho et al. 2015). The unique electronic and optical properties and strong spin–orbit coupling of $MoTe_2$ make it a promising candidate for electronics, optoelectronics and spintronics.

Defects in $MoTe_2$ monolayer can have significant effects on their electronic and magnetic properties. Recently, most of the researchers have focused their attention towards understanding the collective impact of both the defects and dopants on the electronic and magnetic properties of $MoTe_2$ monolayers, with a specific focus on the realization

of enhancement in magnetic ordering. Theoretical studies suggest that the presence of intrinsic structural defects can induce magnetism in the monolayer $MoTe_2$. The presence of both point defects and boundary defects (1D defect) can induce spin polarization thus enabling the magnetic behaviour in monolayer $MoTe_2$ (Li et al. 2018).

(b) **Ferromagnetism by doping**:

Doping is the one of the most important approaches for the realization of ferromagnetic ordering at room temperature. TM doping is a common technique to tune magnetic properties. This approach is also widely explored in 2D TMDs. Below we provide a few specific examples where the dopants induce ferromagnetism in TMDs.

(i) **MoS_2**:

Various transition metal dopants such as V, Cr, Mn, Fe, Co, Ni, Cu, Re, Dy, Ho (Table 15.3) are incorporated in MoS_2 to tailor ferromagnetism (Xia et al. 2018; Zhao et al. 2019a, 2019b; Lee et al. 2014; Sanikop et al. 2021; Shen et al. 2022; Xie and Zhang 2016; Hutten et al. 2021; Yun et al. 2020; Zhang et al. 2020). Table 15.3 lists the M_S and Curie temperature (T_C) values observed in various transition metal-doped MoS_2 systems. The doping, in general, is found to induce room-temperature ferromagnetism (RT-FM) in MoS_2. However, a large variation of reported saturation magnetization (M_S) (at 300 K) is noted with M_S varying from ~0.001 to ~0.4 emu/g. In the case of Fe, Dy and Ho doped MoS_2 synthesized by hydrothermal method, MoS_2 is found to remain stabilized in 2H phase even after the doping (up to ~2.5 at.%). However, doping

concentration dependent ferromagnetism reported in these systems is presented. Enhanced ferromagnetism is observed for doping concentrations up to ~1.5 at.% and with further increase in the concentration the magnetization is reported to decrease. Among all these dopants, Fe doping in MoS_2 has been reported to yield robust ferromagnetism with a saturation magnetization of 0.247 emu/g (1.74 at.%) at 300 K (Xia et al. 2017a). The mechanism for ferromagnetism in these systems is explained based on the bound magnetic polaron model.

Table 15.3 M_S values in various MoS_2 doped systems

Dopant in MoS_2	**Concentration (at.%)**	**Curie temperature T_C (K)**	**M_S (× 10^{-3} emu/g)**	**References**
V	5	10	67	Ahmed et al. (2017)
Cr	4	300	16	Zhang et al. (2019)
Mn	7	50	15	Wang et al. (2016)
Fe	1.74	300	247	Xia et al. (2017a)
Co	3	300	1	Xia et al. (2016)
Re	17	5	16	Xia et al. (2018)
Dy	1.4	300	20	Zhao et al. (2019a)
Ho	1.5	300	55	Zhao et al. (2019b)

Wang et al. also demonstrated robust ferromagnetism in Mn doped MoS_2 nanostructures (Fig. 15.12). Electron paramagnetic resonance measurements were reported to scrutinize the paramagnetic or ferromagnetic nature. With increasing Mn doping concentration to 7 at.%, the

coercivity in the system also increased to 1076 Oe (Fig. 15.12a) (Wang et al. 2016). Further, strong temperature-dependent coercivity was observed, i.e. coercivity decrease was noted with an increase in temperature. This study also reported two distinct magnetic transitions at 150 K and 80 K in the paramagnetic background subtracted M versus T plot (Fig. 15.12b). These transitions are attributed to the strong exchange interaction between carriers in the MoS_2 with Mn^{2+} dopants. It is noteworthy that such ferromagnetic-like transition (with $T_C = 120$ K) is also reported in pristine MoS_2, which is postulated to arise from the strong exchange interaction between spin-1/2 Mo^{5+} and charge carriers due to V_S (Sanikop and Sudakar 2020). Room temperature ferromagnetism is observed in Co doped MoS_2 nanosheets as well. Pristine MoS_2 showed M_S of 2×10^{-3} emu/g. On the contrary to the Mn doping, M_S decreases to 1.7×10^{-3} emu/g and 0.8×10^{-3} emu/g for Co concentrations of 3 at.% and 7 at.%, respectively. The nanosheet thickness increased with an increase in doping concentration and nanosheets became much flat. This decrease in magnetization with Co doping is also explained based on first-principle calculations (Xia et al. 2016).

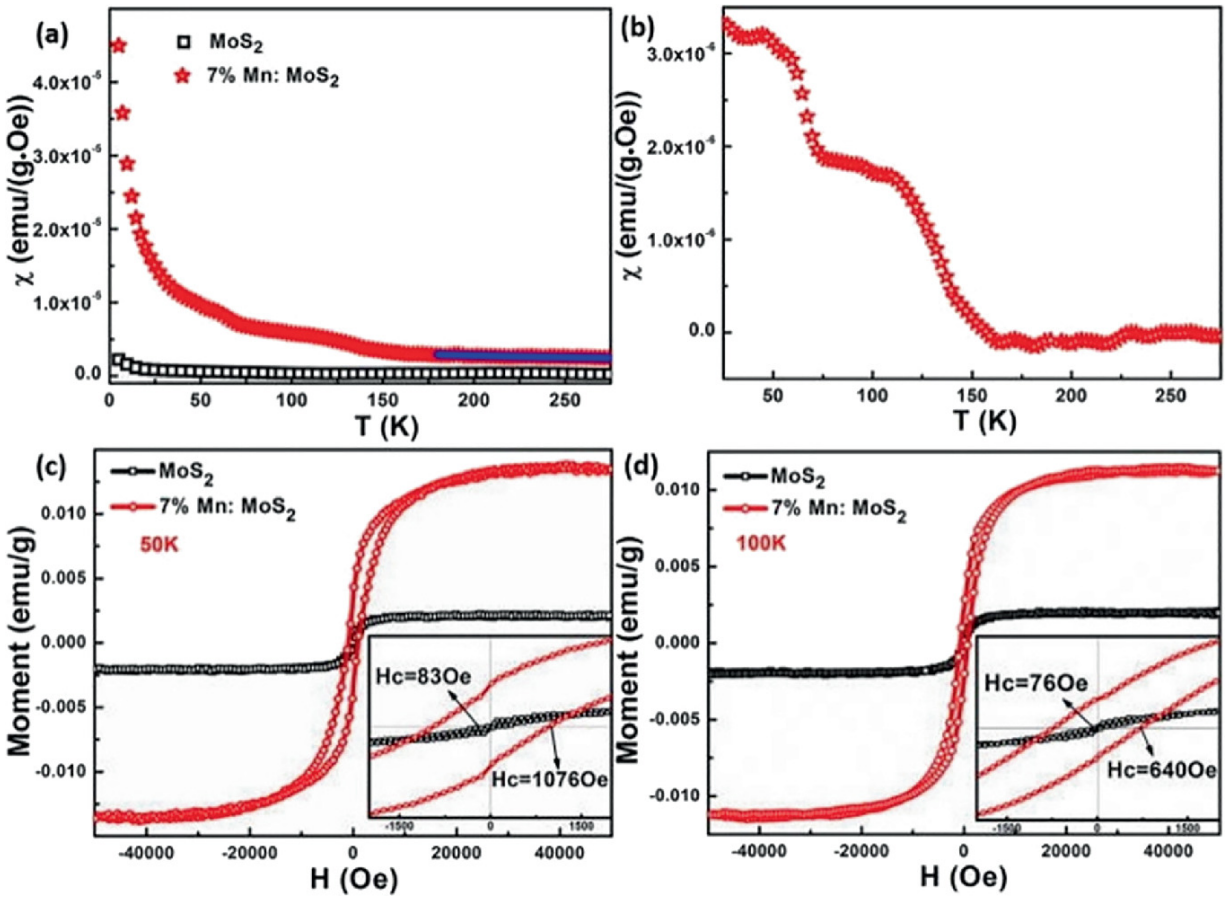

Fig. 15.12 **a** Temperature-dependent susceptibility curve obtained at a field of 500 Oe. The fitting of Curie–Weiss Law at high temperature is shown in blue line. **b** Plot obtained after paramagnetic background subtraction. M versus H plot measured at **c** 50 K and **d** 100 K, respectively.

a–**d** It is reproduced with permission from American Institute of Physics (Wang et al. 2016)

Ahmed et al., demonstrated large coercivity up to 1.87 kOe in 5 at.% V doped MoS_2 nanosheets synthesized by hydrothermal method (Fig. 15.13). This is higher than the reported coercivity values in ZnO based diluted magnetic semiconductors (~1.3 kOe) (Lee et al. 2014). The coercivity also exhibited strong temperature dependence and decreased from 1.87 kOe to 81 Oe with an increase in temperature from 10 to 300 K (Ahmed et al. 2017). Such a large value in coercivity is attributed to the combined effect of the V doping and doping-induced stress or defects in MoS_2. V doping promotes the charge transfer between V

and S ions and generates the anisotropic geometry of V–S bonds (Fig. 15.13b). This anisotropy in localized charge distribution and pinning effect by the defects or induced by stress may induce the high coercivity.

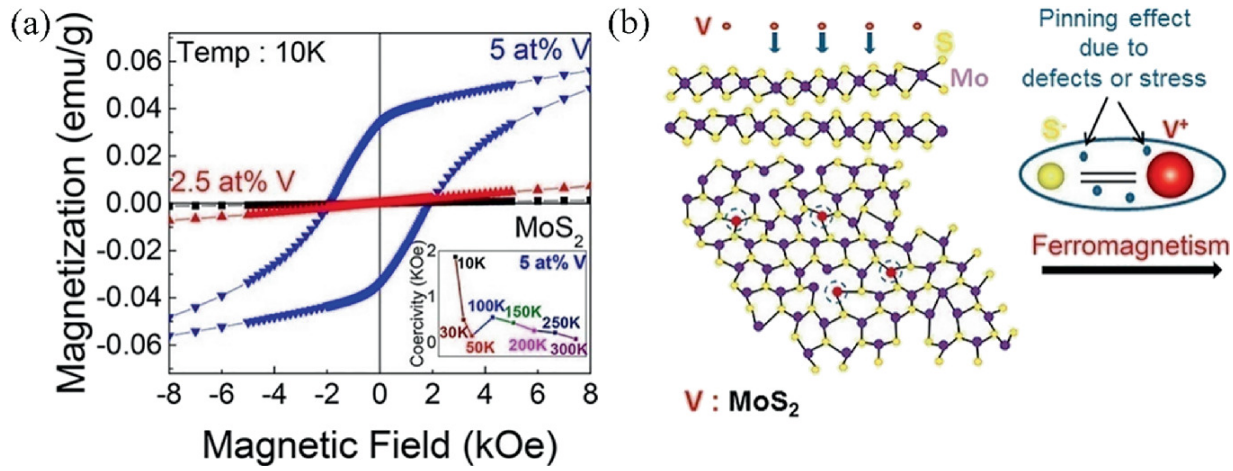

Fig. 15.13 **a** M versus H plot of V doped MoS_2 nanosheets. **b** Vanadium doping in MoS_2 and charge transfer between V and S ions.

It is reproduced with permission from American Chemical Society (Ahmed et al. 2017)

Rohini et al. synthesized pristine MoS_2, and Co/Mn doped MoS_2 nanosheets by wet chemical method to study the dopant-induced ferromagnetism in MoS_2. Doping was carried out in the range of $x = 0$ to 0.25 by a wet chemical process. While X-ray diffraction patterns confirm the 2H polytype of MoS_2 for both pristine and doped nanosheets, for Co doping with $x > 0.05$, Co_9S_8 secondary phase is discerned in the diffraction pattern. Unlike cobalt doping which is found to be very effective, and that Co exists in a mixed oxidation state of 2+/3+, Mn doping in MoS_2 is found to be very ineffective, as discerned from X-ray absorption near-edge spectral studies, for even x up to 0.25 in the initial precursor solution, where Mn predominantly exists in 4+ oxidation state. MoS_2 nanosheets exhibit weak ferromagnetism [magnetization $(M_S) = 19 \times 10^{-3}$ emu/g and

1.3×10^{-3} emu/g at T = 5 K and 300 K] mostly arising from the planar defects. $Mo_{1-x}Mn_xS_2$ and $Mo_{1-x}Co_xS_2$ ($x = 0.025$–0.25) show ferromagnetic S-shaped hysteresis loop superimposed on the diamagnetic background. The curves after subtracting diamagnetic background for $Mo_{1-x}Mn_xS_2$ and $Mo_{1-x}Co_xS_2$ systems are shown in Fig. 15.14. While the magnetization is roughly 6 (3) times higher for Mn-doped MoS_2 than the pristine MoS_2 nanosheets at 300 K (5 K), large enhancement by 7 (37) times is found for Co-doped MoS_2 nanosheets when measured at 300 K (5 K). A small change in M_S for $Mo_{1-x}Mn_xS_2$ nanosheets is due to ineffective Mn substitution at Mo sites. For Co doping three distinct regions are seen: (i) Diluted magnetic semiconductor (DMS) kind with dominant ferromagnetism from $x = 0$ to 0.025, (ii) DMS ferromagnetism coexisting with increasingly becoming antiferromagnetic MoS_2 for $0.025 < x \leq 0.1$, and (iii) Co_9S_8 phase segregations beyond $x > 0.1$ leading to large magnetization (Sanikop et al. 2021). Thus, while the hysteresis loops at 300 K provide evidence for the existence of room temperature ferromagnetism in doped MoS_2 systems some element of uncertainty exists due to the ineffective substitution or phase segregation at higher concentration. However, transition metal doping with appropriate dopants and the right amount of dopants in MoS_2 could set up strong magnetic interactions in the system, making them a promising candidate for diluted magnetic semiconductors.

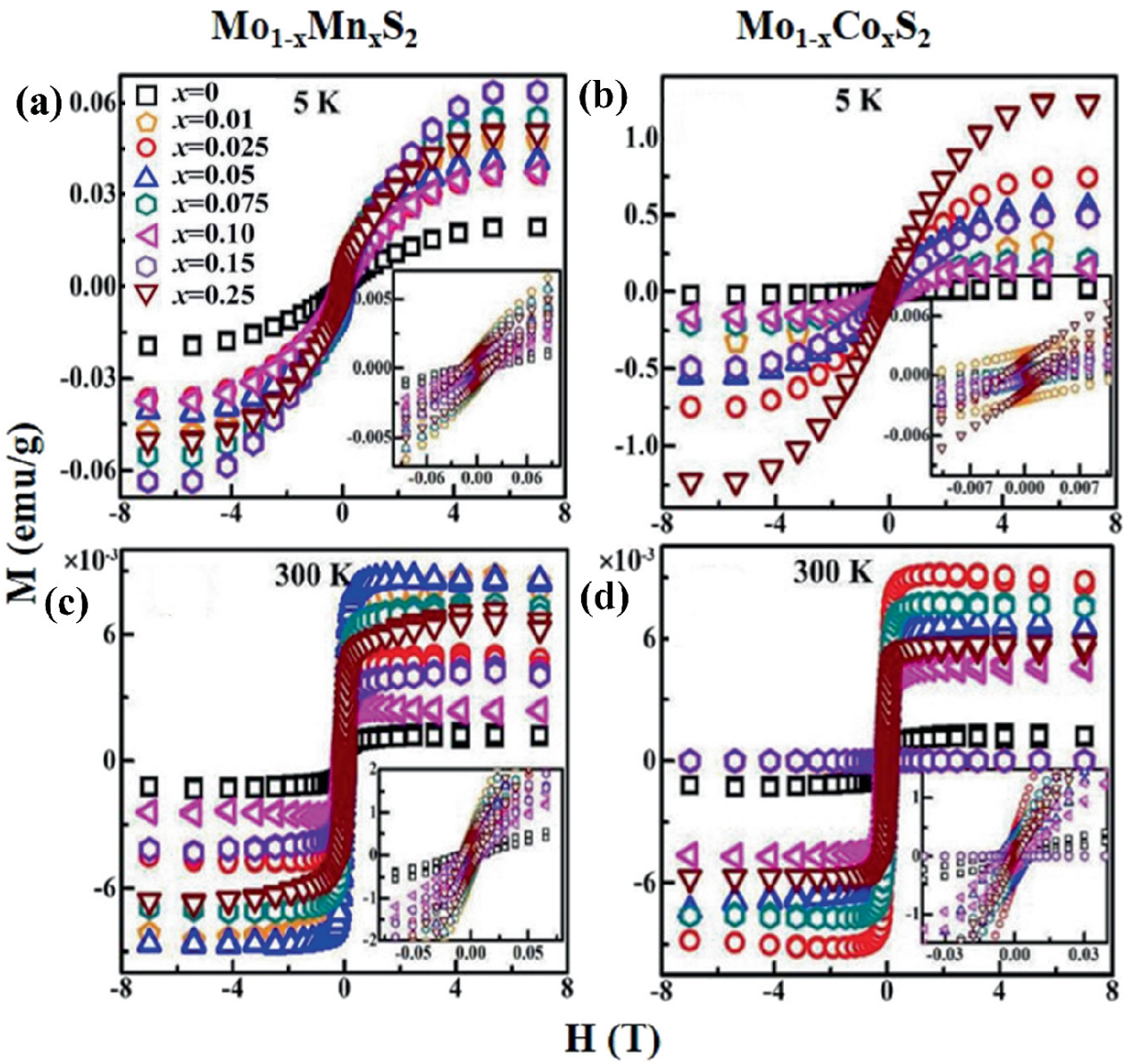

Fig. 15.14 High-field linear change in magnetization subtracted M versus H curves of **a**, **c** $Mo_{1-x}Mn_xS_2$ and **b**, **d** $Mo_{1-x}Co_xS_2$ nanosheets at **a**, **b** 5 K and **c**, **d** 300 K. Inset in all figures show magnified portions of plots at low magnetic field regions.

a–**d** It is reproduced with permission from Elsevier (Sanikop et al. 2021)

(ii) **$MoSe_2$**:

For studying the magnetic properties of these TM (Fe, Co and Ni) doped-$MoSe_2$, Shen et al. (2022) reported direct synthesis via one-pot mixed-salt-intermediated chemical

vapour deposition (MSI-CVD) method. Transition-metal doping of Fe, Co and Ni doped $MoSe_2$ nanosheets was confirmed by high-angle annular dark-field scanning transmission electron microscopy (HAADF-STEM). Ferromagnetic signature in the M-H hysteresis loop measured (Shen et al. 2022) at 10 and 300 K (Fig. 15.15) give clear evidence of near room temperature ferromagnetism. The magnitude of the hysteresis loop is found to shrink at 300 K than at 10 K. The saturation magnetization (M_S) and coercive field (H_C) decrease with increasing temperature due to increasing thermal fluctuation. Further, the temperature dependences of zero-field cooled (ZFC) and field-cooled (FC) magnetization curves indicate that the curie temperature (T_C) of Fe-doped and Ni-doped $MoSe_2$ are ~300 K and the T_C of Co-doped $MoSe_2$ is ~250 K (Shen et al. 2022).

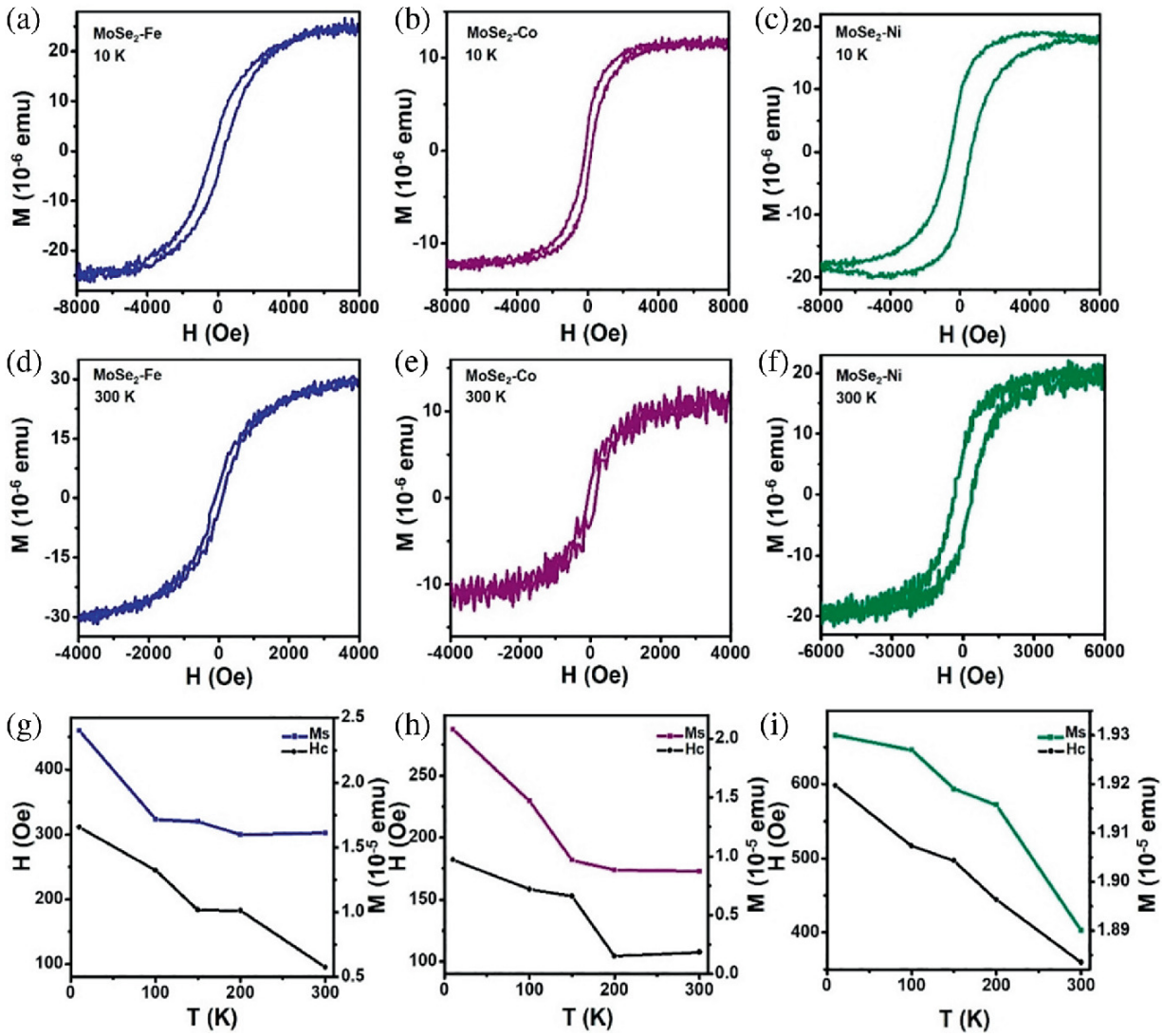

Fig. 15.15 Magnetization characterization of Fe-doped (3.48%), Co-doped, and Ni-doped $MoSe_2$. **a**–**c** Magnetic hysteresis loops for Fe-doped, Co-doped, and Ni-doped $MoSe_2$ at 10 K, respectively. **d**–**f** Magnetic hysteresis loops for Fe-doped, Co-doped, and Ni-doped $MoSe_2$ at 300 K, respectively. **g**–**i** Temperature dependences of M_S and H_C for Fe-doped, Co-doped, and Ni-doped $MoSe_2$.

a–**i** is reproduced with permission from American Chemical Society (Shen et al. 2022)

(iii) $\mathbf{WS_2}$:

Theoretically, Xie et al. have reported the magnetic property of pristine WS_2, doping of single TM and equimolar-dopant of double TM atoms (Mn, Fe, Co, Ni) (Xie and Zhang 2016). Single transition metal doped WS_2 monolayer are predicted to yield half metallic ferromagnet. The origin of magnetic ordering is due to direct exchange interaction for single doped transition metal atoms. Of various TM dopants studied, Mn doped WS_2 is the most stable. But for double equimolar-dopant of double TM doped WS_2, double exchange mechanism is shown to be responsible for ferromagnetic ordering except for Ni system.

Kang et al. have experimentally studied the magnetic property of CVD synthesized pristine and Fe doped WS_2 monolayer shown in Fig. 15.16d (Hutten et al. 2021). Paramagnetic state for the Fe doped system is predicted due to very less charge transfer between Fe dopant and neighbouring S atom. This is suggested to lead to the lack of magnetic ordering in doped WS_2 monolayer. On the other hand, vanadium doped WS_2 monolayer was found to exhibit room temperature ferromagnetic behaviour (Yun et al. 2020). Magnetic properties of the pristine WS_2 and 0.4, 2 and 12% vanadium doped WS_2 were studied by Zhang et al. (2020). A weak ferromagnetic behaviour was observed in the pristine WS_2, whereas, V doped WS_2 showed enhanced ferromagnetic ordering with large saturation magnetization and coercivity. Like most of the studies M_S is largest for an optimum concentration of 2% V doping shown in Fig. 15.16a–c and it reduces beyond it. The theoretical studies reported by this group suggested that the coupling between unpaired 3*d* electron of vanadium atom and the 5*d* and 3*p* states of nearest neighbours, viz W and S, respectively, result in strong exchange interaction (Li et al. 2016b). Zhao et al. theoretically reported that

ferromagnetism can be realized in case of the different X doped (Ni, Pd, Pt) WS_2 monolayer systems. The doping is most suitable under S rich condition due to its lower formation energy and relatively easier to incorporate X atom into WS_2 under S-rich condition than W-rich condition (Zhao et al. 2016a).

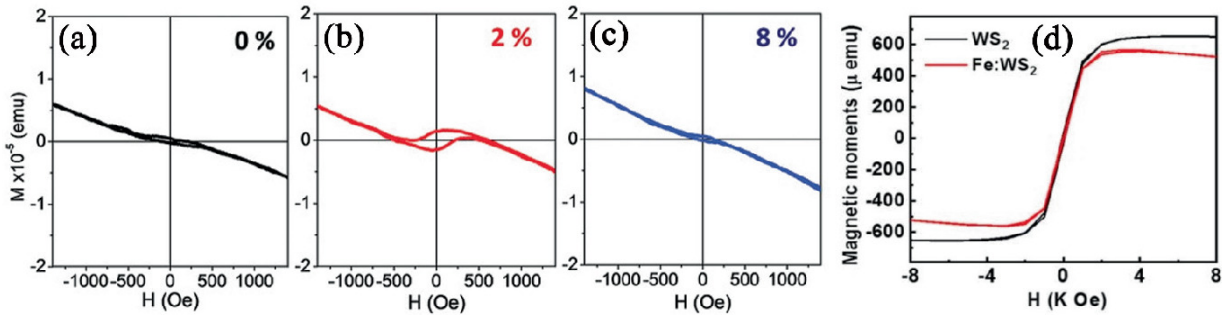

Fig. 15.16 **a–c** Magnetic hysteresis loops of pristine and doped 2, 8 at.% vanadium WS_2 monolayer. It is reproduced with permission from John Wiley and Sons (Xie and Zhang 2016**). d** Magnetization versus applied field measurement of pristine and Fe doped WS_2 monolayer taken at 300 K. It is reproduced with permission from IOP Publishing, Ltd. (Hutten et al. 2021)

(iv) **$MoTe_2$**:

Pristine $MoTe_2$ is nonmagnetic in nature. Kanoun (2018) has theoretically reported the significant modification of the magnetic behaviour by doping various 3d transition metal atoms (Fe, Cr, Mn, Ni) in $MoTe_2$ monolayer. According to their report except for Ni, all transition metal atom doped $MoTe_2$ monolayer leads to the appearance of long-range ferromagnetic ordering with a larger magnetic moment. This is due to strong *p*-*d* hybridization between 3*d* band of the transition metal atom and *p* band of the neighbouring atom. Long-range ferromagnetic ordering in $MoTe_2$ has been realized experimentally by introducing defects via nonmagnetic dopants such as Tantalum. Yang et

al. (2019) have experimentally shown that the CVD synthesized and Ta doped 2H $MoTe_2$ with a few or monolayer mixed nanosheets show long-range ferromagnetic ordering with Curie temperature above 400 K. Approximately four times larger hysteresis is observed in the case of Ta doped mixed $MoTe_2$ nanosheets compared the pristine mixed $MoTe_2$ nanosheets (Fig. 15.17c, d). On the contrary the bulk $MoTe_2$ is diamagnetic in nature (Fig. 15.17a, b). The long-range ferromagnetic ordering in mixed $MoTe_2$ nanosheets is attributed to the presence of Te vacancy, disorder, amorphous imperfection and edge states. Ta doping in $MoTe_2$ nanosheets increases these defect densities, thus resulting in the enhanced long-range ferromagnetic ordering in mixed thin nano sheets. Coelho et al. have studied the magnetic properties of the post-growth incorporation of vanadium and titanium atom in 2D $MoTe_2$ metastable phase (Coelho et al. 2019). In this technique, the $MoTe_2$ surface is coated with Ti and V by using a mini electron beam evaporator at room temperature. They observed room temperature ferromagnetic ordering in the V doped 2H-$MoTe_2$ with Curie temperature above 300 K (Fig. 15.17g), whereas Ti dopant is found to be non-magnetic despite similar incorporation. Ferromagnetic properties have been shown even in low vanadium concentration (0.2%) samples. When the V doped $MoTe_2$ is heated to 500 K, vanadium rearranges itself into thermodynamically favourable impurity configuration and this suppresses the ferromagnetic property. The saturation magnetization is increasing with increasing vanadium concentration for both 10 and 300 K. But this trend is higher in case of 10 K as shown in Fig. 15.17h. This study highlights the importance of controlled magnetic impurity doping and further adjusting the annealing condition in the

post growth process to realize magnetic functionality in the 2D materials.

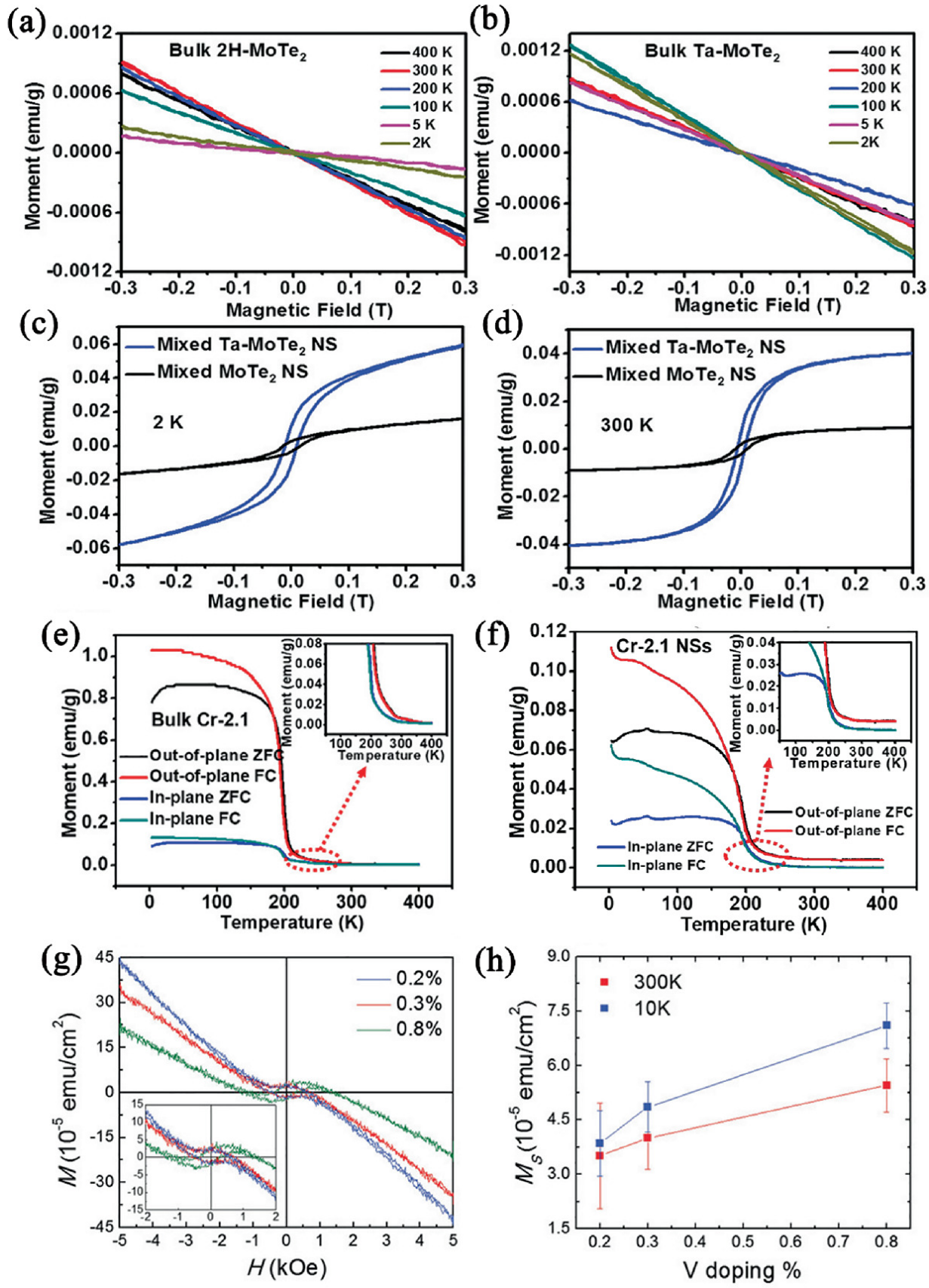
(a)
Bulk 2H-MoTe2
400 K
300 K
200 K
100 K
5 K
2K
Moment (emu/g)
Magnetic Field (T)
(b)
Bulk Ta-MoTe2
400 K
300 K
200 K
100 K
5 K
2K
Moment (emu/g)
Magnetic Field (T)
(c)
Mixed Ta-MoTe2 NS
Mixed MoTe2 NS
2 K
Moment (emu/g)
Magnetic Field (T)
(d)
Mixed Ta-MoTe2 NS
Mixed MoTe2 NS
300 K
Moment (emu/g)
Magnetic Field (T)
(e)
Bulk Cr-2.1
Out-of-plane ZFC
Out-of-plane FC
In-plane ZFC
In-plane FC
Moment (emu/g)
Temperature (K)
(f)
Cr-2.1 NSs
Out-of-plane ZFC
Out-of-plane FC
In-plane ZFC
In-plane FC
Moment (emu/g)
Temperature (K)
(g)
0.2%
0.3%
0.8%
M (10-5 emu/cm2)
H (kOe)
(h)
300K
10K
Ms (10-5 emu/cm2)
V doping %

Fig. 15.17 Magnetic property of bulk and mixed nanosheets of undoped and doped $MoTe_2$ samples. M-H curve of **a** undoped and **b** Ta-doped $MoTe_2$ bulks from 2 to 400 K at a magnetic field range of −0.3 to 0.3 T, respectively. Magnetic hysteresis loop of mixed nanosheets (few/monolayer) of doped and Ta doped $MoTe_2$ at 2 K (**c**) and 300 K (**d**). **a**–**d** is reproduced with permission from John Wiley and Sons (Yang et al. 2019). **e**, **f** Temperature-dependent magnetization of the bulk and Cr-2.1 nanosheet sample with 1000 Oe magnetic field applied for out-of-plane and in-plane orientation respectively. It is reproduced with permission from American Chemical Society (Yang et al. 2021). **g** *M*–*H* hysteresis measurement taken at 10 K for $MoTe_2$ with 0.2, 0.3, and 0.8% of Vanadium concentration. **h** The variation of the linear diamagnetic background is a consequence of different substrate thicknesses. Variation in magnetization saturation with the V concentration.

g, **h** is reproduced with permission from John Wiley and Sons (Coelho et al. 2019)

Recently Yang et al. have shown long range ferromagnetic ordering above room temperature in bulk $MoTe_2$ grown by flux growth method as well as in thin nanosheet of Cr-doped 2H $MoTe_2$ synthesized by ultrasonic exfoliation process of bulk crystals. ZFC and FC magnetization versus temperature measurement has been performed to study the magnetic behaviour for both in-plane and out-of-plane applied magnetic field of 1000 Oe (Yang et al. 2021). They have observed the reduction in Curie temperature from 293 K in the case of 2.1% Cr doping in bulk $MoTe_2$ to 220 K in the case of thin nanosheets (Fig. 15.17e, f). This may be due to thermal fluctuation in the thinner counterpart (Mermin and Wagner 1966). There are also reports on the observation of ferromagnetic ordering with large coercivity and saturation magnetization by defect and doping effect of cobalt in a bulk single crystal of $MoTe_2$ by ion implantation method (Ahmed et al. 2022).

(c) **Ferromagnetism by structural phase transition**:

Structural phase transition in TMDs brings a change in electronic band structure. For example, 2H phase is

semiconducting while 1T phase is metallic. The phase transition from 1 to 1T′ again opens up a small bandgap in monolayers. Thermodynamic stability of these different structural phases is strongly related to material, for example, MoS_2 and WS_2 are mostly stable 2H phase in ambient conditions whereas $CrTe_2$ exists in the 1T phase. As, in general, no growth techniques can directly yield these different phases, several methods are followed to stabilize them. The phase transitions in these materials are mostly accomplished by post-growth treatment like thermal annealing (Ma et al. 2015), laser irradiation (Cho et al. 2015), chemical treatment (Kappera et al. 2014) or ion beam/e-beam irradiation (Voiry et al. 2015; Li and Chen 2017). Mostly the challenge is to stabilize 1T, 1T′, 3R phases. Due to their metastable nature, they convert back to their most thermodynamically stable structure like 1H or 2H. The phase transitions like 1T and 1T′ bring a change in the physical property of the system, and hence observation of exotic properties like magnetoresistance (Ali et al. 2014), superconductivity (Pan et al. 2015), Weyl semi-metallicity (Soluyanov et al. 2015), spin hall effect (Qian et al. 2014) etc.

(i) **MoS_2**:

Yan et al. employed the lithium intercalation method to separate the monolayers from the bulk MoS_2 (Yan et al. 2015). It was demonstrated that the crystal structure underwent a partial transformation from the 2H phase to the 1T phase upon exfoliation. The proportion of the 1T phase formed after exfoliation was found to be 0.82. Magnetic investigations of samples with a 2H:1T phase ratio of 1:0.82 indicated a transition from a diamagnetic to a paramagnetic state. Subsequent annealing at 453 K in an argon atmosphere led to a further reduction in the fraction

of the 1T phase, resulting in a 2H:1T phase ratio of 1:0.08. This reduction caused the magnetization to decrease from 0.015 to 0.002 emu/g. The increase in magnetization due to the structural phase transition is attributed to the Mo atoms occupying octahedral sites instead of their initial trigonal prismatic sites following the phase change. In the trigonal prismatic coordination geometry (as in the 2H phase), Mo^{4+} with an electronic configuration of [Kr]$4d^2 5s^0$ forms three non-degenerate 4d energy levels, namely a', e', and e''. The ground state a' has two electrons paired up, resulting in a net zero magnetic moment for MoS_2. Conversely, in the octahedral coordination geometry (as in the 1T phase), with two non-degenerate sets of 4d orbitals, namely t_{2g} and e_g, Mo accommodates two spin-up electrons in the t_{2g} degenerate levels, leading to a net magnetic moment of 2 μ_B per MoS_2 formula unit. The electronic structure of MoS_2 undergoes modification due to charge transfer from intercalating ions (Py and Haering 1983; Wang et al. 2014; Enyashin and Seifert 2012; Jin et al. 2018). Owing to the large interplanar spacing (approximately 6.2 Å), alkali metal ions (such as lithium and sodium) can occupy interlayer sites between adjacent MoS_2 layers, serving as electron donors. These intercalating ions destabilize the 2H/3R phase, leading the system to stabilize in the 1T phase. Such a phase transition involves intralayer atomic plane gliding via a transverse S-layer displacement. Therefore, the intercalation of alkali metal ions in multilayered MoS_2 nanosheets transforms the structure into the 1T-MoS_2 phase. Despite numerous studies, the impact of lithium intercalation on the magnetic properties of multilayered MoS_2 nanosheets remains unknown.

Cai et al. have demonstrated robust ferromagnetism in MoS_2 nanosheets with localized structural phase transition

from 2H to 1T (Fig. 15.18) (Cai et al. 2015). This structural phase transition is obtained by creating sulphur vacancies in the system during hydrothermal synthesis. Room temperature ferromagnetism with an increase in magnetization from 0.02 to 0.25 μ_B with T_C value of 395 K has been realized by this process. With up to 25% of 1T phase concentration and with an average size of 2 nm of the local 1T phase regions, the distance between two neighbouring 1T lies in the range of 1–3 nm, which is smaller than the size of a polaron (3 nm). Thus, ferromagnetism in such system is enabled by the strong coupling between the vacancy induced 1T phase through bound magnetic polarons (Fig. 15.18d).

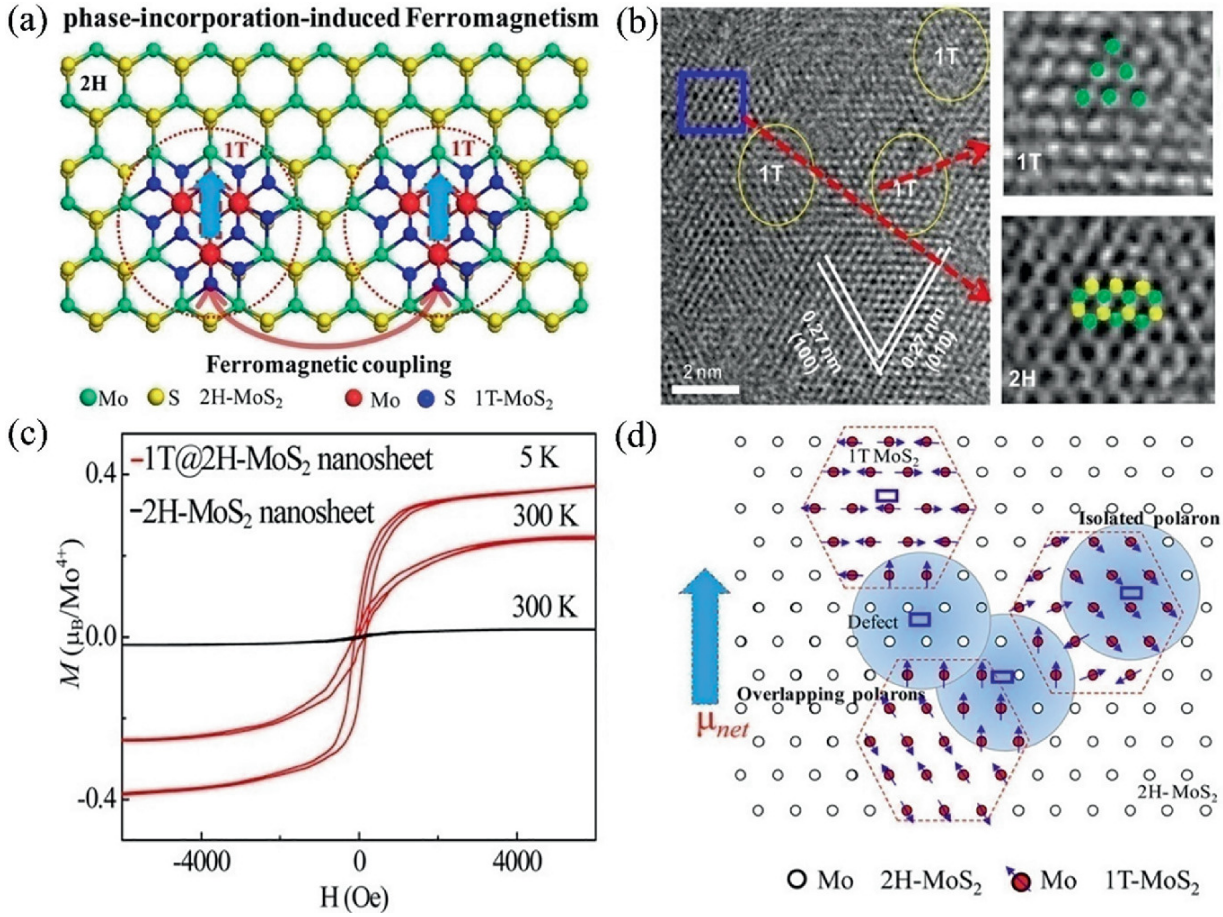

Fig. 15.18 **a** Schematic representation of 1T phase incorporation in 2H inducing ferromagnetism, **b** HRTEM image revealing 1T and 2H, **c** M versus H curve at 5 and 300 K. and **d** Representation of BMP model.

It is reproduced with permission from the American Chemical Society (Cai et al. 2015)

Lithium intercalation and deintercalation in MoS_2 nanosheets: Rohini et al. investigated the magnetic properties of MoS_2 nanosheets subjected to lithium intercalation and subsequent deintercalation, revealing distinct degrees of disorder. MoS_2 nanosheets annealed at low temperature (500 °C), denoted as MoS_2-500, consisting of approximately 5 layers with smaller crystallite size (~3 nm), exhibited a higher density of defects, leading to a notably large fraction of under-coordinated sulphur atoms (Sanikop et al. 2020). In contrast, nanosheets annealed at high temperature (900 °C), labelled as MoS_2-900, comprised an average of 16 layers with larger crystallite size (~9 nm) and demonstrated lower defect density. Upon lithium intercalation, MoS_2-500 exhibited a higher lithium intake ($x \approx 2$) compared to bulk MoS_2 ($x \approx 1$), while MoS_2-900 showed a lithium intake of $x \approx 1.6$. Both MoS_2-500 and MoS_2-900 with lithium intercalation exhibited significantly enhanced ferromagnetism, with magnetization values of 0.4 emu/g and 0.21 emu/g, respectively. Moreover, it was demonstrated that even after deintercalation, a substantial portion of ferromagnetism persisted due to the presence of Mo^{4+} in the distorted octahedral geometry with $S = 1$ in de-lithiated MoS_2 nanosheets.

Intercalation of lithium induces a transformation of the 2H-MoS_2 phase into 1T-Li_xMoS_2, accompanied by alterations in the spin state. Initially, Mo^{4+} ions with a spin (S) of 0 in a trigonal prismatic geometry transition to Mo^{3+} with $S = 3/2$ in an octahedral geometry (Sanikop et al. 2020). However, Mo^{5+} ions situated at defect sites maintain their trigonal prismatic geometry with an oxidation state change to Mo^{4+}, resulting in a net magnetic moment (m) of

0 μ_B. Conversely, Mo^{3+} in MoS_2 yields m = 3 μ_B after lithium intercalation. Raman spectra confirm the presence of the 1T phase, with the J2 and J3 modes at 236 cm^{-1} and 335 cm^{-1}, respectively. These structural features align with the observed magnetic properties. MoS_2-500, rich in defects, exhibits a significant fourfold increase in saturation magnetization (M_S) at 5 K (from 0.1 to 0.4 emu/g) upon lithium intercalation. In contrast, MoS_2-900, with suppressed defects, shows low $M_S = 0.028$ emu/g and experiences a one-order increase in $M_S = 0.21$ emu/g upon lithium intercalation (Fig. 15.19c). Delithiation retains a substantial fraction of lithium at defect sites. The presence of distorted octahedral geometry with S = 1 Mo^{4+} continues to provide a ferromagnetic state for delithiated MoS_2 nanosheets. This investigation highlights that the 1T phase exhibits a favourable ferromagnetic ground state, resulting in significantly greater magnetization in lithiated MoS_2 nanosheets. The ferromagnetic contributions in pristine, lithiated, and delithiated MoS_2 stem from S = 1/2 Mo^{5+} in trigonal prismatic geometry, S = 3/2 Mo^{3+} in octahedral geometry, and S = 1 Mo^{4+} in distorted octahedral geometry, respectively. In all of these cases, a bound magnetic polaron (BMP) is formed with spins from Mo-ions and trapped carriers present at the sulphur vacancies, and the extent of the BMP overlap seems to decide the magnetization values (Fig. 15.19b) (Sanikop et al. 2020). Thus, defect sites with associated phase transition is found to influence magnetic properties of lithiated and delithiated MoS_2 nanosheets as analyzed by Rohini et al. and such approaches with controlled phase change and defect concentration can be utilized to induce the magnetization in a controlled fashion in TMDs.

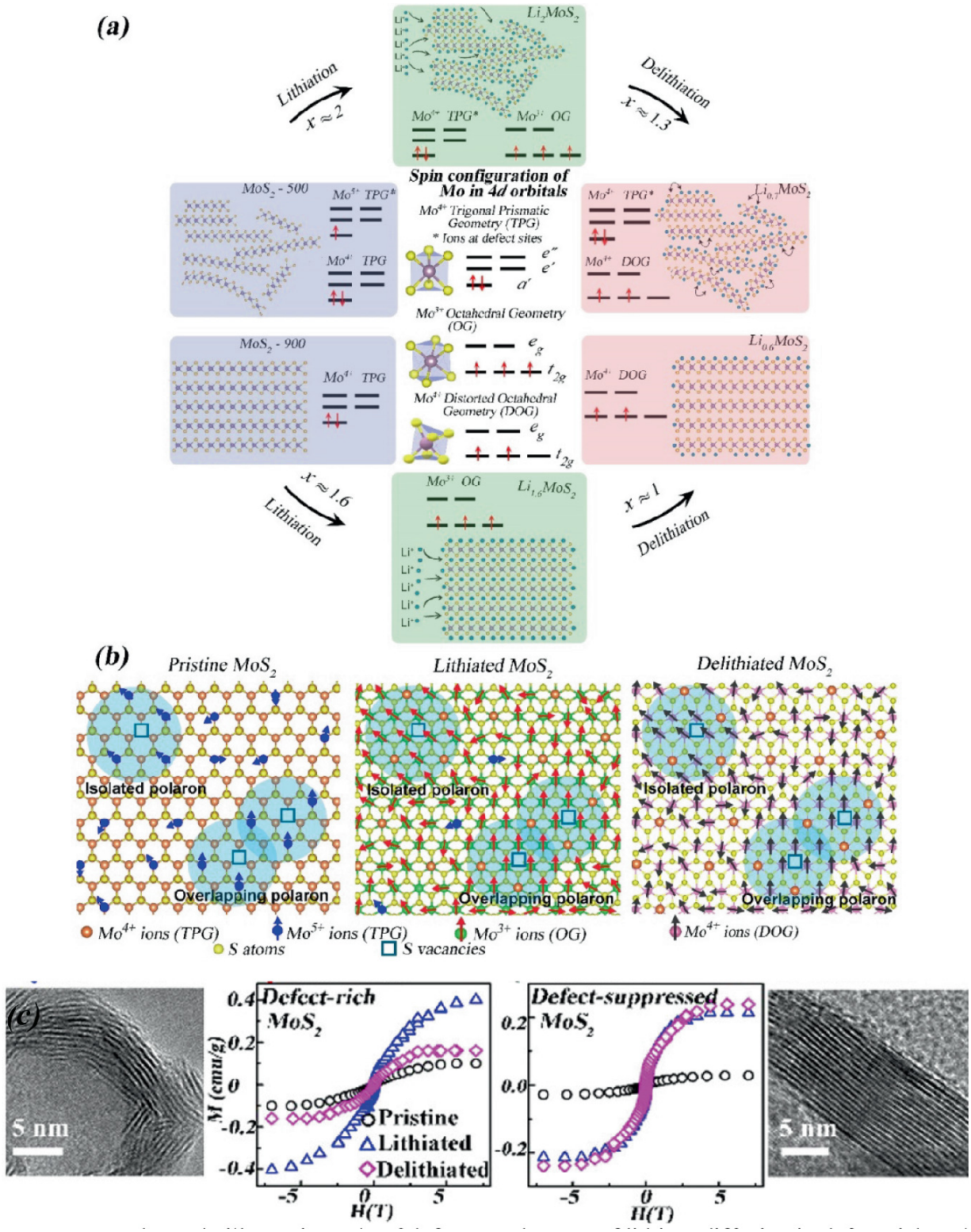

Fig. 15.19 **a** Schematic illustrating role of defects on the ease of lithium diffusion in defect-rich and defect-suppressed MoS_2 nanosheets. The electronic configuration of Mo in pristine, lithiated and delithiated system is represented

within coloured square box. Red arrows represent spins and black dashed lines Mo 4*d*-orbitals. The coordination geometry of Mo in all three phases are shown at the centre. **b** Representation of BMPs (marked by large shaded circles) in MoS_2 systems. V_S are marked by open squares, which donate carriers localized in a volume, allowing spins (blue $S = \frac{1}{2}$, red $S = \frac{3}{2}$ and black $S = 1$ arrows) on the magnetic sites from Mo^{5+}, Mo^{3+} and Mo^{4+} to couple with one another. **c** Magnetic properties of defect-rich MoS_2 and defect-suppressed MoS_2 in the pristine, lithiated and delithiated state. Representative HRTEM image of pristine MoS_2 nanosheets are presented next to the M-H plots.

It is reproduced with permission from Reprinted with permission from American Chemical Society (Sanikop et al. 2020)

Re doping in MoS_2 by hydrothermal method promoted structural phase transition (2H to 1T) in MoS_2 nanosheets (Fig. 15.20) (Xia et al. 2018). The localized 1T phase is thermally stable in all the samples. For doping concentration of 17 at.% large magnetization of 8×10^{-3} emu/g is observed at 300 K. Mo^{4+} in 2H phase does not have unpaired spins giving a net magnetic moment of 0 μ_B, however, with two unpaired spins in 1T phase gives a net magnetic moment of 2 μ_B. Also, Re^{4+} has one and three unpaired electrons in 2H and 1T phase, respectively (Fig. 15.20d). With an increase in Re doping concentration, the fraction of 1T phase increased in the system thus enhancing the ferromagnetism in the system.

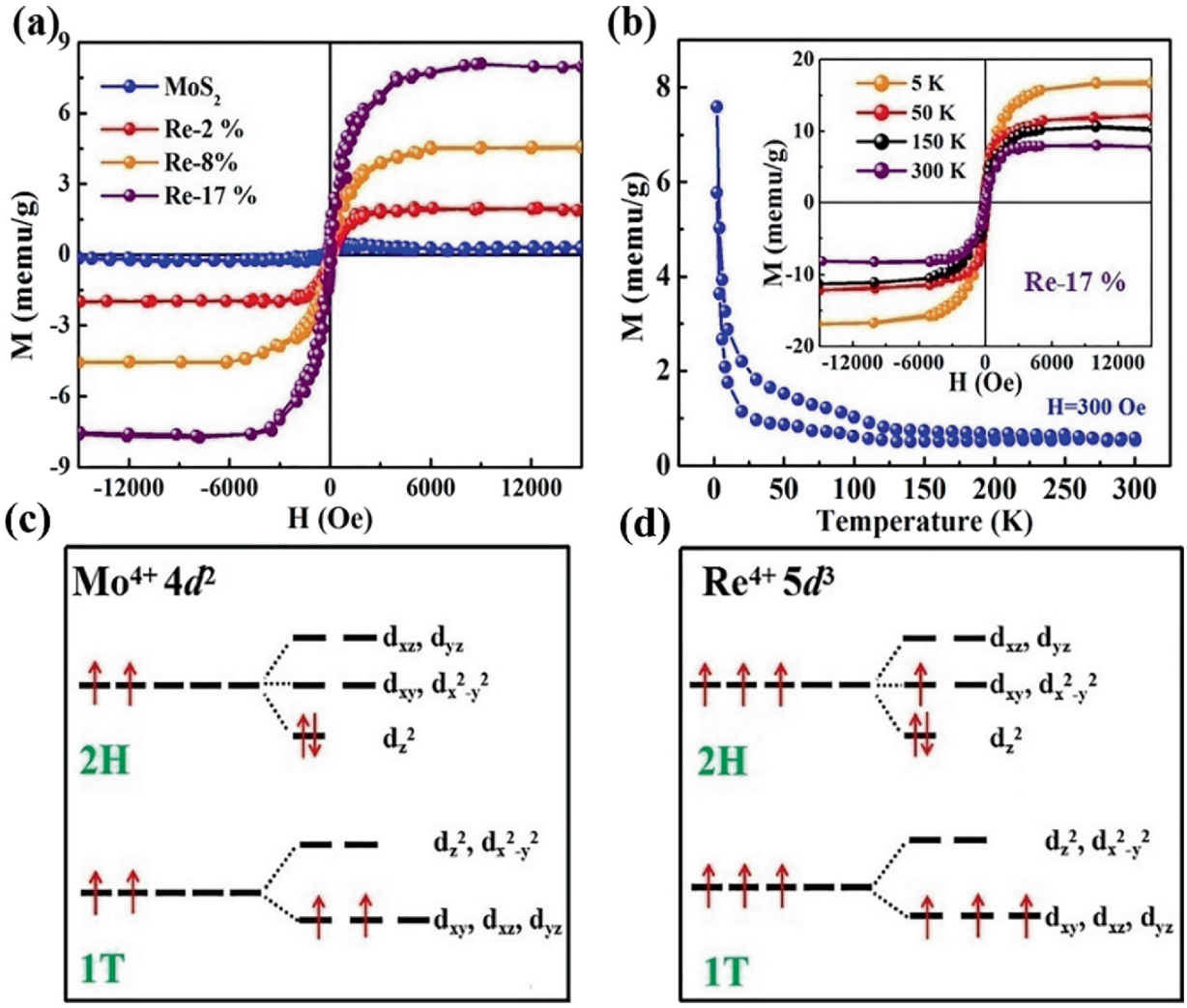

Fig. 15.20 **a** M versus H plots for pristine and Re-doped MoS_2 nanosheets. **b** ZFC and FC plot of Re-doped (8%) MoS_2. The inset shows M versus H plot of Re-17% measured at 5, 50, 150, and 300 K. Coordination geometry of 1T and 2H **c** MoS_2 **d** ReS_2 nanosheets.

It is reproduced with permission from Reprinted with permission from American Institute of Physics (Xia et al. 2018)

(ii) $MoSe_2$:

Xia et al. reported the phase transfer induced ferromagnetic properties of $MoSe_2$ nanosheets (Xia et al. 2017b). These nanosheets were prepared by two-step solvothermal method where the ratio of 2H and 1T phase

changes depending on the timing of heating in autoclave in the 2nd step. With the increase of heating time from 0 to 4 h, 8 h and 20 h the concentration of 1T phase increases to 30.19%, 65.58% and 83.95%, respectively (Fig. 15.21a) (Xia et al. 2017b). It shows that with increasing concentration of 1T phase upon annealing time, M_S also increases from 0.32 to 1.6 memu/g and then to 8.36 memu/g. Such a large increase in M_S indicates the introduction of 1T phase up to 65.58% in $MoSe_2$ nanosheets (Fig. 15.21b). Due to the different splitting of *d* orbitals in 2H and 1T phase Mo^{4+} has magnetic moment 0 μ_B and 2 μ_B respectively. This helps in improving ferromagnetic behaviour. Further, above room temperature T_C of these nanosheets was confirmed by ZFC/FC studies. Ironically, increasing 1T phase further with 1T to 2H ratio of 83.95%, M_S decreases to 2.3 memu/g. With a larger fraction of 1T region in $MoSe_2$ sample and more Mo^{4+} with 2 μ_B spins also form in the lower Se vacancy regions. Due to the majority of Mo atoms in the surroundings of Se atoms rather than Se vacancies, they existed as isolated Mo atoms anti-ferromagnetically coupled with Se atoms. So, enhancing 1T phase ratio above a certain value will not be helpful in increasing M_S further.

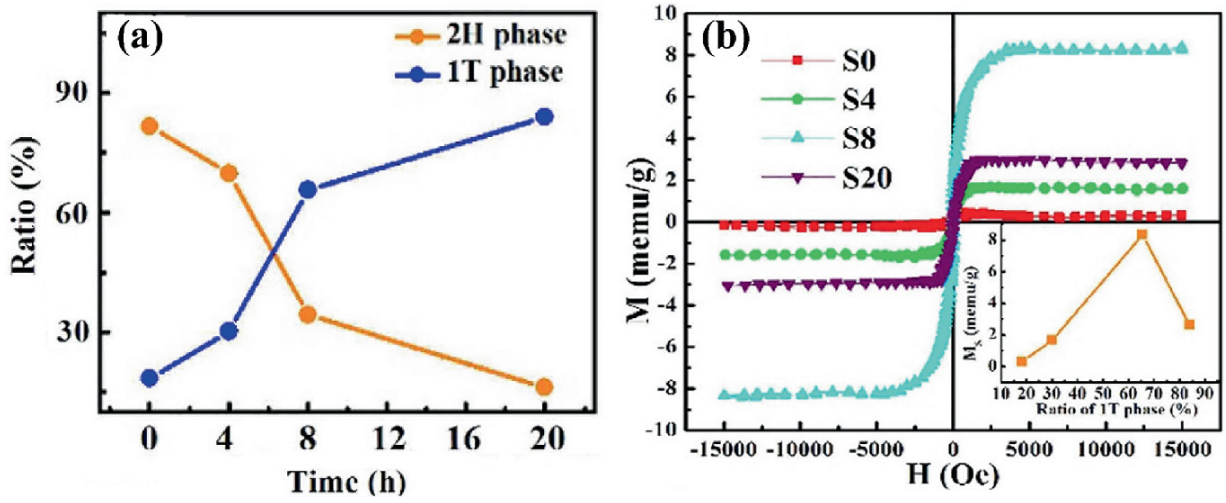

Fig. 15.21 **a** The ratio of 1T and 2H concentrations of four synthesized samples are plotted vs heating time. The ratio is estimated from the XPS results. **b** M-H hysteresis loops of S0, S4, S8 and S20, inset is the saturate magnetization with respect of 1T structure concentration in $MoSe_2$ nanosheets. It is reproduced with permission from Springer Nature (Xia et al. 2017b)

15.3 Theoretical Study of Extrinsic Ferromagnetism in 2D TMDs

Numerous theoretical studies have investigated the magnetic properties of 2D TMDs conducted by various researchers. We offer a brief overview of selected studies that demonstrate the ferromagnetic behaviour through specific defects, dopants, or structural phase stabilization scenarios in the following section. The compiled magnetic moment data from these studies specifically for MoS_2, $MoSe_2$, $MoTe_2$, and WS_2 is presented in Fig. 15.22.

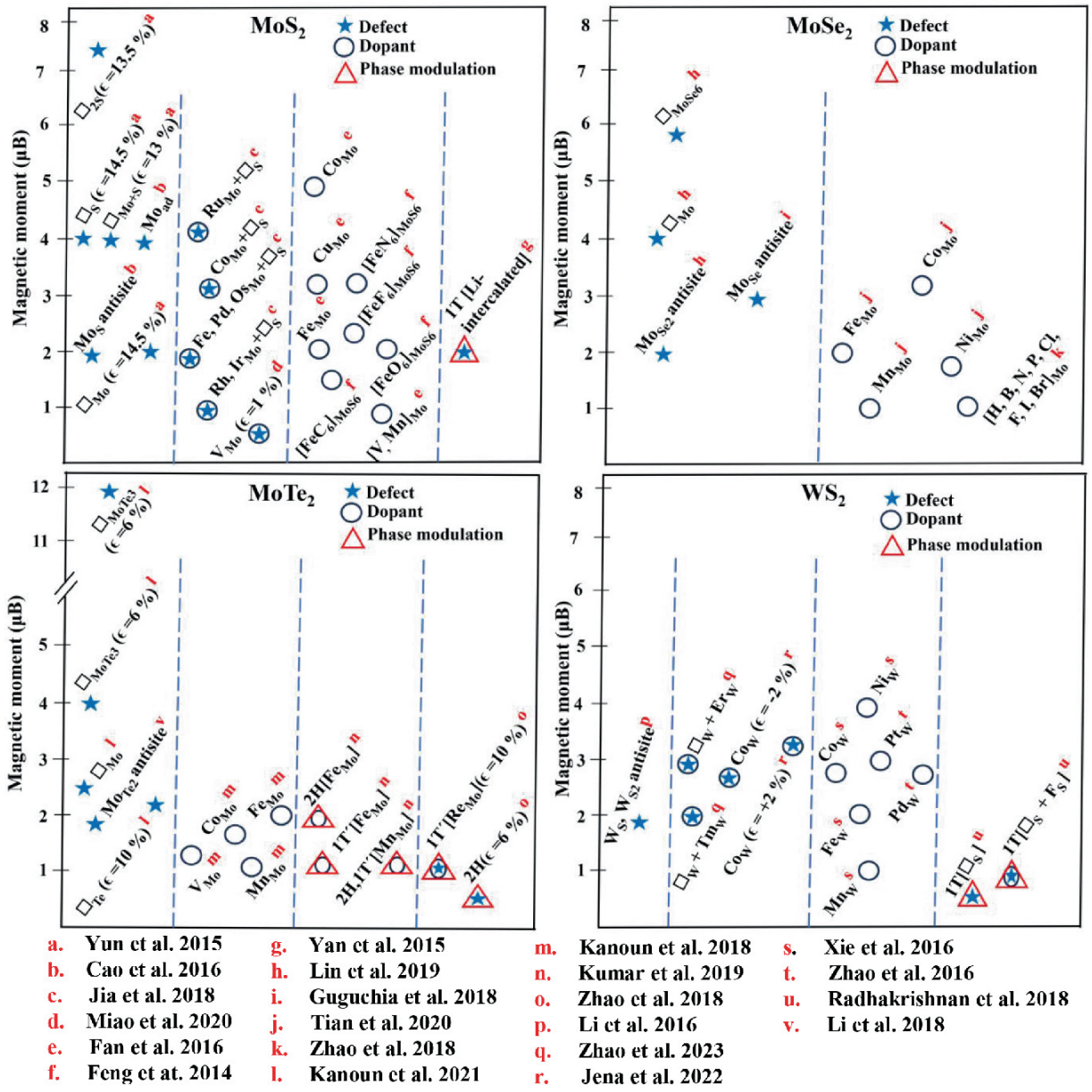

Fig. 15.22 Magnetic moments of various defects (filled star symbols), dopants (open circle) and phase modulated systems (open triangle) or combinations of these (overlapping symbols) in MoS_2, $MoSe_2$, $MoTe_2$ and WS_2. The magnetic moment values are taken from various research works whose references, indicated in the alphabet superscripts (red color), are provided below the figure

(a) **Ferromagnetism by defect engineering**:

(i) **MoS_2**:

In a study conducted by Cao et al., the structural, electronic and magnetic properties of intrinsic defects including Mo or S vacancies, adsorption of metal cations, and anti-site defects in MoS_2 were investigated using first principle calculations (Cao et al. 2016). Adsorption of a Mo atom (Mo_{ad}) on MoS_2 monolayer, which introduces four electrons in the system, can generate a magnetic moment of 4 μ_B. Mo substitution at the S site (Mo_S) can induce spin polarization with a total magnetic moment of 2 μ_B. On the other hand, S substitution at a Mo site (S_{Mo}) and the vacancy of Mo (V_{Mo}) are found to be nonmagnetic, but their n-type and p-type semiconducting properties make them potentially useful in future device applications.

When tensile strain is applied to various vacancy-induced MoS_2 monolayers (1L-MoS_2), they exhibit ferromagnetic and metallic behaviour. In a study employing DFT simulations by Yun and Lee (2015) it was found that vacancy of two S atoms (V_{2S}) with a strain of 13.5% exhibits the highest magnetic moment of 7.45 μ_B and it was also found to be energetically most stable. Additionally, other systems such as V_{Mo}, V_S and V_{Mo+S} with respective strains of 14.5%, 14.5% and 13% also demonstrate ferromagnetic properties with magnetic moments of 2.02 μ_B, 4.07 μ_B and 4.04 μ_B, respectively (Yun and Lee 2015). Cuifang Zia et al. studied the combined effect of doping of group eight atoms via substitution of Mo atom and sulphur (S) vacancy on the electronic and magnetic properties of MoS_2 monolayers by DFT simulations (Jia et al. 2018). It is found that the net magnetic moment of the doped system can vary depending on the distance between the dopant and the S vacancy (V_S), as the V_S diminish the effect of magnetic dopant elements. They have calculated the corresponding T_C using mean field approximation, and

their results indicated T_C values above room temperature for Fe, Co, Rh, Ru, Ir doped MoS_2 monolayers. However, Ni doped system exhibited zero magnetic moment regardless of the presence of V_S. Except for Ni, MoS_2 doped with other group VIII elements, in conjunction with V_S, typically exhibit net magnetic moment ranging from 1 to 3 μ_B. This room temperature ferromagnetism, combined with high magnetic moments, makes them potential candidates for next-generation device applications. First principle calculations reveal that V doped MoS_2 behaves like p-type ferromagnetic half metal with magnetic moment of 0.81 μ_B under zero % of strain (Miao et al. 2020). However, when biaxial tensile and compressive strain is applied to this doped system, the magnetic moment gradually decreases as the strain percentage increases. This reduction is attributed to the diminishing double exchange interaction between V and Mo atoms. Finally, at an applied strain of 3%, the ferromagnetic ground state of V-MoS_2 transitions to antiferromagnetic state.

(ii) **$MoSe_2$**:

To investigate the influence of various types of edges and defects on the magnetism of $MoSe_2$ nanoflakes, Baorui Xia et al. conducted simulations of $MoSe_2$ monolayers with arm-chair and zigzag edges (Xia et al. 2015). The results indicate that the infinitely single-layered $MoSe_2$ and its nanoribbons with arm-chair edges exhibit non-magnetic nature. In contrast, the nanoribbons with zigzag edges, display asymmetric density of states (DOS) near the Fermi level for both spin up and spin down, suggesting their ferromagnetic nature. Magnetic properties of $MoSe_2$ monolayers with various vacancy defects, such as single Mo

or Se vacancies (V_{Mo}/V_{Se}), double Mo or Se vacancies (V_{Mo_2}/V_{Se_2}) and complex defects like V_{Mo} and three/six Se atoms (V_{MoSe_3}/V_{MoSe_6}) were studied by Z. Lin et al. using first principles calculations (Lin et al. 2019). For $MoSe_2$ system with a single V_{Mo}, a magnetic moment of 3.939 μ_B was observed, while the systems with Se vacancies were found to be non-magnetic due to the formation of Mo-Mo metallic bonds around Se vacancies. Among the complex vacancies, V_{MoSe6} defect induces magnetic moment of 5.74 μ_B, whereas the system with V_{MoSe_3} vacancy was shown to be non-magnetic. These edge defects and the vacancies have the potential to modulate the ferromagnetic properties of $MoSe_2$ nanoflakes. Guguchia et al. conducted muon spin rotation (μSR) and scanning tunnelling microscopy (STM) measurements, demonstrating the presence of long-range magnetic ordering in bulk 2H-$MoSe_2$ with the transition temperature of 100 K, a finding supported by DFT calculations (Guguchia et al. 2018). According to these calculations the magnetism in the material arises from various crystal defects such as metal vacancies or chalcogen-metal antisite defects, which exhibit magnetic moments in the range of 0.9–2.8 μ_B.

(iii) **$MoTe_2$**:

Theoretical studies suggest that the intrinsic structural defects can induce magnetism in monolayer $MoTe_2$. Both point defects and boundary defects (1D defect) are capable of inducing spin polarization, resulting in magnetic behaviour (Li et al. 2018). Another report explored the effects of vacancy defects and biaxial strain on monolayer $MoTe_2$ (Kanoun 2021). They found that various vacancy defects, such as V_{Te}, V_{Te_2}, V_{Mo}, V_{Mo_2}, V_{MoTe_3}, V_{MoTe_6} can be

realized in monolayer $MoTe_2$. V_{Te} exhibits the lowest formation energy and V_{MoTe_6} has the highest formation energy, indicating that Te vacancies can be experimentally realized, but $MoTe_6$ vacancies are not thermodynamically stable. The DOS calculation suggests that V_{Mo} exhibits magnetic ordering with magnetic moment of 2.53 μ_B, while the other vacancies are non-magnetic in monolayer $MoTe_2$. Additionally, biaxial strain ranging from 0 to 10% was applied in monolayer $MoTe_2$ with Te and $MoTe_3$ point defects. This study reveals that V_{Te} configuration remains nonmagnetic for biaxial strain less than 3%, but at 10% strain, a magnetic moment of 2.18 μ_B is induced. Similarly, magnetic moments of 3.944 μ_B and 12.021 μ_B were observed with 6% and 10% tensile strain for V_{MoTe_3} configuration. This study combined the effect of vacancies and strain in inducing the magnetic behaviour of $MoTe_2$.

(iv) **WS_2**:

Wun-Fan Li et al. calculated the formation energies of typical point defects, including monovacancies, interstitials and anti-sites and found that the S vacancy (V_S) and adatom S interstitials (S_{int}) have the lowest formation energies (Li et al. 2016a). Additionally, when considering spin–orbit coupling (SOC), V_S as well as W_S and W_{S_2} anti-site defect states exhibit strong splitting. The presence of point defects also exhibits stronger spin–orbit coupling, which is expected to alter the host material's properties significantly. The examination of spin–orbit coupling for each type of vacancy confirmed that this defect is responsible for the observed magnetic state in monolayer WS_2.The effect of substitutional doping in combination with vacancy defects in rare earth atom (Er, Tm, Lu) substituted

WS_2 monolayer is investigated by Zhao et al. for the electronic, optical, and magnetic properties (Zhao et al. 2023). The presence of S defects has shown to have minimal impact on the band gap compared to pristine WS_2 supercells. In contrast, the introduction of V_W causes the host band gap to transition from direct to indirect. To mitigate the impact of metal vacancies, rare earth element was substituted, changing the band gap from indirect to direct. This study reveals that the Lu-doped WS_2 supercell exhibits nonmagnetic properties, whereas Er and Tm-doped supercells display strong magnetic behaviour.

(b) **Ferromagnetism by doping**:

(i) **MoS_2**:

Among various methods to modulate the magnetic properties of 2D TMDs, such as doping, defect engineering and strain engineering, chemical doping of transition metals (TM) is an effective approach. Sintayehu et al. investigated the magnetic properties of V doped monolayer (ML) and bilayer (BL) MoS_2 using density functional theory (DFT) calculations (Mekonnen and Singh 2018). Their study revealed that substituting Mo atoms by V atom can induce near room temperature ferromagnetism. For V doped ML with an impurity concentration of 12.5% and 22.22%, ferromagnetic transition temperature (T_C) of 242 K and 285 K were observed, respectively. In the case of BL MoS_2 with 6.25% and 11.11% V doping, ferromagnetic behaviour was observed up to 187 K and 256 K, respectively. The modulation of structural, electronic and magnetic properties of MoS_2, with low and high doping concentrations of TMs are studied by first principle

calculations. Fan et al. have found that all the TM dopant atoms are preferred to stay at the nearest neighbour configuration showing ferromagnetic coupling with each other and the calculated magnetic moments are 1, 1, 2, 3 and 4.9 μ_B for respective doping of V, Mn, Fe, Cu and Co atoms in MoS_2 monolayers (Fan et al. 2016).

Feng et al. conducted DFT calculations to investigate the electronic and magnetic properties of single Fe and Fe-X_6 (X=C, N, O, F) cluster doped MoS_2 monolayer (Feng et al. 2014). In these systems, Fe and X atoms respectively substitute Mo and nearby S atoms. The results showed that Fe and Fe-F_6 cluster-doped systems are half-metallic, while Fe-C_6 and Fe-N_6 doping, lead to spin-gapless semiconductors. For Fe-O_6 substitutions, MoS_2 monolayers become semiconducting. Furthermore, the Fe-X_6 cluster-doped systems exhibit ferromagnetic behaviour with magnetic moments of 1.93 μ_B, 1.45 μ_B, 3.18 μ_B, 2.08 μ_B, 2.21 μ_B for X=S, C, N, O and F, respectively. The primary contribution to the magnetic moments comes from the doped Fe atom, with the X atoms and nearest neighbour Mo contributing negligibly. Ho et al. conducted a study to understand the induced ferromagnetism in MoS_2 monolayer upon TM (Fe/Ni) bombardment using molecular dynamics (MD) simulations (Ho et al. 2020). When Fe atoms approach the MoS_2 surface, the induced magnetism gradually increases due to the exchange of magnetic moments between Fe 3*d* and Mo 4*d* orbitals. In contrast, Ni bombardment results in a relatively smaller magnetic moment ranging from 1.5 to 4 μ_B.

(ii) **$MoSe_2$**:

Tian et al. systematically investigated the tuning of the magnetic properties of $MoSe_2$ monolayers through doping with TM (Mn, Fe, Co and Ni) using DFT calculations (Tian et al. 2020). Doping these TM atoms with a concentration of 6.25% in a $4 \times 4 \times 1$ supercell of $MoSe_2$ maintained the crystal structure with a slight lattice parameter distortion. The calculations revealed that TM doped systems preferentially exist in spin-polarized states, and the corresponding magnetic moments for Mn, Fe, Co and Ni doped $MoSe_2$ systems were found to be 1.074 μ_B, 1.963 μ_B, 2.760 μ_B, 1.765 μ_B, respectively. Zhao et al. investigated the electronic and magnetic properties of monolayer $MoSe_2$ doped with non-metal (NM) atoms (i.e. H, B, C, Si, N, P, As, O, S, Te, F, Cl, Br and I) (Zhao et al. 2018). The study revealed that $MoSe_2$ doped with NM dopants with an odd number of valence electrons becomes magnetic due to the hybridization of NM-p states and Mo-4d states, leading to the formation of an asymmetrical impurity band (Zhao et al. 2018). In contrast, the NM dopants with an even number of valence electrons do not induce magnetism in the system. Furthermore, H, B, F, Cl, Br and I doped $MoSe_2$ monolayers exhibit a metallic nature with 100% spin polarization at the Fermi level, making them ideal candidates for further device applications.

(iii) **$MoTe_2$**:

Pristine $MoTe_2$ is nonmagnetic in nature, but Kanoun et al. have theoretically demonstrated a significant modification of its magnetic behaviour through the doping of various 3d transition metal atoms (Fe, Cr, Mn, Ni) in $MoTe_2$ monolayer (Kanoun 2018). Their report shows that, except Ni, all transition metal doped $MoTe_2$ monolayers exhibit

long-range ferromagnetic ordering with larger magnetic moments. This is attributed to the strong *p*-*d* hybridization between 3*d* band of the transition metal atom and *p* band of the neighbouring atom.

(iv) **WS_2**:

Theoretical studies conducted by Xie et al., explored the magnetic properties of pristine WS_2, single TM doped and equimolar-dopant of double TM atoms (Mn, Fe, Co, Ni) doped WS_2 monolayers (Xie and Zhang 2016). They found that single TM-doped WS_2 monolayers exhibit half-metallic ferromagnetism driven by direct exchange interactions. Among the various TM dopants studied, Mn-doped WS_2 was the most stable. In the case of double equimolar-dopant TM-doped WS_2, ferromagnetic ordering was attributed to the double exchange mechanism except for Ni system. Luo et al. reported that Ni-doped monolayers and the nearest two Ni-doped systems exhibit magnetic behaviour. This magnetism arises from the *p*-*d* hybridization between the Ni atom and its neighbouring S atoms, resulting in ferromagnetic interaction in Ni-doped monolayer system (Luo et al. 2016).

Jena et al. employed first principle and micro magnetic calculations to investigate the influence of biaxial strain on the magnetic properties of Co-doped WS_2 monolayers (Jena et al. 2022). Their findings revealed that the nonmagnetic WS_2 monolayer exhibits ferromagnetic ordering with a magnetic moment of 2.58 μ_B upon Co-doping. Furthermore, the application of strain enhances the magnetic moment, with 2% tensile strain increasing the magnetic moment to 3.25 μ_B and −2% compressive strain resulting in 2.69 μ_B. The magnetic exchange interaction arises from a double

exchange coupling between Co and W atoms, along with *p*-*d* hybridization between Co and its nearest sulphur atoms. Zhao et al. investigated the influence of doping with various metal elements (Ni, Pd, Pt) on the magnetic characteristics of WS_2 (Zhao et al. 2016b). Their research revealed that monolayer WS_2, when doped with Ni, Pd or Pt, exhibits ferromagnetic behaviour. The magnetic moment associated with Ni-WS_2, Pd-WS_2, and Pt-WS_2 are 3.213 μ_B, 2.841 μ_B, and 2.920 μ_B, respectively.

The effect of Mn, Fe, Co and Ni doping in non-magnetic system such as MoS_2, $MoSe_2$, WS_2, $MoTe_2$ was studied by Mishra et al. (2013). The first principle DFT calculation shows that MoS_2, $MoSe_2$ and WS_2 system exhibit long range ferromagnetic ordering for less than 5% Mn doping (Mishra et al. 2013). This is attributed to the presence of antiferromagnetic coupling between the localized Mn 3*d* state and delocalized *p* state of the chalcogen atoms. This AFM *p*-*d* exchange interaction in turns drives FM ordering of localized spin in other Mn atoms. However, for transition metal Fe, Co and Ni, the system shows FM exchange with the S, Se and Te atoms, which results in a very weak FM. Using first principle calculations, the magnetic properties of several TMDs: MoS_2, $MoSe_2$, $MoTe_2$, WS_2, WSe_2 monolayers with 15% substitutional doping of Ti, V, Cr, Mn, Fe, Co and Ni were investigated by Tiwari et al. (2021). Five different magnetic states were shown to be possible in these systems. Ti and Ni doped systems were shown to be in non-magnetic (paramagnetic) state, whereas Cr doping exhibited AFM ordered state. The latter is found to be so for Co doped MoS_2 and WS_2 and for the V, Cr, and Mn doped $MoTe_2$. V-doping in these systems (except for $MoTe_2$) exhibits strong long-range interactions with the ferromagnetic state observed with their magnetic easy-axis in the out-of-plane direction. However, the Curie

temperatures were far below 300 K with the highest shown to be 224 K for V doped $MoSe_2$. Co doped $MoSe_2$, WSe_2 and $MoTe_2$, and Fe doped MoS_2 and $MoTe_2$ are predicted to exhibit clustered ferromagnetic ordered state, with their magnetic easy-axis in the out-of-plane direction, and strong short-range and weak long-range interactions, where they also observed weakly interacting clusters of FMs. Mn or Fe doped WS_2, $MoSe_2$ and WSe_2 were shown to exhibit X–Y ordered states, i.e., magnets with an in-plane easy axis, where they also observed weakly aligned in-plane FM clusters, but the long-range order remains significantly randomized at any finite temperature. Most of the critical temperatures predicted in these works are at very low temperatures (<200 K). The electronic origin of magnetism in doped TMDs are shown to be a result of super-exchange interaction in the short-range, whereas the interaction is carrier-mediated in the long range.

(c) **Ferromagnetism by structural phase transition**:

(i) **MoS_2**:

Pristine 2H-MoS_2 is diamagnetic in nature, however, through exfoliating it by Li-intercalation, MoS_2 changes its phase from 2H to 1T, resulting in ferromagnetic nature. Yan et al. showed that in the 1T MoS_2 nanoribbon phase, magnetic moments are primarily localized on the Mo atoms, while there is no net magnetic moment in the 2H phase, except at the edge atoms (Yan et al. 2015). The splitting in DOS of Mo 4d orbitals is only observed in the 1T phase of MoS_2. Therefore, it is established that the phase modulation effectively enhances the magnetism of MoS_2.

(ii) **$MoSe_2$**:

Kochat et al. developed a new strategy to grow Re doped $MoSe_2$ monolayer by CVD to show structural phase modulation agrees well with the theoretical prediction of phase transition in these 2D systems (Kochat et al. 2017). Through quantum molecular dynamics simulations, it is determined that $Mo_{1-x}Re_xSe_2$ can exhibit a 2H phase ($x = 0.14$) or 1T′phase ($x = 0.83$) depending on the doping concentration. Due to the slight asymmetry in the DOS at the Fermi level, the magnetization values are 2.779×10^{-3} μ_B and 6.92×10^{-4} μ_B per unit of $Mo_{1-x}Re_xSe_2$ in the 2H and 1T′ phases, respectively. These Re-doped systems exhibit a ferromagnetic nature up to 600 K.

(iii) **$MoTe_2$**:

Zhao et al. have utilized DFT calculations to elucidate the effects of Re doping and strain engineering on the intrinsically nonmagnetic monolayer $MoTe_2$, leading to induce the magnetic behaviour (Zhao et al. 2020). Their study reveals that at different concentrations of Re doping, a structural transformation occurs, transitioning from 2H to 1T′ phase. The phase transition in the $Mo_{1-x}Re_xTe_2$ structure occurs at doping levels between 10% and 11.1%. When subjected to biaxial strain, the system exhibits ferromagnetism. Tensile strain in the range of 4–5% induces a 0.5 μ_B magnetic moment in 2H phase, while strain in the range of 9–10% induces 1 μ_B magnetic moment in the 1T′ phase. The phase transformation in this system and the origin of magnetism can be understood through the crystal field theory. The introduction of an extra electron into the 4*d* orbital of the Mo atom upon Re

atom substitution increases the occupation of the Mo 4*d* orbital, resulting in structural transformation. In the 2H phase, the extra electron occupies a higher energy level of the Mo 4*d* orbital, while in the 1T′ phase, it occupies the lowest $d_{xy,yz,zx}$ orbital with a smaller energy change. This accounts for the higher magnetic moment in the 1T′ phase compared to the 2H phase. Kumar et al. employed DFT calculations to predict the effect of strain and gate voltage for triggering phase transition in $MoTe_2$ doped with 3d and 4d metal (Kumar et al. 2019). The study revealed that even a small amount of doping can significantly influence the energy levels of various crystal phases of $MoTe_2$. Specifically, with 6.3% Mn doping, the phase transition occurs in less than 1 microsecond when subjected to a gate voltage of 1.19 V with magnetic moment of 1 μ_B in both the phases of 2H and 1T′. However, for the same doping concentration of Fe in $MoTe_2$ monolayer, 2H and 1T′ phases possess a magnetic moment of 2 and 1 μ_B, respectively. Notably, the addition of metal-doped atoms not only controls the phase transition but also alters the magnetic behaviour of the $MoTe_2$.

(iv) **WS_2**:

A first-principle based DFT calculation on fluorine (F) doped WS_2, conducted by Radhakrishnan et al. (2018), clearly indicates a phase transition from the 2H phase to 1T phase upon fluorination. At a fluorine concentration of 66.66%, the 1T phase of WS_2 becomes energetically more stable than 2H phase (Radhakrishnan et al. 2018). To investigate the magnetic properties of this 1T-WS_2 system, S vacancies were also induced in it. A 3.125% V_S induces a magnetic moment of 0.67 μ_B. However, when combined

with 2.13% F doping and 3.125% S vacancy, the magnetization of 1T-WS_2 is enhanced to a magnetic moment of 0.7 μ_B. Thus, fluorination is shown not only to facilitate the phase transition but also to enhance the magnetization of WS_2.

15.4 Challenges and Opportunities

2D-TMDs hold significant importance and show promise in various emerging technologies, including spintronics devices. Despite numerous recent research efforts to develop TMD materials and employ various strategies to realize magnetic nature through doping, defects, and strain engineering, there is still considerable need for further exploration to gain robust control over the electronic and magnetic properties of TMDs. In particular, the investigations on the magnetic ordering in extrinsic 2D-TMDs such as MoS_2, WS_2, $MoSe_2$, $MoTe_2$ etc. demand significant attention, despite extensive studies in recent years. While there are numerous reports on the fundamental understanding of the influence of dopant, defects and strain on the magnetic properties of TMDs, pushing the ferromagnetic transition above room temperature in this class of materials is essential for its practical device applications. Generally, ferromagnetic properties in TMDs can be engineered by regulating factors that promote unpaired spins with significant exchange interaction to achieve long-range ordering. One of the challenges has been to experimentally distinguish the long-range magnetic order from defect regions and dopant-specific contributions for the magnetization, as well as to definitively differentiate between strained and unstrained regions. Magnetic probing requires larger area sampling and testing samples locally using advanced magnetic

techniques, including magnetic force microscopy and magneto-optical Kerr effect (MOKE) has been challenging.

While ferromagnetism has been observed under different scenarios, and various new classes of magnetic semiconductors are being proposed, the study of magnetism in 2D TMDs continues to be pursued both experimentally and theoretically. Observation of robust ferromagnetism and applying it to devices remains challenging and pending. Tuning magnetic behaviour through phase modulation has been limited in recent years, presenting challenges to the scientific community. Specifically, using dopants and defects to modulate the phase transition in MX_2 and energetically control the semi-metallic and semiconducting phases appears to be a promising approach. Further control on phase-dependent magnetization to make it more applicable in devices requires in-depth studies. It is anticipated that an optimized combination of engineering these dopants, defects and phase transition factors can yield the best result on the magnetic properties relevant to semiconducting applications.

Methodologies to obtain coexisting defects and dopants with appropriate phase modulation to achieve higher magnetic moment and ordering above room temperature require extensive exploration. A more challenging task is to control the growth of highly ordered TMDs in which the dopants and defects can be inserted in a controlled manner, altering the magnetic and semiconducting properties suitable for spin-electronic applications. The development of efficient doping techniques to introduce elements at specific sites within the TMD structure has been a challenging hurdle. Another challenge is to control the type of defect, the density, and the distribution of defects. Achieving uniformity in defect creation across a

large area is crucial for practical applications and remains a far-reaching goal.

Despite these challenges, ferromagnetism has been observed to exist in extrinsic 2D TMDs, with signatures of Curie transition above room temperature. This has implications for spintronics and memory device applications. Other potential solutions include exploiting interface-induced magnetic phenomena and utilising heterostructured extrinsic 2D TMDs with robust magnetic and semiconducting properties, making them more suitable for device applications.

15.5 Summary

We reviewed the experimental approach widely adopted to induce and control the magnetic properties of a wide range of 2D-TMDs via defect control, doping with transition metal elements, and phase control mechanisms. A broad understanding of ferromagnetic systems in various 2D TMDs like MoS_2, WS_2, $MoSe_2$, and $MoTe_2$ are presented. Research investigations via both the theoretical approach and experimental methods that have been reported recently are summarized. Ferromagnetism can be realized in this system by increasing defect concentration, especially chalcogen vacancies, by doping of various magnetic dopants such as Fe, V, Co, Cr, etc. which leads to an increase in the magnetic moment by introducing unpaired electrons and as well as by phase transformation of the different structure of 2D TMDs. While significant promise and possibility seem to exist in realizing the magnetic properties of TMDs with the claims of intrinsic magnetic properties, further studies to confirm the same and demonstrate the spintronic device characteristics need to be performed. One big challenge could be, unlike the high-quality 2D ferromagnetic materials, which itself is of

significant challenge to realize, the magnetic properties obtained via defect, dopant and phase control engineering pose poor crystallinity of the 2D materials and hence significant hurdle towards realizing the practical devices. The mechanism for the ferromagnetic nature is another area that needs significant understanding. Through this report, the importance of defects, dopants and phase control engineering in 2D-TMDs, primarily on understanding the defect-structure–property correlations, is emphasized.

Acknowledgements

C.S. acknowledges the support from SERB-SUPRA (Science and Engineering Research Board—Scientific and Useful Profound Research Advancement) through Grant No. SPR/2021/000499-G. C.S. acknowledges IIT Madras for the support of research initiatives for establishing the Research Center of Excellence on Center for Advanced Materials and Microscopy (CAMM) vide project # SB20210844MMMHRD008277. This initiative is supported by the Ministry of Human Resource and Development, India through the Institutes of Eminence (vide SP20210777DRMHRDDIRIIT).

Author Contributions

The manuscript was written through the contributions of all the authors. All authors have given approval to the final version of the manuscript.

References

Ahmed, S., Ding, X., Bao, N., et al.: Chem. Mater. **29**, 9066–9074 (2017)

Ahmed, S., Cui, X.Y., Murmu, P.P., et al.: J. Alloys Compd. **918**, 0–7 (2022)

Ali, M.N., Xiong, J., Flynn, S., et al.: Nature **514**, 205–208 (2014) [PubMed]

Bonilla, M., Kolekar, S., Ma, Y., Diaz, H.C., Kalappattil, V., Das, R., Eggers, T., Gutierrez, H.R., Phan, M.H., Batzill, M.: Nat. Nanotechnol. **13**, 289–293 (2018) [PubMed]

Cai, L., He, J., Liu, Q., et al.: J. Am. Chem. Soc. **137**, 2622–2627 (2015) [PubMed]

Cao, D., Shu, H.B., Wu, T.Q., Jiang, Z.T., Jiao, Z.W., Cai, M.Q., Hu, W.Y.: Appl. Surf. Sci. **361**, 199–205 (2016)

Castellanos-Gomez, A., Barkelid, M., Goossens, A.M., Calado, V.E., Van Der Zant, H.S.J., Steele, G.A.: Nano Lett. **12**, 3187–3192 (2012) [PubMed]

Chen, B., Yang, J.H., Wang, H.D., Imai, M., Ohta, H., Michioka, C., Yoshimura, K., Fang, M.H.: J. Phys. Soc. Jpn. **82**, 1–7 (2013)

Chen, C., Chen, X., Wu, C., et al.: Adv. Mater. **34** (2022)

Cho, S., Kim, S., Kim, J.H., et al.: Science **349**(80), 625–628 (2015)

Choi, W., Choudhary, N., Han, G.H., Park, J., Akinwande, D., Lee, Y.H.: Mater. Today **20**, 116–130 (2017)

Coelho, P.M., Komsa, H.P., Lasek, K., Kalappattil, V., Karthikeyan, J., Phan, M.H., Krasheninnikov, A.V., Batzill, M.: Adv. Electron. Mater. **5**, 1–6 (2019)

Cotton, F.A., Wilkinson, G.: p. 1171. Wiley (1972)

Coughlin, A.L., Xie, D., Zhan, X., et al.: Nano Lett. **21**, 9517–9525 (2021) [PubMed]

Enyashin, A.N., Seifert, G.: Comput. Theor. Chem. **999**, 13–20 (2012)

Fan, X.L., An, Y.R., Guo, W.J.: Nanoscale Res. Lett. **11**, 154 (2016) [PubMed][PubMedCentral]

Feng, N., Mi, W., Cheng, Y., Guo, Z., Schwingenschlögl, U., Bai, H.: Sci. Rep. **4** (2014)

Gao, G., Chen, C., Xie, X., Su, Y., Kang, S., Zhu, G., Gao, D., Trampert, A., Cai, L.: Mater. Res. Lett. **5**, 267–275 (2017)

Gong, C., Li, L., Li, Z., et al.: Nature **546**, 265–269 (2017) [PubMed]

Guguchia, Z., Kerelsky, A., Edelberg, D., et al.: Sci. Adv. **4** (2018)

Ogale, S. B.: Adv. Mater. **22**, 3125–3155 (2010)

[PubMed]

Han, J.H., Lee, S., Cheon, J.: Chem. Soc. Rev. **42**, 2581–2591 (2013)
[PubMed]

Han, S.A., Bhatia, R., Kim, S.-W.: Nano Converg. **2**, 17 (2015)

Han, W.: APL Mater. **4** (2016)

He, J., Wu, K., Sa, R., Li, Q., Wei, Y.: Appl. Phys. Lett. **96**, 082504 (2010)

Ho, T.H., Hoang, H.T., Dong, H.C., Kawazoe, Y., Le, H.M.: ACS Omega **5**, 16139–16148 (2020)
[PubMed][PubMedCentral]

Huang, B., Clark, G., Navarro-Moratalla, E., et al.: Nature **546**, 270–273 (2017)
[PubMed]

Hutten, U., Daniel, L., Kang, K., Fu, S., Shayan, K., Anthony, Y.: Nanotechnology (2021)

Jena, A.K., Mallik, S.K., Sahu, M.C., Sahoo, S., Sahoo, A.K., Sharma, N.K., Mohanty, J., Gupta, S.K., Ahuja, R., Sahoo, S.: Sci. Rep. **12** (2022)

Jia, C., Zhou, B., Song, Q., Zhang, X., Jiang, Z.: RSC Adv. **8**, 18837–18850 (2018)
[PubMed][PubMedCentral]

Jiang, X., Liu, Q., Xing, J., Liu, N., Guo, Y., Liu, Z., Zhao, J.: Appl. Phys. Rev. **8**, 1–69 (2021)

Jin, Q., Liu, N., Chen, B., Mei, D.: J. Phys. Chem. C **122**, 28215–28224 (2018)

Kanoun, M.B.: J. Alloys Compd. **748**, 938–942 (2018)

Kanoun, M.B.: Surf. Interfaces **27**, 101442 (2021)

Kappera, R., Voiry, D., Yalcin, S.E., Branch, B., Gupta, G., Mohite, A.D., Chhowalla, M.: Nat. Mater. **13**, 1128–1134 (2014)
[PubMed]

Khan, Y., Obaidulla, S.M., Habib, M.R., Gayen, A., Liang, T., Wang, X., Xu, M.: Nano Today **34**, 100902 (2020)

Kochat, V., Apte, A., Hachtel, J.A., et al.: Adv. Mater. **29** (2017)

Kumar, A., Strachan, A., Onofrio, N.: J. Appl. Phys. **125** (2019)

Lee, J.J., Xing, G.Z., Yi, J.B., Chen, T., Ionescu, M., Li, S.: Appl. Phys. Lett. **104** (2014)

Li, Z., Chen, F.: Appl. Phys. Rev. **4**, 011103 (2017)

Li, Y., Zhou, Z., Zhang, S., Chen, Z.: J. Am. Chem. Soc. **130**, 16739–16744 (2008)
[PubMed]

Li, W.F., Fang, C., Van Huis, M.A.: Phys. Rev. B **94**, 1–8 (2016a)

Li, H., Liu, S., Huang, S., Yin, D., Li, C., Wang, Z.: Ceram. Int. **42**, 2364–2369 (2016b)

Li, Y., Ma, Y., Zhao, M., Sun, Q., Dai, Y., Liu, J., Li, H., Dai, X.: J. Alloys Compd. **735**, 2363–2372 (2018)

Li, B., Wan, Z., Wang, C., et al.: Nat. Mater. **20**, 818–825 (2021)
[PubMed]

Lin, Z., Yan, H., Liu, J., An, Y.: J. Alloys Compd. **774**, 160–167 (2019)

Lin, X., Ni, J.: J. Appl. Phys. **116** (2014)

Lin, Z., Carvalho, B.R., Kahn, E., Lv, R., Rao, R., Terrones, H., Pimenta, M.A., Terrones, M.: 2D Mater. **3**, 022002 (2016)

Luo, M., Hao, S.Y., Ling, Y.T.: AIP Adv. **6** (2016)

Ma, Y., Liu, B., Zhang, A., Chen, L., Fathi, M., Shen, C., Abbas, A.N., Ge, M., Mecklenburg, M., Zhou, C.: ACS Nano **9**, 7383–7391 (2015)
[PubMed]

Mao, X., Xu, Y., Xue, Q., Wang, W., Gao, D.: Nanoscale Res. Lett. **8**, 1–6 (2013)

Mathew, S., Gopinadhan, K., Chan, T.K., et al.: Appl. Phys. Lett. **101** (2012)

Mekonnen, S., Singh, P.: Int. J. Mod. Phys. B **32** (2018)

Memarzadeh, S., Roknabadi, M.R., Modarresi, M., Mogulkoc, A., Rudenko, A.N.: 2D Mater. **8** (2021)

Meng, L., Zhou, Z., Xu, M., et al.: Nat. Commun. **12** (2021)

Mermin, N.D., Wagner, H.: Phys. Rev. Lett. **17**, 1133–1136 (1966)

Miao, Y., Bao, H., Fan, W., Ma, F.: J. Phys. Chem. Solids **142** (2020)

Mishra, R., Zhou, W., Pennycook, S.J., Pantelides, S.T., Idrobo, J.C.: Phys. Rev. B—Condens. Matter. Mater. Phys. **88** (2013)

O'Hara, D.J., Zhu, T., Trout, A.H., et al.: Nano Lett. **18**, 3125–3131 (2018)

[PubMed]

Pan, X.C., Chen, X., Liu, H., et al.: Nat. Commun. **6**, 3–8 (2015)

Pekar, S.I.: Collect Pap. LD Landau **419**, 478–483 (1965)

Py, M.A., Haering, R.R.: Can. J. Phys. **61**, 76–84 (1983)

Qian, X., Liu, J., Fu, L., Li, J.: Science **346**(80), 1344–1348 (2014)

Radhakrishnan, S., Das, D., Deng, L., et al.: Adv. Mater. **30** (2018)

Samadi, M., Sarikhani, N., Zirak, M., Zhang, H., Zhang, H.L., Moshfegh, A.Z.: Nanoscale Horizons **3**, 90–204 (2018)
[PubMed]

Sanikop, R., Sudakar, C.: ACS Appl. Nano Mater. **3**, 576–587 (2020)

Sanikop, R., Budumuru, A.K., Gautam, S., Chae, K.H., Sudakar, C.: ACS Appl. Nano Mater. **3**, 11825–11837 (2020)

Sanikop, R., Gautam, S., Chae, K.H., Sudakar, C.: J. Magn. Magn. Mater. **537**, 168226 (2021)

Sarma, S., Ghosh, B., Ray, S.C., Wang, H.T., Mahule, T.S., Pong, W.F.: J. Phys. Condens. Matter. **31** (2019)

Schonfeld, B.B., Huangt, J.J., Moss, S.C.: Acta Crystallogr. **39**, 404–407 (1983)

Shen, D., Zhao, B., Zhang, Z., et al.: ACS Nano **16**, 10623–10631 (2022)
[PubMed]

Soluyanov, A.A., Gresch, D., Wang, Z., Wu, Q., Troyer, M., Dai, X., Bernevig, B.A.: Nature **527**, 495–498 (2015)
[PubMed]

Tian, Y., Zhu, Z., Ge, Z., Sun, A., Zhang, Q., Huang, S., Li, H., Meng, J.: Phys. E Low-Dimens. Syst. Nanostruct. **116** (2020)

Tiwari, S., Van de Put, M.L., Sorée, B., Vandenberghe, W.G.: npj 2D Mater. Appl. **5** (2021)

Tongay, S., Varnoosfaderani, S.S., Appleton, B.R., Wu, J., Hebard, A.F.: Appl. Phys. Lett. **101** (2012)

Torrance, J.B., Shafer, M.W., McGuire, T.R.: Phys. Rev. Lett. **29**, 1168–1171 (1972)

Vazirisereshk, M.R., Martini, A., Strubbe, D.A., Baykara, M.Z.: Lubricants **7**, 57 (2019)

Voiry, D., Mohite, A., Chhowalla, M.: Chem. Soc. Rev. **44**, 2702–2712 (2015) [PubMed]

Wang, X., Shen, X., Wang, Z., Yu, R., Chen, L.: ACS Nano **8**, 11394–11400 (2014) [PubMed]

Wang, J., Sun, F., Yang, S., Li, Y., Zhao, C., Xu, M., Zhang, Y., Zeng, H.: Appl. Phys. Lett. **109**, 1–6 (2016)

Wang, C., Zhou, X., Pan, Y., Qiao, J., Kong, X., Kaun, C.C., Ji, W.: Phys. Rev. B **97**, 1–11 (2018)

Wang, M., Kang, L., Su, J., Zhang, L., Dai, H., Cheng, H., Han, X., Zhai, T., Liu, Z., Han, J.: Nanoscale **12**, 16427–16432 (2020) [PubMed]

Wen, Y., Liu, Z., Zhang, Y., et al.: Nano Lett. **20**, 3130–3139 (2020) [PubMed]

Xia, B., Gao, D., Liu, P., Liu, Y., Shi, S., Tao, K.: Phys. Chem. Chem. Phys. **17**, 32505–32510 (2015) [PubMed]

Xia, B., Guo, Q., Gao, D., Shi, S., Tao, K.: J. Phys. D Appl. Phys. **49**, 165003 (2016)

Xia, B., Yang, Y., Ma, J., Tao, K., Gao, D.: Appl. Phys. Express **10**, 093002 (2017a)

Xia, B., Wang, T., Xiao, W., Zhang, R., Liu, P., Ding, J., Gao, D., Xue, D.: Sci. Rep. **7**, 1–6 (2017b)

Xia, B., Liu, P., Liu, Y., Gao, D., Xue, D., Ding, J.: Appl. Phys. Lett. **113**, 1–6 (2018)

Xiao, H., Zhuang, W., Loh, L., Liang, T., Gayen, A., Ye, P., Bosman, M., Eda, G., Wang, X., Xu, M.: Adv. Mater. Interfaces **9** (2022)

Xie, L.Y., Zhang, J.M.: Superlattices Microstruct. **98**, 148–157 (2016)

Yan, S., Qiao, W., He, X., Guo, X., Xi, L., Zhong, W., Du, Y.: Appl. Phys. Lett. **106**, 012408 (2015)

Yang, L., Wu, H., Zhang, W., Lou, X., Xie, Z., Yu, X., Liu, Y., Chang, H.: Adv. Electron. Mater. **5**, 1–8 (2019)

Yang, L., Wu, H., Zhang, L., Zhang, G., Li, H., Jin, W., Zhang, W., Chang, H.: ACS Appl. Mater. Interfaces **13**, 31880–31890 (2021)
[PubMed]

Yu, W., Li, J., Herng, T.S., et al.: Adv Mater. **31** (2019)

Yun, W.S., Lee, J.D.: J. Phys. Chem. C **119**, 2822–2827 (2015)

Yun, S.J., Duong, D.L., Ha, D.M., Singh, K., Phan, T.L., Choi, W., Kim, Y.M., Lee, Y.H.: Adv. Sci. **7**, 1–6 (2020)

Zhang, R., Li, Y., Qi, J., Gao, D.: Nanoscale Res. Lett. **9**, 1–5 (2014)

Zhang, R., Du, Y., Han, G., Gao, X.: J. Mater. Sci. **54**, 552–559 (2019)

Zhang, F., Zheng, B., Sebastian, A., et al.: Adv. Sci. **7**, 1–9 (2020)

Zhao, X., Xia, C., Wang, T., Dai, X.: J. Alloys Compd. **654**, 574–579 (2016a)

Zhao, X., Xia, C., Dai, X., Wang, T., Chen, P., Tian, L.: J. Magn. Magn. Mater. **414**, 45–48 (2016b)

Zhao, Y., Wang, W., Li, C., Xu, Y., He, L.: Solid State Commun. **281**, 6–11 (2018)

Zhao, Q., Lu, Q., Liu, Y., Zhang, M.: Appl. Surf. Sci. **471**, 118–123 (2019a)

Zhao, Q., Zhai, C., Lu, Q., Zhang, M.: Phys. Chem. Chem. Phys. **21**, 232–237 (2019b)

Zhao, Y., Li, Y., Liu, M., Xu, K., Ma, F.: J. Phys. Chem. C **124**, 4299–4307 (2020)

Zhao, Y., Yan, B., Liang, X., Liu, S., Shi, X., Zhao, H.: Phys. Status Solidi Basic Res. **260** (2023)

Zhou, Q., Su, S., Cheng, P., Hu, X., Zeng, M., Gao, X., Zhang, Z., Liu, J.M.: Nanoscale **10**, 11578–11584 (2018)
[PubMed]

Zhou, W., Chen, M., Guo, M., Hong, A., Yu, T., Luo, X., Yuan, C., Lei, W., Wang, S.: Nano Lett. **20**, 2923–2930 (2020)
[PubMed]

© The Author(s), under exclusive license to Springer Nature Singapore Pte Ltd. 2024
R. S. Ningthoujam, A. K. Tyagi (eds.), *Handbook of Materials Science, Volume 2*, Indian Institute of Metals Series
https://doi.org/10.1007/978-981-97-4646-0_16

16. Magnetic Nanoparticles-Based Coated Materials

Shankar B. Dalavi[1], Anagha B. Patil[1] and Rabi N. Panda[1] ✉
(1) Birla Institute of Technology and Science Pilani, K K Birla Goa Campus, Zuarinagar, 403726, Goa, India

✉ **Rabi N. Panda**
Email: rnp@goa.bits-pilani.ac.in

Keywords Coated Particles – Magnetic properties – Surface structure – Nano-magnetism – Size and surface effects

16.1 Introduction

The nanotechnology field has reached greater heights of scientific development in every area that is responsible for the growth of mankind. The terminology ‘nano’ is because of their small size ranging roughly from 1 to 100 nm or having atleast one dimension in the particular nanometer (nm) range. Different morphologies that can be obtained for nanomaterials include nanoparticles, nanowires, nanosheets, nanorods, nanotubes, flower-like morphology, and nanoclusters (Ariga et al. 2012). These shapes can be obtained by various methods of synthesis employed in the formation of nanosized structures (Ariga et al. 2012; Mirzadeh and Akhbari 2016). Various fields in which nanomaterials have shown miracles are engineering, medicine, electronics, energy storage and conversion, food safety, agriculture, environmental science, etc. (Hamers 2017). Significant classes of compounds that are studied worldwide at the nanoscale include inorganic materials (metal oxides, sulfides), organic materials (compact polymers, liposome, dendrimer, micelles, ferritin), carbon-based sheets like structured (graphene, graphene oxide, graphite), etc. Different properties of nanoparticles that are under study are optical properties, mechanical properties, electrical properties,

magnetic properties, catalytic properties, surface properties (Tan et al. 2017; Chen et al. 2018), etc. These properties need to be tuned in order to employ these nanoparticles in a designated field of application and enhance the efficiency of the process (Baig et al. 2021; Zhu et al. 2018).

Magnetic nanoparticles are important because of their size, shape, and surface dependent magnetic characteristics (Ban et al. 2018; Tartaj et al. 2003). Several studies have been focussed on the development of synthesis methodologies in order to change the size, shape, and surface structures of magnetic nanomaterials (Panda et al. 2003; Ningthoujam et al. 2012). The important aspects lie in improving chemical stability of such nanoparticles by coating the surfaces with various organic and inorganic materials. These coated materials help in preventing the oxidation of magnetic nanoparticles on the surfaces. Further, the surface structure is well protected in some cases so that surface properties can be reflected in the materials. In several other cases, surface atoms are allowed to interact with the coating materials in order to enhance the materials' properties for specific applications. Functionalizing the magnetic materials using biocompatible coating has also been studied for various bio-applications (Ali et al. 2021). As per our above discussion points, it is clear that coating the surface of the nanoparticles can be helpful in three different ways:

(i) Protecting the surface so that intrinsic magnetic properties can be achieved,

(ii) Materials of the coated layer can be functionalized in order to perform specific functions, e.g., biocompatible, self-assembling, drug carrier, etc. and

(iii) Chemical, magnetic, and electronic interactions between the magnetic particles and outer coated surfaces leading to unusual properties suitable for potential applications.

Therefore, studies on coated magnetic nanoparticles have become very important. Several basic concepts of coatings and functionalization of the surfaces are presented in a schematic way in Fig. 16.1 (Kudr et al. 2017; Sun et al. 2008).

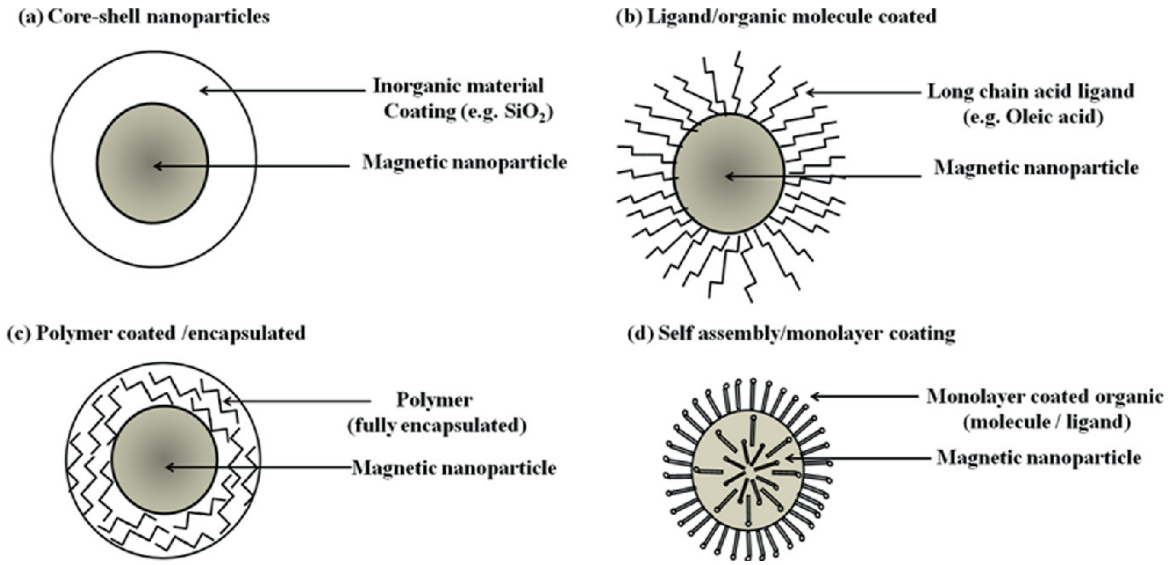

Fig. 16.1 Coating schemes of magnetic nanoparticles: **a** core–shell structure **b** ligand/organic molecule coated **c** polymer coated/encapsulated and **d** self-assembly/monolayer coating (Sun et al. 2008)

During the last few years, numerous coated magnetic and non-magnetic nanoparticles have been investigated for their synthesis, characterization, properties studies, and applications. Some of them are summarized below. Challenges lie in the preparation of non-agglomerated and narrow sized coated magnetic nanostructures with various sizes, shapes, and microstructures. Cobalt alloys are used as hip implants. This can be coated with bioactive hydroxyapatites. Several studies on the stability of particles on metal surfaces at high temperatures have been done (Ortiz et al. 2011; Miyazaki et al. 1997). Stainless steel, Ti-based alloys, and magnesium-based alloys have good biocompatibility but lack in several aspects for practical applications (He et al. 2023). The major disadvantages of steel, Ti-based alloys, and magnesium-based alloys are high modulus, lower hardness, and corrosion, respectively. Coating a layer of inert materials over bio-degradable magnesium alloy may reduce the contact between the corrosive environment and metal surfaces, thereby reducing corrosion.

Cobalt-based alloys are bio-toxic and coating the surface is essential for orthopaedic implant applications. In another development, cobalt-based magnetic nanocrystals are coated with Au, and various nanoparticles with controlled size and shape with core–shell structures, i.e., Au coated Co cores, are synthesized (Bao and Krishnan 2005). Au being biocompatible and nontoxic, these functionalized particles can be used for bio-applications. Another, notable application of magnetic nanoparticles is magnetic

hyperthermia and magnetic resonance imaging (MRI) applications. Magnetic nanoparticles in the colloidal state in physiological conditions in simulated body fluid (SBF) are required for their applications. The basic principle lies in generating heat by applying a magnetic field on the assembly of nanoparticles which can be used to kill diseased cells in the body. Therefore, magnetic particles are coated with a layer of functional materials.

Cobalt-chromium alloys are regarded as dental materials and coating the surface of the particles with a layer of amorphous carbon reduces its efficiency for bacterial adhesion (Chen et al. 2012). Reports are available on coating biocompatible Ta-based multilayers on CoCrMo alloys, in order to reduce metal ion release into the body. CoCrMo alloys have good mechanical strength and are used as artificial joints (Balagna et al. 2012).

The coating of oleic acid on Fe_3O_4 oxides is tested (Soares et al. 2016). Several bimetallic magnetic oxides were tested for MRI applications, such as $MnFe_2O_4$, $CoFe_2O_4$, $CuFe_2O_4$, and $NiFe_2O_4$ (Shin et al. 2015; Putra et al. 2022). Tailoring of their magnetic properties suitable for magnetic-based applications has been an important field of research. It has been seen that nimotuzumab iodine-131 functionalization with $MnFe_2O_4$ particles enhances its potentiality as an MRI contrast agent (Putra et al. 2022). In some studies, iron-oxide particles are coated with PEG which helps in drug loading on the surface of the nanoparticles (Da et al. 2022).

From the above-mentioned literature review, it is evident that magnetic coated particles do possess immense applications in various fields including biological applications. In addition, fundamentally it is important to know the nature of the magnetic nanostructures, their surface forms and functionalization, chemical reactivity and specificity toward other substrate molecules/materials, etc. Although this chapter will focus on all types of coated nano-magnetic materials, the focus will be rendered on describing surface coated cobalt-based magnetic alloys and oxides in the following subsections.

16.1.1 Metal Alloy-Based Magnetic Nanoparticles

One class of magnetic nanoparticles is Fe, Co, and Ni-based metals and alloys. These materials are characterized by their high saturation magnetization (M_S), coercivities (H_C), and remanent magnetizations (M_r). Magnetic moments (per atom) for Fe, Co, and Ni are found to be 2.2, 1.6, and 0.65 μ_B, respectively. The magnetization originates from direct spin–spin exchange interactions in these crystals. In several

cases, alloys based on Fe, Co, and Ni with improved values of magnetizations are found. The reason in part can be magnetic dilution and change in the magnetic structures. In several cases, the presence of interstitial atoms further alters the magnetic parameters. Similarly, a coercive field that is dependent on anisotropy constant and saturation magnetization is found to be quite significant for metal and alloy nanoparticles compared to several other classes of magnetic materials (e.g., metal oxides, metal nitrides, metal carbides, etc.). As many of the particles have characteristics hard or semi-hard nature, magnetic remanent is also quite remarkable. The surface of the metal and alloy-based nanoparticles is very reactive due to large surface energies (Zhu et al. 2023). Therefore, one of the practical difficulties in dealing with metal and alloy nanoparticles is surface oxidation leading to oxide formation. Such kinds of core–shell formation in metallic nanoparticles are well-known in the literature (Li and Hong 2016). However, in order to inhibit surface oxidation which occurs naturally, the metal and alloy surfaces are protected and functionalized in-situ during synthesis.

16.1.2 Metal Oxide-Based Magnetic Nanoparticles

In contrast to the information summarized in Sect. 16.1.1, magnetic parameters obtained using oxide magnetic materials are usually moderate. The intrinsic magnetic moment borne by the metal ions (say from Fe, Co, Ni, Gd, etc.) interacts via oxygen by a super-exchange pathway. The values of Ms, $H_{c,}$ and M_r are moderate. For example, saturation magnetization values obtained for most of the ferrite materials are lesser than 100 emu/g. Similarly, the oxide materials do possess low to moderate (range: 50 Oe–1000 Oe) values of coercive fields and remanent magnetizations. The practical applicability of several materials such kinds are limited to their comparatively lower values of magnetic parameters compared to metal and alloys (Rana et al. 2021). However, this does not limit their widespread use because of ease of preparation cost, better biocompatibility, less sensitive to corrosion, and environmental friendliness. In several cases, non-stoichiometric compositions prevail at the surfaces (Lakshmi et al. 2023; Reddy et al. 2005). These surface defects not only change the magnetic properties but nature of bonding during the functionalization of surfaces, do change. Therefore, this kind of versatilities renders immense potential for applications (Shin et al. 2015; Rana et al. 2021).

16.2 Magnetic Nanomaterials

16.2.1 Various Magnetic Ordering in Bulk and Nanomaterials

In solid-state materials having transition metals, interesting magnetic properties are observed due to the presence of resultant magnetic dipole moments. The origin of magnetic dipoles arises because of the presence of unpaired electrons. These intrinsic magnetic dipole moments interact with each other in order to give ordering of magnetic moments. In particular, metallic materials (e.g., Fe, Co, and Ni) and their alloys with metals or non-metals show ferromagnetism (Brush 1967). Also, there are a few more types of magnetisms are observed depending on the alignment of magnetic moments, such as anti-ferromagnetism, ferrimagnetism, and superparamagnetism. The net magnetization observed in such systems can be explained by spin-up and spin-down concepts (See Fig. 16.2). The spin-up state is more energetically favorable than the spin-down state in ferromagnetic materials and $E_{ex} = -J_{ex}$ S1.S2, where J_{ex} is the corresponding exchange term (Cullity and Graham 2008). When J_{ex} remains positive, ferromagnetic ordering is observed. However, in ferromagnetic materials containing oxygen ions, the magnetization is due to super-exchange phenomena via oxygen and can be explained by two sub-lattice models rather than spin-up and spin-down concepts quite satisfactorily.

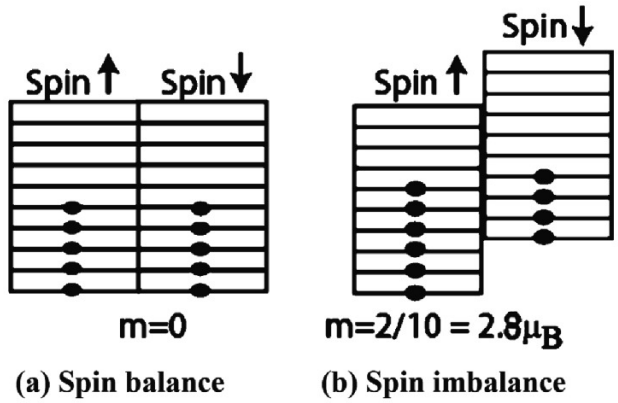

Fig. 16.2 Spin-up and spin-down concepts explaining the origin of net magnetization in **a** spin balanced and **b** spin imbalanced 3d transition metal systems, respectively (Brush 1967)

The behavior of ferromagnetic materials under an external applied magnetic field (H) is shown in Fig. 16.3. In the absence of a field (H = 0), all the domains are randomly oriented, and net magnetization is

small. This state is considered as de-magnetized state. After applying the field, magnetization in the material increases slowly and then drastically up to a certain value and then gets saturated (curve a). The saturation magnetization is denoted as M_S, and 'curve a' is called the initial magnetization curve. At this stage, the direction of H is reversed, the magnetization will not follow the initial curve, and instead, it will follow the (curve b). Some magnetization is retained even when $H \rightarrow 0$, which is called remanence or residual magnetization (M_r). The field required to bring the magnetization value to zero is called the coercive field or coercivity (H_C) of the material. With the further field in the opposite direction, the magnetization will saturate at a negative M_S value. Again increasing the field in the forward direction (curve c), magnetization will complete loop formation which is called a hysteresis loop. Based on different characteristics of magnetic behavior, values of M_S, H_C, and M_r, and both temperature and field dependence of thermal relaxation curves one can address different types of magnetic phenomena as described in the following subsection (Sect. 16.2.2) briefly.

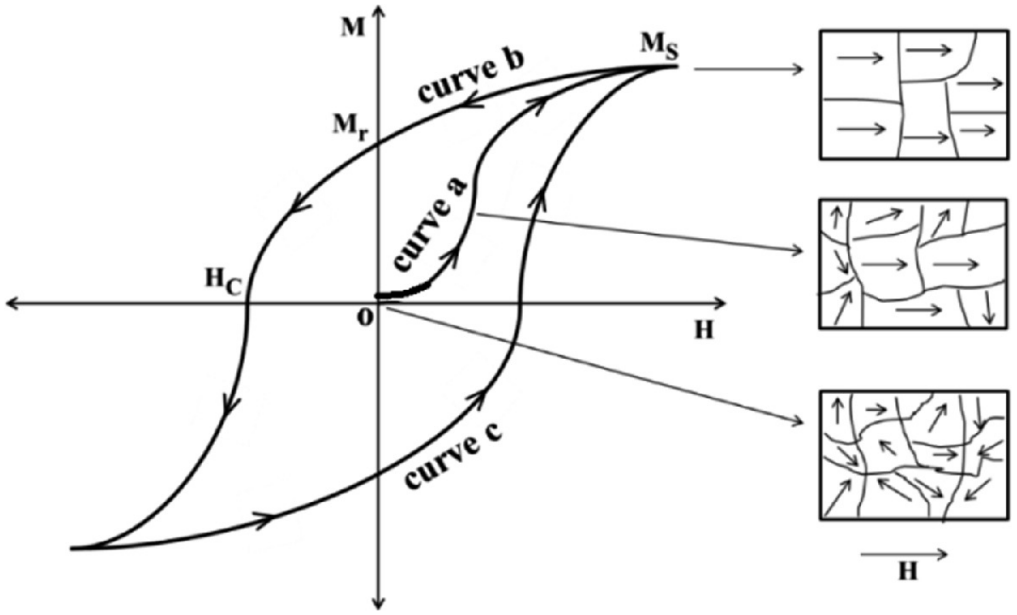

Fig. 16.3 Typical magnetization reversal and corresponding domain structures in ferromagnetic materials. Curve **a** is the initial magnetization plot and curves (**b**, **c**) represent parts of hysteresis loops in reverse and forward directions, respectively

16.2.2 Magnetic Behavior of Nanomaterials

16.2.2.1 Paramagnetic Nanomaterials

Schematic presentations of alignments of atomic magnetic moments for paramagnetic, ferromagnetic, ferrimagnetic, and antiferromagnetic materials are shown in Fig. 16.4a–d. The materials containing unpaired electrons in their atoms, molecules, or ions do possess magnetic dipole and may show paramagnetism. In the absence of the magnetic field, the atomic magnetic moments are randomly oriented and the net magnetic moment becomes zero for such paramagnetic materials (Fig. 16.4a). When the magnetic field is applied, partial alignments of magnetic moments occur and give positive molar susceptibility (χ_m) values in the order of 10^{-5} to 10^{-3} $cm^3\ mol^{-1}$. Paramagnetic materials obey Curie law which gives variation of χ with temperature (T′) as shown in Eq. 16.1.

$$\chi = \frac{C}{T'} \tag{16.1}$$

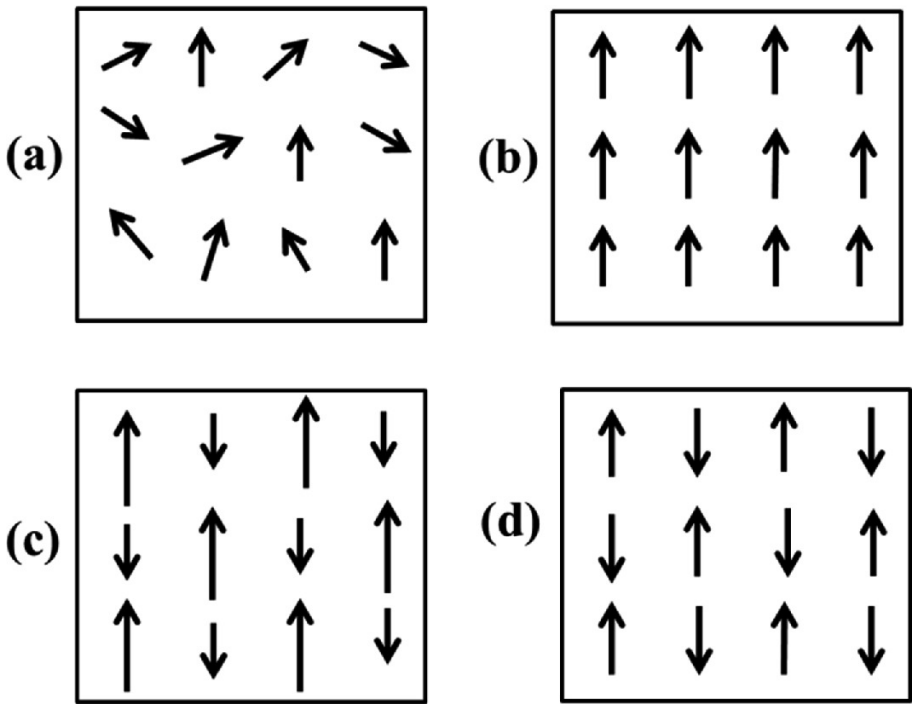

Fig. 16.4 Schematic representations of alignments of atomic magnetic moments; **a** paramagnetic, **b** ferromagnetic, **c** ferrimagnetic, and **d** antiferromagnetic materials

where C is Curie's constant.

Examples of paramagnetic transition metals include W ($\chi_m = 5.3 \times 10^{-5}$ $cm^3\ mol^{-1}$), Pt ($\chi_m = 1.93 \times 10^{-4}$ $cm^3\ mol^{-1}$), etc. (Schenck 1996).

16.2.2.2 Ferromagnetic Nanomaterials

Ferromagnetic materials contain unpaired electrons and possess magnetic dipole-like paramagnetic materials. However, these magnetic dipoles strongly interact with magnetic dipoles of neighboring atoms due to exchange interactions, and the phenomenon is called exchange coupling. Due to exchange coupling, atomic moments are aligned parallel to neighboring moments and hence possess net magnetization (Fig. 16.4b). The occurrence of such net magnetization in the absence of a field is called spontaneous magnetization. Ferromagnetic materials have higher positive χ_m values than paramagnetic materials in the order of $>10^{-3}$ cm^3 mol^{-1}. The value of χ decreases with increasing temperature, loses its ferromagnetic characteristics at a critical temperature called Curie temperature (T_C), and becomes paramagnetic above T_C. Examples of the ferromagnetic materials are Fe ($\chi_m = 1.1 \times 10^5$ cm^3 mol^{-1}), Co ($\chi_m = 132$ cm^3 mol^{-1}), Ni ($\chi_m = 315$ cm^3 mol^{-1}), etc. (Schenck 1996).

16.2.2.3 Ferrimagnetic Nanomaterials

In ferrimagnetic materials, the magnetic moment ordering is composed of two unequal and antiparallel magnetic sublattices which are separated by oxygen anions as shown in Fig. 16.4c. The exchange interactions occur through the oxygen anions, called indirect or super-exchange interactions. The strongest super-exchange interactions were observed for an antiparallel alignment between two sublattices. These materials have similar characteristics like ferromagnetic materials being spontaneously magnetized with Curie Temperature (T_c) at finite temperature. Examples of ferrimagnetic materials include transition metal oxides such as MFe_2O_4 (M = Fe, Mn, Co, Ni, etc.). These materials crystalize with either normal spinel or inverse spinel or mixture structure. M^{2+} ions occupy tetrahedral sites and $2Fe^{3+}$ ions occupy octahedral sites (normal spinel). In the case of inverse spinel, M^{2+} ions occupy half of octahedral sites. $2Fe^{3+}$ ions occupy tetrahedral and octahedral sites equally. Magnetization of MFe_2O_4 materials depends on the nature and concentration of M^{2+} ions. The tetrahedral and octahedral sites form the two magnetic sublattices which are antiparallel to each other with different magnetic moments. Therefore, the net magnetization of the ferrimagnetic materials is lesser than that of pure metal or alloys. For example, for Fe_3O_4 spinel, saturation magnetization, and Curie temperature are found to be 92 emu/g and 580 °C compared to those

observed at 220 emu/g and 770 °C for metallic Fe, respectively (Hu et al. 2017; Danan et al. 1968).

16.2.2.4 Antiferromagnetic Nanomaterials

The atomic moments in these materials are aligned antiparallel to each other as shown in Fig. 16.4d. Antiferromagnetic materials have χ_m values in the order of 10^{-5} to 10^{-3} cm^3 mol^{-1}. In these materials, antiferromagnetic ordering exists at sufficiently lower temperatures up to a critical temperature known as Neel Temperature (T_N), and above T_N the antiferromagnetic ordering gets disturbed and the susceptibility value enters into the paramagnetic regime. Examples of antiferromagnetic materials include hematite (α-Fe_2O_3) ($\chi_m = 3.5 \times 10^{-3}$ cm^3 mol^{-1}), Cr ($\chi_m = 1.8 \times 10^{-4}$ cm^3 mol^{-1}), etc. (Schenck 1996). Hematite has a corundum (Al_2O_3) crystal structure that may be indexed as hexagonal or rhombohedral. Here oxygen ions are situated in a hexagonal close packed framework and Fe^{3+} ions occupy octahedral interstices. The magnetic moments of the Fe^{3+} ions are ferromagnetically coupled within the same c-plane but antiferromagnetically coupled between the different planes (Morin transition) (Morrish 1994).

16.2.2.5 Superparamagnetic Behavior of Nanomaterials

In the case of well crystalline ferromagnetic or ferrimagnetic nanoparticle system, when the particle diameter reduces below a threshold ($D < D_t$), the relaxation time of the magnetic moments at finite temperature is very small and is of the order of 10^{-9} s (Néel 1949). Under these conditions, the magnetization of single-domain nanoparticles fluctuates rapidly along the easy magnetization axis, being always in thermodynamic equilibrium. After applying an external magnetic field, magnetic moments respond instantly to the field variations. This behavior of a system of nanoparticles is magnetically equivalent (i.e., M vs. H response) to a system of paramagnetic atoms (Langevin's paramagnetism) (Langevin 1905), where the non-interacting atomic magnetic moments exist instead of the nanoparticle magnetic moments. Hence, such a system of nanoparticle assembly is called a superparamagnetic (SPM) system (Bean and Livingston 1959), and the phenomenon is called superparamagnetism.

Thus, the magnetization of an SPM system can be expressed by the Langevin formula derived from the classical theory of paramagnetism.

$$\mathrm{M_{SPM}(H,T) = nm_{NP}}\left(\coth\frac{\mu_0 \mathrm{m_{NP}H}}{\mathrm{k_B T}} - \frac{\mathrm{k_B T}}{\mu_0 \mathrm{m_{NP}H}}\right) \quad (16.2)$$

where n is the concentration of nanoparticles in the system, m_{NP} is the magnetic moment of a nanoparticle, and the parenthesis contains the Langevin function.

16.2.3 Different Classes of Magnetic Nanomaterials

Magnetic nanomaterials can be made up of single metal, intermetallic alloys, metal oxides, core of metals covered with shell of another metal or oxide or other compounds, etc. Based on these compositions and surface structures, magnetic nanomaterials can be majorly categorized into the following classes.

16.2.3.1 Metal Nanomaterials

Metallic nanomaterials are made up of single metal atoms such as Fe, Co, or Ni. Iron nanomaterials contain only Fe atoms ordered in body centered cubic crystal structure, Co nanomaterials contain only Co atoms ordered in hexagonal close packed or face centered cubic crystal structure, whereas Ni nanomaterials contain only Ni atoms ordered in face centered cubic crystal structure.

16.2.3.2 Metallic Alloy Nanomaterials

Alloys of magnetic nanomaterials are generally made up of two or more number of metal atoms in which at least one metal should be from the iron group (i.e., Fe, Co, or Ni). Alloy nanomaterials form a single crystalline phase of an ordered or random mixture (or solid solution) of corresponding metal atoms. For example, Fe-Co alloys nanomaterials can form body centered cubic structure rather than a mixture of individual crystal structures. Similarly, Co–Ni alloys crystallize in face centered cubic structures. Depending on the number of metals that consist in alloys formation, they can be called as binary, ternary, or quaternary alloys if the metals involved are 2, 3, or 4, respectively.

16.2.3.3 Metal Oxide/Mixed Metal Oxide Nanomaterials

Metallic oxide nanomaterials can be further divided into two types; (i) the first is binary oxides comprised of single metal ion and (ii) the second is the ternary or higher order oxides comprised of two or more metal ions. Single metal oxides, e.g., Fe_3O_4, Fe_2O_3, Co_3O_4, NiO, etc. crystallize in their corresponding crystal structure only. Whereas

mixed metal oxides, e.g., $CoFe_2O_4$, $NiFe_2O_4$, Cr doped $CoFe_2O_4$, etc., crystallize in crystal structure corresponding to one of the oxides and other atoms incorporated in the same crystal structure.

16.2.3.4 Core–Shell Structures

Core–shell structures of nanomaterials consist of a core of one type of metal atom (A) surrounded by a shell of another metal atom (B). These materials can be represented as $A_{core}B_{shell}$. Core–shell nanomaterials show a mixture of two crystal structures corresponding to core material and shell material separately.

16.2.3.5 Nanomaterials Coated with Inorganic and Organic Layers

In this class, nanomaterials of metals, alloys, metal oxides, and core–shell structures are coated or surface functionalized by inorganic or organic materials such as SiO_2, hypophosphite, carbanious compounds, oleic acid, oleylamine, PEG, and PVP. In coated materials, the inorganic or organic layer forms an amorphous structure and does not effect on core crystal structure of materials.

16.3 Co-Based Uncoated and Coated Metallic Alloy Nanoparticles

16.3.1 Synthetic Methodologies for Uncoated and Coated Co-Based Nanoparticles

In this section, we have focused on the synthesis of coated magnetic alloy nanoparticles by using chemical methods, i.e., functionalization of organic molecules and inorganic shell structures. In some cases, heat treatments of the synthesized coated particles under an inert gas atmosphere are carried out in order to investigate specific properties corresponding to crystalline structure. The synthesis methods described below are nontoxic because it does not involve metal salts with carbonyl, or acetylacetonate groups, hazardous organic medium, and toxic reducing agents.

16.3.1.1 Functionalization with PEG/PVP on the Surface

The functionalization with PEG on Co, $Co_{30}Fe_{70}$ (Kim et al. 2006), and Fe–Ni-Co ternary alloy nanoparticles can be achieved by the $NaBH_4$ reduction method in an aqueous medium. This synthesis can be carried out in an ambient atmosphere and at a pH value below 6.5

during the reaction. This is understood as the nanoparticle surface reacts with hydroxyl ions at pH above 6.82 (Dalavi and Panda 2015a, b; Dalavi et al. 2013). Samples were dried at room temperature (as-prepared and coated materials) and subjected to annealing at 600 °C under high purity N_2 (g) flow for 2 h (annealed and uncoated materials).

The functionalization with PVP on Co and $Co_{50}Ni_{50}$ can be achieved by the modified polyol method (Dalavi et al. 2018). In this method, a stoichiometric amount of metal salts, e.g., $CoCl_2$ for Co, and a 1:1 molar ratio of $CoCl_2$:$NiCl_2$ salts for $Co_{50}Ni_{50}$ synthesis should be used. PVP as capping agent and PEG-200 as reducing agent was added in N, N dimethyl formamide (DMF) and heated to 100–110 °C. Then, reduction was achieved by the addition of NaOH pellets. For as-prepared/coated materials, solids were washed with distilled water to remove excess NaOH and NaCl. Further, annealing of the materials (to get uncoated materials) was done by two routes. In annealing route 1, as-prepared materials were annealed at 600 °C for 6 h (i.e., without NaCl matrix). And in annealing route 2, solids obtained after centrifugation were annealed at 600 °C for 6 h (i.e., with NaCl matrix) and then washed with water.

16.3.1.2 Functionalization with Oleic Acid and Oleylamine

The functionalization with oleic acid and oleylamine on Co, Fe–Co, Co–Ni, etc. can be achieved by the superhydride reduction process. This method is well-known in order to prepare nano-meter-sized particles of transition metal/alloys with controlled size and shape morphologies (Dalavi and Panda 2015c; Dalavi et al. 2015). The resulting controlled size and shape may be obtained by using different concentrations of metal ions in organic solvents along with suitable capping agents. Then, the reduction was carried out at 200 °C by the addition of a superhydride solution (Lithium triethylborohydride, 1 M in THF). The reaction mixture was stirred at 200 °C for 30 min followed by heating to 240 °C for 30 min in order to get uniform in-situ growth of nanocrystals. After workup, solids were dried at RT for coated samples and annealed at 400–600 °C under N_2 (g) flow for uncoated samples.

16.3.1.3 Nanoparticles Coated Mesoporous Silica

The functionalization with mesoporous silica on Co–Ni alloy nanoparticles can be achieved by the superhydride reduction method

using silica KIT-6 as capping agents (Dalavi and Panda 2016). The chemicals and experimental procedure were similar to the superhydride reduction method (see Sect. 16.3.1.2). Additional changes in the synthetic procedure are described as follows: firstly, a mesoporous silica matrix (KIT-6) was prepared as per the literature reported procedure (Kleitz et al. 2003) for obtaining a cubically ordered phase. Different loading of nanoparticles (4–12 weight%) in silica matrix can be achieved by this method.

16.3.2 Structural and Morphological Characterizations of Coated Co-Based Nanoparticles

16.3.2.1 Crystal Structures and Crystallite Sizes

The phase purity of the synthesized materials can be analyzed by XRD studies. Crystalline materials have sharp diffraction lines in their XRD patterns due to ordered atomic arrangements while amorphous materials have more diffuse diffraction lines due to a lack of atom-to-atom long range ordering. The crystallite size (t) can be calculated by Scherrer equation (Cullity 1956).

Typical XRD patterns for Co and Fe–Ni–Co alloys were represented in Figs. 16.5 and 16.6, respectively. As-prepared or coated samples show amorphous XRD patterns whereas annealed or uncoated samples show crystalline patterns. The detailed XRD analysis gives information about the crystalline phase, structure, lattice parameters, crystallite sizes, etc. Some XRD data for Co and Fe–Co, Fe–Ni–Co, and Co–Ni@Silica nanomaterials are summarized in Table 16.1.

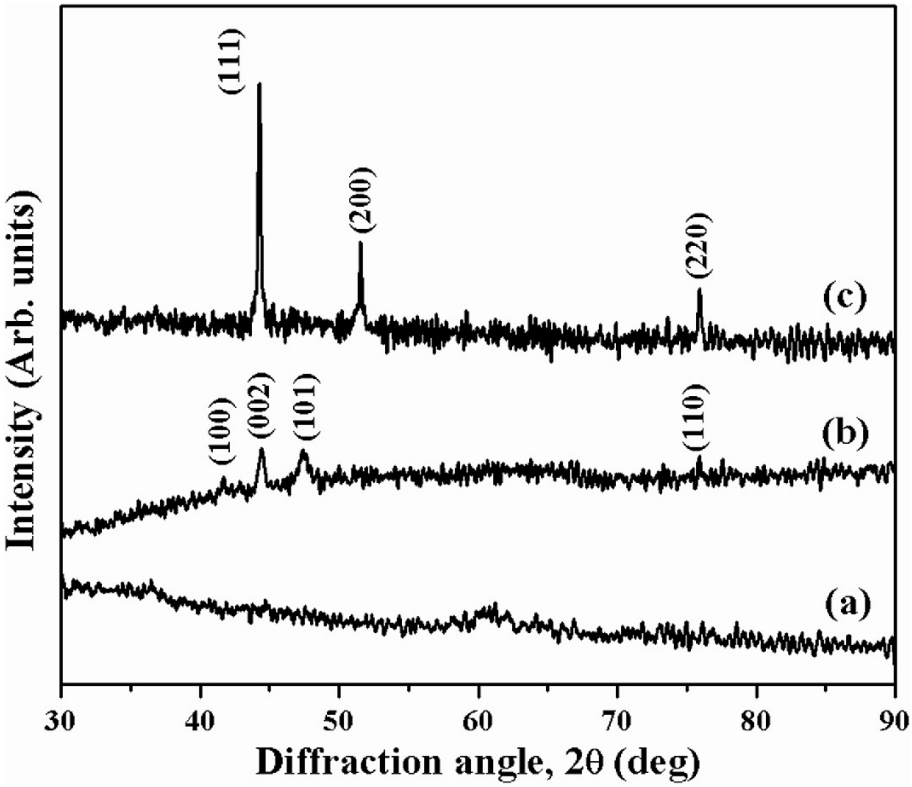

Fig. 16.5 XRD patterns for Co with **a** amorphous, **b** hcp, and **c** fcc phases. Reprinted from reference (Dalavi et al. 2018).

Copyright © 2018, MDPI, Basel, Switzerland (CC BY)

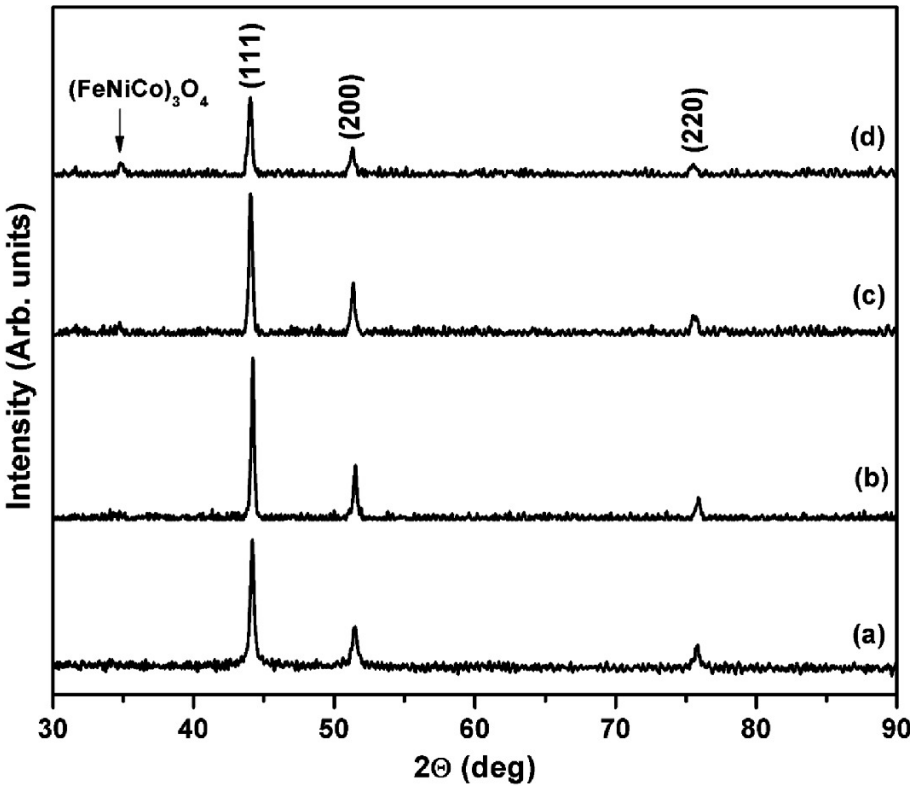

Fig. 16.6 XRD patterns for fcc phases of Fe–Ni–Co alloys with various compositions; **a** $Fe_{20}Ni_{60}Co_{20}$, **b** $Fe_{30}Ni_{50}Co_{20}$, **c** $Fe_{40}Ni_{40}Co_{20}$, and **d** $Fe_{50}Ni_{30}Co_{20}$. Reprinted with permission from reference (Dalavi et al. 2013).
Copyright © 2013, Elsevier

Table 16.1 Experimental parameters obtained from XRD, SEM, and TEM analysis for Co, Fe–Ni–Co, Fe–Co, and CoNi @silica nanomaterials of various coating and compositions

Materials	Coating on as-prepared	Crystal phase	Lattice parameter, (Å)	Crystallite size by XRD (nm)	SEM particle size (nm)	TEM particle size (nm)	References
Co	PEG	Fcc	a = 3.54	42	80	47	Dalavi and Panda (2015a)
Co route 1	PVP	Hcp	a = 2.4972, c = 4.0734	16.4	–	D = 2.8 L = 15–26	Dalavi et al. (2018)
Co route 2		Fcc	a = 3.5403	37.1		5.2	
Co	OA & OlAm	hcp + fcc	a = 2.5049, c = 4.0856 a = 3.5383	15	–	20	Dalavi and Panda (2015c)
$Fe_{20}Ni_{60}Co_{20}$	PEG	Fcc	a = 3.546	27.5	83	24	
$Fe_{30}Ni_{50}Co_{20}$		Fcc	a = 3.546	27.0	76	–	Dalavi et al. (2013), Dalavi and Panda (2015b)
$Fe_{40}Ni_{40}Co_{20}$		Fcc	a = 3.555	24.0	63	36	
$Fe_{50}Ni_{30}Co_{20}$		Fcc	a = 3.558	22.8	60	–	
$Fe_{40}Co_{60}$	OA & OlAm	Bcc	a = 2.852	37.9	–	51	
$Fe_{60}Co_{40}$		Bcc	a = 2.559	26	–	35	Dalavi et al. (2015)
$Fe_{80}Co_{20}$		Bcc	a = 2.868	38.3	–	24	
Co–Ni	–	Fcc	a = 3.54	16.3	–	13.6	
4 wt% Co–Ni	Silica	Fcc	a = 3.53	15.1	–	–	
8 wt% Co–Ni	Silica	Fcc	a = 3.53	14.9	–	8.9	Dalavi and Panda (2016)
12 wt% Co–Ni			a = 3.53				
	Silica	Fcc		13.6	–	–	

16.3.2.2 Morphology Studies

In SEM and TEM micrographs, one can identify the microstructure, size, and shape of nanomaterials. The SEM and TEM particle sizes of

the nanoparticles can be determined by using image analyzing software (e.g., Image J). SAED pattern is used to determine the crystal structure and lattice parameters of the sample.

The above-mentioned technical points of analysis have been demonstrated by SEM and TEM analysis of some Co-based alloys (see Figs. 16.7, 16.8, and 16.9). Typical SEM micrographs for various compositions (annealed at 600 °C) of nanocrystalline Fe–Ni–Co alloys, i.e., $Fe_{20}Ni_{60}Co_{20}$, $Fe_{30}Ni_{50}Co_{20}$, $Fe_{40}Ni_{40}Co_{20,}$ and $Fe_{50}Ni_{30}Co$, are shown in Fig. 16.7 with SEM particles sizes 80 nm, 76 nm, 63 nm, and 60 nm, respectively (Dalavi et al. 2013). Nearly spherical nanostructures with narrow size distributions are shown in the figures. Typical TEM micrographs and SAED patterns for two Fe–Ni–Co alloys, i.e., $Fe_{20}Ni_{60}Co_{20}$ and $Fe_{40}Ni_{40}Co_{20}$ are shown in Fig. 16.8. TEM particle sizes for $Fe_{20}Ni_{60}Co_{20}$ and $Fe_{40}Ni_{40}Co_{20}$ are 24 nm and 36 nm, respectively, and SAED patterns show rings for crystalline planes corresponding to (111), (200), etc. In a similar way, Fig. 16.9a and b shows the TEM micrographs of Co–Ni alloys at the as-prepared stage and 8 wt% Co–Ni@silica with TEM particle sizes 13.6 nm and 8.9 nm, respectively. Further, corresponding SAED patterns show crystalline nature for Co–Ni as-prepared and amorphous for Co–Ni@silica (Fig. 16.9c and d), respectively (Dalavi and Panda 2016).

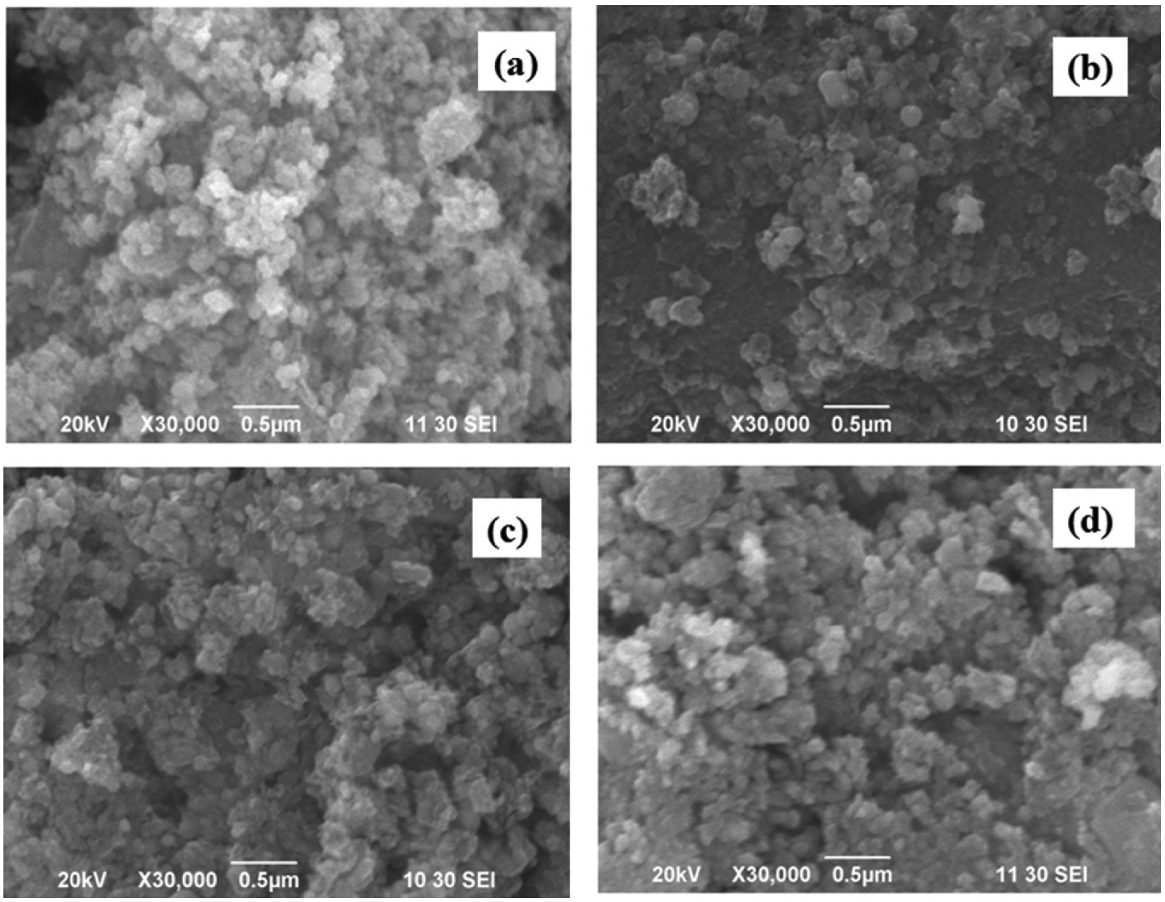

Fig. 16.7 SEM micrographs for Fe–Ni-Co alloys, **a** $Fe_{20}Ni_{60}Co_{20}$, **b** $Fe_{30}Ni_{50}Co_{20}$, **c** $Fe_{40}Ni_{40}Co_{20}$, **d** $Fe_{50}Ni_{30}Co_{20}$. Reprinted with permission from Ref. (Dalavi et al. 2013). Copyright © 2013, Elsevier

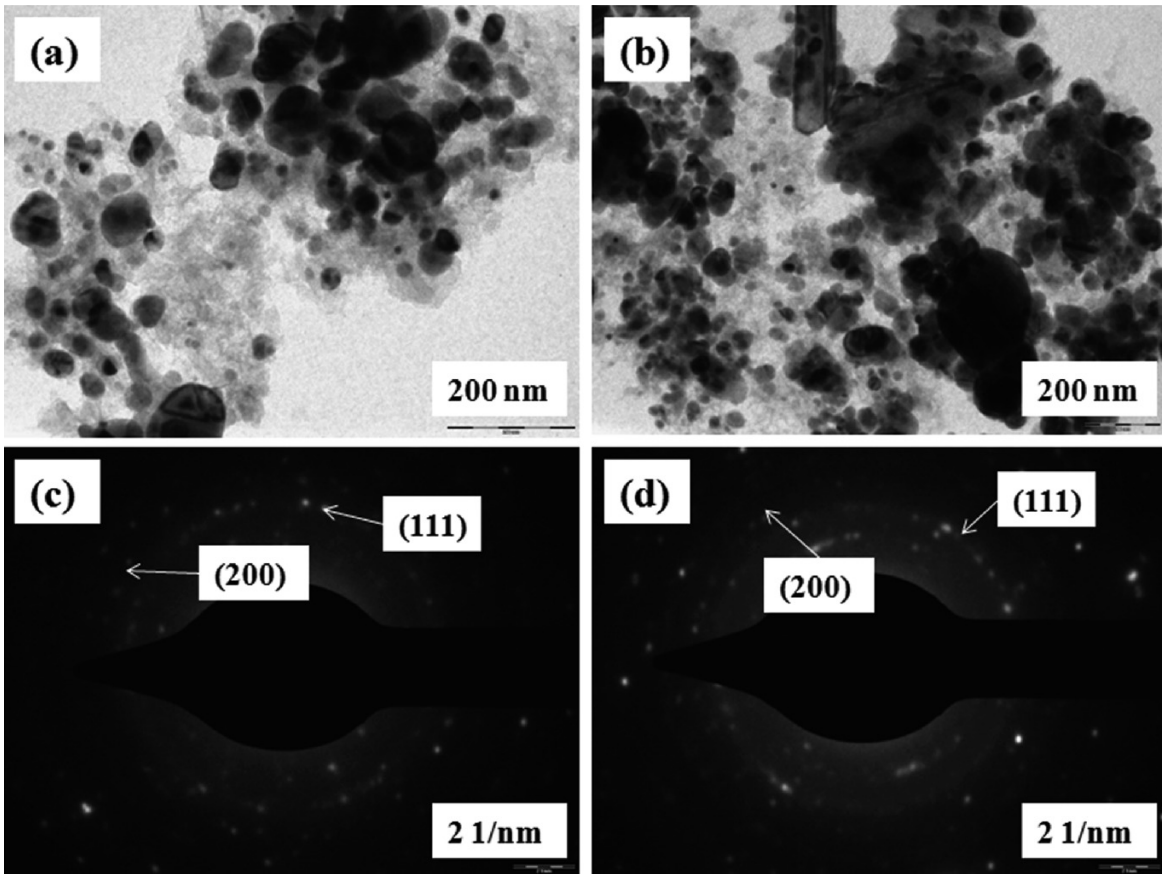

Fig. 16.8 TEM micrographs of nanocrystalline Fe–Ni–Co alloys with various compositions **a** $Fe_{20}Ni_{60}Co_{20}$, **b** $Fe_{40}Ni_{40}Co_{20}$, and **c** and **d** are SAED patterns of corresponding alloys. Reprinted with permission from Ref. (Dalavi and Panda 2015b). Copyright ©2015, Springer Nature

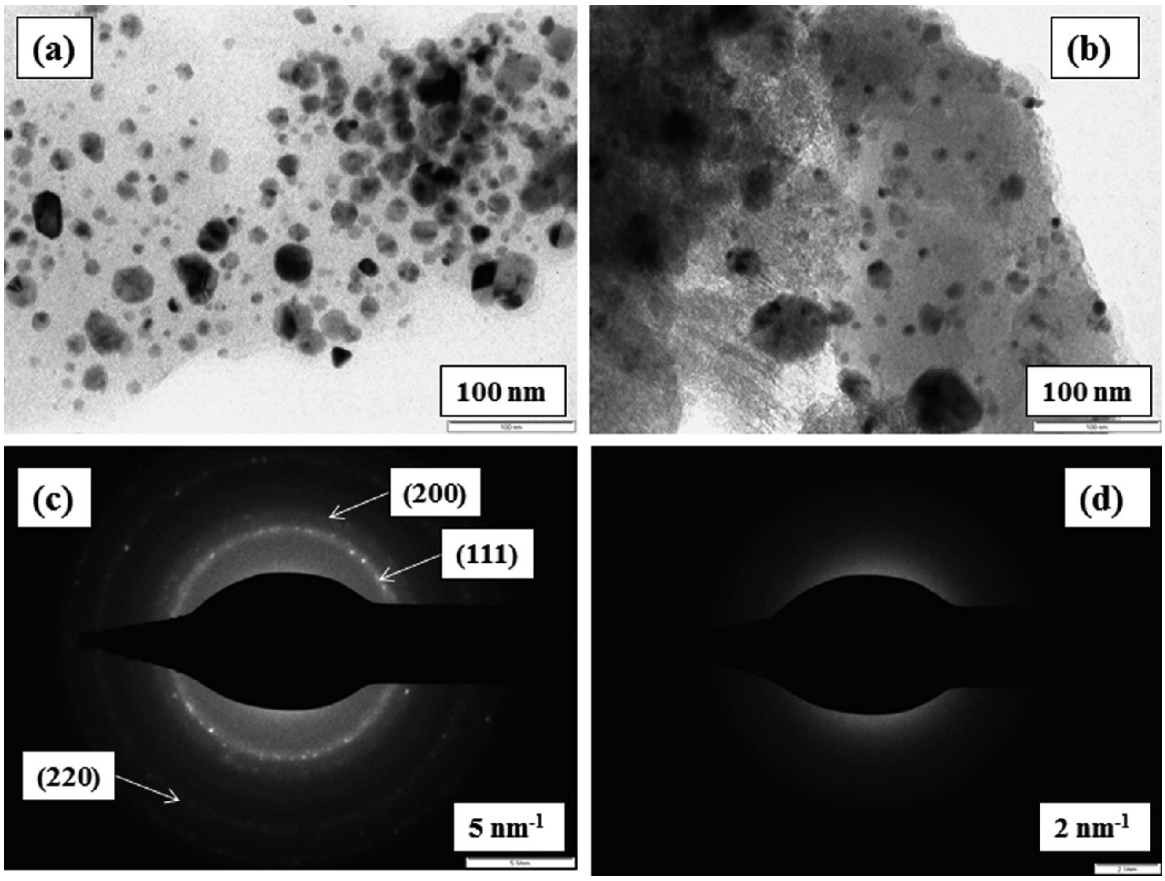

Fig. 16.9 TEM micrographs of nanocrystalline Co–Ni alloys, **a** as-prepared, **b** 8 wt% Co–Ni@silica, **c** and **d** represent corresponding SAED patterns, respectively. Reprinted with permission from Ref. (Dalavi and Panda 2016). Copyright ©2016, Springer Nature

16.3.2.3 Coated Layer Analysis

Analysis of the coated layer can be done using FTIR measurements and a CHNS elemental analyzer. In the case of Oleic acid/Oleylamine coated Co nanomaterials (Dalavi and Panda 2015c), the peaks at 2924 and 2854 cm^{-1} correspond to the CH_2 group, peaks at 1430–1565 cm^{-1} correspond to the carboxylate ($–COO^-$) group. As there is the absence of peaks at 1708, 1592, and 3325 cm^{-1} correspond to ν (C=O) stretch, NH_2 scissoring mode, and ν (N–H) stretch, respectively, confirms the absence of pure oleic acid and oleylamine on the surface of nanoparticles. These results indicate that the capping of oleic acid and oleylamine is in the form of their acid–base complex consisting of $–COO^-$ and $–NH3^+$ ions. However, the peaks in the region of 2854–2924 cm^{-1} were absent after annealing at 600 ºC which indicates the decomposition of the oleyl group to form nanomaterials coated with unknown carbonaceous compounds.

CHNS analysis for Oleic acid/Oleylamine coated/as-prepared materials shows a C:H ratio of about 6:1 as per stoichiometric amount used for preparation. However, after annealing same samples show an increase in the C:H ratio to the range of 10:1 to 20:1. These higher C:H ratios in the annealed or uncoated materials indicate the presence of carbanious materials which are chemically and structurally different from the oleic acid, oleylamine and/or their complex combinations (Dalavi et al. 2015). The CHN contents for annealed Fe-Co alloys are reported to be 34.9, 32.7, and 23.4 wt% for $Fe_{40}Co_{60}$, $Fe_{60}Co_{40,}$ and $Fe_{80}Co_{20}$, respectively.

16.3.3 Magnetic Properties Study Uncoated and Coated Co-Based Nanoparticles

16.3.3.1 Room Temperature Magnetic Properties

The VSM can be used to measure magnetization (M) generated in the materials with varying applied fields ($-20\ \text{kOe} < H < 20\ \text{kOe}$). The hysteresis loops (i.e., M vs. H plots) can be obtained at various temperatures ranging from a lower limit of ~5 K to a higher limit of ~800 K. From the M–H plot, one can determine the values of magnetic parameters such as M_s, M_r, and H_c. The values of M_s of the materials can be determined by (1/H) law, i.e., M vs. (1/H) plot of H values near saturation field (Bean and Jacobs 1960). There are size, shape, and surface effects on the M_s and H_c of nanoparticles. As the size of the particle decreases, the energy that holds the magnetic moment in a particular direction (i.e., anisotropy energy) decreases which randomizes the magnetic moments and leads to a reduction in M_s (Kolhatkar et al. 2013). As the particle size of the material is reduced, coercivity is found to increase, reaches to maximum value (at critical size), and then tends toward zero (Kneller and Luborsky 1963). The particles with size above critical value have multi-domains magnetic structure with stable and non-uniform magnetization whereas particles below critical value become single domains with stable and uniform magnetization. Then, the value of M_s is equal to the intercept on the magnetization axis of the M vs. (1/H) plot. M_s values for coated nanoparticles were generally observed less than uncoated ones because the former has nonmagnetic amorphous structure on the surface while the latter has a crystalline structure without such coating. Magnetic properties for various materials are summarized in Table 16.2.

Table 16.2 Summary of magnetic properties of Co-based alloys nanomaterials at RT and LT conditions

Materials	Annealing conditions in N_2 (ºC/h)	RT magnetic properties			LT magnetic properties		References
		M_S (emu/g)	H_C (Oe)	Mr (emu/g)	T_B (K)	K_{eff} (kJ/m^3)	
Co	600/2	122	111	8	–	–	Dalavi and Panda (2015a)
Co route 1	600/6	162.5	220	17	–	–	Dalavi et al. (2018)
Co route 2		26.7	185	5	–	–	
Co	600/2	64	436	10	>300	>25	Dalavi and Panda (2015c)
$Fe_{20}Ni_{60}Co_{20}$	600/2	54.3	148	10	300	14.0	
$Fe_{30}Ni_{50}Co_{20}$		43.7	122	4	–	–	Dalavi et al. (2013), Dalavi and Panda (2015b)
$Fe_{40}Ni_{40}Co_{20}$		44.3	144	4	300	4.2	
$Fe_{50}Ni_{30}Co_{20}$		41.2	170	2	–	–	
$Fe_{40}Co_{60}$	600/2	92.5	244	2.2	>300	>1.5	
$Fe_{60}Co_{40}$		67.1	400	9.3	>300	>4.6	Dalaviet al. (2015)
$Fe_{80}Co_{20}$		71.1	472	10.4	>300	>14.3	
Co–Ni	400/2	3.59	205	0.58	>300	>280	
4 wt% Co–Ni		1.22	100	0.11	–	–	
8 wt% Co–Ni		1.96	175	0.37	300	78	Dalavi and Panda (2016)
12 wt% Co–Ni		3.96	158	0.50	–	–	

In the case of Co, M_s value for hcp Co is 162 emu/g which matches to bulk value (162.5 emu/g) due to larger crystallites and chain-like structures. M_s value for fcc Co is 29.7 emu/g which is less than the bulk value (172 emu/g) due to nanocrystal size and surface effects (Fig. 16.10) (Dalavi et al. 2018). Similarly, the H_c value is higher for hcp Co (220 Oe) being the magnetically hard phase, and lower for fcc Co (185 Oe) being the magnetically soft phase. Further, M_s and H_c values for Fe–Ni–Co alloys are shown in Fig. 16.11 which shows variation with respect to composition, size, and surface effects (Dalavi et al. 2013). Further, the magnetic properties of Fe–Co alloys vary with their alloy compositions, nano-size, and surface effects and are

attributed to the combined effects of altered crystal anisotropies, disordered structure, reduction in particle size, and spin canting at the surface of nanomaterials (Kaur et al. 2012). The reduced values of the ratios of M_r/M_S for Fe–Co alloys are found to be 0.02, 0.13, and 0.14 which indicates an increase in crystal anisotropies with the increase in Fe content and supports the increasing trend in the H_c values (Ung et al. 2005). Magnetic properties of Co–Ni alloys, before and after silica coating, show significant differences and enhancement in M_S value after silica coating. With the increase of weight % of CoNi in silica matrix, i.e., from 4 wt% to 12 wt%, an increasing trend in the M_s has been observed (Table 16.2). These results show that as dilution effect of CoNi nanoparticles coated with non-magnetic silica along with alteration of nanomaterials dimensions other than spherical inside the porous structure of silica. The intergrain exchange interactions mediated by the silica matrix may be a dominant factor for the enhancement of magnetization in Co–Ni@silica materials as similar effects are found in magnetically diluted systems too (Peng et al. 2008; Prestgard et al. 2013). The values of coercivity for Co–Ni alloy NPs, i.e., 100 Oe–205 Oe, are in the regime of single-domain NPs. The H_c values for Co–Ni@silica with various weight % (4–12 wt%) start increasing from 100 to 175 Oe with an increase in crystallite sizes, i.e., 13.6–15.1 nm due to size, surface effects and lattice strains in the silica coated materials.

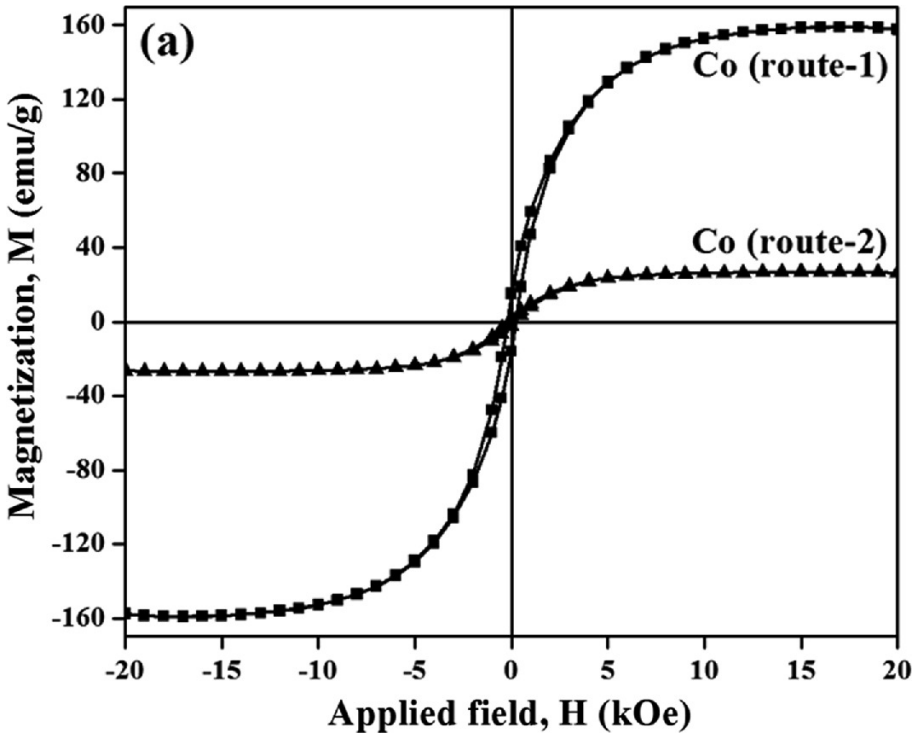

Fig. 16.10 Room temperature magnetic measurement, M versus H curve, and M_S, H_C representation for **a** Co-hcp (route 1) and Co-fcc (route 2). Reprinted from Ref. (Dalavi et al. 2018).

Copyright © 2018, MDPI, Basel, Switzerland (CC BY)

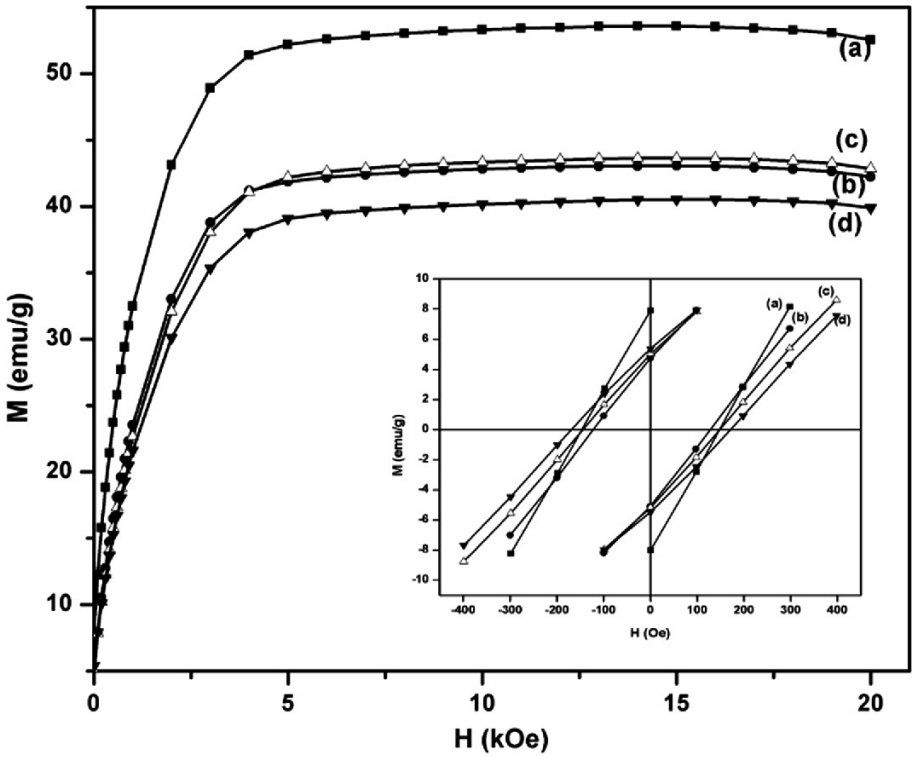

Fig. 16.11 Room temperature magnetic measurement, M versus H curve, and M_S, H_C representation for Fe–Ni–Co alloys with compositions **a** $Fe_{20}Ni_{60}Co_{20}$, **b** $Fe_{30}Ni_{50}Co_{20}$, **c** $Fe_{40}Ni_{40}Co_{20}$, **d** $Fe_{50}Ni_{30}Co_{20}$. Reprinted with permission from reference (Dalavi et al. 2013).

Copyright © 2013, Elsevier

16.3.3.2 Low Temperature Magnetic Properties

Temperature dependent magnetic properties of the nanomaterials, especially superparamagnetism, can be studied by measuring magnetization in the temperature range of 5–300 K (M vs. T plot) as shown in Figs. 16.12 and 16.13. These measurements were carried out in field cooled (FC) and zero field cooled (ZFC) conditions by applying a small magnetic field (~50 Oe–500 Oe). For SPM particles, ZFC curve shows maximum magnetization at blocking temperature, T_B.

$$T_B = \frac{K_{eff} v}{25\ k_B} \tag{16.3}$$

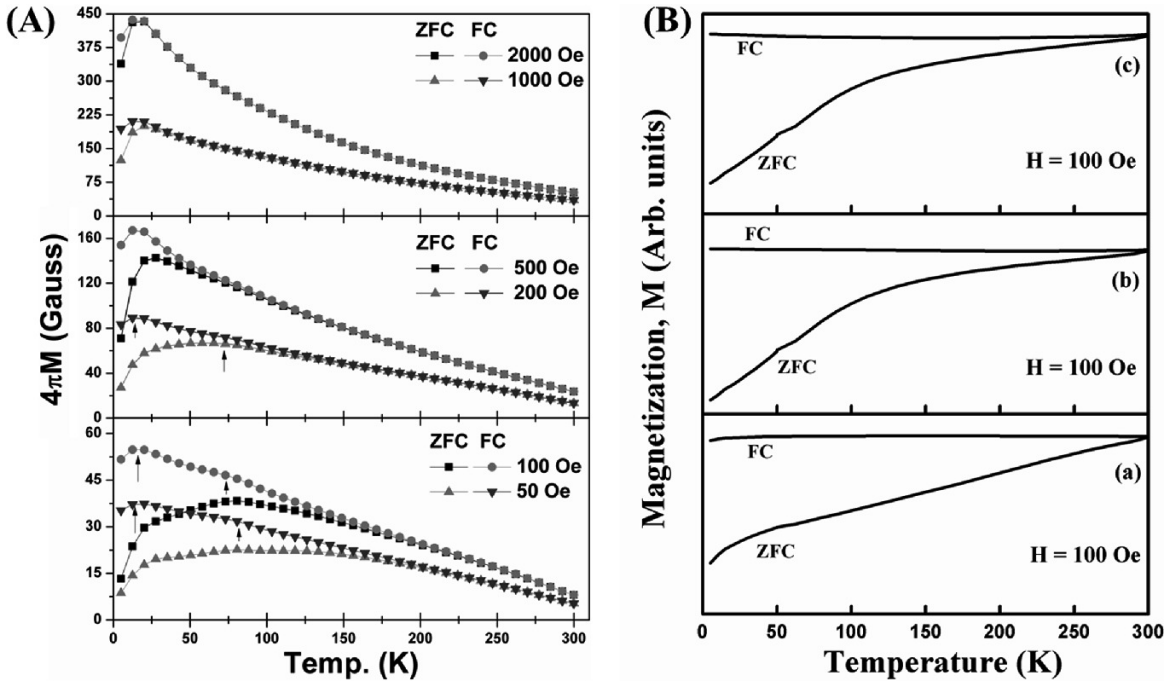

Fig. 16.12 **a** Low temperature FC/ZFC curves for $ZnFe_2O_4$ nanomaterials, and variation with respect to the applied field. Reprinted with permission from ref. (Sahu et al. 2018). Dalavi et al. 2015

Copyright © 2018, MDPI, Basel, Switzerland (CC BY). **b** Low temperature magnetic properties of Fe-Co alloys of various compositions **a** $Fe_{40}Co_{60}$, **b** $Fe_{60}Co_{40}$, **c** $Fe_{80}Co_{20}$. Reprinted with permission from Ref. (). Copyright © 2015, Royal Society of Chemistry

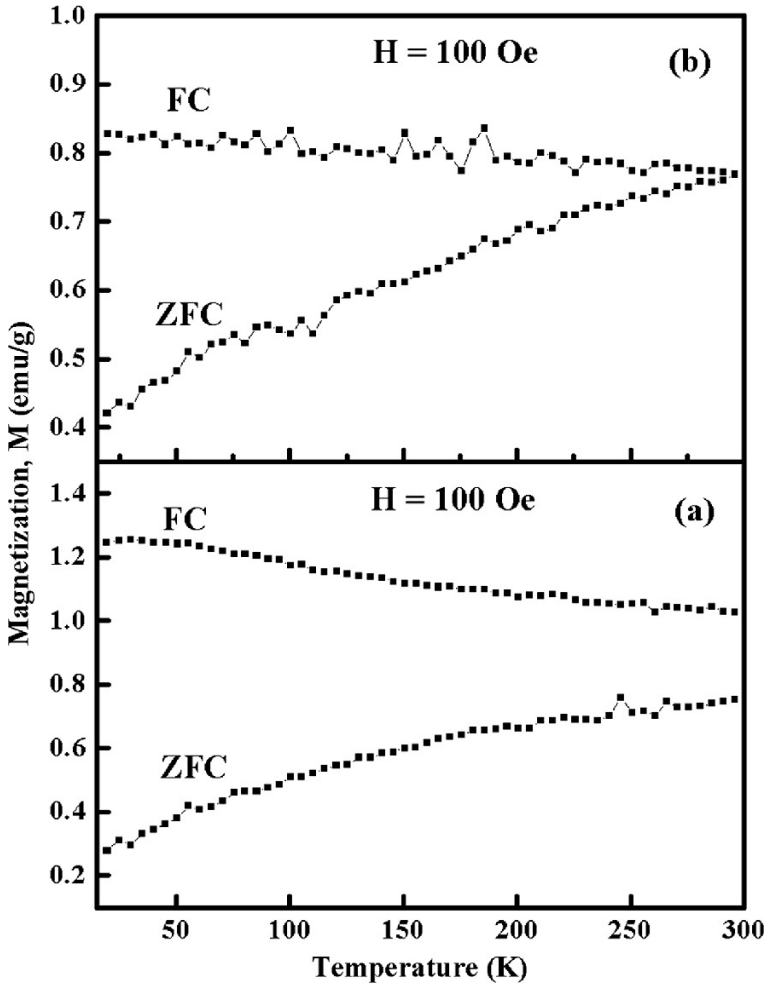

Fig. 16.13 Low temperature magnetic properties of Co–Ni alloys **a** AP Co–Ni, **b** 8 wt% Co–Ni@silica. Reprinted with permission from Ref. (Dalavi and Panda 2016).
Copyright © 2016, Springer Nature

where K_{eff} is the effective anisotropy constant, V is nanoparticle volume and k_B is the Boltzmann constant. The divergence in magnetization of FC and ZFC curves below T_B is due to magnetic anisotropy energy barrier and spin relaxation. SPM particles have a low anisotropy barrier and can be overcome by thermal energy (k_BT). Thermal energy causes the random flipping of the magnetic moments above T_B which results in the decrease of magnetization. Low temperature magnetic parameters, i.e., T_B and K_{eff} for various Co-based nanomaterials are summarized in Table 16.2.

Figure 16.12a shows typical FC/ZFC curves for $ZnFe_2O_4$ nanomaterials at various applied magnetic fields (Sahu et al. 2018). The divergence/irreversibility in FC/ZFC curves below T_B can be clearly seen and decrease with increasing applied magnetic field. This

variation is due to spin freezing phenomena in nanoparticles and is field and temperature dependent. Depending upon field strength, the barrier height is observed for magnetic phase transition in these spintronic systems. Figure 16.12b represents M versus T plot for Fe–-Co alloys with various compositions and shows magnetic irreversibility below 300 K. The higher FC magnetization values than the ZFC values indicate the presence of ferromagnetism in Fe–Co alloys up to 300 K. Further, the ZFC magnetization increases rapidly with temperature but not superimposed with the FC curve up to 300 K. This indicates that NPs are in the magnetically blocked state which may be attributed to stronger dipolar interparticle magnetic interactions (Wei et al. 2008). The strength of such dipolar interactions increases with an increase in particle magnetic moments and a decrease in distance between them. Above 300 K, superimposition of FC/ZFC curves can occur and hence superparamagnetic behavior of the Fe-Co alloys. K_{eff} values for Fe-Co alloys (1.5–14.3 kJ/m^3) are at lower side than literature reported values (40–200 kJ/m^3) for Fe–Co NPs (Peng et al. 2009; Bansmann et al. 2010). This may be attributed to an alteration in the size and surface anisotropy contribution.

Typical FC/ZFC plots for pure CoNi and 8 wt% CoNi@silica are shown in Fig. 16.13. Here, we can see the effect of silica coating which increases interparticle separation and reduces dipolar interaction effects as explained above. The T_B lies significantly above 300 K for pure CoNi whereas 300 K for 8 wt% CoNi/silica. The K_{eff} values are found to be >280 kJ/m^3 and 78 kJ/m^3 for Co–Ni and 8 wt% Co–Ni@silica, respectively. The reduction in T_B and K_{eff} value for 8 wt% Co–Ni@silica signifies altered size and magnetic structure at the surface. These results indicate that silica supports to enhance dipolar interactions although the separation between NPs is higher than that of Co–Ni without silica coating (Dalavi and Panda 2016).

16.4 Co-Based Uncoated and Coated Metal Oxide Nanoparticles

This subsection deals with the synthesis, magnetic properties, and applications of cobalt (Co) based metal oxide nanomaterials in uncoated and coated form. As a representative class of coated materials pure and doped $CoFe_2O_4$ are focused. The magnetic properties have made $CoFe_2O_4$ nanomaterials, excellent contenders

for biomedical applications along with their standard magnetic properties (Amiri and Shokrollahi 2013). In order to eliminate the disadvantage of cytotoxicity of these materials, surface coating, and surface functionalization can be utilized such that the toxic nature due to the presence of cobalt can be overcome. A selection of surface coated materials on these $CoFe_2O_4$-based nanomaterials includes polyethylene glycol (De et al. 2021), polysaccharides (Choppadandi et al. 2023), lipids, dendrimers (Kanwar et al. 2019), etc. The significant aspects of this section include synthetic methodologies, structural characterization, morphological characterization, and magnetic property study (at room temperature and low temperature) of the Co-based uncoated and coated metal oxide nanoparticles.

16.4.1 Synthetic Methodologies for Co-Based Uncoated and Coated Metal Oxide Nanoparticles

16.4.1.1 Wet Chemical Method Based on the Formation of Precursor

In a precursor method, atomic level mixing of metal ions takes place by forming a solid compound (precursor). In a precursor, the elements of the required compound exist in the correct stoichiometric ratio. The precursor is then heated to decompose and to obtain the desired product. Hence, the formation of precursors with proper composition is one of the most important steps in all the wet chemical methods for the synthesis of nanomaterials (Chang et al. 2021). The precursor methods form homogeneous products comparatively at lower temperatures. Here, starting materials such as nitrates, chlorides, and carbonates may be used in order to synthesize precursor materials. Examples of wet chemical methods based on the formation of precursors include the sol–gel autocombustion route (also known as the citrate precursor route) (Das et al. 2021; Kiran and Sumathi 2017), coprecipitation method hydrothermal method (Maaz et al. 2009), etc. The solid-state precursors thus obtained are heat treated at elevated temperatures in order to give uncoated or coated oxide products. Furthermore, uncoated nanoparticles can be coated with inorganic or solid-state materials after suitable surface modifications. A few selected methodologies pertaining to the synthesis of uncoated nanoparticles are described in the subsections below (Sects. 16.4.1.2, 16.4.1.3, 16.4.1.4).

16.4.1.2 Sol–Gel Autocombustion Method

Sol–gel autocombustion method is one of the most extensively used wet chemical methods for the synthesis of spinel ferrites (e.g., $CoFe_2O_4$ based) nanomaterials. Among all the other methods of synthesis of magnetic nanoparticles, the sol–gel autocombustion method is very efficient to use as it has various advantages such as formation of nanometer particle size, formation of highly pure-single phase crystalline products, reproducibility of results, and homogeneity in particle size distribution (Sajjia et al. 2014). This is a liquid phase process that involves hydrolysis and condensation, in which metal salt precursors in stoichiometric ratios are dissolved in a minimum quantity of distilled water and generally followed by the addition of chelating agent (citric acid, tartaric acid, etc.) and/or fuels such as nitrate, glycine, and polyethylene glycol (Kiran and Sumathi 2017; Sajjia et al. 2014; Patta et al. 2020). The representative schematic diagram for the sol–gel autocombustion technique for substituted cobalt ferrite nanomaterials is shown in Fig. 16.14. In the schematic diagram, the metal salt precursor solutions (Fe, Co, and X-substituent) are prepared with complete homogeneity and combined together to form a mixed metal salt solution. At this stage, a chelating agent is added in excess so as to form a complex. Upon refluxing, a completely homogenized sol is obtained which is converted to viscous gel by evaporation. The heat treatment to this viscous gel gives the swollen gel which is then fired/combusted at a low temperature of 300–400 ºC. For various pure and substituted cobalt ferrite nanoparticles, sol–gel autocombustion method is suitable so as to obtain single pure phase products with tuneable saturation magnetization and high coercivity values (Mund and Ahuja 2017).

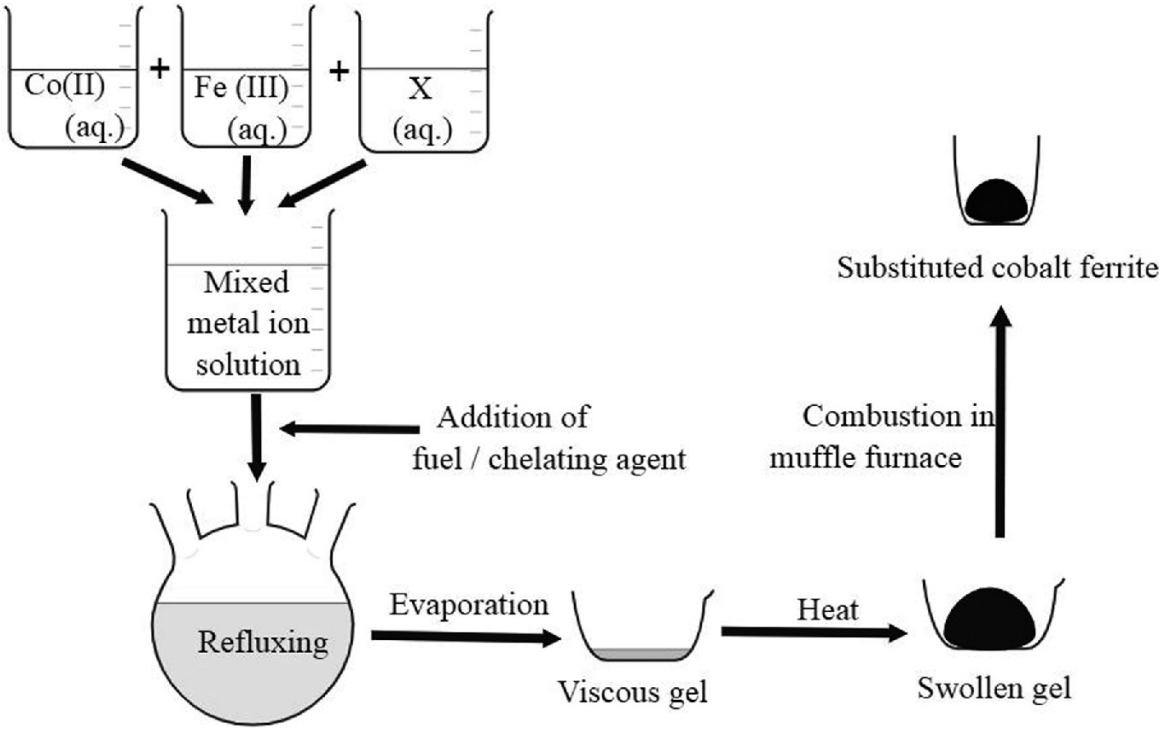

Fig. 16.14 Schematic diagram representing sol–gel autocombustion route of synthesis of oxide nanomaterials

Various methods are adopted in the literature for coating cobalt-based oxide materials with surface modifiers. The $Co_{0.37}Zn_{0.63}Fe_2O_4$ nanoparticles were synthesized by sol–gel method and these synthesized bare $CoZnFe_2O_4$ were subjected to surface modification using chitosan (Choppadandi et al. 2023). In this work cobalt-zinc ferrite nanoparticle loaded with the drug was studied for cancer treatment on the MCF-7 cell line. The drug loading was accomplished by surface modification of the magnetic nanoparticle by using chitosan (Choppadandi et al. 2023). The parameters such as pH and temperature-controlled drug release are significantly considered for high drug loading affinity (86%) on the magnetic nanoparticles. Also, under in-vitro conditions, the Co–-Zn nanoferrites were loaded with doxorubicin through a surface conjugation technique caused considerable apoptosis (genetically regulated form of cell death) in MCF-7 cells (72%) and showed an overall cell death result less than 95% (Choppadandi et al. 2023). From the above research study, it is clear that coating/surface functionalization of the substituted cobalt ferrite with standard magnetic properties leads to significant applications which are certainly functional for the benefit of mankind.

16.4.1.3 Co-Precipitation Method

Co-precipitation is one of the most standard and conventional methods for the synthesis of metal oxide nanoparticles. Besides, coprecipitation is a fast and cost-effective chemical process. In brief, in this method, metal salt precursor (chloride, nitrate, or oxychloride) is dissolved in water and then, by addition of a base such as ammonium hydroxide or sodium hydroxide, the respective hydroxide is precipitated. The coprecipitation technique is not limited to the use of hydroxides, but many other precipitating agents are used, say for example, hydrazine hydrate (Kazi et al. 2023). The coprecipitation method of synthesis is considered better compared to the solid-state method. It overcomes the limitations of solid-state methods such as lack of homogeneity, non-uniform particle size, grinding impurities, and use of high temperatures. Hence, this method is suitable for the synthesis of nanoparticles with mild reaction conditions. The control of particle size and its distribution is often attained by controlling the relative rates of nucleation and growth of nanoparticles during the synthesis process. The comparative study of combustion and coprecipitation synthesis methods for $CoFe_2O_4$ nanoparticles was reported by Houshiar et al. (2014) where size, structure, and magnetic properties were compared of $CoFe_2O_4$ obtained by both synthesis methods (Houshiar et al. 2014). It has been observed that materials quality and properties are quite sensitive to the method of preparation. In a research study conducted by Salunkhe et al. (2016), noteworthy results with respect to coated $CoFe_2O_4$ nanoparticles for magnetic fluid hyperthermia were reported (Salunkhe et al. 2016). The surface modification/coating of nanoparticles was carried out by oleic acid (OA) and OA-conjugated polyethylene glycol (OA-PEG). The in-vitro cytotoxicity studies were carried out based on the Tryptan Blue Dye Exclusion Assay confirmed that the OA-PEG coating upon $CoFe_2O_4$ nanoparticles efficiently enhanced their cytocompatibility (Salunkhe et al. 2016). Another example of a recent study wherein the coprecipitation route was used to synthesize uncoated cobalt ferrite nanoparticles was reported by Anila et al. (2023). These $CoFe_2O_4$ nanoparticles were surface functionalized using chitosan in acetic acid (Anila et al. 2023).

16.4.1.4 Mixed Hydroxides Precipitation and Subsequent Digestion

Transition metal-based magnetic oxide materials can be prepared by co-precipitating their corresponding hydroxides and subsequently digesting or aging the suspension at low temperatures for several

hours (Belhadj et al. 2022; Andhare et al. 2020). In a typical synthesis, metal chlorides are mixed in stoichiometric ratios in distilled water. The molar concentrations of the metal salts were kept in the range of 0.1–1 M. Next, NaOH solution in the range of 1–3 M was added dropwise till all the hydroxides precipitates. The pH of the final solution mixture was kept at 11. The resulting suspension was agitated at low temperatures (range 50–90 ºC) for several hours with constant stirring. During this process, the desired cobalt-based oxide products are obtained which are extracted by centrifugation. For example, in a representative synthesis, reported by Houshiar et al. (2014), salt solutions of 0.4 M iron chloride and 0.2 M cobalt chloride were taken (Houshiar et al. 2014). The NaOH solution (3 M) was then added to the reactants. The reaction mixture was subjected to stirring until a pH value of 12 was reached. Next, aging was done at 80 ºC in order to obtain $CoFe_2O_4$ products. This methodology has its importance since surfactants can be added to the precipitated solutions in order to prepare coated $CoFe_2O_4$ nanoparticles.

16.4.1.5 In-Situ Functionalization of Oxide Material

The in-situ method of synthesis of nanoparticles in a polymer matrix is an effective and simple method to synthesize nanocomposites. The in-situ method is a one-step synthesis of nanocomposites with in-situ production of nanoparticles from the resultant precursors. The surface functionalization of the oxide nanomaterials is carried out in order to enhance the properties of the nanomaterial under study. Various reports of surface functionalized $CoFe_2O_4$ and related nanomaterials are available which present the enhancement in the properties of the materials such as mechanical properties, magnetic properties, thermal properties, and electrical properties.

For instance, citric acid-coated $CoFe_2O_4$ nanoparticles were synthesized using in-situ procedures (Leonel et al. 2018). In this report, in-situ (one-step method) resulted in a small core size (2.9 nm), high stability in aqueous solution, and high surface charge density ($\zeta = -52$ mV). The range of surface charge density values was assigned to various coordinations of the tricarboxylate anion to the nanoparticle surface. The higher surface reactivity and colloidal stability both with very low hydrodynamic size of 4.8 nm and high magnetization (45 emu/g), the $CoFe_2O_4$ prepared by the one-step route was proved to be suitable for subsequent conjugation of bioactive groups, focusing at biological applications (Leonel et al. 2018). Another study reports the hydrothermal synthesis of $Co_{(1-}$

$_{x)}Zn_xFe_2O_4$ (x = 0.3, 0.5, 0.7) nanodot functionalized by polyaniline (PANI) carried out by in-situ polymerization (Kumar et al. 2021). The highly crystalline product, pure-single phase spinel structure, photo-degradation kinetic study and efficient nano-photocatalysts are some of the significant factors of this study. The results depicted that the nanostructure $Co_{0.5}Zn_{0.5}Fe_2O_4$/PANI showed the highest efficiency for the photo-degradation of azo dyes (Kumar et al. 2021).

16.4.2 Structural and Morphological Characterizations of Some Selected Co-Based Uncoated and Coated Metal Oxide Nanoparticles

16.4.2.1 Crystal Structures and Crystallite Sizes

The synthesized nanomaterials are subjected to characterization using the X-ray diffraction (XRD) technique to gain insights into the pure-single phase product formation. The XRD analysis is carried out in order to determine the structure and crystallite size of the synthesized coated Co-based metal oxide nanoparticles. The use of crystalline phase analysis and the Scherrer equation to determine the crystallite size (t) has already been described in Sect. 16.3.2.1. From various calculations carried out by using the Scherrer equation, crystallite size, microstrain, lattice parameters, crystallite structure and residual strain (macrostrain) are the important parameters that can be determined successfully for coated Co-based metal oxide nanoparticles. The major important aspect of this technique is the study of the effect of synthesis method, synthesis temperature, annealing temperatures, surface modification, etc. on the XRD peak intensity, peak broadening, shift in the peak position, etc. For instance, the effect of the synthesis method and the effect of synthesis parameters, such as: pH, synthesis temperature, and duration of thermal treatment were the major points considered in a report on cobalt ferrite nanomaterials (Medeiros et al. 2017). As per the report published by de Medeiros et al. (2017), a correlation between experimental parameters and crystallite sizes obtained using various methods in the synthesis of $CoFe_2O_4$ is summarized in Table 16.3. It can be easily seen that uncoated oxide nanoparticles of various tuneable size ranges can be obtained by adopting suitable methodology and processing parameters. The as-prepared cobalt-based oxide materials can be coated with various surface functionalization molecules/groups. In a recent report, the XRD studies for $Co_{0.37}Zn_{0.63}Fe_2O_4$ nanoparticles and that of the corresponding particles with surface modified with chitosan were

compared and found that no appreciable change in the crystalline structures occur (Choppadandi et al. 2023). Based on the reports mentioned in this subsection, it can be concluded that XRD studies are significant for the determination of the crystalline nature of nanoparticles and crystallite sizes which plays an important role in fine particle magnetism (Zhang et al. 2011).

Table 16.3 Summary of correlation between experimental parameters and crystallite sizes obtained using various methods in the synthesis of $CoFe_2O_4$ (Medeiros et al. 2017)

Sr. no	Method of synthesis	Value of pH	Temperature (ºC)	Time of thermal treatment (h)	Minimum crystallite size (nm)
1	Hydrothermal method	8	120	6	2.3
		9	140	15	7.7
		10	160	24	11.4
2	EDTA/citrate complexing method	8	600	2	22.2
		9	800	4	67.3
		10	1000	6	162.0

16.4.2.2 Morphology Studies: A Comparison Between Uncoated and Coated Nanostructures

The importance of SEM and TEM micro-structural techniques is seen in various literature reports related to oxide nanoparticles and their coated forms (Sajjia et al. 2014). For instance, Fig. 16.15 represents the SEM micrograph of $CoFe_2O_4$ nanoparticles synthesized via the sol–gel synthesis technique (Sajjia et al. 2014). Based on the complete study in this research paper, the particle size obtained from SEM particle size analysis varied over a range of 7–28 nm (Sajjia et al. 2014). Several particles are agglomerated to form aggregates with a variety of irregular shapes. In another study, uncoated and chitosan coated cobalt ferrite nanoparticles were characterized by TEM analysis and it was confirmed that coated layers do not alter the crystalline structure including crystallinity and crystallite sizes significantly (Anila et al. 2023). This indicates that the properties arising from the core structural parameters in nanomaterials remain intact and any change in materials properties can be attributed to changes in surface structure and inter-granular interactions in such kind of coated particles.

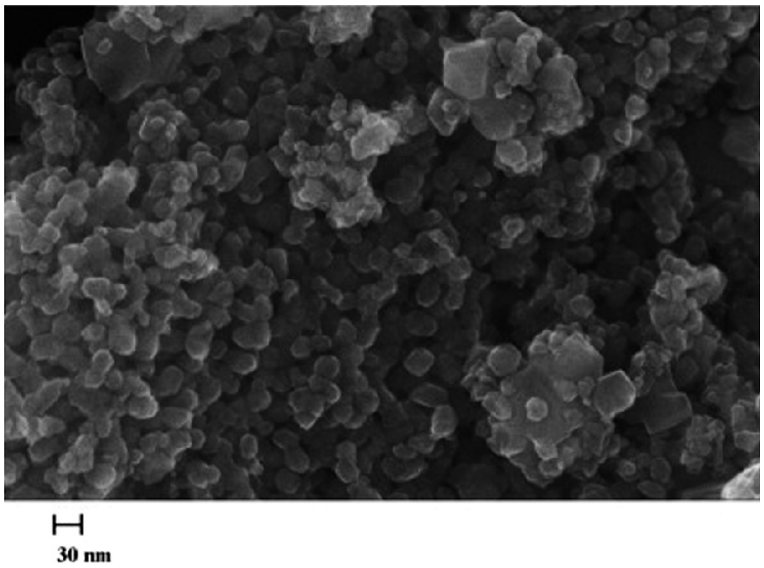

Fig. 16.15 SEM micrograph showing the $CoF_{e2}O_4$ nanoparticles heat treated at 250 ºC for 10 h**.** Reprinted with permission from reference (Sajjia et al. 2014).
Copyright © 2013, Elsevier

16.4.2.3 Elemental Composition Analysis

The fundamental analysis technique used for the determination of elements is energy dispersive spectroscopy (EDS) which is mostly accompanied by the SEM technique. The EDS determines the elements present in a particular material composition. The EDS spectrum shows the presence of different elements and the data obtained by the EDS analysis gives weight % and atomic % of all the elements present in the sample under study. For example, the EDS analysis of $NiFe_2O_4$, $CoFe_2O_4$, and nickel doped cobalt ferrite ($Co_{0.5}Ni_{0.5}Fe_2O_4$) nanoparticles synthesized by coprecipitation method was analyzed and compared (Maaz et al. 2009).

16.4.3 Magnetic Properties of Coated and Uncoated Co-Based Metal Oxide Nanoparticles

One of the most studied and researched properties of cobalt-based metal oxide nanoparticles is their magnetic properties because of their ferrimagnetic behavior with spontaneous magnetization. Different parameters on which magnetic properties of these nanoparticles are dependent include method of synthesis, chemical composition, synthesis temperature, annealing temperature, nature of substituent, particle size, crystallite size, morphology, interaction between particles, cation distribution, etc. The detailed discussion of magnetic nanomaterials, magnetic behavior, classification of nanomaterials showing magnetic properties, etc. is discussed in

Sect. 16.2 of this chapter. The magnetic properties of nanomaterials are highly affected by the influence of the temperature to which they are subjected and can flip the original nature of magnetism exhibited by them. Therefore, this section focuses on the magnetic properties exhibited by uncoated and coated Co-based metal oxide nanoparticles at room temperature (300 K) (Houshiar et al. 2014) and at lower temperatures (range of 5–300 K) (Ounacer et al. 2021; Hassanzadeh-Tabrizi et al. 2021). Various reports in the literature emphasize on the significant magnetic behavior of $CoFe_2O_4$ (uncoated and coated) nanoparticles which are responsible for various applications of magnetic nanomaterials beneficial to mankind (Hassanzadeh-Tabrizi et al. 2021).

16.4.3.1 Room Temperature Magnetic Properties

The room temperature hysteresis (M-H) curve is obtained and analyzed for uncoated and coated $CoFe_2O_4$ nanoparticles. In most cases, various parameters studied from the hysteresis curve are saturation magnetization (M_S), coercivity (H_C), and remanent magnetization (M_r) based on which significant conclusions can be made. For instance, in a study of magnetic properties of $Co_{1-x}Mg_xFe_2O_4$ ($0.0 \leq x \leq 1.0$) nanoparticles synthesized by the coprecipitation method, the M-H curves measured at 300 K were reported (Ounacer et al. 2021). The surface modified $CoZnFe_2O_4$ nanoparticles with chitosan were studied for magnetic properties and compared with uncoated $CoZnFe_2O_4$ nanoparticles and found a substantial increase in the value of magnetization for coated particles (Choppadandi et al. 2023). In another report, the biocompatible hydroxyapatite (HA) coated cobalt ferrite core–shell structures were reported by Hassanzadeh-Tabrizi et al. (2021), wherein the crystalline structure of HA is retained. However, these core–shell structures with increasing content of HA show reduced magnetizations compared with pure cobalt ferrites along with the observation of sizable coercivities (see Fig. 16.16). The values of M_S for CoFe, CoFe-10HA, CoFe-30HA and CoFe-50HA were estimated to be 59.9 emu/g, 43.4 emu/g, 18.3 emu/g and 11.4 emu/g, respectively. As per the fundamental understanding, the magnetic properties of ferrites are in associated with various parameters such as morphology of the particles, composition, particle size, distribution of ions, method of synthesis, and defects in the structure. In this particular study, the particle size of the $CoFe_2O_4$ and the synthesis method parameters

were kept constant and it can be implied that these factors do not have a significant impact on the reduction of magnetization values (Hassanzadeh-Tabrizi et al. 2021). This decrease in M_s shown by the HA-coated $CoFe_2O_4$ materials can be attributed to the separation of adjacent nanoparticles by a non-magnetic HA coating or film, resulting into the decrease in the magneto-static coupling among the nanoparticles. This type of phenomenon was also reported in some other reports as referred by Hassanzadeh-Tabrizi et al.

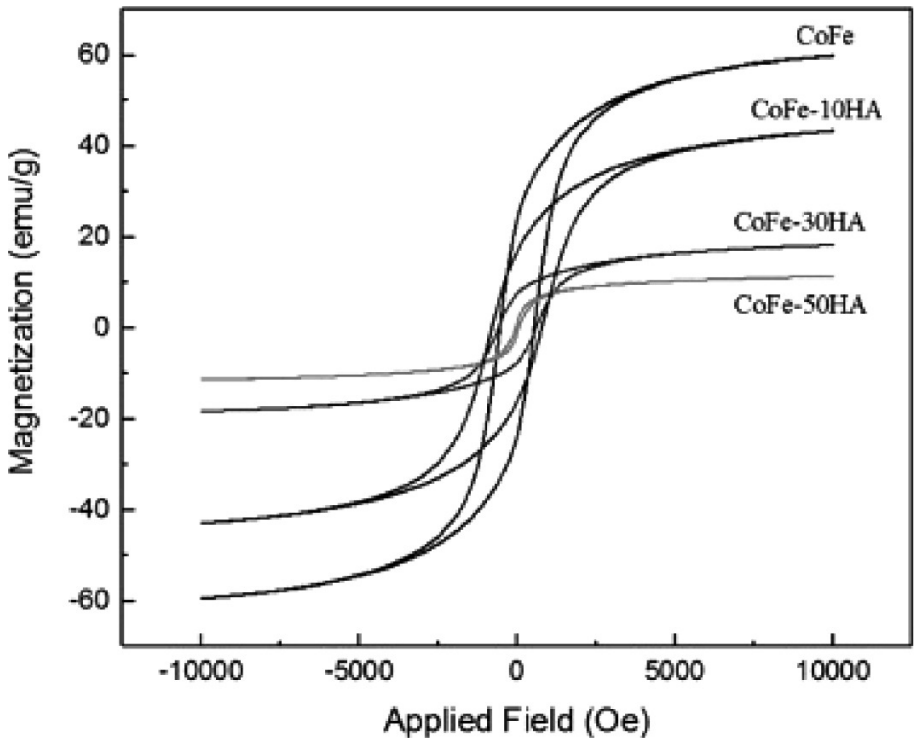

Fig. 16.16 M versus H plots of various nanocomposites with various wt% of HA coating at the surfaces. Reprinted with permission from reference (Hassanzadeh-Tabrizi et al. 2021). Copyright © 2021, Elsevier

16.4.3.2 Low Temperature Magnetic Properties

In order to understand superparamagnetic behaviors and superferromagnetic transition, low temperature magnetic properties of uncoated and coated Co-based oxide materials are studied (Ojha and Kant 2021). The magnetic studies include M versus H plots at different temperatures and their testing for Langevin fit and M versus T plots for estimation of blocking temperature of the magnetic assembly (Bean and Livingston 1959). These studies are important for magnetic oxide systems having low values magneto-crystalline anisotropies. Furthermore, from temperature dependence magnetization studies one can extract conclusions regarding surface

contribution in case of coated particles and interparticle interactions (Ojha and Kant 2021).

16.5 Applications of Magnetic Nanoparticle-Based Coated Materials

16.5.1 Magnetic Recording Head

Magnetic NPs including metals, alloys, metal oxides, and carbides have a wide range of applications in magnetic recording, magnetic sensors, etc. The advantages of magnetic nanomaterials over bulk magnetic materials are due to their small particle size, unique morphologies, and size-surface effects. This section deals with a variety of applications of these nanoparticles that can be significant for the benefit and growth of mankind. For instances, high magnetization and low coercivity materials such as Co and Fe-Co are generally suitable for recording heads. Further, non-spherical shape NPs (e.g., needle and disc shaped) have shape anisotropy, are more easily susceptible to magnetic texturing or ordering of the directions of the magnetic axes, and have been used in magnetic recording tape (Veitch et al. 1999).

16.5.2 Biosensing

Biosensing is important in the area of high performance clinical diagnosis. Nanosized magnetic materials are significant sources of markers for biosensing because of their prominent magnetic properties, and required alteration in composition and particle size. These factors also help to allow their use in respective instruments and formats utilized for biosensing. Also, significant factors that affect the ferrite magnetic nanoparticles-based biosensors are tuned nanoparticles as detection probes to generate specific and large biological signals with negligible non-specific binding. To develop a suitable sensing device, for the detection of disease and intracellular measurements, various factors that need to be supervised are reduction in particle size, a suitable method of synthesis, sensitivity toward targeted intracellular biological small particles, surface functionalization, and lesser signal-to-noise ratio (Tripathy et al. 2021; Srinivasan et al. 2018). Researchers worldwide are focusing on such types of biosensing applications that can be made available for the benefit of mankind. In one of such research study, the development of a biosensor was reported for the detection of a glycoprotein called CEA (Carcinoembryonic antigen) which is over-expressed in cancer-

causing colorectal cancer (Chen and Tang 2007). Based on a quartz crystal microbalance (QCM) immunosensor was developed with $CoFe_2O_4/SiO_2$ which was immobilized on the surface and conjugated with an anti-CEA antibody. Then, by using piezoelectric immunosensing, the CEA antigen was detected (Chen and Tang 2007). In another study, a novel biosensor which is $CoFe_2O_4$-based comprising nanocomposite of $CoFe_2O_4$-chitosan modified using glassy carbon electrode ($CoFe_2O_4$/CT/GCE) was developed in order to determine the non-enzymatic detection of uric acid (UA) (Charan and Shahi 2016). The significant properties of this novel biosensor system are particle size (~10 nm) and high surface area (235 m^2/g). The major advantages of $CoFe_2O_4$/CT/GCE biosensor was reported as the sensitivity and its highly selective nature for the non-enzymatic detection of UA even in the presence/interference of other components like glucose, urea, cholesterol, ascorbic acid, and mixture of these (Charan and Shahi 2016).

16.5.3 Ferrofluid

The stable colloidal suspensions of magnetic nanoparticles (ferromagnetic or ferrimagnetic) that are dispersed in a carrier liquid are defined as ferrofluids. The size of the particles is around 10 nm (in diameter) or smaller and are generally coated with surfactants such as stearic acid and oleic acid. These magnetic fluids consist of colloidal systems comprising single-domain magnetic nanoparticles dispersed in a carrier liquid and can be analyzed as suitable model systems to investigate the basic properties of magnetic nanoparticles structures. Ferrofluid is a topic of interest as it has potential applications in the field of optical, biomedical, and mechanical industries (Kharat et al. 2018). The various applications of ferrofluids are in shaft seals, vacuum chambers, computer disk drives, loudspeakers, etc. The detailed study on ferrofluids states the influence of the external magnetic field on Fe_3O_4 and $CoFe_2O_4$ nanoparticles present in ferrofluids (Kuraica et al. 2018). The $CoFe_2O_4$ nanoparticles were synthesized by the coprecipitation method and surface functionalized (coated) with starch. In this study, simple optical measurements resulted in confirmation of the selective spectral nature of Fe_3O_4 and $CoFe_2O_4$ nanoparticles, which was observed by means of switching on/off the external field. For the optical study, the spectral region of 650–670 nm was considered because significant changes in the intensity of transmitted light exist

in this spectral range. The results obtained by this study can be significant for laser treatment of the patients who are exposed to contrasting agents based on ferrite during MRI scans (Kuraica et al. 2018).

16.5.4 Magnetic Data Storage

Magnetic NPs with high magnetization, coercivity values (in few thousand Oe), and very high K_{eff} values have applications in magnetic data storage fields. The alloys made up of 3d metals (e.g., Fe, Co, and Ni) having large magnetic moments and 4d metals (e.g., Rh) with strong spin–orbit coupling give a high magnetic moment and anisotropy which is required in high-density magnetic storage media (Fromen et al. 2006). Similarly, the 3d–5d nanoalloys (e.g., Fe–Pt and Co–Pt) have applications in ultrahigh density magnetic storage media due to their high magnetic anisotropy with associated high magnetic susceptibility and coercivity values (Dalavi and Panda 2017).

16.5.5 MRI and Hyperthermia Applications

The superparamagnetic Co-based NPs are suitable for contrast agents in magnetic resonance imaging (MRI) due to their smaller size and good dispersion in the hematic flux. Co coated with carbanion materials shows stable superparamagnetic behavior due to surface protection by carbon (Kwong et al. 2010). Fe–Ni, Fe–Ni-Co, and Fe–Pt alloy NPs are utilized in MRI as potential contrast agents due to high magnetic or superparamagnetic properties, and low toxicity in living cells. Bigger size superparamagnetic NPs (30–40 nm) can be used for magnetic hyperthermia by multiple magnetic heating mechanisms. In hyperthermia therapy, the temperature in tumor cells is increased to 40–45 ºC under the alternating magnetic field leading to direct killing of cancer cells. Superparamagnetic NPs of iron-oxide (Fe_3O_4 or Fe_2O_3) coated with aminosilane, antibodies, PEG-phospholipids, or cyclic tripeptide of arginine-glycine-aspartic acid may be used for hyperthermia applications (Xie et al. 2014).

16.5.6 Catalysis and Electrocatalysis

Magnetic NPs have been used as catalysts for several reactions such as hydrogenation and gaseous reactions because of their high surface area, high reactivity, and magnetically separable. Further, alloy NPs are more active than monometallic NPs of the same metals because of the structural effect, i.e., core–shell or disordered structure, composition, and synergistic effects, arising from altered d-band

electronic structure (Schmid et al. 1991). Magnetic NPs coated with various functional entities such as OA, OlAm, PEG, PVP, carbon, and silica have more specific applications in catalysis. In addition to conventional catalysis, bimetallic alloy/core–shell NPs such as CoPt and Fe-Pt have been proven activities in the field of electrocatalysis. They have significant applications in phosphoric acid fuel cells, direct methanol fuel cells, H_2/O_2 evolution reactions, and O_2 reduction reactions (Dalavi et al. 2021).

16.6 Summary and Future Scope

This chapter specifically focused on surface functionalized cobalt-based nanomaterials, such as Co, Co–Fe alloys, Co–Ni alloys, Co–Pt alloys, and cobalt ferrite ($CoFe_2O_4$) based coated particles for potential applications. However, bottlenecks for applications in various fields are stability at the nano-scale, nontoxic synthesis methods, control of size, dispersion in an aqueous medium, biocompatible surfaces, etc. Therefore, we have described the synthesis of Co-based metal/alloy nanomaterials via aqueous/organic mediated chemical reduction routes using $NaBH_4$, $Li(Et)_3BH$ (superhydride), polyol as reducing agents and stabilized via coating the surface with various capping agents, i.e., PEG, PVP, oleic acid, oleyl amine, mesoporous silica, etc. The presence of cobalt is cytotoxic to the cells in its vicinity. Therefore, in this chapter pure and doped $CoFe_2O_4$-based coated magnetic materials coated with organic functionalization or biomaterials were described.

Based on literature reported results, crystal structure, phase purity, and crystallite sizes were explained by XRD studies. Particle sizes and surface morphology are studied from electron microscopy studies (SEM and TEM). Elemental composition studies can be performed from SEM–EDX. The surface structure of the coated particles can be studied from FTIR spectroscopy. Magnetic characterization using magnetic hysteresis (M vs. H) and temperature dependent magnetization (M vs. T) at low temperature was described. The highest M_s values were seen for hcp Co (162 emu/g) due to larger crystallites and chain-like structures whereas the low M_s value for fcc Co (29.7 emu/g) due to nano-size and surface effects. Similarly, the H_c value is higher for hcp Co (magnetically hard phase) and lower for fcc Co (magnetically soft phase). Magnetic properties of Fe–Ni–Co and Fe–Co alloys can be tailored with their compositions, nano-size, and surface effects, altered crystal anisotropies, disordered structure, and

spin canting at the surface of nanomaterials. Magnetic properties of Co–Ni@silica show enhancement in M_S value compare to Co–Ni alloy. These results are attributed to intergrain exchange interactions mediated by the silica matrix. M versus T plots for Fe–Co and Co–Ni alloys show magnetic irreversibility, and NPs are in the magnetically blocked state below 300 K which may be attributed to stronger dipolar interparticle magnetic interactions. Further, silica coating supports enhanced dipolar interactions in Co–Ni@silica.

The synthesis of various cobalt-based coated and uncoated metal oxide nanoparticles was summarized. The methods of synthesis include sol–gel autocombustion, coprecipitation, mixed hydroxides precipitation, and in-situ functionalization of oxide materials. For coated $Co_{0.37}Zn_{0.63}Fe_2O_4$ nanoparticles were synthesized by sol–gel autocombustion and then surface modification was carried out using chitosan. This surface modified $Co_{0.37}Zn_{0.63}Fe_2O_4$ was loaded with the drug and was studied for cancer treatment. Here, high drug loading affinity (86%) was observed. In another study, $CoFe_2O_4$ nanoparticles were synthesized via the coprecipitation method and were coated with oleic acid and oleic acid-conjugated polyethylene glycol. The in-vitro cytotoxicity studies were analyzed and it was established that OA-PEG coated $CoFe_2O_4$ nanoparticles extensively increased the cytocompatibility. The in-situ preparation of citric acid-coated $CoFe_2O_4$ nanoparticles was confirmed to have a 2.9 nm core size, high stability in aqueous solution, high surface charge density ($\zeta = -52$ mV), and high magnetization (45 emu/g). The synthesis of $Co_{(1-x)}Zn_xFe_2O_4$ nanodot functionalized by polyaniline (PANI) was carried out by in-situ polymerization. This study has confirmed the formation of highly crystalline products and pure-single-phase spinel structures. These results showed the nanostructure $Co_{0.5}Zn_{0.5}Fe_2O_4$/PANI has the highest efficiency for the photo-degradation of azo dyes.

The next important step is the structural and morphological characterizations of these synthesized cobalt-based uncoated and coated metal oxide nanoparticles. The X-ray diffraction studies confirmed the crystal structure and crystallite sizes. The correlation between crystallite sizes and experimental factors used in different methods of synthesis gives good insight into the significance of various aspects utilized in synthesis. For the hydrothermal method, varying crystallite size (3–11.4 nm) was obtained within the pH range of 8–10 and annealing temperature range (120–160 ºC) for different time intervals. Similar optimization studies using the above-mentioned

experimental parameters were carried out for $CoFe_2O_4$ nanoparticles synthesized by the EDTA/citrate complexing method. The morphology studies obtained from the results of SEM micrographs confirm the agglomerated and irregular shapes of the $CoFe_2O_4$ nanoparticles. Along with the morphology of the nanoparticles, particle size was also determined to be in the range of 7–28 nm as reported in one of the research studies. By using TEM analysis for chitosan coated $CoFe_2O_4$ nanoparticles, it was noted that the coated layers do not change crystallinity and crystallite sizes significantly. This proves that the properties occurring due to the core structural parameters in nanomaterials remain unaffected and any variation in materials properties can be due to the change in surface structure and inter-granular interactions in coated particles. The elemental composition is determined by EDS analysis using atomic % and weight % data of all the elements present in particular compositions such as $Co_{0.5}Ni_{0.5}Fe_2O_4$ nanoparticles.

For the purpose of specific applications of these cobalt-based coated and uncoated metal oxide nanoparticles, the structure–property correlation studies are important. Here, the review of room temperature and low temperature magnetic properties is summarized based on the M versus H plot and the obtained values of magnetic parameters such as M_s, $H_{c,}$ and M_r. Based on the coating material used such as biocompatible hydroxyapatite (HA), the HA-coated cobalt ferrite core–shell structures with 30% of HA gave reduced magnetizations compared with uncoated $CoFe_2O_4$ and fairly large coercivity values which were more suitable for hyperthermia applications. The low temperature magnetic studies help to analyze the low values of magneto-crystalline anisotropies shown by the magnetic oxides.

The applicability of these coated nanoparticles (NPs) in magnetic, catalysis, and biomedical field is possible due to their availability in nano-scale sizes (10–30 nm), high surface-to-volume ratios, controlled magnetic properties, biocompatibility, and capability of further surface functionalization. Hence, we are looking forward that coated Co-based nanomaterials being highlighted in various fields so that they can be put into practice in the near future. The variety of applications of these nanomaterials in the field of catalysis, magnetic data storage, biosensing, and biomedicine (drug delivery, hyperthermia applications, etc.) can be significant for the benefit and growth of mankind.

Acknowledgements
The authors acknowledge the financial support in part from the Birla Institute of Technology and Science, Pilani, Goa campus, India. We acknowledge DST, India, and CSIR, India for financial support during the execution of this work. Also, the authors acknowledge the valuable support including suggestions during these investigations from Dr. R. S. Ningthoujam, BARC, Dr. Manivel Raja, DMRL Hyderabad, Prof. G. Balaji, BITS Hyderabad and Prof. Sayan Bhattacharya, IISER Kolkata, India. Technical and scientific assistance in the laboratory received from Dr. Pragnya Paramita Mishra is also acknowledged. We acknowledge sophisticated instrumental facilities located at IIT Kanpur, BITS Pilani, Karunya University, Anna University, IIT Madras, and IIT Mumbai, India for data procurement.

Author Contributions
“The manuscript was written through the contributions of all authors. All authors have given approval to the final version of the manuscript.”

References

Ali, A., Shah, T., Ullah, R., Zhou, P., Guo, M., Ovais, M., Tan, Z., Rui, Y.: Front. Chem. **9**, 629054 (2021)
[PubMed][PubMedCentral]

Amiri, S., Shokrollahi, H.: Mater. Sci. Eng. C **33**(1), 1–8 (2013)

Andhare, D.D., Patade, S.R., Kounsalye, J.S., Jadhav, K.M.: Physica B Condens. Matter. **583**, 412051 (2020)

Anila, I., Lahiri, B.B., John, S.P., Mathew, M.J., Philip, J.: Ceram. Int. **49**, 15183–15199 (2023)

Ariga, K., Ji, Q., McShane, M.J., Lvov, Y.M., Vinu, A., Hill, J.P.: Chem. Mater. **24**(5), 728–737 (2012)

Baig, N., Kammakakam, I., Falath, W.: Mater. Adv. **2**(6), 1821–1871 (2021)

Balagna, C., Faga, M.G., Spriano, S.: Mater. Sci. Eng. C **32**(4), 887–895 (2012)

Ban, I., Stergar, J., Maver, U.: Nanotechnol. Rev. **7**(2), 187–207 (2018)

Bansmann, J., Kleibert, A., Getzlaff, M., Rodriguez, A.F., Nolting, F., Boeglin, C., Meiwes-Broer, K.H.: Phys. Status Solidi B **247**(5), 1152–1160 (2010)

Bao, Y., Krishnan, K.M.: J. Magn. Magn. Mater. **293**(1), 15–19 (2005)

Bean, C.P., Jacobs, I.S.: J. Appl. Phys. **31**(7), 1228–1230 (1960)

Bean, C.P., Livingston, U.D.: J. Appl. Phys. **30**(4), S120–S129 (1959)

Belhadj, H., Messaoudi, Y., Khelladi, M.R., Azizi, A.: Int. J. Hydrog. Energy **47**(46), 20129–20137 (2022)

Brush, S.G.: Rev. Mod. Phys. **39**(4), 883–893 (1967)

Chang, H., Kim, B.H., Lim, S.G., Baek, H., Park, J., Hyeon, T.: Inorg. Chem. **60**(7), 4261–4268 (2021)
[PubMed]

Charan, C., Shahi, V.K.: RSC Adv. **6**(64), 59457–59467 (2016)

Chen, Z.G., Tang, D.Y.: Bioprocess Biosyst. Eng. **30**, 243–249 (2007)
[PubMed]

Chen, G., Wang, Z., Wang, H., Zhao, X., Hu, J., Wang, S., Zhang, S.: Surf. Coat. Technol. **206**(15), 3386–3392 (2012)

Chen, Y., Fan, Z., Zhang, Z., Niu, W., Li, C., Yang, N., Chen, B., Zhang, H.: Chem. Rev. **118**(13), 6409–6455 (2018)
[PubMed]

Choppadandi, M., Parmar, K., Rao, K.S., Rao, K.H., Singh, A., Kumar, H., Guduru, A.T., Shard, A., Kapusetti, G.: Colloids Surf. B **222**, 113077 (2023)

Cullity, B.D.: Elements of X-Ray Diffraction. Addison-Wesley Publishing, MA (1956)

Cullity, B.D., Graham, C.D.: Introduction to Magnetic Materials, 2nd edn. Publisher, John Wiley and Sons, USA (2008)

Da, X., Li, R., Li, X., Lu, Y., Gu, F., Liu, Y.: Mater. Lett. **309**, 131357 (2022)

Dalavi, S.B., Panda, R.N.: Part. Sci. Technol. **33**(1), 97–101 (2015a)

Dalavi, S.B., Panda, R.N.: Trans. Indian Inst. Met. **68**, 253–257 (2015b)

Dalavi, S.B., Panda, R.N.: J. Magn. Magn. Mater. **374**, 411–416 (2015c)

Dalavi, S.B., Panda, R.N.: J. Mater. Res. **31**, 2430–2437 (2016)

Dalavi, S.B., Theerthagiri, J., Raja, M.M., Panda, R.N.: J. Magn. Magn. Mater. **344**, 30–34 (2013)

Dalavi, S.B., Raja, M.M., Panda, R.N.: New J. Chem. **39**, 9641–9649 (2015)

Dalavi, S.B., Raja, M.M., Panda, R.N.: J. Nanomater. Mol. Nanotechnol. **7**(6), 1000257 (2018)

Dalavi, S.B., Agarwal, S., Deshpande, P., Joshi, K., Prasad, B.L.V.: J. Phys. Chem. C **125**(14), 7611–7624 (2021)

Dalavi, S.B., Panda, R.N.: J. Magn. Magn. Mater. **428**, 306–312 (2017)

Danan, H., Herr, A., Meyer, A.J.: J. Appl. Phys. **39**(2), 669–670 (1968)

Das, S.B., Singh, R.K., Kumar, V., Kumar, N., Kumar, S.: Mater. Today: Proc. **46**, 6527–6533 (2021)

De, D., Upadhyay, P., Das, A., Ghosh, A., Adhikary, A., Goswami, M.M.: Colloids Surf. A Physicochem. Eng. Asp **627**, 127202 (2021)

de Medeiros, I.A., Lopes-Moriyama, A.L., de Souza, C.P.: Ceram. Int. **43**(5), 3962–3969 (2017)

Fromen, M.C., Morillo, J., Casanove, M.J., Lecante, P.: EPL **73**(6), 885 (2006)

Hamers, R.J.: Acc. Chem. Res. **50**(3), 633–637 (2017)
[PubMed]

Hassanzadeh-Tabrizi, S.A., Norbakhsh, H., Pournaja, R., Tayebi, M.: Ceram. Int. **47**, 18167–18176 (2021)

He, M., Chen, L., Yin, M., Xu, S., Liang, Z.: J. Mater. Res. Technol. **23**, 4396–4419 (2023)

Houshiar, M., Zebhi, F., Razi, Z.J., Alidoust, A., Askari, Z.: J. Magn. Magn. Mater. **371**, 43–48 (2014)

Hu, P., Kang, L., Chang, T., Yang, F., Wang, H., Zhang, Y., Yang, J., Wang, K.S., Du, J., Yang, Z.: J. Alloys Compd. **728**, 88–92 (2017)

Kanwar, R., Rathee, J., Salunke, D.B., Mehta, S.K.: ACS Omega **4**(5), 8804–8815 (2019)
[PubMed][PubMedCentral]

Kaur, M., McCloy, J.S., Jiang, W., Yao, Q., Qiang, Y.: J. Phys. Chem. C **116**(23), 12875–12885 (2012)

Kazi, S., Inamdar, S., Kamble, D., Tigote, R.: Mater Today: Proc **73**, 448–454 (2023)

Kharat, P.B., Somvanshi, S.B., Kounsalye, J.S., Deshmukh, S.S., Khirade, P.P., Jadhav, K.M.: AIP Conf. Proc. **1942**(1), 050044 (2018)

Kim, C.W., Kim, Y.H., Cha, H.G., Kwon, H.W., Kang, Y.S.: J. Phys. Chem. B **110**, 24418–24423 (2006)
[PubMed]

Kiran, V.S., Sumathi, S.: J. Magn. Magn. Mater. **421**, 113–119 (2017)

Kleitz, F., Choi, S.H., Ryoo.: Chem. Commun. **17**, 2136–2137 (2003)

Kneller, E.F., Luborsky, F.E.: J. Appl. Phys. **34**(3), 656–658 (1963)

Kolhatkar, A.G., Jamison, A.C., Litvinov, D., Willson, R.C., Lee, T.R.: Int. J. Mol. Sci. **14**(8), 15977–16009 (2013)
[PubMed][PubMedCentral]

Kudr, J., Haddad, Y., Richtera, L., Heger, Z., Cernak, M., Adam, V., Zitka, O.: Nanomaterials **7**(9), 243 (2017)
[PubMed][PubMedCentral]

Kumar, S., Verma, V., Walia, R.: AIP Adv. **11**, 015106 (2021)

Kuraica, M.M., Iskrenović, P., Perić, M., Krstić, I., Nikolić, A.S.: Chem. Pap. **72**, 1535–1542 (2018)

Kwong, H.Y., Wong, M.H., Leung, C.W., Wong, Y.W., Wong, K.H.: J. Appl. Phys. **108**(3), 034304 (2010)

Lakshmi, Y.K., Bharadwaj, S., Chanda, S., Reddy, C.V., Pola, S., Kumar, K.S.: Mater. Chem. Phys. **295**, 127172 (2023)

Langevin, P.: Ann. Chem. Phys. **8**, 70–127 (1905)

Leonel, L.V., Barbosa, J.B., Miquita, D.R., Oliveira, F.P., Fernandez-Outon, L.E., Oliveira, E.F., Ardisson, J.D.: Solid State Sci. **86**, 45–52 (2018)

Li, X., Hong, X.: Catal. Commun. **83**, 70–73 (2016)

Maaz, K., Karim, S., Mashiatullah, A., Liu, J., Hou, M.D., Sun, Y.M., Duan, J.L., Yao, H.J., Mo, D., Chen, Y.F.: Physica B Condens. Matter. **404**(21), 3947–3951 (2009)

Mirzadeh, E., Akhbari, K.: Cryst. Eng. Comm. **18**(39), 7410–7424 (2016)

Miyazaki, T., Kim, H.M., Miyaji, F., Kokubo, T., Nakamura, T.: Bioceramics **10**, 497 (1997)

Morrish, A.H.: Canted Antiferromagnetism: Hematite. Publisher, World Scientific Publishing, Singapore (1994)

Mund, H.S., Ahuja, B.L.: Mater. Res. Bull. **85**, 228–233 (2017)

Néel, L.: Ann. Geophys. **5**, 99–136 (1949)

Ningthoujam, R.S., Panda, R.N., Gajbhiye, N.S.: Mater. Chem. Phys. **134**(1), 377–381 (2012)

Ojha, V.H., Kant, K.M.: J. Phys. Chem. Solids **148**, 109655 (2021)

Ortiz, J.C., Cortés, D.A., Escobedo, J.C., Almanza, J.M., Muñiz, C.R., Luna, J.S., Rodríguez, N.A.: Mater. Lett. **65**(2), 329–332 (2011)

Ounacer, M., Essoumhi, A., Sajieddine, M., Razouk, A., Fnidiki, A., Richomme, F., Juraszek, J., Dubiel, S.M., Sahlaoui, M.: J. Phys. Chem. Solids **148**, 109687 (2021)

Panda, R.N., Shih, J.C., Chin, T.S.: J. Magn. Magn. Mater. **257**(1), 79–86 (2003)

Patta, G.R., Kumar, V.R., Ragavaiah, B.V., Veeraiah, N.: Appl. Phys. A **126**, 64 (2020)

Peng, K., Zhou, L., Hu, A., Tang, Y., Li, D.: Mater. Chem. Phys. **111**, 34–37 (2008)

Peng, D.L., Chen, Y., She, H., Katoh, R., Sumiyama, K.: J. Alloys Compd. **469**(1–2), 276–281 (2009)

Prestgard, M.C., Siegel, G., Ma, Q., Tiwari, A.: Appl. Phys. Lett. **103**(10), 102409 (2013)

Putra, A.R., Yulizar, Y., Ritawidya, R., Apriandanu, D.O., Juliyanto, S., Fikri, A., Surya, R.M.: Mater. Sci. Eng. B Solid State Mater. Adv. Technol. **286**, 116016 (2022)

Rana, G., Dhiman, P., Kumar, A., Vo, D.V., Sharma, G., Sharma, S., Naushad, M.: Chem. Eng. Res. Des. **175**, 182–208 (2021)

Reddy, N.R., Ramana, M.V., Rajitha, G., Rajagopal, E., Sivakumar, K.V., Murthy, V.R.: J. Magn. Magn. Mater. **292**, 159–163 (2005)

Sahu, B.N., Suresh, K.G., Venkataramani, N., Prasad, S., Krishnan, R.: AIP Adv. **8**, 056118 (2018)

Sajjia, M., Oubaha, M., Hasanuzzaman, M., Olabi, A.G.: Ceram. Int. **40**(1), 1147–1154 (2014)

Salunkhe, A.B., Khot, V.M., Ruso, J.M., Patil, S.I.: J. Magn. Magn. Mater. **419**, 533–542 (2016)

Schenck, J.F.: Med. Phys. **23**(6), 815–850 (1996)
[PubMed]

Schmid, G., Lehnert, A., Malm, J.O., Bovin, J.O.: Angew. Chem. Int. Ed. **30**(7), 874–876 (1991)

Shin, T.H., Choi, Y., Kim, S., Cheon, J.: Chem. Soc. Rev. **44**(14), 4501–4516 (2015)
[PubMed]

Soares, P.I., Laia, C.A., Carvalho, A., Pereira, L.C., Coutinho, J.T., Ferreira, I.M., Novo, C.M., Borges, J.P.: Appl. Surf. Sci. **383**, 240–247 (2016)

Srinivasan, S.Y., Paknikar, K.M., Bodas, D., Gajbhiye, V.: Nanomedicine (lond.) **13**(10), 1221–1238 (2018)
[PubMed]

Sun, C., Lee, J.S., Zhang, M.: Adv. Drug Deliv. Rev. **60**(11), 1252–1265 (2008)
[PubMed][PubMedCentral]

Tan, C., Cao, X., Wu, X.J., He, Q., Yang, J., Zhang, X., Chen, J., Zhao, W., Han, S., Nam, G.H., Sindoro, M., Zhang, H.: Chem. Rev. **117**(9), 6225–6331 (2017)
[PubMed]

Tartaj, P., del Puerto, M.M., Veintemillas-Verdaguer, S., Gonzalez-Carreno, T., Serna, C.J.: J. Phys. D **36**(13), R182–R197 (2003)

Tripathy, A., Nine, M.J., Silva, F.S.: Adv. Colloid Interface Sci. **290**, 102380 (2021)
[PubMed]

Ung, D., Viau, G., Ricolleau, C., Warmont, F., Gredin, P., Fiever, F.: Adv. Mater. **17**(3), 338–344 (2005)

Veitch, R.J., Ilmer, A., Lenz, W., Richter, V.: J. Magn. Magn. Mater. **193**(1–3), 279–283 (1999)

Wei, X.W., Zhu, G.X., Liu, Y.J., Ni, Y.H., Song, Y., Xu, Z.: Chem. Mater. **20**(19), 6248–6253 (2008)

Xie, J., Zhang, Y., Yan, C., Song, L., Wen, S., Zang, F., Chen, G., Ding, Q., Yan, C., Gu, N.: Biomaterials **35**(33), 9126–9136 (2014)
[PubMed]

Zhang, K., Holloway, T., Pradhan, A.K.: J. Magn. Magn. Mater. **323**(12), 1616–1622 (2011)

Zhu, K., Ju, Y., Xu, J., Yang, Z., Gao, S., Hou, Y.: Acc. Chem. Res. **51**(2), 404–413 (2018)
[PubMed]

Zhu, F., Zhang, J., Demidenko, O., Sun, H., Wang, C., Wang, J.: J. Non Cryst. Solids **600**, 122035 (2023)

© The Author(s), under exclusive license to Springer Nature Singapore Pte Ltd. 2024
R. S. Ningthoujam, A. K. Tyagi (eds.), *Handbook of Materials Science, Volume 2*, Indian Institute of Metals Series
https://doi.org/10.1007/978-981-97-4646-0_17

17. Probing Magnetism in Thin Films and Superlattices Using Polarized Neutron Reflectivity

Surendra Singh[1, 2] ✉ and Harsh Bhatt[1, 2]
(1) Solid State Physics Division, Bhabha Atomic Research Centre, Mumbai, 400085, India
(2) Homi Bhabha National Institute, Anushaktinagar, Mumbai, 400094, India

✉ **Surendra Singh**
Email: surendra@barc.gov.in

Keywords Thin films and multilayers – Interface magnetism – Polarized neutron reflectivity

17.1 Introduction

Magnetism, in the form of magnetite, a strong ferrimagnet at room temperature (RT), has been known to mankind for the last 2000 years, however, it was only over the last few centuries that many magnetic phenomena could be explained and understood. Phenomenological theories were developed by Curie and Wiess to explain the intrinsic magnetism in Fe, Co, and Ni elements. The basic understanding of magnetism for more complex materials

like strongly correlated electrons, e.g., $La_xSr_{1-x}MnO_3$, etc., which was the next hurdle in the field of magnetism, was also explained by developing simple models, but the electronic correlations in these systems are still far from being understood. Influence on different magnetic phenomena through interface effects in thin films, and nanostructured magnetic systems has become a trending topic of research as it may give rise to novel magnetic ground states and interactions. In addition, nanostructures with controlled geometry and dimensionality, especially, artificially engineered epitaxial superlattices/multilayers, provide an extraordinary platform to present and discover competing physical phenomena in functional materials, which cannot be realized with the individual constituents.

Nanoscale magnetism has been a subject of intense research, not only for technological development but also for understanding material science and fundamental physics. Magnetism in the nanoscale, especially magnetism across interfaces in thin films and multilayer systems, is an interdisciplinary subject, with researchers from both basic sciences and engineering equally interested in developing novel materials with improved functionalities (Basu and Singh 2022). In addition, the modern state-of-the-art thin film growth techniques (Chopra et al. 1983), such as magnetron sputtering, electron beam epitaxy, pulsed laser deposition (PLD), and molecular beam epitaxial (MBE), have paved the way for the creation of atomically precise ultrathin films and epitaxial interfaces of dissimilar materials. Such engineered structures exhibit exotic physical phenomena, particularly at the interfaces, thereby providing a rigorous test for established theories of magnetism.

In the last two decades, magnetic thin films and multilayers have attracted considerable attention and have emerged as an important area of magnetism research

because of their wide range of applications in micromagnetic devices such as inductors, transformers, valves, motors, sensors, and actuators; magnetic data storage devices such as hard discs, magnetic random-access memory, and perpendicular magnetic recording media. The most important feature of current-day magnetic thin films is the ability to deposit material with immense flexibility in the growth parameters, which allows control over individual atomic layers and enables the creation of artificial heterostructures with new and unique properties due to the possibility of tuning their crystallographic and morphological properties, especially at interfaces. The Nobel Prize in 2007 to Albert Fert and Peter Grũnberg is a high point in the field of magnetic thin films and multilayer (Prize and in Physics 2007), which gave birth to a new kind of memory chip based on Giant-Magneto-Resistance (GMR) phenomena (Baibich et al. 1988). The GMR and spin-valve effects in magnetic multilayers are being used successfully in magnetic data storage device applications. Spintronics is another emerging phenomenon that utilizes the spin degree of freedom of electrons and/or holes. It is an important field for the next-generation nanoelectronic devices with reduced power consumption and increased memory and processing capabilities. The associated field in spintronics also deals with the injection of spins across an interface between ferromagnetic (FM) metal/semiconductors as well as its interaction with their orbital moments and it is being studied extensively in thin film heterostructures at the moment (Žutić et al. 2004). In bulk systems, the search for spintronics material was started earlier and a particular geometrically frustrated non-collinear antiferromagnetic (AFM) order with chirality in bulk crystals was stabilized in the ground state, where chirality was determined by the Dzyaloshinskii-Moriya interaction (DMI) (Dzyaloshinsky 1958; Moriya 1960) due to a crystal structure with broken inversion symmetry (Yu et al. 2010a). The material choice

of bulk chiral magnets with a broken inversion symmetry is still limited. In magnetic multilayer systems, many emergent phenomena, such as perpendicular magnetic anisotropy (PMA) (Yang et al. 2011), DMI (Bode et al. 2007), Rashba effect (Manchon et al. 2015), spin Hall effect (SHE) (Sinova et al. 2015), spin-transfer torque (STT) (Ralph and Stiles 2008), and spin–orbit torque (SOT) (Brataas et al. 2012), have been studied for both fundamental research and applied perspectives. All these phenomena are closely associated with spin–orbit coupling (SOC), a phenomenon widely used for thin film-based spintronic applications.

Many other emerging phenomena have been studied in thin film and multilayer which include the discovery of a highly conducting (Ohtomo and Hwang 2004) and long-range magnetic (Brinkman et al. 2007; Fitzsimmons et al. 2011) interfacial layer at the interface of two oxide insulators, the coexistence of superconductivity and ferromagnetism in non-magnetic and insulating oxides (Dikin et al. 2011), magnetic dead-layers at the interface of magnetic and superconducting layers (Hoppler et al. 2009), tunneling of Cooper pairs across an interface from a superconductor to a ferromagnet through an insulator (Prajapat et al. 2016; Singh et al. 2020; Bhatt et al. 2022), the widely studied phenomena of exchange coupling/bias (EB) at the interface of an FM and an antiferromagnetic (AFM) films (Nogués and Schuller 1999). Emerging ferromagnetism is also observed at the interfaces between two AFM thin layers (He et al. 2012), paramagnetic and AFM layers (Grutter et al. 2013), FM and AFM (multiferroic) oxide films (Singh et al. 2014, 2015; Prajapat et al. 2020) and paramagnetic and FM layers (Bhatt et al. 2020), and these systems also showed unexpected EB. Apart from intriguing phenomena at the interfaces, it is also important to investigate and understand the effect of roughness, and alloying phase at the interfaces of

multilayers as these modifications at interfaces provide additional interactions and magnetic properties at interfaces in thin film and superlattices. Interface alloy formation in ultrathin films (tens of nanometers) via the annealing of heterostructures is another perspective route that allows the formation of alloys at a much lower temperature than the melting point of the individual elements. Figure 17.1 illustrates different phenomena in thin film heterostructures and multilayers and their use in technological applications.

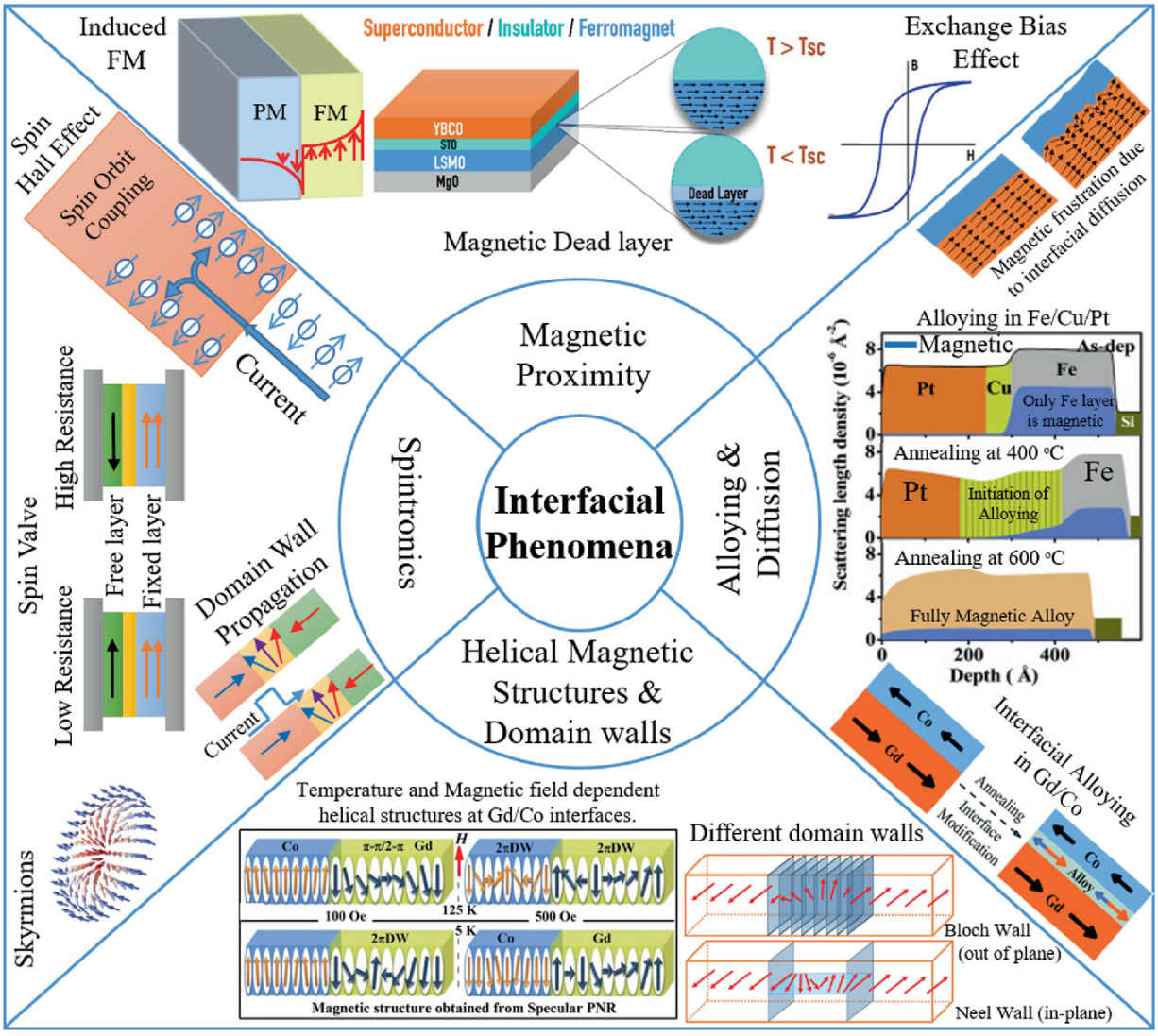

Fig. 17.1 Important phenomena studied in thin film heterostructures and superlattices and their technological applications

Since exotic functionality in thin film heterostructures is obtained from the interactions across interfaces, the intrinsic defects and disorders of the materials in combination with extrinsic effects, such as roughness, interdiffusion of atoms/ions, polar discontinuity, and alloying at the interfaces can induce novel emergent phenomena in magnetic heterostructures. In many cases, these interfacial effects dictate the overall physical properties of heterostructures and can even be used to control them. Thus, an understanding of the interfacial structure and properties is critically important and requires sensitive characterization tools to enable advanced investigation of emerging phenomena at interfaces (importantly buried interfaces) vis-à-vis their structure with inherent good resolution. The surface microstructure and magnetic properties of layered heterostructures can be probed using techniques such as magnetic-force-microscopy (MFM), magneto-optic-Kerr effect (MOKE), and scanning electron microscopy with polarization analysis (SEMPA). Scattering-based techniques such as X-ray reflectivity (XRR), X-ray resonant scattering, and polarized neutron reflectivity (PNR) are ideal for investigating the structure, electronic, and magnetic properties of the buried layers and interfaces. Among these, PNR has the distinct advantage of being highly sensitive to interfacial magnetism in addition to its ability to investigate depth-dependent structural and magnetic properties in thin film heterostructure and multilayer systems with sub-nanometer resolution.

This chapter focuses on how the interfaces in magnetic multilayers can hugely impact their physical properties and the importance of characterizing these interfaces precisely. First, we briefly discuss different techniques for the growth and characterization of thin films and multilayers. This is followed by a short description of some of the important techniques (mentioned above) available for the

characterization of magnetic thin films. Then we highlight the role and significance of PNR in the investigation and understanding of structure and magnetism in thin film heterostructures with the help of several recent examples. We have discussed the effect of parameters like annealing, phase transitions, and interface morphology on several emergent magnetic phenomena, such as the exchange bias (EB) effect, magnetization modulation, alloying, and induced ferromagnetism, in different thin film and multilayer systems. Next, we discuss some applications of magnetic thin films with respect to research as well as technological frontiers, emphasizing the importance of thin films and the extremely important techniques capable of probing interfaces. The chapter ends with a summary and future direction in this exciting field.

17.2 Growth of Thin Films and Superlattices

The physical properties of thin films and multilayer systems are highly sensitive to parameters such as layer thickness, density, and interface roughness which must be controlled precisely to explore and tune the desirable properties. Recent advances in thin film deposition technology have made possible the growth of high-quality thin films and multilayer systems with precise control over different growth parameters, atomic precision, and ample uniformity. Here, we briefly discuss some thin film deposition techniques that are routinely used by researchers to grow layered heterostructures with required parameters. In general, thin film deposition techniques can be categorized into two processes: (i) chemical vapor deposition (CVD) and (ii) physical vapor deposition (PVD). CVD follows a bottom-up approach that involves precursor materials undergoing a chemical reaction, either on the

substrate (probably heated) itself or in the solution, to form the desired material which may precipitate and get deposited on the substrate. Electrodeposition and electroplating are possibly the most widely exploited techniques of CVD. The metal–organic CVD technique is also used widely to grow epitaxial metal films on semiconductor/insulator surfaces in the semiconductor industry. The versatility for depositing thin films of a large variety of elements and compounds at relatively low temperatures and at atmospheric pressure makes CVD important for depositing films at a large scale. PVD, on the other hand, is a top-down approach of thin film deposition where a bulk target of the material to be deposited is physically ablated to produce the atomic or molecular vapors which are deposited as a thin film on a substrate. It offers greater control over growth parameters and is often carried out in a high vacuum or very controlled gas environment and thus, is preferred for the deposition of cleaner films with desirable thickness, density, and interface properties. Here we first describe the general process involved in a PVD technique and then talk about some specific PVD techniques used extensively for growing films in almost any lab dealing with research on thin films and multilayers.

A schematic of a typical PVD setup is shown in Fig. 17.2. Primarily there are three processes associated with any PVD technique:

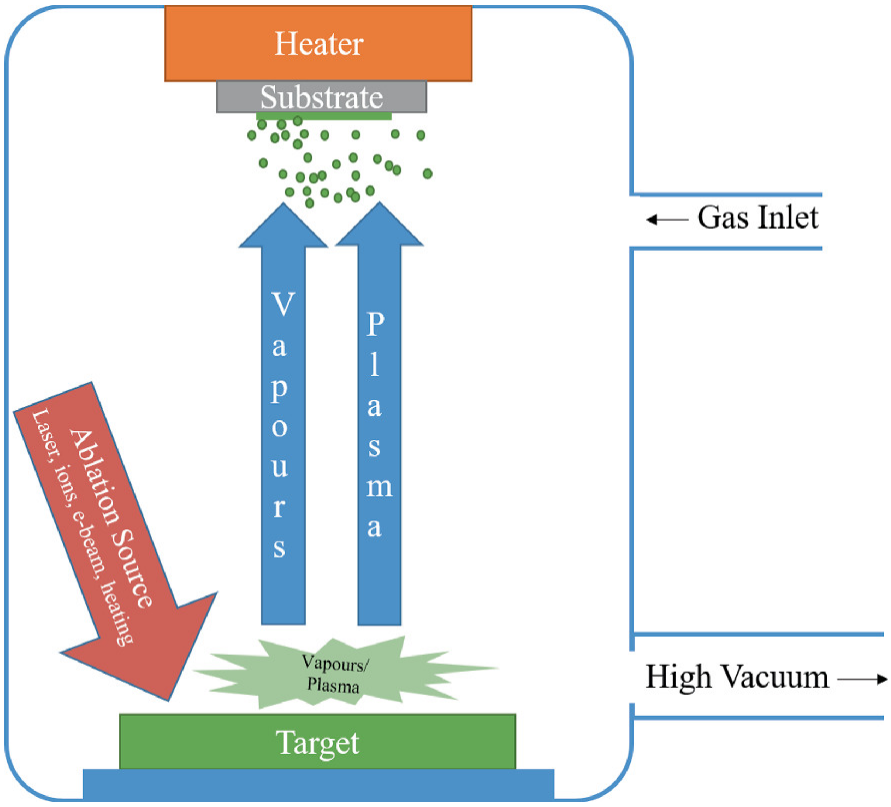

Fig. 17.2 A general schematic of physical vapor deposition and depending upon the technique one can use different means for heating/ablating the target material

(a) generation of atomic or molecular vapor/plasma at the target using a source of ablation such as ions, laser, and electron beam heat. This is the fundamental difference in different PVD techniques and hugely impacts the properties of the films deposited.

(b) transportation of the vapor/plasma to the substrate, which takes place either in a very high vacuum (pressure $<10^{-6}$ mbar) or a controlled gas environment. The chamber gas helps in directing the vapor/plasma toward the substrate and even helps maintain the stoichiometry of the films by adsorption. In any case, the deposition chamber in all the PVD techniques is initially evacuated to ensure a clean environment.

(c) deposition of the atoms/molecules on the substrate and possible heat-assisted redistribution to form the desired thin film.

Often several parameters, that strongly influence the growth of thin film heterostructures, such as type of deposition methods, partial pressure of chamber gas, deposition rates, and substrate temperature, are optimized before the deposition of thin film heterostructures, which are essential for controlling thermal stability, adhesion, stoichiometry, low porosity, etc. of the deposited films (Chopra et al. 1983). Hence choosing the right deposition technique for the thin film growth is crucial for controlling the properties of the system. Depending on the processes mentioned above, different PVD techniques like (i) Thermal Evaporation (ii) Sputtering, (iii) Molecular Beam Epitaxy (MBE), and (iv) Pulsed Laser Deposition (PLD), etc. have been developed. Different methods can be employed for the deposition of thin film heterostructures and multilayers depending on the availability and advantages of one technique over another (Chopra et al. 1983). We have briefly described these different deposition techniques below.

17.2.1 Thermal Evaporation

This technique is one of the oldest and relatively straightforward techniques used for depositing thin films and it is widely used in the laboratory and industry for depositing metal and metal alloys. In this technique, the target and the substrate are placed inside a vacuum (better than 10^{-5} torr) chamber and the target is heated close to or above its melting temperature by different means such as resistive heating and electron beam. The evaporated source (target) materials are condensed on a substrate. In the case of resistive heating, the entire target is heated and vapor is spread evenly throughout the chamber while in the case of

e-beam heating, the target is heated locally by the electron beam which behaves like a point source and generates a vapor plume of the target. Depending on the heating source this technique can be used to deposit films of different materials (metal, alloy, insulators) which also influences the growth quality of thin films. Deposition systems for both types of heating sources are almost similar and one may use more than one target with similar heating processes. The technique is most suitable for the deposition of films with simple stoichiometry such as a single element or simple alloys. However, co-evaporation for compound films and systematic deposition of periodic multilayers by using one target after another is possible.

17.2.2 Sputtering

In the case of sputtering, the source of ablation is an ionized plasma, (usually Ar) created by accelerating ions in the sputtering chamber using a high electric field. The positive gas ions (Ar^+) are accelerated toward the target in the same electric field and hit the target (treated as a cathode) with high kinetic energy, that ejects or sputters the atoms out of the target. Magnets are placed behind the target to enhance the ion density near the target. The magnetic field sets the electrons into helical paths along the field lines, enhancing the path length and time to reach the anode and meanwhile ionizing more gas leading to enhanced plasma density. The ejected atoms are transported to the substrate which is the anode in the system and get deposited. Since plasma can be large in volume, one can deposit larger-size films using this technique. Unlike thermal evaporation, sputtering does not require the melting of the target for deposition. There are three variants of the sputtering technique available and which are (i) Direct current (DC) sputtering: in this case, DC power is used for depositing conductive materials such

as metals and it is an effective and economical choice for growing the thin film of these materials; (ii) Radio frequency (RF) sputtering: in this case, a radio-frequency voltage (typically 13.5 MHz) is applied to create the plasma and it is an effective way to deposit insulating films; (iii) Reactive sputtering: In this case, reactive gas like oxygen and nitrogen together with the inert gas used for plasma generation is introduced into the sputtering chamber and thus mainly used for growing oxide and nitride films.

In comparison to the evaporation techniques, sputtering provides (a) high uniformity and density of deposited film, (b) better adhesion of atoms on the substrate, and (c) growth of a larger surface area film. Therefore, with a better understanding of different growth parameters, sputtering is one of the versatile techniques for preparing high-quality thin films and multilayers.

17.2.3 Molecular Beam Epitaxy (MBE)

In principle, this technique is a part of thermal evaporation as it follows a similar process for heating the target. MBE is considered to be the most controllable and highest purity deposition technique which is used for both research and commercial purposes. The technique is used for the growth of epitaxial films on a heated single crystal substrate under UHV conditions (10^{-8} torr to 10^{-12} torr). The term ‘epitaxy’ is derived from the Greek word ‘epi’ means ‘top’ and ‘taxis’ means ‘ordered’. It refers to the deposition of crystalline layers on top of the crystalline substrate. The evaporated molecular or atomic beam has thermal energy and it falls on the substrate atom (molecule) by atom (molecule), which makes the growth process much slower compared to other techniques. This is a special technique that can be used to grow precise ultrathin and epitaxial films along with atomically abrupt interfaces and a large number of epitaxial semiconductor layers are grown by this technique

preferably. These properties make this technique suitable for the fabrication of specialized semiconductor devices particularly those based on III–V materials.

17.2.4 Pulsed Laser Deposition (PLD)

In this case, a high-power pulsed laser beam (a KrF excimer laser) hits a target inside a PLD chamber and ablates the target. Excimer and solid-state lasers are popular choices for the PLD that offer a short pulse width (~20 nm) and high-energy density. The chamber after initial evacuation is generally filled with a gas (e.g., O_2, $N_{2,}$ etc.) suitable for the material to be deposited. The high-energy density locally ionized the target material to form plasma. This plasma travels in the form of a plume and deposits the target ions on the substrate. The dynamics of the plasma plume can be adjusted by controlling the partial pressure of the chamber gas. The ions on reaching the substrate recombine to form a thin film of the target material. The substrate holder generally has provision to heat the substrate, if required, which may assist the recombination of the ions and provide better crystallinity for the thin films thus formed. PLD offers great flexibility in terms of deposition parameters such as laser energy, pulse rate, substrate temperature, chamber gas, and pressure all of which impact the quality of the films grown. This technique is preferred for the deposition of compound films since the plasma generated in the process maintains the stoichiometry of the target compound. However, the spatial uniformity of the films grown by PLD is restricted to $10\ \text{mm} \times 10\ \text{mm}$, which makes it difficult to incorporate in commercial setups. A large number of functional materials like oxide ferroelectrics and high-temperature superconductors are routinely deposited using this technique. Especially in compounds, where oxygen

stoichiometry is an important issue like oxide superconductors, this is a preferred technique.

17.3 Different Techniques for Probing Magnetism in Thin Films and Superlattices

Magnetic thin film heterostructures and multilayers have played increasingly important parts in all multidisciplinary areas, e.g., magnetic recording devices and advanced electronics, spintronics, and sensors in automotive, health care, and security applications. Interfacial exchange interaction and coupling as well as the structure and morphology of interfaces between different layers in magnetic heterostructures play a crucial role in determining overall properties. Therefore, properly characterizing and understanding the interfacial coupling and interfacial magnetization configuration in magnetic thin film heterostructures and multilayers are essential in guiding material design for their applications. Here we discussed a few techniques that are mostly used for the characterization of thin film heterostructures and multilayers including the surfaces and interfaces of thin films and superlattices.

17.3.1 SEMPA

The SEMPA is an advanced imaging technique that provides detailed information about the magnetic microstructure of thin films at the nanoscale. It is an extension of a regular scanning electron microscope (SEM) and works on the principle of detecting the secondary electrons, carrying spin-polarization information, emitted from a magnetic sample in an SEM experiment, that can be used to quantitatively estimate the magnetization of the samples. The spin-polarization of these secondaries reflects

the net spin density in a material which is correlated to its magnetization. By polarization analyses of the secondary electrons, SEMPA can provide direct images of the direction as well as relative magnetization with high spatial resolution up to 10 nm.

The magnetic contrast generated in the SEMPA image is because of the spin-polarization of the secondary electrons which probes the spin component of the magnetization. Although the polarization of spin is proportional to the magnetization of materials, the proportionality constant is difficult to determine owing to several factors such as energy dependence of polarization in a sample and accepted energy ranges of the polarization analyzer. Hence, SEMPA generally gives the relative and not the absolute magnitude of the magnetization. However, the electrons retain their polarization during the emission process, hence, polarizations of the emitted secondary electrons can precisely determine the direction of magnetization in samples.

The essential components of a SEMPA setup include (i) An SEM column to generate an electron beam and raster it over the sample, (ii) electron optics including polarization detectors and analyzers to collect the secondary electrons and measure their polarizations, (iii) An ultrahigh vacuum chamber (10^{-7} mbar) to avoid surface contamination and lastly (iv) a data acquisition system to record, store and display the collected data and its output. The most significant element of any SEMPA apparatus is the spin-polarization analyzer. The most commonly employed analyzers use low energy diffused scattering from amorphous Au films and rely on the asymmetry of the spin–orbit scattering of different polarization. A detailed discussion about the SEMPA setup and its working can be found in several reviews (Unguris 2001; Oepen and Hopster 2005).

High surface sensitivity, the possibility of in-situ sample preparation, and the natural ability to separate topographic and magnetic contrast make SEMPA especially well-suited for quantitative mapping of magnetization direction in thin films and magnetic surfaces. Due to its large depth of focus, it can also be applied to image magnetic structures of rough samples. It has found application in material research to study spin reorientation transitions, magnetic exchange coupling in multilayer systems, and patterned magnetic structures for spintronics applications. In some cases, SEMPA combined with ion milling can also be used for magnetic depth profiling in weakly coupled magnetic multilayers. High spatial resolution, large depth of field, and ease of operation make SEMPA a very flexible technique for studying magnetic microstructures such as magnetic domains, domain walls, and spin structures. Combined with complementary techniques such as reflection high-energy electron diffraction (RHEED), scanning tunneling microscopy (STM), and Auger spectroscopy, SEMPA can provide insights into the correlation of magnetic structure with atomic-scale chemical structure.

17.3.2 MFM

MFM is a type of scanning probe microscopy that uses magnetostatic interactions between a tip and a flat surface to image its magnetic domains at the nanoscale. MFM offers a resolution of up to 10 nm depending upon the sharpness of the probe. The geometry offered by thin films is flat surfaces with nanoscale pattering or roughness which makes them a particularly well-suited candidate for MFM imaging. MFM can be considered a derivative of atomic force microscopy and uses a sharp magnetic tip attached at the end of a cantilever that scans the stray magnetic field at the surface. The cantilever deflection is monitored through a laser interferometry-based optical

feedback system to obtain the magnetic morphology of a thin film (Fig. 17.3). Since the deflections are small, the cantilever can be modeled effectively as a damped harmonic oscillator having a spring constant and resonant frequency typically of the order of hundreds of kilohertz. The image of the magnetic stray field is obtained by slow raster scanning the cantilever over the sample surface. Typical scan areas vary from a few to 200 μm with scan timing ranging from 5 to 30 min. The MFM probes are generally prepared from the conventional silicon or carbon micromachined tip/cantilever assembly by sputtering it with a thin film of FM materials like cobalt–nickel or iron. Typical probe dimensions are a cantilever length of 200 μm, a diameter of 50 nm, and a tip length of 4 μm. The typical forces measured in MFM are of the order of 30 pN leading to the cantilever deflection of the order of a few nm. An extensive discussion about various aspects of MFM is described in the reference (Magnetic et al. 2017).

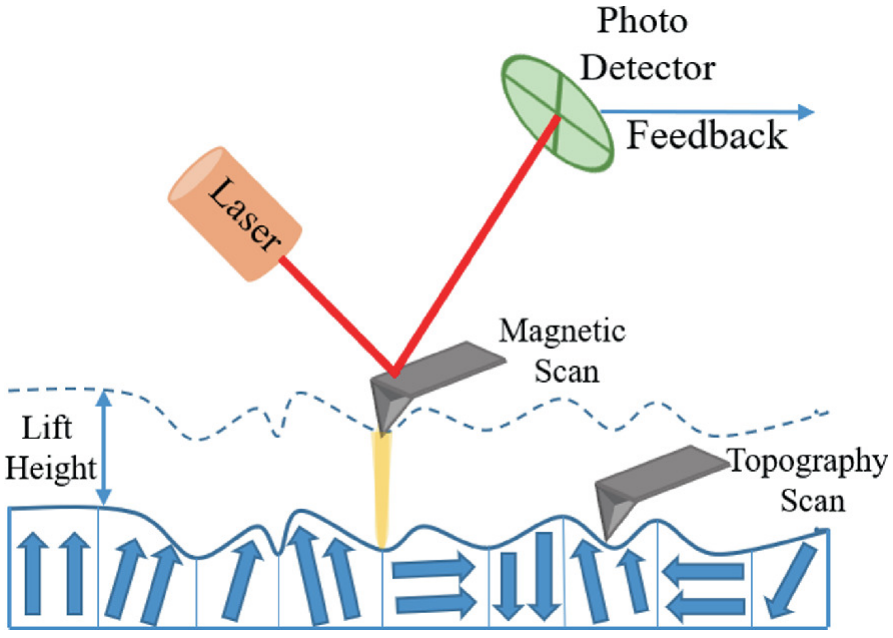

Fig. 17.3 Schematic of the working principle of the MFM technique to investigate the surface magnetic topography. The magnetic tip performs two raster scans, one close to the surface (5–10 nm) which gives topography

information, and the other at a prescribed height (~30 nm) to get magnetic information that can be deconvoluted from the topography

Like the operating principle of atomic force microscopy, an MFM is operated in amplitude modulation mode (tapping mode). In this mode, an image of a magnetic stray field emancipating from the sample is obtained by oscillating the magnetic tip at the cantilever resonance frequency and raster scanning it over the surface of the sample. The tips do not touch the surface and are usually kept at a distance of about 30 nm where they can interact with the magnetic field. The gradients in the magnetic forces near the surface modify the effective spring constant of the cantilever changing its resonant frequency and phase of the oscillation. An attractive magnetic force gradient causes the lowering of resonant frequency and a decrease in the phase shift leading to dark contrast, while the repulsive force gradient has an opposite effect on resonant frequency and phase shift, respectively, and gives a bright contrast. The MFM maps the frequency, amplitude, and phase of the cantilever as it scans the surface at an optimized height to create an image of magnetic morphology at the surface.

The tip-to-sample distance is a critical parameter in MFM image optimization. If the distance is too short it would lead to the convolution of tomographic effects into the MFM signal which might complicate its interpretation significantly. A simple solution is to increase the tip-surface distance to ~100 nm, but that would severely limit the lateral resolution to ~100 nm. The remedy for this is the dual pass setup or the lift mode, where the cantilever scans the surface twice (Fig. 17.3). During the first scan, the tip is in contact with the surface as it maps out the topography in amplitude mode with feedback switched off. In the second scan, the tip is lifted to a prescribed height, decided by the first scan (typically a few tens of nm) above the surface follows the topography contours, and maintains a

constant tip-to-surface distance. Hence, in the double scan mode, both the topography and magnetic images are acquired allowing an effective method to deconvolute the surface topography from the magnetic information.

MFM has evolved as a versatile technique for micromagnetic imaging in a variety of magnetic materials. It is used to study technologically important magnetic materials such as magnetic and magneto-optic recording media. The advantage of MFM is that it can image the magnetic domains through non-magnetic overcoats applied to data storage devices. MFM is also extensively used in magnetic material research to study interesting magnetic systems such as phase-separated manganites having FM domains, ultrathin metallic films exhibiting spin reorientation, and domain wall pinning by grain boundaries (Frisbie and Meyers 2003).

17.3.3 MOKE

The magneto-optic Kerr effect (MOKE) is a widely used technique for studying the magnetic properties of thin films due to its high sensitivity, non-destructive nature, and ability to provide detailed information about magnetic properties (Kuch et al. 2015). MOKE measures the change in light polarization reflected off a magnetized thin film. When polarized light is incident on a magnetic thin film, the reflected light is elliptically polarized due to the interaction between the light and the magnetic field. The degree of ellipticity depends on the magnetization direction in films, and the angle between the plane of incidence and the magnetization direction. By analyzing the polarization of the reflected light, various magnetic properties of the thin film, including its magnetization direction, anisotropy, coercivity, magnetic domain structure, and magnetization dynamics can be determined.

The Kerr effect in a media is dictated by the dielectric tensor of a media which depends on the anisotropy of the

material and its response to the magnetic field. When polarized light propagates through a magnetic media, the right and left circularly polarized components of light experience different refractive indexes. Since the reflection coefficients depend on the refractive index, the two polarizations are reflected with different reflectivity say r^+ and r^-. When r^+ and r^- have a phase difference, the resultant reflected beam exhibits a rotation in polarization and if the magnitudes of $|r^+|$ and $|r^-|$ are different then some degree of ellipticity is introduced in the reflected beam (Kuch et al. 2015).

The Kerr effect is quite general and can be observed with the plane of incident light oriented arbitrarily to the direction of magnetization. However, three different geometries are distinguished: (i) Polar MOKE: When sample magnetization is perpendicular to the plane of the surface, (ii) Longitudinal MOKE: When sample magnetization is parallel to both the plane of the surface and the plane of incidence and (iii) Transverse MOKE: When sample magnetization is parallel to the plane of the surface but perpendicular to the plane of incidence. Both longitude and transverse MOKE are about an order of magnitude weaker than the polar MOKE. In a typical MOKE setup, (Fig. 17.4) focused optical laser first passes through a polarizer filter with an option to switch the polarization to linear or circular based on geometry. The laser also passes through a photoelastic material (PEM) device which allows measurement of the Kerr ellipticity of the samples. The laser is then reflected off the surface of a sample placed in a magnetic field which causes a change in its polarization direction and ellipticity. The reflected light is then passed through an analyzer filter which converts the changes in polarization into a change in visible intensity. In general, the spatial resolution of MOKE is limited by the diffraction of light and the size of the focused laser spot and depends

on factors such as the wavelength of the light used, the numerical aperture of the objective lens, the quality of the optics, and also the thickness and homogeneity of the thin film being studied.

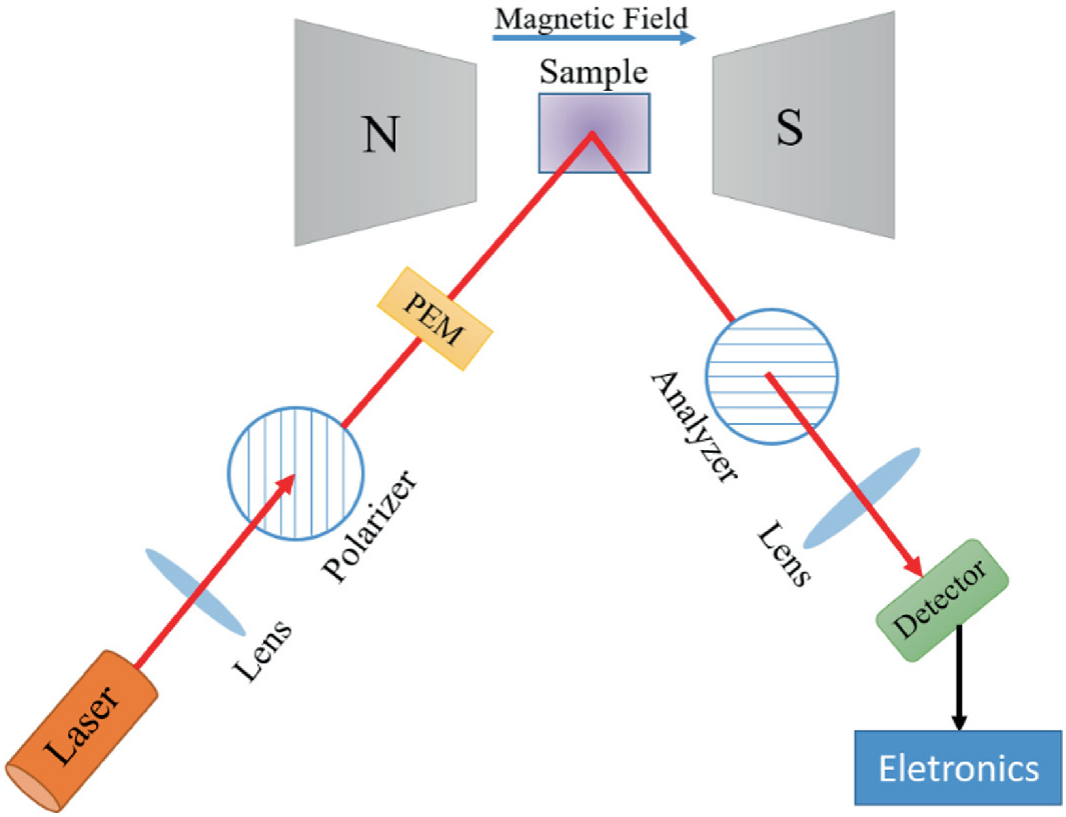

Fig. 17.4 Schematic of MOKE setup with different components. Changes in the intensity of polarized laser light reflected off the sample surface, give information regarding its magnetism

17.3.4 Resonant X-ray Scattering

Resonant magnetic scattering using polarized X-rays offers a unique probe that can provide element, valance, and site-specific electronic and magnetic structure with nanoscopic resolution. The magnetic behavior of the transition metals is dictated by the electrons in *d* orbitals which can be explored by X-ray absorption at the L-edge of the particular elements involved. The resonant X-ray scattering involves the excitation of core electrons (*p* orbitals in the case of transition metals) into the vacant *d* orbitals near the Fermi

level. The possibility to tune X-ray energy at synchrotron sources to core-level electrons has given rise to two popular techniques namely X-ray absorption (XAS) and X-ray resonant magnetic scattering (Laan 2008).

The XAS spectra show huge polarization sensitivity for electric dipole-allowed transitions of electrons from the core level to the valance level that are magnetically polarized. Hence, the difference in absorption level of X-rays with different polarizations shows a different level of absorption upon passing through a magnetic material. This phenomenon is referred to as dichroism and the difference in X-ray absorption levels can provide information about the magnetic properties. The use of either linearly or circularly polarized X-rays is made in this technique called X-ray magnetic linear and circular dichroism (XMLD and XMCD, respectively) that measures the change in the helicity of these polarized X-rays by a magnetic material in XAS spectra.

Meanwhile, the X-Ray Resonant Magnetic Scattering (XRMS) (Singh et al. 2016) is a resonant MOKE in the X-ray regime. The excitation of a core electron may resonant transition causing the formation of a core hole which is subsequently followed by an electron transition from a higher level to the core. This electronic transition may further result either in the emission of an Auger electron or a fluorescence photon. Accordingly, the XRMS measurement can be performed in two modes (i) Total electron yield (TEY) and (ii) Fluorescence yield (FY). In TEY the total drain currents due to the Auger electrons and the escaping photoelectrons are measured which is sensitive only to surfaces as the electrons from bulk are not able to reach the detectors and depths of only up to a few nm can be probed. In FY the intensity of emitted photos is measured and hence contributions from buried interfaces and layers up to a few hundred nm depths can be obtained.

The spin–orbit interaction of the *2p* core–shell electrons gives rise to two primary peaks in the XAS spectra of transition metals, and the sum of the intensities of these peaks is directly proportional to the number of vacant*3d*orbitals. Hence, the valance state of an element can be easily probed using this technique. The angular momentum of circularly polarized X-rays can be changed to the photoelectrons during the emission process and even to the spin utilizing the spin–orbit coupling interaction. The spin-polarization at $p_{3/2}$ (L_3) and $p_{1/2}$ (L_2) levels is opposite because of the opposite spin–orbit coupling. Hence, the difference in absorption signals for the right and left circularly polarized X-ray gives information regarding the magnetism in the sample. The sum of these signals provides information regarding the electronic environment surrounding the *3d* orbitals in the transition metals.

17.3.5 Polarized Neutron Reflectivity

Polarized neutron reflectometry (PNR) is a unique non-contact and non-destructive technique to investigate magnetic properties and interfacial effects in thin film heterostructures and multilayer superlattices with sub-nanometre resolution. The neutron refractive index for most of the materials is slightly less than 1, which allows total reflection at grazing angles. Neutrons also carry an intrinsic magnetic moment of $-1.91\ \mu_N$ and can be polarized either parallel (spin up, +) or antiparallel (spin down, −) with respect to an applied magnetic field. The refractive index of neutrons for magnetic materials is different for these two polarizations which makes PNR inherently sensitive to magnetism. Hence, neutrons interact with both nuclei and magnetization (due to unpaired electrons) and undergo reflection at interfaces separating different nuclear or magnetic media. This allows PNR to simultaneously probe both depth-dependent

chemical and magnetic structures and also makes it a highly sensitive tool to explore interfacial phenomena such as emergent magnetism, diffusion, and alloying. A detailed discussion of various theoretical as well as experimental aspects of PNR is provided in references (Basu and Singh 2022, 2006; Singh et al. 2015, 2018).

In contrast to other techniques such as superconducting quantum interference device (SQUID) and vibrating sample magnetometer (VSM) which give only an average picture of magnetism in the sample (including the substrate), PNR can provide an entire magnetization profile along the depth of heterostructures and efficiently explore the contribution of any emergent interfacial magnetic effects while completely avoiding any substrate contribution. Other techniques like SEMPA, MOKE, and XRMS use the focused beams of electrons and electromagnetic waves as probes that have a very short penetration depth, and hence are only surface sensitive and give very local information. However, neutrons have a very high penetration depth due to weak interaction with matter making PNR an excellent technique to study magnetism in buried layers that are laterally averaged in-plane of the film. Weak interaction of neutrons with most of the materials also assists in implementing sophisticated sample environments such as low temperature, magnetic and electric field, etc. for different PNR experiments.

A specular (angle of incidence = angle of reflection) PNR experiment on a multilayer system can give parameters such as density, thickness, interface, and surface roughness as well as the magnetization profile for each layer. Neutrons with both spin up and spin down polarizations are incident on thin film heterostructure at a grazing angle of incidence and the corresponding reflectivity is recorded as a function of wave vector transfer, Q (= $\frac{4\pi}{\lambda} sin\theta$, where θ is the angle of incidence and

λ is the wavelength of the neutron). Experimentally Q can be varied by either changing θ (adopted at continuous beam sources with monochromatic λ, such as nuclear reactors) or by using a white neutron source consisting of multiple wavelengths (adopted mostly in time of flight experiments using a pulsed beam from neutron spallation source). A schematic of a typical PNR experiment is shown in Fig. 17.5. Neutrons with different polarizations (±) feel the same nuclear-scattering potential but opposite magnetic potential giving rise to spin-dependent reflectivities $R^{\pm}(Q)$. Figure 17.5 illustrates the different components of a PNR instrument. Unpolarized neutrons from a neutron source (either a continuous reactor or pulsed spallation source) are polarized using a supermirror polarizer. The spin of the polarized (spin up, R^{+}) neutron can be flipped (spin down, R^{-}) by switching on the electric current (magnetic field) in the flipper, which works on the principle of Larmor precession. Polarized neutrons fall on the thin film or superlattice sample at a grazing incidence and the reflected neutron is then captured in a neutron detector. For collecting neutrons with different polarization an additional flipper and an analyzer (a supermirror, the same as a polarizer) are placed between the sample table and the detector. Collecting spin-dependent PNR with spin analysis [non spin-flip (R^{++} and R^{--}) and spin-flip (R^{+-} and R^{-+})] of reflected neutrons from the magnetic thin film heterostructure, one can reveal the vector magnetization (magnitude as well as direction) depth profile of the sample (Basu and Singh 2022; Singh et al. 2018).

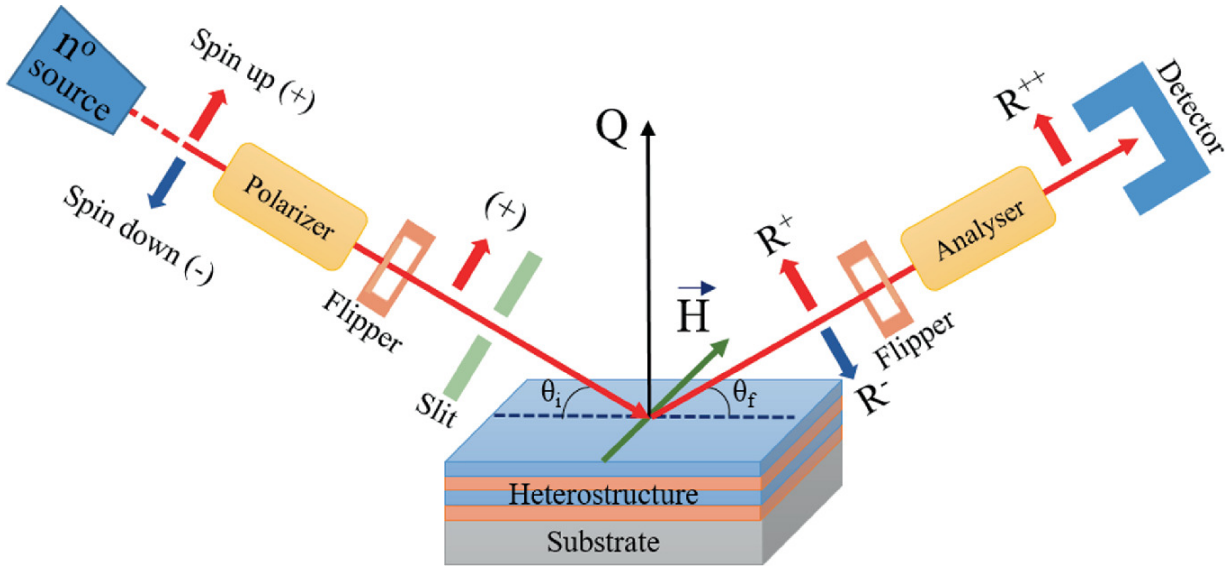

Fig. 17.5 Schematic of a typical PNR instrument with polarization analysis, which measures the spin-dependent reflectivities, i.e., Non-spin-flip (R^{++} and R^{+-}) and spin-flip ($R^{+-}$and R^{-+}). Different components are marked in the schematic

In general, the specular reflectivity normal to a smooth surface is proportional to the square of the Fourier transform of the scattering length density (SLD) depth profile, ρ(z) averaged laterally in the plane of the film. In the case of PNR, the SLD ρ(z) comprises two components, with the first being the nuclear part (NSLD) and the second being the magnetic (MSLD) part (Singh et al. 2018). The NSLD is invariant to the neutron spin, but MSLD changes its direction dependent on the neutron spin. Hence the total SLD is also spin-dependent, such that $\rho^{\pm}(z) = \rho_n(z) \pm \rho_m(z) = \rho_n(z) \pm CM(z)$, where $C = 2.9109 \times 10^{-9}$ Å^{-2} cm^3/emu, and M(z) is the magnetization (emu/cm^3) depth profile. Thus, by measuring spin-dependent reflectivities R$^+$(Q) and R$^-$(Q), both NSLD ($\rho_n(z)$) and MSLD ($\rho_m(z)$) [or $M(z)$] can be obtained separately. The difference between R$^+$(Q) and R$^-$(Q), gives a quantitative estimate of the magnetization ($M(z)$) depth profile in magnetic heterostructures. In addition to the magnitude of the magnetization, PNR measurements with

spin-polarization analysis provide information about the projection of the net magnetization vector (depth-dependent magnetic structure) onto the film plane. The reflectivity data obtained from a PNR experiment is fitted using the dynamical formalism of Parratt and the parameters of the model are adjusted for the goodness of fit. PNR is a versatile technique that can be used to gain insights into different interfacial phenomena in a variety of systems, such as interfacial magnetic modulation in FM/I/SC heterostructures, emergent ferromagnetism, and EB effect in FM/PM heterostructures and helical magnetism in rare-earth/transition metallic multilayers. Some of these systems are discussed in the next section which highlights the significance of PNR in the study of interfacial phenomena in magnetic multilayer systems.

17.4 Investigation of Emerging Interface Magnetization by Polarized Neutron Reflectivity

The surfaces and interfaces in thin film and magnetic multilayer systems induce intriguing phenomena influencing the magnetic properties of these systems. In addition to the finite thickness of thin films, these phenomena may be attributed to interfacial effects such as symmetry breaking, loss of coordination number, atomic and electronic reconstructions, exchange interaction, and proximity effects. These effects are intrinsic in the heterostructure and multilayer systems and occur even at ideal and defect-free interfaces. Lattice mismatch and the consequent epitaxial strain at the interfaces in heterostructures and multilayers can also induce defects that are intrinsic to the heterostructure. The intrinsic defects and disorders in combination with extrinsic effects in magnetic films such as interdiffusion, roughness, and

alloying at interfaces can induce and even control, novel emergent phenomena in magnetic heterostructures. To induce additional magnetic coupling at interfaces which is responsible for intriguing properties, annealing of the thin films and multilayers is a widely used technique in this field that may modify the interface morphology (roughness, interdiffusion, intermixing, etc.) and/or induce alloying at the interfaces. The biggest challenge in investigating interfacial phenomena is that these are confined to a very small volume close to the interface. Moreover, it is difficult to distinguish the intrinsic effects from those caused due to extrinsic factors such as defects and interface roughness. Thus, sensitive characterization tools are required to empower advanced investigation of emerging phenomena at interfaces (importantly buried interfaces) vis-à-vis their structure with inherent good depth resolution. As mentioned earlier PNR is a non-destructive technique that provides layer-resolved vector magnetometry in the entire thickness of the multilayer and more importantly, can resolve the magnetic state as well as coupling across buried interfaces. Here we will provide a few studies related to the emergent magnetic properties of interfaces where the PNR technique has played an important role.

17.4.1 Emerging Phenomena at Complex Oxide Interfaces

In complex transition metal perovskite oxides having a general formula of ABO_3, A site is occupied by a lanthanide cation, an alkali earth cation, or even a stoichiometric combination of both, while the B site is commonly a transition metal cation. These cations are bonded to oxygen anions through a framework of ionic bonds to form an oxygen octahedral, which is very important for some of the remarkable properties observed in these materials. The oxygen anion creates the possibility of intra- and inter-

atomic exchange interactions by acting as a bridge between the magnetic transition metal elements and contributes constructively to different functionalities at interfaces. Figure 17.6 shows various heterostructures with a combination of materials having different magnetic properties which exhibited unexpected interfacial properties and were investigated primarily using the PNR technique. Novel magnetic orders and emergent coupling at the interface of the heterostructure or multilayer may arise, e.g., (a) two AFM oxide layers giving rise to an FM interface (Santos et al. 2011; Aguiar et al. 2015) (Fig. 17.6a, b) an FM interface for heterostructure comprising paramagnetic metal and an AFM insulator (He et al. 2012; Grutter et al. 2013; Hoffman et al. 2013) (Fig. 17.6b) and enhanced interfacial magnetization at an interface of FM with PM/AFM/TI (He et al. 2012; Grutter et al. 2013; Hoffman et al. 2013) (Fig. 17.6c), etc. Macroscopic magnetometry combined with resonant x-ray magnetic scattering experiments has revealed the FM phase at the interface in $CaMnO_3$ (CMO)/$CaRuO_3$ (CRO) superlattices (He et al. 2012), where CMO is an AFM insulator and CRO is a metallic paramagnet.

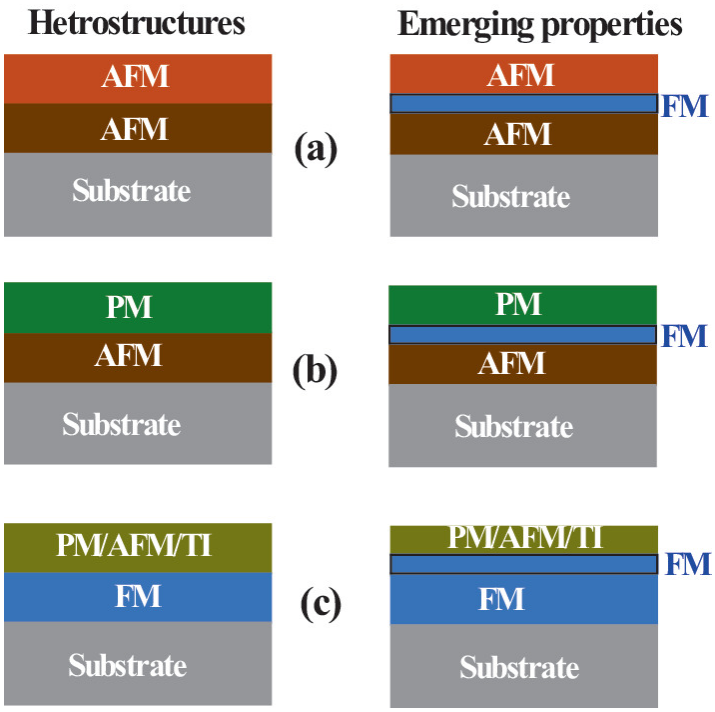

Fig. 17.6 Different heterostructures with a combination of ferromagnetic (FM) and other non-FM materials and associated emergent interfacial phenomena. Heterostructures comprising of (**a**) two antiferromagnetic (AFM) materials, (**b**) an AFM and a paramagnetic (PM), and (**c**) an FM and one of PM/AFM/topological insulator (TI) systems showing emergent FM at the interface

An unexpected interfacial magnetization limited to a single unit cell of CMO and EB effect was also later observed for CMO/CRO superlattice using the depth sensitivity of the PNR (He et al. 2012). In another study, the existence of an interfacial FM phase between a paramagnetic metal $LaNiO_3$ (LNO) and AFM CMO was reported (Grutter et al. 2013) using PNR measurements and was attributed to charge transfer at interfaces. Several enthralling interfacial phenomena have also been observed in heterostructures involving oxide PM and FM, topological insulator (TI) and FM and AFM and FM (Fig. 17.6c), such as $La_{0.67}Sr_{0.33}MnO_3$ (LSMO)/$BiFeO_3$ (BFO) (Singh et al. 2014; Prajapat et al. 2020) and LSMO/LNO (Bhatt et al. 2020), due to competing interactions among different degree of freedom such as orbital, lattice, spin and charge.

Theoretical calculations have suggested weak FM (~0.03 μB) in BFO as a result of canting of the AFM structure in LSMO/BFO heterostructures. PNR investigation (Singh et al. 2014, 2015; Prajapat et al. 2020) on BFO/LSMO heterostructure suggest the emergence of magnetic interfacial layers in BFO with a thickness of ~25–35 Å with the magnetization of ~100 emu/cc. In addition, PNR studies have suggested the presence of different magnetic couplings: FM and AFM in this system (Prajapat et al. 2020). Different magnetic coupling of the layers across interfaces might be a result of different polar terminations of the oxide layers. Low-temperature PNR measurements on PM/FM system of LNO/LSMO heterostructures grown on MgO (001) substrate, discovered an unexpected EB effect, which was attributed to the emergence of a thin FM layer in LNO with thickness ≈22–35 Å (≈6–9 unit cell) and magnetization ≈ 80 emu/cc near the LNO/LSMO interface for $T < 100$ K (Bhatt et al. 2020).

17.4.2 Interface Morphology-Driven Magnetization in Gd/Co Multilayer

Rare earth (RE)–transition metal (TM) heterostructures, viz., Gd–Fe, Gd–Co, etc., are known to exhibit several magnetic structures at different magnetic fields and temperatures because of the strong antiferromagnetic (AF) interaction at interfaces. The interface structure and morphology play a crucial role in deciding the magnetic configuration in Gd/TM multilayers that have been studied using a combination of characterization techniques. The interface morphology of such thin films and multilayers can be artificially varied either during the growth process by the adoption of different techniques/ growth conditions or by post-deposition processes such as heat treatment or mechanical strain. Co and Gd show a long-range magnetic order with a Curie temperature of ~1400 K and 293 K,

respectively, giving rise to interesting magnetic behavior at the interfaces of the Gd/Co multilayer system. Using the polarized neutron reflectometer at Dhruva, research reactor at Mumbai, India (Basu and Singh 2006), we have investigated the structural and magnetic properties of Gd/Co multilayers at a nanometer length scale with an emphasis on interface-induced phenomena (Basha et al. 2018; Singh et al. 2022). Interfacial dependence of magnetic properties in this system was determined using both (i) by depositing multilayers using different argon partial pressure while sputtering and (ii) by annealing multilayers at different temperatures.

A Gd/Co multilayer with a repeat of 10 bilayers of the Gd (thickness = 135 Å) and Co (thickness = 80 Å) was grown by sputtering. Figure 17.7 depicts the schematic of a bilayer of Gd/Co multilayer grown with two partial pressures of Ar (the top panel and the middle panel of column (i) of Fig. 17.7 corresponds to multilayers grown at an Ar pressure of 0.4 Pa and 0.2 Pa, respectively) and after annealing the multilayer (grown at 0.2 Pa) at a temperature of 600 °C for 0.5 h (bottom panel of the column (i) of Fig. 17.7). The corresponding macroscopic magnetizations [$M(T)$] for three multilayers, measured using a SQUID magnetometer under field-cooled, FC, (in the applied field of 500 Oe) and zero fields cooled (ZFC), are shown in column (ii) of Fig. 17.7, suggesting temperature-dependent modulation in the magnetization. Spin-dependent (R^+ and R^-) neutron reflectivity data (symbols) and the corresponding fit (solid lines) from these multilayers are shown in column (iii) in Fig. 17.7. The periodicity of two multilayers (top and middle panel) grown under different Ar pressure was evident from the Bragg peak in PNR data. Whereas annealing of multilayer at 600 °C produces an alloy at the interfaces. We did not find any Bragg peak for this case due to loss of multilayer periodicity. The depth

profiles for magnetization obtained from PNR data for each condition are shown in column (iv) of Fig. 17.7. PNR results predicted higher interface roughness and reduction in the magnetization for the Co layer for Gd/Co multilayer grown at 0.4 Pa Ar pressure (top panel). On annealing the multilayer at 600 °C an alloy is formed, which is ferromagnetic at RT with reduced magnetization.

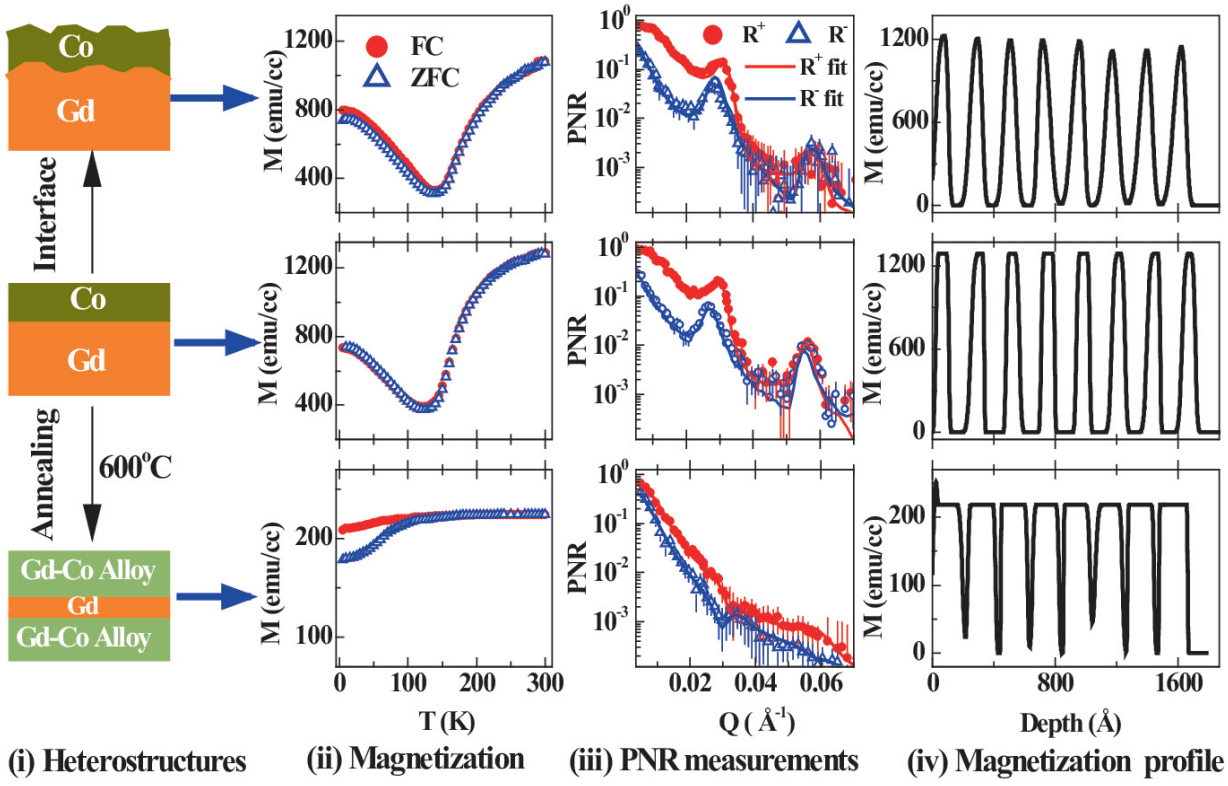

Fig. 17.7 Column (i) represents the schematic of a bilayer of Gd/Co multilayers grown at two different Ar pressures (0.4 Pa and 0.2 Pa for top and middle panels) and after annealing the multilayer grown at 0.2 Pa at 600 °C (bottom pane). Columns (ii), (iii), and (iv) show the corresponding $M(T)$ data in FC and ZFC mode, PNR data, and magnetization depth profile obtained from PNR data, respectively, for these multilayers. It is adapted and redrawn from Elsevier Publishers (Basha et al. 2021)

PNR results investigated a change in the macroscopic magnetic properties of the multilayer, which is attributed to the modification in the exchange interaction at interfaces due to corresponding changes in structure and morphology at interfaces. Therefore, the PNR measurements for Gd/Co multilayer systems (Basha et al.

2018, 2021; Singh et al. 2022) with different interface structures and morphologies offered interesting information that helped us to understand the mechanisms of interface-induced magnetization in RE/TM systems. These findings also revealed that a more complicated magnetic model that takes account of interface roughness and morphology in RE/TM systems is required to study these systems micro-magnetically for possible future applications.

17.4.3 Annealing-Driven Exchange Bias in Fe/Cu/Pt Heterostructure

Many spin-dependent phenomena like spin–orbit torques, spin pumping, spin Hall effect, and the DMI have been studied in FM/heavy metal systems. Fe (FM)/Pt (heavy metal) is such a system (Basha et al. 2020a), which has attracted considerable attention in recent years due to its magnetic properties that are deployable in ultrahigh-density storage applications. The as-deposited FePt is disordered face-centered cubic (fcc) and requires a high-temperature annealing for transforming it to the ordered L_{10}/face-centered tetragonal (fct) FePt phase. The fct phase exhibits high uniaxial magnetic anisotropy along the *c* direction of the crystal structure and shows high PMA, which found strong application in high-density recording media. However, a high-temperature annealing is required to get the required fct phase. The addition of Cu element to FePt and realizing the formation of $(FePt)_{1-x}Cu_x$ ternary alloys was considered one of the effective ways to reduce the ordering (fcc to fct) temperature of FePt films. The ternary alloy shows different magnetic properties as compared to that of FePt. Here we provide an example of a metallic Fe/Cu/Pt heterostructure grown on a Si (001) substrate, where using PNR measurements in combination with other macroscopic techniques (Basha et al. 2020a) we

studied the modification in magnetization of the heterostructure by modifying the interface morphology using annealing treatment at different temperatures. We observed an annealing-induced RTEB effect in Fe/Cu/Pt heterostructure grown on Si substrate. The system, which exhibited soft ferromagnetism with an easy axis along the plane of the film in the pristine state, showed many interesting macroscopic magnetic properties after annealing at relatively higher temperatures.

Figure 17.8a represents the macroscopic magnetization as a function of temperature for the heterostructure in a pristine state and at different annealing temperatures. The FC (field = 500 Oe) and ZFC M(T) show different behavior at different annealing temperatures. An irreversible magnetic behavior (the non-zero difference between FC and ZFC data) with reduced saturation magnetization is evident on annealing the heterostructure both at 400 °C and 600 °C. The M(H) data for different annealing conditions are depicted in Fig. 17.8b. The heterostructure annealed at 400 °C showed a shift in the hysteresis curve toward the positive field axis, suggesting a positive EB in the system at RT. The modulation in macroscopic magnetization of the system at different annealing temperatures, as indicated by different techniques, maybe because of the formation of an alloy phase at the interface (Basha et al. 2020a). To reveal the influence of annealing on the depth-dependent structure and magnetization of this system we performed PNR measurements and Fig. 17.8c–e shows the spin-dependent PNR ($R^{\pm}$) data represented in another form for clear representation, called normalized spin asymmetry (NSA) and defined as (Basu and Singh 2022; Singh et al. 2018) $NSA = (R^{+}–R^{-})/(R^{+} + R^{-})$. PNR data indicates modification upon annealing the heterostructure and thus suggests a change in structure and magnetic properties.

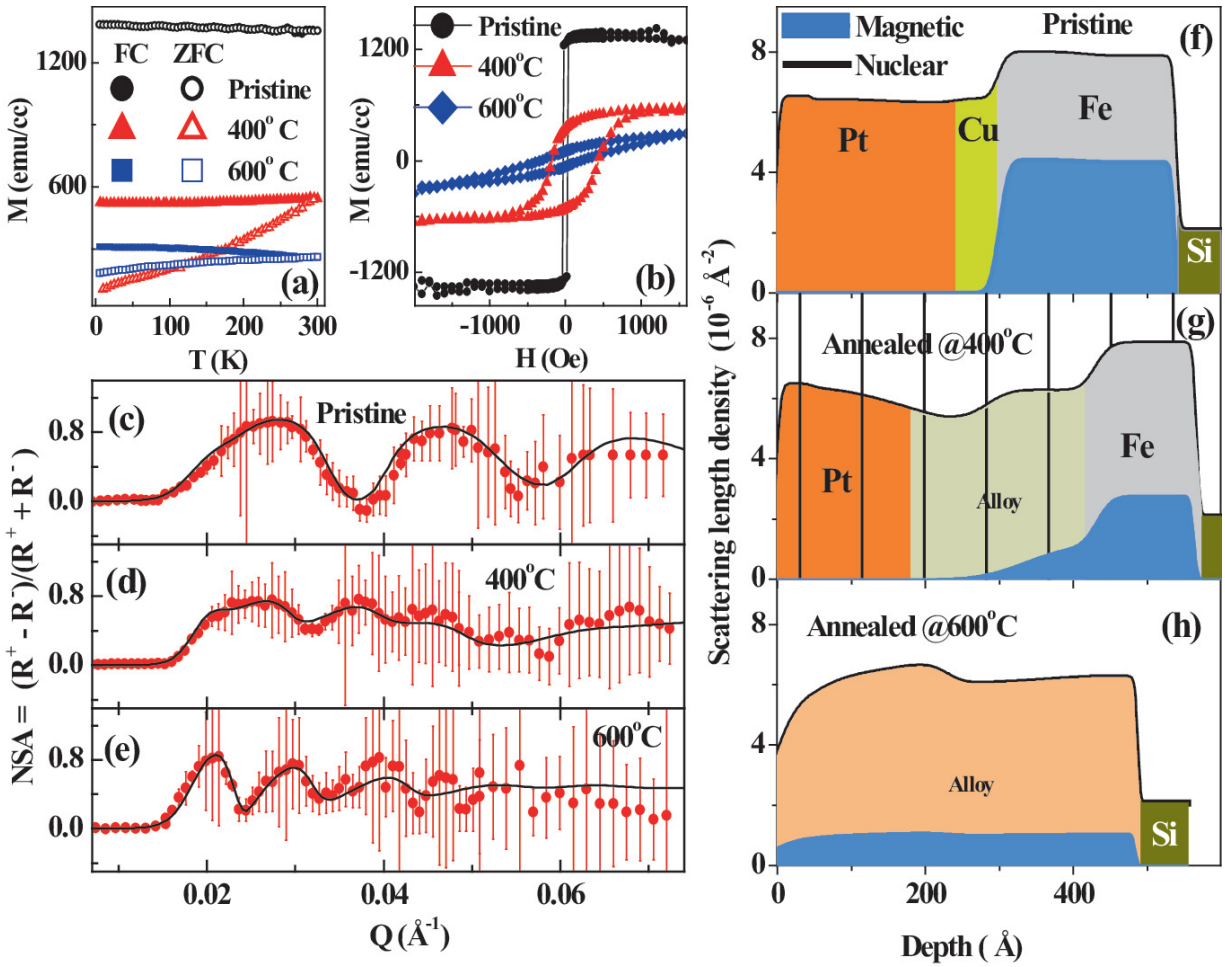

Fig. 17.8 **a** M(T) data under FC (cooling field 500 Oe) and ZFC mode and **b** M(H) data for pristine and annealed Fe/Cu/Pt heterostructure. NSA (PNR) data (solid circles) and corresponding fit (solid lines) for **c** pristine and **d**, **e** annealed heterostructure. **f**–**h** The nuclear and magnetic SLD depth profiles, extracted from PNR data, for heterostructure under different cases of annealing. It is adapted and redrawn from Elsevier Publishers (Basha et al. 2020a)

Analysis of PNR data simultaneously provides the nuclear (structure) and magnetic depth profile of thin films and superlattices (Basu and Singh 2022; Singh et al. 2018). The NSLD and MSLD depth profiles of the Fe/Cu/Pt heterostructure in pristine and annealed (at 400 °C and 600 °C) are shown in Fig. 17.8f–h. The depth-dependent structure of annealed heterostructure at 400 °C suggests the formation of an alloy layer, which is initiated through the interface due to interdiffusion and is ferromagnetic at RT. On further annealing of the heterostructure at 600 °C a

complete alloy phase is formed which shows a reduction in saturation magnetization. The average in-plane magnetization obtained from PNR and SQUID matches well. SQUID data suggested the positive EB for heterostructure annealed at 400 °C which reverses (negative EB) on further annealing at a higher temperature of 600 °C. The observed EB phenomena in the system are attributed to the additional exchange interaction because of the coexistence of soft and hard magnetic phases (Basha et al. 2020a). This study demonstrated an annealing-induced EB effect in the low-field region that is strongly dependent on the majority phases (hard/soft), present in the system and hence can be useful for application in magnetic devices.

17.4.4 Exchange Bias and Thin Ferromagnetic LNO Layer at the LNO/LSMO Interface

There has been a large interest in growing complex oxide heterostructures comprising near RT FM manganites and paramagnetic (PM) nickelates because of the discovery of interface-driven exotic properties in such systems. The $La_{0.67}Sr_{0.33}MnO_3$ (LSMO)/$LaNiO_3$ (LNO) heterostructure is one of the FM manganite/PM nickelate systems that has gained attention in the scientific community recently due to its exotic interfacial properties. The most unexpected magnetic property of this system was the finding of the EB effect in the LSMO/LNO heterostructure, which has been attributed to many phenomena like the existence of a frustrated magnetic phase at the interface, charge transfer between Mn and Ni ions at interface inducing the superexchange interaction, the non-collinear magnetic structure at interfaces, etc. (Bhatt et al. 2020; Rojas Sánchez et al. 2012). The EB in the LNO/LSMO heterostructures were relatively small in magnitude but reported for the entire thickness range up to 30 nm,

suggesting that this phenomenon is intrinsic and may be related to interface exchange interactions. Using temperature-dependent PNR measurements, we have studied the structure and magnetic depth profile of LSMO/LNO/LSMO heterostructures grown on MgO (001) substrate with a special emphasis on revealing the interaction across interfaces (Bhatt et al. 2020). We obtained detailed depth-dependent magnetization profiles of heterostructures giving a quantitative estimate of the magnetization in the interfacial LNO layer and the nature of the magnetic exchange coupling across the interfaces. EB was observed below 50 K by SQUID measurements. In the same temperature range, the PNR results indicate the emergence of an ordered magnetization in the interfacial LNO layers with a thickness of ≈22–35 Å, and the strength of this magnetization increased as the temperature was reduced, reaching a maximum magnetization of ~80 emu cc^{-1} observed at 5 K. PNR results also suggested that the stacking order of the layers plays a significant role in deciding the magnitude and sign of the interfacial exchange interaction in these heterostructures.

Figure 17.9a presents the schematic of the structure of the LSMO/LNO/LSMO heterostructure grown on a single crystal MgO substrate. The structure and morphology of this heterostructure were carried out using X-ray scattering techniques such as X-ray diffraction (XRD) and X-ray reflectivity (XRR) and suggest a high quality of interfaces and layer structure (Bhatt et al. 2020). We found that the EB for heterostructure was strongest at 5 K. The EB was confirmed by measuring M(H) curves, shown in Fig. 17.9b, on cooling the heterostructure in a field of ± 500 Oe. The EB can be calculated by the average of the sum of the coercive fields, respectively, for the positive and negative field axes and defined as EB = $(H_c^+ + H_c^-)/2$ (Basha et al. 2020b). A clear shift in the hysteresis loops toward the field

axis opposite to the direction of the applied field is evident from Fig. 17.9b, indicating a negative EB in the system. To investigate the possibility of any interfacial magnetic exchange interaction and coupling being responsible for observed EB in this system, we carried out specular PNR measurements under FC (+500 Oe) conditions at different temperatures.

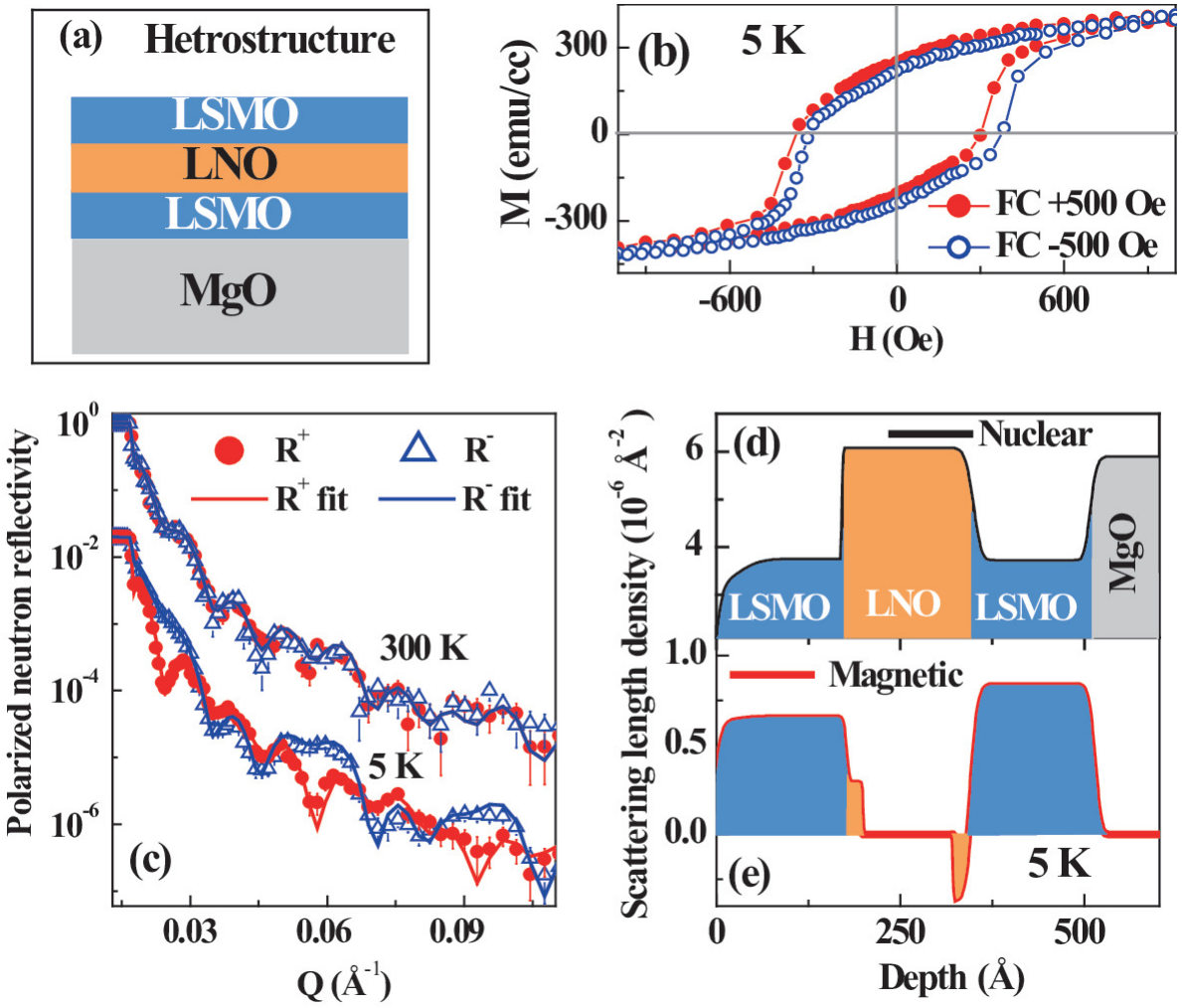

Fig. 17.9 **a** Schematic of the layer structure of LSMO/LNO/LSMO trilayer grown on MgO substrate. **b** M(H) curves at 5 K on cooling the heterostructure in an applied magnetic field of ±500 Oe. **c** PNR data (symbols) and the best fit (solid line) for LSMO/LNO/LSMO/MgO at 300 and 5 K. Nuclear SLD **d** and magnetic SLD **e** depth profile for the heterostructure obtained from PNR data. It is adapted and redrawn from Wiley Publishers (Bhatt et al. 2020)

Figure 17.9c shows the PNR ($R^{\pm}$) data (symbols) and corresponding fits (solid lines) from the LSMO/LNO/LSMO heterostructure at 300 and 5 K, which are shifted vertically for better visualization. We observed no difference in the spin-dependent (R^{+} and R^{-}) neutron reflectivities at 300 K, indicating no net magnetic ordering. The NSLD depth profile (layer structure) of the heterostructure obtained from 300 K, PNR data is shown in Fig. 17.9d and confirms a high-quality layer structure. The analysis of PNR data at 5 K provided a detailed magnetic scattering length density (MSLD) or magnetization depth profile as shown in Fig. 17.9e, suggesting the emergence of a ferromagnetic interfacial layer in LNO at both interfaces. PNR data also revealed different coupling (AFM and FM) of interfacial magnetization at two interfaces suggesting the dependence of interfacial exchange interaction on the layer stacking order. PNR measurements on these systems also confirmed the existence of EB in these systems (Bhatt et al. 2020) which was also attributed to the emergent FM layers at the interfaces. We believe the PNR results obtained in this study provided quantitative information to test theoretical models of the EB effect and emerging phenomena at non-conventional oxide interfaces.

17.4.5 Proximity and Tunneling at Interfaces in Superconductor and Ferromagnet Oxide Heterostructures

It is well-known that superconductors are perfect diamagnets and do not coexist with ferromagnets. However, it is interesting to study the properties of a system when a superconductor (SC) and a ferromagnet (FM) are brought closer to each other. Recently these systems have attracted several interesting studies on a phenomenon known as the *"magnetic proximity effect"* (Hoppler et al. 2009; Prajapat et al. 2016; Singh et al.

2020; Bhatt et al. 2022; Satapathy et al. 2012; Kumar et al. 2021), which shows suppression of magnetism of the interfacial FM layer with the formation of a magnetic depleted (MD) layer below superconducting transition temperature (T_{SC}). A step further, using the inherent capability of PNR, we studied the proximity effect in a tunneling geometry of heterostructures where FM and SC layers are separated by an insulator (I), e.g., LSMO (FM)/$SrTiO_3$ (STO)(I)/ $YBa_2Cu_3O_{7-\delta}$ (YBCO) (SC), and surprisingly we observed modulation in the interfacial magnetization of the FM layer below $T_{SC,}$ even separating the FM layer from the SC layer by an insulator (I). This phenomenon was attributed to the leakage of the spin-triplet Cooper pairs into the FM layer, leading to a modulation in the magnetism of the interfacial FM layer (Prajapat et al. 2016; Singh et al. 2020; Bhatt et al. 2022; Kumar et al. 2021). Here we describe the proximity effect observed in one such heterostructure system, i.e., YBCO/STO/LSMO grown on MgO substrate as well as the influence of ion irradiation and sequence of layer stacking on the proximity effect in this system. The hybrid heterostructures were grown on a single crystal MgO substrate by pulsed laser deposition technique (Singh et al. 2020). Combining different measurements, we correlated the structural and magnetic properties across $T_{SC.}$

Figure 17.10 shows the comparison of different measurements (SQUID and PNR) on three hybrid heterostructures, which are schematically shown in column (i) of Fig. 17.10. The top panel of Fig. 17.10 shows the schematic and different measurements for the MgO/YBCO/STO/LSMO heterostructure. The middle panel of Fig. 17.10 shows different measurements from the same heterostructure after ion irradiation with 120 MeV Ag^{15+} ions at a dose of 1×10^{12} ions/cm^2. The bottom panel of

Fig. 17.10 shows the schematic and measurements from the MgO/LSMO/STO/YBCO heterostructure, where we have reversed the sequence of the layer growth for FM and SC. We observed the crystalline structure for the YBCO layer which was highly textured in the [00 l] direction for three systems, using XRD (Singh et al. 2020; Bhatt et al. 2022; Kumar et al. 2021). A comparison of SQUID data (column (ii) of Fig. 17.10) for heterostructures suggested different values of T_{SC} with a value of ~68 K for MgO/YBCO/STO/LSMO (upper panel), 30 K (middle panel) for ion irradiated heterostructure and 86 K (lower panel) for reversed stacking (MgO/LSMO/STO/YBCO) heterostructures, as compared to its bulk value T_{SC} of ~92 K. Detailed analysis of XRD data demonstrated that the change in T_{SC} is directly correlated to the atomic structure of the YBCO layer (Bhatt et al. 2022). The PNR data were taken on these heterostructures across T_{SC}at different temperatures and NSA (spin-dependent PNR) data (symbols) and corresponding fits (solid lines) from these heterostructures at 300 and 10 K are shown in column (iii) of Fig. 17.10. The PNR results revealed the detailed depth profiling of magnetization at different temperatures (Singh et al. 2020; Bhatt et al. 2022; Kumar et al. 2021). The magnetization depth profiles at 10 K from these heterostructures are shown at the extreme left (column (iv) of each panel in Fig. 17.10, suggesting the formation of the MD layer at the STO/LSMO interface. The interfacial LSMO layer in the magnetization depth profiles is highlighted as a shaded region. A thicker MD layer of thickness ~35 Å was observed for the MgO/YBCO/STO/LSMO heterostructure (upper panel), which reduces to (a) zero Å upon ion irradiation of the heterostructure (middle panel) and (ii) to a thickness of

~20 Å for heterostructure with reversed sequence (lower panel) below T_{SC}.

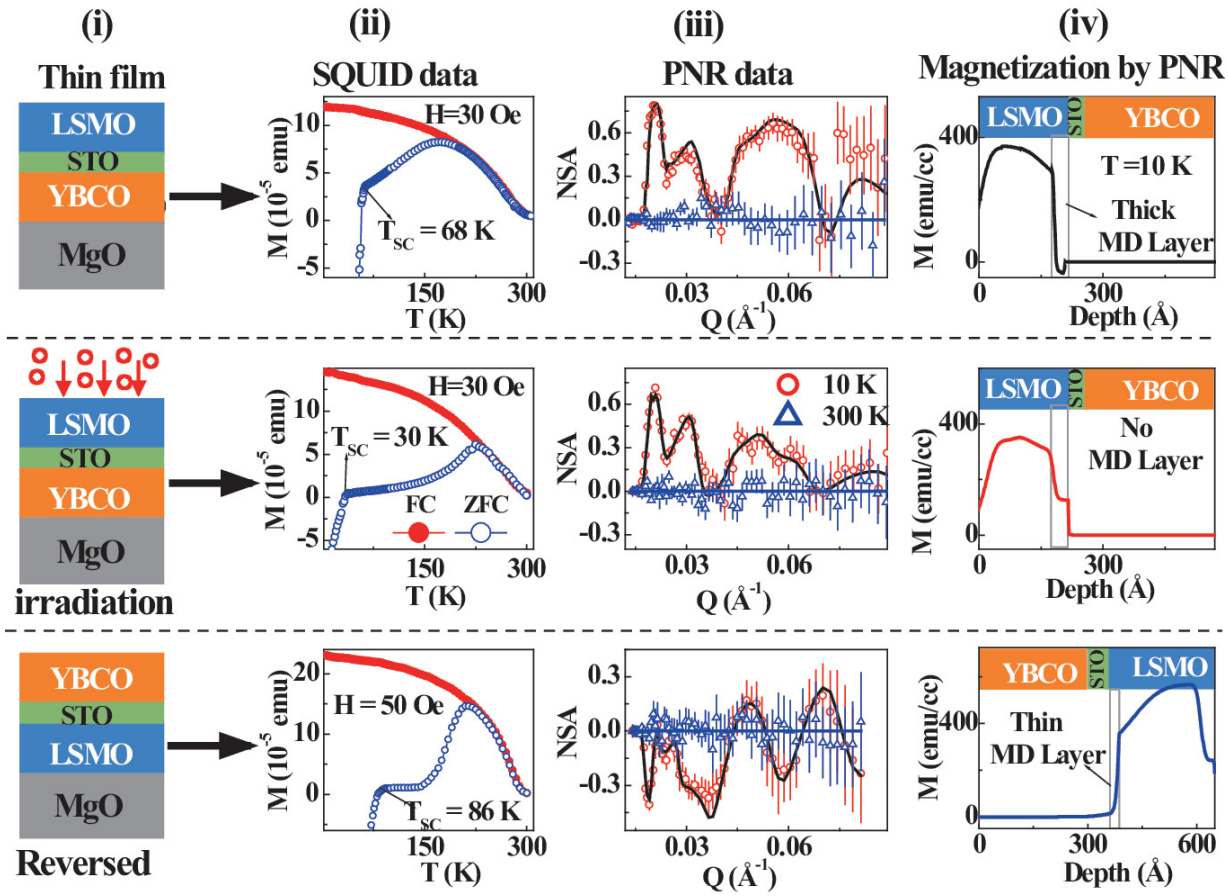

Fig. 17.10 Comparison of SQUID (column (ii)), PNR measurements (column (iii)), and magnetization (column (iv)) depth profiles (PNR results) from trilayer heterostructures of YBCO/STO/LSMO grown on MgO substrates. (top panel): schematic of MgO/YBCO/STO/LSMO heterostructure with different measurements. (middle panel): ion irradiated MgO/YBCO/STO/LSMO heterostructure with different measurements. (lower panel): schematic of MgO/LSMO/STO/YBCO (reversed sequence) heterostructure with different measurements. The magnetization depth profiles extracted from PNR measurements for these heterostructures at 10 K are shown at the extreme right (column iv) of each panel. It is adapted and redrawn from ACS Publishers (Bhatt et al. 2022)

The formation of the MD layer below T_{sc} in these heterostructures is attributed to the tunneling of Cooper pairs across the insulator. In addition, the comparison of these studies suggested that the strength of the magnetic proximity effect highly depends on the interplay of SC and

FM properties such as T_{SC} and magnetization in general, as these parameters may provide additional energies and length scale for observing the magnetic proximity effect. This finding has demonstrated the need and significance of PNR to understand the interplay of superconductivity and magnetism in such hybrid systems.

17.4.6 Induced Interface Magnetism at Ferromagnetic/Multiferroic Interface

Perovskite oxide heterostructures comprising FM such as $La_{0.67}Sr_{0.33}MnO_3$ (LSMO) and AFM such as $BiFeO_3$ (BFO) are some of the most extensively explored FM/multiferroic complex oxide heterostructures (Singh et al. 2014, 2015; Prajapat et al. 2020; Yu et al. 2010b; Jain et al. 2015) for revealing interesting physics at interfaces. BFO is a single-phase multiferroic material that exhibits magnetoelectric coupling between ferroelectric, FE, ($T_C = 1103$ K) and antiferromagnetism, AFM, ($T_N = 643$ K) order parameters (Wang et al. 2003). A weak FM for BFO (~0.03 μB) as a consequence of the canting of the AFM structure due to the DMI has been indicated by theoretical calculations (Ederer and Spaldin 2005). Experimental investigations on BFO/LSMO heterostructure have reported, an enhanced interfacial magnetic moment (~0.75 μ_B) in the BFO which was attributed to orbital reconstruction due to Fe–Mn hybridization (Yu et al. 2010b). Depth dependent magnetic characterization of these heterostructures using PNR suggested a similar enhancement of interfacial magnetization in the BFO layer magnetization (~0.75 μ_B to 1.5 μ_B) for the Interfacial BFO layer up to a thickness of ~6 to 8 unit cells. and Additionally, the PNR measurements suggested the presence of both types of magnetic coupling, FM (magnetic moment of interfacial BFO layer and LSMO are in same directions along the applied field) and AFM

(moments are opposite, i.e., the magnetic moment of the interfacial BFO layer is opposite to applied field and LSMO layer) (Singh et al. 2014; Prajapat et al. 2020; Jain et al. 2015). The different magnetic couplings in this system have also been confirmed by the first principal calculations and it was attributed to different surface terminations (Singh et al. 2014; Prajapat et al. 2020).

The normalized spin asymmetry, NSA (spin-dependent PNR), data (symbols), and the corresponding fit (solid lines) at 300 K and 5 K for the LSMO/BFO/LSMO heterostructure grown on the MgO substrate are shown in Fig. 17.11a, b, respectively. Spin-dependent (R^+ and R^-) PNR data (NSA ~ 0) at 300 K did not show any difference (R^+ and R^- are the same) suggesting the system is non-magnetic at this temperature and a detailed NSLD depth profile (Fig. 17.11b) for the system was obtained from PNR data at 300 K. PNR measurements at low temperatures showed a splitting in R^+ and R^- data (i.e., non-zero NSA), suggesting FM behavior of the system and detail MSLD depth profiles obtained at 5 K for heterostructure is shown in Fig. 17.11d. PNR data at 5 K suggested that the interfacial BFO layer (thickness ~20–35 Å) at both the interfaces (BFO on LSMO and LSMO on BFO) is ferromagnetic with its magnetization aligned opposite to the applied field and magnetization of the LSMO layer (AFM coupling). To justify the magnetization depth profile obtained from PNR at 5 K we have also assumed different possible magnetization profiles and tried to fit these into the experimental PNR data. A comparison of fit to PNR data of different magnetization profiles suggested that the magnetization depth profile assuming AFM coupling between the LSMO layer and the interfacial BFO layer best fitted the PNR data at 5 K (Prajapat et al. 2020). We have also studied different heterostructures of LSMO/BFO, having different morphologies, using PNR and observed

both FM and AFM coupling as depicted in Fig. 17.11e and it is attributed to different interface termination for two polar materials (Prajapat et al. 2020) as hinted by theoretical calculations (Singh et al. 2014). PNR results also confirmed the existence of EB in this system (Prajapat et al. 2020).

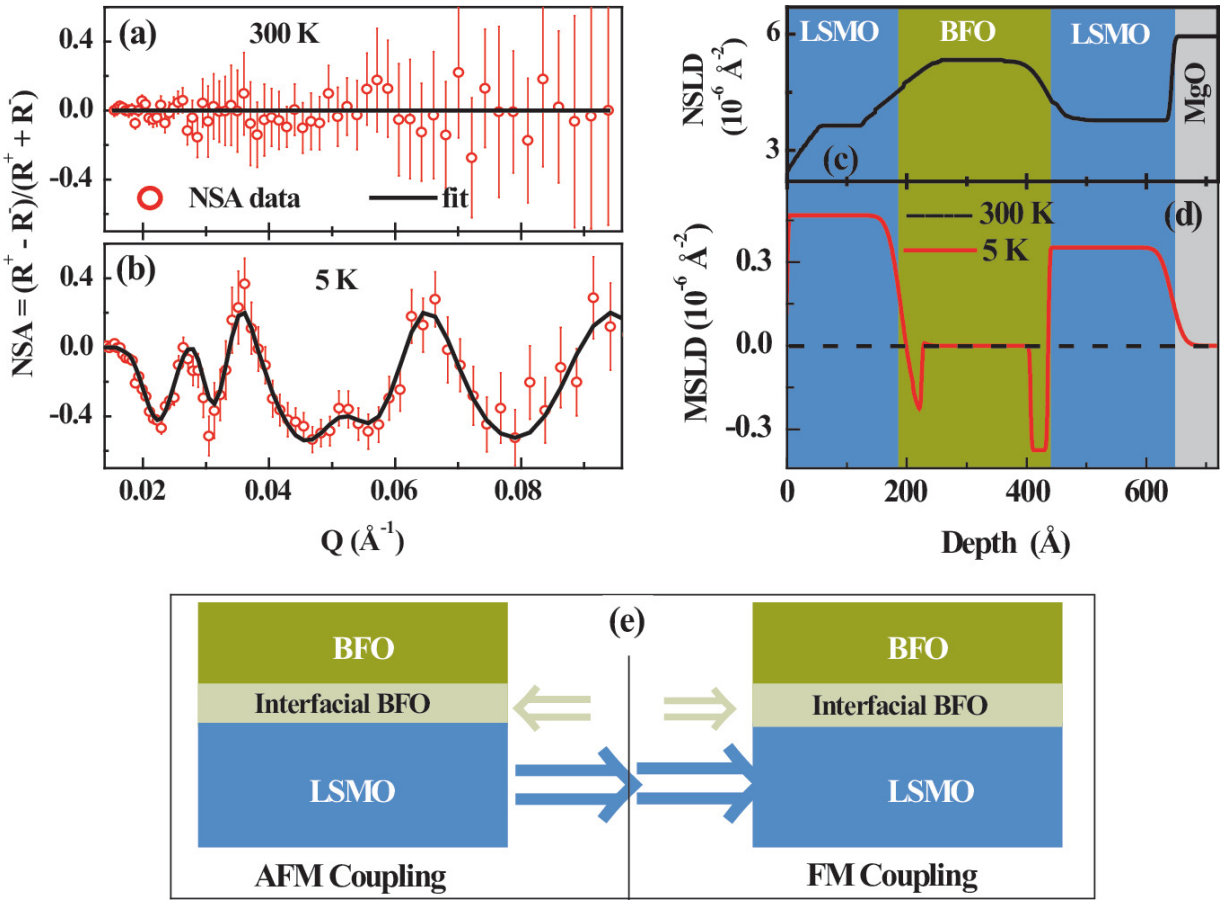

Fig. 17.11 NSA (PNR) measurements from a MgO/LSMO/BFO/LSMO heterostructure at **a** 300 K and **b** 5 K. The NSLD **c** and MSLD **d** depth profiles of the system, as obtained from PNR. **e** schematic representation of different magnetic coupling between the LSMO layer and the interfacial BFO layer observed in this heterostructure depending on surface termination. It is adapted and redrawn from ACS Publishers (Prajapat et al. 2020)

17.5 Application of Magnetic Thin Films and Superlattices

Magnetic thin films hold significant importance to both technological applications as well as fundamental research due to their exotic properties and versatility. They are utilized in diverse fields due to their unique magnetic properties, which can be tailored by adjusting their composition, thickness, and structure to meet specific application requirements. Magnetic thin films exhibit a variety of interesting phenomena such as (i) anisotropy which may give rise to phenomena such as the EB effect and PMA, (ii) giant magneto-resistance which is a spin-dependent transport phenomenon, (iii) magnetic domain structures and domain wall dynamics which can be controlled by external stimuli such as magnetic fields, temperature, and currents, (iv) spin–orbit coupling leading to phenomena such as spin splitting, spin textures, and topological spin transport, and (v) interfacial effects and exchange coupling giving rise to emergent magnetic phenomena such as helical magnetic structures, electronic phase separation, and interfacial magnetization modulation. The most exciting part about thin films is that most of the above-mentioned fundamental phenomena are either already found or are potential candidates for technological applications.

One significant advantage of magnetic thin films is that they enable the miniaturization of devices and systems. This has revolutionized fields such as electronics, telecommunications, and medical devices, allowing for smaller, lighter, and more efficient technologies. A few of the prominent applications of magnetic thin films include:

1. Data storage: Magnetic thin films are the most crucial components for data storage devices such as computer hard disk drives. The phenomena such as GMR combined with high magnetic coercivity and stability of magnetic thin films allow for reliable and long-term

data storage, making them an essential component of the digital age.

2. Magnetic Memory: Magnetic thin films are also used in non-volatile magnetic memories, such as magnetic random-access memory (MRAM) and magnetic cache memories which use the magnetization orientation of a magnetic thin film to store data. MRAM has the potential for high-speed, high-density, and low-power data storage applications due to its non-volatility and fast switching speed.

3. Spintronics Devices: Technologies such as spin valves, magnetic tunnel junctions (MTJs), and spin-transfer torque (STT) devices and spin filters utilize the unique properties of magnetic thin films for functionalities such as spin filtering, spin-polarized current generation, and magnetization manipulation. These devices have potential applications in areas such as magnetic sensors, non-volatile memories, and logic devices, and they are being actively researched for spintronics and related technologies.

4. Magnetic Sensors: Magnetic thin films are commonly used in magnetic sensors, such as magneto-resistive sensors and Hall effect sensors. Magnetoresistive sensors exploit the change in electrical resistance of a magnetic thin film when subjected to an external magnetic field, and they are used in applications such as magnetic field detection, compasses, and current sensors. Hall effect sensors, on the other hand, utilize the magnetic field-induced Hall voltage across a magnetic thin film to measure the strength and direction of a magnetic field, and they are used in various applications, including position sensing, current sensing, and speed sensing.

5. Neutron Supermirrors: Neutron supermirrors are devices used in neutron scattering facilities to transport neutrons from the source to the desired beamline. These use alternate magnetic and non-magnetic multilayers such as Ni/Ti with gradually changing layer thickness to enhance the reflectivity of neutrons and minimize the flux loss during transportation. By choosing certain combinations of the layer materials such as Fe/Si. these supermirrors can also be used to polarize the incoming neutron beam with respect to an applied magnetic field into spin up (parallel to the field) or spin down (antiparallel to the field) orientations.

6. 2 D Quantum Materials: These are thin layers of materials that exhibit quantum properties due to reduced dimensionality, for example, high electron mobility and mechanical strength in graphene and strong light-matter interactions in transition metal dichalcogenides. They have potential applications in many different fields such as electronics to make high-speed transistors, optoelectronics to make efficient photodetectors and light-emitting diodes, and quantum computing to preserve quantum states on the edges and surfaces of topological insulators.

7. Energy Harvesting: Energy harvesting and conversion is a blooming field where magnetic thin films have found significant applications in devices that convert mechanical vibrations, thermal energy, or other forms of energy into electrical energy.

Examples of such applications include magnetostrictive devices made of materials, such as Fe/Ga, Fe/Al, and TbDy alloys, and thermomagnetic devices based on the spin Seebeck effect.

These are just a few examples of the many phenomena observed in magnetic thin films. The rich and diverse behavior of magnetic thin films makes them a fascinating area of research with numerous novel phenomena waiting to be explored, understood, used, and improvised technological applications.

17.6 Summary and Future Direction

Advancements in interface engineering of thin films and superlattices offer an opportunity to control and tailor the structural, electronic, and magnetic properties, where even minor changes in the interface structure and morphology can induce drastic changes in macroscopic magnetic properties. Designing artificially engineered heterostructures to obtain emerging properties and investigating the subsequent new physics arising from the interfacial effects have always been interesting topics for both fundamental research and possible technological applications in the fields of spintronics, magnetic devices, etc. In this chapter, we briefly discussed the successful use of the PNR technique for the investigation of magnetism occurring in films of ultrathin 3*d* transition metal-based systems, antiferromagnetically coupled ultrathin Gd/Co multilayers, and complex oxide interfaces. These systems are technologically relevant and could find interesting applications in devices controlled by interfacial phenomena. We have also provided a brief introduction to different thin film growth techniques such as evaporation, sputtering, MBE, and PLD. This was followed by a small discussion about characterization techniques, e.g., MFM, MOKE, PNR, and x-ray resonant scattering to study magnetism in thin films and multilayer systems. However, in comparison to PNR, most of these other characterizing techniques are either surface sensitive, microscopic, or do

not provide information about the buried interfaces. PNR together with magnetic/non-magnetic X-ray scattering provides a unique means of revealing the structural and vector magnetization details near the surface as well beneath the surface of the heterostructures. We are sure that these techniques will be highly desirable for resolving the exotic properties in quantum material heterostructures, including superconductors, and topological materials, which provide exceptional promise for the advancement of next-generation computers, new energy technologies, and high-precision sensors. Thus, PNR with its inherent sensitivity to detect minute magnetic features at sub-nanometer depth resolution and its ease of implementation under complex experimental conditions stands out as a pivotal tool in the dynamic realm of research on two-dimensional magnets. Advancement in thin film growth techniques allowing high quality and homogeneous artificially engineered heterostructure and the development of high-intensity neutron reflectivity techniques will provide an excellent opportunity to enable real-time studies of interfaces of the heterostructures for technological applications.

References

Aguiar, E.C., Ramirez, M.A., Cortes, J.A., Rocha, L.S., Borsari, E., Simões, A.Z.: Magnetoelectric coupling of $LaFeO_3$/$BiFeO_3$ heterostructures. Ceramics Int. **41**(10, Part A), 13126–34 (2015)

Baibich, M.N., Broto, J.M., Fert, A., Van Dau, F.N., Petroff, F., Etienne, P., Creuzet, G., Friederich, A., Chazelas, J.: Giant Magnetoresistance of (001)Fe/(001)Cr magnetic superlattices. Phys. Rev. Lett. **61**(21), 2472–2475 (1988)
[PubMed]

Basha, M.A., Prajapat, C.L., Gupta, M., Bhatt, H., Kumar, Y., Ghosh, S.K., Karki, V., Basu, S., Singh, S.: Interface induced magnetic properties of Gd/Co heterostructures. Phys. Chem. Chem. Phys. **20**(33), 21580–21589 (2018)
[PubMed]

Basha, M.A., Bhatt, H., Kumar, Y., Prajapat, C.L., Gupta, M., Karki, V., Basu, S., Singh, S.: Annealing driven positive and negative exchange bias in Fe–Cu–Pt heterostructures at room temperature. J. Alloy. Compd. **815**, 152640 (2020a)

Basha, M.A., Prajapat, C.L., Bhatt, H., Kumar, Y., Gupta, M., Kinane, C.J., Cooper, J.F.K., Caruana, A., Gonal, M.R., Langridge, S., Basu, S., Singh, S.: Helical magnetic structure and exchange bias across the compensation temperature of Gd/Co multilayers. J. Appl. Phys. **128**(10), 103901 (2020b)

Basha, M.A., Bhatt, H., Kumar, Y., Prajapat, C.L., Gupta, M., Basu, S., Singh, S.: Formation of an intermetallic $GdCo_2$ alloy on controlled annealing of a Gd/Co multilayer. Mater. Lett. **283**, 128879 (2021)

Basu, S., Singh, S.:Neutron and X-ray Reflectometry: Emerging Phenomena at Heterostructure Interfaces. IOP Publishing, Bristol, UK (2022). https://doi.org/10.1088/978-0-7503-4695-5

Basu, S., Singh, S.: A new polarized neutron reflectometer at Dhruva for specular and off-specular neutron reflectivity studies. J. Neutron Res. **14**, 109–120 (2006)

Bhatt, H., Kumar, Y., Prajapat, C.L., Kinane, C.J., Caruana, A., Langridge, S., Basu, S., Singh, S.: Emergent interfacial ferromagnetism and exchange bias effect in paramagnetic/ferromagnetic oxide heterostructures. Adv. Mater. Interfaces **7**(21), 2001172 (2020)

Bhatt, H., Kumar, Y., Prajapat, C.L., Kinane, C.J., Caruana, A., Langridge, S., Basu, S., Singh, S.: Correlation of magnetic and superconducting properties with the strength of the magnetic proximity effect in $La_{0.67}Sr_{0.33}MnO_3/SrTiO_3/YBa_2Cu_3O_{7-\delta}$ Heterostructures. ACS Appl. Mater. Interfaces **14**(6), 8565–74 (2022)

Bode, M., Heide, M., von Bergmann, K., Ferriani, P., Heinze, S., Bihlmayer, G., Kubetzka, A., Pietzsch, O., Blügel, S., Wiesendanger, R.: Chiral magnetic order at surfaces driven by inversion asymmetry. Nature **447**(7141), 190–193 (2007) [PubMed]

Brataas, A., Kent, A.D., Ohno, H.: Current-induced torques in magnetic materials. Nat. Mater. **11**(5), 372–381 (2012) [PubMed]

Brinkman, A., Huijben, M., van Zalk, M., Huijben, J., Zeitler, U., Maan, J.C., van der Wiel, W.G., Rijnders, G., Blank, D.H.A., Hilgenkamp, H.: Magnetic effects at the interface between non-magnetic oxides. Nat. Mater. **6**(7), 493–496 (2007) [PubMed]

Chopra, K.L., Kaur, I.: Thin Film Technology: An Introduction. In: Chopra, K.L., Kaur, I. (eds.) Thin Film Device Applications, pp. 1–54. Springer, US, Boston, MA (1983)

Dikin, D.A., Mehta, M., Bark, C.W., Folkman, C.M., Eom, C.B., Chandrasekhar, V.: Coexistence of superconductivity and ferromagnetism in two dimensions. Phys. Rev. Lett. **107**(5), 056802 (2011)
[PubMed]

Dzyaloshinsky, I.: A thermodynamic theory of "weak" ferromagnetism of antiferromagnetics. J. Phys. Chem. Solids **4**(4), 241–255 (1958)

Ederer, C., Spaldin, N.A.: Weak ferromagnetism and magnetoelectric coupling in bismuth ferrite. Phys. Rev. B **71**(6), 060401 (2005)

Fitzsimmons, M.R., Hengartner, N.W., Singh, S., Zhernenkov, M., Bruno, F.Y., Santamaria, J., Brinkman, A., Huijben, M., Molegraaf, H.J.A., de la Venta, J., Schuller, I.K.: Upper limit to magnetism in $LaAlO_3/SrTiO_3$ heterostructures. Phys. Rev. Lett. **107**(21), 217201 (2011)
[PubMed]

Frisbie, C.D.: Scanning Probe Microscopy. In: Meyers, R.A. (ed.) Encyclopedia of Physical Science and Technology, 3rd edn., pp. 469–484. Academic Press, New York (2003)

Grutter, A.J., Yang, H., Kirby, B.J., Fitzsimmons, M.R., Aguiar, J.A., Browning, N.D., Jenkins, C.A., Arenholz, E., Mehta, V.V., Alaan, U.S., Suzuki, Y.: Interfacial ferromagnetism in $LaNiO_3/CaMnO_3$ superlattices. Phys. Rev. Lett. **111**(8), 087202 (2013)
[PubMed]

He, C., Grutter, A.J., Gu, M., Browning, N.D., Takamura, Y., Kirby, B.J., Borchers, J.A., Kim, J.W., Fitzsimmons, M.R., Zhai, X., Mehta, V.V., Wong, F.J., Suzuki, Y.: Interfacial ferromagnetism and exchange bias in $CaRuO_3/CaMnO_3$ superlattices. Phys. Rev. Lett. **109**(19), 197202 (2012)
[PubMed]

Hoffman, J., Tung, I.C., Nelson-Cheeseman, B.B., Liu, M., Freeland, J.W., Bhattacharya, A.: Charge transfer and interfacial magnetism in $(LaNiO_3)_n/(LaMnO_3)_2$ superlattices. Phys. Rev. B **88**(14), 144411 (2013)

Hoppler, J., Stahn, J., Niedermayer, C., Malik, V.K., Bouyanfif, H., Drew, A.J., Rössle, M., Buzdin, A., Cristiani, G., Habermeier, H.U., Keimer, B., Bernhard, C.: Giant superconductivity-induced modulation of the ferromagnetic magnetization in a cuprate–manganite superlattice. Nat. Mater. **8**(4), 315–319 (2009)
[PubMed]

Jain, P., Wang, Q., Roldan, M., Glavic, A., Lauter, V., Urban, C., Bi, Z., Ahmed, T., Zhu, J., Varela, M., Jia, Q.X., Fitzsimmons, M.R.: Synthetic magnetoelectric coupling in a nanocomposite multiferroic. Sci. Rep. **5**(1), 9089 (2015) [PubMed][PubMedCentral]

Kuch, W., Schäfer, R., Fischer, P., Hillebrecht, F.U.: Magneto-optical effects. In: Kuch, W., Schäfer, R., Fischer, P., Hillebrecht, F.U. (Eds.), Magnetic Microscopy of Layered Structures, p. 19–95. Springer, Berlin, Heidelberg (2015)

Kumar, Y., Bhatt, H., Prajapat, C.L., Singh, A.P., Singh, F., Kinane, C.J., Langridge, S., Basu, S., Singh, S.: Suppression of the superconducting proximity effect in ferromagnetic-superconducting oxide heterostructures with ion-irradiation. J. Appl. Phys. **129**(16), 163902 (2021)

Magnetic, A.L., Microscopy, F.: In: Lindon, J.C., Tranter, G.E., Koppenaal, D.W. (eds.) Encyclopedia of Spectroscopy and Spectrometry (Third Edition), pp. 675–684. Academic Press, Oxford (2017)

Manchon, A., Koo, H.C., Nitta, J., Frolov, S.M., Duine, R.A.: New perspectives for Rashba spin–orbit coupling. Nat. Mater. **14**(9), 871–882 (2015) [PubMed]

Moriya, T.: Anisotropic superexchange interaction and weak ferromagnetism. Phys. Rev. **120**(1), 91–98 (1960)

Nogués, J., Schuller, I.K.: Exchange bias. J. Magn. Magn. Mater. **192**(2), 203–232 (1999)

Oepen, H.P., Hopster, H.: SEMPA studies of thin films, structures, and exchange coupled layers. In: Hopster, H., Oepen, H.P. (Eds.), Magnetic Microscopy of Nanostructures, p. 137–67. Springer, Berlin, Heidelberg (2005)

Ohtomo, A., Hwang, H.Y.: A high-mobility electron gas at the $LaAlO_3/SrTiO_3$ heterointerface. Nature **427**(6973), 423–426 (2004) [PubMed]

Prajapat, C.L., Singh, S., Paul, A., Bhattacharya, D., Singh, M.R., Mattauch, S., Ravikumar, G., Basu, S.: Superconductivity-induced magnetization depletion in a ferromagnet through an insulator in a ferromagnet–insulator–superconductor hybrid oxide heterostructure. Nanoscale **8**(19), 10188–10197 (2016) [PubMed]

Prajapat, C.L., Bhatt, H., Kumar, Y., Rao, T.V.C., Mishra, P.K., Ravikumar, G., Kinane, C.J., Satpati, B., Caruana, A., Langridge, S., Basu, S., Singh, S.: Interface-induced magnetization and exchange bias in LSMO/BFO multiferroic heterostructures. ACS Appl. Electron. Mater. **2**(8), 2629–2637 (2020)

Ralph, D.C., Stiles, M.D.: Spin transfer torques. J. Magn. Magn. Mater. **320**(7), 1190–1216 (2008)

Rojas Sánchez, J.C., Nelson-Cheeseman, B., Granada, M., Arenholz, E., Steren, L.B.: Exchange-bias effect at $La_{0.75}Sr_{0.25}MnO_3/LaNiO_3$ interfaces. Phys. Rev. B **85**(9), 094427 (2012)

Santos, T.S., Kirby, B.J., Kumar, S., May, S.J., Borchers, J.A., Maranville, B.B., Zarestky, J., te Velthuis, S.G.E., van den Brink, J., Bhattacharya, A.: Delta doping of ferromagnetism in antiferromagnetic manganite superlattices. Phys. Rev. Lett. **107**(16), 167202 (2011)
[PubMed]

Satapathy, D.K., Uribe-Laverde, M.A., Marozau, I., Malik, V.K., Das, S., Wagner, T., Marcelot, C., Stahn, J., Brück, S., Rühm, A., Macke, S., Tietze, T., Goering, E., Frañó, A., Kim, J.H., Wu, M., Benckiser, E., Keimer, B., Devishvili, A., Toperverg, B.P., Merz, M., Nagel, P., Schuppler, S., Bernhard, C.: Magnetic proximity effect in $YBa_2Cu_3O_7/La_{2/3}Ca_{1/3}MnO_3$ and $YBa_2Cu_3O_7/LaMnO_{3+\delta}$ superlattices. Phys. Rev. Lett. **108**(19), 197201 (2012)
[PubMed]

Singh, S., Freeland, J.W., Fitzsimmons, M.R., Jeen, H., Biswas, A.: Composition dependence of charge and magnetic length scales in mixed valence manganite thin films. Sci. Rep. **6**(1), 29632 (2016)
[PubMed][PubMedCentral]

Singh, S., Swain, M., Basu, S.: Kinetics of interface alloy phase formation at nanometer length scale in ultra-thin films: X-ray and polarized neutron reflectometry. Prog. Mater Sci. **96**, 1–50 (2018)

Singh, S., Basha, M.A., Bhatt, H., Kumar, Y., Gupta, M.: Interface morphology driven exchange interaction and magnetization reversal in a Gd/Co multilayer. Phys. Chem. Chem. Phys. **24**(11), 6580–6589 (2022)
[PubMed]

Singh, S., Haraldsen, J.T., Xiong, J., Choi, E.M., Lu, P., Yi, D., Wen, X.D., Liu, J., Wang, H., Bi, Z., Yu, P., Fitzsimmons, M.R., MacManus-Driscoll, J.L., Ramesh, R., Balatsky, A.V., Zhu, J.-X., Jia, Q.X.: Induced MAGNETIZATION IN $La_{0.7}Sr_{0.3}MnO_3/BiFeO_3$ superlattices. Phys. Rev. Lett. **113**(4), 047204 (2014)

Singh, S., Xiong, J., Chen, A.P., Fitzsimmons, M.R., Jia, Q.X.: Field-dependent magnetization of $BiFeO_3$ in an ultrathin $La_{0.7}Sr_{0.3}MnO_3/BiFeO_3$ superlattice. Phys. Rev. B **92**(22), 224405 (2015)

Singh, S., Bhatt, H., Kumar, Y., Prajapat, C.L., Satpati, B., Kinane, C.J., Langridge, S., Ravikumar, G., Basu, S.: Superconductivity-driven negative

interfacial magnetization in $YBa_2Cu_3O_{7-\delta}/SrTiO_3/La_{0.67}Sr_{0.33}MnO_3$ heterostructures. Appl. Phys. Lett. **116**(2), 022406 (2020)

Sinova, J., Valenzuela, S.O., Wunderlich, J., Back, C.H., Jungwirth, T.: Spin Hall effects. Rev. Mod. Phys. **87**(4), 1213–1260 (2015)

The Nobel Prize in Physics 2007; https://www.nobelprize.org/prizes/physics/2007/press-release/ (2007).

Unguris, J.: Scanning electron microscopy with polarization analysis (SEMPA) and its applications. In: De Graef, M., Zhu, Y. (Eds.), Experimental Methods in the Physical Sciences, p. 167–XVI. Academic Press (2001)

van der Laan, G.: Soft X-ray resonant magnetic scattering of magnetic nanostructures. C R Phys. **9**(5), 570–584 (2008)

Wang, J., Neaton, J.B., Zheng, H., Nagarajan, V., Ogale, S.B., Liu, B., Viehland, D., Vaithyanathan, V., Schlom, D.G., Waghmare, U.V., Spaldin, N.A., Rabe, K.M., Wuttig, M., Ramesh, R.: Epitaxial $BiFeO_3$ multiferroic thin film heterostructures. Science **299**(5613), 1719–1722 (2003)
[PubMed]

Yang, H.X., Chshiev, M., Dieny, B., Lee, J.H., Manchon, A., Shin, K.H.: First-principles investigation of the very large perpendicular magnetic anisotropy at Fe/MgO and Co/MgO interfaces. Phys. Rev. B **84**(5), 054401 (2011)

Yu, X.Z., Onose, Y., Kanazawa, N., Park, J.H., Han, J.H., Matsui, Y., Nagaosa, N., Tokura, Y.: Real-space observation of a two-dimensional skyrmion crystal. Nature **465**(7300), 901–904 (2010a)
[PubMed]

Yu, P., Lee, J.S., Okamoto, S., Rossell, M.D., Huijben, M., Yang, C.H., He, Q., Zhang, J.X., Yang, S.Y., Lee, M.J., Ramasse, Q.M., Erni, R., Chu, Y.H., Arena, D.A., Kao, C.C., Martin, L.W., Ramesh, R.: Interface ferromagnetism and orbital reconstruction in $BiFeO_3$-$La_{0.7}Sr_{0.3}MnO_3$ heterostructures. Phys. Rev. Lett. **105**(2), 027201 (2010)

Žutić, I., Fabian, J., Das Sarma, S.: Spintronics: fundamentals and applications. Rev. Mod. Phys. **76**(2), 323–410 (2004)

© The Author(s), under exclusive license to Springer Nature Singapore Pte Ltd. 2024
R. S. Ningthoujam, A. K. Tyagi (eds.), *Handbook of Materials Science, Volume 2*, Indian Institute of Metals Series
https://doi.org/10.1007/978-981-97-4646-0_18

18. Introduction and Classification of Organic Molecule Based Magnetic Materials

Pramod Bhatt[1, 2] ✉ and S. M. Yusuf[1, 2] ✉
(1) Solid State Physics Division, Bhabha Atomic Research Centre, Mumbai, 400 085, India
(2) Homi Bhabha National Institute, Anushaktinagar, Mumbai, 400 094, India

✉ **Pramod Bhatt (Corresponding author)**
Email: prabhatt@barc.gov.in

✉ **S. M. Yusuf**
Email: smyusuf@barc.gov.in

Keywords Molecular magnet – Magnetic anisotropy – Single molecule magnet – Prussian blue analogues

18.1 Introduction to Magnetism

Magnetic materials are important and find many applications in our day-to-day lives. Some of the examples include motors, generators, loudspeakers, microphones, sensors, data storage devices, switches, frictionless

bearings, medical devices, magnetic separators, etc. Most of the above applications of magnetic materials are based on conventional or traditional magnets. These magnets fabricated using high temperature metallurgical methods are based on inorganic atoms, mostly transition metal or lanthanide metals. The bulk magnetic properties of such materials are mainly arising due to the various spin–spin interactions, and spatial arrangement of spin within the solids. Here, we provide an introduction related to the conventional bulk magnetism. In this section, different magnetic materials, magnetic interactions, magnetic anisotropy etc. are discussed.

(I) Origin of Magnetism

The unpaired electrons in the atoms or more precisely spin associated with unpaired electrons lead to the magnetic properties of the compound. The electron circulating in the outer shell produces its orbital magnetic moment, apart from the spin magnetic moment associated with it due to the electron spinning itself. Therefore, the origin of magnetism is inherently based on the atom's magnetic moment and material response to the applied magnetic field evaluated by susceptibility $\chi = M/H$, where M is the magnetization of the material and H is the applied magnetic field. Materials with positive and negative susceptibility are called paramagnetic and diamagnetic respectively.

(II) Types of Magnetic Materials

The materials are divided into mainly five categories (paramagnetic, diamagnetic, ferromagnetic, ferrimagnetic, and antiferromagnetic) depending upon their magnetic response to the applied magnetic field. Diamagnetic

materials are substances that exhibit a weak negative response to a magnetic field i.e., repelled by a magnetic field. This behaviour is due to the induced magnetic moment in the opposite direction to the applied field. The electron orbits are filled in diamagnetic materials, and hence no net magnetic moment exists. When an external magnetic field is applied, the electrons in diamagnetic materials rearrange their orbits to create a weak opposing magnetic field. The induced magnetic moment of these materials follows Lenz law *i.e*. the induced magnetic moment in diamagnetic materials opposes the change in the external magnetic field. The negative susceptibility of these materials is given by equation.

$$\chi = \frac{\mu_0 Z e^2 n \left\langle r^2 \right\rangle}{6 m_e} \tag{18.1}$$

where Z and n are the number of electrons and the number of atoms, The e and m_{e} are electronic charge and electronic mass. The mean square distance of the electrons from the nucleus is $< r^2 >$.

In the absence of a magnetic field, if spins do not interact with each other are called paramagnetic materials. The susceptibility of such materials follows Curie law as a function of temperature (T)

$$\chi = \frac{C}{T} \tag{18.2}$$

where C is a Curie constant (units: emu $\mathrm{K}\,\mathrm{mol}^{-1}$ in cgs). However, in the presence of a magnetic field, all the spins tend to align in the direction of the applied magnetic field, resulting in a net magnetic moment for the paramagnetic material. Within the proximity of spins, there is the possibility of their coupling either in a parallel or anti-parallel direction. The susceptibility increases for the parallel and decrease for the anti-parallel alignment which

can be expressed by Curie–Weiss law by incorporating the concept of Weiss's molecular field.

$$\chi = \frac{C}{T - \theta} \tag{18.3}$$

where, θ is a temperature constant (units: K), often referred to as the Curie–Weiss temperature. θ could be negative, zero, or positive. When θ = 0, the Curie–Weiss law is the same as the Curie law for the paramagnetic state. There is an interaction among neighboring spins in case when θ is non-zero, which can lead to a magnetic ordering. With a positive value of θ, the susceptibility is enhanced and all spins tend to align in parallel, however, with negative value of θ, spins align into anti-parallel and susceptibility is suppressed. The parallel (↑ ↑) arrangement of spins leads to the long-range ferromagnetic order, whereas an antiferromagnetic ordering is a consequence of the antiparallel (↑ ↓) arrangement between spins. A ferromagnetic material behaves like paramagnetic above Curie temperature and their susceptibility depends on the temperature according to the Curie-Wies law. A systematic representation of the coupling of the neighboring spins leading to various magnetic ordering is shown in Fig. 18.1.

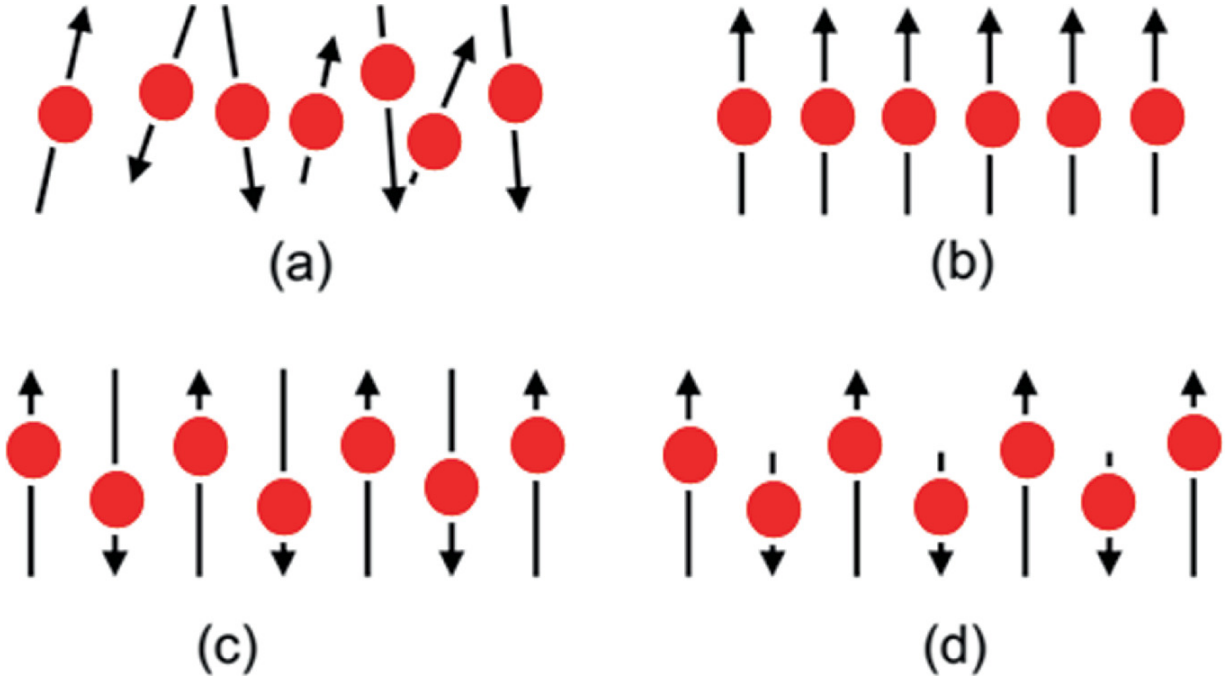

Fig. 18.1 Schematic representations on the spin–spin orientation behavior in (**a**) paramagnetic, (**b**) ferromagnetic, (**c**) anti-ferromagnetic, and (**d**) ferrimagentic materials

Antiferromagnetic materials remain in their magnetic ordering state below a certain temperature called Neel temperature and above that, they also behave like a paramagnetic one that obeys Curie-Wies law with negative value of θ. Ferrimagnetic ordering also arises from the same anti-ferromagnetic coupling but does not lead to a complete cancellation of the spin's magnetic moment. The ferrimagnetism can be observed in ferrite compounds.

The μ_{eff} {Bohr magnetons (μ_{B}), effective paramagnetic moment per formula unit} is directly proportional to the number of unpaired electrons and can be calculated using the Curie constant, C by

$$\mu_{eff} = \sqrt{8C}\mu_B \tag{18.4}$$

The μ_{eff} may be also calculated theoretically (spin only) as

$$(\mu_{eff})^2 = \sum [g^2 \{n.J\,(J+1)\}]\mu_B^2 \tag{18.5}$$

where n is the number of magnetic ions, g is the gyromagnetic ratio (~2), and J is the total angular momentum and summation Σ runs over all magnetic ions per formula unit.

(III) Temperature Dependent Magnetic Properties

The magnetic property of the material is temperature dependent and characterized by susceptibility measurement as a function of temperature. It is carried out using a combined examination of the (*i*) susceptibility (χ), (*ii*) susceptibility temperature product (χT) and (*iii*) inverse susceptibility (χ^{-1}) as a function of temperature. These measurements provide complete information of bulk magnetism of the material.

Figure 18.2 shows temperature dependent response curve of the magnetic susceptibility of paramagnetic, ferromagnetic, and antiferromagnetic materials. The antiferromagnetic materials show a maximum at low temperature which provides information on the strength of the magnetic interaction. The dimensionality of interactions is also related to the shape of the maximum. For example, 1-D and 2-D antiferromagnets show a rounded maximum, whereas a sharp peak appears for the 3-D antiferromagnet.

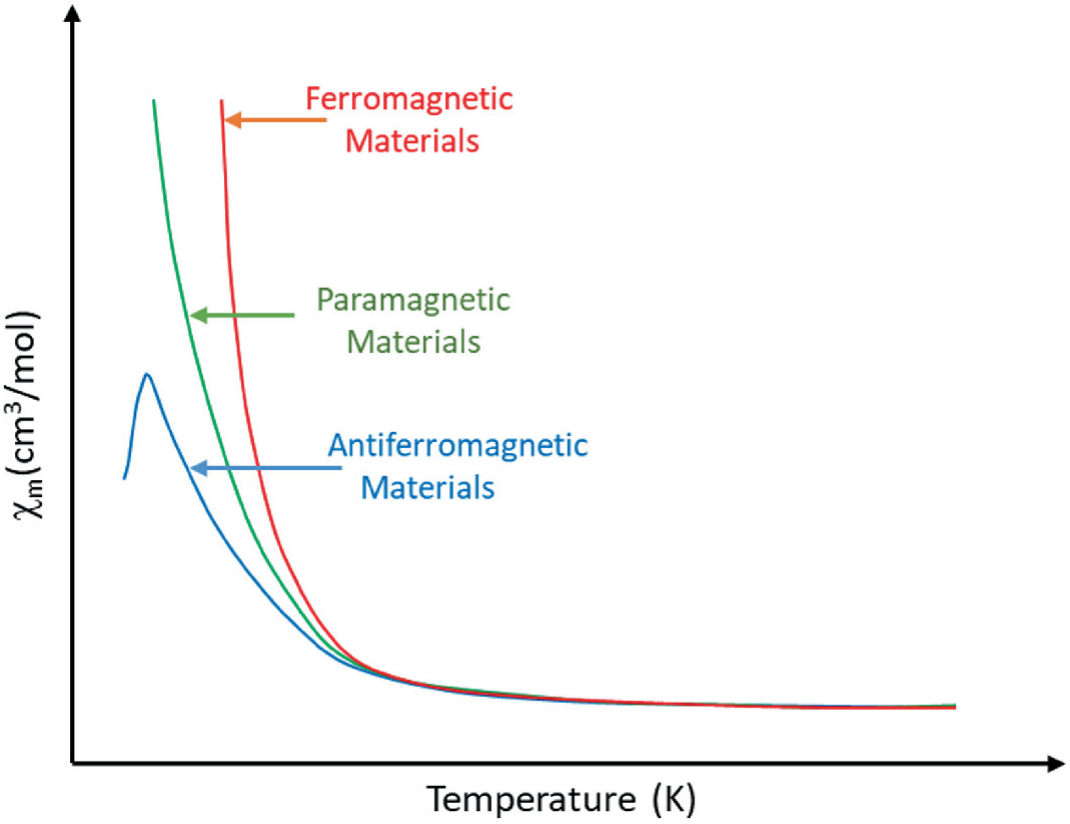

Fig. 18.2 Response of the magnetic susceptibility as a function of temperature for different magnetic materials

The susceptibility temperature product as a function of temperature for magnetic materials is shown in Fig. 18.3. The analysis of the susceptibility temperature product provides information about the nature of magnetic interactions present in the materials. For the paramagnetic compound, Fig. 18.3 shows that the temperature susceptibility product does not vary with temperature. At higher temperatures, mainly above their magnetic ordering temperature, cooperative magnetism for all the magnetic materials is due to their effective paramagnetic behaviour. The ferromagnetic compound shows the upward deviation in the curve concerning paramagnetic materials because the ferromagnetic interaction energy overcomes thermal energy at lower temperatures. However, for antiferromagnetic materials susceptibility temperature product shows downside curve with decreasing

temperature because magnetic moment for the compound decreasing to zero. Ferrimagnetic compounds first show slight downward curvature with decreasing temperature before the rise of the curvature in the upward direction mainly because correlation length increases.

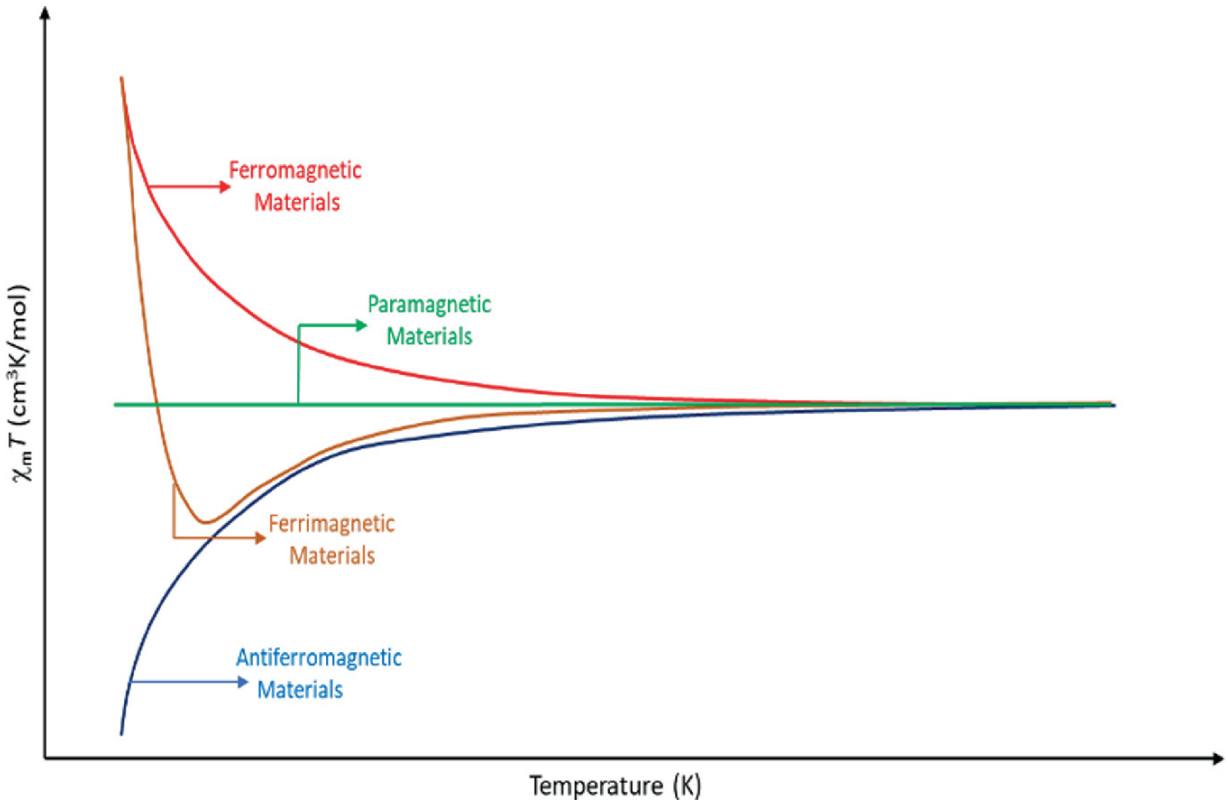

Fig. 18.3 Schematic plot for the response of the magnetic susceptibility temperature product as a function of temperature for different magnetic materials

The inverse susceptibility vs. temperature for the magnetic materials is shown in Fig. 18.4. For the perfect paramagnet, a linear line that intersects at zero is defined by the Curie law. For the magnetic materials, deviation from the linear relationship and the Curie law provide information on the magnetic properties. For example, ferromagnetic material shows a downward deviation, while antiferromagnetic materials show upward deviations with respect to paramagnetic materials. The θ(Weiss temperature constant) is proportional to the magnetic

interaction strength. Positive θ value shows ferromagnetic interactions, whereas the negative θ provides information about antiferromagnetic interactions.

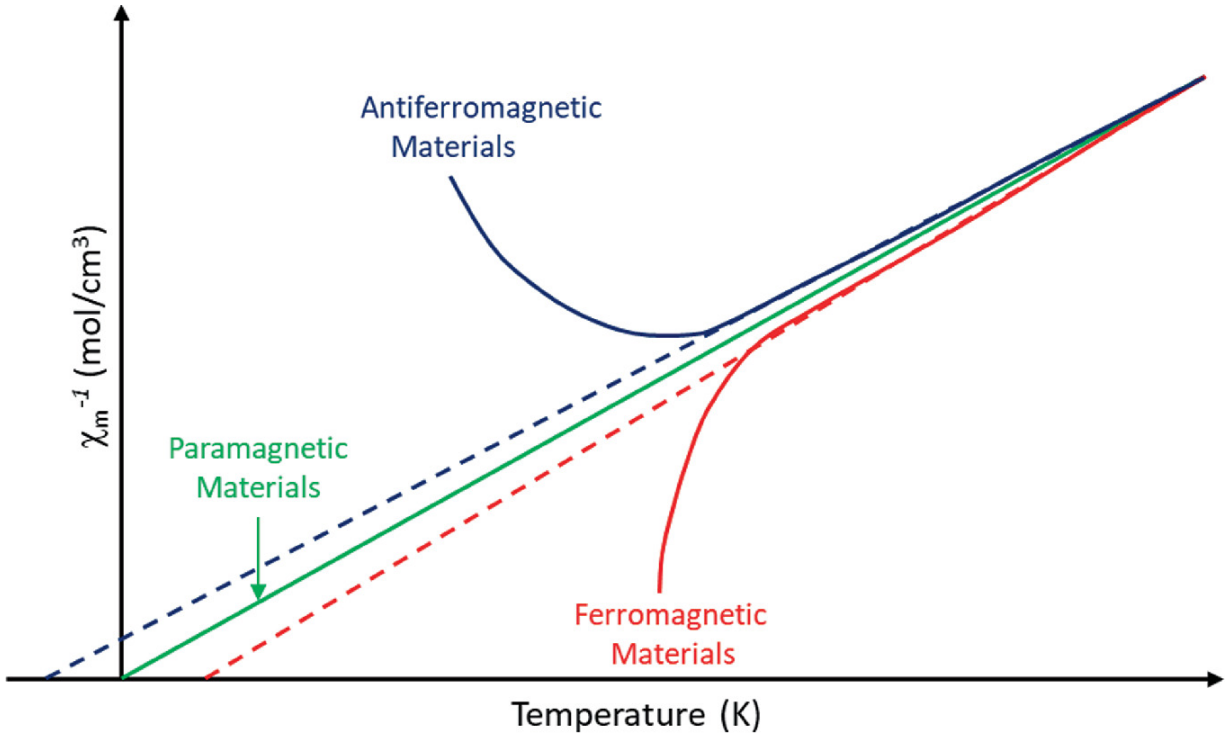

Fig. 18.4 Inverse of the magnetic susceptibility as a function of temperature for different magnetic materials. The dotted line shows the deviation for the paramagnetic materials

(IV) Magnetic Hysteresis

The magnetic hysteresis, which is a response of magnetization as a function of an applied magnetic field is one of the most distinctive features of the magnetic materials which provide information about their bulk magnetism. The observation of hysteresis is mainly related to the ferromagnetic and ferrimagnetic compounds which occur below their magnetic ordering temperature. The origin of hysteresis is due to the rearrangement of domain walls within the material. A bulk ferromagnet exhibits a hysteresis curve as shown in Fig. 18.5.

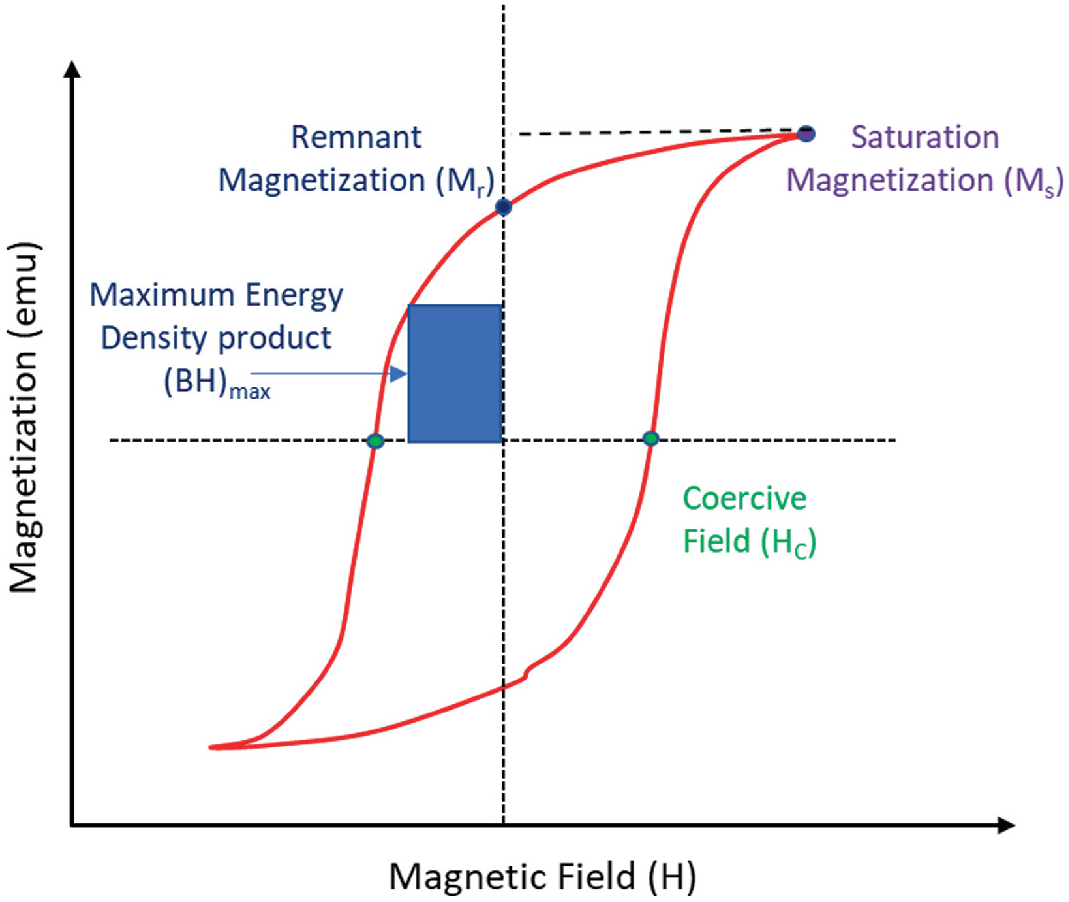

Fig. 18.5 Typical hysteresis curve for ferromagnetic or ferrimagnetic magnetic material

There are mainly three distinctive points $M_{s,}$ M_r and H_C in the hysteresis curve, which describe the magnetic properties of the compound. The M_s (saturation magnetization) is the value of magnetization which originated in the case where all the magnetic moments are aligned and saturate along the applied magnetic field. The M_r (remanent magnetization) or remanence is the value of magnetization i.e., residual magnetic field that left behind in a ferromagnetic material after removal of an external magnetic field. Similarly, the H_C (coercive field) is the value of field needed to bring back the magnetization of a compound to zero. Depending upon the value of high (> 500 G) and low (< 1 G) coercive fields, the magnetic

materials are known as hard and soft magnetic, respectively.

(V) Magnetic Exchange Interactions

To explain the magnetic properties of a material, the magnetic exchange (direct, indirect and super-exchange) interactions need to be understood. Because of the exchange interaction, a range of magnetic behaviors arises in magnetic materials. For example, both Fe and Ni, is ferromagnetic whereas, MnO behaves as antiferromagnetic. Similarly, LaCuO is a layered antiferromagnetic material, which becomes superconducting with doping. Few compounds do not show magnetic ordering but show frustrated magnetism. In order to explain all these magnetic properties, a classical approach does not work because in a classical system there is no thermal equilibrium magnetization. Hence, origin of such properties can be derived from a quantum mechanical theory of magnetism. The overlap of wave functions of different atoms results in an exchange integral or exchange energy, which is generally used when interplay between two magnetic moments arise.

The Heisenberg model is a model for describing the exchange interaction between spins and therefore ideal for modelling ferromagnetism. The interactions between two electron spins (i and j) are expressed by the Hamiltonian (H) as.

$$H = -\sum_{ij} 2JS_i.S_j \tag{18.6}$$

where, $\sum_{ij}$ is the directional independent summation of all neighbouring spins S_i, S_j *and* J is the exchange constant. If anisotropy (due to crystal fields) arises in the exchange parameter J. The Hamiltonian of directional dependent

spins (the anisotropy is along only one direction), can be described as.

$$H = -\sum_{ij} 2J\{(S_i^z.S_j^z + \gamma(S_i^y.S_j^y + S_i^x.S_j^x)\} \quad (18.7)$$

where, γ is a spin anisotropy parameter, when $\gamma = 1$, the same value of exchange will exist for all pair of spins on adjacent sites *i* and *j*. The case when $\gamma = 0$, only z component of the spin is important, known as Ising like spins. For γ» 0, "*xy*" or 2-D model exists. This equation has been extensively used for the study of the magnetic phenomenon in crystalline systems. For the case of molecule based magnetic materials, exchange and random anisotropy terms has also been added to the Hamiltonian of the Heisenberg model due to the disordered nature of the compounds. Hence, the Eq. (7) in which isotropic interaction between spins are modified due to randomness as follows.

$$H = -\sum_{ij} 2J(S_i.S_j) - D_r \sum_i (n_i.S_i)^2 - D_C \sum_i (N_i.S_i)^2 - g\mu_B \sum_i (H.S_j) \quad (18.8)$$

In the above equation, the first term is exchange integral, second is random magnetic anisotropy, third is constant magnetic anisotropy, and the fourth term is the Zeeman interaction which originated due to the interaction between an external field and the magnetic moments. The parameters D_r, D_c are anisotropy constants and n_i, N_i are unit vectors in the direction of local and constant anisotropy.

(VI) Magnetic Anisotropy

The directional dependent magnetic properties are described by the magnetic anisotropy. In the absence of anisotropy, there will be no preferable crystallographic

direction for which the magnetic moment aligns in a particular direction, i.e., the magnetization of the material will be same in all directions irrespective of the direction of the applied magnetic field. These types of materials are known as magnetic isotropic. In contrast, if the material in the applied magnetic field is found to be easier or harder to magnetize in a particular crystallographic direction with respect to the direction of the applied magnetic field are known to be anisotropic. There are generally two easiest directions to magnetize the material, which are 180° rotation apart known as easy and hard axis respectively. Along the easy axis, small amount of magnetic field is required to get the saturation whereas, larger magnetic field is needed to reach the saturation magnetization along the hard axis. In ferromagnetic materials, the origin of hysteresis is due to magnetic anisotropy, without it, a ferromagnet is superparamagnetic. In other words, in the magnetic material, a certain amount of energy is needed to bring the material back from the demagnetized state to the saturated state and this energy is dependent on a certain preferred direction in the crystal in which the magnetic field is applied. The free energy needed to break up such symmetry is known as magnetic anisotropy. It can be intrinsic (due to magneto-crystalline) or extrinsic (anisotropy induced by external effect such as elastic stress or some shape effect). In order to design a good molecular magnet, the molecular compound should possess a magnetic anisotropy. Microscopically magnetic anisotropy originates from the large coupling between orbital and spin angular momentum {spin–orbit coupling (SOC)} which gives rise to zero-field splitting (ZFS) of the magnetic sublevels. The magnetic anisotropy also yields slow magnetic relaxation of the compound. For the ferromagnetic materials, the formation of magnetic domains is originated by minimizing the total free energy of the compound. The free energy of the magnetic material is

a sum of various energies that can be presented as exchange, anisotropy, Zeeman, and demagnetizing energies.

$$E = E_{\mathrm{ex}} + E_{\mathrm{an}} + E_{\mathrm{Z}} + E_{\mathrm{d}} \tag{18.9}$$

where, E_{ex} is the exchange energy and E_{an} is anisotropy energy, E_z is the Zeeman energy and E_{d} is the demagnetization energy. The exchange energy is responsible for the basic interaction which causes cooperative magnetic ordering, represented by the Hamiltonian.

$$H = -\sum_{ij} 2JS_i.S_j$$

The magnetic anisotropy energy is the combination of different anisotropies like magnetocrystalline (E_{MC}) anisotropy, shape (E_{S}) and surface and interface anisotropy (E_{IS}).

$$E_{\mathrm{an}} = E_{\mathrm{MC}} + E_{\mathrm{S}} + E_{\mathrm{IS}} \tag{18.10}$$

The magneto-crystalline anisotropy is dependent on the crystallographic axis. For cubic crystals, the magnetocrystalline anisotropy energy is given by:

$$E_{MC} = K_1 \left({\alpha_1}^2{\alpha^2}_2 + {\alpha_2}^2{\alpha^2}_3 + {\alpha_4}^2{\alpha^2}_5 1\right) + K_2{\alpha_1}^2{\alpha^2}_2{\alpha_3}^2$$

where K_1 and K_2 are anisotropy constants. The α_1, α_2, and α_3 are directional cosines of the magnetization vector with respect to the main crystallographic direction. The shape anisotropy (E_{S}) arises due to the to the anisotropic shape of the magnetic compound particularly in thin films. Further, the broken symmetry at surfaces of magnetic thin films also induces surface and interface anisotropy. It is expressed as.

$$E_{\mathrm{IS}} = K_{\mathrm{S}}\mathrm{Sin}^2\theta$$

where θ is the angle between the magnetization and the z axis, and K_S the surface anisotropy constant.

(VII) Crystal Field Splitting

The splitting of energy levels occurs when the orbital is situated in a close vicinity of higher electron density of ligands. The interaction between metal ion and ligands are electrostatic in nature. If the ligands are negative in nature, the interaction will be ion-ion interaction, whereas ion–dipole interaction exist if the ligand is neutral.

Most common geometries observed in coordination compounds are octahedral and tetrahedral. In octahedral complexes, six ligands surround the central metal ion are arranged in an octahedral shape, whereas in the case of tetrahedral complexes, four ligands are arranged in a tetrahedral shape around the central metal ion. Let us consider the case for octahedral geometry as shown in Fig. 18.6, when the metal centre is away from ligand, all five *d*-orbitals are in the same energy (degenerated). When the ligand approaches the metal centre, the *d*-orbitals become differently influenced due to the electrostatic repulsion resulting in splitting of energy levels. The *d* orbital spilts into the new orbitals (e_g and t_{2g}), however negative charge of ligand leads to destabilization. The $d_{x2\text{-}y2}$ and d_z^2 orbitals possess higher energy in contrast to d_{xy}, d_{yz}, and d_{xz} orbitals. The difference in energy between e_g ($d_{x2\text{-}y2}$ and d_{z2}) and t_{2g} (d_{xy}, $d_{xz,,}$and d_{yz}) is splitting energy (Δ). A higher value of Δ suggests a stronger metal ligands coordination bond. In the case of tetrahedral geometry, the splitting of *d* orbitals is depicted in Fig. 18.6. The electrons residing in $d_x^2\text{-}_y^2$ and d_z^2 orbitals experience weak repulsion compared to electrons residing in d_{xy}, d_{yz}, and d_{xz}

orbitals. Hence, the d_{xy}, d_{yz}, and d_{xz} orbital are in higher energy than d_{x2-y2} and d_{z2} orbitals. The crystal field splitting in a tetrahedral compound is generally lower than that of the octahedral compounds. Based on the field splitting parameter Δ, the compounds are classified as low-spin and high-spin complexes (Fig. 18.7). The compounds which show high crystal field splitting value (Δ) are known as low-spin complexes whereas, smaller value of Δ results in high-spin complexes. In Prussian blue analogues (PBAs) compounds, represented by, $X_jA_k[B(CN)_6]_l{\cdot}mH_2O$, *A* and *B* is in high and low spin state respectively. The *A* and *B* are surrounded by –N≡C– and –C≡N– units octahedrally as shown in Fig. 18.7. Here, –C≡N– ligand induces a strong field to split the 3*d* orbitals of the metal ions. Since the length of *B*–C bonds is smaller to *A*–N bonds, *B* atom will experience a stronger field (larger Δ) compared to *A* atoms. Hence, atom *B* will be in low spin state as splitting energy will be higher than the pairing energy.

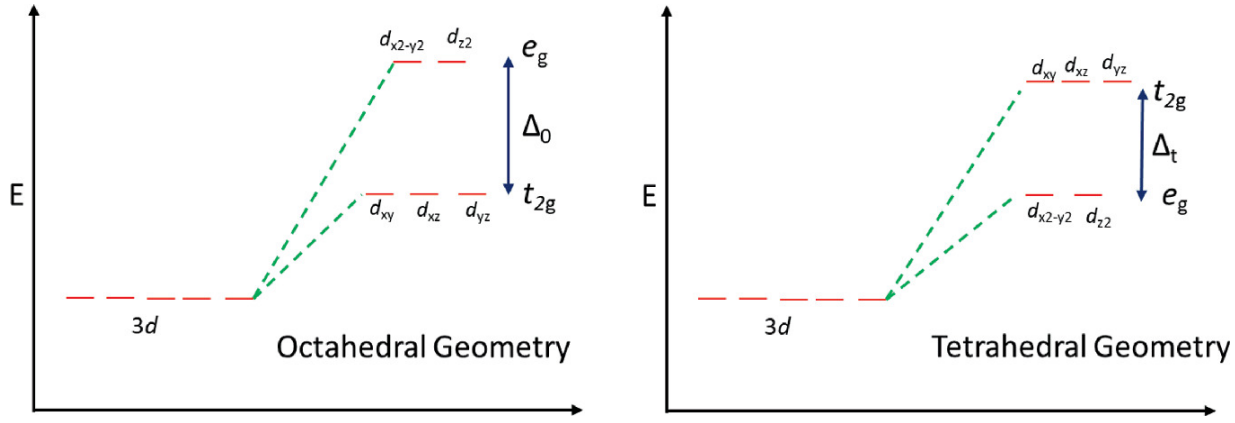

Fig. 18.6 Crystal field splitting of 3d states in octahedral and tetrahedral coordination geometry

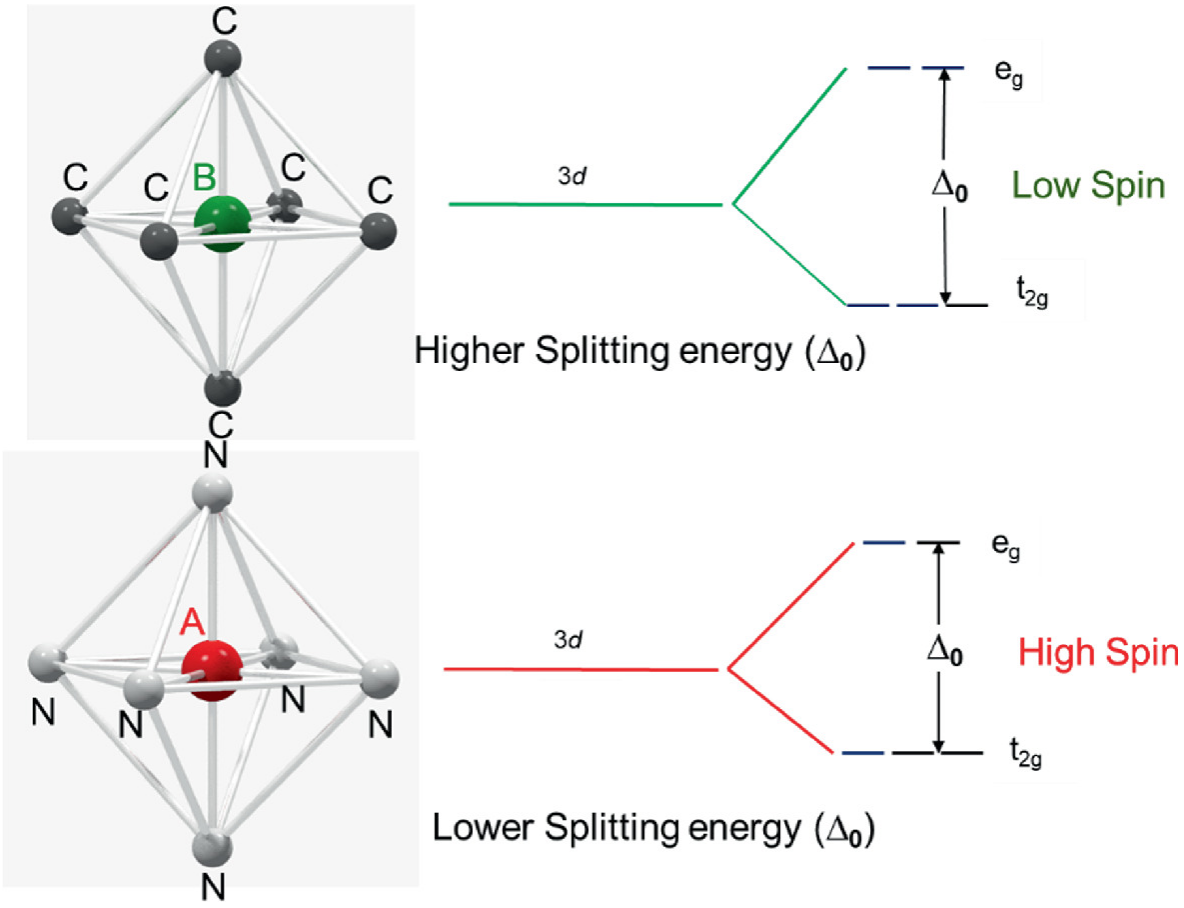

Fig. 18.7 Low spin and high spin state of metal ions in octahedral geometry of PBAs compounds

18.2 Classifications of Molecule Based Magnetic Materials

The materials creating their own persistent magnetic fields, known as permanent magnets are becoming very important in our day-to-day life and in the development of modern society. Those magnets are one of the main components like in computer hard drives to store information on magnetic media, in electricity production, in automobile industry for electric vehicles, in medical science and telecommunications industry etc. Therefore, due to their vast range of possible applications, there is always been a quest for design and development of new magnets with

better efficiency, better performance, low weight, low cost of synthesis. Most of the magnets used so far for technological applications are based on mainly inorganic metals or combinations of more than two inorganic metals in alloy form. However, recently organic or molecule-based magnets have also shown great interest for their unusual magnetic properties and possible technological applications. The first molecule-based magnet was discovered in 1986(Miller et al. 1986) by Prof. Miller and Prof. Epstein. Despite the material was magnetically ordered at low temperature, a novel pathway of synthesising new class of molecule-based magnets has been demonstrated for the first time. Later in year 1991, other major discoveries like first purely organic magnet (Tamura et al. 1991), first room temperature molecular magnet (Manriquez et al. 1991), and first fullerene based purely organic magnet (Allemand et al. 1991) were also reported. All these research activities then opened a new area of magnetism presently know as molecular magnetism (Kahn et al. 1993). The molecular compound can represent as a discrete magnetic unit which can be operated without the need for any long-range ordering. The study of magnetic properties of the paramagnetic metal center in combination with organic ligand or molecular compound is the primary objective of the field of molecular magnetism. It is a multidisciplinary research field which attract great interest for the chemists, physicists, and materials scientists extensible (Benelli and Gatteschi 2015). The ability to tailor the magnetic properties with tunability of their structural and chemical properties results in large number of advantages of molecule-based magnets over conventional magnets. For example, molecule-based magnets are light weight in nature due to their low density, flexible, transparent, and easy synthesis. Moreover, due to their low-temperature synthesis as compared to energy-consuming high-temperature metallurgical synthetic

methodologies, molecular magnets offer low-cost manufacture over conventional magnets.

Lattice structure of various dimensionality like 0-D (single), 1-D (chain), 2-D (layer) and 3-D (open framework) can be synthesized using appropriate choice of molecular ligand or building blocks. Usually, molecular magnets are classified into two main categories: (i) purely organic magnets, and (ii) organic–inorganic hybrid magnets as shown in Fig. 18.8. In the case of purely organic magnets, the spin will reside solely on the organic ligands, whereas in the case of hybrid magnets, the spin carriers will either be active or passive. Active means spin will reside on both of the inorganic and organic ligands whereas passive means the spin will reside only on the inorganic part. These are low dimensional molecular structures which allow us to study exciting and unusual phenomena of quantum magnetism, condensed matter physics and quantum information science. Both experimental and theoretical research have been motivated to find their possible application in quantum computing. The main focus has been given on the hybrid class of molecule-based magnets which are now presented in more details.

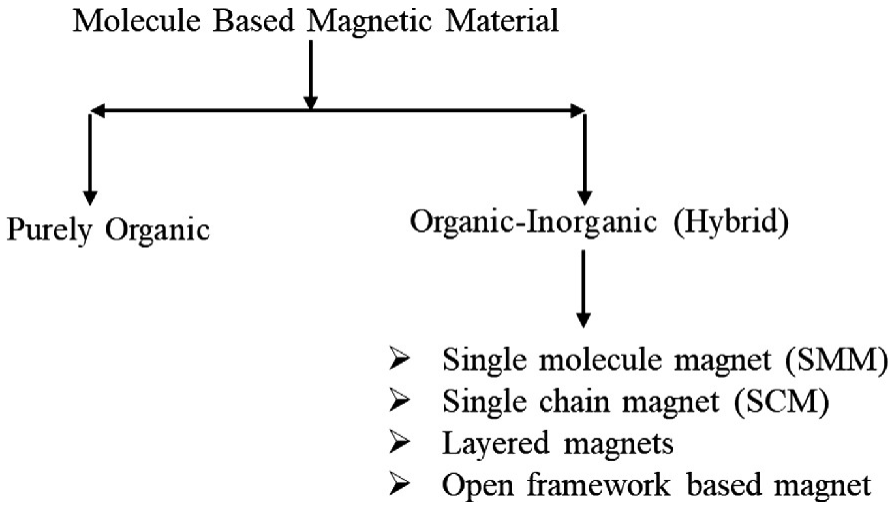

Fig. 18.8 Classifications of molecular magnets

(I) Single Molecule Magnet (SMM)

The molecular compound dodecametallic manganese-acetate cage $[Mn_{12}O_{12}(ac)_{16}(H_2O)_4]$ (where ac is acetate = O_2CCH_3) discovered by Sessoli and co-workers is the first compound which behaves as a single molecule magnet (Sessoli et al. 1993). As the name suggests the SMM compound Mn_{12}ac contains 12 metallic centers of Mn with mixed oxidation states. Four Mn are in Mn^{IV} oxidation and eight Mn are in Mn^{III} ions as shown in Fig. 18.9. The $Mn_{12}O_{12}$ core is surrounded by 16 acetate groups in this compound. The magnetization curve, recorded at low temperature, shows steps due to quantum tunneling of magnetization (Thomas et al. 1996). It's an example of slow relaxation of magnetization, which does not occur in the compounds having bulk magnetism.

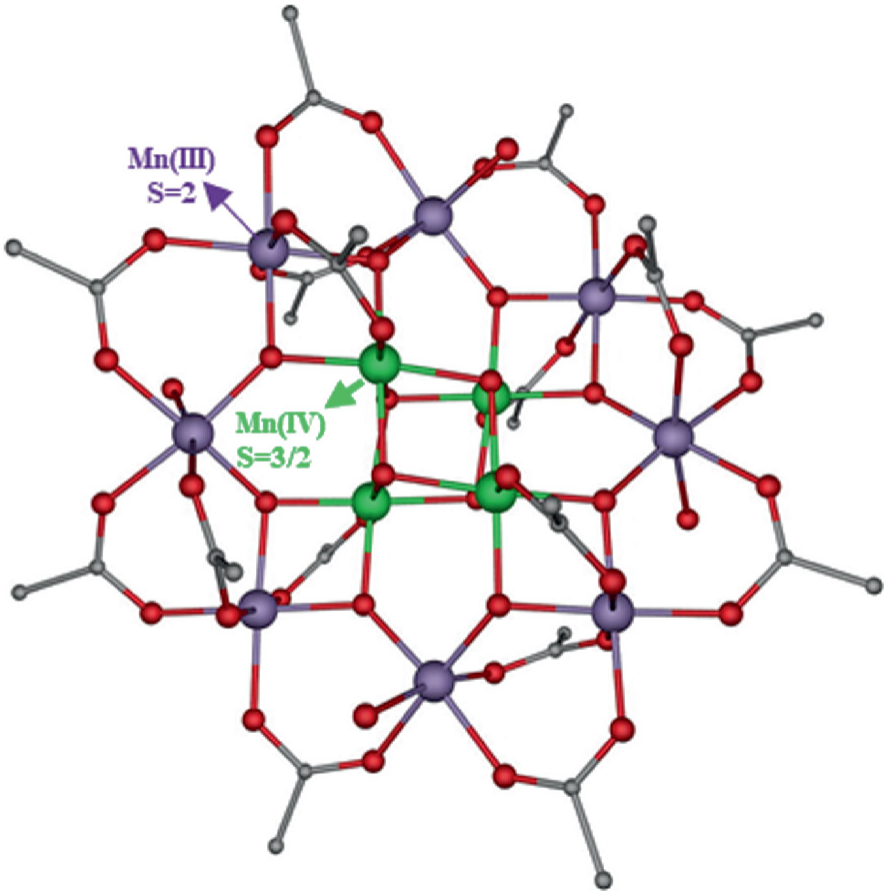

Fig. 18.9 Crystal structure of SMM compound Mn_{12}-ac (**a**). This figure has been adapted with permission from Elsevier publishers reference (Zabala-Lekuona et al. 2021). Creative common license

It shows magnetic properties at very low temperatures, however, it retains its magnetization for long periods of time in the absence of an external magnetic field. Since, the unusual properties of SMM were accessible at very low temperature, the possible application in molecular spintronics was not feasible. Moreover, the design and development of efficient SMM was also difficult, however, offering numerous possible future applications (Zabala-Lekuona et al. 2021). For example, SMMs offer the realization of the smallest practical unit for magnetic memory of quantum computer due to their large, bi-stable spin anisotropy. Another application for SMMs could be in the field of magnetocaloric refrigerants. The important parameter for SMM is the blocking temperature (T_B), a

highest temperature at which SMM displays magnetic hysteresis of molecular origin. Similarly, the coercive field (H_C), is the strength of the magnetic field required to reverse the magnetization back to zero after saturation, and anisotropy/energy barrier (U_{eff}) the amount of effective energy required to reverse the SMM back into a paramagnetic state are also important. Among all, U_{eff} is a crucial parameter for characterizing SMM. It can be also described by the Ising-type magnetic anisotropy. The zero-field splitting (D), and the total spin (S), is expressed as $U_{eff} = |D|S^2$ (integer spin) and $|D|(S^2 - 0.25)$ for non-integer total spin.

There is an antiferromagnetic interaction among the metallic centers and different oxidation states of Mn give rise to a ground state of the compound according to $(2S + 1)$ where S is the total spin value of 10 *i.e*. 21-fold degenerate. However, 21 sublevels are separated by the by the energy barrier DS^2. The axial anisotropy is related to the zero-field splitting (ZFS) which is responsible for the separation of their sublevels as shown in Fig. 18.10.

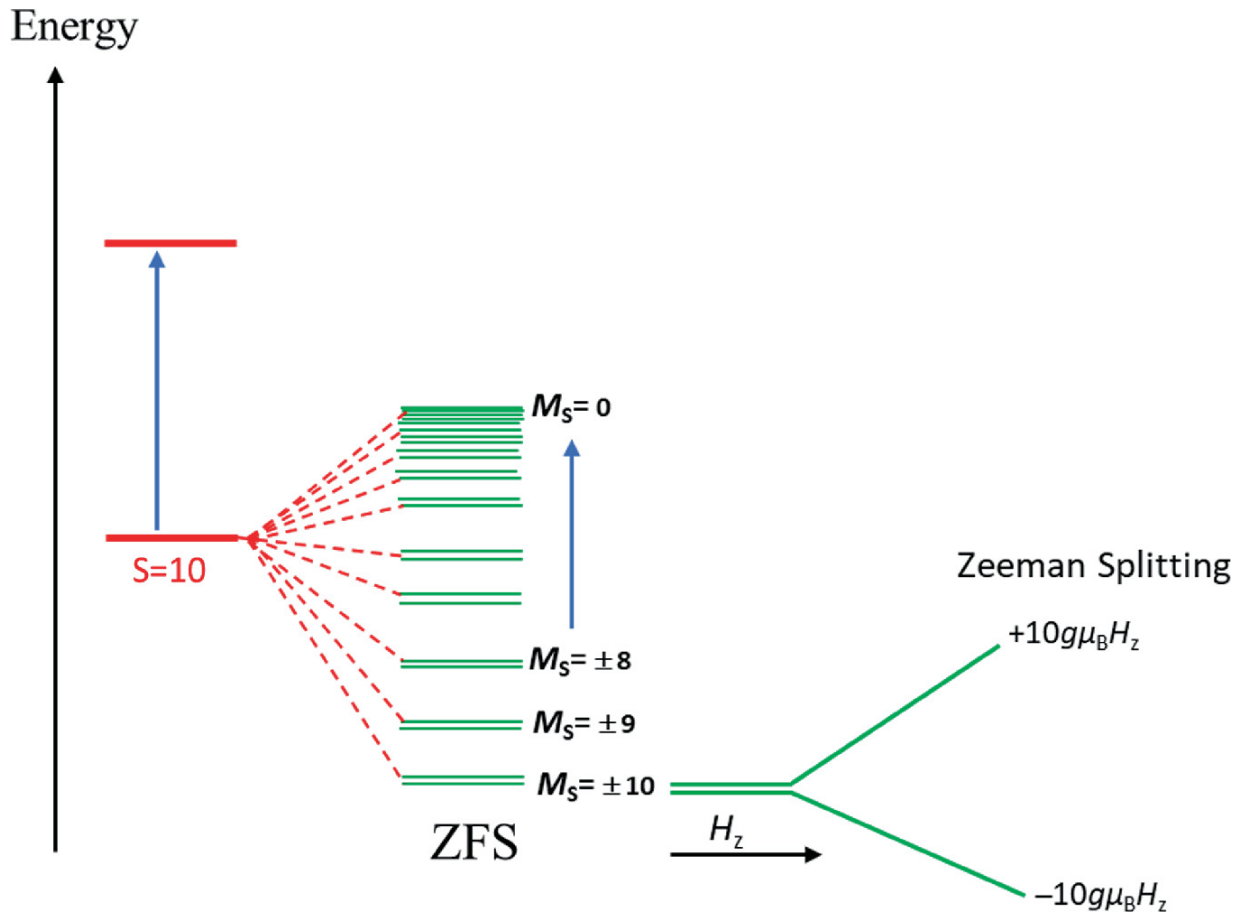

Fig. 18.10 Schematic representation of qualitative energy splitting diagram of Mn_{12}-ac compound. Ground spin state (S = 10) is split by an axial zero-field splitting (ZFS) and ground doublet $M_S = \pm 10$ by Zeeman interactions. This figure is adapted and redrawn with permission from Elsevier publishers Ref No. (Zabala-Lekuona et al. 2021). Creative common license

Consider the cases when (i) $D < 0$, all the energy levels will be stable and will have higher value of magnetization $M_S = \pm 10$. The magnetization of sublevel of each value of M_S will have a particular orientation along the axial anisotropy axis so two states $M_S = 10$ and $M_S = -10$ will exist. The energy, that is the difference between the highest excited state and the ground state equivalent to the energy barrier (U), required to switch from one state of magnetization ($M_S = 10$) to the other state of magnetization ($M_S = -10$). However, for the case of $D > 0$, the sublevels will orient in a reverse direction resulting in unstable

sublevels and lower value of magnetization $M_S = 0$. In this case, only one state of magnetization exists (Neese and Pantazis 2011).

It can be also understood that in the case of the absence of the external magnetic field, all the sublevels $M_s = \pm 10$ will have the same energy and will be equally populated as shown in Fig. 18.11. When the external magnetic field is present, one of the M_S sublevels is stabilized as compared to the other resulting presence of magnetization. Once the magnetic field is removed, the sublevels tend to achieve the original positions, however, it depends upon the thermal energy ($k_B T$). If thermal energy is higher than the barrier energy (U), the material will tend to achieve the equilibrium state between the two orientations (positive and negative). However, if thermal energy is lower than U, which usually occurs at lower temperature ($T < T_B$), the magnetization will be in the blocked state.

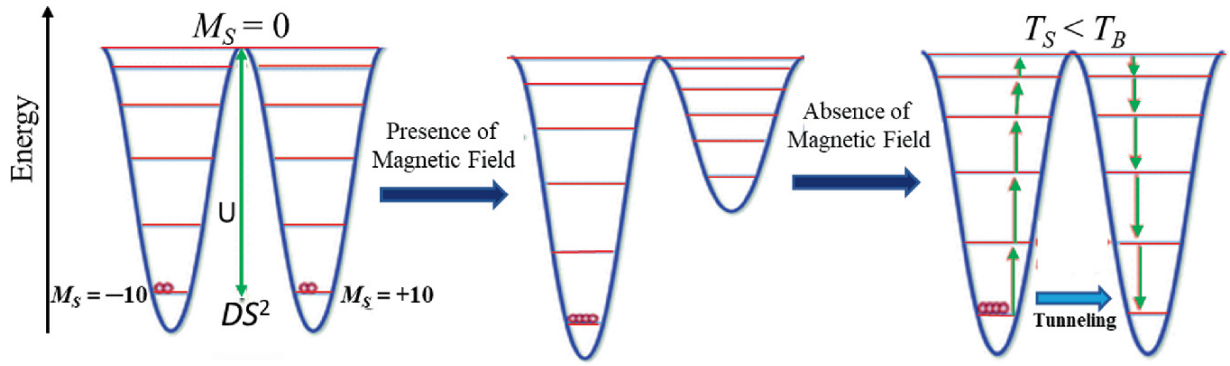

Fig. 18.11 Schematic diagram representing the magnetization relaxation processes in a single molecule magnet. Magnetization equilibrium in the presence, absence and blocking state of external magnetic field. This figure is adapted and redrawn with permission from Elsevier publishers Ref No. (Zabala-Lekuona et al. 2021). Creative common license

There were many efforts to increase the U_{eff} (either by increasing D or S) by synthesizing various types of SMMs. For example, for the case like compound $Mn_{12}Ac$ have U_{eff}

of 51 cm^{-1}, because of the value of D (-0.51 cm^{-1}) and $S = 10$. Similarly, for the SMM compound hexametallic manganese (III) {Mn_6} or $[Mn_6O_2(sao)_6(O_2CPh)_2(EtOH)_4]$ where $saoH_2$ = 2-hydroxybenzaldehye oxime, exhibit $U_{eff} = 62$ cm^{-1} due to the values of $D = -0.43$ cm^{-1} and $S = 12$ (Milios et al. 2007). These examples show that the compounds which have a high spin value would have high U_{eff}. However, that is not always true because for the compound like {Mn_{19}} or $Mn_{19}[Mn_{19}O_8(N_3)_8(HL)_{12}(MeCN)_6]^{2+}$, where ($H_3L$ = 2,6-bis(hydroxymethyl)-4-methylphenol), which has a large total spin of $S = 83/2$, does have the lower value of $U_{eff} = 4$ cm^{-1}(Ako et al. 2006). This is due to the high symmetry ($D = 0$) of M_{19} molecules in which anisotropies on the individual manganese (III) cancel out each other resulting lower U_{eff}.

The SMM based on cobalt (II) complex $[Co(hfpip)_2\{D_2py_2(TBA)\}]_2$, where hfpip is hexafluoro-4-(4-tert-butylphenylimino)-2-pentanoate and D_2py_2(TBA) is a diazo-dipyridyl ligand exhibiting higher U_{eff} of 67 cm^{-1}(Yoshihara et al. 2008). The series of linear two-coordinate complexes of iron (II) also exhibit larger barriers of 104 – 181 cm^{-1}. That means even though if the total spin of the compound is higher, there should be some anisotropy present in the compound. In this regard, SMM with higher single ion anisotropy has been synthesized and investigated across the periodic table including lanthanides and actinides. SMMs using coordination compounds of the *d* and *f*-elements have shown great advance particularly for the *f* element-based compounds in the field of molecular magnetism (Woodruff et al. 2013). Hybrid SMM based on *d* and *f* elements was also investigated. A list below is related

to all about SMMs, investigated for their magnetic properties till date.

SMMs	Type	Blocking Temp. (K)	U_{eff} (cm^{-1})	Ref
$[Mn_{12}O_{12}(OAc)_{16}(H_2O)_4]$	cluster	3	42	Sessoli et al. 1993)
$Tb(Cp^{iPr5})_2$ Cp^{iPr5} = penta-iso-propylcyclopentadienyl	single-ion	52	1205	Gould et al. 2019)
$(Cp^{iPr5})Dy(Cp^*)]^+$ Cp* = pentamethylcyclopentadienyl)	single-ion	80	1541	Guo et al. 2018)
$[Dy(Cp^{iPr4Me})_2][B(C_6F_5)_4]$	single-ion	62	1468	Randall McClain et al. 2018)
$[Dy(Cp^{ttt})_2][B(C_6F_5)_4]$*	single-ion	56	1219	Goodwin et al. 2017)
$[Dy(Cp^{iPr4}H)_2][B(C_6F_5)_4]$	single-ion	17	1285	Goodwin et al. 2017)
$[Dy(Cp^{iPr4}Et)_2][B(C_6F_5)_4]$	single-ion	59	1380	Goodwin et al. 2017)
$[L_2Dy(H_2O)_5][I]_3{\cdot}L_2{\cdot}(H_2O)]$ L = $(^tBuPO(NH^iPr)_2)]$	single-ion	2.4	452	Gupta et al. 2016)
$[K(18\text{-crown-}6)THF)_2]$ $[\{[(Me_3Si)_2N]_2(THF)Tb\}_2(\mu\text{-}\eta^2{:}\eta^2\text{-}N_2)]$	cluster	14	227	Rinehart et al. 2011)
$[Dy(OtBu)_2(py)_5][BPh_4]$	single-ion	12	1264	Ding et al. 2016)
$[Dy(Cp^{iPr5})_2][B(C_6F_5)_4]$	single-ion	56	1334	Goodwin et al. 2017)
$[Dy(Cp^{iPr5})(CpMe_5)][B(C_6F_5)_4]$	single-ion	67	1541	Guo et al. 2018)

Over the years, it has been seen that the research for achieving higher blocking temperature is proceeding with

tremendous pace. The $T_B = 60–80$ K for Dy based SMM has been achieved from 3 K (first SMMs). There is more progress for synthesis of new compounds with high blocking temperatures based on di-nuclear systems by manipulating a magnetic coupling between metal ions using radicals (Vieru et al. 2023).

(II) Single-Chain Magnet (SCM)

$[Co^{II}(hfac)_2(NITphOMe)]$, (Hhfac = hexafluoroacetylacetone, NITPhOMe = 4′ − methoxy-phenyl-4,4,5,5-tetramethylimidazoline-1-oxyl-3-oxide), first single − chain magnet (SCM)(Caneschi et al. 2001) was reported by Gatteschi in 2001(Caneschi et al. 2001). The origin of magnetism was purely molecular in nature and was observed below 4 K. The SCMs have a greater potential as compared to SMM as relaxation of magnetization is controlled by the spin dynamics emergences due to spin–spin correlation at lower temperature. The antiferromagnetic interactions between cobalt (II) and the NITPhOMe radical result in the ferrimagnetic nature of the compound. The chains therefore behave as 1-D ferrimagnets, because of the non-compensation of the magnetic moments of the cobalt (II) centre and the radical. The unit cell structure of the compound is representing a chain like magnets. The magnetic study shows that the susceptibility below 50 K is strongly anisotropic with easy axis of magnetization along the trigonal axis resulting in Ising-type anisotropy. There are many reports available on the SCM based on 3*d* and 4*f* metal ions with unusual magnetic properties (Gatteschi and A. Vindigni in Single-Chain Magnets, 2008). One of the examples is the $[M(hfac)_3(NITPhOPh)]$, rare-earth-based SCM, where PhOPh is nitronyl-nitroxide radical (2,4′-benzoxo-4,4,5,5-

tetramethylimidazoline-1-oxyl-3-oxide) and $M =$, Gd, Eu, Tb, Ho, Er, Yb or Dy, and with tailoring of anisotropy[24c]. The magnetic property and crystal structure of the [Dy(hfac)$_3$NITPhOPh] and [Tb(hfac)$_3$(NITPhOPh) compound is shown in Fig. 18.12.

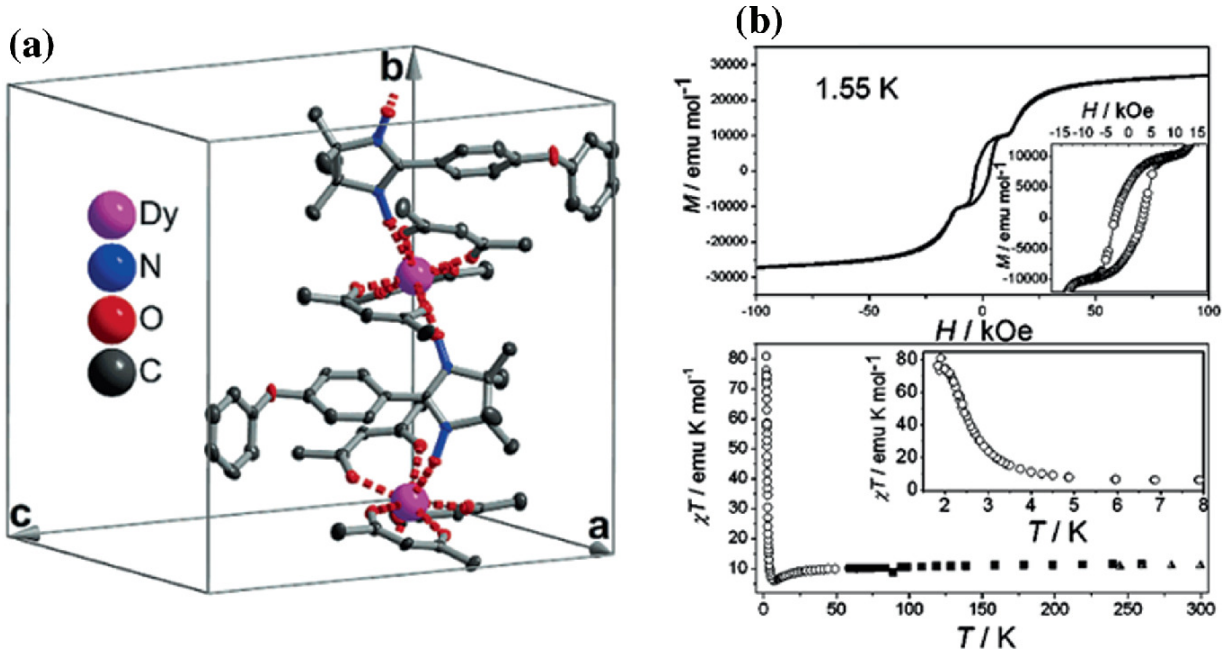

Fig. 18.12 Unit cell of SCM compound [Dy(hfac)$_3$NITPhOPh] (**a**), and magnetization with respect to field and temperature of the [Tb(hfac)$_3$(NITPhOPh)compound (**b**). This figure is reprinted with permission from reference [24c].

Copyright © 2006, American Chemical Society

The blocking of the magnetization is common in both SMMs and SCMs, however, basic physics and mechanisms of slow relaxation of SCMs is somewhat different from the SMM. In order to get the signature of the SCM behaviour, there should be a large easy-axis magnetic anisotropy and minimum interchain magnetic interactions. The magnetic anisotropy of the spin carriers can influence the SCM property. If spin centres are isotropic in nature, Heisenberg chains are to be expected. Whereas, if the metal centres are anisotropic in nature, the chain are Ising type. The NIT (nitronyl-nitroxide) radical act as a bridge between metal

ions (3*d* or 4*f) and is* one of the most studied classes of SCM. The NIT ligand facilitates magnetic interaction along the chain and effectively isolates each chain through the presence of its substituting organic groups.

SCM based on the metal and π functional group, coordinated with oxalate ligand are found to be interesting (Huang et al. 2002). The reason is that the occurrence of spontaneous magnetization in π − functional containing magnetic materials is a rare phenomenon to observe. The physical properties are dependent upon the π − π interaction, and affecting the magnetic interaction between the metal centres (Giri and Saha 2011). The variation in ligands with π − π interactions, coordinating ligand, their coordinating angle result in ferromagnetic and antiferromagnetic interaction. 1–D cobalt-radical coordination magnet {[Co(hfac)$_2$,BPNN] (BPNN)p-butoxyphenyl-NN)} is studied and found to have a huge coercivity (Ishii et al. 2008). Figure 18.13 shows the magnetization as a function of temperature and field of the compound.

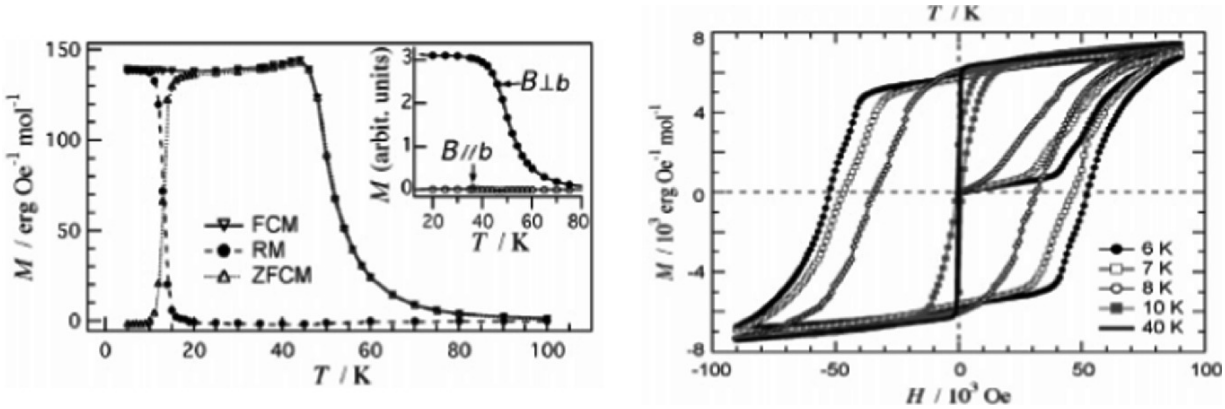

Fig. 18.13 FC and ZFC along with remanent magnetization of the compound {[Co(hfac)$_2$,BPNN] under magnetic field of 5 Oe. Inset shows FC magnetization under 100 Oe applied magnetic field in the directions parallel and perpendicular to the b-axis. Hysteresis loops of the compound measured at various temperatures. This figure has been produced with permission from reference (Ishii et al. 2008).

Copyright © 2008, American Chemical Society

Recently, molecular magnets having π–π interactions between ligands are also studied. One such example is phenanthroline and oxalate ligands-based magnets $[\{Fe^{II}(\Delta)Fe^{II}(\Lambda)\}_x(ox)_2(phen)_2]$. This compound is found to exhibit the magnetic ordering below 10 K (Li et al. 2006). Other magnet with π–π interaction is also found to exhibit room temperature magnetic ordering (Giri and Saha 2011). The π–π interactions among ligands may provide long–or–short range magnetic interactions resulting in an unusual magnetic state of the materials. Nevertheless, the magnetic properties do not only depend upon the exchange interactions but also upon the intermolecular or intramolecular interactions mediated through the connected ions.

In the studied chain molecular magnets, mainly (*i*) interaction mediated by hydrogen bonding (Maspoch et al. 2002) and (*ii*) interaction due to π − π stacking (Li et al. 2006) are investigated. The chain molecular magnets based on oxalate and π functional (phenthrolinene) ligand are synthesised using the hydrothermal method for investigating their structural and magnetic properties (Bhatt et al. 2013a). The structural analysis carried out using X-ray and neutron diffraction confirmed the formation of chain like structure consisting of $Fe^{II}(\Delta)$ and $Fe^{II}(\Lambda)$ atoms coordinated alternatively with oxalate and phenanthroline ligands as shown in Fig. 18.14. The 1– D chains lie in the crystallographic *ac* plane with large inter-chain distance of ~ 8.8 Å, providing negligible interactions between the chains. The material crystallizes in the space group $P2_{1,}$ a monoclinic structure. The phenanthroline ligands provide π–π interactions between them.

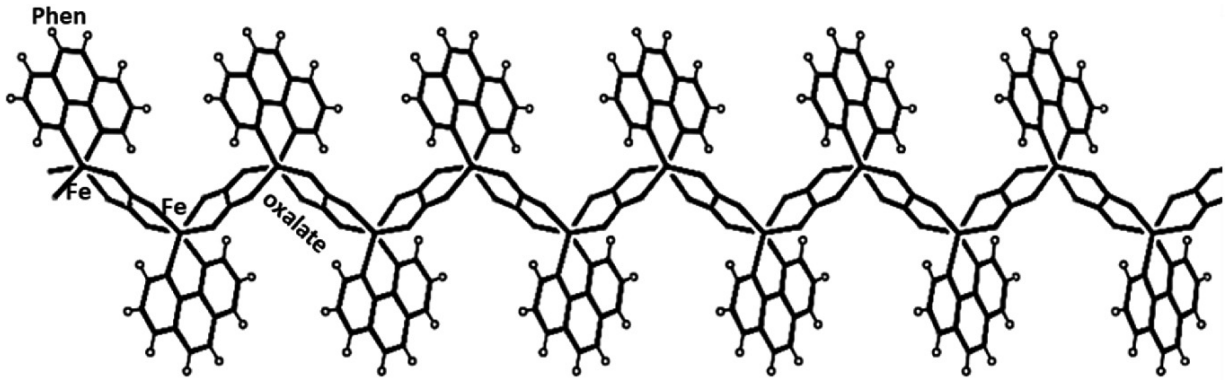

Fig. 18.14 Schematic representation of crystal structural of [{Fe(Δ)Fe(Λ)}$(ox)_2(phen)_2]_n$ compound showing an infinite 1–D zigzag chain like structure. Fe atoms are coordinated with the oxalate and phen ligands

The magnetization studied using *dc* magnetization measurements carried out confirm the existence of 1–D ferrimagnetic nature of the compound. The *ZFC* (zero − field-cooled) and *FC* (Field cooled) data show a maximum in the magnetization which suggest an antiferromagnetic like ordering. However, a weak ferromagnetic-like − transition seems evident from the magnetic saturation data. The magnetic ordering temperature was found to be ~ 8.7 K for $x = 0$ which decreases with higher Cr doping as shown in Fig. 15a. The magnetization (M) vs magnetic field (H) up to ± 9 Tesla at various temperatures shown in Fig. 15b, confirms large coercivity of ~ 3.2 Tesla. The observation of giant magnetic hysteresis in the absence of long-range magnetic ordering could be of great interest for chain molecular magnets. The observation of larger magnetic hysteresis in 1–D single chain magnets (Ishii et al. 2008; Clérac et al. 2002) has been also reported.

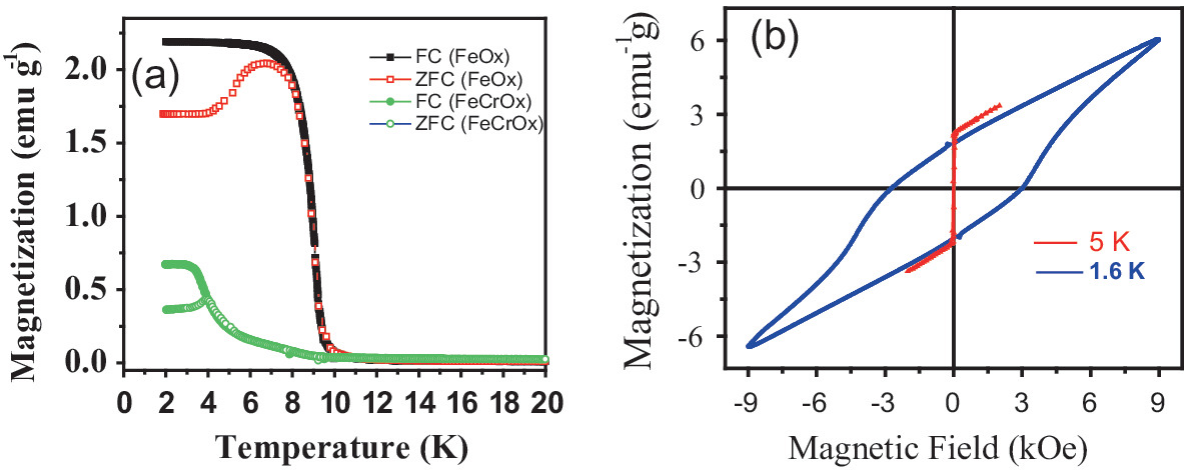

Fig. 18.15 The field-cooled (FC) and zero–field cooled (ZFC) magnetization versus as a function of temperature (T) curves under 50 Oe external applied magnetic field (**a**) and Hysteresis curve (**b**) of the compound $[\{Fe(\Delta)Fe(\Lambda)\}_{1-x}\{Cr(\Delta)Cr(\Lambda)\}_x(ox)_2(phen)_2]_n$

Another SCM $[M\text{-}(hfac)_2NaphNN]_n$ [$M = Co^{II}$ or Mn^{II} and NaphNN = 1-naphthyl nitronyl nitroxide] with high coercive field and high blocking temperature has been also synthesised (Cassaro et al. 2015). The compound shows exceptionally high coercive field of ~ 49 kOe at low temperature of 4.0 K and slower magnetic relaxation with higher T_B ≈13.2 K. The compound shows strong exchange coupling between antiferromagnetic metal and radical as represented in Fig. 18.16.

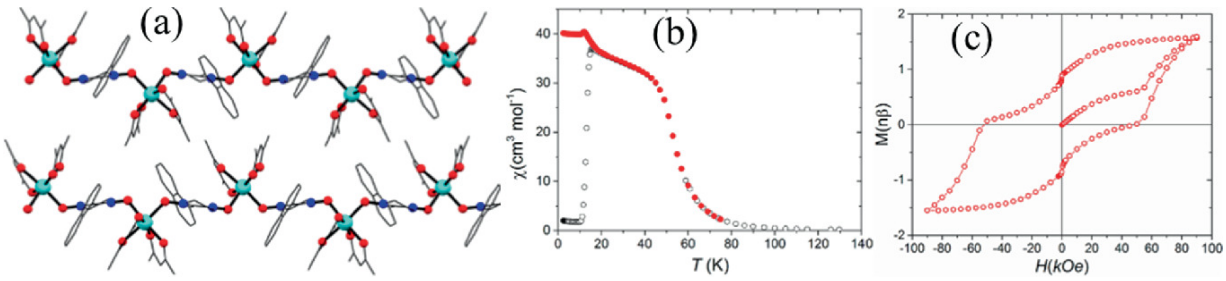

Fig. 18.16 Crystal structure viewed along a axes (**a**) FC and ZFC curve at 10Oe, (**b**) and magnetization hysteresis at 4.0 K (**c**) of SCM $[Co(hfac)_2NaphNN]_n$. This figure has been produced with permission from reference (Cassaro et al. 2015).

Copyright © 2015 American Chemical Society

(III) Layered Magnets

The molecular compounds are also synthesised in the form of layered structures. The layered structures arise due to the special arrangement of atoms in the chemical or magnetic unit cell.

The magnetic cooperativity observed in 2-D molecular magnets stems from the exchange interaction among localized spins within the coordination network, which is formed by radicals and metal cations. The magnetic interactions among ions within unit cell of 2-D molecular compounds will lie over the plane. For example, $M_2(OH)_3X$ ($M =$ Co and Cu) compound, where $X =$ anion is found to be ferromagnetic in-plane. The structure for layered compounds is shown in Fig. 18.17. The magnetic interactions in these compounds depend upon the interlayer spacing d such that the antiferromagnetic interaction occurs for smaller d spacings.

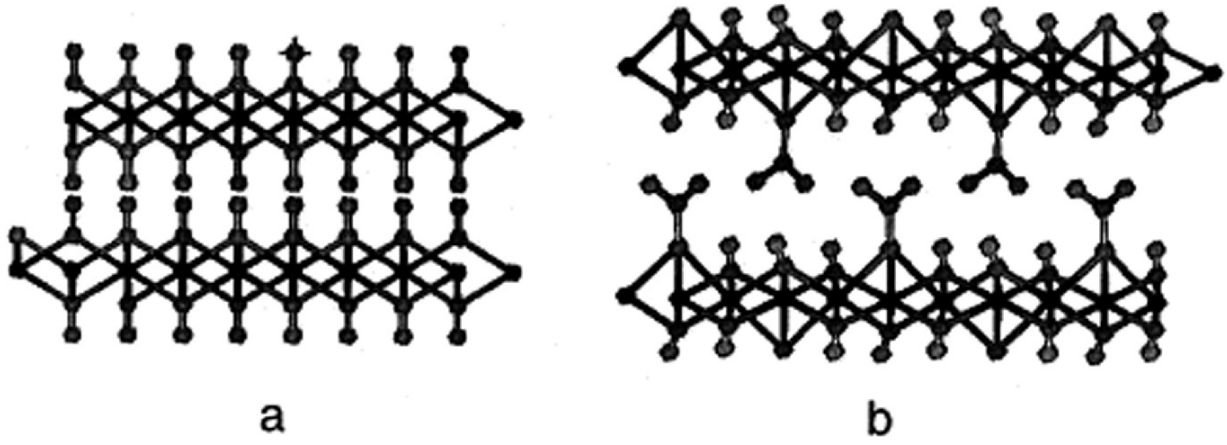

Fig. 18.17 Schematic representation of layered structures $M(OH)_2$ hydroxide (**a**) and $M_2(OH)_3(NO_3)$ hydroxide nitrate, (**b**) compounds. This figure has been produced with permission from reference (Laget et al. 1998).
Copyright © 1998 Elsevier Science

Layered compound based on the NIT radicals and Manganese hexafluoroacetylacetonate are studied for

magnetic properties (Caneschi et al. 1993). The compound crystallised in the monoclinic $P2_1$ space group in which chains of $Mn(hfac)_2$ units are coordinated by the radical NIT using the two oxygen atoms of NO groups.

These chains are connected to another $Mn(hfac)_2$ unit to form planes parallel to the [201] crystallographic axes as shown in **Fig. 18.18**. The magnetic properties of the compound show an increase with respect to temperature. The value of χT is supposed to be similar to the interactions with the spin $S = 5/2$ for Mn within the chain and $S = 1/2$ of the radicals.

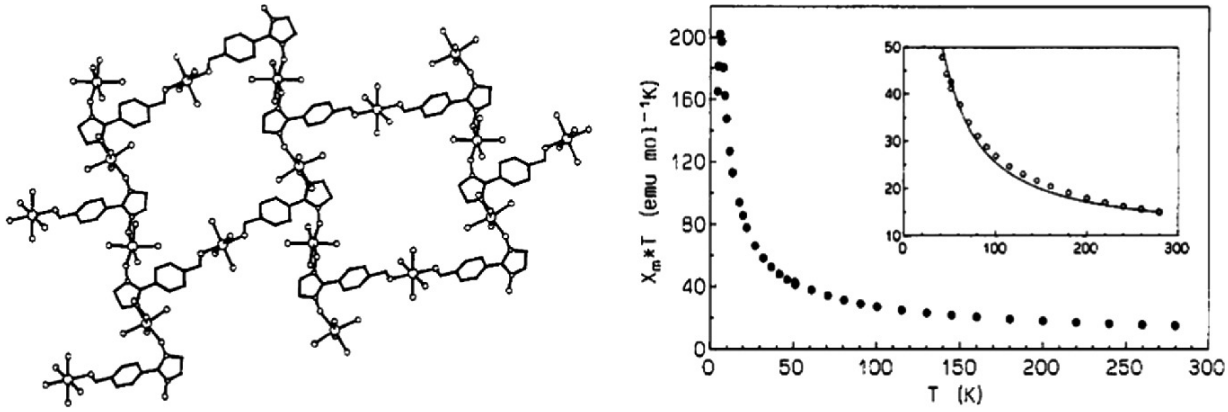

Fig. 18.18 Schematic crystal structure of layered compound $[Mn(hfac)_2]_3(NITBzald)_2$ and Magnetic properties as a function of temperature of the compounds. This figure has been produced with permission from reference (Caneschi et al. 1993).

© American Chemical Society

The magnetic properties of other layered molecular compounds are also investigated by various techniques as well. For example, the magnetic properties of the layered magnets $Ni_2(OH)_3\{N(CN)_2\}$, $Co_5(OH)_8(C_7H_{15}CO_2)_2{\cdot}4H_2O$, $Co_5(OH)_8(C_{12}H_{25}SO_4)_2{\cdot}2NH_3$ and $Co_5(OH)_8\{N(CN)_2\}{\cdot}6H_2O$, are investigated by μ^+SR (muon spin relaxation) (Jestadt et al. 1999). The measurement finds a loss of initial muon spin polarization during phase transitions. In another example, the study of magnetic ordering temperature of metals such

as Cu^{2+} ($S = 1/2$) coordinated with organic ligands like pyrazine based layered quasi-two-dimensional molecular antiferromagnets that are investigated for their magnetic properties using muon relaxation (Steele et al. 2011). The $[Cu(HF_2)(pyz)_2]X$ compound where $X = ClO^-_4$, BF^-_4, and SbF^-_6 represented the first highly stable structure. The structure comprises infinite 2-D $[Cu(pyz)_2]^{2+}$ sheets which lie in the *ab* plane. The HF_2^- (bifluoride) ions below and above the metal ions, act as a bridge for the formation of pseudo-cubic network. Within each cubic pore, the X^- anions occupy the *bcc* position. μ^+SR study allowed to identify the magnetic ordering temperature and critical behaviour near Neel temperature. The effective inter-layer exchange coupling and in-layer correlation lengths at Neel temperature are also estimated for the compound (Steele et al. 2011). Similarly, magnetic properties of oxalate ligand based molecular layer compound are studied using Mössbauer spectroscopy. The linewidth increases with increasing temperature (Pyalling and Ovanesyan 2007). Recently, magnetic ordering temperature of 510 K for $Li_{0.7}Cr(pyz)_2Cl_{0.7}$ (LCPC, pyz = pyrazine) and 480 K for potassium substitution $K_xCr(pyz)_2Cl_x$ (KCPC) are observed for the layered magnet (Huang et al. 2023a). The antiparallel spins of Cr and N from pyrazine and d-π* t spin interactions of Cr-pyrazine lead to the magnetic ordering higher than room temperature for such 2-D molecule-based magnets. The crystal structure and their magnetic properties are presented in Fig. 18.19.

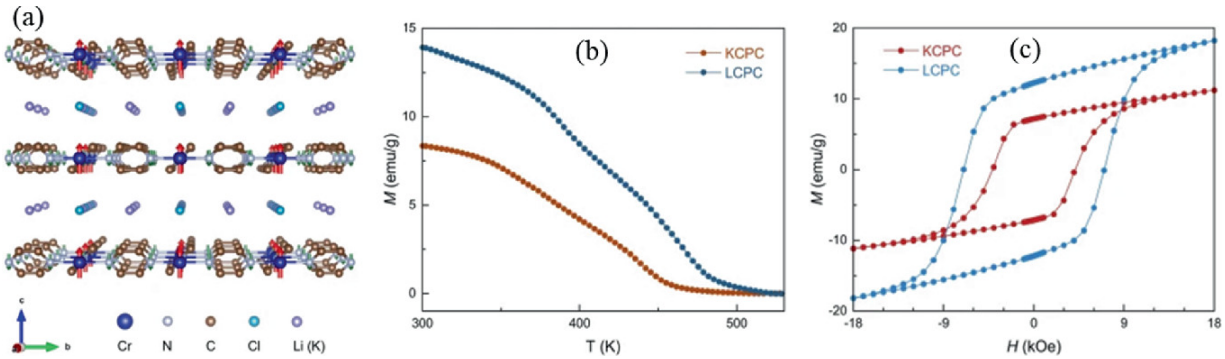

Fig. 18.19 Schematic crystal structure of compound LCPC or KCPC representing the layered structure (**a**). Magnetic properties in terms of temperature-dependent magnetization recorded at magnetic field of 5Oe (**b**), and M-H loops of LCPC and KCPC magnets at room temperature (**c**). This figure has been produced with permission from reference (Huang et al. 2023a). Creative Commons license

One of the oxalate-based compounds, represented by $AM^{II}M'^{III}(C_2O_4)_3$ {A and M is an organic cation and transition metal respectively}, is a layer type magnet (Tamaki et al. 1992). The M ion can be replaced by other divalent and trivalent metal ions. The organic cation can also be replaced along with M^{II} and M^{III} bridged by oxalate in a hexagonal planar honeycomb lattice. Depending upon the nature and choice of M, the magnetic interactions could be either ferro- or antiferromagnetic. It has been observed that small chemical variations in A also lead to the different magnetic ground state.

Another family of oxalate based layered magnetic compound is represented by the chemical formula $[Z^{III}Cp_2^*]$ $[M^{II}Ru^{III}(ox)^3]$ (where ox = oxalate, Cp* = pentamethylcyclopentadienyl, and Z^{III} = Fe and Co; and M^{II} = Mn, Co, Fe, Zn, and Cu). It is found that the Fe^{II} and Co^{II} based compound show magnetic ordering of 12.8 and 2.8 K, respectively. In addition absence of long-range magnetic ordering is observed upto 2 K (Eugenio Coronado et al. 2001). The crystal structure of one of the compounds of this family is shown in Fig. 18.20. The recently reported compound $Cr(pyz)_2{\cdot}x$LiCl$\cdot y$THF with magnetic ordering

temperature higher than room temperature and ferrimagnetic properties is also an example of a 2-D molecular layered compound (Perlepe et al. 2000). Their crystal structure and their magnetic properties are investigated. The compound, a metal–organic ferrimagnet, is found to exhibit a critical temperature as high as up to 242 °C with a 7500 Oe room-temperature coercivity. The synthesis of the compound involved chemically reducing $Cr(OSO_2CH_3)_2(pyz)_2$(pyz = pyrazine) and $CrCl_2(pyz)_2$ (where pyz = pyrazine) to enhance magnetic interactions and thereby increase the magnetic ordering temperature, promoting the development of resulting ferrimagnetic order.

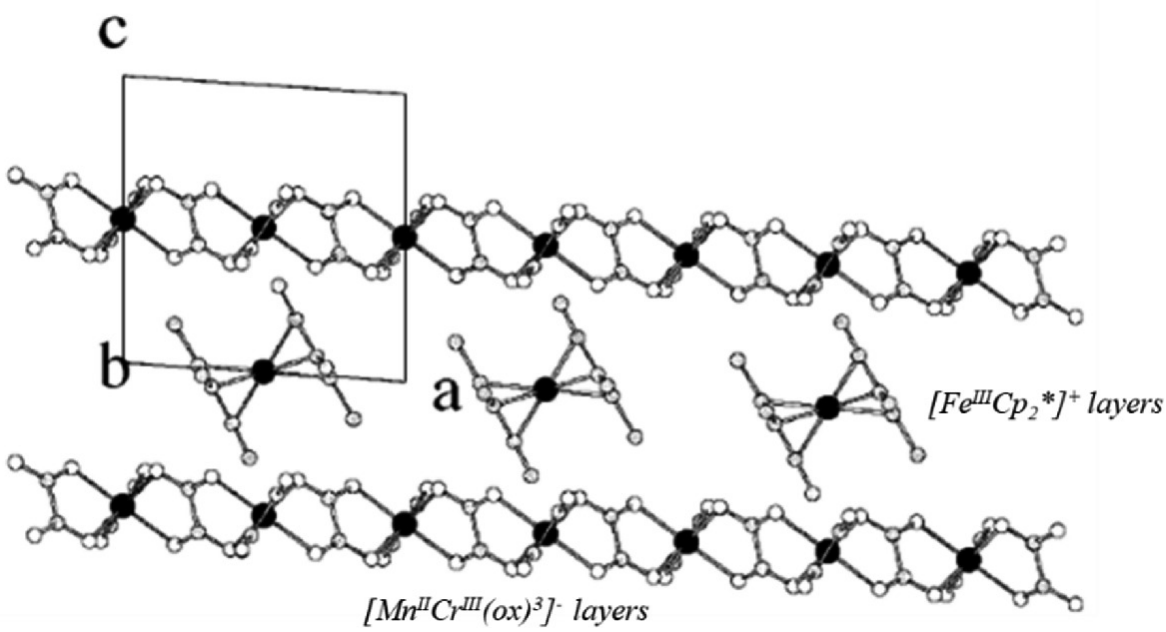

Fig. 18.20 Crystal structure of layered molecule-based magnets $[Fe^{III}Cp_2^*]$ $[Mn^{II}Cr^{III}(ox)_3]$ compound, showing the alternating $[Fe^{III}Cp_2^*]^+$ and $[Mn^{II}Cr^{III}(ox)^3]^-$ layers. This figure is taken with permission from reference (Eugenio Coronado et al. 2001).

Copyright © 2001 Academic Press

This compound is further studied and synthesised in–situ using chemical tuning route (Huang et al. 2023b). This led to a desired and controlled transformation from low-

temperature phase to room-temperature phase of $Cr(pyz)_2 \cdot x LiCl \cdot y THF$. It has been observed that the chemical tuning in terms of solvation/desolvation and lithiation could achieve room temperature magnet with coercivity of 8500 Oe and energy product of 0.6 MGOe. Further, it is correlated with the different amount of lithiation and solvation which modify the stoichiometry. In addition, recently, graphene-based molecular magnets are also found to have interesting electric, thermal, and mechanical properties. The magnetic properties of the aminoferrocene-based graphene molecular compounds are shown in Fig. 18.21. It demonstrates superparamagnetic behavior at room temperature with long-range magnetic order, showcasing colossal magnetocrystalline anisotropy of 3×10^7 and 8×10^5 J/m^3 in graphene-based aminoferrocene and aminoferrocene, respectively (Getahun et al. 2023). These results show that a chemical tuning is able to control the anisotropy and magnetic properties of such 2-D at room temperature, leading to possible suitable applications in the magnetic refrigeration, spintronics, and data storage like qubit arrays and quantum systems.

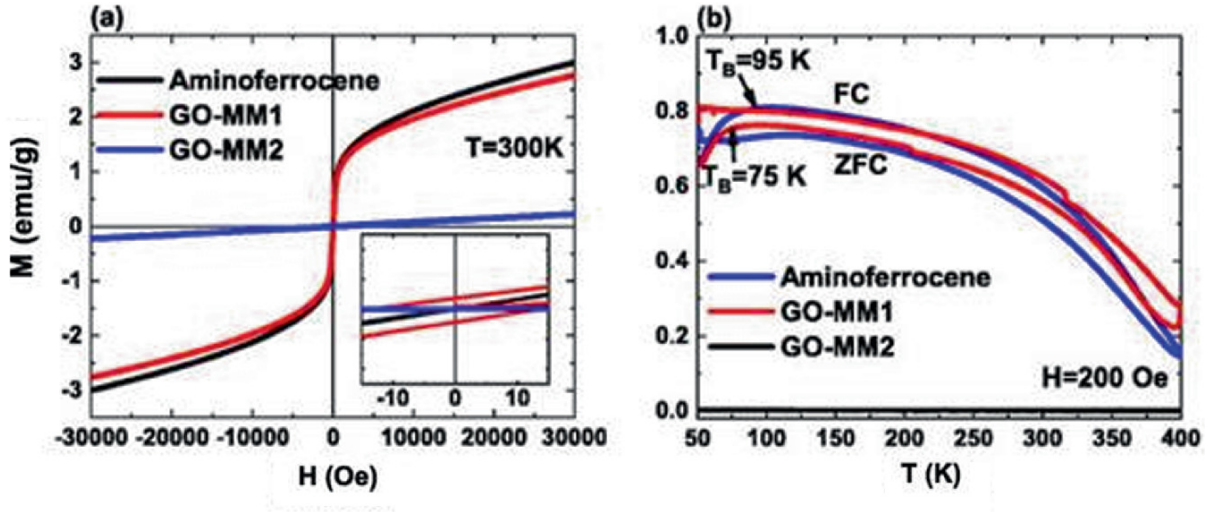

Fig. 18.21 Hysteresis loop at 300 K (**a**), magnetization at zero-field-cooled (ZFC) and field-cooled (FC) at 200 Oe (**b**) of the aminoferrocene-based graphene molecular compounds. The inset show magnetified view of the

hysteresis curve. This figure is reprinted from Getahun et al. (2023) with the permission of AIP Publishing

(IV) Open Framework-Based Magnets

Three-dimensional open framework type molecular compounds are the most studied molecular magnets with unusual magnetic properties. The metal–organic frameworks (MOFs), covalent organic frameworks (COF) are examples of the open framework type compounds having a porous crystalline material. These consist of metal ions linked by organic ligands. The compounds are important for gas storage such as for hydrogen, carbon dioxide, and methane and catalysts. The compound $(rad)_2Mn_2[Cu(opba)]_3(DMSO)_2.2H_2O$, where DMSO is dimethyl sulfoxide, rad^+ is 2-(4-N-methylpyridinium)-(Thorarinsdottir and Harris 2020) 4,4,5,5-tetramethylimidazoline-1 -oxyl-3-oxide, and opba is orthophenylenebis (oxamato), is the three-dimensional molecular magnet showing magnetic properties below 22.5 K (Stumpf et al. 1993). The structure of the compound reveals antiferromagnetic coupling arrangement of Cu(II) and Mn(II) through oxamato and rad^+ radical cations. The metal ions Cu(ll)/Mn(II) ions are also bridged using NIT ligands. Another example of open framework 3-D magnet are trimetallic units of $[Mn_3(4\text{-pyridone})_6]^{6+}$ coordinated by $[WV(CN)_8]^{3-}$. The magnetic properties and crystal structure are shown in Fig. 18.22. The compound is found to behave as ferrimagnetic below magnetic ordering temperature of 20 K. It is reported that the magnet like interactions between $Mn-W$ as well as between $Mn-Mn$ are antiferromagnetic in nature with $J_{MnW} = -3.9\ cm^{-1}$ and $J_{MnMn} = -5.9\ cm^{-1}$, exchanging coupling constants respectively (Komine et al. 2019).

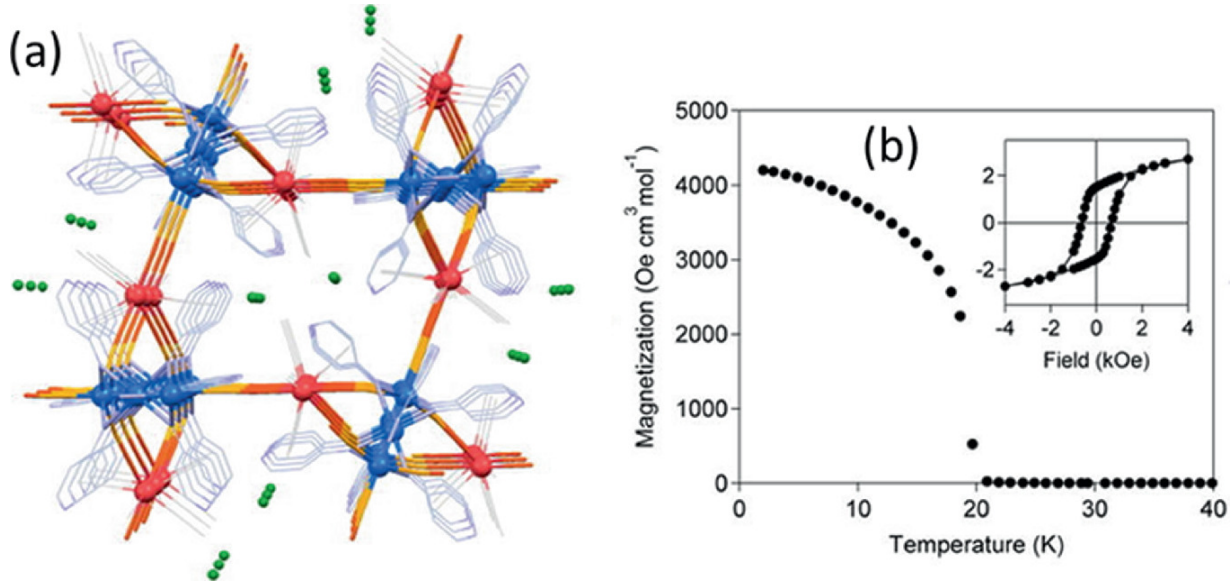

Fig. 18.22 Crystal structure (**a**) and magnetization as function of temperature (**b**) of $[Mn_3(4\text{-pyridone})_6][W(CN)_8]_2{\cdot}2H_2O$ compound. The inset of fig. (**b**) show M-H curve. This figure has been produced with permission from reference (Komine et al. 2019).

© 2019 Elsevier B.V

Prussian blue analogues (PBAs) chemically denoted by $A^{II}{}_k[B^{III}(CN)_6]_l{\cdot}zH_2O$ (A and B: transition metals ions) are also one type of open framework compound with interesting multifunctional properties, like negative thermal expansion (Goodwin et al. 2005), photo-magnetic behavior (Sato et al. 1996), spontaneous magnetization, magnetic pole inversion (Ohkoshi et al. 1999), and slow magnetic relaxation, etc. The possible technological applications of PBAs include ion sensing, hydrogen storage (Bhatt et al. 2014), memory storage, photo switching and biomedical. In general, two types of water molecules are present in PBA compounds depending on their stoichiometry and vacancies namely coordinated and non-coordinated. The cubic crystal structure of PBAs is shown in Fig. 18.23.

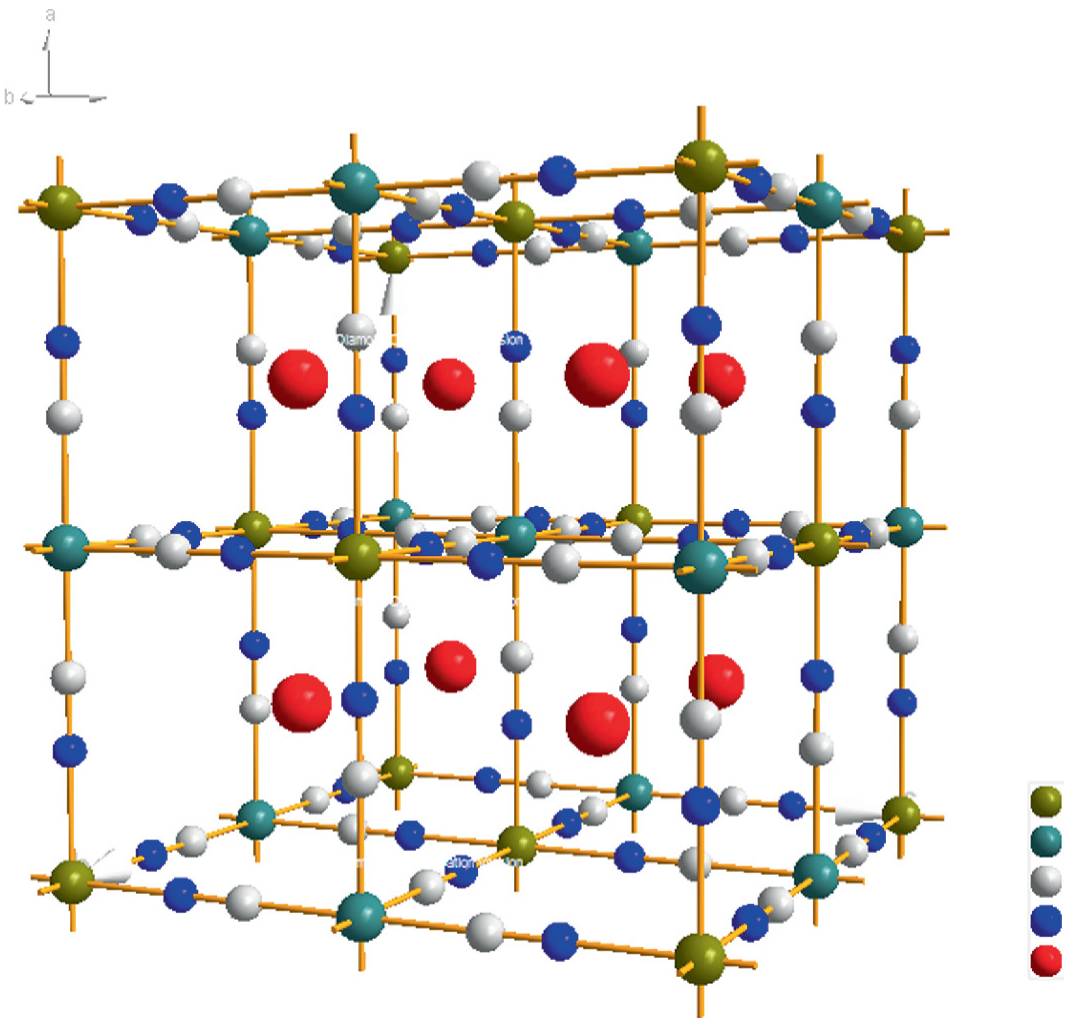

Fig. 18.23 Crystal structure of $A^{II}_{k}[B^{III}(CN)_6]_l{\cdot}nH_2O$ PBAs. The uncoordinated oxygen molecules are denoted by red, reside at the interstitial sites 8c (1/4, 1/4, 1/4)

Open framework compounds based on PBAs $Fe^{II}_{1.5}[Cr^{III}(CN)_6].nH_2O$ and $Co^{II}_{1.5}[Cr^{III}(CN)_6].nH_2O$ are synthesised using the co-precipitation method and investigated for their magnetic properties (Bhatt et al. 2013b). The field-cooled magnetization versus temperature curves recorded at a magnetic field of 200 Oe for both the compounds are shown in Fig. 24a. The values of T_C are found to be ~ 17 and ~ 22 K for $Fe^{II}_{1.5}[Cr^{III}(CN)_6].nH_2O$ and $Co^{II}_{1.5}[Cr^{III}(CN)_6].nH_2O$ compound respectively. Figure 24b shows the magnetic field dependent magnetization at 1.5 K

for $Fe_{1.5}[Cr(CN)_6].nH_2O$ and at 5 K for $Co_{1.5}[Cr(CN)_6].nH_2O$ compounds. The hysteresis curves reveal ferromagnetic characteristics of compounds with a coercive field of 400 Oe and 1200 Oe for $Fe_{1.5}[Cr(CN)_6].nH_2O$ and $Co_{1.5}[Cr(CN)_6].nH_2O$ compounds respectively.

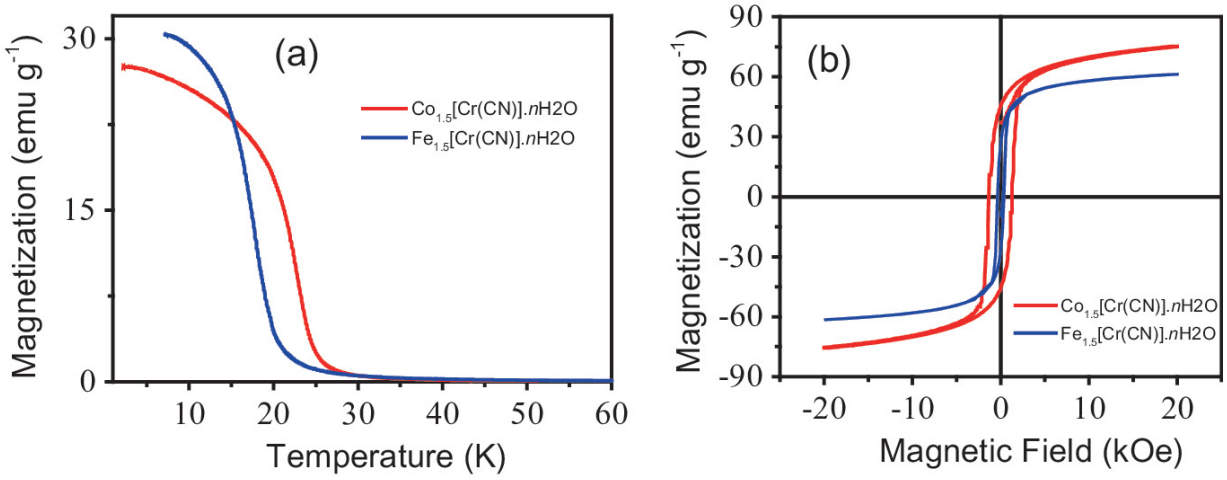

Fig. 18.24 The field-cooled magnetization versus as a function of temperature curves (**a**) and Hysteresis curve (**b**) for PBAs compounds

Few other CN based coordination networks with various dimensionality has been also synthesized using $[Ni(cyclam)]^{2+}$ (cyclam = 1,4,8,11-tetraazacyclotetradecane) and $[W(CN)_8]^{4-}$. Various forms of molecular compounds are synthesized as straight chain 1-D, $Li_2[Ni(cyclam)][W(CN)_8]\cdot 2H_2O$ zigzag chain 2-D, honeycomb-like network of $Li_2[Ni(cyclam)]_3[W(CN)_8]_2\cdot 24H_2O$, as well as the 3-D $Ni(cyclam)]_5[Ni(CN)_4][W(CN)_8]_2\cdot 11H_2O$ [(Heczko et al. 2022). Similarly, $[M^{II}(H_2O)_2]_2[Nb^{IV}(CN)_8]\cdot 4H_2O\}_n$ (M = Fe and Mn) compounds are synthesized which are found to be a magnetically ordered phase at $T_C = 43$ and 50 K for Fe and Mn based compound (Pełka et al. 2018).

18.3 Conclusions

It is summarized that the molecular magnetic materials are generally classified on the basis, nature, and type of the ligands, and building blocks, and on the dimensionalities of their crystal structures. Purely organic molecular magnets in terms of radicals or biradicals are showing interesting physical properties, however, possess low magnetic ordering temperature compared to hybrid molecular magnets. Whereas, organic–inorganic “hybrid” magnets categorized as SMMs, SCMs have future technological applications in the spin-mediated molecular electronics, quantum computer devices, and molecular spintronic devices.

References

Miller, J.S., Calabrese, J.C., Epstein, A.J., Bigelow, R.W., Zhang, J.H., Reiff W.M.: J. Chem. Soc., Chem. Commun. 1026–1028 (1986)

Tamura, M., Nakazawa, Y., Shiomi, D., Nozawa, K., Hosokoshi, Y., Ishikawa, M., Takahashi, M., Kinoshita, M.: Chem. Phys. Lett. **186**, 401 (1991) [Crossref]

Manriquez, J.M., Yee, G.T., Mclean, R.S., Epstein, A.J., Miller, J.S.: Science **252**, 1415–1417 (1991) [Crossref][PubMed]

Allemand, P.-M., Khemani, K.C., Koch, A., Wudl, F., Holczer, K., Donovan, S., Grüner, G., Thompson, J.D.: Science **253**, 301–302 (1991) [Crossref][PubMed]

a) Kahn, O.: Molecular Magnetism, VCH, New York (1993); b) Gatteschi, D., Kahn O., Miller J.S., Palacio F.: Molecular magnetic materials, Kluwer, Dordrecht, 1991; c) Miller, J.S., Epstein, A.J.: MRS Bulletin. 25, 21–30 (2000); d) Miller J.S.: Chem. Soc. Rev. 40, 3266–3296 (2011)

Benelli, C., Gatteschi D.: Introduction to Molecular Magnetism: From Transition Metals to Lanthanides. Wiley-VCH Verlag GmbH & Co. KGaA (2015)

Sessoli, R., Gatteschi, D., Caneschi, A., Novak, M.A.: Nature **365**, 141–143 (1993)

[Crossref]

Thomas, L., Lionti, F., Ballou, R., Gatteschi, D., Sessoli, R., Barbara, B.: Nature **383**, 145–147 (1996)
[Crossref]

Zabala-Lekuona, A., Seco, J.M., Colacio, E.: Coord. Chem. Rev. **441**, 213984 (2021)
[Crossref]

Neese, F., Pantazis, D.A.: Faraday Discuss. **148**, 229–238 (2011)
[Crossref][PubMed]

Milios, C.J., Vinslava, A., Wernsdorfer, W., Moggach, S., Parsons, S., Perlepes, S.P., Christou, G., Brechin, E.K.: J. Am. Chem. Soc. **129**, 2754–2755 (2007)
[Crossref][PubMed]

Ako, A.K., Hewitt, I.J., Mereacre, V., Clérac, R., Wernsdorfer, W., Anson, C.E., Powell, A.K.: Angew. Chem., Int. Ed. 45, 4926 (2006)

Yoshihara, D., Karasawa, S., Koga N.: J. Am. Chem. Soc. 130, 10460–10461 (2008)

Woodruff, D.N., Winpenny, R.E.P., Layfield, R.A.: Chem. Rev. **113**, 5110–5148 (2013)
[Crossref][PubMed]

Gould, C.A., McClain, K.R., Yu, J.M., Groshens, T.J., Furche, F., Harvey, B.G., Long, J.R.: J. Am. Chem. Soc. **141**, 12967–12973 (2019)
[Crossref][PubMed]

Guo, F.-S., Day, B.M., Chen, Y.-C., Tong, M.-L., Mansikkamäki, A., Layfield, R.A.: Science **362**, 1400–1403 (2018)
[Crossref][PubMed]

Randall McClain K., Gould, C.A., Chakarawet, K., Teat, S.J., Groshens, T.J, Long, J.R., Harvey, B.G.: Chem. Sci. 9, 8492–8503 (2018)

Goodwin, C.A.P., Ortu, F., Reta, D., Chilton, N.F., Mills, D.P.: Nature **548**, 439–442 (2017)
[Crossref][PubMed]

Gupta, S.K., Rajeshkumar, T., Rajaraman, G., Murugavel, R.: Chem. Sci. **7**, 5181–5191 (2016)
[Crossref][PubMed][PubMedCentral]

Rinehart, J.D., Fang, M., Evans, W.J., Long, J.R.: J. Am. Chem. Soc. **133**, 14236–14239 (2011)
[Crossref][PubMed]

Ding, Y.-S., Chilton, N.F., Winpenny, D.R.E.P., Zheng, D.Y.-Z.: Angew. Chem. **55**, 16071–16074 (2016)
[Crossref]

Vieru, V., Gómez-Coca, S., Ruiz, E., Chibotaru, L.F.: Angew. Chem.Int. Ed. e202303146 (2023)

Caneschi, A., Gatteschi, D., Lalioti, N., Sangregorio, C., Sessoli, R., Venturi, G., Vindigni, A., Rettori, A., Pini, M.G., Novak, M.A.: Angew. Chem. Int. Ed. **40**, 1760–1763 (2001)
[Crossref]

a) Bogani, L., Vindigni, A., Sessoli, R., Gatteschi, D.: J. Mater. Chem. 18, 4750–4758 (2008); b) Sun, H.-L., Wang, Z.-M. Gao, S.: Coord. Chem. Rev. 254, 1081–1100 (2010); c) Bernot, K., Bogani, L., Caneschi, A., Gatteschi, D., Sessoli, R.: J. Am. Chem. Soc. 128, 7947–7956 (2006); d) Gatteschi, D., Vindigni, A.: Single-Chain Magnets (Eds.): Bartolomé, J., L.F, Fernández, F.J.), Springer, Berlin, Heidelberg, (2014)

a) Huang, L.-W., Yang, C.-J., Lin, K.-J.: Chem. Eur. J. 8, 396–400 (2002); b) Russell, V., Craig, D., Scudder, M., Dance, I.: Cryst. Eng. Comm. 3, 96–106 (2001); c) Kim, J., Lee, U., Koo, B.K.: Bull. Korean Chem. Soc. 31, 487–490 (2010)

Giri, S., Saha, S.K.: J. Phys. Chem. Lett. **2**, 1567–1571 (2011)
[Crossref]

Ishii, N., Okamura, Y., Chiba, S., Nogami, T., Ishida, T.: J. Am. Chem. Soc. **130**, 24–25 (2008)
[Crossref][PubMed]

Li, L.-L., Lin, K.-J., Ho, C.-J., Sun, C.-P., Yang, H.-D.: Chem. Commun. 1286–1288 (2006)

Maspoch, D., Catala, L., Gerbier, P., Ruiz-Molina, D., Vidal-Gancedo, J., Wurst, K., Rovira, C., Veciana, J.: Chem.-Eur. J. 8, 3635–3645 (2002)

Bhatt, P., Thakur, N., Meena, S.S., Mukadam, M.D., Yusuf, S.M.: J. Mater. Chem. C **1**, 6637–6652 (2013a)
[Crossref]

Clérac, R., Miyasaka, H., Yamashita, M., Coulon, C.: J. Am. Chem. Soc. **124**, 12837–12844 (2002)
[Crossref][PubMed]

Cassaro, R.A.A., Reis, S.G., Araujo, T.S., Lahti, P.M., Novak, M.A., Vaz, M.G.F.: Inorg. Chem. **54**, 9381–9383 (2015)
[Crossref][PubMed]

Laget, V., Hornick, C., Rabu, P., Drillon, M., Ziessel, R.: Coord. Chem. Rev. **178–180**, 1533–1553 (1998)
[Crossref]

Caneschi, A., Gatteschi, D., Sessoli, R.: Inorg. Chem. **32**, 4612–4461 (1993)
[Crossref]

Jestadt, T., Kurmoo, M., Blundell, S.J., Lovettr, B.W., Pratt, F.L., Hayes, W.: SyntheticMetals **103**, 2325–2326 (1999)

Steele, A.J., Lancaster, T., Blundell, S.J., Baker, P.J., Pratt, F.L., Baines, C., Conner, M.M., Southerland, H.I., Manson, J.L., Schlueter, J.A.: Phys. Rev. B **84**, 064412 (2011)
[Crossref]

Pyalling, A.A., Ovanesyan, N.S.: Bull. Russ. Acad. Sci. Phys. **71**, 1310 (2007)
[Crossref]

Huang, Y., Pathak, A.K., Tsai, J.-Y., Rumsey, C., Ivill, M., Kramer, N., Hu, Y., Trebbin, M., Yan, Q., Ren, S.: Nat. Commun. **14**, 3186 (2023a)
[Crossref][PubMed][PubMedCentral]

Tamaki, H., Zhong, Z.J., Matsumoto, N., Kida, S., Koikawa, M., Achiwa, N., Hashimoto, Y., Okawa, H.: J. Am. Chem. Soc. **114**, 6974–6979 (1992)
[Crossref]

Eugenio Coronado, J. R. GalaHn-MascaroHs, C. J. GoHmez-GarcmHa, JoseH M. MartmHnez-Agudo, Eugenia MartmHnez-Ferrero, J. C. Waerenborgh, M. Almeida: J. Solid State Chem. 159, 391–402 (2001)

Perlepe, P., Oyarzabal, I., Mailman, A., Morgane Yquel, M.P., Dovgaliuk, I., Rouzières, M., Négrier, P., Mondieig, D., Suturina, E.A., Dourges, M.-A., Bonhommeau, S., Musgrave, R.A., Pedersen, K.S., Chernyshov, D., Wilhelm, F., Andrei Rogalev, C.M., Clérac, R.: Science 370, 587–592 (2000)

Getahun, Y.W., Manciu, F.S., Pederson, M.R., El-Gendy, A.A.: Appl. Phys. Lett. **122**, 241903 (2023)
[Crossref]

Huang, Y., Zhang, Q., Li, Y.C., Yu., Yao: Yong Hu and S. Ren, Advanced Materials **35**, 2208919 (2023b)
[Crossref]

Thorarinsdottir, A.E., Harris, T.D.: Chem. Rev. **120**, 8716–8789 (2020)
[Crossref][PubMed]

Stumpf, H.O., Yu., Pei, Kahn, O.: Lahcéne Ouahab and D. Grandjean **261**, 447–449 (1993)

Komine, M., Nakabayashi, K., Stefańczyk, O., Ohkoshi, S.-I.: Inorg. Chim. Acta **488**, 120–124 (2019)
[Crossref]

Goodwin, A.L., Chapman, K.W., Kepert, C.J.: J. Am. Chem. Soc. **127**, 17980–17981 (2005)
[Crossref][PubMed]

Sato, O., Iyoda, T., Fujishima, A., Hashimoto, K.: Science **272**, 704–705 (1996)
[Crossref][PubMed]

a) Ohkoshi, S.I., Abe, Y., Fujishima, A., Hashimoto, K.: Phys. Rev. Lett. 82, 1285–1288 (1999); b) Kumar, A., Yusuf, S.M., Keller, L., Yakhmi, J.V.: Phys. Rev. Lett. 101, 207206 (2008)

a) Bhatt, P., Banerjee, S., Anwar, S., Mukadam, M.D., Meena, S.S., Yusuf, S.M.: ACS Appl. Mater. & Interfaces 6, 17579–17588 (2014); b) Bhatt, P., Banerjee, S., Mukadam, M.D., Jha, P., Navaneethan, M., Yusuf, S.M.: J. Power Sources 542, 231816 (2022)

Bhatt, P., Thakur, N., Mukadam, M.D., Meena, S.S., Yusuf, S.M.: J. Phys. Chem. C **117**, 2676–2687 (2013b)
[Crossref]

Heczko, M., Sumińska, E., Pinkowicz, D., Nowicka, B.: Inorg. Chem. 61, 13817–13828 (2022)

Pełka, R., Pinkowicz, D., Sieklucka, B., Fitta, M.: J. Alloy. Compd. **765**, 520–526 (2018)
[Crossref]

© The Author(s), under exclusive license to Springer Nature Singapore Pte Ltd. 2024
R. S. Ningthoujam, A. K. Tyagi (eds.), *Handbook of Materials Science, Volume 2*, Indian Institute of Metals Series
https://doi.org/10.1007/978-981-97-4646-0_19

19. HSP90: An Emerging Molecular Target for Improvement of Nanoparticle Based Magnetic Hyperthermia Therapy

Neena G. Shetake[1, 3], Amit Kumar[1, 3], Raghumani S. Ningthoujam[2, 3] and Badri Narain Pandey[1, 3] ✉
(1) Radiation Biology and Health Sciences Division, Bhabha Atomic Research Centre, Mumbai, 400085, India
(2) Chemistry Division, Bhabha Atomic Research Centre, Mumbai, 400085, India
(3) Homi Bhabha National Institute, Anushakti Nagar, Mumbai, 400094, India

✉ **Badri Narain Pandey**
Email: bnp@barc.gov.in
Email: badrinarain@yahoo.co.in

Keywords Heat shock proteins – Nano-thermotherapy – Magnetic nanoparticles – Hyperthermia therapy – Thermo-resistance – Chaperons

Abbreviation

AMF Alternating Current Magnetic Field

AKT/PKB Protein Kinase B

17-AAG 17-Allylamino-17-demethoxygeldanamycin

BiP Immunoglobulin heavy chain-binding protein

CHT Conventional Hyperthermia Therapy

CHK1 Checkpoint Kinase 1

CRT Chemo-Radiotherapy

DNA Deoxyribose Nucleic Acid

17-DMAG 17-Dimethylaminoethylamino-17-demethoxygeldanamycin

FDA Food And Drug Administration

GRP78 78 KDa glucose-regulated protein

HSC70 Heat shock cognate 71 kDa protein

HSP Heat Shock Protein

HSR Heat Shock Response

MHT Magnetic Hyperthermia Therapy

MNPs Magnetic Nanoparticles

NPs Nanoparticles

RAD51 DNA repair protein RAD51 homolog 1

19.1 Introduction

Cancer is a major global health problem and despite substantial advancements in the treatment modalities, there has been only a modest improvement in the clinical outcome of the disease. In this direction, surgery, chemo- and radio-therapy are the most common approaches. Approximately 60% of solid tumors are treated by chemo-radiotherapy, although their success rates are compromised by the non-specificity to tumor, resulting in significant normal tissue toxicities. Immuno-therapy, targeted chemo-therapy, stem cell therapy and hormonal therapy are other advanced cancer therapeutic strategies (Anand et al. 2021). These targeted therapies employ tumor moieties such as small molecule inhibitor against molecules associated with signaling pathway(s) controlling cancer cell proliferation or inhibiting hormone receptors up-regulated in a particular type of cancer. These approaches can be categorized as molecular targeted therapies which act by specifically targeting the cancer cells thereby reducing the damage to normal tissues. However, these strategies also suffer some limitations. Firstly, as cancer is governed by multiple signaling networks, inhibition or targeting a specific molecule does not necessarily result in significant tumor control; and secondly, most of these small molecule inhibitors have poor solubility, bio-availability and pharmaco-kinetics, resulting in inadequate clinical doses at patient level, compromising their efficacy (Zhong et al. 2021). Thus, there is

a significant scope to develop better and tumor-specific strategies. Nanoparticles (NPs) could be excellent candidates to be exploited for tumor-specific delivery of hydrophilic/hydrophobic cargo and to address the issue of solubility and pharmaco-kinetic behavior of small molecule inhibitors/drugs. NPs which usually refer to materials having a size of less than 100 nm in any one dimension have several bio-physical favorable properties such as high surface area, amenability for functionalization, improved pharmaco-kinetics and better stability of NP-bound drugs, which make them ideal candidate for delivery of anti-cancer agents to the tumor site. Sustained or triggered release nano-systems that deliver the cargo in response to the external stimuli such as pH, temperature, light, etc. can also be designed for a controlled and efficient cancer treatment.

Hyperthermia is one of the modalities of cancer treatment mostly used in combination with chemo-and/or radio-therapy. Classically, hyperthermia therapy involves raising the tumor temperature to 40–43 °C, which induces denaturation of cellular proteins and lipids, affecting important biological processes such as membrane transport, DNA replication/repair machinery, cell proliferation/survival (Cheng et al. 2019; Crezee et al. 2021). Combining hyperthermia with radiation and chemotherapy has been known to substantially improve the therapeutic efficacy of these cancer therapeutic modalities. Hyperthermia can be delivered as local, regional or whole body, utilizing different types of energies such as ultrasound, radio-waves or microwaves. However, conventional hyperthermia therapy (CHT) has several dis-advantages which hindered its clinical application in cancer patients. Some of the disadvantages are (i) in-homogenous heating of the tumor as heating is achieved using applicators placed either on the surface or probes placed inside the tumor, (ii) for the core of the tumor to be heated to hyperthermic temperature, the surface has to be heated at much higher temperature resulting in blisters, burn and pain to the patient, (iii) there is a temperature gradient from the place of applicator to core of tumor, which results in insufficient heating and thus poor tumor cell killing and (iv) the heterogenous heating of tumor causes thermo-resistance during subsequent sessions of hyperthermia. Compared to CHT, more recently MHT has gained attention of researchers and clinicians as the specially designed nanoparticles targeted to tumor could cause selective heating and killing of cancer cells when an external

magnetic field is applied. Since in case of MHT, therapeutic heating is within the tumor at nanoscale level (in the range of dimension of nanoparticles), for the first time we used the term “nano-thermotherapy” (Shetake and Pandey 2019). Thus, MHT is a more controlled and tumor-specific heat inducing system compared to conventional hyperthermia.

Heat Shock Proteins (HSPs) are well studied in the mechanism of thermo-resistance under CHT, however, its regulation and role in hyperthermia, especially induced by MHT is poorly known. HSPs are class of proteins including HSP40, HSP60, HSP70, HSP90 and HSP100. Amongst HSPs, HSP90, an evolutionarily conserved 90 KDa molecular chaperone protein, has been implicated in the re-folding or stabilization of client proteins central to the hallmarks of cancer (Miyata et al. 2013; Barrott and Haystead 2013). Moreover, HSP90 has been found to be elevated in response to heat stress and plays a pivotal role in the HSF-1 mediated Heat Shock Response (HSR) (Yamada et al. 2007). Thus, inhibition of HSP90 appears to be a promising strategy and an armamentarium of more than eighteen HSP90 inhibitors are currently in different phases of clinical trials for cancer treatment. Despite the favorable efficacy of these HSP90 inhibitors none have received FDA approval mainly due to poor bioavailability and toxicities. These observations necessitate the need to develop strategies to deliver these inhibitors specifically to tumor and/or selective inhibition of HSP90 isoform/binding-site. In this direction, nanoparticles have provided an excellent option for tumor targeted delivery of HSP90 inhibitors (Rochani et al. 2020; Smalley et al. 2020; Yang et al. 2020) and have been explored in combination with CHT (Liu et al. 2021; Scutigliani et al. 2022) as well as MHT (Rochani et al. 2016; Ito et al. 2009; Yang et al. 2015). Present review is aimed to delineate the role of HSP90 in biological response of magnetic nanoparticles especially after MHT of cancer. We have also brought out the molecular targets of HSP90 involved in interaction with nanoparticles and nanoparticle-based strategies to overcome the limitations of delivery and action of HSP90 inhibitors for effective cancer therapy.

19.2 Heat Shock Proteins and Cancer

In early 1960s, Italian scientist Ferruccio Ritossa made the seminal discovery of heat induced puffs in the polytene chromosomes of salivary glands of *Drosophila melanogaster* when by mistake

temperature of the incubator was changed, (discovery was published in Cell Stress Chaperones (Ritossa 1996)) which a decade later were shown to correspond to activation of HSPs (Maio 2011). Over the last decades, HSPs are well known as molecular chaperones playing pivotal role in protein folding, maturation and re-folding of mis-folded proteins. They are expressed in almost all plant and animal species including humans. HSPs are also made by prokaryotic cells, namely, bacterial and archaean. HSPs are known to be involved in various biological processes and play crucial role in manifestation of effects not only limited to heat but other stress agents like toxins, heavy metals, viruses and free radicals. HSPs are characterized by their molecular weights, ranging from 10 to >100 kDa, categorized into six families: small HSPs, HSP40 (J-proteins), HSP60, HSP70, HSP90 and HSP100 (Jee 2016). A comprehensive description of the members of the HSP families with their sub-cellular localization and predominant function has been mentioned in Table 19.1. At protein folding and assembly, they function as holdase (HSPB, HSP70), foldase (HSP90, HSP60), sequestrase (HSPB), aggregase (regulation of protein aggregation) or disaggregase (control of protein disaggregation) (Hu et al. 2020). The HSPs work as a network to keep the proteostasis in cells and also an efficient first line of defense under various stress conditions. Most of these HSPs are inducible in response to heat shock or stress conditions (such as anoxia, hypoxia, drugs, chemical agents, metals, etc.). Other HSPs such as HSC70 (HSPA8), mortalin (HSPA9) and GRP78 (HSPA5) are constitutively expressed in mammalian systems (Hen et al. 2022; Dubey et al. 2015). Heat Shock Factors (HSFs) are the main transcriptional regulators of stress induced expression of *hsp* genes. HSFs bind to the heat shock elements (HSEs), cis-acting sequences present in multiple copies, upstream of the *hsp* genes and regulate the expression of inducible HSPs. The induction of HSPs in response to proteotoxic stress conditions constitutes the “Heat Shock Response (HSR)”. The proteotoxic stress is characterized by accumulation of aggregated and mis-folded proteins due to exposure to high temperature or other stress conditions (such as nutrient and oxygen deficiencies). HSPs function as molecular chaperones to maintain the protein homeostasis in stress conditions by preventing protein aggregation or facilitating the re-folding of the mis-folded proteins. Wide range of human cancers manifest up-regulation of HSPs (Table 19.1)

wherein they play pivotal role in tumor cell proliferation, differentiation, invasion, metastasis, death. The upregulated expression of HSPs are often associated with poor prognosis or poor response to cancer therapy (Alex and Jaeger 2019; Birbo et al. 2021). The mechanism of HSP induced thermo-resistance in tumor cells has been discussed in subsequent Section of the Chapter.

Table 19.1 Classification of HSPs with their cellular localization, functional role and modulation in different types of cancer

S. no.	HSP family	Names	Alternate names	Predominant cellular localization	Biological function	Expression in different types of Cancer (ONCOMINE) (Fan et al. 2020)
1	HSPA	HSP1A	HSP70-1, HSP72, HSPA1	Cytosol, Lysosome	Client protein binding	Up-regulated in Liver, Prostate, Colorectal, Breast, Lung, Ovarian, Uterine, Melanoma, Oral, Bladder Cancer and Myeloid Leukemia (Murphy 2013)
		HSPA5	BIP, GRP78	Endoplasmic reticulum (E.R.)	E.R. chaperone	–
		HSPA8	HAS70	Cytosol	Client binding	–
		HSPA9	GRP75, HSP70-9, Mortalin	Mitochondria	Protein import	–
2	HSPC	HSPC1	HSP90	Cytosol	Client binding	Up-regulated in Bladder, Colorectal, Head and Neck, Kidney Cancer and Myeloma (Fan et al. 2020)

S. no.	HSP family	Names	Alternate names	Predominant cellular localization	Biological function	Expression in different types of Cancer (ONCOMINE) (Fan et al. 2020)
3	DNAJ					
	DNAJA	DNAJA2	Rdj2		Protein scaffold?	-
		DNAJA3	Tid1	Postsynaptic membrane	nACh-R clustering	-
	DNAJB	DNAJB1	HSP40, Hdj-1		HSPA, C recruitment, co-chaperone	Colorectal Cancer (Kanazawa et al. 2003)
		DNAJB2	Hsj-1	Cytosol, Cytoplasmic face of E.R		–
		DNAJB6	Mrj	Cytosol		–
	DNAJC	DNAJC5	CSPα	Cytosol (synapse)	SNARE assembly, neurotransmitter release	–
		DNAJC6	Auxilin	Cytosol (synapse)	Clathrin disassembly	–
		DNAJC13	RME-8	Cytosol (endosome)	Endocytosis/trafficking	–
		DNAJC26	GAK	Cytosol, nucleus	Clathrin disassembly	–
4	HSPH	HSPH1	HSP105	α—cytosol β—nucleus	Nucleotide exchange factor for HSPA, promoter of STAT-3	Up-regulated in Breast, Colorectal, Esophageal, Head & Neck, Leukemia, Liver and melanoma cancer

S. no.	HSP family	Names	Alternate names	Predominant cellular localization	Biological function	Expression in different types of Cancer (ONCOMINE) (Fan et al. 2020)
5	HSPB	HSPB1	HSP27, HSP25	Chaperone	Cytoplasmic	Up-regulated in Prostate, Lung, Ovarian, Colon, Cervical, Pancreatic, Esophageal Cancer and Thymic epithelial tumors (Yang et al. 2021)
		HSPB2		Chaperone	Cytoplasmic, Nuclear	–
		HSPB5	αβ-crystallin	Chaperone	Cytoplasmic, Nuclear	–
		HSPB6	HSP20	Chaperone	Cytoplasmic, Nuclear	–
		HSPB8	HSP22	Chaperone	Cytoplasmic, Nuclear	–
6	HSPD	HSPD1	HSP60	Mitochondrial matrix, may be cytosolic, extracellular	Mitochondrial protein folding	Up-regulated in Cervical, Colorectal, Head & Neck, Lymphoma, Myeloma and Sarcoma (Fan et al. 2020)
7	HSPE	HSPE1	HSP10	Mitochondrial matrix	HSPD co-chaperone	–
8	HSP100	HSP100		Mitochondria	Disaggregation	–

Data on expression levels of HSP90 and HSP60 in different types of cancer has been taken from ONCOMINE database

19.3 Modulation of HSP90 Expression During Hyperthermia and Its Role in Thermo-Tolerance

Hyperthermia therapy (HT) has been used as an adjuvant therapy to enhance the therapeutic efficacies of radiation and chemotherapy

due to its several effects at physiological and cellular levels. Tumor cells exposed to temperatures in the range of 40–42 °C have been observed to die at exponential rate (Griffin et al. 2010). HT is one of the most ancient techniques (dating back to 3000 B.C.) of killing tumor cells by application of heat, a process known as cauterization in ancient India, Egypt, and China. Typically, the heating was achieved using heat from natural heat sources (e.g., hot mud baths and volcanic steam). Similar observations have been made by ancient philosophers like Parmenides, Hippocrates and Celsus from ancient Greece and Rome around 500 B.C.–50 A.D, wherein heat was able to cure cancer; when other treatment options failed (Scutigliani et al. 2022). Later, two surgeons William B. Coley and Carl D.W. Busch (in early 1850s) observed a positive correlation between systemic body fever and tumor regression and overall patient survival. This lead to the development of “Coley toxin”, wherein an injection of a mixture of dead bacterial strains was found to be induce artificial fever and showed positive impact on tumor control (Scutigliani et al. 2022). In fact, this observation formed the basis of modern immunotherapy and showed the effectiveness of HT in cancer cure.

Temperatures in the range of 42–43 °C causes vasodilation which is hypothesized to be mediated via heat induced activation of nitric oxide synthase and nitric oxide production in the endothelial cells lining the blood vessels (Griffin et al. 2010). Vasodilation triggers an increase in the blood flow resulting in increased oxygen and drug delivery to the tumor site. These physiological changes greatly enhance the sensitivity of hypoxic tumor regions to thermal-radiotherapy. Further, at cellular level, HT is known to induce changes in plasma membrane permeability and alter intracellular signaling, macromolecule synthesis, interfere with repair processes [such as DNA double-strand break (DSB) repair], affect the chromatin stability and structure, resulting in significant radio-sensitization of the cells (Griffin et al. 2010). However, several pre-clinical studies have demonstrated the induction of HSR mediated thermo-tolerance; a phenomenon characterized by increased expression of several HSPs (Fig. 19.1), specifically HSP70 and HSP90 (Li et al. 2009).

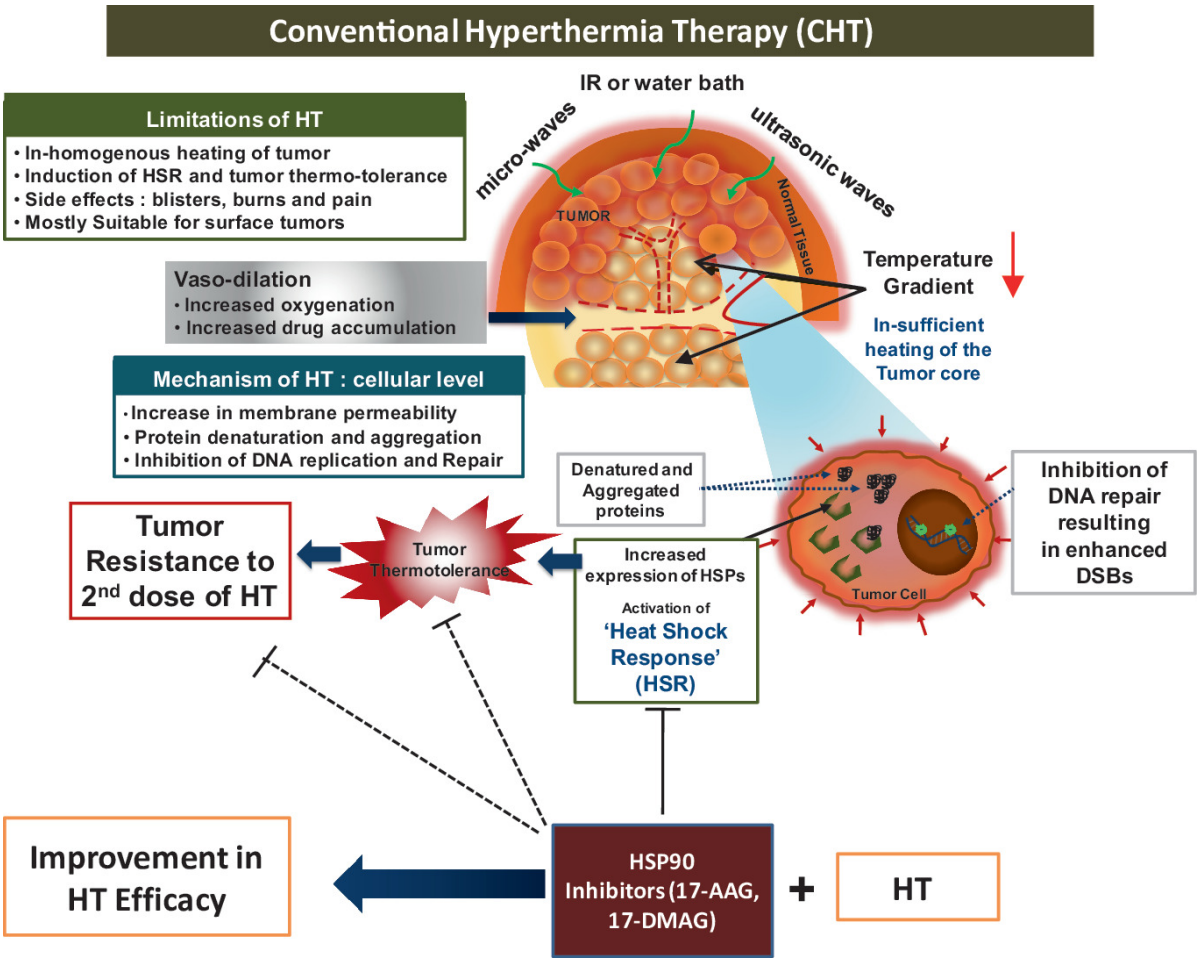

Fig. 19.1 Scheme for thermal sensitization of tumors at physiological and cellular level following conventional hyperthermia therapy (HT). The mechanism of heat stress induced activation of Heat Shock Response (HSR) mediated by up-regulation of HSPs (specifically HSP90) and its role in induction of tumor thermo-tolerance and resistance of tumors to subsequent second round of HT. The promising approach of combining HSP90 inhibitors with HT would prevent induction of thermo-tolerance and improve the efficacy of HT

Central to HSR is the proteo-toxic stress induced by HT wherein an abnormal accumulation of misfolded or disaggregated or damaged proteins triggers the activation of HSF-1, a master regulator of protein quality-control machinery expression. Heat stress triggers trimerization and nuclear translocation of HSF-1 activating the expression of HSPs, which in turn increases the protein-folding capacity, re-establishment in balance of proteo-stasis and support cellular survival. Subsequent heat treatments makes the cancer cells susceptible due to persistent over-expression of HSPs, which in turn severely hampers the HT efficacy.

Similar to pre-clinical studies, in clinical settings as well, the efficacy of HT has been found to be compromised by up-regulation of HSPs following heating. Tanja Grimmig and co-workers observed

that in human colon cancer patients, a significant up-regulation of HSP27, HSP70, and HSP90 was induced during hyperthermic chemotherapy treatment (Grimmig et al. 2017). Their results suggested that the HSR triggered by up-regulation of these HSPs enhanced the HSP-associated anti-apoptotic and proliferative effects. Thus, the efficacy of hyperthermic chemotherapy was severely compromised. These results were also validated in HT-29/SW480/SW620 colon cancer cells. In accordance with these observations, Yinuo Tu et al. observed a similar trend of elevated HSP90 levels in case of gastric adenocarcinoma patients undergoing HT (Tu et al. 2018). Interestingly, serum levels of HSP90 were also found to be up-regulated in gastric cancer patients (22) following Hyperthermic Intraperitoneal Chemoperfusion (HIPEC) therapy. Therefore, inhibition of HSR or the HSPs becomes a promising strategy to ensure successful clinical outcome of HT. In support of this, Vriend et al. (2017) showed the efficacy of an HSP90 inhibitor, Ganetespib (binding to the ATP binding pocket of NTD of HSP90) in potentiating the cytotoxic as well as radio- and chemo-sensitizing effects of hyperthermia and reducing the thermo-tolerance in cervix cancer cell lines (Vriend et al. 2017). Another recent study by Scutigliani et al. authenticated the efficacy of Ganetespib in boosting the thermo-chemotherapy and thermo-radiotherapy in a cervix cancer xenograft (Scutigliani et al. 2022).

In addition to tumor thermo-resistance, multiple HT treatments have been observed to induce a state of vascular thermotolerance in tumors, wherein pre-heated tumors show decreased therapeutic response to a second dose of HT. Vascular thermo-tolerance has also been found to be negatively correlated with the tumor oxygenation rate which ultimately influences the therapy response (Griffin et al. 2010). Although no direct association has yet been reported between HSP90 expression and vascular thermo-tolerance, it would be interesting to delineate the contribution of HSP90 in induction of vascular thermo-tolerance, which is likely due to increased surface expression of HSP90 in endothelial cells in case of pathologies such as atherosclerosis (Profumo et al. 2018).

19.4 Magnetic Hyperthermia Therapy (MHT): Factors Affecting Heat Generation in Tumor

MHT utilizes super-paramagnetic magnetic nanoparticles (MNPs) to induce heat generation (in the range of 40–43 °C) in the tumor under the influence of an alternating current (*AC*) magnetic field (AMH) generated by radiofrequency (RF) induction coils. Heating under AMH occurs due to four different mechanism: (i) hysteresis, (ii) eddy current, (ii) Néel or Brownian relaxation and (iv) frictional losses. However, in case of MNPs, Néel or Brownian relaxation is the predominant mechanism of heat generation (Fatima et al. 2021). The efficiency of MNPs for MHT depends on several factors such as their (i) colloidal stability, (ii) specific absorption rate (SAR), (iii) targetability or specificity for tumor cells, (iv) residence time in tumor and (v) intra-cellular distribution inside the tumor cells. SAR dictates the heating ability of MNPs, a property influenced by amongst others (magnetic anisotropy, composition, applied field and frequency), the MNPs size and its colloidal stability. Thus, higher SAR enables heating of tumors to hyperthermic temperatures achievable even at lower intra-tumor doses of MNPs (Kritika 2022). The tumor specific delivery of MNPs is an attribute that distinguishes the better hyperthermia inducing ability of MHT as compared to CHT. Unlike CHT, in MHT, MNPs can be functionalized using tumor targeting surface ligands to specifically internalize in the tumor cells and distribute to cellular compartments more sensitive to heat. Such as plasma membrane is known to be a more sensitive target of heat as compared to cytosolic compartment. Such targeted heating of the tumor cells can substantially improve the therapeutic efficacy of MHT, but maximizing the damage to tumor cells and minimizing the heat damage to surrounding normal tissue. Another important consideration for successful application of MHT is the maximum limit of the magnetic field to which the biological samples/living tissues can be exposed without inducing severe and/or irreversible patho-physiological consequences. In 1984, the limit of magnetic field-frequency product ($H \times f = 4.85 \times 10^8$ Am^{-1} s^{-1}) was proposed by Atkinson–Brezovich as a limit for safe application of MHT based on temperature distributions computed for tissue models using thermal seeds (Atkinson et al. 1984). However, recently, Borja Herrero de la Parte et al., has re-assessed this limit and proposed that exceeding the Atkinson–Brezovich limit upto 9.59×10^9 Am^{-1} s^{-1} seems to be safe. however, this revised limit needs further experimental evaluation (Herrero de la Parte et al. 2022).

19.5 HSP90: A Druggable Target for Nanoparticle Based Magnetic Hyperthermia Therapy of Cancer

Amongst HSPs, HSP90 received a great deal of attention and has been explored as a prospective molecular/drug target for the treatment of cancer and neurodegenerative diseases (Chaudhury et al. 2021; Sumi and Ghosh 2022). HSP90 is an evolutionarily conserved molecular chaperone that ensures cellular proteo-stasis by maintaining the folding, stabilization, activation, and degradation of over 400 proteins termed as 'clients'. The clientele of HSP90 involves protein kinases and nuclear receptors, participating in essential cellular activities such as cell growth, proliferation, and survival (Sanchez et al. 2020). The candidacy for HSP90 to be explored as a potent anti-cancer target is further strengthened by its indirect selectivity towards tumor cells over normal cells (Kamal et al. 2003). One reason for this selectivity is due to the differential molecular assembly of HSP90 machinery in cancer cells, wherein it exists as a multi-chaperone complex with unusually high affinity for ATP and drugs. Whereas in case of normal cells, HSP90 exists as in un-complexed or latent state. Additionally, Kamal et al. reported the unusually higher (~100 folds) client protein binding affinity of cancer cell HSP90 as compared to its counterpart in normal cells (Kamal et al. 2003). Furthermore, studies have reported tumor-specific accumulation of HSP90 inhibitors (17-AAG, 17-DMAG, IPI-504, radicicol derivatives and purine scaffold inhibitors), however, the mechanism of tumor specificity remains elusive. These observations corroborate the anti-cancer potential of HSP90 inhibitors (Li et al. 2009; Chiosis and Neckers 2006).

Presently, it has been identified that HSP90 has four isoforms: HSP90α, HSP90β, glucose-regulated protein 94 (GRP94) and TNF receptor associated protein 1 (TRAP-1). Out of the two major cytoplasmic isoforms (HSP90α and HSP90β), HSP90α is an inducible HSP, whereas HSP90β is constitutively expressed. Both the isoforms (HSP90α and HSP90β) share ~ 86% homology. These isoforms differ in their cellular roles and speed of action, for instance, HSP90α plays a cytoprotective role, whereas HSP90β is involved in cellular adaptation. Further, HSP90α is a fast responder as compared to HSP90β which is known to show slower response to proteo-toxic stress conditions. Although there are some differences

between the two isoforms, HSP90 is often used to refer to both isoforms HSP90α and HSP90β, since they are similar in structure and function (Zhong et al. 2021). The other two isoforms of HSP90 namely, GRP94 and TRAP-1are localized in the endoplasmic reticulum and mitochondria, respectively and have been implicated in processes such as tumor cell proliferation, metastasis and drug resistance (Jackson 2013). All the isoforms of HSP90 share common structure and exist as homodimers of two identical monomers each having three distinct functional domains, namely a C-terminal dimerization domain (CTD), a substrate binding middle domain (MD) for binding of client proteins as well as co-chaperones and a nucleotide binding N-terminal domain (NTD) which binds to ATP. Out of the three domains of HSP90, NTD has been exploited as an HSP90 inhibition site by competitively binding to its ATP binding pocket. Moreover, all four HSP90 isoforms are known to share high sequence identity in the NTD region, making it a highly prospective site for inhibition of HSP90. Till date, more than 170 clinical trials have taken place to test 18 different HSP90 inhibitors as therapeutic agents in humans (Jhaveri et al. 1823). However, adverse effects including induction of the pro-survival resistance and detrimental dose-limiting toxicities have prevented HSP90 inhibitors acting on HSP90-NTD from gaining FDA approval. Moreover, certain NTD inhibitors have been found to be non-effective against non-cytosolic isoforms of HSP90 such as TRAP-1 (Li and Luo 2023). These limitations raised the need to explore other HSP sites for effective HSP90 inhibition while simultaneously reducing the activation of HSR. Bhatia et al., recently demonstrated the HSP90 inhibition efficacy of a small molecule inhibitor that interferes with the dimerization of CTD of HSP90 and doesn’t induce HSR in a therapy-resistant xeno-transplanted leukemia cells in zebra fish model (Bhatia et al. 2022). Another prospective approach was developed by Csermely and co-workers wherein they identified the presence of a second ATP-binding site in the C-terminus of HSP90 (Soti et al. 2003). In addition to ATP, other molecules (e.g. cisplatin, novobiocin, epilgallocatechin-3-gallate (EGCG) and taxol) were found to be able to bind to this pocket in CTD, leading to newer possibilities for development of a more effective and less toxic HSP90 inhibitor (Soti et al. 2003; Donnelly and Blagg 2008).

In addition to the NTD and CTD, MD of HSP90 has also been evaluated as a probable drug target site. Recently, Kristine Donahue

and co-workers, demonstrated the efficacy of Diptoindonesin G (Dip G) as a middle domain HSP90 modulator for cancer treatment, by promoting degradation of HSP90 clients without triggering the HSR which is major reason for development of clinical resistance to HSP90 inhibitor monotherapy (Donahue et al. 2022). Unlike dip G, which is a small molecule inhibitor of HSP90 MD, preliminary studies in our laboratory identified the novel ability of oleic acid functionalized iron oxide nanoparticles (MN-OA) to bind to HSP90 and induce down-regulation of several of its client proteins playing role in DNA repair and cellular proliferation (AKT) (Fig. 19.2). MN-OA has a highly hydrophobic coating of oleic acid which increases its probability to bind to the substrate/client binding MD of HSP90 which is known to have high affinity for proteins exposing long patches of hydrophobic residues (Shetake et al. 1863). However more experiments are needed to identify the binding characteristics of MN-OA with intra-cellular HSP90. Interestingly, MN-OA being super-paramagnetic in nature was able to induce significant thermal sensitization of fibrosarcoma cancer cells by inducing down-regulation of HSP90, thereby preventing activation of HSR (Shetake et al. 2015). Furthermore, in combination with radiotherapy, MN-OA showed significant radio-sensitization of cancer cells by inducing twofold higher DNA double strand breaks and slower repair kinetics (Shetake et al. 1863). These observations open new scope for designing nanoparticles against HSP90 for MHT applications as they may offer better therapeutic response. Moreover, magnetic nanoparticle coated with agents with property of HSP90 inhibitor could serve the dual purpose of inhibiting the intra-cellular HSP90 as well as delivering MHT (Figs. 19.2 and 19.3).

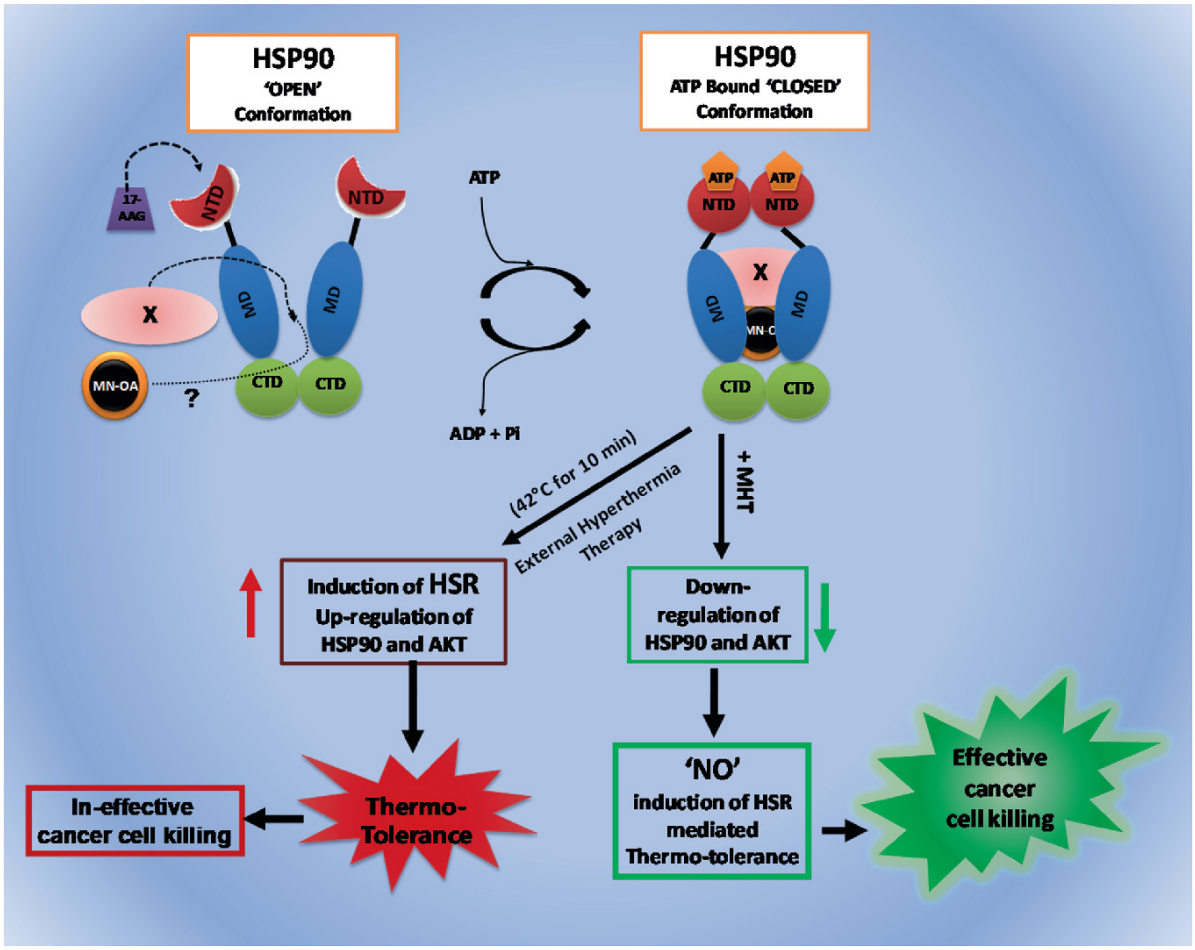

Fig. 19.2 HSP90 structure and interaction with magnetic nanoparticles. Pincer-like structure of HSP90 cycling between the 'Open' and ATP bound 'Closed' conformation. The middle domain (MD) binds to the substrate/client proteins. Novel approach of HSP90 binding magnetic nanoparticles was evaluated in our laboratory to enhance the efficacy of MHT. Probable mechanism for binding of MN-OA (oleic acid coated iron oxide nanoparticles) to the MD of HSP90 resulting in HSP90 inhibition and down-regulation of HSP90 client protein (AKT) similar to 17-AAG (NTD binding HSP90 inhibitor) (Shetake et al. 1863, 2015). In combination with MHT, MN-OA induces down-regulation of both HSP90 and AKT. However, in case of external hyperthermia therapy (42 °C for 10 min), up-regulation of both HSP90 and AKT is observed suggesting activation of Heat Shock Response (HSR) and thermo-tolerance

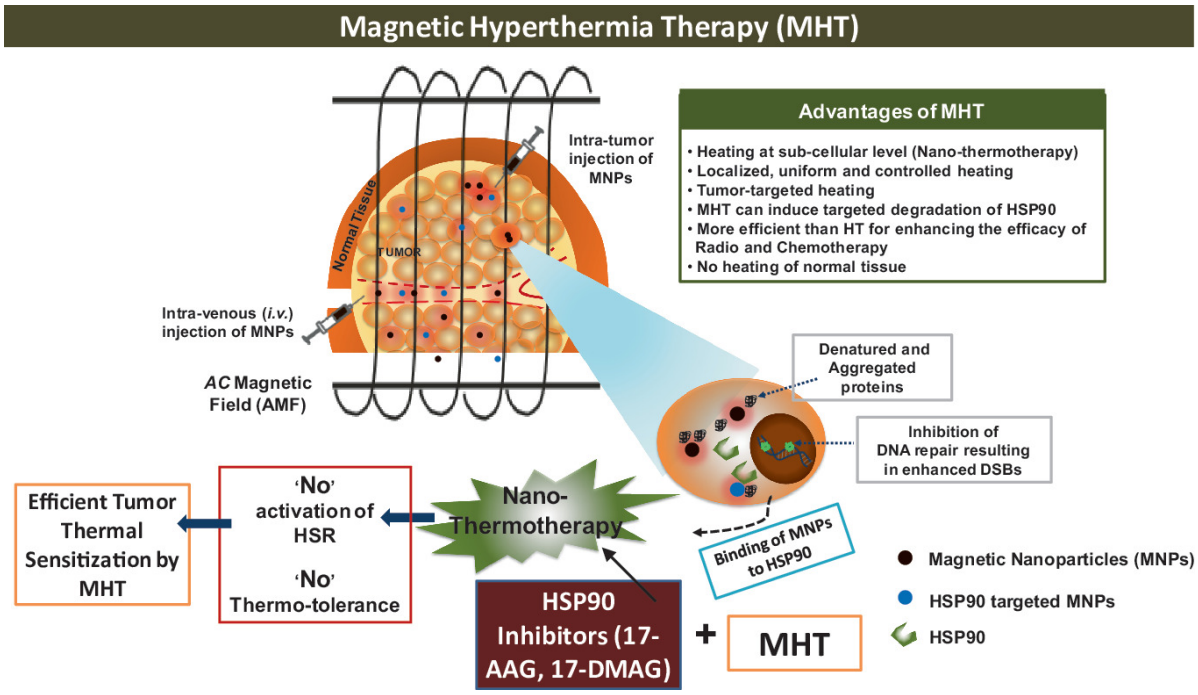

Fig. 19.3 Scheme for Mechanism of Magnetic Hyperthermia Therapy (MHT) and its advantages. The scheme depicts a novel approach of targeting intra-cellular HSP90 with oleic acid coated magnetic nanoparticles (MN-OA) to induce 'Nano-thermotherapy' mediated degradation of HSP90 thereby preventing induction of HSR and tumor thermo-tolerance. Additionally, combining other HSP90 inhibitors (17-AAG, 17-DMAG) can also improve the efficacy of MHT by inhibiting induction of HSR

Classically, successful application of HT as a stand-alone therapy has been severely hampered by thermo-tolerance phenomena, which in turn also prohibits the use of multiple heat treatments when used as an adjuvant to fractionated radiotherapy. As discussed in previous section, heat stress induces HSR via up-regulating the expression of several HSPs. Amongst HSPs, HSP90 being already highly abundant in cell (1–2% of total cellular protein under non-stress conditions) plays a major role in heat stress-induced thermo-tolerance. Although HSP90 inhibitors have been utilized to overcome the problem of thermo-tolerance, several clinical trials have shown their moderate performance when used in combination with HT or HT in combination with CRT. There are three major limiting factors for these inhibitors in the process of their clinical translation (i) poor solubility, bioavailability and pharmaco-kinetics, (ii) induction of HSR by inducing synthesis of other HSPs (like HSP70) during HSP90 inhibitor monotherapy and (iii) dose-limiting toxicities (Jhaveri et al. 1823; Tibor et al. 2023). Unlike the small molecule inhibitors, nanoparticles based magnetic hyperthermia therapy (MHT) can help to overcome the induction of

HSR following heating, thereby enhancing the efficacy of HT. Moreover, the nanoparticles would have an added advantage of improving the solubility, bioavailability and pharmaco-kinetics while targeted delivery of these inhibitors to the tumor site. Few reports demonstrate the beneficial effect of combining MHT with HSP90 inhibitors mainly via inhibiting the activation of HSR mediated thermo-tolerance. Yang R. et al. synthesized CD90-targeted thermosensitive magneto-liposomes (TMs)-encapsulated with 17-AAG (CD90@17-AAG/TMs) for targeted delivery of HSP90 inhibitor and MHT to liver cancer stem-like cells (LCSCs). Direct correlation was observed between the levels of HSP90 and efficacy of MHT. In case of TMs without the HSP90 inhibitor, the MHT treatment resulted in increased expression of HSP90. Whereas, in case of 17-AAG loaded TMs, significant decrease in HSP90 expression was observed which correlated with enhancement in the killing of LCSCs both in culture and in hepatocellular carcinoma-burdened nude mice model. Similar observation was made by Miyagawa and co-workers, wherein MHT was found to be more effective in killing melanoma cells both in vitro and in vivo, in case of pre-treatment with HSP90 inhibitor (17-DMAG) and HSP70 inhibitor (quercitin) (Miyagawa et al. 2014). These findings suggest the potential of combining HSP90 inhibitor and MHT for improving the efficacy of hyperthermia therapy for cancer (Fig. 19.3). It is pertinent to mention that above studies observed an increase in expression of HSP90 in response to MHT monotherapy.

19.6 Potential of HSP90 as a Prognotic Bio-marker for Hyperthermia Response

As discussed in the previous sections, tumor cells have been found to show increased expression of HSPs, particularly HSP90 which in turn has shown negative correlation with prognosis and overall survival of patients. Dionysios Th. Dimas and co-workers observed a correlation between high HSP90 expression and worse overall survival (pooled RR = 1.48, 95%CI = 1.21–1.82) and marginally with worse disease-free survival in 23 breast cancer patients (Dimas et al. 2018). Similar correlations have also been observed between serum levels of HSP90 and overall survival in case of cancer patients of lung, gastric and liver cancer (Rong et al. 2014; Shi et al. 2014; Han et al. 2021). Contrary to these studies in lung, breast,

liver and gastric cancer patients, an independent study by Dorota Pawlik-Gwozdecka and co-workers in 21 newly diagnosed childhood acute lymphoblastic leukemia (ALL) observed a negative correlation between HSP90 serum levels and peripheral blood lymphoblasts on the 8^{th} day of treatment (Pawlik-Gwozdecka et al. 2021). The authors explained that the trend was specific for pediatric patients, whereas in case of adult ALL patients, serum HSP90 levels were found to be elevated and correlated with poor overall survival or poor response to chemotherapy. Furthermore, few reports observed modulation of serum levels of HSP90 after hyperthermia suggesting the predictive capabilities of HSP90 for therapy response. Moreover, changes in the serum levels of HSP90/HSP70 after first round of HT has shown close association with a transient resistance of cells towards a subsequent second heat shock, which in turn may offer protection to cells from damage induced by a second round of HT (Tu et al. 2018). For instance, Tu et al., observed increase in the serum levels of HSP90 in 22 gastric cancer patients following hyperthermic intraperitoneal chemoperfusion (HIPEC), peaking at 18 h and returning to normal levels 24 h post-exposure (Tu et al. 2018).

Thus, these findings suggest that HSP90 levels in serum could serve as an indicator of response of cancer patients to HT and can also help in deciding the time interval between two HT sessions to maximize its cyto-toxic effect. Additionally, basal levels of HSP90 in serum of cancer patients could also serve as a parameter for patient stratification in terms of identifying patients (having low basal levels of HSP90) that are likely to respond positively to HT in combination with CRT. In similar lines, our laboratory carried out a preliminary study in head and neck cancer (HNSCC) patients and observed a significant up-regulation of serum HSP90 levels in HNSCC patients compared to healthy controls. Moreover, a retrospective analysis revealed a positive correlation between decreased serum levels of HSP90 after HT and CRT and complete response to therapy as compared to partial or non-responders (Shetake et al. 2023). Thus, HSP90 expression could serve as a promising bio-marker not only for cancer diagnosis but also for predicting the prognostic capability of HT in cancer patients or for patient stratification to reduce treatment failures.

19.7 Conclusions and Future Directions

Several clinical findings have established the therapeutic efficacy of HT modality mainly as an adjuvant therapy in combination with CRT. However, recent investigation into the physiological and molecular changes induced by HT in cancer cells highlights the critical role of HSPs, especially HSP90 expression in deciding the success or failure of HT. Nanoparticle based approaches have opened newer opportunities to tackle the problem of HSR induced by HT or HSP90 inhibitors for enhancing their therapeutic capabilities. Moreover, MHT using HSP90 targeted NPs could help to overcome the limitations of conventional HT and thus facilitating the translation of this promising target to clinical settings. Substantial research needs to be carried out in designing and validating NPs for MHT which could serve as the future of hyperthermia modality in treatment of cancer.

References

Alex, M., Jaeger, L.: Whitesell, HSP90: enabler of cancer adaptation. Annu. Rev. Cancer Biol. **3**, 275–297 (2019)
[Crossref]

Anand, S, Chan, T.A., Hasan, T., Maytin, E.V., Current prospects for treatment of solid tumors via photodynamic, photothermal, or ionizing radiation therapies combined with immune checkpoint inhibition (a review). Pharmaceuticals (Basel) **14**, 447 (2021)

Atkinson, W.J., Brezovich, I.A., et al.: Usable frequencies in hyperthermia with thermal seeds. IEEE Trans. Biomed. Eng. BME **31**, 70–75 (1984)

Barrott, J.J., Haystead, T.A.J.: Hsp90, an unlikely ally in the war on cancer. FEBS J **280**, 1381–1396 (2013)

Bhatia, S., Spanier, L., Bickel, D., Dienstbier, N., Woloschin, V., Vogt, M., Pols, H., Lungerich, B., Reiners, J., Aghaallaei, N., Diedrich, D., Frieg, B., Schliehe-Diecks, J., Bopp, B., Lang, F., Gopalswamy, M., Loschwitz, J., Bajohgli, B., Skokowa, J., Borkhardt, A., Hauer, J., Hansen, F.K., Smits, S.H.J., Jose, J., Gohlke, H., et al.: Development of a first-in-class small-molecule inhibitor of the C-terminal Hsp90 dimerization. ACS Cent. Sci. **8**, 636–655 (2022)

Birbo, B., Madu, E.E., Madu, C.O., Lu, Y., Jain, A.: Role of HSP90 in Cancer. Int. J. Mol. Sci. **22**, 10317 (2021)

Chaudhury, S., Keegan, B., Blagg, B.: The role and therapeutic potential of Hsp90, Hsp70, and smaller heat shock proteins in peripheral and central neuropathies. Med. Res. Rev. **41**, 202–222 (2021)
[Crossref][PubMed]

Cheng, Y., Weng, S., Yu, L., Zhu, N., Yang, M., Yuan, Y.: The role of hyperthermia in the multidisciplinary treatment of malignant tumors. Integr. Cancer Ther. **18**, 1534735419876345 (2019)

Chiosis, G., Neckers, L.: Tumor selectivity of Hsp90 inhibitors: the explanation remains elusive. ACS Chem. Biol. **1**, 279–284 (2006)

Crezee, J., Franken, N.A.P., Oei A.L.: Hyperthermia-based anti-cancer treatments. Cancers (Basel) **13**, 1240 (2021)

De Maio, A.: Extracellular heat shock proteins, cellular export vesicles, and the Stress Observation System: a form of communication during injury, infection, and cell damage. Cell Stress Chaperones **16**, 235–249 (2011)
[Crossref][PubMed]

Dimas, D.T., Perlepe, C.D., Sergentanis, T.N., Misitzis, I., Kontzoglou, K., Patsouris, E., Kouraklis, G., Psaltopoulou, T., et al.: The prognostic significance of Hsp70/Hsp90 expression in breast cancer: a systematic review and meta-analysis. Anticancer Res. **38**, 1551–1562 (2018)

Donahue, K., Xie, H., Li, M., Gao, A., Ma, M., Wang, Y., Tipton, R., Semanik, N., Primeau, T., Li, S., Li, L., Tang, W., Xu, W.: Diptoindonesin G is a middle domain HSP90 modulator for cancer treatment. J. Biol. Chem. **298**, 102700 (2022)
[Crossref][PubMed][PubMedCentral]

Donnelly, A., Blagg, B.S.J.: Novobiocin and additional inhibitors of the Hsp90 C-terminal nucleotide-binding pocket. Curr. Med. Chem. **15**, 2702–2717 (2008)

Dubey, A., Prajapati, K.S., Swamy, M., Pachauri, V.: Heat shock proteins: a therapeutic target worth to consider. Vet World **8**, 46–51 (2015)

Fan, G., Tu, Y., Wu, N., Xiao, H.: The expression profiles and prognostic values of HSPs family members in Head and neck cancer. Cancer Cell Int. **20**, 220 (2020)

Fatima, H., Charinpanitkul, T., et al.: Fundamentals to apply magnetic nanoparticles for hyperthermia therapy. Nanomaterials **11**, 1203 (2021)

Griffin, R.J., Dings, R.P., Jamshidi-Parsian, A., et al.: Mild temperature hyperthermia and radiation therapy: role of tumour vascular thermotolerance and relevant physiological factors. Int. J. Hyperthermia. **26**, 256–263 (2010)

Grimmig, T., Moll, E.-M., Kloos, K., Thumm, R., Moench, R., Callies, S., Kreckel, J., Pelz, J.: Upregulated heat shock proteins after hyperthermic chemotherapy point to induced cell survival mechanisms in affected tumor cells from peritoneal carcinomatosis. Cancer Growth Metastasis **10** (2017)

Han, Y., Zhang, Y., Cui, L., Li, Z., Feng, H., Zhang, Y., Sun, D., et al.: Plasma heat shock protein 90alpha as a biomarker for the diagnosis of liver cancer: in patients with different clinicopathologic characteristics. World J. Surg. Oncol. **19**, 228 (2021)

Herrero de la Parte, B., Rodrigo, I., Gutiérrez-Basoa, J., Iturrizaga Correcher, S., Mar Medina, C., Echevarría-Uraga, J.J., Garcia, J.A., Plazaola, F., et al.: Proposal of new safety limits for in vivo experiments of magnetic hyperthermia antitumor therapy. Cancers (Basel) **14**, 3084 (2022)

Hu, C., Yang, J., Qi, Z., Wu, H., Wang, B., Zou, F., Mei, H., Liu, J., Wang, W., Liu, Q.: Heat shock proteins: biological functions, pathological roles, and therapeutic opportunities. MedComm **3**, e161 (2022)

Ito, A., Saito, H., Mitobe, K., Minamiya, Y., Takahashi, N., Maruyama, K., Motoyama, S., Katayose, Y., Ogawa, J.-I.: Inhibition of heat shock protein 90 sensitizes melanoma cells to thermosensitive ferromagnetic particle-mediated hyperthermia with low Curie temperature. Cancer Sci. **100**, 558–564 (2009) [Crossref][PubMed][PubMedCentral]

Jee, H.: Size dependent classification of heat shock proteins: a mini-review. J. Exerc. Rehabil. **12**, 255–259 (2016)

Jackson, S.E.: Hsp90: structure and function. Top Curr. Chem. **328**, 155–240 (2013)

Jhaveri, K., Taldone, T., Modi, S., Chiosis, G.: Advances in the clinical development of heat shock protein 90 (Hsp90) inhibitors in cancers. Biochimica et Biophysica Acta (BBA)—Mol. Cell Res. **1823**, 742–755 (2012)

Rochani, A.K., Balasubramanian, S., Ravindran Girija, A., Maekawa, T., Kaushal, G., Kumar, D.S.: Heat shock protein 90 (Hsp90)-inhibitor-luminespib-loaded-protein-based nanoformulation for cancer therapy. Polymers **12**, 1798 (2020)

Kamal, A., Thao, L., Sensintaffar, J., Zhang, L., Boehm, M.F., Fritz, L.C., et al.: A high-affinity conformation of Hsp90 confers tumour selectivity on Hsp90 inhibitors. Nature **425**, 407–410 (2003)

Kanazawa, Y., Isomoto, H., Oka, M., Yano, Y., Soda, H., Shikuwa, S., Takeshima, F., Omagari, K., Mizuta, Y., Murase, K., Nakagoe, T., Ohtsuka, K., et al.: Expression of heat shock protein (Hsp) 70 and Hsp 40 in colorectal cancer. Med. Oncol. **20**, 157–164 (2003)

Kritika, Roy, I.: Therapeutic applications of magnetic nanoparticles: recent advances. Mater. Adv. **3**, 7425–7444 (2022)

Li, Z.N., Luo, Y.: HSP90 inhibitors and cancer: prospects for use in targeted therapies (Review). Oncol. Rep. **49**, 6 (2023)

Li, Y., Zhang, T., Schwartz, S.J., et al.: New developments in Hsp90 inhibitors as anti-cancer therapeutics: mechanisms, clinical perspective and more potential. Drug Resist. Updat. **12**, 17–27 (2009)

Liu, L., Deng, Y., Zheng, Z., Deng, Z., Zhang, J., Li, J., Liang, M., Zhou, X., Tan, W., Yang, H., Neckers, L.M., Zou, F., Chen, X.: Hsp90 inhibitor STA9090 sensitizes hepatocellular carcinoma to hyperthermia-induced DNA damage by suppressing DNA-PKcs protein stability and mRNA transcription. Mol. Cancer Ther. **20**, 1880–1892 (2021)

Murphy, M.E.: The HSP70 family and cancer. Carcinogenesis **34**: 1181–1188 (2013)

Miyagawa, T., Saito, H., Minamiya, Y., Mitobe, K., Takashima, S., Takahashi, N., Ito, A., Imai, K., Motoyama, S., et al.: Inhibition of Hsp90 and 70 sensitizes melanoma cells to hyperthermia using ferromagnetic particles with a low Curie temperature. Int. J. Clin. Oncol. **4**, 722–730 (2014)

Miyata, Y., Nakamoto, H., Neckers, L., The therapeutic target Hsp90 and cancer hallmarks. Curr. Pharm. Des. **19**, 347–365 (2013)

Pawlik-Gwozdecka, D., Górska-Ponikowska, M., Adamkiewicz-Drożyńska, E., et al.: Serum heat shock protein 90 as a future predictive biomarker in childhood acute lymphoblastic leukemia. Cent. Eur. J. Immunol. **46**, 63–67 (2021)

Profumo, E., Buttari, B., Tinaburri, L., D'Arcangelo, D., Sorice, M., Capozzi, A., Garofalo, T., Facchiano, A., Businaro, R., Kumar, P., Singh, B.K., Parmar, V.S., Saso, L., et al.: Oxidative stress induces HSP90 upregulation on the surface of primary human endothelial cells: role of the antioxidant 7,8-dihydroxy-4-methylcoumarin in preventing HSP90 exposure to the immune system. Oxid. Med. Cell. Longev. **2018**, 2373167 (2018)

Ritossa, F.: Discovery of the heat shock response. Cell Stress Chaperones. **1**, 97–98 (1996)

Rochani, A.K., Balasubramanian, S., Girija, A.R., Raveendran, S., Borah, A., Nagaoka, Y., Nakajima, Y., Maekawa, T., Kumar, D.S.: Dual mode of cancer cell destruction for pancreatic cancer therapy using Hsp90 inhibitor loaded polymeric nano magnetic formulation. Int. J. Pharm. **511**, 648–658 (2016)

Rong, B., Zhao, C., Liu, H., Ming, Z., Cai, X., Gao, W., et al.: Identification and verification of Hsp90-beta as a potential serum biomarker for lung cancer. Am. J. Cancer Res. **4**, 874–885 (2014)

Sanchez, J., Carter, T.R., Cohen, M.S., et al.: Old and new approaches to target the Hsp90 chaperone. Curr. Cancer Drug Targets **20**, 253–270 (2020)

Scutigliani, E.M., Liang, Y., IJff, M., Rodermond, H., Mei, X., Korver, M.P., Orie, V.S., Hoebe, R.A., Picavet, D.I., Oei, A.E.A.: Evaluation of the heat shock protein 90 inhibitor ganetespib as a sensitizer to hyperthermia-based cancer treatments. Cancers **14**, 5250 (2022)

Shetake, N.G., Kumar, A., et al.: Iron-oxide nanoparticles target intracellular HSP90 to induce tumor radio-sensitization. Biochim. Biophys. Acta Gen. Subj. **1863**, 857–869 (2019)

Shetake, N.G., Kumar, A., Gaikwad, S., Ray, P., Desai, S., Ningthoujam, R.S., Pandey, B.N.: Magnetic nanoparticle-mediated hyperthermia therapy induces tumour growth inhibition by apoptosis and Hsp90/AKT modulation. Int. J. Hyperth. **31**, 909–919 (2015)

Shetake, N. G., Kumar, A., Huilgol, N., Pandey, B. N.: Diagnostic potential of serum HSP90 beta for HNSCC and its therapeutic prognosis after local hyperthermia therapy. PLoS ONE **18**(11), e0281919 (2023). https://doi.org/10.1371/journal.pone.0281919

Shetake, N., Pandey, B.: Hyperthermia therapy of cancer: need for deeper biological insights for improved therapeutic outcome. J. Radiat. Cancer Res. **10**, 170–173 (2019) [Crossref]

Shi, Y., Liu, X., Lou, J., Han, X., Zhang, L., Wang, Q., Li, B., Dong, M., et al.: Plasma levels of heat shock protein 90 alpha associated with lung cancer development and treatment responses. Clin. Cancer Res. **20**, 6016–6022 (2014)

Smalley, M., Natarajan, S.K., Mondal, J., Best, D., Goldman, D., Shanthappa, B., Pellowe, M., Dash, C., Saha, T., Khiste, S., Ramadurai, N., Eton, E.O., Smalley, J.L., Brown, A., Thayakumar, A., Rahman, M., Arai, K., Kohandel, M., Sengupta, S., Goldman, A.: Nanoengineered disruption of heat shock protein 90 targets drug-induced resistance and relieves natural killer cell suppression in breast cancer. Cancer Res. **80**, 5355–5366 (2020)

Soti, C., Vermes, A., Haystead, T.A., et al.: Comparative analysis of the ATP-binding sites of Hsp90 by nucleotide affinity cleavage: a distinct nucleotide specificity of the C-terminal ATP-binding site. Eur. J. Biochem. **270**, 2421–2428 (2003)

Sumi, M.P., Ghosh, A.: Hsp90 in human diseases: molecular mechanisms to therapeutic approaches. Cells **11**, 976 (2022)

Tibor, C., Magyar, J., Vashist, Y.K., Stroka, D., Kim-Fuchs, C., Berger, M.D., Banz, V.M.: Heat shock protein 90 (HSP90) inhibitors in gastrointestinal cancer: where do we currently stand?—A systematic review. J. Cancer Res. Clin. Oncol. (2023)

Tu, Y., Tian, Y., Wu, Y., et al.: Clinical significance of heat shock proteins in gastric cancer following hyperthermia stress: Indications for hyperthermic intraperitoneal chemoperfusion therapy. Oncol. Lett. **15**, 9385–9391 (2018)

Vriend, L.E.M., van den Tempel, N., Oei, A.L., L'Acosta, M., Pieterson, F.J., Franken, N.A.P., Kanaar, R., et al.: Boosting the effects of hyperthermia-based anticancer treatments by HSP90 inhibition. Oncotarget **8**, 97490–97503 (2017)

Yamada, K., Fukao, Y., Hayashi, M., Fukazawa, M., Suzuki, I., Nishimura, M.: Cytosolic HSP90 regulates the heat shock response that is responsible for heat acclimation in Arabidopsis thaliana. J. Biol. Chem. **282**, 7794–37804 (2007)

Yang, S., Xiao, H., Cao, L.: Recent advances in heat shock proteins in cancer diagnosis, prognosis, metabolism and treatment. Biomed. Pharmacother. **142**, 112074 (2021) [Crossref][PubMed]

Yang, R., Tang, Q., Miao, F., An, Y., Li, M., Han, Y., Wang, X., Wang, J., Liu, P., Chen, R.: Inhibition of heat-shock protein 90 sensitizes liver cancer stem-like cells to magnetic hyperthermia and enhances anti-tumor effect on hepatocellular carcinoma-burdened nude mice. Int. J. Nanomed. **10**, 7345–7358 (2015)

Yang, M., Zhang, F., Yang, C., Wang, L., Sung, J., Garg, P., Zhang, M., Merlin, D.: Oral targeted delivery by nanoparticles enhances efficacy of an Hsp90 inhibitor by reducing systemic exposure in murine models of colitis and colitis-associated cancer. J. Crohns. Colitis. **14**, 130–141 (2020)

Zhong, L., Li, Y., Xiong, L., Wang, W., Wu, M., Yuan, T., Yang, W., Tian, C., Miao, Z., Wang, T., Yang, S.: Small molecules in targeted cancer therapy: advances, challenges, and future perspectives. Signal Transduct. Target. Ther. **6**, 201 (2021)

© The Author(s), under exclusive license to Springer Nature Singapore Pte Ltd. 2024
R. S. Ningthoujam, A. K. Tyagi (eds.), *Handbook of Materials Science, Volume 2*, Indian Institute of Metals Series
https://doi.org/10.1007/978-981-97-4646-0_20

20. Magnetic–Luminescent Nanocomposites for Cancer Hyperthermia Therapy

Goutam Singh Ningombam[1] ✉ and Nongmaithem Rajmuhon Singh[1, 2]
(1) Department of Chemistry, Manipur University, Imphal, 795003, Manipur, India
(2) Dhanamanjuri University, Imphal, 795001, Manipur, India

✉ **Goutam Singh Ningombam**
Email: ningombam12@gmail.com

Keywords Magnetic nanoparticles – Magnetic–luminescent nanocomposites – Magnetic fluid hyperthermia – Cancer therapy

20.1 Introduction

Cancer is one of the dreaded diseases causing a serious threat to life expectancy and deep emotional issues to patients as well as the near and dear ones. The strategic efforts for early diagnosis, prevention, and cure of the disease is one of the many goals extensively pursued by researchers from various disciplines including physicists,

chemists, and medicine. According to a report released by The International Agency for Research on Cancer (IARC), there were 19.3 million new cases of cancer and almost 10 million deaths from cancer in 2020 (Sung et al. 2021). It is expected that the global burden of cancer occurrence could grow to 27.5 million new cancer cases and 16.3 million cancer deaths simply due to the growth and aging of the population by the year 2040 (Global Cancer Facts & Figures, American Cancer Society, https://www.cancer.org/research/cancer-facts-statistics/global.html). The number of new cancer cases has been alarmingly shocking and indicates the need for all possible interventions to save human lives from this deadliest disease. There are well-known methods of treatment of cancers such as chemotherapy, radiotherapy, immunotherapy, surgical removal of cancerous tissues or organs, and conventional hyperthermia. Chemotherapy uses chemicals or drugs to destroy cancer cells. Immunotherapy relies on activating the anticancer immune response in the patient using various approaches (e.g., monoclonal antibodies, checkpoint inhibitors, etc.). Radiotherapy usually uses a specific dose range typically used in clinics to kill cancer cells and shrink tumors. Chemotherapy and radiotherapy are known to cause certain side effects which may sometimes be severe leading to visible hair loss, fertility issues, organ stress, etc. Hyperthermia therapy involves controlled elevation of temperature of body tissues that could destroy blood vessels, disrupt cellular functions of cancer cells, and ultimately kill the cancer. It is based on the difference in sensitivity of the normal and cancerous tissues toward the heat which is governed by the difference in physiological conditions. The hyperthermia can be localized, regional, or whole-body hyperthermia depending on the type of cancer and severity of the issues (Zee 2002). One of the new approaches and highly envisaged method is magnetic fluid hyperthermia, i.e., the thermal destruction

of cancerous tissues through intratumoral heat generation from the magnetic particles accumulated in the vicinity of the cancerous tissues on exposure to alternating magnetic field. The cancerous tissues are very sensitive and can be destroyed when heated above 41 °C to about 46 °C and above this temperature, the over-heating can lead to thermal ablation of normal cells (Zee 2002). The use of superparamagnetic iron oxide nanoparticles and magnetic–luminescent nanocomposites composed of magnetic iron oxide and luminescent inorganic-based components, mainly quantum dots and lanthanide-based oxides, are encouraged for the use in magneto-thermal killing of cancer cells. The magnetic nanoparticles can be functionalized with various biocompatible molecules or the surfaces can be modified with targeting receptor molecules to specifically deliver to cancer tissues. Chemotherapeutic drugs are also loaded onto the modified nanoparticles for delivery and accumulation by magnetic guidance. The combined approach of hyperthermia with radiotherapy, chemotherapy, or gene therapy can increase the therapeutic efficacy in cancer therapy (Zee 2002; Wust et al. 2002). The surroundings of the cancerous tissues are hypoxic and it makes the tissues radioresistant (Reinhold and Endrich 1986; Engin et al. 1995). The radiosensitivity and compliance of chemotherapeutic drugs were observed to increase when hyperthermia was administered in combination in which the latter complementary method increased blood flow and tissue oxygenation, intracellular drug uptake or intratumor drug accumulation, and subsequent DNA damage (Song et al. 2005; Dunne et al. 2019). The heating of the tissues also resulted in the disruption of the actin and tubulin cytoskeletons, protein denaturation, protein misfolding and aggregation, DNA crosslinking, and cellular damage leading to the death of cancer cells (Goldstein et al. 2003; Prasad et al. 2007; Rand et al. 1982; Fairbairn et al. 1995). Consequently, the

intracellular heating of tissues using magnetic iron oxide nanoparticles can be studied as a potential means of cancer therapy.

The use of magnetic iron oxide nanoparticles in the thermal destruction of cancerous tissues or magnetic fluid hyperthermia was pursued by many researchers. Here, the dispersion of the magnetic nanoparticles in a suitable solvent and subsequent delivery either magnetically or by enhancing chemically targeting capability to the vicinity of the cancerous tissues and generation of heat under the influence of an external alternating magnetic field were the important methodologies adopted. The elevation of temperature above the said temperature range may lead to thermal ablation of normal cells and therefore a controlled methodology is extremely important. Some of the citable factors which make the iron oxide-based magnetic nanoparticles and magnetic–luminescent nanocomposites potential candidates for magnetic fluid hyperthermia are mentioned below:

(a) Biocompatible nature, physiological stability, and easy removal through metabolic pathways of iron oxide nanoparticles compared to metal alloy nanoparticles (e.g., FeCo and FePt) (Ling and Hyeon 2013);

(b) Efficient magnetization of iron oxide NPs and their response to external alternating magnetic field for heat generation and magnetic resonance imaging;

(c) Possibility of conjugation of iron oxide nanoparticles with various therapeutic drugs, magnetically activated drug delivery, and accumulation at the target tissues which could minimize the side effects of the chemotherapeutic chemicals;

(d) Composite formation with various luminescent components such as organic dyes, quantum dots

(QDs), and downconversion or upconversion lanthanide-based inorganic oxides without losing the magnetic character, though magnetization may be reduced with low MNPs content;

(e) Multimodality of the nanocomposites for combined (in vitro, in vivo) imaging and hyperthermia, drug delivery, photodynamic therapy, and photothermal therapy.

Keeping in view of the present trends of research in the field of cancer therapy using magnetic nanoparticles and magnetic–luminescent nanocomposites, the designing of multimodal nanocomposites capable of optical-imaging-guided-hyperthermia, drug delivery, and photodynamic and photothermal therapy is in a younger stage and still marching toward a maturity level for clinical administration. A typical illustration of magnetic fluid hyperthermia with multimodal magnetic–luminescent nanocomposite is shown in Fig. 20.1. It is therefore important to cover the various fundamental aspects of magnetic nanoparticles and magnetic–luminescent nanocomposites.

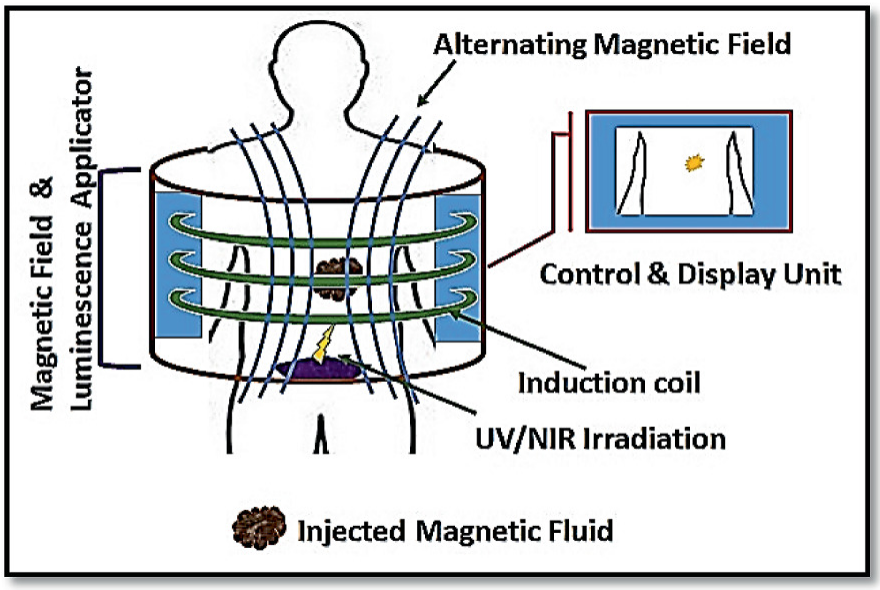

Fig. 20.1 Typical illustration of magnetic fluid hyperthermia with multimodal magnetic–luminescent nanocomposite

20.2 A Brief History of Tissue Heating: The Path to Magnetic Fluid Hyperthermia

The word “hyperthermia” is derived from a combination of two words—an English word “*hyper*” which means beyond and a Greek word *“therme”* meaning heat which became popular in the late nineteenth century. By definition, it is the condition of having a body temperature greatly above normal. On a medical note, hyperthermia is a technique of induced heating within the temperature range of 40–46 °C to destroy cancer cells (Wust et al. 2002). The method of hyperthermia is considered to be non-invasive compared to chemotherapy and radiotherapy or the combined administration of hyperthermia plus chemotherapy/radiotherapy was found to show substantial additive therapeutic effects. The conventional techniques of hyperthermia for treatment of cancer use radiowaves (10–100 MHz), microwaves (>300 MHz), and infrared or ultrasonic radiations for heating the cancer tissues. Later, in order to achieve efficient local heating, the use of magnetic nanoparticles for induced heating was being envisaged by the scientific community, which is now commonly known by the term “magnetic fluid hyperthermia (MFH).” This new approach is based on the ability of the magnetic particles to generate heat under the influence of an alternating magnetic field (AMF).

The concept and experiment on killing of cancerous tissues with the use of magnetic nanoparticles started early in the latter part of the 1950s. It was in 1957 that Gilchrist et al. used Fe_2O_3 for selective induction heating of lymph nodes to destroy metastases of cancerous cells in lymph

nodes which were left out during the surgical operation (Gilchrist et al. 1957). A magnetic field strength of 200–240 Oersteds and 5 mg of iron oxide (0.02–0.1 μ in size) per gram of lymph nodes was administered where a dog was used for the purpose. Again in 1959, Medal et al. demonstrated the gross induction heating effect in rabbit. The Fe_2O_3 suspension was administered to the scrotal sac of the animal. A deposition of 30–70 mg of Fe_2O_3 per gram of tissue was observed and after treatment for only 3 min, the local necrosis in the intertesticular area at the site of iron oxide deposition can be seen. Further, local hyperemia and coagulation necrosis were observed in and about the deep nodes in the inguinal region (Medal et al. 1959). Their study focused on the achievement of maximum heat generated from the magnetic particle which further observed that higher frequency can cause the heating up of normal tissues and therefore the operating frequency has to be reduced to achieve better differential heating of tissues in animals. The reduction of frequency is necessary to reduce eddy current heating in normal tissues. These two reports have opened the further possibility and modifications of strategy for applications of magnetic nanoparticles mediated hyperthermia for destruction of cancerous tissues.

For many years that followed, the study on the potentials of the magnetite, ferric hydroxide, and ferri-/ferromagnetic microparticles continued with a great zeal. In 1979, R. T. Gordon and coworkers demonstrated tumor cell destruction in spontaneous mammary tumors in Sprague Dawley rats via intracellular hyperthermia with the use of dextran magnetic iron oxide particles (Gordon et al. 1979). The selective uptake of magnetic particles and the heating-induced intracellular alteration of the biophysical properties of the cancer cells were illustrated. The cancer cells have a far greater affinity and uptake of

foreign particles than do the normal cells. Their report emphasized the therapeutic enhancement by intracellular heating in precise increments and selective destruction of cancer cells without affecting the functions of the normal cells and the surroundings. Rand and coworkers, in 1982, demonstrated the ischemic necrosis followed by heating-induced coagulation necrosis in an experimental rabbit VX_2 renal cancer model. They employed needle-shaped microferromagnetic (0.1–1 μm) particles and sufficiently low-frequency alternating magnetic fields to reduce eddy current and dielectric heating (Rand et al. 1982). In 1983, Luderer et al. used ferromagnetic glass–ceramic particles (about 1.5 μm in size) administered intravenously and exposure to external alternating magnetic field (500 Oe, 10 kHz) for 2 h to treat Meth-A sarcoma in 33 Balb/cJ mice models (Luderer et al. 1983). 17 out of 33 mice showed tumor regrowth delay and ultimately permanent control in 4 mice. In the later part of the 1980s, there were also some other works which showed antitumor activity by induction heating of magnetic materials. These works have opened the opportunity toward understanding and advancing a step further for the utilization of magnetic nanoparticles for magnetic fluid hyperthermia of cancer therapy.

However, the reports mentioned above utilized multidomain magnetic materials and do not present a qualitative and quantitative picture regarding the nature of heating and the factors to be considered for efficient delivery of heat. Then in 1993, Jordan and his coworkers, who can be called the pioneers of magnetic fluid hyperthermia, put forward the potential of colloidal subdomain ferrite particle suspensions (also called magnetic fluids) exposed to an alternating magnetic field for applications in hyperthermia (Jordan et al. 1993). Their works have emphasized the mechanisms of energy absorption of the magnetic materials and the heating

efficiencies based on their morphology, the frequency, and the strength of the magnetic field. This was one of the important reports regarding the utilization of subdomain magnetic ferrite materials with the size less than 10 nm which were prepared into magnetic colloidal fluids. A stabilized fluid containing dextran–coated particles of about 3 nm and a poorly stabilized fluid of about 7 nm. The term specific absorption rate (SAR) which is well distinguished from the hysteresis and eddy heating was used to express the inductive heating abilities of the particles. Their studies have suggested that the heat generation ability was dependent on the dynamic behavior of the single subdomain particles—Neel and Brownian relaxation of the magnetic moments of the magnetic particles—in an alternating magnetic field and the single subdomain ferrite particles are superior to the multidomain particles. The physical interpretation of these relaxation mechanisms was reported earlier by Shliomis et al. and Hanson et al. (Shliomis et al. 1990; Hanson 1991). Also in 1993, a similar analysis was reported by Chan and coworkers (Chan et al. 1993). In their work, the absorption rates of dextran stabilized colloidal superparamagnetic iron oxide (magnetite) were measured at certain frequencies, magnetic field strengths, and colloidal iron oxide in polyacrylamide (1–20%) gels. The distinguishing contributions from the Neel and Brownian relaxation in the heat generation were studied and observed the dominant contribution from the Neel relaxation in their studies. The human lung adenocarcinoma cell line A549 and breast carcinoma cell line ZR75 experienced a significant cell death on exposure to temperatures in the range of 42–45 °C. The heating was achieved either through hyperthermia induced by an alternating magnetic field in the presence of magnetic particles or water bath. Therefore, heating therapy was shown to be a good approach for tumor inactivation.

Later, from the quantitative analysis of the magnetism and heat generation characteristics of the multidomain and subdomain magnetic particles, the realm of research has transformed into in vitro and preclinical in vivo analyses. During 1996–2001, Jordan and coworkers reported experiments on various cell lines such as WiDr (ATCC CCL 218) human colonic adenocarcinoma, C3H mammary carcinoma, BT20 (ATCC HTB 19) mammary carcinoma, human fibroblast, RuSi-RS1 malignant glioma, prostate carcinoma, normal cortical neuronal cells (Jordan et al. 1996, 1997, 1999, 2001). Depending on the types of cell lines and the ferrofluid materials used for the studies, differential endocytosis was observed. In most of these works, modified dextran-coated magnetite and aminosilane-coated magnetite nanoparticles were used. Efficient inactivation of cells was observed after exposure of the cells treated with magnetic ferrofluids to alternating magnetic fields. There was either homogeneous or heterogenous inactivation of tumor cells in case of intravenously administered ferrofluids (dextran-coated ferrofluids) in mice models with WiDr (ATCC CCL 218) human colonic adenocarcinoma and C3H mammary carcinoma, respectively. The heterogeneous inactivation was supposed to be due to inadequate homogeneous distribution of ferrofluid throughout the tumor. These works used a frequency of 520 kHz and a magnetic field of 4–12.5 kA/m to raise the temperature to 43 °C and 47 °C, respectively, in the above cells. The team urged the therapeutic approach by interstitial magnetic fluid hyperthermia to be an effective method for tumor control. Hilger et al. also observed intratumoral variations of deposited heat dosage (DHD which is defined as the area between the time-dependent temperature curves during treatments and the temperature level without heating) in SCID mice implanted with human breast adenocarcinomas (Hilger et al. 2002). The region of heating underdosages

arises from the low dosage distribution of magnetic fluid within the tumor affected by the morphology of iron oxide nanoparticle distribution and divergent texture of the tumor tissue. Meanwhile, administration of large amount of magnetic particles was not encouraged as it would increase interstitial pressure of the tumor and migration of tumor cells into the surrounding could occur fast. The nanoparticles were preferentially washed out from the intratumoral deposition by the circulatory system. The difference in the distribution of magnetic particles in lungs, liver spleen, and blood after 50 min of intratumoral injection was ascribed to the nature of particle agglomeration and surface chemistry. The detailed chemistry of the surface modification was not mentioned in the literature and therefore no specific reasons were pointed out. During 2004–2006, Johannsen and coworkers described the in vivo magnetic fluid hyperthermia in MatLyLu prostate cancer cells inducted in Copenhagen rat models after intratumoral injection of aminosilane-coated magnetic fluids which showed promising results (Johannsen et al. 2004, 2005a, 2006). The instraprostatic nanoparticle infiltration was genuinely significant and the intratumoral accumulation was found to be approximately 79% after 4 days of MFH treatment (Johannsen et al. 2004). Later, another study showed that approximately 82.5% of the intratumorally injected nanoparticles were found in the prostate of the MFH-treated and untreated Copenhagen rats, whereas 5.3% in liver, 1.0% in lungs, and 0.5% in spleen. Two consecutive MFH treatments after a single intratumoral injection reduced the local tumor growth by about 50% in the orthotopic tumor of rats (Johannsen et al. 2005a). Another very exciting achievement was the combined treatment using MFH and radiotherapy which showed a significant and additive reduction of local tumor at comparatively 3 times lower radiation exposure when combined with magnetic fluid

hyperthermia (Johannsen et al. 2006). In 2006, a pre-clinical trial was again reported for the treatment of glioblastoma multiforme (malignant intracranial tumor) in 120 male Fisher rats (Jordan et al. 2006). The reported works used dextran-coated and aminosilane-coated magnetic iron oxide nanoparticles for the thermotherapeutic pre-clinical treatments. The aminosilane-coated magnetic nanoparticles showed high therapeutic efficiency which increased the survival time of the rats by 4.5 times over the control rat groups whereas the dextran-coated materials do not show any significant efficiency. The aminosilane-coated nanoparticles showed stable interstitial deposition as well as homogeneous distribution within the tumor tissue even after the heat treatments. On the other hand, the dextran-coated nanoparticles spread into the surrounding tissues. These studies demonstrated the feasibility of the new form of hyperthermia based on magnetic fluid to proceed for the clinical trial stage.

The regulation of heat shock proteins and enhancement of antitumor immunity with the use of intratumoral hyperthermia methods were beneficial for regression of tumors (Yanase et al. 1998; Ito et al. 2003a, 2009; Tanaka et al. 2005; Sato et al. 2010; Takada et al. 2009). Yanase et al. observed disappearance of tumors in female F344 rats due to antitumor immunity effects (Yanase et al. 1998). Glioma T-9 cells were transplanted on the left and right femurs of the rats. After injection of magnetic cationic liposomes, the left femoral tumor was subjected to alternating magnetic field (118 kHz, 384 Oe) for 30 min thrice at 24-h intervals. The tumors disappeared in both the femoral regions, however after a period of transient growth. From the immune-cytochemical assay, it was obvious that the hyperthermia treatment induced a host immune response mediated by both $CD8^+$ and $CD4^+$ T cells

and accompanied by a marked augmentation of tumor-selective cytotoxic T-lymphocyte activity. Kawai et al. used magnetic cationic liposomes (MCL) to analyze the effect of repeated hyperthermia on experimental prostate cancer in mice models (Kawai et al. 2005, 2006). The prostate cancer—PLS10, PC3, and LNCap—inducted mice were subjected to hyperthermia temperature of 45 °C for 30 min. The LNCap cells were found to be more sensitive to hyperthermia. Suppression or complete regression of the tumors was observed after different numbers of days in each mouse. In case of PLS10 mice, the heat treatment led to appearance of heat shock protein (HSP70) in viable tissue at its boundary with necrotic tissue, while immune response was also induced specifically in PLS10 cells. The induced immune response was eventually complementing antitumor immune reaction and complete tumor regression. In another parallel work published shortly afterward, an in vitro and in vivo anticancer efficacy of combined hyperthermia plus chemotherapy was demonstrated with the use of 4-S-cysteaminylphenol loaded onto magnetic cationic liposomes (4-S-CAP/MCL) on B16 melanoma cells (Ito et al. 2007). The C57BL/6 mice carrying B16 melanoma tumors received the therapeutic materials via intratumoral injection and were subjected to 45 °C for 30 min for in vivo hyperthermia. The tumors showed progressive growth in mice treated with or without magnetic cationic liposomes. The tumors were suppressed significantly in mice treated with 4-S-CAP/MCL alone or MCL with hyperthermia. Strong suppression of tumor was observed when mice were treated with 4-S-CAP/MCL plus hyperthermia and 17% (1/6) of subcutaneous tumors were regressed completely. Ito et al. and Tanaka et al. also demonstrated tumor regressions, respectively, in glioma-induced F344 mice and melanoma induced in C57BL/6 mice due to antitumor response caused by the heat-induced expression of heat shock protein 70 (HSP70) (Tanaka et al.

2005). While Ito et al. used magnetic cationic liposomes, Tanaka et al. used a combination of magnetic cationic liposomes and immature dendritic cells. This method was proposed to be an in situ vaccination to boost immunity against tumor growth. The intratumoral hyperthermia on B16-OVA mouse melanoma (B16F1, B16F10, and B16 OVA) transplanted C57BL/6 mice using magnetic nanoparticles conjugated with melanogenesis substrate, N-propionyl-4-S-cysteaminylphenol (NPr-CAP) is encouraged to be a promising treatment for advanced metastatic melanomas subject to clinical effectiveness (Sato et al. 2010; Takada et al. 2009). This is a combination strategy of chemotherapy, thermotherapy, and immune therapy. The NPr-CAP inhibits the growth of melanoma by producing cytotoxic free radicals and the magnetite generates heat under the influence of an alternating magnetic field which consequently leads to release of heat shock protein–peptide complexes and activated antitumor immune response through the tumor antigen-specific cytotoxic T-lymphocytes (CTL) that destroys cancer tissues. Another strategy of magnetic fluid hyperthermia followed by injection of immunotherapeutic drugs into the tumor site with efficient tumor regression, hinted at combined methodology for patients with advanced malignancies, was reported (Ito et al. 2003b). Interleukin-2 (IL-2) or granulocyte macrophage-colony stimulating factor (GM-CSF) were used in the study. Female C57BL/6 mice bearing B16 melanoma were either treated with hyperthermia, immunotherapy, or combined methods. The immunotherapeutic drugs were injected into the melanoma nodule after 24 h of heat therapy in a group of mice. The group of mice which were heat treated prior to injection of interleukin-2 (IL-2) or granulocyte macrophage-colony stimulating factor (GM-CSF) showed complete regression of tumors—75% (i.e., 6/8 in IL-2 treated) and 40% (i.e., 4/10 in GM-CSF treated) of the mice, whereas other groups treated by heating or immunotherapy alone

had not caused to kill tumor cells. Here, the prior heating served as in situ vaccination followed by drugs served the purpose of augmenting the vaccine-induced response against tumor cells. On the other hand, heat shock protein 90 (HSP90) is a key participant in oncogenesis and it mediates thermotolerance during hyperthermia therapy. It is necessary to inhibit this particular protein to enhance the effect of heat therapy. Geldanamycin (GA) is one kind of an inhibitor to deactivate the HSP90 expression. The combined administration of Geldanamycin (GA) with ferromagnetic particles (specific material was not mentioned in the literature) in melanoma transplanted C57BL/6 mice increased the apotosis of the melanoma cells up to 76.2 ± 20.0 apoptotic cells per high-powered field compared to 53.9 ± 9.6 (hyperthermia alone) and 44.0 ± 16.5 (Geldanamycin alone) (Ito et al. 2009). The porphyrin-coated Fe/Fe_3O_4 core–shell nanoparticles exhibited antitumor effects in B16-F10 melanoma transplanted mice under hyperthermia even with less amount of nanoparticles in microgram iron content (Balivada et al. 2010). A significant decrease in tumor weight was observed with short time (10 min, increased by 11 °C) exposure to an alternating magnetic field. The uptake of porphyrin-coated nanoparticles was not sure in their works; however, the possibility was expressed since the cancer cells overexpress porphyrin receptors. Further, the possibility of release of iron within the tumor regions due to biocorrosion and subsequent increase in concentration of reactive oxygen species (ROS) in tumor environment was speculated. The short duration of exposure and administration of low doses of magnetic nanoparticles for antitumor effect was a challenging one at this point of time in comparison with the contemporary works.

The significant benefitting results from the in vitro and in vivo studies have brought an optimistic vision toward the

clinical trials in already known patients with certain types of cancers either treated or untreated with other therapeutic methods and prove the feasibility of the magnetic fluid hyperthermia. Johannsen et al. reported the first-ever clinical trial of interstitial hyperthermia using magnetic nanoparticles in locally recurrent prostate cancer (Johannsen et al. 2005b). A 67-year-old patient with biopsy-proven local tumor progression following high-dose-rate brachytherapy (2×15 Gy boost to the prostate using Iridium 192, 5×1.8 Gy up to 50.4 Gy external radiation to the prostate and pelvis) for clinical T3 prostate carcinoma 4 years earlier, who did not tolerate hormonal therapy was the subject of this trial. Based on their previous experience and subsequent calculations, a total of 12.5 mL of magnetic fluid was injected at a prostate size of 35 ml as 24 depots covering the prostate. The injection of the fluid was guided by transrectal ultrasound and fluoroscopy. The heat therapy session was started at a magnetic field strength of 2.5 kAm^{-1} and gradually increased to 5.0 kAm^{-1} which was kept constant for 60 min. At weekly intervals, six hyperthermia treatment sessions were performed. The method was well tolerated though some minor discomforts were observed. Thus, it opened the path to further Phase 1 clinical study to evaluate feasibility, toxicity, and quality of life during hyperthermia using magnetic nanoparticles in patients with recurrent prostate cancer post-radiotherapy with curative intent. Later, during 2006–2007, there prospective Phase 1 trials in patients treated with radiotherapy and biopsy-proven locally recurrent prostate cancer were reported (Johannsen et al. 2007a, 2007b, 2010). In these studies, 10 patients were enrolled and 6 thermotherapy sessions were performed at weekly intervals. All these works demonstrated a high tolerance of interstitial heating and durable deposition of magnetic nanoparticles in the prostate. Local discomforts are

observed in patients at high magnetic field strengths due to boundary effects between tissues of different dielectric constants and conductivity (between bone surfaces and soft tissues) and increases in current density at skin level. The irregular intratumoral heat distribution was also one issue that needs to be resolved. Maier-Hauff and coworkers carried out clinical trials on 14 patients (Phase 1 trial, 2 with primary tumors, and 12 with recurrent) using magnetic nanoparticles combined with external beam radiotherapy for the treatment of recurrent glioblastoma multiforme (Maier-Hauff et al. 2007). Their study was stared in 2003 and published in 2007. The magnetic fluid constituted of aminosilane-coated iron oxide nanoparticles was administered intratumorally via three-dimensional image guidance. The dosages were 0.1–0.7 mL (median: 0.2) of fluid per mL of tumor volume and single fractions (2 Gy) of a radiotherapy series of 16–70 Gy (median: 30). The magnetic fields applied within 3.8–13.5 kA/m (median: 8.5) showed high tolerance with some minor effect only. Their work has demonstrated the ability of magnetic fluid hyperthermia for treatment of brain tumor and control of therapeutic temperature from hyperthermia to thermoablation range. In 2009, Van Landegham et al. presented the postmortem neuropathological analysis of three glioblastoma patients (males aged 41, 57, and 69 years) treated with magnetic fluid hyperthermia (Landeghem et al. 2009). Macrophages are dominant in the internalization of administered magnetic nanoparticle, while glioblastoma cells showed lesser uptake. The administration of heat therapy further enhanced the uptake of nanoparticles by macrophages which was hypothesized to be due to therapy-induced formation of necrosis with subsequent infiltration and activation of phagocytes. Since the administered nanoparticles are restricted in distribution to the sites of instillation, the findings indicated the need for instillation of magnetic nanoparticles

in multiple locations. Again in 2010 (published online), Maier-Hauff and coworkers reported another clinical trial (Phase II) in 66 patients out of which 59 with recurrent glioblastoma multiforme (Maier-Hauff et al. 2011). The group commenced the research in 2005 and the compilation of the results was completed in 2009. In this work, aminosilane-coated Fe_3O_4 nanoparticles of 12 nm diameter and the aqueous dispersion of superparamagnetic nanoparticle with Fe concentration of 112 mg/mL was administered via neuronavigationally controlled intratumoral instillation. Further, the treatment methodology was magnetic fluid hyperthermia combined with external beam radiotherapy. From these works, the hyperthermia therapy combined with radiotherapy was observed to be an optimistic model due to its efficacy and tolerance.

From the above-mentioned pre-clinical studies as well as clinical trials, it is becoming a more of a confident emerging approach for cancer therapy. These works cited above used magnetic nanoparticles mostly Fe_3O_4 being surface-modified with organic molecules such as aminosilane and dextran or chemisorbed drugs and protein regulators for heat shock expression effect. Still, several works on the designing of various multimodal magnetic nanoparticles capable of enhancing therapeutic effects have been continuing. Basically, the therapeutic method utilized the ability of the magnetic nanoparticle to generate heat under the influence of alternating magnetic field. Therefore, it would be more enlightening to discuss the mechanism of heat generation and the factors affecting it and the tunability of the magnetism that can enhance the heating properties in the following section.

20.3 Heat Generation of Iron Oxide Nanoparticles: Mechanism and Factors

One of the fundamental requirements for the application of iron oxide in magnetic fluid hyperthermia is its magnetization and ability to generate heat under the influence of alternating magnetic field. There are other factors like size distribution and surface chemistry to enhance physicochemical stability, biocompatibility, targeting capacity, long-time circulation. These other factors will not be discussed in detail in this section. The designing and engineering of magnetism will be discussed in the later section of this chapter. Their heating efficiencies are dependent on the morphology, magnetic anisotropy, and the viscosity of the medium (Lv et al. 2015; Fortin et al. 2007; Presa et al. 2012; Salas et al. 2014; Jeun et al. 2009).

The heat dissipation of the magnetic nanoparticles on exposure to alternating magnetic field is governed mainly by four mechanisms: (i) Neel relaxation, (ii) Brownian relaxation, (iii) hysteresis loss, and (iv) eddy currents (Shliomis et al. 1990; Hanson 1991; Lima et al. 2012). When magnetic iron oxide nanoparticles are suspended in a fluid, each particle behaves like a magnetic dipole in suspension. In the absence of a magnetic field, the orientations of the magnetic moments are random and the prevailing orientation is called easy axis. This easy axis tends to flip back and forth when an alternating magnetic field is applied. In a system of non-agglomerating nanoparticles, the Neel and Brownian relaxations are predominantly contributing to the heat generation. However, in case of agglomerated nanoparticles, the dipolar–dipolar interaction is quite importantly occurring and there is a dominant contribution from the hysteresis

effect when Neel relaxation may not be significantly encountered (Jeun et al. 2009; Lima et al. 2012). The possible mechanisms undergone by magnetic iron oxide nanoparticles under the influence of alternating magnetic field are illustrated in Fig. 20.2.

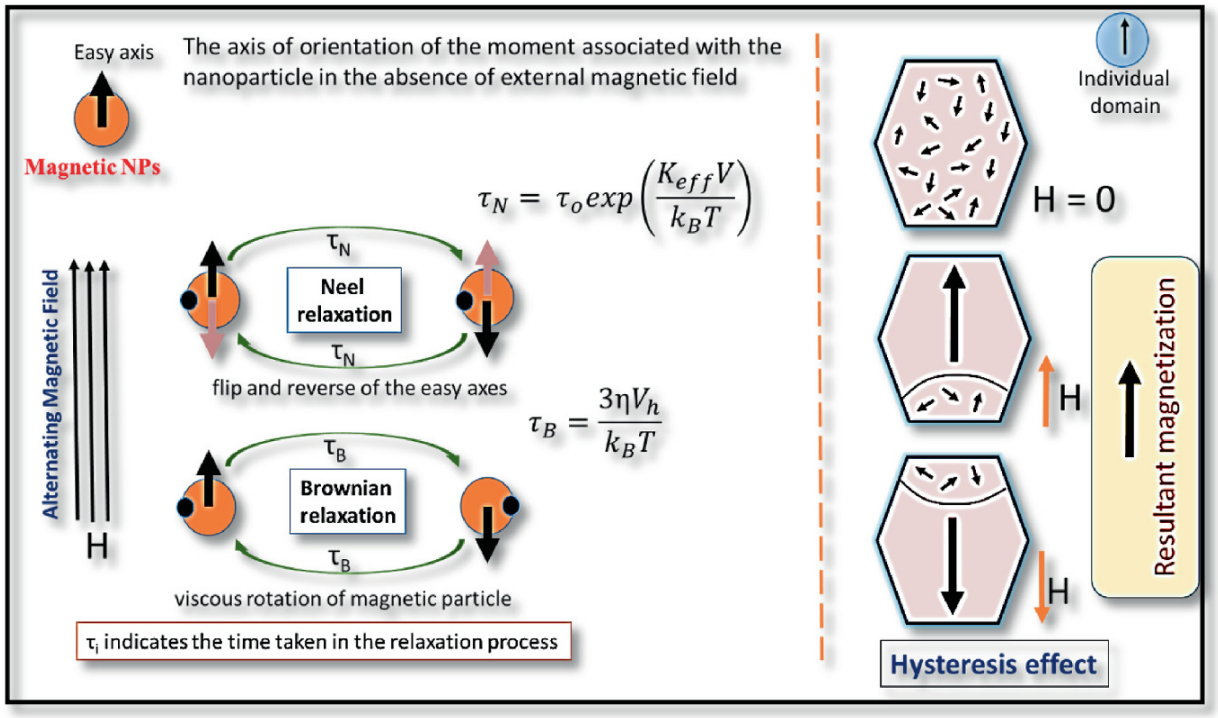

Fig. 20.2 Schematic presentation of Neel and Brownian relaxation of magnetic moment in single domain superparamagnetic nanoparticles; hysteresis effect in polydispersed (multidomain) magnetic nanoparticles

Neel relaxation refers to the flipping of the magnetic moment vector associated with the nanoparticles relative to the applied alternating magnetic field upholding the particle embodying the moments in a particular position, that is, the flipping of the easy axis back and forth. This mode of relaxation is very pronounced in very small nanoparticles, usually <10 nm which attain a superparamagnetic regime and each particle behaves as a single domain possessing spin, which can orient from $+z$ to $-z$ direction with relaxation time of $\sim 10^{-9}$ s. It is so fast that the measurement time window (0.1 s^{-1} min in VSM) cannot distinguish the change of spin. During the

relaxation, the heat is released to the surrounding medium. It is assumed that domains are non-interacting and net moment is almost zero in superparamagnetic regime. The relaxation process is temperature-dependent. The Neel relaxation time (τ_N) is given by Shliomis et al. (1990), Suto et al. (2009)

$$\tau_N = \tau_o \exp\left[\frac{\Delta E}{k_B T}\right] = \tau_o \exp\left[\frac{K_{\text{eff}} V}{k_B T}\right] \tag{20.1}$$

Here, τ_o 0 is in the order of 10^{-9} s; ΔE, the anisotropic energy barrier; k_B, Boltzmann's constant and T, the temperature. The energy barrier ΔE is equal to the product of an effective anisotropic energy constant (K_{eff}) and the volume of the particle (V). The dependence of Neel relaxation time (τ_N) on temperature T, in agglomerated system and the relaxation process perturbed by the dipolar interactions between particles, is described by the Vogel–Fulcher law,

$$\tau_N = \tau_o \exp\left(\frac{E_A}{k_B (T - T_o)}\right) = \tau_o \exp\left(\frac{K_{\text{eff}} V}{k_B (T - T_o)}\right) \tag{20.2}$$

where T_o is a measure of the strength of the dipole–dipole interparticle interactions (Umut et al. 2012).

The Brownian relaxation is a viscosity-dependent mechanism and it refers to the rotation of particle itself as a whole under the influence of alternating magnetic field. The relaxation time (τ_B) of particles in a liquid medium having dynamic viscosity (η) at a particular temperature (T) is given by

$$\tau_B = \frac{4\pi\eta {r_h}^3}{k_B T} = \frac{3\eta V_h}{k_B T} \tag{20.3}$$

where r_h is the hydrodynamic radius and V_h is the hydrodynamic volume of the particle.

When both these relaxations are present, an effective relaxation time may be defined by

$$\tau_R = \frac{\tau_N \tau_B}{\tau_N + \tau_B} \tag{20.4}$$

The Neel relaxation time depends exponentially on the volume of the particle which implies that magnetic relaxation is faster in smaller particles. The $k_B T$ is the thermal activation energy associated with the particle in the magnetic fluid. When the $k_B T$ becomes comparable to $K_{\text{eff}} V$, the nanoparticles become superparamagnetic and there is random flipping of the relaxation process (Liu et al. 2000). Mössbaeur spectroscopy can be used to determine the magnetic state of the nanoparticles. When the relaxation time τ_N is longer than 10^{-9} s, the Mössbauer absorption analysis provides a spectrum with a ferromagnetic sextet peak. But, if the relaxation time τ_N is shorter than 10^{-9} s, the Mössbauer spectrum will only be a paramagnetic doublet. The τ_N for a single domain becomes longer with decrease in temperature, increase in magnetic field, and increase in magnetic interaction among domains (Liu et al. 2000). Both the Neel and Brownian relaxation times increased with the increase in particle size (Presa et al. 2012). The respective τ_N values for the particles having sizes of 8, 11, and 13 nm are 0.9×10^{-7}, 2.4×10^{-7}, and 3.3×10^{-7} s, whereas the respective τ_B values for the size of 8, 11, and 13 nm are 1.9×10^{-7}, 5.0×10^{-7}, and 8.3×10^{-7} s, respectively. According to Shliomis (Shliomis et al. 1990), the magnetic nanoparticles in suspension can exhibit the condition $\tau_N = \tau_B$ at a characteristic particle size (D) and a characteristic frequency:

$$\vartheta = \frac{1}{2\pi\tau_B D} \tag{20.5}$$

When the particle size is less than the d, the heat dissipation by the Neel relaxation mechanism dominates; and when the particle size exceeds the D, the Brownian relaxation mechanism dominantly contributes to the heat dissipation.

AC field has the frequency (f) as well as magnetic field (H). In such a situation, relaxation has real and imaginary components. These window times corresponding to the operating AC frequency can distinguish the orientation of spin of single domain and net magnetic moment of domains can be observed. Also, the presence of small magnetic field can generate the hysteresis loop, which can produce heat to the surrounding medium and hysteresis area (A) is given by

$$A = f \int M dH \tag{20.6}$$

where M is magnetization at the applied magnetic field (H). Also, if the particles are small (the particle size is less than the critical size/single domain), the heat generation from the hysteresis loop will be negligible. For a polydispersed nanoparticle system, the heating can be originated from the magnetic relaxations, hysteresis loss, and the random stirring of the particles in solution. The critical size of the nanoparticles below which the inductive heating originated equally from the Neel and Brownian relaxations is defined by the following relation (Vallejo-Fernandez et al. 2013):

$$D_p(0) = \left\{ \frac{6k_B T \ln(f\tau_o)}{\pi K_{\text{eff}}} \right\}^{\frac{1}{3}} \tag{20.7}$$

The above relation shows the dependence of the critical size of the magnetic nanoparticles on the effective

anisotropy constant. For a particular K_{eff} value, as the size of the particle exceeds the $D_p(0)$, the inductive heating arises from the hysteresis losses and stirring of the nanoparticles in the solution. The critical diameter for which the hysteresis loss has dominantly contributed to the heat generation is given by the relation (Vallejo-Fernandez et al. 2013):

$$D_p(H) = \left\{1 - \frac{HM_s}{0.9K_{\text{eff}}}\right\}^{-\frac{2}{3}} D_p(0) \tag{20.8}$$

The heating from the stirring becomes predominant when the particle size exceeds the $D_p(H)$. The above relations were reported by Vallejo-Fernandez et al. for nanoparticles in a small field—an applied field of 250 Oe and 115 kHz for a K_{eff} value of 30 kJ m^{-3}.

Even though the nanoparticles are superparamagnetic at room temperature, heat generation due to hysteresis losses is also possible if high frequencies are used in measurements (Giri et al. 2000). At high frequencies, the magnetization response of the nanoparticles lags behind the applied field and the hysteresis effect occurs. Here, a parameter called the blocking frequency (f_b) is coined whereby at a frequency below f_b, the nanoparticles are superparamagnetic but hysteresis is observed above this frequency (Giri et al. 2000). In case of agglomerated nanoparticles, the heating capability is dependent on the hysteresis losses under optimal conditions where the particle diameter is about 15 nm. However in a system of dispersed non-agglomerated nanoparticles, for a similar size range of the particles, the heat generation is dominantly contributed from the Neel and Brownian relaxations. The heat generation due to hysteresis loss is also significant at higher applied filed strength (Lv et al. 2015).

The heat loss due to eddy currents arises as a result of the interaction of a conductive material with an oscillating magnetic field according to Faraday's and Lenz's laws. The heat loss due to eddy currents (ED) is given by

$$\mathrm{ED} = \frac{(\mu\pi df H_0)^2}{20\rho} \tag{20.9}$$

where μ is the permeability of a material, d is the diameter of the particle, and ρ is the resistivity of the material. The eddy effect is negligible in semiconducting Fe_3O_4 materials with high resistivity ($\rho = 10^2$ Ohm-cm) and therefore heat generation under an AC magnetic field will be negligible from eddy currents. The application of high-frequency electromagnetic radiation could cause heating up of normal tissues due to the eddy currents which flow in ionized conducting fluid within the body.

Rosensweig derived the relation to express the total heat dissipation per time, denoted by P, of the magnetic ferrofluid system from the concept of the first law of thermodynamics (Rosensweig 2002):

$$P = f\Delta U = \mu_0 \pi \chi'' f H_o^2 \tag{20.10}$$

and the components of susceptibility—χ''—is expressed as

$$\chi'' = \frac{\omega\tau_\mathrm{R}}{1 + (\omega\tau_\mathrm{R})^2}\chi_\mathrm{o} \tag{20.11}$$

where τ_R is the total relaxation provided from Brownian (τ_B) and Neel's (τ_N) terms.

Therefore,

$$P = \mu_0 \pi f H_o^2 \frac{\omega\tau_R}{1 + (\omega\tau_R)^2}\chi_\mathrm{o} \tag{20.12}$$

Equation (20.12) expresses the power dissipation density for a monodispersed ferrofluid system which assumes susceptibility is constant. Based on the above

expression, the evolution of temperature for the given system is computed as

$$\Delta T = P\frac{\Delta t}{c} \tag{20.13}$$

For a polydispersed system,

$$\Delta\,\bar{T} = \bar{P}\,\frac{\Delta t}{c} \tag{20.14}$$

where c is the specific heat (the volume average of solid and liquid constituents) of the magnetic fluid and Δt is the duration of the heating.

An alternative utilization and expression to Eq. (20.13) is introduced by the term specific loss power (SLP) or specific absorption rate (SAR), a measure of the heating efficiency which is defined as the ratio of the heat power dissipated and the mass of the magnetic nanoparticles in the ferrofluid (Chou 1990).

$$\mathrm{SAR} = C\frac{\Delta T}{\Delta t}\,\frac{1}{m} \tag{20.15}$$

where C = specific heat of water (4.18 $\mathrm{Jg^{-1}\ K^{-1}mol^{-1}}$), m = mass of the magnetite per total amount of magnetite + liquid (water), and $\Delta T/\Delta t$ = initial slope of the temperature versus time plot. The value of a specific absorption rate (SAR) is expressed in W/g. The SAR is a quantitative interpretation of the rate at which energy is absorbed per unit mass of the magnetic materials when exposed to radiofrequency or alternating magnetic field.

When two more solvents such as water and hydrogel are used for the dissolution of the magnetic nanoparticles in the ferrofluid, Eq. (20.15) is modified as (Suto et al. 2009)

$$\mathrm{SAR} = \sum_i C_i m_i \frac{\Delta T}{\Delta t}\frac{1}{m} \tag{20.16}$$

where $c_i s$ are the specific heats and m_is are the mass of each component in the system.

Sometimes, in order to bring a real comparative analysis of the SAR or SLP values, this can be expressed as an intrinsic loss power (ILP) or intrinsic absorption rate (IAR) which accounts for the dependence on ${H_o}^2$ and f of the applied field (Ortega et al. 2013), given by

$$\mathrm{ILP} = \mathrm{IAR} = C\frac{\Delta T}{\Delta t}\frac{1}{m}\frac{1}{H_o^2 f} \tag{20.17}$$

or

$$\mathrm{ILP} = \mathrm{IAR} = \sum_i C_i m_i \frac{\Delta T}{\Delta t}\frac{1}{m}\frac{1}{H_o^2 f} \tag{20.18}$$

The term ILP has been coined previously which has a terminological coincidence with SLP. The term IAR is new and used here to visualize terminological coincidence with SAR in this chapter.

For a non-adiabatic system, the SAR value was calculated by the introduction of a correction parameter called a thermal loss parameter, L, because the heating curve starts to drop as higher temperatures are reached due to thermal losses. The parameter L can be estimated by determining the slope for multiple temperatures along the heating curves. The corrected equation is presented as

$$\mathrm{SAR}_{\mathrm{corrected}} = \left(CV_s\frac{\Delta T}{\Delta t} + L\mathrm{d}T\right)\frac{1}{m} \tag{20.19}$$

where dT is the average temperature difference between the sample and the baseline (adiabatic) (Wildeboer et al. 2014).

Hergt et al. have propounded that there is a tolerance limit of the applied alternating magnetic field (H) and the operating frequency (f) for which the product Hf value for hyperthermia application must be lower than 5×10^6

kAm^{-1} s^{-1} (Hergt and Dutz 2007). The application of higher frequency is not biophysically suitable as it causes non-selective heating of both cancerous as well as healthy tissue due to generation of eddy currents. The achievement of high heating efficieny or SAR values of the magnetic nanoparticles was targeted in order to reduce the quantity of materials being administered for hyperthermia therapy into the tumor or reduced the applied field and frequency to an optimum level within the threshold limit. Therefore, to enhance the SAR values of the nanoparticles, certain factors such as the morphology and composition of the nanoparticles, carrier liquids, frequency, and amplitude of the applied magnetic field are important (Lv et al. 2015; Presa et al. 2012; Glöckl et al. 2006; Hugounenq et al. 2012; Ningombam et al. 2018, 2022). In case of γ-Fe_2O_3 spherical nanoparticles, the heating efficiency has near cubic dependence on the radius of the nanoparticles (Presa et al. 2012), i.e., SAR α $(d/2)^3$, whereas the dependence on field strength is quadratic (Das et al. 2016a). At a particular applied field strength and concentration of the particles, the SAR values are higher as the size of the nanoparticles increases with the increase in applied frequency (Presa et al. 2012). And at a particular frequency and concentration, the heating efficiency decreases as the viscosity of the carrier solvent increases. This effect is significant at larger particle size. However, the heating efficiency for smaller nanoparticles seems to be independent of the media viscosity. That is, there is an optimal size for the nanoparticles at which the viscosity of the medium does not affect the heating efficiency, as in γ-Fe_2O_3 is 12 nm where both the Neel and the Brownian relaxations are both augmenting the magnetic fluctuations for narrow size distribution (Presa et al. 2012). The Mn^{2+}-doped Fe_3O_4 showed better heat generation than the undoped Fe_3O_4 possessing almost similar morphology

under similar dispersion medium and applied magnetic field strengths (Ningombam et al. 2022).

The morphology of magnetic iron oxide nanoparticles is playing an important role in tuning the heating efficiency. It was observed that, for a particular morphology, optimum SAR could be achieved when the size distribution is sufficiently narrow and size is tuned to the transition range between superparamagnetic and ferromagnetic regimes of the magnetic nanoparticles (Hergt et al. 2006). Size-dependent heating performance was observed when iron oxide nanocubes of different sizes—12, 19, 25, and 38 nm—were studied at different fields and frequencies (Guardia et al. 2012). The 19 nm showed the highest heating efficiency and this corroborated the hypothesis that the size exhibited a transition of magnetism between superparamagnetic and ferromagnetic regimes. The octahedral Fe_3O_4 nanoparticles are reported to have high SAR values with wide nanoparticle size ranges—13, 22, 43, 98, and 260 nm (Lv et al. 2015). Comparatively, the octahedral particles exhibited higher heating efficiency than the spherical nanoparticles of nearly similar volume. This work also illustrated that the SAR values are directly dependent on the strength of the applied field strength which has been attributed to hysteresis loss. The heating efficiency increases with the size from 13 to 43 nm and maintains a plateau in 43 nm–98 nm particles and then falls as the size becomes bigger in 260 nm particles. Also, the Fe_3O_4 nano-octopods present a better heating efficiency than their spherical counterparts, especially in the high field region (Nemati et al. 2016).

The enhancement of heating can also be achieved by tuning of the magnetic anisotropy. The flower-shaped structure (nanoflowers) of maghemite nanoparticles has higher heat generation compared to spherical counterparts (Gazeau et al. 1998; Demortière et al. 2011; Lartigue et al. 2011). These nanoflowers have lower K_{eff} values than the

spherical nanoparticles. Another similar observations are made in the 8, 11, and 13 nm γ-Fe_2O_3 particles where the corresponding K_{eff} values are 6.7×10^4 J/m^3, 3.3×10^4 J/m^3, and 2.1×10^4 J/m^3 whereas the SAR values are 10 W/g, 42 W/g, and 55 W/g, respectively, at applied H = 7.5 kA/m and f = 522.3 kHz (Hf = 4×10^6 kAm^{-1} s^{-1}) (Presa et al. 2012). The 26 nm Fe_3O_4 nano-octopods show better heating efficiency compared to the 25 nm Fe_3O_4 sphere; the nano-octopods (17 and 47 nm) are better than the nanocubes (20 and 40 nm) due to enhanced shape anisotropy of the nano-octopods (Nemati et al. 2016). The 17 nm and 47 nm nano-octopods have shape anisotropy values of 8×10^4 J/m^3 and 1.2×10^5 J/m^3, respectively, whereas the 25 nm spherical particles have anisotropy a value of 6.5×10^4 J/m^3, and the 20 nm and 40 nm nanocubes have anisotropy values of 7.7 $\times 10^4$ J/m^3 and 4.2×10^4 J/m^3, respectively (Martinez-Boubeta et al. 2013). Among the nano-octopods, the smallest size (17 nm) possessed the largest SAR, but, for higher AC fields (>400 Oe), the SAR tends to increase with increasing particle size, reaching maximum values up to 415 W/g for the 47 nm nano-octopods. The cause of heating efficiency was attributed to viscous losses in the case of the smaller nano-octopods and hysteresis losses in the case of the bigger ones. Also, Fe_3O_4 nanorods exhibited better heating than the spheres or cubes of similar volumes due to larger M_s and effective anisotropy. Among the nanorods, the ones with higher aspect ratios show superior heat generation ability (Das et al. 2016a). The 65 nm × 5.7 nm (aspect ratio of 11) nanorods give a SAR value of 862 W/g which is superior to spherical (140 W/g) and cubic (314 W/g) nanoparticles of similar volumes. It is therefore obvious that (i) for a particle of similar morphology, high K_{eff} values and small size give higher heating effect at low

field strength whereas the larger ones with low K_{eff} show superior heating at high field strength, (ii) for different morphology with nearly similar size and volume, high K_{eff} values are favorable for greater heating effect. The composition of the nanoparticles also influences the heating efficiency of the magnetic fluids (Ningombam et al. 2018, 2022). At the field strength of 4.58×10^6 kAm^{-1} s^{-1} and concentration of 2 mg/mL dispersed in water, the Fe_3O_4, $Mn_{0.2}Fe_{2.8}O_4$, and $Mn_{0.5}Fe_{2.5}O_4$ nanoparticles of similar synthesis procedure and morphology give SAR values of 57 W/g, 73 W/g, and 139 W/g, respectively, when the corresponding magnetization values of the nanoparticles are 38.5 emu/g, 47.75 emu/g and 63.67 emu/g (Ningombam et al. 2022). Spherical $Zn_{0.4}Fe_{2.6}O_4$ (438.6 W/g) have higher magnetization and two times higher heating efficiency compared to its undoped Fe_3O_4 (189.6 W/g) (Bauer et al. 2016). Therefore, tuning the composition to enhance magnetization is beneficial for enhancing the heating efficiencies.

The dispersed state of the nanoparticles also influences the heating efficiency of the magnetic fluid (Presa et al. 2012; Suto et al. 2009; Nemati et al. 2016). The heating efficiency decreases when the Brownian relaxation is suppressed by increasing the viscosity of the dispersion medium and hence the increase in Brownian relaxation times (τ_B). The room temperature magnetization of the two different magnetite nanoparticles—12.5 nm and 15.7 nm was 43.2 emu/g and 50.3 emu/g, respectively. These two nanoparticles dispersed in water showed SAR values of 2.29×10^{-8} $Wg^{-1}Oe^{-2}Hz^{-1}$ (21.98 Wg^{-1}) and 2.95×10^{-8} $Wg^{-1}Oe^{-2}Hz^{-1}$(28.61 Wg^{-1}), respectively, at $H_o = 40$ Oe and $f = 600$ kHz (Suto et al. 2009). However, the respective SAR values of magnetite nanoparticles dispersed in hydrogel are reduced to 1.68×10^{-8} $Wg^{-1}Oe^{-2}Hz^{-1}$ (16.8 Wg^{-1},

27% decrease with respect to water medium) and 9.69×10^{-9} $Wg^{-1}Oe^{-2}Hz^{-1}$(9.3 Wg^{-1}, 67% decrease with respect to water medium). At the applied $H_o f = 4 \times 10^6$ kAm^{-1} s^{-1}, the magnetic fluid of 14 nm particle dispersed in water gives SAR of 58 Wg^{-1} and that in agar gel (1 wt.%) reduced SAR value to 40 Wg^{-1} (Presa et al. 2012). The dispersion of 17 nm particles in 2 wt.% agar medium is drastically decreased to 25% of that in water at the low field region of 200 Oe; however, at 800 Oe, the SAR reduces to 77% of that in water (Nemati et al. 2016).

20.4 Tunable Magnetism of Fe_3O_4 Nanoparticles

In an undisturbed stoichiometric formula of Fe_3O_4 with inverse spinel lattice, the Fe^{2+} ions occupy octahedral (O_h) sites, whereas the Fe^{3+} ions occupy the octahedral (O_h) and tetrahedral (T_d) sites in equal proportions. These cations can be labeled as $Fe^{2+}(O_h)$, $Fe^{3+}(O_h)$, and $Fe^{3+}(T_d)$. Electronically, the Fe^{2+} has a d^6 (high spin) state and the Fe^{3+} has a d^5 (high spin) state. The electronic spins and hence the magnetic moment vectors are oriented randomly and there is no resultant magnetization in the absence of an external magnetic field. But, when a magnetic field is applied, their moment vectors tend to align along the field. The magnetic moment of the $Fe^{3+}(O_h)$ and $Fe^{3+}(T_d)$ align opposite to each other and therefore only the $Fe^{2+}(O_h)$ contributed to the magnetization of the material. The magnetic moment per unit Fe_3O_4 is 4.1 μB (Bohr Magnetons, magnitude equal to $9.27 \times 10^{-24} A/m^2$) approximately (Kittel 2005).

The magnetic nature of a material is defined by its susceptibility, saturation magnetization (M_s), remnant magnetization (M_r), and coercivity (H_c) values. The magnetic behavior of the bulk Fe_3O_4 is altered when the size comes down to a nanodimensional regime. In the nanodimensional regime, other properties such as blocking temperature (T_b) and magnetocrystalline anisotropy constant (K) become significantly important. An individual atom constituting a nanoparticle has its own magnetic moment but it is not actually treatable alone. When a nanoparticle is constituted, the magnetic moments of the constituent atoms are collectively coupled via the exchange interactions so that the nanoparticle as a whole possesses a super-atomic scale magnetic moment referred to as a "superspin". Ultimately, the superspin of the nanoparticle can be viewed as a single entity with a preferred axis of magnetization. The moment associated with each superspin aligned randomly and independently along an axis called the easy axis in the absence of an external magnetic field. When an external alternating magnetic field is applied, the axis of magnetization tends to flip back and forth when the characteristic time for the superspin flipping is smaller than the experimental time scale. The easy axis is dependent on the nature of the material and the shape of the particle. This superspin alignment ultimately influences the magnetic properties of the nanocrystals. The quantities —M_s, M_r, T_b—are dependent on particle size but H_c is shape-dependent because of surface anisotropy effects.

Magnetic ferrite materials in their bulk form may be ferrimagnetic having a large hysteresis loop with high coercivity and remanent magnetization due to the antiferromagnetic coupling among Fe^{3+} in their inverse spinel structure. At room temperature, bulk Fe_3O_4 has a saturation magnetization of 92 emu/g and a coercivity of

323 Oe (Cullity and Graham 2009; Goya et al. 2003). As the size of the Fe_3O_4 goes into the nanodimensional regime, the M_s, $M_{r,}$ and H_c values drop below the bulk value and it reaches a state of zero or negligible Mr and Hc values called the superparamagnetic state. At this point, Fe_3O_4 nanoparticles are called superparamagnetic iron oxide magnetic nanoparticles (SPIONs). Usually, the saturation of magnetization for nanoparticles is not reached even at high field and the M_s is calculated from the extrapolation of M versus 1/H using the M-H measurement at room temperature (Ningombam et al. 2018). An illustration on the variation of magnetism on attaining superparamegntic state with an example of iron oxide nanoparticle is presented in Fig. 20.3. Certain factors such as size, shape, composition, blocking temperature, and magnetocrystalline anisotropy energy are indispensable factors governing the magnetic behavior of iron oxide nanoparticles.

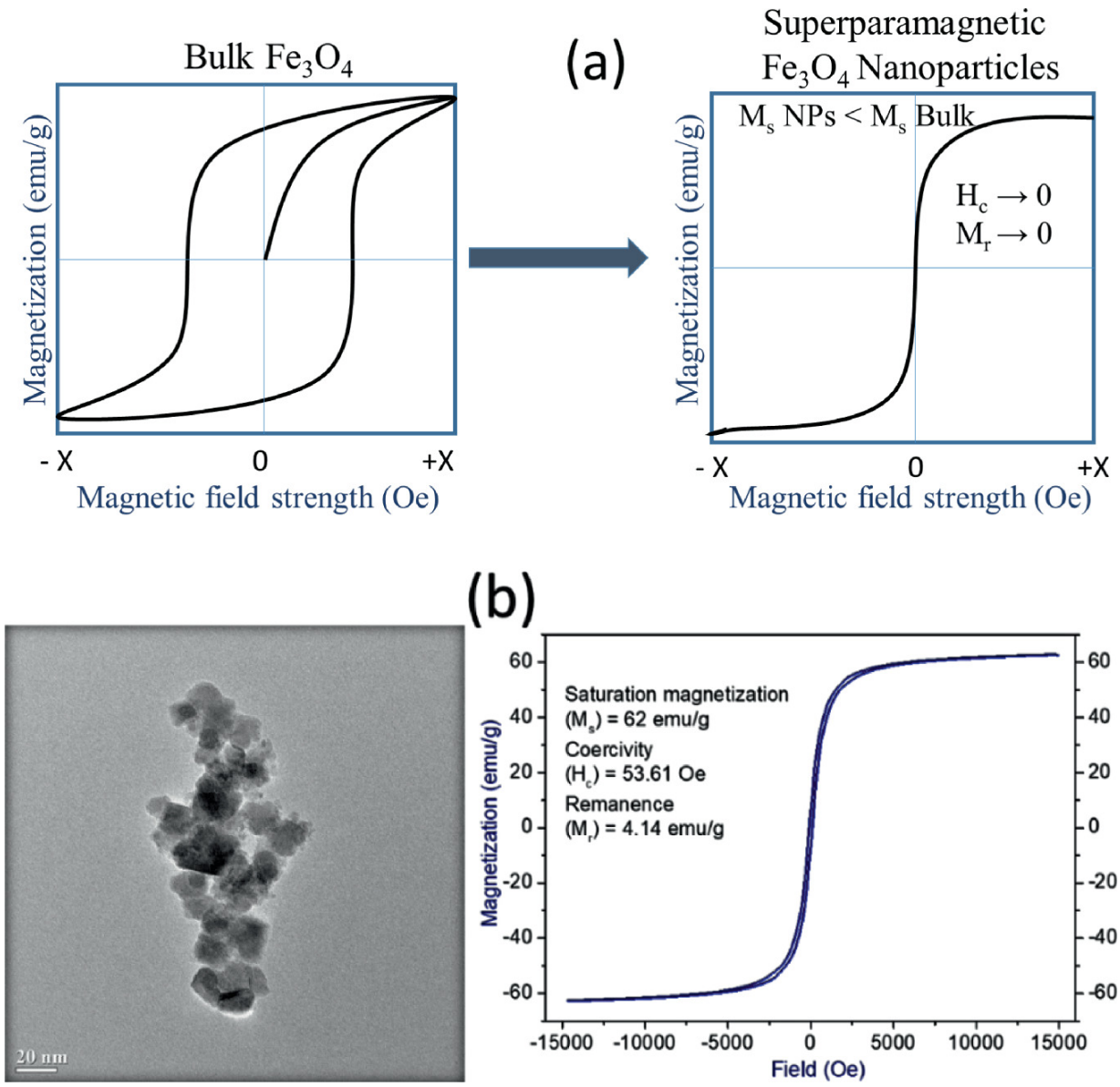

Fig. 20.3 **a** Typical illustration of change of magnetic properties (M_S, H_C, M_r) of Fe_3O_4 from ferromagnetic in bulk to superparamagnetic in nanodimensional regime. **b** TEM image and magnetization of Fe_3O_4 nanoparticles synthesized by coprecipitation in aqueous 300 mM glycine medium

Magnetocrystalline anisotropy energy (E_A) and blocking temperature (T_b) are important parameters that need to be ascertained to understand the ferromagnetic to superparamagnetic transformation of magnetic particles as the size is reduced. The magnetocrystalline anisotropy energy (E_A) serves as an energy barrier for blocking the

flips of magnetic moments and it competes with thermal activation energy, $k_B T$ of the material, where k_B is the Boltzmann constant and T, the temperature. According to the Stoner–Wolfarth model (Stoner and Wohlfarth 1991), the energy E_A of a single domain particle can be approximated as $E_A = K_{\text{eff}}\, V \sin^2\theta$, where K_{eff} = effective anisotropy constant, V = volume of the magnetic nanoparticles, and θ = angle between the magnetization direction and the easy axes of the nanoparticles. For spherical nanoparticles, this energy E_A can be regarded as the total magnetic anisotropy energy (Moumen et al. 1996). In bulk materials, the $E_A >> k_B T$ and the random flipping of the magnetization direction aligns with the applied field and there is a resultant coercivity of the materials when the field is reversed. However, in nanoparticle, when $E_A \approx k_B T$ is attained, the thermal energy surpasses the anisotropy barrier and the inversion of the magnetization direction occurs readily. The random flipping of magnetization direction led to cancellation of resultant magnetization and loss of ability to retain magnetization when the magnetic field is reversed. And the hysteresis disappears, i.e., coercivity of the material tends to reach zero value. At this point, the nanoparticles attain a superparamagnetic state. Thus, the quantity K_{eff} is a physical constant and it quantitatively reflects the energy required to change the direction of magnetization from easy to hard axes. The effective anisotropy decreases with the increase in particle size and the magnetization of the particles (Presa et al. 2012; Nemati et al. 2016; Martinez-Boubeta et al. 2013; Carrey et al. 2011) which are presented in Table 20.1.

Table 20.1 Effective anisotropy (K_{eff}) values of magnetic nanoparticles possessing different morphology and chemical formulas

Formula	Shape	Size	Effective anisotropy (K_{eff}) values	References
γ-Fe_2O_3	Spherical	7.1 nm	1.6×10^4 J/m^3	Fortin et al. (2007)
		8 nm	6.7×10^4 J/m^3	Presa et al. (2012)
		11 nm	3.3×10^4 J/m^3	
		13 nm	2.1×10^4 J/m^3	
Fe_3O_4	Spherical	25 nm	6.5×10^4 J/m^3	Nemati et al. (2016)
	Nano-octopods	17 nm	8.0×10^4 J/m^3	
		47 nm	1.2×10^5 J/m^3	
	Nanocubes	20 nm	7.7×10^4 J/m^3	Martinez-Boubeta et al. (2013)
		40 nm	4.2×10^4 J/m^3	
	–	Bulk	1.1×10^4 J/m^3	Cullity and Graham (2009)
$CoFe_2O_4$	Spherical	6 nm	5.5×10^5 J/m^3	Hyeon et al. (2002)
		9 nm	2.0×10^5 J/m^3	
		Bulk	$(1.8–3.0) \times 10^5$ J/m^3	
$MnFe_2O_4$	Spherical	5–10 nm	$(9–4) \times 10^4$ J/m^3	Kang et al. (2004)
		Bulk	2.5×10^3 J/m^3 (100 K)	
Au–Fe_3O_4 hybrid nanoparticles	Spherical Fe_3O_4	7.48 nm	3.7×10^4 J/m^3	Umut et al. (2012)
	Au–Fe_3O_4 dimer	Au = 5–8 nm; dimer = 11 0.07 nm	5.6×10^4 J/m^3	
	Au–Fe_3O_4 core–shell	Au = 5–8 nm; diameter = 15.92 nm	6.2×10^4 J/m^3	

The superparamagnetism of magnetic nanoparticles is attained when they are smaller than a critical size and

above a temperature called blocking temperature. The size limit for Fe_3O_4 to be superparamagnetic at room temperature is reported to be smaller than 20 nm in diameter, whereas the cubic and spherical particles have a size limit of 76 nm and 128 nm, respectively, for transition into multi-domain regime (Yavuz et al. 2006; Li et al. 2017; Leslie-Pelecky and Rieke 1996). The blocking temperature is defined by the relation: $T_b = K_{\text{eff}}V/25k_B$, where the symbols have usual significance (Liu et al. 2000; Song and Zhang 2006). It is the temperature at which the nanoparticles show maximum magnetization and higher beyond this temperature the magnetic behavior transforms from ferro- or ferrimagnetic phase to paramagnetic phase with a fall in magnetization. The T_b values, considering the intrinsic magnetization of the crystal, are obtained by using the Neel–Arrhenius formula (Sjögren et al. 1997):

$$T_b = \frac{\beta}{k_B}\frac{K_{\text{eff}}V_m}{\ln\left(\tau_m/\tau_o\right)} \tag{20.20}$$

where β is a constant depending on the crystal size distribution, K is the effective anisotropy, V_m is the median crystal volume, k_B is the Boltzmann constant, τ_m is the measurement time, and τ_o is a characteristic relaxation time of crystal of 10^{-11} s (Johansson et al. 1993). The blocking temperature of nanoparticles increases with the increase in size, as well as with the magnetocrystalline anisotropy energy as summarized in Table 20.1 (Presa et al. 2012; Kang et al. 2004). As the temperature increases, the magnetic hysteresis becomes weaker and eventually disappears above the blocking temperature. Theoretically, the temperature dependence of the coercive field for a single domain follows the equation (Kang et al. 2004): $H_c/H_c^o = 1 - (T/T_b)^2$, where H_c is the measured coercive

field and H_c^o the estimated coercive field at 0 K, T_b the measured blocking temperature and T the measuring temperature. The calculated T_b at 100 kHz for the agglomerated 8 nm and 15 nm Fe_3O_4 samples are found to be greater than 300 K, whereas that of the dispersed non-agglomerated 8 and 14 nm Fe_3O_4 samples have the respective values of 82 and 267 K (Lima et al. 2012). Thus, it is known that the state of nanoparticles in the fluid also influences the blocking temperature. The agglomerated system of nanoparticles has stronger interparticle interactions which elevate the energy barrier and consequently an increase in T_b is resulted (Lima et al. 2012; Kwon and Hyeon 2011). The blocking temperatures of the 5, 7, and 10 nm-sized $MnFe_2O_4$ nanocrystals were found to be approximately 30, 60, and 85 K, respectively (Kang et al. 2004). The addition of Gd^{3+} in $Mn_{0.5}Zn_{2.5}Gd_xFe_{2-x}O_4$ increases the Curie temperature (T_c) whereas the blocking temperature (T_b) decreases with an increase in Gd^{3+} content (Jadhav et al. 2019). The corresponding T_c values for $x = 0.025$, 0.05, 0.075, and 0.1 are 315, 317, 320, and 326 K. The corresponding T_b values for $x = 0.025$, 0.05, 0.075, and 0.1 are 88, 78, 57, and 49 K. The size of the reported particles increased from 11 to 14 nm as Gd^{3+} content increased. The reported T_b value of spherical $Mn_{0.5}Zn_{2.5}Fe_2O_4$ nanoparticles of 11.4 nm is 45 K (Parekh et al. 2012). The higher T_b of $Mn_{0.5}Zn_{2.5}Gd_xFe_{2-x}O_4$ particles than the $Mn_{0.5}Zn_{2.5}Fe_2O_4$ nanoparticles of similar size could be attributed to higher K_{eff} of the materials. The T_b is dependent on K_{eff} when the anisotropy is inversely related to size of the particles. This explains why the T_b of $Mn_{0.5}Zn_{2.5}Gd_xFe_{2-x}O_4$ particles decreases as the size increases.

The influence of L-S coupling (orbital angular momentum–electron spin coupling) on the blocking temperature and hence the superparamagnetism is illustrated in Fe_3O_4, $MgFe_2O_4$, and $CoFe_2O_4$ spinel ferrite nanoparticles (Liu et al. 2000; Song and Zhang 2006). All of these nanoparticles showed an increase in T_b with the increase in size. But, the blocking temperature of $CoFe_2O_4$ nanoparticles is about 100 K higher than Fe_3O_4 and 150 K higher than that for $MgFe_2O_4$ nanoparticles of the same size indicating much higher anisotropy energy in $CoFe_2O_4$ nanoparticles. The coercivity of $CoFe_2O_4$ nanocrystals at 5 K is over 50 times higher than the same-sized Fe_3O_4 nanocrystals (Song and Zhang 2006). The metal ions are in a weak ligand field and they have high spin states. The contribution of Fe^{3+} to the magnetic anisotropy is considered insignificant in these studies. It was reasoned that a Fe^{3+} cation with a $3d^5$ electron configuration usually has its orbital angular momentum quenched in a weak ligand field (Song and Zhang 2006). Another reason is that a similar Fe^{3+} distribution in their crystal lattices and thus Fe^{3+} sites contributes similarly to the magnetic anisotropy is these nanoparticles (Liu et al. 2000). The $Fe^{2+}(O_h)$ in Fe_3O_4, $Co^{2+}(O_h)$ in $CoFe_2O_4$, and $Mg^{2+}(O_h)$ in $MgFe_2O_4$ took an important role in tuning magnetic anisotropy energy, ultimately the blocking temperature and the superparamagnetism. Here, (O_h) denotes the lattice site of these divalent ions. The nanocrystals obtained in these two works have spherical morphology but different size distribution and therefore these works must be discussed independently. Here, the $Mg^{2+}(2p^63s^0)$ cation has no unpaired electrons and therefore zero total electron spin. The $Fe^{2+}(3d^6)$ has four unpaired, whereas the $Co^{2+}(3d^7)$ has three unpaired electrons. Evidently, the larger

magnetocrystalline anisotropy of $CoFe_2O_4$ nanoparticles compared to $MgFe_2O_4$ is due to the strong L-S couplings at $Co^{2+}(O_h)$ sites. There is an anomalous behavior in L-S coupling strength between Co^{2+} and Fe^{2+} despite the number of unpaired electrons that affects the relative magnitude of magnetic anisotropy. The lowering of symmetry and crystal field splitting is solely cited for the resultant magnitudes of magnetic anisotropy. In spinel lattice structures, the cubic symmetry is often lowered to a trigonal field due to the structural distortion from the Jahn–Teller effect and/or the nonstructural distortion from the interactions between the central cation and the cations outside the nearest neighborhood of the central ion. In an ideal cubic system, the $Fe^{2+}(O_h)$ with $3d^6$ electron configuration has the $^5T_{2g}$ ground state. But in the distorted system, the triplet degenerated energy state of T_{2g} split into two levels—E and B_2 (ground state). The orbital angular momentum in a Fe^{2+} cation with a B_2 ground state is quenched. Consequently, there is little contribution from the Fe^{2+} in the magnetic anisotropy of Fe_3O_4, whereas a $Co^{2+}(O_h)$ has a triplet $^4T_{1g}$ ground state in ideal system which gets split into A_2 and E states in the trigonal field. The Co^{2+} cation with an E ground state has a stronger L-S coupling. This mechanism enhanced the magnetic anisotropy of $CoFe_2O_4$ more than that case of Fe_3O_4.

Surface modification or hybrid formation can alter the blocking temperature of the magnetic nanoparticles. For example, the T_b for Fe_3O_4 coated with Au and methoxy polyethylene glycol (MPEG-5000) are 80 K and 130 K, respectively (Mikhaylova et al. 2004). The higher T_b in MPEG-coated sample is attributed to high density of

interactions between the particles embedded in the polymer matrix. The T_b of Fe_3O_4 alters after the formation of hybrid with Au nanoparticles (Umut et al. 2012). The T_b values for spherical Fe_3O_4 (7.48 nm), Au–Fe_3O_4 dimer (size of Au = 5–8 nm, size of dimer = 11 0.07 nm), and core–shell Au–Fe_3O_4 (core Au = 5–8 nm, total diameter = 15.92 nm) are 80 K, 100 K, and between 150 and 200 K, respectively. The increased K_{eff} in Au-Fe_3O_4 hybrid is observed (Table 20.1) which is ascribed to additional surface anisotropy induced by the Au/Fe_3O_4 interface and the effect is bigger in core–shell structures due to their larger Au/Fe_3O_4 contact area. Therefore, the T_b is highest for core–shell Au–Fe_3O_4.

A linear correlation between saturation magnetization and the particle size of ferrites has been reported. A decrease in M_s values was observed when the size of the nanoparticles was reduced. For instance, at room temperature (300 K), the M_s values of octahedral Fe_3O_4 nanoparticles are 68, 73, 85, 90, and 92 emu/g for 13 nm, 22 nm, 43 nm, 98 nm, and 260 nm, respectively (Lv et al. 2015); Fe_3O_4 nano-octopods have M_s values of 50.6, 68.4, 66.7, 65.3, 65.5, and 81.7 emu/g for the sizes of 17 nm, 20 nm, 26 nm, 35 nm, 40 nm, and 47 nm, respectively (Nemati et al. 2016). In the case of Fe_3O_4 nanorods, higher M_s values are observed in the shorter rods with smaller aspect ratio (Das et al. 2016a). At 300 K, the measured M_s values are determined to be 86, 84, and 87 emu/g for the rod of dimensions 41 nm × 7 nm (aspect ratio 5.8), 65 nm × 5.7 nm (aspect ratio 11), and 56 nm × 10 nm (aspect ratio 5.6), respectively. But, the nanorods have a higher M_s value than the spherical nanoparticles (20–25 nm diameter, M_s = 58 emu/g) of nearly same volume. The mass magnetization

value (χH) of 4, 6, 9, and 12 nm spherical Fe_3O_4 nanoparticles are 25, 43, 80, and 102 emu/g (Fe), respectively (Jun et al. 2005). The significant causes of size effect were the defects at the particle surface such as the presence of disordered passivating layer, structural vacancy order–disorder, and spin canting at the surface and inside the particle (Varanda et al. 2002; Morales et al. 1999). Smaller nanoparticles with larger curvature have a magnetically disordered crystal orientation on the surface which diminishes with increasing size. The increasing spin disorder can be observed on the nanoparticle's surface due to weaker spin–spin exchange coupling at the surface with more ordered interior spins. Also, the canting of internal spin canting as well as the surface spins contribute to the effect due to increased interactions between the surface and internal spins. The saturation magnetization (Ms) of a nanoparticle can be approximately related to the bulk magnetization, Ms(bulk) as $Ms = Ms(bulk)[(a\text{-}d)/a]^3$, where a is the radius of the particle and d is the characteristic thickness of the disordered surface layer. The value of d is typically of the order of 1–2 nm (Morales et al. 1999). The significance of the equation is well appreciated for very small nanoparticles less than 5 nm because of the increased interaction between the surface and internal spins. Meanwhile, a wide size distribution of nanoparticles enhanced the interparticle dipole interaction energy and exchange coupling energy among the nanoparticles. These effects increase the total magnetic moment leading to increased saturation magnetization of the nanoparticles. This phenomenon is observed in MFe_2O_4 (M=Mg, Ni, Co) nanoparticles (Jeun et al. 2009).

The coercivity of the magnetic nanoparticles has been expressed as a function of the particle size from the multi- to single-domain region as below

$$H_c(D) = H_M \left(\frac{D}{D_1}\right)^{-0.6} \left[1 - e^{\left(-\frac{D}{D_1}\right)^5}\right] \tag{20.21}$$

where H_M and D_1 are the material-specific parameters (Hergt et al. 2008). The dependence of coercive field on effective magnetic anisotropy K_{eff}, saturation magnetization Ms, particle volume V, and absolute temperature T is given by Hernando et al. (1995)

$$H_c = \left(\frac{2K_{\text{eff}}}{\mu_o M_s}\right) \left[1 - \left(\frac{25 k_B T}{K_{\text{eff}} V}\right)\right] \tag{20.22}$$

Accordingly, the coercivity increases as the size increases when *Ms* and K_{eff} are volume-independent. This relation is exemplified in the case of γ-Fe_2O_3 nanoparticles where the coercivity increases as 100, 200, and 300 Oe for the 8, 11, and 13 nm, respectively, at 10 K (Presa et al. 2012). Similar patterns of coercivity changes are observed in octahedral Fe_3O_4 nanoparticles, where H_c values are 0 Oe, 22 Oe, 37 Oe, 80 Oe, and 118 Oe for 13 nm, 22 nm, 43 nm, 98 nm, and 260 nm, respectively (Lv et al. 2015). In the case of Fe_3O_4 nano-octopods, 0 Oe coercivity is observed for 17 nm nanoparticles and 151 Oe for 40 nm nanoparticles but unexpectedly lower to 103 Oe in 47 nm nanoparticle (Nemati et al. 2016). The octahedral particles have uniform morphology as observed by microscopy but the octopods are deformed cubes which may pose certain defect-related variations. Consequently, the octopods could have higher coercivity compared to uniform smooth octahedral nanoparticles.

The magnetism of the iron oxide can also be tuned by the addition of certain metal ions to the crystal structure which alters the saturation magnetization as well as the magnetic anisotropy of the materials (Colombo et al. 2012; Sun et al. 2004; Lee et al. 2007; Aslibeiki et al. 2019). In a

data proved by Colombo et al., the nanoparticles of Fe_3O_4, ɣ-Fe_2O_3, $MgFe_2O_4$, $MnFe_2O_4$, $CoFe_2O_4$, and $NiFe_2O_4$ have bulk magnetization values of 98, 82, 31, 110, 94 and 56 emu/g, respectively (Colombo et al. 2012). The coercivity of the 16 nm $CoFe_2O_4$ nanoparticles is about 20 kOe at 10 K which is much larger than the 16 nm Fe_3O_4 nanoparticles (450 Oe at 10 K) (Sun et al. 2004). The abrupt change in the magnetic configuration is due to the increase in magnetic anisotropy of the materials by incorporation of Co^{2+} in the Fe–O matrix. On the other hand, incorporation of Mn^{2+} cation in the Fe–O matrix reduces the magnetic anisotropy of the materials and hence 14 nm $MnFe_2O_4$ nanoparticles show coercivity of only 140 Oe at 10 K (Lee et al. 2007). In a similar manner, Co^{2+} substitution in $MnFe_2O_4$ ($Mn_{1-x}Mn_xFe_2O_4$) nanoparticles too enhanced the magnetic anisotropy and dipolar interaction (Aslibeiki et al. 2019). The effective anisotropy values increased from 2×10^4 Jm^{-3} $MnFe_2O_4$ to 7.44×10^5 Jm^{-3} in $CoFe_2O_4$. The Mossbauer spectral data suggest that the superparamagnetic fraction is maximum in $MnFe_2O_4$ which then decreases with Co^{2+} doping when the $CoFe_2O_4$ has maximum ferromagnetic sextets. The remnant magnetization (21 emu/g in $MnFe_2O_4$ to 43 emu/g in $Mn_{0.75}Co_{0.25}Fe_2O_4$, rather irregular pattern) and the saturation magnetization (51 emu/g in $MnFe_2O_4$ to 68 emu/g in $CoFe_2O_4$, irregular pattern) increase with increasing Co^{2+} doping when it is expected to lower due to low magnetic moment contribution from Co^{2+} ($3d^7$, $3\mu_B$) compared to Mn^{2+} ($3d^5$, $5\mu_B$). The variation in anisotropy and magnetization is attributed to inhomogeneous distribution of Co^{2+} ions throughout the particles, i.e., differential occupation of O_h and T_d sites.

In another report which presented a comparative analysis for $MnFe_2O_4$, $CoFe_2O_4$, and $NiFe_2O_4$ nanocrystals, the T_b values are 129 K, 303 K, and 70 K, respectively; the K_{eff} values are 1.17×10^5 Jm^{-3}, 9.24×10^5 Jm^{-3}, and 2.14×10^5 Jm^{-3}, respectively; the H_c values are 316 Oe, 14,286 Oe, and 542 Oe, respectively; the M_s values are 11.2 emu/g, 9.9 emu/g, and 5.6 emu/g, respectively (Carta et al. 2009). The M_s variation is different from that reported, in reference (Aslibeiki et al. 2019), for which there cannot be any relevant common explanation to offer but size variation can be seen. These observations suggest that Mn^{2+} ion would be a better dopant than Co^{2+} ion in tuning superparamagnetic behavior. However, there is a suggestion that the studies on coercivities should not be limited to 300 K only but it is needed to pursue above 300 K also. The substitution of Fe^{2+} by Zn^{2+} is beneficial for tuning of saturation magnetization M_s values (Behdadfar et al. 2012). The M_s values of $Zn_xFe_{3-x}O_4$ nanoparticles increased as 65.77, 75.1, 79.89, and 82.5 emu/g for $x = 0$, 0.25, 0.3, and 0.37, respectively, and the M_s falls to 67.5 emu/g in $Zn_{0.4}Fe_{2.6}O_4$. The change of M_s values with Zn^{2+} substitution is attributed to preferential occupation Zn^{2+} in the $Fe^{3+}(O_h)$ sites and the subsequent resultant magnitude of $M^{3+}(T_d)$–O–$M^{3+}(O_h)$, $M^{3+}(T_d)$–O–$M^{3+}(T_d)$, and $M^{3+}(O_h)$–O–$M^{3+}(O_h)$ superexchange interactions. In $Zn_{0.37}Fe_{2.63}O_4$, $M^{3+}(T_d)$–O–$M^{3+}(O_h)$ is dominant which then shifted to $M^{3+}(O_h)$–O–$M^{3+}(O_h)$ in $Zn_{0.4}Fe_{2.6}O_4$. The $Co_xZn_yFe_{3-x-y}O_4$ nanocrystals exhibited a shift from ferromagnetic at $y = 0$ ($CoFe_2O_4$) and 0.2 ($Co_{0.8}Zn_{0.2}Fe_2O_4$) to superparamagnetic to paramagnetic at $y = 1$ ($ZnFe_2O_4$) (Kumar et al. 2012). The

Curie temperature as well as the magnetization decreases with increasing concentration of Zn. This observation is attributed to the inclusion of a higher concentration of non-magnetic Zn^{2+} instead of Co^{2+} in the T_d sites. The La^{3+} substitution in $ZnFe_2O_4$ at the Fe^{3+} sites yields nanoclusters of different sizes (Zhao and Nan 2012). A compositional and size-dependent magnetization was observed in these samples. The $ZnLa_{0.02}Fe_{1.98}O_4$ with the largest size of nanoclusters possesses the highest M_s value of 86 emu/g when $ZnFe_2O_4$, $ZnLa_{0.01}Fe_{1.99}O_4$, $ZnLa_{0.03}Fe_{1.97}O_4$, and $ZnLa_{0.04}Fe_{1.96}O_4$ have Ms values of 74, 80, 76, and 75 emu/g, respectively. The substitution of $Fe^{2+}(O_h)$ by Mn^{2+} enhanced the Ms values but the substitution by Co^{2+} and Ni^{2+} lowers the Ms values compared to Fe_3O_4 (Ningombam et al. 2018, 2022; Lee et al. 2007). Here, Mn^{2+} ($3d^5$), Fe^{2+} ($3d^6$), Co^{2+} ($3d^7$), and $Ni^{2+}(3d^8)$ have 5, 4, 3, and 2 unpaired electrons, respectively. The contribution from the unpaired electrons to the net magnetization is presented as a possible reason for enhanced magnetization. Some other phenomena like $M^{3+}(T_d)$–O–$M^{3+}(O_h)$ superexchange interaction, cited earlier in $Zn^{2+}(3d^{10})$ substituted Fe_3O_4, are probable. But it would need another study to bring a better reasoning about the observations revealed above. In the case of $Mn_{0.5}Zn_{2.5}Gd_xFe_{2-x}O_4$ particles, the M_s values decreased from 48.6 emu/g in $Mn_{0.5}Zn_{2.5}Gd_{0.025}Fe_{1.975}O_4$ to 28.2 emu/g in $Mn_{0.5}Zn_{2.5}Gd_{0.1}Fe_{1.9}O_4$ (Jadhav et al. 2019). The decrease in M_s values was explained by the fact that Gd^{3+} tends to occupy the $Fe^{3+}(O_h)$ sites and the consequential decline of the $M^{3+}(T_d)$–O–$M^{3+}(O_h)$ superexchange interaction which could create spin canting spins at the surface of the particles.

20.5 Magnetic–Luminescent Nanocomposites: A Bimodal Integration of Magnetic and Luminescent Nanoparticles

As the clinical trials of magnetic nanoparticles advanced, the use of the materials for cancer therapy was enlightened broader. Several efforts were made by many researchers to obtain better targeting and heating. Many new synthetic methods were reported to obtain highly monodispersed particles, controlled shape and size, high effective anisotropy which exhibit better heating effect. Meanwhile, the development of nanocomposites based on magnetic iron oxide and luminescent/non-luminescent parts have been envisaged with much interest because of the possible multifunctionalities that can be derived such as drug delivery, enzyme catalysis, protein separation, immobilization of biomolecules, cell separation, optical imaging, and magnetic imaging (Obaidat et al. 2019; Corr et al. 2008; Zhao et al. 2020; Serrano et al. 2018). A design of multimodal magnetic–luminescent nanocomposite either surface-modified and/or drug-loaded is illustrated in Fig. 20.4. Magnetic–luminescent nanocomposites derived from lanthanide-doped luminescent materials or quantum dots integrated with magnetic materials are becoming a new hotspot of multifunctional materials, aiming at combined optical imaging and magnetic fluid hyperthermia. The conjunction of luminescence and magnetism added an advantage—high sensitivity of the luminophores though the depth of penetration is to be accounted and high spatial resolution mediated by the magnetic materials—to enhance the bioimaging application (Xia et al. 2011; Zhou et al. 2010). Despite the efficiency of the nanocomposites based on fluorescent dye for biological staining and labeling, the

dyes suffer a setback due to stability short Stokes shift, poor photochemical stability, susceptibility to photobleaching and decomposition under repeated excitation, and some non-specific cellular interactions (Wang et al. 2005). Comparativley, quantum dots of fluorescent semiconductor nanocrystals have better photostability, tunability of emissions spectra with the particle size or composition, and bright emissions making them very suitable for optical imaging. However, quantum dots have acute toxicity concerns due to its influence on particle–cell interaction, slow clearance, and long-term toxicity and generation of reactive oxygen species causing cell death (Tsoi et al. 2013), whereas the lanthanide-doped inorganic oxide-based materials are relatively non-toxic and the lanthanides in the rigid inorganic matrix have large Stokes shift, sharp and durable emission spectra, reduced photobleaching, excellent photostability, low cytotoxicity, and 4f–4f or 4f–5d transitions are unaffected by the crystal field (Wang et al. 2005; Nichkova et al. 2005). Further, the composite designed with upconversion inorganic nanoparticles is capable of temperature sensing or infra-red induced heat generation may serve more purposes such as combined photothermal and magnetothermal therapy with the sensing of evolved temperature in the therapeutic zone where the magnetic materials were injected. Many reports were available on cell targeting, detection of target site, and imaging based on magnetic–luminescent nanocomposites. However, there were not many literatures available on the use of such nanocomposites for magnetic fluid hyperthermia in cancer therapy and no advancing trial stage has been reached, though few in vitro cellular analyses were found in the literatures.

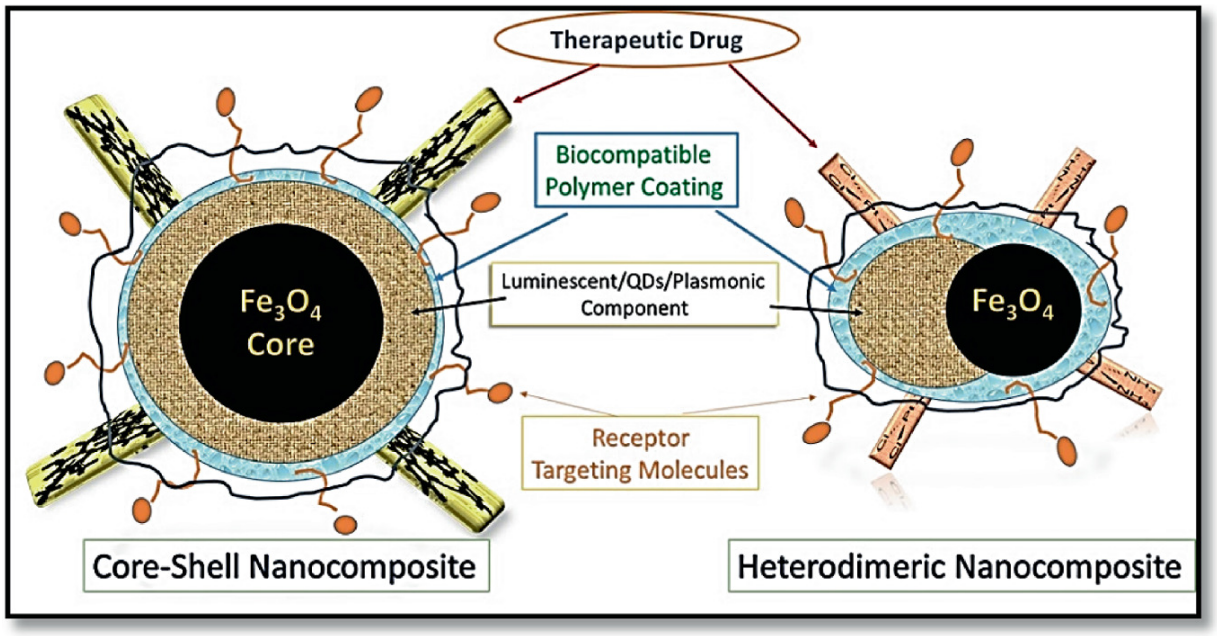

Fig. 20.4 Design of the basic components of a multimodal magnetic–luminescent nanocomposites anticipated for magnetic fluid hyperthermia

The coating of magnetic nanoparticles with a layer of silica (SiO_2) was indeed a wise choice for the designing of magnetic–luminescent nanocomposites owing to the versatile properties of silica such as chemically robustness, hydrophilicity, biological inertness and no toxicity concern, and versatility in surface modification/functionalization, optical transparency and protective layer that prevents the quenching of luminescence by the magnetic materials (Ling and Hyeon 2013; Corr et al. 2008). Superparamagnetic SiO_2-coated Fe_3O_4 which is further conjugated with bright orange emitting CdSe-ZnS QDs was studied for conventional radiofrequency hyperthermia (Xu et al. 2010). The cellular uptake study of pancreatic human cancer cells (Panc-1) revealed that the luminescent composite materials were observed to present everywhere the cells had grown after 24 h of treatment and agglomerated around the nuclear membrane, while a small amount reached the nucleus. The cytotoxicity was also relatively low for the composite concentration below 50 μg/mL or 200 μg/mL. The layers of stable ZnS and 3-mercaptopropionic acid

(MPA) coating over the CdSe significantly reduce the toxicity. Further, on treatment with radiofrequency, the cells were sensitive and went through an accelerated apoptotic process leading to cellular decomposition. The saturation magnetization (M_s) value for the nanocomposite was 15.4 emu/g which may be good enough for response to alternating magnetic field but was not studied when reported. Superparamagnetic–luminescent nanocomposite derived from APTES functionalized Fe_3O_4 and 3-mercaptossuccinic acid (MSA) capped CdTe showed the M_s value of 59.2 emu/g (Cabrera et al. 2017). Here, a very low quantity of goethite α-FeOOH evolved in APTES conjugation, whereas both the goethite α-FeOOH and maghemite γ-Fe_2O_3 phases evolved negligibly in the final quantum dot incorporated nanocomposite. The magnetic properties were however not affected. The nanocomposite exhibited bright red luminescence and efficient internalization by HeLa cells with some aggregation at the cell membrane without significant changes in their morphology. The Fe_3O_4@SiO_2/Y_2O_3:Tb^{3+} nanocomposite was obtained by assembling Y_2O_3:Tb^{3+} nanorods onto the surface of Fe_3O_4@SiO_2 core–shell nanostructures (Zhang et al. 2008). Under 240 nm excitation, the nanocomposite displays four strong characteristic emissions of Tb^{3+}—489, 544, 585, and 622 nm of which 544 nm (green) is the strongest. Therefore the composite Fe_3O_4@SiO_2/Y_2O_3:Tb^{3+} displayed green emissions. Similarly, other lanthanide dopants displayed respective color emissions—red for Eu^{3+}, blue for Tm^{3+}, near white for Dy^{3+}, orange red for Sm^{3+}, green for Er^{3+}, and red for Ho^{3+}.

Erogbogbo et al. designed a magnetic composite MSiQD-Mag which contains silicon quantum dots coupled with superparamagnetic Fe_3O_4 which emits red light on

exposure to 365 nm UV radiation (Erogbogbo et al. 2010). It was emphasized that the designed multimodal nanocomposite would be non-toxic compared to those integrated with other heavy metal-based quantum dots (Fujioka et al. 2008; Erogbogbo et al. 2011). The cellular uptake of nanoparticles was also enhanced with the aid of the magnetic force. The composite is stable and the luminescence is significantly preserved in water or in bovine serum plasma. The in vivo demonstration of the bioimaging capability was overwhelming that the magnetic composite injected to the prostate tumor mouse model exhibited a 20% increase in luminescence intensity post 24 h of injection compared to the luminescence observed immediately after injection. This shows the potential of tracking the delivery of nanoparticle or drug into the target tumor site. Later, Xia et al. also fabricated a red-to-near infrared emitting luminescent nanocomposites from porous Si nanoparticles and Fe_3O_4 (Xia et al. 2017). This nanocomposite has excellent fluorescence and magnetic resonance imaging multimodalities in both the cancer cells in vitro and tumor tissues in vivo. The materials have excellent biodegradability and biocompatibility when studied after intravenously injected (20 mg/kg dose) into Balb/C mice. Most of the administered materials were distributed in the liver (20.6 ± 2.3%ID Si/g; 63.9 ± 6.5%ID Fe/g), spleen (16.1 ± 2.1%ID Si/g; 37.6 ± 5.2%ID Fe/g), and lungs post 1 day of injection, while small amounts of the materials were found in the kidney and brains. After 7 days, the accumulation of Si and Fe have been reduced significantly in the liver (8.7 ± 1.8%ID Si/g; 34.1 ± 4.0%ID Fe/g) and spleen (6.4 ± 1.1%ID Si/g; 20.5 ± 2.9%ID Fe/g). Post 28 day of intravenous injection, total clearance of the Si and Fe was observed from liver (5.7 ± 1.0%ID Si/g; 6.7 ± 1.7%ID Fe/g) and spleen (4.0 ± 1.2%ID Si/g; 8.0 ± 0.6%ID Fe/g) after 28 days which was close to the control groups:

liver (4.8 ± 0.3%ID Si/g; 6.2 ± 1.0%ID Fe/g) and spleen (3.9 ± 0.6%ID Si/g; 8.7 ± 1.3%ID Fe/g). Although the works mentioned above demonstrated optimistic model for imaging magnetic-targeted drug delivery and magnetic hyperthermia therapy, the study on the heating ability of the materials essential for killing tumor tissues have not been carried out.

Monodispersed uniform Fe_3O_4@YPO_4:Ln^{3+} (Ln=Tb, Eu) spheres obtained from fluffy nanostructures of spherical YPO_4:Ln^{3+} integrated with Fe_3O_4 nanoparticles attained a larger size distribution of about 500–600 nm (Wang et al. 2010). The composites have Ms values of about 1–2 emu/g with near superparamagnetic behavior. The fluffy structure provides an efficient surface morphology for drug loading and the doxorubicin-loaded was released in a sustainable manner with low initial burst release pattern. The hybrid spheres were actively internalized by live HeLa cells after 96 h of incubation. The magnetization may not be favorable for hyperthermia applications. Biotin-functionalized magnetic Fe_3O_4@Y_2O_3:Eu^{3+} nanocomposite with red color emission was demonstrated for cellular targeting, cell separation, and bioimaging using avidin-coupled polystyrene beads as a model cellular mimic (Ma et al. 2009). Amine-functionalized Tb^{3+}-doped γ-Fe_2O_3 nanocrystals have green luminescence and are highly water dispersible with capability of cellular imaging (Zhang et al. 2009). The iron oxide conjoined upconversion nanocomposites capable of excitation by harmless infrared radiations are more interesting than that excited by ultraviolet radiation. They acquire duality of T2-enhanced magnetic resonance and NIR-to-NIR upconversion luminescent imaging. The Fe_3O_4/γ-Fe_2O_3@$NaGdF_4$:Yb^{3+},Er^{3+} (~15 nm) nanocomposites acquire negligible coercivity and an excellent green

[($^2H_{11/2}$, $^4S_{3/2}$) → $^4I_{15/2}$ (540 nm)] upconversion luminescence emission from Er^{3+} when excited at 980 nm (Shrivastava et al. 2018). The in vivo studies in mouse using mesoparticles of Fe_3O_4@LaF_3:Yb^{3+},Er^{3+} as a T_2 contrast agent to visualize a tumor system as well as optical imaging via upconversion green emission was impressive (Zhang et al. 2012). Similarly, core–shell $NaYF_4$:Yb^{3+},Tm^{3+}@Fe_3O_4 nanocomposite has T_2 relaxivity coefficient (r_2) of about 189 mm^{-1} s^{-1}, which is almost twice that of the commercial iron oxide-based T_2 contrast agent Feridex ($r_2 = 108$ mm^{-1} s^{-1}) and the upconversion luminescence imaging detection has high signal-to-noise ratio (Xia et al. 2011). The thickness of the Fe_3O_4 layer affected the r_2 values. The in vivo studies in Sprague–Dawley nude mouse demonstrated the capability of magnetic resonance imaging and upconversion optical imaging. The mouse was injected with 1 mg/mL of a suspension into its right forepaw and the upconversion luminescence was monitored at 800 nm. After 10 min of injection, the materials were diffused along the lymphatic basins in the right antebrachium of the nude mouse, from the injected point to axillary lymph nodes along the right antebrachium and finally after 20 min, the materials were detected by 800 nm signal in the lymph node and forepaw. The 800 nm signal could be detected even after one week at the forepaw and the lymph node. The composite has relatively low toxicity indicated by the viability of KB cells after incubation for 24 h and 48 h, which were greater than 80% when the concentration was lower than 100 mg/mL and the calculated IC_{50} values of about 295 and 190 mg/mL, respectively. Considering the above facts, such upconversion luminescence-based magnetic

nanocomposites still open more opportunities for high-resolution imaging and hyperthermia.

Luwang et al. obtained dendrimer stabilized $YPO_4:Tb^{3+}@Fe_3O_4$ nanocomposite which has zero coercivity and remanence (Luwang et al. 2012). The composite give green emission when excited at 266 nm (Tb–O charge transfer) and efficient heat generation was observed from the Fe_3O_4 (39.22 W/g) with an applied field of 110 Oe and frequency of 425 kHz. However, the heating profile of the composite was low and stated the difficulty to achieve desirable hyperthermia temperature. The low heating effect was attributed to low magnetization values as a consequence of large content of dendrimer and luminescent $YPO_4:Tb^{3+}$ component. However, treatment of the biphasic suspension of the composite with HeLa cell lines subjection to AC magnetic field (110 Oe, 425 kHz, 15 min to achieve 43 °C) twice showed a large proportion of cell death with visible morphological changes in dead cells. The intracellular uptake study of $Fe_3O_4@YPO_4:Eu$ hybrid nanoparticles in mouse fibrosarcoma (WEHI 164) cells showed high internalization and accumulation in tumor cells (Prasad et al. 2013). The composite has red emission from the Eu^{3+} ions. Here, the Fe_3O_4 nanoparticles can reach hyperthermia temperature even at lower concentrations (5 mg/mL) at 6.9×10^6 kA m^{-1} s^{-1}, whereas the $Fe_3O_4@YPO_4:Eu^{3+}$ could attain the hyperthermia temperature at higher concentration (10 mg/mL) in the same applied field strength. The polyethylene glycol-coated $Fe_3O_4@CaMoO_4:Eu^{3+}$ nanocomposites showed that the particles are readily internalized into the cytoplasm of the cells, and further exhibited selective cytotoxicity toward human liver cancer cells (HepG2 cells) but biocompatible with mesenchymal stem cells (hTERT) (Parchur et al. 2014). Mesoporous silica encapsulated biphasic

nanocomposite composed of Fe_3O_4 and $YVO_4:Eu^{3+}$ nanoparticles have shown pH-dependent release of doxorubicin loaded into the composite and high in vitro death of Hela (43% cell death) and MCF-7 (57% cell death) cells (Shanta et al. 2013). The application of alternating magnetic field for 15 min to generate the hyperthermia temperature of 42 °C in cells treated with the drug-loaded nanocomposite enhanced the tumour cell death more than 90%. Singh et al. reported luminescent $Fe_3O_4@SnO_2:Tb^{3+}$, $Fe_3O_4@YVO_4:Eu^{3+}$, and $Fe_3O_4@CaF_2:Eu^{3+}$ nanocomposites which give green and red emission under ultraviolet (240–270 nm) excitation (Singh et al. 2014, 2015a, 2015b). The Ms value of Fe_3O_4 is reported to be ~ 62 emu/g, whereas that of $Fe_3O_4@SnO_2:Tb^{3+}$, $Fe_3O_4@YVO_4:Eu^{3+}$, and $Fe_3O_4@CaF_2:Eu^{3+}$ nanocomposites are 13.9, 13.28, and 13.38 emu/g, respectively. These nanocomposites have excellent biocompatibility with the cell viabilities of ~ 80 in HeLa and ~ 98% in WEHI-164 after 24 h treatment at 100–200 µg/mL concentration of nanocomposites. High intracellular uptake of luminescent $YVO_4:Eu^{3+}$ nanoparticles and $Fe_3O_4@YVO_4:Eu^{3+}$ nanocomposite in the cytoplasm of WEHI-164 cells can be seen through confocal laser scanning microscopy. The cell viabilities of the WEHI-164 cells were reduced to ~ 89% and ~ 80%, respectively, for 100 and 200 µg/mL concentration of $Fe_3O_4@YVO_4:Eu^{3+}$ nanocomposites when external magnetic field was applied for 10 min. The nanocomposite fluid was obtained by mixing Fe_3O_4 and the luminescent $SnO_2:Tb^{3+}/YVO_4:Eu^{3+}/CaF_2:Eu^{3+}$ nanoparticles in the 1:4 weight ratio and dispersed in 1 mL of aqueous polyethyleneglycol solution. The $Fe_3O_4@SnO_2:Tb^{3+}$ nanocomposite achieves the hyperthermia temperature of

42 °C for the 4 and 6 mg of Fe_3O_4 per 1 mL dispersion at the applied field (*Hf*) strengths of 5.3×10^6 kAm^{-1} s^{-1} (20 kAm^{-1}, 265 kHz) and 7.16×10^6 kAm^{-1} s^{-1} (27 kAm^{-1}, 265 kHz). The 6 mg dispersion reached the hyperthermia temperature in 149 and 57 s, respectively, at the former and the latter field strengths. However, the 4 mg dispersion reached the hyperthermia temperature in 68 s at $Hf = 7.16 \times 10^6$ kAm^{-1} s^{-1}. The dispersion containing 4 and 6 mg of Fe_3O_4 per 1 mL for the Fe_3O_4@YVO_4:Eu^{3+} nanocomposite reached the hyperthermia temperature of 42 °C 379 and 334 s, respectively, at the applied $Hf = 7.16 \times 10^6$ kAm^{-1} s^{-1}. For the Fe_3O_4@CaF2:Eu^{3+} nanocomposite, the 2, 4, and 6 mg of Fe_3O_4 per 1 mL of the dispersion reached 42 °C in 200, 50, and 40 s, respectively, at applied field $Hf = 7.16 \times 10^6$ kAm^{-1} s^{-1}. The corresponding SAR values for 6 mg of Fe3O4 per mL dispersion of Fe_3O_4@SnO_2:Tb^{3+}, Fe_3O_4@YVO_4:Eu^{3+}, and Fe_3O_4@CaF_2:Eu^{3+} at $Hf = 7.16 \times 10^6$ kAm^{-1} s^{-1} are 53, 58, and 122 Wg^{-1}, respectively. In the case of Fe_3O_4@CaF_2:Eu^{3+}, a possible exchange interaction between the f-orbitals in antiferromagnetic Eu_3O_4 phase and d-orbitals in superparamagnetic Fe_3O_4 phase was a probable reason for the increased heating efficiency of the composite compared to the pure Fe_3O_4.

The cell viability study found that polyethylene glycol (PEG)-modified water dispersible (Y/Eu/Li)VO_4@Fe_3O_4@PEG (abbreviated as YELF-PEG in Table 20.2) nanocomposite shows 60% cell viability for up to 400 µg/mL concentrations and LD_{50} value of 677.00 µg/mL (Ningombam et al. 2021). The particles of nanocomposite have a biphasic nature with the Fe_3O_4 particles forming an adsorbed layer over the rod-like luminescent (Y/Eu/Li)VO_4 particle. The nanocomposite

gives a strong red emission under excitation at 280 nm which is good for optical imaging. The saturation magnetization of the materials is 18.92 emu/g and their induction heating profiles showed efficient heating at higher magnetic field strength. In all the measurements, the heating curve showed a rapid rise in the first 200–300 s. At the applied field of $Hf = 2.15 \times 10^6$ kAm^{-1} s^{-1}, the concentrations of fluid which are higher than 10 mg/mL in water generate the hyperthermia temperature range. When $Hf = (3.05–3.22) \times 10^6$ kAm^{-1} s^{-1}, the concentrations of 10, 15, and 20 mg/mL can reach the hyperthermia temperature. And for $Hf = 4.58 \times 10^6$ kAm^{-1} s^{-1}, even the 5 mg/mL dispersion achieves the hyperthermia temperature in 465 s in the region of slow rising temperature curve. The time taken to achieve the hyperthermia temperature for different concentrations of (Y/Eu/Li)VO_4@ Fe_3O_4@PEG under different field strengths is summarized in Table 20.2. In this work, a linear dependence of heating rate $\Delta T/\Delta t$ and concentration was considered and an explanation was offered on the low values of $\Delta T/\Delta t$ that that expected from the linear dependence. It was reasoned that there could be cancellation of magnetic orientation flipping and cross-relaxation among the magnetic particles or a part of the heat energy released dissipated in overcoming the energy barrier to induce sufficient Brownian relaxation at higher concentration resulting in loss of magnetic energy in causing Brownian flipping in the congested suspension.

Table 20.2 Time taken to reach the hyperthermia temperature for different concentrations of YELF-PEG, MF-Gly, and MFEu-PEG under different field strengths

Materials	Amount of sample	Magnetic field strength (*Hf* in $kAm^{-1}\ s^{-1}$)				References
		2.15×10^6	3.22×10^6	3.05×10^6	4.58×10^6	
		Time taken to achieve the hyperthermia temperature				
YELF-PEG	10 mg/mL	*	402 s	330 s	248 s	Ningombam et al. (2021)
	15 mg/mL	270 s	207 s	160 s	132 s	
	20 mg/mL	180 s	134 s	100 s	70 s	
MF-Gly	2 mg/mL	*	*	462 s	284 s	Ningombam et al. (2018)
	5 mg/mL	495 s	330 s	209 s	138 s	
	10 mg/mL	202 s	110 s	86 s	58 s	
	15 mg/mL	110 s	70 s	55 s	49 s	
	20 mg/mL	56 s	39 s	38 s	33 s	
MFEu-PEG	2 mg/mL	*	*	*	500 s	
	5 mg/mL	*	*	*	285 s	
	10 mg/mL	*	600 s	330 s	180 s	
	15 mg/mL	*	180 s	190 s	80 s	
	20 mg/mL	*	100 s	105 s	60 s	

* The blank cells indicate inability to achieve the hyperthermia temperature in a measurement time of 600 s

Polymeric coatings such as polyethyleneglycol and chitosan have also enhanced the hemocompatibility and biocompatibility of the $Mn_xFe_{3-x}O_4$-based nanocomposites (Ningombam et al. 2018, 2022). The comparative hemolysis profile of glycine-modified $Mn0_{0.5}Fe_{2.5}O_4$ (abbreviated as (MF-Gly in Table 20.2) and PEG-modified $Mn0_{0.5}Fe_{2.5}O_4$@YVO_4:Eu^{3+} (abbreviated as MFEu-PEG in Table 20.2) revealed that the former has 5.18 (±1.68)% hemolysis, whereas the latter has 2.53 (±0.73)% hemolysis

(Ningombam et al. 2018). The reason to higher percentage of hemolysis in glycine-modified one was not established in the report. Further in vitro and in vivo analyses may be able to establish the reasoning. The cell viability analysis showed that 200, 500, and 1000 µg/M of MFEu-PEG killed 15, 26, and 56% of the MCF-7 cell after incubation for 24 h but at 1000 µg/mL, only 15% of the cell survived. This is an indication of cytotoxic nature toward MCF-7 cell lines. The MF-Gly and MFEu-PEG have the respective M_s values of 63.37 emu/g and 9.96 emu/g with the magnetic content being 16.4 wt.% magnetic content in the nanocomposite. The MF-Gly and MFEu-PEG showed an efficient heating performance. At $Hf = (2.15–4.58) \times 10^6$ KAm^{-1} s^{-1}, for the 5 mg/mL suspension of MF-Gly nanoparticles, the SAR values were recorded to be 51–90 Wg^{-1}; and 5 mg/mL suspension of MFEu-PEG nanocomposite have SAR values of 13–40 Wg^{-1}. The time taken by the nanoparticles and the nanocomposites to achieve the hyperthermia temperature is listed in Table 20.2. Again, in the case of $Mn_xFe_{3-x}O_4$ nanoparticles prepared in PEG media, the percentage hemolysis of Fe_3O_4, $Mn_{0.2}Fe_{2.8}O_4$, and $Mn0_{0.5}Fe_{2.5}O_4$ nanoparticles were 0.345 (±0.004)%, 2.677 (±0.034)% and 5.028 (±0.189)%, respectively (Ningombam et al. 2022). For the $Mn_{0.5}Fe_{2.5}O_4$, the glycine or PEG coated gave a nearly equal hemolysis value, whereas, in the case of $Mn_{0.2}Fe_{2.8}O_4$@YVO_4:Dy@Chitosan and $Mn_{0.5}Fe_{2.5}O_4$@YVO_4:Eu@PEG, the corresponding values are 2.822 (±0.003)% and 5.0839 (±0.127)% hemolysis, respectively. All these values are well within the acceptable limits of hemocompatibility for a biomaterial. The cell viability studies in HeLa cell lines clearly indicated at low cytotoxicity of the materials. After incubation for 24 h, the viability stood at 95–80% for the 200 µg/mL–600 µg/mL

concentrations. The PEG-coated nanocomposite has relatively lesser cytotoxicity than the chitosan-coated one.

The comparative analysis of $Mn_xFe_{3-x}O_4$ nanoparticles prepared in polyethylene glycol and the derived nanocomposites revealed that Mn^{2+} doping has enhanced the saturation magnetization (Ms) as well as heating better performance when *Hf* is below the clinical threshold limit (Ningombam et al. 2022). The Ms values of Fe_3O_4, $Mn_{0.2}Fe_{2.8}O_4$ and $Mn0_{0.5}Fe_{2.5}O_4$ nanoparticles are 38.55 emu/g, 47.75 emu/g and 63.67 emu/g, respectively, whereas the $Mn_{0.2}Fe_{2.8}O_4$@YVO_4:Dy@Chitosan (abbreviated as M2Dy-Chi) and $Mn0_{0.5}Fe_{2.5}O_4$@YVO_4:Eu@PEG (abbreviated as M5Eu-PEG) have Ms values of 16.35 emu/g and 18.48 emu/g, respectively. The elemental analysis data confirmed that the corresponding magnetic content in the materials—$Mn_{0.2}Fe_{2.8}O_4$, $Mn_{0.5}Fe_{2.5}O_4$, M2Dy-Chi, and M5Eu-PEG are 96.02, 92.13, 28.45, and 20 wt.%. Even though the magnetic content is lowered, the magnetization is higher which clearly indicates the enhanced magnetic properties of Mn^{2+} doping in the case of nanoparticles as well as nanocomposites. The Fe_3O_4 and $Mn_{0.2}Fe_{2.8}O_4$ nanoparticles can achieve the hyperthermia temperature when the concentration is ≥10 mg/mL at the $Hf = 3.05 \times 10^6$ kA m^{-1} s^{-1}; however, the $Mn_{0.5}Fe_{2.5}O_4$ nanoparticles can reach the required temperature even at 2 mg/mL in 495 s. And, at the $Hf = 4.58 \times 10^6$ kA m^{-1} s^{-1}, the Fe_3O_4 can reach the hyperthermia temperature for the concentrations of ≥5 mg/mL and the respective times taken are 297, 170, 104, and 65 s for 5, 10, 15, and 20 mg/mL. For this $Hf = 4.58 \times 10^6$ kA m^{-1} s^{-1}, the concentration of 2 mg/mL is enough to reach the hyperthermia temperature for $Mn_{0.2}Fe_{2.8}O_4$ (597 s) and $Mn0_{0.5}Fe_{2.5}O_4$ (279 s)

nanoparticles. The time taken to achieve the required temperatures is shorter in nanoparticles with higher saturation magnetization since the heat dissipation is proportional to susceptibility and magnetization given in Eqs. (20.12) and (20.19). The corresponding SAR values for 2 mg/mL of Fe_3O_4, $Mn_{0.2}Fe_{2.8}O_{4,}$ and $Mn0_{0.5}Fe_{2.5}O_4$ nanoparticles are 69, 72, and 122 Wg^{-1} at at $Hf = 3.05 \times 10^6$ kA m^{-1} s^{-1}; 57, 73, and 139 Wg^{-1} at $Hf = 4.58 \times 10^6$ kA m^{-1} s^{-1}. Again, the $Mn_{0.2}Fe_{2.8}O_4$@YVO_4:Dy@Chitosan (abbreviated as M2Dy-Chi) and $Mn_{0.5}Fe_{2.5}O_4$@YVO_4:Eu@PEG (abbreviated as M5Eu-PEG) nanocomposites attained the SAR values of 40 and 43 W g^{-1}, respectively, when $Hf =$ is 3.05×10^6 kA m^{-1} s^{-1}; 60 and 62 W g^{-1} at $Hf = 4.58 \times 10^6$ kA m^{-1} s^{-1}. Ignoring the synthetic procedure and weight content of magnetic material but taking into account the constituents—$Mn_{0.5}Fe_{2.5}O_4$, YVO_4:Eu^{3+}, polyethyleneglycol—in the nanocomposites, the nanocomposite shows lesser toxicity toward HeLa cells but higher toxicity in MCF-7 cells (Ningombam et al. 2018, 2022).

The magnetic–luminescent nanocomposites fabricated from luminescent upconversion, metal (Ag/Au) plasmonic and Fe_3O_4 nanoparticles possess the capability of combined imaging (optical and magnetic), phtotothermal as well as magnetic fluid hyperthermia therapy. The safer infrared wavelengths can be used for imaging, tracking, or photothermal therapy applications. The hybrid nanocomposite, $NaYF_4$:Er^{3+},Yb^{3+}@PE_3@Fe_3O_4 exhibited enhanced absorption at 808 nm and efficient near-infrared photothermal therapeutic performance in killing of the mouse 4T1 breast cancer cells (Fu et al. 2019). The term PE_3 denotes the polyelectrolytes—polyethylenimine, poly(allylamine hydrochloride), and poly(sodium 4-styrenesulfonate)—used in the synthesis of the

nanocomposite. The saturation magnetization of Fe_3O_4 is about 59.2 emu/g and that of $NaYF_4:Er^{3+},Yb^{3+}@PE_3@Fe_3O_4$ nanocomposites is about 37.4 emu/g. upon 808 nm laser irradiation at the power density of 1 W/cm^2, the hyperthermia temperature of 42.0 °C was achieved at 7 min for $NaYF_4:Er^{3+},Yb^{3+}@PE_3@Fe_3O_4$ nanocomposites, but 11 min for Fe_3O_4 dispersion. The presence of external magnetic field further enhanced the fluorescent imaging sensitivity as well as the photothermal killing of cancer cells. In the absence of external magnetic field, 808 nm laser irradiation at the power density of 1 W/cm2 for 10 min after 24 h incubation reduced the cell viability to 41.2% for Fe_3O_4 NPs, and 26.4% for $NaYF_4:Er^{3+},Yb^{3+}@PE_3@Fe_3O_4$ nanocomposites. When external magnetic field is assisted, the cell viability is further reduced to 13.9% for the cells incubated with $NaYF_4:Er^{3+},Yb^{3+}@PE_3@Fe_3O_4$ nanocomposites. The comparative heat generation ability of Fe_3O_4, UCNP@SiO_2 (UCNP = $NaYF_4:Er^{3+},Yb^{3+}$), and UCNP@SiO_2@Au@Fe_3O_4 nanocomposites indicated the partial involvement of the heating generated by the AuNPs because the interaction between the electrical conductive gold and oscillating magnetic field could induce eddy effects in heat generation (Soni et al. 2019). The Fe_3O_4 dispersed in water (2 mg/mL) reaches the temperature 42 °C within 5 min. The UCNP@SiO_2@Fe_3O_4 (1 and 2 mg added in 1 mL UCNP@SiO_2) hyperthermia temperature is reached by 30 and 26 min, respectively. Whereas the hybrid UCNP@SiO_2@Au@Fe_3O_4 (1 and 2 mg added in 1 mL UCNP@SiO_2 and 600 µL Au), the hyperthermia temperature was attained within 26 and 20 min. The composite UCNP@SiO_2@Au@Fe_3O_4 reaches hyperthermia

temperature 4 min before that of UCNP@SiO_2@Fe_3O_4 under the same induction heating conditions. The UCNP@SiO_2@Au nanocomposites responded well in heat generation when exposed to near-infrared radiation. Under 980 nm CW NIR laser light excitation (below 600 mW), the elevation of temperature to 41–44 °C is observed for the UCNP@SiO_2@Au which contains 400–600 µL Au nanoparticle suspension when AuNPs and UCNP@SiO_2 reached about ~28–30 °C. At the irradiation time of up to 30 min, even the addition of 100 µL of Au is enough to reach hyperthermia temperature. As the concentration of Au is increased, the irradiation time to achieve hyperthermia temperature is shortened. The hybrid containing 800 µL of AuNPs reaches a hyperthermia treatment temperature of about 43 °C in less than 15 min. The cause of NIR heating is based on the Förster or fluorescence resonance energy transfer (FRET) crowded in the UCNP@SiO_2@Au hybrid.

A summarized pictorial representation of the emission of colors from some typical magnetic–luminescent nanocomposites on irradiation with various wavelengths ranging from ultraviolet to infrared regions is presented in Fig. 20.5. It would also be more interesting to highlight some of the characteristic features of the magnetic–plasmon nanocomposites for hyperthermia purposes. The plasmonic component Ag or Ag incorporation into the Fe_3O_4 provides multimodality for photothermal and magnetic fluid hyperthermia with enhanced performance in a single platform (Das et al. 2016b; Mohammad et al. 2010; Lu et al. 2018). The plasmonic component played a synergistic role in increasing the heat generation through laser irradiation and this could solve the reduction of high magnetic field applied for magnetic fluid hyperthermia. The Ag/Fe_3O_4 core–shell nanoflowers (2 mg/mL dispersed in 2

wt.% agar in water) could not reach 40 °C when the applied field is below 47.75 kAm^{-1} ($f = 310$ Hz), whereas a power density of 0.93 W/cm^2 is required to reach temperatures above 40 °C (Das et al. 2016b). The final temperature increases with increasing magnetic field and power density of the 442 nm laser. The heating rate was increased when the magnetic field was assisted by the constant laser power densities of 0.53 W/cm^2 and 0.93 W/cm^2. The magnetic field required to reach the 40 °C is 47.75 kAm^{-1} in the absence of laser radiation. However, the magnetic field requirement was reduced to about 31.8 kAm^{-1} and 15.9 kAm^{-1} when 442 nm laser power densities of 0.53 W/cm^2 and 0.93 W/cm^2, respectively, were applied simultaneously. Further, the 210 nm Ag/Fe_3O_4 nanoflowers with 70 nm Ag core have better heating efficiency than the 120 nm Ag/Fe_3O_4 nanoflowers with 45 nm Ag core. This clearly suggests that the heating efficiency of Ag/Fe_3O_4 nanoflowers can be tuned by varying the size of Ag core and/or thickness of Fe_3O_4 shell. The Au nanoshell formation over the Fe_3O_4 core enhanced the saturation magnetization from 55 emu/g in Fe_3O_4 (5.4 nm) to 58 emu/g in Fe_3O_4@Au (6.3 nm) as well as the heating rate (Mohammad et al. 2010). Meanwhile, the blocking temperatures of Fe_3O_4 and Fe_3O_4@Au are 19.1 and 44.3 K, respectively. This was claimed to be the first report of enhanced hyperthermia using Fe_3O_4@Au in low-frequency oscillating magnetic fields. In the presence of an AC magnetic field (37 kAm^{-1}, 44 Hz), the Fe_3O_4@Au achieved the therapeutic temperature faster and the heating rate was higher by about 4–5 times compared to Fe_3O_4 based on the pure Fe_3O_4 content after subtracting the weight of the ligand and gold shell. The heating efficiency of the

Fe_3O_4@Au decreased with the increase in applied frequency and increase in concentration in the dispersion. The quenching of heat at higher concentration by Au since it is a good conductor was the probable reason. The Fe_3O_4@Au composite showed excellent biocompatibility with Hc92 and MCF-7 cell lines. For 500 µg/mL, the cell viability was decreased by 18% (Fe_3O_4) and 14% (Fe_3O_4@Au) in Hc92 cell lines; 30% (Fe_3O_4) and 23% (Fe_3O_4@Au) in MCF-7 cell lines. Another study on core–shell Fe_3O_4@Au composed of Fe_3O_4 nanocubes (35–40 nm) and ultrathin Au (2–3 nm) layer showed a slight decrease in magnetization values after core–shell formation (Abdulla-Al-Mamun et al. 2013). The magnetization drops from 65.56 emu/g in Fe_3O_4 to 63.51 emu/g in Fe_3O_4@Au. The observation is opposite to that mentioned above in Ref. (Mohammad et al. 2010). It is also to be noted that Fe_3O_4 in these two independent works have different shapes and sizes as well as thickness of Au coating. In this latter work, the combined application of alternating magnetic field (5 kAm^{-1}, 560 kHz) and photoirradiation (350–800 nm Xe lamp, 30 mW cm^{-2} power) for a length of 5–30 min achieve the best heating and highest efficiency of HeLa cell death compared to sole magnetic field or photoirradiation. When AMF is applied alone, Fe_3O_4 has better heating effect and if the photoirradiation is solely applied, the core–shell Fe_3O_4@Au produced more heat. The Cy3-modified S6-aptamer-conjugated-Fe_3O_4-Au core–shell nanocomposite has the ability of selective photothermal killing of SK-BR-3 human cancer cells which overexpresses the epithermal growth factor receptor HER2/c-erb-2/Neu (HER2) on the cell surface (Fan et al. 2012). This was observed when photoirradiation was performed on SK-BR-3, MDA-MB (HER2-negative human breast cancer cell line), LNCaP

(human prostate cancer cell line which overexpresses prostate-specific membrane antigen, PSMA), HaCaT keratinocytes (normal human skin cell line) with 670 nm at 2.5 W/cm^{-2} for 20 min. Cell viability analysis revealed that more than 80% of the SK-BR-3 cancer cells were killed within 10 min, whereas the survival was about 93% in the MDA-MB and LNCaP cells and 96% in the HaCaT cells. Such a selective destruction can be useful for a specific type of tumor-targeted therapy which can also be combined with hyperthermia. A citable work on combined magnetic–photothermal–chemotherapeutic nanocomposite was the C225 (another name for Cetuximab, an anti-neoplastic targeted therapy) loaded onto core–shell Fe_3O_4@Au denoted as Fe_3O_4@Au-C225 (Lu et al. 2018). Either in an AC magnetic field (30 A, 230 Hz) and NIR (635 nm, 0.3 Wcm^{-2}) exposure alone or combined exposure, the Fe_3O_4@Au-C225 composite showed a rapid rise of temperature at first and then stabilized after a certain time. However, a higher heating rate was observed when the AC magnetic field and NIR were applied simultaneously. The combined exposure increased the antiproliferative effect mediated by Fe_3O_4@Au-C225 MNPs against U251 cells and the cell viability was significantly decreased compared to sole exposure to magnetic field or NIR. This combined treatment also increased therapeutic efficacy for U251 cells by induction of apoptosis. The in vivo studies in mice with tumor model of human glioma demonstrated the superiority of the combined exposure over the sole exposure of the Fe_3O_4@Au-C225 nanocomposite wherein the materials were diffused throughout the tumor and enlarged the zone of necrosis. This particular magnetic–photothermal–chemotherapeutic nanocomposite with combined heating is claimed to be a promising one for future human clinical trials in patients with glioma.

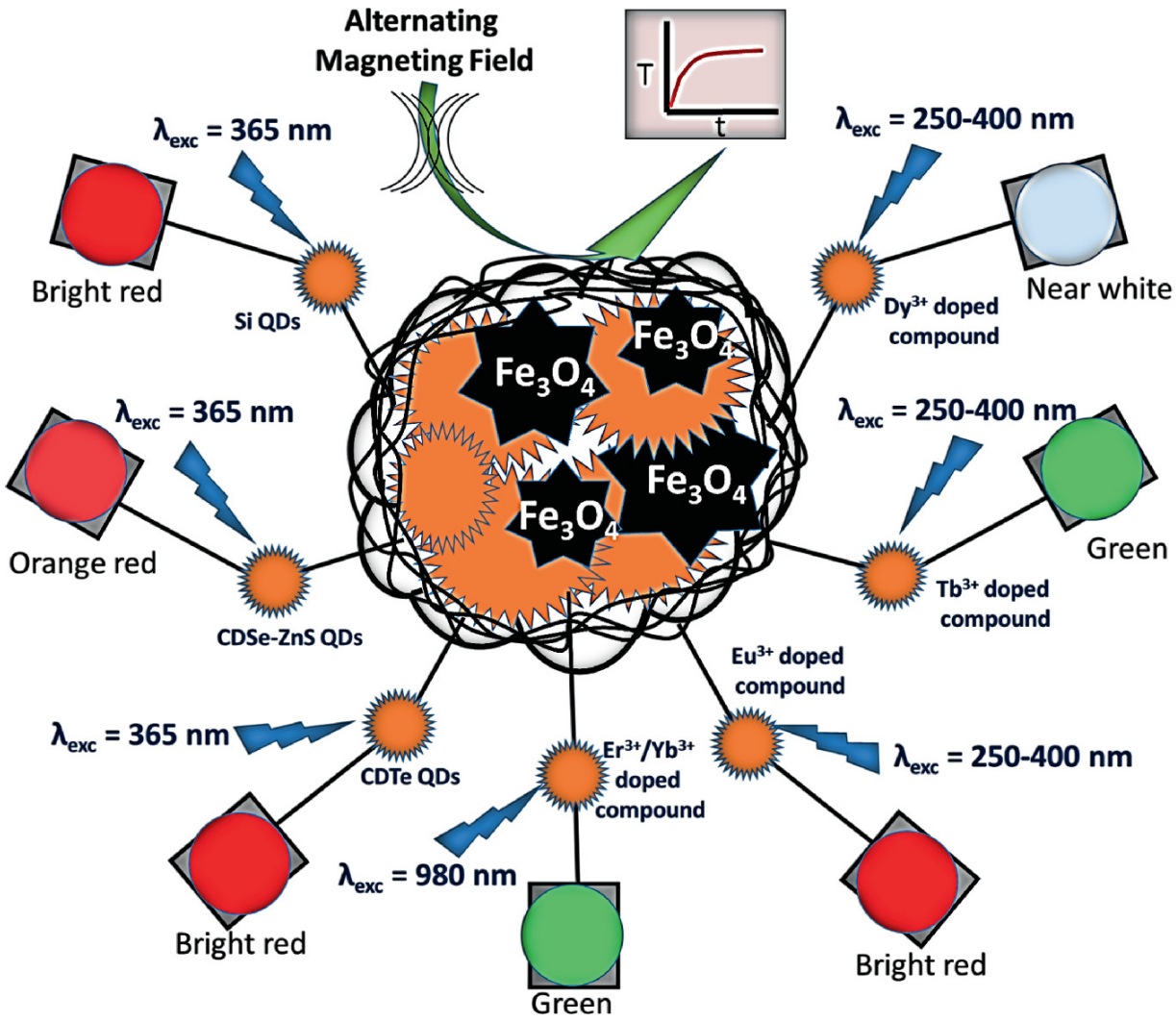

Fig. 20.5 Schematics of color emissions from some typical magnetic–luminescent nanocomposites in combination with heat generation under alternating magnetic field

20.6 Summary and Conclusions

Summarily, this chapter has highlighted a brief background of the evolution of concept of magnetic fluid hyperthermia, envisaged to be an emergent alternative or additional approach to cancer therapy, from the idea of heating tissue to destruction of cancer cells deciphering the concept by biophysical approach and clinical trials. The physical characteristics and biological model studies on magnetic iron oxide have shown the path to its use for cancer

therapy. Later, clinical trials have found out the possible mechanism of administration and the optimistic feasibility of magnetic fluid hyperthermia for full-fledged applications on cancer therapy. The combinatorial approach of thermo-radiotherapy, thermo-chemotherpay, chemo-thermo-immunotherapy, or protein regulation assisted by hyperthermia were presented in brief. Further, the various aspects for heat generation including the mechanisms and factors affecting the heating properties of iron oxide have been discussed. The dependent factors such as shape, size, composition, state of dispersion, and other inherent physical parameters are presented from the available literatures. Also, this chapter highlighted a number of surface-functionalized magnetic nanocomposites for imaging and/or hyperthermia purposes that have been developed in the recent years. The design of magnetic–luminescent composites on integration of iron oxide with quantum dots and inorganic lanthanide-based phosphors as well as some characteristic features of magnetic-plasmon nanocomposites with special emphasis on hyperthermia potentials were covered for information to readers. The works on magnetic iron oxide nanoparticles and magnetic–liminescent nanocomposites are, at present, pursued by many researchers to find a multimodal platform with optimum output in the sense of heat generation, drug loading, imaging, and killing of cancer tissues.

In most of the magnetic–luminescent nanocomposites, the heating originates from the magnetic component and therefore the heating rate and the maximum temperature achieved were lowered as the magnetic content was lowered after incorporation into bimodal nanocomposites. Therefore, the need for enhancing the magnetic characteristics of the particles and response to alternating magnetic field within the threshold limit of applied field and frequency has to be stressed. Otherwise, the combined magnetic and infrared heating from luminescent

counterpart in the magnetic–upconversion nanocomposites was demonstrated to have better effect.

For quite many studies on conventional hyperthermia, computational techniques to monitor three-dimensional heat distribution throughout the tumor tissues have been developed based on SAR-based optimization and temperature-based optimization (Kok et al. 2015; Greef et al. 2010). A detailed review stated that SAR-based optimization can be very useful to improve tumor temperatures but the discrepancies between specific absorption rate (SAR) and temperature predictions due to dielectric and conductive properties of tissues are very significant. This optimization methodology does not take into account the cooling processes inside the tissues such as perfusion, conduction, and bolus cooling during heating of the tumor tissues. The errors posed due to SAR-based optimization were proposed to be solved by temperature-based optimization, a more computationally efficient and least expensive methodology to monitor thermal dosage distribution during hyperthermia treatment. Consequently, the potentials of magnetic iron oxide nanoparticles for intracellular heat generation had to be designed to enhance heat generation which could compensate for the simultaneous heat loss during the heating process.

Studies on dose-dependent cellular response, heat dosage distribution inside the tumor, biodistribution of nanocomposites, potential toxicity, activity, and specificity of drug-loaded or polymer-modified nanocomposites in different tumors would present a deeper insight and broader spectrum to the application of nanocomposites for various type of tumors. Moreover, there is a need to realize the quantity of nanocomposite-based drugs accumulated at the tumor site and the surrounding during the experimental or treatment period. This will help in finding solution precautious to any undesired or unimagined side effects which may arise later. The development is at an early

stage, the progress is overwhelmingly significant and the efforts of the researchers to revolutionize the nanobiomedicine sector are very much needed. Many in vitro and in vivo studies have presented us the possibility of combined targeting, imaging, and therapeutic applications. It is highly confident that the magnetic iron-oxide-based luminescent nanocomposites for diagnosis and therapy will be boosting the convergence of biotechnology and medicine through the nanotechnological approaches in the near future.

Acknowledgements

G. S Ningombam is grateful to the Council of Scientific and Industrial Research (CSIR), New Delhi, for the award of CSIR-Research Associate [09/476(0091)/2019-EMR-I].

References

Abdulla-Al-Mamun, M., Kusumoto, Y., Zannat, T., Horie, Y., Manaka, H.: RSC Adv. **3**(21), 7816–7827 (2013)

Aslibeiki, B., Kameli, P., Salamati, H., Concas, G., Salvador, F.M., Talone, A., Muscas, G., Peddis, D.: Beilstein J. Nanotechnol. **10**, 856–865 (2019) [PubMed][PubMedCentral]

Balivada, S., Rachakatla, R.S., Wang, H., Samarakoon, T.N., Dani, R.K., Pyle, M., Kroh, F.O., Walker, B., Leaym, X., Koper, O.B., Tamura, M., Chikan, V., Bossmann, S.H., Troyer, D.L.: BMC Cancer **10**(1), 119 (2010) [PubMed][PubMedCentral]

Bauer, L.M., Situ, S.F., Griswold, M.A., Samia, A.C.S.: Nanoscale **8**(24), 12162–12169 (2016) [PubMed]

Behdadfar, B., Kermanpur, A., Sadeghi-Aliabadi, H., Morales, M.P., Mozaffari, M.: J. Magn. Magn. Mater. **324**(14), 2211–2217 (2012)

Cabrera, M.P., Filho, P.E.C., Silva, C.M.C.M., Oliveira, R.M., Geraldes, C.F.G.C., Castro, M.M.C.A., Costa, B.F.O., Henriques, M.S.C., Paixão, J.A., Carvalho, L.B., Santos, B.S., Hallwass, F., Fontes, A., Pereira, G.A.L.: Nanotechnology **28**(28), 285704 (2017) [PubMed]

Carrey, J., Mehdaoui, B., Respaud, M.: J. Appl. Phys. **109**(8), 083921 (2011)

Carta, D., Casula, M.F., Falqui, A., Loche, D., Mountjoy, G., Sangregorio, C., Corrias, A.: J. Phys. Chem. C **113**(20), 8606–8615 (2009)

Chan, D.C.F., Kirpotin, B.D., Bunn, P.A.: J. Magn. Magn. Mater. **122**(1), 374–378 (1993)

Chou, C.K.: Int. J. Hyper. **6**(2), 367–370 (1990)

Colombo, M., Carregal-Romero, S., Casula, M.F., Gutiérrez, L., Morales, M.P., Böhm, I.B., Heverhagen, J.T., Prosperi, D., Parak, W.J.: Chem. Soc. Rev. **41**(11), 4306–4334 (2012)
[PubMed]

Corr, S.A., Rakovich, Y.P., Gun'ko, Y.K.: Nanoscale Res. Lett. **3**(3), 87–104 (2008)

Cullity, B.D., Graham, C.D.: Introduction to Magnetic Materials, 2nd edn. Wiley, USA (2009)

Das, R., Alonso, J., Nemati, P.Z., Kalappattil, V., Torres, D., Phan, M.H., Garaio, E., García, J.Á., Sanchez, L.J.L., Srikanth, H.: J. Phys. Chem. C **120**(18), 10086–10093 (2016a)

Das, R., Rinaldi-Montes, N., Alonso, J., Amghouz, Z., Garaio, E., García, J.A., Gorria, P., Blanco, J.A., Phan, M.H., Srikanth, H.: ACS Appl. Mater. Interfaces **8**(38), 25162–25169 (2016b)
[PubMed]

de Greef, M., Kok, H.P., Correia, D., Bel, A., Crezee, J.: Med. Phys. **37**(9), 4540–4550 (2010)
[PubMed]

de la Presa, P., Luengo, Y., Multigner, M., Costo, R., Morales, M.P., Rivero, G., Hernando, A.: J. Phys. Chem. C **116**(48), 25602–25610 (2012)

Demortière, A., Panissod, P., Pichon, B.P., Pourroy, G., Guillon, D., Donnio, B., Bégin-Colin, S.: Nanoscale **3**(1), 225–232 (2011)
[PubMed]

Dunne, M., Epp-Ducharme, B., Sofias, A.M., Regenold, M., Dubins, D.N., Allen, C.: J. Control. Release **308**, 197–208 (2019)
[PubMed]

Engin, K., Leeper, D.B., Cater, J.R., Thistlethwaite, A.J., Tupchong, L., McFarlane, J.D.: Int. J. Hyper. **11**(2), 211–216 (1995)

Erogbogbo, F., Yong, K.T., Hu, R., Law, W.C., Ding, H., Chang, C.W., Prasad, P.N., Swihart, M.T.: ACS Nano **4**(9), 5131–5138 (2010)
[PubMed]

Erogbogbo, F., Yong, K.T., Roy, I., Hu, R., Law, W.C., Zhao, W., Ding, H., Wu, F., Kumar, R., Swihart, M.T., Prasad, P.N.: ACS Nano **5**(1), 413–423 (2011)
[PubMed]

Fairbairn, J.J., Khan, M.W., Ward, K.J., Loveridge, B.W., Fairbairn, D.W., O'Neill, K.L.: Cancer Lett. **89**(2), 183–188 (1995)
[PubMed]

Fan, Z., Shelton, M., Singh, A.K., Senapati, D., Khan, S.A., Ray, P.C.: ACS Nano **6**(2), 1065–1073 (2012)
[PubMed][PubMedCentral]

Fortin, J.P., Wilhelm, C., Servais, J., Ménager, C., Bacri, J.C., Gazeau, F.: J. Am. Chem. Soc. **129**(9), 2628–2635 (2007)
[PubMed]

Fu, S., Ding, Y., Cong, T., Yang, X., Hong, X., Yu, B., Li, Y., Liu, Y.: Dalton Trans. **48**(34), 12850–12857 (2019)
[PubMed]

Fujioka, K., Hiruoka, M., Sato, K., Manabe, N., Miyasaka, R., Hanada, S., Hoshino, A., Tilley, R.D., Manome, Y., Hirakuri, K., Yamamoto, K.: Nanotechnology **19**(41), 415102 (2008)
[PubMed]

Gazeau, F., Bacri, J.C., Gendron, F., Perzynski, R., Raikher, Y.L., Stepanov, V.I., Dubois, E.: J. Magn. Magn. Mater. **186**(1), 175–187 (1998)

Gilchrist, R.K., Medal, R., Shorey, W.D., Hanselman, R.C., Parrott, J.C., Taylor, C.B.: Ann. Surg. **146**(4), 596–606 (1957)
[PubMed][PubMedCentral]

Giri, A.K., Chowdary, K.M., Humfeld, K., Majetich, S.A.: AC magnetic properties of compacted FeCo nanocomposites. In: IEEE International Magnetics Conference (INTERMAG), pp. 241–241 (2000)

Global Cancer Facts & Figures, American Cancer Society, https://www.cancer.org/research/cancer-facts-statistics/global.html. Accessed 23 May 2022

Glöckl, G., Hergt, R., Zeisberger, M., Dutz, S., Nagel, S., Weitschies, W.: J. Condens. Matter Phys. **18**(38), S2935–S2949 (2006)

Goldstein, L.S., Dewhirst, M.W., Repacholi, M., Kheifets, L.: Int. J. Hyper. **19**(3), 373–384 (2003)

Gordon, R.T., Hines, J.R., Gordon, D.: Med. Hypotheses **5**(1), 83–102 (1979)
[PubMed]

Goya, G.F., Berquó, T.S., Fonseca, F.C., Morales, M.P.: J. Appl. Phys. **94**(5), 3520–3528 (2003)

Guardia, P., Di Corato, R., Lartigue, L., Wilhelm, C., Espinosa, A., Garcia-Hernandez, M., Gazeau, F., Manna, L., Pellegrino, T.: ACS Nano **6**(4), 3080–3091 (2012)
[PubMed]

Hanson, M.: J. Magn. Magn. Mater. **96**(1), 105–113 (1991)

Hergt, R., Dutz, S., Müller, R., Zeisberger, M.: J. Condens. Matter Phys. **18**(38), S2919–S2934 (2006)

Hergt, R., Dutz, S., Röder, M.: J. Condens. Matter Phys. **20**(38), 385214 (2008)

Hergt, R., Dutz, S.: Magnetic particle hyperthermia—biophysical limitations of a visionary tumour therapy. In: Proceedings of the Sixth International Conference on the Scientific and Clinical Applications of Magnetic Carriers, vol. 311(1), pp. 187–192 (2007)

Hernando, A., Vázquez, M., Kulik, T., Prados, C.: Phys. Rev. B **51**(6), 3581–3586 (1995)

Hilger, I., Hiergeist, R., Hergt, R., Winnefeld, K., Schubert, H., Kaiser, W.A.: Invest. Radiol. **37**(10), 580–586 (2002)
[PubMed]

Hugounenq, P., Levy, M., Alloyeau, D., Lartigue, L., Dubois, E., Cabuil, V., Ricolleau, C., Roux, S., Wilhelm, C., Gazeau, F., Bazzi, R.: J. Phys. Chem. C **116**(29), 15702–15712 (2012)

Hyeon, T., Chung, Y., Park, J., Lee, S.S., Kim, Y.W., Park, B.H.: J. Phys. Chem. B **106**(27), 6831–6833 (2002)

Ito, A., Shinkai, M., Honda, H., Yoshikawa, K., Saga, S., Wakabayashi, T., Yoshida, J., Kobayashi, T.: Cancer Immunol. Immunother. **52**(2), 80–88 (2003a)
[PubMed][PubMedCentral]

Ito, A., Tanaka, K., Kondo, K., Shinkai, M., Honda, H., Matsumoto, K., Saida, T., Kobayashi, T.: Cancer Sci. **94**(3), 308–313 (2003b)
[PubMed][PubMedCentral]

Ito, A., Fujioka, M., Yoshida, T., Wakamatsu, K., Ito, S., Yamashita, T., Jimbow, K., Honda, H.: Cancer Sci. **98**(3), 424–430 (2007)
[PubMed][PubMedCentral]

Ito, A., Saito, H., Mitobe, K., Minamiya, Y., Takahashi, N., Maruyama, K., Motoyama, S., Katayose, Y., Ogawa, J.: Cancer Sci. **100**(3), 558–564 (2009) [PubMed][PubMedCentral]

Jadhav, S.V., Shewale, P.S., Shin, B.C., Patil, M.P., Kim, G.D., Rokade, A.A., Park, S.S., Bohara, R.A., Yu, Y.S.: J. Colloid Interface Sci. **541**, 192–203 (2019) [PubMed]

Jeun, M., Bae, S., Tomitaka, A., Takemura, Y., Park, K.H., Paek, S.H., Chung, K.-W.: Appl. Phys. Lett. **95**(8), 082501 (2009)

Johannsen, M., Jordan, A., Scholz, R., Koch, M., Lein, M., Deger, S., Roigas, J., Jung, K., Loening, S.: J. Endourol. **18**(5), 495–500 (2004) [PubMed]

Johannsen, M., Gneveckow, U., Eckelt, L., Feussner, A., Waldöfner, N., Scholz, R., Deger, S., Wust, P., Loening, S.A., Jordan, A.: Int. J. Hyper. **21**(7), 637–647 (2005b)

Johannsen, M., Thiesen, B., Gneveckow, U., Taymoorian, K., Waldöfner, N., Scholz, R., Deger, S., Jung, K., Loening, S.A., Jordan, A.: Prostate **66**(1), 97–104 (2006) [PubMed]

Johannsen, M., Gneveckow, U., Taymoorian, K., Thiesen, B., Waldöfner, N., Scholz, R., Jung, K., Jordan, A., Wust, P., Loening, S.A.: Int. J. Hyper. **23**(3), 315–323 (2007a)

Johannsen, M., Gneveckow, U., Thiesen, B., Taymoorian, K., Cho, C.H., Waldöfner, N., Scholz, R., Jordan, A., Loening, S.A., Wust, P.: Eur. Urol. **52**(6), 1653–1662 (2007b) [PubMed]

Johannsen, M., Thiesen, B., Wust, P., Jordan, A.: Int. J. Hyper. **26**(8), 790–795 (2010)

Johannsen, M., Thiesen, B., Jordan, A., Taymoorian, K., Gneveckow, U., Waldöfner, N., Scholz, R., Koch, M., Lein, M., Jung, K., Loening, S.A.: Prostate **64**(3), 283–292 (2005)

Johansson, C., Hanson, M., Hendriksen, P.V., Mørup, S.: J. Magn. Magn. Mater. **122**(1), 125–128 (1993)

Jordan, A., Wust, P., Fähling, H., John, W., Hinz, A., Felix, R.: Int. J. Hyper. **9**(1), 51–68 (1993)

Jordan, A., Wust, P., Scholz, R., Tesche, B., Fähling, H., Mitrovics, T., Vogl, T., Cervós-navarro, J., Felix, R.: Int. J. Hyper. **12**(6), 705–722 (1996)

Jordan, A., Scholz, R., Wust, P., Schirra, H., Thomas, S., Schmidt, H., Felix, R.: J. Magn. Magn. Mater. **194**(1), 185–196 (1999)

Jordan, A., Scholz, R., Maier-Hauff, K., van Landeghem, F.K.H., Waldoefner, N., Teichgraeber, U., Pinkernelle, J., Bruhn, H., Neumann, F., Thiesen, B., von Deimling, A., Felix, R.: J. Neuro-Oncol. **78**(1), 7–14 (2006)

Jordan, A., Scholz, R., Wust, P., Fähling, H., Krause, J., Wlodarczyk, W., Sander, B., Vogl, T., Felix, R.: Int. J. Hyper. **13**(6), 587–605 (1997)

Jordan, A., Scholz, R., Maier-Hauff, K., Johannsen, M., Wust, P., Nadobny, J.., Schirra, H., Schmidt, H., Deger, S., Loening, S., Lanksch, W., Felix, R.: Presentation of a new magnetic field therapy system for the treatment of human solid tumors with magnetic fluid hyperthermia. In: Proceedings of the Third International Conference on Scientific and Clinical Applications of Magnetic Carriers, vol. 225(1), pp. 118–126 (2001)

Jun, Y., Huh, Y.M., Choi, J., Lee, J.H., Song, H.T., Kim, S., Yoon, S., Kim, K.S., Shin, J.S., Suh, J.S., Cheon, J.: J. Am. Chem. Soc. **127**(16), 5732–5733 (2005) [PubMed]

Kang, E., Park, J., Hwang, Y., Kang, M., Park, J.G., Hyeon, T.: J. Phys. Chem. B **108**(37), 13932–13935 (2004)

Kawai, N., Ito, A., Nakahara, Y., Futakuchi, M., Shirai, T., Honda, H., Kobayashi, T., Kohri, K.: Prostate **64**(4), 373–381 (2005) [PubMed]

Kawai, N., Ito, A., Nakahara, Y., Honda, H., Kobayashi, T., Futakuchi, M., Shirai, T., Tozawa, K., Kohri, K.: Prostate **66**(7), 718–727 (2006) [PubMed]

Kittel, C.: Introduction to Solid State Physics, 8th edn. Wiley, USA (2005)

Kok, H., Wust, P., Stauffer, P., Bardati, F., van Rhoon, G., Crezee, J.: Radiat. Oncol. **10**(1), 196 (2015) [PubMed][PubMedCentral]

Kumar, S., Singh, V., Aggarwal, S., Mandal, U.K., Kotnala, R.K.: J. Magn. Magn. Mater. **324**(22), 3683–3689 (2012)

Kwon, S.G., Hyeon, T.: Small **7**(19), 2685–2702 (2011) [PubMed]

Lartigue, L., Innocenti, C., Kalaivani, T., Awwad, A., Sanchez, D.M., Guari, Y., Larionova, J., Guérin, C., Montero, J.L.G., Barragan-Montero, V., Arosio, P., Lascialfari, A., Gatteschi, D., Sangregorio, C.: J. Am. Chem. Soc. **133**(27), 10459–10472 (2011)

Lee, J.H., Huh, Y.M., Jun, Y., Seo, J., Jang, J., Song, H.T., Kim, S., Cho, E.J., Yoon, H.G., Suh, J.S., Cheon, J.: Nat. Med. **13**(1), 95–99 (2007)
[PubMed]

Leslie-Pelecky, D.L., Rieke, R.D.: Chem. Mater. **8**(8), 1770–1783 (1996)

Li, Q., Kartikowati, C.W., Horie, S., Ogi, T., Iwaki, T., Okuyama, K.: Sci. Rep. **7**(1), 9894 (2017)
[PubMed][PubMedCentral]

Lima, E., De Biasi, E., Mansilla, M.V., Saleta, M.E., Granada, M., Troiani, H.E., Effenberger, F.B., Rossi, L.M., Rechenberg, H.R., Zysler, R.D.: J. Phys. D Appl. Phys. **46**(4), 045002 (2012)

Ling, D., Hyeon, T.: Small **9**(9–10), 1450–1466 (2013)
[PubMed]

Liu, C., Zou, B., Rondinone, A.J., Zhang, Z.J.: J. Am. Chem. Soc. **122**(26), 6263–6267 (2000)

Lu, Q., Dai, X., Zhang, P., Tan, X., Zhong, Y., Yao, C., Song, M., Song, G., Zhang, Z., Peng, G., Guo, Z., Ge, Y., Zhang, K., Li, Y.: Int. J. Nanomed. **13**, 2491–2505 (2018)

Luderer, A.A., Borrelli, N.F., Panzarino, J.N., Mansfield, G.R., Hess, D.M., Brown, J.L., Barnett, E.H., Hahn, E.W.: Radiat. Res. **94**(1), 190–198 (1983)
[PubMed]

Luwang, M.N., Chandra, S., Bahadur, D., Srivastava, S.K.: J. Mater. Chem. **22**(8), 3395–3403 (2012)

Lv, Y., Yang, Y., Fang, J., Zhang, H., Peng, E., Liu, X., Xiao, W., Ding, J.: RSC Adv. **5**(94), 76764–76771 (2015)

Ma, Z.Y., Dosev, D., Nichkova, M., Gee, S.J., Hammock, B.D., Kennedy, I.M.: J. Mater. Chem. **19**(27), 4695–4700 (2009)
[PubMed][PubMedCentral]

Maier-Hauff, K., Rothe, R., Scholz, R., Gneveckow, U., Wust, P., Thiesen, B., Feussner, A., von Deimling, A., Waldoefner, N., Felix, R., Jordan, A.: J. Neuro-Oncol. **81**(1), 53–60 (2007)

Maier-Hauff, K., Ulrich, F., Nestler, D., Niehoff, H., Wust, P., Thiesen, B., Orawa, H., Budach, V., Jordan, A.: J. Neuro-Oncol. **103**(2), 317–324 (2011)

Martinez-Boubeta, C., Simeonidis, K., Makridis, A., Angelakeris, M., Iglesias, O., Guardia, P., Cabot, A., Yedra, L., Estradé, S., Peiró, F., Saghi, Z., Midgley, P.A., Conde-Leborán, I., Serantes, D., Baldomir, D.: Sci. Rep. **3**(1), 1652 (2013)

[PubMed][PubMedCentral]

Medal, R., Shorey, W., Gilchrist, R.K., Barker, W., Hanselman, R.: AMA Arch. Surg. **79**(3), 427–431 (1959)

Mikhaylova, M., Kim, D.K., Bobrysheva, N., Osmolowsky, M., Semenov, V., Tsakalakos, T., Muhammed, M.: Langmuir **20**(6), 2472–2477 (2004)
[PubMed]

Mohammad, F., Balaji, G., Weber, A., Uppu, R.M., Kumar, C.S.S.R.: J. Phys. Chem. C **114**(45), 19194–19201 (2010)

Morales, M.P., Veintemillas-Verdaguer, S., Montero, M.I., Serna, C.J., Roig, A., Casas, L., Martínez, B., Sandiumenge, F.: Chem. Mater. **11**(11), 3058–3064 (1999)

Moumen, N., Bonville, P., Pileni, M.P.: J. Phys. Chem. **100**(34), 14410–14416 (1996)

Nemati, Z., Alonso, J., Martinez, L.M., Khurshid, H., Garaio, E., Garcia, J.A., Phan, M.H., Srikanth, H.: J. Phys. Chem. C **120**(15), 8370–8379 (2016)

Nichkova, M., Dosev, D., Gee, S.J., Hammock, B.D., Kennedy, I.M.: Anal. Chem. **77**(21), 6864–6873 (2005)
[PubMed]

Ningombam, G.S., Ningthoujam, R.S., Kalkura, S.N., Singh, N.R.: J. Phys. Chem. B **122**(27), 6862–6871 (2018)
[PubMed]

Ningombam, G.S., Chattopadhyay, D., Sarkar, K., Kalkura, S.N., Singh, N.R.: Colloids Surf A Physicochem Eng Asp **625**, 126826 (2021)

Ningombam, G.S., Srinivasan, B., Chidananda, A.H., Kalkura, S.N., Sharma, Y., Singh, N.R.: Dalton Trans. **51**(21), 8510–8524 (2022)
[PubMed]

Obaidat, I.M., Narayanaswamy, V., Alaabed, S., Sambasivam, S., Muralee Gopi, C.V.V.: Magnetochemistry **5**(4), 67 (2019). (1–40)

Ortega, D., Pankhurst, Q.A.: Magnetic hyperthermia. In: O'Brien, P. (ed.) Nanoscience: Volume 1: Nanostructures Through Chemistry, pp. 60–88. The Royal Society of Chemistry, Cambridge, UK (2013)

Parchur, A.K., Ansari, A.A., Singh, B.P., Hasan, T.N., Syed, N.A., Rai, S.B., Ningthoujam, R.S.: Integr. Biol. **6**(1), 53–64 (2014)

Parekh, K., Almásy, L., Lee, H.S., Upadhyay, R.V.: Appl. Phys. A **106**(1), 223–228 (2012)

Prasad, N.K., Rathinasamy, K., Panda, D., Bahadur, D.: J. Mater. Chem. **17**(48), 5042–5051 (2007)

Prasad, A.I., Parchur, A.K., Juluri, R.R., Jadhav, N., Pandey, B.N., Ningthoujam, R.S., Vatsa, R.K.: Dalton Trans. **42**(14), 4885–4896 (2013)
[PubMed]

Rand, R.W., Snow, H.D., Brown, W.J.: J. Surg. Res. **33**(3), 177–183 (1982)
[PubMed]

Reinhold, H.S., Endrich, B.: Int. J. Hyper. **2**(2), 111–137 (1986)

Rosensweig, R.E.: Heating magnetic fluid with alternating magnetic field. In: Proceedings of the 9th International Conference on Magnetic Fluids, vol. 252, pp. 370–374 (2002)

Salas, G., Camarero, J., Cabrera, D., Takacs, H., Varela, M., Ludwig, R., Dähring, H., Hilger, I., Miranda, R., Morales, M.P., Teran, F.J.: J. Phys. Chem. C **118**(34), 19985–19994 (2014)

Sato, A., Tamura, Y., Sato, N., Yamashita, T., Takada, T., Sato, M., Osai, Y., Okura, M., Ono, I., Ito, A., Honda, H., Wakamatsu, K., Ito, S., Jimbow, K.: Cancer Sci. **101**(9), 1939–1946 (2010)
[PubMed][PubMedCentral]

Serrano, G.R., Stafford, S., Gun'ko, Y.K.: Appl. Sci. **8**(2), 172 (2018)

Shanta, S.N., Kulkarni, H., Pradhan, L., Bahadur, D.: Nanotechnology **24**(6), 065101 (2013)

Shliomis, M.I., Pshenichnikov, A.F., Morozov, K.I., Shurubor, I.Y.: J. Magn. Magn. Mater. **85**(1), 40–46 (1990)

Shrivastava, N., Rocha, U., Muraca, D., Jacinto, C., Moreno, S., Vargas, J.M., Sharma, S.K.: AIP Adv. **8**(5), 056710 (2018)

Singh, L.P., Srivastava, S.K., Mishra, R., Ningthoujam, R.S.: J. Phys. Chem. C **118**(31), 18087–18096 (2014)

Singh, L.P., Singh, N.P., Srivastava, S.K.: Dalton Trans. **44**(14), 6457–6465 (2015a)
[PubMed]

Singh, L.P., Jadhav, N.V., Sharma, S., Pandey, B.N., Srivastava, S.K., Ningthoujam, R.S.: J. Mater. Chem. C **3**(9), 1965–1975 (2015b)

Sjögren, C.E., Johansson, C., Nævestad, A., Sontum, P.C., Briley-Sæbø, K., Fahlvik, A.K.: Magn. Res. Imaging **15**(1), 55–67 (1997)

Song, Q., Zhang, Z.J.: J. Phys. Chem. B **110**(23), 11205–11209 (2006)
[PubMed]

Song, C.W., Park, H.J., Lee, C.K., Griffin, R.: Int. J. Hyper. **21**(8), 761–767 (2005)

Soni, A.K., Joshi, R., Singh, B.P., Kumar, N.N., Ningthoujam, R.S.: ACS Appl. Nano Mater. **2**(11), 7350–7361 (2019)

Stoner, E.C., Wohlfarth, E.P.: IEEE Trans. Magn. **27**(4), 3475–3518 (1991)

Sun, S., Zeng, H., Robinson, D.B., Raoux, S., Rice, P.M., Wang, S.X., Li, G.: J. Am. Chem. Soc. **126**(1), 273–279 (2004)
[PubMed]

Sung, H., Ferlay, J., Siegel, R.L., Laversanne, M., Soerjomataram, I., Jemal, A., Bray, F.: CA: A Cancer J. Clin. **71**(3), 209–249 (2021)

Suto, M., Hirota, Y., Mamiya, H., Fujita, A., Kasuya, R., Tohji, K., Jeyadevan, B.: Heat dissipation mechanism of magnetite nanoparticles in magnetic fluid hyperthermia. In: Proceedings of the Seventh International Conference on the Scientific and Clinical Applications of Magnetic Carriers, vol. 321(10), pp. 1493–1496 (2009)

Takada, T., Yamashita, T., Sato, M., Sato, A., Ono, I., Tamura, Y., Sato, N., Miyamoto, A., Ito, A., Honda, H., Wakamatsu, K., Ito, S., Jimbow, K.: J. Biotechnol. Biomed. **2009**(1–13), 457936 (2009)

Tanaka, K., Ito, A., Kobayashi, T., Kawamura, T., Shimada, S., Matsumoto, K., Saida, T., Honda, H.: Int. J. Cancer **116**(4), 624–633 (2005)
[PubMed]

Tsoi, K.M., Dai, Q., Alman, B.A., Chan, W.C.W.: Acc. Chem. Res. **46**(3), 662–671 (2013)
[PubMed]

Umut, E., Pineider, F., Arosio, P., Sangregorio, C., Corti, M., Tabak, F., Lascialfari, A., Ghigna, P.: J. Magn. Magn. Mater. **324**(15), 2373–2379 (2012)

Vallejo-Fernandez, G., Whear, O., Roca, A.G., Hussain, S., Timmis, J., Patel, V., O'Grady, K.: J. Phys. D Appl. Phys. **46**(31), 312001 (2013)

van der Zee, J.: Ann. Oncol. **13**(8), 1173–1184 (2002)
[PubMed]

van Landeghem, F.K.H., Maier-Hauff, K., Jordan, A., Hoffmann, K.T., Gneveckow, U., Scholz, R., Thiesen, B., Brück, W., von Deimling, A.: Biomaterials **30**(1), 52–57 (2009)

[PubMed]

Varanda, L.C., Jafelicci, M., Tartaj, P., O'Grady, K., González-Carreño, T., Morales, M.P., Muñoz, T., Serna, C.J.: J. Appl. Phys. **92**(4), 2079–2085 (2002)

Wang, F., Tan, W.B., Zhang, Y., Fan, X., Wang, M.: Nanotechnology **17**(1), R1–R13 (2005)

Wang, W., Zou, M., Chen, K.: Chem. Comm. **46**(28), 5100–5102 (2010)
[PubMed]

Wildeboer, R.R., Southern, P., Pankhurst, Q.A.: J. Phys. D Appl. Phys. **47**(49), 495003 (2014)

Wust, P., Hildebrandt, B., Sreenivasa, G., Rau, B., Gellermann, J., Riess, H., Felix, R., Schlag, P.: Lancet Oncol. **3**(8), 487–497 (2002)
[PubMed]

Xia, A., Gao, Y., Zhou, J., Li, C., Yang, T., Wu, D., Wu, L., Li, F.: Biomaterials **32**(29), 7200–7208 (2011)
[PubMed]

Xia, B., Li, J., Shi, J., Zhang, Y., Zhang, Q., Chen, Z., Wang, B.: ACS Biomater. Sci. Eng. **3**(10), 2579–2587 (2017)
[PubMed]

Xu, Y., Karmakar, A., Wang, D., Mahmood, M.W., Watanabe, F., Zhang, Y., Fejleh, A., Fejleh, P., Li, Z., Kannarpady, G., Ali, S., Biris, A.R., Biris, A.S.: J. Phys. Chem. C **114**(11), 5020–5026 (2010)

Yanase, M., Shinkai, M., Honda, H., Wakabayashi, T., Yoshida, J., Kobayashi, T.: Jap. J. Cancer Res. **89**(7), 775–782 (1998)

Yavuz, C.T., Mayo, J.T., Yu, W.W., Prakash, A., Falkner, J.C., Yean, S., Cong, L., Shipley, H.J., Kan, A., ToMson, M., Natelson, D., Colvin, V.L.: Science **314**(5801), 964–967 (2006)

Zhang, Y., Pan, S., Teng, X., Luo, Y., Li, G.: J. Phys. Chem. C **112**(26), 9623–9626 (2008)

Zhang, Y., Das, G.K., Xu, R., Yang, T.T.T.: Tb-doped iron oxide: bifunctional fluorescent and magnetic nanocrystals. J. Mater. Chem. **19**(22), 3696–3703 (2009)

Zhang, L., Wang, Y.S., Yang, Y., Zhang, F., Dong, W.F., Zhou, S.Y., Pei, W.H., Chen, H.D., Sun, H.B.: Chem. Comm. **48**(91), 11238–11240 (2012)
[PubMed]

Zhao, B., Nan, Z.: J. Mater. Chem. **22**(14), 6581–6586 (2012)

Zhao, S., Yu, X., Qian, Y., Chen, W., Shen, J.: Multifunctional magnetic iron oxide nanoparticles: an advanced platform for cancer theranostics. Theranostics **10**(14), 6278–6309 (2020)
[PubMed][PubMedCentral]

Zhou, J., Sun, Y., Du, X., Xiong, L., Hu, H., Li, F.: Biomaterials **31**(12), 3287–3295 (2010)
[PubMed]